UC Berkeley
UC Berkeley Electronic Theses and Dissertations

Title

Biologically Driven Design of Molecular and Molecular-Materials Platforms for Electrochemical Carbon Dioxide Reduction

Permalink

https://escholarship.org/uc/item/3hh142fs

Author

Derrick, Jeffrey S

Publication Date

2022

Peer reviewed|Thesis/dissertation

eScholarship.org Powered by the California Digital Library
University of California

Biologically Driven Design of Molecular and Molecular-Materials Platforms for Electrochemical Carbon Dioxide Reduction

By

Jeffrey S. Derrick

A dissertation submitted in partial satisfaction of the

requirements for the degree of

Doctor of Philosophy

in

Chemistry

in the

Graduate Division

of the

University of California, Berkeley

Committee in charge:

Professor Christopher J. Chang, Chair
Professor Jeffrey R. Long
Professor Jeffrey A. Reimer

Spring 2022
Biologically Driven Design of Molecular and Molecular-Materials Platforms
for Electrochemical Carbon Dioxide reduction

© 2022

by Jeffrey S. Derrick

Abstract

Biologically Driven Design of Molecular and Molecular-Materials Platforms for Electrochemical Carbon Dioxide Reduction

by

Jeffrey S. Derrick

Doctor of Philosophy in Chemistry

University of California, Berkeley

Professor Christopher J. Chang, Chair

Chapter 1. An overview of the field of electrochemical carbon dioxide reduction with homogenous, molecular catalyst. Discussion in this chapter is focused on the motivation, challenges, and strategies to convert carbon dioxide into value-added chemicals and ends with a brief primer on electrochemistry.

Chapter 2. Inspired by the role of redox reservoirs in nature, we explore the application of the chelate effect to adhere molecular catalysts onto the surface of a palladium cathode to give a new molecular-material hybrid catalyst platform. These palladium functionalized electrodes show marked improvements in catalyst stability and selectivity for the electrochemical reduction of carbon dioxide into C1 products compared to both bare, unfunctionalized palladium electrodes and palladium surfaces modified with monodentate carbenes.

Chapter 3. Biological systems utilize precisely positioned hydrogen bonding networks to direct redox reactions with high selectivity and efficiency. Inspired by this, we report the design, synthesis, and characterization of a series of iron porphyrin complexes that are equipped with amide pendants at various positions along the periphery of the metal core. We show through electrochemical analysis that proper positioning of these hydrogen bond donors greatly affects the electrocatalytic activity for carbon dioxide reduction and that these second coordination spheres can be utilized to break the electronic scaling relationships that often limit catalyst performance by entangling the overpotential with the turnover frequency.

Chapter 4. The application of appropriately positioned hydrogen bonding networks into the second coordination sphere of molecular porphyrin catalysts is further explored. Here, we exchange the single-point hydrogen bond donor amides for two-point urea-appended porphyrin analogs. We report the design, synthesis, and characterization of iron porphyrin complexes that incorporate a bis-aryl urea moiety at *ortho* or *para* positions of the *meso* aryl ring of tetraphenylporphyrin. We show that these urea-complexes can template bicarbonate into the second coordination sphere resulting in a large enhancement in electrochemical carbon dioxide reduction catalysis. This work illustrates the importance of understanding bicarbonate speciation

in organic electrolytes and demonstrates how these equilibria can be exploited to enhance the performance of homogeneous catalysts.

Chapter 5. Biological systems often exhibit a high degree of electronic delocalization that serves to minimize energy input and maximize selectivity for desired chemical transformations. Here we report the design, synthesis, and characterization of a molecular iron catalyst that captures this design concept through the use of a redox non-innocent terpyridine-based polypyridine ligand. Due to strong metal–ligand exchange coupling between an intermediate-spin Fe(II) center an a doubly reduced ligand, this iron complex displays redox behavior at extremely mild potentials. This electronic interaction enables electrochemical reduction of CO_2 to CO at low overpotentials with high selectivity and fast turnover frequencies in organic and aqueous electrolytes. This work provides a starting point for the design of systems that exploit metal–ligand cooperativity for electrocatalysis where the electrochemical potential of redox non-innocent ligands can be tuned through secondary metal-dependent interactions.

Chapter 6. The origins of the exceptional catalytic performance of the iron polypyridyl complex developed in the previous chapter are explored here though the use of a combined computational and experimental study. This work establishes two distinct mechanistic pathways for electrochemical CO_2 reduction catalyzed by $[Fe(tpyPY2Me)]^{2+}$ ($[Fe]^{2+}$) as a function of applied overpotential. Comparison of experimental kinetic data to rates obtained from the energetic span model support a PCET pathway as the most likely mechanism. This study serves as a foundation from which we build upon this mechanistic understanding to propose the design of an improved ligand framework. Taken together, this work highlights the value of synergistic computational/experimental approaches to decipher mechanisms of new electrocatalysts and direct the rational design of improved platforms.

Chapter 7. The work presented in this final chapter seeks to explore the extent to which the concept of metal–ligand exchange coupling from Chapter 5 can be utilized to reduce carbon dioxide by more than two electrons to give access to more value-added products. The design, synthesis, characterization, and analysis of two new redox-active ligand platforms for electrochemical carbon dioxide reduction is discussed.

Appendix A. The synthesis, characterization, and screening of a library of nickel bis(iminopyridine) complexes as catalysts for the electrochemical reduction of CO_2.

Appendix B. Metal–ligand cooperativity enable by the tpyPY2Me ligand from Chapter 5 is leveraged for controlling the product selectivity of single-electron transfers to alkyl halides through an outer sphere pathway.

Acknowledgements

There are so many people that I owe an immense amount of gratitude to for their kindness, friendship, and mentorship throughout this very long and at times frustrating process of completing a PhD. I truly believe that the relationships I've made throughout my time at Berkeley have been instrumental in shaping me as the scientist and person that I am today, and I owe much of my professional and personal successes to all of you. I could not have completed my PhD without your help and I will forever cherish the memories, laughs, and hangovers we shared together along the way. I must admit that the task of writing this acknowledgment section has seemed somewhat more daunting at times than writing the actual thesis. Naturally, this is because this section will most likely be the only part of this document that most people will read. No worries though, I too have been guilty of skimming the acknowledgements sections of my friends and colleagues' theses to see what they had written about me. For this reason, and perhaps due to my "good Midwest upbringing" as Chris would put it, I feel the need to individually acknowledge everyone.

First, and foremost I would like to thank the advisors and mentors I've had along the way. To my PhD advisor, Professor Chris Chang, thank you for giving me the opportunity to come to Berkeley and work in your lab. I am grateful that you were willing to take a chance on some random person that you met once at a small train station in Ulsan, South Korea. I hope I was worth the gamble! Your support and mentorship throughout these past six years are what have allowed me to grow into an independent and confident scientist. Beyond the scientific training, I would also like to thank you for giving me the opportunity to work alongside and befriend some of the greatest people "in the business." You have an amazing ability to attract not only incredibly intelligent and skilled scientists, but also unbelievably kind people. I have been fortunate to have made lifelong friendships with many of them. Next, I would also like to thank the members of my Qualifying Exam and Dissertation Committees for their time and guidance throughout my graduate studies: Professors Jeff Long, Jeff Reimer, Don Tilley, John Arnold, and Nicholas Ingolia. Finally, I would like to thank my undergraduate and master's research advisor, Professor Mi Hee Lim. You were the first person to give me a chance to fall in love with science. I was headed in a completely different direction in life until you gave me the opportunity to work in your lab and I owe what feels like a random mix of opportunities and adventures since then to you. Beyond just chemistry, you taught me so much about the value of hard work and dedication. I know at times that I must have been a very challenging and frustrating student to mentor, but you never gave up on me and you always had my best interests in mind. Even when those interests didn't align with what was best for you. Because of you, I was able to leave Michigan and travel the world doing science. The two years I spent in Korea were truly transformative and humbling. I hope in the future that I can repay you for all your time and support throughout the years. FIGHTING!!!

To all the Changstas, past and present, thank you for creating a fun and intellectually stimulating environment. I'd like to take the opportunity to acknowledge and thank many of you individually:

Eva (Nichols; context is key!) – You were the first mentor I had in the lab, and I owe so much of my success to the guidance and training you provided. Thank you for your time and patience! I would not have wanted to go down the rabbit hole of searching for the illusive acetaldehyde with anyone else! Your generosity to include me into the amide porphyrin project

when the nickel bis(iminopyridine) work finally hit a dead-end was what gave me an opportunity to quickly gain the experience required to become independent in the lab. It was such a great experience to work on that project with you and I am happy that I was able to continue that research direction after you graduated. Yay to us for finally wrapping up the urea study after what felt like four long years of confusion and hard work! I look forward to watching the amazing science that comes out of your group in the years to come!

Zhi – Thank you for your kindness and mentorship when I first joined the lab. I learned so much electrochemistry from you by working together on the Pd-NHC project. I wish we could have gotten one of the follow up projects we discussed to work but it was not for lack of effort. I hope that you find as much success in your independent career!

Peter – Thanks for being a great friend. I enjoyed or many science discussions throughout my time in the lab and your input has been invaluable. Perhaps the most enjoyable moments with you were the many long nights spent drinking with you and Chris after group dinners. I could always count on you to hang in until the end with me and make sure that I got home safely even after I'd lost the ability to walk and communicate. I look forward to future nights of drunken debauchery.

Diana – I think it is no exaggeration to say that I could not have completed any of the iron polypyridyl chemistry without your guidance. You taught me so much about spectroscopy and inorganic chemistry and were always my "go-to" person when I had questions or needed to talk about science. Thank you for always being available to listen to my ramblings and for providing support and advice along the way. I am so happy that we have continued to keep in touch since you have started your own lab, and I hope that we continue to as both of our lives go in new directions. I wish you all of the best and can't wait to see the exciting chemistry that comes out of your lab.

Kevin – Thanks for always being your sassy and supportive self. Boyfriends supporting boyfriends! I wish you much success and happiness as you start your own exciting career at Eli Lilly. I look forward to our continued friendship in the years to come.

Carson – My other "boyfriend," I knew we were going to be great friends the moment you told me about the first reaction you ran in the lab that didn't require column purification. It's been an honor to be your "SSB." You made lab life during the pandemic truly tolerable. The long PM shifts in lab with you and Young Aidan were some of the best times of my PhD. Thank you for all your advice and input as I navigated trying to find an industry job. I cherish the time spent with you and Alice (A.K.A "The Gurt") outside of the lab and look forward to the many more years of exciting activities that lie ahead. You will always have a place to crash if you ever find yourself in New Jersey.

Steven – You are genuinely one of the smartest and kindest people I've ever met. Thanks for taking the time read through many of the chapters in this thesis and for providing thoughtful and insightful comments. I have always respected and looked up to your incredible work ethic and deep understanding of organic chemistry. I hope to become a fraction of the scientist that you are!

I wish you all the best as you begin your search for a job, and I selfishly hope that you end up in New Jersey as well so we can continue to share delicious meals and drinks together in the future.

Marco – Thanks for all the casual and pleasant chats throughout the years. I could always count on you to be down for a couple drinks and some solid laughs. I wish you the best as you begin your own academic career!

Mina – I think it is fair to say that you and I got put on perhaps the hardest inorganic chemistry project. Thanks for getting in the N_2 reduction trenches with me and for always being optimistic and extremely hard working. Sorry, that we couldn't get something to work in that space, but I am so happy to see that you found your own scientific direction in the lab and am very excited to read about your upcoming porphyrin chemistry once it's published! Please be sure to stay in touch as you begin your own career and do not hesitate to ever reach out if you need anything from me!

Lun – You are not only one of the hardest workers I've ever met, but also one of the nicest. I have always admired your work ethic and mastery of organic chemistry. It is amazing how much you have been able to accomplish during your time in the lab while also being a new dad! I am so happy to see that all your dedication is finally paying off in what will certainly be a few very exciting publications. I wish you and your family the best in all your future endeavors.

Young Aidan – I've enjoyed shooting the proverbial "shit" with you for the past couple of years. Much luck as you get through the second half of your PhD. Remember to stay optimistic, do your best, and don't be afraid to ask others for help! We are all in this together.

Logan – I'm glad that we got to overlap in my last couple of years. I respect your tastes in coffee, alcohol, and sad girl music and have enjoyed the time we have spent together. Keep working hard and keep your head up!

To my mentees, Luke and Aila – I've enjoyed working with you both and have been extremely impressed by the speed that you both learn and master new techniques and chemistry. Watching you both progress has been one of the most enjoyable parts of my time in the lab, and I know there are many great discoveries to come from you both! Take advantage of this opportunity to learn as much as you can and to build your own lifelong relationships with lab members and scientists throughout the department. I can't wait to see what both of you accomplish!

Matthias – It has truly been a pleasure collaborating with you throughout my PhD. Your intelligence and work ethic are unmatched! Thank you for all your help with the calculations and theory on these CO_2 reduction projects and all the laughs we shared along the way. As you asked, I'll be sure to "put in a good word for you at Merck" if you ever decide you want to jump ship and come work with me again!

Next, to my roommates: Ed, Danny, Trevor, and honorary roommate, John Lee, thank you for being some of the best friends I've ever had. I was worried that going to a place as prestigious as Berkeley would mean that I wouldn't be able to find the type of degenerate friends I had grown accustomed to. Thanks to you all for proving me entirely wrong. The amount of debauchery and

ridiculousness that we got into will never be forgotten and I'm sure will be the subject of endless stories that we will continue to tell for years to come.

Danny – I knew from the first moment we met in orientation that we were going to be great friends. There is so much to thank you for that I don't even know where to begin so I'll just rattle off some of the first things that come to mind. Thanks for always supporting my rage quits and often joining in on them. My liver is a little more damaged and I never want to drink another gin and tonic again because of you, but it was all worth it. Thanks for always supporting my spouts of retail therapy. I learned from the best in that department. You are the only person I'd ever want to get tattooed with and those trips to see Jakoh in San Jose were some of the best memories during my time here. Don't forget we still have to plan a trip to see Helge because he owes us both some new ink and a real fun time in Germany! Football Sundays were some of my fondest memories. Thanks for giving me an opportunity to root for a team that actually wins. Go Cowboys! On a more serious note, you work harder than anyone else I know, and you and Ed have always been the first people I turn to with any organic chemistry questions. I have always admired and looked up to your mastery of organic chemistry and your commitment and dedication to your craft. I know that you are going to do incredible things and I look forward to cheering you on along the way. I'm glad we both are ending up on the east coast. Feel free to come and see Nigel whenever you want. That last point was obviously a joke, I know you're pulling a "noodle" with him.

Ed – In the movies they often talk about how lucky you are to be fortunate enough to find your "one true love". Well, I sometimes feel like I was fortunate enough to find my one special Ed. I think it is fair to say that I've never met anyone like you. We have definitely been through a lot and had our fair share of laughs and squabbles. I think what truly makes us unique as friends is our mutual willingness to laugh at and enjoy in each other's successes in addition to our failures. Like that time during first year that you got your computer stolen out of Danny's car while we were eating Korean BBQ. Great stuff! But for real, you taught me the importance of waiting at least a couple minutes before making a joke and certainly the dangers associated with "blaming the victim." In all seriousness though, time spent with you was some of the best time spent in Berkeley. The speed that you learn things is truly impressive and also frustrating. I wish that I could learn things as quickly and with as little effort as you do! Thanks for the almost daily lunches and commutes between lab and home. I look forward to the continued years of friendship and I know that you are going to be extremely successful no matter what direction you decide to take your career.

Trevor – You were the first person I met at Berkeley when we got paired up as roommates during our visitation weekend and I am so grateful to have gotten the opportunity to build a friendship with you since then. You have always been the kind, calm, and level-headed personability that was required to keep the peace between all our "strong" personalities. I sometimes wonder if I may have talked you into doing a PhD at Berkeley because I remember during our conversation back to the airport that you were on the fence about it. If that is the case, I hope you don't regret that decision as you have been one of the best parts about my graduate school experience and I look forward to many more years of friendship in the future. It sounds repetitive to keep saying how intelligent you all are but it's the truth. Between you Ed, and Danny, I've often felt like the dumbest one in the group. I know that you are going to be crazy successful in the next step in your career. I hope you find all the happiness that you deserve. Finally, thanks

for co-parenting Erwin and Nigel with me and for everything you put up with and do for them. While we often make jokes about it, I know that they are going to be devastated to no longer be able to see you every day. Know that you always have an open invitation to come and see them and don't ever hesitate to ask for updates!

John – I wish that we had gotten to overlap more during our time at Berkeley. Some of my most enjoyable moments were hanging out with you and Ed late at night in the Toste lab. We could always count on you to organize and plan a night full of fun and debauchery. Thanks for being a great friend and I look forward to many for fun nights to come. Also, keep sending those crab pics!

Cam – Thanks for the countless hours of pain and great conversation. Because of you, I'm leaving Berkeley much more "colorful" than when I came here!

To my feline friends: Johnny, Christopher (R.I.P.), Cow Cat, Loud Cat, Clown Cat, and Hippo, thanks for all the soft pets and pleasant meows. I hope that your futures are full of sun-warmed napping spots and lots of food.

To my parents, grandma, brother, and sister, I would like to thank you for your unconditional love, support, and encouragement as I've gone on this long journey around the world to study chemistry. I could not have done any of this without you.

To my children, Erwin and Nigel, thanks for making my life at home so much more fulfilling and enjoyable. I am a firm believer that you can't have nice things if you have cats but that's been a trade that has been more than worth it. I look forward to many more cuddles and the destruction of many more nice things with you both in New Jersey.

Lastly, I want to thank my partner, Eva. My last few years in Berkeley have been some of the best years of my life because it was time spent with you. Thank you for everything that you do and for changing my life for the better.

Table of Contents

Chapter 1: A Biologically Directed Design Strategy for the Development of Molecular Carbon Dioxide Reduction Catalysis 1
1.1 Background and Motivation 2
1.2 Chemical Challenges of Electrochemical CO_2 Reduction 2
1.3 Catalyst Design Inspired by Biological Systems 4
1.4 Privileged Scaffolds for Electrochemical CO_2 Reduction 7
1.5 Electrochemical Analysis and Benchmarking Catalysts 11
1.6 Conclusion 23
1.7 References 25
Chapter 2: Chelating N-Heterocyclic Carbene Ligands Enable Tuning of Electrochemical Carbon Dioxide Reduction to Formate and Carbon Monoxide Through Surface Organometallic Chemistry 34
2.1 Abstract 35
2.2 Introduction 36
2.3 Results and Discussion 37
2.4 Conclusion 49
2.5 Materials and Methods 50
2.5.1 General Methods 50
2.5.2 Iodide Analysis 50
2.5.3 Preparation of Pd foil and NHC Functionalized Pd Electrodes 51
2.5.4 X-Ray Photoelectron Spectroscopy (XPS) 51
2.5.5 External Reflection Fourier Transform Infrared Spectroscopy (ER-FTIR) 51
2.5.6 Solid-State $^{1}H-^{13}C$ Cross-Polarization (CP) Magic-Angle Spinning (MAS) NMR Spectroscopy 52
2.5.7 Electrochemical Cell Design 52
2.5.8 Controlled Potential Electrolysis (CPE) 52
2.5.9 Cyclic Voltammetry (CV) 53
2.5.10 Stripping Experiments 53
2.5.11 Double Layer Capacitance Measurements 53
2.5.12 Computational Methods 54
2.5.13 Synthesis of [timtmbMe(H)][(I)3] 55
2.5.14 Synthesis of [timtmb^{Me}(H)][$(HCO_3)_3$] 55
2.5.15 Synthesis of [timtmb^{iPr}(H)][$(I)_3$] and [timtmb^{iPr}(H)][$(HCO_3)_3$] 56
2.5.16 Synthesis of [timtmb^{tBu}(H)][$(I)_3$] and [timtmb^{tBu}(H)][$(HCO_3)_3$] 56
2.5.17 Synthesis of [mimtmb^{Me}(H)][I] and [mimtmb^{Me}(H)][HCO_3] 57
2.5.18 NMR Spectra 59
2.6 References 71
Chapter 3: Positional Effects of Second-Sphere Amide Pendants on Electrochemical Carbon Dioxide Reduction Catalyzed by Iron Porphyrins 75
3.1 Abstract 76

3.2 Introduction 77
3.3 Results and Discussion 79
3.3.1 Bis(aryl)amide Additive Promotes CO_2 Reduction with Fe Porphyrin. 79
3.3.2 Synthesis of Covalently Modified Porphyrins Bearing Intramolecular Amide Groups. 80
3.3.3 Structural Characterization of Zn-*ortho*-1-amide. 82
3.3.4 Cyclic Voltammetry Studies in Dimethylformamide. 83
3.4 Conclusion 109
3.5 Materials and Methods 110
3.5.1 General Synthetic and Physical Methods 110
3.5.2 General Methods for X-ray Crystallography 110
3.5.3 General Methods for Electrochemistry 110
3.5.4 Details for CO_2 Concentration Dependence Experiments 111
3.5.5 Details for Foot-Of-The-Wave Analysis (FOWA) and Determination of k_{obs} 111
3.5.6 Details for Controlled Potential Electrolysis Experiments 111
3.5.7 Details for Measurement of CO_2 Binding Constant (K_{CO_2}) 113
3.5.8 Details for Spectrophotometric pK_a Titration Experiments 113
3.5.9 Details for Measurement of KIE 118
3.5.10 Computational Details 118
3.5.11 Synthesis of [3,5-Bis(trifluoromethyl)phenyl]amide (amide) 119
3.5.12 Synthesis of 5-[2-Nitrophenyl]-10,15,20-triphenyl Porphyrin (1) 120
3.5.13 Synthesis of 5-[2-Aminophenyl]-10,15,20-triphenyl Porphyrin (2) 120
3.5.14 Synthesis *Ortho*-1-amide 121
3.5.15 Synthesis of 2-Ethoxyindene (3) 121
3.5.16 Synthesis of 2-Formylphenyl Acetic Acid Ethyl Ester (4) 122
3.5.17 Synthesis of 5-[2-Phenylacetic acid ethyl ester]-10,15,20-triphenyl Porphyrin (5) 123
3.5.18 Synthesis of 5-[2-Phenylacetic acid]-10,15,20-triphenyl Porphyrin (6) 123
3.5.19 Synthesis of Ortho-2-amide 124
3.5.20 Synthesis of 5-[4-Nitrophenyl]-10,15,20-triphenyl Porphyrin (7) 125
3.5.21 Synthesis of 5-[4-Aminophenyl]-10,15,20-triphenyl Porphyrin (8) 125
3.5.22 Synthesis of *Para*-1-amide 126
3.5.23 Synthesis of 5-[4-Phenylacetic acid methyl ester]-10,15,20-triphenyl Porphyrin (9) 126
3.5.24 Synthesis of 2-(4-(10,15,20-Triphenylporphyrin-5-yl)phenyl)acetic Acid (10) 127
3.5.25 Synthesis of *Para*-2-amide 127
3.5.26 Synthesis of *Para*-$(CF_3)_4$ 128
3.5.27 General Procedure for Synthesis of Fe Porphyrins 128
3.5.28 NMR Specta 132
3.6 References 160
Chapter 4: Templating Bicarbonate in the Second Coordination Sphere Enhances Electrochemical Carbon Dioxide Reduction Catalyzed by Iron Porphyrins 166
4.1 Abstract 167
4.2 Introduction 168
4.3 Results and Discussion 170

4.3.1 Design and Synthesis of Well-Defined Iron Porphyrin Catalysts Modified with Second-Sphere Urea Pendants to Template Bicarbonate Binding 170
4.3.2 Structural Characterization Establishes the Ability of Urea Pendants to Poise Anions Proximal to the Porphyrin Metal Center 171
4.3.3 Electrochemical Carbon Dioxide Reduction Catalyzed by Urea-Modified Iron Porphyrin Complexes 172
4.3.4 Positional Effects of Second-Sphere Urea Pendants on Bicarbonate-Mediated Enhancement of Electrochemical Carbon Dioxide Reduction 176
4.3.5 Second-Sphere Urea Pendants Increase Acidity of Templated Bicarbonate as a Proton Source to Promote Carbon Dioxide Reduction 186
4.4 Conclusion 190
4.5 Materials and Methods 191
4.5.1 General Methods 191
4.5.2 Cyclic Voltammetry 191
4.5.3 CO_2 Concentration-Dependent Experiments 191
4.5.4 Details for Foot-Of-The Wave Analysis (FOWA) and Determination of k_{obs} 192
4.5.5 Controlled Potential Electrolysis 192
4.5.6 Determination of Faradaic Efficiency 193
4.5.7 X-ray Crystallography 194
4.5.8 Spectrophotometric pK_a Titrations 194
4.5.9 Computational Details 197
4.5.10 Synthesis of 5-(2-Nitrophenyl)-10,15,20-triphenylporphyrin (1) 198
4.5.11 Synthesis of 2-(10,15,20-Triphenylporphyrin-5-yl)aniline (2) 198
4.5.12 Synthesis of 1-(3,5-Bis(trifluoromethyl)phenyl)-3-(2-(10,15,20-triphenylporphyrin-5-yl)phenyl)urea (*ortho*-urea) 199
4.5.13 Synthesis of 5-(4-nitrophenyl)-10,15,20-triphenylporphryin (3) 200
4.5.14 Synthesis of 4-(0,15,20-Triphenylporphyrin-5-yl)aniline (4) 200
4.5.15 Synthesis of 1-(3,5-Bis(trifluoromethyl)phenyl)-3-(4-(10,15,20-triphenylporphyrin-5-yl)phenyl)urea (*para*-urea) 201
4.5.16 General Procedure for the Synthesis of Iron Porphyrins 201
4.5.17 Crystallographic Data 203
4.5.18 NMR Spectra 204
4.6 References 214
Chapter 5: Metal–Ligand Cooperativity via Exchange Coupling Promotes Iron-Catalyzed Electrochemical Carbon Dioxide Reduction at Low Overpotentials 219
5.1 Abstract 220
5.2 Introduction 221
5.3 Results and Discussion 223
5.3.1 Design, Synthesis, and Characterization of the tpyPY2Me Ligand and its Metal Coordination Complexes 223
5.3.2 Cyclic Voltammetry of tpyPY2Me Fe(II) and Zn(II) Complexes and comparison to $PY5Me_2$ Analogs. 232
5.3.3 Electrochemical Reduction of CO_2 Catalyzed by $[Fe(tpyPY2Me)]^{2+}$ in Organic Solution 232

5.3.4 Controlled Potential Electrolysis Studies in Organic Solution 235
5.3.5 Kinetic Analysis in Organic Solution 246
5.3.6 Chemical Reduction and Characterization of $[Fe(tpyPY2Me)]^0$ ($[Fe1]^0$) 249
5.3.7 Electronic Structure Calculations 255
5.3.8 Electrochemical CO_2RR Catalyzed by $[Fe(tpyPY2Me)]^{2+}$ in Water 259
5.4 Conclusion 267
5.5 Materials and Methods 269
5.5.1 General Methods 269
5.5.2 Cyclic Voltammetry 269
5.5.3 Controlled Potential Electrolysis 270
5.5.4 Determination of Overpotential (η) 273
5.5.5 Determination of Faradaic Efficiency (FE) 274
5.5.6 Determination of k_{obs} and Turn Over Frequency (TOF) 274
5.5.7 Mössbauer Spectroscopy 275
5.5.8 X-Ray Absorption Spectroscopy (XAS) 276
5.5.9 X-Ray Crystallography 276
5.5.10 Quantum Chemical Calculations 276
5.5.11 Computational Details 278
5.5.12 Synthesis of 6-Bromo-2,2':6',2"-terpyridine 280
5.5.13 Synthesis of 6-(1,1-Di(pyridin-2-yl)ethyl)-2,2':6',2"-terpyridine (tpyPY2Me) 281
5.5.14 Synthesis of $[Fe(tpyPY2Me)(CH_3CN)][OTf]_2$ ($[Fe1]^{2+}$) 281
5.5.15 Synthesis of $[Fe(tpyPY2Me)(NO_3)][NO_3]$ 282
5.5.16 Synthesis of $[Zn(tpyPY2Me)][OTf]_2$ ($[Zn1]^{2+}$) 283
5.5.17 Synthesis of $[Fe(tpyPY2Me)]^0$ ($[Fe1]^0$) 283
5.5.18 Synthesis of $[Zn(tpyPY2Me)]^0$ ($[Zn1]^0$) 284
5.5.19 X-Ray Crystallographic Data 285
5.5.20 DFT Calculation Coordinates (x,y,z) 293
5.5.21 NMR Spectra 316
5.6 References 324
Chapter 6: Deciphering Distinct Overpotential Dependent Pathways for Electrochemical Carbon Dioxide Reduction Catalyzed by an Iron-Terpyridine Complex 332
6.1 Abstract 333
6.2 Introduction 334
6.3 Results and Discussion 337
6.3.1 Observation of Two Distinct Overpotential-Dependent Regimes for Electrochemical CO_2 Reduction Catalyzed by $[Fe(tpyPY2Me)]^{2+}$ 337
6.3.2 Low Overpotential Pathway 338
6.3.3 Reduction 338
6.3.4 CO_2 Binding 340
6.3.5 Protonation 343
6.3.6 CO Release 343
6.3.7 High Overpotential Pathway 345
6.3.8 Kinetic Analysis of Proposed Mechanistic Pathways 349
6.3.9 Selectivity Versus HER 359

6.3.10 Rational Catalyst Design Driven by Mechanistic Insights 361
6.4 Conclusion 365
6.5 Materials and Methods 366
6.5.1 Computational Model 366
6.5.2 Quantum Chemistry 367
6.5.3 Redox Potential Calculations 370
6.5.4 General Experimental Methods 370
6.5.5 Cyclic Voltammetry (CV) 371
6.5.6 Controlled Potential Electrolysis (CPE) 371
6.5.7 Determination of Half-Maximum Catalytic Potentials ($E_{cat/2}$) 372
6.5.8 Determination of Overpotential (η) 373
6.5.9 Determination of Faradaic Efficiency (FE) 374
6.5.10 Determination of k_{obs} and Turnover Frequency (TOF) 374
6.5.11 Determination of Kinetic Isotope Effects (KIE) 375
6.6 References 376
Chapter 7: Expanded π^* Systems Integrated into Molecular Polypyridyl Coordination Complexes for Electrochemical Carbon Dioxide Reduction Beyond Two-Electron Reduction Products: Synthesis, Characterization, and Catalytic Analysis 383
7.1 Abstract 384
7.2 Introduction 385
7.3 Results and Discussion 389
7.3.1 Rational Design of the tpy(Iso)Quin2Me Ligands 389
7.3.2 Synthesis and Characterization of Metal tpy(Iso)Quin2Me Complexes 393
7.3.3 Electrochemical Properties of the Metal tpy(Iso)Quin2Me Complexes 398
7.3.4 Screening Metal tpy(Iso)Quin2Me Complexes as Catalysts for Electrochemical CO_2 Reduction 402
7.3.5 Future Directions Towards the Production of More Reduced Products 408
7.4 Conclusion 412
7.5 Materials and Methods 413
7.5.1 General Methods 413
7.5.2 Cyclic Voltammetry 413
7.5.3 Controlled Potential Electrolysis 414
7.5.4 Determination of Faradaic Efficiency (FE) 414
7.5.5 X-Ray Crystallography 414
7.5.6 Detection and Quantification of Liquid Products 415
7.5.7 Evans Method Analysis 415
7.5.8 Synthesis of Di(quinolin-2-yl)methane (7a) 416
7.5.9 Synthesis of 2,2'-(Ethane-1,1-diyl)diquinoline (7b) 416
7.5.10 Synthesis of Di(isoquinolin-1-yl)methane (7c) 417
7.5.11 Synthesis of 1,1'-(Ethane-1,1-diyl)diisoquinoline (7d) 417
7.5.12 Synthesis of 6-Fluoro-2,2':6',2''-terpyridine (F-tpy) 418
7.5.13 Synthesis of 2,2'-(1-([2,2':6',2''-Terpyridin]-6-yl)ethane-1,1-diyl)diquinoline (tpyQuin2Me) 419

7.5.14 Synthesis of 1,1'-(1-([2,2':6',2"-Terpyridin]-6-yl)ethane-1,1-diyl)diisoquinoline (tpyIsoQuin2Me) ... 420
7.5.15 Synthesis of $Cr(OTf)_2(CH_3CN)_2$ ... 420
7.5.16 Synthesis of $[Cr(tpyQuin2Me)(Cl)_2][Cl]$ ... 421
7.5.17 Synthesis of $[Cr(tpyQuin2Me)(Cl)_2][OTf]$ ... 421
7.5.18 Synthesis of $[Cr(tpyQuin2Me)][OTf]_2$ (Cr-tpyQuin2Me) ... 422
7.5.19 Synthesis of $[Fe(tpyQuin2Me)][OTf]_2$ (Fe-tpyQuin2Me) ... 422
7.5.20 Synthesis of $[Co(tpyQuin2Me)][OTf]_2$ (Co-tpyQuin2Me) ... 423
7.5.21 Synthesis of $[Ni(tpyQuin2Me)][OTf]_2$ (Ni-tpyQuin2Me) ... 424
7.5.22 Synthesis of $[Zn(tpyQuin2Me)][OTf]_2$ (Zn-tpyQuin2Me) ... 424
7.5.23 Synthesis of $[Cr(tpyIsoQuin2Me)(Cl)_2][Cl]$ ... 425
7.5.24 Synthesis of $Cr(tpyIsoQuin2Me)(OTf)_2$ (Cr-tpyIsoQuin2Me) ... 425
7.5.25 Synthesis of $Fe(tpyIsoQuin2Me)(OTf)_2$ (Fe-tpyIsoQuin2Me) ... 426
7.5.26 Synthesis of $Co(tpyIsoQuin2Me)(OTf)_2$ (Co-tpyIsoQuin2Me) ... 427
7.5.27 Synthesis of Ni(tpyIsoQuin2Me)(OTf)2 (Ni-tpyIsoQuin2Me) ... 427
7.5.28 Synthesis of $Zn(tpyIsoQuin2Me)(OTf)_2$ (Zn-tpyIsoQuin2Me) ... 428
7.5.29 X-Ray Crystallography Data ... 429
7.5.30 Supplemental Controlled Potential Electrolysis Data ... 450
7.5.31 NMR Spectra ... 454
7.6 References ... 484

Appendix A: Development of Nickel Bis(iminopyridine) Complexes Directed Toward Electrochemical Carbon Dioxide and Carbon Monoxide Reduction ... 490
A.1 Introduction ... 491
A.2 Results and Discussion ... 493
A.2.1 Design Rationale and Preparation of Nickel Bis(iminopyridine) Complexes ... 493
A.2.2 X-Ray Crystallographic Characterization of Ni(5) ... 494
A.2.3 Electrochemical CO_2 Reduction ... 496
A.2.4 Electrochemical CO Reduction and Efforts Toward Product Detection ... 500
A.2.5 Controlled Potential Electrolysis in ^{13}CO Atmosphere ... 504
A.3 Conclusion ... 506
A.4 Materials and Methods ... 507
A.4.1 General Methods ... 507
A.4.2 Electrochemical Measurements ... 507
A.4.3 Detection of CPE Products by NMR ... 508
A.4.4 UV-Visible DNPH Experiments for Acetaldehyde (AA) Detection ... 508
A.4.5 General Synthetic Procedure for the Preparation of Bis(iminopyridine) Ligands ... 508
A.4.6 General Procedure for the Preparation of Nickel Complexes ... 510
A.4.7 X-Ray Crystallography Data ... 513
A.5 References ... 514

Appendix B: Controlled Single-Electron Transfer via Metal–Ligand Cooperativity Drives Divergent Nickel-Electrocatalyzed Radical Pathways ... 516
B.1 Abstract ... 517
B.2 Introduction ... 518
B.3 Results and Discussion ... 520

B.3.1 Synthesis and characterization of Ni complexes 520
B.3.2 Single-Electron Activation of Alkyl Iodide Substrates by [Ni-1] 524
B.3.3 Single-Electron Activation of Alkyl Iodide Substrates by $[Ni\text{-}2]^{+}$ 545
B.3.4 Computational Characterization of Reduced Electroactive Species [Ni-1] and $[Ni\text{-}2]^{+}$ 547
B.3.5 Mechanistic Model for Controlled Single-Electron Transfer Manipulated via Metal–Ligand Cooperativity 550
B.4 Conclusion 553
B.5 Materials and Methods 554
B.5.1 General Methods 554
B.5.2 Electrochemical Methods for Cyclic Voltammetry 554
B.5.3 Bulk Electrolysis Procedures 555
B.5.4 Electrochemical Simulation Methods 555
B.5.5 Determination of Electron Transfer Rate Constant for $[Ni\text{-}2]^{2+}$ 556
B.5.6 Determination of Electron Transfer Rates for EC Mechanism Involving Catalyst Deactivation 556
B.5.7 Determination of Electron Transfer Rates for Total Catalysis (TC) 557
B.5.8 Determination of Electron Transfer Rates for Chemical Catalysis (CC) 558
B.5.9 X-Ray Crystallography 558
B.5.10 Evans Method Analysis 558
B.5.11 Quantum Chemical Computations 559
B.5.12 Synthesis of Dimethyl 2-(but-3-en-1-yl)-2-(iodomethyl)malonate (11) 559
B.5.13 Synthesis of Dimethyl 2-butyl-2-(iodomethyl)malonate (3) 560
B.5.14 Synthesis of $[Ni(tpyPY2Me)(MeCN)](PF_6)_2$ ($[Ni\text{-}1]^{2+}$) 560
B.5.15 Synthesis of $[Ni(PY5Me2)(MeCN)](PF_6)_2$ ($[Ni\text{-}2]^{2+}$) 560
B.5.16 Synthesis of [Ni(PY5Me2)(I)](I) 561
B.5.17 Synthesis of Tetramethyl 3,3'-(ethane-1,2-diyl)bis(cyclopentane-1,1-dicarboxylate) 561
B.5.18 Synthesis of Dimethyl 3-(iodomethyl)cyclopentane-1,1-dicarboxylate 561
B.5.19 Synthesis of Dimethyl 3-methylcyclopentane-1,1-dicarboxylate 562
B.5.20 Synthesis of dimethyl 2-(but-3-en-1-yl)succinate 562
B.5.21 X-Ray Crystallography Data 563
B.5.22 DFT Calculation Coordinates (x,y,z) 566
B.5.23 NMR Spectra 579
B.6 References 594

Chapter 1: A Biologically Directed Design Strategy for the Development of Molecular Carbon Dioxide Reduction Catalysis

1.1 Background and Motivation

Nature is miraculous in its ability to maintain complex ecosystems that sustain diverse life with precisely balanced and intertwined natural cycles that interconvert the small molecules that are essential for life: water (H_2O), dinitrogen (N_2), and carbon dioxide (CO_2). For example, the carbon cycle is naturally balanced by aerobic organisms that release CO_2 into the atmosphere through cellular respiration, while plants uptake and use the CO_2 along with water and light in photosynthesis to generate energy-rich sugars. Disruption of the natural balance of these cycles can have severe, far-reaching consequences, some of which we are now starting to experience.[1] The start of the Industrial Revolution marked a major improvement in the standard of living for many people by gaining increased wealth, healthier diets, better housing, and cheaper goods. Unfortunately, these improvements were acquired by exploiting the combustion of fossil fuels, severely disrupting the innate balance of the carbon cycle through the release of large amounts of CO_2 into the atmosphere. Without an equal increase in photosynthetic processes to mitigate this spike, CO_2 has accumulated in the atmosphere at high concentrations. Atmospheric CO_2 levels were almost constant throughout the history of humankind at 280 ppm.[2,3] Current levels today measured at the Mauna Loa Observatory in Hawaii exceed 419 ppm.[3,4] This drastic increase in atmospheric CO_2 has had direct impacts on global warming,[5–8] increased sea levels,[9,10] ocean acidification,[11] severe weather patterns,[12] and decreased biodiversity.[13,14] Recent increased global awareness of these consequences has led to a push for political, societal, and economic reforms to transition away from a carbon-based economy toward a more sustainable, environmentally conscientious one. Scientific and technological innovation to capture and reduce the CO_2 footprint must first occur for these goals to ultimately realized. The conversion of CO_2 into value-added materials that can be used to produce fuels, plastics, foods, or medicines represents a promising pathway especially if these technologies can be driven with the use of renewable and thus carbon-free energy sources (*e.g.*, solar, wind, and hydroelectric power) (**Figure 1.1**).[15,16] We direct the reader to a few recent articles that discuss the technologies and feasibility of integrating these systems in much more detail.[15–21] The work presented in this thesis explores the design and development of catalytic systems to electrochemically reduce CO_2 and convert it into value-added products such as carbon monoxide (CO), formate (HCO_2H), formaldehyde (CH_2O), or methanol (CH_3OH).

1.2 Chemical Challenges of Electrochemical CO_2 Reduction

In order to design effective catalysts that can electrochemically convert CO_2 into value-added products, it is important to understand the chemical challenges that are associated with the reduction and conversion of CO_2.[22,23] The single-electron reduction of CO_2 to generate a bent, radical anion presents a major thermodynamic hurdle. This can be observed experimentally by the extremely negative redox potential of –1.90 V vs the standard hydrogen electrode (SHE)[24] that is required to drive this reaction (equivalent to approximately –2.5 V vs Fc/Fc^+)[25] and qualitatively understood by considering the amount of energy required to rearrange the linear CO_2 molecule into the bent geometry of $CO_2^{\bullet-}$. Fortunately, the thermodynamic barriers are greatly reduced by supplying protons and electrons together in pairs. **Figure 1.1** illustrates this point by showing how the thermodynamic redox potentials for CO_2 reduction increase as more electrons and protons are supplied simultaneously. For example, the thermodynamic potential for the two-electron reduction of CO_2 into CO and H_2O is a remarkable 1.37 V more positive than the potential for the single-

electron reduction of CO_2. These high energy barriers also don't account for additional electrochemical interfacial phenomena that result in the formation of an overpotential (vide infra), but these barriers can be greatly reduced with the use of transition metal catalysts as the critical potential required for catalysis is often no longer determined by the onset potential for CO_2 reduction but is instead directed by the reduction potential of the catalyst. Additionally, the reduction of protons in solution to generate hydrogen gas (H_2) occurs at thermodynamic potentials comparable to those for the CO_2 reduction reaction (CO_2RR), making the hydrogen evolution reaction (HER) an undesirable but competitive catalytic pathway (**Figure 1.1**). Reaction pathways for hydrogen production often evoke the formation of metal hydride intermediates and therefore most rational ligand design strategies incorporate methods to suppress the formation of such species (vide infra).

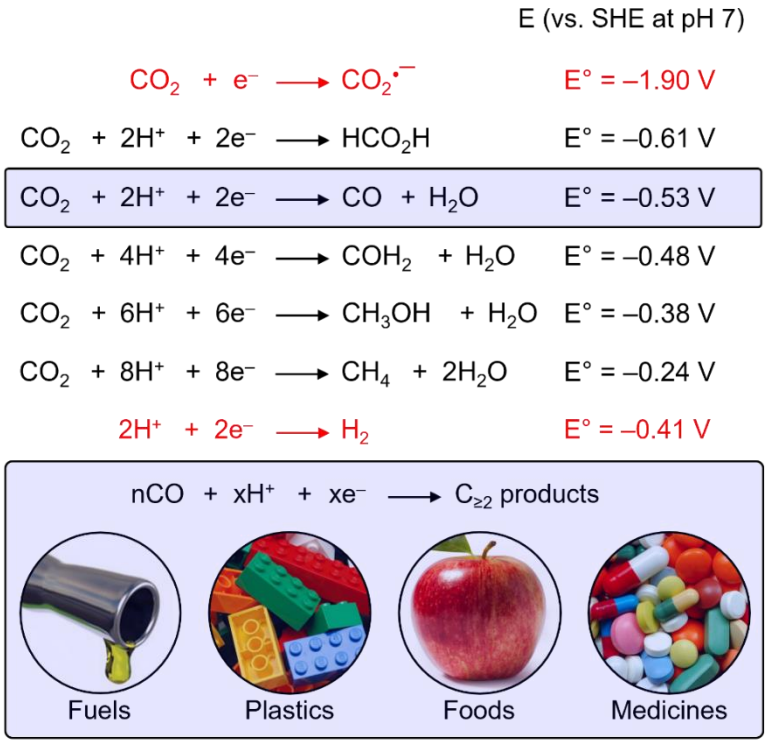


Figure 1.1. Chemical challenges associated with the electrochemical reduction of CO_2. The single electron reduction of CO_2 requires extremely reducing potentials that can be mitigated with the simultaneous delivery of multiple proton and electrons to generate higher-value products. The competitive reduction of protons to generate hydrogen gas occurs at similar redox potentials and represents a major competitive, undesirable pathway.

While the thermodynamic requirements are mitigated by the supply of multiple protons and electrons, the production of highly reduced products remains challenging due to the kinetic barriers associated with the need to precisely control the delivery of the proton and electrons. As a result, very few homogenous catalytic systems can reduce CO_2 beyond the two-electron reduction products, CO and formate. Most catalysts capable of producing these products are heterogenous copper-based materials.[26–28] Of the few molecular catalysts that have been reported, several mechanistic pathways have been proposed for the reduction of CO_2 into highly reduced C_1

products such as CH_2O, CH_3OH, and CH_4 based on theoretical and to some degree, experimental studies.[29] These studies suggest that the production of highly reduced C_1 products go through reaction pathways that are dependent on CO or formate intermediates that remain bound to the active site (**Figure 1.2**).[29] Therefore, the understanding required to generate more reduced products comes down to comprehending how to stabilize and activate these CO and/or formate intermediates for further reductive transformations.[29] The reduction of carbonyl intermediates is strongly dictated by the Sabatier principle[30] which describes how the strength of CO binding to the active site can prohibit catalysis through either ligand dissociation if binding is weak or catalyst poisoning if strong π-backbonding is operative.[31,32] If π-backbonding doesn't completely shut down the catalyst it can instead degrade its selectivity by requiring the use of more negative operating potentials which often favor the production of H_2 over CO_2 reduction. This reasoning has been used to explain the remarkable reactivity of copper-based materials to produce highly reduced C_1 and C_2 products[33] as they appear to operate in an effective "goldilocks zone" with a CO binding strength that is "just right." The Sabatier principle has been further applied to explain the strong metal center dependence of metal phthalocyanine complexes for CO_2 reduction into methane and was used to predict the remarkable reactivity the cobalt complex relative to the analogous Ni and Fe complexes.[34–37] Many additional pathways have been proposed to explain CO_2 reduction beyond two-electrons through a formate intermediate; however, many of them involve bimetallic pathways that incorporate one metal center to bind and activate CO_2 while another serves to generate the hydrides required to promote further reduction.[38] These points and how they direct rational ligand design are discussed further in Chapter 7 and have been recently reviewed elsewhere in greater detail.[29,39]

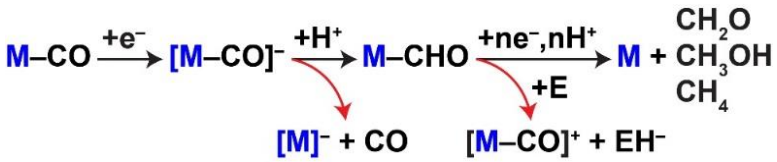


Figure 1.2. Proposed mechanistic pathways for the activation and reduction of CO to produce highly reduced C_1 products from CO_2 at a metal complex catalyst. Figure is adapted from Reference 29 with permission. Deactivation pathways are denoted with red arrows. The first shows the dissociation of the carbonyl complex to give a reduced metal center and CO and the second deactivation pathway depicts the hydride transfer to an electrophile (*i.e.*, CO_2) yielding an oxidized carbonyl complex.

1.3 Catalyst Design Inspired by Biological Systems

With these chemical challenges in mind, we turn toward nature for inspiration to rationally design catalytic platforms to electrochemically reduce CO_2 into value-added products. In particular, the work presented in this thesis is inspired by three characteristics that metalloenzymes utilize to catalyze reactions with exceptional selectivity and efficiency (**Figure 1.3**). The first is the use of electron reservoirs to facilitate and control electron transfer reactions. Their use in nature is ubiquitous but some key examples relevant to small molecule activation and reduction include the metalloenzymes periplasmic nitrate reductases and nitrogenases that both utilize iron-sulfur clusters to couple electron transfer processes to catalysis.[40,41] Nitrogenases in particular are remarkable in their ability to catalyze the six-electron reduction of N_2 into the ammonia (NH_3) that

is required to generate the fertilizers needed to sustain the current human population. Industrially this is accomplished at high temperatures and pressures through the Haber-Bosch process.[42,43] Nitrogenases achieve this amazing feat at ambient conditions through a complex process that involves the cycling of electrons between the [4Fe-4S] cluster of the Fe protein, to the P cluster of the MoFe protein, and finally to the buried active site of the FeMo-cofactor. Once two electrons have been up taken, they can eventually combine with protons to generate the hydride equivalents required to ultimately release two NH_3 molecules from N_2. This overall reaction involves eight rounds of Fe and MoFe protein redox cycling and the hydrolysis of a minimum of 16 ATP molecules.[44–50] Integration of a synthetic analog to such redox reservoirs into a molecular scaffold could provide a solution to overcome the steep kinetic barriers associated with delivering the multiple reduction equivalents required to reduce CO_2 into the desired value-added products. Extensive efforts have been directed towards the development and study of organometallic electron reservoirs that can withstand single or multiple redox changes without molecular disruption, decomposition, and with minimal structural changes.[51] Most of these coordination complexes tend to be derivatives of transition metal sandwich complexes because of their exceptional electrochemical stability and ability to tune their redox potentials in a predictable manner through the identity of the metal center or substitutions to the aryl rings. For these reasons, we had initially explored the integration of metallocenes as redox reservoirs onto molecular scaffolds for electrochemical CO_2 reduction but ultimately found this approach to be quite limiting. The metallocene derivatives that are reducing enough to be redox matched to the standard potential for CO_2 such as cobaltocene, ($CoCp_2$; –1.33 V vs Fc/Fc^+), decamethylcobaltocene ($CoCp^*_2$; –1.94 V vs Fc/Fc^+) or hexamethylbenzene cyclopentadienyliron ([$FeCp^*(\eta\text{-}C_6Me_6)$]; –2.30 V vs Fc/Fc^+) have limited air stability, are challenging to synthetically modify, and possess undesirable background catalytic activity.[52–56] Therefore, to pursue this approach we settled on the exploration and development of a molecular-material hybrid platform where a robust solid metal cathode material that behaves as an electron reservoir is paired with a molecular capping ligand that greatly enhances the selectivity and stability of the cathode for electrochemical CO_2 reduction to formate.[57] The details of this work are presented and discussed in further detail in Chapter 2.

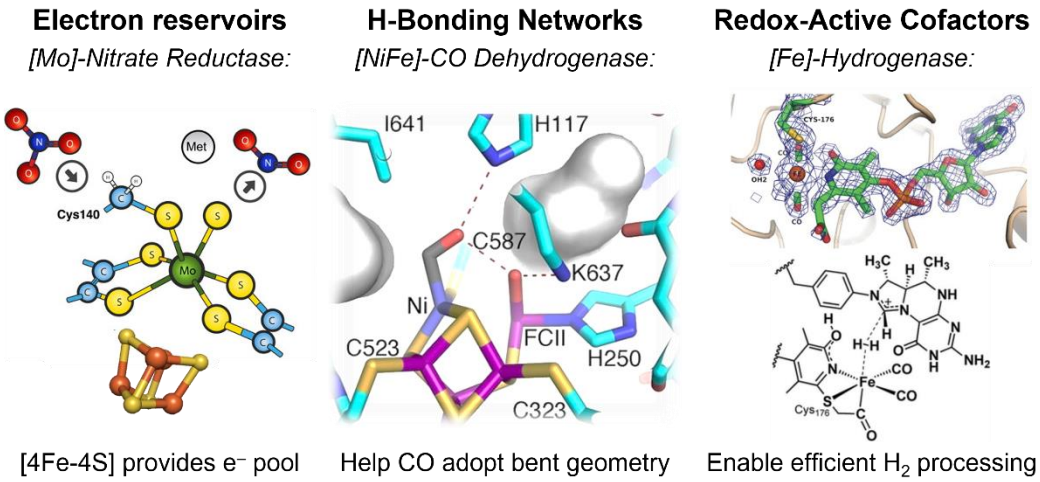


Figure 1.3. Catalyst design inspired by biological systems. Enzymes take advantage of precisely placed electron reservoirs, hydrogen bonding networks, and redox active cofactors to direct the delivery of proton and electrons in a highly controlled manner.

The use of precisely positioned hydrogen bonding networks to stabilize key transition states is the second area of biologically inspired molecular catalyst design. This approach takes inspiration from metalloenzymes such as [NiFe] carbon monoxide dehydrogenase (CODH) that catalyzes the reverse of the CO_2RR, the oxidation of CO to CO_2.[58–62] Hydrogen bonding between nickel-bound CO and the proximal histidine and lysine residues enforces a unique bent conformation that serves to prime and activate it for attack by a nearby iron-bound hydroxide, whose negative charge is also stabilized through hydrogen bonding to a cysteine residue.[58–60] These types of bioinorganic systems have inspired and directed an entire field of biomimetic catalysts that incorporate second-sphere functionality to enhance the activation and transformation of small molecule substrates.[63–66] In particular, modifications to the second coordination sphere to improve electrochemical CO_2RR is a vastly expanding field and as such we will not cover it in exhaustive detail here but instead will highlight some of the major advances in the following section, which is devoted to discussing the canonical privileged ligand scaffolds for electrochemical reduction of CO_2. More detailed and recent reviews on the role of second-sphere effects in catalysis were recently published by Drover and Machan and coworkers.[67,68] The work that is presented in this thesis is focused on investigating how the relative positioning and number of hydrogen bond donors that are integrated into the second coordination sphere of a molecular CO_2 reduction catalyst impacts the overall performance. Chapter 3 discusses how the positioning of a bis-aryl amide pendant onto an iron porphyrin framework can be utilized to greatly enhance the rates of catalysis and break inherent scaling relationships between the thermodynamic operating potentials and the maximum turnover frequency. Chapter 4 expands on this work by exploring how the addition of a second hydrogen bond donor in the form of a bis-aryl urea moiety alters the catalytic performance by toggling the complex equilibrium between soluble sources of bicarbonate and CO_2 in organic electrolytes.

The remaining body of work presented in this thesis is inspired by metalloenzymes' use of redox active cofactors to minimize energy input and maximize reaction selectivity through the separation of reducing equivalents in an organized way via electronic delocalization and tunneling

pathways.[69,70] For example, we were inspired by enzymes like mononuclear iron hydrogenases that take advantage of redox-active cofactors such as tautomeric 2-hydroxypridine/pyridone ligands and pterins to enable efficient hydrogen processing without redox cycling of the iron center.[71] The ability to catalyze the reduction of small molecules without having to change oxidation states on the metal center was intriguing as we reasoned that it could improve the thermodynamics and selectivity for CO_2 reduction by delocalizing electron density across an extended ligand framework and suppressing the formation of metal hydrides that are often generated through protonation of Lewis basic metal centers. This directed us to explore the use and integration of redox-active ligands into homogenous electrocatalysts that could mimic the chemistry of these types of cofactors. Whether the use of redox-active ligands serves to benefit or impede electrochemical CO_2 and proton reduction reactions is still a matter of some debate.[72] Beneficial effects that have been claimed in the literature include: (1) increased CO_2 reduction selectivity by suppressing background HER activity,[73–75] (2) decreased overpotentials required for catalysis by introducing ligand-centered redox chemistry that is more accessible at less reducing potentials,[76–78] and (3) enhancing rates through access to a local concentration of protons *via* protonation of reduced ligand intermediates.[79,80] Alternatively, deleterious effects such as undesired ligand-centered chemical reactivity and metal-centered chemical trapping have been reported where both pathways lead to either the trapping of electron density and eventual catalyst poisoning through irreversible chemical bond formation or a metal center that is not nucleophilic enough to react with CO_2.[75,81–86] Taken together, it is likely that a combination of both pathways can be engendered by redox-active ligands as too little delocalization can promote HER pathways while too much can suppress CO_2RR. Clearly, further study and comparison to the appropriate redox-innocent control ligand systems are required to firmly establish a quantitative measure for the exact role that redox-active ligands play in CO_2 reduction catalysis. A more detailed discussion of these points and how they are applied to some recent literature examples was recently published in a perspective article written by Queyriaux.[72] Moreover, the work presented in Chapter 5 explores the use of incorporating a redox active terpyridine moiety into a polypyridyl ligand scaffold to turn-on and enhance catalysis for electrochemical CO_2 reduction. Comparison to the appropriate redox-silent ligand and zinc controls allows the role of the terpyridine-appended redox active ligand to be disentangled from the role of iron metal center.[87] Chapter 6 expands upon this system to establish a mechanistic understanding of the exceptional catalytic performance of the iron terpyridine-based molecular catalyst. Finally, Chapter 7 seeks to further expand the extent of redox-activity in this polypyridyl ligand scaffold so that it can enable the reduction of CO_2 beyond the two-electron products.

1.4 Privileged Scaffolds for Electrochemical CO_2 Reduction

The first homogenous catalysts for the electrochemical reduction of CO_2 were reported almost 50 years ago. Since then, the field has evolved rapidly with many additional catalysts reported and much complexity integrated into the molecular scaffolds. To give a brief overview of the chemical space for homogenous catalyst development, we give a general discussion on some of the canonical catalytic systems that have been developed for the conversion of CO_2. Unlike most review articles, we organize this section based on the type of ligand rather than the identity of the metal center. This approach makes more sense as the objective of this thesis to develop biologically inspired novel homogenous catalysts and thus the design and synthesis of a new ligand framework opens an entire chemical space through which the role of the central metal ion can be

systematically screened. The classes of ligands discussed in this section represent a set of "privileged" scaffolds in the sense that they have been shown to impart exceptional catalytic stability and performance when paired with the appropriate metal centers. As such, these types of ligands represent an ideal starting platform to incorporate the biologically inspired design principles that were discussed above. The four types of ligands that will be discussed in this section are (1) porphryins/phthalocyanines, (2) tetraaza macrocycles, (3) bipyridine-based tris-carbonyls, and (4) phosphines (**Figure 1.4**). The ligand categories discussed here are far from exhaustive. For more detailed reviews on the application and use of transition metal complexes as molecular electrochemical CO_2 reduction catalysts we direct the reader to these recent reviews articles.[3,88,89]

Macrocyclic transition metal complexes comprise some of the most active and well-studied electrochemical CO_2 reduction catalysts. Of these complexes, metal phthalocyanines, porphyrins, and corroles were some of the first molecular systems reported to catalyze the reduction of CO_2. In 1974, Meshitsuka and coworkers published the first report on a series of metal phthalocyanine complexes for the reduction of CO_2 although they did not analyze or quantify the products and instead identified the Co and Ni complexes as active catalysts based on the size of the catalytic waves measured by cyclic voltammetry.[90] A few years later this work was expanded to include metalloporphyrins in a seminal report by Katsuhiro et al. who investigated free-base meso-tetra(4-carboxyphenyl)porphyrin (TCPP) and tetraphenylporphine sulfonate ligands and their respective metal complexes (M = Co, Fe, and Cu) as CO_2 reduction catalysts.[91] Only the cobalt complexes were identified as competent catalysts for converting CO_2 into formate as confirmed by a resorcinol test.[91] Savéant and coworkers have since greatly expanded the use and understanding of such porphyrin complexes with much of their work focused on the study of iron tetraphenylporphyrin complexes (Fe-TPP).[92,93] Their mechanistic electrochemical studies have identified the active catalytic species as a formal Fe(0) complex. Elegant spectroscopic and computational work by Römelt et al. characterized the electronic structure of the Fe(0) complex as an open-shell singlet formulated as an intermediate-spin Fe(II) center that is antiferromagnetically coupled to a diradical anion porphyrin ligand.[94] Electronically, this systems is almost identical to the one discussed in Chapter 5. Moreover, Savéant and coworkers were also some of the first to further modify the second coordination spheres of these ligands via the incorporation of phenolic groups which have been shown to enhance catalytic rates by over two orders of magnitude.[95] As the CO_2RR is a proton-dependent reaction, the incorporation of a highly acidic, local concentration of protons at the active site of the catalyst is proposed to greatly enhance catalysis through a proton relay pathway. Similarly, these types of acidic second sphere groups may also serve to stabilize key transitions states through hydrogen bonding interactions or help to facilitate the often rate-limiting cleavage of the C–O bond and release of water through a push-pull mechanism with the conjugate base of the tethered acidic functional group.[3] More recent work in this space has expanded to incorporate positively charged functional groups into the second coordination sphere to give remarkable improvements in catalytic performance due to through-space coulombic interactions.[96–99]

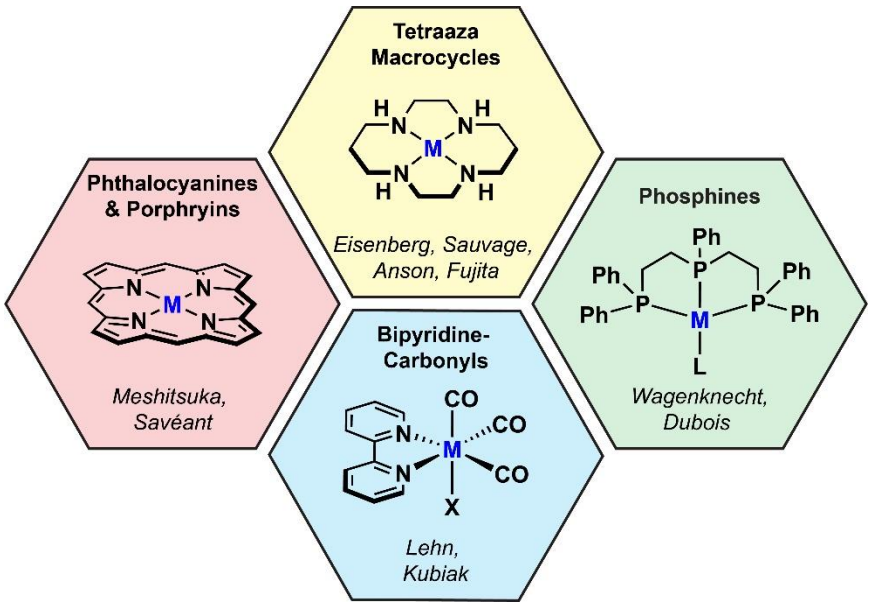


Figure 1.4. Privileged ligand scaffolds for electrochemical CO_2 reduction. Ligands can be characterized into four categories: (1) Phthalocyanine and porphyrin frameworks first reported on by Meshitsuka and greatly expanded upon by Savéant and coworkers; (2) Metal cyclams and other tetraaza macrocycles based on pioneering working from Eisenberg, Sauvage, Anson, and more recent work from Fujita and coworkers; (3) tricarbonyl bipyridine-based complexes first discovered by Lehn and coworkers and further expanded by Kubiak et al. (4) Phosphine complexes were first reported by Wagenknecht and largely applied and expanded by Dubois.

In addition to porphyrins, 1,4,8,11-tetraazacyclotetradecane, also known as cyclam, is the other macrocyclic ligand platform that is renowned for its extremely effective electrochemical reduction of CO_2 (**Figure 1.4**). In 1980, Eisenberg and coworkers published the first report using Ni and Co tetraaza macrocycles for the electrochemical reduction of CO_2 to CO although the performance was somewhat modest as significant amounts of H_2 was also generated under their electrochemical conditions.[100] Shortly after in 1984, Sauvage reported that the closely related complex, $[Ni(cyclam)]^{2+}$, has almost quantitative selectivity towards CO_2 reduction to CO at remarkably mild operating potentials of –1.00 V vs NHE in aqueous electrolyte.[101] Additional electrochemical and pulse radiolysis follow-up studies were conducted by Kelly et al.[102] and Balazs et al.[103] to explain how nickel cyclam is able to reduce CO_2 at potentials that are almost 1.0 V more positive than the formal Ni(II/I) redox couple. The influence of the working electrode material was identified as a critical factor in explaining the remarkable catalytic performance of Ni(cyclam). Ni(cyclam) was shown to adsorb strongly onto the Hg-based working electrodes that were commonly used back then due to their inertness towards catalyzing the HER. It is believed that electrode adsorption alters the solution equilibrium distributions of the different configurational isomers of Ni(cyclam) towards a specific conformation that is more active toward the CO_2RR. The exact structure of the Ni(cyclam) isomer that is active towards catalyzing the CO_2RR however is still debated. A follow up study by Bujno et al.[104] supports the computational findings of Sakaki[105,106] and coworkers that suggests that the active catalytic species needs to undergo isomerization from the major *trans*-III conformer in solution to the *trans*-I isomer prior to CO_2 binding and activation. This finding is contradicted by a computational study from Wu and

colleagues which suggests that the Hg surface favors the *trans*-III conformer over the *trans*-I.[107] In addition to electrode adsorption, Ni(cyclam) can also be poisoned by CO through the formation and precipitation of insoluble $[Ni(cyclam)CO]^0$ onto the Hg electrode or the formation of gaseous and toxic nickel tetracarbonyl ($Ni(CO)_4$), depending on the relative CO concentration.[104,108] To circumvent these issues, Kubiak and coworkers have attempted to convert Ni(cyclam) into a "true" homogenous catalyst that is compatible with more desirable glassy carbon working electrodes through the use of a CO scavenger.[108,109] Detailed computational investigation into the mechanism of homogenous CO_2 reduction catalyzed by Ni(cyclam) was performed by Neese, Ye, and coworkers.[110] More recent work to develop a structure-activity relationship and further expand the application of these cyclam-based catalysts has been undertaken by Fujita and coworkers.[111–115]

The next major class of privileged ligand scaffolds are polypyridyl-based metal complexes that are comprised of bipyridine (bpy) and carbonyl ligands (**Figure 1.4**). These types of complexes are ubiquitous in the field and are the most frequently reported ligands used to produce of CO from CO_2. The first of these types of coordination complexes was reported by Lehn and coworkers in 1984 where they established $Re(bpy)(CO)_3Cl$ as an exceptionally selective catalyst for the CO_2RR at very positive operating potentials.[116] Extensive spectroscopic and computational mechanistic follow-up studies have been conducted on the related Re and Mn catalytic systems that have focused on the role that bpy plays as a redox-active ligand.[117–120] While the bpy ligand is certainly integral to the catalytic performance of this platform, the strong π-accepting carbonyl ligands have been shown in follow up studies to also contribute significantly to the catalytic performance.[117] For example, the hexacarbonyl derivatives of these bpy catalysts still showed catalytic performance with maximum efficiencies for CO production close to 100%.[121] Indeed quantum chemical calculations and spectroscopic measurements on $[Re(bpy)(CO)_3]^-$ (and its Mn derivative) do support these experimental findings by establishing that one electron occupies the bpy π^* orbital but the second electron is placed into a metal d_{z^2} orbital that is strongly delocalized into the three carbonyl ligands.[118–120] More current work on these systems has been largely done by Kubiak, Fujita, and coworkers who have greatly expanded the mechanistic understanding and performance of these ligand frameworks by incorporating bulky substituents that aid in shutting down deleterious dimerization pathways and by tethering the catalysts to electrodes and other heterogeneous supports. This work has been summarized in detail in a recent report by Fujita.[122]

Phosphines are the final class of ligands that will be discussed in this section. The first of these catalysts was reported in 1984 by Slater and Wagenknecht who showed that $Rh(dppe)_2Cl$ (dppe = 1,2-bis(diphenylphosphino)ethane) could reduce CO_2 to formate in acetonitrile with reasonable selectivity.[123] They were able to isolate and characterize a Rh hydride species that showed slow reactivity with CO_2 accounting the propensity of the reduced catalyst to build up in solution leading to the formation of catalytically inactive dimers. DuBois and coworkers later expanded these chelating phosphine systems and showed that product selectivity can be switched to CO formation with the exchange of the Rh metal center for Pd; however, the long-term activity of these types of complexes still appears to be quite limited due to detrimental formation of Pd dimers.[124] The catalytic performance was significantly improved through the synthesis of a bimetallic Pd phosphine complex that was stitched together with a 1,3-bis(phosphaneyl)benzene linker.[125] Kinetic analysis however showed that the reaction is 0.5 order in catalyst, and due to the geometric orientation of the two metal centers they operate independently as opposed to cooperatively – which could greatly enhance reaction rates or shift product distributions towards

more value-added products. Renewed interest in the use of phosphine complexes was sparked by a recent report by Bi et al. who showed that an Fe-triphos complex can reduce CO_2 to into formate and methanol at high efficiencies (97% and 69%, respectively) with the addition of diethylamine.[126] They propose the diethylamine is critical to the formation of a carbamic acid intermediate that is on-pathway to methanol formation.

1.5 Electrochemical Analysis and Benchmarking Catalysts

The effectiveness of a molecular catalyst is determined by its properties; more specifically, the robustness, selectivity, turnover frequency (i.e. rate), and overpotential (η) of a catalyst for the CO_2RR are what defines a catalyst as "good". Quantitation of these metrics allows for it to be directly compared and benchmarked to other molecular systems reported in the literature. In this section, we will provide an outline for how to go about experimentally investigating a new coordination complex as a potential electrocatalyst for CO_2 reduction. First, we will discuss a few of the key electrochemical techniques that are used to screen and evaluate a new perspective catalyst. These techniques are utilized throughout this thesis so a fundamental understanding on how they operate and how to interpret the data generated from these measurements is integral to understanding the work presented in the following chapters. Next, we will define the benchmarking metrics listed above and discuss the methods available to quantify them. Finally, the discussion will be expanded to include the construction and analysis of catalytic Taffel plots that allow for a more accurate comparison between catalytic systems by accounting for differences in electrochemical operating conditions (e.g., applied potential, electrode materials, electrolyte composition, identity, concentration of acids, etc.).

The go-to "bread and butter" techniques for the experimental electrochemist are cyclic voltammetry (CV) and controlled potential electrolysis (CPE), also known as bulk electrolysis. CV is a non-destructive, diffusion-controlled technique that allows for the electrochemical and catalytic properties of a new coordination complex to be evaluated extremely fast (data collected on minute timescales) with the use of little material (mg quantities). **Figure 1.5a** and **1.5b** depicts the basics of a typical CV experiment using the reversible, single-electron reduction of ferrocenium (Fc^+) into ferrocene (Fc) as an example system.[127] The accompanying concentration profiles for Fc^+ (blue line) and Fc (green line) are also depicted which show how the concentrations of the reactant (Fc^+) and product (Fc) change as a function of applied potential (V vs Fc/Fc^+) and distance (d) from the electrode surface to the bulk solution. In a typical CV experiment, the potential of the working electrode is systematically swept in the negative direction from an initial, starting potential (point A) to a switching potential denoted by point D in **Figure 1.5**. In the forward sweep, the cathodic process occurs where the Fc^+ near the electrode surface is reduced by a single electron to Fc. The current response does not continue to increase as the current is swept to more reducing potentials and instead a characteristic peak-shaped wave is produced. This occurs because CV is a diffusion-controlled process and therefore eventually the concentration of Fc^+ near the electrode surface begins to deplete causing the decay in current that is observed from point C to D. After the cathodic process has occurred, the switching potential is reached (point D) where, as the name denotes, the potential is swept in the reverse, positive direction where the anodic process (i.e. the oxidation of Fc to Fc^+) occurs. An identical peak-shaped wave is observed for the oxidation of Fc back to Fc^+ as the reverse process is also diffusion controlled; this produces the "duck" shaped plot that is characteristic of cyclic voltammetry. Experimentally, the chemist has

control over the selection of the initial, switching, and final potentials, the scan rate (ν), and number of cycles conducted in the voltammetry experiment. This allows the redox properties of new potential catalyst to be screened and characterized under inert atmosphere in a fast and effective manner. Moreover, the ability to control the potential window and the electron transfer rate by changing the scan rate provides powerful experimental handles to probe the mechanisms of electrochemical reactions and to some extent, chemical reactions that are coupled to electron transfer processes. For a more comprehensive, detailed introduction into the world of electrochemistry that includes both theoretical and practical aspects we direct the reader to the excellent reviews written by the Dempsey group and the textbook "*Understanding Voltammetry*" by Compton and Banks.[127–130]

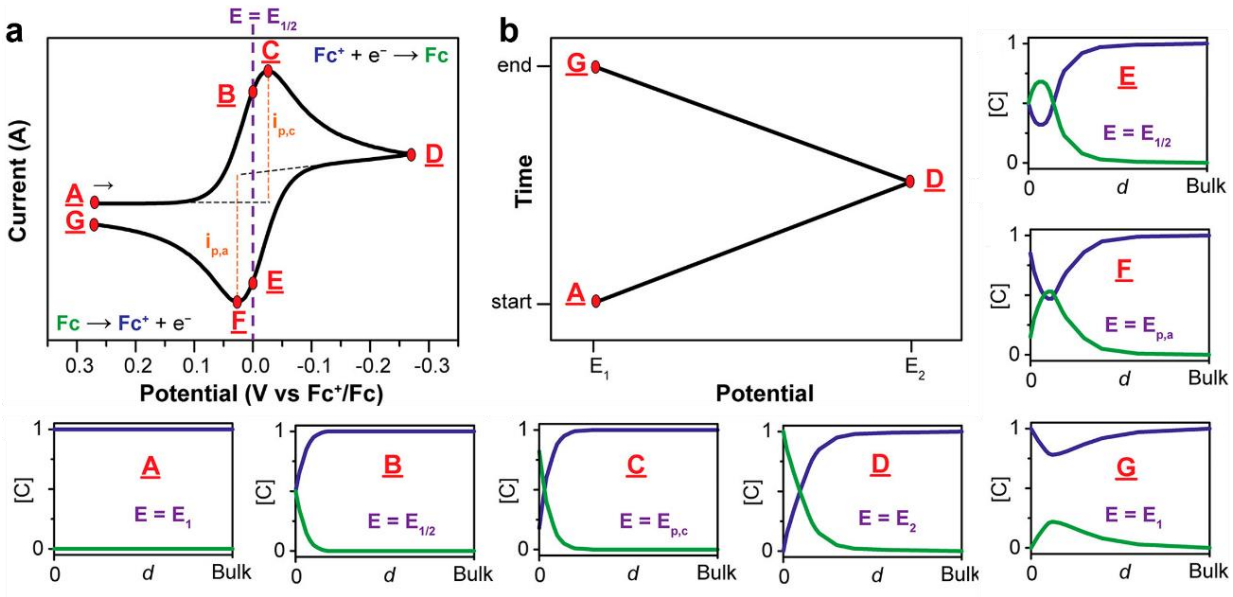


Figure 1.5. Basics of a CV experiment. (a) Voltammogram for the reversible, single-electron reduction of Fc^+ into Fc. (b) Schematic representation of the CV experiment showing the change in applied potential over time from the initial potential, A, to the switching potential, D, finally back to the final potential, G. Concentration profiles for Fc^+ (blue) and Fc (green) as a function of distance, d, from the electrode surface to the bulk solution are provided in the accompanying smaller graphs. Adapted with permission from Reference 127.

Once the electrochemical properties of a potential catalyst have been evaluated by CV under inert atmosphere (typically N_2 or Ar is used), its catalytic properties can be efficiently screened quickly by looking at how the voltammograms change in the presence of substrate (i.e. CO_2 and protons). Generally, if a complex is an active CO_2 reduction catalyst, it should change in three characteristic ways upon addition of CO_2 and a proton source. These changes can be understood by considering **Figure 1.6** which depicts a simplified general mechanistic scheme for electrocatalysis. In this general electrocatalytic scheme, a heterogenous electron transfer event first occurs with n electrons being transferred from the electrode to the molecular catalyst, Cat^{n+}, at a specified heterogenous rate constant, k_h, to produce the active catalytic species, Cat. Cat then reduces the substrate (i.e. CO_2) and converts it into the desired product (e.g. CO) through additional electrochemical and chemical steps that are not depicted in this simplified scheme. This type of

catalytic process alters the voltametric response by first causing a significant increase in the diffusion limited current because the current response is no longer entirely limited by the concentration of unreduced catalyst (Cat^{n+}) near the electrode surface. Electron transfer from the reduced, active catalytic species, Cat, to CO_2 drives the formation of the desired products (i.e. CO) and replenishes the supply of Cat^{n+} near the electrode surface thus explaining the large increase in current relative to what is observed in the absence of CO_2. Second, because a catalyst enhances the rate of a chemical reaction by lowering the activation barrier, the diffusion-controlled current should also be shifted anodically, towards less reducing potentials. Finally, the reversibility in the return oxidation wave is lost due to the chemical reaction between Cat and CO_2 because Cat is re-oxidized chemically via an electron transfer reaction with CO_2 rather than being electrochemically oxidized at the electrode surface. Taken together, these three changes constitute what we refer to throughout this thesis as a catalytic wave or a catalytic response; a representative example data set is given in **Figure 1.7a** to clearly illustrate these characteristics. This analysis illuminates why CV is such a powerful technique as it allows many potential catalysts to be screened across a wide range of experimental conditions and to very quickly (minutes) determine if it is a promising catalyst by simply looking at how the shape of the electrochemical wave changes (vide infra).

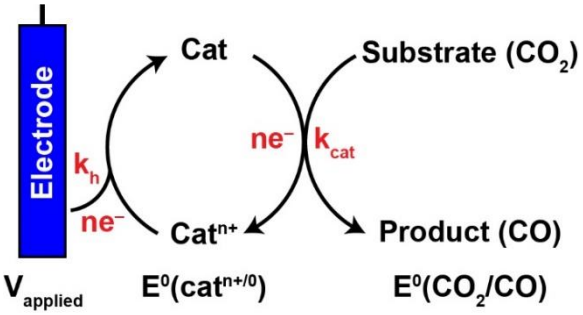


Figure 1.6. General schematic representation of electrocatalysis. Electrons (ne^-) are shuttled from the electrode to the catalyst (Cat^{n+}) to generate the active, reduced catalyst (Cat) that can then interact with and reduce the substrate (CO_2) at an appreciable rate constant, k_{cat}. An optimal catalyst participates in both the electron transfer reaction and accelerates the chemical reaction. To do so, the thermodynamics of the system must be appropriately redox matched such that the redox potential for the electron transfer reaction ($E^0(cat^{n+/0})$) matches the redox potential of the chemical reaction that is being catalyzed, $E^0(CO_2/CO)$.

While CV is an extremely powerful technique for quickly screening and identifying promising catalysts and electrochemical conditions, it doesn't provide any information regarding which products are generated. To address these questions, we turn to CPE experiments. In a typical bulk electrolysis experiment, the potential is held constant at select potentials along the catalytic wave and the corresponding current is measured over time (see **Figure 1.7b**). The goal of the experiment is to pass as much charge (Q, reported in units of Coulombs, C) as possible to generate as much product as possible so that it can be detected and quantified by complementary analytical techniques. For example, gaseous products can be detected and quantified by gas chromatography while liquid products are typically analyzed by ^1H NMR or various colorimetric assays depending on the specific analyte of interest. From these experiments, the selectivity of the catalyst for the reaction of interest can be determined relative to other undesirable background reactions or decomposition pathways. The robustness of a catalyst can also be probed through CPE

experiments by monitoring how the current density (current divided by the geometric surface area of the working electrode) changes over the course of the experiment. The details and nuances of this are beyond the scope of this chapter but is covered in an excellent review by Lee et al. on probing catalyst decomposition and degradation with CPE and other complimentary electrochemical techniques.[131] Some of these analyses are discussed and performed in later chapters to establish the homogenous, molecular nature of our iron catalyst.

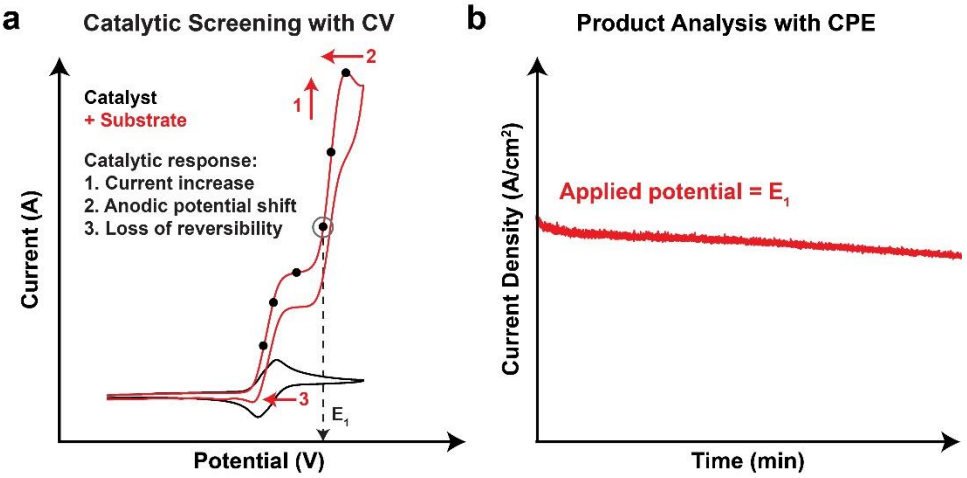


Figure 1.7. Representative electrochemical data for catalyst screening. (a) CV analysis of a catalyst in the absence and presence of substrate to illustrate how the catalytic wave should change. Note that this data is discussed in Chapters 5 and 6 and displays the formation of two distinct catalytic waves. (b) CPE analysis is done at selected points (e.g., applied potential, E_1) along the catalytic wave that are indicated by black dots. The potential is held constant over time and the resultant products are detected and analyzed using complementary analytical measurements.

Once a catalyst and the appropriate electrochemical conditions have been identified, it is important to determine how the catalyst performs relative to other systems reported in the literature. When benchmarking a new catalyst, there are three metrics that are often considered. The first is the Faradaic efficiency (FE) of the catalysts. FE is a selectivity measurement that reports the reaction yield with respect to electrons. Mathematically, it is describing how many electrons are going to produce the desired product (charge used to produce the product, $Q_{product}$) over the total electrons that are passed during the electrolysis experiment (total charged passed during experiment, Q_{total}; see **Equation 1.1**).

$$FE(\%) = \left(\frac{Q_{product}}{Q_{total}}\right) * 100 = \left(\frac{znF}{Q}\right) * 100 \qquad \textbf{Equation 1.1}$$

In practice, $Q_{product}$ is not an experimental observable as there is no effective way to measure how much of the charge that is being passed during the CPE experiment goes towards the production of products. Instead, $Q_{product}$ can be determined indirectly by measuring the amount of product generated (in mols, n) and multiplying it by the number of electrons required to produce the desired product (z) and Faraday's constant (F = 96486 C mol^{-1}) which describes the amount of charge produced by a mol of electrons. Dividing by the total charge (Q) passed during the electrolysis experiment, which is measured directly by the potentiostat, then gives the desired FE, which is

multiplied by 100 so that it can be reported as a percentage (**Equation 1.1**). Naturally, a desirable catalyst will operate with FE's that are as close to 100% as possible for the preferred product.

The next metric that is important to determine for a novel catalyst is the overpotential (η) at which it operates. The overpotential is a thermodynamic parameter that describes the additional potential, beyond the thermodynamic requirement, needed to drive the half-cell reaction at a specific rate. Mathematically, it is defined for reductive half-reactions as the difference between the standard redox potential for the formation of product B from substrate A ($E^0_{A/B}$) (also referred to as the equilibrium potential) and the applied potential ($E_{applied}$; see **Equation 1.2**); where the "best" catalysts operate at an overpotential as close to the thermodynamic potential as possible (i.e., η = 0) as that represents conditions where the minimum amount of excess energy is required to drive the catalytic reaction. If done correctly (see discussion below), reporting the performance of the catalyst in terms of overpotential is extremely helpful for comparison with other catalysts, because overpotential is independent of the experimental conditions used (e.g., electrolyte composition, acid identity, acid concentration, etc.).

$$\eta = E^0_{A/B} - E_{applied} \qquad \textbf{Equation 1.2}$$

Therefore, to experimentally determine the overpotential range through which a catalyst operates one only needs to know the equilibrium potential for the transformation of interest, $E^0_{A/B}$, because $E_{applied}$ is selected by the experimentalist and is often systematically varied in order to evaluate how the accompanying rates of catalysis change as a function of overpotential (i.e., Catalytic Tafel plot analysis, vide infra). For the purposes of the work presented in this thesis, where the major CO_2 reduction product is CO, we will focus the remainder of this discussion on how to accurately determine values for $E^0_{CO_2/CO}$. To accurately convert and report the overpotential of a catalyst, the standard redox potential must be known under the exact experiment conditions employed. While the standard thermodynamic potential for the conversion of CO_2 into CO is well known in aqueous electrolyte (−0.106 V vs SHE[132] which converts to approximately −0.730 V vs Fc/Fc^+[25]), it is much more complicated to determine accurately in organic electrolytes because it varies much more extensively with changes to the electrolyte identity (e.g. organic solvent identity) and composition (e.g. identity and concentration of acid source). As most molecular electrocatalysts operate in organic electrolytes due to solubility constraints, this represents a major problem and source of inaccuracy when benchmarking catalytic performance. Naturally, the performance of a catalyst can be artificially inflated by selecting an inaccurate value for $E^0_{CO_2/CO}$ that is more negative than the actual value, leading to much smaller overpotentials. For these reasons, it is extremely important that both the correct method is utilized to calculate $E^0_{CO_2/CO}$ and thus the overpotential, and that the method that is used is made transparent to the reader.

Two main methods are utilized in the literature to convert applied potentials into overpotentials in organic electrolyte in the presence of an exogenous acid source. The first approach is based on a protocol published by Savéant and coworkers where they derive a relationship between $E^0_{CO_2/CO}$ and the pK_a of the acid using a series of thermodynamic cycles obtained for standard states in acetonitrile and N,N-dimethylformamide (DMF) (**Equations 1.3** and **1.4**).[95]

$$E^0_{CO_2/CO,CH_3CN,AH} = 0.349 - \frac{RTln10}{F} pK_{a,HA,CH_3CN} \text{ (V vs NHE)} \quad \textbf{Equation 1.3}$$

$$E^0_{CO_2/CO,DMF,AH} = -0.259 - \frac{RTln10}{F} pK_{a,HA,DMF} \text{ (V vs NHE)} \quad \textbf{Equation 1.4}$$

These equations require that the pK_a of the strongest acid present in solution be considered. If any significant amount of water is present in the system, the most acidic species in solution is carbonic acid (H_2CO_3). Using additional thermodynamic square schemes, Savéant and coworkers extracted pK_a's in acetonitrile and DMF of 7.37 and 17.03, respectively.[95] Using **Equations 1.3** and **1.4**, this then equates to values for $E^0_{CO_2/CO}$ of –0.650 (–1.28 V vs Fc/Fc^+)[25] and –6.90 V (–1.32 V vs Fc/Fc^+)[25] vs NHE, respectively. These values are heavily utilized within the literature because they are significantly more negative than the ones reported by Matsubara and Mayer et al., which result in more "favorable" overpotentials values that are closer to zero (see below). Moreover, some reports take even further steps to, in our opinion, to artificially "inflate" the performance of their catalysts by using the pK_a of phenol rather than carbonic acid to calculate the overpotentials of their catalysts.[133] The $E^0_{CO_2/CO}$ with phenol as an acid source is –0.821 V vs NHE in acetonitrile which represents a shocking decrease in overpotential by 171 mV if one claims that no water is present in their catalytic conditions. Given that most electrolytes and acid sources utilized for electrochemistry are hydroscopic (tetrabutylammonium salts in particular) and that most groups do not report rigorously drying and storing these salts in dry environments, this claim seems to be dubious at best. Furthermore, as water is often a product of electrochemical CO_2 reduction, it seems highly unlikely that an electrochemical system is "rigorously" dry without the use of some sort of desiccant in the electrolysis cell which is far from commonplace.

The major critique to Savéant's method is that their derivation and equations rely on thermodynamic assumptions that do not often rigorously apply to the actual experimental conditions. For example, they define the CO_2 and CO standard states to be 1 M. This assumption is far from accurate given that the solubility of 1 atmosphere of CO_2 in acetonitrile[134] and DMF[135] at room temperature is reported as 0.28 and 0.20 M, respectively. Mayer et al. correct these assumptions and report an alternative method to estimate overpotential based on thermodynamic cycles that combine the free energy for transferring water from aqueous solution to organic solvent.[136] Their method gives a much more conservative measure for $E^0_{CO_2/CO}$ of –0.12 V and –0.73 V vs Fc/Fc^+ in acetonitrile and DMF, respectively.[136] These values are shockingly 1.16 V and 0.59 V more positive than the analogous ones reported above by Savéant. Granted, the values reported by Mayer do not account for the addition of a proton source such as phenol or 2,2,2-trifluorethanol, which are often utilized in CO_2 reduction catalysis at molar quantities. Matsubara has further expanded upon this method to include calculations for $E^0_{CO_2/CO}$ in acetonitrile and DMF with varying concentrations of water as the proton source using **Equation 1.5**.[137–139]

$$E^0_{CO_2/CO,CH_3CN,AH}(vs\ SHE) = \frac{-1}{2F}[\Delta_f G^0(CO_{(g)}) + \Delta_f G^0(H_2O_{(l)}) + \Delta^{1\rightarrow sol}_{tr} G^0(H_2O) - \Delta_f G^0(CO_{2(g)}) + 2RT(ln10) pK^{H_2O}_{a,abs}(CO_{2(g)} + H_2O_{(sol,x)})] \quad \textbf{Equation 1.5}$$

Where F is Faraday's constant and $\Delta_f G^0(CO_{(g)})$, $\Delta_f G^0(CO_{2(g)})$, and $\Delta_f G^0(H_2O_{(l)})$ are the standard formation Gibbs energy changes of CO and CO_2 in the gas phase, and pure liquid H_2O, respectively. At standard pressure (1 bar) and temperature (298.15 K) these values are reported as

–137.163, –394.389, and –237.178 kJ/mol. The term $\Delta_{tr}^{1\rightarrow sol}G^{0}(H_2O)$ is the standard Gibbs energy change upon transfer of water from pure liquid to an acetonitrile-water mixture, for which both standard states are taken as unit mole fractions of water. R is the gas constant, and T the temperature. $pK_{a,abs}^{H_2O}\left(CO_{2(g)}+H_2O_{(sol,x)}\right)$ is the absolute acidity constant for acetonitrile-water mixtures which can be measured and have been tabulated by Matsubara.[139] We have utilized this method throughout this thesis to calculate the overpotential since the strongest acid present in our solution is water, making this analysis most appropriate. Even with this more accurate approach, $pK_{a,abs}^{H_2O}\left(CO_{2(g)}+H_2O_{(sol,x)}\right)$ varies significantly as a function of water concentration in acetonitrile mixtures which causes the tabulated standard redox potentials to fluctuate by up to 500 mV across the water-acetonitrile mixtures examined by Matsubara (*i.e.*, –1.57 V vs Fc/Fc^+ for 0.5 M water; –0.95 V vs Fc/Fc^+ for 55 M water). Experimentally, it is hard to determine the exact amount of water present. Therefore, as a conservative estimate, we selected the midpoint value of –1.27 V vs Fc/Fc^+ because conditions of high-water concentration do not apply for our experimental conditions reported throughout this thesis, and low-water concentrations (less than 0.5 M water) leads to an estimated CO_2 standard redox potential that is more negative than where some of our reported catalysts operate for CO_2 reduction, which would then result in negative overpotential values. We do further note that this value of –1.27 V vs Fc/Fc^+ for $E_{CO_2/CO}^{0}$ agrees well with our calculated value reported in Chapter 6 (see Materials and Methods for further details). Overall, the purpose of this discussion is to illustrate the complexities and challenges associated with calculating overpotentials and to further encourage the reader to exercise caution when comparing the thermodynamics of catalytic systems based solely on reported overpotential. It is essential that the method used to calculate the overpotential is determined to be accurate and equivalent across all catalysts under comparison. Moreover, for the purposes of transparency, we believe it is also best practice to provide the reduction potential relative to the Fc/Fc^+ couple whenever reporting an overpotential. This is routinely done throughout this thesis. All references to overpotential are accompanied by the applied potential relative to Fc/Fc^+. For a more detailed discussion regarding the practices and challenges surrounding accurate overpotential determination, we direct the reader to the recent review article published by Miller and coworkers.[140]

The final benchmarking metric that is important to measure is the turnover frequency (TOF) of the catalyst. The TOF is a potential-dependent kinetic parameter that reports the number of mols of product (e.g. CO) that is evolved per unit of time per mole of catalyst. When the applied potential is sufficiently negative of the redox couple of the catalyst such that effectively all the catalyst in the diffusion layer is in the active form, the TOF is no longer dependent on potential. The resulting value represents the observed rate constant (k_{obs}) which is also often referred to as the TOF_{max}. This is what gives rise to the distinctive "hockey stick" shape of the catalytic Tafel plots used to directly compare the performance of catalytic systems (vide infra). Measuring the TOF can be complex for homogenous molecular catalyst because the TOF describes only the activity of the catalyst molecules that are contained within the reaction-diffusion layer of the electrode and therefore is not equal to the concentration of catalyst in the bulk solution. Utilization of the concentration of the catalyst in bulk solution would result in grossly underestimated values for TOF. Therefore, in order to measure the TOF, we must know what the concentration of "active" catalyst is near the electrode surface. To estimate the TOF based solely on the CV responses various approximations must be made to ensure that the concentration of the catalyst is accounted for appropriately. The TOF can be estimated quite quickly by CV with a few different methods

depending on the shape of the CV response; however, because CV waveshapes are dependent on factors such as scan rate and catalyst and substrate concentration, the accurate estimation of rate constants by CV requires some understanding of the mechanisms that are operative. Thankfully, much of the "hard work" required to derive these relationships and simulate the shape of the CV waveforms that apply to each method to estimate the TOF has already been mapped out by Savéant and coworkers.[141,142] They have determined how the CV responses change for a one-electron reduction where the rate-limiting step is homogenous electron transfer (i.e. an $E_r C_i'$ mechanism) as a function of the parameters λ and γ. Where λ is a kinetic parameter that is defined by **Equation 1.6** and is dependent on the rate constant for the homogenous electron transfer (k_e) and γ is the excess factor that accounts for how much excess substrate (C_A^0) exist in the bulk solution relative to the bulk concentration of catalyst (C_P^0) (**Equation 1.7**).

$$\lambda = \left(\frac{RT}{F}\right)\left(\frac{k_e C_P^0}{\nu}\right) \qquad \textbf{Equation 1.6}$$

$$\gamma = \frac{C_A^0}{C_P^0} \qquad \textbf{Equation 1.7}$$

A kinetic zone diagram can be generated from this analysis by creating a two-dimensional plot of the log(λ) as a function of the log(γ) which is depicted in **Figure 1.7**.[128,129] This kinetic zone diagram is immensely useful because it provides vital kinetic information about a catalyst based entirely on the shape of the catalytic wave which then informs which equations can be applied to extract the TOF and TOF_{max} values for the catalyst. Moreover, it also shows how one can traverse into other kinetic zones by altering experimental handles such as substrate concentration (C_A^0), bulk catalyst concentration (C_P^0), and scan rate (ν) (please refer to the compass rose in **Figure 1.7**).

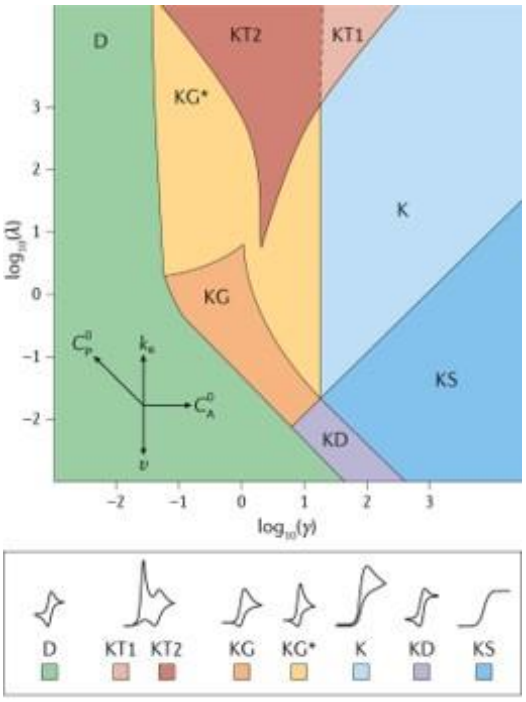


Figure 1.8. Kinetic zone diagram and the accompanying simulated CV waveshapes for the one electron reduction of substrate A to product B via a catalytic redox mediator, P. Adapted with permission from Reference 129.

Below we give a very brief description of the kinetic zones plotted in **Figure 1.8** and the appropriate methods and accompanying equations that can be used to extract rate information. A more detailed discussion of this kinetic zone diagram and how it relates to more complex mechanism is beyond the scope of this introduction chapter. For a more in-depth discussion on these topics we direct the reader to the excellent reviews written by the Dempsey group and the work from Savéant and coworkers.[128,129,141,142]

Zone D (no catalysis): The CV waveshape illustrated in zone D (green) is typical of a reversible, fast single-electron transfer process and therefore is characteristic of a region where no catalysis occurs.

Zone KS (Pure catalytic condition without substrate consumption): Zone KS (blue) can be determined by its distinctive "S-shaped" wave where the current on the reverse scan is superimposed upon what was recorded in the forward scan. This plateau occurs because the substrate concentration at the electrode surface is equal to the bulk solution and therefore catalysis is limited by the rate determining step and not by mass transport. In this region, catalytic rates and TOF_{max} can be determined very easily by measuring CVs in the absence and presence of substrate and using catalytic plateau analysis which is given by **Equation 1.8** for a general multistep catalytic reaction:

$$\frac{i_{pl}}{i_p} = \frac{1}{0.446}\sqrt{\left(\frac{RT}{nFv}\right)n'k_{obs}} \qquad \textbf{Equation 1.8}$$

Where i_{pl} is the current at the plateau of the "S-shaped" wave observed when substrate is present and i_p is the peak current of the catalytic wave that is obtained in the absence of substrate. The number of electrons transferred to the catalyst is described by n and n' is the number of catalyst equivalents used per turnover. The mathematical form of this approach changes slightly depending on the specific mechanistic pathway; deviations of this equation are discussed and reported in much more detail in Reference 128. It is also important to note that this approach is independent of the CV scan rate, ν, used to record the voltammograms. In fact, if the plateau current increases as a function of scan rate then catalytic plateau analysis does not rigorously apply and the rates obtained using it will be underestimates. The scan rate appears in the equation because the Randles-Sevcik equation is utilized to derive the relationship between i_{pl} and i_p. Collecting CV data at very fast scan rates where there is no longer a dependence on the catalytic current can sometimes be utilized to overcome this requirement. For examples of this see the case studies discussed in Reference 129.

Zone K (Pure kinetic conditions with substrate consumption): Zone K (light blue) is defined by the formation of a peak-shaped wave in the catalytic voltammogram. This type of response is exceptionally common for molecular electrocatalysts. In this region, the kinetics are controlled by the competition between substrate consumption by the rate determining step and the diffusion of fresh substrate to the electrode surface. Additionally, other nonideal side phenomena such as catalyst degradation or poisoning can also result in the formation of a peak-shaped wave. In this region catalytic plateau current analysis no longer applies because obviously a plateau is no longer observed and therefore there is significant ambiguity surrounding how to extract an accurate value for i_{pl}. Furthermore, most peak-shaped waves increase as a function of the scan rate which makes its even more unclear how to extract an accurate value for i_{pl} from these data. Instead, foot-of-the-wave analysis (FOWA) can be used to estimate rates following a method that was developed and pioneered by Savéant. A general expression for FOWA is given in **Equation 1.9**:

$$\frac{i}{i_p^0} = \frac{2.24\sqrt{\frac{k_{obs}}{f}}}{1+e^{[f(E-E^0_{cat})]}} \qquad \textbf{Equation 1.9}$$

where i is the current, E is the potential, v is the scan rate (V/s), k_{obs} is the observed rate constant, and $f = F/RT = 38.94\ V^{-1}$. Thus, a "FOW" plot of $\frac{i}{i_p^0}$ versus $\frac{1}{1+e^{[f(E-E^0_{cat})]}}$ yields a straight line with the slope of $2.24\sqrt{\frac{k_{obs}}{fv}}$, from which k_{obs} may be determined. A more detailed discussion regarding how this equation changes with mechanism is provided in Reference 128. FOWA is used in Chapters 3 and 4 of this thesis to extract CO_2 reduction rates for the iron porphyrin catalysts investigated as they have sufficient linear FOW regions that can easily be fit. The kinetics of the iron polypyridyl catalyst discussed in Chapters 5 and 6 are not described accurately by FOWA due to the small linear region which makes linear fitting ambiguous (see Chapter 5 for more details).

Zones KT1 and KT2 (total catalysis limited by substrate consumption). Zone KT1 (light red) and KT2 (red) are characteristic of catalytic CV waveshapes that display a large peak shaped catalytic wave followed by a reversible redox couple. In this region catalysis occurs so fast that all the substrate is entirely consumed within the reaction-diffusion layer. This gives rise to the large,

peak shaped wave. Therefore, because the substrate is entirely consumed by fast catalysis, there is a significant amount of reduced catalyst remaining at the electrode surface that can be re-oxidized heterogeneously upon application of the cathodic potentials on the return CV scan. Rates for CVs showing total catalysis behavior can be extracted using peak shift analysis which uses the shift in redox potential of the catalytic wave as a function of scan rate to estimate the observed rate constant. A general mathematical description of this relationship is provided in **Equation 1.10**:

$$E_p = E^{0\prime} - 0.78\frac{RT}{F} + \frac{RT}{2F}\ln\left(\frac{RT}{F}\frac{k_{obs}}{v}\right) \qquad \textbf{Equation 1.10}$$

where E_p is the new peak potential relative to the original potential prior to the shift described by $E^{0\prime}$ and k_{obs} is the observed rate constant for the irreversible chemical step. For a more detailed discussion of this method and some case study examples we refer to the reader to Reference 129.

Zones KD, KG, and KG*: Catalysis described by zones KD (purple), KG (orange), and KG* (light orange) are characterized by the formation of peak-shaped catalytic waves along with an additional smaller redox wave corresponding to re-oxidation of the catalyst that is observed on the return scan. In zone KD, no substrate consumption is observed because its operating in a region where the excess factor (γ) is large (**Equation 1.7**). A canonical "S-shaped" wave however is not produced because the kinetics are relatively sluggish as distinguished by the smaller λ value in this region relative to the KS region. Plateau current analysis (**Equation 1.8**) can still be applied to extract rate information from catalysts that express waveshapes consistent with this KD region.[128] Alternatively, it is often possible to transition into the KS region where plateau current analysis rigorously applies by decreasing the scan rate or increasing the substrate concentration. Zones KG and KG* differ from KD in the sense that they are in fact substrate limited. While appropriate rates in these regions can be determined with the peak shift analysis, the catalytic conditions such as scan rate and substrate or catalyst concentrations can also be altered to traverse into another kinetic region where the kinetics can be extracted more easily.

Alternatively, instead of estimating the rates from CV, the observed rate constants can also be directly measured from CPE data collected across a range of applied potentials. While this method is much more time-consuming and requires a lot more catalyst, it does provide absolute determination of the rates which is enable by the direct measurement and quantification of products that is assumed to be close to 100% in the above methods. This assumption is often not rigorously true for most molecular catalysts and therefore extraction of rates with either of the three CV-based methods described above represents an optimistic estimate for their actual performance. **Equation 1.11** describes the relationship between the experimental specific current density (I) that is averaged across the entire CPE experiment and the observed rate constant (*k*) as originally reported by Savéant and coworkers.[143,144] It is important to note that the specific current density is defined as the fraction of current density that goes to generate the desired product and is therefore calculated by multiplying the current density by the FE. For this reason, this method accounts for the selectivity of the catalyst when determining its TOF.

$$\frac{I}{F} = \sqrt{2kC_A^0 D_p}\,\frac{C_p}{1+exp\left[\frac{F}{RT}\left(E-E^0_{redox}\right)\right]} \qquad \textbf{Equation 1.11}$$

Where E is the applied potential, E^0_{redox}, is the redox potential of the catalyst in the absence of substrate, D_p is the diffusion coefficient of the catalyst that can be easily measured by CV using the Randles-Sevcik equation. This is the method that is used in Chapters 5 and 6 to obtain TOFs for our iron polypyridyl complexes.

Finally, now that we have covered the basics of CV and CPE, defined the main benchmarking parameters, and provided some discussion into the nuances associated with their calculations, we can end this section with a discussion on how to effectively compare multiple catalysts to one another once we have benchmarked their performance. To do this it is often instructive to construct a catalytic Tafel plot by plotting the log(TOF) of a catalyst as a function of its overpotential. **Equation 1.12** describes the mathematical relationship between the TOF and the overpotential that is used to construct the Tafel plot.

$$TOF = \frac{k_{obs} * n}{1 + e^{\left[\frac{F}{RT}(E - E^0_{redox})\right]}} \qquad \textbf{Equation 1.12}$$

An example Tafel plot is displayed in **Figure 1.9** so that the utility and power of Tafel analysis can be easily conveyed. Each catalyst in **Figure 1.9** is represented by a single-colored line that fully describes its thermodynamic properties (η) on the x-axis and the accompanying kinetic parameters (TOF) on the y-axis. Therefore, this allows for immediate relative determination of which catalysts are "good" and which are "bad" because an excellent catalyst will operate with fast reaction rates at small input of energy beyond the thermodynamic minimum (i.e. small η). These catalysts thus appear in the upper left-hand corner of the Tafel plot. Alternatively, a poorly preforming catalyst will occur on the opposite, lower right-hand corner because those complexes operate with very slow rates even when extremely large overpotentials are applied. This type of catalytic Tafel analysis is conducted throughout this thesis so that the performance of the novel molecular catalytic systems developed here can be compared and contextualized to other competitive systems in the field. Taken, together we hope that this electrochemistry overview serves as the "crash-course" required to fully understand the data and discussion presented in the following chapters.

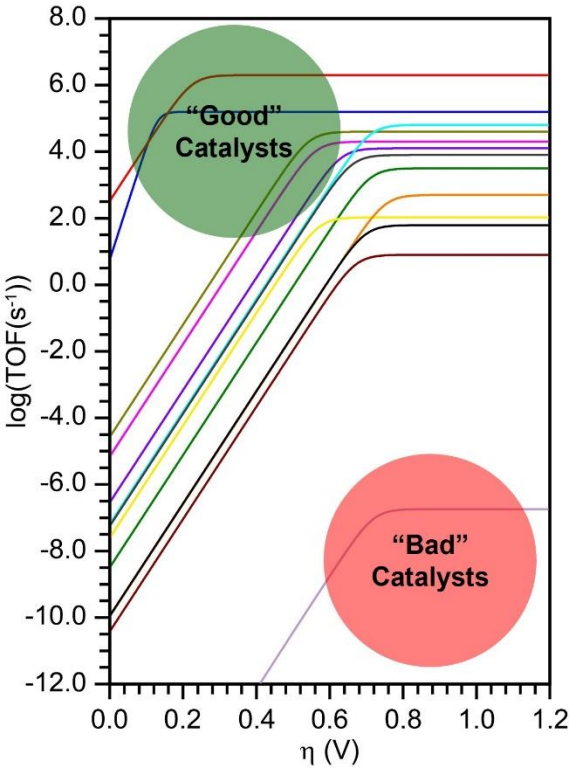


Figure 1.9. Representative example of a catalytic Tafel plot comparing multiple homogenous catalysts for the conversion of CO_2 to CO. Each colored line represents a single catalyst. The "best" catalysts occur in the upper left and corner which is denoted by the green circle. Poor catalysts display behavior depicted in the opposite corner in the region highlighted by the red circle.

1.6 Conclusion

In summary, the goal of this chapter is to briefly outline the motivations for this work. As carbon emissions continue to increase, society will continue to face major scientific challenges that must be overcome in order to restore natural balance to the carbon cycle. The electrochemical conversion of CO_2 using renewable sources of electricity represents a promising solution, but it requires the use of exceptionally cheap, abundant, selective, and robust catalysts for these goals to be met. The content of this thesis is focused on the development of new catalytic systems to electrochemically reduce CO_2 into value-added products. The thesis is structured as follows: Chapter 2 discusses the development of a molecular-material hybrid approach to converting CO_2 into CO and formate that is inspired by how enzymes utilize redox-reservoirs.[57] Chapter 3 explores the use of hydrogen bond donor mimics to enhance CO_2 reduction catalysis on an iron porphyrin scaffold by incorporating bis-aryl amides at various points along the second coordination sphere.[145] Chapter 4 expands upon this concept to investigate how the number of hydrogen-bond donors can alter the catalytic performance by switching the one-point amide donor with a two-point hydrogen bond donating, urea moiety. Chapter 5 takes inspiration from natures' use of redox active cofactors to perform catalysis without the need to toggle oxidation states. We show how this concept of electron delocalization can be used to engender exceptional catalytic activity onto an iron polypyridyl scaffold through metal–ligand cooperativity.[87] A detailed combined experimental and theoretical mechanistic study of this system is presented in Chapter 6. Finally, Chapter 7 attempts

to expand the ligand design strategy from Chapters 5 and 6 to enable the reduction of CO_2 beyond the two electron products, CO and formate. Together, these chapters illustrate how nature can direct the rational design of new and interesting molecular catalysts.

1.7 References

(1) Schmalensee, R.; Stoker, T. M.; Judson, R. A. World Carbon Dioxide Emissions: 1950–2050. *Rev. Econ. Stat.* **1998**, *80*, 15–27.

(2) Solomon, S., Qin, D.; Manning, M.; Chen, Z.; Marquis, M.; Averyt, K. B.; Tignor, M.; Miller, H. L. Climate Change 2007: The Physical Science Basis. Contribution of Working Group I to the Fourth Assessment Report of the Intergovernmental Panel on Climate Change, IPCC, Cambridge, United Kingdom and New York, NY, USA, **2007**.

(3) Kinzel, N. W.; Werlé, C.; Leitner, W. Transition Metal Complexes as Catalysts for the Electroconversion of CO_2: An Organometallic Perspective. *Angew. Chem. Int. Ed.* **2021**, *60*, 11628–11686.

(4) Dlugokencky, E.; Tans, P. US Department of Commerce, N. Global Monitoring Laboratory - Carbon Cycle Greenhouse Gases. *NOAA/GML* (gml.noaa.gov/ccgg/trends/).

(5) Florides, G. A.; Christodoulides, P. Global Warming and Carbon Dioxide through Sciences. *Environ. Int.* **2009**, *35*, 390–401.

(6) Garrett, C. W. On Global Climate Change, Carbon Dioxide, and Fossil Fuel Combustion. *Prog. Energy Combust. Sci.* **1992**, *18*, 369–407.

(7) Zhou, P.; Wang, M. Carbon Dioxide Emissions Allocation: A Review. *Ecol. Econ.* **2016**, *125*, 47–59.

(8) Houghton, J. The Science of Global Warming. *Interdiscip. Sci. Rev.* **2001**, *26*, 247–257.

(9) Titus, J. G. Greenhouse Effect, Sea Level Rise, and Costal Wetlands. U.S. Environmental Protection Agency, **1988**, 1–35.

(10) Raper, S. C. B.; Wigley, T. M. L.; Warrick, R. A. Global Sea-Level Rise: Past and Future; Sea-Level Rise and Costal Subsidence. Coastal Systems and Continental Margins, Springer, Dordrecht, Netherlands, **1996**, 11–45.

(11) Doney, S. C.; Fabry, V. J.; Feely, R. A.; Kleypas, J. A. Ocean Acidification: The Other CO_2 Problem. *Annu. Rev. Mar. Sci.* **2009**, *1*, 169–192.

(12) Khandekar, M. L.; Murty, T. S.; Chittibabu, P. The Global Warming Debate: A Review of the State of Science. *Pure Appl. Geophys.* **2005**, *162*, 1557–1586.

(13) Bradshaw, C. J. A.; Bowman, D. M. J. S.; Bond, N. R.; Murphy, B. P.; Moore, A. D.; Fordham, D. A.; Thackway, R.; Lawes, M. J.; McCallum, H.; Gregory, S. D.; Dalal, R. C.; Boer, M. M.; Lynch, A. J. J.; Bradstock, R. A.; Brook, B. W.; Henry, B. K.; Hunt, L. P.; Fisher, D. O.; Hunter, D.; Johnson, C. N.; Keith, D. A.; Lefroy, E. C.; Penman, T. D.; Meyer, W. S.; Thomson, J. R.; Thornton, C. M.; VanDerWal, J.; Williams, R. J.; Keniger, L.; Specht, A. Brave New Green World – Consequences of a Carbon Economy for the Conservation of Australian Biodiversity. *Biol. Conserv.* **2013**, *161*, 71–90.

(14) Cusack, D. F.; Karpman, J.; Ashdown, D.; Cao, Q.; Ciochina, M.; Halterman, S.; Lydon, S.; Neupane, A. Global Change Effects on Humid Tropical Forests: Evidence for Biogeochemical and Biodiversity Shifts at an Ecosystem Scale. *Rev. Geophys.* **2016**, *54*, 523–610.

(15) De Luna, P.; Hahn, C.; Higgins, D.; Jaffer, S. A.; Jaramillo, T. F.; Sargent, E. H. What Would It Take for Renewably Powered Electrosynthesis to Displace Petrochemical Processes? *Science* **2019**, *364*, eaav3506.

(16) Papanikolaou, G.; Centi, G.; Perathoner, S.; Lanzafame, P. Catalysis for E-Chemistry: Need and Gaps for a Future De-Fossilized Chemical Production, with Focus on the Role of Complex (Direct) Syntheses by Electrocatalysis. *ACS Catal.* **2022**, *12*, 2861–2876.

(17) Birdja, Y. Y.; Pérez-Gallent, E.; Figueiredo, M. C.; Göttle, A. J.; Calle-Vallejo, F.; Koper, M. T. M. Advances and Challenges in Understanding the Electrocatalytic Conversion of Carbon Dioxide to Fuels. *Nat. Energy* **2019**, *4*, 732–745.
(18) Centi, G.; Perathoner, S. Redesign Chemical Processes to Substitute the Use of Fossil Fuels: A Viewpoint of the Implications on Catalysis. *Catal. Today* **2022**, *387*, 216–223.
(19) Linnemann, J.; Kanokkanchana, K.; Tschulik, K. Design Strategies for Electrocatalysts from an Electrochemist's Perspective. *ACS Catal.* **2021**, *11*, 5318–5346.
(20) Zhao, K.; Quan, X. Carbon-Based Materials for Electrochemical Reduction of CO_2 to C_{2+} Oxygenates: Recent Progress and Remaining Challenges. *ACS Catal.* **2021**, *11*, 2076–2097.
(21) Li, C.; Li, J.; Qin, L.; Yang, P.; Vlachos, D. G. Recent Advances in the Photocatalytic Conversion of Biomass-Derived Furanic Compounds. *ACS Catal.* **2021**, *11*, 11336–11359.
(22) Elouarzaki, K.; Kannan, V.; Jose, V.; Sabharwal, H. S.; Lee, J.-M. Recent Trends, Benchmarking, and Challenges of Electrochemical Reduction of CO_2 by Molecular Catalysts. *Adv. Energy Mater.* **2019**, 1900090
(23) Savéant, J.-M. Molecular Electrochemistry: Recent Trends and Upcoming Challenges. *ChemElectroChem* **2016**, *3*, 1967–1977.
(24) Sun, Z.; Ma, T.; Tao, H.; Fan, Q.; Han, B. Fundamentals and Challenges of Electrochemical CO_2 Reduction Using Two-Dimensional Materials. *Chem* **2017**, *3*, 560–587.
(25) Pavlishchuk, V. V.; Addison, A. W. Conversion Constants for Redox Potentials Measured versus Different Reference Electrodes in Acetonitrile Solutions at 25°C. *Inorganica Chim. Acta* **2000**, *298*, 97–102.
(26) Nitopi, S.; Bertheussen, E.; Scott, S. B.; Liu, X.; Engstfeld, A. K.; Horch, S.; Seger, B.; Stephens, I. E. L.; Chan, K.; Hahn, C.; Nørskov, J. K.; Jaramillo, T. F.; Chorkendorff, I. Progress and Perspectives of Electrochemical CO_2 Reduction on Copper in Aqueous Electrolyte. *Chem. Rev.* **2019**, *119*, 7610–7672.
(27) Popović, S.; Smiljanić, M.; Jovanovič, P.; Vavra, J.; Buonsanti, R.; Hodnik, N. Stability and Degradation Mechanisms of Copper-Based Catalysts for Electrochemical CO_2 Reduction. *Angew. Chem.* **2020**, *132*, 14844–14854.
(28) Ni, Z.; Liang, H.; Yi, Z.; Guo, R.; Liu, C.; Liu, Y.; Sun, H.; Liu, X. Research Progress of Electrochemical CO_2 Reduction for Copper-Based Catalysts to Multicarbon Products. *Coord. Chem. Rev.* **2021**, *441*, 213983.
(29) Boutin, E.; Robert, M. Molecular Electrochemical Reduction of CO_2 beyond Two Electrons. *Trends Chem.* **2021**, *3*, 359–372.
(30) Ooka, H.; Huang, J.; Exner, K. S. The Sabatier Principle in Electrocatalysis: Basics, Limitations, and Extensions. *Front. Energy Res.* **2021**, *9*, 1–20.
(31) Costentin, C.; Savéant, J.-M. Towards an Intelligent Design of Molecular Electrocatalysts. *Nat. Rev. Chem.* **2017**, *1*, 0087.
(32) Exner, K. S. Is Thermodynamics a Good Descriptor for the Activity? Re-Investigation of Sabatier's Principle by the Free Energy Diagram in Electrocatalysis. *ACS Catal.* **2019**, *9*, 5320–5329.
(33) Peterson, A. A.; Nørskov, J. K. Activity Descriptors for CO_2 Electroreduction to Methane on Transition-Metal Catalysts. *J. Phys. Chem. Lett.* **2012**, *3*, 251–258.
(34) Wu, Y.; Jiang, Z.; Lu, X.; Liang, Y.; Wang, H. Domino Electroreduction of CO_2 to Methanol on a Molecular Catalyst. *Nature* **2019**, *575*, 639–642.

(35) Tripkovic, V.; Vanin, M.; Karamad, M.; Björketun, M. E.; Jacobsen, K. W.; Thygesen, K. S.; Rossmeisl, J. Electrochemical CO_2 and CO Reduction on Metal-Functionalized Porphyrin-like Graphene. *J. Phys. Chem. C* **2013**, *117*, 9187–9195.
(36) Ju, W.; Bagger, A.; Hao, G.-P.; Varela, A. S.; Sinev, I.; Bon, V.; Roldan Cuenya, B.; Kaskel, S.; Rossmeisl, J.; Strasser, P. Understanding Activity and Selectivity of Metal-Nitrogen-Doped Carbon Catalysts for Electrochemical Reduction of CO_2. *Nat. Commun.* **2017**, *8*, 944.
(37) Zhang, Z.; Xiao, J.; Chen, X.-J.; Yu, S.; Yu, L.; Si, R.; Wang, Y.; Wang, S.; Meng, X.; Wang, Y.; Tian, Z.-Q.; Deng, D. Reaction Mechanisms of Well-Defined Metal–N_4 Sites in Electrocatalytic CO_2 Reduction. *Angew. Chem. Int. Ed.* **2018**, *57*, 16339–16342.
(38) Ahmed, M. E.; Adam, S.; Saha, D.; Fize, J.; Artero, V.; Dey, A.; Duboc, C. Repurposing a Bio-Inspired NiFe Hydrogenase Model for CO_2 Reduction with Selective Production of Methane as the Unique C-Based Product. *ACS Energy Lett.* **2020**, *5*, 3837–3842.
(39) Boutin, E.; Merakeb, L.; Ma, B.; Boudy, B.; Wang, M.; Bonin, J.; Anxolabéhère-Mallart, E.; Robert, M. Molecular Catalysis of CO_2 Reduction: Recent Advances and Perspectives in Electrochemical and Light-Driven Processes with Selected Fe, Ni and Co Aza Macrocyclic and Polypyridine Complexes. *Chem. Soc. Rev.* **2020**, *49*, 5772–5809.
(40) Sparacino-Watkins, C.; Stolz, J. F.; Basu, P. Nitrate and Periplasmic Nitrate Reductases. *Chem. Soc. Rev.* **2013**, *43*, 676–706.
(41) Tanifuji, K.; Ohki, Y. Metal–Sulfur Compounds in N_2 Reduction and Nitrogenase-Related Chemistry. *Chem. Rev.* **2020**, *120*, 5194–5251.
(42) Humphreys, J.; Lan, R.; Tao, S. Development and Recent Progress on Ammonia Synthesis Catalysts for Haber–Bosch Process. *Adv. Energy Sustain. Res.* **2021**, *2*, 2000043.
(43) Martín, A. J.; Shinagawa, T.; Pérez-Ramírez, J. Electrocatalytic Reduction of Nitrogen: From Haber-Bosch to Ammonia Artificial Leaf. *Chem* **2019**, *5*, 263–283.
(44) Seefeldt, L. C.; Dean, D. R. Iron-Sulfur Cluster Proteins, Nitrogenases. *Encyclopedia of Metalloproteins*; Springer: New York, NY, **2013**, 1053–1057.
(45) Seefeldt, L. C.; Hoffman, B. M.; Dean, D. R. Mechanism of Mo-Dependent Nitrogenase. *Annu. Rev. Biochem.* **2009**, *78*, 701–722.
(46) Rutledge, H. L.; Tezcan, F. A. Electron Transfer in Nitrogenase. *Chem. Rev.* **2020**, *120*, 5158–5193.
(47) Seefeldt, L. C.; Yang, Z.-Y.; Lukoyanov, D. A.; Harris, D. F.; Dean, D. R.; Raugei, S.; Hoffman, B. M. Reduction of Substrates by Nitrogenases. *Chem. Rev.* **2020**, *120*, 5082–5106.
(48) Van Stappen, C.; Decamps, L.; Cutsail, G. E.; Bjornsson, R.; Henthorn, J. T.; Birrell, J. A.; DeBeer, S. The Spectroscopy of Nitrogenases. *Chem. Rev.* **2020**, *120*, 5005–5081.
(49) Einsle, O.; Rees, D. C. Structural Enzymology of Nitrogenase Enzymes. *Chem. Rev.* **2020**, *120*, 4969–5004.
(50) Burén, S.; Jiménez-Vicente, E.; Echavarri-Erasun, C.; Rubio, L. M. Biosynthesis of Nitrogenase Cofactors. *Chem. Rev.* **2020**, *120*, 4921–4968.
(51) Astruc, D. How to Design Organometallic "Electron-Reservoirs." *Comments Inorg. Chem.* **1987**, *6*, 61–84.
(52) Connelly, N. G.; Geiger, W. E. Chemical Redox Agents for Organometallic Chemistry. *Chem. Rev.* **1996**, *96*, 877–910.

(53) Grice, K. A.; Saucedo, C.; Sovereign, M. A.; Cho, A. P. The Electrochemical Behavior of Early Metal Metallocene Cp_2MCl_2 Complexes under CO_2. *Electrochimica Acta* **2016**, *218*, 110–118.
(54) Lee, D.; Choi, S.; Choe, M. S.; Kim, S.-Y.; Park, K.; Kim, C. H.; Son, H.-J.; Kang, S. O. Photochemical CO_2-to-Formate/CO Conversion Catalyzed by Half-Metallocene Ir(III) Catalyst and Its Mechanistic Investigation. *Organometallics* **2021**, *40*, 2430–2442.
(55) Vanicek, S.; Jochriem, M.; Hassenrück, C.; Roy, S.; Kopacka, H.; Wurst, K.; Müller, T.; Winter, R. F.; Reisner, E.; Bildstein, B. Redox-Rich Metallocene Tetrazene Complexes: Synthesis, Structure, Electrochemistry, and Catalysis. *Organometallics* **2019**, *38*, 1361–1371.
(56) Chalkley, M. J.; Oyala, P. H.; Peters, J. C. Cp* Noninnocence Leads to a Remarkably Weak C–H Bond via Metallocene Protonation. *J. Am. Chem. Soc.* **2019**, *141*, 4721–4729.
(57) Cao, Z.; Derrick, J. S.; Xu, J.; Gao, R.; Gong, M.; Nichols, E. M.; Smith, P. T.; Liu, X.; Wen, X.; Copéret, C.; Chang, C. J. Chelating N-Heterocyclic Carbene Ligands Enable Tuning of Electrocatalytic CO_2 Reduction to Formate and Carbon Monoxide: Surface Organometallic Chemistry. *Angew. Chem. Int. Ed.* **2018**, *57*, 4981–4985.
(58) Drennan, C. L.; Heo, J.; Sintchak, M. D.; Schreiter, E.; Ludden, P. W. Life on Carbon Monoxide: X-Ray Structure of Rhodospirillum Rubrum Ni-Fe-S Carbon Monoxide Dehydrogenase. *Proc. Natl. Acad. Sci.* **2001**, *98*, 11973–11978.
(59) Jeoung, J.-H.; Dobbek, H. Carbon Dioxide Activation at the Ni,Fe-Cluster of Anaerobic Carbon Monoxide Dehydrogenase. *Science* **2007**, *318*, 1461–1464.
(60) Gong, W.; Hao, B.; Wei, Z.; Ferguson, D. J.; Tallant, T.; Krzycki, J. A.; Chan, M. K. Structure of the $\alpha_2\varepsilon_2$ Ni-Dependent CO Dehydrogenase Component of the Methanosarcina Barkeri Acetyl-CoA Decarbonylase/Synthase Complex. *Proc. Natl. Acad. Sci.* **2008**, *105*, 9558–9563.
(61) Mondal, B.; Song, J.; Neese, F.; Ye, S. Bio-Inspired Mechanistic Insights into CO_2 Reduction. *Curr. Opin. Chem. Biol.* **2015**, *25*, 103–109.
(62) Volbeda, A.; Fontecilla-Camps, J. C. Structure–Function Relationships of Nickel–Iron Sites in Hydrogenase and a Comparison with the Active Sites of Other Nickel–Iron Enzymes. *Coord. Chem. Rev.* **2005**, *249*, 1609–1619.
(63) Gamba, I. Biomimetic Approach to CO_2 Reduction. *Bioinorg. Chem. Appl.* **2018**, *2018*, e2379141.
(64) Ilic, S.; Gesiorski, J. L.; Weerasooriya, R. B.; Glusac, K. D. Biomimetic Metal-Free Hydride Donor Catalysts for CO_2 Reduction. *Acc. Chem. Res.* **2022**, *55*, 844–856.
(65) Kalyanasundaram, K.; Graetzel, M. Artificial Photosynthesis: Biomimetic Approaches to Solar Energy Conversion and Storage. *Curr. Opin. Biotechnol.* **2010**, *21*, 298–310.
(66) English, N. J.; El-Hendawy, M. M.; Mooney, D. A.; MacElroy, J. M. D. Perspectives on Atmospheric CO_2 Fixation in Inorganic and Biomimetic Structures. *Coord. Chem. Rev.* **2014**, *269*, 85–95.
(67) Drover, M. W. A Guide to Secondary Coordination Sphere Editing. *Chem. Soc. Rev.* **2022**, 51, 1861–1880.
(68) Nichols, A. W.; Machan, C. W. Secondary-Sphere Effects in Molecular Electrocatalytic CO_2 Reduction. *Front. Chem.* **2019**, *7*, 397.
(69) Reda, T.; Plugge, C. M.; Abram, N. J.; Hirst, J. Reversible Interconversion of Carbon Dioxide and Formate by an Electroactive Enzyme. *Proc. Natl. Acad. Sci.* **2008**, *105* (31), 10654–10658.

(70) Evans, R. M.; Siritanaratkul, B.; Megarity, C. F.; Pandey, K.; Esterle, T. F.; Badiani, S.; Armstrong, F. A. The Value of Enzymes in Solar Fuels Research – Efficient Electrocatalysts through Evolution. *Chem. Soc. Rev.* **2019**, *48*, 2039–2052.
(71) Dey, S.; Das, P. K.; Dey, A. Mononuclear Iron Hydrogenase. *Coord. Chem. Rev.* **2013**, *257*, 42–63.
(72) Queyriaux, N. Redox-Active Ligands in Electroassisted Catalytic H^+ and CO_2 Reductions: Benefits and Risks. *ACS Catal.* **2021**, *11*, 4024–4035.
(73) Su, X.; McCardle, K. M.; Panetier, J. A.; Jurss, J. W. Electrocatalytic CO_2 Reduction with Nickel Complexes Supported by Tunable Bipyridyl-N-Heterocyclic Carbene Donors: Understanding Redox-Active Macrocycles. *Chem. Commun.* **2018**, *54*, 3351–3354.
(74) Su, X.; McCardle, K. M.; Chen, L.; Panetier, J. A.; Jurss, J. W. Robust and Selective Cobalt Catalysts Bearing Redox-Active Bipyridyl-N-Heterocyclic Carbene Frameworks for Electrochemical CO_2 Reduction in Aqueous Solutions. *ACS Catal.* **2019**, *9*, 7398–7408.
(75) Elgrishi, N.; Chambers, M. B.; Fontecave, M. Turning It off! Disfavouring Hydrogen Evolution to Enhance Selectivity for CO Production during Homogeneous CO_2 Reduction by Cobalt–Terpyridine Complexes. *Chem. Sci.* **2015**, *6*, 2522–2531.
(76) Gonell, S.; Massey, M. D.; Moseley, I. P.; Schauer, C. K.; Muckerman, J. T.; Miller, A. J. M. The Trans Effect in Electrocatalytic CO_2 Reduction: Mechanistic Studies of Asymmetric Ruthenium Pyridyl-Carbene Catalysts. *J. Am. Chem. Soc.* **2019**, *141*, 6658–6671.
(77) Gonell, S.; Assaf, E. A.; Duffee, K. D.; Schauer, C. K.; Miller, A. J. M. Kinetics of the Trans Effect in Ruthenium Complexes Provide Insight into the Factors That Control Activity and Stability in CO_2 Electroreduction. *J. Am. Chem. Soc.* **2020**, *142*, 8980–8999.
(78) Gonell, S.; Lloret-Fillol, J.; Miller, A. J. M. An Iron Pyridyl-Carbene Electrocatalyst for Low Overpotential CO_2 Reduction to CO. *ACS Catal.* **2021**, *11*, 615–626.
(79) Drosou, M.; Kamatsos, F.; Mitsopoulou, C. A. Recent Advances in the Mechanisms of the Hydrogen Evolution Reaction by Non-Innocent Sulfur-Coordinating Metal Complexes. *Inorg. Chem. Front.* **2019**, *7*, 37–71.
(80) Solis, B. H.; Hammes-Schiffer, S. Computational Study of Anomalous Reduction Potentials for Hydrogen Evolution Catalyzed by Cobalt Dithiolene Complexes. *J. Am. Chem. Soc.* **2012**, *134*, 15253–15256.
(81) Nie, W.; McCrory, C. C. L. Electrocatalytic CO_2 Reduction by a Cobalt Bis(Pyridylmonoimine) Complex: Effect of Acid Concentration on Catalyst Activity and Stability. *Chem. Commun.* **2018**, *54*, 1579–1582.
(82) Andrez, J.; Guidal, V.; Scopelliti, R.; Pécaut, J.; Gambarelli, S.; Mazzanti, M. Ligand and Metal Based Multielectron Redox Chemistry of Cobalt Supported by Tetradentate Schiff Bases. *J. Am. Chem. Soc.* **2017**, *139*, 8628–8638.
(83) Rossi, L. Electrochemical Methodologies for the Carboxylation Reactions in Organic Synthesis. An Alternative Re-Use of Carbon Dioxide. *Curr. Green Chem. 2*, 77–89.
(84) Queyriaux, N.; Abel, K.; Fize, J.; Pécaut, J.; Orio, M.; Hammarström, L. From Non-Innocent to Guilty: On the Role of Redox-Active Ligands in the Electro-Assisted Reduction of CO_2 Mediated by a Cobalt(II)-Polypyridyl Complex. *Sustain. Energy Fuels* **2020**, *4*, 3668–3676.
(85) Queyriaux, N.; Giannoudis, E.; Windle, C. D.; Roy, S.; Pécaut, J.; Coutsolelos, A. G.; Artero, V.; Chavarot-Kerlidou, M. A Noble Metal-Free Photocatalytic System Based on a Novel Cobalt Tetrapyridyl Catalyst for Hydrogen Production in Fully Aqueous Medium. *Sustain. Energy Fuels* **2018**, *2*, 553–557.

(86) Myren, T. H. T.; Alherz, A.; Stinson, T. A.; Huntzinger, C. G.; Lama, B.; Musgrave, C. B.; Luca, O. R. Metalloradical Intermediates in Electrocatalytic Reduction of CO_2 to CO: Mn versus Re Bis-N-Heterocyclic Carbene Pincers. *Dalton Trans.* **2020**, *49*, 2053–2057.
(87) Derrick, J. S.; Loipersberger, M.; Chatterjee, R.; Iovan, D. A.; Smith, P. T.; Chakarawet, K.; Yano, J.; Long, J. R.; Head-Gordon, M.; Chang, C. J. Metal–Ligand Cooperativity via Exchange Coupling Promotes Iron- Catalyzed Electrochemical CO_2 Reduction at Low Overpotentials. *J. Am. Chem. Soc.* **2020**, *142* (48), 20489–20501.
(88) Rotundo, L.; Gobetto, R.; Nervi, C. Electrochemical CO_2 Reduction with Earth-Abundant Metal Catalysts. *Curr. Opin. Green Sustain. Chem.* **2021**, *31*, 100509.
(89) Apaydin, D. H.; Schlager, S.; Portenkirchner, E.; Sariciftci, N. S. Organic, Organometallic and Bioorganic Catalysts for Electrochemical Reduction of CO_2. *ChemPhysChem* **2017**, *18*, 3094–3116.
(90) Meshitsuka, S.; Ichikawa, M.; Tamaru, K. Electrocatalysis by Metal Phthalocyanines in the Reduction of Carbon Dioxide. *J. Chem. Soc. Chem. Commun.* **1974**, 158–159.
(91) Takahashi, K.; Hiratsuka, K.; Sasaki, H.; Toshima, S. Electrocatalytic Behavior of Metal Porphyrins in the Reduction of Carbon Dioxide. *Chem. Lett.* **1979**, *8*, 305–308.
(92) Hammouche, M.; Lexa, D.; Savéant, J. M.; Momenteau, M. Catalysis of the Electrochemical Reduction of Carbon Dioxide by Iron("0") Porphyrins. *J. Electroanal. Chem. Interfacial Electrochem.* **1988**, *249*, 347–351.
(93) Hammouche, M.; Lexa, D.; Momenteau, M.; Saveant, J. M. Chemical Catalysis of Electrochemical Reactions. Homogeneous Catalysis of the Electrochemical Reduction of Carbon Dioxide by Iron("0") Porphyrins. Role of the Addition of Magnesium Cations. *J. Am. Chem. Soc.* **1991**, *113*, 8455–8466.
(94) Römelt, C.; Song, J.; Tarrago, M.; Rees, J. A.; van Gastel, M.; Weyhermüller, T.; DeBeer, S.; Bill, E.; Neese, F.; Ye, S. Electronic Structure of a Formal Iron(0) Porphyrin Complex Relevant to CO_2 Reduction. *Inorg. Chem.* **2017**, *56*, 4745–4750.
(95) Costentin, C.; Drouet, S.; Robert, M.; Savéant, J.-M. A Local Proton Source Enhances CO_2 Electroreduction to CO by a Molecular Fe Catalyst. *Science* **2012**, *338*, 90–94.
(96) Azcarate, I.; Costentin, C.; Robert, M.; Savéant, J.-M. Through-Space Charge Interaction Substituent Effects in Molecular Catalysis Leading to the Design of the Most Efficient Catalyst of CO_2-to-CO Electrochemical Conversion. *J. Am. Chem. Soc.* **2016**, *138*, 16639–16644.
(97) Gotico, P.; Boitrel, B.; Guillot, R.; Sircoglou, M.; Quaranta, A.; Halime, Z.; Leibl, W.; Aukauloo, A. Second-Sphere Biomimetic Multipoint Hydrogen-Bonding Patterns to Boost CO_2 Reduction of Iron Porphyrins. *Angew. Chem. Int. Ed.* **2019**, *58*, 4504–4509.
(98) Gotico, P.; Roupnel, L.; Guillot, R.; Sircoglou, M.; Leibl, W.; Halime, Z.; Aukauloo, A. Atropisomeric Hydrogen Bonding Control for CO_2 Binding and Enhancement of Electrocatalytic Reduction at Iron Porphyrins. *Angew. Chem. Int. Ed.* **2020**, *59*, 22451–22455.
(99) Khadhraoui, A.; Gotico, P.; Leibl, W.; Halime, Z.; Aukauloo, A. Through-Space Electrostatic Interactions Surpass Classical Through-Bond Electronic Effects in Enhancing CO_2 Reduction Performance of Iron Porphyrins. *ChemSusChem* **2021**, *14*, 1308–1315.
(100) Fisher, B. J.; Eisenberg, R. Electrocatalytic Reduction of Carbon Dioxide by Using Macrocycles of Nickel and Cobalt. *J. Am. Chem. Soc.* **1980**, *102*, 7361–7363.

(101) Beley, M.; Collin, J.-P.; Ruppert, R.; Sauvage, J.-P. Nickel(II)-Cyclam: An Extremely Selective Electrocatalyst for Reduction of CO_2 in Water. *J. Chem. Soc. Chem. Commun.* **1984**, 1315–1316.
(102) Kelly, C. A.; Blinn, E. L.; Camaioni, N.; D'Angelantonio, M.; Mulazzani, Q. G. Mechanism of CO_2 and H^+ Reduction by $Ni(Cyclam)^+$ in Aqueous Solution. A Pulse and Continuous Radiolysis Study. *Inorg. Chem.* **1999**, *38*, 1579–1584.
(103) Balazs, G. B.; Anson, F. C. The Adsorption of $Ni(Cyclam)^+$ at Mercury Electrodes and Its Relation to the Electrocatalytic Reduction of CO_2. *J. Electroanal. Chem.* **1992**, *322*, 325–345.
(104) Bujno, K.; Bilewicz, R.; Siegfried, L.; Kaden, T. A. Effects of Ligand Structure on the Adsorption of Nickel Tetraazamacrocyclic Complexes and Electrocatalytic CO_2 Reduction. *J. Electroanal. Chem.* **1998**, *445*, 47–53.
(105) Sakaki, S. Can Carbon Dioxide Coordinate to a Nickel(I) Complex? An Ab Initio MO/SD-CI Study. *J. Am. Chem. Soc.* **1990**, *112*, 7813–7814.
(106) Sakaki, S. An Ab Initio MO/SD-CI Study of Model Complexes of Intermediates in Electrochemical Reduction of Carbon Dioxide Catalyzed by $NiCl_2$(Cyclam). *J. Am. Chem. Soc.* **1992**, *114*, 2055–2062.
(107) Wu, Y.; Jiang, J.; Weng, Z.; Wang, M.; Broere, D. L. J.; Zhong, Y.; Brudvig, G. W.; Feng, Z.; Wang, H. Electroreduction of CO_2 Catalyzed by a Heterogenized Zn–Porphyrin Complex with a Redox-Innocent Metal Center. *ACS Cent. Sci.* **2017**, *3*, 847–852.
(108) Froehlich, J. D.; Kubiak, C. P. The Homogeneous Reduction of CO_2 by $[Ni(Cyclam)]^+$: Increased Catalytic Rates with the Addition of a CO Scavenger. *J. Am. Chem. Soc.* **2015**, *137*, 3565–3573.
(109) Froehlich, J. D.; Kubiak, C. P. Homogeneous CO_2 Reduction by Ni(Cyclam) at a Glassy Carbon Electrode. *Inorg. Chem.* **2012**, *51*, 3932–3934.
(110) Song, J.; Klein, E. L.; Neese, F.; Ye, S. The Mechanism of Homogeneous CO_2 Reduction by Ni(Cyclam): Product Selectivity, Concerted Proton–Electron Transfer and C–O Bond Cleavage. *Inorg. Chem.* **2014**, *53*, 7500–7507.
(111) Schneider, J.; Jia, H.; Kobiro, K.; Cabelli, D. E.; Muckerman, J. T.; Fujita, E. Nickel(II) Macrocycles: Highly Efficient Electrocatalysts for the Selective Reduction of CO_2 to CO. *Energy Environ. Sci.* **2012**, *5*, 9502–9510.
(112) Fujita, E.; Haff, J.; Sanzenbacher, R.; Elias, H. High Electrocatalytic Activity of RRSS-$[Ni^{II}HTIM](ClO_4)_2$ and $[Ni^{II}DMC](ClO_4)_2$ for Carbon Dioxide Reduction (HTIM = 2,3,9,10-Tetramethyl-1,4,8,11-Tetraazacyclotetradecane, DMC = C-Meso-5,12-Dimethyl-1,4,8,11-Tetraazacyclotetradecane). *Inorg. Chem.* **1994**, *33*, 4627–4628.
(113) Szalda, D. J.; Fujita, E.; Sanzenbacher, R.; Paulus, H.; Elias, H. Syntheses and Properties of Nickel(I) and Nickel(II) Complexes of a Series of Macrocyclic N4 Ligands: Crystal Structures of C-RSSR-$[Ni^{I}HTIM](ClO_4)$, C-RSSR-$[Ni^{II}HTIM](ClO_4)_2$, C-RRSS-$[Ni^{II}HTIM](ClO_4)_2$, and $[Ni^{II}TIM](ClO_4)_2$ (HTIM = 2,3,9,10-Tetramethyl-1,4,8,11-Tetraazacyclotetradecane, TIM = 2,3,9,10-Tetramethyl-1,4,8,11-Tetraazacyclotetradeca-1,3,8,10-Tetraene). *Inorg. Chem.* **1994**, *33*, 5855–5863.
(114) Fujita, E.; Brunschwig, B. S.; Cabelli, D.; Rentier, M. W.; Furenlid, L. R.; Ogata, T.; Wada, Y.; Yanagida, S. Photochemical Carbon Dioxide Reduction with Metal Complexes: Differences between Cobalt and Nickel Macrocycles. In *Studies in Surface Science and Catalysis*; Advances in Chemical Conversions for Mitigating Carbon Dioxide; Elsevier, **1998**, *114*, 97–106.

(115) Ogata, T.; Yanagida, S.; Brunschwig, B. S.; Fujita, E. Mechanistic and Kinetic Studies of Cobalt Macrocycles in a Photochemical CO_2 Reduction System: Evidence of Co-CO_2 Adducts as Intermediates. *J. Am. Chem. Soc.* **1995**, *117*, 6708–6716.
(116) Hawecker, J.; Lehn, J.-M.; Ziessel, R. Electrocatalytic Reduction of Carbon Dioxide Mediated by Re(Bipy)$(CO)_3$Cl (Bipy = 2,2′-Bipyridine). *J. Chem. Soc. Chem. Commun.* **1984**, 328–330.
(117) Benson, E. E.; Sampson, M. D.; Grice, K. A.; Smieja, J. M.; Froehlich, J. D.; Friebel, D.; Keith, J. A.; Carter, E. A.; Nilsson, A.; Kubiak, C. P. The Electronic States of Rhenium Bipyridyl Electrocatalysts for CO_2 Reduction as Revealed by X-Ray Absorption Spectroscopy and Computational Quantum Chemistry. *Angew. Chem. Int. Ed.* **2013**, *52*, 4841–4844.
(118) Riplinger, C.; Sampson, M. D.; Ritzmann, A. M.; Kubiak, C. P.; Carter, E. A. Mechanistic Contrasts between Manganese and Rhenium Bipyridine Electrocatalysts for the Reduction of Carbon Dioxide. *J. Am. Chem. Soc.* **2014**, *136*, 16285–16298.
(119) Keith, J. A.; Grice, K. A.; Kubiak, C. P.; Carter, E. A. Elucidation of the Selectivity of Proton-Dependent Electrocatalytic CO_2 Reduction by Fac-Re(Bpy)$(CO)_3$Cl. *J. Am. Chem. Soc.* **2013**, *135*, 15823–15829.
(120) Clark, M. L.; Cheung, P. L.; Lessio, M.; Carter, E. A.; Kubiak, C. P. Kinetic and Mechanistic Effects of Bipyridine (Bpy) Substituent, Labile Ligand, and Brønsted Acid on Electrocatalytic CO_2 Reduction by Re(Bpy) Complexes. *ACS Catal.* **2018**, *8*, 2021–2029.
(121) Grice, K. A.; Saucedo, C. Electrocatalytic Reduction of CO_2 by Group 6 $M(CO)_6$ Species without "Non-Innocent" Ligands. *Inorg. Chem.* **2016**, *55*, 6240–6246.
(122) Fujita, E.; Grills, D. C.; Manbeck, G. F.; Polyansky, D. E. Understanding the Role of Inter- and Intramolecular Promoters in Electro- and Photochemical CO_2 Reduction Using Mn, Re, and Ru Catalysts. *Acc. Chem. Res.* **2022**, *55*, 616–628.
(123) Slater, S.; Wagenknecht, J. H. Electrochemical Reduction of Carbon Dioxide Catalyzed by $Rh(Diphos)_2Cl$. *J. Am. Chem. Soc.* **1984**, *106*, 5367–5368.
(124) DuBois, D. L.; Miedaner, A.; Haltiwanger, R. C. Electrochemical Reduction of Carbon Dioxide Catalyzed by [Pd(Triphosphine)(Solvent)]$(BF_4)_2$ Complexes: Synthetic and Mechanistic Studies. *J. Am. Chem. Soc.* **1991**, *113*, 8753–8764.
(125) Raebiger, J. W.; Turner, J. W.; Noll, B. C.; Curtis, C. J.; Miedaner, A.; Cox, B.; DuBois, D. L. Electrochemical Reduction of CO_2 to CO Catalyzed by a Bimetallic Palladium Complex. *Organometallics* **2006**, *25*, 3345–3351.
(126) Bi, J.; Hou, P.; Liu, F.-W.; Kang, P. Electrocatalytic Reduction of CO_2 to Methanol by Iron Tetradentate Phosphine Complex Through Amidation Strategy. *ChemSusChem* **2019**, *12*, 2195–2201.
(127) Elgrishi, N.; Rountree, K. J.; McCarthy, B. D.; Rountree, E. S.; Eisenhart, T. T.; Dempsey, J. L. A Practical Beginner's Guide to Cyclic Voltammetry. *J. Chem. Educ.* **2018**, *95*, 197–206.
(128) Rountree, E. S.; McCarthy, B. D.; Eisenhart, T. T.; Dempsey, J. L. Evaluation of Homogeneous Electrocatalysts by Cyclic Voltammetry. *Inorg. Chem.* **2014**, *53*, 9983–10002.
(129) Lee, K. J.; Elgrishi, N.; Kandemir, B.; Dempsey, J. L. Electrochemical and Spectroscopic Methods for Evaluating Molecular Electrocatalysts. *Nat. Rev. Chem.* **2017**, *1*, 0039.
(130) Compton, R., G.; Banks, C., E. *Understanding Voltammetry*, 2nd ed.; Imperial College Press: London, 2011.

(131) Lee, K. J.; McCarthy, B. D.; Dempsey, J. L. On Decomposition, Degradation, and Voltammetric Deviation: The Electrochemist's Field Guide to Identifying Precatalyst Transformation. *Chem. Soc. Rev.* **2019**, *48*, 2927–2945.
(132) Bard, A. *Standard Potentials in Aqueous Solution*; Routledge, 2017.
(133) Hooe, S. L.; Dressel, J. M.; Dickie, D. A.; Machan, C. W. Highly Efficient Electrocatalytic Reduction of CO_2 to CO by a Molecular Chromium Complex. *ACS Catal.* **2020**, *10*, 1146–1151.
(134) Fujita, Etsuko.; Szalda, D. J.; Creutz, Carol.; Sutin, Norman. Carbon Dioxide Activation: Thermodynamics of Carbon Dioxide Binding and the Involvement of Two Cobalt Centers in the Reduction of Carbon Dioxide by a Cobalt(I) Macrocycle. *J. Am. Chem. Soc.* **1988**, *110*, 4870–4871.
(135) Gennaro, A.; Isse, A. A.; Vianello, E. Solubility and Electrochemical Determination of CO_2 in Some Dipolar Aprotic Solvents. *J. Electroanal. Chem. Interfacial Electrochem.* **1990**, *289*, 203–215.
(136) Pegis, M. L.; Roberts, J. A. S.; Wasylenko, D. J.; Mader, E. A.; Appel, A. M.; Mayer, J. M. Standard Reduction Potentials for Oxygen and Carbon Dioxide Couples in Acetonitrile and N,N-Dimethylformamide. *Inorg. Chem.* **2015**, *54*, 11883–11888.
(137) Matsubara, Y.; Grills, D. C.; Kuwahara, Y. Thermodynamic Aspects of Electrocatalytic CO_2 Reduction in Acetonitrile and with an Ionic Liquid as Solvent or Electrolyte. *ACS Catal.* **2015**, *5*, 6440–6452.
(138) Matsubara, Y. Standard Electrode Potentials for the Reduction of CO_2 to CO in Acetonitrile–Water Mixtures Determined Using a Generalized Method for Proton-Coupled Electron-Transfer Reactions. *ACS Energy Lett.* **2017**, *2*, 1886–1891.
(139) Matsubara, Y. Unified Benchmarking of Electrocatalysts in Noninnocent Second Coordination Spheres for CO_2 Reduction. *ACS Energy Lett.* **2019**, *4*, 1999–2004.
(140) Stratakes, B. M.; Dempsey, J. L.; Miller, A. J. M. Determining the Overpotential of Electrochemical Fuel Synthesis Mediated by Molecular Catalysts: Recommended Practices, Standard Reduction Potentials, and Challenges. *ChemElectroChem* **2021**, *8*, 4161–4180.
(141) Savéant, J. M.; Su, K. B. Homogeneous Redox Catalysis of Electrochemical Reaction: Part VI. Zone Diagram Representation of the Kinetic Regimes. *J. Electroanal. Chem. Interfacial Electrochem.* **1984**, *171*, 341–349.
(142) Savéant, J.-M. *Elements of Molecular and Biomolecular Electrochemistry*; John Wiley & Sons, Inc.: Hoboken, NJ.
(143) Costentin, C.; Drouet, S.; Robert, M.; Savéant, J.-M. Turnover Numbers, Turnover Frequencies, and Overpotential in Molecular Catalysis of Electrochemical Reactions. Cyclic Voltammetry and Preparative-Scale Electrolysis. *J. Am. Chem. Soc.* **2012**, *134*, 11235–11242.
(144) Costentin, C.; Drouet, S.; Robert, M.; Savéant, J.-M. Correction to Turnover Numbers, Turnover Frequencies, and Overpotential in Molecular Catalysis of Electrochemical Reactions. Cyclic Voltammetry and Preparative-Scale Electrolysis. *J. Am. Chem. Soc.* **2012**, *134*, 19949–19950.
(145) Nichols, E. M.; Derrick, J. S.; Nistanaki, S. K.; Smith, P. T.; Chang, C. J. Positional Effects of Second-Sphere Amide Pendants on Electrochemical CO_2 Reduction Catalyzed by Iron Porphyrins. *Chem. Sci.* **2018**, *9*, 2952–2960.

Chapter 2: Chelating N-Heterocyclic Carbene Ligands Enable Tuning of Electrochemical Carbon Dioxide Reduction to Formate and Carbon Monoxide Through Surface Organometallic Chemistry

Portions of this work were published in the following scientific journal:
Cao, Z.‡; Derrick, J. S.‡; Xu, J.‡; Gao, R.; Gong, M.; Nichols, E. M.; Smith, P. T.; Liu, X.; Wen, X.; Coperet, C.; Chang, C. J. Chelating *N*-Heterocyclic Carbene Ligands Enable Tuning of Electrochemical CO_2 Reduction to Formate and Carbon Monoxide Through Surface Organometallic Chemistry. *Angewandte Chemie International Edition* **2018**, *57*, 4981–4985. (‡Denotes equal contribution)

Specific contributions: Dr. Zhi Cao helped with electrochemical measurements. Dr. Jun Xu did the solid-state NMR measurements. Dr. Rui Gao, Dr. Xingwu Liu, and Dr. Ming Gong helped characterize the surface functionalization.

2.1 Abstract

Reported here is the Chelate effect as a design principle for tuning heterogeneous catalysts for electrochemical CO_2 Reduction. Palladium functionalized with a chelating tris-*N*-heterocyclic carbene (NHC) ligand (Pd–timtmb^{Me}) exhibits a 32-fold increase in activity for electrochemical reduction of CO_2 to C1 products with high Faradaic efficiency (FE_{C_1} = 86%) compared to the parent unfunctionalized Pd foil (FE = 23%), with sustained activity relative to a monodentate NHC-ligated Pd electrode (Pd–mimtmb^{Me}). The results highlight the contributions of the chelate effect for tailoring and maintaining reactivity at molecular-materials interfaces enabled by surface organometallic chemistry.



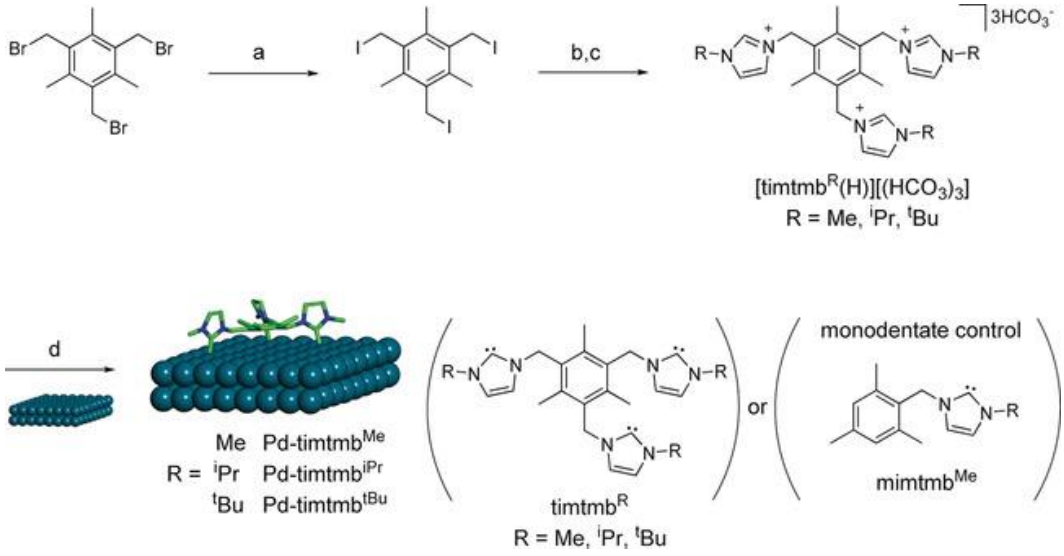
2.2 Introduction

The previous chapter introduced the concept of taking inspiration from biological systems to direct the design of new catalytic platforms for electrochemical CO_2 Reduction. Here we provide further detail on the incorporation of redox reservoirs as a pool of reducing equivalents into a catalyst framework by integrating molecular scaffolds onto solid metal cathodes to generate hybrid molecular-material catalysts for CO_2 reduction. This work establishes the chelate effect as an effective strategy to tailor electrochemical activity by improving the selectivity of CO_2 reduction to formate with enhanced rates and electrode stability.

The chelate effect is a classic principle of molecular chemistry that enables formation of metal-ligand coordination complexes with enhanced stability.[1] Given our interests in developing molecular approaches to hybrid catalyst platforms for electrochemical CO_2 reduction,[2–4] and drawing inspiration from the emerging use of N-heterocyclic carbenes (NHCs) as privileged ligands for influencing reactivity at metal surfaces,[5–28] we sought to explore the use of chelating NHC ligands to tune the reactivity of heterogeneous catalysts for electrochemical CO_2 reduction through surface organometallic chemistry. We now report that palladium electrodes functionalized with tridentate NHCs show enhanced activity and selectivity for electrochemical CO_2 reduction over parent unfunctionalized Pd counterparts, along with improved stability relative to Pd electrodes decorated with monodentate NHCs. By exploiting the chelate effect to achieve more robust attachment of molecular ligands to materials interfaces, this approach offers further opportunities to tailor heterogeneous catalysts and alter the surface with molecular-level precision.

2.3 Results and Discussion

Noting catalytic organic transformations mediated by heterogeneous Pd, including asymmetric α-arylations,[7] hydrogenations of olefins,[16,24,28] and Buchwald-Hartwig aminations,[27] as well as molecular Pd-NHC complexes for reductive transformations of CO_2,[29–31] tripodal tris-NHCs were prepared following slight modifications to previous literature methods[23,32–35] to give the benchtop stable, desired tripodal tris-imidizolium bicarbonate salts ([timtmb^{R}(H)][$(HCO_3)_3$], R = Me, ^{i}Pr, ^{t}Bu; **Scheme 2.1**). Pd functionalized electrodes (Pd–timtmb^{Me}, Pd–timtmb^{iPr}, and Pd–timtmb^{tBu}) were then generated by soaking pretreated, thermally annealed Pd foils in 10 mM methanol solutions of [timtmb^{R}(H)][$(HCO_3)_3$] for 12 h to generate the free tridentate carbenes, timtmb^{R}, in situ and washing with methanol to remove excess uncoordinated ligands. The resulting NHC-functionalized Pd electrodes were then dried, characterized, and evaluated for electrocatalytic studies.



Scheme 2.1. Synthetic scheme for the preparation of tripodal *N*-heterocyclic carbenes and functionalization of palladium surfaces: (a) NaI, Me_2CO, RT, 5 min; (b) imidazole (1-methylimidazole, 1-isopropylimidazole, or 1-*tert*-butylimidazole), Me_2CO, RT, 5 h; (c) CO_2, H_2O_2, RT, 1 h; (d) MeOH, Pd foil.

The attachment of the timtmb^{Me} ligand to the palladium surface was first identified by high-resolution N1s X-ray photoelectron spectroscopy (XPS). The N1s peaks at 401.3 and 399.6 eV are consistent with previously reported spectra assigned to a surface-capped NHC layer,[26] thus confirming the existence of timtmb^{Me} on the palladium surface (Pd-timtmb^{Me}; **Figure 2.1a**). Additional analysis of the Pd-timtmb^{Me} electrode by external-reflection FT-IR spectroscopy shows two broad bands at about 1602 and 1339 cm^{-1}, which are consistent with C–C and C–N stretching vibrations of the imidazole[34] and are identical to those observed for [timtmb^{Me}(H)][$(HCO_3)_3$], thus further supporting the successful functionalization of the electrode surface (**Figure 2.1b**). Interaction of the tris-NHC ligands with the palladium surfaces was further reflected by the changes in ^{13}C NMR peaks resulting from interactions between the ^{13}C nuclei of the ligands and the Pd^{0} surface,[3,26,34,35] which typically leads to broadening and shifting of resonance peaks as

observed in the solid-state ^{13}C NMR spectra of [timtmb^{tBu}(H)][$(HCO_3)_3$] versus that of Pd-timtmb^{tBu} (**Figure 2.2**).

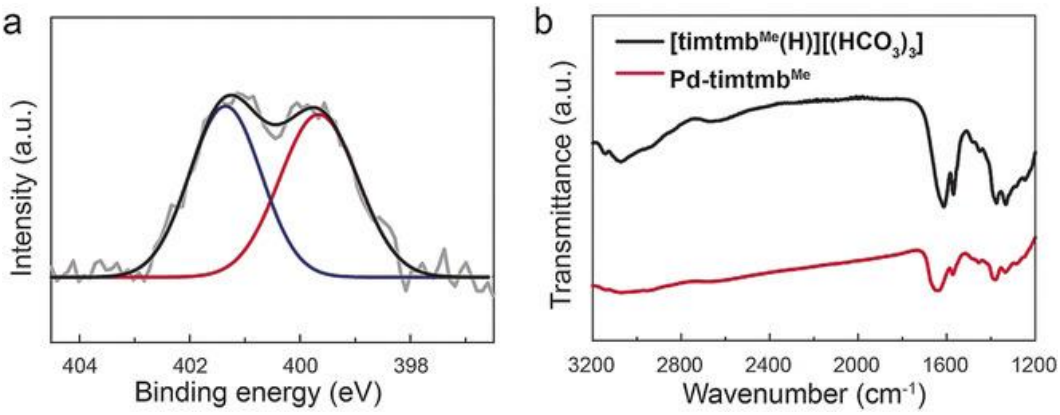


Figure 2.1. Surface attachment of timtmb^{Me} onto Pd foil. (a)High-resolution XPS spectrum of N1s region of Pd-timtmb^{Me}. (b) External-reflective IR spectra of [timtmb^{Me}(H)][$(HCO_3)_3$] and Pd-timtmb^{Me}.

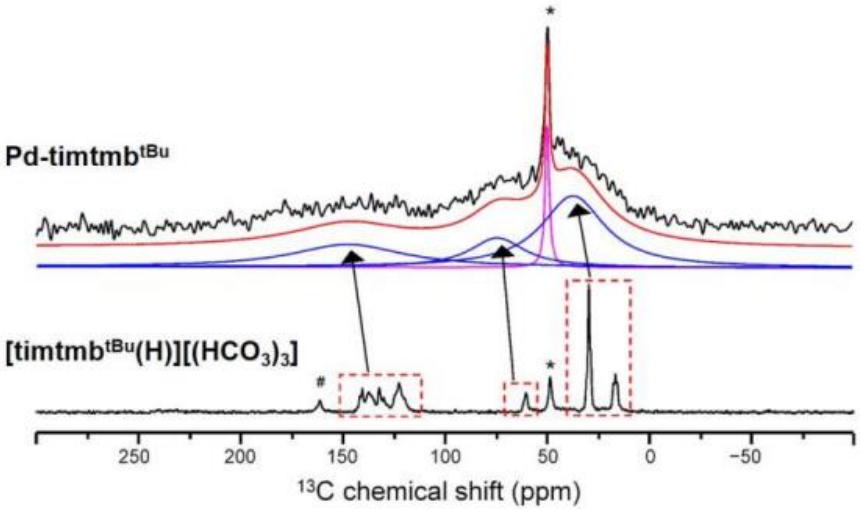


Figure 2.2. Solid-state ^{13}C NMR spectra of [timtmb^{tBu}(H)][$(HCO_3)_3$] and Pd–timtmb^{tBu}. * indicates methanol and # denotes HCO_3^-.

With characterization of the tripodal NHC-functionalized palladium surfaces in hand, we assessed the catalytic activity of the methyl-NHC derivative Pd-timtmb^{Me} for electrochemical CO_2 reduction, compared to that of the unmodified control palladium foil, in pH 7 aqueous media using 0.5 M $KHCO_3$ as the electrolyte. The current density was normalized to the geometric area of the working electrode and all potentials reported herein are referenced to the reversible hydrogen electrode (RHE). The Pd-timtmb^{Me} catalyst exhibits larger total current densities and positively shifted onset potentials relative to the control palladium foil according to cyclic voltammetry (CV) studies (**Figure 2.3a**). The onset potential at –0.12V, positively shifted by 265 mV relative to the palladium control, reflects a superior catalytic activity of NHC-functionalized Pd-timtmb^{Me} for

electrochemical reduction of CO_2 in neutral aqueous media. No increase in current or anodic shift in onset potential was observed for NHC-functionalized palladium foils under Ar atmosphere, thus suggesting that this phenomenon is not the result of the reduction of surface-bound timtmb^{Me} (see **Figure 2.4**).

Controlled potential electrolysis (CPE) experiments were performed in CO_2-saturated $KHCO_3$ buffer under different applied potentials between –0.37 V and –0.87 V to quantify the catalytic products of CO_2 reduction. Gaseous products were analyzed by gas chromatography (GC) and liquid products were characterized by ^{1}H NMR spectroscopy. Analysis of the head-space and electrolyte solutions following CPE experiments identified CO and H_2 as the gaseous products for both Pd-timtmb^{Me} and palladium foil as the catalyst while the functionalized electrode, Pd-timtmb^{Me}, generated a significant amount of formate relative to the unfunctionalized palladium electrode. The calculated Faradaic efficiencies (FEs) for C1 products (formate and CO) for Pd-timtmb^{R} and unmodified palladium are shown in **Figure 2.3b**. The Pd-timtmb^{R} catalysts show higher FEs for C1 products compared to the control palladium foil at all potentials examined. At a potential of –0.57V, the Pd-timtmb^{Me} catalyst displays an optimal FE for C1 production (FE = 86%; 82% of formate and 4% of CO) with a moderate overpotential of 360 mV (**Figures 2.3c,d**), with the remaining current going to H_2 production. The control palladium foil shows a peak FE of 23% with CO as the major C1 product. For comparison, the FEs of both Pd-timtmb^{iPr} and Pd-timtmb^{tBu} were obtained and also show improved formate selectivity (**Figure 2.3c**) over the control palladium, but slightly lower than Pd-timtmb^{Me}. In addition to the superior selectivity of Pd-timtmb^{Me} for CO_2 reduction products, Pd-timtmb^{Me} also showed significantly enhanced specific current densities (j_{C_1}) at all potential ranges compared to the unfunctionalized palladium foil. Indeed, at the applied potential of –0.57 V, Pd-timtmb^{Me} exhibits a 32-fold increase in specific current density compared to the unfunctionalized palladium foil (**Figure 2.3e**).

To evaluate the contributions of the timtmb^{Me} ligand to the observed improvements in catalytic activity and selectivity, we first investigated the electrochemically active surface area (ECSA) of the palladium foil with and without timtmb^{Me} functionalization by a CO stripping method (**Figure 2.3f**).[36,37] The calculated ECSA of Pd-timtmb^{Me} is 51% of the unmodified palladium foil, presumably resulting from the occupation of palladium sites by timtmb^{Me} ligands on the surface. Despite its smaller ECSA relative to control palladium foil, the higher activity and selectivity for CO_2 reduction observed on Pd-timtmb^{Me} shows the high intrinsic activity of the molecular-materials interface formed by NHC ligation. Another interesting factor extracted from the CO stripping voltammograms is the observed positive shift of the anodic CO oxidation peak upon timtmb^{Me} functionalization, which is suggestive of increased electron density on palladium surface by NHC functionalization and may contribute to the activity for electrochemical CO_2 reduction.

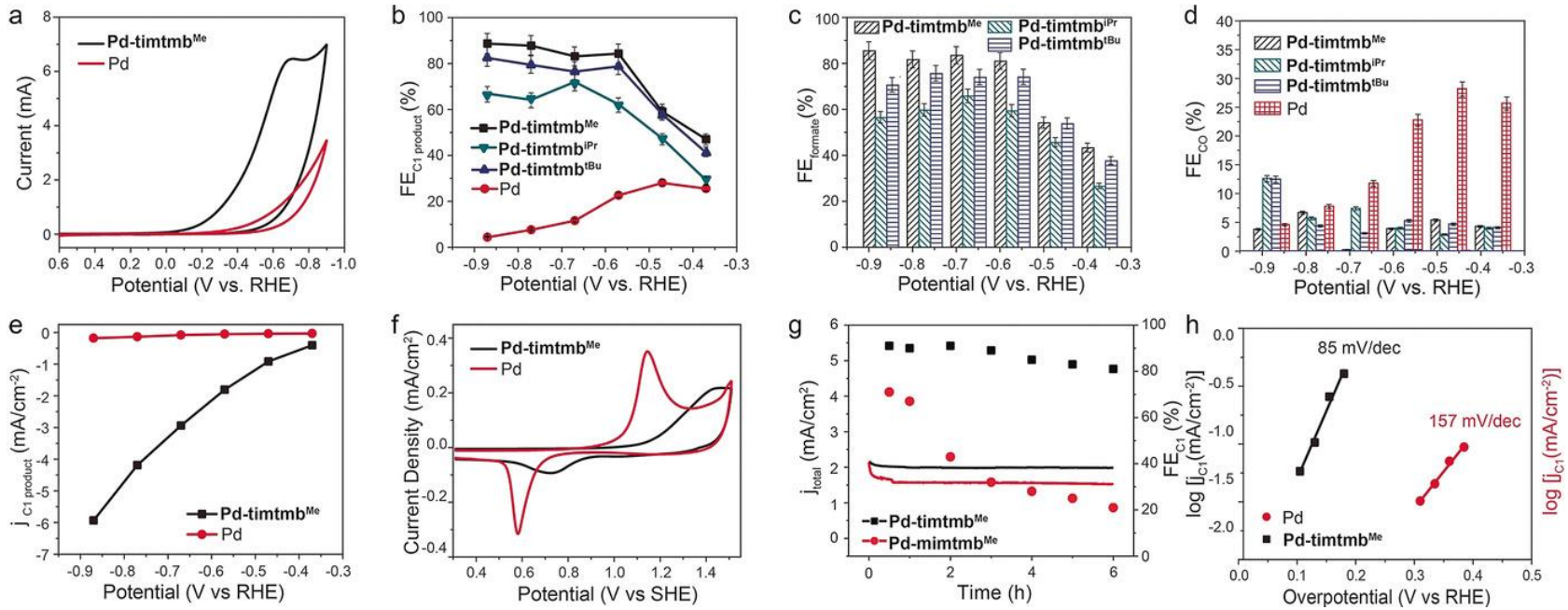


Figure 2.3. Electrochemical analysis of palladium catalysts. (a) CV scans of Pd and Pd-timtmb^{Me} electrodes in CO_2-saturated 0.5 M $KHCO_3$ at pH 7.3. (b) FEs of C1 products (CO for Pd; formate and CO for Pd-timtmb^{R}) produced by Pd and Pd-timtmb^{R} electrodes. (c) FEs of formate generation by the Pd-timtmb^{R} electrodes. (d) Faradaic efficiencies of CO generation by the Pd and Pd-timtmb^{R} electrodes. (e) Specific current densities of C1 products generated by Pd and Pd-timtmb^{Me} electrodes. (f) CO stripping voltammograms on Pd and Pd-timtmb^{Me} electrodes in 0.5 M H_2SO_4 electrolyte. The scan rate is 100 mV s^{-1}. (g) CPE of tridentate-NHC Pd-mimtmb^{Me} and monodentate-NHC Pd-timtmb^{Me} electrodes at −0.57 V over a 6 h time course. (h) Tafel plots of Pd and Pd-timtmb^{Me} electrodes.

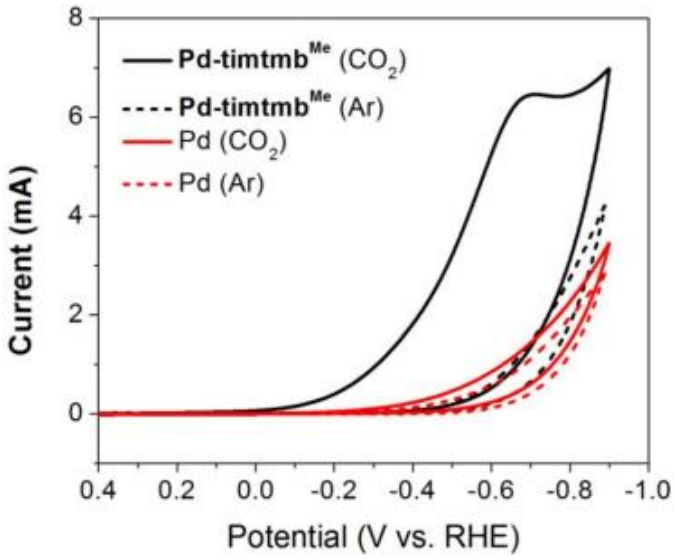
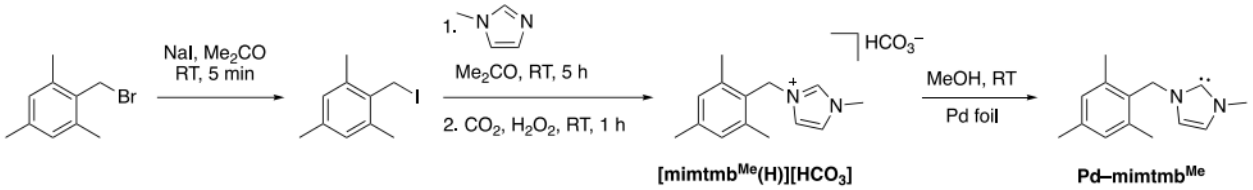


Figure 2.4. CV scans of Pd and Pd–timtmb^{Me} electrodes under Ar-saturated 0.5 M $KHCO_3$ at pH 7.3.

Longer-term CPE experiments at a potential of –0.57 V vs. RHE show that the Pd-timtmb^{Me} catalyst maintains activity and high FE for C1 product formation for up to 6 hours (**Figure 2.3g**). To evaluate the contributions of the chelate effect to catalyst stability, we prepared a monodentate NHC analogue (mimtmb^{Me}; **Scheme 2.2**) and made a functionalized palladium foil in MeOH to generate Pd-mimtmb^{Me}. First, to explore possible differences in coordination modes between the tridentate timtmb^{Me} and the monodentate mimtmb^{Me} ligands with the palladium surface, differences resulting from the decreased steric bulk associated with the elimination of two of the NHC arms, CO stripping voltammograms were measured for Pd-mimtmb^{Me}.[38–40] As can be seen in **Figure 2.5**, the CO stripping voltammogram for Pd-mimtmb^{Me} was similar to that of Pd-timtmb^{Me} but with a slightly smaller CO oxidation peak. The positive shift in the CO stripping peak suggests that a similar donation effect exists between mimtmb^{Me} and the palladium surface. Taken together, these results suggest a similar interaction mode between mimtimb^{Me} and timtmb^{Me} with the palladium electrode, with mimtmb^{Me} having a slightly higher surface coverage than Pd-timtmb^{Me}. To further deconvolute the role of coordination modes from denticity in this system, a more thorough molecular level investigation into the exact coordination chemistry of these molecules to metallic surfaces will be the subject of future study. CPE experiments under CO_2 atmosphere with Pd-mimtmb^{Me} show that Pd-mimtmb^{Me} does enhance the electrocatalysis of CO_2 compared to native palladium foil at early time points, however it exhibits inferior stability and activity over the same 6 hour time period as reflected by the significant FE loss for C1 down to less than 40% within 2 hours of electrolysis (**Figure 2.3g**). These data suggest that the chelate effect may be essential for maintaining electrochemical activity for selective CO_2 reduction.



Scheme 2.2. Synthetic scheme for the preparation of the monodentate control carbene. [mimtmb^{Me}(H)][HCO_3] was prepared through an analogous synthetic route used for the preparation of the tripodal imidazolium bicarbonate salts. The monodentate *N*-heterocyclic carbene**,** mimtmb^{Me}, was prepared in situ in a solution of MeOH in the presence of Pd foil following an identical procedure that was used for the tridentate ligands.

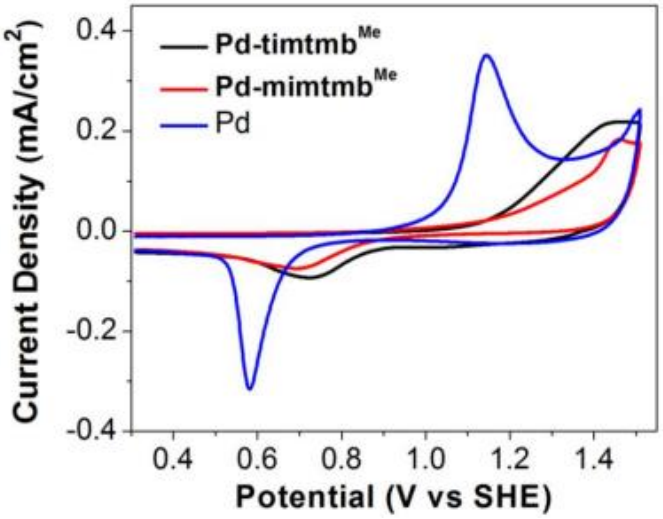


Figure 2.5. CO stripping voltammograms on Pd–timtmb^{Me}, Pd–mimtmb^{Me} and Pd electrodes in 0.5 M H_2SO_4 electrolyte. The scan rate is 100 mV/s.

The stability of Pd-timtmb^{Me} under electrochemical conditions was further evaluated by FT-IR, double-layer capacitance,[41,42] and XPS measurements. Indeed, the Pd-timtmb^{Me} catalyst possesses nearly identical FT-IR features prior to and immediately after electrolysis, thus reflecting its electrochemical durability (see **Figure 2.6**). Furthermore, the electrochemically accessible palladium surface area for the same Pd-timtmb^{Me} working electrode before and after electrolysis is nearly identical as evidenced by only subtle observed differences in measured area for double-layer capacitance (see **Figures 2.6** and **2.7**). Moreover, high-resolution N1s XPS peaks are persistent after bulk electrolysis, thus confirming the existence of timtmb^{Me} on the palladium surface (see **Figure 2.8**) throughout the reaction.

We next explored the kinetics of CO_2 reduction on the control palladium and NHC-functionalized palladium electrodes using Tafel analysis (**Figure 2.3h**). The data establish that NHC functionalization influences the mechanistic pathways for CO_2 reduction. A Tafel slope of 157 mV/decade is observed for the control palladium, and is comparable to the 118 mV/decade expected for rate-limiting single-electron transfer from the adsorbed CO_2 to generate the surface adsorbed $CO_2^{\bullet-}$.[43] In contrast, the Tafel slope for Pd-timtmb^{Me} is 85 mV/decade, thus reflecting

the possibility that Pd-timtmb^{Me} may undergo a pre-equilibrating one-electron transfer followed by a rate-limiting chemical step. Strong σ-donation from the NHC ligands can make the palladium surface of Pd-timtmb^{Me} more electron-rich, which in turn can promote fast electron transfer to CO_2 prior to the rate-determining step.

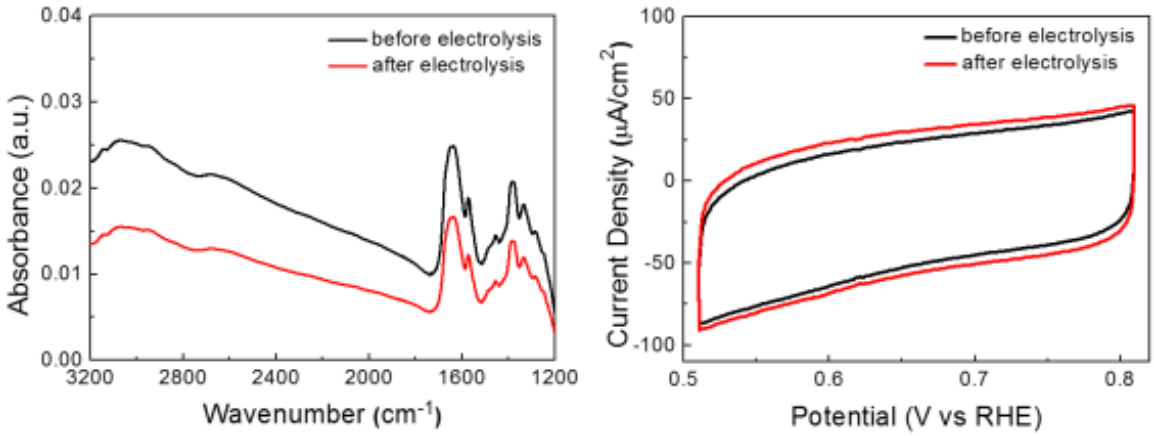


Figure 2.6. Reflective IR spectra of Pd-timtmb^{Me} before and after 1 h bulk electrolysis at –0. 57 V vs RHE (left). Cyclic voltammetry curves of Pd-timtmb^{Me} in 0.5 M H_2SO_4 for determining double-layer capacitance before and after 1h bulk electrolysis at –0.57 V vs RHE (right).

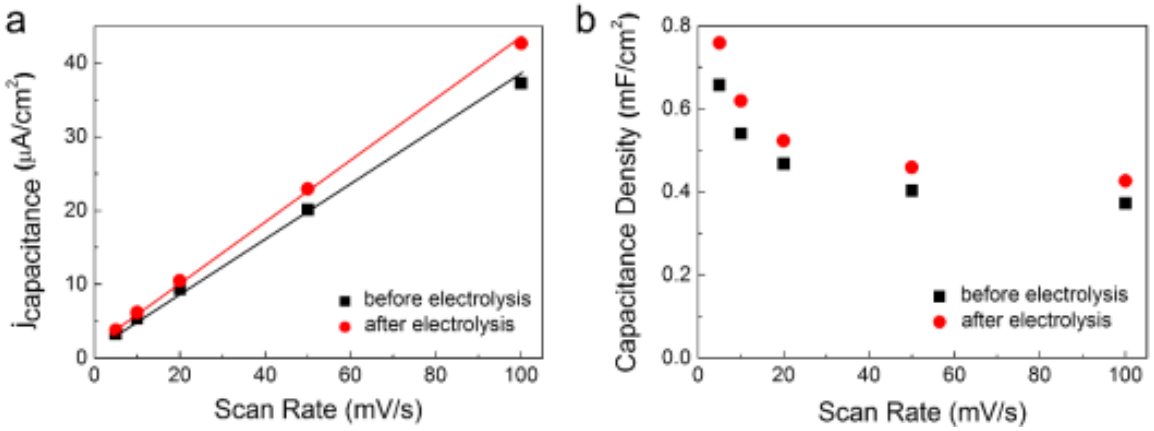


Figure 2.7. (a) Current density due to double-layer charge/discharge plotted against CV scan rate. (b) Capacitance density due to double-layer charge/discharge as a function of CV scan rate.

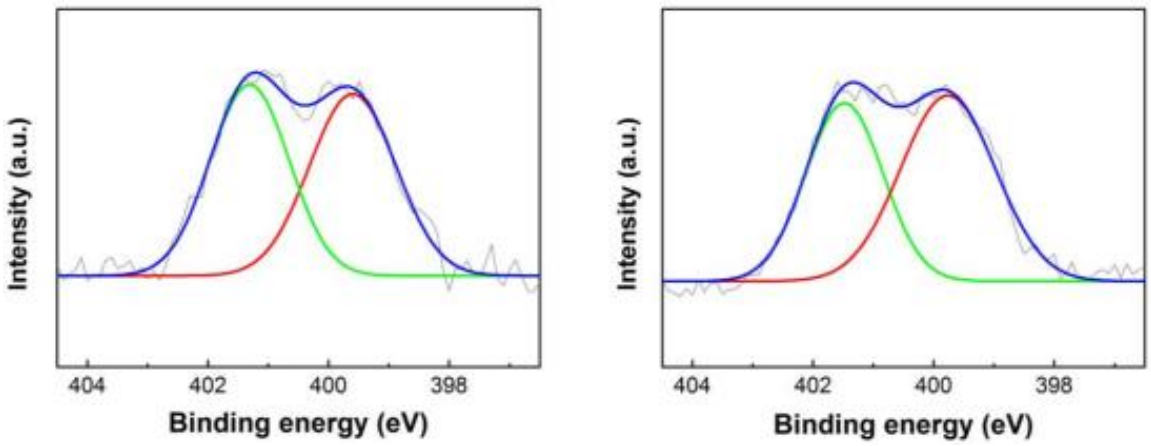


Figure 2.8. High resolution XPS spectra of N1s region of Pd–timtmb^{Me} before electrolysis (left) and after electrolysis (right).

Finally, we performed DFT calculations to further probe the effects of NHC ligation on the palladium surface and its reactivity consequences. In particular, we computed the possible pathways of CO_2 hydrogenation into HCOOH on two surface models of Pd(111) and Pd(111)-timtmb^{Me} (**Figures 2.9** and **2.10**). The initial step of CO_2 hydrogenation (CO_2 + H* → COOH*) generates COOH*, a key reaction intermediate of CO_2 reduction,[8,10,13,20–22,25,44] with an energy barrier of 0.85 eV for Pd-timtmb^{Me}, compared to a 1.23 eV barrier for a parent Pd(111) surface, thus reflecting a more energetically favored pathway for COOH* formation on Pd-timtmb^{Me}. HCOOH formation was further computed by COOH* hydrogenation on the two models. For COOH* + H* → HCOOH, the calculated barriers are 1.24 and 1.00 eV on Pd(111) and Pd(111)-timtmb^{Me}, thus indicating that HCOOH formation on Pd-timtmb^{Me} over the control palladium is favored as well. These computational findings are consistent with the experimental observations that formate is formed as the dominant C1 product in Pd-timtmb^{Me} mediated CO_2 reduction. CO formation on the Pd(111)-timtmb^{Me} is predicted to be energetically unfavored as reflected by the larger required energy compared with Pd(111) (see **Figure 2.11**). Moreover, the improved electrochemical stability of Pd-NHC electrodes, formed from tridentate versus monodentate NHCs effect arising from timtmb^{Me} functionalization, is calculated to be borne out by the significantly favored adsorption energy of Pd(111)-timtmb^{Me} (–1.21 eV) relative to Pd(111) (–0.39 eV), as shown by our DFT calculations (see **Figure 2.12**).

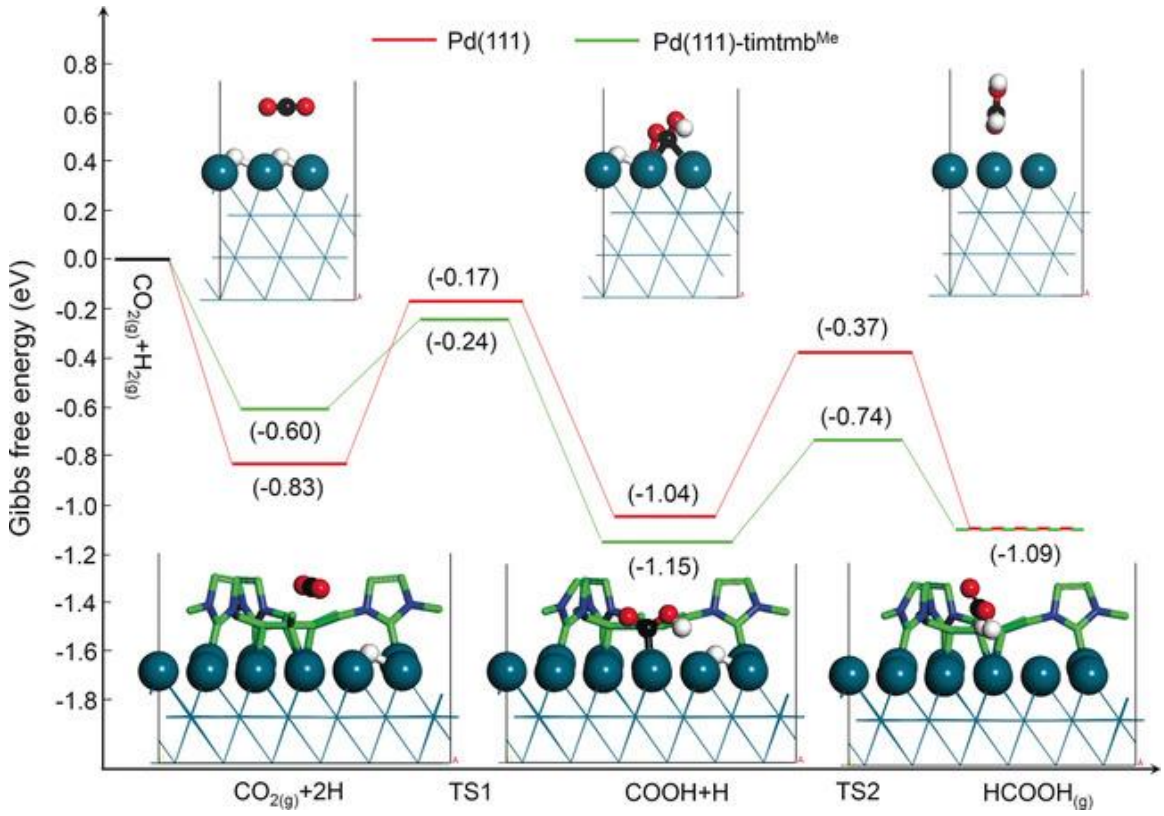


Figure 2.9. Free-energy diagrams for CO_2 reduction to HCOOH on Pd(111) (red line) and Pd(111)-timtmb^{Me} (green line).

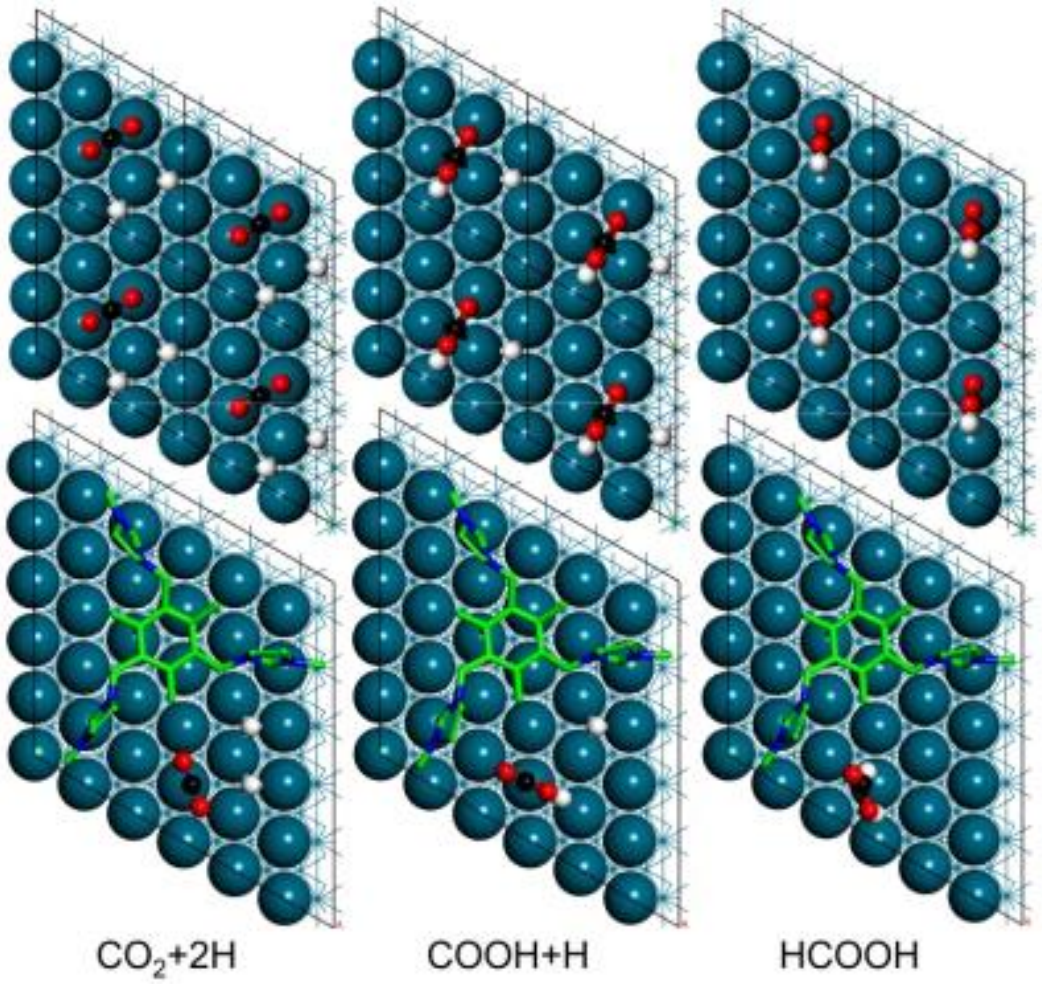


Figure 2.10. Top view of equilibrium structures for the adsorption of CO_2+2H, COOH+H, and HCOOH on the surface of Pd(111) (top) and Pd(111)-timtmb^{Me} (bottom), respectively. The catalyst surface and intermediates are represented in ball, whereas the carbene molecule is given in stick. The Pd, C, N, O and H atoms are in navy, green, blue, red, and white, respectively; whereas the C atom from CO_2 is depicted in black to distinguish it from other carbons.

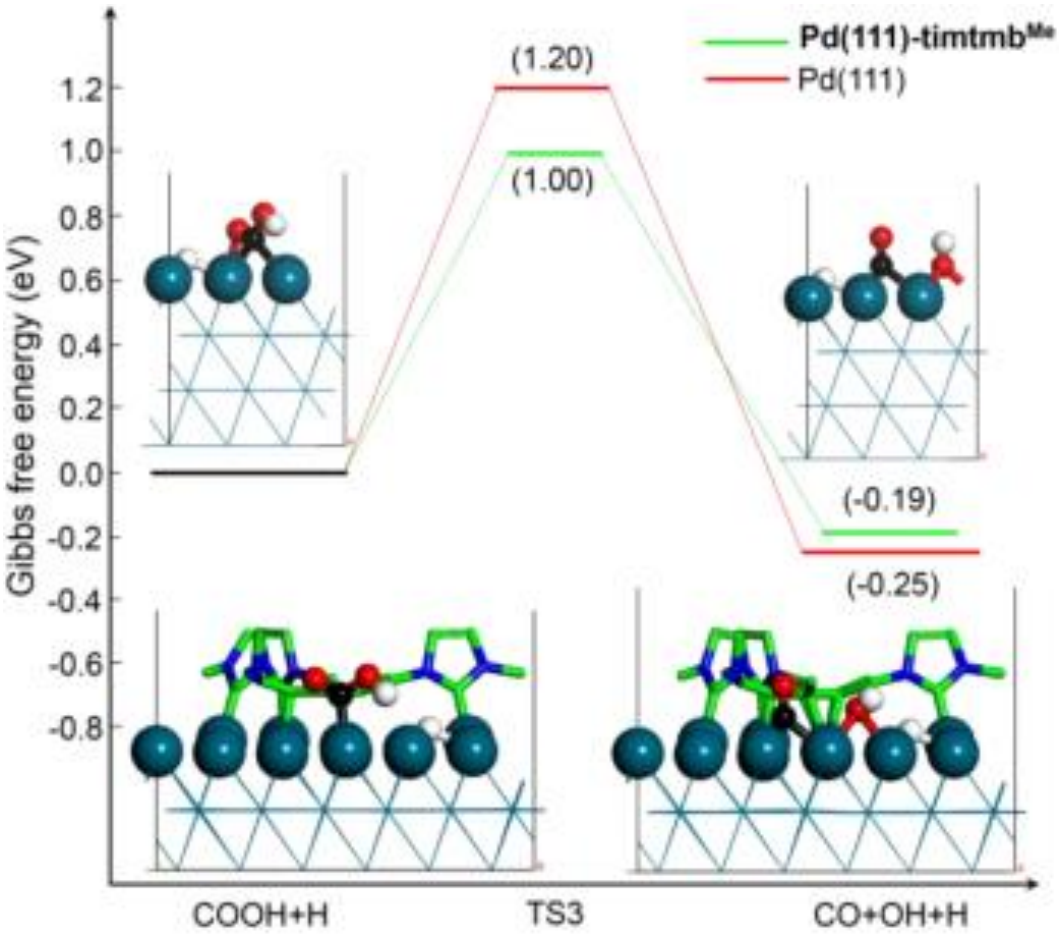


Figure 2.11. Free energy diagram of COOH dissociation to generate CO on Pd(111) (red line) and Pd(111)-timtmb^{Me} (green line), respectively. The catalyst surface and intermediates are represented in ball, whereas the carbene molecule is given in stick. The Pd, C, N, O and H atoms are in navy, green, blue, red, and white, respectively, whereas the C atom from CO_2 is depicted in black to distinguish it from other carbons.

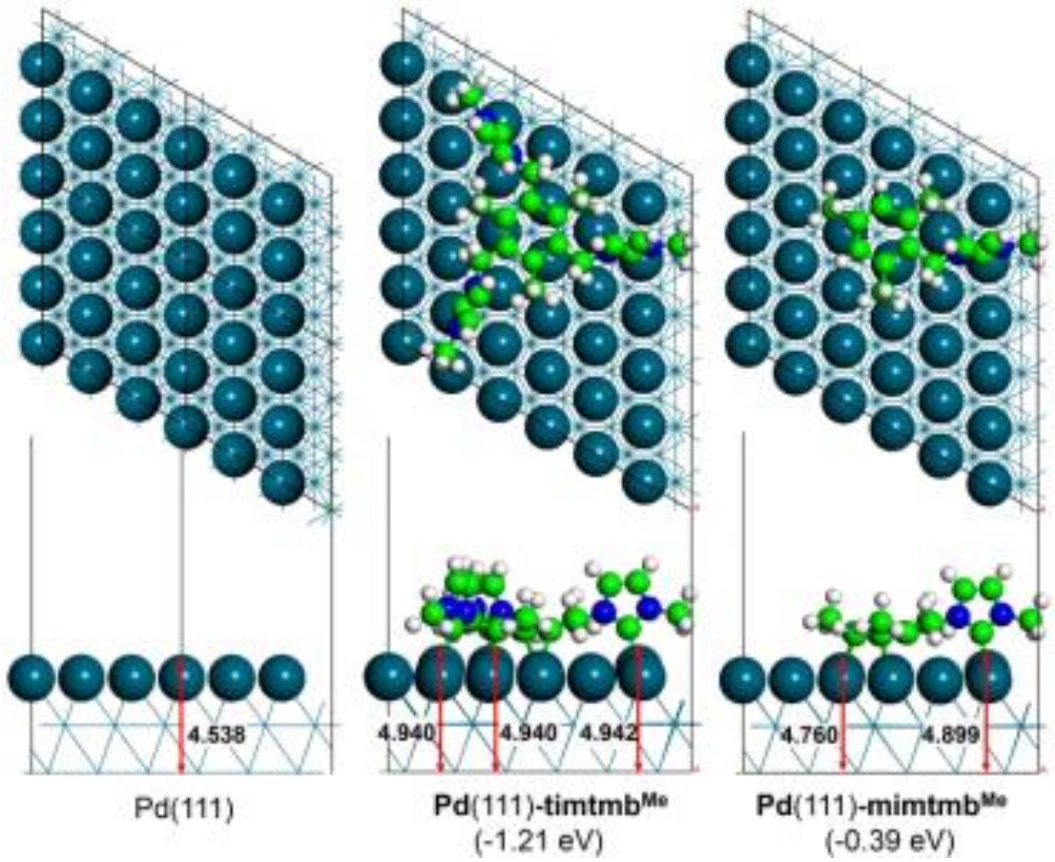


Figure 2.12. The top and side view of equilibrium structures of Pd(111), Pd(111)-timtmb^{Me} , and Pd(111)-mimtmb^{Me} . Pd, C, N and H atoms in navy, green, blue, and white, respectively. Herein, we speculate that carbene coordination may influence the palladium surface through a combination of both electronic and geometric effects. Strong σ-donation from the carbenes can make the palladium surface more electron rich, which may explain the observed change in mechanism for NHC-functionalized Pd, in which a fast electron transfer to CO_2 occurs prior to the rate determining step. From a geometric perspective, the strong carbene–palladium bond can also potentially destabilize Pd–Pd bonding with neighboring atoms. This destabilization may lead to restructuring of the Pd surface, thereby increasing the number of defect sites with better kinetics for the CO_2 reduction reaction.[3]

2.4 Conclusion

Taken together, this work establishes the chelate effect as a molecular design approach for tuning heterogeneous catalysts, as illustrated by observed improvements in activity, selectivity, and stability for electrochemical CO_2 reduction on Pd electrodes modified through tris-NHC ligation. We anticipate that this surface organometallic chemistry strategy,[45] in which molecular-materials analogs to homogeneous coordination complexes can be developed and studied, will be applicable for a broader range of catalytic processes and other applications.

2.5 Materials and Methods

2.5.1 General Methods

All chemicals were obtained from commercial suppliers and used without further purification, unless otherwise mentioned. 1,3,5-tris(bromomethyl)-2,4,6-trimethylbenzene, 1-methylimidazole, and 1-tert-butylimidazole, were purchased from TCI America. 2-(bromomethyl)-1,3,5-trimethylbenzene was purchased from Enamine. 1-isopropylimidazole was purchased from Santa Cruz Biotechnology. Sodium iodide was purchased from Alfa Aesar. Sulfuric acid (ACS reagent, 95.0-98.0%), potassium bicarbonate (≥99.99% trace metals basis, 99.7-100.5% dry basis), palladium foil (99.95% trace metals basis, thickness 0.05 mm) and silver wire (99.9% trace metal basis, 0.5 mm diameter) were purchased from Sigma Aldrich. Deionized water was obtained from a Millipore Autopure system. All reagents were of analytical grade and used without further purification. Carbon dioxide (5.0 UHP), carbon monoxide (5.0 UHP), hydrogen (5.0 UHP) and argon (5.0 UHP) gas were purchased from Praxair.

2.5.2 Iodide Analysis

To evaluate the removal of iodine, a qualitative silver nitrate test was performed according to a previous literature report.[23] The results from these experiments are shown in **Figure 2.13**. Upon addition of [timtmb^{R}(H)][$(I)_3$] and [timtmb^{R}(H)][$(HCO_3)_3$] (or [mimtmb^{Me}(H)][I], and [mimtmb^{Me}(H)][HCO_3]) to 1.0 M solutions of $AgNO_3$, light yellow (AgI) and white ($AgHCO_3$) precipitates were generated, respectively. Further addition of 1 M nitric acid to the vial containing [timtmb^{Me}(H)][$(HCO_3)_3$] (or [mimtmb^{Me}(H)][HCO_3]) resulted in the solution becoming transparent (solubilizing $AgHCO_3$) while the vail with [timtmb^{Me}(H)][$(I)_3$] (or [mimtmb^{Me}(H)][I]) remained opaque (**Figure 2.13**). The presence of the bicarbonate anions in [timtmb^{R}(H)][$(HCO_3)_3$] and [mimtmb^{Me}(H)][HCO_3] was further validated from the ^{13}C NMR spectrum (peak at 161 ppm). Quantitative analysis for removal of iodide was determined by elemental analysis via Schoniger combustion (Midwest Microlab; Indianapolis, IN).

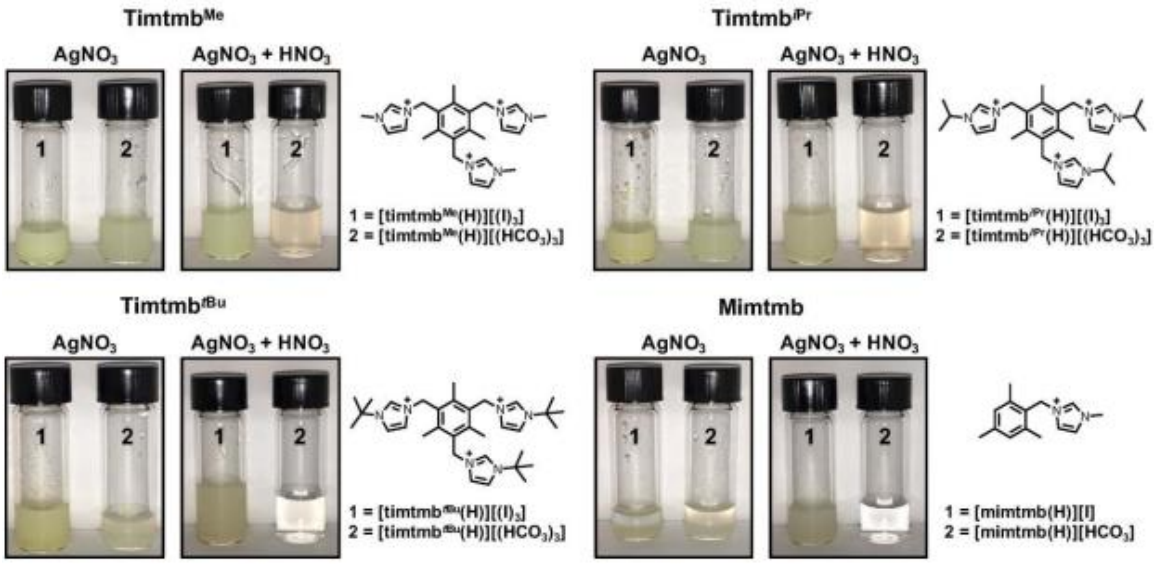


Figure 2.13. Qualitative silver nitrate ($AgNO_3$) chemical test for iodide removal in [timtmb^R(H)][$(I)_3$], [timtmb^R(H)][$(HCO_3)_3$], [mimtmb^{Me}(H)][I], and [mimtmb^{Me}(H)][HCO_3].

2.5.3 Preparation of Pd foil and NHC Functionalized Pd Electrodes

A polycrystalline palladium foil (Sigma Aldrich, 99.95% trace metals basis, thickness 0.05 mm) was used as a reference for the NHC functionalized palladium samples. The foil was cut into pieces of approximately 1 cm × 2 cm with immersed area of 1 cm^2, and the pieces were cleaned with acetone, methanol, and deionized water. The dried foil pieces were then put into a quartz tube furnace. The system was evacuated for 10 minutes, and the temperature was then gradually increased to 600 °C over a course of 1 hour and held at 600 °C under a H_2/Ar (1:9) mixture for 8 h to anneal the Pd foil. After slowly cooling down to room temperature, the pre-treated Pd foils are ready for use for electrochemical measurements or functionalization with timtmb^R (R = Me, iPr, tBu). The NHC carbene functionalized electrodes were then prepared by soaking pretreated Pd foils in 10 mM methanol solutions of [timtmb^R(H)][$(HCO_3)_3$] (R = Me, iPr, tBu) for 12 h (suspension of [timtmb^R(H)][$(HCO_3)_3$] in methanol generates the desired carbenes, timtmb^R, *in situ*) and washing with methanol to remove the excess uncoordinated ligand. The resulting functionalized electrodes were then dried and ready for use in electrochemical studies.

2.5.4 X-Ray Photoelectron Spectroscopy (XPS)

XPS spectra were recorded with an ECSA3057, (ULVAC Phi.) using an Al Kα X-ray source (1486.7 eV). Narrow multiple scans were obtained with a pass energy of 35.75 eV and 0.1 eV energy steps. The binding energy scale was corrected setting C1s peak in 284.6 eV.

2.5.5 External Reflection Fourier Transform Infrared Spectroscopy (ER-FTIR)

The spectra were recorded on an FT-IR spectrometer in a diffuse reflectance mode (4 cm^{-1} resolution, FT/IR-4200, JASCO). The incident IR beam was reflected off the sample substrate at

the incident angle of 60 degrees, and the spectra were acquired with a resolution of 1 cm^{-1}. Absorption due to air (CO_2 and water vapor) was subtracted from the spectra.

2.5.6 Solid-State $^{1}H-^{13}C$ Cross-Polarization (CP) Magic-Angle Spinning (MAS) NMR Spectroscopy

The experiments were performed on a Bruker Avance III HD spectrometer at 9.4 T using a Bruker 4 mm double-resonance probe. The CP conditions were optimized on glycine. A pulse delay of 4 s and a short contact time of 0.5 ms were used. The spinning rate was 10 kHz. ^{13}C chemical shifts were referenced to the methylene signal of adamantane, which is 38.48 ppm relative to the primary reference TMS.

2.5.7 Electrochemical Cell Design

Controlled-potential electrolysis was conducted using a custom-made, three-piece glass cell made by Adams & Chittenden Scientific Glass, which includes a working compartment body, a working compartment lid, and a counter compartment body. The main bodies of the two compartments were assembled together using an O-ring and a Teflon clamp and were separated by a Selemion membrane. The body of the working compartment was charged with a 3 cm long Teflon-coated stir bar and 130 mL of electrolyte solution (0.5 M aqueous $KHCO_3$, unless otherwise noted), and the lid was fitted with a functionalized palladium working electrode (1 cm × 2 cm fixed onto an alligator clip with immersed area of 1 cm^2) and an Ag/AgCl reference electrode. Both electrodes were connected to the outside through a stainless steel rod (1/16 inch diameter × 2 inch length, connected to the palladium through the alligator clip and the reference electrode through a two-way metal socket). The lid was also equipped with a Teflon sparging line that extends into the electrolyte solution and a gas outlet that connects to the headspace of the cell. Both gas ports were connected to a two-way Swagelok valve, and the valve at the gas outlet was also fitted with a Swagelok male miniature quick-connect. During sample analysis, this quick-connect was connected to a female miniature quick-connect on the injection inlet of the GC. The lid and the main body of the working compartment were assembled using an o-ring and a Teflon clamp, and the position of the working electrode was adjusted so that only the area covered with the catalyst was immersed in the solution while the silver wire was not. The resulting working compartment has a headspace volume of ~120 mL. The counter compartment was filled with 50 mL of electrolyte solution (0.5 M aqueous $KHCO_3$), and equipped with a Teflon cap with a septum, as well as a graphite auxiliary electrode connected to the outside with a stainless-steel alligator clip and a silver wire.

2.5.8 Controlled Potential Electrolysis (CPE)

CPE experiments were performed using a BASi EC Epsilon potentiostat/galvanostat. Ag/AgCl reference electrodes were obtained from BASi and stored in 3 M KCl solution before use. Gas production was measured on an SRI gas chromatography instrument (model #8610C) equipped with a Haysep D column (1/8" × 6') and a 13 × Mol Sieve column (1/8" × 6'), with ethylene (C_2H_4) as the internal standard; carbon monoxide (CO) was quantified using flame ionization detector (FID) and hydrogen (H_2) using thermal conductivity detector (TCD). All potentials in this study were measured against the Ag/AgCl reference electrode and converted to

the RHE reference scale by E (vs. RHE) = E (vs. Ag/AgCl) + 0.21 V + 0.0591 × pH. After the electrochemical cell was assembled, the electrolyte solution in the working compartment was sparged for 30 minutes with CO_2. Then, 1 mL ethylene was injected into the headspace as the internal standard for GC analysis. The solutions were electrolyzed at a constant potential for a desired test period. Following electrolysis, the headspace of the cell was analyzed by the GC. The $KHCO_3$ solution after electrolysis was collected and analyzed on a Bruker 500 MHz NMR spectrometer to quantify liquid products. Samples of the $KHCO_3$ solution after electrolysis were analyzed by quantitative ^1H NMR using dimethyl sulfoxide as an internal standard. The ^1H spectrum was measured with water suppression by a pre-saturation method. The concentration of liquid products was determined by comparing the standard curves made from various known concentrations (0.05, 0.1, 0.5 and 1 mM) of purchased chemicals. The area ratio of the formate peak to the dimethyl sulfoxide peak was compared to the standard curve to quantify the concentration of formate.

2.5.9 Cyclic Voltammetry (CV)

Using the same electrochemical setup as described above, the electrolyte solution in the working compartment was sparged for 20 minutes with Ar or CO_2. CV scans were then taken from 0 to –1.50 V vs. Ag/AgCl with a scan rate of 50 mV/s. Multiple consecutive cycles were taken until the voltammogram from each cycle overlays. The initial few cycles were not recorded until a stable polarized curve was observed.

2.5.10 Stripping Experiments

Experiments were carried out in an electrolyte of 0.5 M H_2SO_4. CO stripping voltammograms were obtained after bubbling CO through the cell for 10 min while keeping the electrode in the electrolyte at 0.1 V vs SHE, followed by Ar purging for 20 min to remove the excess CO that is not adsorbed. The working electrode was then subject to cyclic voltammetry studies for obtaining CO stripping voltammograms. The scan rate is 100 mV/s and the scanning polarity is toward the positive direction. For the determination of electrochemically active surface area of the electrodes we used stripping charge of saturated CO adlayer (see **Figure 2.3f**). On palladium electrodes, CO_{ad} oxidation takes place in the range between –0.65 and –1.2 V (vs Ag/AgCl). The net Faradaic charge for the oxidation of a saturated CO adlayer (Q_{CO} oxidation) net is determined by the difference of Faradaic charge between with and without CO_{ad} obtained from the integration of CV diagram between –0.65 and –1.2 V (vs Ag/AgCl) divided by the scan rate.

2.5.11 Double Layer Capacitance Measurements

Cyclic voltammetry was performed in the same electrochemical cell as in the CPE experiments with a Nafion proton exchange membrane and 0.5 M H_2SO_4 electrolyte. The capacitance current density was calculated by averaging the current density over the tested potential range within which no Faradaic process is occurring. The slope of the linear regression gives the capacitance over the scan rate.

2.5.12 Computational Methods

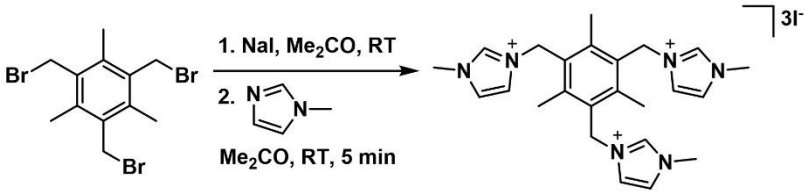
All calculations were performed using the plane wave based periodic DFT method as implemented in the Vienna Ab Initio Simulation Package (VASP).[46,47] The electron-ion interaction was described with the projector augmented wave (PAW) method.[48,49] The electron exchange and correlation energies were treated within the generalized gradient approximation in the Perdew-Burke-Ernzerhof functional (GGA-PBE).[50] The plane wave basis was set up to 450 eV. Electron smearing was used via the Methfessel-Paxton technique with a smearing width consistent to σ = 0.2 eV. The adsorption energies spin polarization was included. All transition states were estimated using the climbing image nudged elastic band method (CI-NEB).[51] The stretching frequencies were predicted to verify whether the stationary point is a minimal state associates a solely imaginary frequency.

The calculated lattice constant of cubic Pd cell (fcc) is 3.9433 Å (experimental = 3.8907 Å), and the Pd–Pd bond is 2.788 Å. In three structure models (see **Figure 2.11**), a unit cell p(3×3) was used for Pd(111) surface, whereas a unit cell of P(6×6) was used for Pd(111)-timtmb^{Me} and Pd(111)-mimtmb^{Me}. The k-point sampling of 3×3×1 was set for Pd(111), and 2×2×1 for the two NHC-adsorbed surfaces. In total, the Pd(111) surface has 36 Pd atoms, in which 18 Pd were fixed; the Pt(111)-NHC has 108 Pd atoms, and 36 Pd were fixed.

The adsorption energy was calculated according to $E_{ads} = E_{X/slab} - [E_{slab} + E_X]$, where $E_{X/slab}$ is the total energy of the slab with adsorbates in its equilibrium geometry, E_{slab} is the total energy of the bare slab, and E_X is the total energy of the free adsorbates in the gas phase. Therefore, the more negative the E_{ads}, the stronger the adsorption. The barrier (E_a) and reaction energy (ΔE_r) are calculated according to $E_a = E_{TS} - E_{IS}$ and $\Delta E_r = E_{FS} - E_{IS}$, where E_{IS}, E_{FS} and E_{TS} are the energies of the corresponding initial state (IS), final state (FS), and transition state (TS), respectively.

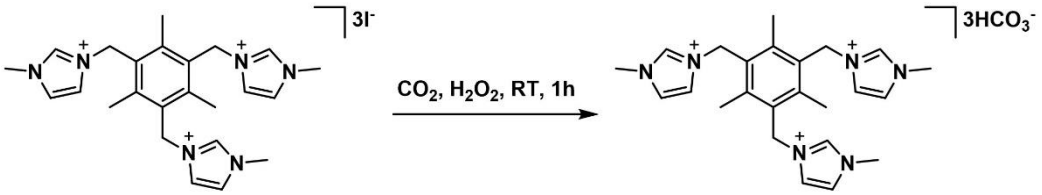
The computational hydrogen electrode[52] was used to study the reaction energy as a function of potential. At U = 0 V versus RHE, protons and electrons are at equilibrium with H_2 at ambient temperature and pressure, as well as all pH. At a given U ≠ 0 V versus RHE, $\mu(H^+) + \mu(e^-) = 1/2\mu(H_2) - eU$. Therefore, for example, the free energy change of the proton–electron transfer to CO_2 can be calculated as the following equation: $\Delta G = \mu(COOH^*) - \mu(CO_2) - [1/2\mu(H_2) - eU]$. Where $\mu = E + E_{ZPE} - TS$ was calculated by including zero-point energies and entropy contributions. According to our calculations, E_{ZPE} and TS are 0.27 and 0.41 eV in $\mu(H_2)$; 0.91 and 0.77 eV in μ(HCOOH); the E_{ZPE} in μ(2H*) is 0.32 eV. For the chemical potentials of the surface adsorbed species, such as COOH, CO, and OH, the E_{ZPE} and TS are neglected, e.g. μ(COOH*) = E(COOH*), as they are minimal for the free energy change. It is worthy to highlight that in our calculation the free energy of H_2 desorption, defined as $\Delta G = \mu(H_2) - \mu(2H^*)$, was not taken into consideration for the potential correction of U, as the elementary step for evolving H_2 in HER ($2H^* \leftrightarrow H_2 + 2^*$) is a Tafel reaction. It is worthy to note that the Tafel reaction is a homolytic reaction (a Langmuir-Hinshelwood type reaction), and thus not necessary to explicitly include water, ions, electric potentials, or electric fields in order to describe it in an electrochemical environment.[53,54]

2.5.13 Synthesis of [timtmbMe(H)][(I)3]



[timtmb^{Me}(H)][$(I)_3$] was prepared following slight modifications to previous literature reports.[23,32,33] To a flame-dried round-bottom flask equipped with a stir bar was added 1,3,5-tris(bromomethyl)-2,4,6-trimethylbenzene (400 mg, 1.0 mmol) and acetone (10 mL). The reaction was allowed to stir, protected from the light, until the reagent was fully soluble. To a separate flame-dried round bottom flask loaded with a stir bar was added sodium iodide (600 mg, 4.0 mmol) and acetone (10 mL). The reaction was allowed to stir, protected from the light, until the reagent was fully soluble. Once, fully soluble, the sodium iodide solution was quickly added to the round bottom flask containing the 1,3,5-tris(bromomethyl)-2,4,6-trimethylbenzene solution. The reaction was protected from light and allowed to proceed for exactly 5 min. After 5 min, the reaction was filtered through a flame-dried frit to remove precipitated sodium bromide. The resultant filtrate containing 1,3,5-tris(iodomethyl)-2,4,6-trimethylbenzene was then quickly transferred to a clean, flame-dried, round bottom flask and stirred at RT, protected from the light. To this solution was added 1-methylimidazole (248 µL, 3.11 mmol), which caused the immediate formation of a white precipitate. The reaction was allowed to stir for an additional 5 h at room temperature, protected from the light. After 5 h, the reaction mixture was filtered, and the white solid was collected and dried under vacuum to afford the iodide tridentate imidazolium salt. Yield: 566 mg (72%). ^{1}H NMR (400 MHz, $(CD_3)_2SO$)/ δ (ppm): 8.85 (3H, s), 7.76 (3H, t, *J* = 1.70 Hz), 7.67 (3H, t, *J* = 1.79 Hz), 5.54 (6H, s), 3.83 (9H, s), 2.31 (9H, s).

2.5.14 Synthesis of [timtmb^{Me}(H)][$(HCO_3)_3$]

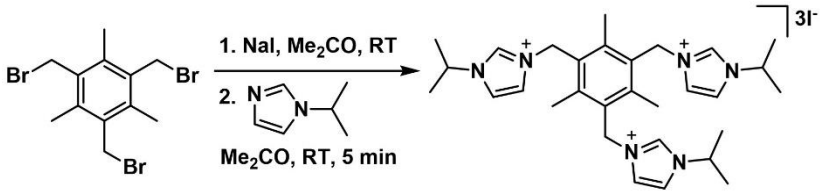


A final salt metathesis reaction was then carried out on the iodide imidazolium salt ([timtmb^{Me}(H)][$(I)_3$]) to exchange the iodide anions for bicarbonate anions that will participate as the base in methanol to generate the free carbene, timtmb^{Me}, *in situ* during the functionalization of the Pd foil. To a 10 mL round bottom flask loaded with a stir bar was added 200 mg (0.25 mmol) of the iodide imidazolium salt. 5 mL of water (pH 8.0) was added to the reaction flask and the reaction was then sparged with CO_2 for 1 min. 30% hydrogen peroxide solution (w/w) was then added to the reaction mixture (60 µL) and the reaction was stirred vigorously under CO_2 atmosphere for 1 h or until a dark purple precipitate was visible and the reaction solution was colorless. The reaction mixture was then filtered and the filtrate was evaporated under a steady flow of N_2 to yield [timtmb^{Me}(H)][$(HCO_3)_3$] as a crystalline white solid. The final desirable product, timtmb^{Me}, was obtained in situ by stirring [timtmb^{Me}(H)][$(HCO_3)_3$] in methanol. Yield:

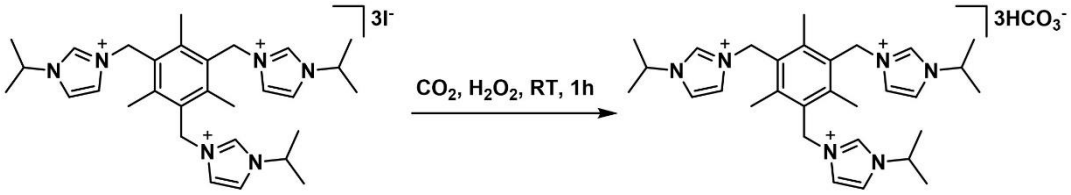
75 mg (51%). ^{1}H NMR (400 MHz, $(CD_3)_2SO$)/ δ (ppm): 7.62 (3H, d, *J* = 1.92 Hz), 7.58 (3H, d, *J* = 1.92 Hz), 5.59 (6H, s), 3.91 (9H, s), 2.37 (9H, s). ^{13}C NMR (100 MHz, CD_3OD)/ δ (ppm): 161.31, 143.28, 130.84, 125.48, 125.34, 123.65, 40.60, 36.83, 16.91. ESI-MS (CH_3OH): $[M–2H]^+$ calcd for $C_{24}H_{31}N_6$ 403.28 m/z; Found 403.18 m/z. Iodide analysis by Schoniger combustion (Midwest MicroLab): Found: I, 1.25%.

2.5.15 Synthesis of [timtmb^{iPr}(H)][(I)$_3$] and [timtmb^{iPr}(H)][(HCO$_3$)$_3$]

[timtmb^{iPr}(H)][(I)$_3$] and [timtmb^{iPr}(H)][(HCO$_3$)$_3$] were synthesized following an identical procedure that was used for the preparation of [timtmb^{Me}(H)][(I)$_3$] and [timtmb^{Me}(H)][(HCO$_3$)$_3$], by reacting 1,3,5-tris(bromomethyl)-2,4,6-trimethylbenzene (400 mg, 1.0 mmol) with 1-isopropylimidazole (353.32 µL, 3.11 mmol).



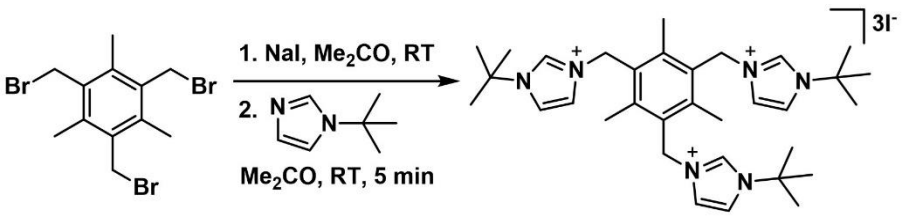
The iodine imidazolium salt, [timtmb^{iPr}(H)][(I)$_3$], was isolated as a white powder. Yield (220 mg, 25%). ^{1}H NMR (400 MHz, $(CD_3)_2SO$)/ δ (ppm): 9.14 (3H, s), 7.98 (3H, s), 7.62 (3H, s), 5.55 (6H, s), 4.68 (3H, quin, *J* = 6.70 Hz), 2.30 (9H, s), 2.08 (6H, s), 1.46 (18H, d, *J* = 6.62 Hz).



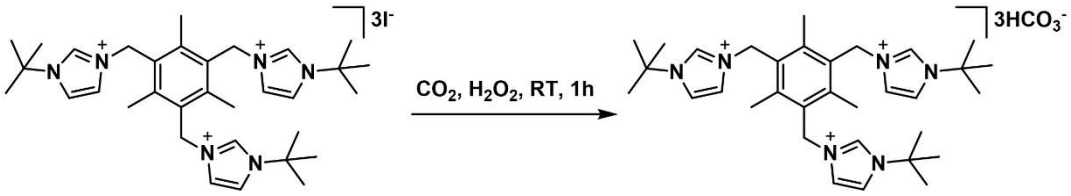
The bicarbonate imidazolium salt, [timtmb^{iPr}(H)][(HCO$_3$)$_3$], was isolated as a crystalline white solid. Yield (107 mg, 69%). ^{1}H NMR (400 MHz, CD_3OH)/ δ (ppm): 7.79 (3H, d, *J* = 1.96 Hz), 7.50 (3H, d, *J* = 1.98 Hz), 5.61 (6H, s), 4.70 (3H, quin, *J* = 6.70 Hz), 2.36 (9H, s), 1.55 (18H, d, *J* = 6.70 Hz). ^{13}C NMR (100 MHz, CD_3OD)/ δ (ppm): 161.31, 143.21, 130.88, 123.71, 121.89, 121.76, 54.77, 48.81, 23.16, 16.92. ESI-MS (CH_3OH): $[M–2H]^+$ calcd for $C_{30}H_{43}N_6$ 487.37 m/z; Found 487.18 m/z. Iodide analysis by Schoniger combustion (Midwest MicroLab): Found: I, 2.90%.

2.5.16 Synthesis of [timtmb^{tBu}(H)][(I)$_3$] and [timtmb^{tBu}(H)][(HCO$_3$)$_3$]

[timtmb^{tBu}(H)][(I)$_3$] and [timtmb^{tBu}(H)][(HCO$_3$)$_3$] were synthesized following an identical procedure that was use for the preparation of [timtmb^{Me}(H)][(I)$_3$] and [timtmb^{Me}(H)][(HCO$_3$)$_3$], by reacting 1,3,5-tris(bromomethyl)-2,4,6-trimethylbenzene (400 mg, 1.0 mmol) with 1-tertbutylimidazole (419.82 µL, 3.11 mmol).



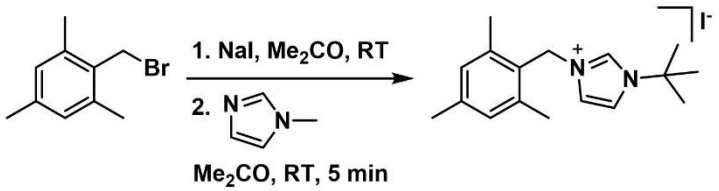
The iodine imidazolium salt, [timtmb^{tBu}(H)][$(I)_3$], was isolated as a white powder. Yield (395.0 mg, 43%). ^{1}H NMR (400 MHz, $(CD_3)_2SO$)/ δ (ppm): 9.29 (3H, s), 8.02 (3H, t, *J* = 1.47 Hz), 7.40 (3H, t, *J* = 1.62 Hz), 5.52 (6H, s), 2.27 (9H, s), 1.57 (27H, s).



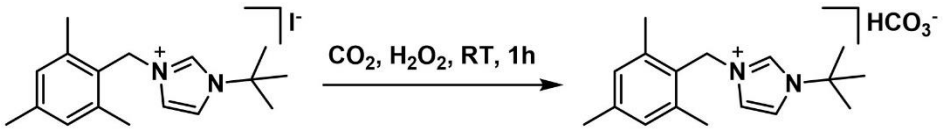
The bicarbonate imidazolium salt, [timtmb^{tBu}(H)][$(HCO_3)_3$], was isolated as a crystalline white solid. Yield (74.9 mg, 48%). ^{1}H NMR (400 MHz, CD_3OH)/ δ (ppm): 7.88 (3H, d, *J* = 2.10 Hz), 7.35 (3H, d, *J* = 2.09 Hz), 5.66 (6H, s), 2.39 (9H, s), 1.69 (27H, s). ^{13}C NMR (100 MHz, CD_3OD)/ δ (ppm): 161.42, 143.20, 130.89, 123.02, 121.96, 121.83, 61.78, 49.44, 29.95, 17.03. ESI-MS (CH_3OH): $[M–2H]^+$ calcd for $C_{33}H_{49}N_6$ 529.42 m/z; Found 529.18 m/z. Iodide analysis by Schoniger combustion (Midwest MicroLab): Found: I, 5.83%.

2.5.17 Synthesis of [mimtmb^{Me}(H)][I] and [mimtmb^{Me}(H)][HCO_3]

[mimtmb^{Me}(H)][I] and [mimtmb^{Me}(H)][HCO_3] were synthesized following an identical procedure that was used for the preparation of [timtmb^{Me}(H)][$(I)_3$] and [timtmb^{Me}(H)][$(HCO_3)_3$], by reacting 2-(bromomethyl)-1,3,5-trimethylbenzene (400 mg, 1.9 mmol) with 1-methylimidazole (165.8 µL, 2.08 mmol).



The iodine imidazolium salt, [mimtmb^{Me}(H)][I], was isolated as a white powder. Yield (806 mg, 56%). ^{1}H NMR (400 MHz, $(CD_3)_2SO$)/ δ (ppm): 8.79 (1H, s), 7.70 (1H, s), 7.61 (1H, s), 6.97 (2H, s), 5.37 (2H, s), 3.80 (3H, s), 2.25 (9H, s).



The bicarbonate imidazolium salt, [mimtmb^{Me}(H)][HCO_3], was isolated as a crystalline white solid. Yield (375.8 mg, 72%). ^{1}H NMR (400 MHz, CD_3OH)/ δ (ppm): 7.57 (1H, d, *J* = 1.77 Hz), 7.45 (1H, d, *J* = 1.85 Hz), 7.01 (2H, s), 5.44 (2H, s), 3.88 (3H, s), 2.30 (9H, s). ^{13}C NMR (100 MHz, CD_3OD)/ δ (ppm): 161.54, 141.22, 139.65, 131.01, 127.31, 125.30, 123.45, 48.72, 36.66, 21.29, 19.74. Iodide analysis by Schoniger combustion (Midwest MicroLab): Found: I, 2.38%.

2.5.18 NMR Spectra

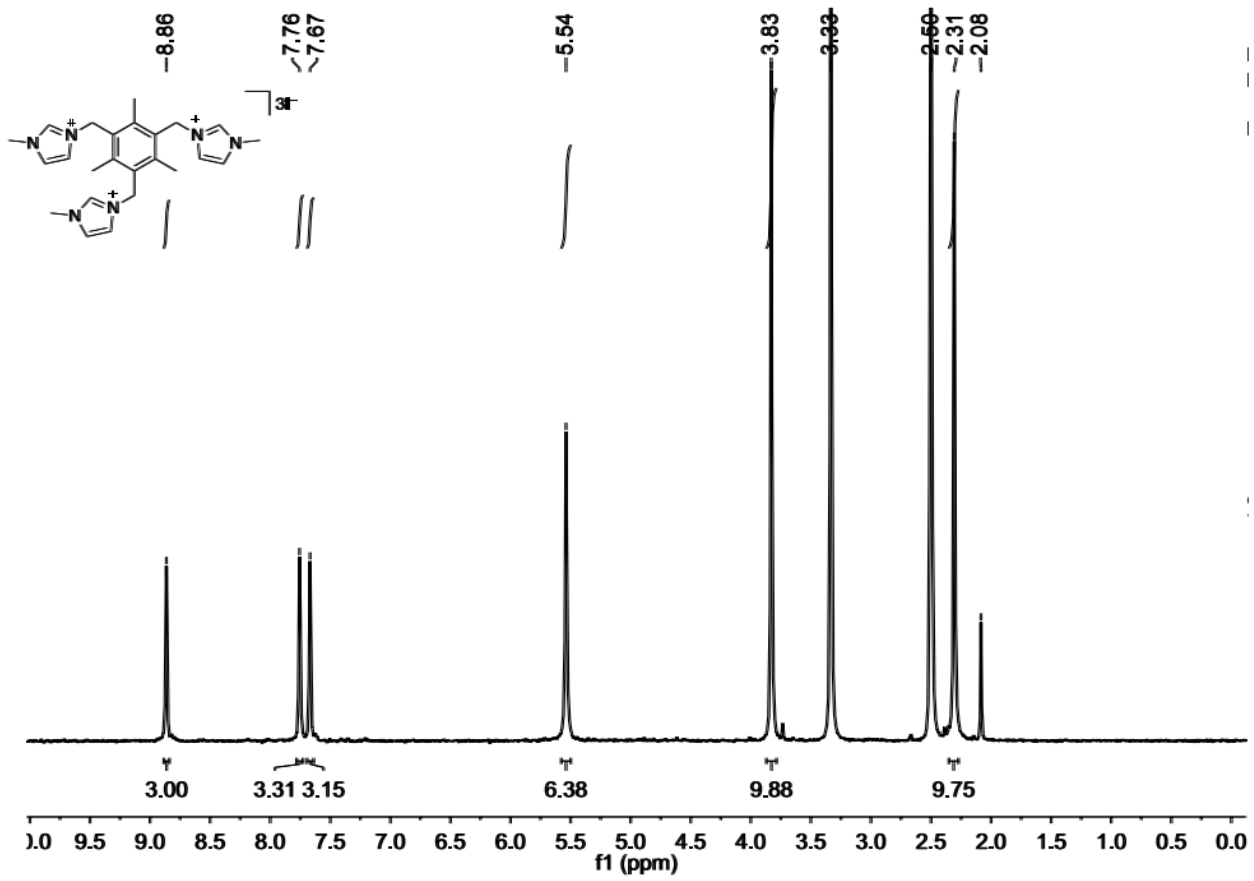


Figure 2.14. ^{1}H NMR spectrum of [timtmb^{Me}(H)][(I)$_3$].

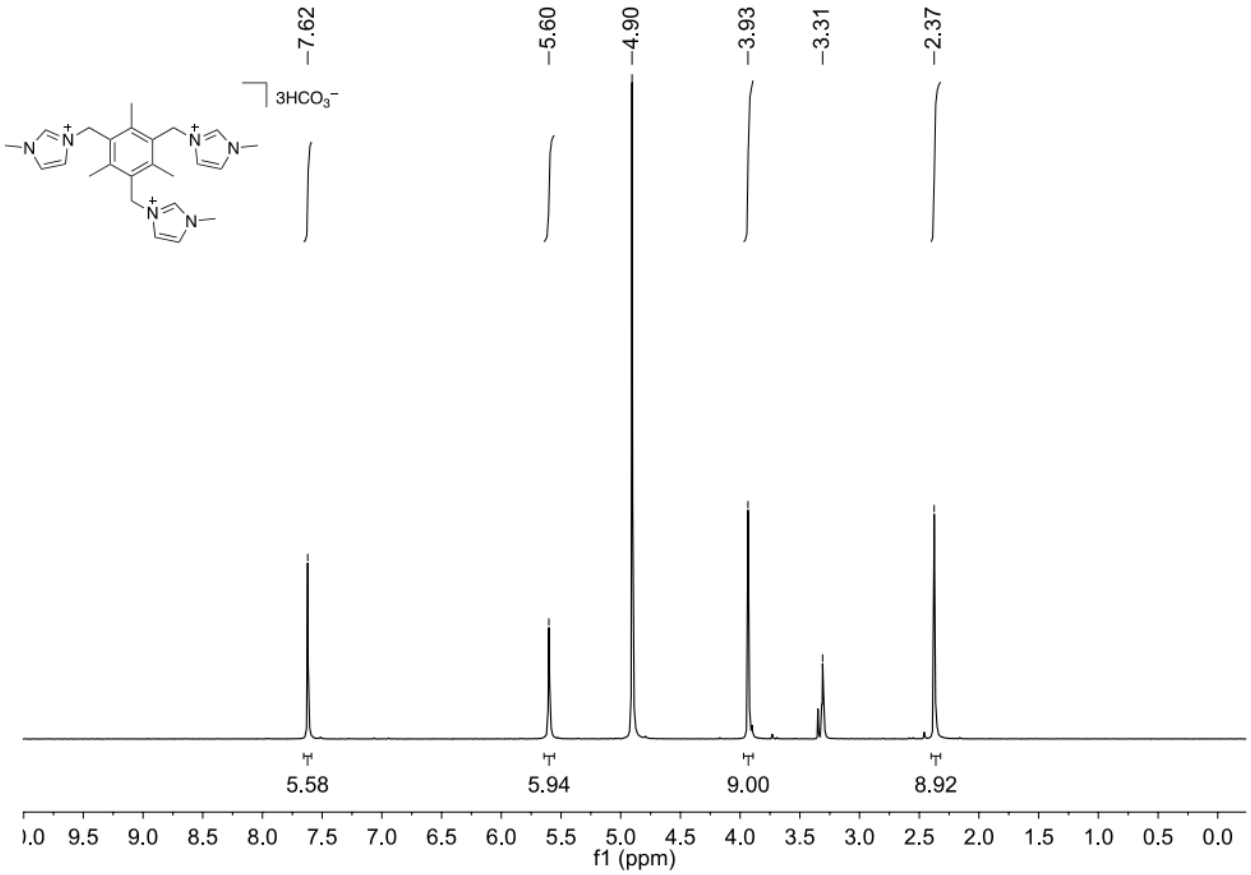


Figure 2.15. ^{1}H NMR spectrum of [timtmb^{Me}(H)][$(HCO_3)_3$].

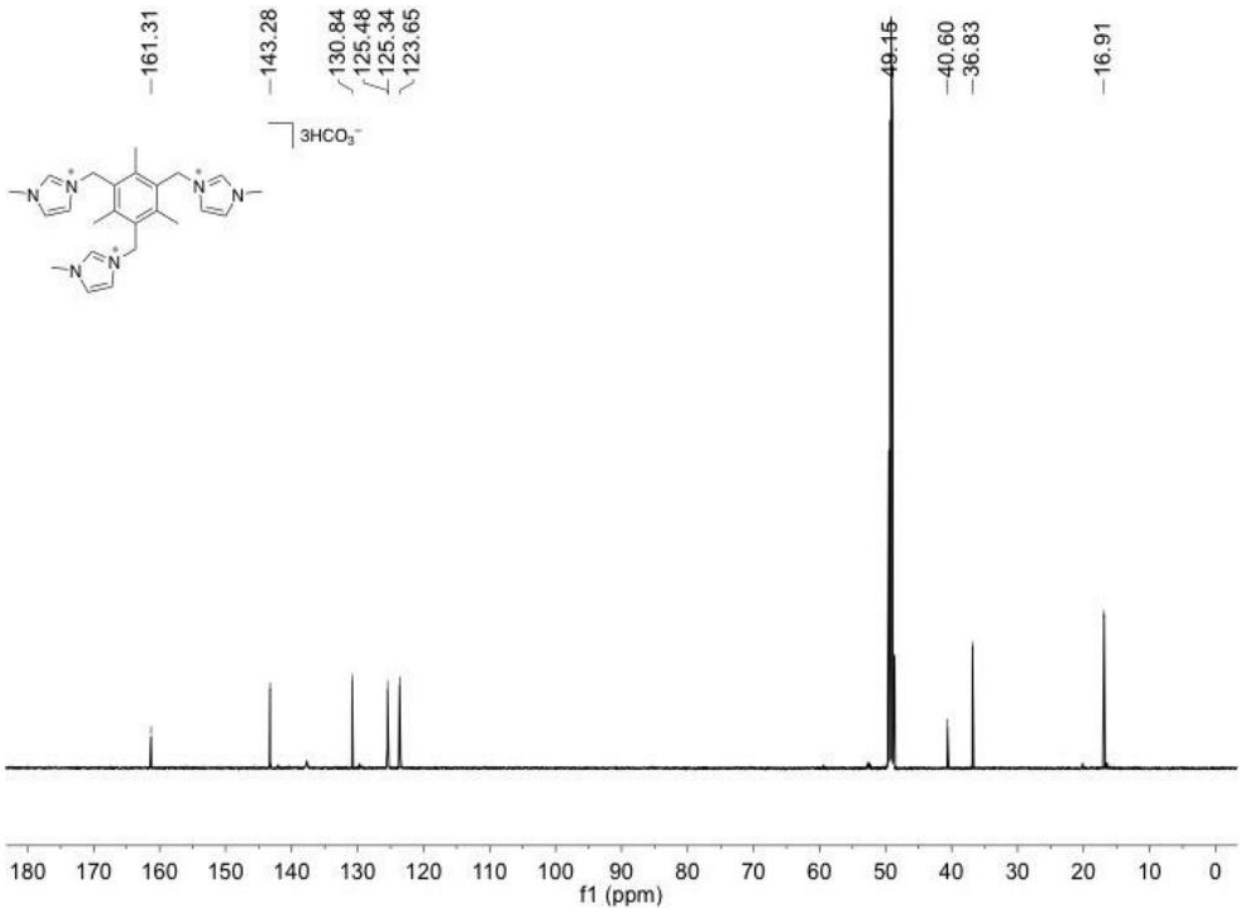


Figure 2.16. ^{13}C NMR spectrum of [timtmb^{Me}(H)][$(HCO_3)_3$].

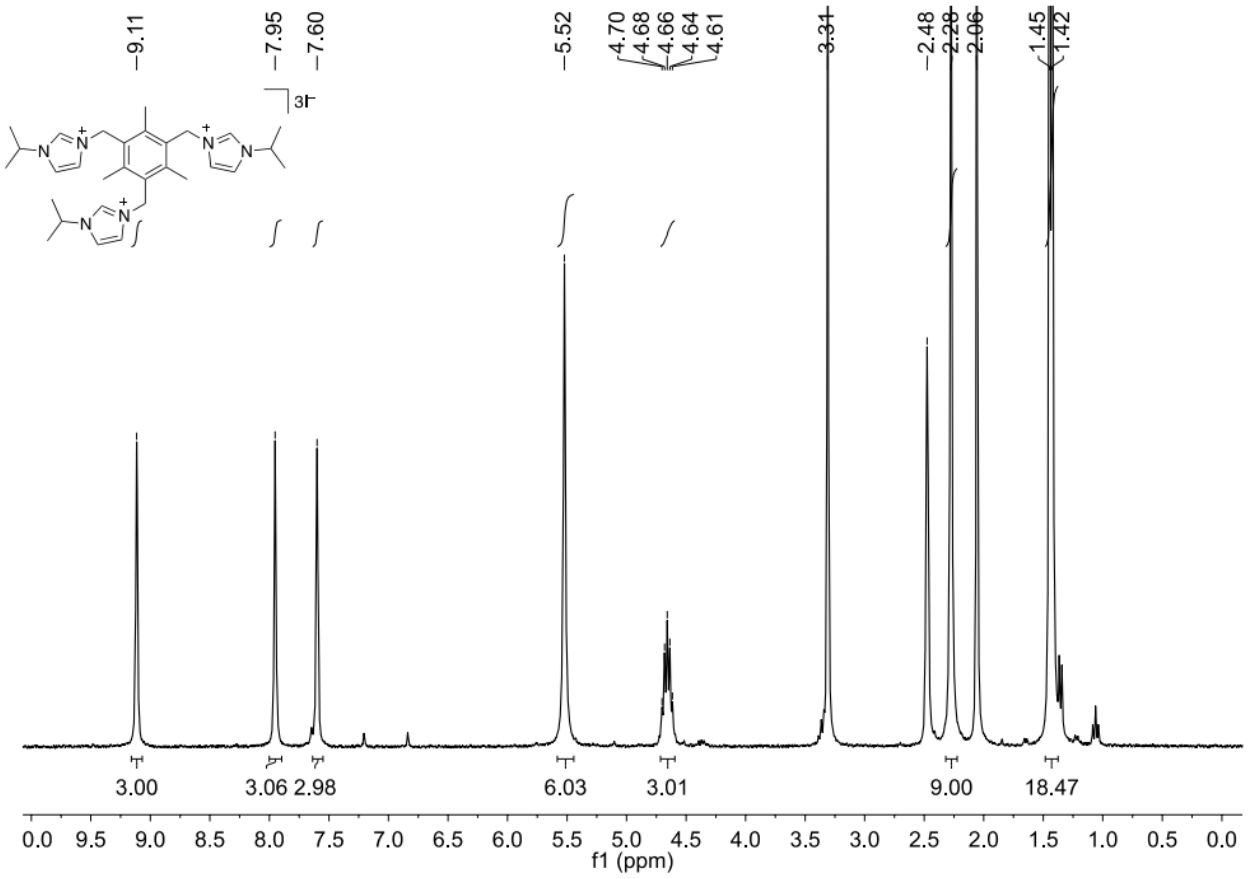


Figure 2.17. ^{1}H NMR spectrum of [timtmb^{iPr}(H)][(I)$_3$].

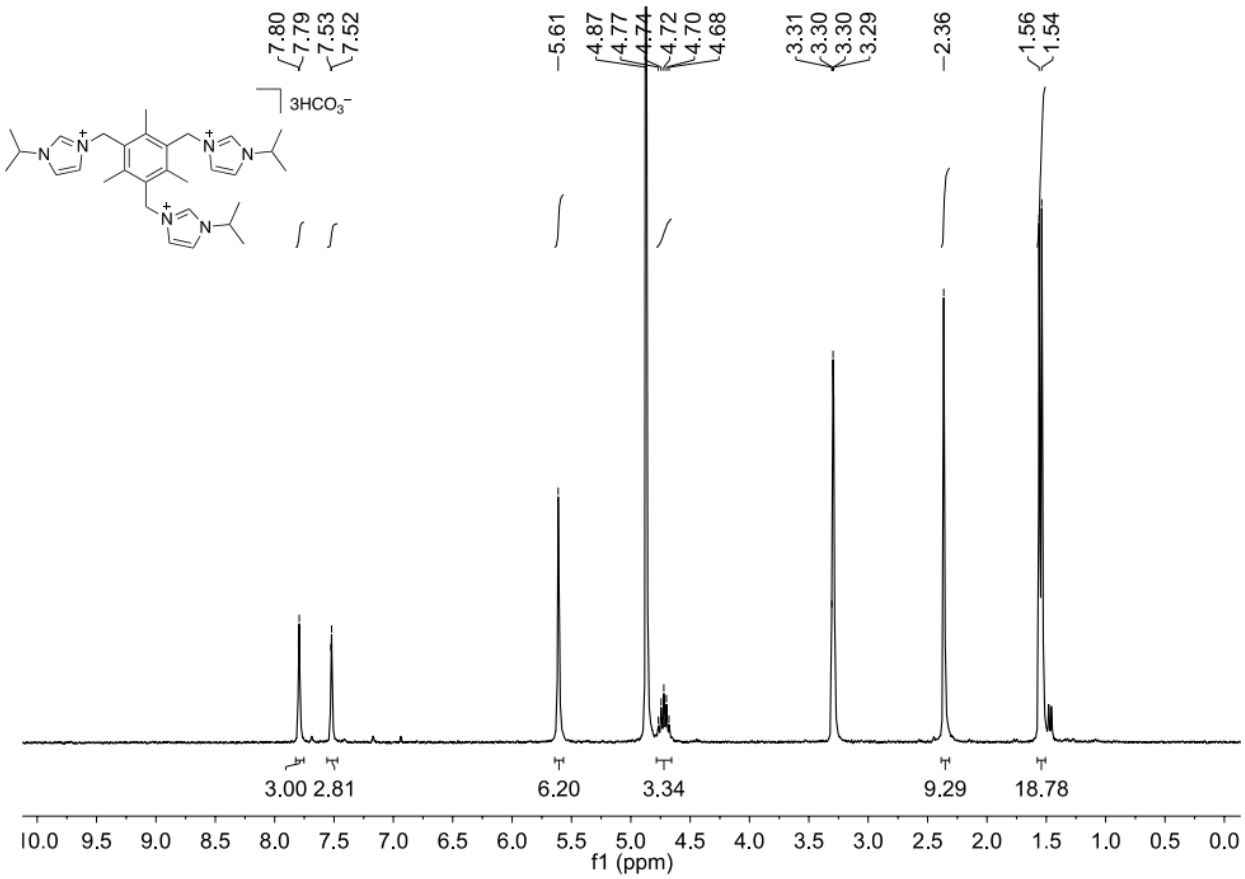


Figure 2.18. ^{1}H NMR spectrum of [timtmb^{iPr}(H)][$(HCO_3)_3$].

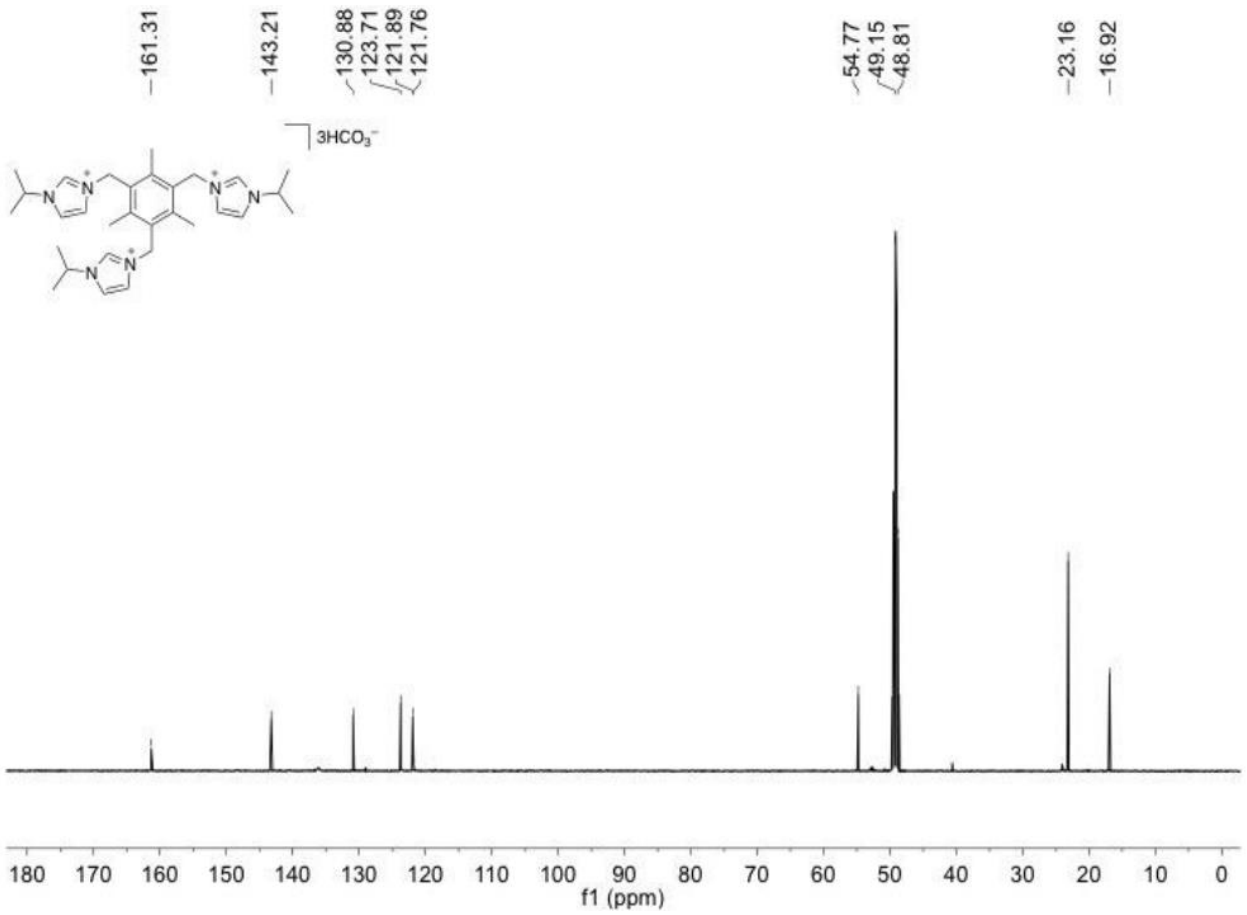


Figure 2.19. ^{13}C NMR spectrum of [timtmb^{iPr}(H)][$(HCO_3)_3$].

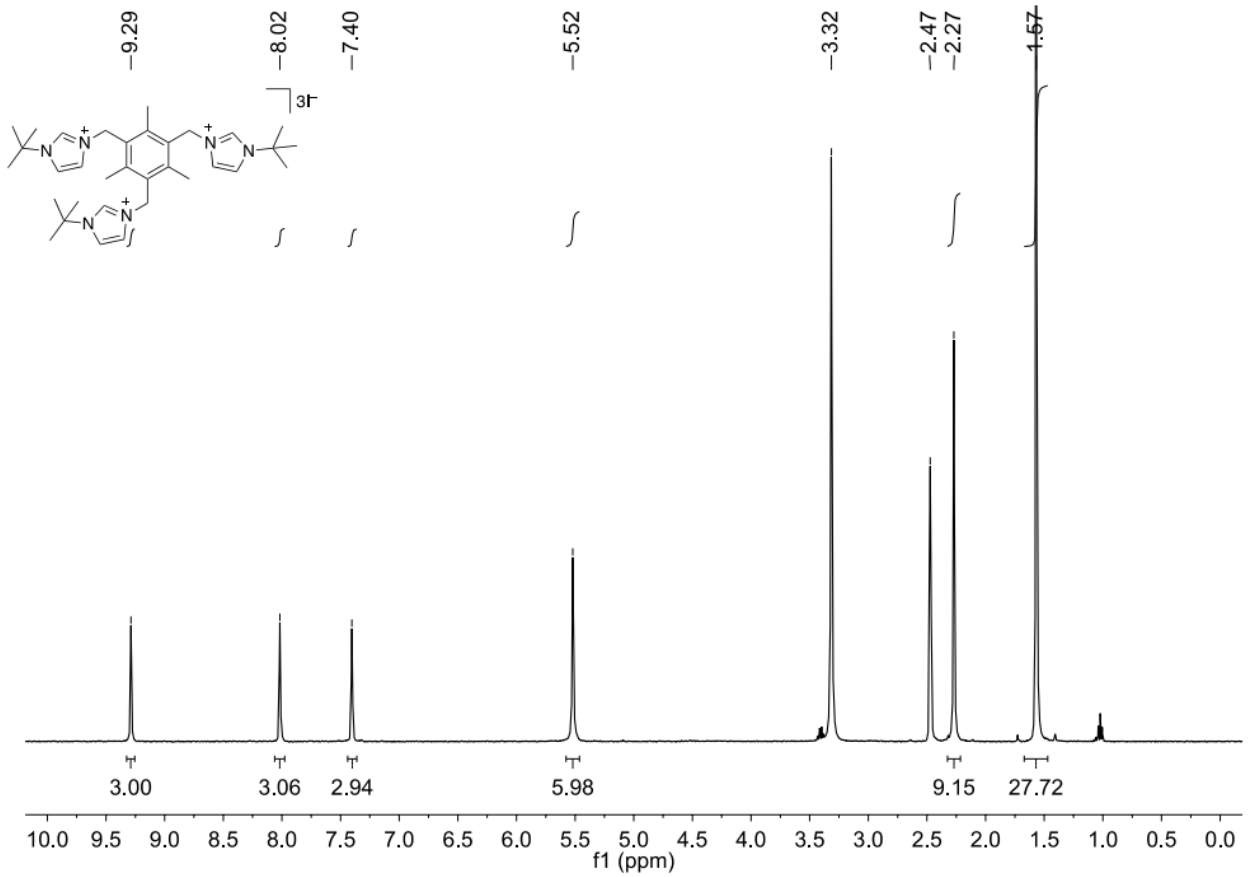


Figure 2.20. ^{1}H NMR spectrum of [timtmb^{tBu}(H)][(I)$_3$].

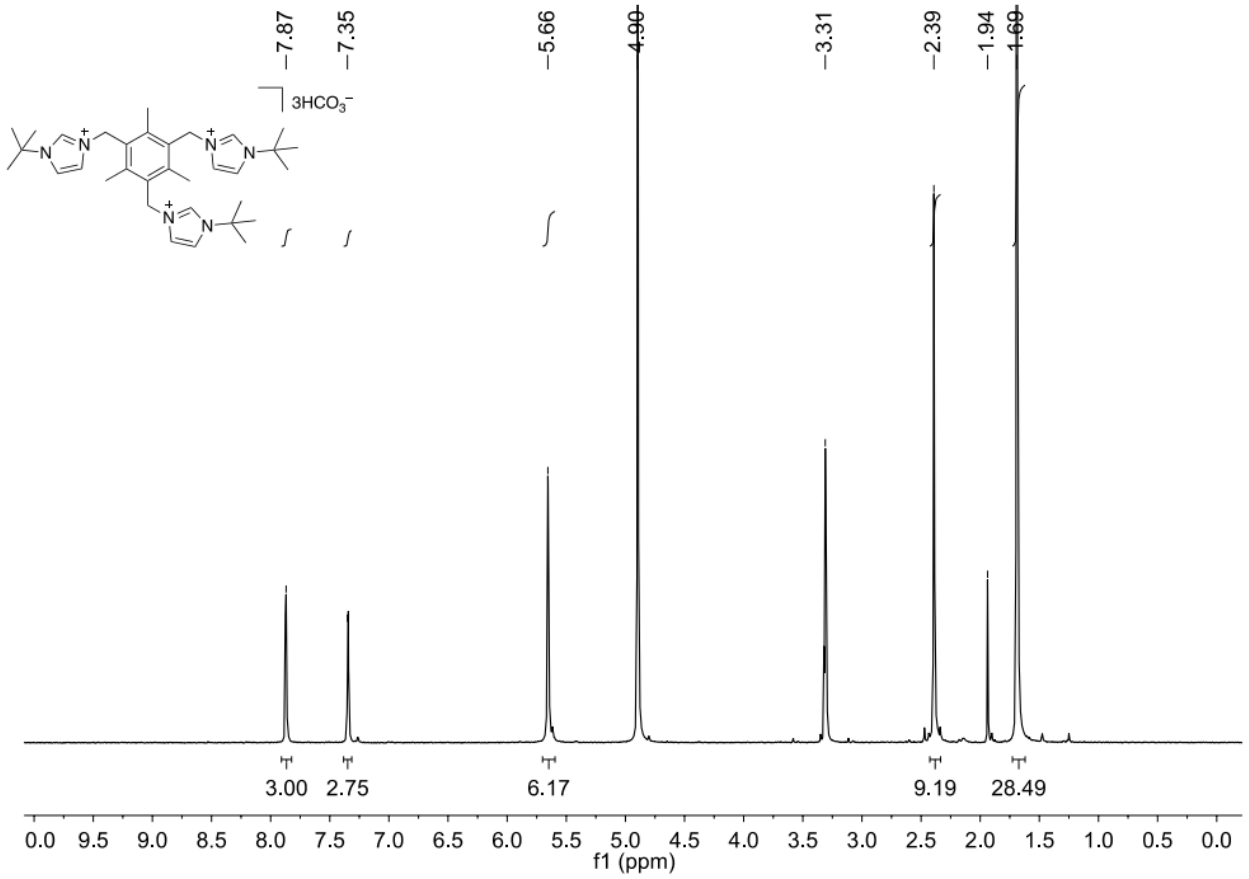


Figure 2.21. ^{1}H NMR spectrum of [timtmb^{tBu}(H)][$(HCO_3)_3$].

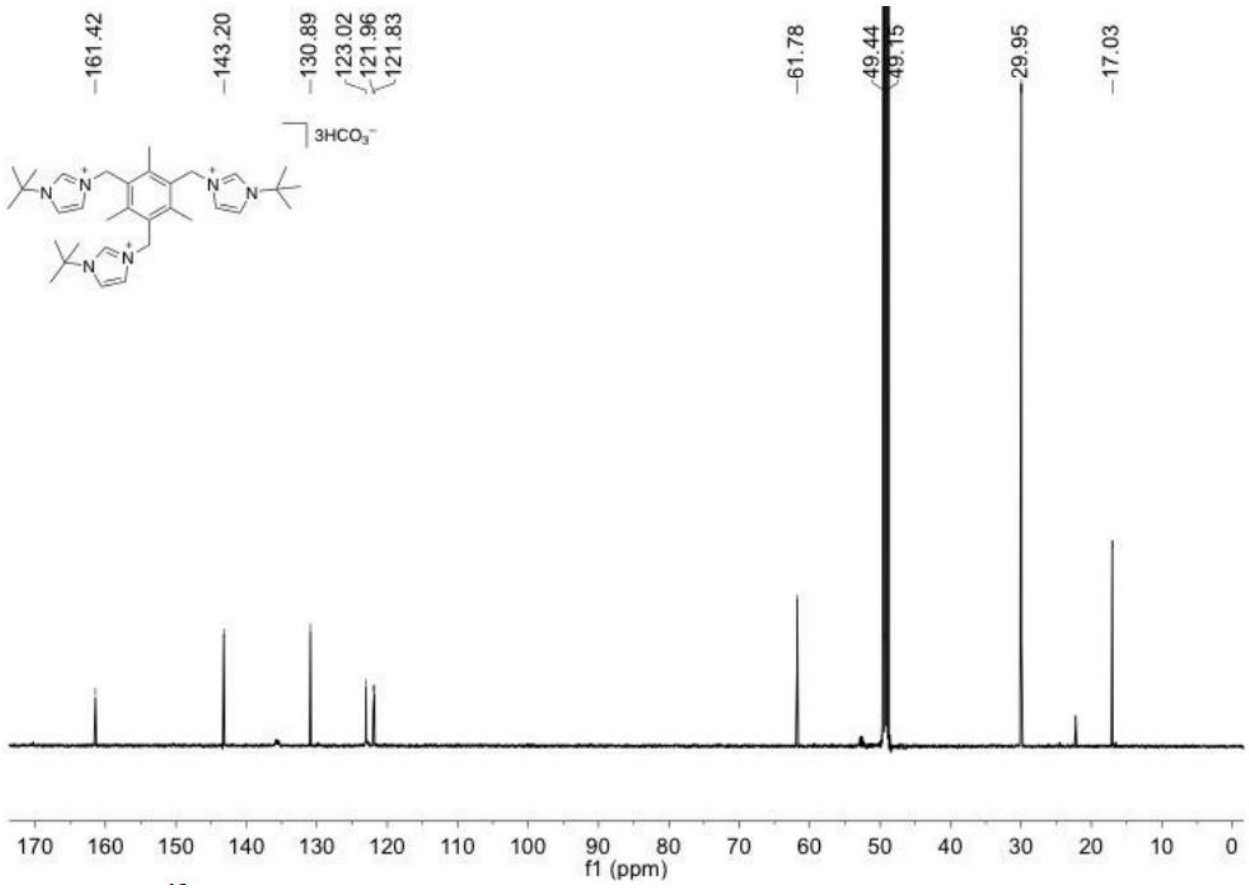


Figure 2.22. ^{13}C NMR spectrum of [timtmb^{tBu}(H)][$(HCO_3)_3$].

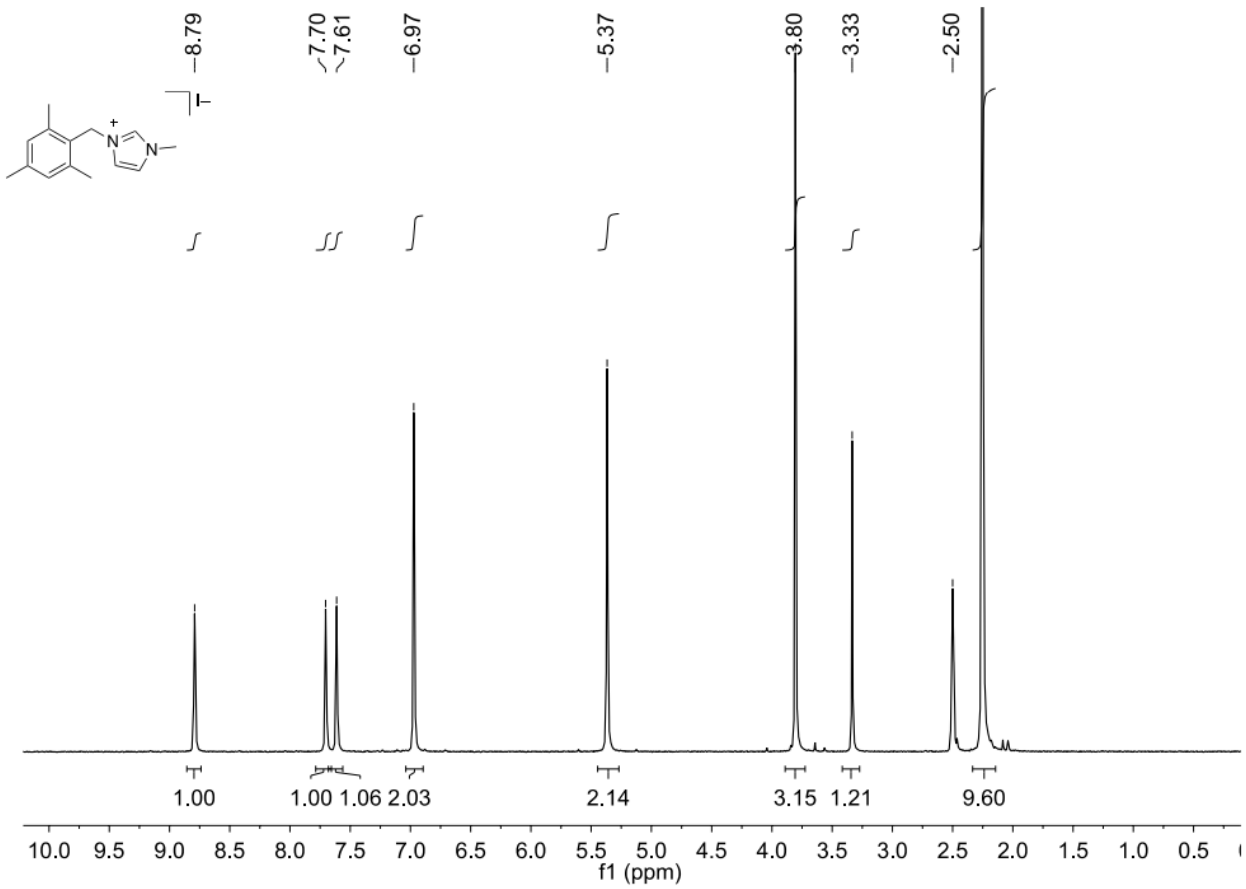


Figure 2.23. ^{1}H NMR spectrum of [mimtmb^{Me}(H)][I].

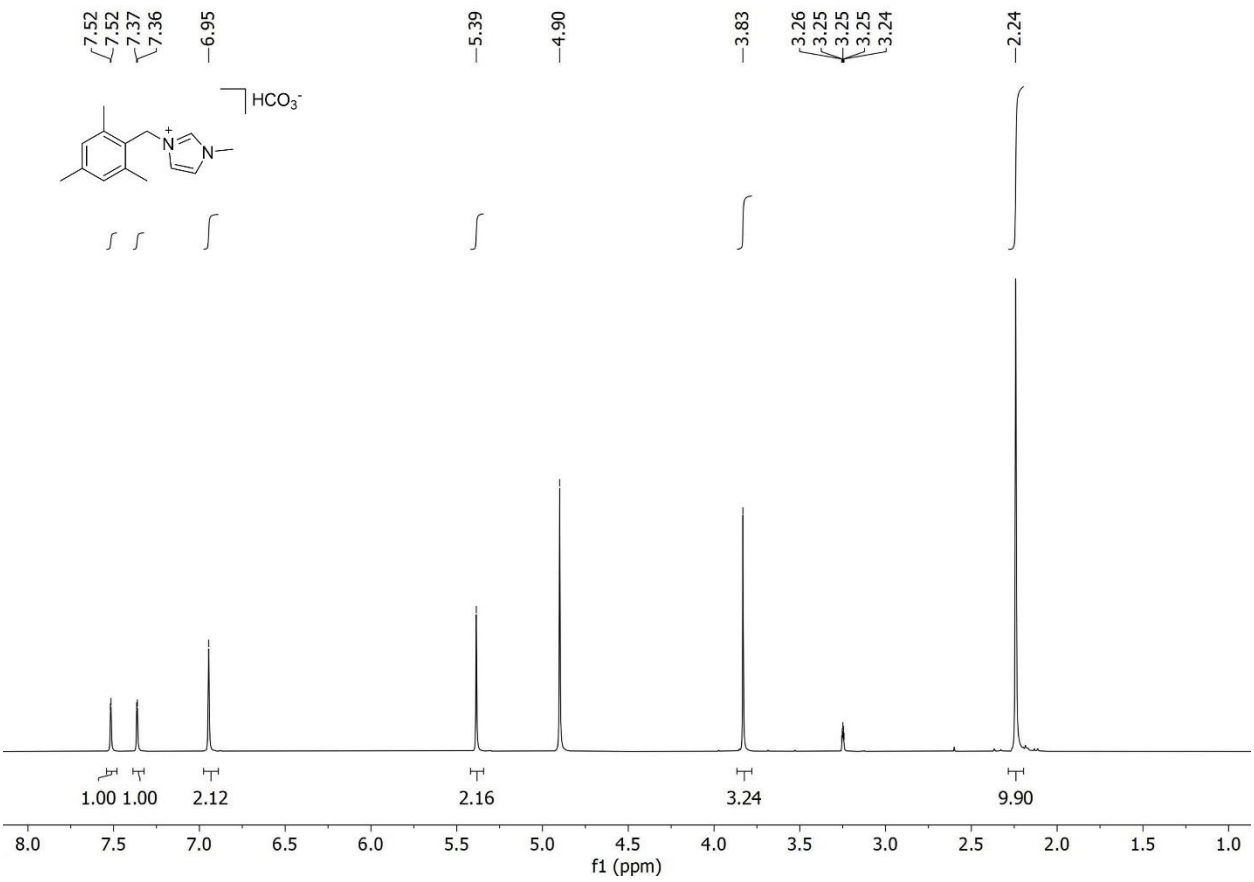


Figure 2.24. ^{1}H NMR spectrum of [mimtmb^{Me}(H)][HCO_3].

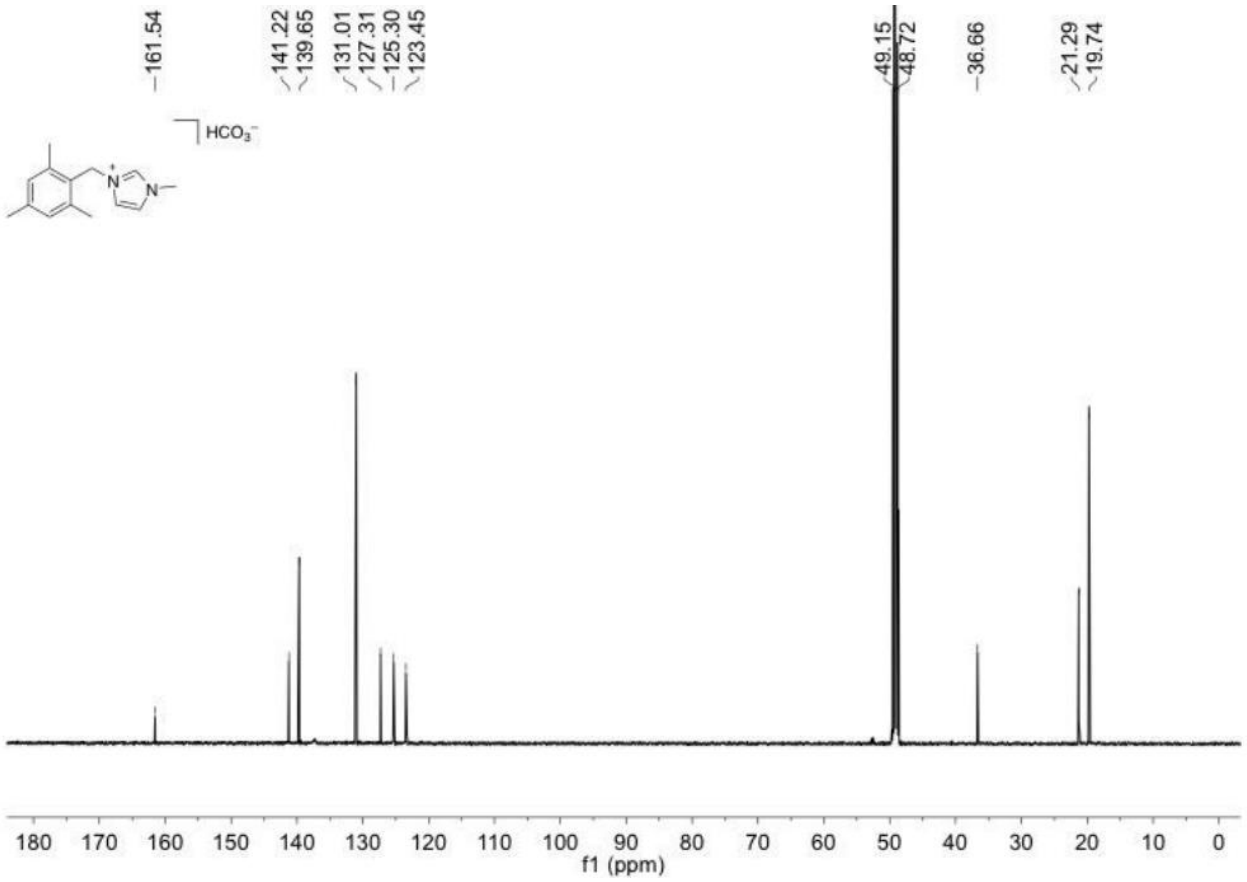


Figure 2.25. ^{13}C NMR spectrum of [mimtmb^{Me}(H)][HCO_3].

2.6 References

(1) Cotton, A. F.; Wilkinson, G.; Bochmann, C. A.; Murillo, C. A. Advanced Inorganic Chemistry, 6th ed., Wiley, New York, 1999.

(2) Lin, S.; Diercks, C. S.; Zhang, Y.-B.; Kornienko, N.; Nichols, E. M.; Zhao, Y.; Paris, A. R.; Kim, D.; Yang, P.; Yaghi, O. M.; Chang, C. J. Covalent Organic Frameworks Comprising Cobalt Porphyrins for Catalytic CO_2 Reduction in Water. *Science* **2015**, *349*, 1208–1213.

(3) Cao, Z.; Kim, D.; Hong, D.; Yu, Y.; Xu, J.; Lin, S.; Wen, X.; Nichols, E. M.; Jeong, K.; Reimer, J. A.; Yang, P.; Chang, C. J. A Molecular Surface Functionalization Approach to Tuning Nanoparticle Electrocatalysts for Carbon Dioxide Reduction. *J. Am. Chem. Soc.* **2016**, *138*, 8120–8125.

(4) Gong, M.; Cao, Z.; Liu, W.; Nichols, E. M.; Smith, P. T.; Derrick, J. S.; Liu, Y.-S.; Liu, J.; Wen, X.; Chang, C. J. Supramolecular Porphyrin Cages Assembled at Molecular–Materials Interfaces for Electrocatalytic CO Reduction. *ACS Cent. Sci.* **2017**, *3*, 1032–1040.

(5) Hurst, E. C.; Wilson, K.; Fairlamb, I. J. S.; Chechik, V. N-Heterocyclic Carbene Coated Metal Nanoparticles. *New J. Chem.* **2009**, *33*, 1837–1840.

(6) Vignolle, J.; Tilley, T. D. N-Heterocyclic Carbene-Stabilized Gold Nanoparticles and Their Assembly into 3D Superlattices. *Chem. Commun.* **2009**, 7230–7232.

(7) Ranganath, K. V. S.; Kloesges, J.; Schäfer, A. H.; Glorius, F. Asymmetric Nanocatalysis: N-Heterocyclic Carbenes as Chiral Modifiers of Fe_3O_4/Pd Nanoparticles. *Angew. Chem. Int. Ed.* **2010**, *49*, 7786–7789.

(8) Lara, P.; Rivada-Wheelaghan, O.; Conejero, S.; Poteau, R.; Philippot, K.; Chaudret, B. Ruthenium Nanoparticles Stabilized by N-Heterocyclic Carbenes: Ligand Location and Influence on Reactivity. *Angew. Chem.* **2011**, *123*, 12286–12290.

(9) Zhukhovitskiy, A. V.; Mavros, M. G.; Van Voorhis, T.; Johnson, J. A. Addressable Carbene Anchors for Gold Surfaces. *J. Am. Chem. Soc.* **2013**, *135*, 7418–7421.

(10) Gonzalez-Galvez, D.; Lara, P.; Rivada-Wheelaghan, O.; Conejero, S.; Chaudret, B.; Philippot, K.; Leeuwen, P. W. N. M. van. NHC-Stabilized Ruthenium Nanoparticles as New Catalysts for the Hydrogenation of Aromatics. *Catal. Sci. Technol.* **2012**, *3*, 99–105.

(11) Crudden, C. M.; Horton, J. H.; Ebralidze, I. I.; Zenkina, O. V.; McLean, A. B.; Drevniok, B.; She, Z.; Kraatz, H.-B.; Mosey, N. J.; Seki, T.; Keske, E. C.; Leake, J. D.; Rousina-Webb, A.; Wu, G. Ultra Stable Self-Assembled Monolayers of N-Heterocyclic Carbenes on Gold. *Nat. Chem.* **2014**, *6*, 409–414.

(12) Baquero, E. A.; Tricard, S.; Flores, J. C.; de Jesús, E.; Chaudret, B. Highly Stable Water-Soluble Platinum Nanoparticles Stabilized by Hydrophilic N-Heterocyclic Carbenes. *Angew. Chem.* **2014**, *126*, 13436–13440.

(13) Lara, P.; Suárez, A.; Collière, V.; Philippot, K.; Chaudret, B. Platinum N-Heterocyclic Carbene Nanoparticles as New and Effective Catalysts for the Selective Hydrogenation of Nitroaromatics. *ChemCatChem* **2014**, *6*, 87–90.

(14) Zhukhovitskiy, A. V.; MacLeod, M. J.; Johnson, J. A. Carbene Ligands in Surface Chemistry: From Stabilization of Discrete Elemental Allotropes to Modification of Nanoscale and Bulk Substrates. *Chem. Rev.* **2015**, *115*, 11503–11532.

(15) MacLeod, M. J.; Johnson, J. A. PEGylated N-Heterocyclic Carbene Anchors Designed to Stabilize Gold Nanoparticles in Biologically Relevant Media. *J. Am. Chem. Soc.* **2015**, *137*, 7974–7977.

(16) Ferry, A.; Schaepe, K.; Tegeder, P.; Richter, C.; Chepiga, K. M.; Ravoo, B. J.; Glorius, F. Negatively Charged N-Heterocyclic Carbene-Stabilized Pd and Au Nanoparticles and Efficient Catalysis in Water. *ACS Catal.* **2015**, *5*, 5414–5420.
(17) Martínez-Prieto, L.; Ferry, A.; Lara, P.; Richter, C.; Philippot, K.; Glorius, F.; Chaudret, B. New Route to Stabilize Ruthenium Nanoparticles with Non-Isolable Chiral N-Heterocyclic Carbenes. *Chem. Eur. J.* **2015,** *21*, 17495 – 17502.
(18) Wang, G.; Rühling, A.; Amirjalayer, S.; Knor, M.; Ernst, J. B.; Richter, C.; Gao, H.-J.; Timmer, A.; Gao, H.-Y.; Doltsinis, N. L.; Glorius, F.; Fuchs, H. Ballbot-Type Motion of N-Heterocyclic Carbenes on Gold Surfaces. *Nat. Chem.* **2017**, *9*, 152–156.
(19) Lara, P.; Martínez-Prieto, L. M.; Roselló-Merino, M.; Richter, C.; Glorius, F.; Conejero, S.; Philippot, K.; Chaudret, B. NHC-Stabilized Ru Nanoparticles: Synthesis and Surface Studies. *Nano-Struct. Nano-Objects* **2016**, *6*, 39–45.
(20) Ernst, J. B.; Muratsugu, S.; Wang, F.; Tada, M.; Glorius, F. Tunable Heterogeneous Catalysis: N-Heterocyclic Carbenes as Ligands for Supported Heterogeneous Ru/K-Al_2O_3 Catalysts to Tune Reactivity and Selectivity. *J. Am. Chem. Soc.* **2016**, *138*, 10718–10721.
(21) Martínez-Prieto, L. M.; Ferry, A.; Rakers, L.; Richter, C.; Lecante, P.; Philippot, K.; Chaudret, B.; Glorius, F. Long-Chain NHC-Stabilized RuNPs as Versatile Catalysts for One-Pot Oxidation/Hydrogenation Reactions. *Chem. Commun.* **2016**, *52*, 4768–4771.
(22) Fedorov, A.; Liu, H.-J.; Lo, H.-K.; Copéret, C. Silica-Supported Cu Nanoparticle Catalysts for Alkyne Semihydrogenation: Effect of Ligands on Rates and Selectivity. *J. Am. Chem. Soc.* **2016**, *138*, 16502–16507.
(23) Crudden, C. M.; Horton, J. H.; Narouz, M. R.; Li, Z.; Smith, C. A.; Munro, K.; Baddeley, C. J.; Larrea, C. R.; Drevniok, B.; Thanabalasingam, B.; McLean, A. B.; Zenkina, O. V.; Ebralidze, I. I.; She, Z.; Kraatz, H.-B.; Mosey, N. J.; Saunders, L. N.; Yagi, A. Simple Direct Formation of Self-Assembled N-Heterocyclic Carbene Monolayers on Gold and Their Application in Biosensing. *Nat. Commun.* **2016**, *7*, 12654.
(24) Rühling, A.; Schaepe, K.; Rakers, L.; Vonhören, B.; Tegeder, P.; Ravoo, B. J.; Glorius, F. Modular Bidentate Hybrid NHC-Thioether Ligands for the Stabilization of Palladium Nanoparticles in Various Solvents. *Angew. Chem. Int. Ed.* **2016**, *55*, 5856–5860.
(25) Martínez-Prieto, L.; Rakers, L.; López-Vinasco, A.; Cano, I.; Coppel, Y.; Philippot, K.; Glorius, F.; Chaudret, B.; van Leeuwen, P. Soluble Platinum Nanoparticles Ligated by Long-Chain N-Heterocyclic Carbenes as Catalysts. *Chem. Eur. J.* **2017**, *23*, 12779–12786.
(26) Ernst, J. B.; Schwermann, C.; Yokota, G.; Tada, M.; Muratsugu, S.; Doltsinis, N. L.; Glorius, F. Molecular Adsorbates Switch on Heterogeneous Catalysis: Induction of Reactivity by N-Heterocyclic Carbenes. *J. Am. Chem. Soc.* **2017**, *139*, 9144–9147.
(27) Salorinne, K.; Man, R. W. Y.; Li, C.-H.; Taki, M.; Nambo, M.; Crudden, C. M. Water-Soluble N-Heterocyclic Carbene-Protected Gold Nanoparticles: Size-Controlled Synthesis, Stability, and Optical Properties. *Angew. Chem. Int. Ed.* **2017**, *56*, 6198–6202.
(28) Richter, C.; Schaepe, K.; Glorius, F.; Ravoo, B. J. Tailor-Made N-Heterocyclic Carbenes for Nanoparticle Stabilization. *Chem. Commun.* **2014**, *50*, 3204–3207.
(29) Therrien, J. A.; Wolf, M. O. The Influence of Para Substituents in Bis(N-Heterocyclic Carbene) Palladium Pincer Complexes for Electrocatalytic CO_2 Reduction. *Inorg. Chem.* **2017**, *56*, 1161–1172.
(30) Therrien, J. A.; Wolf, M. O.; Patrick, B. O. Electrocatalytic Reduction of CO_2 with Palladium Bis-N-Heterocyclic Carbene Pincer Complexes. *Inorg. Chem.* **2014**, *53*, 12962–12972.

(31) Therrien, J. A.; Wolf, M. O.; Patrick, B. O. Polyannulated Bis(N-Heterocyclic Carbene)Palladium Pincer Complexes for Electrocatalytic CO_2 Reduction. *Inorg. Chem.* **2015**, *54*, 11721–11732.
(32) Nakai, H.; Tang, Y.; Gantzel, P.; Meyer, K. A New Entry to N-Heterocyclic Carbene Chemistry: Synthesis and Characterisation of a Triscarbene Complex of Thallium(I). *Chem. Commun.* **2003**, 24–25.
(33) Dias, H. V. R.; Jin, W. A Stable Tridentate Carbene Ligand. *Tetrahedron Lett.* **1994**, *35*, 1365–1366.
(34) Fahlbusch, T.; Frank, M.; Schatz, J.; Schmaderer, H. Influence of the Number and Geometry of Binding Sites on Host–Guest Affinity: Imidazolium-Substituted Receptor Molecules for Small Inorganic Anions. *Eur. J. Org. Chem.* **2006**, *2006*, 1899–1903.
(35) Planellas, M.; Pleixats, R.; Shafir, A. Palladium Nanoparticles in Suzuki Cross-Couplings: Tapping into the Potential of Tris-Imidazolium Salts for Nanoparticle Stabilization. *Adv. Synth. Catal.* **2012**, *354*, 651–662.
(36) Klinkova, A.; De Luna, P.; Dinh, C.-T.; Voznyy, O.; Larin, E. M.; Kumacheva, E.; Sargent, E. H. Rational Design of Efficient Palladium Catalysts for Electroreduction of Carbon Dioxide to Formate. *ACS Catal.* **2016**, *6*, 8115–8120.
(37) Bauskar, A. S.; Rice, C. A. Spontaneously Bi Decorated Carbon Supported Pt Nanoparticles for Formic Acid Electro-Oxidation. *Electrochimica Acta* **2013**, *93*, 152–157.
(38) Jiang, L.; Zhang, B.; Médard, G.; Seitsonen, A. P.; Haag, F.; Allegretti, F.; Reichert, J.; Kuster, B.; Barth, J. V.; Papageorgiou, A. C. N-Heterocyclic Carbenes on Close-Packed Coinage Metal Surfaces: Bis-Carbene Metal Adatom Bonding Scheme of Monolayer Films on Au, Ag and Cu. *Chem. Sci.* **2017**, *8*, 8301–8308.
(39) Larrea, C. R.; Baddeley, C. J.; Narouz, M. R.; Mosey, N. J.; Horton, J. H.; Crudden, C. M. N-Heterocyclic Carbene Self-Assembled Monolayers on Copper and Gold: Dramatic Effect of Wingtip Groups on Binding, Orientation and Assembly. *Chemphyschem* **2017**, *18*, 3536–3539.
(40) Man, R. W. Y.; Li, C.-H.; MacLean, M. W. A.; Zenkina, O. V.; Zamora, M. T.; Saunders, L. N.; Rousina-Webb, A.; Nambo, M.; Crudden, C. M. Ultrastable Gold Nanoparticles Modified by Bidentate N-Heterocyclic Carbene Ligands. *J. Am. Chem. Soc.* **2018**, *140*, 1576–1579.
(41) Waszczuk, P.; Zelenay, P.; Sobkowski, J. Surface Interaction of Benzoic Acid with a Copper Electrode. *Electrochimica Acta* **1995**, *40*, 1717–1721.
(42) Li, C. W.; Ciston, J.; Kanan, M. W. Electroreduction of Carbon Monoxide to Liquid Fuel on Oxide-Derived Nanocrystalline Copper. *Nature* **2014**, *508*, 504–507.
(43) Chen, Y.; Kanan, M. W. Tin Oxide Dependence of the CO_2 Reduction Efficiency on Tin Electrodes and Enhanced Activity for Tin/Tin Oxide Thin-Film Catalysts. *J. Am. Chem. Soc.* **2012**, *134*, 1986–1989.
(44) Feaster, J. T.; Shi, C.; Cave, E. R.; Hatsukade, T.; Abram, D. N.; Kuhl, K. P.; Hahn, C.; Nørskov, J. K.; Jaramillo, T. F. Understanding Selectivity for the Electrochemical Reduction of Carbon Dioxide to Formic Acid and Carbon Monoxide on Metal Electrodes. *ACS Catal.* **2017**, *7*, 4822–4827.
(45) Copéret, C.; Comas-Vives, A.; Conley, M. P.; Estes, D. P.; Fedorov, A.; Mougel, V.; Nagae, H.; Núñez-Zarur, F.; Zhizhko, P. A. Surface Organometallic and Coordination Chemistry toward Single-Site Heterogeneous Catalysts: Strategies, Methods, Structures, and Activities. *Chem. Rev.* **2016**, *116*, 323–421.

(46) Kresse, G.; Furthmüller, J. Efficiency of Ab-Initio Total Energy Calculations for Metals and Semiconductors Using a Plane-Wave Basis Set. *Comput. Mater. Sci.* **1996**, *6*, 15–50.
(47) Kresse, G.; Furthmüller, J. Efficient Iterative Schemes for Ab Initio Total-Energy Calculations Using a Plane-Wave Basis Set. *Phys. Rev. B* **1996**, *54*, 11169–11186.
(48) Blöchl, P. E. Projector Augmented-Wave Method. *Phys. Rev. B* **1994**, *50*, 17953–17979.
(49) Kresse, G.; Joubert, D. From Ultrasoft Pseudopotentials to the Projector Augmented-Wave Method. *Phys. Rev. B* **1999**, *59*, 1758–1775.
(50) Perdew, J. P.; Burke, K.; Ernzerhof, M. Generalized Gradient Approximation Made Simple. *Phys. Rev. Lett.* **1996**, *77*, 3865–3868.
(51) Henkelman, G.; Uberuaga, B. P.; Jónsson, H. A Climbing Image Nudged Elastic Band Method for Finding Saddle Points and Minimum Energy Paths. *J. Chem. Phys.* **2000**, *113*, 9901–9904.
(52) Liu, X.; Xiao, J.; Peng, H.; Hong, X.; Chan, K.; Nørskov, J. K. Understanding Trends in Electrochemical Carbon Dioxide Reduction Rates. *Nat. Commun.* **2017**, *8*, 15438.
(53) Skúlason, E.; Karlberg, G. S.; Rossmeisl, J.; Bligaard, T.; Greeley, J.; Jónsson, H.; Nørskov, J. K. Density Functional Theory Calculations for the Hydrogen Evolution Reaction in an Electrochemical Double Layer on the Pt(111) Electrode. *Phys. Chem. Chem. Phys.* **2007**, *9*, 3241–3250.
(54) Skúlason, E.; Tripkovic, V.; Björketun, M. E.; Gudmundsdóttir, S.; Karlberg, G.; Rossmeisl, J.; Bligaard, T.; Jónsson, H.; Nørskov, J. K. Modeling the Electrochemical Hydrogen Oxidation and Evolution Reactions on the Basis of Density Functional Theory Calculations. J. Phys. Chem. C **2010**, *114*, 18182–18197.

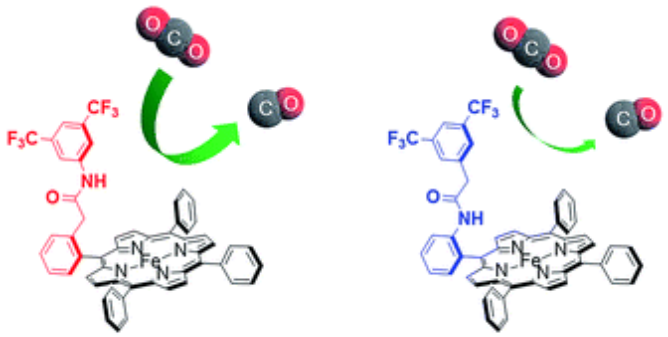
Chapter 3: Positional Effects of Second-Sphere Amide Pendants on Electrochemical Carbon Dioxide Reduction Catalyzed by Iron Porphyrins

Portions of this work were published in the following scientific journal:
Nichols, E. M.‡; Derrick, J. S.‡; Nistanaki, S. K.; Smith, P. T.; Chang, C. J. Positional Effects of Second-Sphere Amide Pendants on Electrochemical CO_2 Reduction Catalyzed by Iron Porphyrins. *Chemical Science*, *2018*, *9*, 2952–2960. (‡Denotes equal contribution).

Specific contributions: Dr. Eva M. Nichols and Sepand K. Nistanaki helped with synthesis and collection and interpretation of electrochemical data.

3.1 Abstract

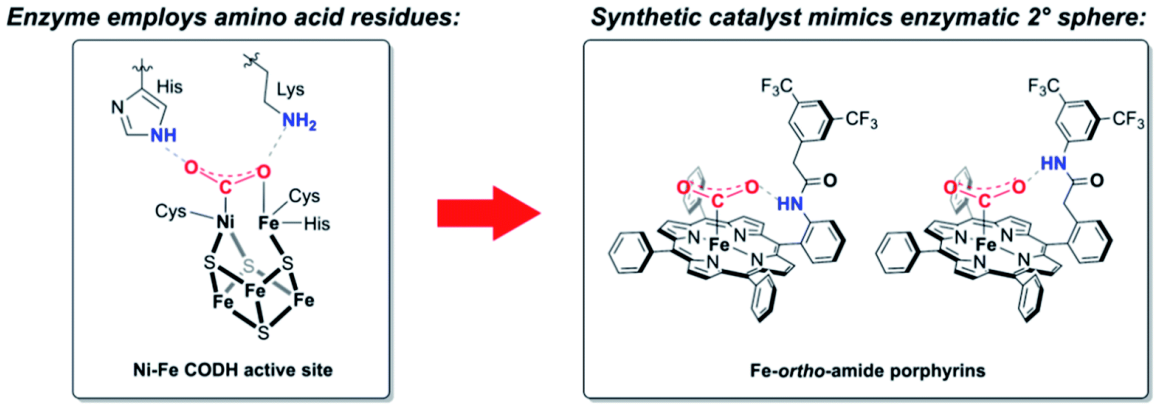
The development of catalysts for electrochemical reduction of carbon dioxide offers an attractive approach to transforming this greenhouse gas into value-added carbon products with sustainable energy input. Inspired by natural bioinorganic systems that feature precisely positioned hydrogen-bond donors in the secondary coordination sphere to direct chemical transformations occurring at redox-active metal centers, we now report the design, synthesis, and characterization of a series of iron tetraphenylporphyrin (Fe-TPP) derivatives bearing amide pendants at various positions at the periphery of the metal core. Proper positioning of the amide pendants greatly affects the electrocatalytic activity for carbon dioxide reduction to carbon monoxide. In particular, derivatives bearing proximal and distal amide pendants on the *ortho* position of the phenyl ring exhibit significantly larger turnover frequencies (TOF) compared to the analogous *para*-functionalized amide isomers or unfunctionalized Fe-TPP. Analysis of TOF as a function of catalyst standard reduction potential enables first-sphere electronic effects to be disentangled from second-sphere through-space interactions, suggesting that the *ortho*-functionalized porphyrins can utilize the latter second-sphere property to promote CO_2 reduction. Indeed, the distally-functionalized *ortho*-amide isomer shows a significantly larger through-space interaction than its proximal *ortho*-amide analogue. These data establish that proper positioning of secondary coordination sphere groups is an effective design element for breaking electronic scaling relationships that are often observed in electrochemical CO_2 reduction.



Proper pendant placement enhances catalysis

3.2 Introduction

Environmental challenges associated with rising atmospheric CO_2 concentrations and the promise of CO_2 as a cheap and abundant C1 feedstock motivate the research into technologies to convert CO_2 into value-added chemical products.[1–3] Electrochemical reduction of CO_2 offers an attractive approach to meet this goal using sustainable energy input, but the kinetic and thermodynamic barriers to CO_2 activation provide significant chemical challenges, necessitating the development of catalysts that can promote CO_2 reduction selectively over the competing background reduction of protons to hydrogen that can occur at comparable potentials. Indeed, despite broad interest in electrochemical CO_2 reduction, molecular catalysis efforts have focused largely on a limited number of primary coordination sphere motifs, including metal complexes with porphyrins[4–8] and aza-macrocycles,[9–15] bipyridine,[16–23] phosphine,[24–26] and carbene[27–29] ligands. In contrast, biological systems for CO_2 redox catalysis, such as the carbon monoxide dehydrogenase (CODH) enzymes that catalyze the reversible interconversion of CO_2 and CO, modulate activity using precisely positioned hydrogen-bond and proton-relay groups in the second coordination sphere.[30] For example, second-sphere histidine and lysine residues in Ni–Fe CODH are positioned to stabilize a CO_2-metal adduct and assist in C–O bond cleavage (**Scheme 3.1**).[31–33]



Scheme 3.1. The active site of Ni–Fe CO dehydrogenase, showing activated CO_2 in red and the nearby network of hydrogen bond donor amino acid residues in blue (left), inspires the design of *ortho*-amide-functionalized Fe porphyrins examined in this work (right).

The aforementioned bioinorganic systems provide inspiration for the design of metal complexes bearing second-sphere groups to aid with activation or transformation of small molecule substrates. Notable advances in utilizing intramolecular hydrogen-bond donors to promote oxygen binding/activation include picket fence-, picnic basket-, and hangman porphyrins by Collman, Reed, C. K. Chang, and Nocera,[34–39] dicopper complexes by Masuda,[40,41] and tripodal systems by Borovik.[42–45] Second-sphere donors have also been shown to play important roles in structural mimics of alcohol dehydrogenase,[46,47] as well as in complexes for stoichiometric reduction of nitrite,[48,49] nitrate,[50] and nitrogen.[51] Furthermore, second-sphere pendants have been incorporated into electrocatalyst scaffolds to facilitate protonation steps relevant to H_2 evolution[52–54] and O_2 reduction,[55,56] and to stabilize adducts or promote C–O bond cleavage in CO_2 reduction.[11,12,57–59] With specific regard to CO_2 reduction, elegant work on iron

tetraphenylporphyrins by Savéant, Costentin, and Robert has explored the use of phenol-based pendants for enhancing electrochemical CO_2 reduction.[57,60]

Against this backdrop, we targeted the study of functionalized porphyrin complexes that could yield insight into questions of optimal placement of second-sphere pendants on a conserved first-sphere metal core. In this report, we describe the synthesis and electrochemical study of positional isomers of iron porphyrin CO_2 reduction catalysts bearing pendant amides in the secondary coordination sphere. Intermolecular addition of a parent iron tetraphenylporphyrin catalyst, Fe-TPP, with an aryl amide additive results in a dose-dependent increase in CO_2 reduction activity. Building upon this result, we designed and evaluated a series of positional isomers bearing intramolecular amide pendants in the *ortho* or *para* positions of the *meso* aryl ring, both proximal and distal to the porphyrin plane. Comparison of the catalytic activities of these isomers establishes that *ortho* orientation of the second-sphere groups is critical for an enhancement in catalysis. Correlation between the turnover frequency (TOF) and standard potential of the formal $Fe^{I/0}$ couple indicates that through-space interactions play a role in enhancing the rate of CO_2 reduction for both *ortho* amide-functionalized catalysts, with the distal donor exhibiting a more significant through-space component. In contrast, such effects are largely absent in the *para*-functionalized congeners. These data provide a starting point for more sophisticated design of second-sphere functionalities as bioinspired design elements for redox catalysis of CO_2 and other small-molecule substrates.

3.3 Results and Discussion

3.3.1 Bis(aryl)amide Additive Promotes CO_2 Reduction with Fe Porphyrin.

As a starting point to explore the use of amides as functional secondary coordination sphere pendants, we examined the effects of an electron-deficient aryl amide additive on CO_2 reduction catalyzed by Fe-TPP. Titration of 3,5-[bis(trifluoromethyl)phenyl]amide to Fe-TPP in dimethylformamide (DMF) reveals a dose-dependent increase in catalytic activity (**Figure 3.1**), with the additive acting as a proton source as well as a potential hydrogen bond donor/acceptor. Foot-of-the-wave analysis (FOWA), as described by Savéant, Costentin, Robert and co-workers,[61] can be used to extract kinetic information from cyclic voltametric data, especially in cases where a plateau current is not observed due to substrate consumption or catalyst inhibition. Using this approach, the rate of CO_2 reduction was examined as a function of amide concentration under pseudo-first order conditions of excess CO_2, and the rate was found to exhibit a first-order dependence on the amide additive (**Figure 3.2**). Cyclic voltammograms under a nitrogen atmosphere show a negligible change between 50 equivalents of amide additive and Fe-TPP alone, indicating that background processes such as proton reduction are likely to be minimal with this additive (**Figure 3.3**). With this pilot result in hand, we sought to explore the effects of introducing intramolecular amide substituents onto the porphyrin scaffold in a spatially well-defined fashion.

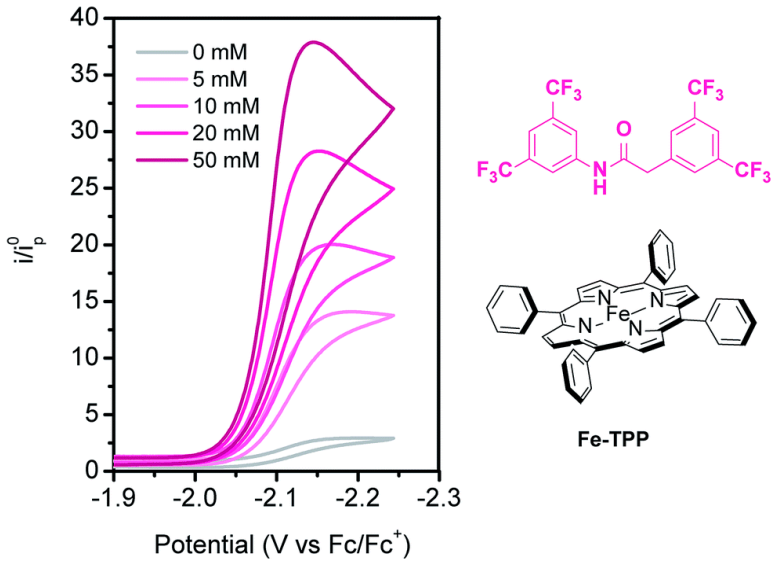


Figure 3.1. Titration of 3,5-[bis(trifluoromethyl)phenyl]amide to Fe-TPP under CO_2 showing current increases with increasing concentrations of amide. Conditions: 0.1 M $TBAPF_6$ in DMF, 1 mM Fe-TPP.

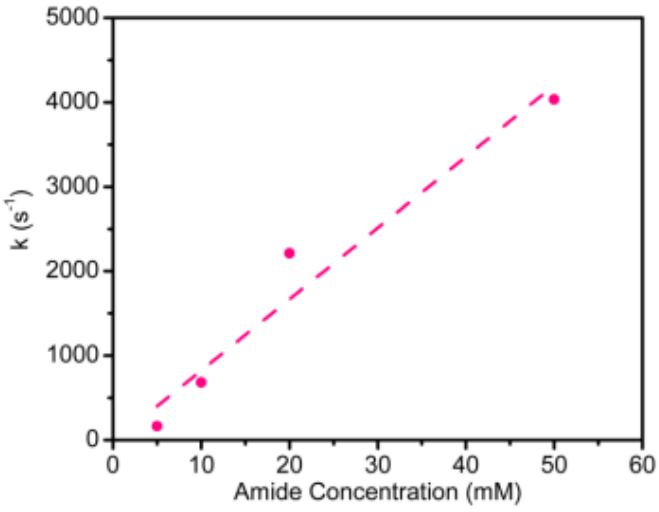


Figure 3.2. Intramolecular addition of amide additive to Fe-TPP shows that CO_2 reduction rate exhibits first-order dependence on amide concentration. Cyclic voltammograms recorded for 1 mM Fe-TPP in 0.1 M $TBAPF_6$ in DMF under 1 atm of CO_2. Rates were determined using Foot-of-the-Wave analysis.

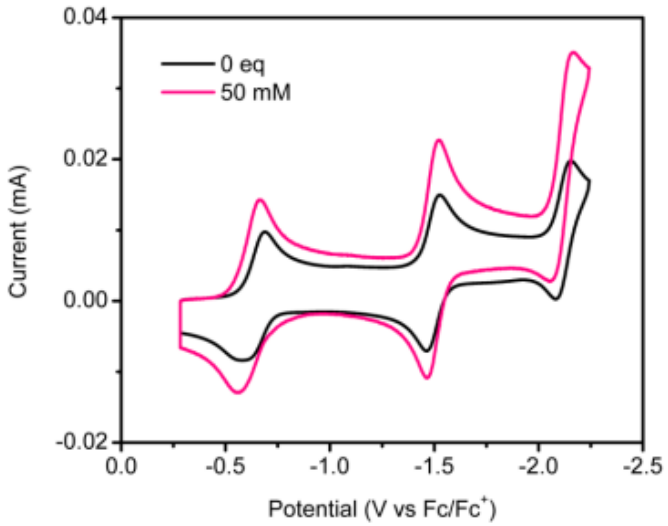


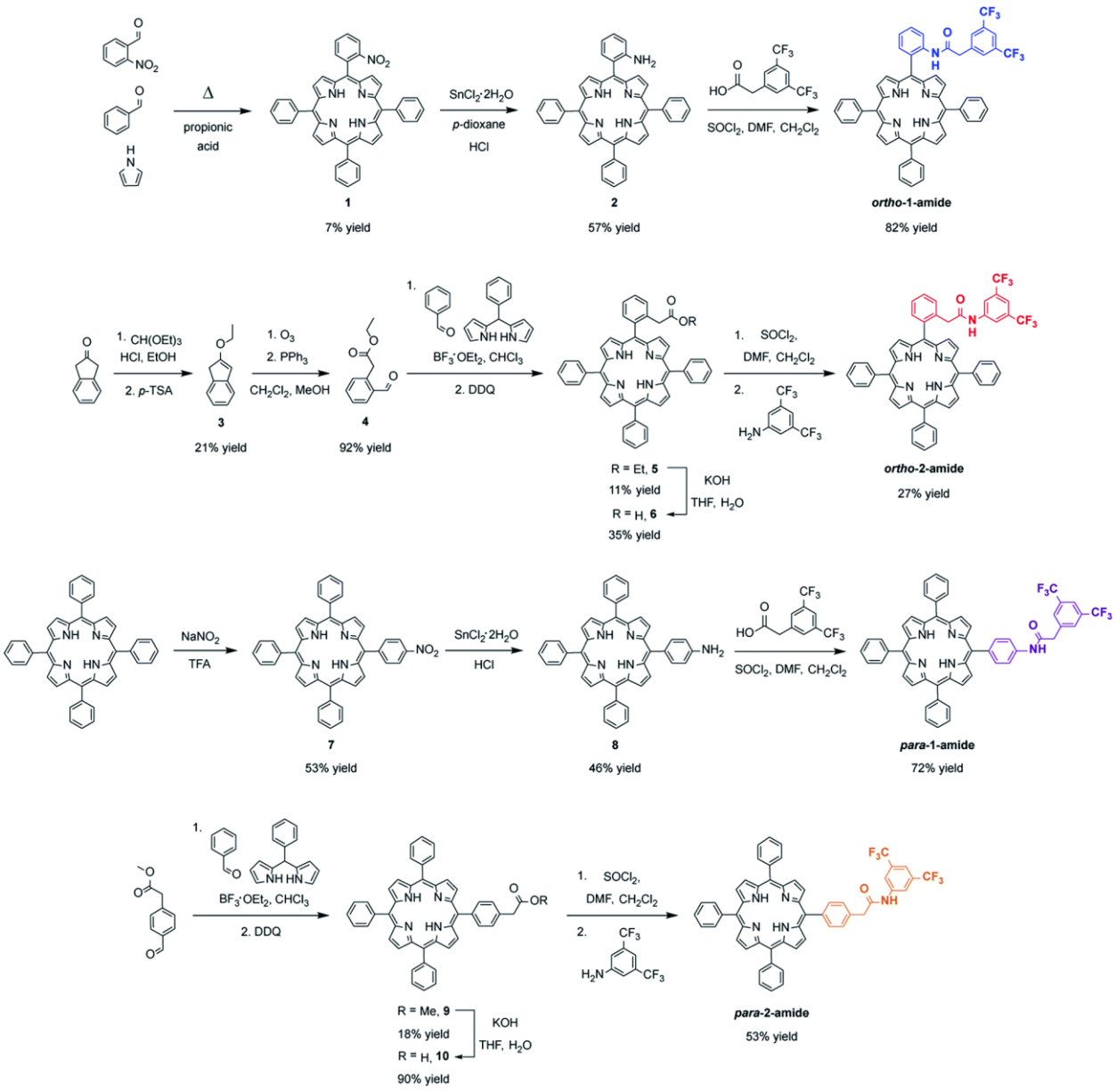
Figure 3.3. Cyclic voltammograms of Fe-TPP (1 mM) in 0.1 M $TBAPF_6$ under Ar atmosphere in the absence (black) or presence (pink) of 50 mM of amide additive.

3.3.2 Synthesis of Covalently Modified Porphyrins Bearing Intramolecular Amide Groups.

As only amide groups located at the *ortho* position of the porphyrin *meso* aryl rings are expected to engage in intramolecular proton donor- or hydrogen bonding interactions with CO_2-derived intermediates bound at the iron center, we envisioned two positional isomers: *ortho*-1-amide, bearing the NH proximal to the porphyrin ring, and *ortho*-2-amide, bearing the NH distal to the porphyrin ring. Most porphyrin-based catalysts bearing second-sphere groups, especially those evaluated for CO_2 reduction, feature these functionalities in the proximal location for reasons

of synthetic practicality. We were interested in interrogating the effect of distal group positioning given a previous report showing that proximal second-sphere groups are located too far away from the metal center and are less effective at promoting oxygen binding at iron.[36] The corresponding *para*-1-amide and *para*-2-amide porphyrins were targeted to serve as control compounds, where the amide NH group at the *para* position of the *meso* aryl rings is not expected to interact productively with CO_2 or CO_2-derived intermediates. The synthesis of all four functionalized porphyrin ligands is shown in **Scheme 3.2**. Condensation of 2-nitrobenzaldehyde and benzaldehyde with pyrrole results in the mono-(2-nitrophenyl)porphyrin starting material **1**, which can be subsequently reduced to the mono-(2-aminophenyl)porphyrin synthon **2**. Reaction with 3,5-bis(trifluoromethyl)phenylacyl chloride affords the proximal target *ortho*-1-amide. The distal *ortho* congener was prepared by condensation of 2-formylphenylacetic acid ethyl ester **4** (obtained in two steps from 2-indanone) and benzaldehyde with 5-phenyldipyrromethane to afford porphyrin **5**. Subsequent hydrolysis, followed by *in situ* generation of the acyl chloride and reaction with 3,5-bis(trifluoromethyl)aniline affords *ortho*-2-amide. Porphyrin *para*-1-amide is obtained from mono-(4-aminophenyl)porphyrin **8**, which is in turn prepared by regioselective *para*-nitration of tetraphenylporphyrin and subsequent reduction. A precursor to *para*-2-amide was accessed by condensation of commercially available 4-formylphenylacetic acid methyl ester and benzaldehyde with 5-phenyldipyrromethane to afford porphyrin **9**. Hydrolysis, followed by *in situ* generation of the acyl chloride and reaction with 3,5-bis(trifluoromethyl)aniline, gave the desired ligand.

The iron complexes of the aforementioned porphyrin ligands were obtained by metalation with $FeBr_2$ in anhydrous tetrahydrofuran in the presence of 2,6-lutidine as a base. All porphyrin ligands were characterized by ^{1}H-, ^{13}C-, and ^{19}F-NMR spectroscopy, and freebase and metalloporphyrins were additionally characterized by UV-visible spectroscopy and ESI mass spectrometry (see materials and methods for details).



Scheme 3.2. Synthesis of *ortho*- and *para*-functionalized tetraphenylporphyrin ligands *ortho*-1-amide, *ortho*-2-amide, *para*-1-amide, and *para*-2-amide.

3.3.3 Structural Characterization of Zn-*ortho*-1-amide.

We sought structural characterization of the amide-appended porphyrins to confirm the expected connectivity. Owing to a lack of success in obtaining suitable quality single crystals for structural characterization of the iron complexes, the corresponding zinc complexes were targeted. Porphyrin Zn–*ortho*-1-amide was prepared by metalation of the ligand with $Zn(OAc)_2$. Crystals suitable for X-ray diffraction were grown by vapor diffusion of water into a concentrated DMF solution. The solid-state structure is shown in **Figure 3.4**, where a DMF molecule occupies the fifth axial coordination site. As is typical for pentacoordinate Zn porphyrins, the Zn atom is

displaced from the porphyrin plane. As desired, the amide is oriented such that it may engage CO_2 directly or act as a proton relay or hydrogen bond donor with CO_2-bound intermediates during catalysis. We have been unable to obtain X-ray quality crystals of Zn–*ortho*-2-amide, perhaps due to enhanced flexibility of the amide group caused by the presence of the methylene spacer.

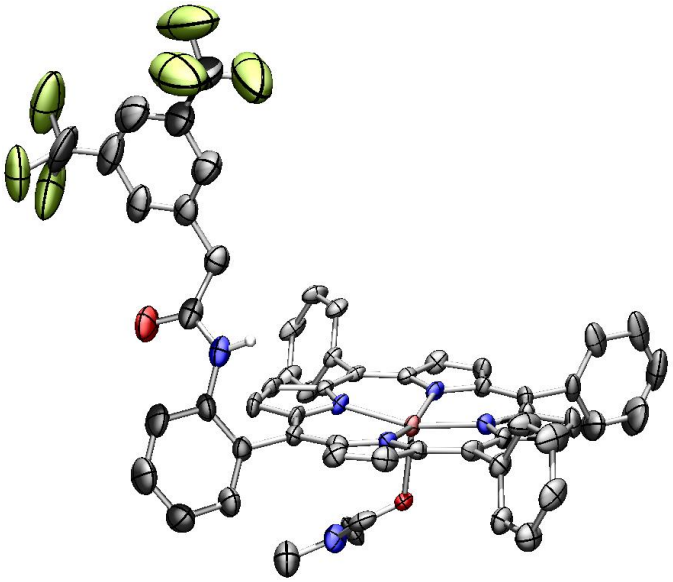
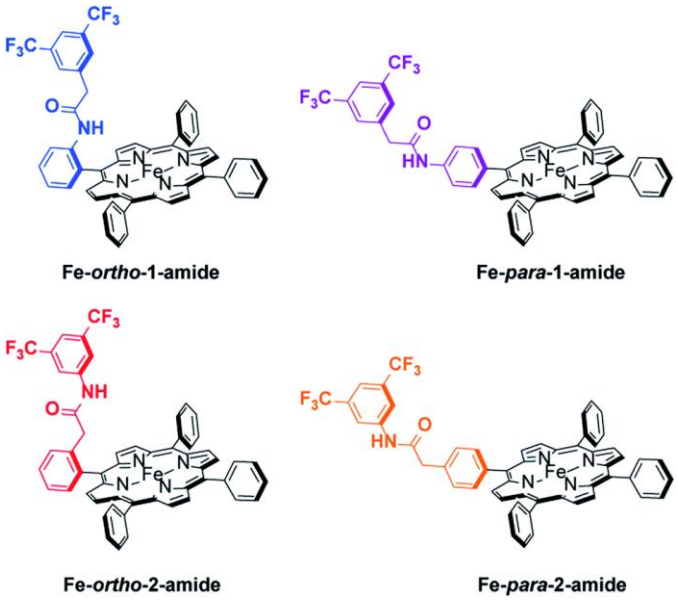


Figure 3.4. Solid-state structure of Zn–*ortho*-1-amide. Non-coordinated solvent molecules and non-amide hydrogen atoms have been omitted for clarity. Thermal ellipsoids are shown at the 50% level.

3.3.4 Cyclic Voltammetry Studies in Dimethylformamide.

With these positional isomers in hand (**Scheme 3.3**), we next evaluated their electrochemical characteristics under an inert atmosphere and under CO_2. Cyclic voltammograms (CVs) of the functionalized iron porphyrins and parent Fe-TPP measured in DMF under argon atmosphere (0.1 M $TBAPF_6$, 1 mM catalyst) show three distinct redox events corresponding to formal $Fe^{III/II}$, $Fe^{II/I}$, and $Fe^{I/0}$ couples (**Figure 3.5**). Reversible $Fe^{I/0}$ couples are observed at a scan rate of 100 mV s^{-1} under these conditions. Scan rate-dependence studies show a linear correlation between peak current and $(\text{scan rate})^{1/2}$, indicating that all the complexes are freely diffusing under non-catalytic conditions (**Figure 3.6**). The $Fe^{I/0}$ standard potentials, E^0_{cat}, are given in **Table 3.1** for each porphyrin complex. The E^0_{cat} potentials trend with the electron-withdrawing nature of the substituent, with *ortho* substituents exerting a larger electronic effect than *para* substituents: the proximal *ortho* amide is inductively electron-withdrawing, followed by the proximal *para* amide and unsubstituted TPP. The distal amides are rendered electron-donating by the methylene substituent, with the *ortho* positional isomer being more electron-rich than the *para*-substituted analogue.



Scheme 3.3. Positional isomers of amide-functionalized iron tetraphenylporphyrins examined in this work.

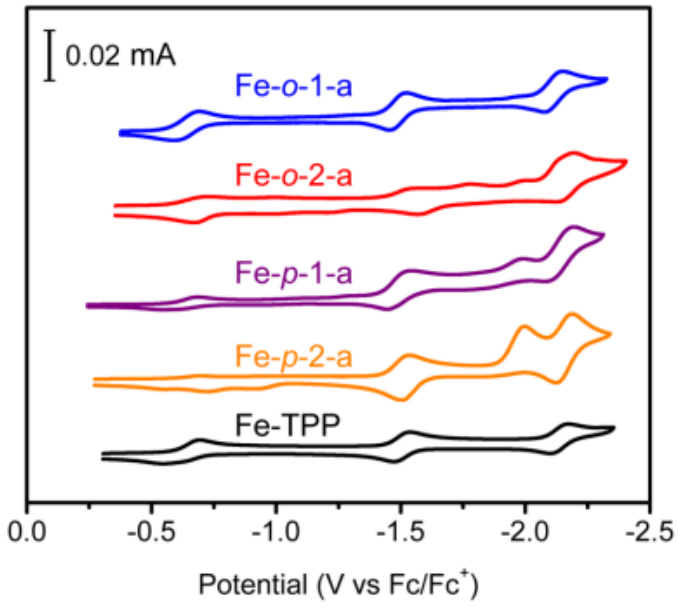


Figure 3.5. Cyclic voltammograms of the pendant amide Fe porphyrin complexes compared to unfunctionalized FeTPP, [Fe] = 1 mM. Voltammograms were recorded in 0.1 M $TBAPF_6$ in DMF under Ar atmosphere at 100 mV/sec.

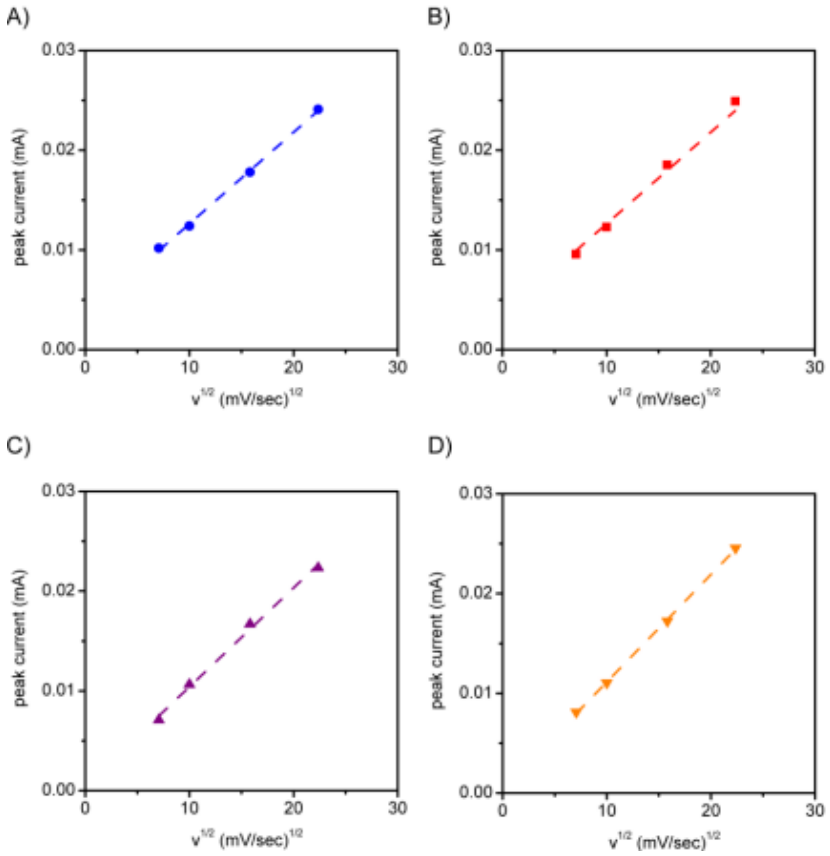


Figure 3.6. Scan rate dependence for (a) Fe–*ortho*-1-amide, (b) Fe–*ortho*-2-amide, (c) Fe–*para*-1-amide, and (d) Fe–*para*-2-amide measured under Ar atmosphere in 0.1 M $TBAPF_6$ in DMF. Peak currents for the $Fe^{II/I}$ couple were used.

Table 3.1. Summary of electrochemical properties of iron porphyrin catalysts.

Catalyst	E^0_{cat} (V vs Fc/Fc$^+$)[a]	TOF$_{max}$ (s^{-1})[b]	log(TOF$_{max}$)	k_{cat} (M^{-2}s^{-1})[c]	FE$_{CO}$ (%)[d]
Fe-*ortho*-1-amide	–2.12	2.24 x 10^4	4.35	1.01 x 10^6	83 ± 3
Fe-*ortho*-2-amide	–2.18	5.50 x 10^6	6.75	3.33 x 10^8	92 ± 2
Fe-*para*-1-amide	–2.15	1.70 x 10^2	2.23	1.03 x 10^4	74 ± 8
Fe-*para*-2-amide	–2.16	6.76 x 10^3	3.84	4.20 x 10^5	79 ± 8
Fe-TPP	–2.15	6.76 x 10^2	2.83	2.13 x 10^5	90 ± 6
Fe-TPP + 50 mM amide	–2.15	4.04 x 10^3	3.61	3.18 x 10^5	–

[a] The standard reduction potential for the formal Fe$^{I/0}$ couple, E^0_{cat}, is reported as an average over three independent experiments. [b] TOF$_{max}$ values are reported in presence of 100 mM PhOH and 0.23 M CO_2 except for the last entry, which is in presence of 50 mM amide additive and 0.23 M CO_2. [c] k_{cat} values are reported as an average over three sets of experimental conditions (different [PhOH], 0.23 M CO_2, in the regime where rate is linearly dependent on [PhOH]). [d] FE for CO is reported as an average over three CPE experiments, see materials and methods for details

Under 1 atmosphere of CO_2 and in the presence of phenol as an acid source, catalytic responses indicative of CO_2 reduction are observed by cyclic voltammetry for all catalysts examined. In the presence of 100 mM phenol, Fe–*ortho*-1-amide exhibits a slightly more positive catalytic onset than Fe–*ortho*-2-amide, but both show significantly higher catalytic responses than the corresponding *para*-functionalized positional congeners or unfunctionalized Fe-TPP (**Figure 3.7**). In the presence of low phenol concentrations (5 mM), Fe–*ortho*-2-amide shows a significantly larger peak current compared to all other catalysts and a comparable onset potential to that of Fe–*ortho*-1-amide (**Figure 3.8**). In contrast, at higher phenol concentrations of 250 mM, Fe–*ortho*-1-amide displays a larger peak current and a more anodic onset potential than Fe–*ortho*-2-amide (**Figure 3.8**). These findings suggest that the role of phenol may differ among the positional isomers, or that altered mechanisms of catalyst inactivation are at play.

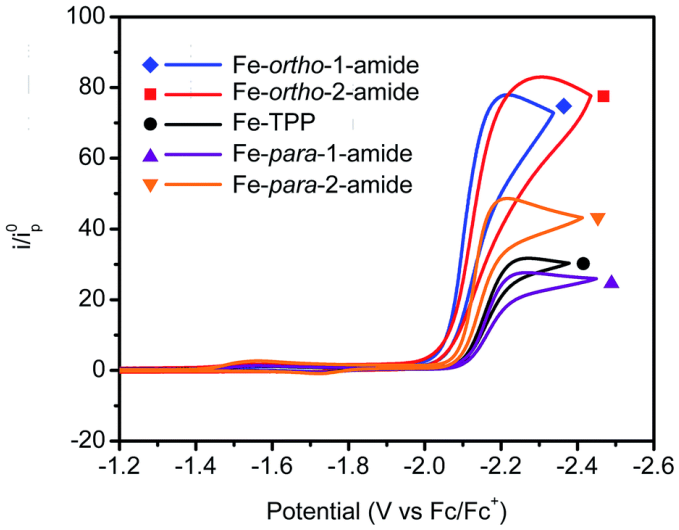


Figure 3.7. Cyclic voltammograms of amide-functionalized porphyrins and unfunctionalized Fe-TPP under CO_2 atmosphere. Conditions: 1 mM catalyst, 100 mM phenol, 0.1 M $TBAPF_6$ in DMF, saturated with CO_2 (0.23 M); scan rate 100 mV s^{-1}. *i* represents current under catalytic conditions; i^0_p represents the cathodic peak height of the formal $Fe^{II/I}$ couple under inert atmosphere.

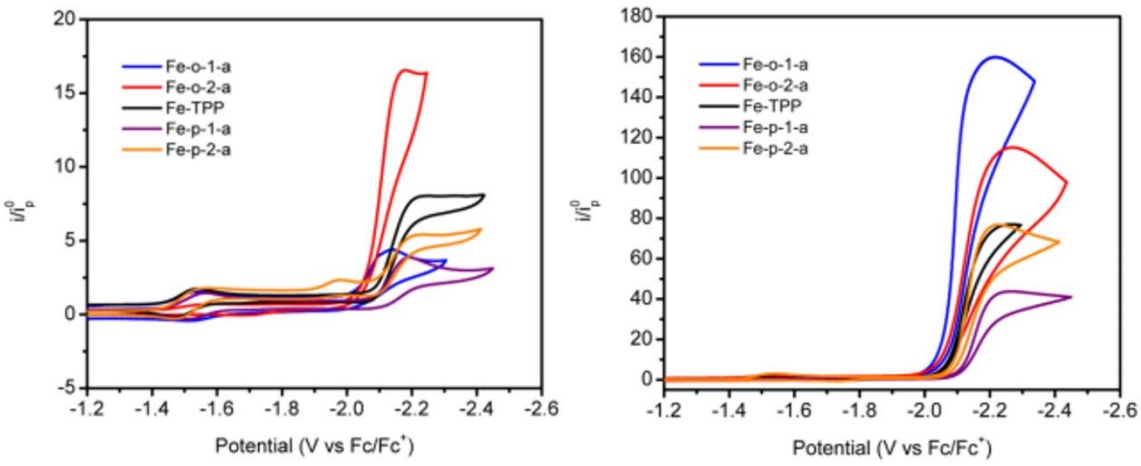


Figure 3.8. Cyclic voltammograms of amide-functionalized porphyrins and unfunctionalized Fe-TPP under CO_2 atmosphere in the presence of 5 mM phenol (left) and 250 mM phenol (right). Conditions: 0.1 M $TBAPF_6$ in DMF, saturated with CO_2 (0.23 M); scan rate 100 mV/sec.

To gain further insight into CO_2 reduction catalyzed by this series of amide-functionalized porphyrins, the observed rate constants (k_{obs} = TOF_{max}, s^{-1}) determined by FOWA were examined as a function of phenol and CO_2 concentration. Under pseudo-first order conditions, all four functionalized catalysts display first-order dependence on phenol concentration (**Figure 3.9** – **3.13**). Fe–*ortho*-2-amide achieves the largest observed rate constants (k_{obs}) of all catalysts tested, but exhibits non-linearity at higher phenol concentrations, possibly as a result of catalyst inhibition or local depletion of CO_2. Fe–*ortho*-1-amide exhibits the next highest set of k_{obs} values, followed by Fe–*para*-2-amide and finally Fe–*para*-1-amide. Maximum turnover frequencies (TOF_{max}) in the presence of 100 mM phenol are summarized in **Table 3.1**. Likewise, all four catalysts show first-order dependence on CO_2 concentration in the presence of excess (500 mM) phenol (**Figure 3.14**), as well as on catalyst concentration (**Figure 3.15**). Taken together, in the linear regimes of [PhOH] and [CO_2] where secondary phenomena are minimal, all four catalysts follow the rate law

$$\frac{-d[CO_2]}{dt} = k_{obs}[cat] = k_{cat}[PhOH][CO_2][cat]$$

Where k_{cat} (M^{-2} s^{-1}) is the intrinsic third-order rate constant. Average values for k_{cat}, determined at several phenol concentrations in the linear regime, are reported in **Table 3.1**. TOF_{max} and k_{cat} values for unfunctionalized Fe-TPP in the presence of 50 mM amide additive are also shown for comparison, demonstrating that *ortho* pendant amide groups are necessary to observe large enhancements in activity.

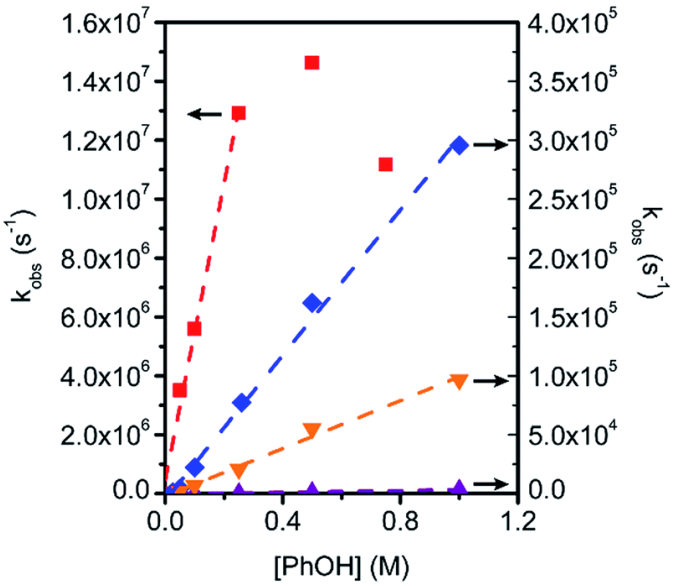


Figure 3.9. Observed rate constants (s^{-1}) for catalytic CO_2 reduction as a function of PhOH concentration for Fe–*ortho*-1-amide (blue diamonds), Fe–*ortho*-2-amide (red squares), Fe–*para*-1-amide (purple upward triangles), and Fe–*para*-2-amide (orange downward triangles). Conditions: 1 mM catalyst, 0.1 M $TBAPF_6$ in DMF; 0.23 M CO_2; scan rate is 100 mV s^{-1}. k_{obs} values were determined by FOWA.

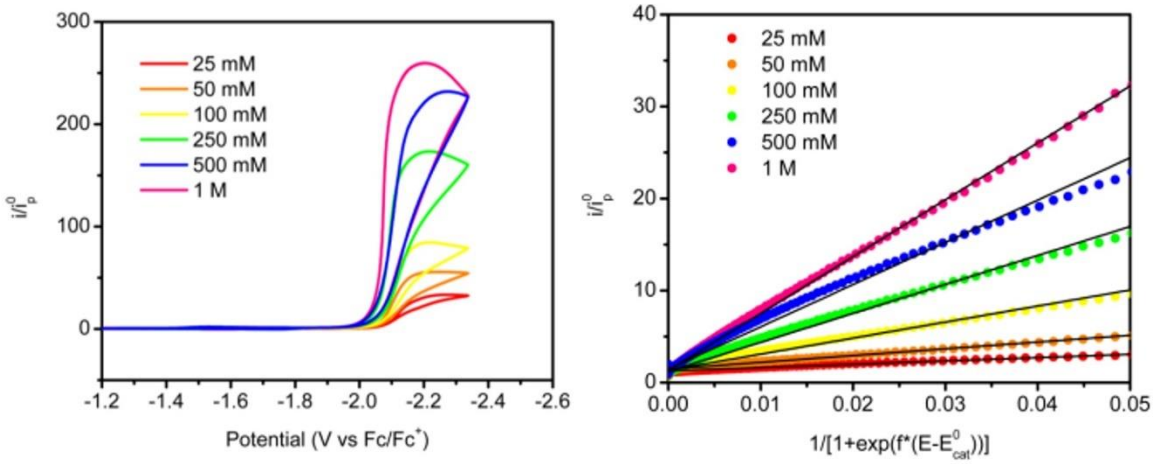


Figure 3.10. Cyclic voltammograms of Fe–*ortho*-1-amide (1 mM) in the presence of 25 – 1000 mM phenol under CO_2 atmosphere (0.23 M) in 0.1 M $TBAPF_6$ in DMF at a scan rate of 100 mV/sec (left). FOW plots for Fe–*ortho*-1-amide (1 mM) as a function of phenol concentration (right). Black lines denote linear fits used to obtain k_{obs}.

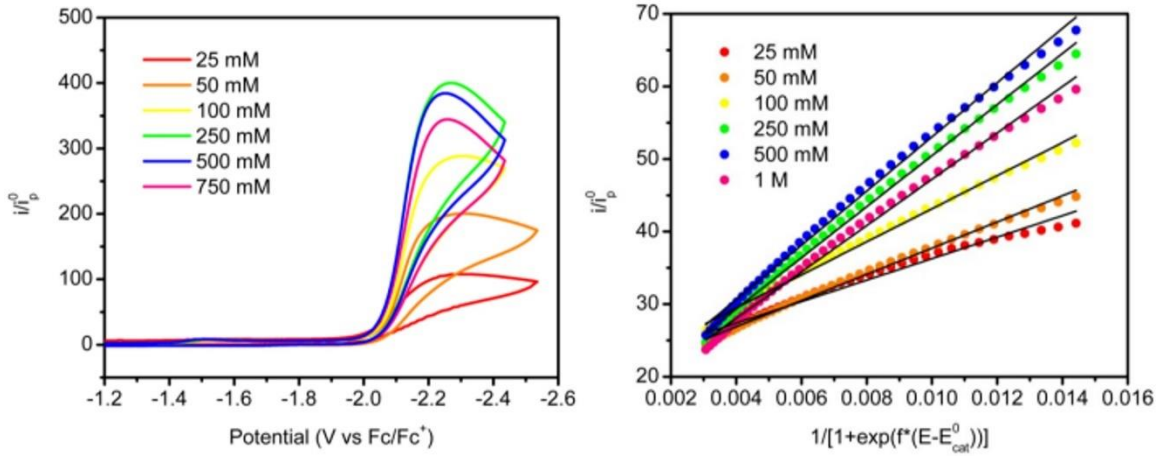


Figure 3.11. Cyclic voltammograms of Fe–*ortho*-2-amide (1 mM) in the presence of 25 – 1000 mM phenol under CO_2 atmosphere (0.23 M) in 0.1 M $TBAPF_6$ in DMF at a scan rate of 100 mV/sec (left). FOW plots for Fe–*ortho*-2-amide (1 mM) as a function of phenol concentration (right). Black lines denote linear fits used to obtain k_{obs}.

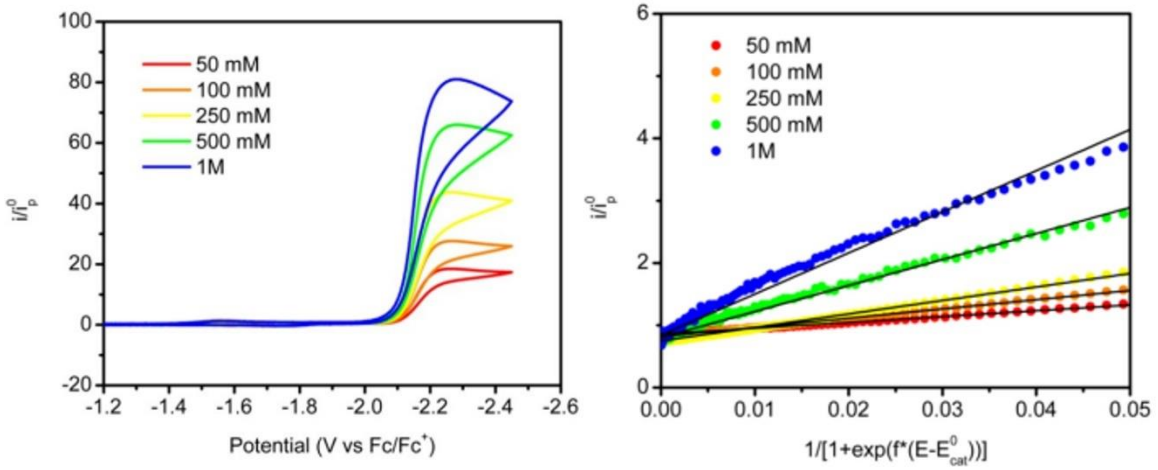


Figure 3.12. Cyclic voltammograms of Fe–*para*-1-amide (1 mM) in the presence of 50 – 1000 mM phenol under CO_2 atmosphere (0.23 M) in 0.1 M $TBAPF_6$ in DMF at a scan rate of 100 mV/sec (left). FOW plots for Fe–*para*-1-amide (1 mM) as a function of phenol concentration (right). Black lines denote linear fits used to obtain k_{obs}.

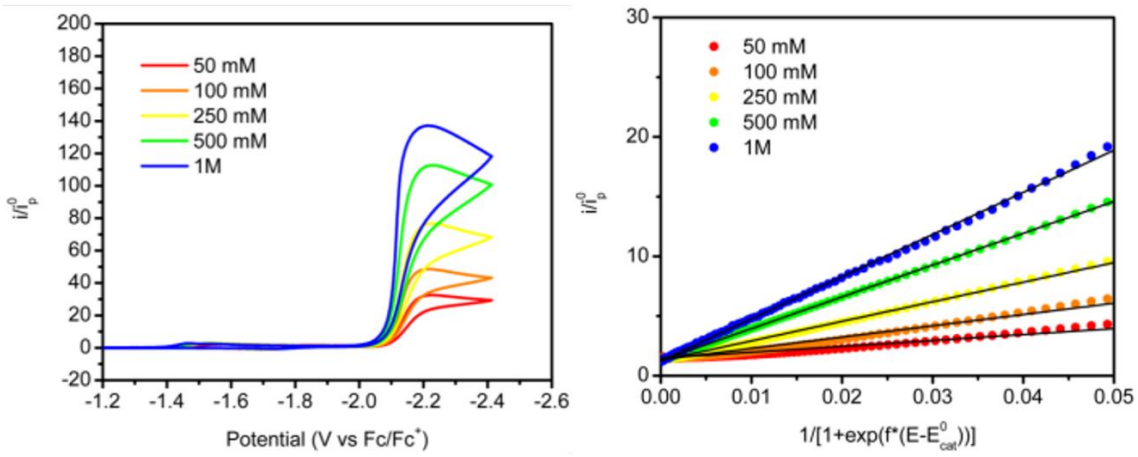


Figure 3.13. Cyclic voltammograms of Fe–*para*-2-amide (1 mM) in the presence of 50 – 1000 mM phenol under CO_2 atmosphere (0.23 M) in 0.1 M $TBAPF_6$ in DMF at a scan rate of 100 mV/sec (left). FOW plots for Fe–*para*-2-amide (1 mM) as a function of phenol concentration (right). Black lines denote linear fits used to obtain k_{obs}.

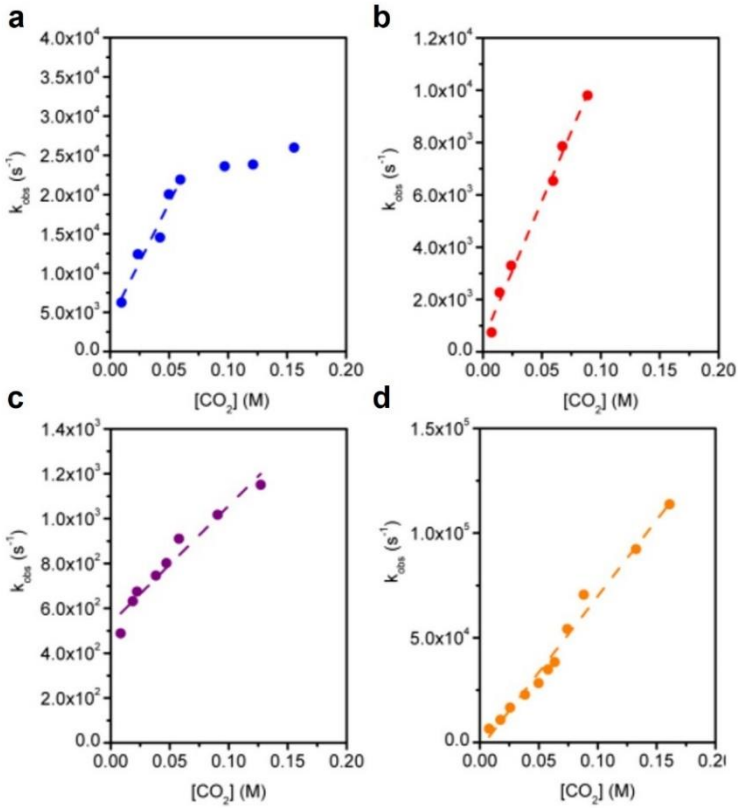


Figure 3.14. Observed rate constants (s^{-1}) as a function of CO_2 concentration for (a) Fe–*ortho*-1-amide, (b) Fe–*ortho*-2-amide, (c) Fe–*para*-1-amide, and (d) Fe–*para*-2-amide. Conditions: 1 mM catalyst, 0.1 M $TBAPF_6$ in DMF; 0.5 M PhOH; scan rate is 100 mV/sec. k_{obs} values were determined by Foot-of-the-Wave analysis.

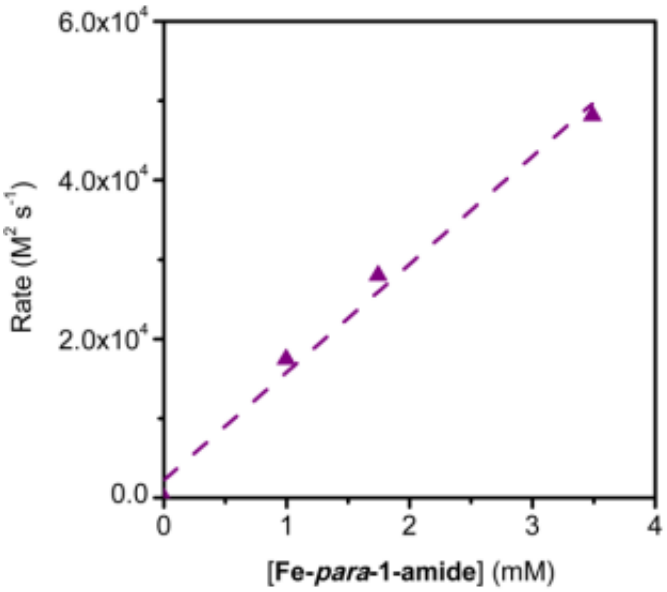


Figure 3.15. Observed rate constant, k_{obs} (s^{-1}), as a function of catalyst concentration for Fe–*para*-1-amide, indicating first-order dependence on catalyst concentration. Experiments performed in the presence of 0.5 M PhOH and 0.23 M CO_2; rates determined by Foot-of-the-Wave analysis.

For the purposes of catalyst benchmarking, it is illustrative to examine the log(TOF) *vs.* overpotential (η) relationships as indicated by a catalytic Tafel plot.[61] More effective catalysts operate with higher TOFs at lower overpotentials and are displayed in the upper left portion of such plots. As shown in **Figure 3.16**, Fe–*ortho*-2-amide exhibits higher TOFs over all overpotential values compared to Fe–*ortho*-1-amide, which in turn exhibits higher TOFs compared to Fe-TPP and both *para*-substituted porphyrins. The values at the plateau of such curves represent log(TOF_{max}), the maximum turnover frequency achievable at large overpotential (when the catalyst is fully present in its reduced state). The selectivity and stability of the aforementioned catalysts were examined by controlled potential electrolysis (CPE). A solution of catalyst in CO_2-saturated DMF electrolyte (0.1 M $TBAPF_6$, 0.5 mM catalyst, 0.5 M phenol as acid source) was electrolyzed at potentials between −2.1 and −2.2 V *vs.* Fc/Fc^+ in a homemade gas-tight electrolysis cell (see materials and methods for details). Gas chromatographic measurements of the headspace reveal that all four amide-functionalized catalysts have high selectivity for CO, with faradaic efficiencies (FE) between 74% and 92% (**Tables 3.1** – **3.3**). No hydrogen was observed for any catalyst under these conditions. Representative CPE traces are provided in **Figure 3.17**.

Though the previous metrics indicate that Fe–*ortho*-2-amide is a superior catalyst compared to Fe–*ortho*-1-amide, it is important to stress that the difference in E^0_{cat} values between catalysts must be considered when attempting to resolve questions of optimal second-sphere pendant placement. As illustrated previously,[62,63] electron withdrawing- or donating substituents on the porphyrin aryl rings modulate E^0_{cat} and consequently alter the driving force for electrochemical CO_2 reduction. In such cases, a linear scaling relationship between log(TOF_{max}) and E^0_{cat} is observed, where catalysts having more negative E^0_{cat} values exhibit larger TOFs. Deviation from this relationship occurs when second-sphere interactions either promote or inhibit catalysis, as has been previously documented for electrostatic effects.[64]

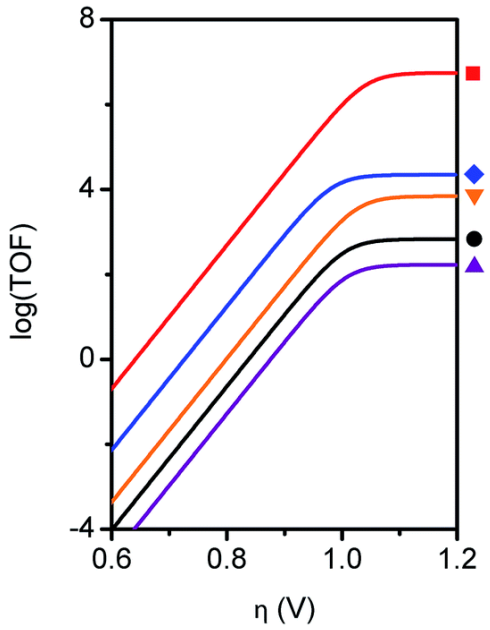


Figure 3.16. Catalytic Tafel plots for Fe–*ortho*-1-amide (blue diamond), Fe–*ortho*-2-amide (red square), Fe–*para*-1-amide (purple upward triangle), Fe–*para*-2-amide (orange downward triangle), and Fe-TPP (black circle). Conditions: 0.1 M $TBAPF_6$ in DMF; 0.23 M CO_2; 100 mM PhOH; scan rate is 100 mV s^{-1}. TOF = k_{obs} and was determined by FOWA.

Table 3.2. Summary of equilibrium CO_2 binding constants (K_{CO_2}), amide pK_a values, and kinetic isotope effects (KIE) for the iron porphyrin catalysts.

Catalyst	K_{CO_2} [a] (M^{-1})	Amide pK_a	KIE [b]
Fe-TPP	2.3	N/A	1.5 – 2.5[c]
Fe-*ortho*-1-amide	17.1	18.7 ± 0.2	1.47
Fe-*ortho*-2-amide	14.4	19.3 ± 0.1	1.77
Fe-*para*-1-amide	–	18.8 ± 0.1	1.88
Fe-*para*-2-amide	3.6	18.7 ± 0.5	1.84

[a] The binding constant for Fe–*para*-1-amide could not be measured but is expected to be between 2 – 4 M^{-1}. [b] KIE values represent the ratio of k_H/ k_D measured using water as the proton source (see materials and methods for details). [c] Values reported for various proton sources, see [65]

Table 3.3. Raw results for controlled potential electrolysis replicates for all iron porphyrin complexes including electrolysis potential *E*, the charge passed Q, amount of CO measured by headspace GC versus expected based on charge (mL), and the resulting Faradaic Efficiency (%). No H_2 gas was detected in any case.

Catalyst	E (V vs Fc/Fc^+)	Q (C)	CO measured (mL)	CO expected (mL)	FE_{CO} (%)
Fe-*ortho*-1-amide	–2.12	2.22	0.224	0.281	80
	–2.15	3.67	0.399	0.465	86
	–2.14	3.04	0.316	0.385	82
Fe-*ortho*-2-amide	–2.19	8.78	1.030	1.113	93
	–2.15	8.15	0.964	1.034	93
	–2.17	8.55	0.978	1.084	90
Fe-*para*-1-amide	–2.19	1.76	0.184	0.223	82
	–2.22	1.67	0.153	0.212	72
	–2.27	2.74	0.229	0.348	66
Fe-*para*-2-amide	–2.16	3.01	0.329	0.381	86
	–2.16	1.99	0.180	0.253	71
	–2.16	3.40	0.343	0.431	80
Fe-*para*-$(CF_3)_4$	–2.06	2.75	0.246	0.349	71
	–2.10	4.40	0.408	0.558	73
	–2.09	5.04	0.508	0.639	80
Fe-TPP	–2.15	10.0	1.066	1.268	84
	–2.14	9.0	1.102	1.141	97
	–2.22	9.0	1.019	1.141	89
Fe-*para*-$(OMe)_4$	–2.18	2.51	0.200	0.318	63
	–2.21	2.71	0.253	0.344	74
	–2.20	2.86	0.269	0.363	74

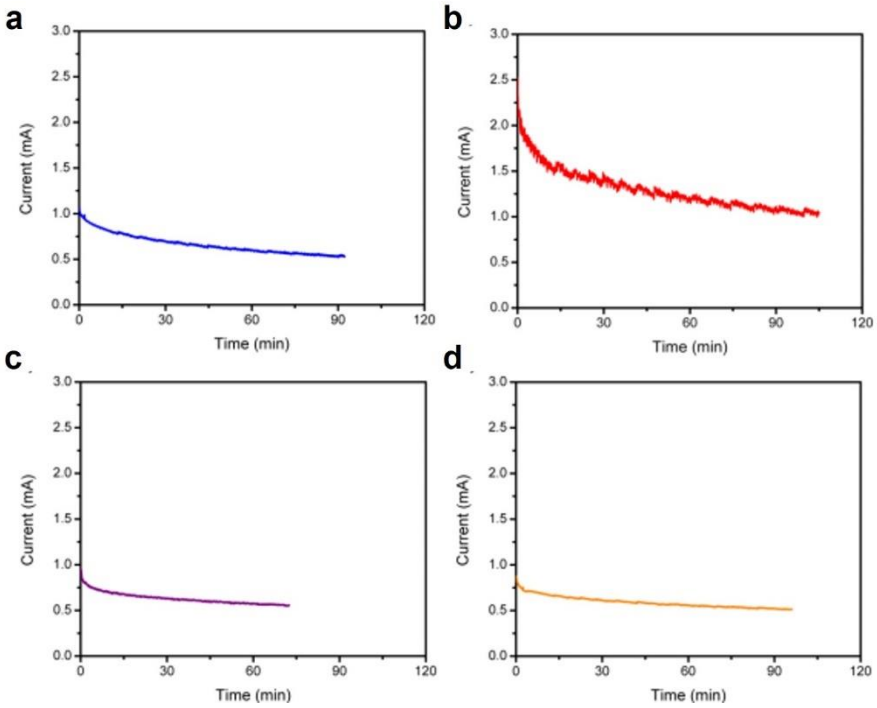


Figure 3.17. Representative CPE traces for (a) Fe–*ortho*-1-amide held at –2.15 V vs Fc/Fc^+, (b) Fe–*ortho*-2-amide held at –2.15 V vs Fc/Fc^+, (c) Fe–*para*-1-amide held at –2.27 V vs Fc/Fc^+, and (d) Fe–*para*-2-amide held at –2.16 V vs Fc/Fc^+.

In order to benchmark the electronic scaling relationship, Fe-TPP and two additional iron porphyrins with no second-sphere influences were investigated: Fe–*para*-$(CF_3)_4$, the iron complex of *meso*-tetra(4-trifluoromethylphenyl)porphyrin, and Fe–*para*-$(OMe)_4$, the iron complex of *meso*-tetra(4-methoxyphenyl)porphyrin. The synthesis and characterization of these two additional complexes are provided in the materials and methods section. Cyclic voltammograms of Fe–*para*-$(CF_3)_4$ and Fe–*para*-$(OMe)_4$ in the presence of phenol and CO_2 show characteristic responses indicative of CO_2 reduction (**Figures 3.18** and **3.19**). FOWA was applied to determine TOF_{max} values under conditions identical to those given above for the amide-functionalized porphyrins (**Figures 3.18** – **3.20**). Controlled potential electrolysis experiments (**Figure 3.21**) show that CO is also a major product for these two catalysts, with FE_{CO} of 70–74% (**Table 3.4**). The similar product selectivity permits meaningful comparisons with the amide-functionalized complexes. The electrochemical parameters for Fe–*para*-$(CF_3)_4$ and Fe–*para*-$(OMe)_4$ are summarized in **Table 3.4**. Together with Fe-TPP, these two catalysts exhibit the expected linear relationship between $\log(TOF_{max})$ and E^0_{cat} (circles, **Figure 3.22**).

To examine the contribution of through-space interactions on catalysis by the *ortho*- and *para*-amide-substituted porphyrins, each complex was added to the plot of $\log(TOF_{max})$ *vs.* E^0_{cat} shown in **Figure 3.22**. Both Fe–*ortho*-1-amide and Fe–*ortho*-2-amide lie significantly above the line corresponding to electronic-only effects, confirming that second-sphere interactions enhance the rate of CO_2 reduction for both complexes. Fe–*ortho*-2-amide shows a much larger departure from the electronic correlation line compared to Fe–*ortho*-1-amide, suggesting that the extent of through-space stabilization of the iron-bound CO_2 adduct is larger for the distal *ortho* isomer than

for the proximal congener. In contrast, the log(TOF_{max}) for Fe–*para*-2-amide is very slightly higher, and that for Fe–*para*-1-amide is very slightly lower, than that predicted by the electronic scaling relationship, suggesting that the *para*-substituted positional isomers do not exhibit notable through-space effects.

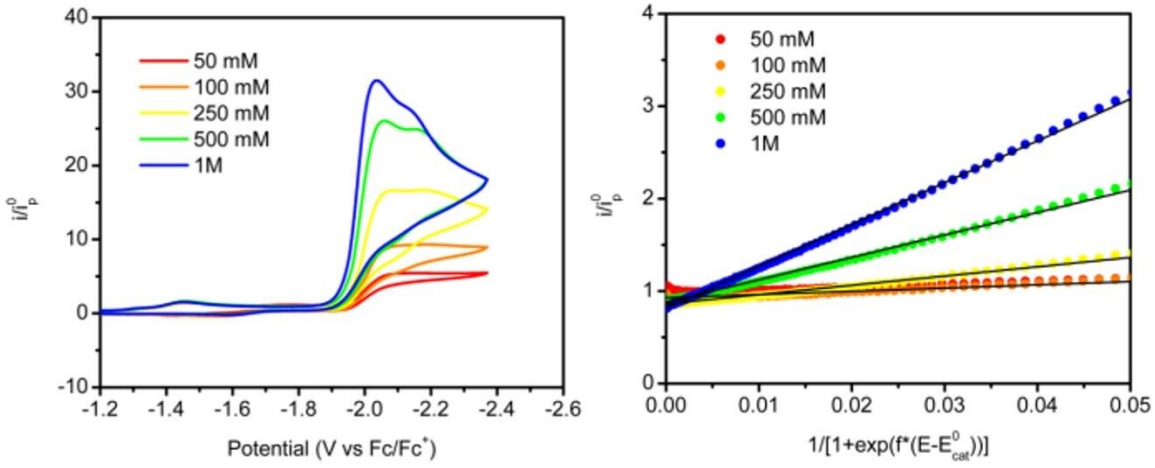


Figure 3.18. Cyclic voltammograms of Fe–*para*-$(CF_3)_4$ (1 mM) in the presence of 50 – 1000 mM phenol under CO_2 atmosphere (0.23 M) in 0.1 M $TBAPF_6$ in DMF at a scan rate of 100 mV/sec (left). FOW plots for Fe–*para*-$(CF_3)_4$ (1 mM) as a function of phenol concentration (right). Black lines denote linear fits used to obtain k_{obs}.

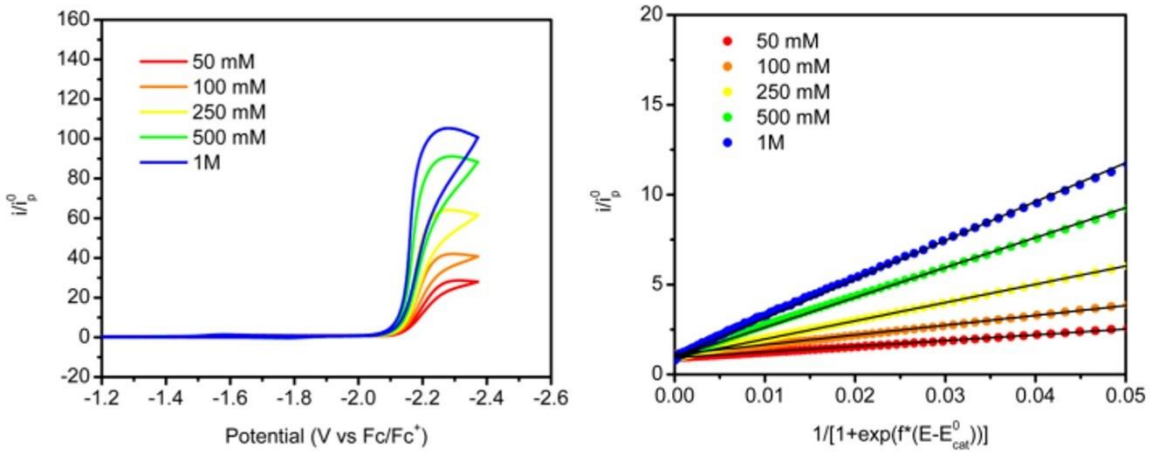


Figure 3.19. Cyclic voltammograms of Fe–*para*-$(OMe)_4$ (1 mM) in the presence of 50 – 1000 mM phenol under CO_2 atmosphere (0.23 M) in 0.1 M $TBAPF_6$ in DMF at a scan rate of 100 mV/sec (left). FOW plots for Fe–*para*-$(OMe)_4$ (1 mM) as a function of phenol concentration (right). Black lines denote linear fits used to obtain k_{obs}.

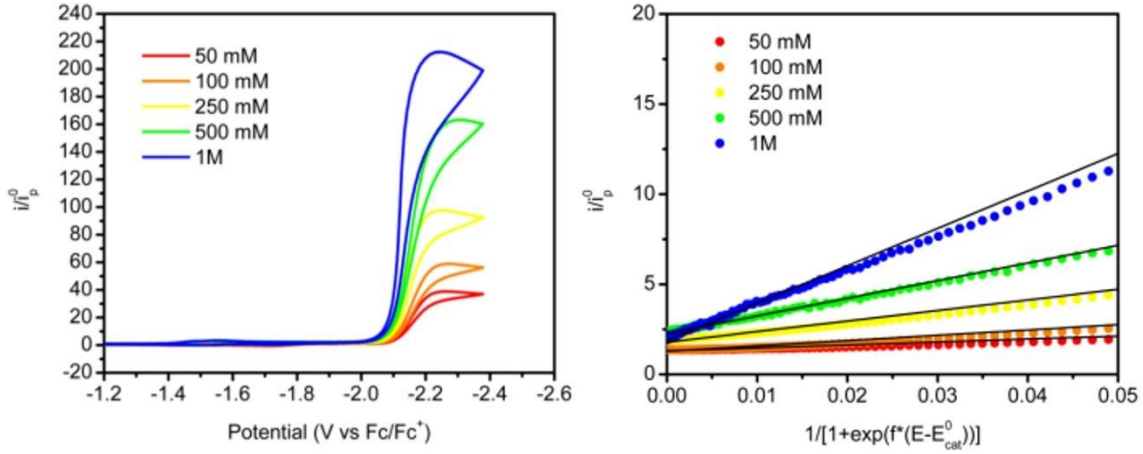


Figure 3.20. Cyclic voltammograms of Fe-TPP (1 mM) in the presence of 50 – 1000 mM phenol under CO_2 atmosphere (0.23 M) in 0.1 M $TBAPF_6$ in DMF at a scan rate of 100 mV/sec (left). FOW plots for Fe-TPP (1 mM) as a function of phenol concentration (right). Black lines denote linear fits used to obtain k_{obs}.

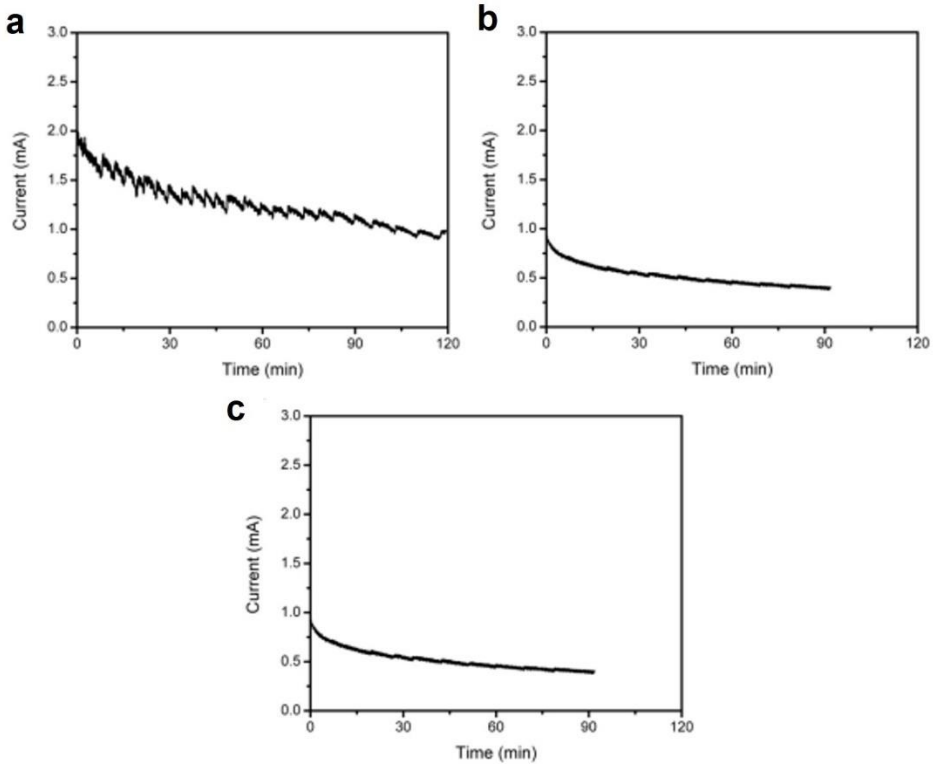


Figure 3.21. Representative CPE traces for (a) Fe-TPP held at –2.22 V vs Fc/Fc^+, (b) Fe–*para*-$(OMe)_4$ held at –2.20 V vs Fc/Fc^+ , and (c) Fe–*para*-$(CF_3)_4$ held at –2.09 V vs Fc/Fc^+.

Table 3.4. Summary of electrochemical properties of iron porphyrin catalysts.

Catalyst	E^0_{cat} (V vs Fc/Fc$^+$)[a]	TOF_{max} (s^{-1})[b]	log(TOF_{max})	k_{cat} ($M^{-2}s^{-1}$)	FE_{CO} (%)[c]
Fe-*para*-$(CF_3)_4$	–2.00	9.33×10^0	0.97	1.01×10^6	74 ± 5
Fe-TPP	–2.15	6.76×10^2	2.83	2.13×10^5	90 ± 6
Fe-*para*-$(OMe)_4$	–2.19	2.75×10^3	3.44	3.33×10^8	70 ± 6

[a]The standard reduction potential for the formal $Fe^{I/0}$ couple, E^0_{cat}, is reported as an average over three independent experiments. [b] TOF_{max} values are reported as an average over three sets of experimental conditions (different [PhOH], 0.23 M CO_2, in the regime where rate is linearly dependent on [PhOH]). [c] FE for CO is reported as an average over three CPE experiments.

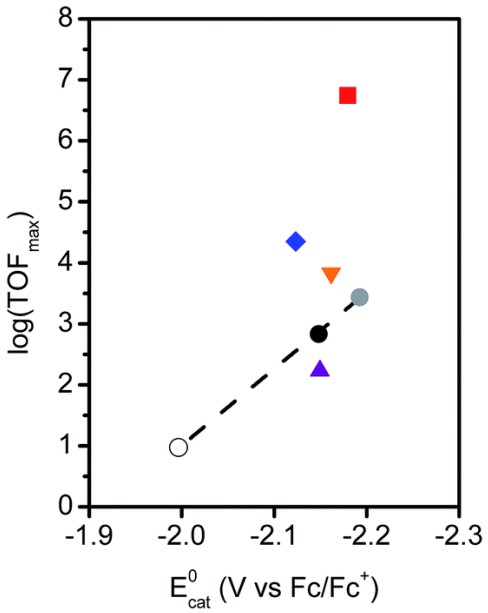


Figure 3.22. Correlation between log(TOF_{max}) and E^0_{cat} illustrating the through-space interactions that promote catalysis in the case of Fe–*ortho*-1-amide (blue diamond) and Fe–*ortho*-2-amide (red square). Porphyrin catalysts with no through-space interactions are shown in black: Fe–*para*-$(CF_3)_4$ (white circle), Fe-TPP (black circle), and Fe–*para*-$(OMe)_4$ (gray circle). Fe–*para*-2-amide (orange downward triangle) and Fe–*para*-1-amide (purple upward triangle) show minimal through-space effects. TOF_{max} determined by FOWA in the presence of 100 mM phenol and 0.23 M CO_2.

In order to gain further insight into the role of the *ortho* amide pendants in promoting catalysis, we determined the equilibrium constants for CO_2 binding, K_{CO_2}, based on the potential shift of the formal $Fe^{I/0}$ couple under Ar and CO_2. These experiments were performed at fast scan rates (2 – 10 V s^{-1}) in the absence of an added proton source to prevent subsequent catalytic turnover (**Figure 3.23**). As shown in **Table 3.2**, Fe-TPP and Fe–*para*-2-amide, which lack the ability to engage in productive through-space interactions, exhibit low K_{CO_2} values (2 – 4 M^{-1}). In contrast, Fe–*ortho*-1-amide and Fe–*ortho*-2-amide exhibit significantly larger K_{CO_2} values (14 – 17 M^{-1}), indicating that properly positioned amide pendants act to increase the affinity for CO_2 *via* hydrogen bonding interactions. Quantum chemical calculations on the Fe–CO_2 adducts of both *ortho*-functionalized complexes reveal differences in the length of the amide-CO_2 hydrogen bond (see materials and methods for details), with an H–O distance of 1.61 Å for Fe–*ortho*-1-amide and 1.45 Å for Fe–*ortho*-2-amide (**Figures 3.24** and **3.25**). The shorter H-bond distance for the latter complex is in agreement with the larger through-space interaction seen electrochemically (**Figure 3.22**).

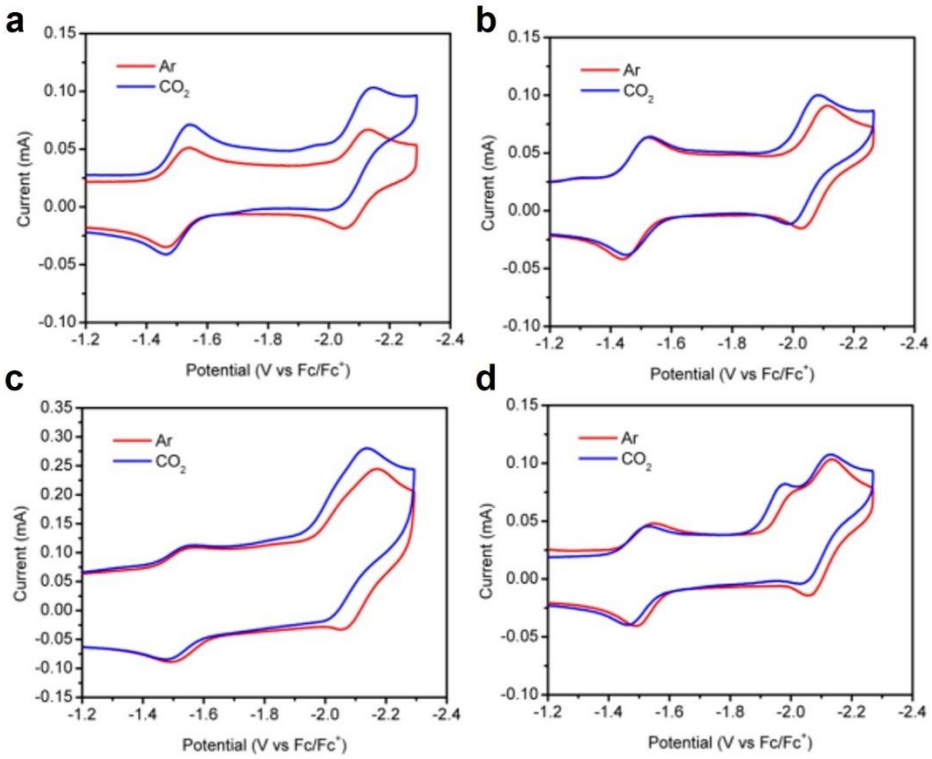


Figure 3.23. Cyclic voltammograms used to determine CO_2 equilibrium binding constant, K_{CO_2}. (a**)** Fe-TPP (measured at 2 V/sec), ΔE = 0.011 V. (b) Fe–*ortho*-1-amide (measured at 2 V/sec), ΔE = 0.041 V. (c) Fe–*ortho*-2-amide (measured at 10 V/sec), ΔE = 0.038 V. (d) Fe–*para*-2-amide (measured at 2 V/sec), ΔE = 0.016 V. K_{CO_2} for Fe–*para*-1-amid**e** was not able to be determined using this method.

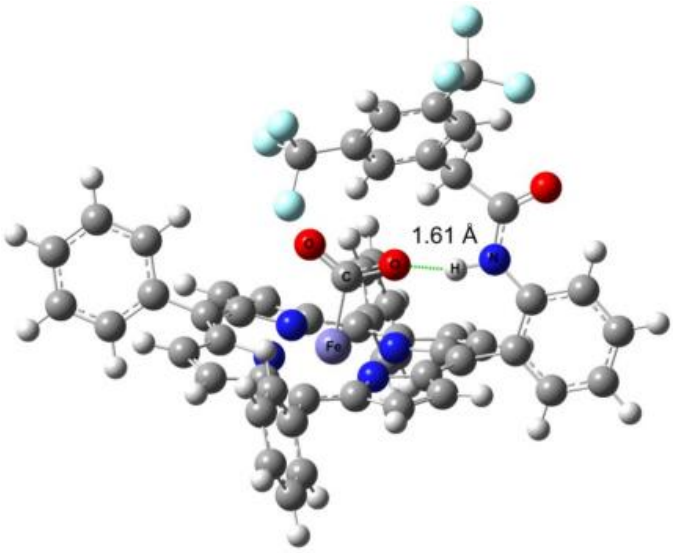


Figure 3.24. Optimized structure of the Fe^0–CO_2 adduct of Fe–*ortho*-1-amide, The hydrogen bond between the amide and bound CO_2 is represented by the green dashed line. Key: gray, carbon; white, hydrogen; red, oxygen; blue, nitrogen; light purple, iron; light blue, fluorine.

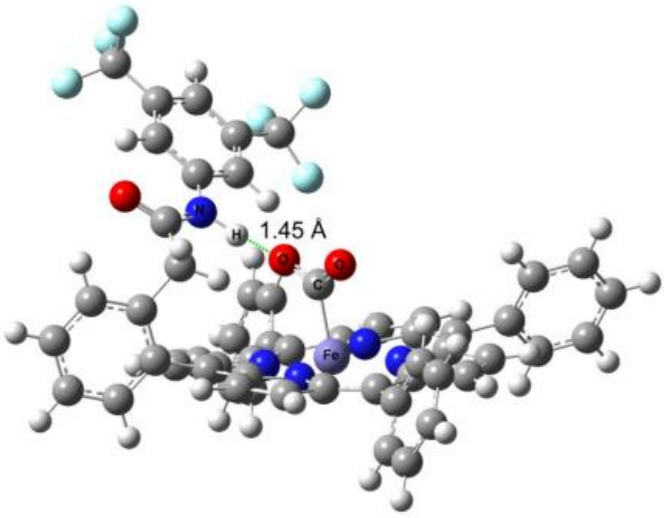


Figure 3.25. Optimized structure of the Fe^0–CO_2 adduct of Fe–*ortho*-2-amide, The hydrogen bond between the amide and bound CO_2 is represented by the green dashed line. Key: gray, carbon; white, hydrogen; red, oxygen; blue, nitrogen; light purple, iron; light blue, fluorine.

The role of proton transfer during catalysis was examined by measuring the pK_a values of all four amide pendants, as well as the H/D kinetic isotope effects. The pK_a values of all four amide pendants were determined spectrophotometrically (**Figures 3.26** – **3.29**) in DMSO, as shown in **Table 3.2**. Importantly, the amide of Fe–*ortho*-2-amide is less acidic (pK_a = 19.3 ± 0.1) than that of Fe–*ortho*-1-amide (pK_a = 18.7 ± 0.2). Thus, the higher catalytic activity of Fe–*ortho*-2-amide cannot be ascribed simply to a more acidic amide pendant. In addition, kinetic isotope effects for all four positional isomers were measured using H_2O or D_2O as the proton source (**Figures 3.30** –

3.37). Normal primary H/D kinetic isotope effects were observed for all four amide-functionalized catalysts (k_H/k_D between 1.47 and 1.88, see **Table 3.2**), suggesting that proton transfer is involved in the rate-determining step regardless of amide positioning.

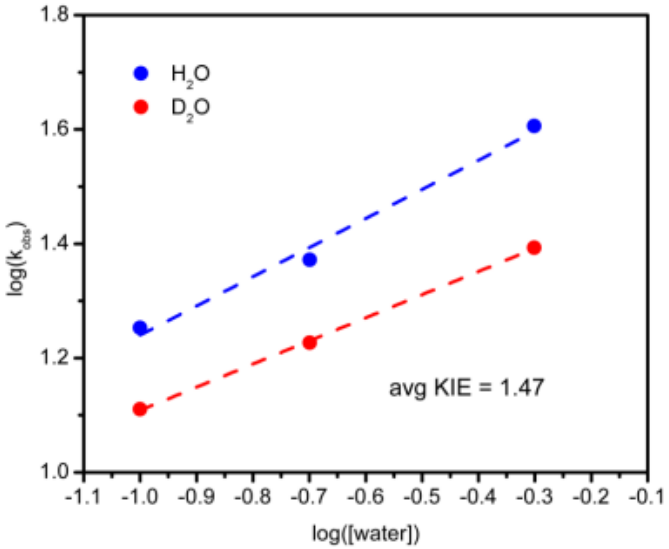


Figure 3.26. Variation of k_{obs} as a function of water concentration for Fe–*ortho*-1-amide. KIE was determined as an average of $k_{obs}(H_2O)/ k_{obs}(D_2O)$ for the three concentration points.

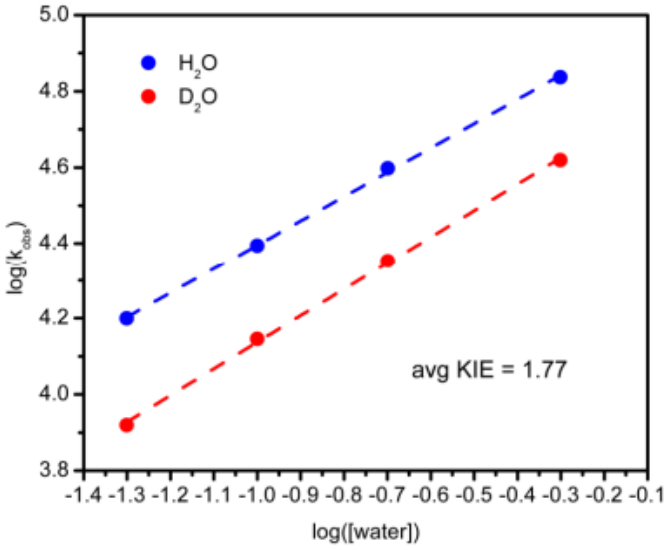


Figure 3.27. Variation of k_{obs} as a function of water concentration for Fe–*ortho*-2-amide. KIE was determined as an average of $k_{obs}(H_2O)/ k_{obs}(D_2O)$ for the four concentration points.

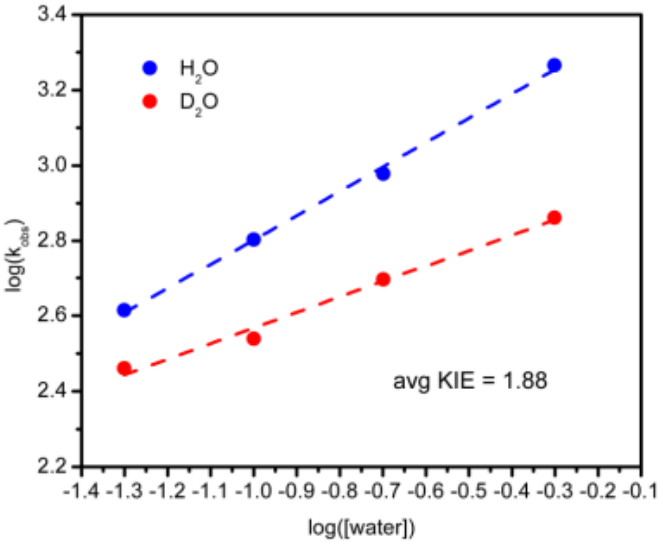


Figure 3.28. Variation of k_{obs} as a function of water concentration for Fe–*para*-1-amide. KIE was determined as an average of $k_{obs}(H_2O)/ k_{obs}(D_2O)$ for the four concentration points.

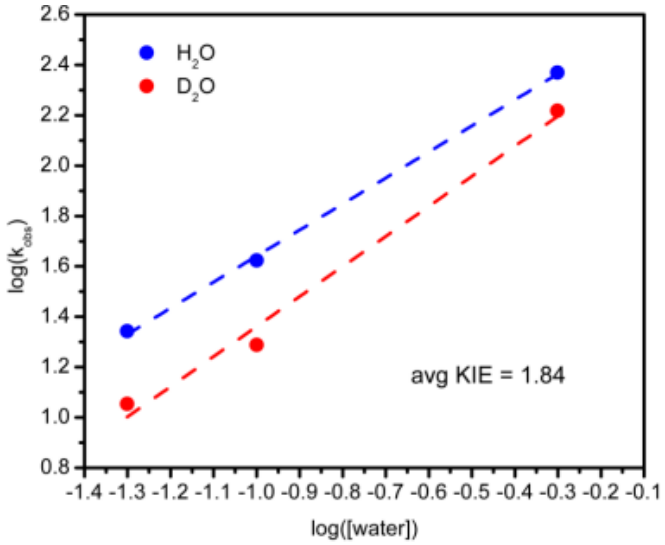


Figure 3.29. Variation of k_{obs} as a function of water concentration for Fe–*para*-2-amide. KIE was determined as an average of $k_{obs}(H_2O)/ k_{obs}(D_2O)$ for the three concentration points.

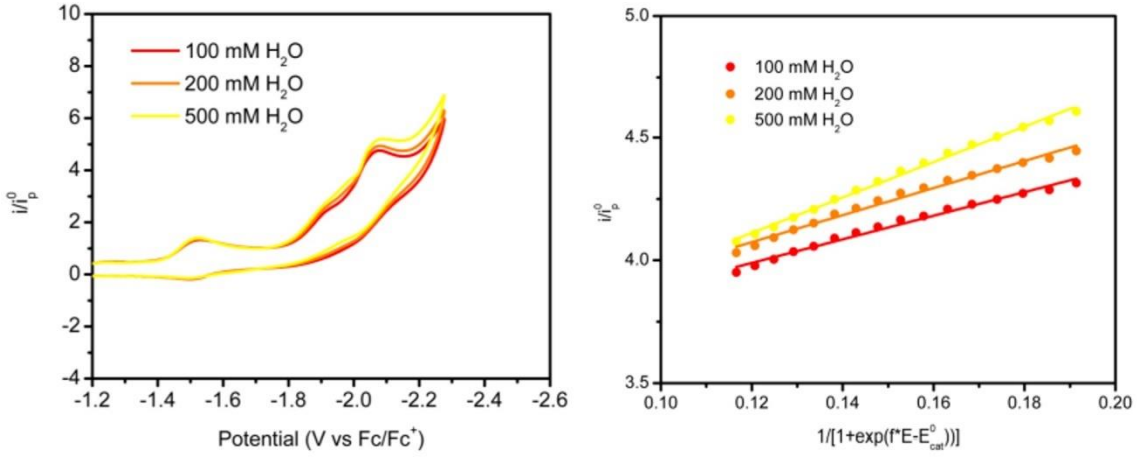


Figure 3.30. Cyclic voltammograms of Fe–*ortho*-1-amide (1 mM) in the presence of 100 – 500 mM H_2O under CO_2 atmosphere (0.23 M) in 0.1 M $TBAPF_6$ in DMF at a scan rate of 100 mV/sec (left). FOW plots for Fe–*ortho*-1-amide (1 mM) as a function of H_2O concentration (right). Lines denote linear fits used to obtain k_{obs}.

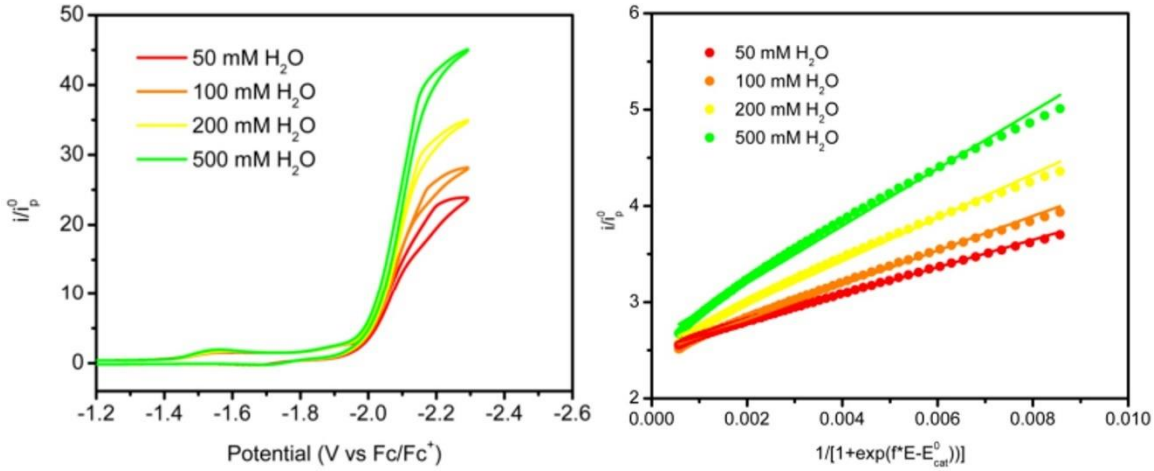


Figure 3.31. Cyclic voltammograms of Fe–*ortho*-2-amide (1 mM) in the presence of 50 – 500 mM H_2O under CO_2 atmosphere (0.23 M) in 0.1 M $TBAPF_6$ in DMF at a scan rate of 100 mV/sec (left). FOW plots for Fe–*ortho*-2-amide (1 mM) as a function of H_2O concentration (right). Lines denote linear fits used to obtain k_{obs}.

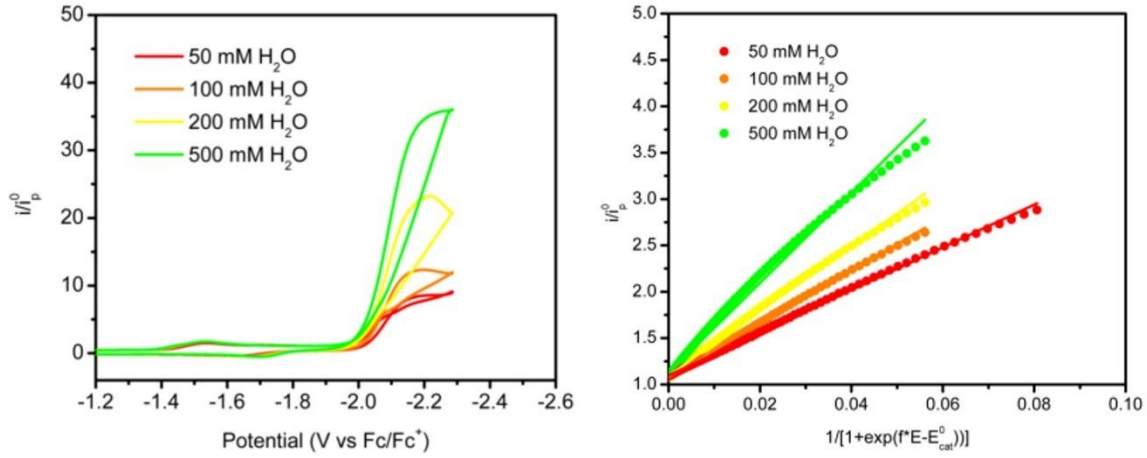


Figure 3.32. Cyclic voltammograms of Fe–*para*-1-amide (1 mM) in the presence of 50 – 500 mM H_2O under CO_2 atmosphere (0.23 M) in 0.1 M $TBAPF_6$ in DMF at a scan rate of 100 mV/sec (left). FOW plots for Fe–*para*-1-amide (1 mM) as a function of H_2O concentration (right). Lines denote linear fits used to obtain k_{obs}.

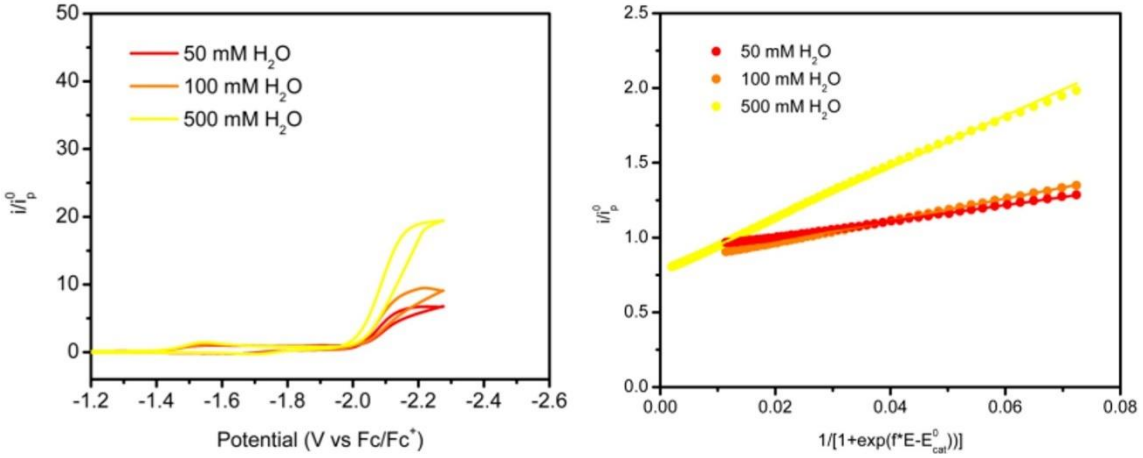


Figure 3.33. Cyclic voltammograms of Fe–*para*-2-amide (1 mM) in the presence of 50 – 500 mM H_2O under CO_2 atmosphere (0.23 M) in 0.1 M $TBAPF_6$ in DMF at a scan rate of 100 mV/sec (left). FOW plots for Fe–*para*-2-amide (1 mM) as a function of H_2O concentration (right). Lines denote linear fits used to obtain k_{obs}.

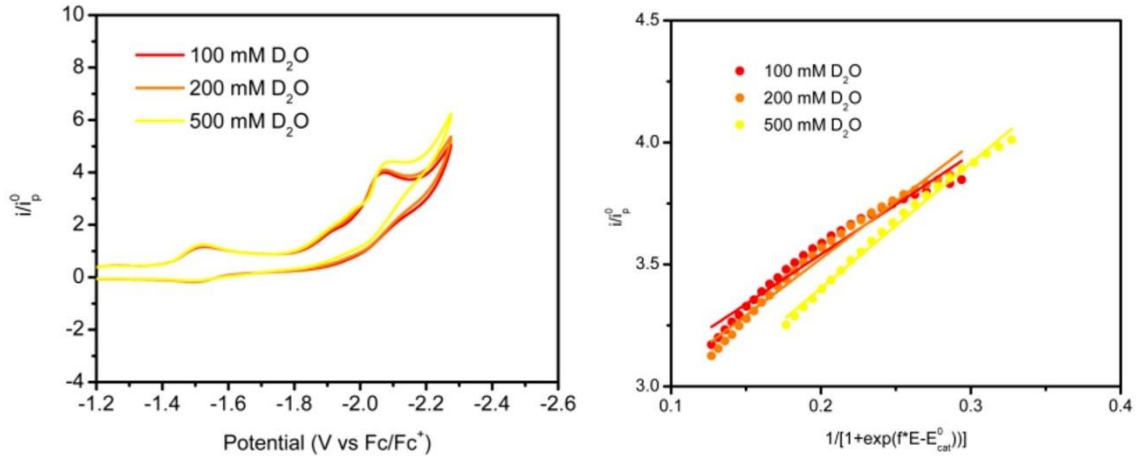


Figure 3.34. Cyclic voltammograms of Fe–*ortho*-1-amide (1 mM) in the presence of 100 – 500 mM D_2O under CO_2 atmosphere (0.23 M) in 0.1 M $TBAPF_6$ in DMF at a scan rate of 100 mV/sec (left). FOW plots for Fe–*ortho*-1-amide (1 mM) as a function of D_2O concentration (right). Lines denote linear fits used to obtain k_{obs}.

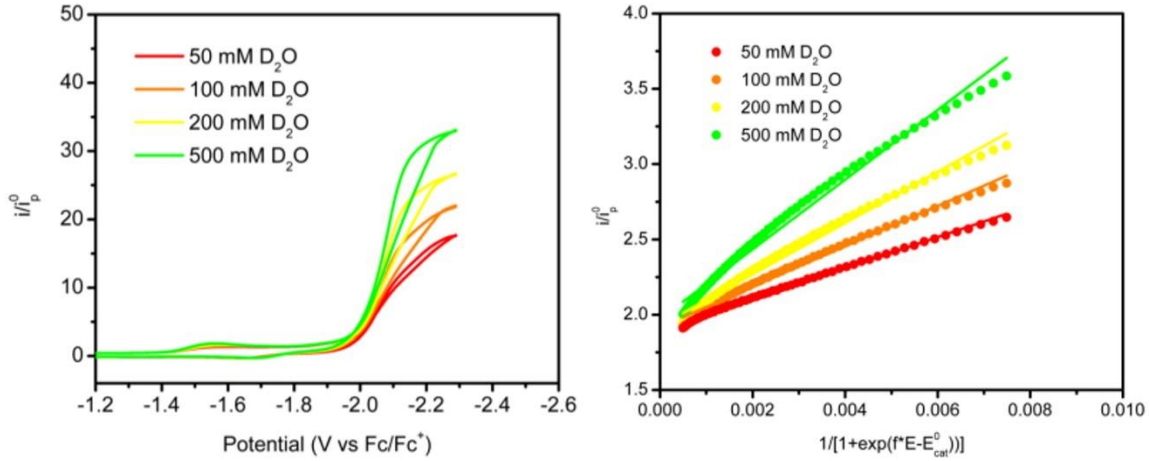


Figure 3.35. Cyclic voltammograms of Fe–*ortho*-2-amide (1 mM) in the presence of 50 – 500 mM D_2O under CO_2 atmosphere (0.23 M) in 0.1 M $TBAPF_6$ in DMF at a scan rate of 100 mV/sec (left). FOW plots for Fe–*ortho*-2-amide (1 mM) as a function of D_2O concentration (right). Lines denote linear fits used to obtain k_{obs}.

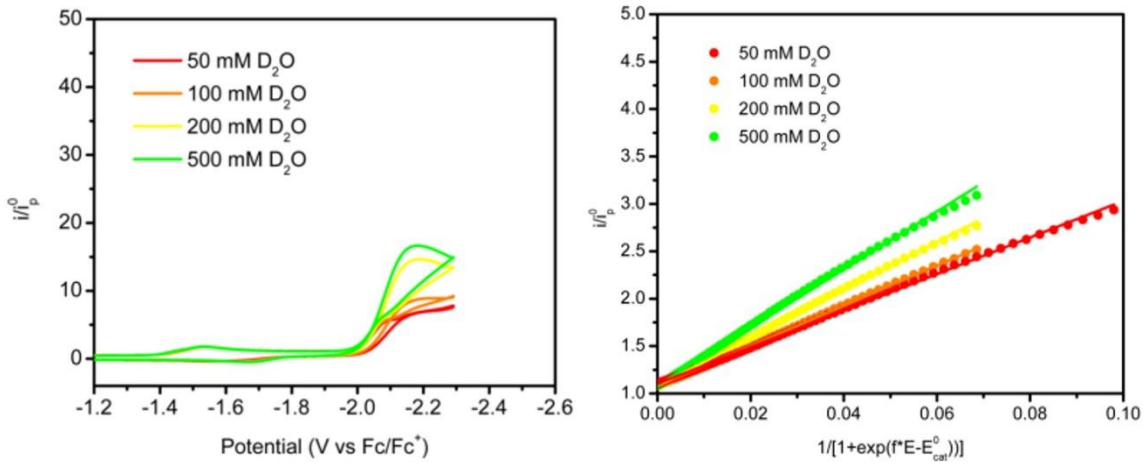


Figure 3.36. Cyclic voltammograms of Fe–*para*-1-amide (1 mM) in the presence of 50 – 500 mM D_2O under CO_2 atmosphere (0.23 M) in 0.1 M $TBAPF_6$ in DMF at a scan rate of 100 mV/sec (left). FOW plots for Fe–*para*-1-amide (1 mM) as a function of D_2O concentration (right). Lines denote linear fits used to obtain k_{obs}.

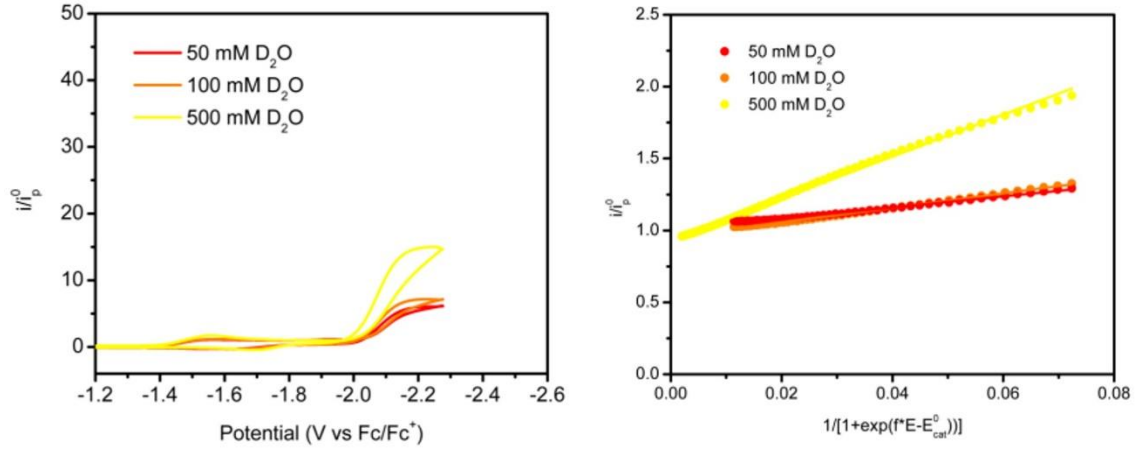


Figure 3.37. Cyclic voltammograms of Fe–*para*-2-amide (1 mM) in the presence of 50 – 500 mM D_2O under CO_2 atmosphere (0.23 M) in 0.1 M $TBAPF_6$ in DMF at a scan rate of 100 mV/sec (left). FOW plots for Fe–*para*-2-amide (1 mM) as a function of D_2O concentration (right). Lines denote linear fits used to obtain k_{obs}.

These results confirm, unsurprisingly, that second-sphere donors must be located at the *ortho*-positions of the porphyrin scaffold to exhibit productive interactions with catalytically-relevant intermediates. More interestingly, we show that a distally-located second-sphere amide group is more effective at breaking the electronic scaling relationship for CO_2 reduction than the proximal positional isomer due to enhanced hydrogen bond stabilization of the Fe–CO_2 intermediate. Differences in pK_a of the four amide pendants are minimal, indicating that their position with respect to the iron-bound CO_2 is more likely what governs differences in catalytic activity. The primary kinetic isotope effects observed for all four amide-functionalized catalysts are in agreement with those measured with other proton sources[65] or for other CO_2 reduction

catalysts,[22] and indicate that proton transfer is involved in the rate-determining step. Given the pK_a of the amide pendants, they are expected to act as proton relays in addition to hydrogen bond donors. We therefore conclude that distal *ortho* positioning allows the pendant to adopt a configuration that is more ideally suited to both hydrogen bond stabilization and proton transfer.

3.4 Conclusion

In summary, we investigate the positional dependence of secondary coordination sphere groups on the reactivity of a conserved primary iron porphyrin core for electrochemical CO_2 reduction. To this end, four positional isomers were synthesized, varying the location of the second-sphere amide group *ortho*- and *para*-, as well as proximal and distal, to the porphyrin plane. Cyclic voltammetry and controlled potential electrolysis were used to fully characterize the electrochemical behavior of this family of functionalized porphyrins, including kinetic parameters, catalytic Tafel plots, and faradaic efficiencies for the product CO. Studying the correlation between $\log(TOF_{max})$ and the $Fe^{I/0}$ standard potential, E^0_{cat}, reveals that through-space interactions enhance the rate of catalysis in both *ortho*-functionalized positional isomers, with the distally-located amide exhibiting a more significant enhancement. In contrast, the *para*-functionalized congeners display no significant through-space effects. These results demonstrate that fine-tuning the location of second-sphere pendants is an effective design strategy for the development of highly active biomimetic catalysts for CO_2 reduction, and by extension, for a wider range of chemical transformations.

3.5 Materials and Methods

3.5.1 General Synthetic and Physical Methods

Unless noted otherwise, all manipulations were carried out at room temperature under a dinitrogen atmosphere in a VAC glovebox or using high-vacuum Schlenk techniques. THF, DCM, toluene and DMF were dried using a JC Meyer solvent purification system; in addition to desiccant columns, DMF was passed through an isocyanate column to remove dimethylamine impurities. Thionyl chloride was purified by distillation. 2,6-Lutidine was dried over $AlCl_3$ then purified by distillation. All other reagents and solvents were purchased from commercial sources and used without further purification. Meso-tetra(4-methoxyphenyl)porphyrin was purchased from Frontier Scientific (Logan, UT). Fe-para-$(OMe)_4$ was prepared according to previously published procedures.[66] NMR spectra were recorded on Bruker spectrometers operating at 300, 400, or 500 MHz as noted. Chemical shifts for ^1H and $^{13}C\{1H\}$ spectra are reported in ppm relative to residual protiated solvent; those for ^{19}F spectra are reported in ppm relative to an external $CFCl_3$ standard. Coupling constants are reported in Hz.

3.5.2 General Methods for X-ray Crystallography

Single-crystal X-Ray diffraction was performed at the University of California, Berkeley College of Chemistry X-Ray Crystallography Facility. Crystals were mounted on nylon loops in Paratone-N hydrocarbon oil. Data collection was performed on a Bruker AXS diffractometer using Mo Kα radiation and an APEX II CCD area detector. A low temperature apparatus was used to keep crystals at 100 K during data collection. Determination of collection strategy, integration, scaling, and space group was performed using Bruker APEX2 software. Structure solution was performed using SHELXT-2014 and refinement was performed using SHELXL-2014.2

3.5.3 General Methods for Electrochemistry

Non-aqueous electrochemical experiments were conducted under Ar or CO_2 atmosphere in 0.1 M NBu_4PF_6 electrolyte in fresh anhydrous DMF that had been purified of dimethylamine by passing through an isocyanate column. Phenol was purified by repeated recrystallization from its melt and stored in the dark in a vacuum desiccator. Cyclic voltammetry and controlled potential electrolysis experiments were performed using an Epsilon potentiostat from Bioanalytical Systems, Inc. The working electrode for cyclic voltammetry was a 3.0 mm diameter glassy carbon disk (from Bioanalytical Systems, Inc.) and was polished between every scan with 0.05-micron alumina powder on a felt pad. The counter electrode was a platinum wire. A silver wire in porous Vycor tip glass tube filled with 0.1 M NBu_4PF_6 in DMF was used as a pseudo-reference electrode. At the conclusion of a series of experiments, the pseudo-reference potentials were referenced against ferrocene/ferrocenium as an external standard. The scan rate for all cyclic voltammograms was 100 mV/sec unless otherwise noted. All scans were compensated for internal resistance.

3.5.4 Details for CO_2 Concentration Dependence Experiments

The concentration of CO_2 in solution was varied by changing the percentage of CO_2 to N_2 balance using a gas proportioner (G21A2-BA0; Aalborg Instruments; Orangeburg, NY) fitted with sapphire/Viton-A flowtubes (112-02-SA; Aalborg Instruments; Orangeburg, NY). Using metering pressures of 50 psi for N_2 and 15 psi for CO_2 and correlating flow rate with meter reading using calibration curves published at Aalborg.com, the percentage of CO_2 in each gas mixture was calculated. It was assumed that the solution concentration of CO_2 is equal to 0.23 M times the CO_2 percentage in the mixed gas. Cyclic voltammetry experiments were performed by sparging the solution with gas mixtures containing increasing percentages of CO_2 for 10 min, then maintaining the same gas mixture in the headspace for the duration of the scan.

3.5.5 Details for Foot-Of-The-Wave Analysis (FOWA) and Determination of k_{obs}

Foot-of-the-Wave Analysis was applied to cyclic voltammetry measurements as described by Savéant and coworkers[61] in order to determine k_{obs} = TOF under the specified conditions. At the outset of each experiment, a cyclic 3 voltammogram was measured of catalyst alone under inert atmosphere in the absence of proton source, from which E^0_{cat} could be determined. The peak height of the formal $Fe^{II/I}$ couple, i^0_p, was determined by taking the difference between peak cathodic current and baseline current before the $Fe^{II/I}$ couple. As described previously,[57,61] CO_2 reduction with iron porphyrin catalysts may be described as an EC' process

$$Fe(I) + e^- \rightarrow Fe(0)$$

$$Fe(0) + CO_2 + 2H^+ \rightarrow Fe(II)CO + H_2O \text{ (RDS)}$$

$$Fe(II)CO + Fe(0) \rightarrow 2Fe(I) + CO$$

in which the rate-determining step involves pre-equilibrium CO_2 binding to the nucleophilic Fe(0) center and subsequent proton transfer. The following relationship may be derived:

$$\frac{i}{i^0_p} = \frac{2.24\sqrt{\frac{k_{obs}}{fv}}}{1+e^{[f(E-E^0_{cat})]}} \qquad \textbf{Equation 3.1}$$

where i is the current, E is the potential, v is the scan rate (V/s), k_{obs} is the observed rate constant, and f = F/RT = 38.94 V^{-1}. Thus, a "FOW" plot of $\frac{i}{i^0_p}$ *versus* $\frac{1}{1+e^{[f(E-E^0_{cat})]}}$ yields a straight line with slope of $2.24\sqrt{\frac{k_{obs}}{fv}}$, from which k_{obs} may be determined.

3.5.6 Details for Controlled Potential Electrolysis Experiments

Controlled potential electrolysis experiments were conducted in a homemade PEEK electrolysis cell (**Figure 3.38**). The cell has a working compartment (30 mL liquid volume) and counter compartment (12 mL liquid volume) that are separated by an ultra-fine glass frit. The cell is comprised of five distinct pieces: a main (working compartment) body, a lid, a window covering,

a side (counter compartment) cell, and a spacer to hold the glass frit. The cell features quartz windows on both working and counter sides.

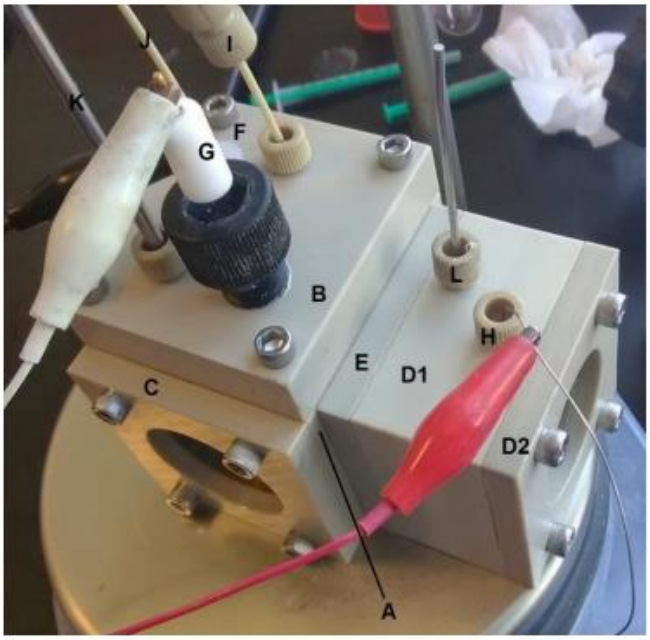


Figure 3.38. Photograph of the PEEK two-compartment cell. Important design features are (a) main body/working electrode compartment, (b) lid, (c) quartz window covering, (d1) counter electrode compartment, (d2) counter electrode window covering, (e) spacer for glass frit, (f) working electrode feedthrough, (g) non-aqueous reference electrode, (h) counter electrode, (i) gas injection port, (j) gas sparging line, (k) gas sampling line to GC, (l) opening to counter electrode compartment.

The cell windows are made from 1/16” thick x 1.5” diameter quartz discs (7500-05; GM Associates; Oakland, CA). A 25 mm diameter x 3-3.5 mm thick ultra-fine glass frit separates the working and counter compartments (7176; Ace Glass; San Francisco, CA). All junctions are sealed with PTFE-coated o-rings (orange with colorless coating) of the appropriate size. The working electrode is attached to 6”-long stainless steel rod (1 /16” OD) which passes through the lid and is sealed with a 1 /16” Tefzel ferrule and flangeless male nut (P-200 and XP-235X, respectively; Upchurch Scientific). The non-aqueous reference electrode consists of a silver wire in a glass tube with a CoralPor frit and is filled with the electrolyte used for the CPE experiment (MW-1085; Bioanalytical Systems, Inc.; West Lafayette, IN). The reference electrode is held in place with a ½-13 UNC plastic bushing and o-ring that makes a gas-tight fitting to the electrode. The gas injection port is constructed using a PEEK union (P-703, Upchurch Scientific) with a Teflon septum cut to size and held in place with a Delrin flat-bottom plug (P-309; Upchurch Scientific). The gas sparging line is made from 1/16” OD PEEK tubing (1531, Upchurch Scientific) that is once again sealed to the lid using 1/16” Tefzel ferrules and flangeless male nuts (P-200 and XP-235X, respectively; Upchurch Scientific). A Tefzel ETFE shut-off valve (P-782; Upchurch Scientific) was used to seal the gas sparging line. The outlet for GC sampling is constructed from 1/8” OD stainless steel tubing (sealed to the lid with a 1/8” Tefzel ferrule and nut (P-300X and P-335X, respectively; Upchurch Scientific)) that is connected to a Swagelok ball valve (40 series

1/8” tube fitting; Swagelok; Solon, OH). A piece of 1/8” OD stainless steel tubing is used to connect the other end of the ball valve to the stem of a Quick-Connect (SS-QM2-S-200, Swagelok), which is attached directly to the GC inlet that has been modified with a Quick-Connect body (SS-QM2-B-200, Swagelok).

Controlled potential electrolysis experiments were conducted by preparing a 0.5 mM solution of catalyst in 30 mL of 0.1 M $TBAPF_6$/DMF electrolyte. Phenol was added at a concentration of 0.5 M. The counter electrode chamber was filled with 12 mL of 0.1 M $TBAPF_6$/DMF electrolyte with 20 mM tetrabutylammonium acetate. This soluble source of acetate was sacrificially oxidized via the Kolbe reaction to generate CO_2 and ethane, thereby preventing GC detection of solvent oxidation byproducts. Both compartments were sealed to be gas-tight. The working compartment was sparged with CO_2 for 15 min, then closed and injected with 0.5 mL ethylene as a gaseous internal standard. A CV scan was collected to benchmark CPE potential, then the CPE experiment was initiated while stirring the solution at 300 rpm with a 1 cm stir bar. Upon completion, the headspace was injected into a SRI-GC equipped with 6’ Hayesep D and 13X Molecular Sieve chromatographic columns, as well as a second Hayesep D guard column which is used to trap solvent volatiles. Two in-line detectors were used: a TCD for H_2 detection, and a FID equipped with a methanizer for $CO/CO_2/C_2H_4$ detection. Temperature and pressure ramping was adjusted so that the analytes of interest eluted separately and not during valve turns. Analytes of interest were quantified by comparing a ratio of analyte:internal standard peak integrals to a calibration curve with known amounts of analyte.

3.5.7 Details for Measurement of CO_2 Binding Constant (K_{CO_2})

Equilibrium binding constants were determined electrochemically following methods detailed elsewhere.[67] Cyclic voltammograms were recorded in 0.1 M NBu_4PF_6 in anhydrous DMF (prepared as described in the section “General methods for electrochemistry”), first under an atmosphere of argon and then upon saturation with carbon dioxide. Fast scan rates (2 – 10 V/sec) were necessary to observe a reversible $Fe^{I/0}$ couple under CO_2. Proton sources (other than adventitious water) were omitted to prevent subsequent catalytic turnover. K_{CO_2} was calculated based on the difference between the standard potentials under Ar and CO_2, ΔE, using the **Equation 3.2**:

$$K_{CO_2} = \frac{e^{(f*\Delta E)} - 1}{[CO_2]} \qquad \textbf{Equation 3.2}$$

where f = F/RT = 38.94 V^{-1} and $[CO_2]$ (for CO_2-saturated DMF) is 0.23 M.

3.5.8 Details for Spectrophotometric pK_a Titration Experiments

The pK_a values of the amide pendants on the iron porphyrin complexes were determined in DMSO by following slight modifications to a previous literature report.[68] DMSO, base (K-dimsyl), indicator (4-choloro-2-nitroaniline; Sigma Aldrich), and porphyrin stock solutions were freshly prepared (as detailed below) before the spectrophotometric titration experiments were performed. Amounts of indicator, porphyrin, and DMSO, as well as amounts of indicator and porphyrin solutions, were determined gravimetrically using a microbalance.

DMSO. Rigorously dry and degassed DMSO was required for accurate determination of pK_a values. DMSO was dried following a previous report.[69] A commercial source of DMSO was dried over freshly activated alumina (Al_2O_3) overnight. The DMSO was filtered with a Schlenk-frit into a clean, flame-dried Schlenk flask equipped with a stir bar and dried over calcium hydride (CaH_2) overnight. Subsequent distillation under reduced pressure and degassing via three freeze-pump-thaw cycles afforded the dry DMSO, which was brought into a nitrogen filled glovebox and stored over 4 Å molecular sieves overnight before use. The fresh solvent was used within a two-day period.

K-dimsyl base. A clean Schlenk tube equipped with a glass stir bar was pre-weighed and flame dried. To this tube was added approximately 100 mg of potassium hydride (KH; Alfa Aesar) (30–35 w% 5 dispersion in mineral oil) under N_2 atmosphere and was washed with pentane (1 mL x3). The solvent was removed with a syringe, and the remaining solid was dried under vacuum for at least 1 hr. Once dry, the Schlenk tube was again weighed under N_2 atmosphere so that the amount of KH could be determined. With vigorous stirring, 20 mL of freshly dried DMSO was added to the Schlenk tube and allowed to stir until the KH was fully dissolved and no more H_2 was released. The K-dimsyl stock solution was then sealed and brought into a nitrogen filled glovebox and used within a two-day period. The concentration of the K-dimsyl base stock solution was calculated and was used to prepare an approximately 5 mM K-dimsyl solution. The 5 mM K-dimsyl base solution was protected from the light and used for the spectrophotometric titration experiments.

Indicator solution. 4-chloro-2-nitroaniline (pK_a in DMSO = 18.9; λ_{max} of deprotonated indicator = 520 nm; Sigma Aldrich)[68] was selected as the appropriate indicator due to its pK_a and lack of spectral overlap with Fe-amide porphyrins. The indicator was recrystallized from hot ethanol and dried under vacuum overnight prior to use. To a pre-weighed, oven-dried vial was added approximately 4.5 mg of 4-chloro-2-nitroaniline, with the exact amount determined gravimetrically using a microbalance. The vial was then brought into the glovebox and approximately 5 mL of dry DMSO was added. The vial was tightly sealed and taken out of the glovebox, quickly weighed using a microbalance, and brought back into the glovebox where it was stored in the absence of light. The exact concentration of the indicator solution was determined gravimetrically, assuming that the dilute stock solutions had the same density as pure DMSO (1.1 g/mL). A 2.59 mM indicator solution was utilized in these studies (*i.e.*, 4.40 mg of 4-chloro-2-nitroaniline in 9.71 mL dry DMSO). The indicator solution was used within a two-day period.

Fe porphyrin solutions. Approximately 1.10 – 2.50 mg of each iron porphyrin complex was added to pre-weighed, oven-dried vials, with the exact amount determined gravimetrically using a microbalance. The vials were then brought into the glovebox and 2.5 – 5.0 mL of dry DMSO was added. The vials were then tightly sealed and taken out of the glovebox, quickly weighed using a microbalance, and brought back into the glovebox where they were stored in the absence of light. The exact concentrations of the iron porphyrin solutions were determined gravimetrically, assuming that the dilute stock solutions had the same density as pure DMSO. The following concentrations were utilized for the iron porphyrin complexes reported in these studies: Fe–*para*-1-amide (0.46 mM; 2.30 mg in 4.89 mL DMSO); Fe–*para*-2-amide (0.43 mM; 2.30 mg

in 4.97 mL DMSO); Fe–*ortho*-1-amide (0.49 mM; 2.50 mg in 4.97 mL DMSO); Fe–*ortho*-2-amide (0.44 mM; 1.1 mg in 2.48 mL DMSO).

Titration experiment. In the first phase of each experiment, a solution of indicator was titrated into a K-dimsyl solution, allowing for determination of the extinction coefficient of the deprotonated indicator. This phase of the titration was repeated separately for each porphyrin measured.

An oven-dried semi-micro rectangular quartz cuvette with a screw cap and septum (d = 1 cm) (Starna Scientific; Atascadero, CA) was pre-weighed and brought into the glovebox. The cell was charged with 1 mL of freshly distilled DMSO, tightly sealed shut, and brought outside of the glovebox and weighed again to determine the amount of DMSO used. The cell was brought back into the glovebox, where 70 μL of the 5 mM K-dimsyl solution was carefully added to the cuvette with an oven-dried Hamilton syringe. The cuvette was sealed tightly with the screw septum cap and re-weighed outside the glovebox. The first UV-visible (UV-vis) spectrum was then recorded to determine the base line, and the titration was started. An oven-dried 100 μl Hamilton syringe was loaded with the indicator solution in the glovebox and then plugged with a rubber gasket. Approximately a 10 μl aliquot of the indicator stock solution was then added to the air-free cuvette and vigorously shaken to ensure proper mixing. The solution in the cuvette should turn pink in color. After addition of indicator, the cuvette was weighed, and the UV-vis spectrum was recorded. The Hamilton syringe was quickly re-plugged with the rubber gasket and stored in the small antechamber of the glovebox under vacuum between each measurement. The addition of 10 μl aliquots of the indicator solution, weighing the cuvette, and recording UV-visible spectra was repeated until no further increase in the absorption spectrum at 520 nm was observed (see **Figure 3.39**).

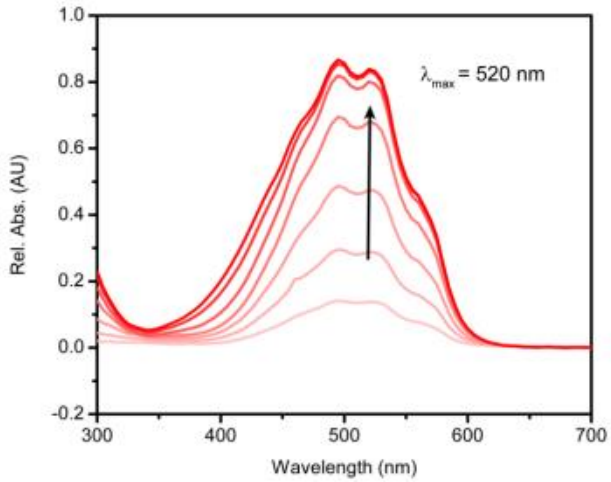


Figure 3.39. Representative spectral changes observed upon titration of 4-chloro-2-nitroaniline into a solution of K-dimsyl base. Aniline was added in small aliquots until no change in absorbance values at 520 nm was observed, signifying complete consumption of K-dimsyl base.

These data were used to determine the extinction coefficient (ε) of the indicator anion by plotting the concentration of the indicator in the cuvette vs. the absorbance at 520 nm (**Figure 3.40**). Dilution effects were taken into account through the volume increase upon sample addition. At the conclusion of this phase of the experiment, all K-dimsyl base (B^-) has been protonated (BH), and the cuvette contains only the two species of 4-chloro-2-nitroaniline indicator (HInd and Ind^-), with the maximum concentration of the deprotonated indicator (Ind^-). It is extremely important that all K-dimsyl base has been consumed before addition of iron porphyrin solutions, as direct protonation of K-dimsyl by the porphyrin amide will lead to significant error in determining the pK_a.

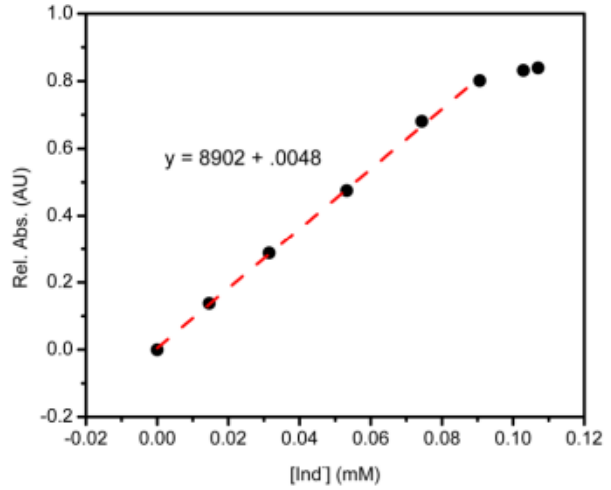


Figure 3.40. Representative determination of extinction coefficient ε (slope) of 4-chloro-2-nitroaniline anion, Ind^-, by titration of the corresponding aniline into a solution of K-dimsyl base.

Once no further spectral change at 520 nm is observed, the second phase of the titration is initiated. An oven-dried Hamilton syringe (25 µl – 200 µL) was loaded with the iron porphyrin solution inside the glovebox and then plugged with a rubber gasket. Small aliquots (10 – 25 µL) of the porphyrin solution were added to the air-free cuvette, which was vigorously shaken, weighed, and the UV-vis spectrum recorded. The syringe loaded with the porphyrin solution was re-plugged with the rubber gasket and stored in the small antechamber of the glovebox between titrations. With each addition of porphyrin solution to the cuvette, a new acid-base equilibrium is established, causing a loss in the absorbance of the deprotonated indicator (Ind^-) at 520 nm as the indicator anion is re-protonated (HInd). At least five titration points were collected for each iron porphyrin complex (**Figure 3.41**).

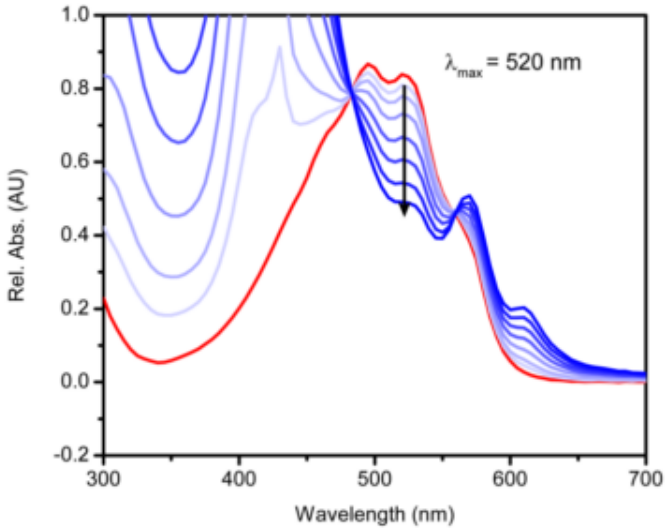


Figure 3.41. Representative spectral changes observed upon titration of Fe–*ortho*-2-amide into the solution of 4-chloro-2-nitroaniline and its anion (from the first phase of the titration experiment). The red trace is identical to that shown in **Figure 3.39**. Note the decrease in absorption at 520 nm as the deprotonated indicator becomes protonated by the pendant amide.

pK_a calculations. The first and second phases of the titration experiment involve the equilibria shown in **Equations 3.3** and **3.4**, where BH/B^-, $HInd/Ind^-$, and HA/A^- are the protonated and deprotonated Kdimsyl base, 4-chloro-2-nitroaniline indicator, and iron porphyrin complexes, respectively. The pK_a value of the iron porphyrin complex was determined using the equilibrium constant (K_{eq}) for **Equation 3.4** and the known pK_a of the indicator. A value for K_{eq} was determined for each titration point; thus, the reported pK_a values represent the average over at least 5 measurements.

$$B^- + HInd \rightarrow BH + Ind^- \qquad \textbf{Equation 3.3}$$

$$Ind^- + HA \rightarrow HInd + A^- \qquad \textbf{Equation 3.4}$$

The equilibrium constant can be determined by measuring the exact concentrations of $HInd/Ind^-$ and HA/A^- (**Equation 3.5**) in the cuvette at each titration point. Once the equilibrium constants have been measured, the pK_a of the iron porphyrin complex can be calculated from

Equation 3.6. In order for the pK_a of the unknown to be determined accurately, the indicator pK_a must be within 2 pK_a units of the unknown porphyrin complex.

$$K_{eq} = \frac{[Hind][A^-]}{[HA][Ind^-]} \quad \textbf{Equation 3.5}$$

$$pK_a = pK_{a\,indicator} - logK_{eq} \quad \textbf{Equation 3.6}$$

The concentration of the deprotonated indicator, [Ind$^-$], was determined by the Beer-Lambert Law, **Equation 3.7**, using the absorbance of the indicator anion at 520 nm. The extinction coefficient (ε) was determined during each experiment from the gradual addition of the indicator solution to the cuvette as described above.

$$[Ind^-] = \frac{Abs\ @520\ nm}{\varepsilon * l} \quad \textbf{Equation 3.7}$$

The concentration of the protonated indicator, [HInd], was determined by subtracting the concentration of [Ind$^-$] from the total concentration of indicator that was added to the cell, [Ind$_{total}$] (**Equation 3.8**).

$$[IH] = [Ind_{total}] - [Ind^-] \quad \textbf{Equation 3.8}$$

Because Ind$^-$ is stoichiometrically protonated by HA, the change in concentration of Ind$^-$ and A$^-$ are equal in magnitude (**Equation 3.9**). The concentration of deprotonated iron porphyrin complex, [A$^-$], was therefore determined from the change in absorption at 520 nm upon addition of the porphyrin.

$$-\Delta[Ind^-] = \Delta[A^-] \quad \textbf{Equation 3.9}$$

Finally, [HA] was determined by subtracting the concentration of deprotonated porphyrin, [A$^-$], from the concentration of the total amount of porphyrin complex added to the cuvette, [porphyrin$_{total}$] according to **Equation 3.10**.

$$[HA] = [porphyrin_{total}] - [A^-] \quad \textbf{Equation 3.10}$$

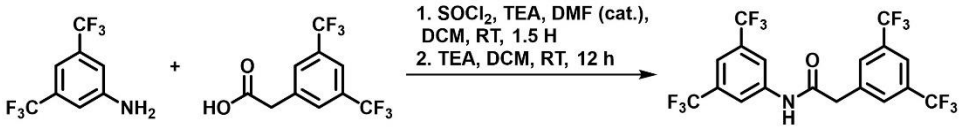
3.5.9 Details for Measurement of KIE

Kinetic isotope effect (KIE) values were measured for each Fe porphyrin bearing a pendant amide group. Water (H_2O or D_2O) was used as the proton source for these studies. Observed rate constants, k_{obs}, were determined using FOWA for various concentrations of H_2O or D_2O as described above. The reported KIE is an average of k_{obs}(H)/k_{obs}(D) over several water concentrations.

3.5.10 Computational Details

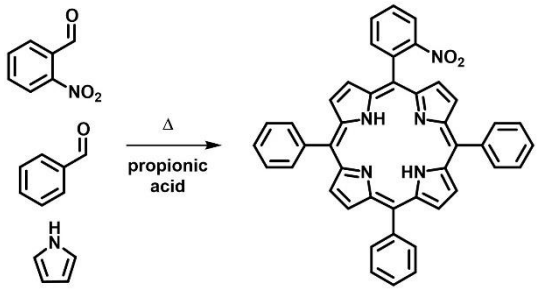
Calculations were performed using Gaussian 16.[70] Calculations were run using the B3LYP functional and LAN12DZ basis set. Minimum energy structures were fully optimized.

3.5.11 Synthesis of [3,5-Bis(trifluoromethyl)phenyl]amide (amide)



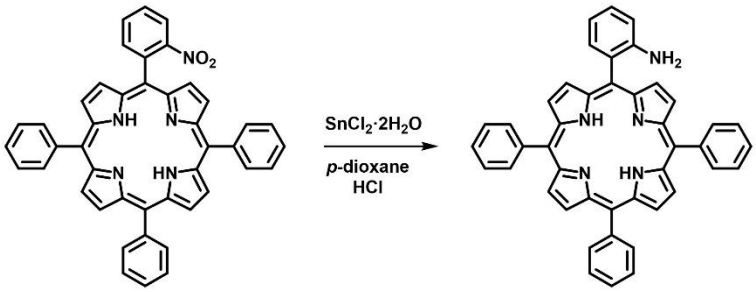
A 50 mL Schlenk flask was charged with 20 mL anhydrous DCM, 3,5-bis(trifluoromethyl)phenylacetic acid (1.00 g, 3.67 mmol), and a catalytic amount of anhydrous DMF (29 μL, 0.37 mmol). Freshly distilled $SOCl_2$ (0.32 mL, 4.41 mmol) was added under a N_2 atmosphere, and the solution was stirred at RT for 1.5 h. Solvent was removed under reduced pressure to afford a yellow oil. Anhydrous toluene (5 mL) was added, then removed under reduced pressure to assist in removal of excess $SOCl_2$. The resulting acid chloride was dissolved in anhydrous DCM (20 mL) and 3,5- bis(trifluoromethyl)aniline (0.86 mL, 5.51 mmol) was added, followed by triethylamine (0.61 mL, 4.41 mmol). After reacting overnight at RT, the solvent was removed under reduced pressure. The product was dissolved in EtOAc and washed with water; combined organic fractions were dried over $MgSO_4$ and solvent was removed under reduced pressure. The crude product was purified by column chromatography (starting at 2:1 hexane:DCM and progressing to 1:3 hexane:DCM) on silica, and obtained as a white solid (0.65 g, 37% yield). ^{1}H NMR (500 MHz, CD_3CN) δ 9.02 (br s, 1H), 8.15 (s, 2H), 7.94 (s, 3H), 7.70 (s, 1H), 3.92 (s, 2H). $^{13}C\{^1H\}$ NMR (126 MHz, CD_3CN) δ 169.80, 141.30, 138.77, 132.46 (q, J = 33.3 Hz), 131.76 (q, J = 32.8 Hz), 131.37 (m), 124.49 (q, J = 271.8 Hz), 124.29 (q, J = 271.9 Hz), 121.87 (m), 120.12, 117.84 (m), 43.06. ^{19}F NMR (376 MHz, $CDCl_3$) δ -62.57, -62.89. IR (ATR, solid, ν (cm^{-1})): 3264 (w), 3222 (w), 3186 (w), 3096 (w), 1670 (m), 1569 (m), 1469 (m), 1374 (s), 1272 (s), 1171 (s), 1127 (s). ESI-MS calculated for $C_{18}H_8F_{12}NO$ $[M-H]^-$ 482.0, found 482.4; $C_{18}H_9ClF_{12}NO$ $[M+Cl]^-$ 518.0 m/z, found 518.4 m/z.

3.5.12 Synthesis of 5-[2-Nitrophenyl]-10,15,20-triphenyl Porphyrin (1)



Porphyrin **1** was synthesized according to a modified literature procedure.[71,72] 2-nitrobenzaldehyde (7.2 g, 47.6 mmol) and benzaldehyde (10.11 g, 95.3 mmol) were added to refluxing propionic acid (400 mL) in a 1 L round bottom flask. Pyrrole (9.9 g, 142.9 mmol) was added dropwise and the solution was heated at reflux for 30 min in the absence of light. Upon cooling to room temperature, methanol (200 mL) was added and the precipitated porphyrins were collected via filtration, then washed with water and methanol several times. A solution of the porphyrin mixture in DCM was run through a basic alumina plug to remove oligomers. Porphyrin 1 (R_f = 0.6) was separated from tetraphenylporphyrin (R_f = 0.75) and other nitroporphyrins by column chromatography (2:1 hexane:DCM) on basic alumina, and finally recrystallized from DCM/MeOH (1.7 g, 7% yield). The ^{1}H NMR spectrum agrees well with the literature reports of this compound. ^{1}H NMR (300 MHz, CD_2Cl_2) δ 8.82 – 8.92 (m, 6H), 8.66 – 8.72 (m, 2H), 8.45 (m, 1H), 8.15 – 8.33 (m, 7H), 7.96 – 8.05 (m, 2H), 7.70 – 7.85 (m, 9H), -2.78 (s, 2H).

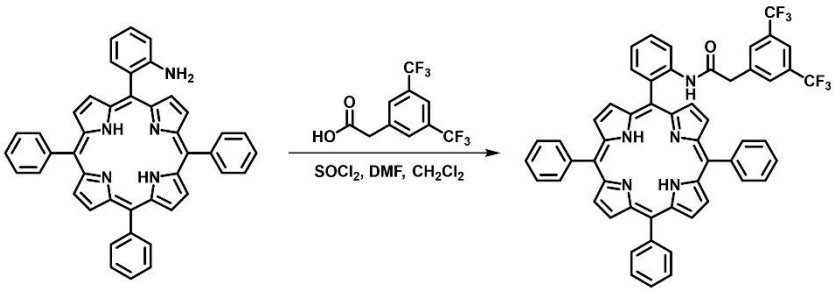
3.5.13 Synthesis of 5-[2-Aminophenyl]-10,15,20-triphenyl Porphyrin (2)



Porphyrin **2** was synthesized by reduction of **1** according to a modified literature procedure.[71,72] A solution of **1** (1.39 g, 2.10 mmol) in p-dioxane (300 mL) was sparged with N_2 and $SnCl_2$•$2H_2O$ (5.68 g, 25.20 mmol) was added as a solid. After 10 min, concentrated HCl (480 mL) was added and the solution was heated to reflux for 1 h under N_2 atmosphere in the absence of light. Upon cooling to room temperature, the solution was neutralized to pH 7 with 6 M NaOH and saturated $NaHCO_3$. The biphasic mixture was extracted three times with EtOAc, then the combined organic phase was rinsed with water and brine and dried over $MgSO_4$. Solvent was removed under reduced pressure to afford crude **2**. The product was purified by column chromatography (starting at 1:1 EtOAc:hexane and progressing to 3:1 EtOAc:hexane) on silica, and finally recrystallized from DCM/MeOH (750 mg, 57% yield). The ^{1}H NMR spectrum agrees well with the literature reports of this compound. ^{1}H NMR (300 MHz, CD_2Cl_2) δ 8.81 – 8.96 (m, 8H), 8.16 – 8.30 (m, 6H), 7.86 (d, *J* = 7.5 Hz, 1H), 7.71 – 7.83 (m, 9H), 7.61 (t, *J* = 7.8 Hz, 1H),

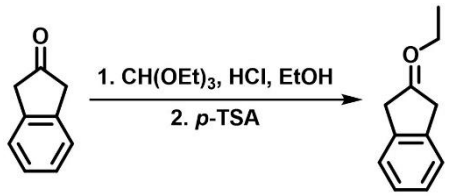
7.16 (t, *J* = 7.4 Hz, 1H), 7.14 (d, *J* = 8.0 Hz, 1H), 3.61 (s, 2H), -2.81 (s, 2H). ESI-MS calculated for $C_{44}H_{33}N_5$ $[M+H]^+$ 630.3 m/z, found 630.8 m/z.

3.5.14 Synthesis *Ortho*-1-amide



A 100 mL Schlenk flask was charged with 40 mL anhydrous DCM, 3,5-bis(trifluoromethyl)phenylacetic acid (525 mg, 1.89 mmol), and a catalytic amount of anhydrous DMF (15 µL). Freshly distilled thionyl chloride (167 µL, 2.30 mmol) was added under a N_2 atmosphere and the solution was stirred at RT for 2 h. Solvent was removed under reduced pressure to afford a yellow oil. Anhydrous toluene (5 mL) was added, then removed under reduced pressure to assist in removal of excess $SOCl_2$. The resulting acid chloride was dissolved in anhydrous THF (20 mL) and added dropwise to a solution of porphyrin **2** (115 mg, 0.183 mmol) dissolved in anhydrous THF (25 mL). After reacting overnight at RT in the absence of light, the solvent was removed under reduced pressure to afford crude *ortho*-1-amide. The product was purified by column chromatography (starting at 2:1 hexane:DCM and progressing slowly to 1:3 hexane:DCM) on silica (132 mg, 82% yield). ^{1}H NMR (400 MHz, CD_2Cl_2) δ 8.82 – 8.97 (m, 6H), 8.77 (d, *J* = 4.7 Hz, 2H), 8.68 (d, *J* = 8.3 Hz, 1H), 8.14 – 8.28 (m, 6H), 8.01 (d, *J* = 7.0 Hz, 1H), 7.72 – 7.88 (m, 10H), 7.54 (t, *J* = 7.7 Hz, 1H), 7.32 (s, 1H), 7.12 (s, 2H), 7.06 (s, 1H), 2.81 (s, 2H), -2.77 (br s, 2H). ^{13}C{^{1}H} NMR (126 MHz, CD_2Cl_2) δ 167.35, 142.24, 142.04, 138.64, 136.95, 135.41, 135.01, 134.93, 134.89, 134.85, 132.04, 131.21 (q, *J* = 33.1 Hz), 129.80, 129.61, 128.26, 127.20, 127.14, 123.60, 123.24 (q, *J* = 272.3 Hz), 121.62, 121.17, 121.02, 120.84 – 120.94 (m), 112.91, 43.08. ^{19}F NMR (376 MHz, CD_2Cl_2) δ -62.73. λ_{max} (CH_2Cl_2) 418, 443, 516, 550, 594, 648 nm. ESI-MS calculated for $C_{54}H_{36}F_6N_5O$ $[M+H]^+$ 884.3 *m/z*, found 884.5 *m/z*.

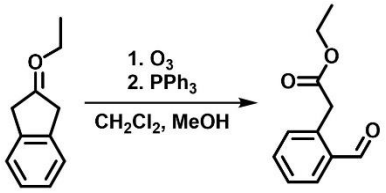
3.5.15 Synthesis of 2-Ethoxyindene (3)



2-ethyoxyindene was synthesized according to modified literature procedure.[73] 2-Indanone (30 g, 227 mmol) was dissolved in absolute ethanol (175 mL) and degassed with N_2. Triethylorthoformate (53 mL, 318 mmol) was added under inert gas, followed by a 4 M solution of HCl in dioxane (1.7 mL, 6.8 mmol). The yellow solution was stirred at room temperature overnight, during which time it turned dark brown. Sodium methoxide (1.44 g, 27 mmol) was

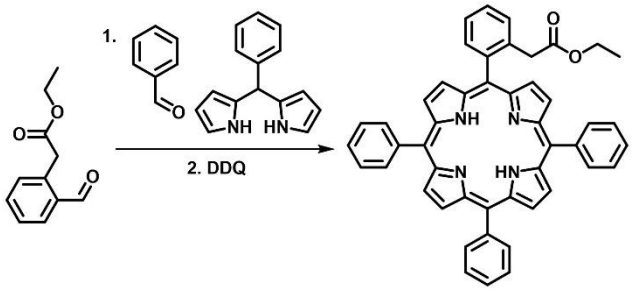
added to basify. Solvent was removed by distillation and the residue was distilled at 100˚C (1.4 mmHg) to afford a mixture of of 2,2-diethoxyindane (pale yellow liquid) and 2-ethoxyindene (white crystalline solid at room temperature). To this distillate was added catalytic *p*-toluenesulfonic acid (10 mg). The mixture was heated to 60 ˚C for 1 hr while distilling away ethanol at 1 atm. The resulting orange oil was purified by Kugelrohr distillation at 135 ˚C (1.4 mmHg) to afford a white crystalline solid (7.60 g, 21% yield over two steps). The purified product was stored cold under Ar to prevent decomposition. ^{1}H NMR (500 MHz, $CDCl_3$) δ 7.28 (dd, *J* = 7.3, 1.3 Hz, 1H), 7.21 (td, *J* = 7.3, 1.3 Hz, 1H), 7.16 (dd, *J* = 7.3, 1.3 Hz, 1H), 7.04 (td, *J* = 7.3, 1.3 Hz, 1H), 5.68 (s, 1H), 4.02 (q, *J* = 7.1 Hz, 3H), 3.42 (s, 2H), 1.44 (t, *J* = 7.1 Hz, 3H). ^{13}C{^{1}H} NMR (126 MHz, $CDCl_3$) δ 166.77, 145.36, 136.07, 126.69, 123.30, 122.34, 118.88, 99.39, 65.75, 37.94, 14.65. IR (ATR, solid, ν (cm^{-1})): 3070 (w), 3043 (w), 3022 (w), 2977 (m), 2935 (w), 2888 (w), 1735 (m), 1698 (m), 1595 (s), 1578 (s), 1456 (s), 1319 (s), 1150 (s), 1036 (s). ESI-GCMS calculated for $C_{11}H_{12}O$ $[M]^+$ 160.09 *m/z*, found 160.10 *m/z*.

3.5.16 Synthesis of 2-Formylphenyl Acetic Acid Ethyl Ester (4)



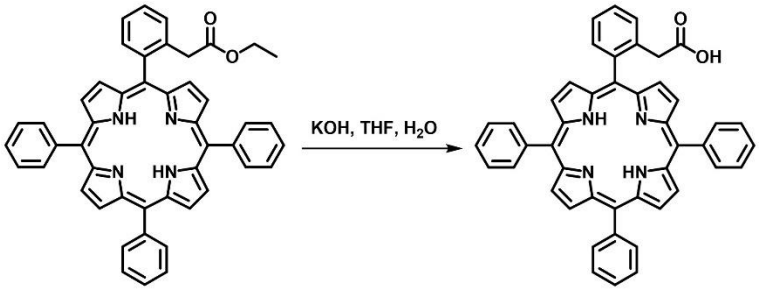
This product was synthesized according to modified literature procedure.[74] A solution of 2-ethoxyindene (1.57 g, 9.81 mmol) in dichloromethane (12 mL) and methanol (50 mL) was cooled to -30˚C. Ozone was bubbled through the cooled solution for 30 min until a faint blue color was apparent. The solution was subsequently sparged with nitrogen for 15 min to remove excess ozone. Triphenylphosphine (10.29 g, 39.23 mmol) was added as a solid. The solution temperature was maintained at -30˚C for 1 hr, then allowed to warm to room temperature slowly and stirred at room temperature overnight. Excess triphenylphosphine was removed by concentrating the solution to approximately 20 mL, then filtering away the white precipitate. This process was repeated several times until a pale yellow oil was obtained. The crude compound was purified by column chromatography (hexane then eventually 3:1 hexane:EtOAc) on silica, with the product eluting as the second spot. Solvent was removed under reduced pressure to afford the product as a white waxy solid (1.73 g, 92% yield). The purified product was stored cold under Ar to prevent decomposition. ^{1}H NMR (300 MHz, $CDCl_3$) δ 10.13 (s, 1H), 7.85 (d, *J* = 7.4 Hz, 1H), 7.67 – 7.40 (m, 2H), 7.30 (d, *J* = 7.3 Hz, 1H), 4.17 (q, *J* = 7.2 Hz, 2H), 4.04 (s, 2H), 1.26 (t, *J* = 7.1 Hz, 3H). ^{13}C{^{1}H} NMR (126 MHz, $CDCl_3$) δ 193.10, 171.13, 135.76, 134.49, 134.36, 133.86, 132.41, 128.01, 61.09, 39.24, 14.30. IR (ATR, solid, ν (cm^{-1})): 2982 (m), 2935 (w), 2906 (w), 2837 (w), 2748 (m), 1724 (vs), 1692 (vs), 1580 (m), 1412 (m), 1367 (m), 1340 (s), 1214 (s), 1201 (s), 1171 (s), 1028 (s).

3.5.17 Synthesis of 5-[2-Phenylacetic acid ethyl ester]-10,15,20-triphenyl Porphyrin (5)



5-phenyldipyrromethane (0.97 g, 4.38 mmol), benzaldehyde (0.20 mL, 1.96 mmol), and 2-formylphenylacetic acid ethyl ester (0.53 g, 2.74 mmol) were dissolved in chloroform (250 mL) and sparged with Ar for 15 min. Boron trifluoride etherate (0.16 mL, 1.33 mmol) was added dropwise while stirring, and the reaction proceeded at room temperature in darkness. After 1 hr, 2,3-dichloro-5,6-dicyano-1,4-benzoquinone (DDQ) (0.65 g, 2.85 mmol) was added, and the dark solution was stirred at room temperature for another 1 hr. Solvent was removed under reduced pressure, and the crude porphyrin was purified by column chromatography (starting at 3:1 hexane:DCM and slowly progressing to 1:3 hexane:DCM). The product was obtained as the second spot. A second column using the above conditions was run to remove remaining traces of tetraphenylporphyrin. The product was obtained as a purple solid (102.9 mg, 8 % yield). ^{1}H NMR (500 MHz, $CDCl_3$) δ 8.96 – 8.88 (m, 6H), 8.77 (d, *J* = 4.6 Hz, 2H), 8.33 – 8.23 (m, 6H), 8.16 (d, *J* = 7.5 Hz, 1H), 7.92 – 7.75 (m, 11H), 7.68 (t, *J* = 7.3 1H), 3.62 (q, *J* = 7.2 Hz, 2H), 3.45 (s, 2H), 0.56 (t, *J* = 7.2 Hz, 3H), -2.66 (br s, 2H). $^{13}C\{^{1}H\}$ NMR (126 MHz, $CDCl_3$) δ 171.46, 142.29, 142.14, 141.86, 136.34, 134.70, 134.60, 134.44, 129.73, 128.90, 127.88, 126.84, 126.82, 125.54, 120.58, 120.32, 117.63, 60.36, 39.85, 13.64. λ_{max} (CH_2Cl_2) 417, 445, 514, 549, 590, 646 nm. ESI-MS calculated for $C_{48}H_{37}N_4O$ $[M+H]^+$ 701.3 *m/z*, found 701.9 *m/z*.

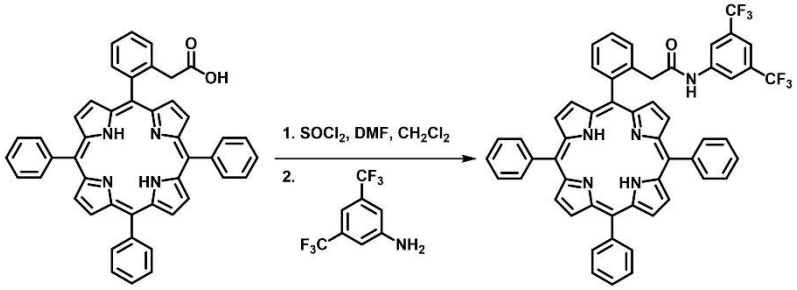
3.5.18 Synthesis of 5-[2-Phenylacetic acid]-10,15,20-triphenyl Porphyrin (6)



Porphyrin **5** (82.5 mg, 0.12 mmol) was dissolved in THF (40 mL). A solution of KOH (0.33 g, 5.88 mmol) in 10 mL water was added, then the reaction was heated to reflux overnight under N_2 in the absence of light. Reaction progress was monitored by the disappearance of the comparatively non-polar methyl ester porphyrin spot by TLC. When complete, the reaction was cooled to room temperature and acidified with 1 M HCl solution, then neutralized by addition of saturated $NaHCO_3$ until the organic phase was pink. The product was extracted into DCM and washed with water, then dried over Na_2SO_4 and solvent was removed under reduced pressure. The crude porphyrin was purified by column chromatography (starting at 1:1 hexane:DCM, then 1:3

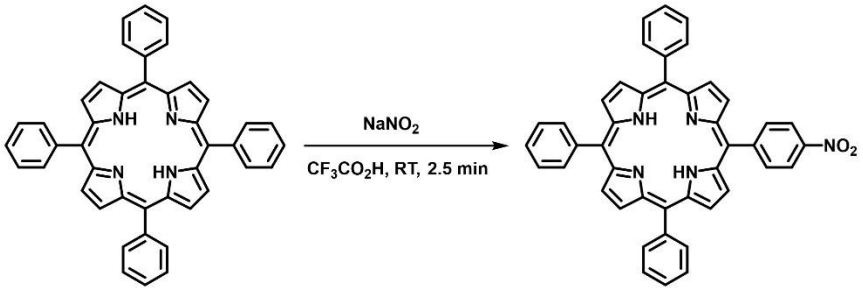
hexane:DCM and finally pure DCM) on silica. The product was obtained as the second spot as a purple solid (28 mg, 35% yield). ^{1}H NMR (500 MHz, $CDCl_3$) δ 8.87 – 8.77 (m, 4H), 8.75 (d, *J* = 4.8 Hz, 2H), 8.63 (d, *J* = 4.7 Hz, 2H), 8.23 (d, *J* = 7.2 Hz, 1H), 8.19 (d, *J* = 7.5 Hz, 1H), 8.15 – 8.10 (m, 4H), 8.05 (d, *J* = 7.5 Hz, 1H), 7.84 – 7.68 (m, 4H), 7.66 – 7.50 (m, 8H), 3.37 (s, 2H), -2.79 (br s, 2H). ^{13}C{^{1}H} NMR (126 MHz, $CDCl_3$) δ 175.36, 142.27, 142.02, 141.93, 135.48, 134.70, 134.61, 134.53, 129.51, 128.86, 127.88, 127.75, 126.81, 126.73, 125.71, 120.60, 120.33, 117.17, 39.06. λ_{max} (CH_2Cl_2) 418, 444, 514, 549, 590, 647 nm. ESI-MS calculated for $C_{46}H_{33}N_4O_2$ $[M+H]^+$ 673.3 *m/z*, found 673.7 *m/z*.

3.5.19 Synthesis of Ortho-2-amide



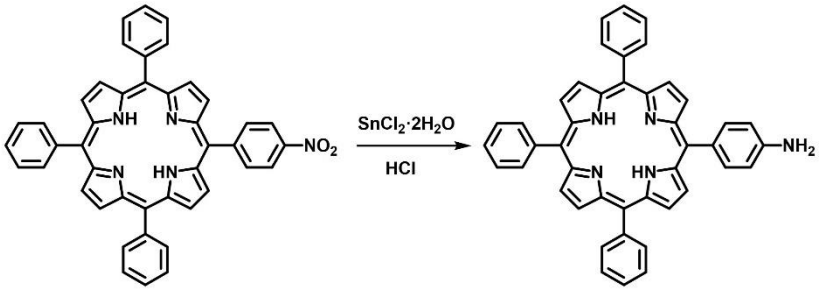
Porphyrin **6** (350 mg, 0.52 mmol) was dissolved in anhydrous DCM (60 mL), and freshly distilled $SOCl_2$ (56 μL, 0.78 mmol) was added under N_2, followed by one drop of anhydrous DMF. The dark green solution was stirred for 2 hr at room temperature in the absence of light. The solvent was removed under reduced pressure. Anhydrous toluene (10 mL) was added, then removed under reduced pressure to assist in removal of excess $SOCl_2$. The resulting acid chloride porphyrin was dissolved in anhydrous DCM (60 mL) and 3,5-bis(trifluoromethyl)aniline (0.41 mL, 2.60 mmol) was added. The solution was stirred for 8 hr at room temperature in the absence of light. Next, the reaction solution was poured into saturated $NaHCO_3$ solution (40 mL) to neutralize the protonated porphyrin and extracted with DCM (3x50 mL). The combined organic fractions were washed with water and dried over Na_2SO_4, and solvent was removed under reduced pressure. The product was purified by column chromatography (starting at 1:1 DCM:hexane and progressing to 5:1 DCM:hexane) on silica. The product was obtained as a purple solid (250 mg, 45% yield). ^{1}H NMR (500 MHz, $CDCl_3$) δ 8.89 (d, *J* = 4.3 Hz, 4H), 8.82 (d, *J* = 4.8 Hz, 2H), 8.71 (d, *J* = 4.7 Hz, 2H), 8.28 (d, *J* = 7.0 Hz, 2H), 8.22 – 8.17 (m, 2H), 8.13 (d, *J* = 6.8 Hz, 2H), 8.01 (d, *J* = 7.4 Hz, 2H), 7.86 – 7.64 (m, 12H), 7.34 (s, 1H), 6.93 (s, 2H), 5.88 (s, 1H), 3.26 (s, 2H), -2.76 (br s, 2H). ^{19}F NMR (376 MHz, $CDCl_3$) δ -62.42. λ_{max} (CH_2Cl_2) 418, 442, 515, 550, 591, 647 nm. ESI-MS calculated for $C_{54}H_{36}F_6N_5O$ $[M+H]^+$ 884.3 *m/z*, found 884.7 *m/z*.

3.5.20 Synthesis of 5-[4-Nitrophenyl]-10,15,20-triphenyl Porphyrin (7)



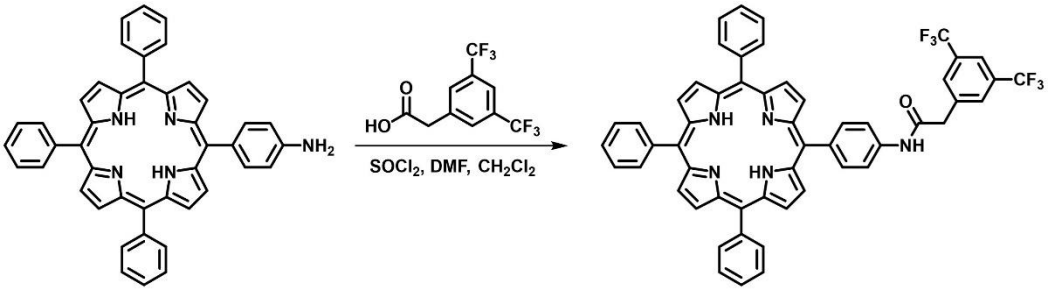
Porphyrin **7** was synthesized according to literature procedure.[75] Tetraphenylporphyrin (600 mg, 0.977 mmol) was dissolved in trifluoroacetic acid (40 mL) and stirred under N_2. Sodium nitrite (120 mg, 1.740 mmol) was suspended in trifluoroacetic acid (20 mL) and added to the porphyrin solution over the course of exactly 30 seconds. After 2.5 additional min, the green solution was quenched by pouring into 300 mL cold water and extracted with DCM. The organic layer was neutralized with saturated $NaHCO_3$ solution and rinsed with water, then dried over $MgSO_4$. Solvent was removed under reduced pressure to afford crude **7**. The product was purified by column chromatography (starting at 2:1 hexane:DCM and ending at 1:1 hexane:DCM) on silica (340 mg, 53% yield). The ^{1}H NMR spectrum agrees well with the literature reports of this compound. ^{1}H NMR (400 MHz, $CDCl_3$) δ 8.83 – 8.93 (m, 6H), 8.72 – 8.76 (m, 2H), 8.64 (d, *J* = 8.6 Hz, 2H), 8.41 (d, *J* = 8.6 Hz, 2H), 8.17 – 8.25 (m, 6H), 7.73 – 7.83 (m, 9H), -2.79 (s, 2H).

3.5.21 Synthesis of 5-[4-Aminophenyl]-10,15,20-triphenyl Porphyrin (8)



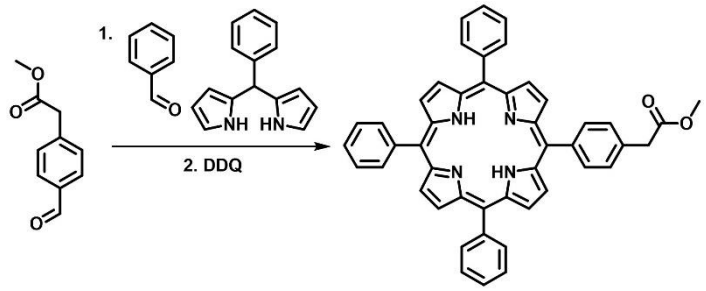
Porphyrin **7** (375 mg, 0.568 mmol) was dissolved in concentrated HCl (125 mL) and $SnCl_2$•$2H_2O$ (1.537 g, 6.811 mmol) was added as a solid. The solution was heated to 65˚C for 1 h, then poured into 300 mL water and neutralized to pH 8 with ammonium hydroxide. The aqueous phase was extracted with DCM, rinsed with water, and dried over $MgSO_4$. Solvent was removed under reduced pressure to afford crude **8**. The product was purified by column chromatography (starting at 2:1 hexane:DCM and progressing slowly to 3:1 DCM:hexane and finally pure DCM) on silica, followed by recrystallization from DCM/MeOH (199 mg, 46% yield). The ^{1}H NMR spectrum agrees well with the literature reports of this compound. ^{1}H NMR (400 MHz, $CDCl_3$) δ 9.04 – 9.12 (m, 2H), 8.96 – 9.04 (m, 6H), 8.30 – 8.41 (m, 6H), 8.06 (d, *J* = 8.0 Hz, 2H), 7.77 – 7.89 (m, 9H), 6.95 (d, *J* = 7.9 Hz, 2H), 3.79 (br s, 2H), -2.55 (s, 2H). ESI-MS calculated for $C_{44}H_{32}N_5$ $[M+H]^+$ 630.3 *m/z*, found 630.5 *m/z*.

3.5.22 Synthesis of *Para*-1-amide



A 100 mL Schlenk flask was charged with 40 mL anhydrous DCM, 3,5-bis(trifluoromethyl)phenylacetic acid (341 mg, 1.22 mmol), and a catalytic amount of anhydrous DMF (15 μL). Freshly distilled $SOCl_2$ (108 μL, 1.49 mmol) was added under a N_2 atmosphere and the solution was stirred at RT for 2 h. Solvent was removed under reduced pressure to afford a yellow oil. Anhydrous toluene (5 mL) was added, then removed under reduced pressure to assist in removal of excess $SOCl_2$. The resulting acid chloride was dissolved in anhydrous DCM (20 mL) and added dropwise to a solution of porphyrin **8** (75 mg, 0.119 mmol) dissolved in anhydrous DCM (40 mL). After reacting overnight at RT in the absence of light, the solvent was removed under reduced pressure to afford crude *para*-1-amide. The product was purified by column chromatography (starting at 2:1 hexane:DCM and progressing slowly to 1:3 hexane:DCM) on silica (76 mg, 72% yield). ^{1}H NMR (400 MHz, $CDCl_3$) δ 8.88 – 8.85 (m, 9H), 8.23 – 8.20 (m, 9H), 7.76 – 7.71 (m, 12H), 4.05 (s, 2H), -2.80 (br s, 2H). ^{19}F NMR (376 MHz, $CDCl_3$) δ -61.93. λ_{max} (CH_2Cl_2) 420, 515, 550, 590, 645 nm. ESI-MS calculated for $C_{54}H_{36}F_6N_5O$ $[M+H]^+$ 884.3 *m/z*, found 884.9 *m/z*.

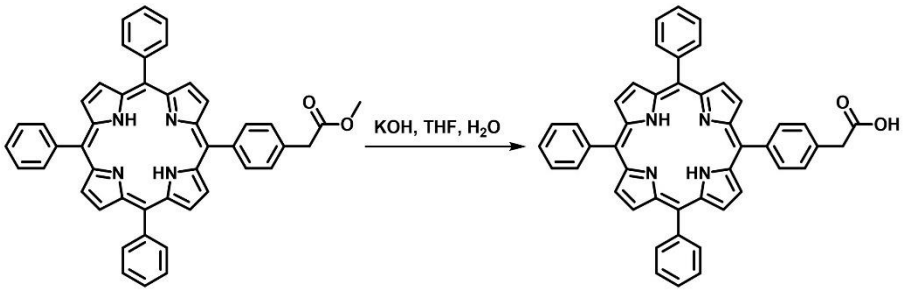
3.5.23 Synthesis of 5-[4-Phenylacetic acid methyl ester]-10,15,20-triphenyl Porphyrin (9)



5-phenyldipyrromethane (3.92 g, 17.64 mmol), benzaldehyde (0.81 mL, 8.02 mmol), and 4-formylphenylacetic acid methyl ester (2.00 g, 11.22 mmol) were dissolved in chloroform (750 mL) and sparged with Ar for 15 min. Boron trifluoride etherate (0.67 mL, 5.45 mmol) was added dropwise while stirring, and the reaction proceeded at room temperature in darkness. After 1 hr, 2,3-dichloro-5,6-dicyano-1,4-benzoquinone (DDQ) (3.64 g, 16.04 mmol) was added, and the dark solution was stirred at room temperature for another 1 hr. Solvent was removed under reduced pressure, and the crude porphyrin was purified by column chromatography (starting at 3:1 hexane:DCM and progressing slowly to 1:3 hexane:DCM) on silica and was obtained as a purple solid (1.0 g, 18% yield). ^{1}H NMR (400 MHz, $CDCl_3$) δ 8.88 – 8.85 (m, 8H), 8.24 – 8.17 (m, 8H),

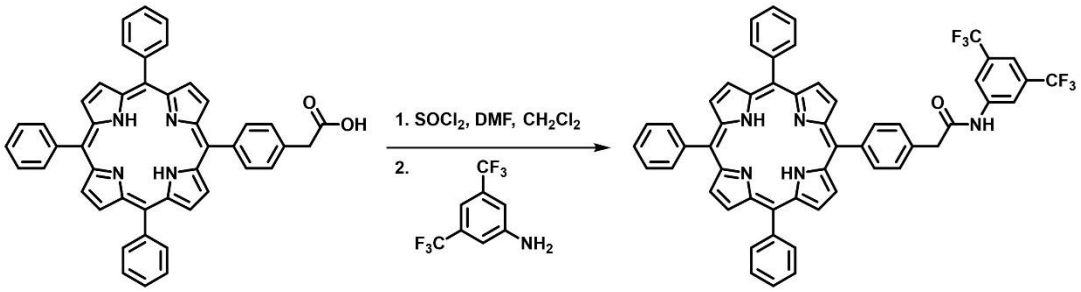
7.77 – 7.72 (m, 9H), 7.68 (d, 2H, *J* = 8.0 Hz) 3.99 (s, 2H), 3.89 (s, 3H), -2.78 (br s, 2H). ESI-MS calculated for $C_{47}H_{34}N_4O_2$ $[M+H]^+$ 687.3 *m/z*, found 687.7 *m/z*.

3.5.24 Synthesis of 2-(4-(10,15,20-Triphenylporphyrin-5-yl)phenyl)acetic Acid (10)



Porphyrin **9** (82.5 mg, 0.12 mmol) was dissolved in THF (40 mL). A solution of KOH (0.33 g, 5.88 mmol) in 10 mL water was added, then the reaction was heated to reflux overnight under N_2 in the absence of light. Reaction progress was monitored by the disappearance of the comparatively non-polar methyl ester porphyrin spot by TLC. When complete, the reaction was cooled to room temperature and acidified with 1 M HCl solution, then neutralized by addition of saturated $NaHCO_3$ until the organic phase was pink. The product was extracted into DCM and washed with water, then dried over Na_2SO_4 and solvent was removed under reduced pressure. The crude porphyrin was purified by column chromatography (starting at 1:1 hexane:DCM, then 1:3 hexane:DCM, then pure DCM, and finally 2% MeOH and DCM) on silica. The product was obtained as the second band as a purple solid (73 mg, 90% yield). ^{1}H NMR (400 MHz, $CDCl_3$) δ 8.92 – 8.89 (m, 8H), 8.27 – 8.25 (m, 8H), 7.80 – 7.75 (m, 11H), 4.09 (s, 2H), -2.74 (br s, 2H). $^{13}C\{^1H\}$ NMR (126 MHz, $CDCl_3$) δ 174.63, 142.04, 141.02, 134.72, 134.54, 133.35, 127.84, 127.74, 126.73, 120.26, 120.23, 119.67, 40.42. λ_{max} (CH_2Cl_2) 420, 515, 550, 590, 645 nm. ESI-MS calculated for $C_{46}H_{32}N_4O_2$ $[M+H]^+$ 673.3 *m/z*, found 673.7 *m/z*.

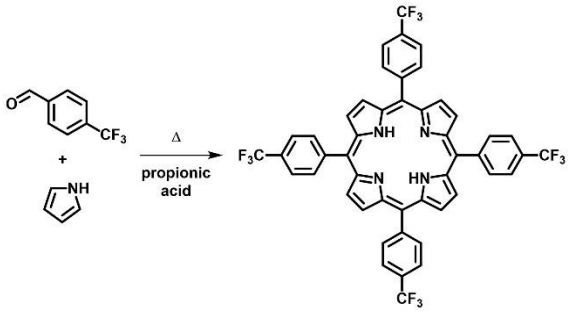
3.5.25 Synthesis of *Para*-2-amide



Porphyrin **10** (400 mg, 0.594 mmol) was dissolved in anhydrous DCM (300 mL), and freshly distilled thionyl chloride (0.144 mL, 1.98 mmol) was added under N_2, followed by one drop of anhydrous DMF. The dark green solution was stirred for 2 hr at room temperature in the absence of light. The solvent was removed under reduced pressure. Anhydrous toluene (5 mL) was added, then removed under reduced pressure to assist in removal of excess $SOCl_2$. The resulting acid chloride porphyrin was dissolved in anhydrous THF (250 mL) and 3,5-bis(trifluoromethyl)aniline (0.464 mL, 2.97 mmol) was added. The solution was stirred for 8 hr at

room temperature in the absence of light. Next, the reaction solution was poured into saturated $NaHCO_3$ solution (20 mL) to neutralize the protonated porphyrin and extracted with DCM (3x25 mL). The combined organic fractions were washed with water and dried over Na_2SO_4, and solvent was removed under reduced pressure. The product was purified by column chromatography (starting at 1:1 DCM:hexane and progressing to 5:1 DCM:hexane) on silica. The product was obtained as a purple solid (278 mg, 53% yield). ^{1}H NMR (400 MHz, CD_2Cl_2) δ 8.88 (d, 8H, *J* = 5.7 Hz), 8.28 – 8.20 (m, 10H), 7.80 – 7.75 (m, 12H), 7.70 (s, 1H), 4.10 (s, 12H), -2.84 (br s, 2H). ^{19}F NMR (376 MHz, CD_2Cl_2) δ - 62.51. λ_{max} (CH_2Cl_2) 420, 515, 545, 590, 645 nm. ESI-MS calculated for $C_{54}H_{36}F_6N_5O$ $[M+H]^+$ 884.3 *m/z*, found 884.6 *m/z*.

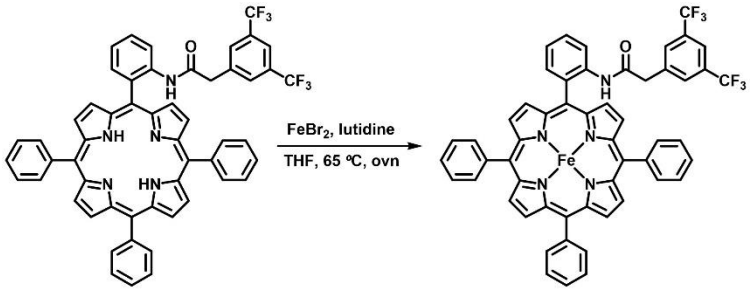
3.5.26 Synthesis of *Para*-$(CF_3)_4$



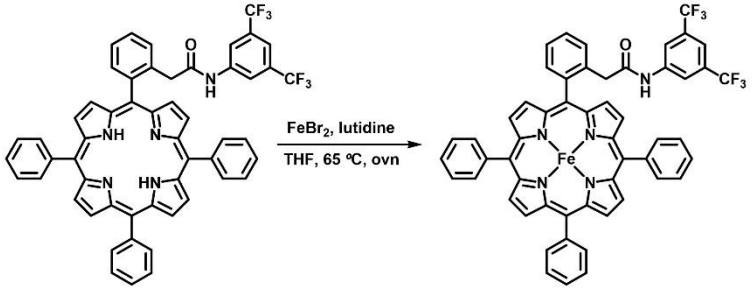
4-Trifluoromethylbenzaldehyde (7.7 mL, 57.43 mmol) and pyrrole (4.0 mL, 57.43 mmol) were dissolved in 250 mL propionic acid and heated to 110˚C in darkness for 1 h. Water (50 mL) and methanol (250 mL) was added to precipitate the porphyrin product, which was filtered and washed with water and methanol. The crude product was purified by column chromatography (2:1 hexane:DCM) on silica and was isolated as a purple powder (2.11 g, 18% yield). ^{1}H NMR (400 MHz, $CDCl_3$) δ 8.83 (s, 8H), 8.35 (d, *J* = 7.8 Hz, 8H), 8.06 (d, *J* = 7.8 Hz, 8H), -2.84 (s, 2H). ^{19}F NMR (376 MHz, $CDCl_3$) δ -61.27. ESI-MS calculated for $C_{48}H_{27}F_{12}N_4$ $[M+H]^+$ 887.2 *m/z*, found 887.1 *m/z*.

3.5.27 General Procedure for Synthesis of Fe Porphyrins

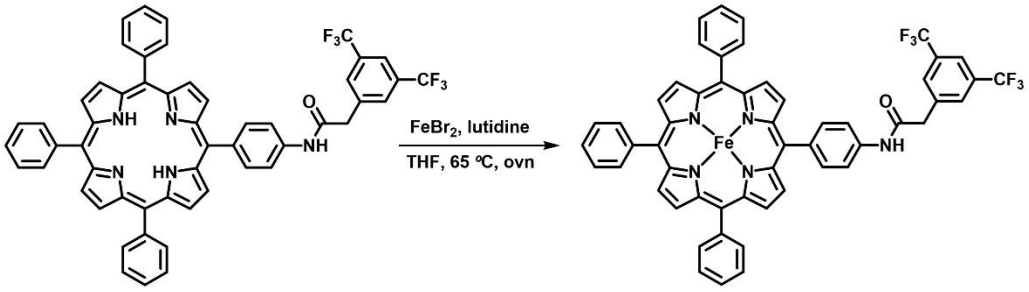
Metalation of porphyrins was performed in a N_2-filled glovebox or using standard Schlenk techniques and dry solvents. To a solution of the free-base porphyrin (1 eq) in dry THF was added anhydrous $FeBr_2$ (15 eq) as a suspension in dry THF. Distilled lutidine (3 eq) was added and the solution was heated to 65˚C overnight in the absence of light. The resulting solution was opened to air and then neutralized by pouring into 1 M HBr. After extraction into EtOAc and rinsing with copious water, the organic phase was dried over $MgSO_4$ and the solvent was removed under reduced pressure. The crude complex was purified according to the conditions specified below.



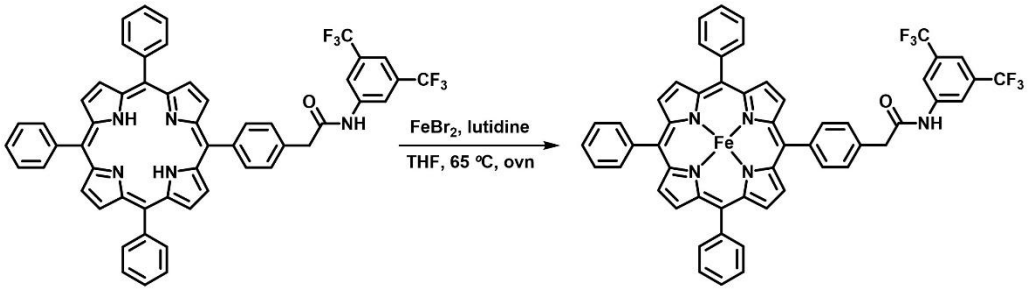
Synthesis of Fe-*ortho*-1-amide. Metalation was performed as described above using 100 mg of *ortho*-1-amide. Purification was achieved by column chromatography (5:1 DCM:hexane then progressing to pure DCM and slowly to 2% MeOH in DCM) on silica (94 mg, 82% yield). λ_{max} (CH_2Cl_2) 380, 417, 514 nm. ESI-MS calculated for $C_{54}H_{33}F_6FeN_5O$ $[M]^+$ 937.2 *m/z*, found 937.3 *m/z*; $C_{55}H_{37}F_6FeN_6O_2$ $[M+MeOH]^+$ 969.2 *m/z*, found 969.4 *m/z*.



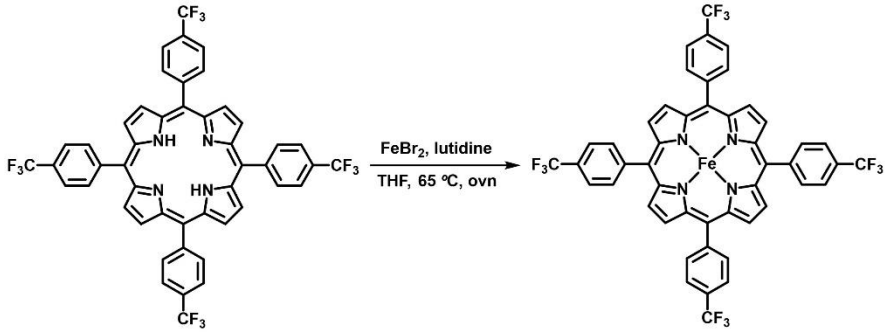
Synthesis of Fe-*ortho*-2-amide. Metalation was performed as described above using 100 mg of *ortho*-2-amide. Purification was achieved by column chromatography (1:1 THF:hexane) on silica (59 mg, 51% yield). λ_{max} (CH_2Cl_2) 383, 414, 510 nm. ESI-MS calculated for $C_{54}H_{33}F_6FeN_5O$ $[M]^+$ 937.2 *m/z*, found 937.7 *m/z*; $C_{55}H_{37}F_6FeN_5O_2$ $[M+MeOH]^+$ 969.2 *m/z*, found 969.7 *m/z*.



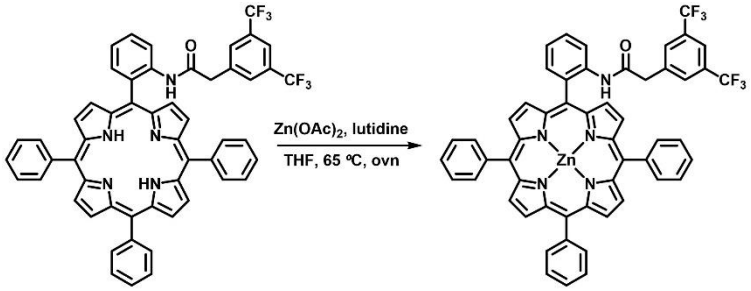
Synthesis of Fe-*para*-1-amide. Metalation was performed as described above using 97 mg of *para*-1-amide. Purification was achieved by column chromatography (pure DCM then progressing slowly to 6% MeOH in DCM) on silica (86 mg, 84% yield). λ_{max} (CH_2Cl_2) 384, 415, 515, 580, and 680 nm. ESI-MS calculated for $C_{54}H_{33}F_6FeN_5O$ $[M+MeOH]^+$ 969.2 *m/z*, found 970.1 *m/z*.



Synthesis of Fe-*para*-2-amide. Metalation was performed as described above using 140 mg of *para*-2-amide. Purification was achieved by column chromatography (pure DCM then progressing slowly to 4% MeOH in DCM) on silica (110 mg, 74% yield). λ_{max} (CH_2Cl_2) 410, 570, 610 nm. ESI-MS calculated for $C_{54}H_{36}F_6FeN_6O_2$ $[M+MeOH]^+$ 969.2 *m/z*, found 970.4 *m/z*.



Synthesis of Fe-*para*-$(CF_3)_4$. Metalation was performed as described above using 740 mg of *para*-$(CF_3)_4$. Purification was achieved by column chromatography (pure DCM then progressing slowly to 2% MeOH in DCM) on silica (480 mg, 61% yield). ESI-MS calculated for $C_{49}H_{28}F_{12}FeN_4O$ $[M+MeOH]^+$ 972.1 *m/z*, found 972.6 *m/z*.



Synthesis of Zn-*ortho*-1-amide. Porphyrin *ortho*-1-amide (31 mg, 0.035 mmol) was dissolved in chloroform (6 mL) and sparged with N_2 for 5 min. A solution of $Zn(OAc)_2$ (16 mg, 0.088 mmol) in methanol (1 mL) was added dropwise. The resulting solution was stirred at RT overnight in the absence of light. The organic phase was washed with saturated $NaHCO_3$ three times followed by water three times, then dried over $MgSO_4$. The product was purified by recrystallization via vapor diffusion of water into a solution of DMF (29 mg, 87% yield). X-ray quality crystals were grown by slow vapor diffusion of water into a solution of Zn-*ortho*-1- amide in DMF. ^{1}H NMR (500 MHz, $CDCl_3$) δ 8.95 – 8.86 (m, 6H), 8.82 (d, *J* = 4.7 Hz, 2H), 8.55 (d, *J* = 8.5 Hz, 1H), 8.26 – 8.04 (m, 6H), 7.94 (d, *J* = 7.4 Hz, 1H), 7.83 – 7.63 (m, 11H), 7.41 (t, *J* = 7.4

Hz, 1H), 7.28 (s, 2H), 7.18 (s, 1H), 7.16 (br s, 1H). $^{13}C\{^{1}H\}$ NMR (126 MHz, $CDCl_3$) δ 152.55, 150.37, 150.33, 150.26, 150.03, 142.98, 142.84, 140.88, 139.52, 134.82, 134.72 (d, J = 4.2 Hz), 134.43, 132.75, 132.08, 132.01, 131.93, 131.71, 131.44, 131.40, 129.25, 127.62, 126.73, 126.61, 126.56, 123.15 (q, J = 272.6 Hz), 121.51, 121.47, 121.09, 119.82, 117.46, 114.96 – 114.44 (m). ^{19}F NMR (376 MHz, $CDCl_3$) δ -62.47. λ_{max} (CH_2Cl_2) 419, 548 nm. ESI-MS calculated for $C_{53}H_{32}F_6N_6OZn$ $[M]^+$ 946.2 *m/z*, found 946.8 *m/z*.

3.5.28 NMR Specta

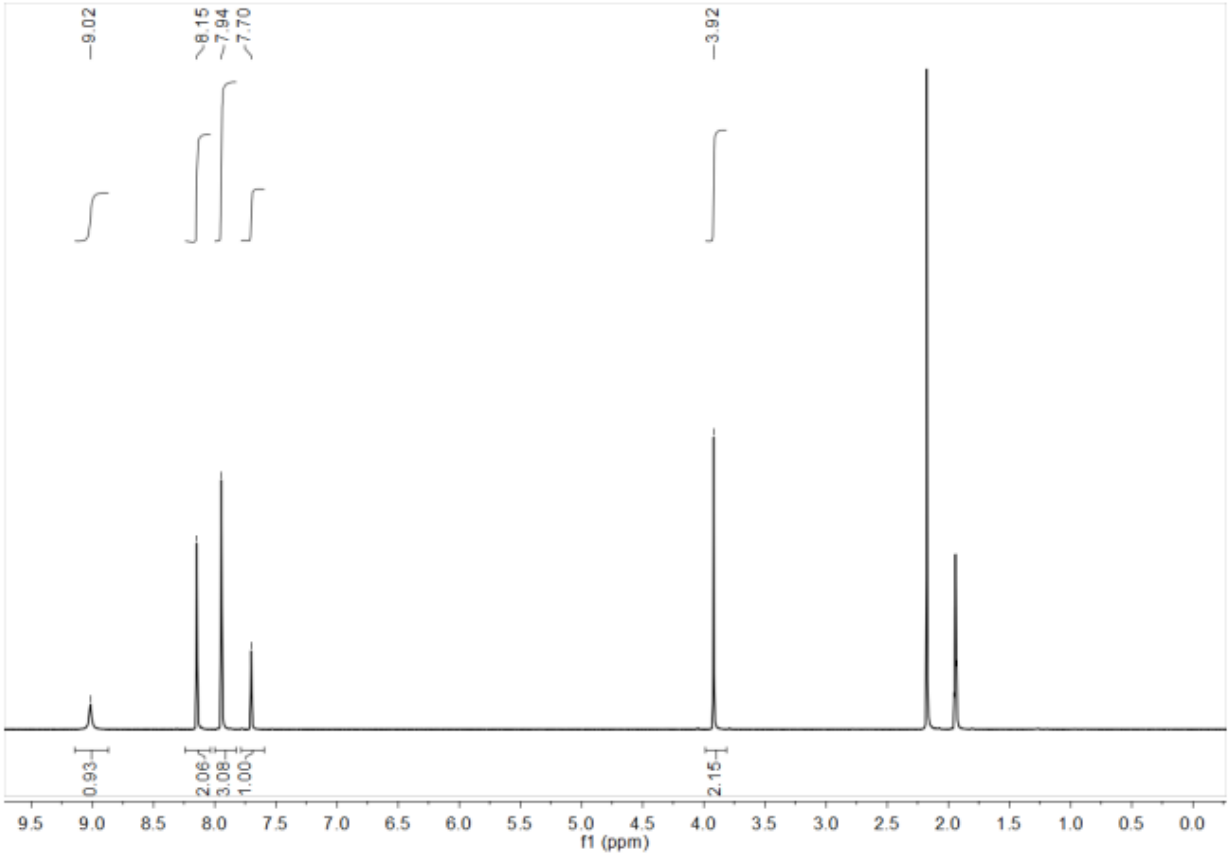


Figure 3.42. ^{1}H-NMR of [3,5-bis(trifluoromethyl)phenyl]amide in CD_3CN.

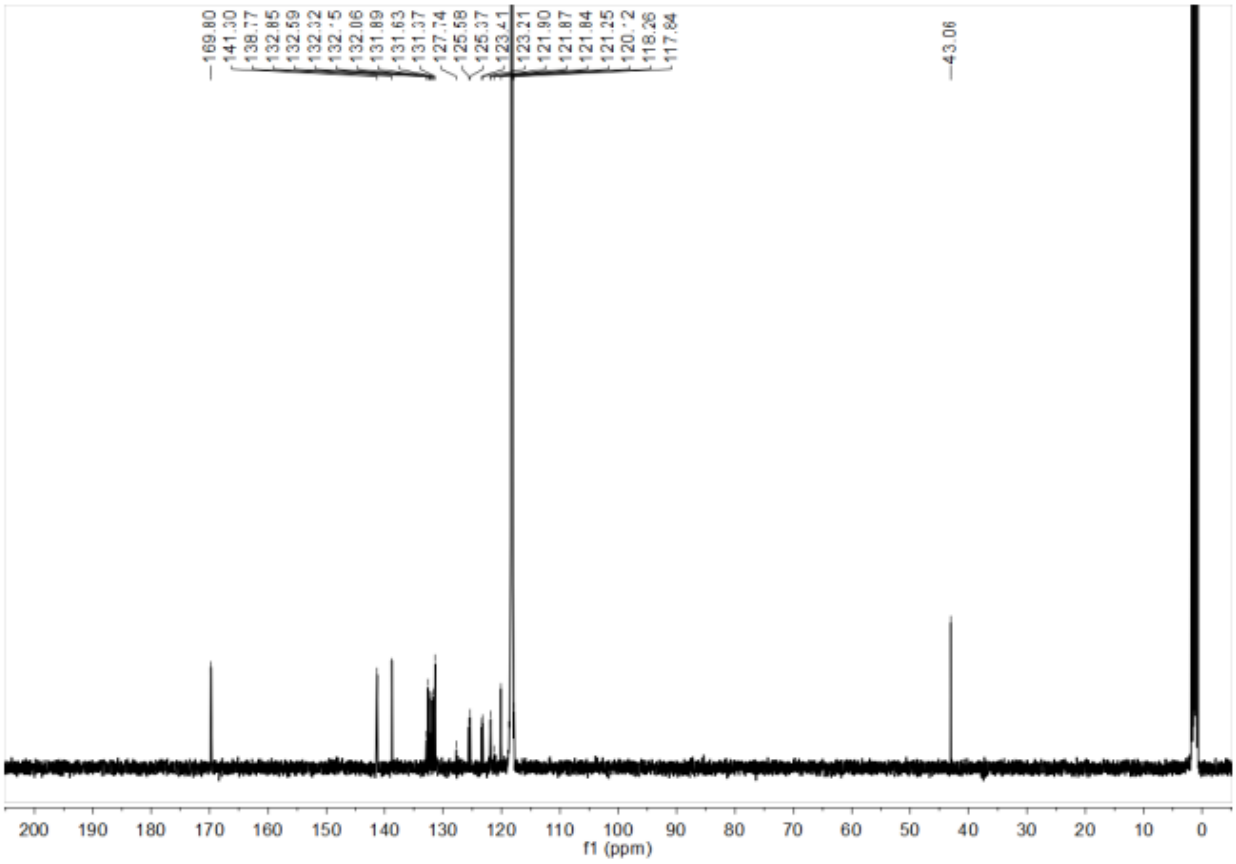


Figure 3.43. ^{13}C-NMR of [3,5-bis(trifluoromethyl)phenyl]amide in CD_3CN.

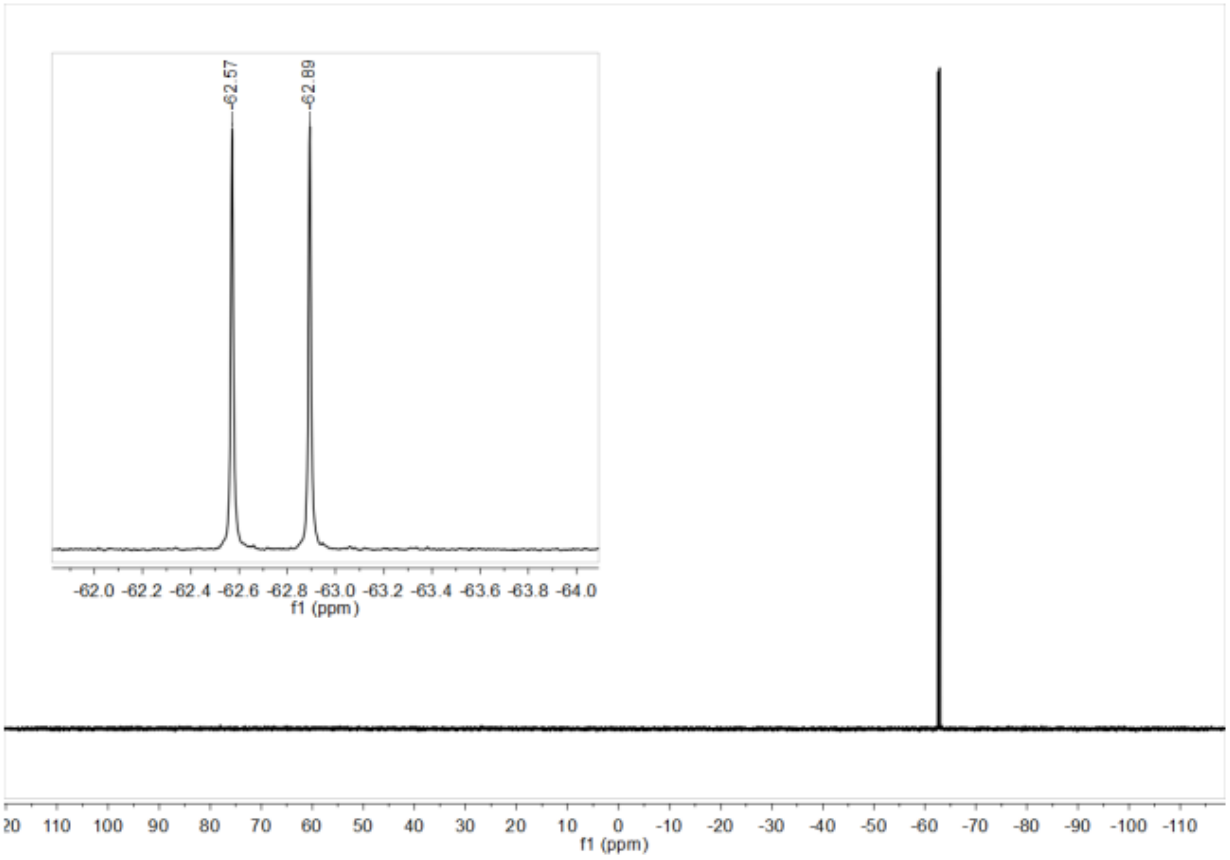


Figure 3.44. ^{19}F-NMR of [3,5-bis(trifluoromethyl)phenyl]amide in CD_3CN.

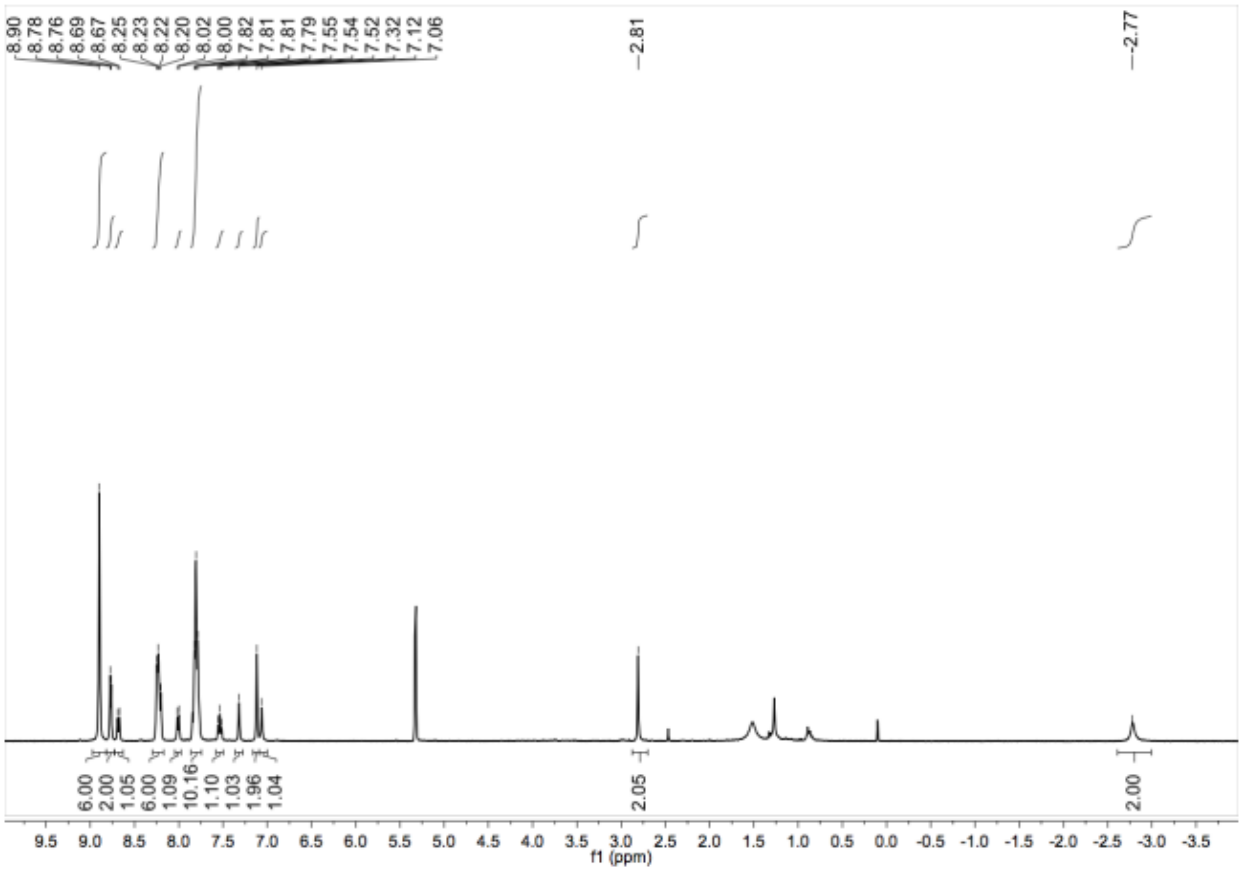


Figure 3.45. ^{1}H-NMR of *ortho*-1-amide in CD_2Cl_2.

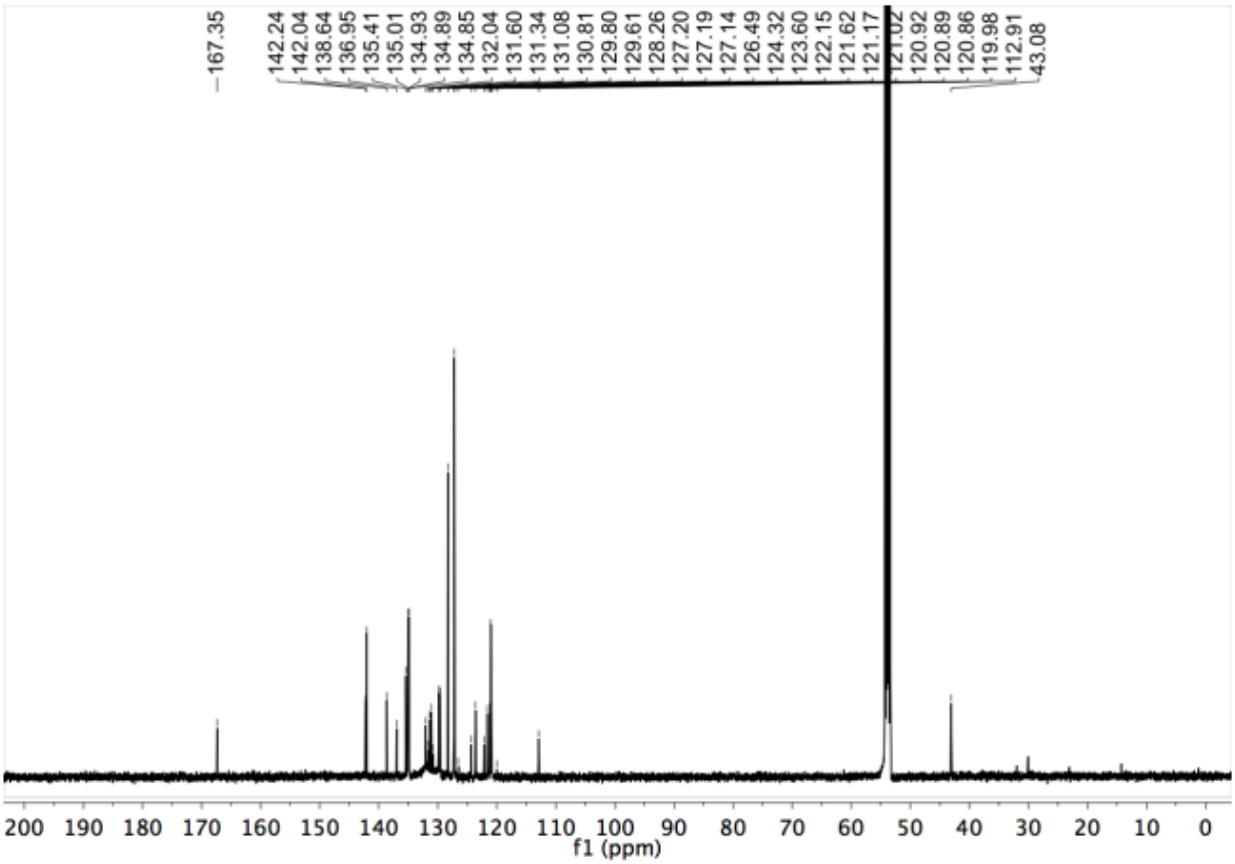


Figure 3.46. ^{13}C-NMR of *ortho*-1-amide in CD_2Cl_2.

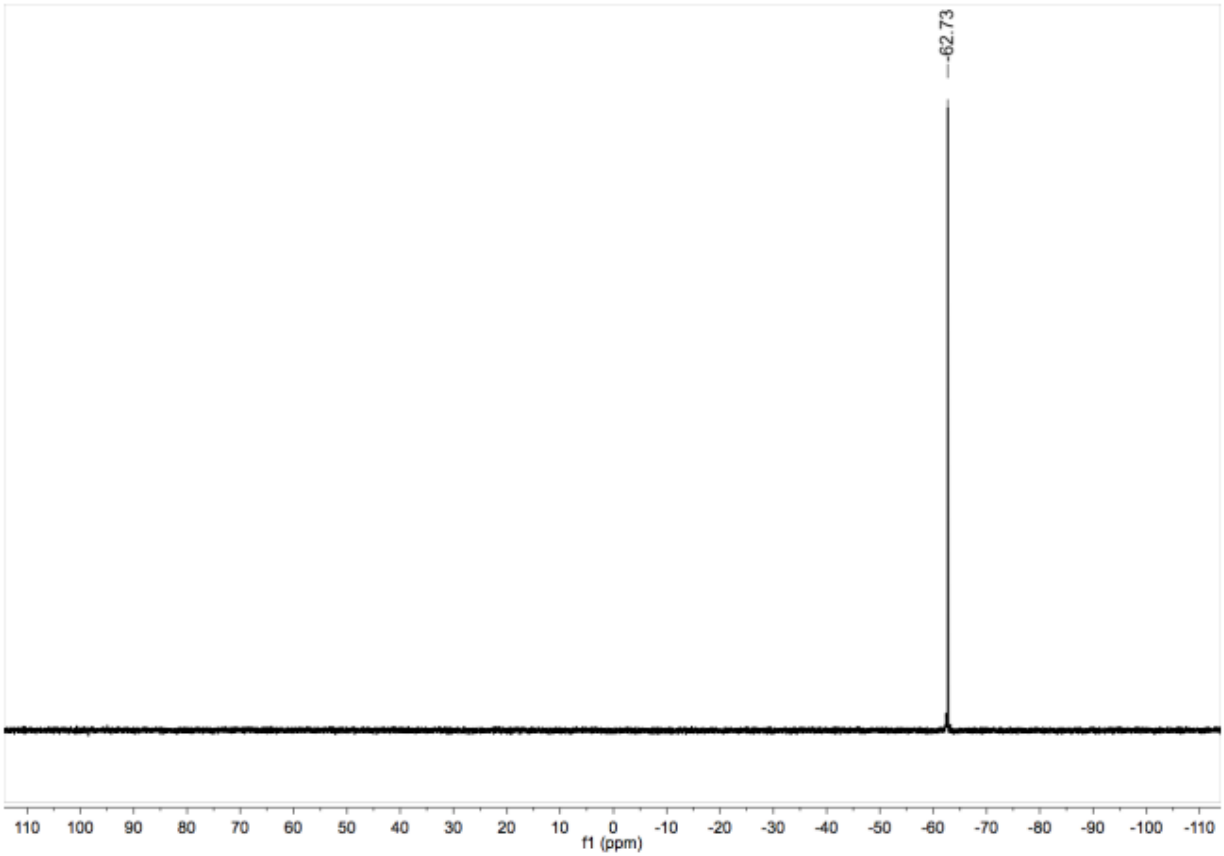


Figure 3.47. ^{19}F-NMR of *ortho*-1-amide in CD_2Cl_2.

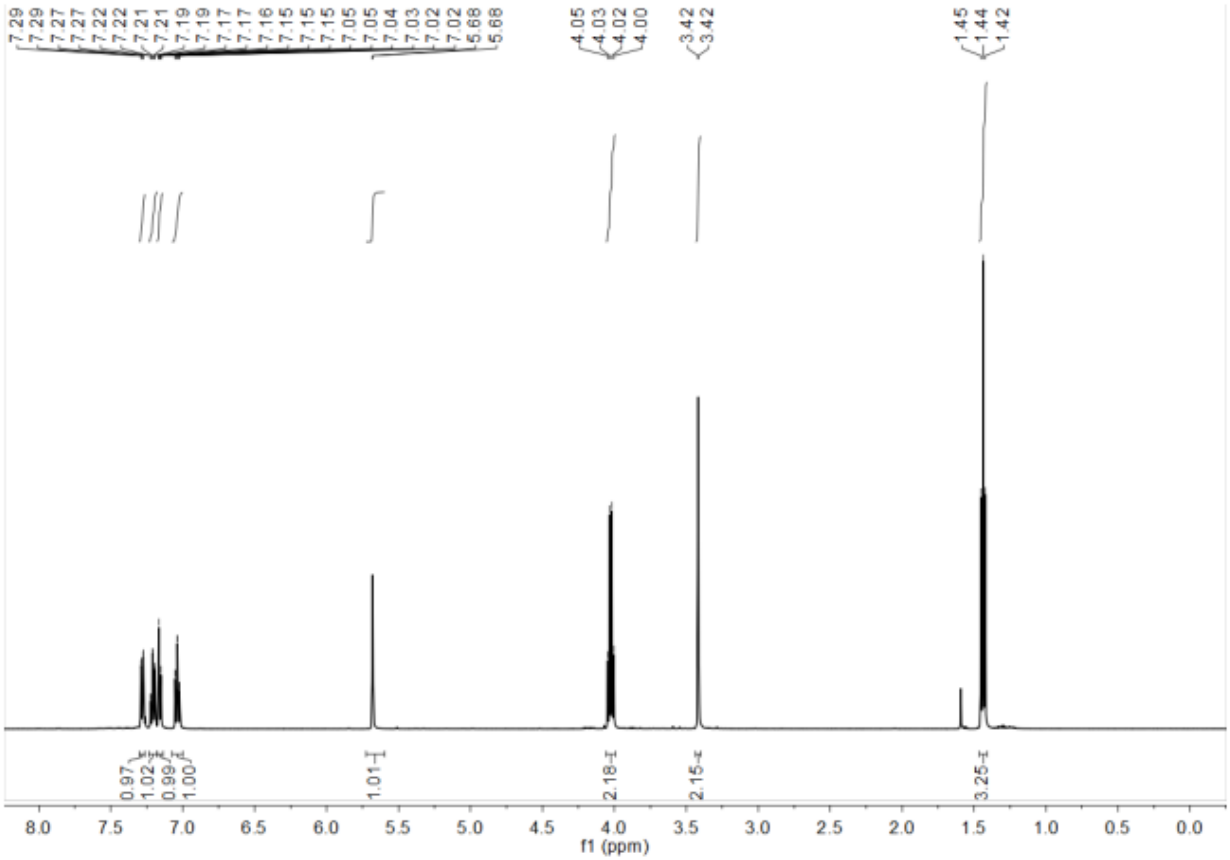


Figure 3.48. ^{1}H-NMR of 2-ethoxyindene (**3**) in $CDCl_3$.

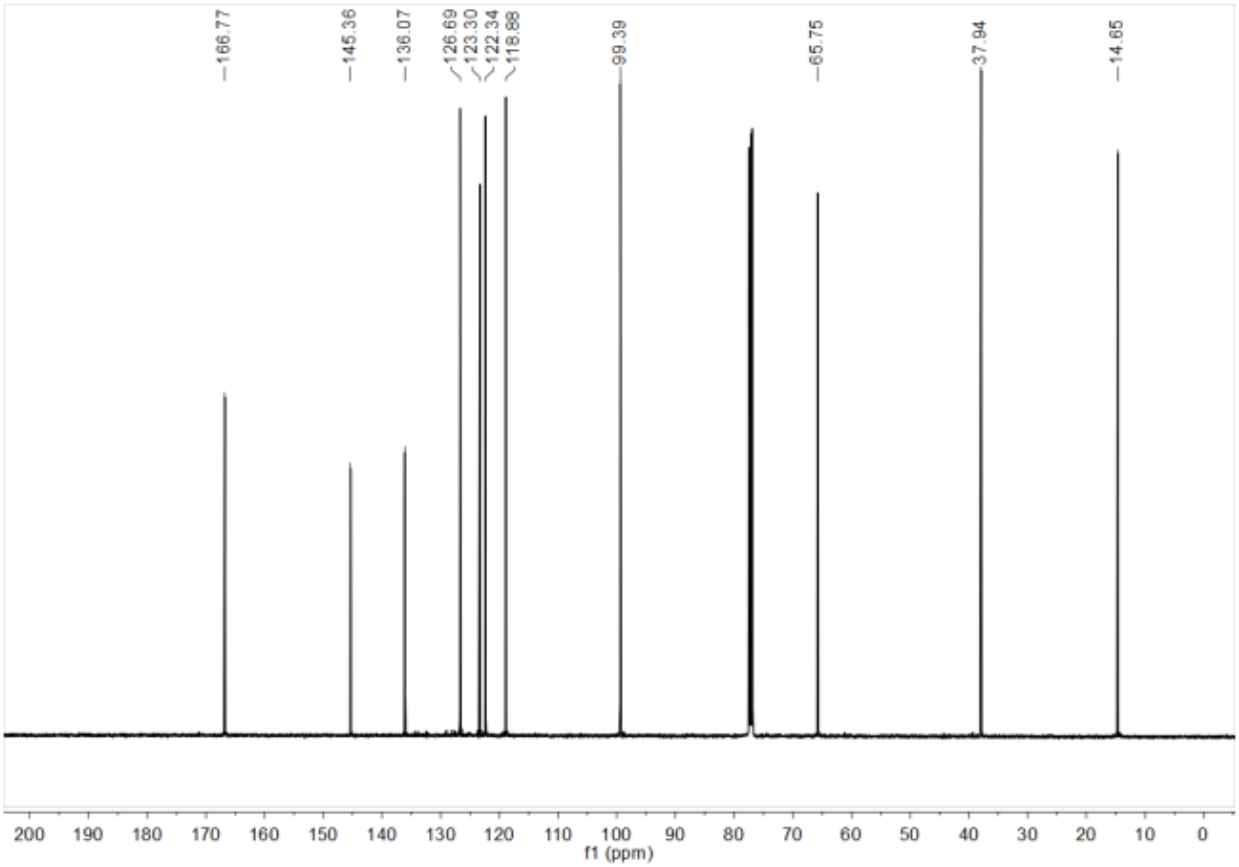


Figure 3.49. ^{13}C-NMR of 2-ethoxyindene (**3**) in $CDCl_3$.

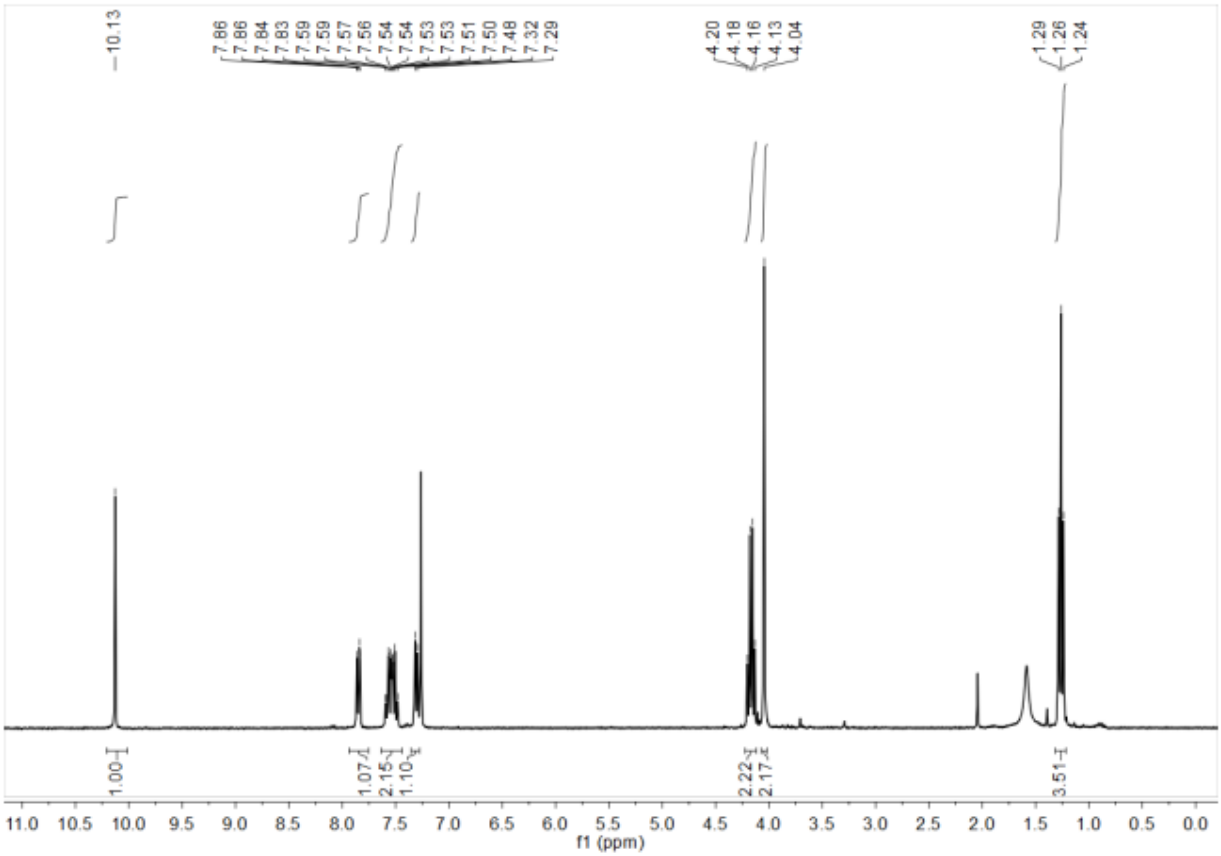


Figure 3.50. ^{1}H-NMR of 2-formylphenylacetic acid ethyl ester (**4**) in $CDCl_3$

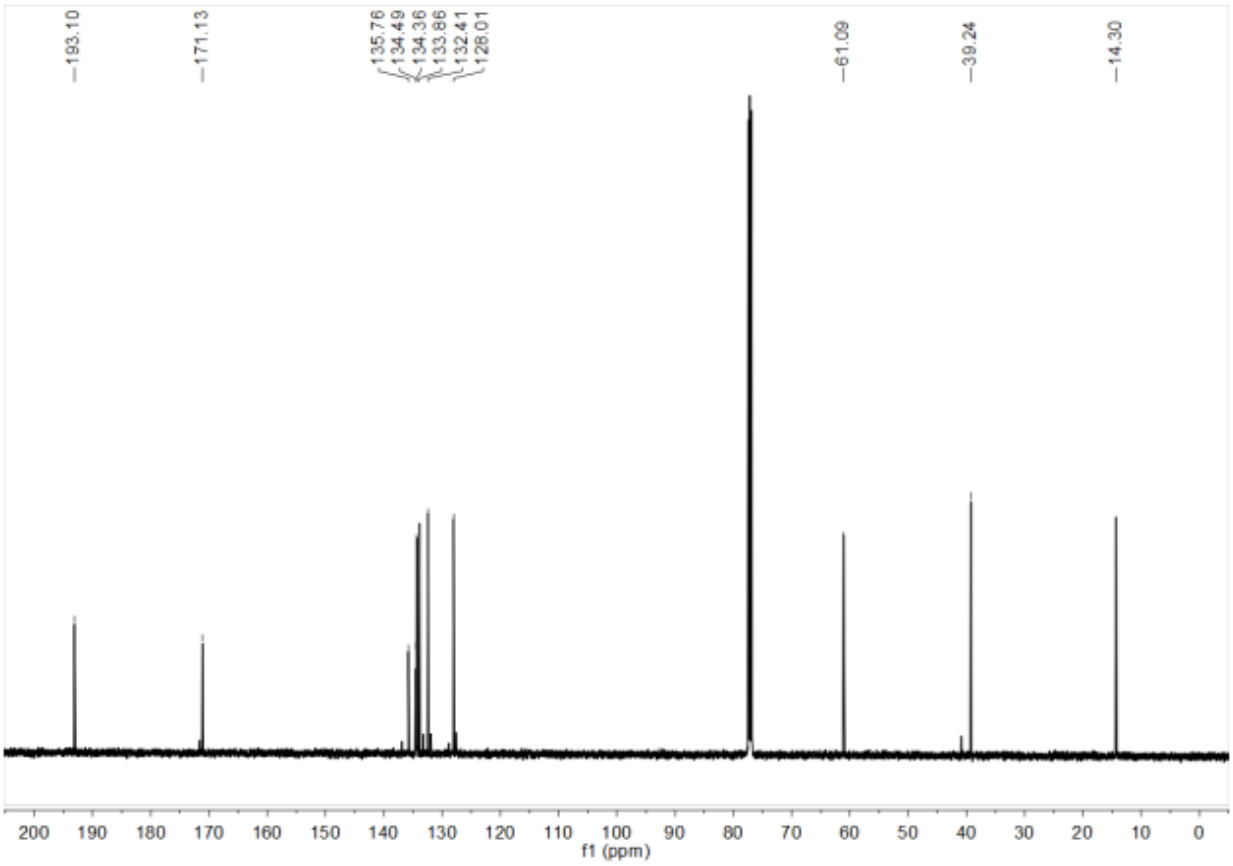


Figure 3.51. ^{13}C-NMR of 2-formylphenylacetic acid ethyl ester (**4**) in $CDCl_3$:

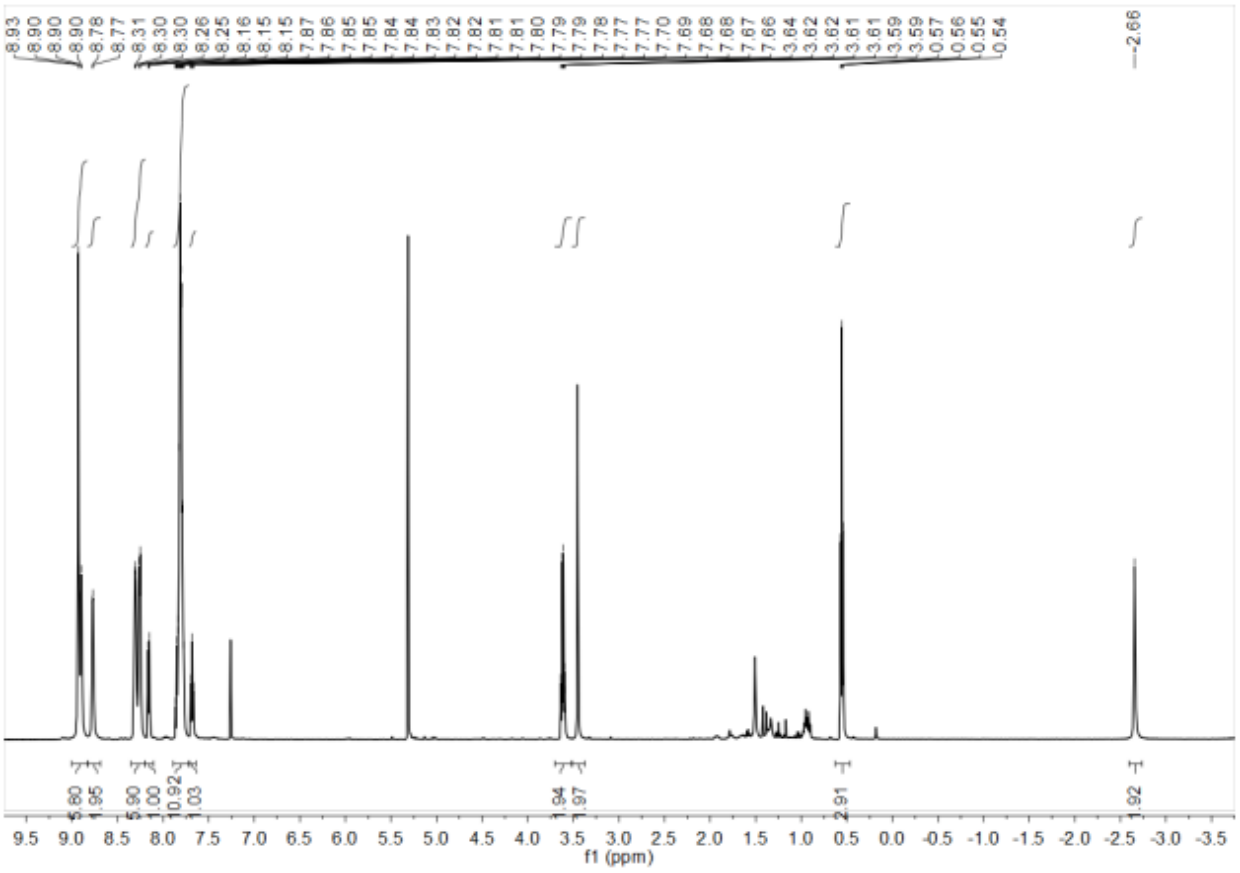


Figure 3.52. ^{1}H-NMR of 5-[phenylacetic acid methyl ester]-10,15,20-triphenyl porphyrin (**5**) in $CDCl_3$.

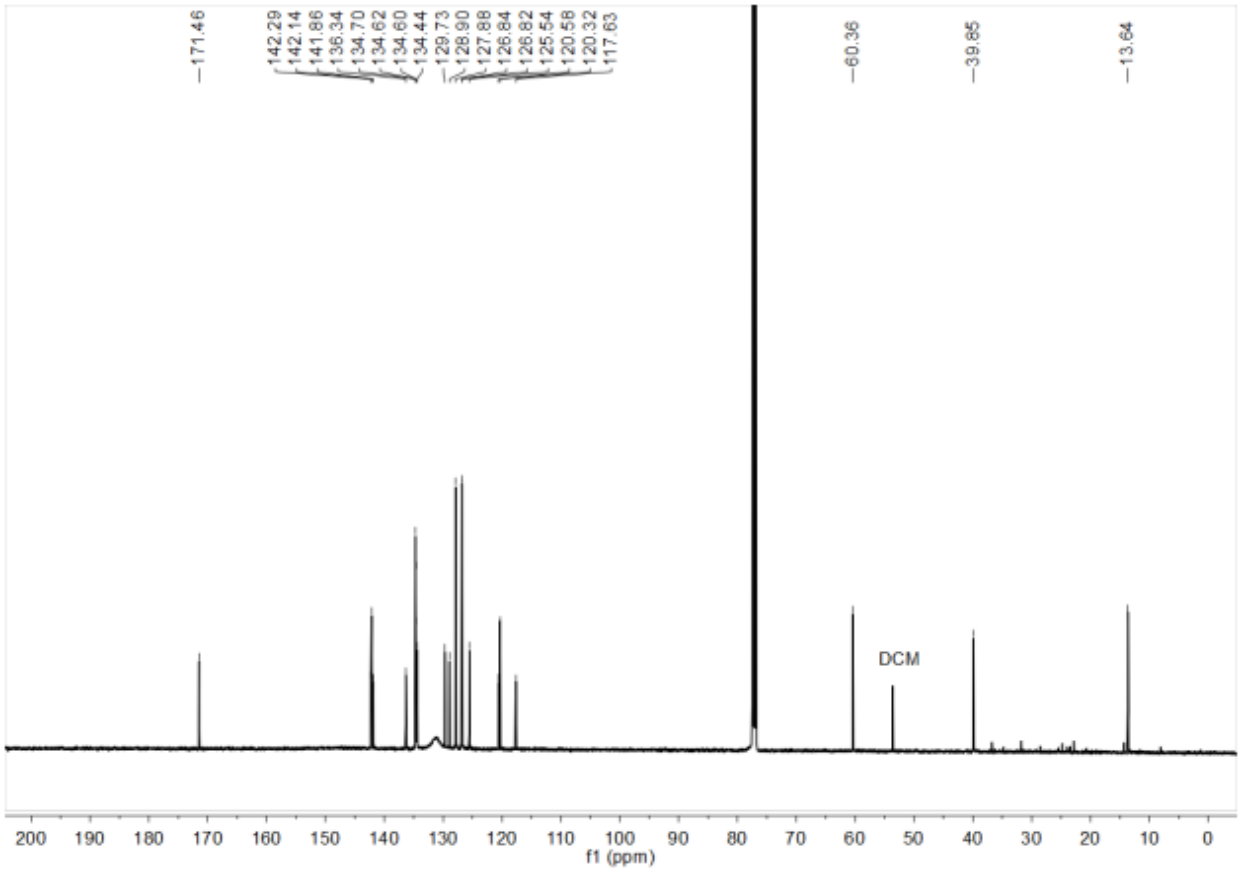


Figure 3.53. ^{13}C-NMR of 5-[phenylacetic acid methyl ester]-10,15,20-triphenyl porphyrin (**5**) in $CDCl_3$.

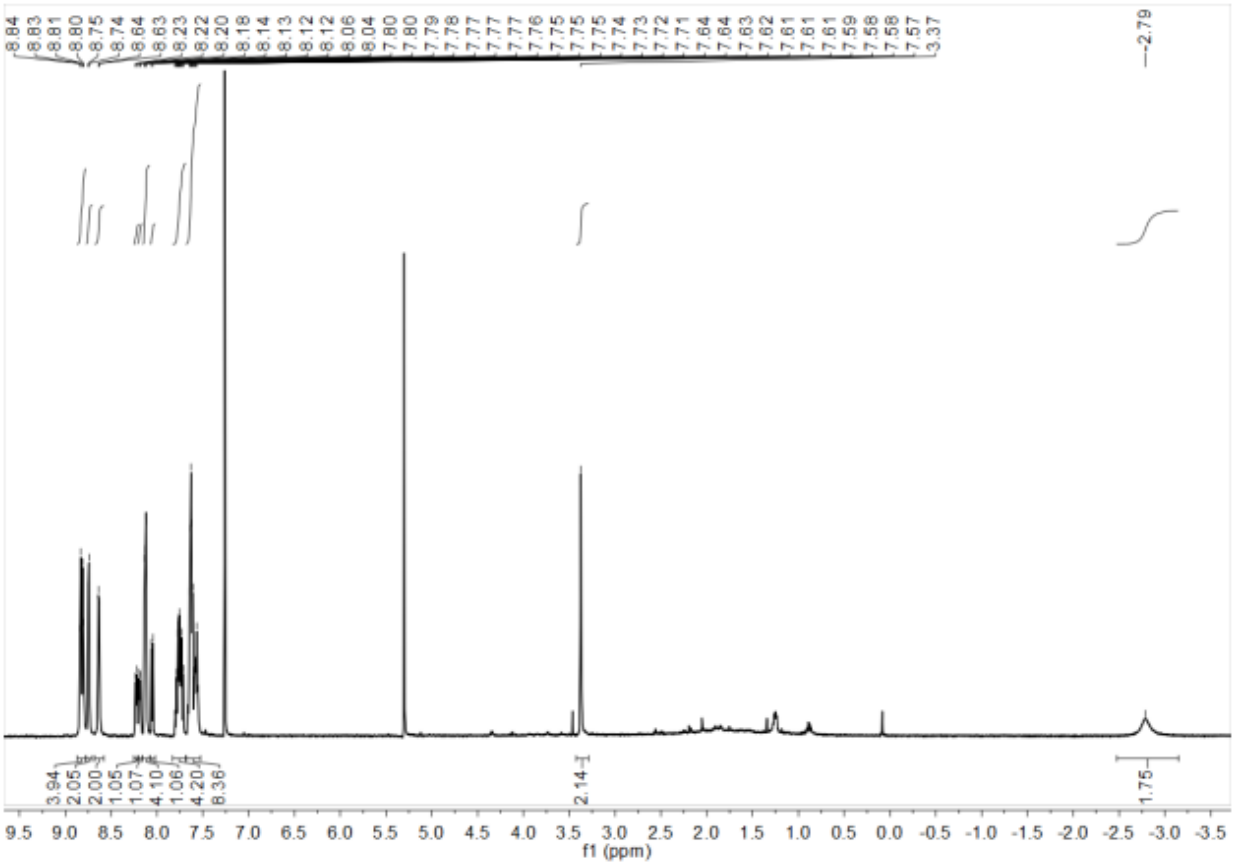


Figure 3.54. ^{1}H-NMR of 5-[phenylacetic acid]-10,15,20-triphenyl porphyrin (**6**) in $CDCl_3$.

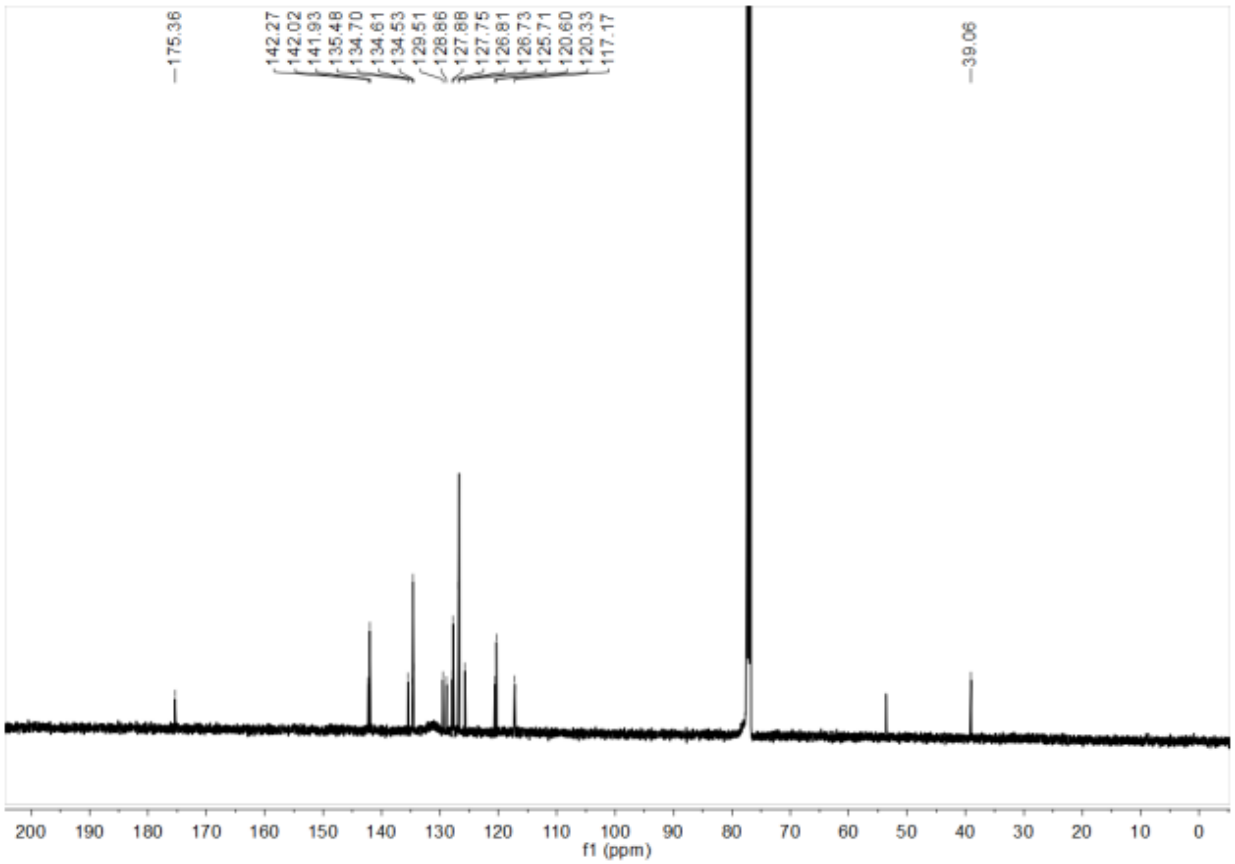


Figure 3.55. ^{13}C-NMR of 5-[phenylacetic acid]-10,15,20-triphenyl porphyrin (**6**) in $CDCl_3$.

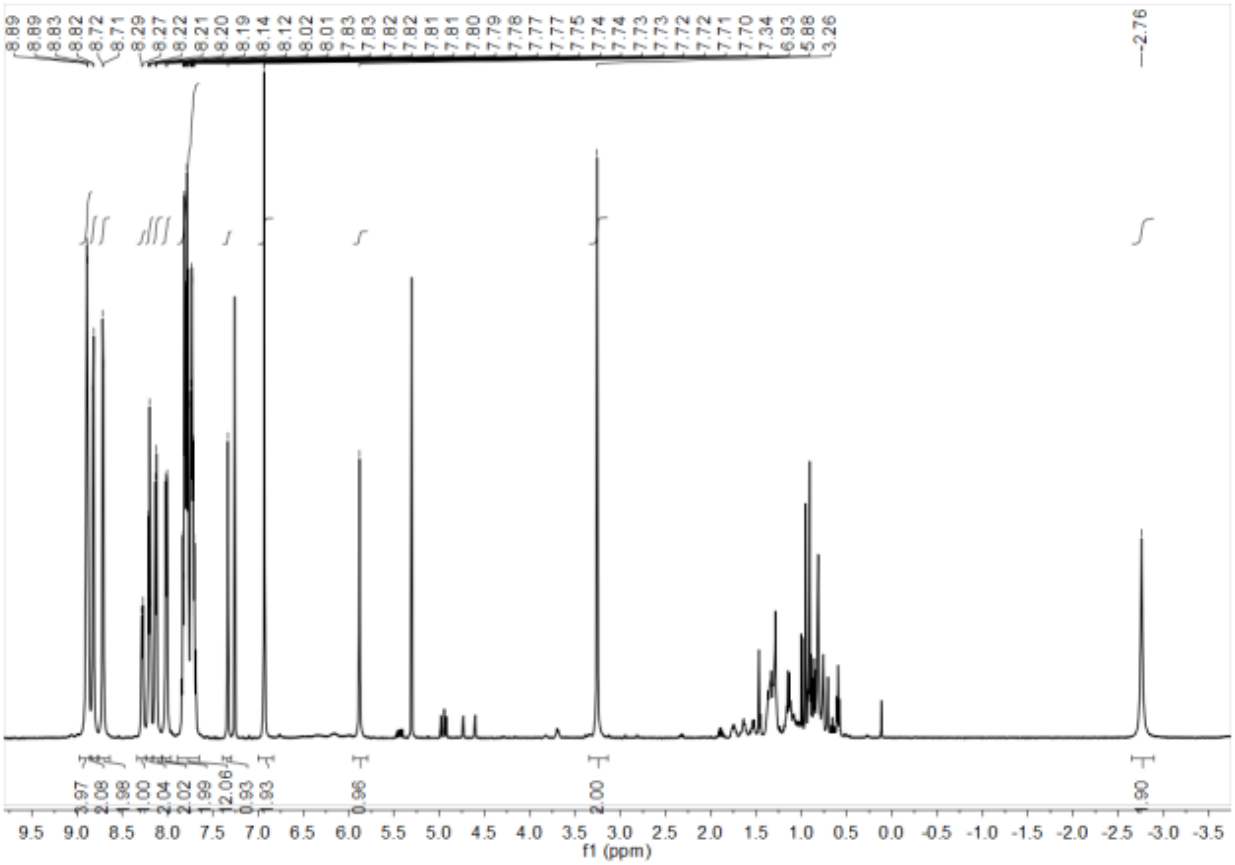


Figure 3.56. ^{1}H-NMR of *ortho*-2-amide in $CDCl_3$.

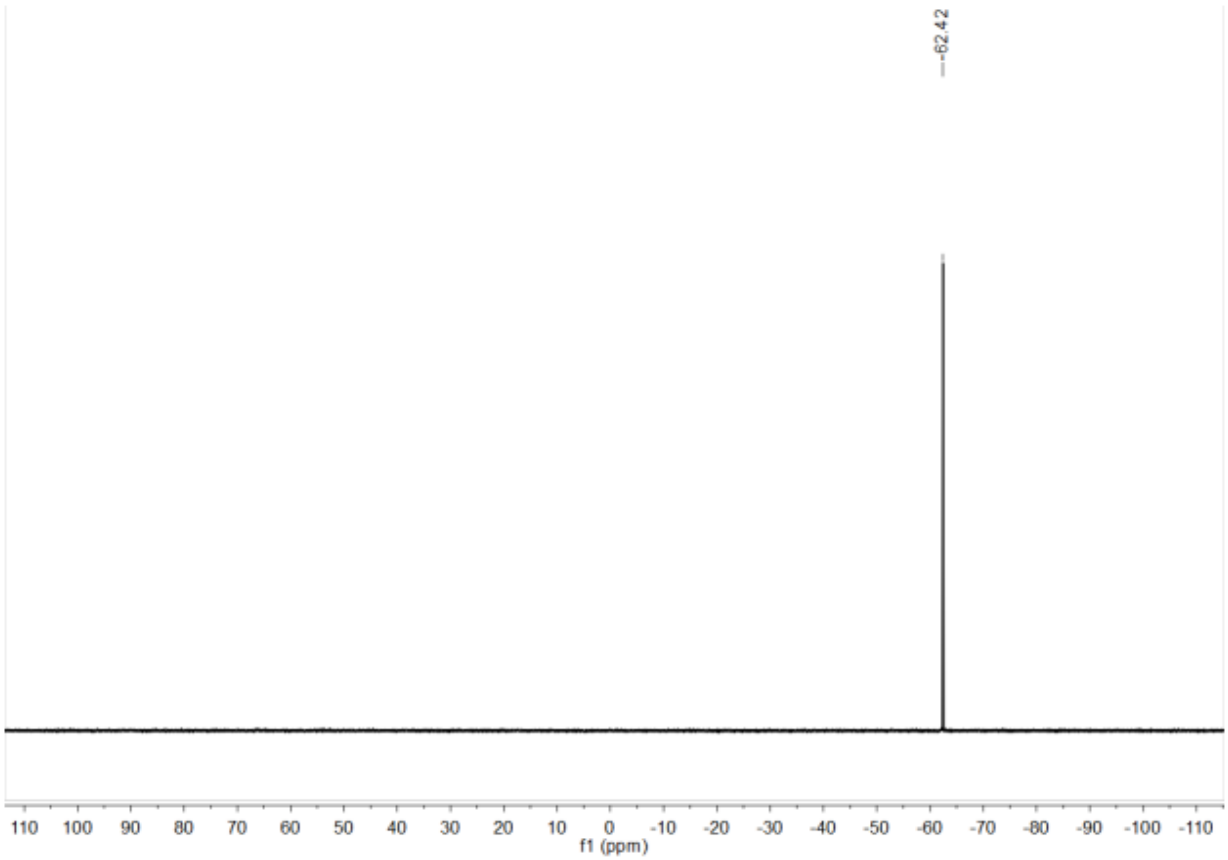


Figure 3.57. ^{19}F-NMR of *ortho*-2-amide in $CDCl_3$.

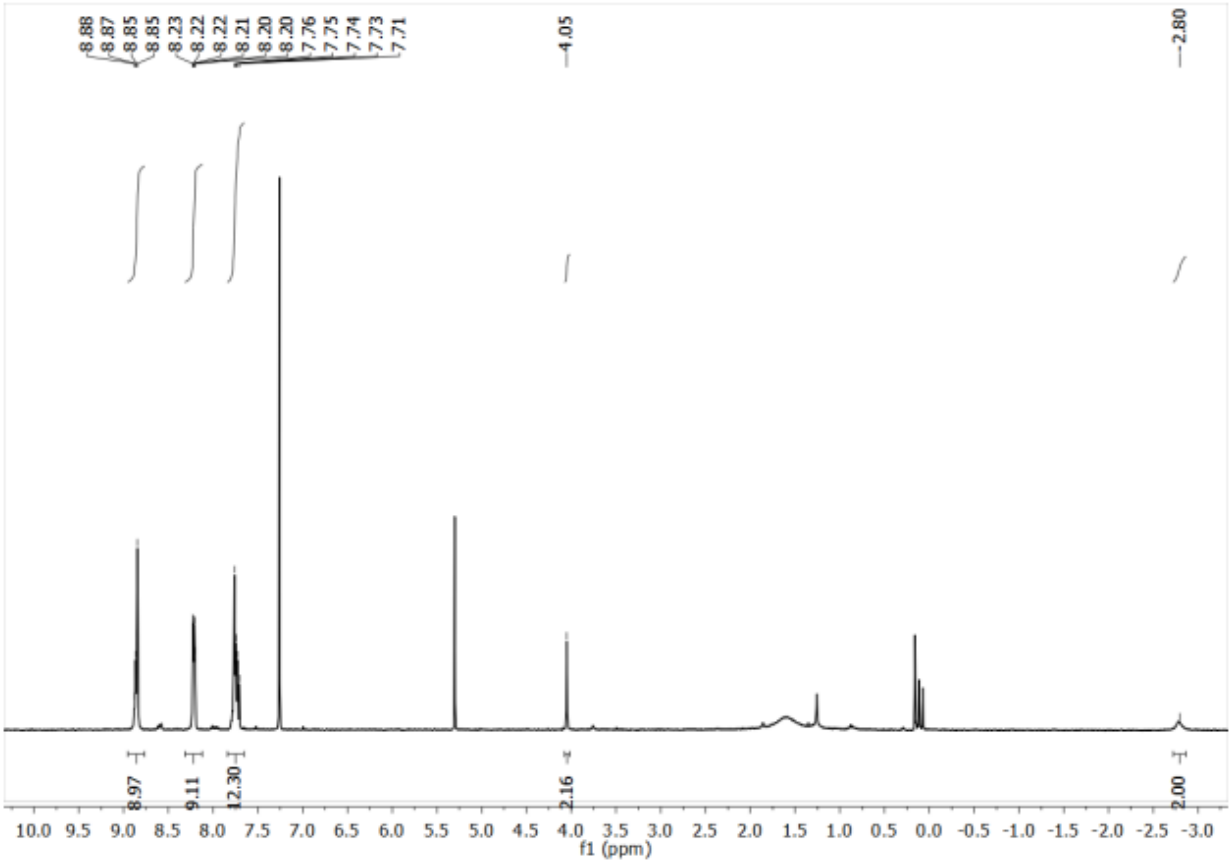


Figure 3.58. ^{1}H-NMR of *para*-1-amide in $CDCl_3$.

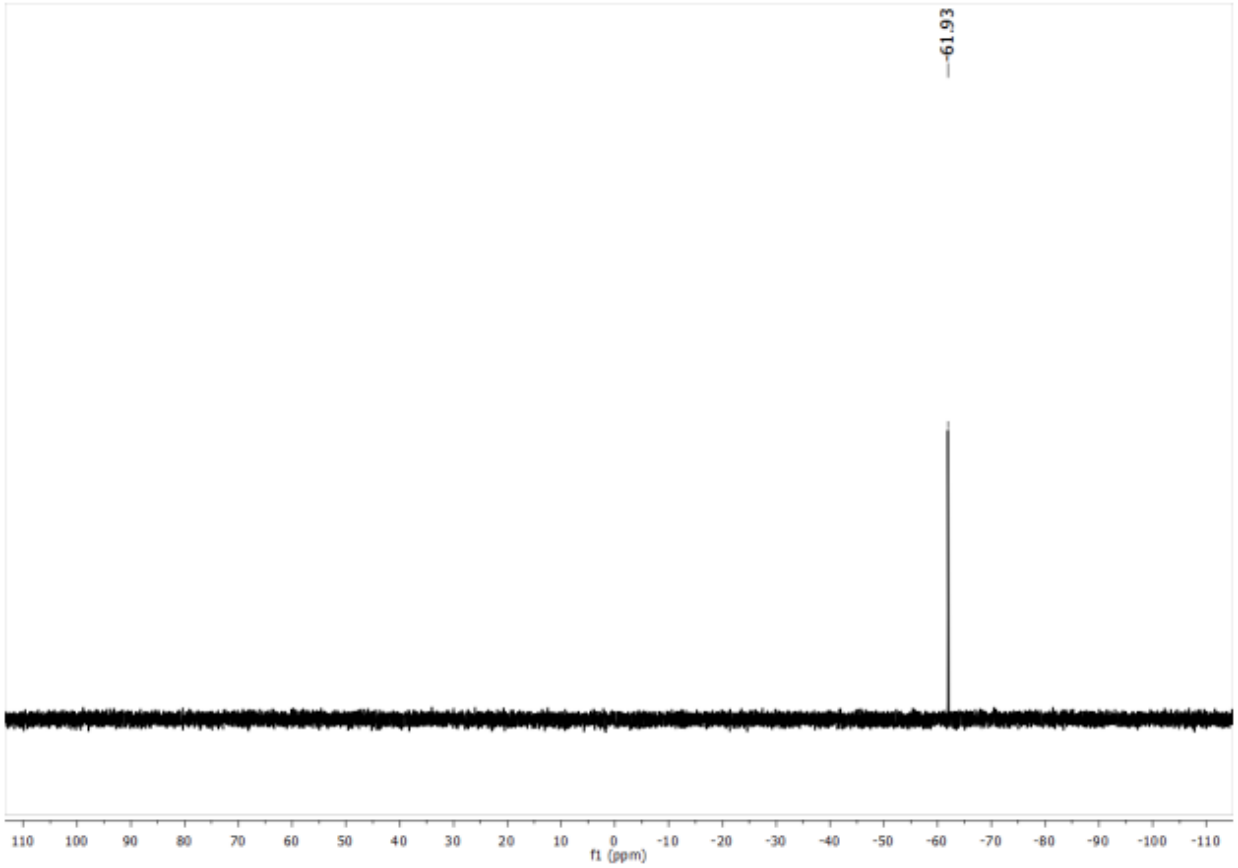


Figure 3.59. ^{19}F-NMR of *para*-1-amide in $CDCl_3$.

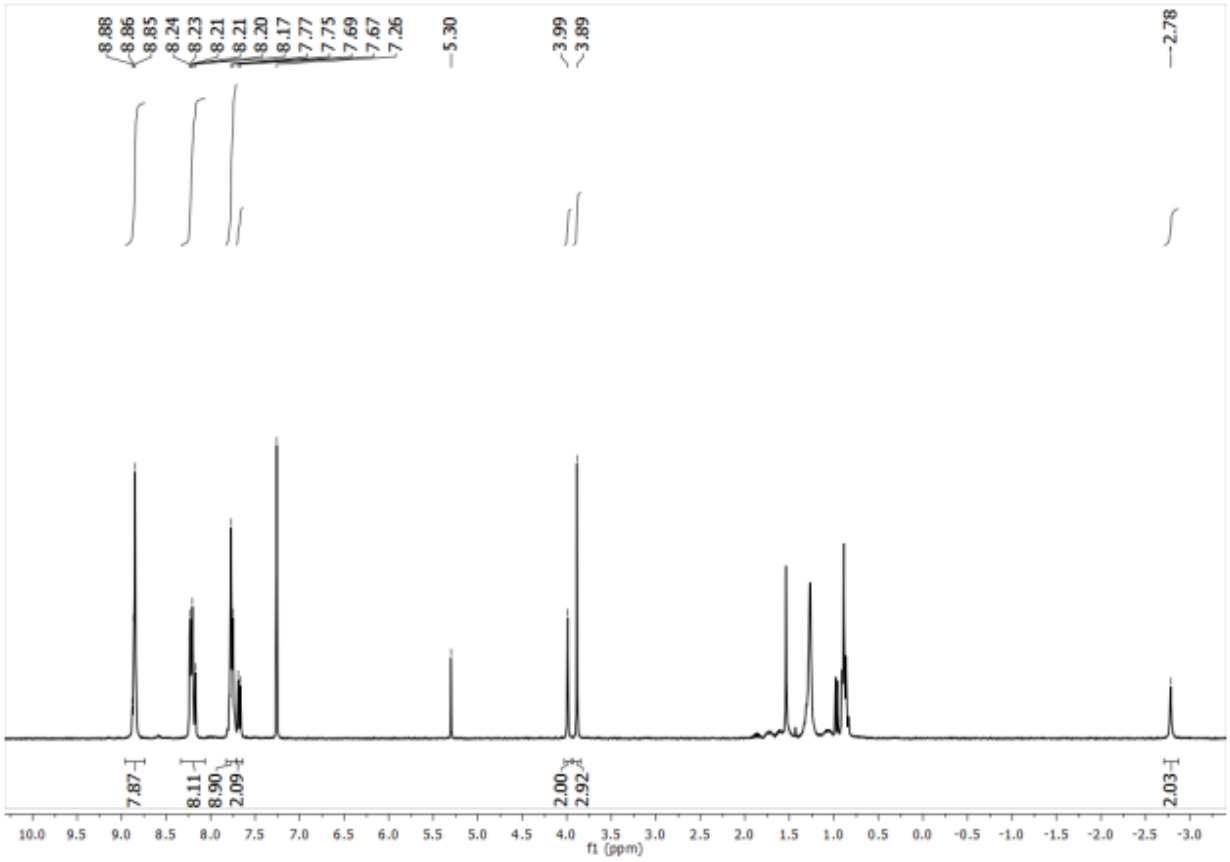


Figure 3.60. ^{1}H-NMR of Ethyl 2-(4-(10,15,20-triphenylporphyrin-5-yl)phenyl)acetate (**9**) in $CDCl_3$.

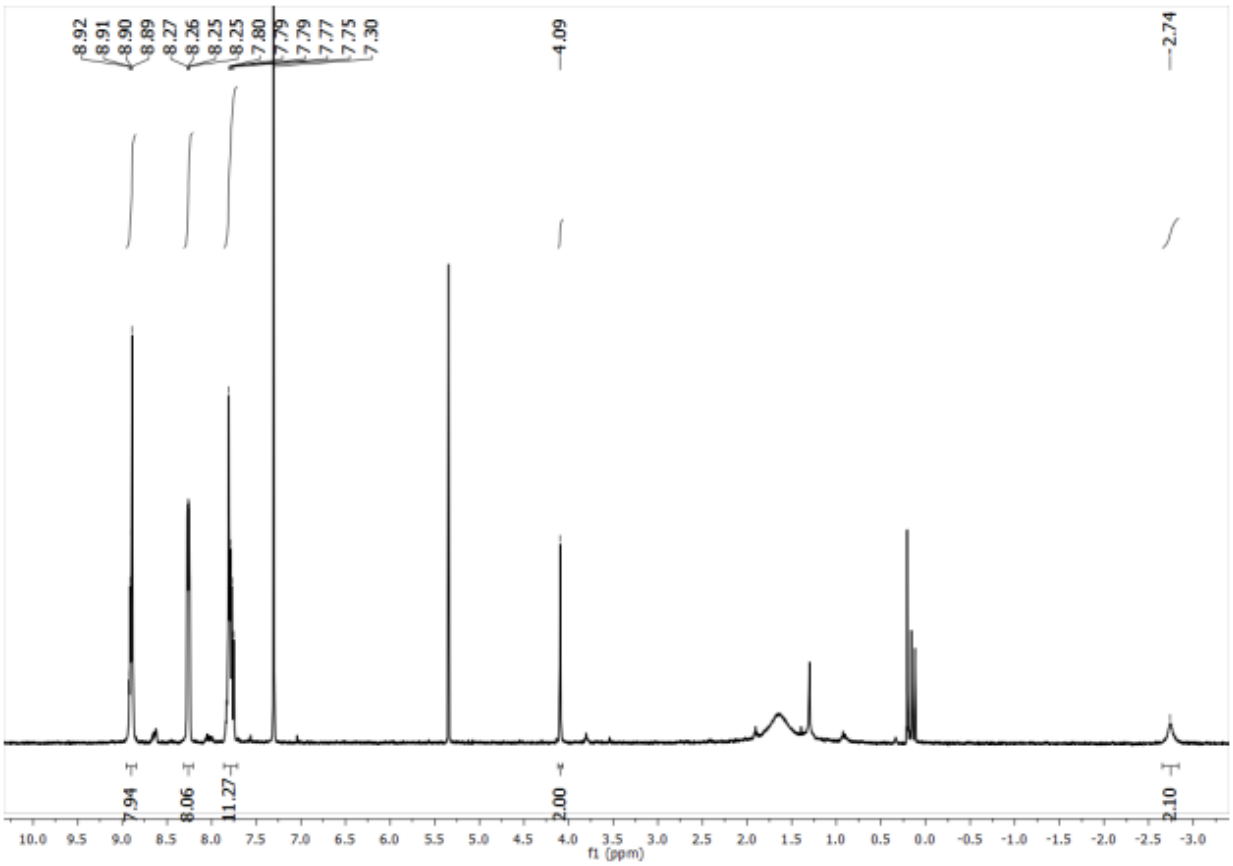


Figure 3.61. ^{1}H-NMR of 2-(4-(10,15,20-Triphenylporphyrin-5-yl)phenyl)acetic acid (**10**) in $CDCl_3$.

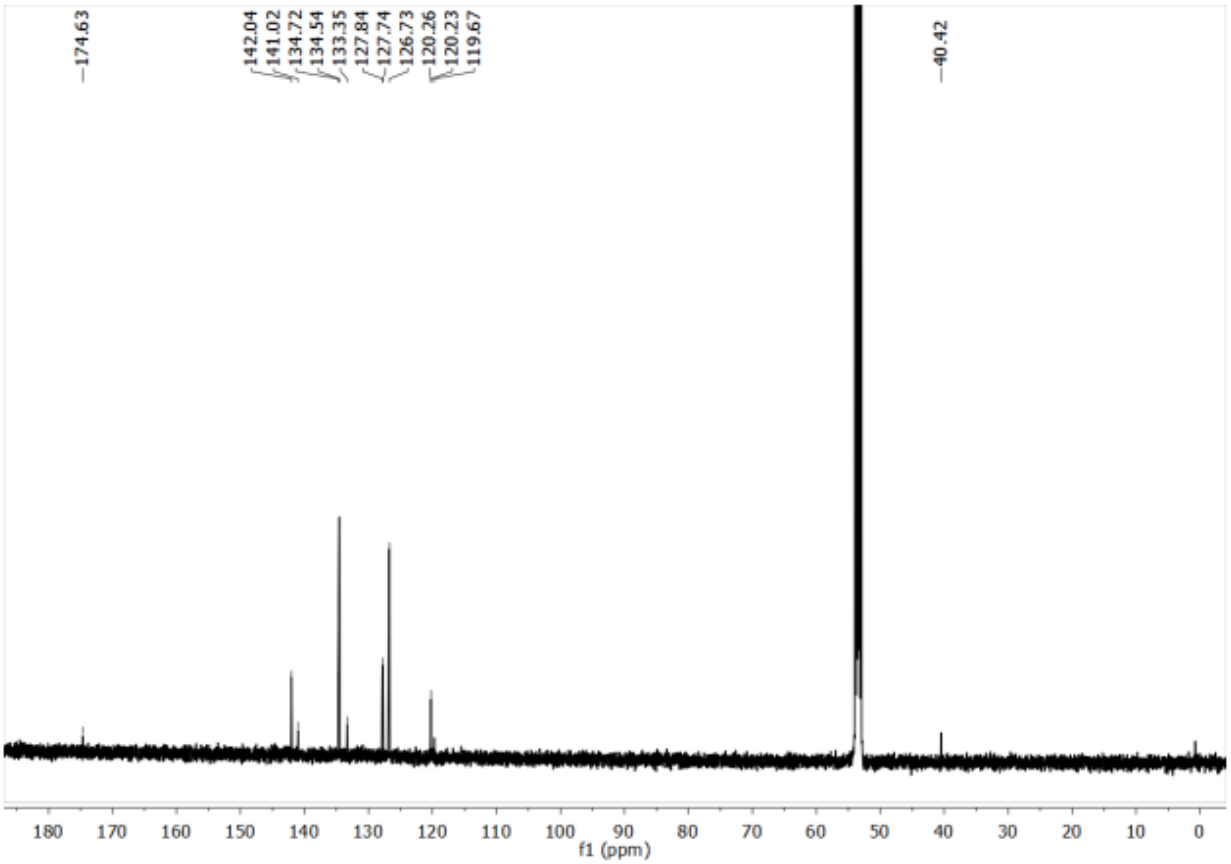


Figure 3.62. ^{13}C-NMR of 2-(4-(10,15,20-Triphenylporphyrin-5-yl)phenyl)acetic acid (**10**) in $CDCl_3$.

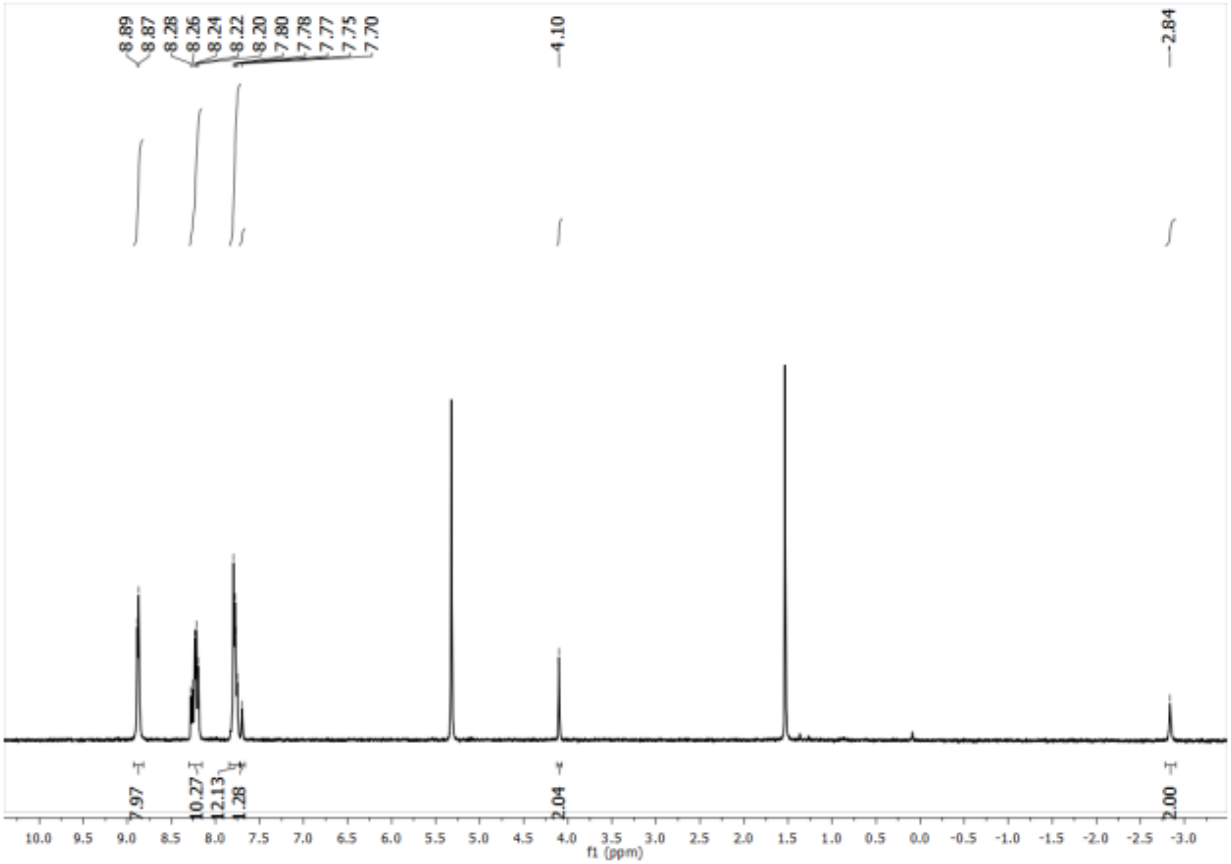


Figure 3.63. ^{1}H-NMR of *para*-2-amide CD_2Cl_2.

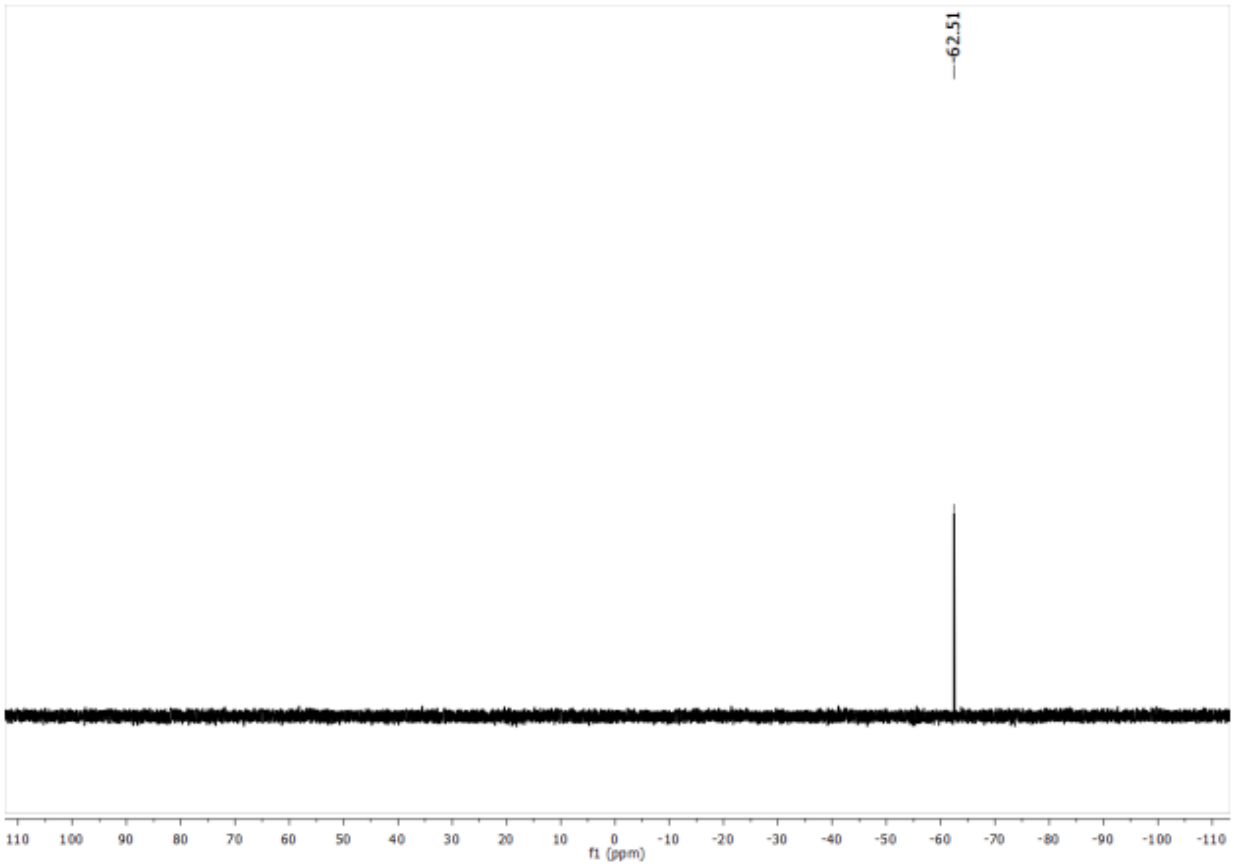


Figure 3.64. ^{19}F-NMR of *para*-2-amide CD_2Cl_2.

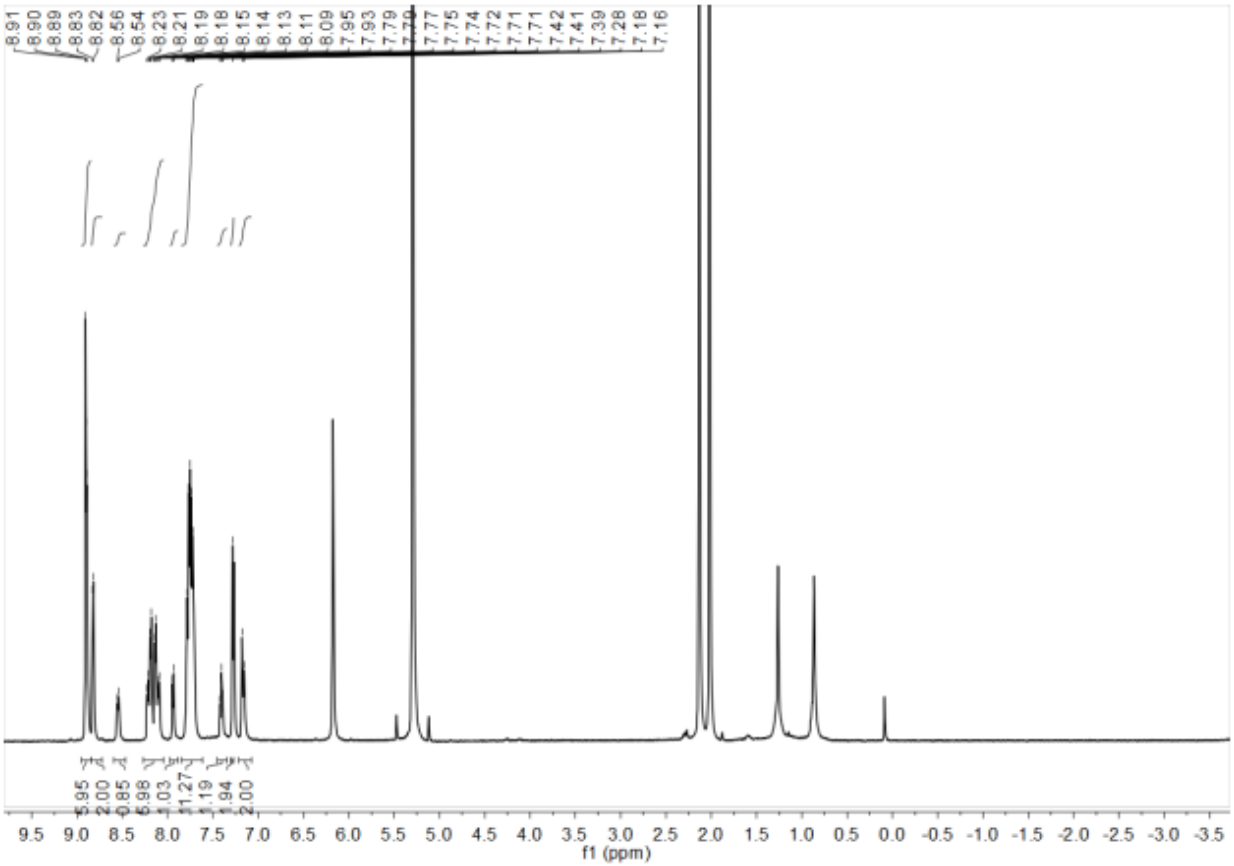


Figure 3.65. ^{1}H-NMR of Zn-*ortho*-1-amide in $CDCl_3$.

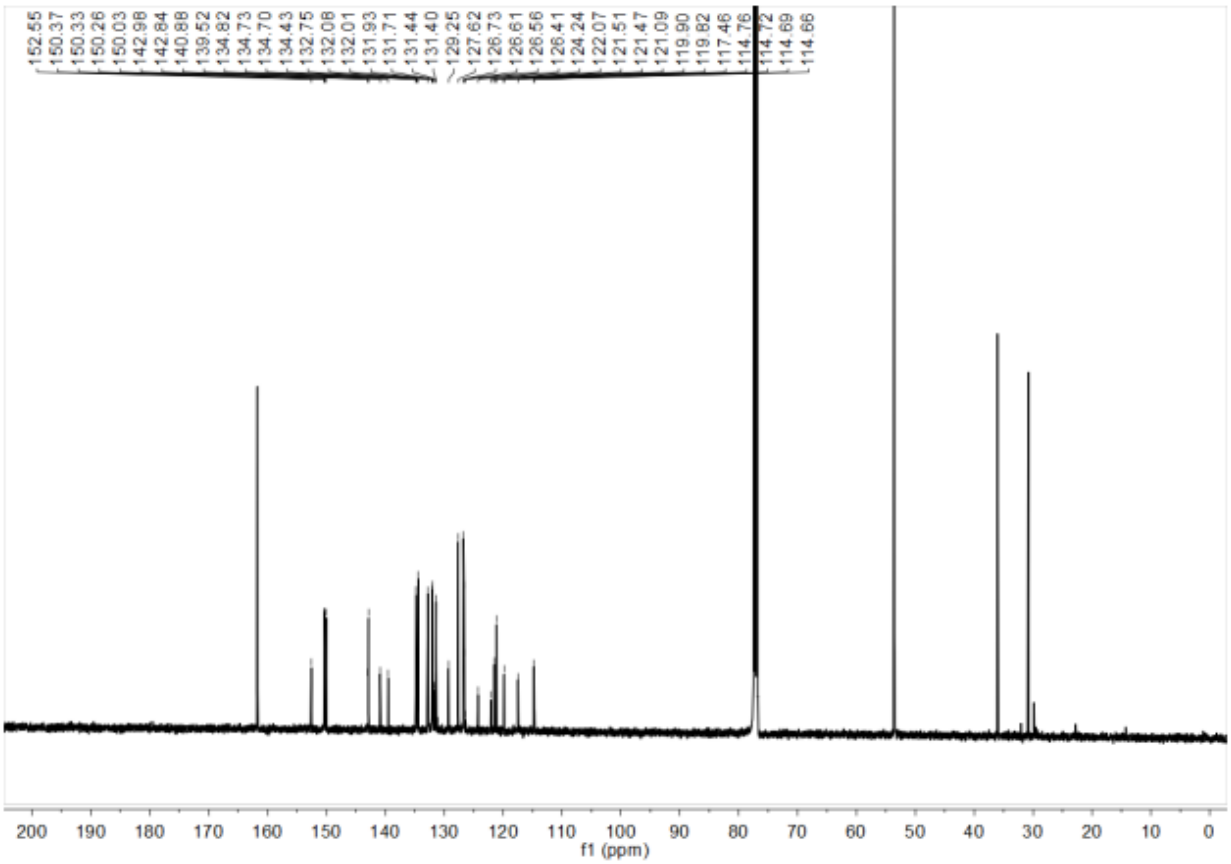


Figure 3.66. ^{13}C-NMR of Zn-*ortho*-1-amide in $CDCl_3$.

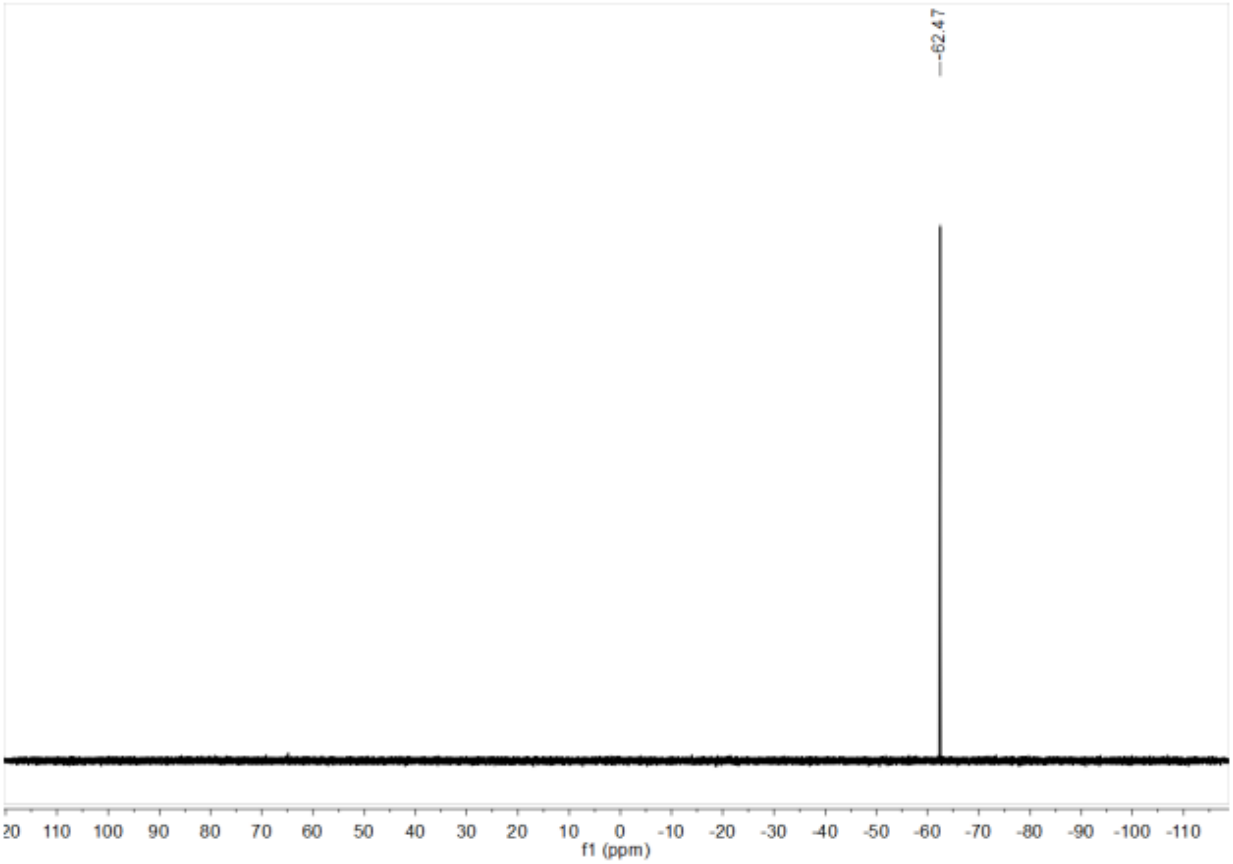


Figure 3.67. ^{19}F-NMR of Zn-*ortho*-1-amide in $CDCl_3$.

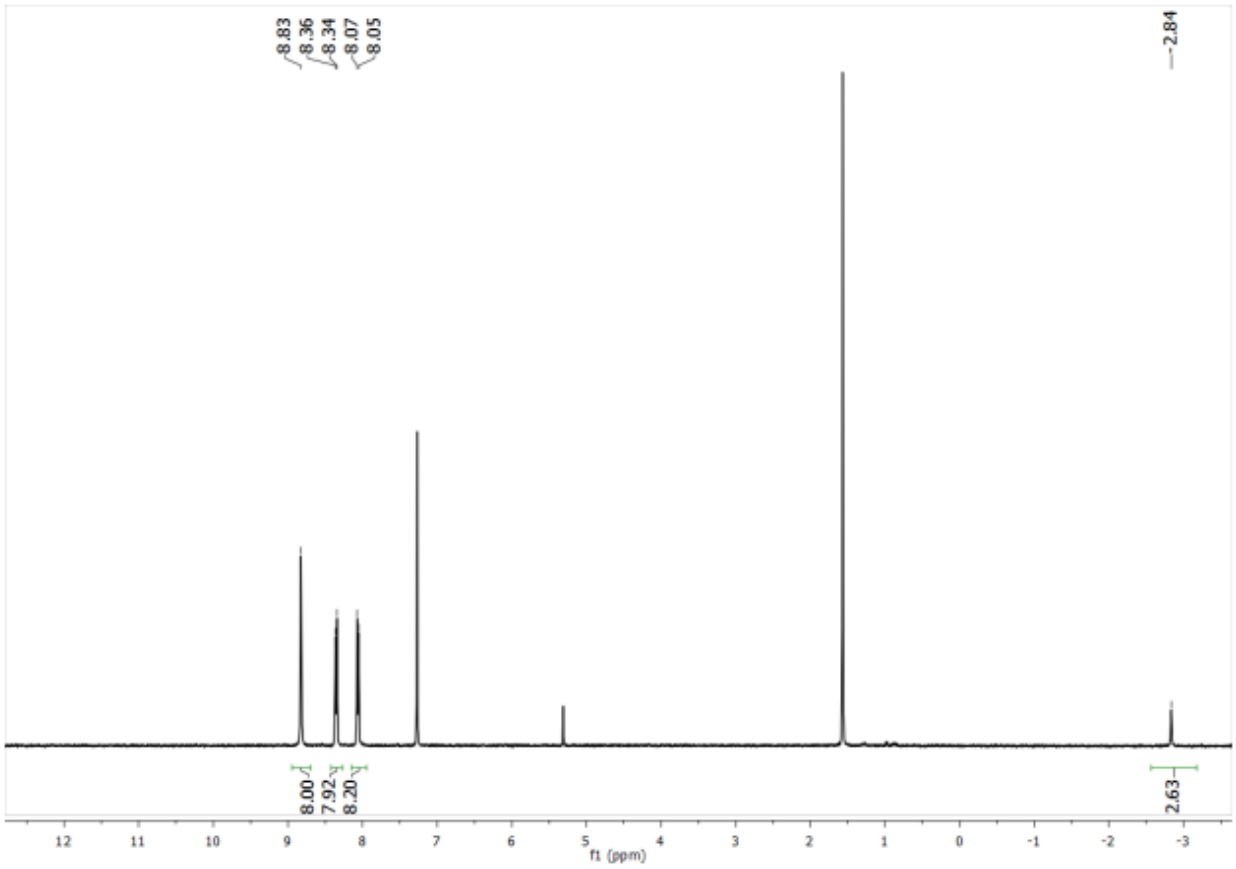


Figure 3.68. ^{1}H-NMR of *para*-$(CF_3)_4$ in $CDCl_3$.

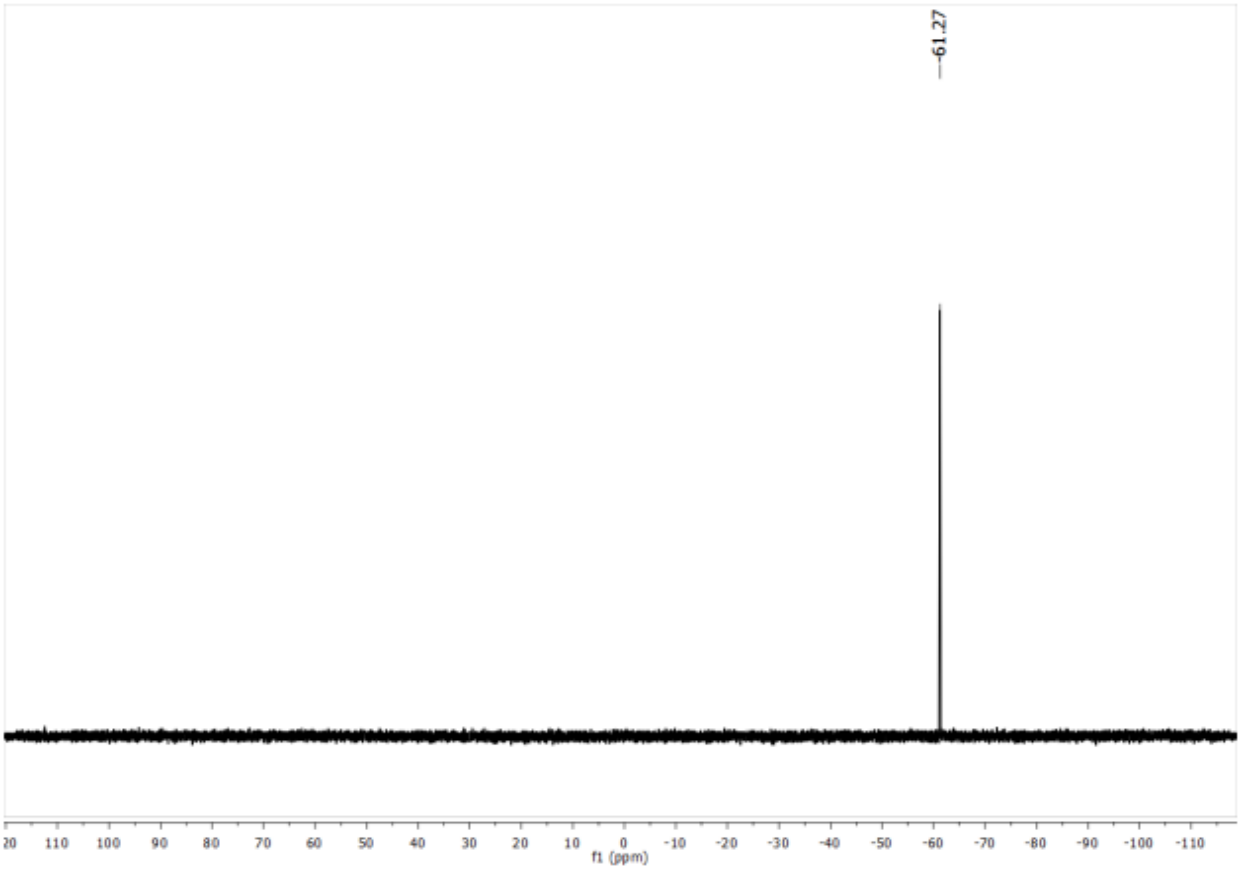


Figure 3.69. ^{19}F-NMR of *para*-$(CF_3)_4$ in $CDCl_3$.

3.6 References

(1) Appel, A. M.; Bercaw, J. E.; Bocarsly, A. B.; Dobbek, H.; DuBois, D. L.; Dupuis, M.; Ferry, J. G.; Fujita, E.; Hille, R.; Kenis, P. J. A.; Kerfeld, C. A.; Morris, R. H.; Peden, C. H. F.; Portis, A. R.; Ragsdale, S. W.; Rauchfuss, T. B.; Reek, J. N. H.; Seefeldt, L. C.; Thauer, R. K.; Waldrop, G. L. Frontiers, Opportunities, and Challenges in Biochemical and Chemical Catalysis of CO_2 Fixation. *Chem. Rev.* **2013**, *113*, 6621–6658.

(2) Benson, E. E.; Kubiak, C. P.; Sathrum, A. J.; Smieja, J. M. Electrocatalytic and Homogeneous Approaches to Conversion of CO_2 to Liquid Fuels. *Chem. Soc. Rev.* **2008**, *38*, 89–99.

(3) Morris, A. J.; Meyer, G. J.; Fujita, E. Molecular Approaches to the Photocatalytic Reduction of Carbon Dioxide for Solar Fuels. *Acc. Chem. Res.* **2009**, *42*, 1983–1994.

(4) Takahashi, K.; Hiratsuka, K.; Sasaki, H.; Toshima, S. Electrocatalytic Behavior of Metal Porphyrins in the Reduction of Carbon Dioxide. *Chem. Lett.* **1979**, *8*, 305–308.

(5) Hammouche, M.; Lexa, D.; Savéant, J. M.; Momenteau, M. Catalysis of the Electrochemical Reduction of Carbon Dioxide by Iron("0") Porphyrins. *J. Electroanal. Chem. Interfacial Electrochem.* **1988**, *249*, 347–351.

(6) Hammouche, M.; Lexa, D.; Momenteau, M.; Saveant, J. M. Chemical Catalysis of Electrochemical Reactions. Homogeneous Catalysis of the Electrochemical Reduction of Carbon Dioxide by Iron("0") Porphyrins. Role of the Addition of Magnesium Cations. *J. Am. Chem. Soc.* **1991**, *113*, 8455–8466.

(7) Bhugun, I.; Lexa, D.; Savéant, J.-M. Catalysis of the Electrochemical Reduction of Carbon Dioxide by Iron(0) Porphyrins: Synergystic Effect of Weak Brönsted Acids. *J. Am. Chem. Soc.* **1996**, *118*, 1769–1776.

(8) Behar, D.; Dhanasekaran, T.; Neta, P.; Hosten, C. M.; Ejeh, D.; Hambright, P.; Fujita, E. Cobalt Porphyrin Catalyzed Reduction of CO_2. Radiation Chemical, Photochemical, and Electrochemical Studies. *J. Phys. Chem. A* **1998**, *102*, 2870–2877.

(9) Fisher, B. J.; Eisenberg, R. Electrocatalytic Reduction of Carbon Dioxide by Using Macrocycles of Nickel and Cobalt. *J. Am. Chem. Soc.* **1980**, *102*, 7361–7363.

(10) Tinnemans, A. H. A.; Koster, T. P. M.; Thewissen, D. H. M. W.; Mackor, A. Tetraaza-Macrocyclic Cobalt(II) and Nickel(II) Complexes as Electron-Transfer Agents in the Photo(Electro)Chemical and Electrochemical Reduction of Carbon Dioxide. *Recl. Trav. Chim. Pays-Bas* **1984**, *103*, 288–295.

(11) Beley, M.; Collin, J.-P.; Ruppert, R.; Sauvage, J.-P. Nickel(II)-Cyclam: An Extremely Selective Electrocatalyst for Reduction of CO_2 in Water. *J. Chem. Soc. Chem. Commun.* **1984**, 1315–1316.

(12) Beley, Marc.; Collin, J. Paul.; Ruppert, Romain.; Sauvage, J. Pierre. Electrocatalytic Reduction of Carbon Dioxide by Nickel $Cyclam^{2+}$ in Water: Study of the Factors Affecting the Efficiency and the Selectivity of the Process. *J. Am. Chem. Soc.* **1986**, *108*, 7461–7467.

(13) Fujita, E.; Creutz, C.; Sutin, N.; Szalda, D. J. Carbon Dioxide Activation by Cobalt(I) Macrocycles: Factors Affecting Carbon Dioxide and Carbon Monoxide Binding. *J. Am. Chem. Soc.* **1991**, *113*, 343–353.

(14) Schneider, J.; Jia, H.; Kobiro, K.; Cabelli, D. E.; Muckerman, J. T.; Fujita, E. Nickel(II) Macrocycles: Highly Efficient Electrocatalysts for the Selective Reduction of CO_2 to CO. *Energy Environ. Sci.* **2012**, *5*, 9502–9510.

(15) Lacy, D. C.; McCrory, C. C. L.; Peters, J. C. Studies of Cobalt-Mediated Electrocatalytic CO_2 Reduction Using a Redox-Active Ligand. *Inorg. Chem.* **2014**, *53*, 4980–4988.
(16) Hawecker, J.; Lehn, J.-M.; Ziessel, R. Electrocatalytic Reduction of Carbon Dioxide Mediated by $Re(Bipy)(CO)_3Cl$ (Bipy = 2,2′-Bipyridine). *J. Chem. Soc. Chem. Commun.* **1984**, 328–330.
(17) Hawecker, J.; Lehn, J.-M.; Ziessel, R. Photochemical and Electrochemical Reduction of Carbon Dioxide to Carbon Monoxide Mediated by (2,2′-Bipyridine)Tricarbonylchlororhenium(I) and Related Complexes as Homogeneous Catalysts. *Helv. Chim. Acta* **1986**, *69*, 1990–2012.
(18) Sullivan, B. P.; Meyer, T. J. Photoinduced Irreversible Insertion of CO_2 into a Metal–Hydride Bond. *J. Chem. Soc. Chem. Commun.* **1984**, 1244–1245.
(19) Bolinger, C. M.; Story, N.; Sullivan, B. P.; Meyer, T. J. Electrocatalytic Reduction of Carbon Dioxide by 2,2'-Bipyridine Complexes of Rhodium and Iridium. *Inorg. Chem.* **1988**, *27*, 4582–4587.
(20) Ishida, Hitoshi.; Tanaka, Koji.; Tanaka, Toshio. Electrochemical CO_2 Reduction Catalyzed by Ruthenium Complexes $[Ru(Bpy)_2(CO)_2]^{2+}$ and $[Ru(Bpy)_2(CO)Cl]^{+}$. Effect of PH on the Formation of CO and $HCOO^{-}$. *Organometallics* **1987**, *6*, 181–186.
(21) Bourrez, M.; Molton, F.; Chardon-Noblat, S.; Deronzier, A. $[Mn(Bipyridyl)(CO)_3Br]$: An Abundant Metal Carbonyl Complex as Efficient Electrocatalyst for CO_2 Reduction. *Angew. Chem. Int. Ed.* **2011**, *50*, 9903–9906.
(22) Smieja, J. M.; Benson, E. E.; Kumar, B.; Grice, K. A.; Seu, C. S.; Miller, A. J. M.; Mayer, J. M.; Kubiak, C. P. Kinetic and Structural Studies, Origins of Selectivity, and Interfacial Charge Transfer in the Artificial Photosynthesis of CO. *Proc. Natl. Acad. Sci.* **2012**, *109*, 15646–15650.
(23) Sampson, M. D.; Nguyen, A. D.; Grice, K. A.; Moore, C. E.; Rheingold, A. L.; Kubiak, C. P. Manganese Catalysts with Bulky Bipyridine Ligands for the Electrocatalytic Reduction of Carbon Dioxide: Eliminating Dimerization and Altering Catalysis. *J. Am. Chem. Soc.* **2014**, *136*, 5460–5471.
(24) Slater, S.; Wagenknecht, J. H. Electrochemical Reduction of Carbon Dioxide Catalyzed by $Rh(Diphos)_2Cl$. *J. Am. Chem. Soc.* **1984**, *106*, 5367–5368.
(25) DuBois, D. L.; Miedaner, A.; Haltiwanger, R. C. Electrochemical Reduction of Carbon Dioxide Catalyzed by $[Pd(Triphosphine)(Solvent)](BF_4)_2$ Complexes: Synthetic and Mechanistic Studies. *J. Am. Chem. Soc.* **1991**, *113*, 8753–8764.
(26) Kang, P.; Meyer, T. J.; Brookhart, M. Selective Electrocatalytic Reduction of Carbon Dioxide to Formate by a Water-Soluble Iridium Pincer Catalyst. *Chem. Sci.* **2013**, *4*, 3497–3502.
(27) Thoi, V. S.; Chang, C. J. Nickel N-Heterocyclic Carbene–Pyridine Complexes that Exhibit Selectivity for Electrocatalytic Reduction of Carbon Dioxide over Water. *Chem. Commun.* **2011**, *47*, 6578–6580.
(28) Thoi, V. S.; Kornienko, N.; Margarit, C. G.; Yang, P.; Chang, C. J. Visible-Light Photoredox Catalysis: Selective Reduction of Carbon Dioxide to Carbon Monoxide by a Nickel N-Heterocyclic Carbene–Isoquinoline Complex. *J. Am. Chem. Soc.* **2013**, *135*, 14413–14424.
(29) Agarwal, V.; Penzel, S.; Szekely, K.; Cadalbert, R.; Testori, E.; Oss, A.; Past, J.; Samoson, A.; Ernst, M.; Böckmann, A.; Meier, B. H. De Novo 3D Structure Determination from Sub-

Milligram Protein Samples by Solid-State 100 KHz MAS NMR Spectroscopy. *Angew. Chem. Int. Ed.* **2014**, *53*, 12253–12256.
(30) Mondal, B.; Song, J.; Neese, F.; Ye, S. Bio-Inspired Mechanistic Insights into CO_2 Reduction. *Curr. Opin. Chem. Biol.* **2015**, 103–109.
(31) Drennan, C. L.; Heo, J.; Sintchak, M. D.; Schreiter, E.; Ludden, P. W. Life on Carbon Monoxide: X-Ray Structure of Rhodospirillum Rubrum Ni-Fe-S Carbon Monoxide Dehydrogenase. *Proc. Natl. Acad. Sci.* **2001**, *98*, 11973–11978.
(32) Jeoung, J.-H.; Dobbek, H. Carbon Dioxide Activation at the Ni,Fe-Cluster of Anaerobic Carbon Monoxide Dehydrogenase. *Science* **2007**, 318, 1461–1464.
(33) Gong, W.; Hao, B.; Wei, Z.; Ferguson, D. J.; Tallant, T.; Krzycki, J. A.; Chan, M. K. Structure of the $\alpha_2\varepsilon_2$ Ni-Dependent CO Dehydrogenase Component of the Methanosarcina Barkeri Acetyl-CoA Decarbonylase/Synthase Complex. *Proc. Natl. Acad. Sci.* **2008**, *105*, 9558–9563.
(34) Collman, J. P.; Gagne, R. R.; Reed, C.; Halbert, T. R.; Lang, G.; Robinson, W. T. Picket Fence Porphyrins. Synthetic Models for Oxygen Binding Hemoproteins. *J. Am. Chem. Soc.* **1975**, *97*, 1427–1439.
(35) Collman, J. P.; Zhang, X.; Wong, K.; Brauman, J. I. Dioxygen Binding in Iron and Cobalt Picnic Basket Porphyrins. *J. Am. Chem. Soc.* **1994**, *116*, 6245–6251.
(36) Wuenschell, G. E.; Tetreau, C.; Lavalette, D.; Reed, C. A. Hydrogen-Bonded Oxyhemoglobin Models with Substituted Picket-Fence Porphyrins: The Model Compound Equivalent of Site-Directed Mutagenesis. *J. Am. Chem. Soc.* **1992**, *114*, 3346–3355.
(37) Momenteau, M.; Reed, C. A. Synthetic Heme-Dioxygen Complexes. *Chem. Rev.* **1994**, *94*, 659–698.
(38) Chang, C. K.; Liang, Y.; Aviles, G.; Peng, S.-M. Conformational Control of Intramolecular Hydrogen Bonding in Heme Models: Maximal Co^{II}-O_2 Binding in a C-Clamp Porphyrin. *J. Am. Chem. Soc.* **1995**, *117*, 4191–4192.
(39) Chang, C. J.; Chng, L. L.; Nocera, D. G. Proton-Coupled O−O Activation on a Redox Platform Bearing a Hydrogen-Bonding Scaffold. *J. Am. Chem. Soc.* **2003**, *125*, 1866–1876.
(40) Wada, A.; Harata, M.; Hasegawa, K.; Jitsukawa, K.; Masuda, H.; Mukai, M.; Kitagawa, T.; Einaga, H. Structural and Spectroscopic Characterization of a Mononuclear Hydroperoxo–Copper(II) Complex with Tripodal Pyridylamine Ligands. *Angew. Chem. Int. Ed.* **1998**, *37*, 798–799.
(41) Wada, A.; Honda, Y.; Yamaguchi, S.; Nagatomo, S.; Kitagawa, T.; Jitsukawa, K.; Masuda, H. Steric and Hydrogen-Bonding Effects on the Stability of Copper Complexes with Small Molecules. *Inorg. Chem.* **2004**, *43*, 5725–5735.
(42) Lucas, R. L.; Zart, M. K.; Murkerjee, J.; Sorrell, T. N.; Powell, D. R.; Borovik, A. S. A Modular Approach toward Regulating the Secondary Coordination Sphere of Metal Ions: Differential Dioxygen Activation Assisted by Intramolecular Hydrogen Bonds. *J. Am. Chem. Soc.* **2006**, *128*, 15476–15489.
(43) Shook, R. L.; Borovik, A. S. Role of the Secondary Coordination Sphere in Metal-Mediated Dioxygen Activation. *Inorg. Chem.* **2010**, *49*, 3646–3660.
(44) Cook, S. A.; Borovik, A. S. Molecular Designs for Controlling the Local Environments around Metal Ions. *Acc. Chem. Res.* **2015**, *48*, 2407–2414.
(45) MacBeth, C., E.; Golombek, A., P.; Young, V., G. Jr.; Yang, C.; Kuczera, K.; Hendrich, M., P.; Borovik, A. S. O_2 Activation by Nonheme Iron Complexes: A Monomeric Fe(III)-Oxo Complex Derived From O_2. *Science*, **2000**, *289*, 938–941.

(46) Berreau, L. M.; Makowska-Grzyska, M. M.; Arif, A. M. Modeling the Active Site Chemistry of Liver Alcohol Dehydrogenase: Mononuclear Zinc Methanol and N,N-Dimethylformamide Complexes of a Nitrogen/Sulfur Ligand Possessing an Internal Hydrogen Bond Donor. *Inorg. Chem.* **2001**, *40*, 2212–2213.
(47) Makowska-Grzyska, M. M.; Jeppson, P. C.; Allred, R. A.; Arif, A. M.; Berreau, L. M. Modeling Substrate- and Inhibitor-Bound Forms of Liver Alcohol Dehydrogenase: Chemistry of Mononuclear Nitrogen/Sulfur-Ligated Zinc Alcohol, Formamide, and Sulfoxide Complexes. *Inorg. Chem.* **2002**, *41*, 4872–4887.
(48) Moore, C. M.; Szymczak, N. K. Nitrite Reduction by Copper through Ligand-Mediated Proton and Electron Transfer. *Chem. Sci.* **2015**, *6*, 3373–3377.
(49) Matson, E. M.; Park, Y. J.; Fout, A. R. Facile Nitrite Reduction in a Non-Heme Iron System: Formation of an Iron(III)-Oxo. *J. Am. Chem. Soc.* **2014**, *136*, 17398–17401.
(50) Ford, C. L.; Park, Y. J.; Matson, E. M.; Gordon, Z.; Fout, A. R. A Bioinspired Iron Catalyst for Nitrate and Perchlorate Reduction. Science, **2016**, *354*, 741–743.
(51) Creutz, S. E.; Peters, J. C. Exploring Secondary-Sphere Interactions in Fe–NxHy Complexes Relevant to N_2 Fixation. *Chem. Sci.* **2017**, *8*, 2321–2328.
(52) Rana, A.; Mondal, B.; Sen, P.; Dey, S.; Dey, A. Activating Fe(I) Porphyrins for the Hydrogen Evolution Reaction Using Second-Sphere Proton Transfer Residues. *Inorg. Chem.* **2017**, *56*, 1783–1793.
(53) Helm, M. L.; Stewart, M. P.; Bullock, R. M.; DuBois, M. R.; DuBois, D. L. A Synthetic Nickel Electrocatalyst with a Turnover Frequency Above 100,000 S^{-1} for H_2 Production. *Science* **2011**, 333, 863–866.
(54) Yang, J. Y.; Smith, S. E.; Liu, T.; Dougherty, W. G.; Hoffert, W. A.; Kassel, W. S.; DuBois, M. R.; DuBois, D. L.; Bullock, R. M. Two Pathways for Electrocatalytic Oxidation of Hydrogen by a Nickel Bis(Diphosphine) Complex with Pendant Amines in the Second Coordination Sphere. *J. Am. Chem. Soc.* **2013**, *135*, 9700–9712.
(55) Dogutan, D. K.; McGuire, R.; Nocera, D. G. Electocatalytic Water Oxidation by Cobalt(III) Hangman β-Octafluoro Corroles. *J. Am. Chem. Soc.* **2011**, *133*, 9178–9180.
(56) Carver, C. T.; Matson, B. D.; Mayer, J. M. Electrocatalytic Oxygen Reduction by Iron Tetra-Arylporphyrins Bearing Pendant Proton Relays. *J. Am. Chem. Soc.* **2012**, *134*, 5444–5447.
(57) Costentin, C.; Drouet, S.; Robert, M.; Savéant, J.-M. A Local Proton Source Enhances CO_2 Electroreduction to CO by a Molecular Fe Catalyst. *Science* **2012**, *338* (6103), 90–94.
(58) Chapovetsky, A.; Do, T. H.; Haiges, R.; Takase, M. K.; Marinescu, S. C. Proton-Assisted Reduction of CO_2 by Cobalt Aminopyridine Macrocycles. *J. Am. Chem. Soc.* **2016**, *138*, 5765–5768.
(59) Roy, S.; Sharma, B.; Pécaut, J.; Simon, P.; Fontecave, M.; Tran, P. D.; Derat, E.; Artero, V. Molecular Cobalt Complexes with Pendant Amines for Selective Electrocatalytic Reduction of Carbon Dioxide to Formic Acid. *J. Am. Chem. Soc.* **2017**, *139*, 3685–3696.
(60) Costentin, C.; Passard, G.; Robert, M.; Savéant, J.-M. Ultraefficient Homogeneous Catalyst for the CO_2-to-CO Electrochemical Conversion. *Proc. Natl. Acad. Sci.* **2014**, *111*, 14990–14994.
(61) Costentin, C.; Drouet, S.; Robert, M.; Savéant, J.-M. Turnover Numbers, Turnover Frequencies, and Overpotential in Molecular Catalysis of Electrochemical Reactions. Cyclic Voltammetry and Preparative-Scale Electrolysis. *J. Am. Chem. Soc.* **2012**, *134*, 11235–11242.

(62) Azcarate, I.; Costentin, C.; Robert, M.; Savéant, J.-M. Dissection of Electronic Substituent Effects in Multielectron–Multistep Molecular Catalysis. Electrochemical CO_2-to-CO Conversion Catalyzed by Iron Porphyrins. *J. Phys. Chem. C* **2016**, *120*, 28951–28960.
(63) Pegis, M. L.; McKeown, B. A.; Kumar, N.; Lang, K.; Wasylenko, D. J.; Zhang, X. P.; Raugei, S.; Mayer, J. M. Homogenous Electrocatalytic Oxygen Reduction Rates Correlate with Reaction Overpotential in Acidic Organic Solutions. *ACS Cent. Sci.* **2016**, *2*, 850–856.
(64) Azcarate, I.; Costentin, C.; Robert, M.; Savéant, J.-M. Through-Space Charge Interaction Substituent Effects in Molecular Catalysis Leading to the Design of the Most Efficient Catalyst of CO_2-to-CO Electrochemical Conversion. *J. Am. Chem. Soc.* **2016**, *138*, 16639–16644.
(65) Costentin, C.; Drouet, S.; Passard, G.; Robert, M.; Savéant, J.-M. Proton-Coupled Electron Transfer Cleavage of Heavy-Atom Bonds in Electrocatalytic Processes. Cleavage of a C–O Bond in the Catalyzed Electrochemical Reduction of CO_2. *J. Am. Chem. Soc.* **2013**, *135*, 9023–9031.
(66) Madadi, M.; Rahimi, R. Zeolite-Immobilized Mn(III), Fe(III) and Co(III) Complexes with 5,10,15,20-Tetra(4-Methoxyphenyl)Porphyrin as Heterogeneous Catalysts for the Epoxidation of (R)-(+)-Limonene: Synthesis, Characterization and Catalytic Activity. *React. Kinet. Mech. Catal.* **2012**, *107*, 215–229.
(67) Gagne, R. R.; Allison, J. L.; Ingle, D. M. Unusual Structural and Reactivity Types for Copper(I). Equilibrium Constants for the Binding of Monodentate Ligands to Several Four-Coordinate Copper(I) Complexes. *Inorg. Chem.* **1979**, *18*, 2767–2774.
(68) Jakab, G.; Tancon, C.; Zhang, Z.; Lippert, K. M.; Schreiner, P. R. (Thio)Urea Organocatalyst Equilibrium Acidities in DMSO. *Org. Lett.* **2012**, *14*, 1724–1727.
(69) Amarego, W. L. F. *Purification of Laboratory Chemicals*, 6th ed. Elsevier **2009**.
(70) Frisch, M; Trucks, G. W.; Schlegel, H. B.; Scuseria, G. E.; Robb, M. A.; Cheeseman, J. R.; Scalmani, G.; Barone, V.; Petersson, G. A.; Nakatsuji, H.; Li, X.; Caricato, M.; Marenich, A. V.; Bloino, J.; Janesko, B. G.; Gomperts, R.; Mennucci, B.; Hratchian, H. P.; Ortiz, J. V.; Izmaylov, A. F.; Sonnenberg, J. L.; Williams-Young, D.; Ding, F.; Lipparini, F.; Egidi, F.; Goings, J.; Peng, B.; Petrone, A.; Henderson, T.; Ranasinghe, D.; Zakrzewski, V. G.; Gao, J.; Rega, N.; Zheng, G.; Liang, W.; Hada, M.; Ehara, M.; Toyota, K.; Fukuda, R.; Hasegawa, J.; Ishida, M.; Nakajima, T.; Honda, Y.; Kitao, O.; Nakai, H.; Vreven, T.; Throssell, K.; Montgomery, J. A.; Peralta, J. E.; Ogliaro, F.; Bearpark, M. J.; Heyd, J. J.; Brothers, E. N.; Kudin, K. N.; Staroverov, V. N.; Keith, T. A.; Kobayashi, R.; Normand, J.; Raghavachari, K.; Rendell, A. P.; Burant, J. C.; Iyengar, S. S.; Tomasi, J.; Cossi, T. M.; Millam, J. M.; Klene, M.; Adamo, C.; Cammi, R.; Ochterski, J. W.; Martin, R. L.; Morokuma, K.; Farkas, O.; Foresman, J. B.; Fox, D. J. Gaussian 16, Revision A.03, Gaussian, Inc., Wallingford CT, **2016**.
(71) Bryden, F.; Boyle, R. W. A Mild, Facile, One-Pot Synthesis of Zinc Azido Porphyrins as Substrates for Use in Click Chemistry. *Synlett*, **2014**, *24*, 1978–1982.
(72) Landrum, J. T.; Grimmett, D.; Haller, K. J.; Scheidt, W. R.; Reed, C. A. Imidazolate- and Oxo-Bridged Metalloporphyrins. *J. Am. Chem. Soc.* **1981**, *103*, 2640–2650.
(73) Parham, W. E.; Wright, C. D. Formation of Naphthalenes from Indenes. IV.[1] The Effect of Substitution at the Ethylenic Double Bond*. *J. Org. Chem.* **1957**, *22*, 1473–1477.
(74) Bleasdale, D. A.; Jones, D. W. 2-Benzopyran-3-Ones as Synthetic Building Blocks; Regioselective Diels–Alder Additions with Simple Olefins Leading to Aromatic Steroids. *J. Chem. Soc. Perkin* **1991**, *1*, 1683–1692.

(75) Harvey, P. D.; Tasan, S.; Gros, C. P.; Devillers, C. H.; Richard, P.; Gendre, P. L.; Bodio, E. Ruthenium and Osmium Complexes of Phosphine-Porphyrin Derivatives as Potential Bimetallic Theranostics: Photophysical Studies. *Organometallics* **2015**, *34*, 1218–1227.

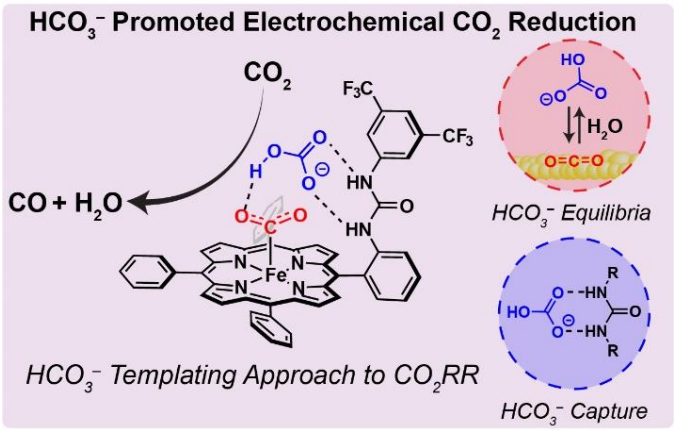
Chapter 4: Templating Bicarbonate in the Second Coordination Sphere Enhances Electrochemical Carbon Dioxide Reduction Catalyzed by Iron Porphyrins

Portions of this work were published in the following scientific journal:
Jeffrey S. Derrick, Matthias Loipersberger, Sepand K. Nistanaki, Martin Head-Gordon, Eva M. Nichols, Christopher J. Chang. Templating Bicarbonate in the Second Coordination Sphere Enhances Electrochemical CO_2 Reduction Catalyzed by Iron Porphyrins. *Journal of the American Chemical Society*, **2022**, *in revision*, 10.26434/chemrxiv-2022-6ctz6.

Specific contributions: Sepand K. Nistanaki helped with synthesis. Dr. Matthias Loipersberger did the bicarbonate modeling and pK_a calculations. Dr. Eva M. Nichols helped with synthesis and collection and interpretation of some of the electrochemical data.

4.1 Abstract

Bicarbonate-based electrolytes are ubiquitous in aqueous electrochemical CO_2 reduction, particularly in heterogenous catalysis, where they demonstrate improved catalytic performance relative to other buffers. In contrast, the presence of bicarbonate in organic electrolytes and its roles in homogenous electrocatalysis remain underexplored. Here, we investigate the influence of bicarbonate on iron porphyrin-catalyzed electrochemical CO_2 reduction. We show that bicarbonate is a viable proton donor in organic electrolyte (pK_a = 20.8 in DMSO) and that urea pendants in the second coordination sphere can be used to template bicarbonate in the vicinity of a molecular iron porphyrin catalyst. The templated binding of bicarbonate significantly decreases its pK_a value, resulting in a 1500-fold enhancement in catalytic rates relative to unmodified parent iron porphyrin. This work emphasizes the importance of bicarbonate speciation in wet organic electrolytes and establishes second-sphere bicarbonate templating as a design strategy to harness this adventitious acid and enhance CO_2 reduction catalysis.



4.2 Introduction

The capture and conversion of CO_2 as a cheap, abundant C1 building block into value-added chemical products represents a promising solution to global climate challenges.[1–3] The use of electricity to drive the transformation of CO_2 is an attractive strategy[4] but it requires the development of efficient and selective catalysts that facilitate the CO_2 reduction reaction (CO_2RR) over competitive side reactions such as the hydrogen evolution reaction (HER).[5,6] Heterogeneous systems represent some of the most active catalysts for aqueous CO_2RR,[7–10] where abundant and non-toxic water can be used both as a solvent and as a proton source. Indeed, bicarbonate-based electrolytes are ubiquitous in these aqueous, heterogenous systems, where they have been shown to lead to higher CO_2RR efficiencies compared to other buffered electrolytes.[11–14]

Under aqueous conditions, CO_2 hydration establishes complex equilibria between dissolved CO_2, carbonic acid, bicarbonate, and carbonate.[11] In this context, the roles that bicarbonate (HCO_3^-) plays to enhance the CO_2RR at heterogeneous metal surfaces are debated. Although there is general consensus that bicarbonate is not a direct substrate for reduction, it has been proposed that it serves in a myriad of roles, including as a proton donor,[11–13,15] pH buffer,[7,12,16] or to facilitate an increase in the local concentration of CO_2 near the electrode surface through fast equilibrium between HCO_3^- and soluble CO_2 (**Figure 4.1**).[16] We hypothesized that bicarbonate may be similarly important in homogenous electrochemical systems operating in organic electrolytes; to the best of our knowledge, this topic has remained largely underexplored. We now report that templating bicarbonate binding in a well-defined molecular electrocatalysts using second-sphere coordination pendants can increase its acidity and enhance electrochemical CO_2 reduction.

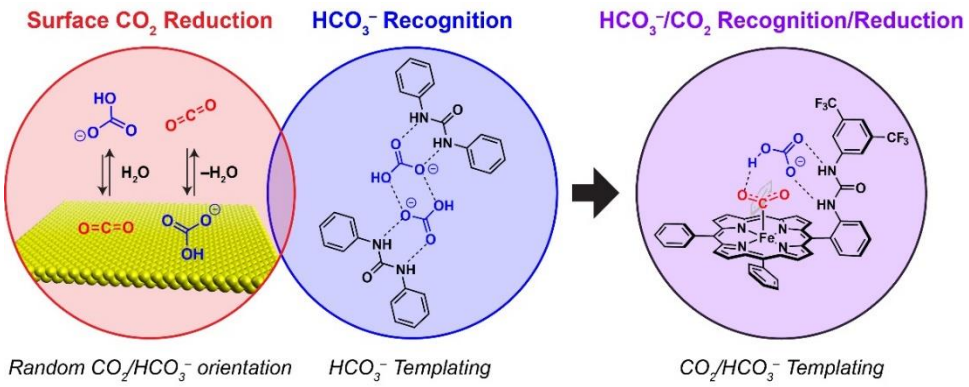


Figure 4.1. Templating bicarbonate in the second-coordination sphere of well-defined molecular catalysts can enhance the electrochemical carbon dioxide reduction reaction (CO_2RR). Merging the concept of the importance of bicarbonate-based aqueous electrolytes in heterogeneous CO_2RR with anion recognition in bis-aryl urea moieties can provide an effective design strategy for promoting homogeneous CO_2RR, as illustrated by the canonical iron porphyrin catalyst platform.

To illustrate the general concept for this current study, we chose iron tetraphenylporphyrin (Fe-TPP) as a representative member of a prototypical class of molecular CO_2RR catalysts.[17–21] Inspired by the field of anion receptor chemistry,[22,23] we sought to enhance the interaction of the Fe-TPP catalyst with bicarbonate by incorporating a bis-aryl urea moiety into the second

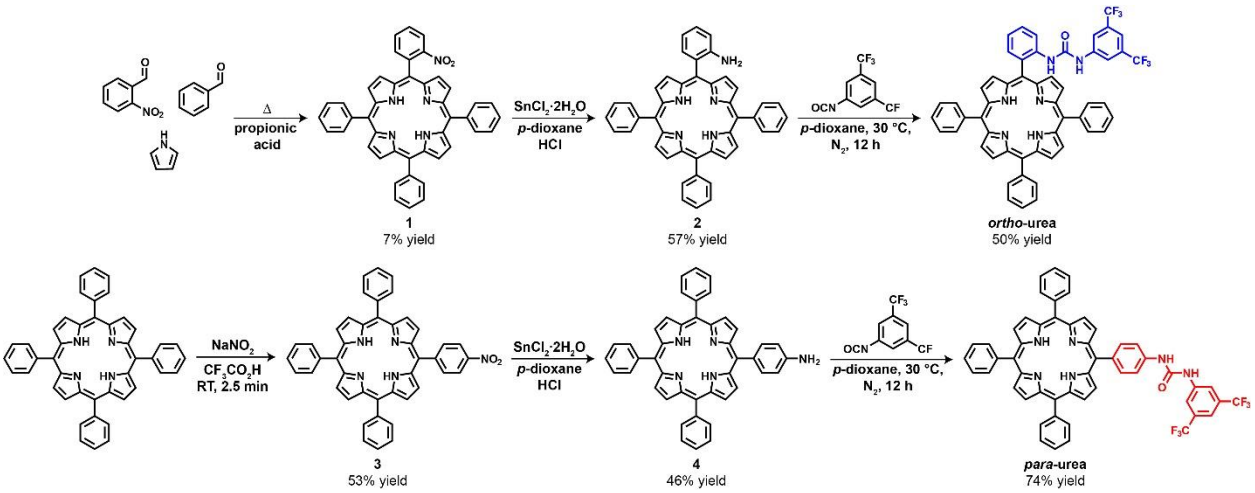
coordination sphere (**Figure 4.1**). (Thio)ureas are known to be highly effective motifs for selective binding of bicarbonate and other oxyanions, and thus have been incorporated into diverse frameworks such as amide-linked macrocycles,[24] cyclopeptide cages,[25] and tripodal[26] and linear[27–31] ligand scaffolds for recognition and sensing applications. Indeed, previous reports from our laboratory[6,32,33] and others[34–47] have established the ability of second coordination sphere pendants to enhance CO_2RR catalysis. As such, we reasoned that functionalization of Fe-TPP with a properly-positioned urea moiety would promote advantageous interactions with bicarbonate through templated hydrogen bonding interactions (**Figure 4.1**). Integration of urea moieties into porphyrin scaffolds to enhance CO_2 reduction through second-sphere hydrogen bonding interactions has been reported by Aukauloo and coworkers[48–51] but to the best of our knowledge, the anion recognition and templating properties of ureas has not been exploited in CO_2 reduction catalysis.

4.3 Results and Discussion

4.3.1 Design and Synthesis of Well-Defined Iron Porphyrin Catalysts Modified with Second-Sphere Urea Pendants to Template Bicarbonate Binding

To illustrate the general concept for this current study, we chose iron tetraphenylporphyrin (Fe-TPP) as a representative member of a prototypical class of molecular CO_2RR catalysts.[17–21] Inspired by the field of anion receptor chemistry,[22,23] we sought to enhance the interaction of the Fe-TPP catalyst with bicarbonate by incorporating a bis-aryl urea moiety into the second coordination sphere (**Figure 4.1**). (Thio)ureas are known to be highly effective motifs for selective binding of bicarbonate and other oxyanions, and thus have been incorporated into diverse frameworks such as amide-linked macrocycles,[24] cyclopeptide cages,[25] and tripodal[26] and linear[27–31] ligand scaffolds for recognition and sensing applications. Indeed, previous reports from our laboratory[6,32,33] and others[34–47] have established the ability of second coordination sphere pendants to enhance CO_2RR catalysis. As such, we reasoned that functionalization of Fe-TPP with a properly-positioned urea moiety would promote advantageous interactions with bicarbonate through templated hydrogen bonding interactions (**Figure 4.1**). Integration of urea moieties into porphyrin scaffolds to enhance CO_2 reduction through second-sphere hydrogen bonding interactions has been reported by Aukauloo and coworkers[48–51] but to the best of our knowledge, the anion recognition and templating properties of ureas has not been exploited in CO_2 reduction catalysis. We now show that proper positioning of this two-point hydrogen-bond moiety in the second sphere can promote bicarbonate-mediated CO_2RR in a well-defined molecular system.

Specifically, we targeted two positional isomers of urea-appended tetraphenylporphyrins, designated *ortho*-urea and *para*-urea according to the pendant's placement around the *meso* aryl ring. We predicted that the pendant group of Fe-*ortho*-urea would be located appropriately to enhance CO_2RR through direct interactions with Fe-bound CO_2 or by positioning a templated bicarbonate in the vicinity of the Fe active site, whereas the Fe-*para*-urea would serve as a positional negative control that was not expected to promote such effects. Synthesis of the functionalized porphyrins was achieved through a similar strategy utilized for amide analogs (**Scheme 4.1**).[32] Briefly, the *ortho* isomer was accessed through the condensation of 2-nitrobenzaldehyde, benzaldehyde, and pyrrole to give the mono-(2-nitrophenyl)porphyrin starting material (1). Reduction with tin chloride gave the subsequent amine, mono-(2-aminophenyl)porphyrin (2), and the reaction with 3,5-bis(trifluoromethyl)phenyl isocyanate afforded the target *ortho*-urea ligand. The *para* positional control was prepared from commercially available *meso*-tetraphenylporphyrin (TPP). Regioselective nitration of TPP with sodium nitrite in trifluoroacetic acid gave the corresponding mono-(4-nitrophenyl)porphyrin (3). Identical reduction and urea formation reaction conditions with tin chloride and 3,5-bis(trifluoromethyl)phenyl isocyanate, respectively, yielded the desired *para*-urea ligand. Metalation with iron bromide in anhydrous tetrahydrofuran with 2,6-lutidine as the base gave the desired urea-appended iron porphyrin complexes.



Scheme 4.1. Synthesis of *ortho*- and *para*-urea functionalized tetraphenylporphyrin ligands.

4.3.2 Structural Characterization Establishes the Ability of Urea Pendants to Poise Anions Proximal to the Porphyrin Metal Center

To establish connectivity and positioning of the urea moiety relative to the metal center, we sought to grow crystals suitable for X-ray diffraction analysis. Unfortunately, we were unable to obtain single crystals of Fe-*ortho*-urea due to severe twinning caused by stacking of the thin plate-shaped crystals. Instead, slow vapor diffusion of water into a concentrated DMF solution of the zinc analog, Zn-*ortho*-urea**,** produced diffraction-quality crystals (**Figure 4.2**, **Table 4.4**). As is typical for pentacoordinate Zn porphyrins, the Zn atom is axially coordinated to a DMF molecule causing displacement from the porphyrin plane by 0.331 Å. Unlike what was observed for the amide analog,[32] the urea moiety is engaged in tight hydrogen bonding with an exogenous DMF molecule and is distorted slightly from planarity in the solid state due to crystal packing interactions. The Zn-*ortho*-urea structure validates the ability of the urea pendant to form hydrogen bonding networks with solvent molecules and presumably also oxyanions such as bicarbonate.

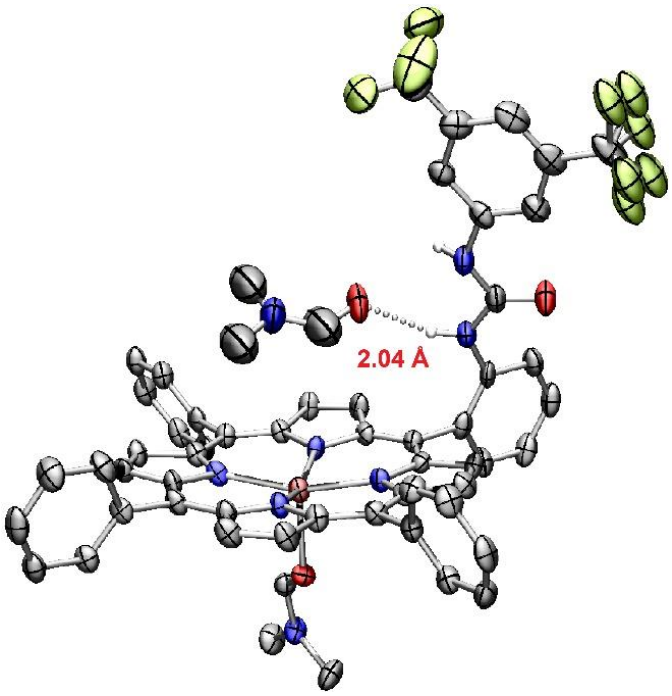


Figure 4.2. Solid-state structure of Zn-*ortho*-urea determined by single-crystal X-ray diffraction, showing the ability of a second-sphere urea pendant to poise an oxyanion proximal to the porphyrin metal center. Non-coordinated solvent molecules not participating in H-bonding interactions and C–H hydrogen atoms have been omitted for clarity. H-bonding is depicted by the dashed line. Brown, grey, blue, red, and green ellipsoids signify Zn, C, N, O, and F atoms, respectively. Thermal ellipsoids are plotted at the 50% probability level.

4.3.3 Electrochemical Carbon Dioxide Reduction Catalyzed by Urea-Modified Iron Porphyrin Complexes

With the iron complexes in hand, we sought to evaluate their electrochemical properties under an inert atmosphere (**Figure 4.3a**). Cyclic voltammograms (CVs) for the urea-functionalized iron porphyrin complexes and Fe-TPP were measured in dry DMF electrolyte (0.10 M $TBAPF_6$, **Figure 4.3a**). Three distinct redox events are observed for all three complexes at approximately –0.6, –1.5, and –2.1 V *vs* Fc/Fc^+ corresponding to the formal Fe(III/II), Fe(II/I), and Fe(I/0) couples, respectively. At a scan rate of 100 mV/s, the Fe(I/0) couples exhibit chemically- and electrochemically reversible behavior. The Fe(I/0) standard potentials, E^0_{cat}, were determined under inert atmosphere by taking an average of three independent scans and are given in **Table 4.1**. CVs of Fe-*ortho*-urea and Fe-*para*-urea show additional redox waves apart from the three discussed above. Given the high affinity of urea moieties for halides,[52] we speculate that these additional waves may arise from electronically-distinct porphyrins where the urea is bound to Br^- or PF_6^-. Variable scan rate data collected for Fe-*ortho*-urea and Fe-*para*-urea establish that the peak cathodic currents are linearly correlated with the square root of the scan rate, indicating that these complexes are freely diffusing in solution (**Figure 4.4**).

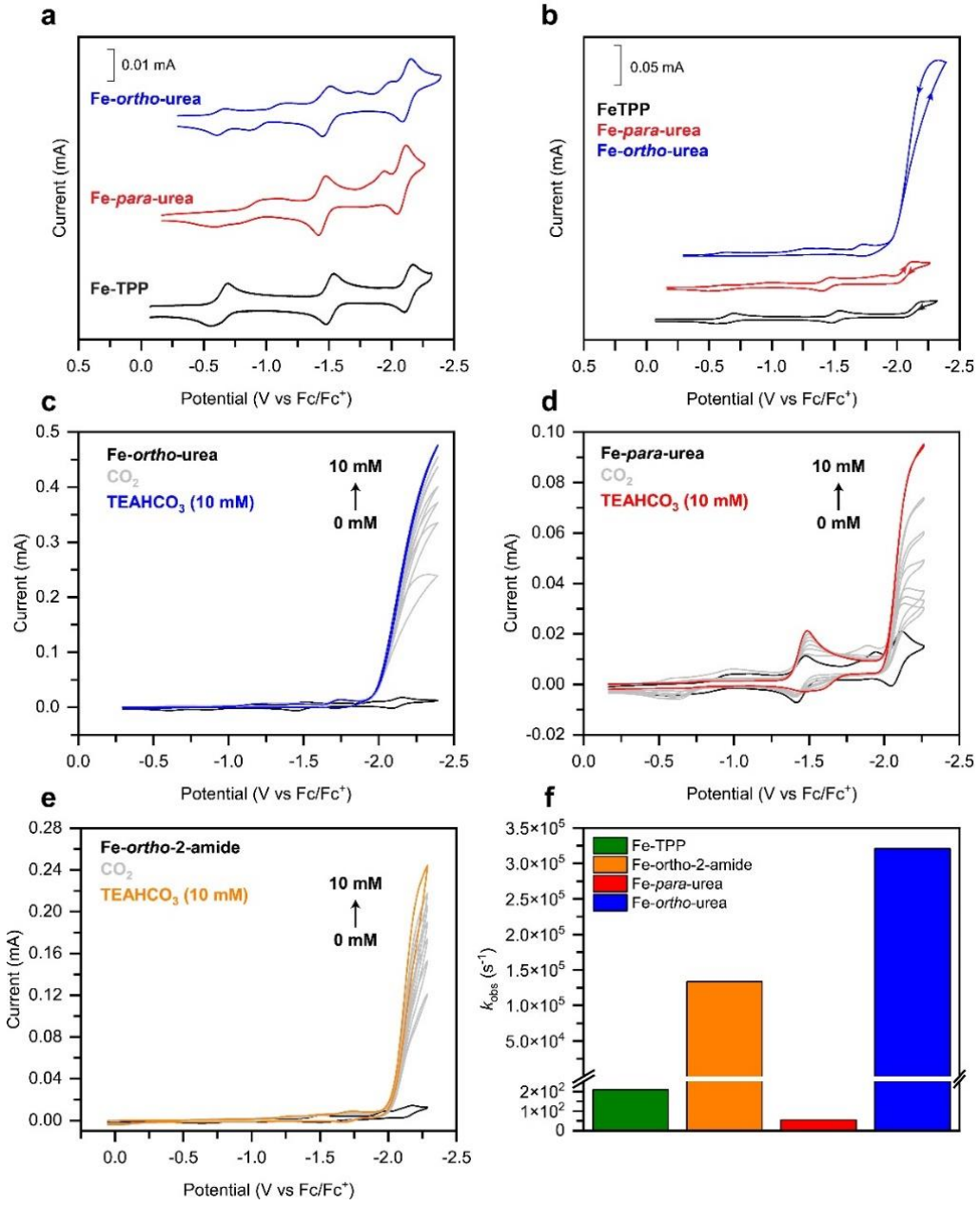


Figure 4.3. Electrochemical analysis of iron porphyrin complexes. Cyclic voltammograms (CVs) of Fe-TPP (black), Fe-*para*-urea (red), and Fe-*ortho*-urea (blue) under (a) Ar and (b) CO_2 atmosphere, showing a marked catalytic current enhancement for the *ortho* analog. Comparison of the catalytic performance of iron porphyrin complexes under CO_2 atmosphere in the presence of bicarbonate. Titrations of $TEAHCO_3$ into solutions of (c) Fe-*ortho*-urea, (d) Fe-*para*-urea, and (e) Fe-*ortho*-2-amide show a marked enhancement of catalytic activity with this additive. (f) Direct comparison of the observed rate constants (k_{obs}) extracted from FOWA of the iron porphyrin complexes under CO_2 saturated electrolyte with 10 mM $TEAHCO_3$ show that the Fe-*ortho*-urea has the largest current enhancement, with a 1500-fold increase over Fe-TPP. Conditions: 0.1 M $TBAPF_6$ in DMF, 1 mM Fe complexes, 0 – 10 mM $TEAHCO_3$, 100 mV/s scan rate.

Table 4.1. Summary of the standard reduction potentials (E^0_{cat}) for Fe-TPP and the urea-functionalized catalysts.

Catalyst	E^0_{cat} (V vs Fc/Fc$^+$)
Fe-TPP	–2.14
Fe-*para*-urea	–2.18
Fe-*ortho*-urea	–2.06

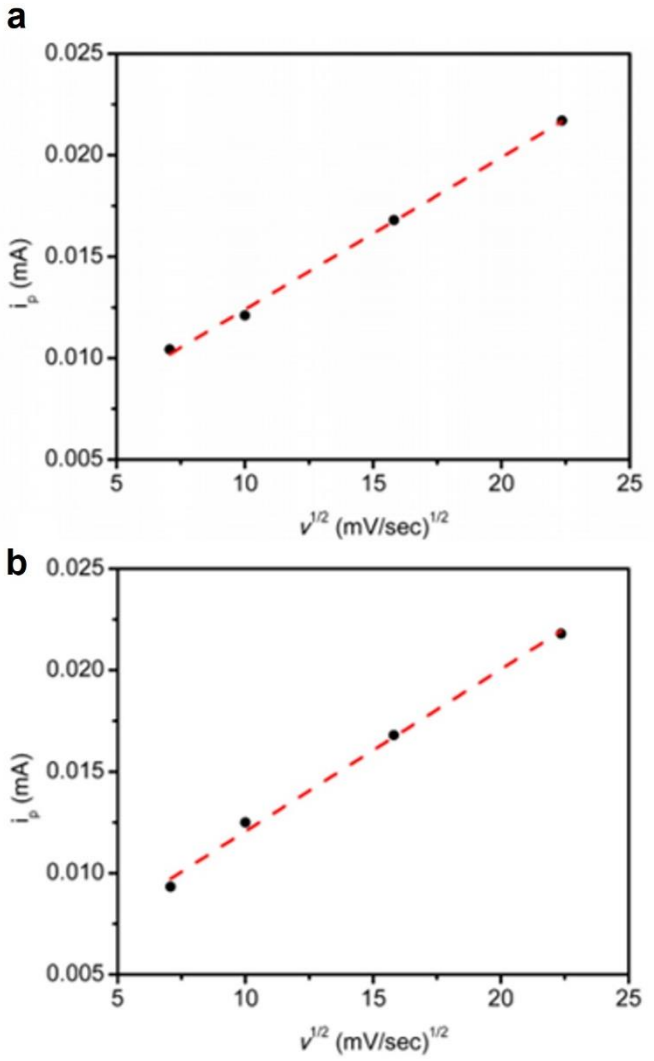


Figure 4.4. Linear correlation between the square root of the scan rate ($v^{1/2}$) and peak cathodic current (i_p) of the formal Fe(I/0) couple in 0.1 M $TBAPF_6$/DMF for (a) Fe-*ortho*-urea and (b) Fe-*para*-urea.

Under a CO_2 atmosphere but with no added proton source, catalytic responses are observed for all three complexes, with Fe-*ortho*-urea exhibiting a much larger current enhancement relative

to positional control Fe-*para*-urea and unmodified Fe-TPP. Fe-*ortho*-urea also displays significant curve-crossing behavior, where current on the return scan is higher than the current on the forward scan (**Figure 4.3b**, blue line). Curve-crossing is often indicative of an initial induction period where a more active catalytic species is generated *in situ* and thus its concentration increases as a function of time.[53] Interestingly, curve-crossing was not observed for Fe-*para*-urea or amide-functionalized analogs,[32] but has appeared in structurally-related urea porphyrins reported by Aukauloo and coworkers,[48–51] though they did not discuss this observation. Together, these data suggest that curve crossing depends on both the positioning and number of H-bond donors in the second coordination sphere, and hints that *ortho* urea groups engage in unique interactions during CO_2RR. Comparing the two control catalysts under CO_2, Fe-*para*-urea has a smaller catalytic response at more negative onset potential than Fe-TPP, which is unexpected given the electronic scaling relationship that exists between E^0_{cat} and catalytic rate, where catalysts with more negative E^0_{cat} values are expected to have greater driving force for CO_2 reduction.[54] A more detailed investigation of Fe-*para*-urea revealed that the observed rate constant for CO_2 reduction, k_{obs}, (obtained from Foot-of-the-Wave Analysis, FOWA, according to procedures described in the Materials and Methods section) exhibits first-order dependence on the catalyst concentration only at concentrations below 0.4 mM (**Figure 4.5**). At the higher concentrations used for cyclic voltammetric and preparative scale electrolysis experiments (*i.e.*, 1 mM), k_{obs} is inversely correlated with the concentration of Fe-*para*-urea, presumably due to a dimerization process occurring in solution (**Figures 4.5**). Similar dimers generated through H-bond templating with exogenous anions have been extensively observed for linear bis-urea ligands,[27] which may explain the lower-than-expected observed activity of Fe-*para*-urea.

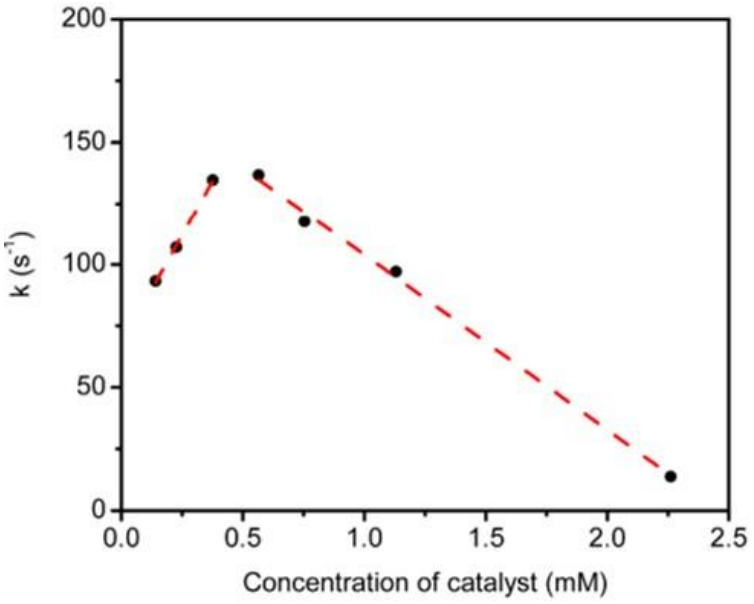


Figure 4.5. Variation of observed catalytic rate constant, k_{obs}, as a function of the concentration of Fe-*para*-urea catalyst showing the effects of presumed dimerization at concentrations above 0.4 mM catalyst. Conditions: 0.1 M $TBAPF_6$ in DMF, 10 mM phenol.

4.3.4 Positional Effects of Second-Sphere Urea Pendants on Bicarbonate-Mediated Enhancement of Electrochemical Carbon Dioxide Reduction

Given our hypotheses regarding the important roles of bicarbonate in non-aqueous CO_2RR and the possible templating ability of the pendant urea, we examined how the catalytic responses of our porphyrins change upon addition of tetraethylammonium bicarbonate ($TEAHCO_3$) in DMF electrolyte ($TBAPF_6$). Titration of $TEAHCO_3$ into a solution of Fe-*ortho*-urea under CO_2 atmosphere results in a large enhancement in the catalytic wave (**Figure 4.3c**). Interestingly, the curve-crossing behavior was eliminated at higher concentrations of bicarbonate (~10 mM). Comparison of the catalytic performance of Fe-*ortho*-urea to Fe-*para*-urea and Fe-TPP in the presence of $TEAHCO_3$ is provided in **Figure 4.3**. The data show that titration of $TEAHCO_3$ into a CO_2-saturated solution of Fe-*para*-urea or Fe-TPP (**Figure 4.6**) also results in a catalytic enhancement, but much less than what is observed for Fe-*ortho*-urea (**Figure 4.7**). Interestingly, the titration of $TEAHCO_3$ into a solution of our previously reported Fe-*ortho*-2-amide catalyst[32] under a CO_2 atmosphere also results in a large increase in the catalytic current (**Figure 4.3e**). Thus, it appears that bicarbonate addition results in a generalizable enhancement in catalytic activity with iron porphyrin catalysts, suggesting that bicarbonate may function as a proton donor under these conditions.

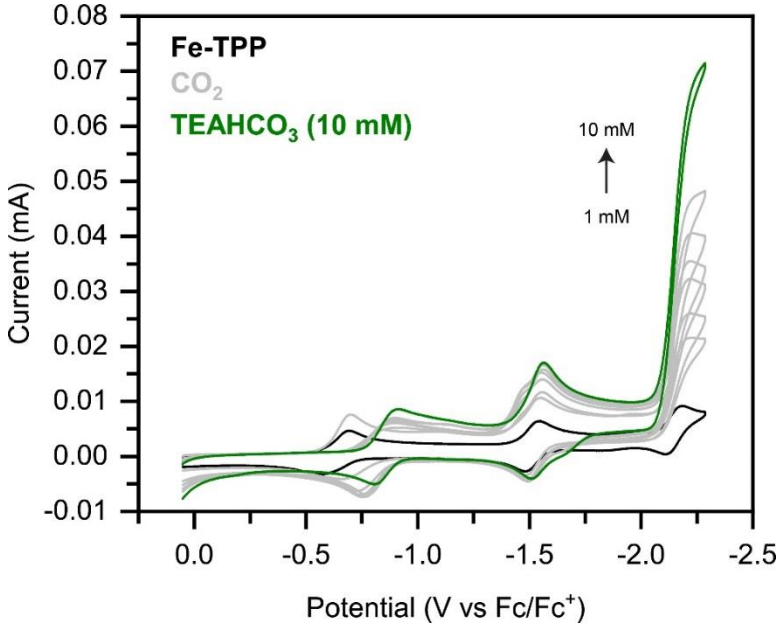


Figure 4.6. Cyclic voltammograms of Fe-TPP in 0.1 M $TBAPF_6$ in DMF under CO_2 atmosphere with the addition of increasing amounts of $TEAHCO_3$ additive (0 – 10 mM). 100 mV/s scan rate was used for all measurements.

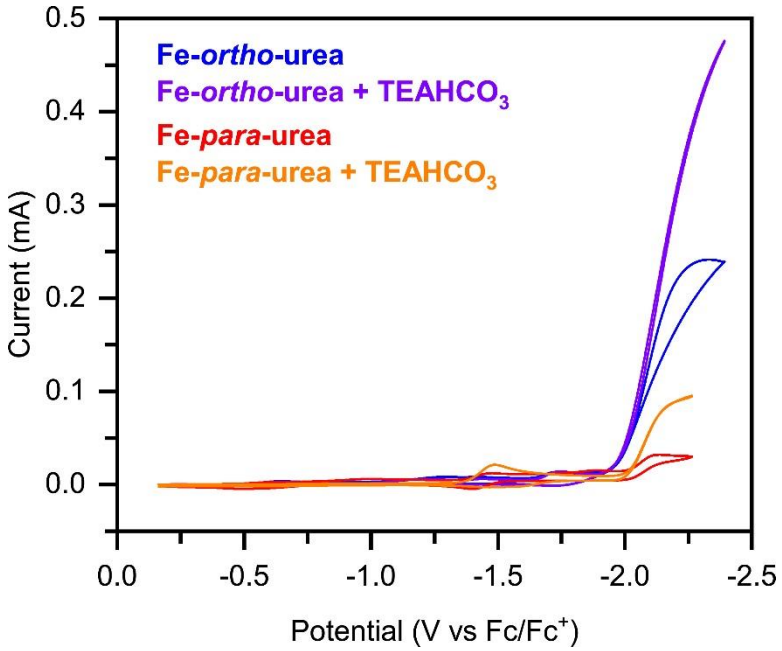


Figure 4.7. Cyclic voltammograms comparing the catalytic waves of Fe-*ortho*-urea in the absence (blue line) and presence (purple line) of $TEAHCO_3$ to Fe-*para*-urea in the absence (red line) and presence of $TEAHCO_3$ (orange) under CO_2 atmosphere. Condition: 0.1 M $TBAPF_6$ in DMF, 10 mM $TEAHCO_3$, 100 mV/s scan rate.

Surprisingly, we were unable to find a reported pK_a value for HCO_3^- in non-aqueous media and therefore measured this value experimentally using a spectrophotometric method; we determined the pK_a of $TEAHCO_3$ in DMSO to be 20.8 ± 0.1 (**Figure 4.8**). This result supports the notion that bicarbonate acts as the principal proton source under our electrolysis conditions. Furthermore, we note that the pK_a (DMSO) of HCO_3^- is comparable to other typical acids for electrochemical CO_2RR in organic solution such as phenol (18.0), 2,2,2-trifluoroethanol (23.6), and water (32.0).[55] As such, we sought to consider the role of equilibria involving HCO_3^-, including the concentration of basic additives or residual water in a non-aqueous electrolyte.

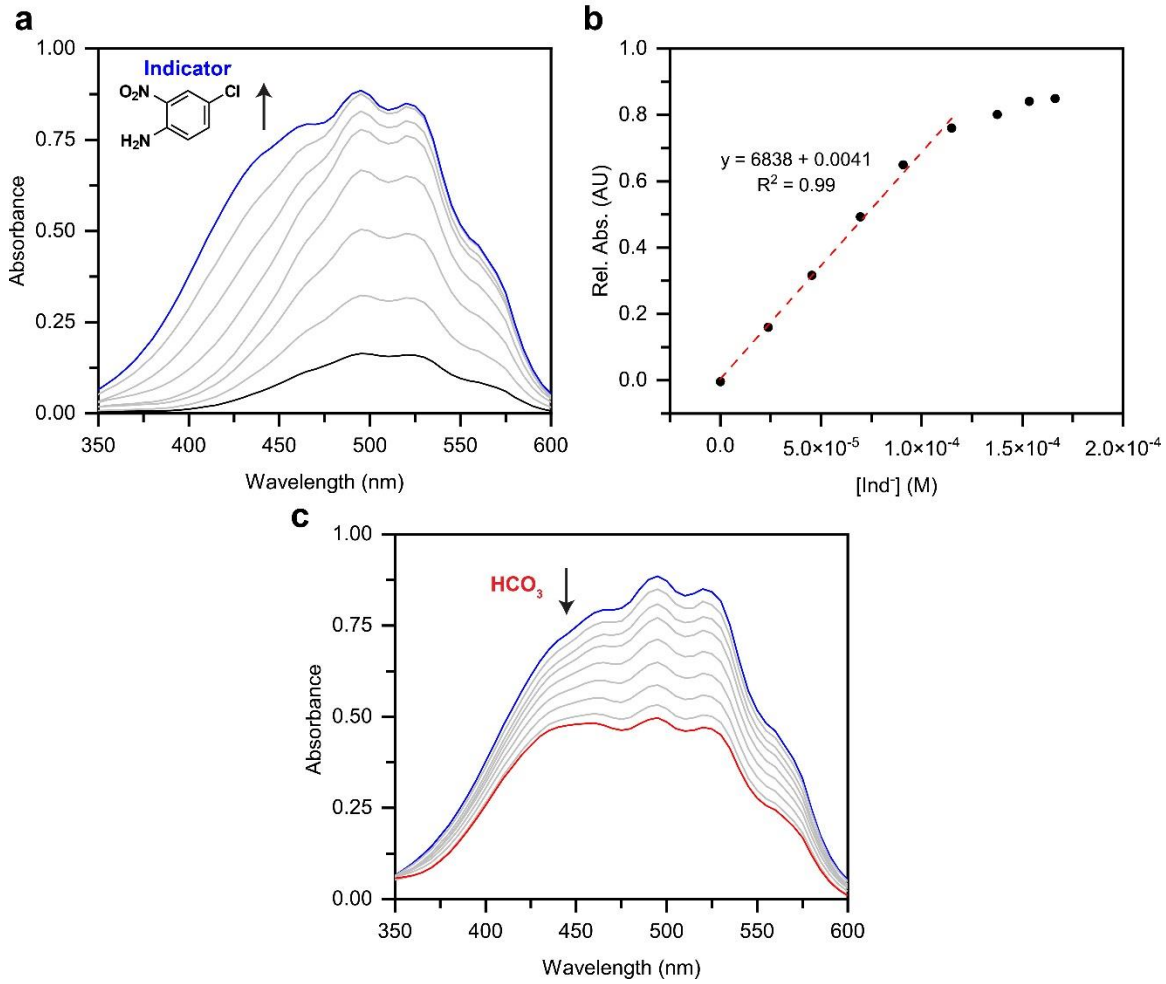


Figure 4.8. Representative spectrophotometric titrations to determine the pK_a of $TEAHCO_3$. (a) Titration of 4-chloro-2-nitroaniline into a solution of K-dimsyl base. (b) The aniline indicator was added in small aliquots until no further spectral change at 520 nm was observed signifying the full consumption of K-dimsyl base. (c) Spectral changes observed upon the titration of $TEAHCO_3$ into a solution of deprotonated 4-chloro-2-nitroaniline. Note that the decrease in the absorption at 530 nm as the deprotonated indicator is protonated by HCO_3^-.

To determine the selectivity and stability for electrochemical CO_2 reduction, preparative-scale controlled potential electrolysis (CPE) experiments were conducted in a CO_2-saturated gas-tight H-cell with and without the addition of 100 mM $TEAHCO_3$ (**Figures 4.9** and **4.10**, **Table 4.2**). The urea-appended catalysts are stable during catalysis, with steady current density maintained across the hour-long CPE experiments. At the same applied potential of -2.18 V *vs* Fc/Fc^+, Fe-*ortho*-urea operates at much higher current densities (1.61 mA/cm^2) compared to Fe-*para*-urea (0.37 mA/cm^2). Moreover, we also observe a stark difference in Faradaic efficiency for CO production (FE_{CO}): Fe-*ortho*-urea achieves an average FE_{CO} of 98% while Fe-*para*-urea achieves an average FE_{CO} of only 3%. Addition of $TEAHCO_3$ (100 mM) causes the average current density of Fe-*ortho*-urea and Fe-*para*-urea to increase to 3.08 mA/cm^2 and 0.98 mA/cm^2, respectively, and are indicative of a large catalytic rate enhancement due to the bicarbonate additive. Fe-*ortho*-urea maintains a high FE_{CO} in the presence of $TEAHCO_3$ (93%) while the FE_{CO}

for Fe-*para*-urea increases to 54%. No H_2 (or a trace amount) is detected for either catalyst under either of these conditions (**Table 4.2**). We speculate that the low FE_{CO} observed for the *para*-functionalized analog may be due to its propensity to dimerize into a catalytically-inactive form *(vide supra)*, where hydrogen bonding between the urea moiety and bicarbonate may disrupt formation of this dimer and lead to an improvement in FE_{CO}.

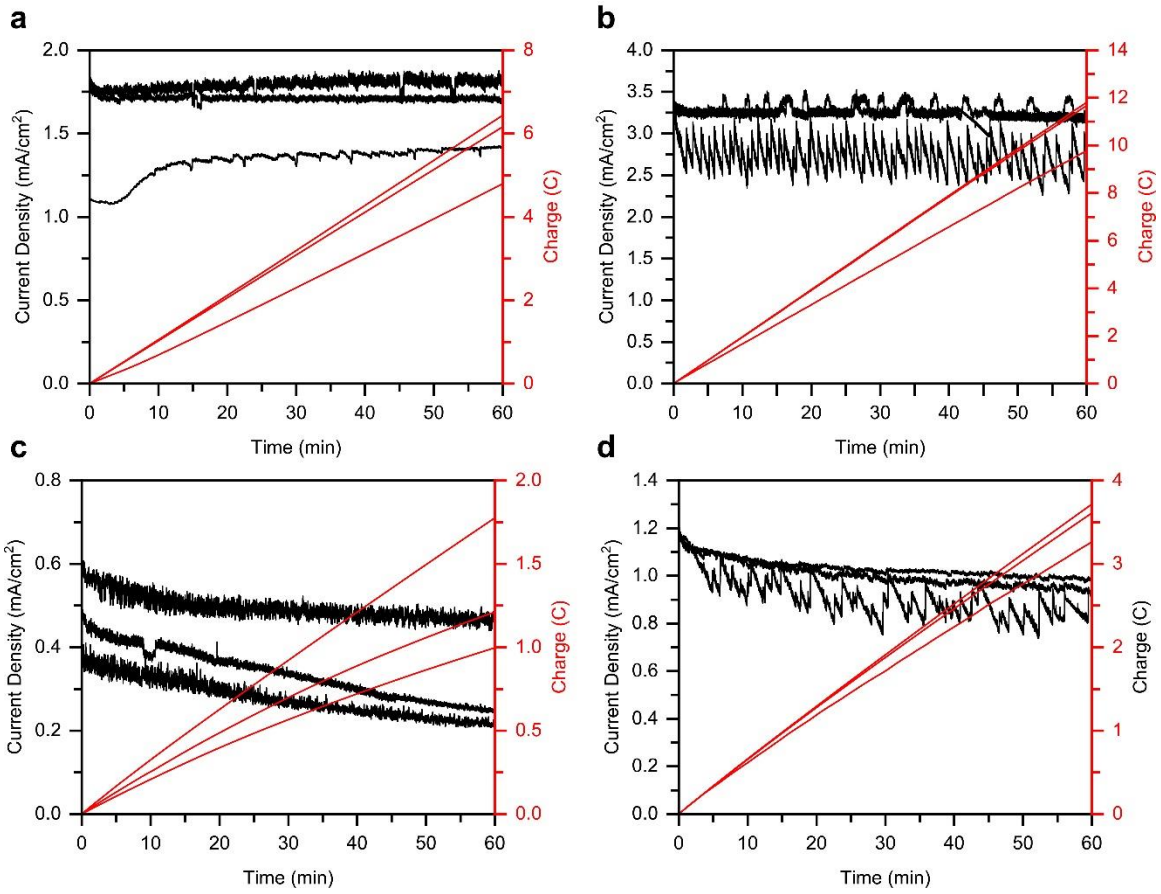


Figure 4.9. Controlled potential electrolysis, collected in triplicate, under CO_2 atmosphere of (a) Fe-*ortho*-urea in the absence and (b) presence of $TEAHCO_3$. (b) Controlled potential electrolysis of the positional control, Fe-*para*-urea, under CO_2 atmosphere in the (c) absence or (d) presence of $TEAHCO_3$. The current density vs time plots are shown in black and the accompanying accumulation of charge across the one-hour electrolysis experiments are plotted in red. Conditions: Onset potential = –2.18 V vs Fc/Fc^+; 1 mM iron prophryins; 100 mM $TEAHCO_3$.

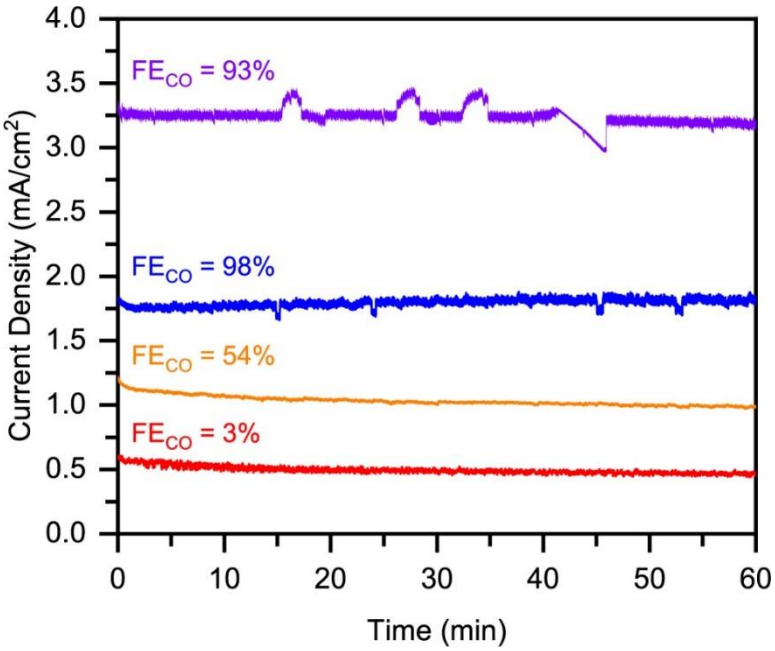


Figure 4.10. Controlled potential electrolysis under CO_2 atmosphere of Fe-*para*-urea (red line) and Fe-*ortho*-urea (blue line) in the absence and presence of $TEAHCO_3$ (purple line = Fe-*ortho*-urea; orange line = Fe-*para*-urea). Faradaic efficiencies for CO production are noted. No H_2 was detected. All CPE data was collected in triplicate. The replicate runs and additional details can be found in **Table 4.2** and **Figure 4.9**. Conditions: 0.1 M $TBAPF_6$ in DMF, 1 mM Fe complexes, 100 mM $TEAHCO_3$.

Table 4.2. Controlled potential electrolysis replicates for Fe-*ortho*-urea and Fe-*para*-urea in the presence and absence of $TEAHCO_3$ (100 mM). The onset potential (E), charge (Q), Faradaic Efficiency for CO production (FE_{CO}), average current density (I_{avg}), and the average specific current density for CO production (j_{CO}) are provided. No H_2 gas was detected in any case.

Catalyst	E (V vs Fc/Fc^+)	Q (C)	FE_{CO} (%)	FE_{H_2} (%)	I_{avg} (mA/cm^2)	j_{CO} (mA/cm^2)
Fe-*ortho*-urea	–2.18	4.80	100	0	1.33	1.33
	–2.18	6.16	95	0	1.71	1.62
	–2.18	6.40	97	0	1.79	1.74
Fe-*ortho*-urea w/ $TEAHCO_3$	–2.18	11.8	100	0	3.28	3.28
	–2.18	11.7	88	0	3.24	2.85
	–2.18	9.80	92	0	2.72	2.50
Fe-*para*-urea	–2.18	1.78	8	0	0.49	0.04
	–2.15	1.20	1	0	0.34	<0.01
	–2.14	1.00	1	0	0.28	<0.01
Fe-*para*-urea w/ $TEAHCO_3$	–2.18	3.70	59	0.5	1.03	0.61
	–2.18	3.60	51	1.1	1.00	0.51
	–2.18	3.26	51	0	0.91	0.46

Having confirmed that CO is the unique catalytic product of electrochemical CO_2RR, we turned to Foot-of-the-Wave Analysis (FOWA) to obtain quantitative catalytic metrics. Observed catalytic rate constants (k_{obs}) of the iron porphyrin complexes were determined using FOWA in the presence of 0-10 mM $TEAHCO_3$ (limiting) and 0.23 M CO_2 (excess) (**Figures 4.11–4.14** and summarized in **Table 4.3**). The data show that catalysis has approximately first-order dependence on bicarbonate concentration for most of the iron porphyrins investigated. **Figure 4.3f** shows a comparison of k_{obs} values at [$TEAHCO_3$] = 10 mM and illustrates that proper positioning of the urea moiety increases k_{obs} by three to four orders of magnitude over parent Fe-TPP. The number of hydrogen bond donors also influences catalytic rates, with the two-point H-bond donor Fe-*ortho*-urea exhibiting a greater than two-fold improvement in k_{obs} relative to its one-point counterpart Fe-*ortho*-2-amide.

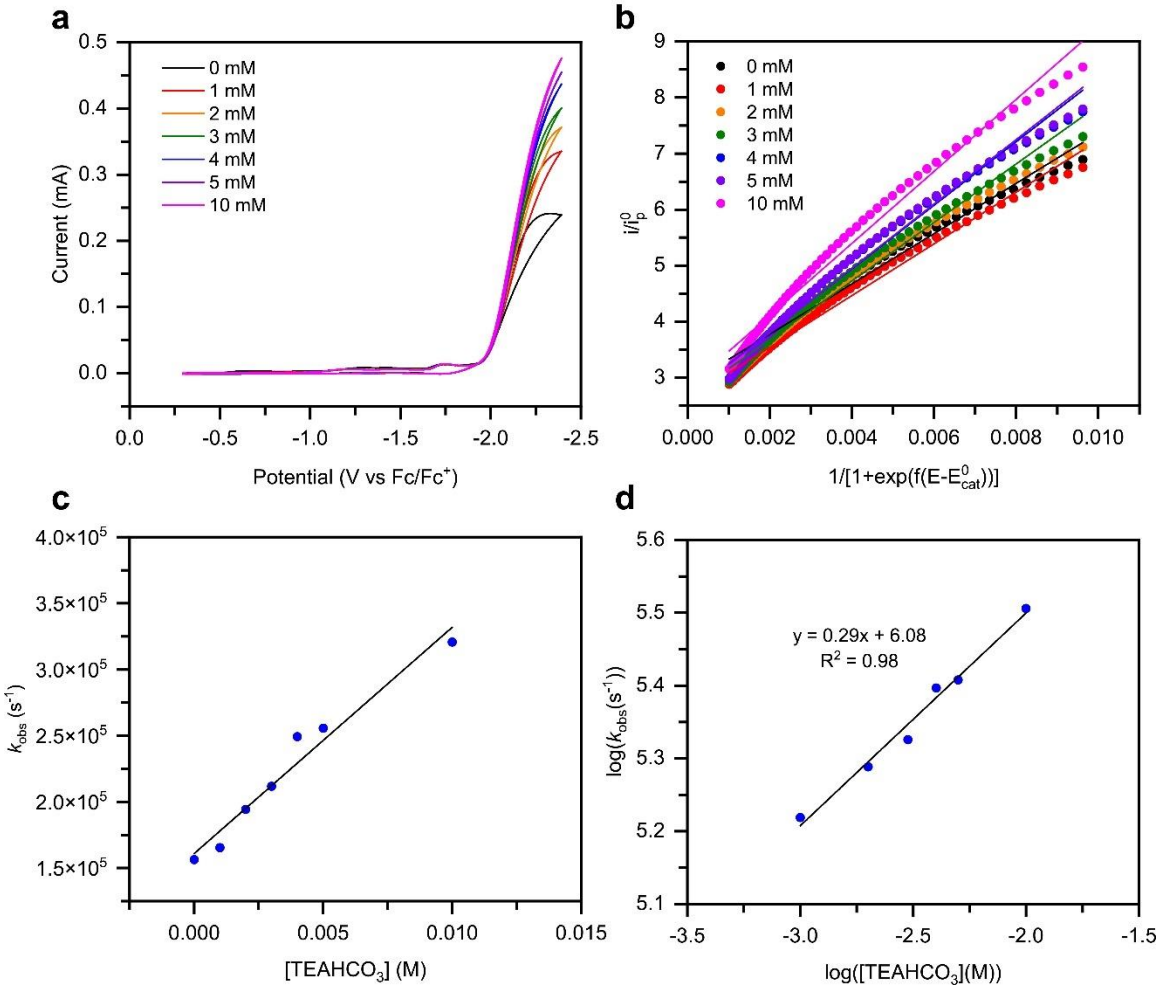


Figure 4.11. Foot-of-the-Wave Analysis (FOWA) of Fe-*ortho*-urea in the presence of bicarbonate additive. (a) Cyclic voltammograms of the titration of $TEAHCO_3$ into a solution of Fe-*ortho*-urea under CO_2 atmosphere. (b) FOW plots for Fe-*ortho*-urea (1 mM) as a function of $TEAHCO_3$ concentration (0 – 10 mM). Solid lines denote linear fits used to obtain the observed rate constants (k_{obs}). (c) k_{obs} as a function of bicarbonate concentration and the accompanying (d) log plots.

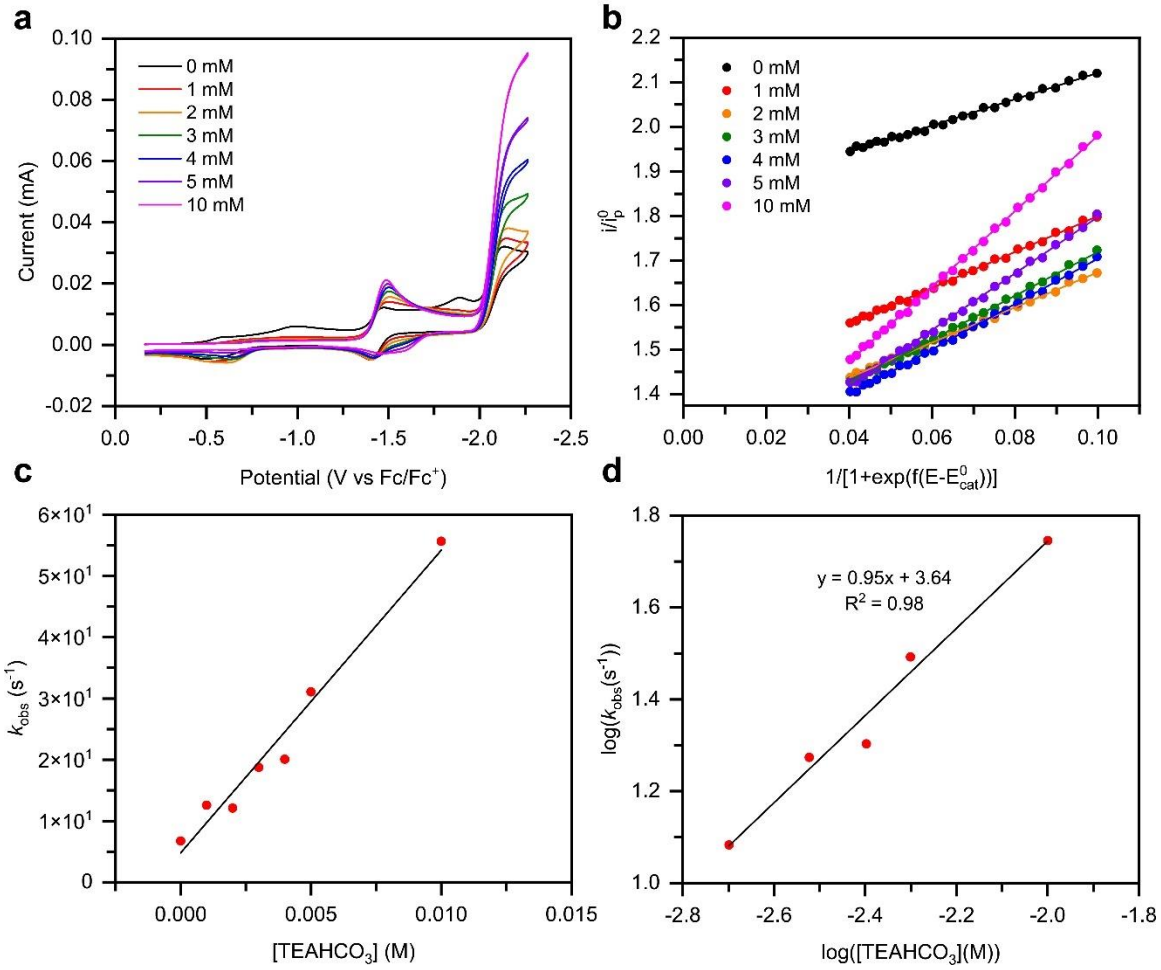


Figure 4.12. FOWA of Fe-*para*-urea in the presence of bicarbonate additive. (a) Cyclic voltammograms of the titration of $TEAHCO_3$ into a solution of Fe-*para*-urea under CO_2 atmosphere. (b) FOW plots for Fe-*para*-urea (1 mM) as a function of $TEAHCO_3$ concentration (0 – 10 mM). Solid lines denote linear fits used to obtain the observed rate constants (k_{obs}). (c) k_{obs} as a function of bicarbonate concentration and the accompanying (d) log plots.

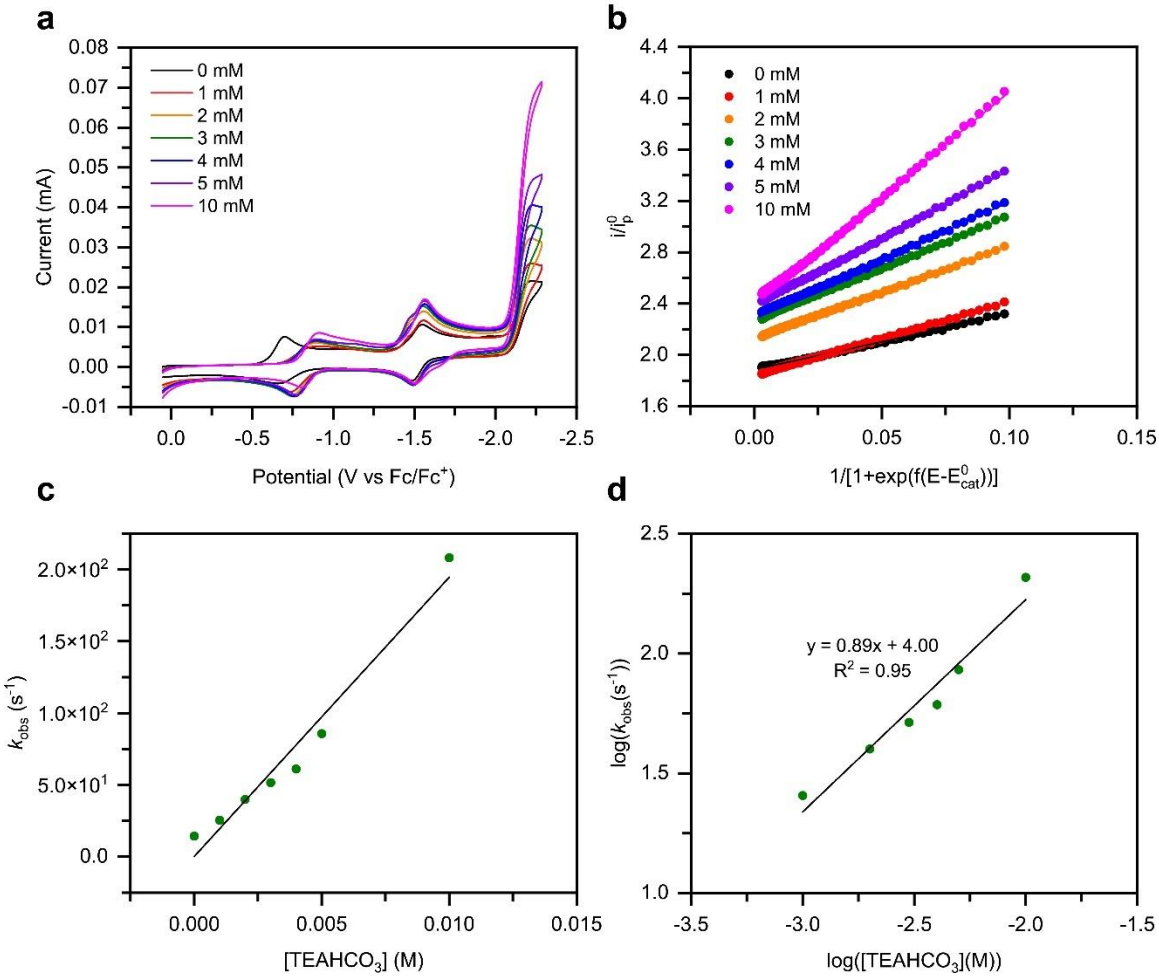


Figure 4.13. FOWA of Fe-TPP in the presence of bicarbonate additive. (a) Cyclic voltammograms of the titration of $TEAHCO_3$ into a solution of Fe-TPP under CO_2 atmosphere. (b) FOW plots for Fe-TPP (1 mM) as a function of $TEAHCO_3$ concentration (0 – 10 mM). Solid lines denote linear fits used to obtain the observed rate constants (k_{obs}). (c) k_{obs} as a function of bicarbonate concentration and the accompanying (d) log plots.

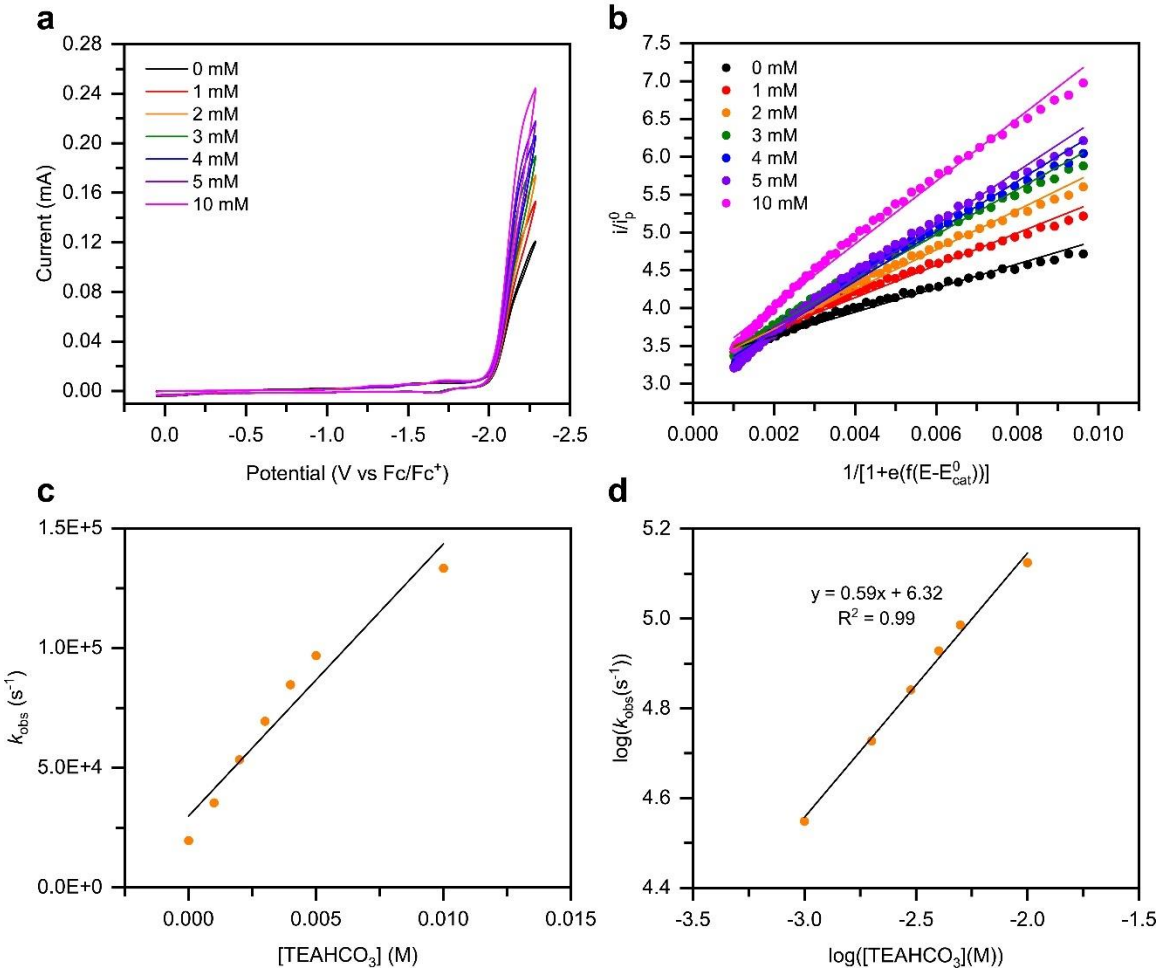


Figure 4.14. FOWA of Fe-*ortho*-2-amide in the presence of bicarbonate additive. (a) Cyclic voltammograms of the titration of $TEAHCO_3$ into a solution of Fe-*ortho*-2-amide under CO_2 atmosphere. (b) FOW plots for Fe-*ortho*-2-amide (1 mM) as a function of $TEAHCO_3$ concentration (0 – 10 mM). Solid lines denote linear fits used to obtain the observed rate constants (k_{obs}). (c) k_{obs} as a function of bicarbonate concentration and the accompanying (d) log plots.

Table 4.3. Summary of the observed rate constants (k_{obs}) for the reported iron porphyrin complexes. Rate constants were extracted using Foot-of-the-wave analysis.

Catalyst	**k_{obs} (s^{-1})**
Fe-TPP	208.2
Fe-*para*-urea	55.7
Fe-*ortho*-urea	320724.9
Fe-*ortho*-2-amide	13355.8

4.3.5 Second-Sphere Urea Pendants Increase Acidity of Templated Bicarbonate as a Proton Source to Promote Carbon Dioxide Reduction

We hypothesized that the *ortho* urea group engages in hydrogen bonding with bicarbonate and that this interaction enhances CO_2RR catalysis by 1) templating the bicarbonate proton close to CO_2-bound intermediates and 2) further lowering the pK_a of bicarbonate, thereby increasing the driving force for proton transfer. We first evaluated the binding of bicarbonate to the free-base *ortho*-urea ligand by ^{1}H NMR (**Figure 4.15**). Sub-stoichiometric titration of $TEAHCO_3$ causes an upfield shift of the aryl resonances and a complete loss of the urea-proton signals due to fast exchange with the bicarbonate proton. The control titration of $TEAHCO_3$ into a solution of unmodified TPP displays no spectral change, even upon the addition of excess bicarbonate, illustrating the strong interaction between the urea moiety and bicarbonate in solution. The interaction between bicarbonate and the porphyrins was further investigated by density functional theory (DFT) (**Figure 4.16** and **4.17**). DFT calculations show that bicarbonate does indeed hydrogen bond tightly to the urea moiety in a bidentate fashion that is not possible for the amide analog (**Figure 4.16**).[32] When the urea is in the *ortho*-position, the hydrogen bonding network positions the bicarbonate proton close (1.85 Å) to the iron-bound CO_2 moiety. This urea-templated bicarbonate binding effectively dangles its proton close to CO_2, enabling stabilization of the transition state and/or promoting proton transfer. This templating effect is not possible with only one hydrogen bond donor as the bicarbonate proton is positioned much further away from the CO_2-bound intermediate in the amide case (~2.33 Å). DFT calculations further predict the pK_a of bicarbonate to decrease by ~5.5 (relative to free HCO_3^-) due to this templated hydrogen bonding with Fe-*ortho*-urea. These computational results support a model in which the Fe-*ortho*-urea complex displays the largest catalytic enhancement owing to its ability to template and activate bicarbonate by synergistic second-sphere interactions. Taken together, these results suggest that the curve-crossing behavior may arise from changes to $CO_2/HCO_3^-/CO_3^{-2}$ equilibria in the diffusion layer over the time course of a CV scan. The kinetics of CO_2 hydration to generate HCO_3^- are relatively slow, so initial CO_2 reduction with Fe-*ortho*-urea likely proceeds *via* a slower proton-limited pathway where one CO_2 molecule serves as a Lewis acid to activate the reduced CO_2, generating CO and CO_3^{2-} as products.[20] Diffusion-controlled proton transfer from adventitious water then rapidly generates HCO_3^-, which is templated and activated by the pendant urea group and helps promote a faster catalytic pathway with bicarbonate as the proton donor.

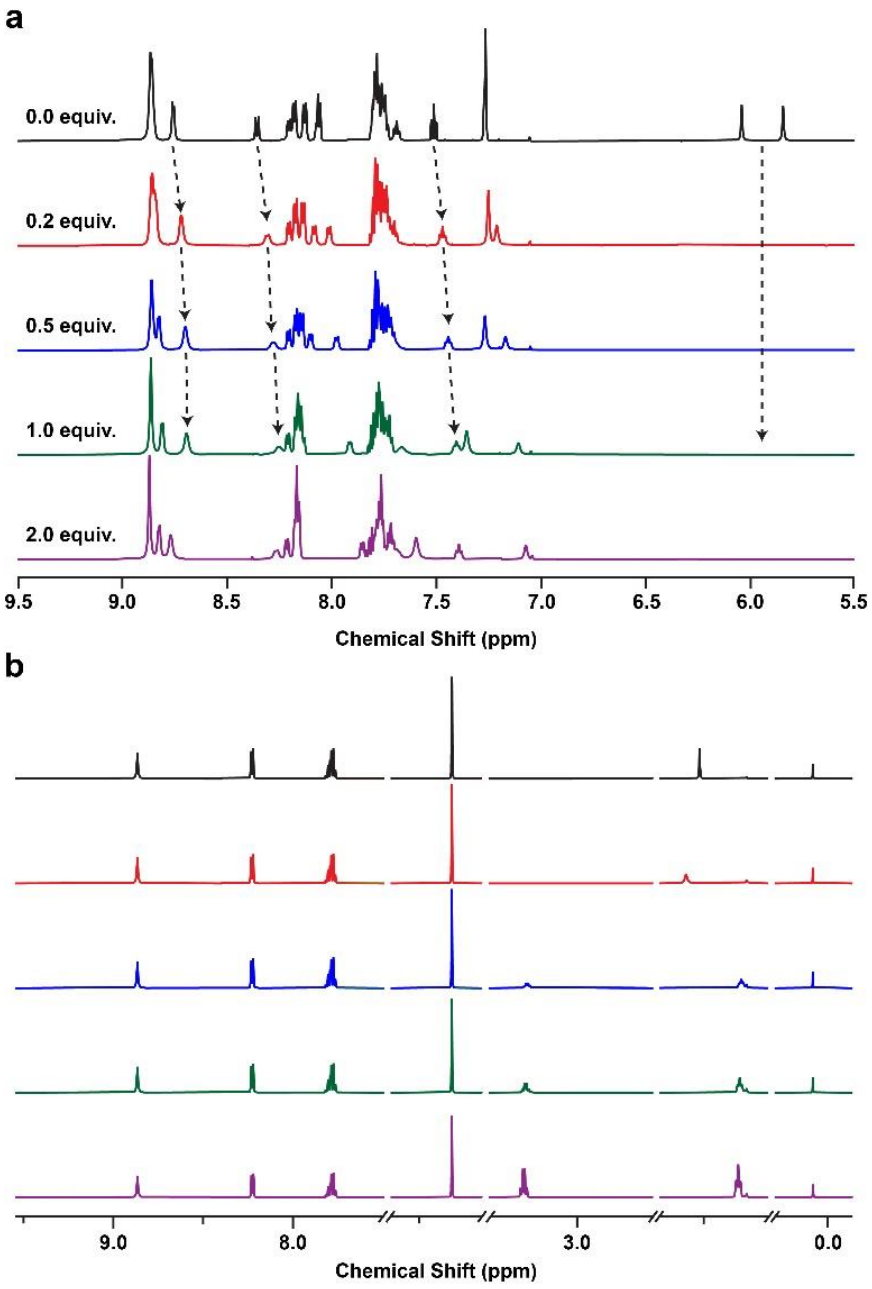


Figure 4.15. Titration of $TEAHCO_3$ into a solution of (a) *ortho*-urea or (b) TPP in DMSO-d6.

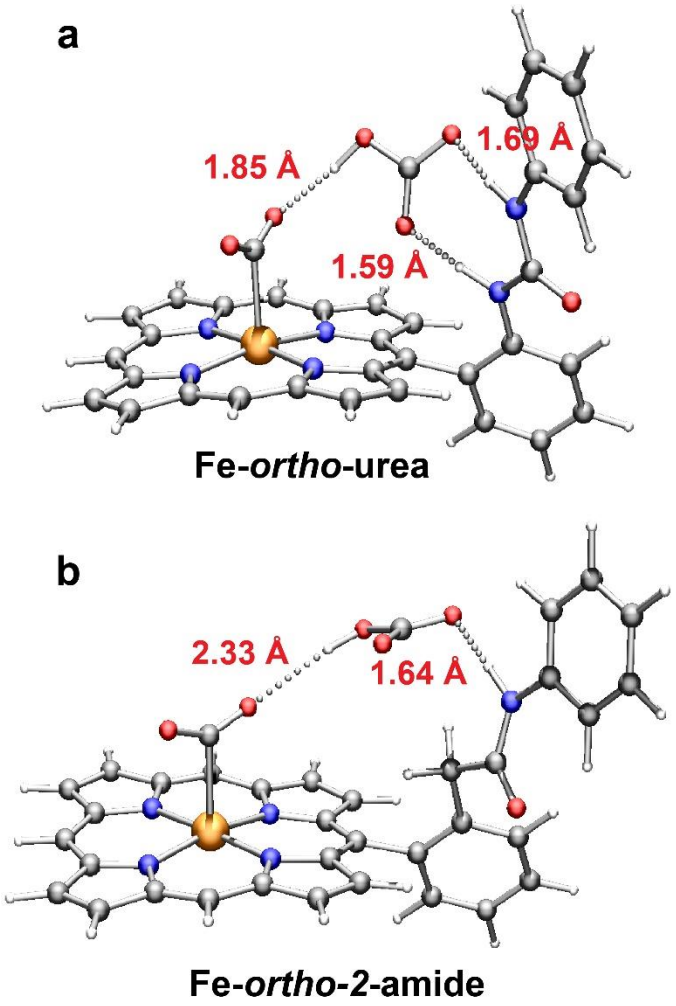


Figure 4.16. Optimized structures from DFT (B97-D)[56] calculations of Fe(0)–CO_2 adducts of (a) Fe-*ortho*-urea and (b) Fe-*ortho*-2-amide,[32] with bicarbonate to probe the H-bond templating of bicarbonate to iron porphyrin scaffolds employing either a 1-point or 2-point H-bond donor. The geometry optimized structure for the *para*-urea control is given in Figure S14. Orange, grey, blue, white, and red atoms signify Fe, C, N, H, and O, respectively. To reduce computational cost, the ligands were truncated to remove the non-functionalized phenyl moieties and the bis(3,5-trifluoromethyl) functional groups. The DFT calculations support the importance of the two-point urea binder to properly position bicarbonate relative to the Fe(0)–CO_2 adduct for substrate reduction as well as increase the acidity of bicarbonate as an acid to facilitate proton transfer in CO_2RR.

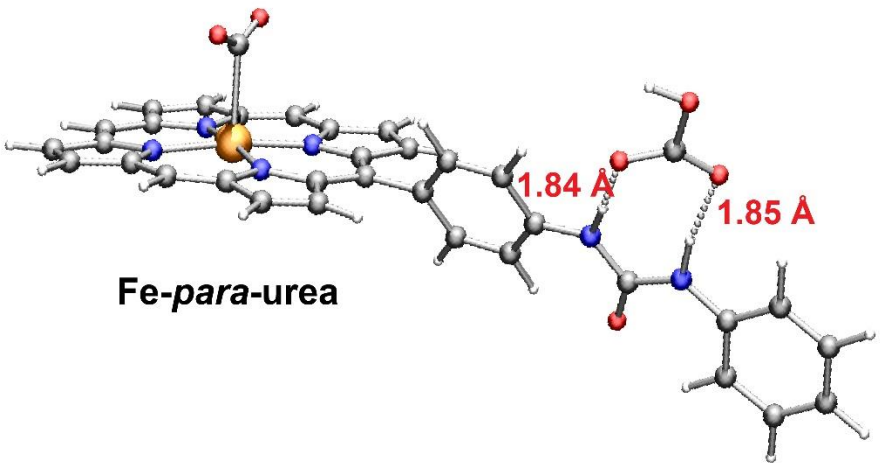


Figure 4.17. Geometry optimization and frequency calculations of Fe(0)–CO_2 adducts of Fe-*para*-urea with bicarbonate. Orange, grey, blue, white, and red atoms signify Fe, C, N, H, and O, respectively. To reduce computational cost, the ligands were truncated to remove the non-functionalized phenyl moieties and the bis(3,5-trifluoromethyl) functional groups.

4.4 Conclusion

In summary, we have shown that bicarbonate, as an additive, causes a large catalytic enhancement in homogenous electrochemical CO_2 reduction in organic electrolyte. Using iron porphyrin as a representative molecular catalyst platform, installation of a properly positioned urea moiety into the second coordination sphere as a bicarbonate anion receptor further facilitates a marked improvement in catalytic rates. Spectrophotometric pK_a measurements, NMR binding studies, and DFT calculations provide support that bicarbonate operates as a competent proton donor and that templated binding to the urea results in the generation of a much stronger acid that is appropriately positioned for rapid proton transfer to a CO_2-bound intermediate. Taken together, this study identifies the importance of understanding the CO_2/HCO_3^- solution equilibria under organic electrolyte conditions where molecular catalysts are often utilized and shows how the second coordination sphere can be designed to exploit these equilibria for CO_2RR catalysis.

4.5 Materials and Methods

4.5.1 General Methods

All manipulations were conducted under air and moisture free conditions using a MBraun LABstar pro glove-box and standard Schlenk line techniques unless otherwise noted. THF, DCM, toluene, and DMF were dried using a JC Meyer solvent purification system. 2,6-lutidine was dried over KOH then purified by distillation. All other reagents and solvents were purchased from commercial suppliers and used without additional purification. Carbon dioxide (99.99%), carbon monoxide (99.5%), hydrogen (99.999%), ethane (99.0%), argon (99.999%) and nitrogen (99.998%) were purchased from Praxair. UV-visible (UV-vis) spectra were collected using an Agilent Cary 60 spectrophotometer at room temperature (RT). NMR spectra were recorded on Bruker spectrometers operating at either 300, 400, 500, or 600 MHz as noted. Chemical shifts for ^{1}H and $^{13}C\{^{1}H\}$ spectra are reported in ppm relative to residual protonated solvent; those for ^{19}F spectra are reported in ppm relative to an external $CFCl_3$ standard. Coupling constants were reported in Hz. MALDI-MS spectra were recorded using an Applied Biosystems Voyager System 6322 with an accelerating voltage of 20,000 V, 200 laser shots per spectrum, and a laser rep rate of 20 Hz. α-Cyano-4-hydroxycinnamic acid was used as the matrix. X-ray crystallography was performed in the Chexray facility at the University of California, Berkeley.

4.5.2 Cyclic Voltammetry

Cyclic voltammetry experiments were performed using either a CH Instruments, Inc. 600E potentiostat or a Bioanalytical Systems, Inc. (BASi) Epsilon potentiostat. Non-aqueous voltammetry studies were conducted in a three-electrode cell equipped with a glassy carbon disk (3.0 mm diameter) working electrode (BASi), a platinum wire counter electrode, and a silver wire in a porous Vycor tipped glass tube filled with electrolyte as a pseudo-reference electrode. The working electrode was polished prior to each experiment with 0.05-micron alumina powder on a felt pad. The electrolyte was 0.1 M tetrabutylammonium hexafluorophosphate ($TBAPF_6$) in dry DMF that had been purified of dimethylamine by passing through an isocyanate column and was saturated with either CO_2 or Ar at 1 atm. We estimate, based on Karl Fischer titration results reported by JC Meyer Solvent Systems,[57,58] water content of approximately 15 ppm on average which equates to 0.8 mM water. This is significant considering catalyst loadings of 1 mM. At the conclusion of each experiment, the pseudo-reference potentials were referenced against ferrocene/ferrocenium (Fc/Fc^{+}) used as an external standard. The scan rates for all cyclic voltammograms were 100 mV/s unless otherwise noted. All voltammograms were obtained with iR compensation.

4.5.3 CO_2 Concentration-Dependent Experiments

The concentration of CO_2 in solution was varied by changing the percentage of CO_2 to N_2 balance using a gas proportioner (G21A2-BA0; Aalborg Instruments; Orangeburg, NY) fitted with sapphire/Viton-A flowtubes (112-02-SA; Aalborg Instruments; Orangeburg, NY). Using metering pressures of 50 psi for N_2 and 15 psi for CO_2, and correlating flow rate with meter reading using calibration curves published at Aalborg.com, the percentage of CO_2 in each gas mixture was calculated. It was assumed that the solution concentration of CO_2 is equal to 0.23 M times the CO_2

percentage in the mixed gas. Cyclic voltammetry experiments were performed by sparging the solution with gas mixtures containing increasing percentages of CO_2 for 10 min, then maintaining the same gas mixture in the headspace for the duration of the scan.

4.5.4 Details for Foot-Of-The Wave Analysis (FOWA) and Determination of k_{obs}

Foot-of-the-Wave Analysis was applied to cyclic voltammetry measurements as described by Savéant and coworkers[57,58] in order to determine k_{obs} (= TOF) under CO_2 saturated solution in the presence of $TEAHCO_3$ (0 to 10 mM). At the outset of each experiment, a CV was measured of the catalysts alone under Ar atmosphere in the absence of proton source ($TEAHCO_3$), from which E^0_{cat} could be determined. The peak height of the formal Fe(II/I) couple, i^0_p, was determined by taking the difference between the peak cathodic current and baseline current before the Fe(II/I) couple. As described previously[34,57,58] CO_2 reduction with iron porphyrin catalysts may be described as an EC' process:

$$Fe(I) + e^- \rightarrow Fe(0)$$

$$Fe(0) + CO_2 + 2H^+ \rightarrow Fe(II)CO + H_2O \text{ (RDS)}$$

$$Fe(II)CO + Fe(0) \rightarrow 2Fe(I) + CO$$

In which the rate-determining step involved pre-equilibrium CO_2 binding to the nucleophilic Fe(0) center and subsequent proton transfer. The following relationship may be derived (**Equation 4.1**):

$$\frac{i}{i_p^0} = \frac{2.24\sqrt{\frac{k_{obs}}{fv}}}{1+e^{[f(E-E^0_{cat})]}} \qquad \textbf{Equation 4.1}$$

where i is the current, E is the potential, v is the scan rate (V/s), k_{obs} is the observed rate constant, and $f = F/RT = 38.94\ V^{-1}$. Thus, a "FOW" plot of $\frac{i}{i_p^0}$ versus $\frac{1}{1+e^{[f(E-E^0_{cat})]}}$ yields a straight line with the slope of $2.24\sqrt{\frac{k_{obs}}{fv}}$, from which k_{obs} may be determined.

4.5.5 Controlled Potential Electrolysis

Controlled potential electrolyses (CPEs) were conducted using either a CH Instruments, Inc. 600E potentiostat or a Bioanalytical Systems, Inc. (BASi) Epsilon potentiostat. Non-aqueous preparative scale controlled potential electrolysis experiments were performed in a miniaturized version of our previously described homemade gastight PEEK electrolysis cell with a working compartment (7 mL liquid volume) and counter compartment (3 mL liquid volume) separated by an ultrafine glass frit.[32] A 1 cm^2 glassy carbon plate (Toki Carbon; Kanagawa, Japan) was used as the working electrode, a 2.5 cm diameter graphite planchet (Ted Pella; Redding, CA) was used as the auxiliary electrode, and an Ag wire in a Vycor tipped glass tube filled with electrolyte ($TBAPF_6$/DMF) was used as a pseudo-reference electrode. The working compartment was filled with 7 mL of a 1 mM solution of porphyrin catalyst dissolved in 0.1 M $TBAPF_6$/DMF containing up to 100 mM $TEAHCO_3$ as a proton source. The counter electrode chamber was filled with 3 mL

of a 20 mM solution of tetrabutylammonium acetate dissolved in 0.1 M $TBAPF_6$/DMF. This soluble source of acetate was sacrificially oxidized to generate CO_2 and ethane, thereby preventing GC detection of solvent oxidation byproducts. Both compartments were sealed to be gastight. The working compartment was sparged with CO_2 for 10 min, then sealed and injected with 0.50 mL of ethane as a gaseous internal standard. A CV scan was collected prior to the CPE measurement to calibrate the potential. The electrolyte solution was constantly stirred during the CPE experiment with a 1 cm stirbar. At the conclusion of the experiment, the headspace was injected directly into an SRI-GC (model #8610C) equipped with 6' Hayesep D and 13X molecular sieve chromatographic columns. Two in-line detectors were used: a TCD for H_2 detection and an FID with a methanizer for $CO/CO_2/C_2H_6$ detection. Analytes of interest were quantified by comparing a ratios of analyte/internal stand peak integrals to a calibration curve with known amounts of analyte (**Figure 4.18**).

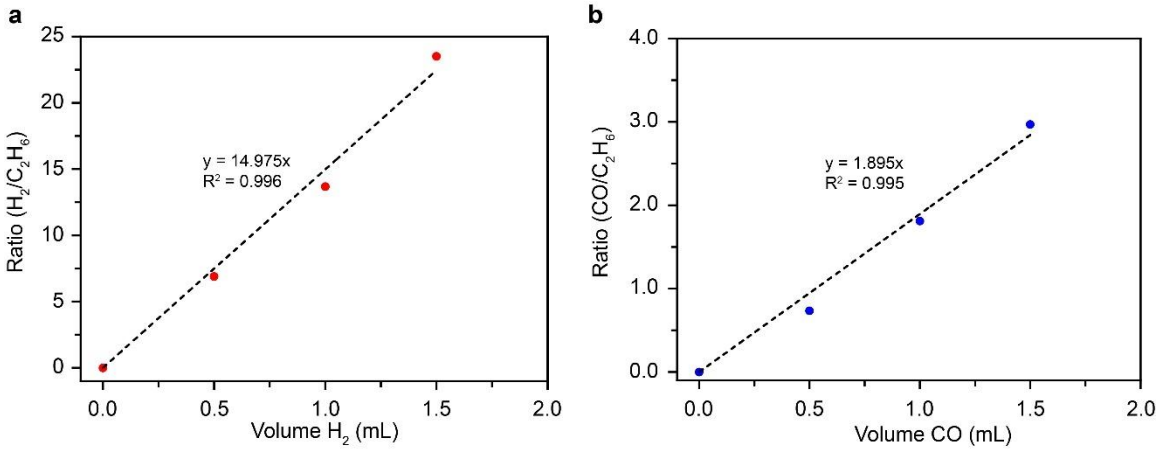


Figure 4.18. GC calibration curves. (a) H_2 and (b) CO calibration curve for CPE experiments conducted in $TBAPF_6$/DMF.

4.5.6 Determination of Faradaic Efficiency

Controlled potential electrolysis (CPE) experiments to determine Faradaic efficiency (FE) values were conducted in gas-tight electrochemical cells at varying applied potentials for 1 h. At the conclusion of the CPE experiment, samples from the headspace of the electrochemical cell were injected into a gas chromatograph for analysis. Calibration curves (Figure 4.18) were constructed using known amounts of H_2 and CO and C_2H_6 (0.50 mL) as internal standards to quantify the volume of gaseous products from the respective chromatograms. The amounts (mols) of gas produced were calculated from the volume of gas using the Ideal Gas Law and Faradaic efficiencies were then determined using **Equation 4.2**:

$$FE(\%) = \frac{Q_{expt}}{Q_{Theory}} x100 = \frac{znF}{Q} x100 \qquad \textbf{Equation 4.2}$$

where *z* is the number of electrons, *n* is the mols of analyte produced, *F* is Faraday's constant and *Q* is the specific charge passed during the CPE experiment.

4.5.7 X-ray Crystallography

Crystals were coated with Paratone-N oil, attached to a Kapton loop, and mounted onto a Bruker AXS diffractometer equipped with an APEX II CCD area detector. Data were collected using Mo Kα radiation (λ = 0.71073 Å). Crystals were kept at 100(2) K throughout the collection. Determination of the collection strategy, integration, scaling, and space group identification was performed using Bruker APEX2 software. Structure solution was performed using SHELXT-2014 and refinement was performed using SHELXL-2014.[59]

4.5.8 Spectrophotometric pK_a Titrations

To evaluate the feasibility of $TEAHCO_3$ functioning as an acid in our system under these electrochemical conditions, we sought to measure its pK_a in DMF. Unfortunately, to the best of our knowledge, the pK_a of bicarbonate in organic solvent is unreported. Therefore, we measured it spectrophotometrically in DMSO (Figure 4.8) because of the extremely limited number of appropriate colorimetric indicators available with known pK_a's in DMF. The pK_a of $TEAHCO_3$ was determined in DMSO by following a previous report and provided here in detail.[32,60] DMSO, base (K-dimsyl), indicator (4-chloro-2-nitroaniline; Sigma Aldrich), and $TEAHCO_3$ stock solutions were freshly prepared (as detailed below) before the spectrophotometric titration experiments were performed. Amounts of indicator, $TEAHCO_3$, and DMSO and their respective solutions, were determined gravimetrically using a microbalance.

DMSO. Rigorously dry and degassed DMSO was required for accurate determination of pK_a values. DMSO was dried following a previous report.[60] A commercial source of DMSO was dried over freshly activated alumina (Al_2O_3) overnight. The DMSO was filtered with a Schlenk-frit into a clean, flame-dried Schlenk flask equipped with a stir bar and dried over calcium hydride (CaH_2) overnight. Subsequent distillation under reduced pressure and degassing via three freeze-pump-thaw cycles afforded the dry DMSO, which was brought into a nitrogen filled glovebox and stored over 4 Å molecular sieves overnight before use. The fresh solvent was used within a two-day period.

K-Dimsyl Base. A clean Schlenk tube equipped with a glass stir bar was pre-weighed and flame dried. To this tube was added approximately 100 mg of potassium hydride (KH; Alfa Aesar) (30 – 35 wt% dispersion in mineral oil) under N_2 atmosphere and was washed with pentanes (1 mL x3). The solvent was removed with a syringe, and the remaining solid was dried under vacuum for at least 1 h. Once dry, the Schlenk tube was again weighed under N_2 atmosphere so that the amount of KH could be determined. With vigorous stirring, 20 mL of freshly dried DMSO was added to the Schlenk tube and allowed to stir until the KH was fully dissolved and no more H_2 was released. The K-dimsyl stock solution was then sealed and brought into a nitrogen filled glovebox and used within a two-day period. The calculation of the K-dimsyl base stock solution was calculated and used to prepare an approximately 5 mM K-dimsyl solution. The 5 mM K-dimsyl base solution was protected from the light and used for the spectrophotometric titration experiments.

Indicator Solution. 4-Chloro-2-nitroaniline (pK_a in DMSO = 18.9; λ_{max} of deprotonated indicator = 520 nm; Sigma Aldrich)[6] was selected as the appropriate indicator due to its pK_a and

lack of spectra overlap with $TEAHCO_3$. The indicator was recrystallized from hot ethanol and dried under vacuum overnight prior to use. To a pre-weighed, oven-dried vial was added approximately 3.2 mg of 4-chloro-2-nitroaniline, with the exact amount determined gravimetrically using a microbalance. The vial was then brought into the glovebox and approximately 5 mL of dry DMSO was added. The vial was tightly sealed and taken out of the glovebox, quickly weighed using a microbalance, and brought back into the glovebox where it was stored in the absence of light. The exact concentration of the indicator solution was determined gravimetrically, assuming that the dilute stock solutions had the same density as pure DMSO (1.1 g/mL). A 2.56 mM indicator solution was utilized in these studies (*i.e.*, 3.20 mg of 4-chloro-2-nitroaniline in 7.24 mL dry DMSO). The indicator solution was used within a two-day period.

$TEAHCO_3$ Solution. Approximately 2 – 3 mg of $TEAHCO_3$ was added to a pre-weighed, oven-dried vial, with the exact amount determined gravimetrically using a microbalance. The vials were then brought into the glovebox and 2 – 5 mL of dry DMSO was added. The vials were then tightly sealed and taken out of the glovebox, quickly weighed using a microbalance, and brought back into the glovebox where they were stored in the absence of light. The exact concentrations of the $TEAHCO_3$ solution were determined gravimetrically, assuming that the dilute stock solution had the same density as pure DMSO. A 7.12 mM $TEAHCO_3$ solution was utilized in these studies (*i.e.*, 2.80 mg of $TEAHCO_3$ in 2.06 mL dry DMSO).

Titration Experiment. In the first phase of each experiment, a solution of indicator was titrated into a K-dimsyl solution, allowing for determination of the extinction coefficient of the deprotonated indicator. An oven-dried semi-micro rectangular quartz cuvette with a screw cap and septum (d = 1 cm) (Starna Scientific, Atascadero, CA) was pre-weighed and brought into the glovebox. The cell was charged with 1 mL of freshly distilled DMSO, tightly sealed shut, and brought outside of the glovebox and weighed again to determine the amount of DMSO used. The cell was brought back into the glovebox, where 70 μL of the 5 mM K-dimsyl solution was carefully added to the cuvette with an oven-dried Hamilton syringe. The cuvette was sealed tightly with the screw septum cap and re-weighed outside the glovebox. The first UV-visible (UV-vis) spectrum was then recorded to determine the baseline, and the titration was started. An oven-dried 100 μl Hamilton syringe was loaded with the indicator[6] solution in the glovebox and then plugged with a rubber gasket. Approximately a 10 μL aliquot of the indicator stock solution was then added to the air-free cuvette and vigorously shaken to ensure proper mixing. The solution in the cuvette should turn pink in color. After addition of indicator, the cuvette was weighed, and the UV-vis spectrum was recorded. The Hamilton syringe was quickly re-plugged with the rubber gasket and stored in the small antechamber of the glovebox under vacuum between each measurement. The addition of 10 μL aliquots of the indicator solution, weighting the cuvette, and recording UV-visible spectra was repeated until no further increase in the absorption spectrum at 520 nm was observed (Figure 4.8a). These data were used to determine the extinction coefficient (ε) of the indicator anion by plotting the concentration of the indicator in the cuvette vs. the absorbance at 520 nm (Figure 4.8b). Dilution effects were taken into account through the volume increase upon sample addition. At the conclusion of this phase of the experiment, all K-dimsyl base (B^-) has been protonated (BH), and the cuvette contains only the two species of 4-chloro-2-nitroaniline indicator (HInd and Ind^-), with the maximum concentration of the deprotonated indicator (Ind^-). It is extremely important that all K-dimsyl base has been consumed before addition of the $TEAHCO_3$ solution, as direct protonation of K-dimsyl by the $TEAHCO_3$ will lead to significant error in determining the

pK_a. Once no further spectral change at 520 nm is observed, the second phase of the titration is initiated. An oven-dried Hamilton syringe (25 μl–200 μL) was loaded with the $TEAHCO_3$ solution inside the glovebox and then plugged with a rubber gasket. Small aliquots (10–25 μL) of the $TEAHCO_3$ solution were added to the air-free cuvette, which was vigorously shaken, weighed, and the UV-vis spectrum recorded. The syringe loaded with the $TEAHCO_3$ solution was re-plugged with the rubber gasket and stored in the small antechamber of the glovebox between titrations. With each addition of the $TEAHCO_3$ solution to the cuvette, a new acid-base equilibrium is established, causing a loss in the absorbance of the deprotonated indicator (Ind^-) at 520 nm as the indicator anion is re-protonated (HInd) (Figure 4.8c). Seven to nine titration points were collected for each titration replicate and the pK_a was calculated based on the average of 3 titration trials.

pK_a Calculations. The first and second phases of the titration experiment involve the equilibria shown in **Equations 4.3** and **4.4**, where BH/B^-, $HInd/Ind^-$, and HA/A^- are the protonated and deprotonated K-dimsyl base, 4-chloro-2-nitroaniline indicator, and $TEAHCO_3$, respectively. The pK_a value of $TEAHCO_3$ was determined using the equilibrium constant (Keq) for **Equation 4.3** and the known pK_a of the indicator. A value for Keq was determined for each titration point; thus, the reported pK_a values represent the average over at least 7 measurements.

$$B^- + HInd \rightarrow BH + Ind^- \qquad \textbf{Equation 4.3}$$

$$Ind^- + HA \rightarrow HInd + A^- \qquad \textbf{Equation 4.4}$$

The equilibrium constant can be determined by measuring the exact concentrations of $HInd/Ind^-$ and HA/A^- (**Equation 4.5**) in the cuvette at each titration point. Once the equilibrium constants have been measured, the pK_a of $TEAHCO_3$ can be calculated from **Equation 4.6**. In order for the pK_a of the unknown to be determined accurately, the indicator pK_a must be within 2 pK_a units of the unknown.

$$K_{eq} = \frac{[Hind][A^-]}{[HA][Ind^-]} \qquad \textbf{Equation 4.5}$$

$$pK_a = pK_{a\,indicator} - logK_{eq} \qquad \textbf{Equation 4.6}$$

The concentration of the deprotonated indicator, $[Ind^-]$, was determined by the Beer-Lambert Law, **Equation 4.7**, using the absorbance of the indicator anion at 520 nm. The extinction coefficient (ε) was determined during each experiment from the gradual addition of the indicator solution to the cuvette as described above.

$$[Ind^-] = \frac{Abs_{520\,nm}}{\varepsilon * l} \qquad \textbf{Equation 4.7}$$

The concentration of the protonated indicator, [HInd], was determined by subtracting the concentration of $[Ind^-]$ from the total concentration of indicator that was added to the cell, $[Ind_{total}]$ (**Equation 4.8**).

$$[Hind] = [Ind_{total}] - [Ind^-] \qquad \textbf{Equation 4.8}$$

Because Ind^- is stoichiometrically protonated by HA, the change in concentration of Ind^- and A^- are equal in magnitude (**Equation 4.9**). The concentration of deprotonated $TEAHCO_3$, $[A^-]$, was therefore determined from the change in absorption at 520 nm upon addition of $TEAHCO_3$.

$$-\Delta[Ind^-] = \Delta[A^-] \qquad \textbf{Equation 4.9}$$

Finally, [HA] was determined by subtracting the concentration of deprotonated $TEAHCO_3$, $[A^-]$, from the concentration of the total amount of $TEAHCO_3$ added to the cuvette, $[TEAHCO_{3,total}]$ according to **Equation 4.10**.

$$[HA] = \left[TEAHCO_{3,total}\right] - [A^-] \qquad \textbf{Equation 4.10}$$

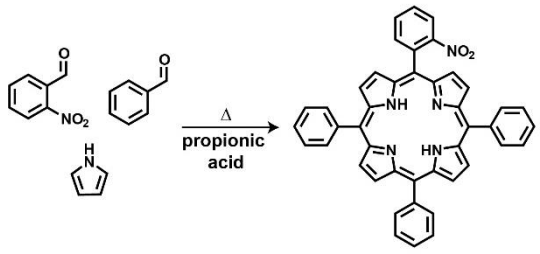
4.5.9 Computational Details

Density functional theory calculations were carried out with the Q-Chem package (version 5.3.0).[61] Geometries were confirmed as minimum structures by frequency calculations. For the Fe-TTP systems, the B97-D functional was used due to its affordability and excellent performance for non-covalent interaction; in combination with a mixed basis set mixed basis using def2-SVP basis for all main group elements and def2-TZVP basis set for Fe.[62]

For the pK_a calculations, the accurate ωB97X-D[63] functional in combination with the def-TZVPD basis set was employed.[62] In both cases a (75, 302) grid (75 radial shells with 302 Lebedev points) was used for exchange correlation functional. The solvation energies were calculated using the C-PCM model (DMSO, ε = 46.7) as implemented in Q-Chem.[61]

The calculation of accurate pK_a's follow the standard thermodynamic cycles and use the experimental value for the free energy of the proton based on the Sackur-Tetrode equation and an estimated solvation energy of $G_{solv}(H^+) = -266.4$ kcal/mol in DMSO was used.[64,65]

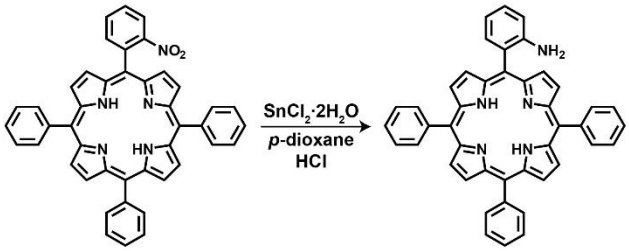
4.5.10 Synthesis of 5-(2-Nitrophenyl)-10,15,20-triphenylporphyrin (1)



1
7% yield

Porphyrin **1** was prepared following pervious literature reports.[66,67] 2-Nitrobenzaldehyde (7.2 g, 47.6 mmol) and benzaldehyde (10.11 g, 95.3 mmol) were added to refluxing propionic acid (400 mL) in a 1 L round bottom flask. Pyrrole (9.9 g, 142.9 mmol) was added dropwise and the solution was heated to reflux for 30 min in the absence of light. Upon cooling to room temperature, methanol (200 mL) was added and the precipitated porphyrins were collected via filtration, then washed with water and methanol several times. A solution of the porphyrin mixture in DCM was run through a basic alumina plug to remove oligomers. **1** (R_f = 0.6) was separated from tetraphenylporphyrin (R_f = 0.75) and other undesired nitroporphyrins by column chromatography (2:1 hexanes: DCM) on basic alumina and finally recrystallized from DCM/MeOH (1.7 g, 7% yield). The ^{1}H NMR spectrum agrees with the literature reports for this compound. ^{1}H NMR (500 MHz, CD_2Cl_2) / δ (ppm): 8.88 (d, *J* = 8.4 Hz, 6H), 8.70 (d, *J* = 4.7 Hz, 2H), 8.49 – 8.40 (m, 1H), 8.35 – 8.15 (m, 7H), 8.04 – 7.95 (m, 2H), 7.84 – 7.72 (m, 9H), -2.77 (s, 2H).

4.5.11 Synthesis of 2-(10,15,20-Triphenylporphyrin-5-yl)aniline (2)

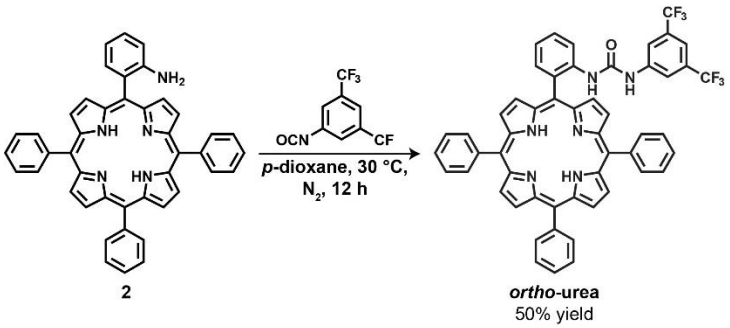


1 **2**
57% yield

Porphyrin **2** was synthesized by a tin mediated reduction of 1 according to previous literature reports.[66,67] A solution of 1 (1.39 g, 2.10 mmol) in p-dioxane (300 mL) was sparged with N_2 and $SnCl_2$•$2H_2O$ (5.68 g, 25.20 mmol) was added as a solid. After 10 min, concentrated HCl (480 mL) was added and the solution was heated to reflux for 1 h under N_2 atmosphere in the absence of light. Upon cooling to room temperature, the solution was neutralized to pH 7 with 6 M NaOH and saturated $NaHCO_3$. The mixture was extracted three time with EtOAc, then the combined organic phase was rinsed with water and brine and dried over MgSO4. Solvent was removed under reduced pressure to afford crude **2**. The product was purified by column chromatography (starting at 1:1 EtOAc:hexanes and progressing to 3:1 EtOAc:hexanes) on silica, and finally recrystallizing from DCM/MeOH (750 mg, 57% yield). The ^{1}H NMR spectrum agrees

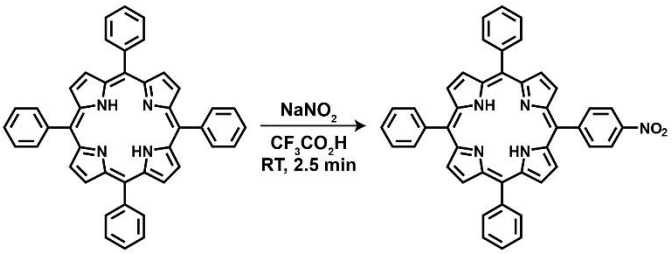
with the literature reports for this compound.[1]H NMR (300 MHz, CD_2Cl_2) / δ (ppm): 8.81 – 8.96 (m, 8H), 8.16 – 8.30 (m, 6H), 7.86 (d, J = 7.5 Hz, 1H), 7.71 – 7.83 (m, 9H), 7.61 (t, J = 7.8 Hz, 1H), 7.16 (t, J = 7.4 Hz, 1H), 7.14 (d, J = 8.0 Hz, 1H), 3.61 (s, 2H), -2.81 (s, 2H). ESI-MS calculated for $C_{44}H_{33}N_5$ $(M+H)^+$ 630.3, found 630.8.

4.5.12 Synthesis of 1-(3,5-Bis(trifluoromethyl)phenyl)-3-(2-(10,15,20-triphenylporphyrin-5-yl)phenyl)urea (*ortho*-urea)



Porphyrin **2** (600 mg, 1.05 mmol) was dissolved in anhydrous *p*-dioxane (100 mL) and 3,5-bis(trifluoromethyl)phenyl isocyanate (0.4 mL, 2.41 mmol) was added under N_2 atmosphere. The solution was heated to 35 ºC for 3 h in the absence of light. MeOH (10 mL) was added to quench any unreacted isocyanate; solvent was removed under reduced pressure to afford crude *ortho*-urea. The crude product was purified by column chromatography (2:1 DCM:hexanes) on silica and finally recrystallized from DCM/MeOH (425 mg, 50% yield). ^{1}H NMR (300 MHz, CD_2Cl_2) / δ (ppm): 8.85 (d, *J* = 4.8 Hz, 2H), 8.77 (dd, *J* = 8.4, 4.8 Hz, 4H), 8.55 (d, *J* = 4.8 Hz, 2H), 8.20 – 8.12 (m, 1H), 8.12 – 8.02 (m, 2H), 8.02 – 7.91 (m, 3H), 7.81 – 7.68 (m, 8H), 7.56 – 7.45 (m, 3H), 7.40 (ddd, *J* = 7.5, 5.4, 3.3 Hz, 1H), 7.32 (d, *J* = 10.7 Hz, 2H), 6.87 (s, 2H), 5.69 (s, 1H), 5.51 (s, 1H), -2.89 (s, 2H). ^{13}C{^{1}H} NMR (151 MHz, DMSO-d_6) / δ (ppm): 152.24, 141.15, 141.06, 141.01, 138.88, 134.96, 134.26, 134.19, 134.15, 134.08, 131.14, 130.78, 130.56, 130.34, 130.13, 129.31, 128.12, 126.98, 125.70, 123.90, 122.09, 121.92, 120.89, 120.58, 120.04, 117.29, 114.45, 114.17. ^{19}F NMR (565 MHz, DMSO-d_6) δ -61.95. λ_{max} (CH_2Cl_2) 418, 441, 521, 549, 590, 648 nm. ESI-MS calculated for $C_{53}H_{35}F_6N_6O$ $(M+H)^+$ 885.3, found 885.8.

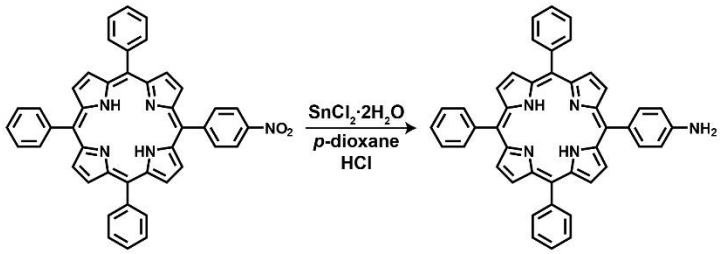
4.5.13 Synthesis of 5-(4-nitrophenyl)-10,15,20-triphenylporphryin (3)



3
53% yield

Porphyrin **3** was synthesized according to previous literature reports.[68] Tetraphenylporphryin (600 mg, 0.977 mmol) was dissolved in trifluoroacetic acid (20 mL) and stirred under N_2. Sodium nitrite (120 mg, 1.740 mmol) was suspended in trifluoroacetic acid (10 mL) and added to the porphyrin solution over 30 seconds. After an addition 2.5 min, the green solution was quenched by pouring into 300 mL cold water and extracted with DCM. The organic layer was neutralized with saturated $NaHCO_3$ solution and rinsed with water, then dried over $MgSO_4$. Solvent was removed under reduced pressure to afford crude **3**. The crude product was purified by column chromatography (starting at 2:1 hexanes:DCM and ended at 1:1 hexanes:DCM) on silica (340 mg, 53% yield). The ^{1}H NMR spectrum agrees with the literature reports of this compound. ^{1}H NMR (400 MHz, CD_2Cl_2) / δ (ppm): 8.90 (d, *J* = 4.7 Hz, 6H), 8.77 (d, *J* = 4.8 Hz, 2H), 8.55 (d, *J* = 8.1 Hz, 2H), 8.35 (d, *J* = 8.2 Hz, 2H), 8.22 (dt, *J* = 6.5, 1.8 Hz, 6H), 7.84 – 7.72 (m, 9H), -2.80 (s, 2H).

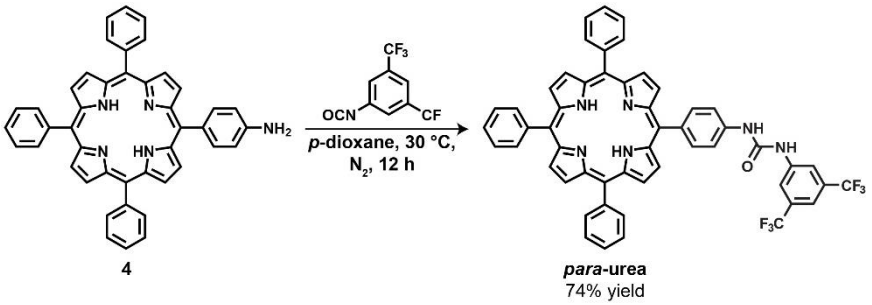
4.5.14 Synthesis of 4-(0,15,20-Triphenylporphyrin-5-yl)aniline (4)



3 **4**
46% yield

Porphyrin **3** (375 mg, 0.568 mmol) was dissolved in concentrated HCl (125 mL) and $SnCl_2$•$2H_2O$ (1.537 g, 6.811 mmol) was added as a solid. The solution was heated to 65 ºC for 1 h, then poured into 300 mL water and neutralized to pH 8 with ammonium hydroxide. The aqueous phase was extracted with DCM, rinsed with water, and dried over $MgSO_4$. Solvent was removed under reduced pressure to afford crude 4. The crude product was purified by column chromatography (starting at 2:1 hexanes:DCM and progressing slowly to 3:1 DCM:hexanes and finally pure DCM) on silica, followed by recrystallization from DCM/MeOH (199 mg, 46% yield). The ^{1}H NMR spectrum agrees well with the literature reports of this compound. ^{1}H NMR (400 MHz, $CDCl_3$) / δ (ppm): 8.97 (d, *J* = 4.8 Hz, 2H), 8.87 (d, *J* = 2.6 Hz, 6H), 8.25 (dt, *J* = 7.8, 1.5 Hz, 6H), 8.06 – 7.99 (m, 2H), 7.85 – 7.71 (m, 9H), 7.12 – 7.04 (m, 2H), 4.02 (s, 2H), -2.72 (s, 2H). ESI-MS calculated for $C_{44}H_{32}N_5$ $(M+H)^+$ 630.3, found 630.5 *m/z*.

4.5.15 Synthesis of 1-(3,5-Bis(trifluoromethyl)phenyl)-3-(4-(10,15,20-triphenylporphyrin-5-yl)phenyl)urea (*para*-urea)



Porphyrin **4** (145 mg, 0.230 mmol) was dissolved in anhydrous *p*-dioxane (20 mL) and 3,5-bis(trifluoromethyl)phenyl isocyanate (0.12 mL, 0.69 mmol) was added under a N_2 atmosphere. The solution was stirred overnight at RT in the absence of light. MeOH (10 mL) was added to quench the remaining isocyanate; solvent was removed under reduced pressure to afford crude *para*-urea. The crude product was purified by column chromatography (starting at 1:1 DCM:hexanes and progressing to pure DCM and finally 1% MeOH in DCM) on silica. A second column (3:1 hexanes:EtOAc to 2:1 hexanes:EtOAc) was run on the purified fractions to obtain the pure product (165 mg, 74%). ^{1}H NMR (400 MHz, DMSO-d_6) / δ (ppm): 9.67 (s, 1H), 9.50 (s, 1H), 8.93 (s, 2H), 8.84 (s, 6H), 8.29 (s, 2H), 8.23 (dt, *J* = 7.9, 2.0 Hz, 6H), 8.18 (d, *J* = 8.1 Hz, 2H), 7.97 (d, *J* = 8.3 Hz, 2H), 7.84 (q, *J* = 6.9 Hz, 9H), 7.73 (s, 1H), -2.90 (s, 2H). ^{13}C{^{1}H} NMR (126 MHz, DMSO-d_6) / δ (ppm): 152.75, 141.97, 141.27, 141.24, 139.15, 135.25, 134.88, 134.27, 130.96, 130.70, 128.13, 127.05, 124.51, 122.34, 120.16, 120.08, 120.02, 119.92, 118.19, 117.40. ^{19}F NMR (376 MHz, DMSO-d_6) / δ (ppm): -60.8. λ_{max} (CH_2Cl_2) 418, 520, 553, 593, 649 nm. ESI-MS calculated for $C_{53}H_{35}F_6N_6O$ $(M+H)^+$ 885.3, found 886.0 *m/z*.

4.5.16 General Procedure for the Synthesis of Iron Porphyrins

Metalation of porphyrins was performed using inside a N_2-filled glovebox or using standard Schlenk techniques and dry solvents to avoid the formation of μ-oxo dimers. To a solution of the free-base porphyrin (1 eq) in dry THF was added anhydrous $FeBr_2$ (15 eq) as a suspension in dry THF. Distilled lutidine (3 eq) was added and the solution was heated to 65 ºC overnight in the absence of light. The resulting solution was neutralized by pouring into 1 M HBr. After extraction into EtOAc and rinsing with copious amounts of water, the organic phase was dried over $MgSO_4$ and the solvent was removed under reduced pressure. The crude complexes were purified according to the conditions specified below.

Fe-*ortho*-urea. Metalation was performed as described above using 360 mg of *ortho*-urea. Purification was achieved by column chromatography (pure DCM then progressing slowly to 2% MeOH in DCM) on silica (250 mg, 60% yield). λ_{max} (CH_2Cl_2) 348, 414, 514 nm. ESI-MS calculated for $C_{53}H_{32}F_6FeN_6O$ $(M)^+$ 938.2, found 938.5; $C_{54}H_{36}F_6FeN_6O_2$ $(M+MeOH)^+$ 970.2, found 970.5.

Fe-*para*-urea. Metalation was performed as described above using 100 mg of *para*-urea. Purification was achieved by column chromatography (pure DCM then progressing slowly to 2% MeOH in DCM) on silica (93 mg, 80% yield). λ_{max} (CH_2Cl_2) 410, 571, 613 nm. ESI-MS calculated for $C_{53}H_{32}F_6FeN_6O$ $(M)^+$ 938.2, found 938.8; $C_{54}H_{36}F_6FeN_6O_2$ $(M+MeOH)^+$ 970.2, found 970.8.

Zn-*ortho*-urea. *Ortho*-urea (31 mg, 0.035 mmol) was dissolved in $CHCl_3$ (6 mL) and sparged with N_2 for 5 min. A solution of $Zn(OAc)_2$ (16 mg, 0.088 mmol) in methanol (1 mL) was added dropwise. The resulting solution was stirred at RT overnight in the absence of light. The organic phase was washed with saturated NaHCO3 (3x) followed by water (3x), then dried over $MgSO_4$. The product was purified by recrystallization via vapor diffusion of water into a solution of DMF (29 mg, 87% yield). Diffraction quality single crystals suitable for X-ray crystallography were grown by slow vapor diffusion of water into a saturated solution of Zn-*ortho*-urea in DMF. ^{1}H NMR (500 MHz, $CDCl_3$) δ 8.95 – 8.86 (m, 6H), 8.82 (d, J = 4.7 Hz, 2H), 8.55 (d, J = 8.5 Hz, 1H), 8.26 – 8.04 (m, 6H), 7.94 (d, J = 7.4 Hz, 1H), 7.83 – 7.63 (m, 11H), 7.41 (t, J = 7.4 Hz, 1H), 7.28 (s, 2H), 7.18 (s, 1H), 7.16 (br s, 1H). ^{13}C{^{1}H} NMR (126 MHz, CDCl3) δ 152.55, 150.37, 150.33, 150.26, 150.03, 142.98, 142.84, 140.88, 139.52, 134.82, 134.72 (d, J = 4.2 Hz), 134.43, 132.75, 132.08, 132.01, 131.93, 131.71, 131.44, 131.40, 129.25, 127.62, 126.73, 126.61, 126.56, 123.15 (q, J = 272.6 Hz), 121.51, 121.47, 121.09, 119.82, 117.46, 114.96 – 114.44 (m). ^{19}F NMR (376 MHz, $CDCl_3$) δ -62.47. λ_{max} (CH_2Cl_2) 419, 548. ESI-MS calculated for $C_{53}H_{32}F_6N_6OZn$ $(M)^+$ 946.2, found 946.8.

4.5.17 Crystallographic Data

Table 4.4. Crystallographic data for Zn-*ortho*-urea.

	Zn-*ortho*-urea
Chemical formula	$C_{66}H_{62}F_6N_{10.5}O_{5.5}Zn$
FW	1269.63
Crystal system, space group	Triclinic, *P*-1
Temperature (K)	100(2)
a (Å)	11.5913(8)
b (Å)	13.7936(9)
c (Å)	22.2041(16)
α (Å)	99.686(4)
β (Å)	93.808(4)
γ (Å)	118.752(3)
V(Å^3)	3023.1(4)
Z	2
μ (mm^{-1})	0.486
F(000)	1319
Crystal size (mm)	0.04 × 0.04 × 0.01
θ range (°) for cell measurement	1.73–25.73
Radiation type	Mo *K*α
No. of reflections for cell measurement	28655
Index ranges	$-11 \leq h \leq 13$
	$-16 \leq k \leq 16$
	$-26 \leq l \leq 25$
Reflections collected / unique	28655 / 10478
R_{int}	0.0778
Data / restraints / parameters	10478 / 12 / 757
Goodness-of-fit on F^2	1.035
Final R indices[a]	$R_1 = 0.105$, $wR_2 = 0.324$
Largest diff. peak and hole, eÅ^{-3}	1.7 and –1.4

[a] $R_1 = \sum||F_0| - F_C||/\sum|F_0|$, $R_2 = \{\sum[w(F_0^2 - F_0^2)^2]/\sum[\ w(F_0^2)^2]\}^{1/2}$.

4.5.18 NMR Spectra

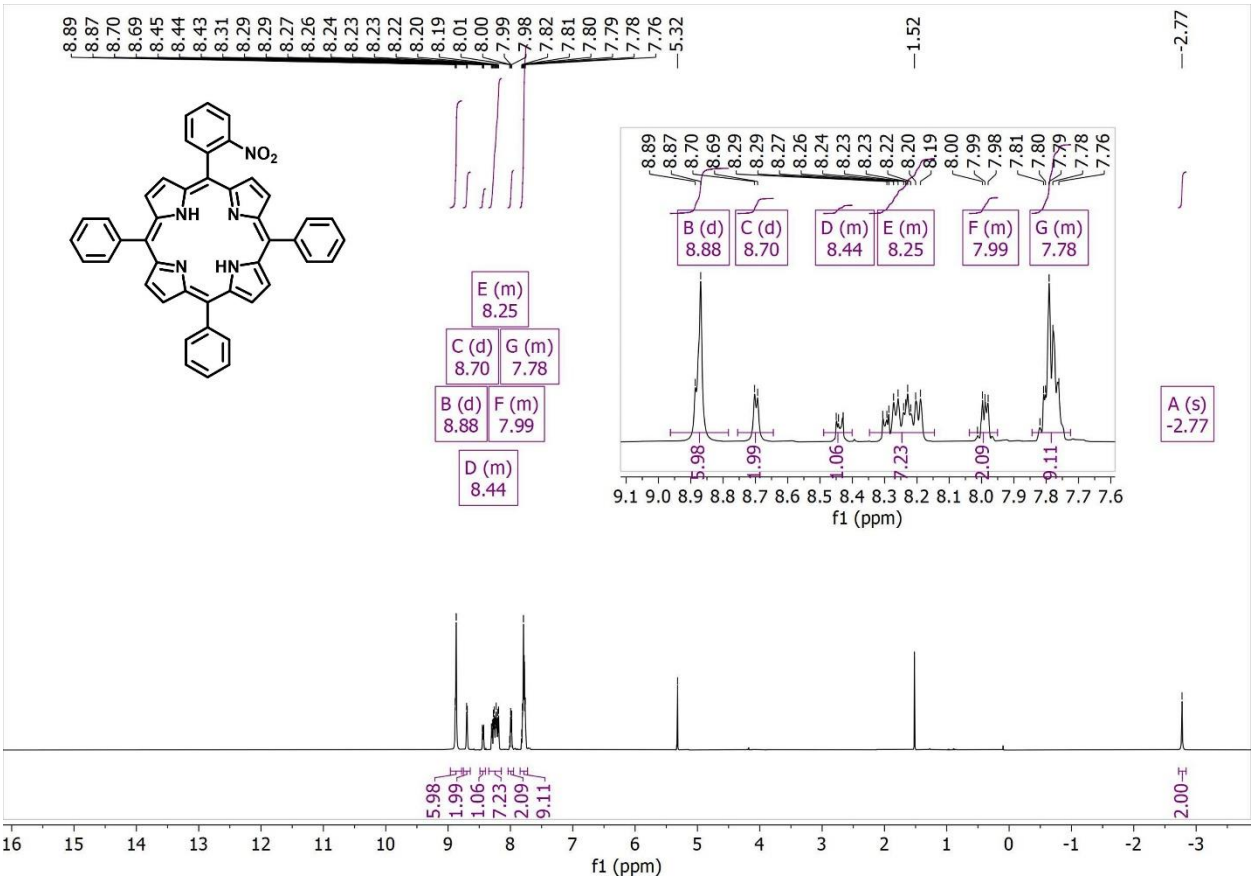


Figure 4.19. ^{1}H NMR of 5-(2-nitrophenyl)-10,15,20-triphenylporphyrin (**1**) in CD_2Cl_2.

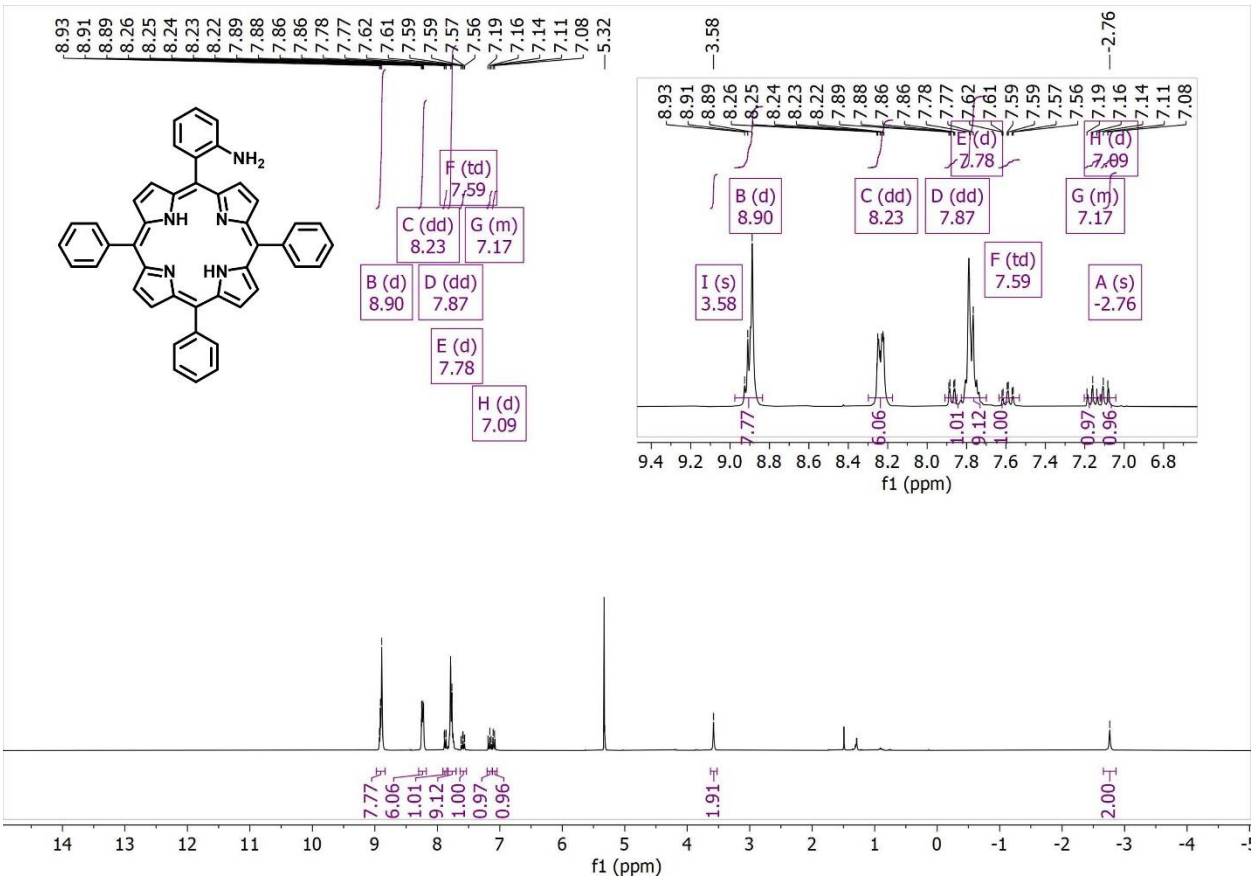


Figure 4.20. ^{1}H NMR of 2-(10,15,20-triphenylporphyrin-5-yl)aniline (**2**) in CD_2Cl_2.

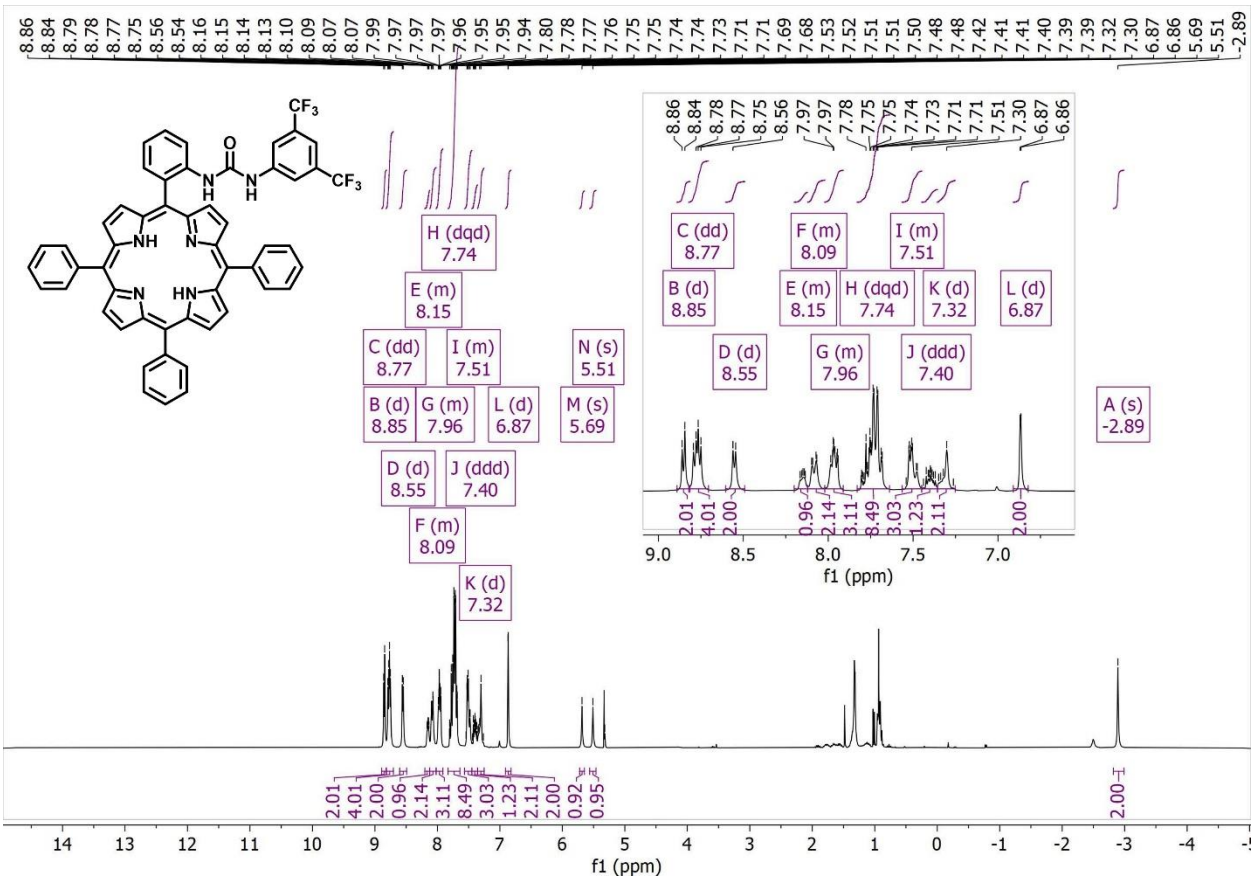


Figure 4.21. ^{1}H NMR of 1-(3,5-bis(trifluoromethyl)phenyl)-3-(2-(10,15,20-triphenylporphyrin-5-yl)phenyl)urea (*ortho*-urea) in CD_2Cl_2.

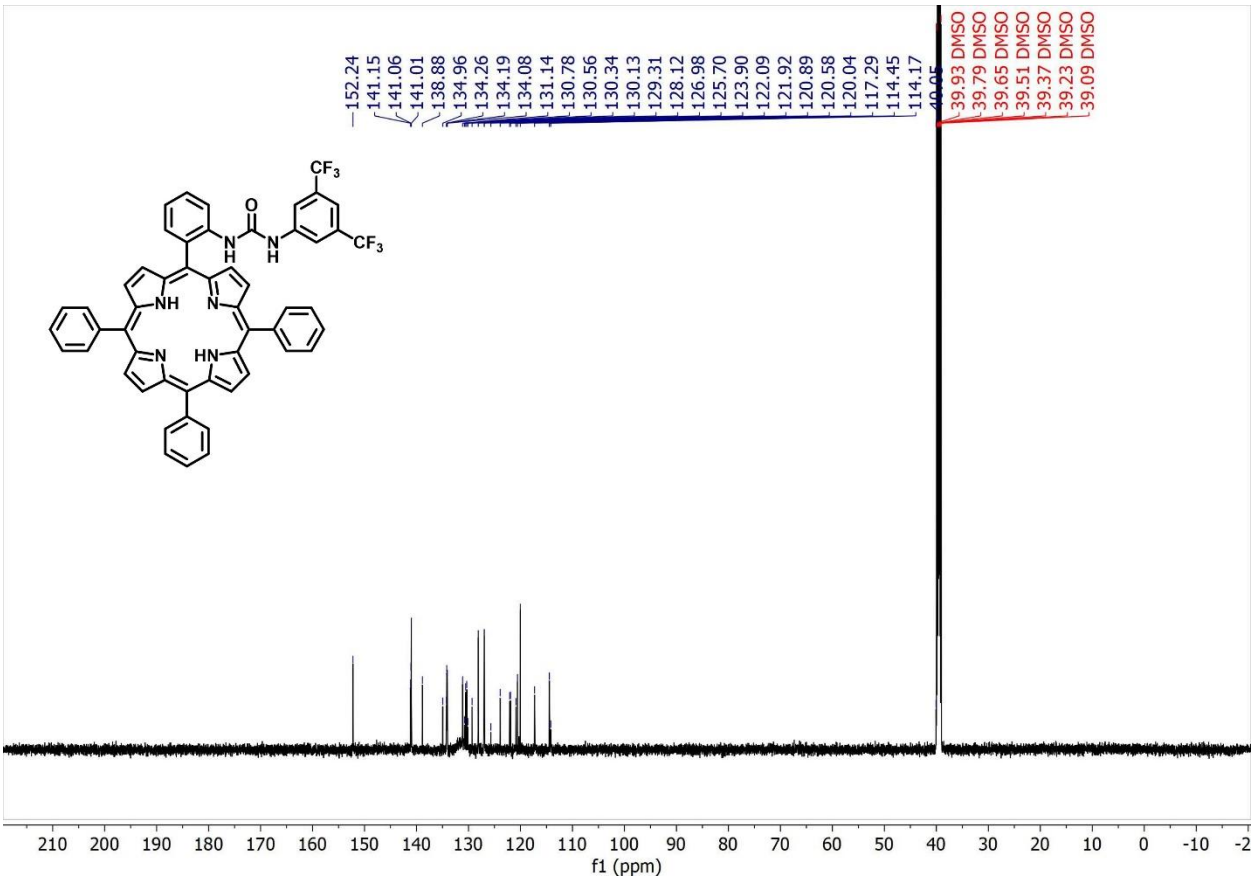


Figure 4.22. ^{13}C NMR of 1-(3,5-bis(trifluoromethyl)phenyl)-3-(2-(10,15,20-triphenylporphyrin-5-yl)phenyl)urea (*ortho*-urea) in DMSO-d_6.

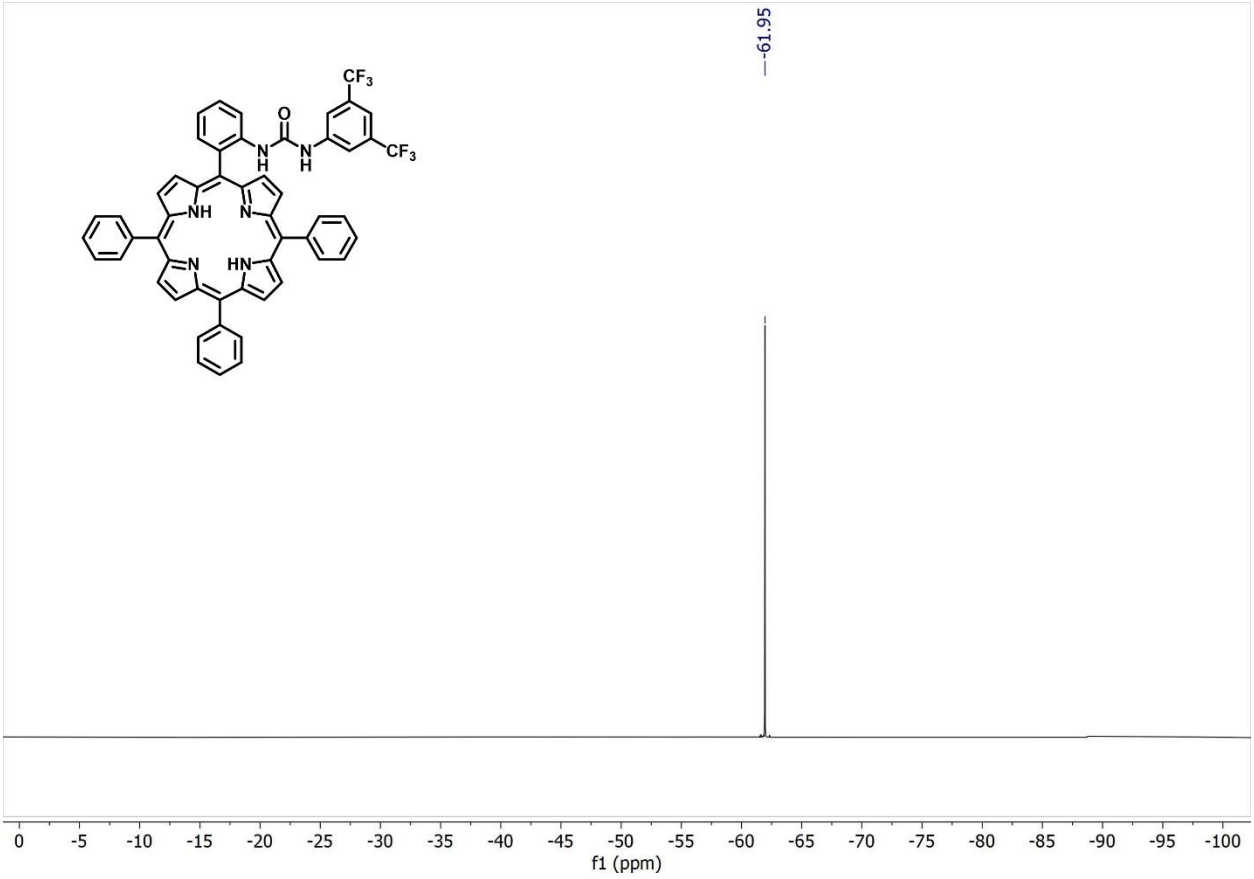


Figure 4.23. ^{19}F NMR of 1-(3,5-bis(trifluoromethyl)phenyl)-3-(2-(10,15,20-triphenylporphyrin-5-yl)phenyl)urea (*ortho*-urea) in DMSO-d_6.

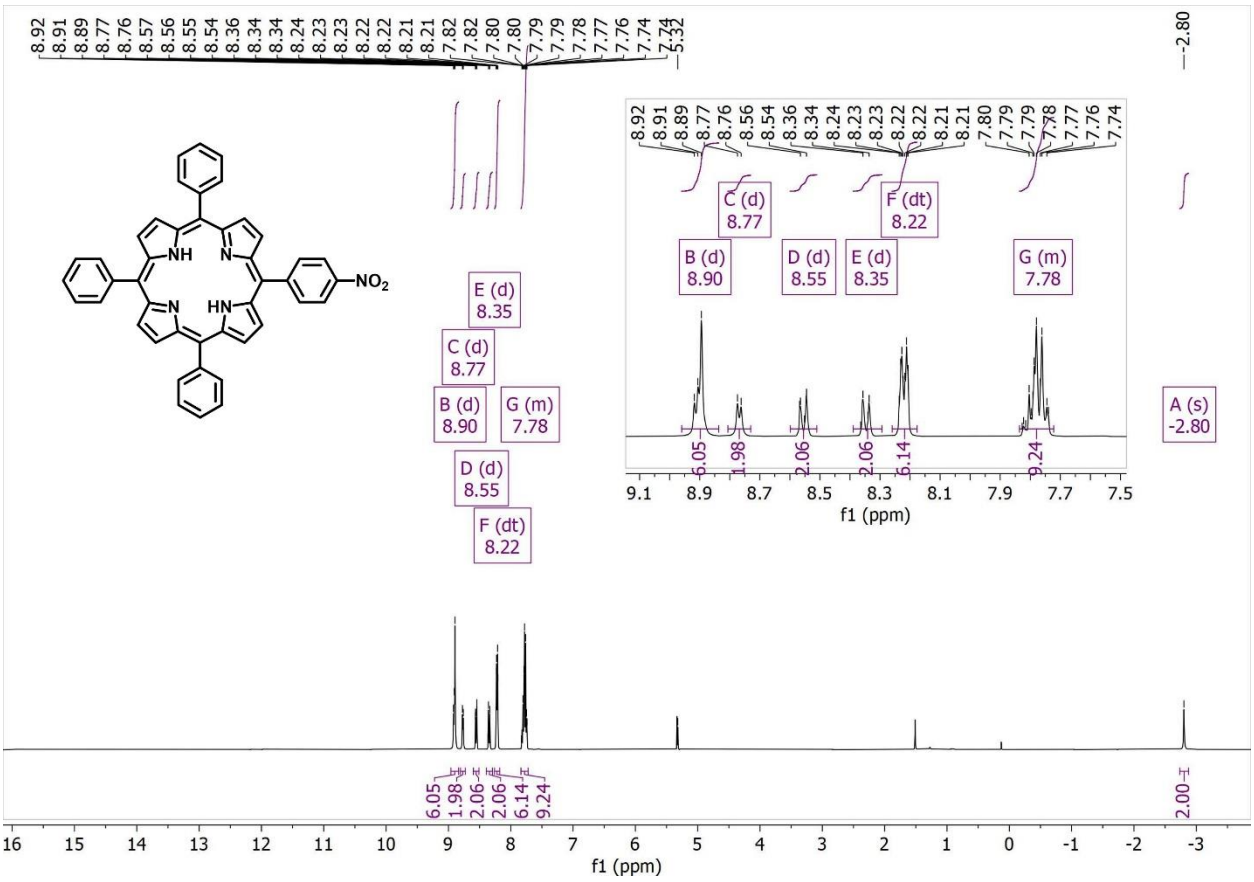


Figure 4.24. ^{1}H NMR of 5-(4-nitrophenyl)-10,15,20-triphenylporphryin (**3**) in CD_2Cl_2.

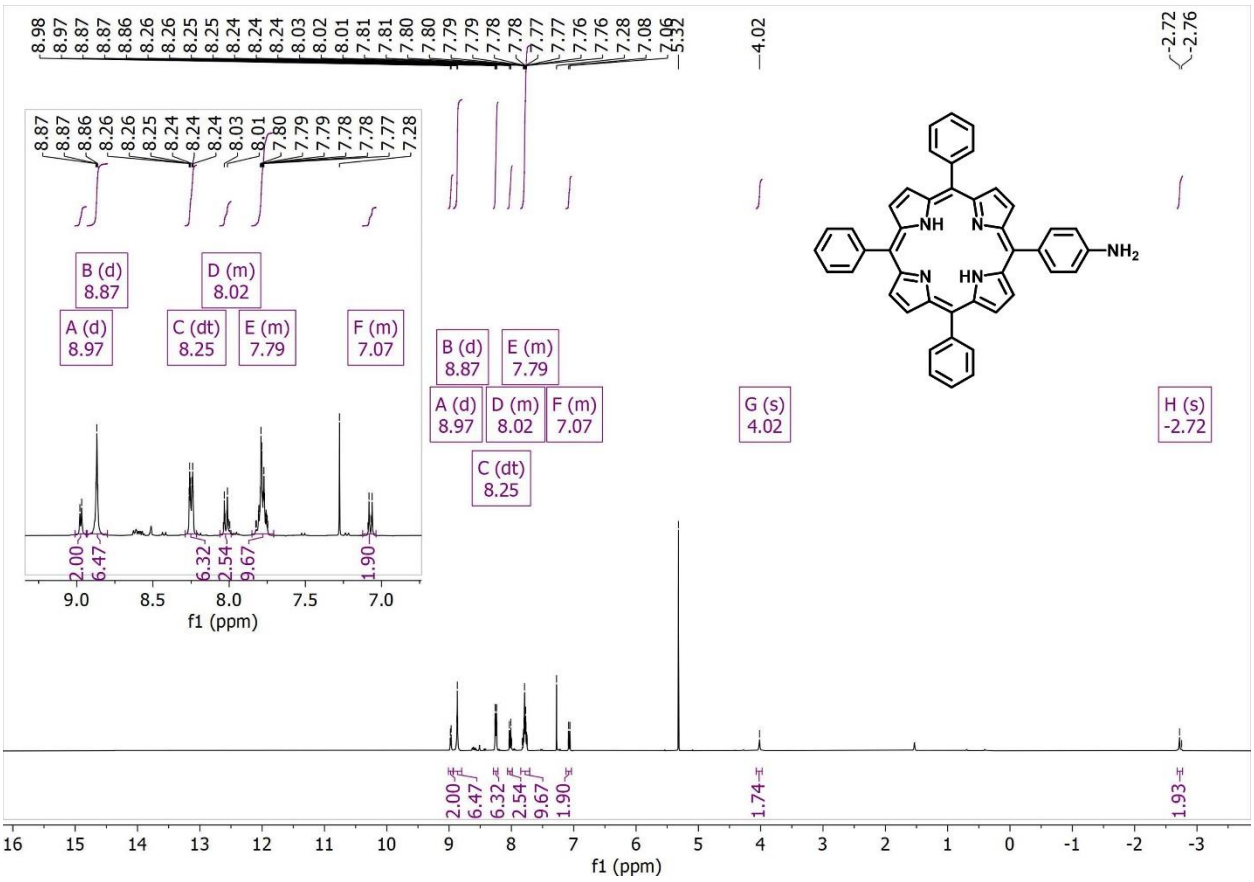


Figure 4.25. ^{1}H NMR of 4-(0,15,20-triphenylporphyrin-5-yl)aniline (**4**) in CD_2Cl_2.

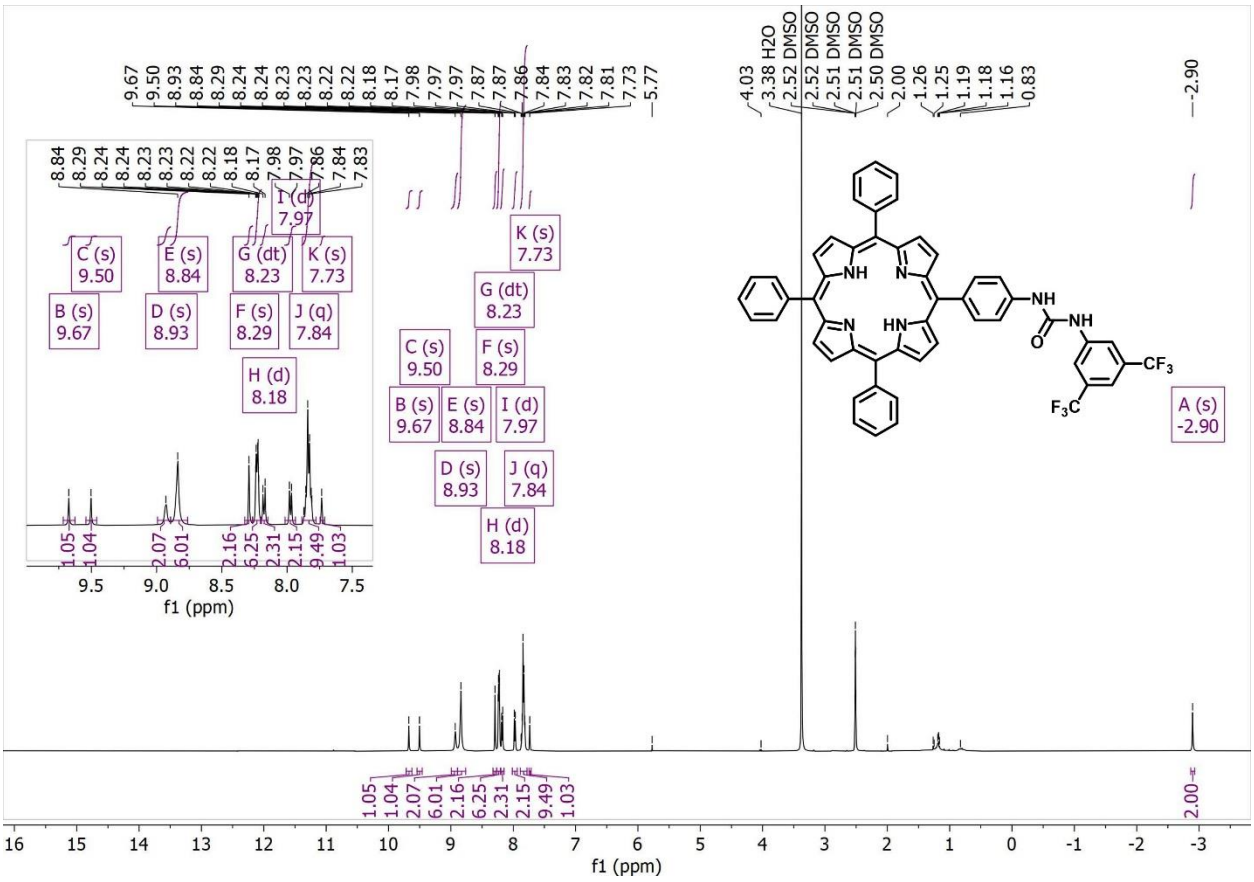


Figure 4.26. [1]H NMR of 1-(3,5-bis(trifluoromethyl)phenyl)-3-(4-(10,15,20-triphenylporphyrin-5-yl)phenyl)urea (*para*-urea).

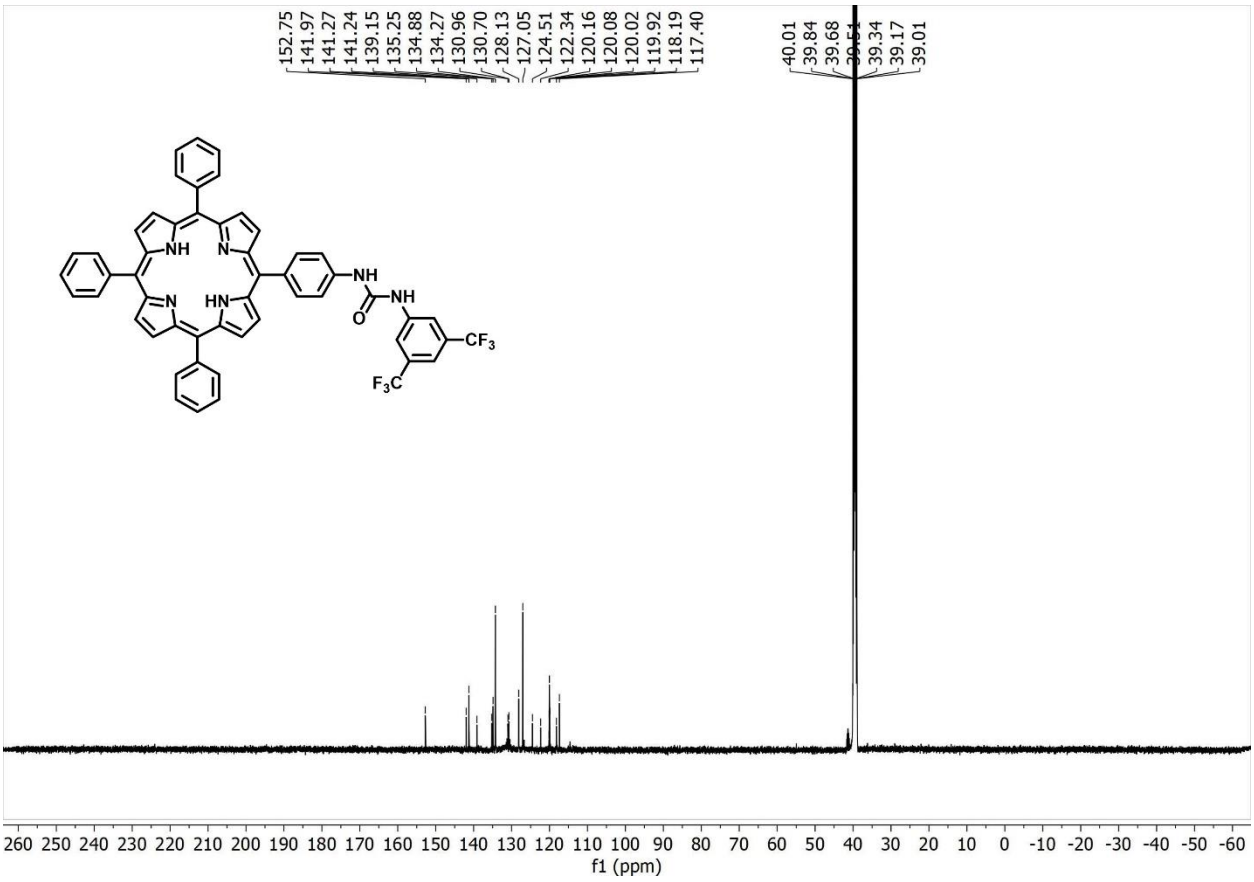


Figure 4.27. ^{13}C NMR of 1-(3,5-bis(trifluoromethyl)phenyl)-3-(4-(10,15,20-triphenylporphyrin-5-yl)phenyl)urea (*para*-urea).

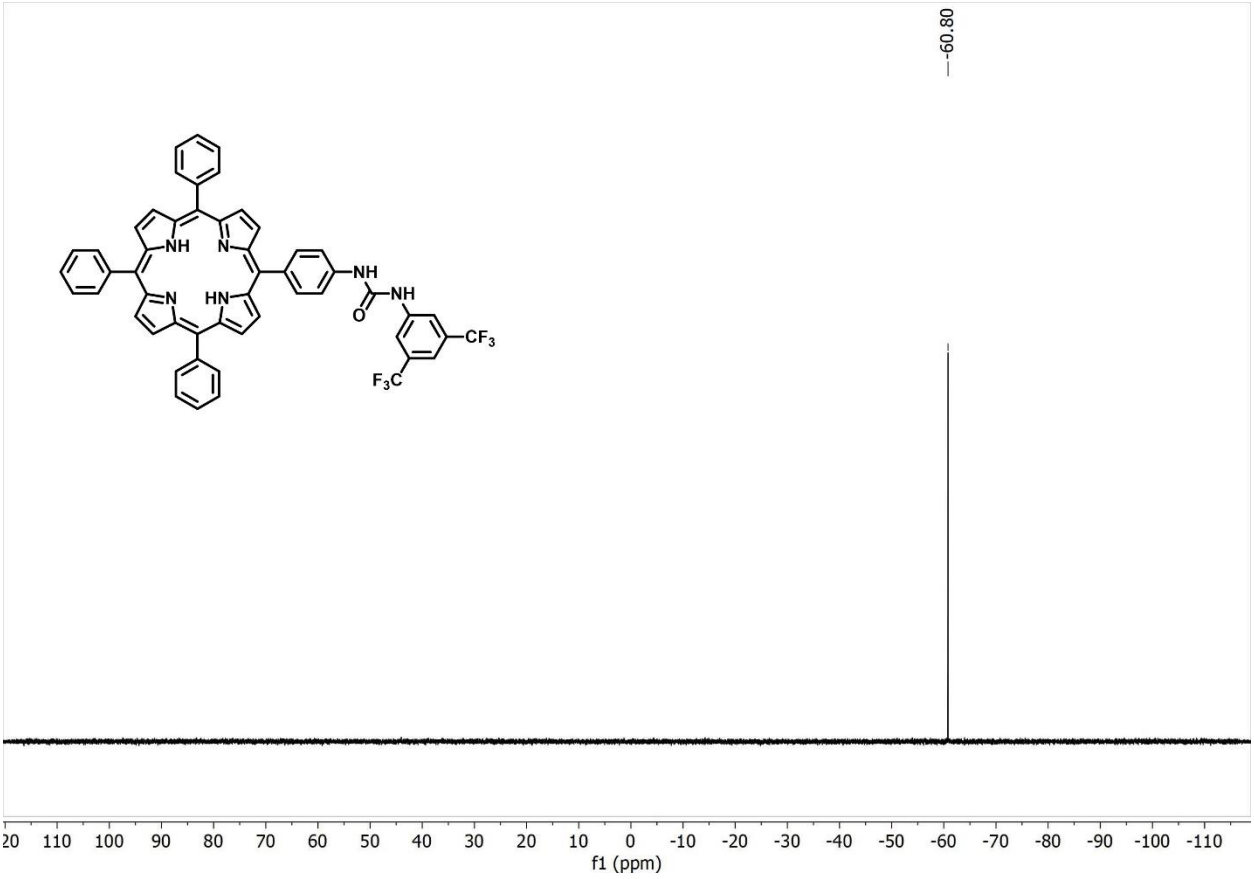


Figure 4.28. ^{19}F NMR of 1-(3,5-bis(trifluoromethyl)phenyl)-3-(4-(10,15,20-triphenylporphyrin-5-yl)phenyl)urea (*para*-urea).

4.6 References

(1) Appel, A. M.; Bercaw, J. E.; Bocarsly, A. B.; Dobbek, H.; DuBois, D. L.; Dupuis, M.; Ferry, J. G.; Fujita, E.; Hille, R.; Kenis, P. J. A.; Kerfeld, C. A.; Morris, R. H.; Peden, C. H. F.; Portis, A. R.; Ragsdale, S. W.; Rauchfuss, T. B.; Reek, J. N. H.; Seefeldt, L. C.; Thauer, R. K.; Waldrop, G. L. Frontiers, Opportunities, and Challenges in Biochemical and Chemical Catalysis of CO_2 Fixation. *Chem. Rev.* **2013**, *113*, 6621–6658.

(2) Benson, E. E.; Kubiak, C. P.; Sathrum, A. J.; Smieja, J. M. Electrocatalytic and Homogeneous Approaches to Conversion of CO_2 to Liquid Fuels. *Chem. Soc. Rev.* **2008**, *38*, 89–99.

(3) Lewis, N. S.; Nocera, D. G. Powering the Planet: Chemical Challenges in Solar Energy Utilization. *Proc. Natl. Acad. Sci.* **2006**, *103*, 15729–15735.

(4) De Luna, P.; Hahn, C.; Higgins, D.; Jaffer, S. A.; Jaramillo, T. F.; Sargent, E. H. What Would It Take for Renewably Powered Electrosynthesis to Displace Petrochemical Processes? *Science* **2019**, *364*, eaav3506.

(5) Francke, R.; Schille, B.; Roemelt, M. Homogeneously Catalyzed Electroreduction of Carbon Dioxide—Methods, Mechanisms, and Catalysts. *Chem. Rev.* **2018**, *118*, 4631–4701.

(6) Smith, P. T.; Nichols, E. M.; Cao, Z.; Chang, C. J. Hybrid Catalysts for Artificial Photosynthesis: Merging Approaches from Molecular, Materials, and Biological Catalysis. *Acc. Chem. Res.* **2020**, *53*, 575–587.

(7) Hori, Y. Electrochemical CO_2 Reduction on Metal Electrodes. In *Modern Aspects of Electrochemistry*; Vayenas, C. G., White, R. E., Gamboa-Aldeco, M. E., Eds.; Modern Aspects of Electrochemistry; Springer: New York, NY, **2008**, 89–189.

(8) Zhao, S.; Jin, R.; Jin, R. Opportunities and Challenges in CO_2 Reduction by Gold- and Silver-Based Electrocatalysts: From Bulk Metals to Nanoparticles and Atomically Precise Nanoclusters. *ACS Energy Lett.* **2018**, *3* , 452–462.

(9) Nitopi, S.; Bertheussen, E.; Scott, S. B.; Liu, X.; Engstfeld, A. K.; Horch, S.; Seger, B.; Stephens, I. E. L.; Chan, K.; Hahn, C.; Nørskov, J. K.; Jaramillo, T. F.; Chorkendorff, I. Progress and Perspectives of Electrochemical CO_2 Reduction on Copper in Aqueous Electrolyte. *Chem. Rev.* **2019**, *119* , 7610–7672.

(10) Proppe, A. H.; Li, Y. C.; Aspuru-Guzik, A.; Berlinguette, C. P.; Chang, C. J.; Cogdell, R.; Doyle, A. G.; Flick, J.; Gabor, N. M.; van Grondelle, R.; Hammes-Schiffer, S.; Jaffer, S. A.; Kelley, S. O.; Leclerc, M.; Leo, K.; Mallouk, T. E.; Narang, P.; Schlau-Cohen, G. S.; Scholes, G. D.; Vojvodic, A.; Yam, V. W.-W.; Yang, J. Y.; Sargent, E. H. Bioinspiration in Light Harvesting and Catalysis. *Nat. Rev. Mater.* **2020**, *5*, 828–846.

(11) Wuttig, A.; Yoon, Y.; Ryu, J.; Surendranath, Y. Bicarbonate Is Not a General Acid in Au-Catalyzed CO_2 Electroreduction. *J. Am. Chem. Soc.* **2017**, *139*, 17109–17113.

(12) Marcandalli, G.; Villalba, M.; Koper, M. T. M. The Importance of Acid–Base Equilibria in Bicarbonate Electrolytes for CO_2 Electrochemical Reduction and CO Reoxidation Studied on Au(hkl) Electrodes. *Langmuir* **2021**, *37*, 5707–5716.

(13) Zeng, J. S.; Corbin, N.; Williams, K.; Manthiram, K. Kinetic Analysis on the Role of Bicarbonate in Carbon Dioxide Electroreduction at Immobilized Cobalt Phthalocyanine. *ACS Catal.* **2020**, *10*, 4326–4336.

(14) Li, T.; Lees, E. W.; Goldman, M.; Salvatore, D. A.; Weekes, D. M.; Berlinguette, C. P. Electrolytic Conversion of Bicarbonate into CO in a Flow Cell. *Joule* **2019**, *3*, 1487–1497.

(15) Chen, Y.; Li, C. W.; Kanan, M. W. Aqueous CO_2 Reduction at Very Low Overpotential on Oxide-Derived Au Nanoparticles. *J. Am. Chem. Soc.* **2012**, *134*, 19969–19972.
(16) Dunwell, M.; Lu, Q.; Heyes, J. M.; Rosen, J.; Chen, J. G.; Yan, Y.; Jiao, F.; Xu, B. The Central Role of Bicarbonate in the Electrochemical Reduction of Carbon Dioxide on Gold. *J. Am. Chem. Soc.* **2017**, *139*, 3774–3783.
(17) Takahashi, K.; Hiratsuka, K.; Sasaki, H.; Toshima, S. Electrocatalytic Behavior of Metal Porphyrins in the Reduction of Carbon Dioxide. *Chem. Lett.* **1979**, *8*, 305–308.
(18) Hammouche, M.; Lexa, D.; Savéant, J. M.; Momenteau, M. Catalysis of the Electrochemical Reduction of Carbon Dioxide by Iron("0") Porphyrins. *J. Electroanal. Chem. Interfacial Electrochem.* **1988**, *249*, 347–351.
(19) Hammouche, M.; Lexa, D.; Momenteau, M.; Saveant, J. M. Chemical Catalysis of Electrochemical Reactions. Homogeneous Catalysis of the Electrochemical Reduction of Carbon Dioxide by Iron("0") Porphyrins. Role of the Addition of Magnesium Cations. *J. Am. Chem. Soc.* **1991**, *113*, 8455–8466.
(20) Bhugun, I.; Lexa, D.; Savéant, J.-M. Catalysis of the Electrochemical Reduction of Carbon Dioxide by Iron(0) Porphyrins: Synergystic Effect of Weak Brönsted Acids. *J. Am. Chem. Soc.* **1996**, *118*, 1769–1776.
(21) Behar, D.; Dhanasekaran, T.; Neta, P.; Hosten, C. M.; Ejeh, D.; Hambright, P.; Fujita, E. Cobalt Porphyrin Catalyzed Reduction of CO_2. Radiation Chemical, Photochemical, and Electrochemical Studies. *J. Phys. Chem. A* **1998**, *102*, 2870–2877.
(22) Evans, N. H.; Beer, P. D. Advances in Anion Supramolecular Chemistry: From Recognition to Chemical Applications. *Angew. Chem. Int. Ed.* **2014**, *53*, 11716–11754.
(23) Chen, L.; Berry, S. N.; Wu, X.; Howe, E. N. W.; Gale, P. A. Advances in Anion Receptor Chemistry. *Chem* **2020**, *6*, 61–141.
(24) Brooks, S. J.; Gale, P. A.; Light, M. E. Anion-Binding Modes in a Macrocyclic Amidourea. *Chem. Commun.* **2006**, 4344–4346.
(25) Busschaert, N.; Karagiannidis, L. E.; Wenzel, M.; Haynes, C. J. E.; Wells, N. J.; Young, P. G.; Makuc, D.; Plavec, J.; Jolliffe, K. A.; Gale, P. A. Synthetic Transporters for Sulfate: A New Method for the Direct Detection of Lipid Bilayer Sulfate Transport. *Chem. Sci.* **2014**, *5*, 1118–1127.
(26) Busschaert, N.; Gale, P. A.; Haynes, C. J. E.; Light, M. E.; Moore, S. J.; Tong, C. C.; Davis, J. T.; William A. Harrell, J. Tripodal Transmembrane Transporters for Bicarbonate. *Chem. Commun.* **2010**, *46*, 6252–6254.
(27) Manna, U.; Das, A.; Das, G. Self-Assemblies of Positional Isomeric Linear Bis-Urea Ligands with Oxyanions/Hydrated Oxyanions: Evidence of F^- and OH^- Induced Atmospheric CO_2 Fixation. *Cryst. Growth Des.* **2018**, *18*, 6801–6815.
(28) Brooks, S. J.; Edwards, P. R.; Gale, P. A.; Light, M. E. Carboxylate Complexation by a Family of Easy-to-Make Ortho-Phenylenediamine Based Bis-Ureas: Studies in Solution and the Solid State. *New J. Chem.* **2006**, *30*, 65–70.
(29) Moore, S. J.; Haynes, C. J. E.; González, J.; Sutton, J. L.; Brooks, S. J.; Light, M. E.; Herniman, J.; Langley, G. J.; Soto-Cerrato, V.; Pérez-Tomás, R.; Marques, I.; Costa, P. J.; Félix, V.; Gale, P. A. Chloride, Carboxylate, and Carbonate Transport by Ortho-Phenylenediamine-Based Bisureas. *Chem Sci* **2013**, *4*, 103–117.
(30) Manna, U.; Kayal, S.; Nayak, B.; Das, G. Systematic Size Mediated Trapping of Anions of Varied Dimensionality within a Dimeric Capsular Assembly of a Flexible Neutral Bis-Urea Platform. *Dalton Trans.* **2017**, *46*, 11956–11969.

(31) Manna, U.; Kayal, S.; Samanta, S.; Das, G. Fixation of Atmospheric CO_2 as Novel Carbonate–(Water)$_2$–Carbonate Cluster and Entrapment of Double Sulfate within a Linear Tetrameric Barrel of a Neutral Bis-Urea Scaffold. *Dalton Trans.* **2017**, *46*, 10374–10386.
(32) Nichols, E. M.; Derrick, J. S.; Nistanaki, S. K.; Smith, P. T.; Chang, C. J. Positional Effects of Second-Sphere Amide Pendants on Electrochemical CO_2 Reduction Catalyzed by Iron Porphyrins. *Chem. Sci.* **2018**, *9*, 2952–2960.
(33) Nichols, E. M.; Chang, C. J. Urea-Based Multipoint Hydrogen-Bond Donor Additive Promotes Electrochemical CO_2 Reduction Catalyzed by Nickel Cyclam. *Organometallics* **2019**, *38*, 1213–1218.
(34) Costentin, C.; Drouet, S.; Robert, M.; Savéant, J.-M. A Local Proton Source Enhances CO_2 Electroreduction to CO by a Molecular Fe Catalyst. *Science* **2012**, *338*, 90–94.
(35) Costentin, C.; Passard, G.; Robert, M.; Savéant, J.-M. Ultraefficient Homogeneous Catalyst for the CO_2-to-CO Electrochemical Conversion. *Proc. Natl. Acad. Sci.* **2014**, *111*, 14990–14994.
(36) Azcarate, I.; Costentin, C.; Robert, M.; Savéant, J.-M. Through-Space Charge Interaction Substituent Effects in Molecular Catalysis Leading to the Design of the Most Efficient Catalyst of CO_2-to-CO Electrochemical Conversion. *J. Am. Chem. Soc.* **2016**, *138*, 16639–16644.
(37) Kinzel, N. W.; Werlé, C.; Leitner, W. Transition Metal Complexes as Catalysts for the Electroconversion of CO_2: An Organometallic Perspective. *Angew. Chem. Int. Ed.* **2021**, *60*, 11628–11686.
(38) Drover, M. W. A Guide to Secondary Coordination Sphere Editing. *Chem. Soc. Rev.* **2022**, *51*, 1861 – 1880.
(39) Haviv, E.; Azaiza-Dabbah, D.; Carmieli, R.; Avram, L.; Martin, J. M. L.; Neumann, R. A Thiourea Tether in the Second Coordination Sphere as a Binding Site for CO_2 and a Proton Donor Promotes the Electrochemical Reduction of CO_2 to CO Catalyzed by a Rhenium Bipyridine-Type Complex. *J. Am. Chem. Soc.* **2018**, *140*, 12451–12456.
(40) Sen, P.; Mondal, B.; Saha, D.; Rana, A.; Dey, A. Role of 2nd Sphere H-Bonding Residues in Tuning the Kinetics of CO_2 Reduction to CO by Iron Porphyrin Complexes. *Dalton Trans.* **2019**, *48*, 5965–5977.
(41) Amanullah, S.; Saha, P.; Dey, A. Activating the Fe(I) State of Iron Porphyrinoid with Second-Sphere Proton Transfer Residues for Selective Reduction of CO_2 to HCOOH via Fe(III/II)–COOH Intermediate(s). *J. Am. Chem. Soc.* **2021**, *143*, 13579–13592.
(42) Johnson, E. M.; Liu, J. J.; Samuel, A. D.; Haiges, R.; Marinescu, S. C. Switching Catalyst Selectivity via the Introduction of a Pendant Nitrophenyl Group. *Inorg. Chem.* **2022**, *61*, 1316–1326.
(43) Chapovetsky, A.; Liu, J. J.; Welborn, M.; Luna, J. M.; Do, T.; Haiges, R.; Miller III, T. F.; Marinescu, S. C. Electronically Modified Cobalt Aminopyridine Complexes Reveal an Orthogonal Axis for Catalytic Optimization for CO_2 Reduction. *Inorg. Chem.* **2020**, *59*, 13709–13718.
(44) Chapovetsky, A.; Welborn, M.; Luna, J. M.; Haiges, R.; Miller, T. F.; Marinescu, S. C. Pendant Hydrogen-Bond Donors in Cobalt Catalysts Independently Enhance CO_2 Reduction. *ACS Cent. Sci.* **2018**, *4*, 397–404.
(45) Yang, J. Y.; Smith, S. E.; Liu, T.; Dougherty, W. G.; Hoffert, W. A.; Kassel, W. S.; DuBois, M. R.; DuBois, D. L.; Bullock, R. M. Two Pathways for Electrocatalytic Oxidation of

Hydrogen by a Nickel Bis(Diphosphine) Complex with Pendant Amines in the Second Coordination Sphere. *J. Am. Chem. Soc.* **2013**, *135*, 9700–9712.
(46) Margarit, C. G.; Asimow, N. G.; Gonzalez, M. I.; Nocera, D. G. Double Hangman Iron Porphyrin and the Effect of Electrostatic Nonbonding Interactions on Carbon Dioxide Reduction. *J. Phys. Chem. Lett.* **2020**, *11*, 1890–1895.
(47) Margarit, C. G.; Schnedermann, C.; Asimow, N. G.; Nocera, D. G. Carbon Dioxide Reduction by Iron Hangman Porphyrins. *Organometallics* **2019**, *38*, 1219–1223.
(48) Gotico, P.; Boitrel, B.; Guillot, R.; Sircoglou, M.; Quaranta, A.; Halime, Z.; Leibl, W.; Aukauloo, A. Second-Sphere Biomimetic Multipoint Hydrogen-Bonding Patterns to Boost CO_2 Reduction of Iron Porphyrins. *Angew. Chem. Int. Ed.* **2019**, *58*, 4504–4509.
(49) Gotico, P.; Roupnel, L.; Guillot, R.; Sircoglou, M.; Leibl, W.; Halime, Z.; Aukauloo, A. Atropisomeric Hydrogen Bonding Control for CO_2 Binding and Enhancement of Electrocatalytic Reduction at Iron Porphyrins. *Angew. Chem. Int. Ed.* **2020**, *59*, 22451–22455.
(50) Khadhraoui, A.; Gotico, P.; Leibl, W.; Halime, Z.; Aukauloo, A. Through-Space Electrostatic Interactions Surpass Classical Through-Bond Electronic Effects in Enhancing CO_2 Reduction Performance of Iron Porphyrins. *ChemSusChem* **2021**, *14*, 1308–1315.
(51) Zhang, C.; Dragoe, D.; Brisset, F.; Boitrel, B.; Lassalle-Kaiser, B.; Leibl, W.; Halime, Z.; Aukauloo, A. Second-Sphere Hydrogen-Bonding Enhances Heterogeneous Electrocatalytic CO_2 to CO Reduction by Iron Porphyrins in Water. *Green Chem.* **2021**, *23*, 8979–8987.
(52) Zhang, Z.; Schreiner, P. R. (Thio)Urea Organocatalysis—What Can Be Learnt from Anion Recognition? *Chem. Soc. Rev.* **2009**, *38*, 1187–1198.
(53) Lee, K. J.; McCarthy, B. D.; Dempsey, J. L. On Decomposition, Degradation, and Voltammetric Deviation: The Electrochemist's Field Guide to Identifying Precatalyst Transformation. *Chem. Soc. Rev.* **2019**, *48*, 2927–2945.
(54) Costentin, C.; Savéant, J.-M. Homogeneous Molecular Catalysis of Electrochemical Reactions: Manipulating Intrinsic and Operational Factors for Catalyst Improvement. *J. Am. Chem. Soc.* **2018**, *140*, 16669–16675.
(55) Bordwell, F. G. Equilibrium Acidities in Dimethyl Sulfoxide Solution. *Acc. Chem. Res.* **1988**, *21*, 456–463.
(56) Antony, J.; Grimme, S. Density Functional Theory Including Dispersion Corrections for Intermolecular Interactions in a Large Benchmark Set of Biologically Relevant Molecules. *Phys. Chem. Chem. Phys.* **2006**, *8*, 5287–5293.
(57) Costentin, C.; Drouet, S.; Robert, M.; Savéant, J.-M. Turnover Numbers, Turnover Frequencies, and Overpotential in Molecular Catalysis of Electrochemical Reactions. Cyclic Voltammetry and Preparative-Scale Electrolysis. *J. Am. Chem. Soc.* **2012**, *134*, 11235–11242.
(58) Costentin, C.; Drouet, S.; Robert, M.; Savéant, J.-M. Correction to Turnover Numbers, Turnover Frequencies, and Overpotential in Molecular Catalysis of Electrochemical Reactions. Cyclic Voltammetry and Preparative-Scale Electrolysis. *J. Am. Chem. Soc.* **2012**, *134*, 19949–19950.
(59) Sheldrick, G. M. Crystal Structure Refinement with *SHELXL*. *Acta Crystallogr. Sect. C Struct. Chem.* **2015**, *71*, 3–8.
(60) Jakab, G.; Tancon, C.; Zhang, Z.; Lippert, K. M.; Schreiner, P. R. (Thio)Urea Organocatalyst Equilibrium Acidities in DMSO. *Org. Lett.* **2012**, *14*, 1724–1727.

(61) Shao, Y.; Gan, Z.; Epifanovsky, E.; Gilbert, A. T. B.; Wormit, M.; Kussmann, J.; Lange, A. W.; Behn, A.; Deng, J.; Feng, X.; Ghosh, D.; Goldey, M.; Horn, P. R.; Jacobson, L. D.; Kaliman, I.; Khaliullin, R. Z.; Kuś, T.; Landau, A.; Liu, J.; Proynov, E. I.; Rhee, Y. M.; Richard, R. M.; Rohrdanz, M. A.; Steele, R. P.; Sundstrom, E. J.; Woodcock, H. L.; Zimmerman, P. M.; Zuev, D.; Albrecht, B.; Alguire, E.; Austin, B.; Beran, G. J. O.; Bernard, Y. A.; Berquist, E.; Brandhorst, K.; Bravaya, K. B.; Brown, S. T.; Casanova, D.; Chang, C.-M.; Chen, Y.; Chien, S. H.; Closser, K. D.; Crittenden, D. L.; Diedenhofen, M.; DiStasio, R. A.; Do, H.; Dutoi, A. D.; Edgar, R. G.; Fatehi, S.; Fusti-Molnar, L.; Ghysels, A.; Golubeva-Zadorozhnaya, A.; Gomes, J.; Hanson-Heine, M. W. D.; Harbach, P. H. P.; Hauser, A. W.; Hohenstein, E. G.; Holden, Z. C.; Jagau, T.-C.; Ji, H.; Kaduk, B.; Khistyaev, K.; Kim, J.; Kim, J.; King, R. A.; Klunzinger, P.; Kosenkov, D.; Kowalczyk, T.; Krauter, C. M.; Lao, K. U.; Laurent, A. D.; Lawler, K. V.; Levchenko, S. V.; Lin, C. Y.; Liu, F.; Livshits, E.; Lochan, R. C.; Luenser, A.; Manohar, P.; Manzer, S. F.; Mao, S.-P.; Mardirossian, N.; Marenich, A. V.; Maurer, S. A.; Mayhall, N. J.; Neuscamman, E.; Oana, C. M.; Olivares-Amaya, R.; O'Neill, D. P.; Parkhill, J. A.; Perrine, T. M.; Peverati, R.; Prociuk, A.; Rehn, D. R.; Rosta, E.; Russ, N. J.; Sharada, S. M.; Sharma, S.; Small, D. W.; Sodt, A.; Stein, T.; Stück, D.; Su, Y.-C.; Thom, A. J. W.; Tsuchimochi, T.; Vanovschi, V.; Vogt, L.; Vydrov, O.; Wang, T.; Watson, M. A.; Wenzel, J.; White, A.; Williams, C. F.; Yang, J.; Yeganeh, S.; Yost, S. R.; You, Z.-Q.; Zhang, I. Y.; Zhang, X.; Zhao, Y.; Brooks, B. R.; Chan, G. K. L.; Chipman, D. M.; Cramer, C. J.; Goddard, W. A.; Gordon, M. S.; Hehre, W. J.; Klamt, A.; Schaefer, H. F.; Schmidt, M. W.; Sherrill, C. D.; Truhlar, D. G.; Warshel, A.; Xu, X.; Aspuru-Guzik, A.; Baer, R.; Bell, A. T.; Besley, N. A.; Chai, J.-D.; Dreuw, A.; Dunietz, B. D.; Furlani, T. R.; Gwaltney, S. R.; Hsu, C.-P.; Jung, Y.; Kong, J.; Lambrecht, D. S.; Liang, W.; Ochsenfeld, C.; Rassolov, V. A.; Slipchenko, L. V.; Subotnik, J. E.; Van Voorhis, T.; Herbert, J. M.; Krylov, A. I.; Gill, P. M. W.; Head-Gordon, M. Advances in Molecular Quantum Chemistry Contained in the Q-Chem 4 Program Package. *Mol. Phys.* **2015**, *113*, 184–215.

(62) Weigend, F.; Ahlrichs, R. Balanced Basis Sets of Split Valence, Triple Zeta Valence and Quadruple Zeta Valence Quality for H to Rn: Design and Assessment of Accuracy. *Phys. Chem. Chem. Phys.* **2005**, *7*, 3297–3305.

(63) Chai, J.-D.; Head-Gordon, M. Long-Range Corrected Hybrid Density Functionals with Damped Atom–Atom Dispersion Corrections. *Phys. Chem. Chem. Phys.* **2008**, *10*, 6615–6620.

(64) Rossini, E.; Knapp, E.-W. Proton Solvation in Protic and Aprotic Solvents. *J. Comput. Chem.* **2016**, *37*, 1082–1091.

(65) Rossini, E.; Knapp, E.-W. Erratum: Proton Solvation in Protic and Aprotic Solvents *J. Comput. Chem.* **2016**, *37*, 2163–2164.

(66) Bryden, F.; Boyle, R. W. A Mild, Facile, One-Pot Synthesis of Zinc Azido Porphyrins as Substrates for Use in Click Chemistry. *Synlett* **2013**, *24*, 1978–1982.

(67) Landrum, J. T.; Grimmett, D.; Haller, K. J.; Scheidt, W. R.; Reed, C. A. Imidazolate- and Oxo-Bridged Metalloporphyrins. *J. Am. Chem. Soc.* **1981**, *103*, 2640–2650.

(68) Harvey, P. D.; Tasan, S.; Gros, C. P.; Devillers, C. H.; Richard, P.; Gendre, P. L.; Bodio, E. Ruthenium and Osmium Complexes of Phosphine-Porphyrin Derivatives as Potential Bimetallic Theranostics: Photophysical Studies. Organometallics 2015, 34, 1218–1227.

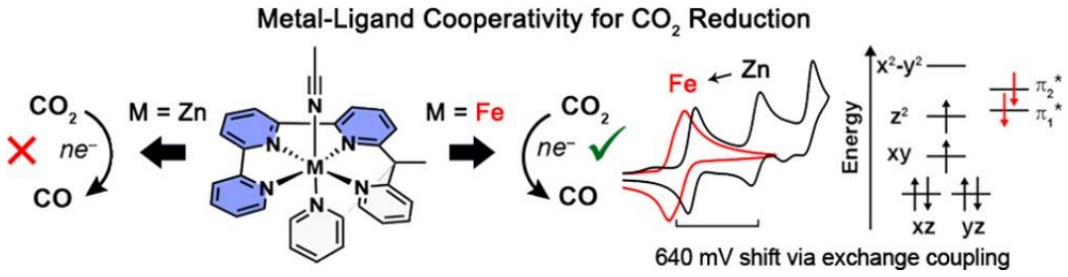
Chapter 5: Metal–Ligand Cooperativity via Exchange Coupling Promotes Iron-Catalyzed Electrochemical Carbon Dioxide Reduction at Low Overpotentials

Portions of this work were published in the following scientific journal:
Derrick, J. S.; Loipersberger, M.; Chatterjee, R.; Iovan, D. A.; Smith, P. T.; Chakarawet, K.; Yano, J.; Long, J. R.; Head-Gordon, M.; Chang, C. J. Metal–Ligand Cooperativity via Exchange Coupling Promotes Iron-Catalyzed Electrochemical CO_2 Reduction at Low Overpotentials. *Journal of the American Chemical Society* **2020**, *142*, 20489 – 20501.

Specific Contributions: Dr. Matthias Loipersberger did the computations and Dr. Ruchira Chatterjee performed the X-ray absorption measurements.

5.1 Abstract

Biological and heterogeneous catalysts for the electrochemical CO_2 Reduction Reaction (CO_2RR) often exhibit a high degree of electronic delocalization that serves to minimize overpotential and maximize selectivity over the hydrogen evolution reaction (HER). Here, we report a molecular iron(II) system that captures this design concept in a homogeneous setting through the use of a redox non-innocent terpyridine-based pentapyridine ligand (tpyPY2Me). As a result of strong metal–ligand exchange coupling between the Fe(II) center and ligand, $[Fe(tpyPY2Me)]^{2+}$ exhibits redox behavior at potentials 640 mV more positive than the isostructural $[Zn(tpyPY2Me)]^{2+}$ analog containing the redox-inactive Zn(II) ion. This shift in redox potential is attributed to the requirement for both an open-shell metal ion and a redox non-innocent ligand. The metal–ligand cooperativity in $[Fe(tpyPY2Me)]^{2+}$ drives the electrochemical reduction of CO_2 to CO at low overpotentials with high selectivity for CO_2RR (>90%) and turnover frequencies of 100,000 s^{-1} with no degradation over 20 h. The decrease in the thermodynamic barrier engendered by this coupling also enables homogeneous CO_2 reduction catalysis in water without compromising selectivity or rates. Synthesis of the two-electron reduction product, $[Fe(tpyPY2Me)]^0$, and characterization by X-ray crystallography, Mössbauer spectroscopy, X-ray absorption spectroscopy (XAS), variable temperature NMR, and density functional theory (DFT) calculations, support assignment of an open-shell singlet electronic structure that maintains a formal Fe(II) oxidation state with a doubly reduced ligand system. This work provides a starting point for the design of systems that exploit metal–ligand cooperativity for electrocatalysis where the electrochemical potential of redox non-innocent ligands can be tuned through secondary metal-dependent interactions.



5.2 Introduction

The electrochemical carbon dioxide reduction reaction (CO_2RR) provides opportunities to synthesize value-added products from this greenhouse gas in a sustainable manner.[1,2] Efficient catalysts for this reaction are required to selectively drive CO_2 reduction over the thermodynamic and kinetically competitive hydrogen evolution reaction (HER).[3] Biological,[4] heterogeneous,[5] and molecular[3] catalysts have been studied for CO_2 reduction, and molecular systems in particular offer potential advantages such as their small size relative to enzymes and the fact that they can be tuned with a level of atomic precision that is inaccessible with heterogeneous materials.[6] However, despite advances in the development of molecular catalysts with highly specialized ligand scaffolds, including cyclams,[7–10] porphyrins and phthalocyanines,[11–15] and tricarbonyl-bipyridines,[16,17] it remains a challenge to design molecules that exhibit low overpotentials, high turnover numbers, and compatibility with aqueous electrolytes to avoid off-pathway HER processes. In this regard, one key advantage of biological and heterogeneous catalysts is their ability to minimize overpotential and maximize selectivity for CO_2 reduction via electronic delocalization, either through electron-tunneling pathways[18,19] or a high local density of states,[20–22] respectively. Such systems can thereby achieve organization and separation of reducing equivalents in a way that is challenging to design in molecular systems.

Previous work from our laboratories has explored the chemistry of the $PY5Me_2$ ligand (2,6-bis(1,1-bis(2-pyridyl)ethyl)pyridine) and its molybdenum[23–25] and cobalt[25,26] derivatives as catalysts for the HER. We reasoned that by incorporating a redox-active pendant such as terpyridine[27–29] within this ligand scaffold, it would be possible to increase metal–ligand orbital mixing and delocalization of electron density away from the metal center to favor CO_2 reduction (**Figure 5.1**). Precedent for the use of redox non-innocent ligands in molecular electrochemical CO_2RR has shown the viability of this strategy,[16,17,27–39] along with classic systems bearing strong metal–ligand cooperativity such as metal-dithiolenes for HER.[40–43] Indeed, the suppression of metal-centered reductions can limit the formation of off-pathway metal hydride intermediates necessary for hydrogen evolution[35,44] and thereby favor CO_2 reduction catalysis. As part of a larger program in electrocatalysis via bioinorganic mimicry,[6,24,25,45–48] our synthetic approach was inspired by mononuclear iron hydrogenase enzymes, which catalyze the reduction of methenyl-H_4MPT^+ to methylene-H_4MPT in methanogenic archaea.[49] In these systems, heterolysis of H_2 and hydride shuttling is enabled by a single redox-innocent iron(II) site that synergistically interacts with a redox non-innocent guanyl pyridinol cofactor in the primary coordination sphere to provide reducing equivalents (**Figure 5.1**).

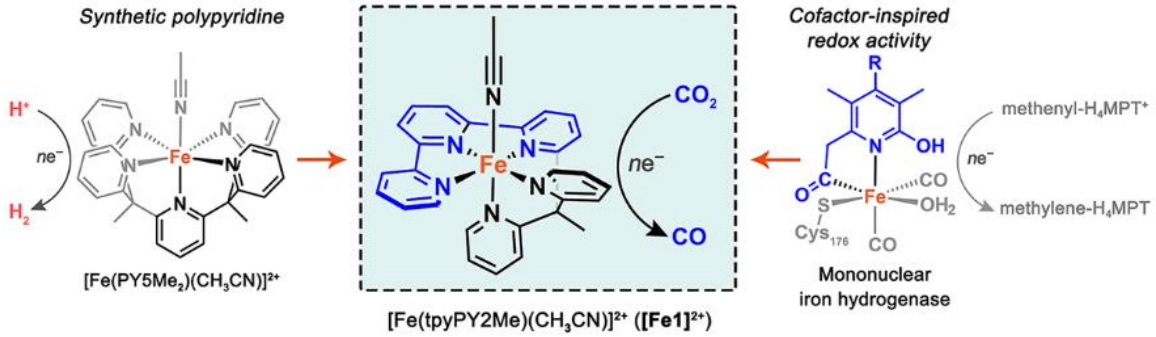


Figure 5.1. Bioinspired design of a molecular iron polypyridyl complex for electrochemical carbon dioxide reduction catalysis. The molecular CO_2 reduction catalyst $[Fe1]^{2+}$ was designed to feature a mononuclear iron center supported by a redox-active pendant in a robust synthetic polypyridyl scaffold, inspired by the active site of mononuclear iron hydrogenase.

Here we report an iron polypyridine complex $[Fe(tpyPY2Me)(CH_3CN)]^{2+}$ ($[Fe1]^{2+}$) (tpyPY2Me = 6-(1,1-di(pyridin-2-yl)ethyl)-2,2′:6′,2″-terpyridine), which features a redox-active terpyridine fragment and demonstrates this principle of electronic delocalization. In particular, metal–ligand cooperativity promotes strong exchange coupling between the redox-active tpyPY2Me ligand and iron(II) center where the $[Fe(tpyPY2Me)]^{2+}$ complex is able to accept two electrons at reduction potentials that are 640 mV more positive than the isostructural $[Zn(tpyPY2Me)]^{2+}$ analog containing the redox-inactive Zn(II) ion, showing that a redox non-innocent ligand alone is not sufficient to promote multielectron redox chemistry with low activation barriers. Upon two-electron reduction of $[Fe(tpyPY2Me)]^{2+}$, strong antiferromagnetic coupling facilitates electrocatalytic reduction of CO_2 to CO at low overpotentials. Under these conditions, $\mathbf{[Fe1]^{2+}}$ exhibits high selectivity for CO production (greater than 90%) at high turnover frequencies. Synthetic reduction of the $[Fe(tpyPY2Me)]^{2+}$ complex enables access to the hypothesized catalytically active species, $[Fe(tpyPY2Me)]^{0}$, which has been characterized by X-ray crystallography, Mössbauer spectroscopy, X-ray absorption spectroscopy (XAS), variable temperature NMR, and density functional theory (DFT) calculations. The collective data support assignment of an open-shell singlet ground state that maintains a formal Fe(II) oxidation state, comprised of an intermediate-spin iron(II) (S_{Fe} = 1) antiferromagnetically coupled to a doubly reduced triplet terpyridine ligand (S_{tpy} = 1). This electronic structure also enables the molecular catalyst to operate at low overpotentials in both organic and neutral aqueous electrolytes, resulting in high selectivity for CO_2RR over HER.

5.3 Results and Discussion

5.3.1 Design, Synthesis, and Characterization of the tpyPY2Me Ligand and its Metal Coordination Complexes

The tpyPY2Me ligand and corresponding iron(II) complex $[Fe(tpyPY2Me)]^{2+}$, abbreviated as $[Fe1]^{2+}$, were prepared following modifications of previously reported procedures for the pentapyridine $PY5Me_2$ ligand and its metal complexes (see materials and methods). Briefly, the pentapyridine ligand tpyPY2Me bearing a redox non-innocent terpyridine fragment was formed by a lithium-mediated coupling between 6-bromo-2,2′:6′,2″-terpyridine and 2,2′-(ethane-1,1-diyl)dipyridine. A series of control coordination complexes were synthesized and evaluated to disentangle the contributions of the redox-active ligand from the metal center (**Figure 5.2**). In order to decipher the role of the iron center in electrochemical behavior and subsequent catalysis, we prepared the diamagnetic, isostructural zinc(II) analog $[Zn(tpyPY2Me)]^{2+}$ ($[Zn1]^{2+}$) that is equipped with the same redox-active tpyPY2Me ligand but with a redox-silent zinc center. To aid in identifying the role of the redox-active terpyridine fragment of the polypyridyl scaffold, $[Fe(PY5Me_2)(CH_3CN)]^{2+}$[50] and $[Zn(PY5Me_2)(CH_3CN)]^{2+}$[26] complexes bearing the related pentapyridine $PY5Me_2$ ligand without polypyridine conjugation were synthesized. Indeed, irreversible reduction of the $PY5Me_2$ ligand occurs at very negative potentials (between −2.0 and −2.5 V vs Fc/Fc^+) and is coupled to catalyst decomposition; thus, it serves as a polypyridyl redox-innocent ligand control (**Figure 5.2**).

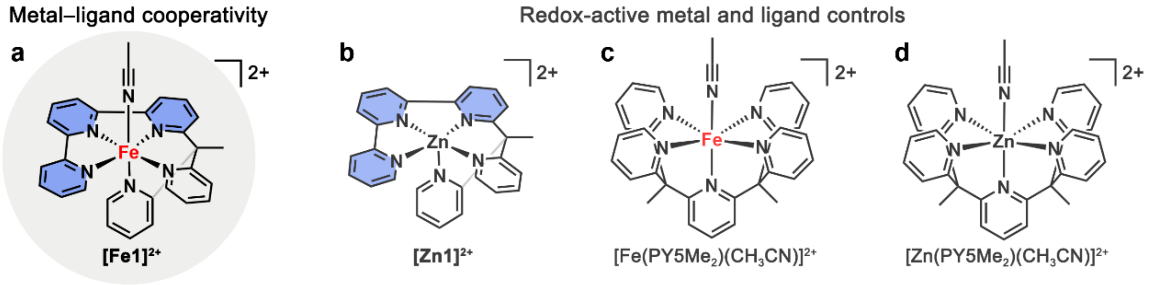


Figure 5.2. Chemical structures of $[Fe1]^{2+}$ and the coordination complexes used as controls to disentangle the contributions of ligand and metal center in catalysis. (a) Chemical structure of **$[Fe1]^{2+}$** highlighting cooperativity between the open-shell iron center and redox non-innocent tpyPY2Me ligand. (b) The diamagnetic analog containing the redox-silent Zn(II) center, $[Zn1]^{2+}$, enables the role of the iron center to be probed with the same redox non-innocent ligand scaffold. Likewise, (c) $[Fe(PY5Me_2)(CH_3CN)]^{2+}$ and (d) $[Zn(PY5Me_2)(CH_3CN)]^{2+}$ both feature the redox-innocent $PY5Me_2$ as a related pentapyridine ligand and thus aid in identifying the contributions of the redox-active terpyridine fragment within the polypyridyl scaffold.

A comparison of the solid-state structures of $[Fe1]^{2+}$ and $[Fe(PY5Me_2)(CH_3CN)]^{2+}$[50] obtained via single-crystal X-ray diffraction (XRD) revealed that the enhanced rigidity of the tpyPY2Me ligand enforces a more distorted *pseudo*-octahedral (O_h) geometry in $[Fe1]^{2+}$ relative to $[Fe(PY5Me_2)(CH_3CN)]^{2+}$, which adopts an almost ideal O_h geometry (**Figure 5.3a**). In particular, occupation of the iron equatorial plane by the three terpyridine nitrogen atoms and coordination of the pyridine arms to axial and equatorial positions induces severe axial distortions in $[Fe1]^{2+}$ that are absent in $[Fe(PY5Me_2)(CH_3CN)]^{2+}$ (see crystallography **Tables 5.9** and **5.10**).

This distortion also significantly compresses the axial bond angle in $[Fe1]^{2+}$ (173.64(6)) whereas the corresponding angle in $[Fe(PY5Me_2)(CH_3CN)]^{2+}$ is nearly linear (178.53(7)) (**Figure 5.3a**). Distortion of the primary coordination sphere as a result of the enhanced ligand rigidity of tpyPY2Me is also observed for the control analog bearing the redox-silent Zn(II) center, $[Zn1]^{2+}$. The solid-state structure of $[Zn1]^{2+}$ (**Figure 5.4**) shows that tpyPY2Me enforces a severely distorted square pyramidal coordination geometry with the terpyridine nitrogen atoms occupying equatorial positions (see crystallography **Tables 5.11** and **5.12**). This structure departs quite significantly from the O_h geometry observed for $[Zn(PY5Me_2)(CH_3CN)]^{2+}$.[26]

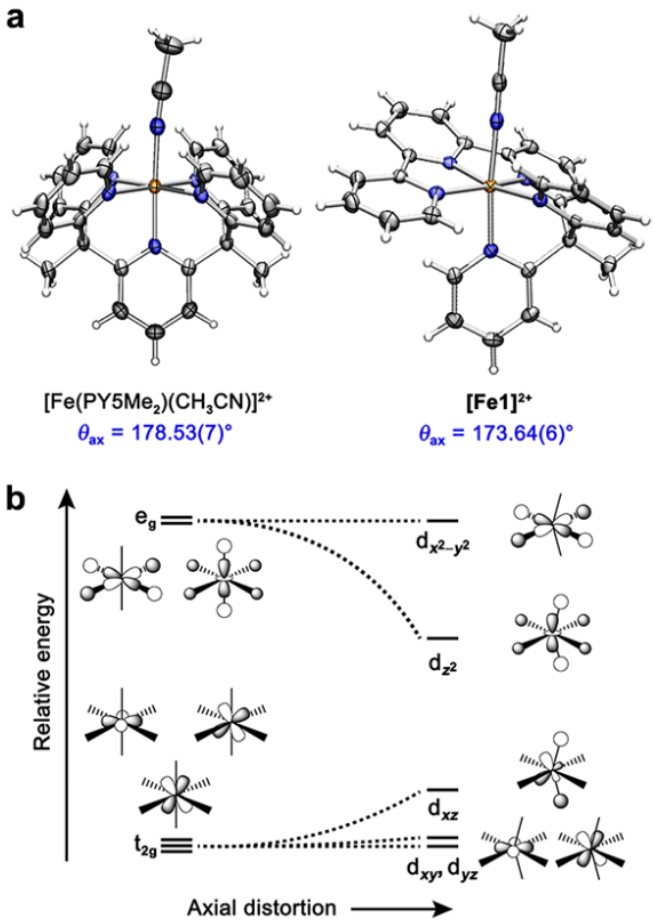


Figure 5.3. Structural characterization of iron polypyridyl complexes. (a) Solid state structures of $[Fe(PY5Me_2)(CH_3CN)]^{2+}$, featuring redox-innocent $PY5Me_2$ ligand, and $[Fe1]^{2+}$, as determined via X-ray diffraction analysis. Thermal ellipsoids are plotted at 80% probability level; orange, blue, and gray ellipsoids represent Fe, N, and C atoms, respectively. Noncoordinating solvent and anions are omitted for clarity. (b) Simplified Walsh diagram illustrating the effect of axial distortion away from the near ideal O_h symmetry in $[Fe(PY5Me_2)(CH_3CN)]^{2+}$ toward C_{2v} symmetry in $[Fe1]^{2+}$.

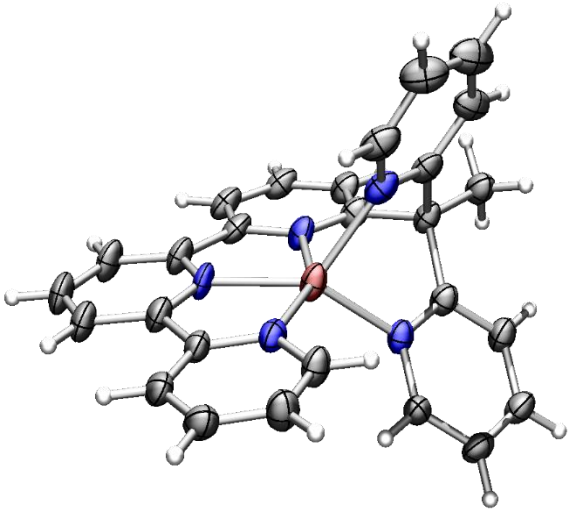


Figure 5.4. Solid state structure of $[Zn1]^{2+}$ at 50% displacement ellipsoid probability. Pink, blue, and gray ellipsoids represent Zn, N, and C atoms, respectively. Calculated H atom positions are shown as white spheres. Anions and residual solvent are omitted for clarity.

The structure of $[Fe1]^{2+}$ remains more distorted than that of $[Fe(PY5Me_2)(CH_3CN)]^{2+}$ in solution, as verified by ^{1}H NMR spectra collected for both complexes in CD_3CN at 295 K. The ^{1}H NMR spectrum of $Fe(PY5Me_2)(CH_3CN)]^{2+}$ features five sharp signals consistent with a C_{2v} symmetric complex with low-spin Fe(II) ($S = 0$), whereas the ^{1}H NMR spectrum of $[Fe1]^{2+}$ features slightly more broadened resonances with no well-defined symmetry (**Figure 5.5**). Alternatively, $[Zn1]^{2+}$ shows a ^{1}H NMR spectrum with all expected ligand resonances accounted for, consistent with its diamagnetic ground state (see materials and methods). Using the Evans method, we measured an effective magnetic moment (μ_{eff}) of 1.27 μ_B for $[Fe1]^{2+}$ at 293 K, which is indicative of a low-spin Fe(II) ground state ($S = 0$) with a population of thermally accessible spin excited states at room temperature (**Figure 5.6**). Because the $[Fe1]^{2+}$ bond lengths measured at 100 K are in agreement with those of other low-spin Fe(II) polypyridyl complexes,[50] the collective data suggest that $[Fe1]^{2+}$ undergoes a spin-state transition between 100 K and room temperature. To further probe the spin-state transition of $[Fe1]^{2+}$, variable-temperature (VT) ^{1}H NMR spectra were collected in CD_3CN across a temperature range of 233 to 353 K (**Figure 5.7**). At 293 K, resonances at 9.47, 7.73, 7.12, and 6.74 ppm appear as very broad singlets and upon heating the sample to 353 K, these peaks become undetectable due to broadening into the baseline (**Figure 5.7b**). Upon stepwise cooling, the resonances start to become fully resolved. At 233 K, integration of the aryl region accounts for the 18 proton signals expected for $[Fe1]^{2+}$. This temperature-dependent signal broadening is in line with our interpretation of a population of thermally accessible spin excited states. Due to the absence of systematic, temperature-dependent paramagnetic shifts of the $[Fe1]^{2+}$ resonances, we were unable to quantify the spin equilibrium from the ^{1}H NMR data alone. Nevertheless, variable temperature Evans method data further revealed a gradual increase in μ_{eff} upon heating, in agreement with the occurrence of a spin transition process in solution (**Figure 5.8**). The limited temperature range available in acetonitrile and limited solubility of $[Fe1]^{2+}$ in alternative solvents to expand this temperature range prevents isolation of a pure population of low-spin Fe(II) (μ_{eff} of 1.20 μ_B at 233 K) and the transition is incomplete at the highest available temperature (μ_{eff} of 1.33 μ_B at 353 K), precluding accurate determination of the spin-equilibrium transition ($T_{1/2}$).

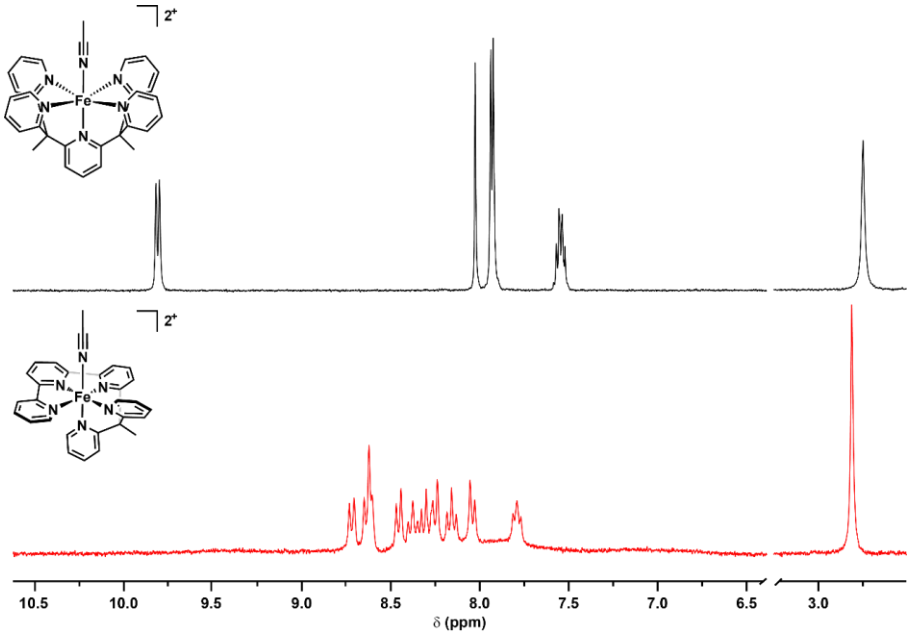
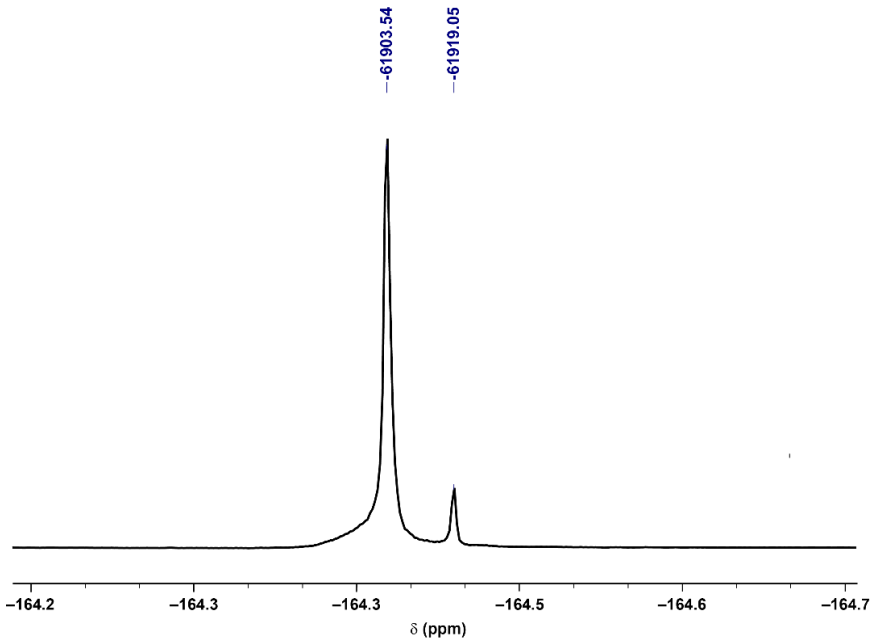


Figure 5.5. ^{1}H NMR spectra of $[Fe(PY5Me_2)(CH_3CN)]^{2+}$ and $[Fe1]^{2+}$ measured in CD_3CN at room temperature.



Figures 5.6. Solution Evans Method of $[Fe1]^{2+}$ in CD_3CN measured by ^{19}F NMR at 293 K. Hexafluorobenzene was used as the internal standard.

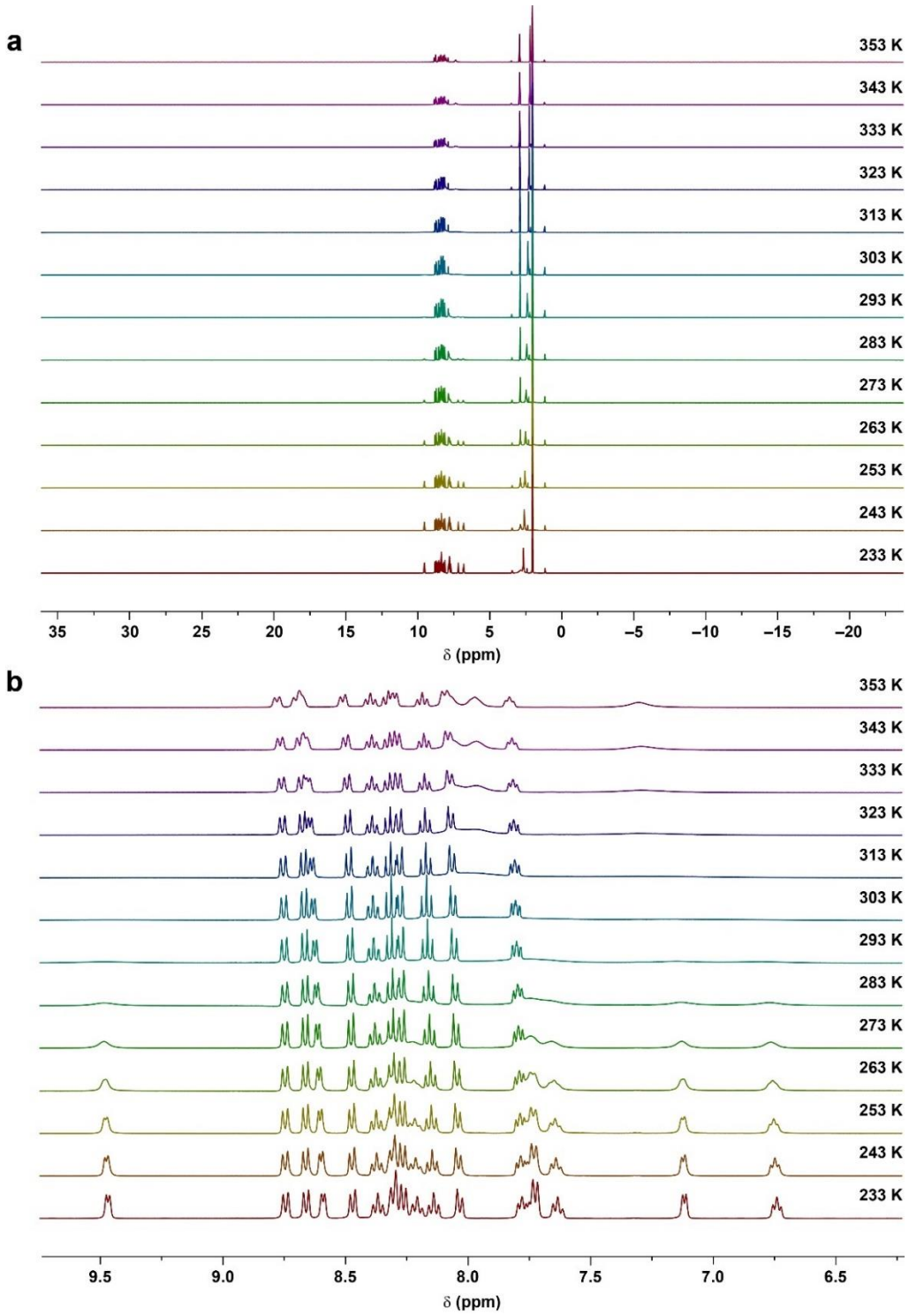


Figure 5.7. Variable-temperature ^{1}H NMR spectra of $[Fe1]^{2+}$ measured across a temperature range of 353 K to 233 K in CD_3CN. (a) The full chemical shift window is given to show the absence of any paramagnetically shifted resonances. (b) The aryl region of $[Fe1]^{2+}$ is provided to clearly show the signal broadening across the temperature range.

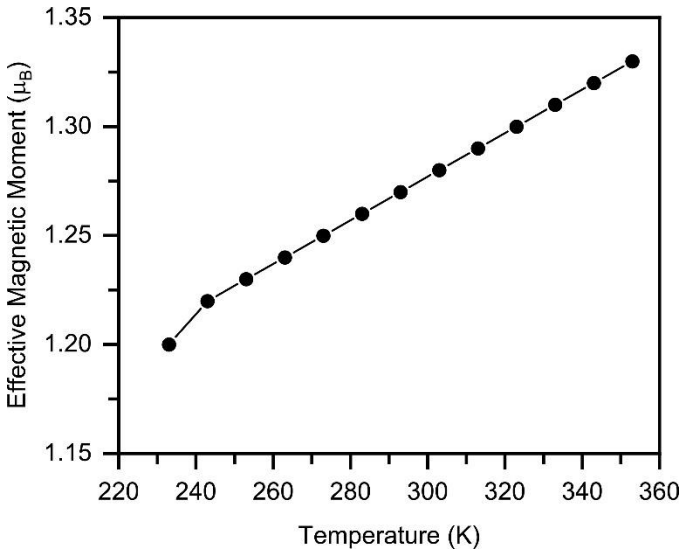


Figure 5.8. Variable-temperature Evans method data for $[Fe1]^{2+}$ measured across a temperature range of 353 K to 233 K in CD_3CN.

Zero-field ^{57}Fe Mössbauer spectra collected for $[Fe1]^{2+}$ at 5 and 295 K further support such a spin state transition for the Fe(II) center (**Figure 5.9** and **Table 5.1**). At 5 K, the spectrum features a symmetric Lorentzian doublet with isomer shift (δ) and quadrupole splitting ($|\Delta E_Q|$) values of 0.3562(4) and 1.0203(8) mm/s, respectively, consistent with a low-spin iron(II) (**Figure 5.9a**). The density functional theory (DFT) computed Mössbauer parameters closely match the experimental values within the well-established uncertainty ranges (~0.10 mm/s for δ and ~0.3 mm/s for $|\Delta E_Q|$),[51,52] thus corroborating the low-spin Fe(II) assignment (**Figure 5.10** and **Table 5.2**). In contrast, the Mössbauer spectrum measured at 295 K features an asymmetric quadrupole doublet that can be fit to two different iron sites (**Figure 5.9b** and **Table 5.1**). The parameters of the major site are nearly identical to the 5 K spectrum when accounting for second-order Doppler shifts (SODS) (δ = 0.285(1) mm/s, $|\Delta E_Q|$ = 1.056(2) mm/s) and are therefore consistent with the same low-spin Fe(II) species observed at 5 K. The isomer shift of the minor site is significantly more positive (0.62(1) mm/s) and is indicative of a higher spin iron(II) species. DFT predicted Mössbauer parameters for these higher-spin Fe(II) species correspond closely to the experimental values for the minor site measured at 295 K, further supporting this assignment (**Figure 5.10** and **Table 5.2**).

The distinct iron(II) spin states in $[Fe1]^{2+}$ and $[Fe(PY5Me_2)(CH_3CN)]^{2+}$ can be understood from the simplified Walsh diagram presented in **Figure 5.3b**. Axial distortions engendered by the rigid tpyPY2Me ligand lead to a decrease in symmetry from idealized O_h to C_{2v}, and this distortion significantly stabilizes the d_z^2 orbital and destabilizes the d_{xz} through *z*-component mixing of the t_{1u} and t_{2g} orbitals. The stabilization of the d_z^2 orbital and disruption of t_{2g} degeneracy can then facilitate the formation of thermally accessible spin excited states near room temperature. We hypothesize that these marked differences in the ground-state electronic structures of $[Fe1]^{2+}$ and $Fe(PY5Me_2)(CH_3CN)]^{2+}$ contribute to their distinct electrochemical and catalytic behavior (vide infra).

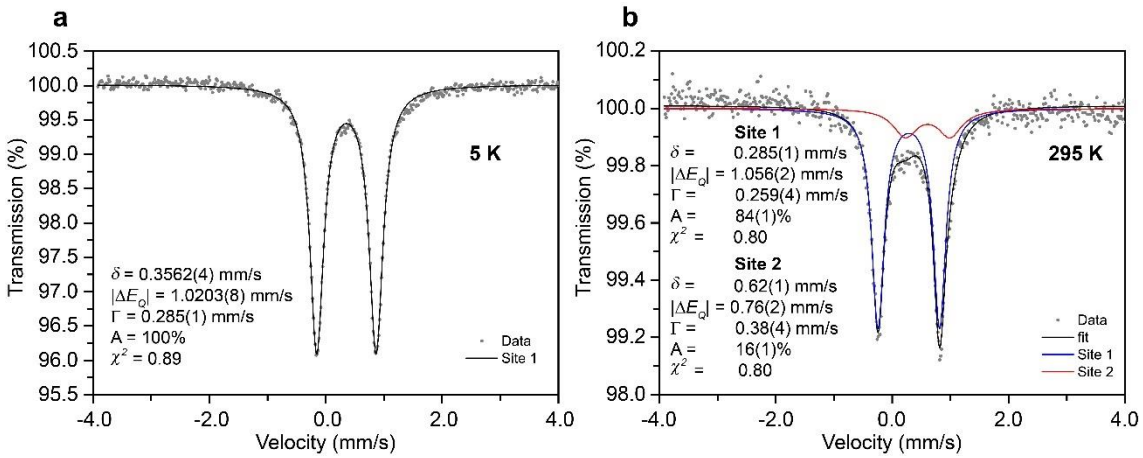


Figure 5.9. Zero-field ^{57}Fe Mössbauer spectrum of $[Fe1]^{2+}$ at (a) 5 K and (b) 295 K. Data are represented by gray dots and fits are given as colored lines. In (b), the blue and red fits correspond to sites 1 and 2, as described in the main text.

Table 5.1. Mössbauer fitting parameters for $[Fe1]^{2+}$ and $[Fe1]^{0}$ collected at 5 K and 295 K.

Compound	**$[Fe1]^{2+}$**		**$[Fe1]^{0}$**	
***T* (K)**	**5**	**295**	**5**	**295**
δ_1 (mm/s)	0.3562(4)	0.285(1)	0.2608(2)	0.1749(6)
$\lvert\Delta E_{Q1}\rvert$ (mm/s)	1.0203(8)	1.056(2)	0.7637(4)	0.722(1)
Γ_1 (mm/s)	0.285(1)	0.259(4)	0.2767(5)	0.278(1)
Area$_1$ (%)	100	84(1)	100	100
δ_2 (mm/s)	–	0.62(1)	–	–
$\lvert\Delta E_{Q2}\rvert$ (mm/s)	–	0.76(2)	–	–
Γ_2 (mm/s)	–	0.38(4)	–	–
Area$_2$ (%)	–	16(1)	–	–

Complex	δ_{exp} (mm/s)	$\lvert\Delta E_q\rvert_{exp}$ (mm/s)	ρ(0) (a.u.)	ρ(0) - C
$[Fe(PY5Me_2)]^{2+}$	0.52	0.34	11816.38	6.38
$[Fe(tpy)_2]^{3+}$	0.07	3.43	11817.51	7.51
$[Fe(tpy)_2]^{2+}$	0.28	1.05	11816.90	6.90
$[Fe(tpy)_2]^{+}$	0.26	1.11	11816.96	6.96
$[Fe(tpy)_2]^{0}$	0.88	0.52	11815.52	5.52
$[Fe(bpy)_3]^{3+}$	0.06	1.80	11817.41	7.41
$[Fe(bpy)_3]^{2+}$	0.37	0.32	11816.65	6.65
$[Fe(bpy)_3]^{+}$	0.33	0.37	11816.76	6.76

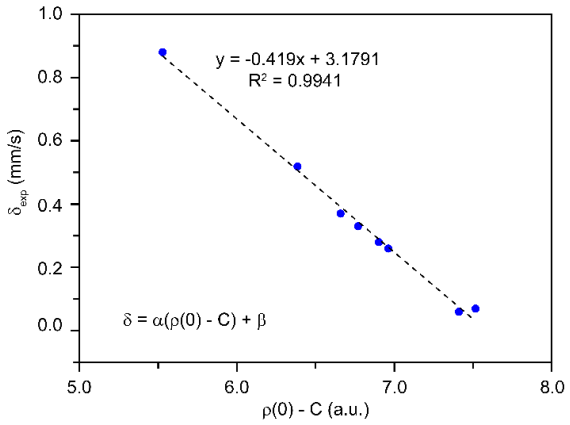


Figure 5.10. Mössbauer correlation diagram of reported polypyridyl iron complexes[50,53,54] α and β constants extracted from the correlation diagram are utilized to predict Mössbauer parameters for $[Fe1]^{2+/0}$ following literature reported methods.[51,51,52]

Table 5.2. Comparison of experimental and predicted Mössbauer parameters of **[Fe1]$^{2+/0}$** at 5 K.

Complex	**δ_{exp} (mm/s)**	**δ_{theory} (mm/s)**	**$\lvert\Delta E_q\rvert_{exp}$ (mm/s)**	**$\lvert\Delta E_q\rvert_{theory}$ (mm/s)**
[Fe1]$^{2+}$ (S_{Fe} = 0)	0.3562(4)	0.360	1.0203(8)	0.933
[Fe1]$^{2+}$, (S_{Fe} = 1)		0.581		1.589
[Fe1]^{0}, (S_{Fe} = 0; S_{tpy} = 0; S = 0)	0.2608(2)	0.319	0.7637(4)	0.976
[Fe1]^{0}, (S_{Fe} = 1; S_{tpy} = 1; S = 0)		0.325		0.826

5.3.2 Cyclic Voltammetry of tpyPY2Me Fe(II) and Zn(II) Complexes and comparison to $PY5Me_2$ Analogs.

The presence of a redox-active terpyridine moiety in tpyPY2Me also gives rise to unique electrochemical behavior for $[Fe1]^{2+}$ and $[Zn1]^{2+}$ relative to their $PY5Me_2$ analogues. The room-temperature cyclic voltammogram (CV) of $[Fe1]^{2+}$ collected in CH_3CN under Ar exhibits three reversible features: a one-electron oxidation at $E_{1/2}$ = 0.66 V (versus Fc/Fc^+) assigned to the iron(III/II) couple and two, closely spaced, one-electron redox processes that are centered at −1.43 V (**Figure 5.11a**). Further chemical characterization of this redox behavior indicates that these redox events are two sequential ligand-based reductions ($tpyPY2Me^{0/1-}$ and $tpyPY2Me^{1-/2-}$) (vide infra). During constant potential coulometry of 7.6×10^{-3} mmol of $[Fe1]^{2+}$ conducted at −1.60 V vs Fc/Fc^+ under Ar atmosphere, 1.58 C of charge was passed equating to 2.1 electrons per molecule of $[Fe1]^{2+}$, supporting this assignment as two closely spaced one-electron redox waves centered at −1.43 V vs Fc/Fc^+ (**Figure 5.12**). No additional features were observed when scanning to more negative potentials.

In contrast, under the same conditions, the cyclic voltammogram of $[Zn1]^{2+}$ exhibits two, well-separated, reversible, one-electron ligand-centered reductions with $E_{1/2}$ of −1.56 and −2.07 V as well as an additional irreversible redox event (tentatively assigned as $tpyPY2Me^{2-/3-}$) at −2.41 V (**Figure 5.11a**). The first ligand centered reduction of $[Zn1]^{2+}$ occurs at a comparable potential to that of $[Fe1]^{2+}$ but the second ligand centered reduction is shifted 640 mV more negative and it is this disparate electrochemical behavior between $[Fe1]^{2+}$ and $[Zn1]^{2+}$ that indicates a degree of communication between the reduced tpyPY2Me ligand and the open-shell iron center that is not possible in the isostructural complex containing the closed-shell, redox-silent zinc center. In contrast, ligand-based reductions in $[Fe(PY5Me_2)(CH_3CN)]^{2+}$ and $[Zn(PY5Me_2)(CH_3CN)]^{2+}$ are electrochemically irreversible and occur at potentials negative of −2.0 V (**Figure 5.11b**), highlighting the crucial role of the terpyridyl fragment in achieving electrochemically reversible reduction events at relatively positive potentials.

5.3.3 Electrochemical Reduction of CO_2 Catalyzed by $[Fe(tpyPY2Me)]^{2+}$ in Organic Solution

Under an atmosphere of CO_2, CV data collected for $[Fe1]^{2+}$ exhibit only a subtle increase in current relative to scans under Ar; however, when excess phenol (3.5 M) is added as a proton source, two large catalytic waves appear at ca. −1.50 and −2.0 V versus Fc/Fc^+ (**Figure 5.11c**). The $PY5Me_2$ analog $[Fe(PY5Me_2)(CH_3CN)]^{2+}$ also displays catalytic currents upon addition of CO_2 and phenol, but the onset current for catalysis is >500 mV more negative than that observed for $[Fe1]^{2+}$ (**Figure 5.11d**). Phenol titrations conducted with solutions of $[Fe1]^{2+}$ under a CO_2 atmosphere revealed a dose-dependence on phenol concentration (**Figure 5.13a**). The electrochemical response is mitigated when control phenol titrations are collected under an Ar atmosphere, suggesting that $[Fe1]^{2+}$ selectively catalyzes electrochemical CO_2 reduction (CO_2RR) over the hydrogen evolution reaction (HER), even at high concentrations of organic acid (**Figure 5.13b**). As anticipated, the isostructural Zn(II) analog $[Zn1]^{2+}$ does not show similar increases in catalytic current at such positive potentials (**Figure 5.14**), establishing that the redox non-innocent tpyPY2Me ligand alone with a Lewis acid center is not sufficient for promoting CO_2RR activity.

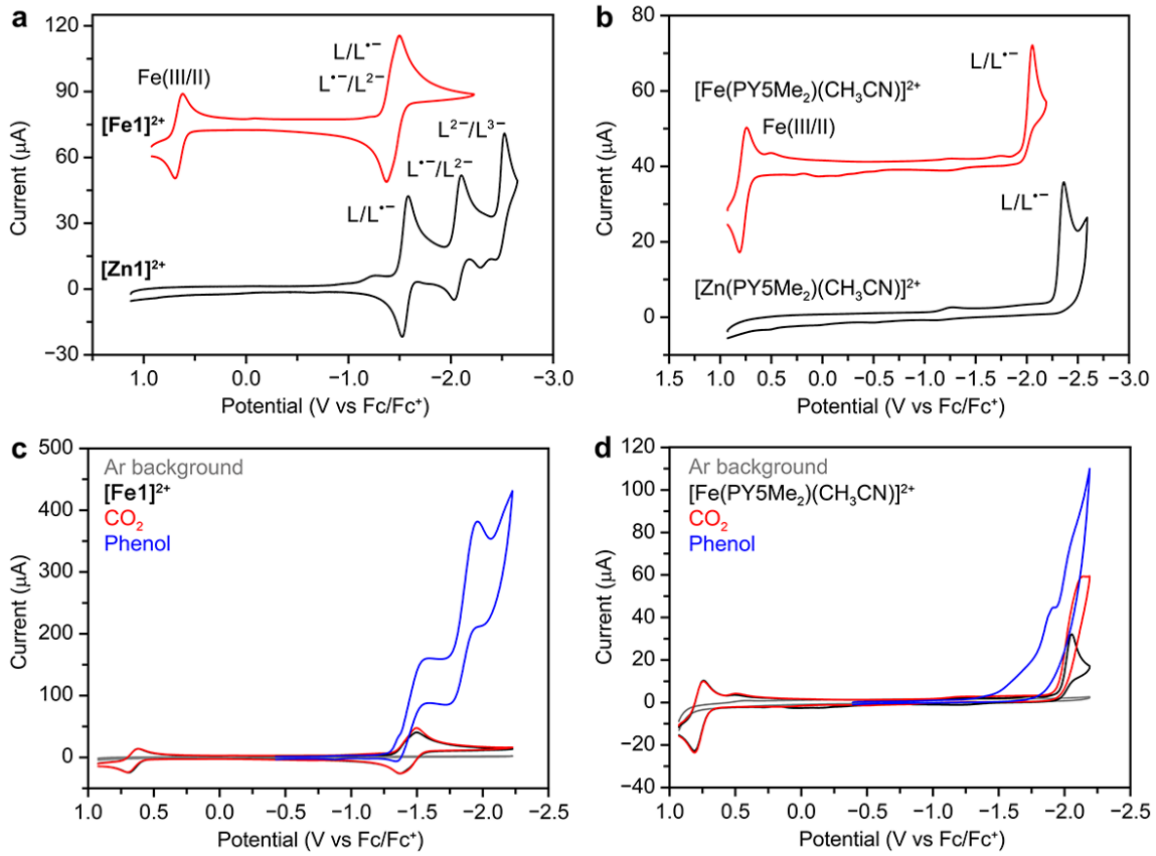


Figure 5.11. Electrochemical characterization. Cyclic voltammograms collected under Ar of (a) $[Fe1]^{2+}$ (red trace) and $[Zn1]^{2+}$ (black trace) complexes and (b) $[Fe(PY5Me_2)(CH_3CN)]^{2+}$ (red trace) and $[Zn(PY5Me_2)(CH_3CN)]^{2+}$ (black trace) complexes supported by redox-innocent $PY5Me_2$. These data show that the unique combination of Fe and redox non-innocent tpyPY2Me ligand led to electrochemically reversible two-electron chemistry, with the Zn-tpyPY2Me analog exhibiting two reversible one-electron reduction waves with the second reduction at potentials over 600 mV more negative than the iron analog. The Fe(II) and Zn(II) $PY5Me_2$ analogs both exhibit irreversible electrochemical reductions at potentials more negative than –2.0 V vs Fc/Fc^+. Cyclic voltammograms of (c) $[Fe1]^{2+}$ and (d) $[Fe(PY5Me_2)(CH_3CN)]^{2+}$ collected under Ar (black), CO_2 (red), and with added phenol (3.5 M, blue). Voltammograms were collected with a scan rate of 100 mV/s with an electrolyte of 0.10 M $TBAPF_6$ dissolved in CH_3CN.

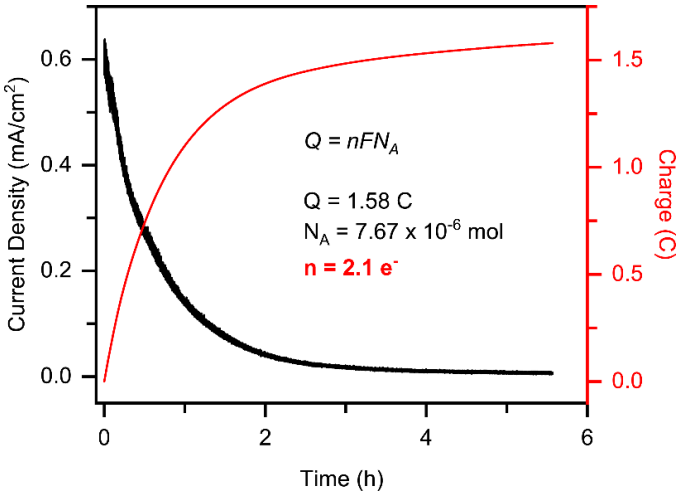


Figure 5.12. Potentiostatic coulometry of $[Fe1]^{2+}$ under Ar atmosphere at –1.60 V vs Fc/Fc^+. Current density as a function of time is shown in black and charge accumulation over time is depicted in red. Conditions: 5.9 mg (7.67 x 10^{-6} mol) $[Fe1]^{2+}$ in 0.10 M $TBAPF_6/CH_3CN$ electrolyte. 1.58 C of charge was passed during the experiment equating to ~2 electrons transferred per molecule of $[Fe1]^{2+}$.

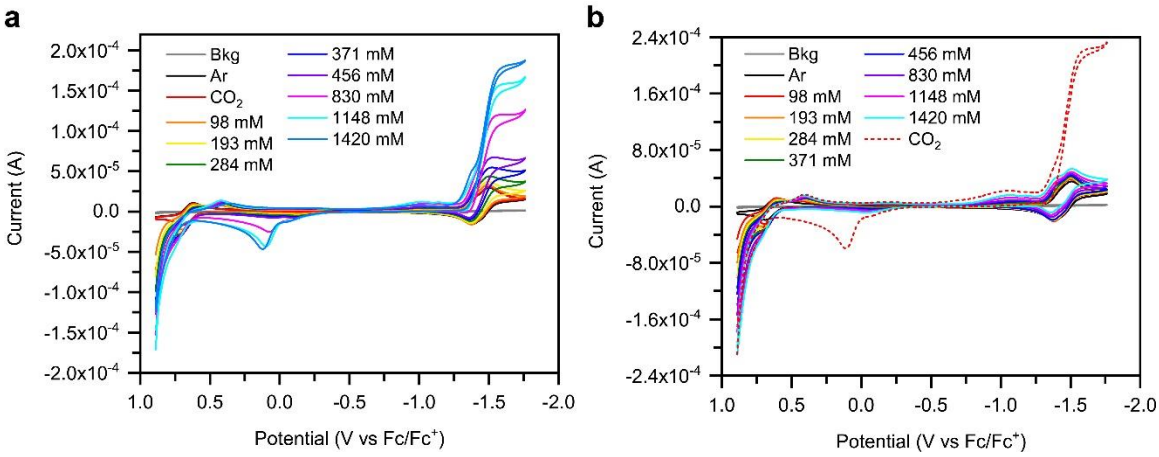


Figure 5.13. Phenol titrations into solutions $[Fe1]^{2+}$ monitored by CV. (a) Titration of phenol (0 – 1420 mM) into a $[Fe1]^{2+}$ solution under CO_2 atmosphere. (b) Control titration of phenol (0 – 1420 mM) under Ar atmosphere to probe the selectivity of $[Fe1]^{2+}$ for CO_2RR over HER. Following titration of phenol under Ar atmosphere, the solution was saturated with CO_2 (dotted red line). Conditions: 1 mM $[Fe1]^{2+}$; 0.10 M $TBAPF_6/CH_3CN$; Phenol (0 – 1420 mM). CV data were corrected for dilution effects from phenol titrations.

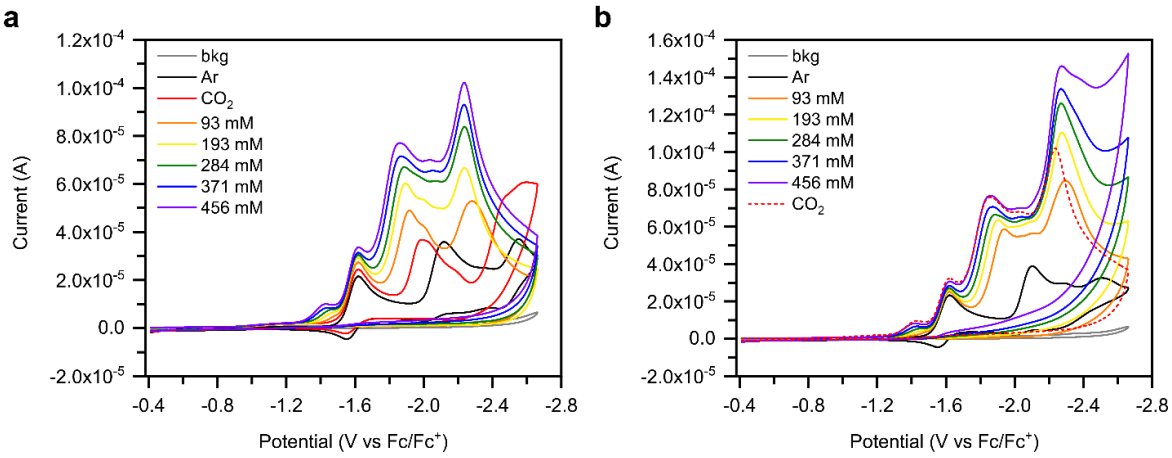


Figure 5.14. Phenol titrations into solutions $[Zn1]^{2+}$ monitored by CV. (a) Titration of phenol (0 – 456 mM) into a $[Zn1]^{2+}$ solution under CO_2 atmosphere. (b) Control titration of phenol (0 – 456 mM) under Ar atmosphere to probe the selectivity of $[Zn1]^{2+}$ for CO_2RR over HER. Following titration of phenol under Ar atmosphere, the solution was saturated with CO_2 (dotted red line). Conditions: 1 mM $[Zn1]^{2+}$; 0.10 M $TBAPF_6/CH_3CN$; Phenol (0 – 456 mM). CV data were corrected for dilution effects from phenol titrations.

5.3.4 Controlled Potential Electrolysis Studies in Organic Solution

Preparative-scale controlled potential electrolysis (CPE) experiments were conducted in CO_2-saturated acetonitrile with 3.5 M phenol across a range of applied potentials (−1.35 to −1.98 V vs Fc/Fc^+), and the products were quantified by gas chromatography. We find that CO is the major product of CO_2RR. Importantly, we note that subsequent turnover number and turnover rate values reported in this work are derived from these direct measurements of product, as opposed to indirect methods derived from transient CV currents with electrochemical assumptions.

Because the utility of a catalyst is benchmarked by its rate and overpotential (η), the applied potentials were also converted into overpotentials following the methods reported by Mayer[55] and Matsubara and co-workers.[56,57] Accurate conversion necessitates that the thermodynamic potential for CO_2 reduction to CO is known under the experimental conditions. Whereas the aqueous standard potential is known (−0.106 V vs SHE;[58] −0.730 V vs Fc/Fc^+[(59)]), it is difficult to experimentally determine in organic solvents where the identity and amount of the proton source complicate the measurements. This caveat often leads to the use of estimated values that do not match the experimental conditions or rely on thermodynamic assumptions that do not rigorously apply, such as taking the CO_2 and CO standard states to be 1 M[12,13] or assuming anhydrous conditions without reporting measured water concentrations or using anhydrous organic acids,[60] leading to potential inconsistencies in the literature with regard to reported overpotentials. With the goal of increasing standardization and transparency in molecular electrocatalysis, we report the applied potentials from our CPE experiments in both overpotential and versus Fc/Fc^+ and use a conservative estimate of $E^0_{CO_2/CO}$ (−1.27 V vs Fc/Fc^+)[57] obtained from measured pK_a values for acetonitrile–water mixtures (see materials and methods for additional details). It should be noted that this value is 770 mV more positive than for "dry" acetonitrile and 70 mV more positive than the previously estimated standard redox potential for "wet" acetonitrile derived by assigning

unusual gas standard states.[12,13] Tafel plots that compare catalyst activity are plotted to show both the calculated overpotential as well as the directly measured potential versus the reference electrode used in the experiments. We reason that reporting both values should lead to more clarity in benchmarking catalysts.

$[Fe1]^{2+}$ is highly selective for CO_2 reduction over hydrogen evolution across the entire potential window examined, with averaged specific current densities for CO production (j_{CO}) reaching as high as 3.6 mA/cm^2 (**Figures 5.15a**, **5.16**, and **5.17** and summarized in **Table 5.3**). The Faradaic efficiency for CO production (FE_{CO}) reaches 94% at an overpotential of 190 mV (−1.46 V vs Fc/Fc^+) and increases to 100% with the application of overpotentials between 320 and 710 mV (−1.59 and −1.98 V vs Fc/Fc^+) (**Figures 5.15a** and **5.16**; **Table 5.3**). This high activity and selectivity for CO production at applied potentials as low as −1.46 V vs Fc/Fc^+ is a substantial decrease in the energy requirements compared to other molecular catalysts and sits among the most efficient reported catalysts.[13,27–29,61–63] Significantly, no CO and only small amounts of H_2 (FE_{H_2} = 44%) were detected in analogous CPE experiments with $[Fe(PY5Me_2)(CH_3CN)]^{2+}$ at much larger overpotentials (**Figure 5.18**). Moreover, variable potential CPE experiments with $[Zn1]^{2+}$ conducted between −1.66 V and −2.41 V vs Fc/Fc^+ produced only trace amounts of CO (FE_{CO} = 1 – 6%) and a small amount of H_2 (FE_{H_2} = 1–20%), further illustrating the importance of metal–ligand cooperativity for efficient CO_2RR catalysis (**Figure 5.19**).

Control experiments strongly support the homogeneous molecular nature of $[Fe1]^{2+}$. First, CO_2 reduction was not observed in the absence of $[Fe1]^{2+}$ (**Figure 5.20**). Furthermore, cyclic voltammetry and UV–vis data collected before and after 1 h CPE experiments are indistinguishable, attesting to the bulk stability of $[Fe1]^{2+}$ under electrolysis conditions (**Figure 5.21**). Finally, the possible formation of an electrode-adsorbed active catalyst was excluded through a series of control experiments. First, peak currents for $[Fe1]^{2+}$ and $[Zn1]^{2+}$ scale linearly with the square root of the scan rate, indicative of freely diffusing species in solution (**Figures 5.22** and **5.23**). Second, CPE rinse tests[64] which probe for electrode deposition, give complete inversion of product selectivity, with H_2 as the predominant product and negligible generation of CO (**Figure 5.24**).

Table 5.3. Summary of electrochemical properties of $[Fe1]^{2+}$. The kinetic data was determined from the average of 1 h variable potential CPE experiments with direct product detections done in triplicate.

V vs Fc/Fc^+	η (V)	FE_{CO} (%)	j_{CO} (mA/cm^2)	k_{obs}	TOF (s^{-1})	logTOF (s^{-1})
−1.35	0.08	22 ± 10	0.1 ± 0.02	$1.7x10^5 \pm 9.6x10^4$	$1.4x10^4 \pm 7.9x10^3$	4.12 ± 0.22
−1.38	0.11	67 ± 11	0.4 ± 0.06	$3.1x10^5 \pm 1.0x10^5$	$7.5x10^4 \pm 2.5x10^4$	4.86 ± 0.14
−1.46	0.19	94 ± 4	0.9 ± 0.10	$5.0x10^4 \pm 1.1x10^4$	$7.6x10^4 \pm 1.7x10^4$	4.87 ± 0.10
−1.48	0.21	92 ± 2	1.0 ± 0.08	$4.8x10^4 \pm 6.8x10^3$	$8.5x10^4 \pm 1.2x10^4$	4.92 ± 0.06
−1.59	0.32	100 ± 1	1.8 ± 0.22	$1.2x10^5 \pm 2.8x10^4$	$2.4x10^5 \pm 5.6x10^4$	5.37 ± 0.10
−1.63	0.36	97 ± 1	1.8 ± 0.21	$1.2x10^5 \pm 2.7x10^4$	$2.4x10^5 \pm 5.4x10^4$	5.36 ± 0.10
−1.73	0.46	99 ± 1	2.4 ± 0.14	$2.0x10^5 \pm 2.4x10^4$	$4.0x10^5 \pm 4.8x10^4$	5.60 ± 0.05
−1.83	0.56	96 ± 3	2.9 ± 0.17	$2.8x10^5 \pm 3.5x10^4$	$5.7x10^5 \pm 6.9x10^4$	5.75 ± 0.05
−1.93	0.66	103 ± 1	2.9 ± 0.06	$3.0x10^5 \pm 1.2x10^4$	$5.9x10^5 \pm 2.4x10^4$	5.77 ± 0.02
−1.98	0.71	97 ± 3	3.6 ± 0.15	$4.5x10^5 \pm 3.9x10^4$	$9.0x10^5 \pm 7.8x10^4$	5.95 ± 0.04

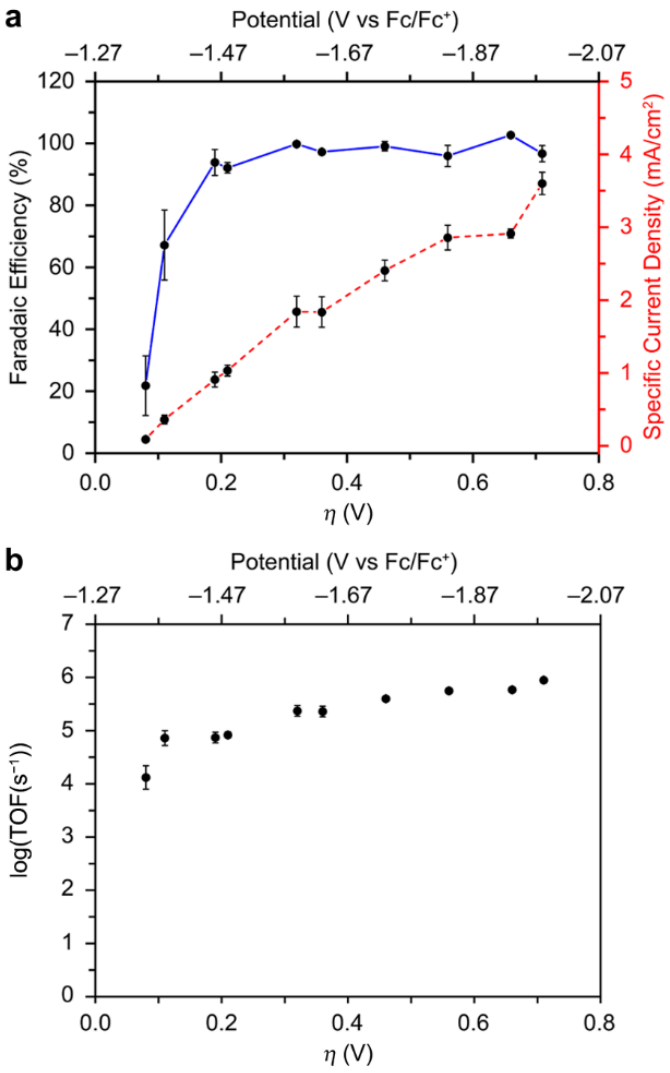


Figure 5.15. Electrochemical CO_2 reduction performance of $[Fe1]^{2+}$. (a) Selectivity of $[Fe1]^{2+}$ for CO_2 reduction to CO at varying overpotentials and specific current densities for CO (j_{CO}) production (averages of three experiments). (b) Catalytic Tafel plot for $[Fe1]^{2+}$ obtained from CPE experiments in acetonitrile with added phenol (3.5 M). CPE experiments were collected in an electrolyte of 0.10 M $TBAPF_6$ dissolved in CH_3CN.

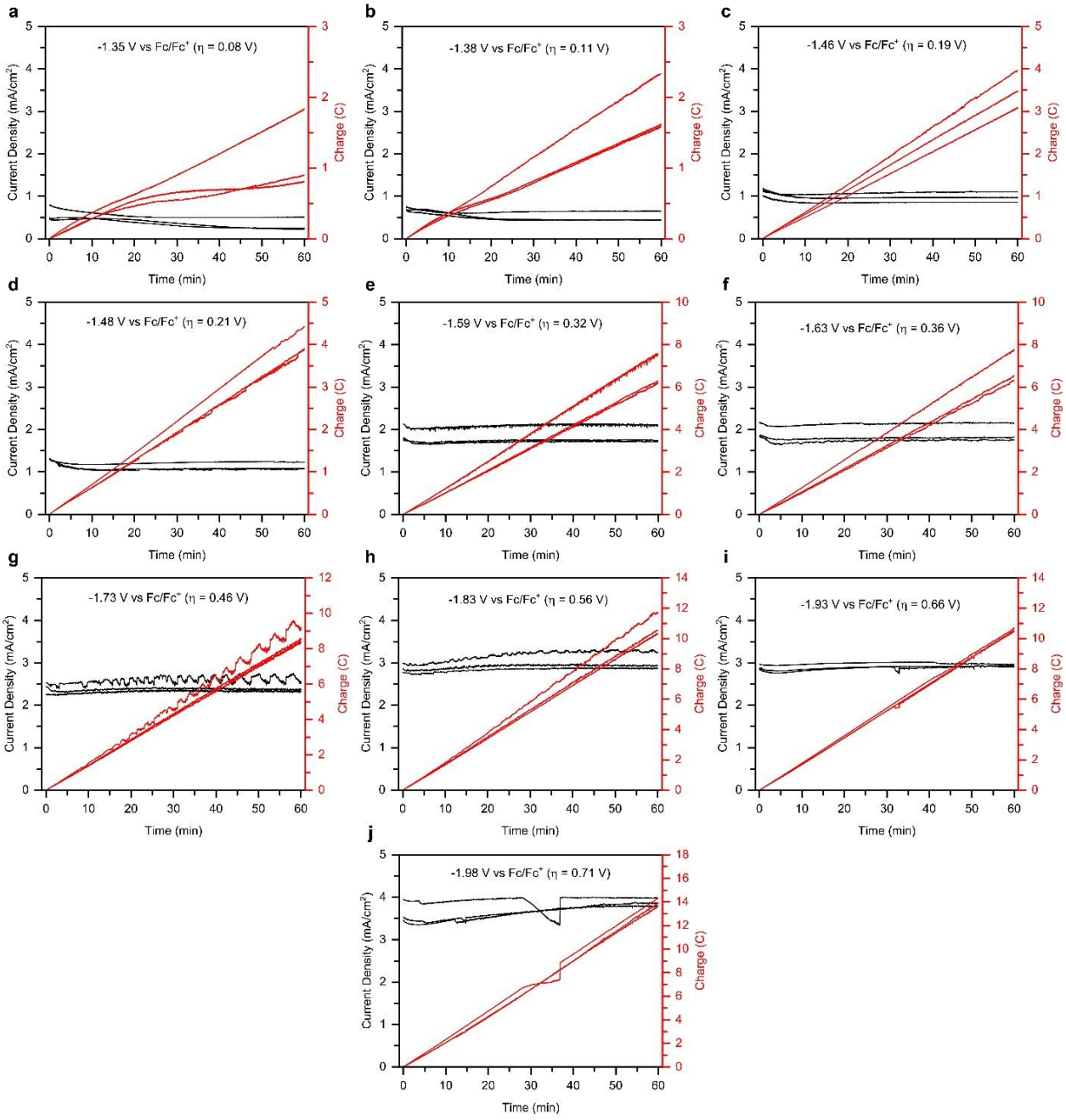


Figure 5.16. Controlled potential electrolysis of $[Fe1]^{2+}$ under CO_2 atmosphere. CPE experiments were conducted in triplicate at varying onset potentials: (a) –1.35 V vs Fc/Fc^+ (η = 0.08 V); (b) –1.38 V vs Fc/Fc^+ (η = 0.11 V); (c) –1.46 V vs Fc/Fc^+ (η = 0.19 V); (d) –1.48 V vs Fc/Fc^+ (η = 0.21 V); (e) –1.59 V vs Fc/Fc^+ (η = 0.32 V); (f) –1.63 V vs Fc/Fc^+ (η = 0.36 V); (g) –1.73 V vs Fc/Fc^+ (η = 0.46 V); (h) –1.83 V vs Fc/Fc^+ (η = 0.56 V); (i) –1.93 V vs Fc/Fc^+ (η = 0.66 V); (j) –1.98 V vs Fc/Fc^+ (η = 0.71 V). Conditions: 1 mM $[Fe1]^{2+}$; 0.10 M $TBAPF_6/CH_3CN$; 3.5 M phenol; 0.020 M tetrabutylammonium acetate.

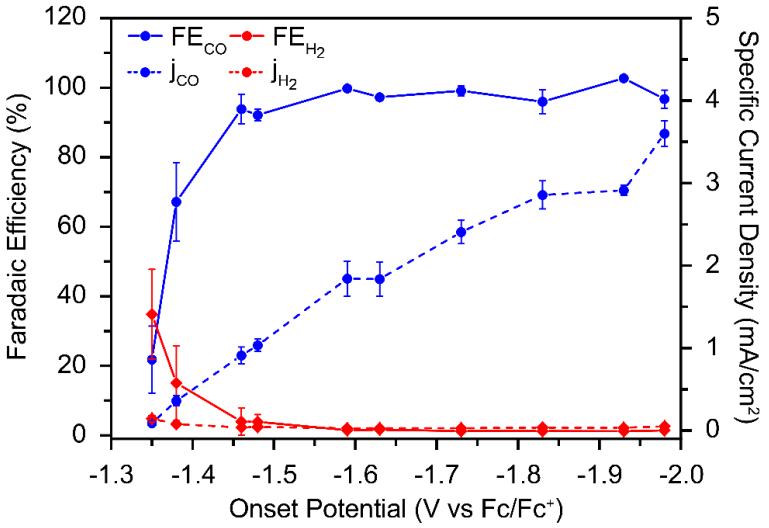


Figure 5.17. Selectivity of $[Fe1]^{2+}$ for CO_2 reduction to CO (blue) over proton reduction at varying applied potentials and specific current densities for CO (j_{CO}) and H_2 (j_{H_2}) production (averages of three experiments).

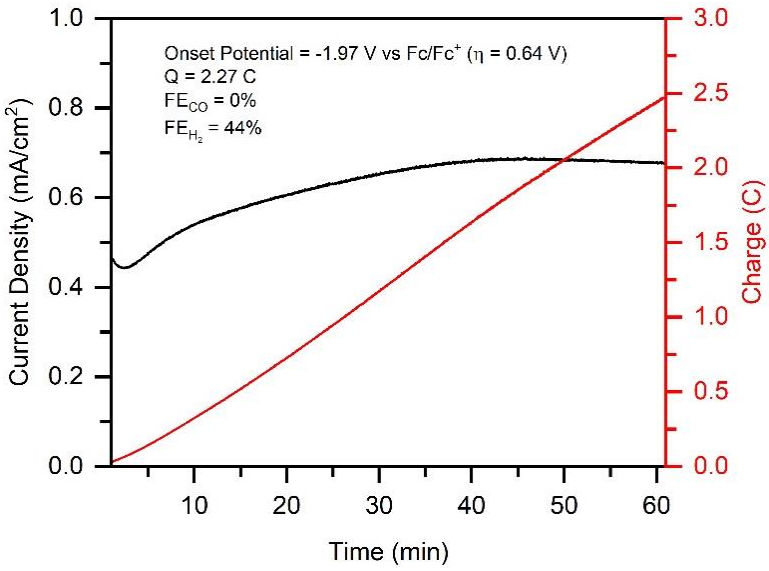


Figure 5.18. Controlled potential electrolysis of $[Fe(PY5Me_2)(CH_3CN)]^{2+}$ under CO_2 atmosphere. The CPE experiment was conducted at –1.97 V vs Fc/Fc^+ (η = 0.70 V). Conditions: 1 mM $[Fe(PY5Me_2)(CH_3CN)]^{2+}$; 0.10 M $TBAPF_6/CH_3CN$; 3.5 M phenol; 0.020 M tetrabutylammonium acetate.

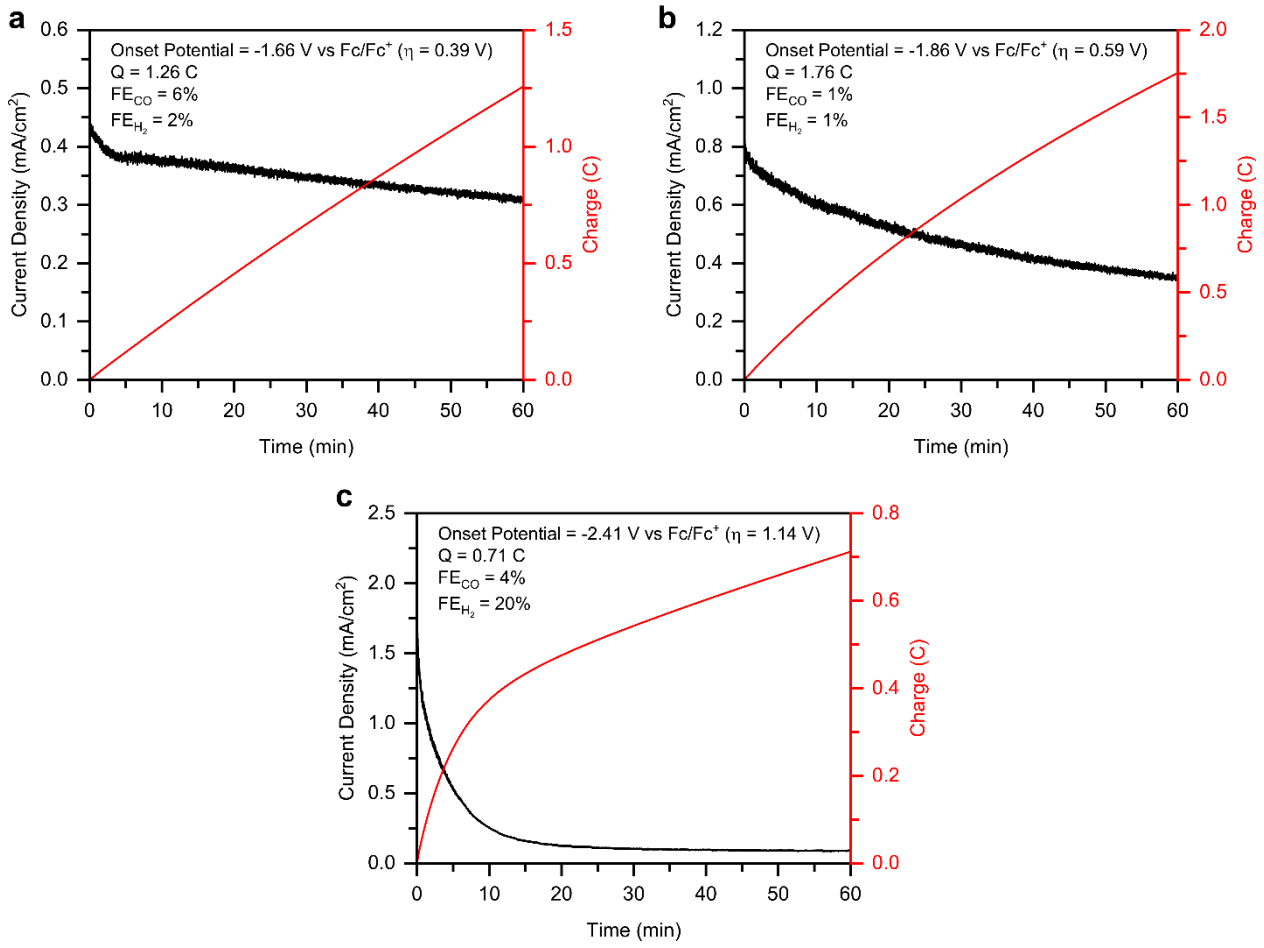


Figure 5.19. Controlled potential electrolysis of $[Zn1]^{2+}$ under CO_2 atmosphere. CPE experiments was conducted at varying onset potentials. (a) –1.66 V vs Fc/Fc^+ (η = 0.39 V); (b) –1.76 V vs Fc/Fc^+ (η = 0.59 V); (c) –2.41 V vs Fc/Fc^+ (η = 1.14 V). Conditions: 1 mM $[Zn1]^{2+}$; 0.10 M $TBAPF_6/CH_3CN$; 3.5 M phenol; 0.020 M tetrabutylammonium acetate.

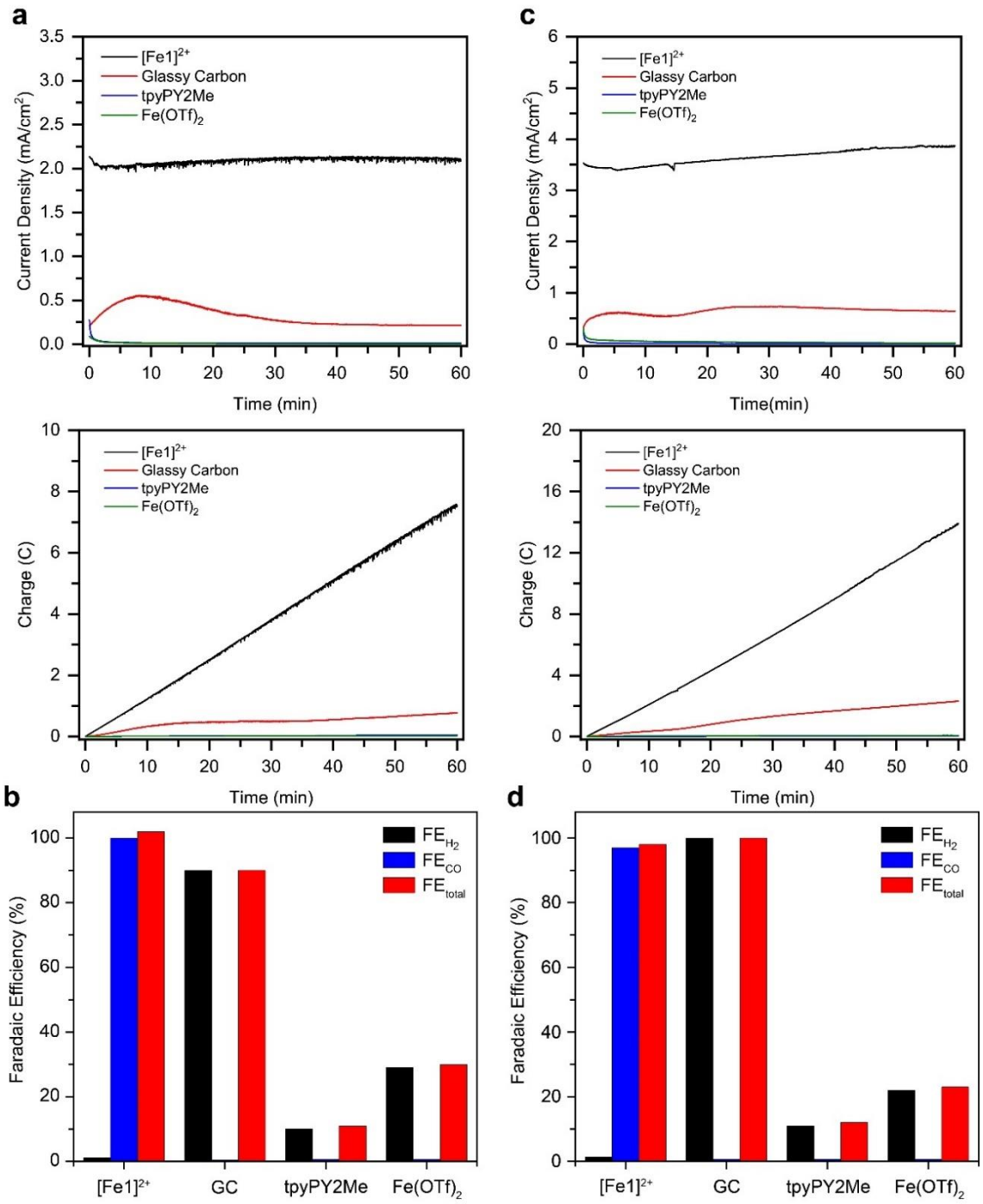


Figure 5.20. Control CPE experiments. Controls were conducted at two different applied potentials. (a) CPE with an onset potential of –1.59 V vs Fc/Fc^+ (η = 0.32 V) and (b) quantification of the gaseous products by GC. (c) CPE with an applied potential of –1.98 V vs Fc/Fc^+ (η = 0.71 V) and (d) quantification of gaseous products by GC. Black = $[Fe1]^{2+}$ (1 mM); Red = glassy carbon control; Blue = tpyPY2Me (1 mM); Green = $Fe(OTf)_2$ (1 mM). Conditions: 0.10 M $TBAPF_6/CH_3CN$; 3.5 M phenol; 0.020 M tetrabutylammonium acetate.

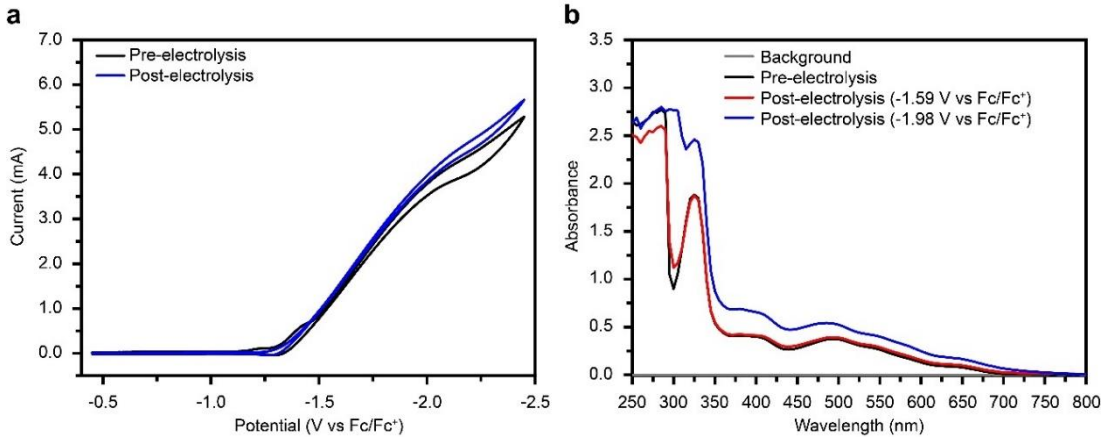


Figure 5.21. Control experiments to support the stability of $[Fe1]^{2+}$ under electrolysis conditions. (a) CVs before and after CPE experiments. (b) Analysis of the electrolyte solution before (black) and after CPE experiments at –1.59 V (η = 0.32 V) (red) and –1.98 V (η = 0.71 V) (blue) vs Fc/Fc^{+}.

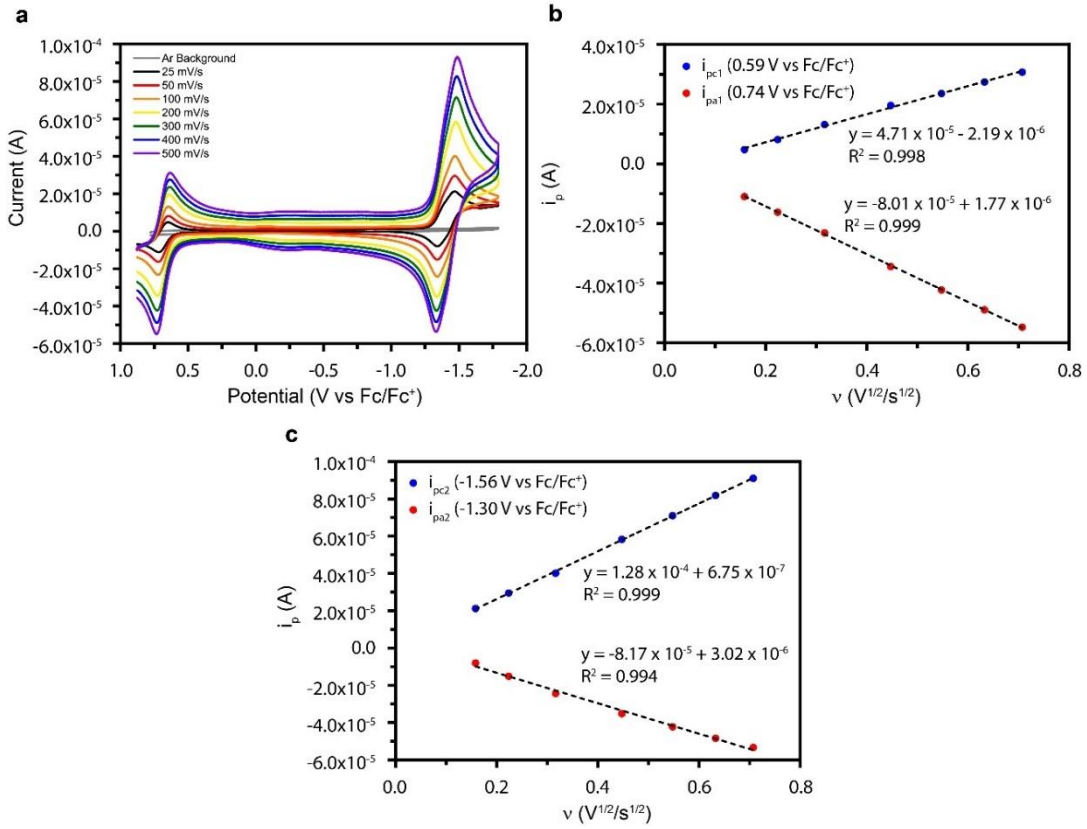


Figure 5.22. Scan rate dependent cyclic voltammograms of $[Fe1]^{2+}$. (a) CVs were recorded at scan rates ranging from 25 to 500 mV/s. (b) Peak current (i) vs square root scan rate $(\nu)^{1/2}$ data for the Fe(III/II) redox couple ($E_{1/2}$ = +0.66 V vs Fc/Fc^{+}). (c) i vs $(\nu)^{1/2}$ plot for the L/L^{2-} redox couple ($E_{1/2}$ = −1.43 V vs Fc/Fc^{+}). Conditions: 1 mM $[Fe1]^{2+}$; 0.10 M $TBAPF_6/CH_3CN$.

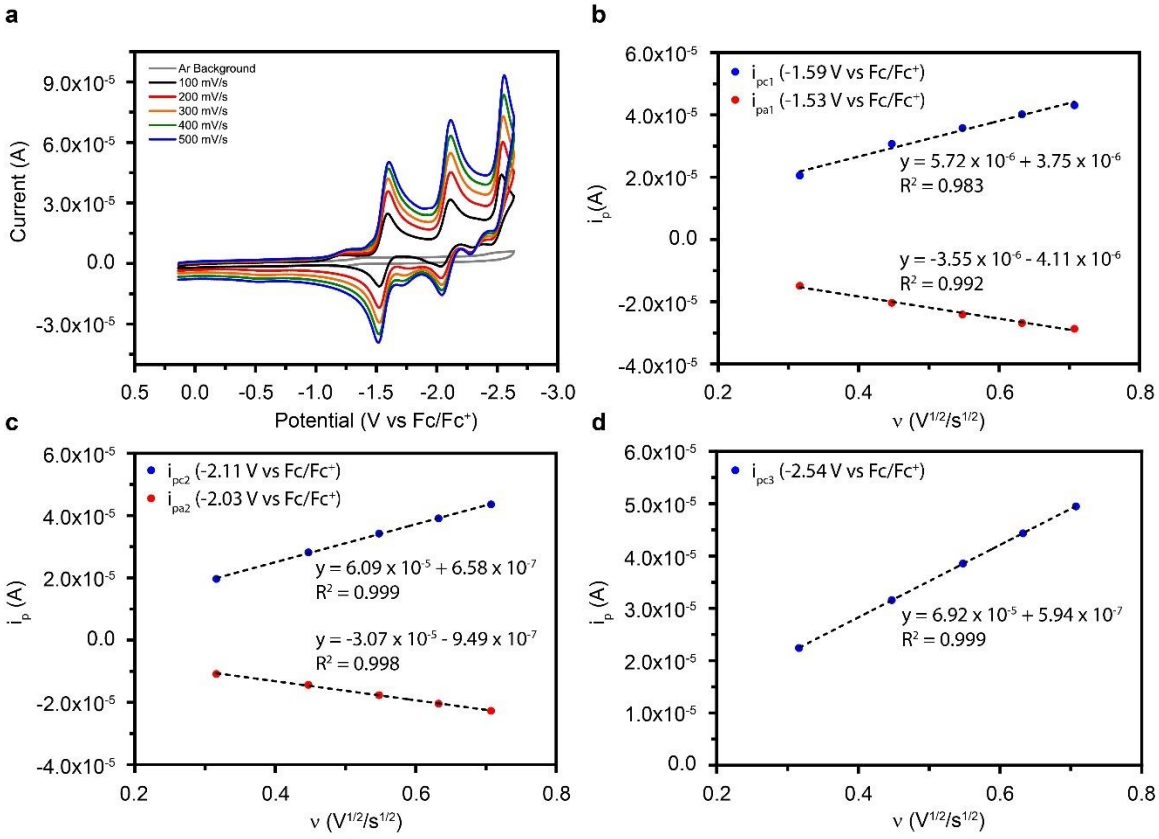


Figure 5.23. Scan rate dependent cyclic voltammograms of $[Zn1]^{2+}$. (a) CVs recorded at scan rates ranging from 100 – 500 mV/s. (b) i vs $(\nu)^{1/2}$ plot for the $L/L^{\bullet-}$ redox couple ($E_{1/2}$ = –1.56 V vs Fc/Fc^{+}). (c) i vs $(\nu)^{1/2}$ plot for the $L^{\bullet-}/L^{2-}$ redox couple ($E_{1/2}$ = –2.07 V vs Fc/Fc^{+}). (d) i vs $(\nu)^{1/2}$ plot for the L^{2-}/L^{3-} reduction (E_{pc} = –2.54 V vs Fc/Fc^{+}). Conditions: 1 mM $[Zn1]^{2+}$; 0.10 M $TBAPF_6/CH_3CN$.

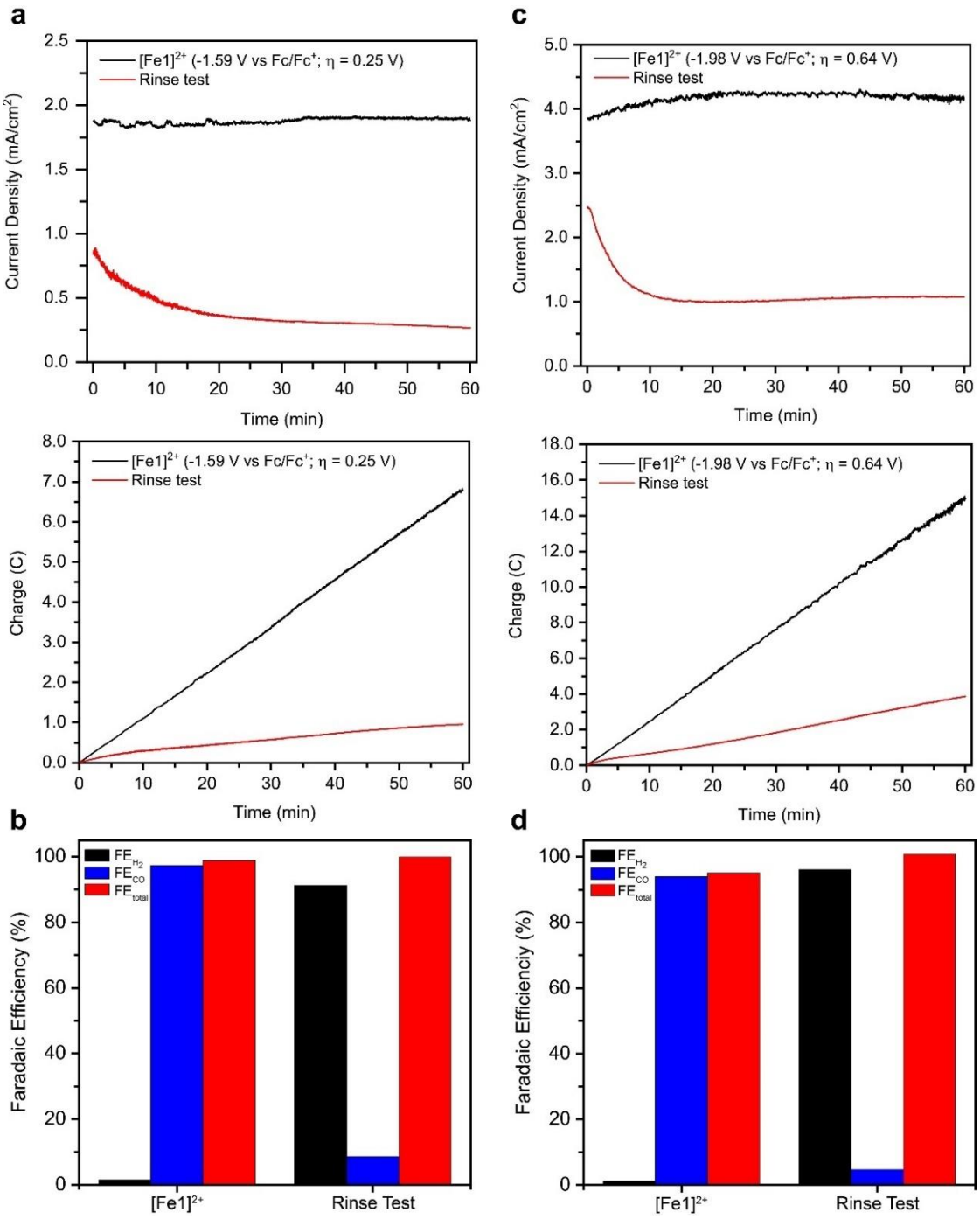


Figure 5.24. Rinse test control CPE experiments. Rinse tests were conducted at two different applied potentials. (a) CPE rinse test with a selected applied potential of –1.59 V vs Fc/Fc^+ (η = 0.32 V). (b) Faradaic efficiencies for rinse test conducted at –1.59 V vs Fc/Fc^+ (η = 0.32 V). (c) CPE rinse test with a selected applied potential of –1.98 V vs Fc/Fc^+ (η = 0.71 V). (d) Faradaic efficiency for rinse test conducted at –1.98 V vs Fc/Fc^+ (η = 0.71 V). Conditions: 0.10 M $TBAPF_6/CH_3CN$; 3.5 M phenol; 0.020M tetrabutylammonium acetate.

5.3.5 Kinetic Analysis in Organic Solution

Encouraged by the high selectivity of $[Fe1]^{2+}$ for electrochemical CO_2RR over competing HER processes, we sought to evaluate its kinetic performance. Cyclic voltammograms acquired for $[Fe1]^{2+}$ under CO_2-saturated electrolyte in the presence of 3.5 M phenol (**Figure 5.25**) exhibit scan rate dependence and noncanonical peak-shaped waves, indicative of competitive, nonideal processes (e.g., substrate consumption, product inhibition, etc.). As a result, k_{obs} (TOF_{max}) obtained from catalytic plateau current analysis is not appropriate here and will lead to underestimations of the rates of CO_2 reduction.[65] Therefore, we instead extracted kinetic parameters directly from our variable potential CPE experiments (**Figure 5.16**), as described by Savéant and co-workers,[66,67] where the products (CO and H_2) were detected and quantified by gas chromatography. The observed rate constants (k_{obs}) at each applied potential were extracted from the averaged specific current density for CO production (j_{CO}) taken across the entire 1 h CPE experiments (**Figure 5.16**) that were conducted in triplicate (see materials and methods for additional details).

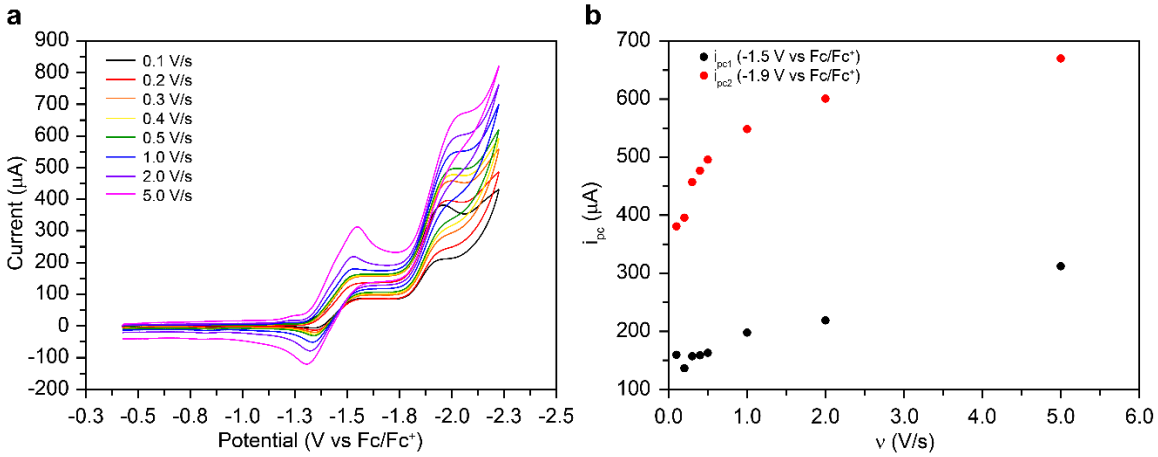


Figure 5.25. (a) Scan rate dependent CVs (0.1 – 5.0 V/s) of $[Fe1]^{2+}$ under CO_2 atmosphere. (b) Plot of the peak cathodic current of $[Fe1]^{2+}$ as a function of scan rate. Black = –1.5 V vs Fc/Fc^+ Red = –1.9 V vs Fc/Fc^+. Conditions: 1 mM $[Fe1]^{2+}$; 0.10 M $TBAPF_6/CH_3CN$; 3.5 M Phenol.

A catalytic Tafel plot was constructed from our CPE experiments with direct product quantification (**Figure 5.15b**) and is summarized in **Table 5.3**. Tafel analysis identifies $[Fe1]^{2+}$ as one of the most active molecular electrocatalysts reported to date with it achieving a turnover frequency (TOF) of 75,000 s^{-1} at an applied overpotential as low as 190 mV (−1.46 V vs Fc/Fc^+) and reaching TOFs > 500 000 s^{-1} between overpotentials of 560 – 710 mV (−1.81 and −1.98 V vs Fc/Fc^+) (**Figure 5.26**). Notably, this rapid, homogeneous CO_2 reduction catalysis is achieved without any modifications to the secondary coordination sphere to introduce hydrogen bond/proton-relay functionalities to break electronic scaling relationships.[12,13,47,68–71]

In parallel, we also attempted to apply foot-of-the-wave analysis (FOWA) as pioneered by Savéant[66,67] to estimate the kinetics based solely on CVs collected in the presence and absence of CO_2. FOWA estimates the idealized catalytic reactivity by considering the initial portion of the catalytic wave where the effects of side phenomena are expected to be minimal. Unfortunately, FOWA does not find clear application here because the linear region of the FOW is very small and

is ill defined due to the appearance of a pre-wave feature at −1.36 V vs Fc/Fc^+ and a multi-segmented catalytic wave with apparent maxima at −1.56 and −1.96 V vs Fc/Fc^+ (**Figures 5.11c** and **5.27**). The existence of this multi-segmented catalytic wave may suggest that the catalytic resting state is changing as more negative potentials are applied. Therefore, the extraction of kinetic data based on our CPE experiments results in more accurate analysis as they are determined from preparative scale experiments that directly detect and measure CO rather than relying on estimations of observed rate constants determined from CV data.

Finally, to assess the long-term catalytic stability and recyclability of $[Fe1]^{2+}$, four consecutive 5 h CPE experiments were conducted at −1.98 V (versus Fc/Fc^+), the highest potential investigated, without addition of fresh $[Fe1]^{2+}$ between each experiment (**Figure 5.28**). $[Fe1]^{2+}$ is remarkably stable with 221 C of charge passed over the 20 h window without any loss in selectivity for CO (average FE_{CO} = 87%).

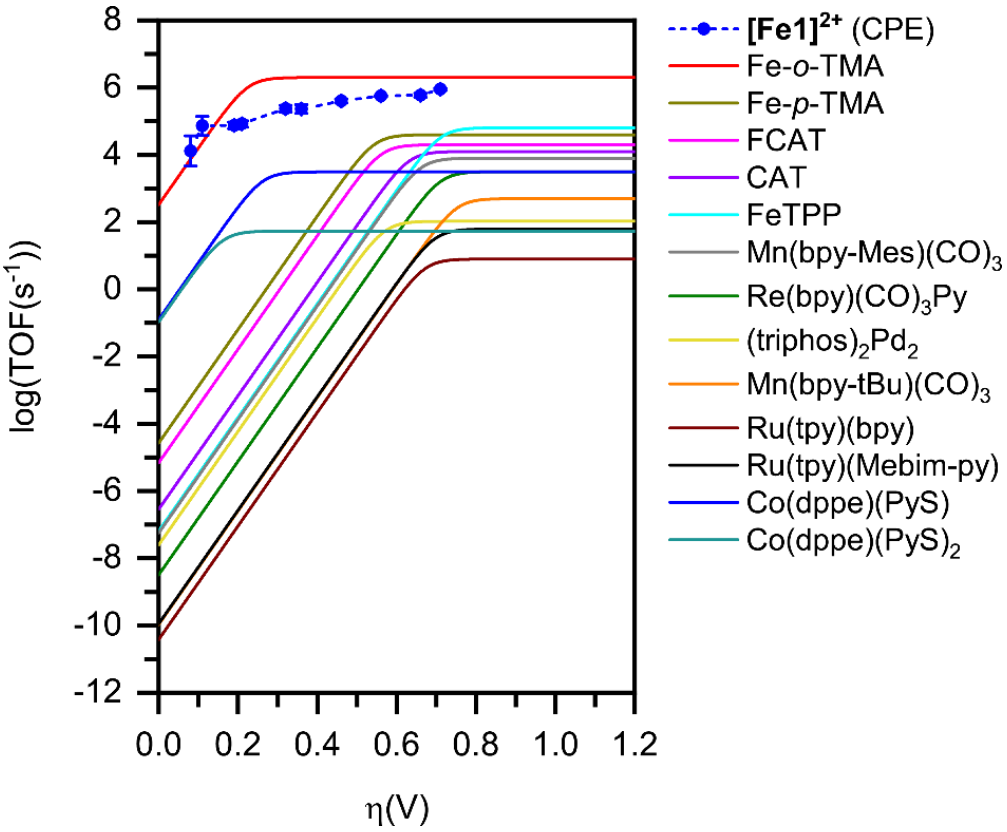


Figure 5.26. Catalytic Tafel plot comparing the CO_2RR of $[Fe1]^{2+}$ to other state-of-the-art literature reported homogenous electrocatalysts. Tafel plots for $[Fe1]^{2+}$ were obtained from CPE experiments with direct product detection (blue, dashed) Data for other electrocatalysts was adapted from Savéant and coworkers previous report[13] and recent literature reports for Co(dppe)(PyS)[62] and Co(dppe)$(PyS)_2$.[63] Conditions: 1 mM $[Fe1]^{2+}$; 0.10 M $TBAPF_6/CH_3CN$; 3.5 M Phenol. Note that CO_2RR activity of $[Fe1]^{2+}$ was measured by direct product detection rather than estimated from FOWA or other analyses.

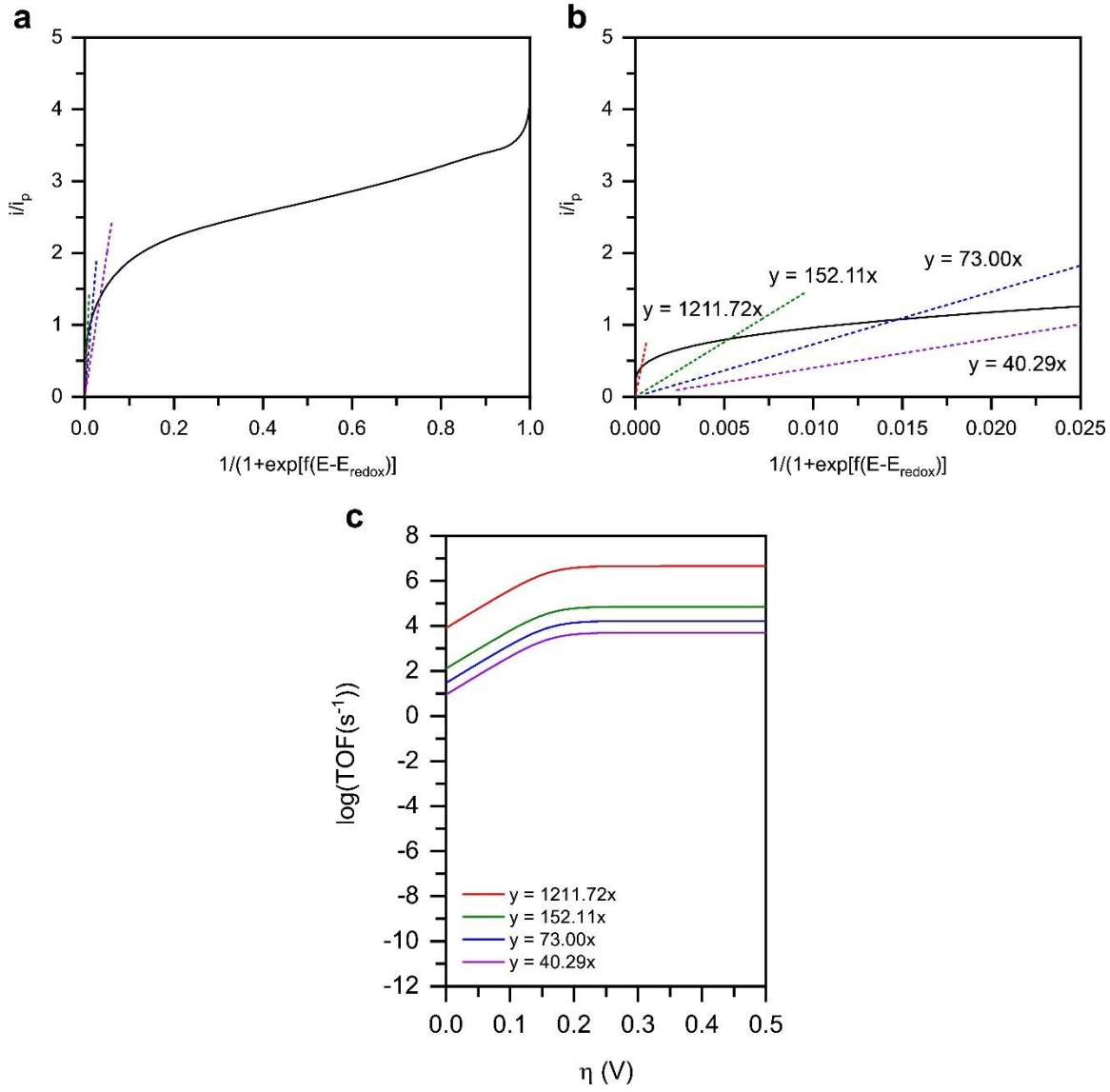


Figure 5.27. Foot-of-the-wave analysis (FOWA) of (a) $[Fe1]^{2+}$ and (b) a smaller region of the x-axis with four linear fits shown to illustrate the small linear FOW region. (c) Catalytic Tafel plots obtained from FOWA fits. The large degree of variation illustrates the limitation of FOWA for determining the kinetics of $[Fe1]^{2+}$ for electrochemical CO_2 reduction. Conditions: 1 mM $[Fe1]^{2+}$; 0.10 M $TBAPF_6/CH_3CN$; 3.5 M Phenol. As such, the CO_2RR activity of $[Fe1]^{2+}$ was measured by direct product detection.

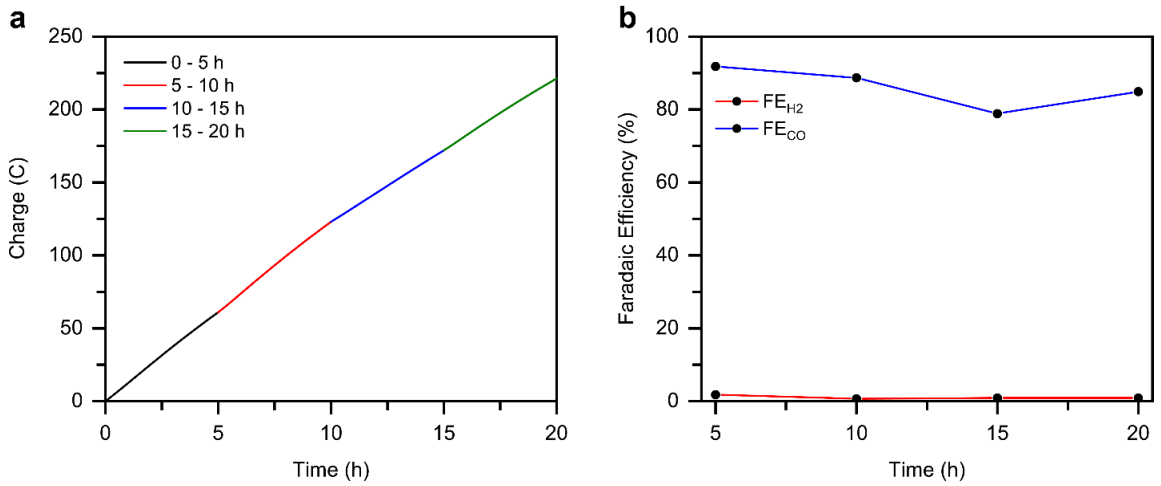


Figure 5.28. Long-term catalytic stability of $[Fe1]^{2+}$. (a) 5 h CPE experiments at –1.98 V vs Fc/Fc^{+} without addition of fresh catalyst between runs. (b) Faradaic yields for the formation of CO (blue) and H_2 (red) during the 20 h CPE.

5.3.6 Chemical Reduction and Characterization of [Fe(tpyPY2Me)]^0 ([Fe1]^0)

We reasoned that the observed electrocatalytic efficiency of $[Fe1]^{2+}$ for CO_2RR stems from a synergistic effect between the iron center and the redox-active tpyPY2Me ligand, as both components are necessary to achieve selective CO_2RR reactivity. To establish a molecular-level framework for understanding this metal–ligand cooperativity, we sought to synthesize, isolate, and characterize the two-electron reduced complex, $[Fe(tpyPY2Me)]^0$ ($[Fe1]^0$), which we hypothesize has putative catalytic relevance. Chemical reduction of $[Fe1]^{2+}$ with 2.2 equiv. of decamethylcobaltocene (**Figure 5.29a**) produced $[Fe1]^0$ as a dark purple solid. Interestingly, room temperature ^{1}H NMR analysis of $[Fe1]^0$ in CD_3CN revealed that the compound is diamagnetic with the aryl and aliphatic signals shifted upfield (**Figure 5.29b**). In support of this result, a nearly identical ^{1}H NMR spectrum was obtained for the product $[Zn1]^0$ generated from the chemical reduction of $[Zn1]^{2+}$ with potassium graphite (see **Figure 5.30** and details in the materials and methods). These data are consistent with our assignment of the reduction features for both $[Fe1]^{2+}$ and $[Zn]^{2+}$ as ligand-centered events. Frozen solution Fe K-edge X-ray absorption near-edge spectroscopy (XANES) was used to characterize metal oxidation states (**Figure 5.31**). Absorption edge energies were determined from the second derivative zero crossings, giving the following values (eV): 7126.9 ($[Fe1]^0$) and 7127.4 ($[Fe1]^{2+}$). These values are similar to compounds in the literature[72] leading to the assignment of the oxidation states of both species as Fe(II).

Given the unique diamagnetic ground state of $[Fe1]^0$, two major electronic structures are possible. The first possibility is a low-spin iron(II) center ($S_{Fe} = 0$) coordinated to a reduced closed-shell singlet ligand ($S_{tpyPY2Me} = 0$) generated by both electrons occupying the same π* orbital (i.e., $[Fe(tpyPY2Me)^{2-}]^0$). The other possibility is an intermediate-spin iron(II) center ($S_{Fe} = 1$) antiferromagnetically coupled to a reduced ligand with an open-shell triplet configuration ($S_{tpyPY2Me} = 1$) through half occupation of both low-lying π* terpyridine orbitals, leading to an overall metal–ligand spin-coupled electronic structure (i.e., $[Fe(tpyPY2Me^{\bullet})^{2-}]^0$). The two electronic configurations are more clearly distinguished here by specifying the spin state of the

ligand as either a singlet $(tpyPY2Me)^{2-}$ or a triplet $(tpyPY2Me^{\bullet\bullet})^{2-}$ in the chemical formula. Because of the large anodic shift (640 mV) in the ligand-based reductions of $[Fe1]^{2+}$ relative to $[Zn1]^{2+}$ (**Figure 5.11a**), the electrochemistry indicates a strong influence of the metal center and supports assignment to a $[Fe(tpyPY2Me^{\bullet\bullet})^{2-}]^{0}$ electronic configuration. In further support of this model, Mössbauer data for $[Fe1]^{0}$ revealed an isomer shift of $\delta = 0.2608(2)$ mm/s and a quadrupole splitting of $|\Delta E_Q| = 0.7637(4)$ mm/s, consistent with the formation of intermediate-spin iron(II) (**Figures 5.29c** and **5.32**).[73] The antiferromagnetic coupling between the reduced biradical ligand, $(tpyPY2Me^{\bullet\bullet})^{2-}$, and the intermediate-spin iron(II) is expected to be quite strong given that a diamagnetic ^{1}H NMR spectrum is observed at room temperature. Indeed, DFT calculations predict a large coupling constant of -1023 cm^{-1}, giving rise to a singlet-quintet gap of 4400 cm^{-1} (see the materials and methods section).

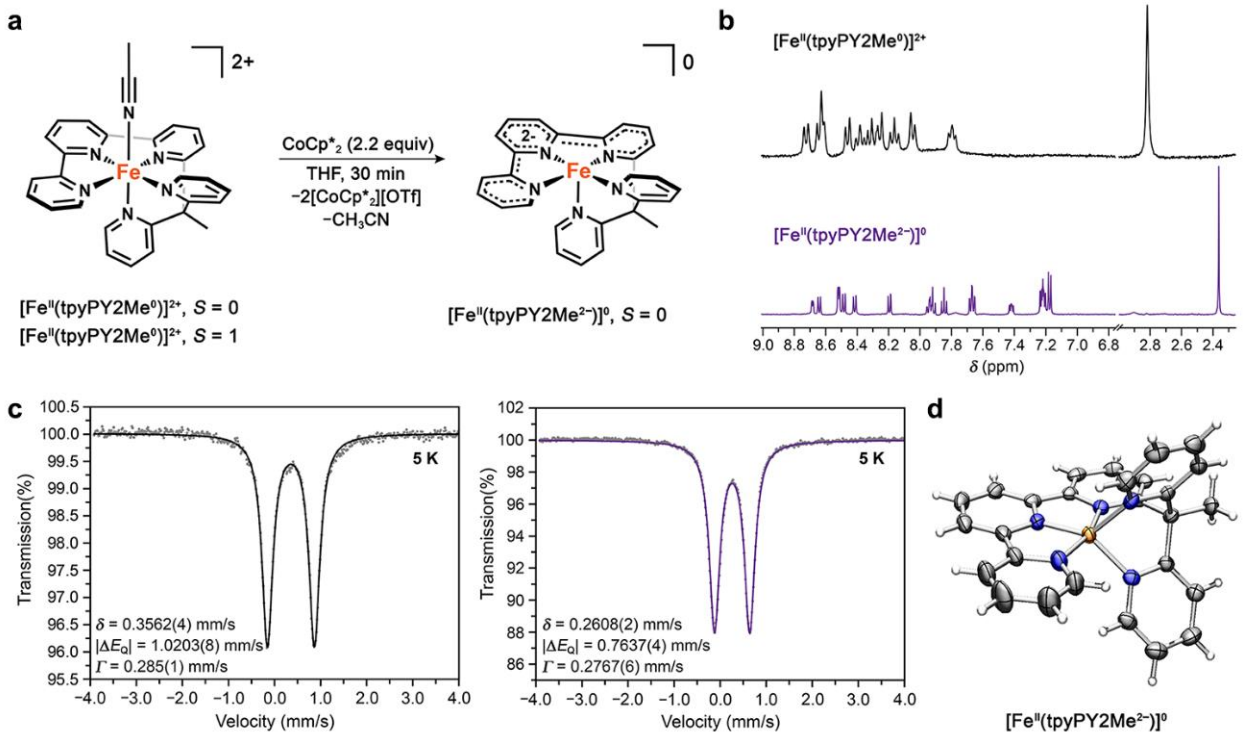
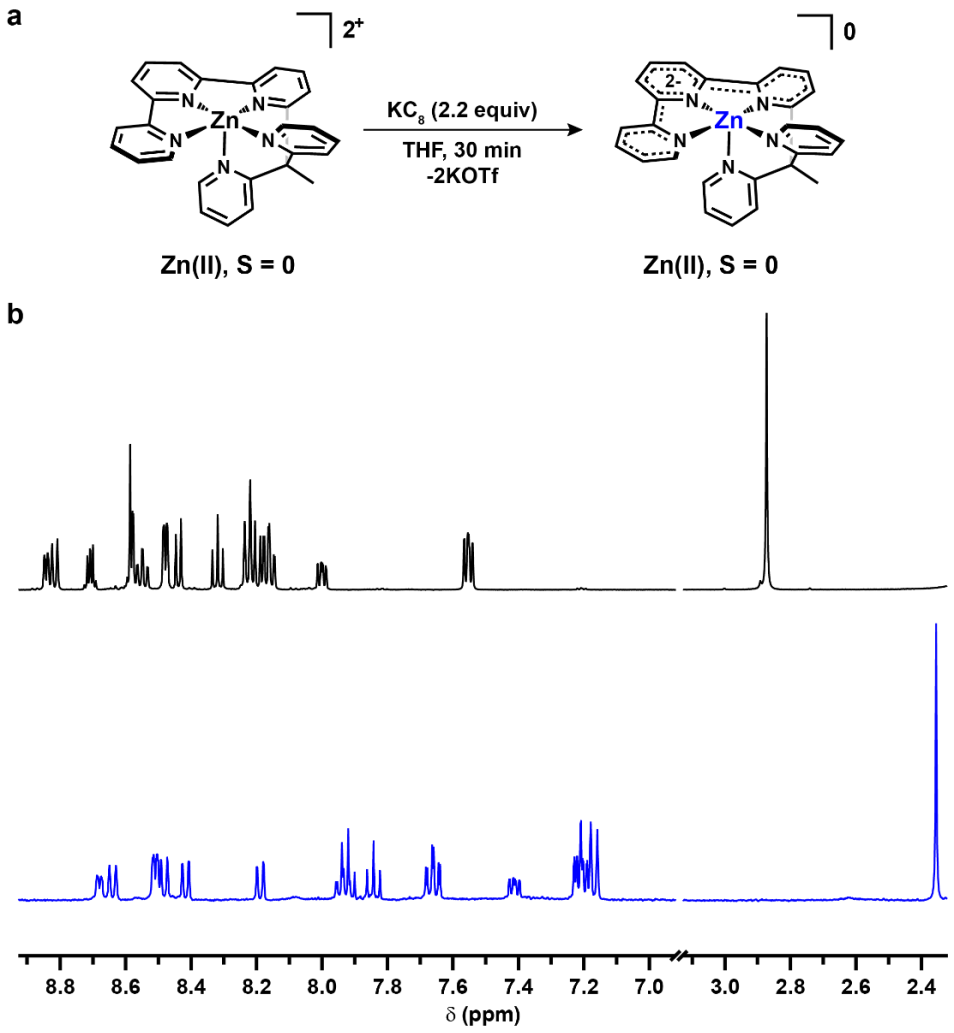


Figure 5.29. Synthetic preparation and characterization of the two-electron reduced species $[Fe1]^{0}$. The collective structural and spectroscopic data support assignment to an open-shell singlet species that maintains a formal Fe(II) oxidation state. (a) Two-electron reduction of $[Fe1]^{2+}$ generates the $[Fe1]^{0}$ complex that is a putatively active species for CO_2 reduction. (b) ^{1}H NMR spectrum of $[Fe1]^{2+}$ (black) and ^{1}H NMR spectrum of the product resulting from chemical reduction of $[Fe1]^{2+}$ with $CoCp^*_2$ (purple); both spectra were in CD_3CN at room temperature. (c) Zero-field ^{57}Fe Mössbauer analysis of $[Fe1]^{2+}$ (black) and $[Fe1]^{0}$ (purple) measured at 5 K. (d) Solid state structure of $[Fe1]^{0}$ from single-crystal X-ray diffraction analysis. Thermal ellipsoids are plotted at 80% probability level; orange, blue, and grey ellipsoids represent Fe, N, and C atoms, respectively. Residual solvent, and co-crystalized $CoCp^*_2$ are omitted for clarity.



Figures 5.30. Chemical reduction of $[Zn1]^{2+}$. (a) Reaction scheme for the two-electron reduction of $[Zn1]^{2+}$ with potassium graphite (KC_8). (b) ^1H NMR spectra of $[Zn1]^{2+}$ (black) and $[Zn1]^0$ (blue) in CD_3CN.

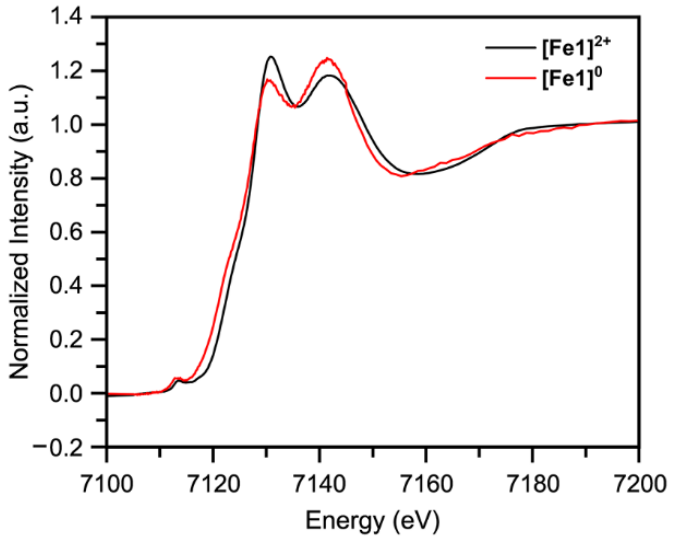


Figure 5.31. Experimental Fe K-edge XAS spectra of $[Fe1]^{2+}$ (black) and two-electron reduced $[Fe1]^{0}$ (red), supporting a formal Fe(II) oxidation state assignment for both species.

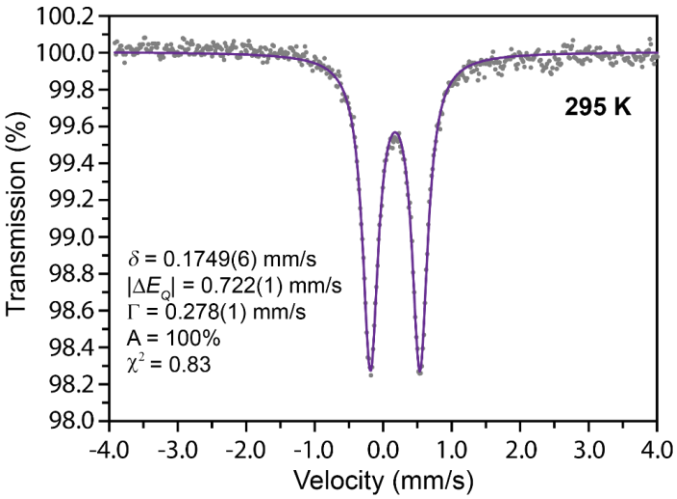


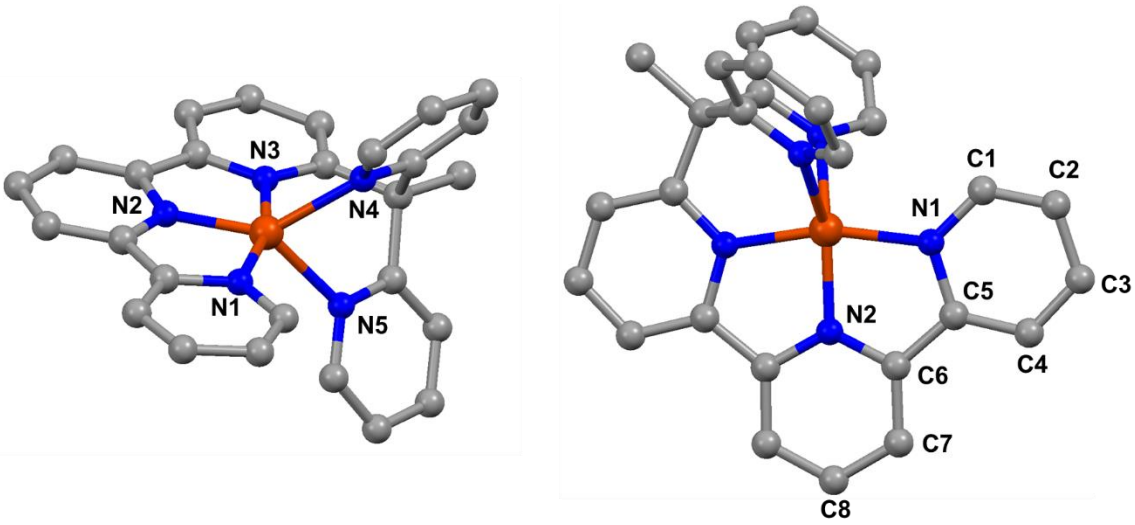
Figure 5.32. Zero-field ^{57}Fe Mössbauer analysis of $[Fe1]^{0}$ measured at 295 K.

Further insights into the electronic structure of $[Fe1]^{0}$ can be gleaned from the solid-state structure of $[Fe1]^{0}$. Single crystals of $[Fe1]^{0}$ were obtained by slow evaporation of a saturated acetonitrile solution, and X-ray diffraction analysis revealed a distorted square pyramidal geometry (**Figure 5.29d**; see crystallography **Tables 5.13** and **5.14**) resulting from the loss of the axial acetonitrile ligand in $[Fe1]^{2+}$. This structure is in good agreement with the reduction pathway predicted by DFT (*vide infra*). The bond metrics of the terpyridine moiety unambiguously supports the two-electron reduction of the tpyPY2Me ligand in the solid state and thus the iron(II) oxidation state assignment. In particular, the contraction of the intra-pyridine bond lengths (C_{py}–C'_{py}), from an average of 1.474(3) Å in $[Fe1]^{2+}$ to 1.434(4) Å in $[Fe1]^{0}$ is consistent with the metrics with which the oxidation levels of terpyridine can be established as determined through structural studies on a series of iron(II) and chromium(III) bis-terpyridine complexes reported by Wieghardt

and co-workers.[53,54] Furthermore, average C–N bond lengths of the terpyridine moiety in $[Fe1]^0$ (1.384(3) Å) depart quite significantly from what would be expected for typical, neutral aromatic pyridine rings (1.35 ± 0.1 Å, respectively)[53] and what was observed in the solid state structure of $[Fe1]^{2+}$ (1.353(2) Å).

Distinguishing between the two possible electronic configurations of $[Fe1]^0$ based on the single crystal X-ray diffraction data is more challenging. The DFT predicted structure for the open-shell singlet ($[Fe(tpyPY2Me^{\bullet\bullet})^{2-}]^0$) more closely matches the experimental bond metrics of $[Fe1]^0$ than does the predicted structure of the closed-shell singlet ($[Fe(tpyPY2Me)^{2-}]^0$); however, the solid-state structures are susceptible to additional packing and dispersion forces that are not accounted for by DFT calculations (**Table 5.4**). In theory, the unique bonding interactions of the two terpyridine LUMOs[53,54,74] should enable us to directly distinguish between the two possible electronic configurations of $[Fe1]^0$, but the change in bond metrics between the dianionic, singlet ligand ($tpyPY2Me^{2-}$) and the triplet, π radical dianion ($tpyPY2Me^{\bullet\bullet 2-}$) is expected to be quite subtle given the metrics reported by Wieghardt and co-workers on a series of reduced homoleptic bis(terpyridine) complexes ($[M(tpy)_2]^{n+}$; M = Cr, Fe).[53,54] Attempts to crystallize $[Zn1]^0$ have been unsuccessful to date, thus preventing direct crystallographic comparison to $[Fe1]^0$.

Table 5.4. Average bond length (Å) comparison of $[Fe1]^0$ to DFT predicted structures of the open-shell singlet ($[Fe(II)(tpyPY2Me^{\bullet\bullet})^{2-}]^0$ S_{Fe} =1; S_L = 1) and the closed-shell singlet ($[Fe(II)(tpyPY2Me)^{2-}]^0$ S_{Fe} = 0; S_L = 0).



Bond Lengths (Å)	$[Fe1]^0$ Experiment	$[Fe1]^0$ Theory (open-shell singlet)	$[Fe1]^0$ Theory (closed-shell singlet)
Fe1—N1	1.8997(18)	1.937	1.943
Fe1—N2	1.8377(18)	1.873	1.811
Fe1—N3	1.8783(17)	1.891	1.901
Fe1—N4	1.9463(18)	2.090	1.945
Fe1—N5	1.9600(19)	2.092	1.945
N1—C1	1.369(4)	1.358	1.351
N1—C5	1.398(4)	1.399	1.380
N2—C6	1.384(4)	1.364	1.393
C1—C2	1.373(4)	1.373	1.379
C2—C3	1.415(5)	1.433	1.414
C3—C4	1.374(5)	1.376	1.378
C4—C5	1.398(4)	1.410	1.409
C5—C6	1.434(4)	1.432	1.431
C6—C7	1.396(4)	1.410	1.377
C7—C8	1.393(4)	1.396	1.402

Although absolute determination of the electronic structure should not be based solely on X-ray diffraction, when it is taken together with the electrochemical, NMR, and Mössbauer results, the collective data support the iron(II) oxidation state assignment of $[Fe1]^0$ as an open-shell singlet ground state ($[Fe(tpyPY2Me^{\bullet\bullet})^{2-}]^0$) composed of an intermediate-spin iron(II) center (S_{Fe} = 1) that is antiferromagnetically coupled to a doubly reduced tpyPY2Me (S_{tpy} = 1) ligand. This strong exchange coupling shifts the tpyPY2Me-based reductions of $[Fe1]^{2+}$ to more positive potentials relative to the analog with the redox-silent Zn(II) center by 640 mV, which we hypothesize

ultimately promotes highly selective CO_2 reduction by $[Fe1]^{2+}$. To further elucidate the electronic structures of $[Fe1]^{2+/0}$, we subsequently applied extensive DFT and multireference methods.

5.3.7 Electronic Structure Calculations

We carried out DFT calculations using the ωB97X-D functional to generate a more accurate molecular orbital picture of our $[Fe1]^{2+}$ system. Optimized structures and predicted redox potentials for $[Fe1]^{2+}$ and $[Zn1]^{2+}$ are in good agreement with experimental data (**Tables 5.5** and **5.6**). Interestingly, although the DFT data indicate the metal center in $[Fe1]^{2+}$ is best described as low-spin iron(II), the calculated singlet-quintet gap is small, explaining the observed thermal population of a higher spin-state at room temperature (**Tables 5.7** and **5.8**). The first reduction of $[Fe1]^{2+}$ to $[Fe1]^{+}$ is predicted to generate a ground state doublet composed of a low-spin iron(II) and a tpyPY2Me-based radical $(tpyPY2Me^{\bullet})^{1-}$ with a predicted redox potential of −1.46 V (**Figure 5.33a–c**). The spin density plot of this $[Fe1]^{+}$ species indicates a ligand-based reduction with almost no excess spin on the iron center (**Figure 5.33b**). The second reduction populates a second low lying π* orbital of tpyPY2Me and induces loss of the axial acetonitrile molecule, providing access to an intermediate-spin iron(II) state (**Figure 5.33a,d,e**). The $S_{Fe} = 1$ iron center is strongly antiferromagnetically coupled to the two electrons in the tpyPY2Me π* orbitals (i.e., $[Fe(tpyPY2Me^{\bullet\bullet})^{2-}]^{0}$; **Figure 5.33e**). Localized orbital bonding analysis confirmed that iron remains in the 2^{+} oxidation state during the second reduction process, which has a predicted reduction potential of −1.51 V. This predicted redox potential is in good agreement with that observed experimentally.

In contrast, the other feasible closed-shell singlet configuration: a low-spin iron(II) center ($S_{Fe} = 0$) coordinated to a reduced closed-shell doubly reduced singlet ligand ($S_{typPY2Me} = 0$) (i.e., $[Fe(tpyPY2Me)^{2-}]^{0}$), does not match the experimental data. The doubly reduced tpy ligand is strongly π basic and thus delocalizes some electron density into the empty metal orbitals (distorted e_g-type). The computed reduction potential of −2.03 V vs Fc/Fc^{+} using the $[Fe(tpyPY2Me)^{2-}]^{0}$ electronic configuration does not match the experimental value of −1.43 V vs Fc/Fc^{+}. This difference can be rationalized by the large free energy gap (12 kcal/mol) between the broken symmetry solution ($[Fe(tpyPY2Me^{\bullet\bullet})^{2-}]^{0}$) and the closed-shell singlet ($[Fe(tpyPY2Me)^{2-}]^{0}$) consisting of low-spin iron(II) ($S_{Fe} = 0$) and doubly reduced ligand ($S_{tpyPY2Me} = 0$) (**Tables 5.7** and **5.8**). It should also be noted that a large variety of different hybrid density functionals all predict the broken symmetry configuration as the ground state on the singlet surface (see **Table 5.8**).

Table 5.5. Predicted redox potentials for $[Fe1]^{2+}$ and $[Zn1]^{2+}$ (vs Fc/Fc^{+}) using the ωB97X-D/def2-TZVPP functional. Total spin (*S*) and coordination number (CN) indicated inside parenthesis (S, CN). [a] Calculated redox potential determined with $[Fe1]^{0}$ possessing an open-shell singlet electronic structure ($[Fe(tpyPY2Me^{\bullet\bullet})^{2-}]^{0}$) and [b] predicted redox potential determined with $[Fe1]^{0}$ having a closed-shell singlet electronic structure ($[Fe(tpyPY2Me)^{2-}]^{0}$).

Reaction	$E_{1/2}$ (V vs Fc/Fc^{+})
$[Fe1]^{2+}$ (0, 6) + e^{-} → $[Fe1]^{+}$ (1/2, 6)	−1.46
$[Fe1]^{+}$ (1/2, 6) + e^{-} → $[Fe1]^{0}$ (0, 5) + CH_3CN	−1.51[a]
$[Fe1]^{+}$ (1/2, 6) + e^{-} → $[Fe1]^{0}$ (0, 5) + CH_3CN	−2.03[b]
$[Zn1]^{2+}$ (0, 5) + e^{-} → $[Zn1]^{+}$ (1/2, 5)	−1.31
$[Zn1]^{+}$ (1/2, 5) + e^{-} → $[Zn1]^{0}$ (0, 5)	−2.02

Table 5.6. Predicted redox potentials of $[Fe1]^{2+}$ (vs Fc/Fc^{+}) using different DFT functionals.

Functional	$E_{1/2}$ ($L/L^{\bullet-}$) (V vs Fc/Fc^{+})	$E_{1/2}$ ($L^{\bullet-}/L^{2-}$)(V vs Fc/Fc^{+})
*ω*B97X-D	–1.46	–1.51
*ω*B97M-V	–1.52	–1.77
*ω*B97X-V	–1.49	–1.63
B3LYP	–1.29	–0.97
PBE0	–1.25	–1.04
PW6B95	–1.36	–1.30
PWB6K	–1.28	–1.17
MN15	–1.67	–1.79

Table 5.7. Adiabatic spin gaps for intermediate spin (IS) and low spin (LS) $[Fe1]^{n+}$ (n = 2, 1, 0) relative to the high-spin configuration; spin gaps were calculated using wB97X-D/def2-TZVPP.

Complex	Δ*G* (IS) (kcal/mol)	Δ*G* (LS) (kcal/mol)
$[Fe1]^{2+}$	11.0 (S = 1)	0.2 (S = 0)
$[Fe1]^{+}$	7.6 (S = 3/2)	−0.7 (S = 1/2)
$[Fe1]^{0}$	−5.0 (S = 1)	−10.4 (S = 0)

Table 5.8. Functional dependent adiabatic spin gaps for intermediate spin (IS) and low spin (LS) $[Fe1]^{n+}$ (n = 2, 1, 0) relative to the high-spin configuration using the def2-TZVPP basis. Energies are provided in kcal/mol; S indicates the total spin state of the ground state.

Functional	**$[Fe1]^{2+}$**		**$[Fe1]^{+}$**		**$[Fe1]^{0}$**		
	IS (S = 1)	LS (S = 0)	IS (S = 3/2)	LS (S = 1/2)	IS (S = 1)	LS (S = 0) RKS	IS (S = 0) BS
ωB97X-D	11.0	0.2	7.6	−0.7	−5.0	−1.6	−10.4
ωB97M-V	11.7	−1.6	9.2	−2.6	−4.5	−0.3	−9.8
ωB97X-V	11.4	−0.1	8.8	−1.3	−4.2	1.6	−9.7
B3LYP	10.8	1.1	4.2	−1.7	−7.4	−10.0	−12.5
PBE0	15.0	6.3	8.8	3.9	−6.2	−5.3	−10.9
PW6B95	12.1	1.6	5.8	−0.2	−6.5	−6.9	−11.2
PWB6K	8.4	3.9	15.8	15.6	−3.2	9.1	−7.1
MN15	4.2	−2.3	−2.8	−3.0	−6.5	−6.0	−7.1

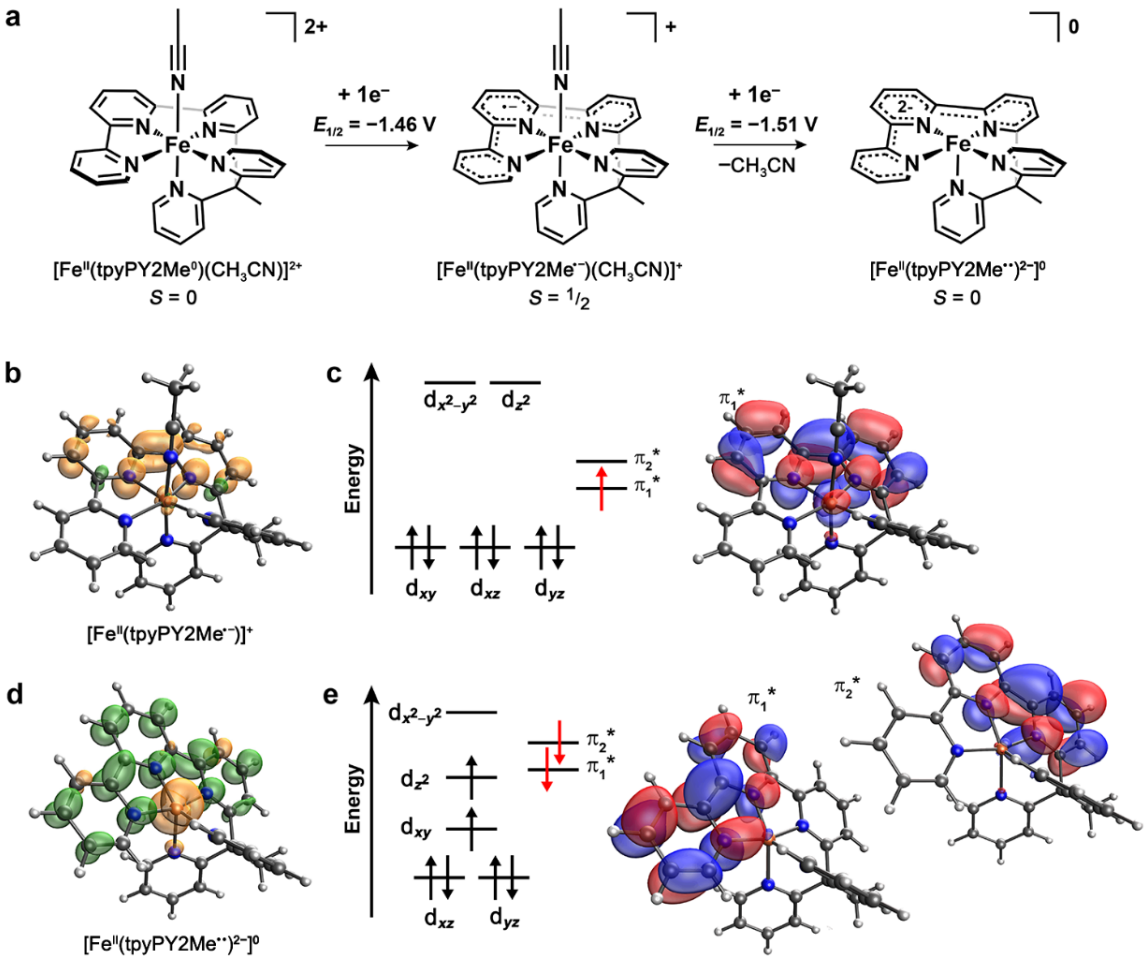
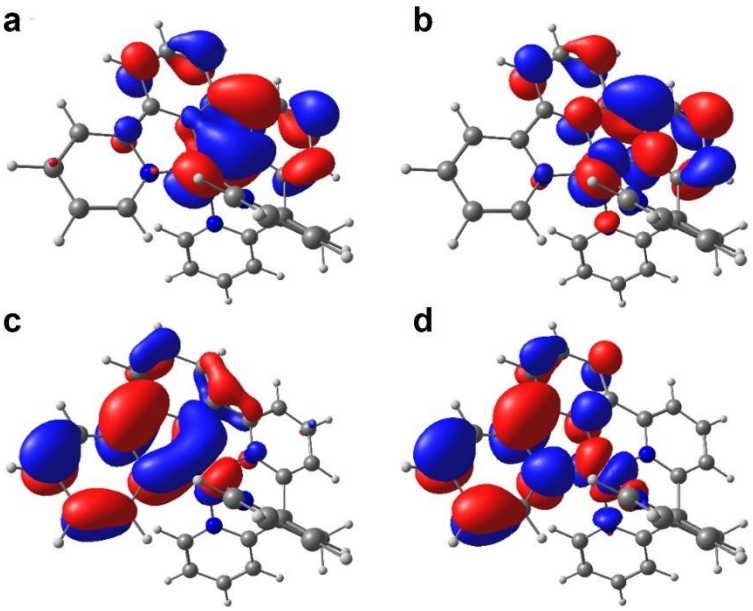


Figure 5.33. DFT analysis and calculated molecular orbitals for $[Fe1]^{+}$ and $[Fe1]^{0}$ species. (a) DFT predicted pathway for reduction of $[Fe1]^{2+}$ to the open-shell singlet $[Fe1]^{0}$, $[Fe(tpyPY2Me^{\bullet\bullet})^{2-}]^{0}$. The computed reduction potentials are given for reduction of $[Fe1]^{2+}$ to $[Fe1]^{+}$ and $[Fe1]^{+}$ to $[Fe1]^{0}$. See **Table 5.5** for the predicted reduction pathways for $[Zn(1)]^{2+/0}$ and for the closed-shell singlet $[Fe1]^{0}$, $[Fe(tpyPY2Me)^{2-}]^{0}$. (b) Spin density plot and (c) simplified molecular orbital diagram of the one electron reduced intermediate $[Fe1]^{+}$. (d) Spin density plot and (e) simplified molecular orbital diagram of $[Fe1]^{0}$ ($[Fe(tpyPY2Me^{\bullet\bullet})^{2-}]^{0}$). Localized metal orbitals are depicted in the supplementary materials.

In addition, multi-reference calculations using complete active space self-consistent field (CASSCF) confirmed the antiferromagnetically coupled ground state (see the materials and methods). This calculation reveals a strong entanglement of the two ligand-based orbitals and the two metal d-orbitals. In particular, the axial distortion away from octahedral symmetry allows the d_z^2 and d_{xy} metal orbitals (or superposition of the two orbitals) to interact with the two tpyPY2Me π* orbitals in a weak π-type interaction (**Figure 5.34**). Hence, the novel ligand framework with two low-lying π* orbitals, a distorted coordination geometry, and a moderate ligand field in combination with the iron metal center stabilizes two excess electrons effectively. The spin transition alters both the energetics of the d-orbitals and local spin on the central metal to facilitate an effective antiferromagnetic coupling. In contrast, in the alternative closed-shell singlet

electronic configuration ($[Fe(tpyPY2Me)^{2-}]^0$; $S_{Fe} = 0$ and $S_{tpy} = 0$), the stabilization of the doubly reduced tpyPY2Me π* ($S_{tpy} = 0$) by the high lying e_g* of the low-spin iron(II) ($S_{Fe} = 0$) is marginal. This feature is illustrated by the almost identical second ligand reduction potentials of $[Zn1]^{2+}$ and $[Fe1]^{2+}$ with a closed-shell singlet electronic structure (−2.02 V for $[Zn1]^{2+}$ and −2.03 V vs Fc/Fc^+ for $[Fe1]^{2+}$ with $S_{Fe} = 0$ and $S_{tpy} = 0$).



Figures 5.34. Natural orbital of the CAS(4,4) of $[Fe1]^0$ bonding (a) and (c) and antibonding (b) and (d) with natural occupation number (NOON) (a) 1.35 (b) 0.65 (c) 1.33 (d) 0.67.

We note that a similar electronic structure involving this intramolecular antiferromagnetic coupling was proposed by Neese and co-workers for the electronic structure of another CO_2 reduction catalyst, the doubly reduced iron tetraphenylporphryin complex, $[Fe(TPP)]^{2-}$.[75] Through quantum mechanical calculations and spectroscopic data (Mössbauer and XAS) they assign both reductions of $[FeTPP]^{2-}$ to the porphyrin ligand framework and show that it is coupled to an intermediate-spin iron center ($S_{Fe} = 1$) giving an overall singlet state.[75] It should be noted that the iron center in the un-reduced iron(II) complex, $[Fe(TPP)]^0$, is intermediate-spin and therefore the metal center does not undergo a spin transition upon reduction. This behavior can be contrasted to the group VII CO_2 reduction catalyst, $[Re(bpy)(CO)_3]^-$ (and its Mn derivative), where the quantum chemical calculations and spectroscopic data revealed that one electron is placed into the π* orbital of the non-innocent bpy ligand and the second electron is placed in the metal d_z^2 orbital but is strongly delocalized into the three carbonyl ligands. Both electrons form a metal–ligand bond (delocalized metal–ligand orbital) with a singlet ground state which is 15 kcal/mol lower in energy than the uncoupled triplet state.[32] Thus, the "initial" d-orbitals are not involved in the stabilization of the excess electrons as they are in $[Fe1]^{2+}$ and [Fe(TPP)].

5.3.8 Electrochemical CO_2RR Catalyzed by $[Fe(tpyPY2Me)]^{2+}$ in Water

Given the low overpotentials required for $[Fe1]^{2+}$ to catalyze homogeneous electrochemical CO_2 reduction in organic solvent, we sought to evaluate its activity in water

(**Figure 5.35**). For this purpose, we prepared the more water-soluble nitrate analog of $[Fe1]^{2+}$ (see the materials and methods), and X-ray diffraction analysis revealed that anion exchange does not alter the catalyst structure (**Figure 5.36**; see crystallography **Tables 5.15** and **5.16**). As a cheap, abundant, and benign solvent and proton source, water is an attractive medium for CO_2 reduction. However, homogeneous molecular CO_2 reduction catalysts typically require mercury working electrodes to operate effectively in aqueous electrolytes because their onset potentials are too negative to be compatible with more desirable carbon-based electrodes that preferentially catalyze competing water reduction.[10,76–79] Owing to the 640 mV positive shift in 2-electron reduction potential upon moving from Zn(II) to Fe(II), we envisioned that CO_2RR could be favored over HER, even with water as both a solvent and proton source.

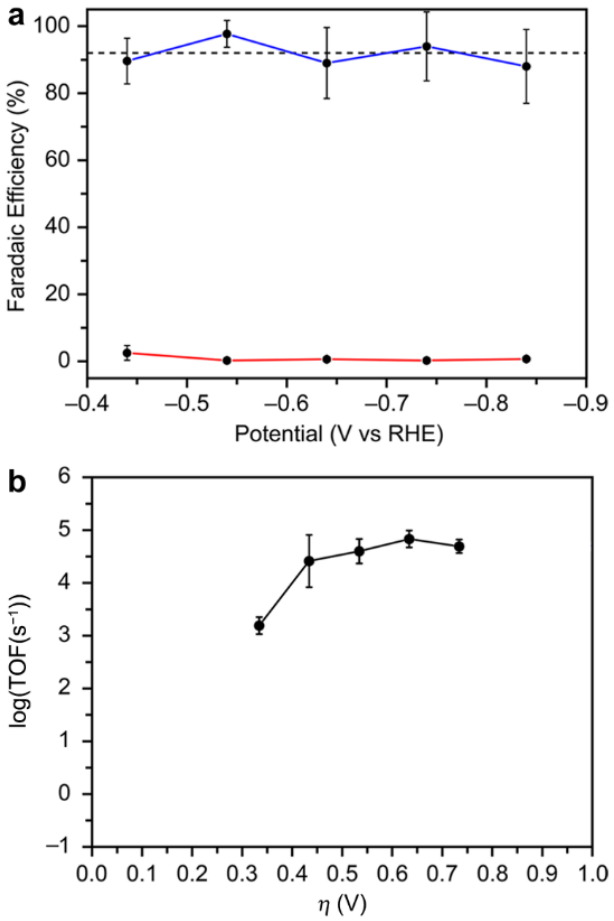


Figure 5.35. Aqueous CO_2 reduction performance for the Fe-tpyPY2Me electrocatalyst. (a) Faradaic efficiencies for CO (blue) and H_2 (red) formation at varying applied potentials for 60 min (averages of three experiments). The average FE_{CO} is indicated by the black dashed line. (b) Catalytic Tafel plot for $[Fe1]^{2+}$ obtained from CPE experiments in 0.10 M $NaHCO_3$.

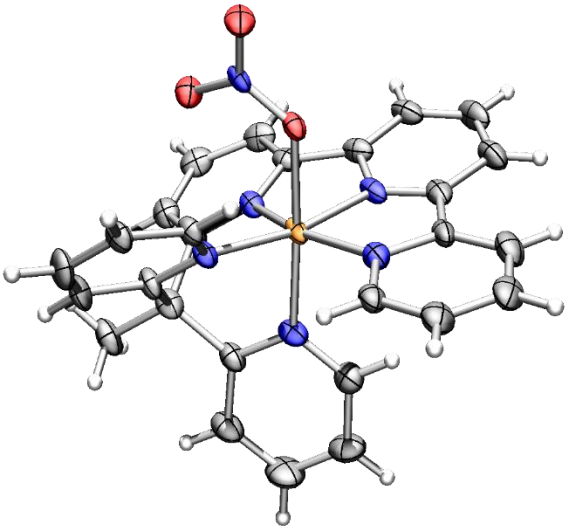


Figure 5.36. Solid state structure of [Fe(tpyPY2Me)(NO_3)][NO_3] at 50% displacement ellipsoid probability. The non-coordinated nitrate anion was omitted for clarity.

Against this backdrop, we were pleased to observe that cyclic voltammograms collected for $[Fe1]^{2+}$ dissolved in 0.10 M $NaHCO_3$ with a carbon paste working electrode show the formation of a catalytic wave when saturated with CO_2 (**Figure 5.37**). Notably, variable potential CPE experiments (**Figures 5.38 – 5.42**) revealed that $[Fe1]^{2+}$ maintains its activity and selectivity for CO_2 reduction to CO in water (average FE_{CO} = 92% and FE_{H_2} < 1%) with maximum turnover frequencies, determined from direct product detection, reaching > 50 000 s^{-1} at overpotentials of 500 mV (**Figure 5.35b**). Importantly, control rinse tests passed negligible current during 1 h CPE experiments, and the selectivity was inverted such that H_2 is the major product (**Figures 5.38–5.43**). UV–visible spectra collected before and after electrolysis are nearly indistinguishable; however, cyclic voltammograms change quite drastically following the 1 h CPE (**Figure 5.44**) indicative of some degree of catalyst deposition and decomposition on the glassy carbon electrode. In line with this observation, electrochemical stripping behavior is also observed, which may contribute to slower catalysis in water relative to organic solvent (**Figure 5.45**). Nevertheless, these data show that $[Fe1]^{2+}$ is an effective molecular catalyst for homogeneous CO_2 reduction in water. Crucially, given its molecular nature, the activity, stability, and overpotential of this catalyst can in principle be tuned through ligand modifications accessible by synthetic chemistry. Further, the study of this catalyst and related systems has the potential to shed important insights on the behavior of materials catalysts bearing atomically dispersed iron sites.[80]

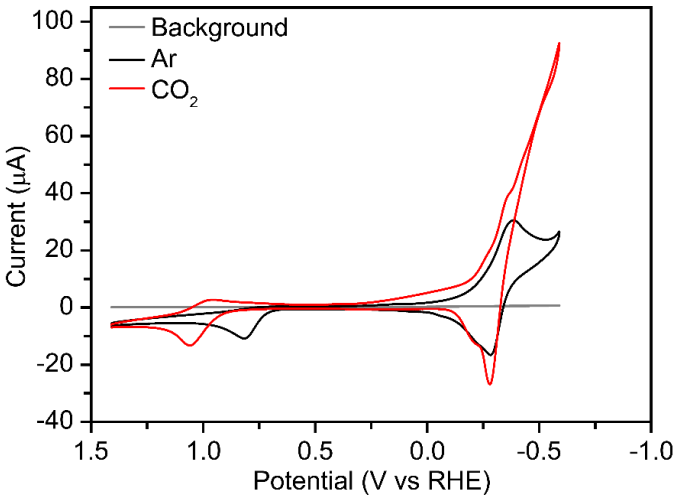


Figure 5.37. CVs of $[Fe1]^{2+}$ (1 mM) under Ar (black) and CO_2 (red) in aqueous 0.10 M $NaHCO_3$.

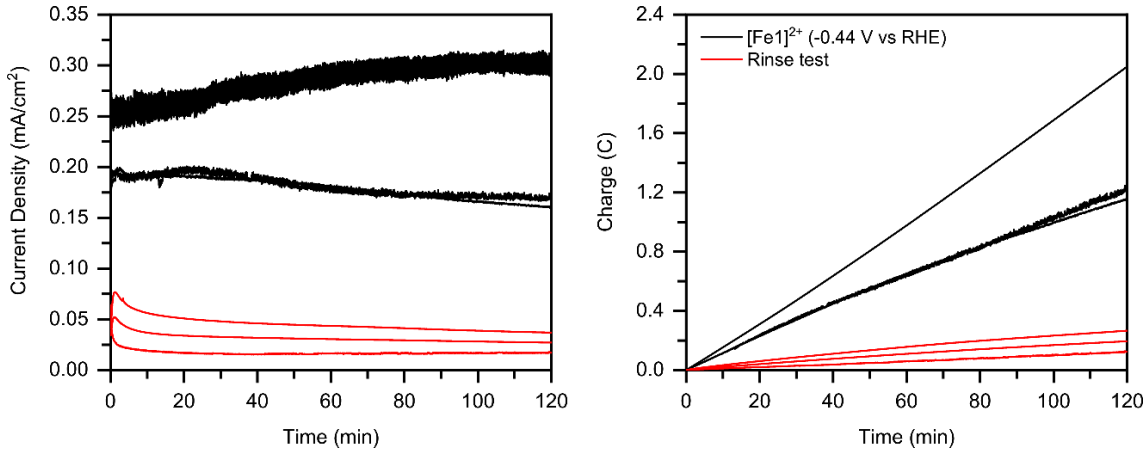


Figure 5.38. Controlled potential electrolysis of $[Fe(tpyPY2Me)][NO_3]_2$ in water at an applied potential of –0.44 V vs RHE. Black = $[Fe1]^{2+}$; Red = rinse test. Conditions: 1 mM $[Fe1]^{2+}$; 0.10 M $NaHCO_3$. Data was collected in triplicate.

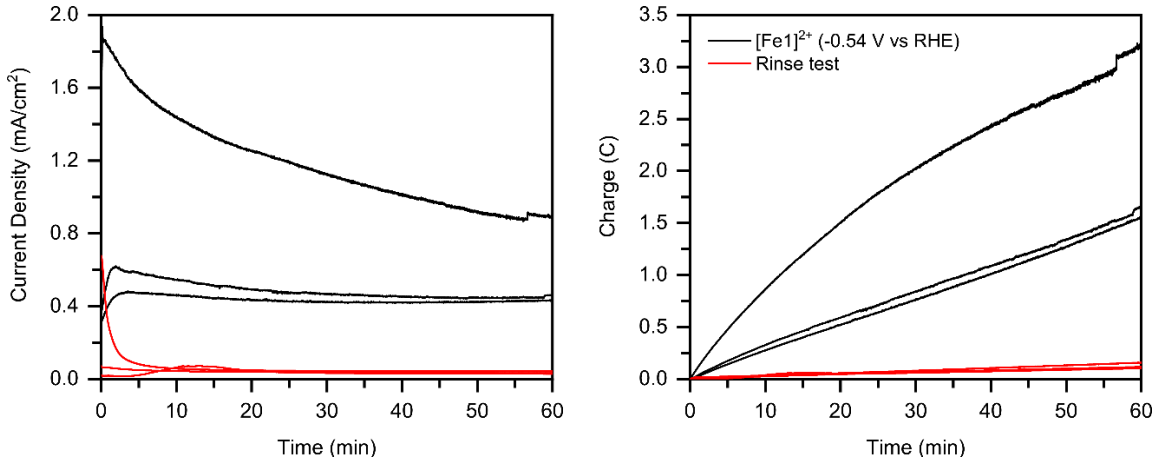


Figure 5.39. Controlled potential electrolysis of [Fe(tpyPY2Me)][NO_3]$_2$ in water at an applied potential of –0.54 V vs RHE. Black = [Fe1]$^{2+}$; Red = rinse test. Conditions: 1 mM [Fe1]$^{2+}$; 0.10 M $NaHCO_3$. Data was collected in triplicate.

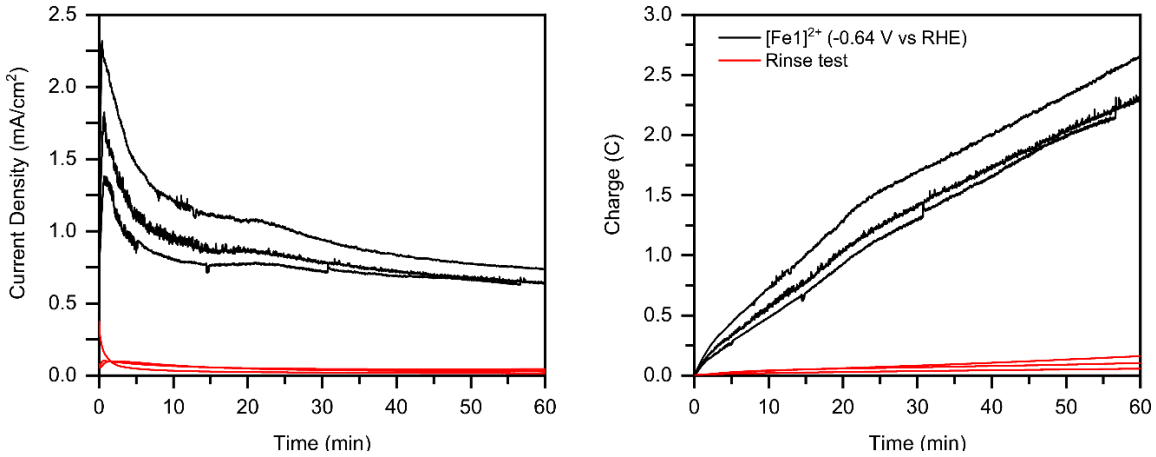


Figure 5.40. Controlled potential electrolysis of [Fe(tpyPY2Me)][NO_3]$_2$ in water at an applied potential of –0.64 V vs RHE. Black = [Fe1]$^{2+}$; Red = rinse test. Conditions: 1 mM [Fe1]$^{2+}$; 0.10 M $NaHCO_3$. Data was collected in triplicate.

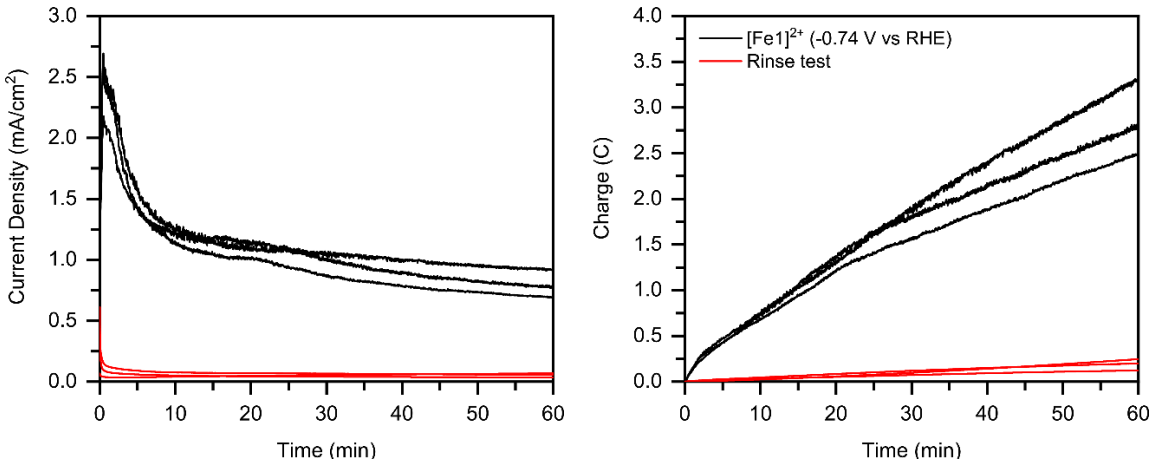


Figure 5.41. Controlled potential electrolysis of [Fe(tpyPY2Me)][NO_3]$_2$ in water at an applied potential of –0.74 V vs RHE. Black = $[Fe1]^{2+}$; Red = rinse test. Conditions: 1 mM $[Fe1]^{2+}$; 0.10 M $NaHCO_3$. Data was collected in triplicate.

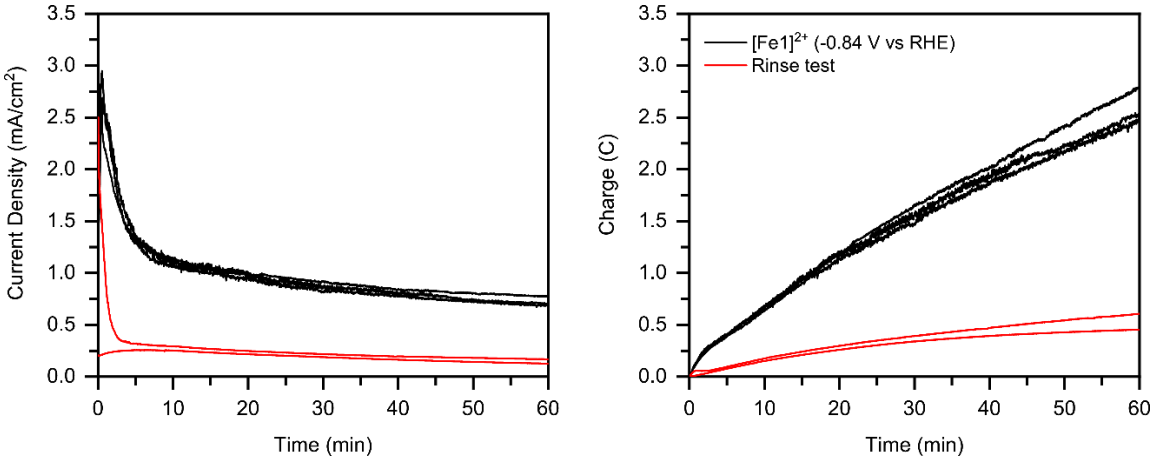


Figure 5.42. Controlled potential electrolysis of [Fe(tpyPY2Me)][NO_3]$_2$ in water at an applied potential of –0.84 V vs RHE. Black = $[Fe1]^{2+}$; Red = rinse test. Conditions: 1 mM $[Fe1]^{2+}$; 0.10 M $NaHCO_3$. Data was collected in triplicate.

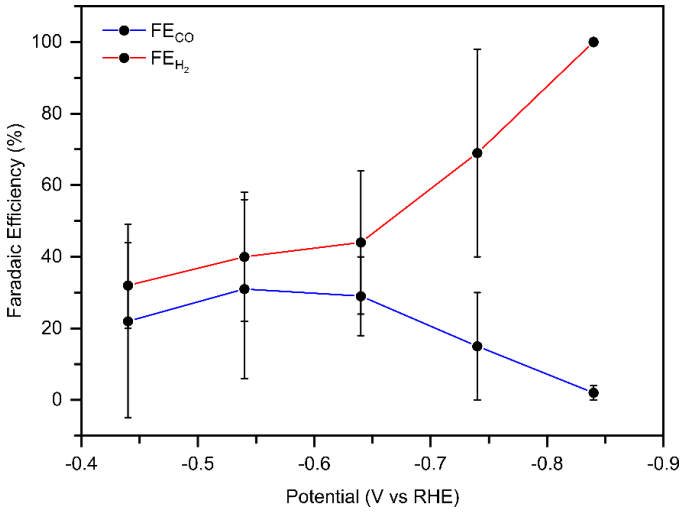


Figure 5.43. Faradaic efficiencies at varying potentials from rinse test CPE experiments with $[Fe1]^{2+}$. Conditions: 1 mM $[Fe1]^{2+}$; 0.10 M $NaHCO_3$.

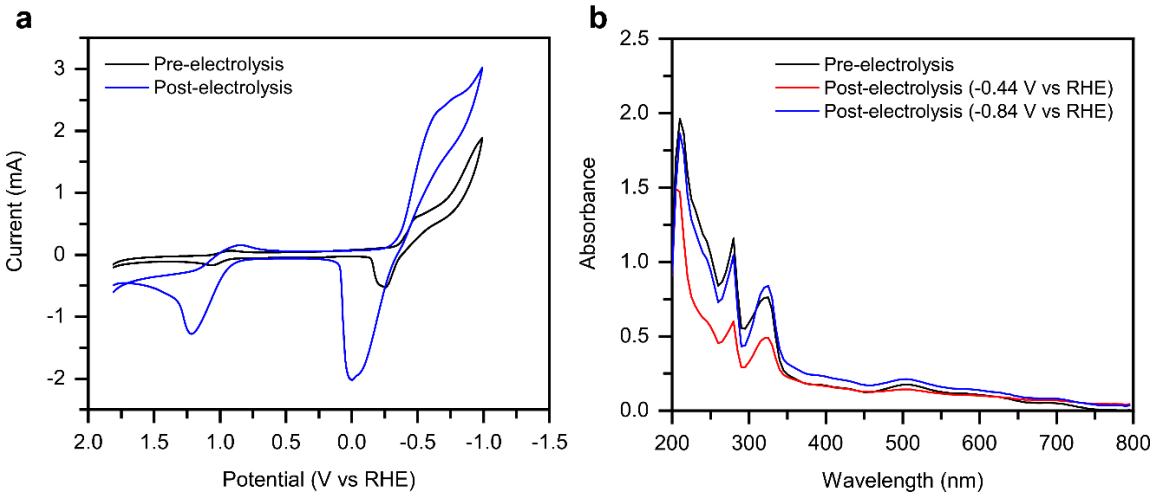


Figure 5.44. Control experiments to investigate the stability of $[Fe1]^{2+}$ under aqueous electrolysis conditions. (a) CVs collected before and after CPE experiments. (b) Analysis of the electrolyte solution before (black) and after CPE experiments at onset potentials of –0.44 V (red) and –0.84 V (blue) vs RHE.

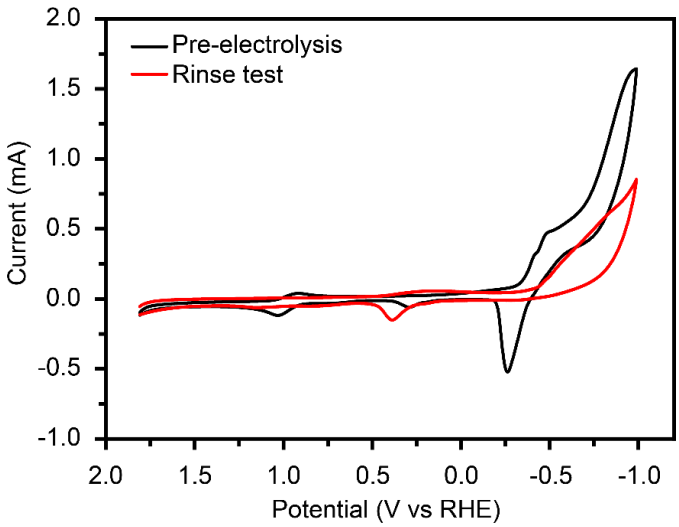


Figure 5.45. Rinse test of [Fe(tpyPY2Me)][NO_3]$_2$. Black = pre-electrolysis scans; Red = rinse test scans. Conditions: 1 mM $[Fe1]^{2+}$; 0.10 M $NaHCO_3$.

5.4 Conclusion

In summary, inspired by the beneficial feature of electronic delocalization exhibited by biological and heterogeneous systems for electrochemical CO_2RR catalysis to minimize overpotentials and favor CO_2RR over competing HER pathways, even in aqueous media, we report a molecular system that captures this design concept. A new ligand framework that incorporates a redox-active terpyridine moiety into a modular polypyridyl scaffold can achieve highly selective and efficient iron-catalyzed electrochemical CO_2 reduction to CO in both organic and aqueous solutions with high specificity over competing hydrogen evolution pathways. Importantly, the combination of both an open-shell metal ion using an earth-abundant, first-row transition metal in conjunction with a redox non-innocent ligand enables metal-cooperativity through strong exchange coupling that shifts electrochemical reduction potentials to promote CO_2RR catalysis. Specifically, the Fe(II)-tpyPYMe2 analog exhibits a 640 mV positive shift in the 2-electron reduction potential relative to the isostructural analog bearing a redox-silent Zn(II) center, poising it for multielectron electrocatalysis with minimized overpotentials. Control experiments with Fe(II) and Zn(II) complexes bearing a related pentapyridine ligand lacking the redox-active terpyridine fragment and the same redox non-innocent ligand but with a redox-silent Zn(II) center show that CO_2RR relies on synergistic coupling between both metal and ligand components.

The combination of distorted coordination geometry, low-lying π* orbitals, and moderate ligand field engendered by the rigid, redox non-innocent tpyPY2Me ligand promotes strong metal–ligand cooperativity with the iron(II) center. $[Fe1]^{2+}$ is shown to catalyze CO_2 reduction at extremely mild redox potentials (η = 190 mV; – 1.46 V vs Fc/Fc^+) relative to the control polypyridyl complexes presented in this study. The positive redox potentials at which CO_2RR catalysis occurs is interpreted through extensive experimental spectroscopic (NMR, Mössbauer, and XAS), XRD, and electrochemical studies, along with electronic structure calculations, which collectively point to a model in which the two-electron reduced iron complex, $[Fe1]^0$, possesses an open-shell singlet ground state electronic structure ($[Fe(tpyPY2Me^{\bullet\bullet})^{2-}]^0$) resulting from a strong intramolecular antiferromagnetic coupling between a triplet reduced ligand (tpyPY2Me tpyPY2Me$^{\bullet\bullet 2-}$; $S_{tpyPY2Me} = 1$) and an intermediate-spin Fe(II) center ($S_{Fe} = 1$). We propose that the multielectron chemistry of $[Fe1]^{2+}$ at relatively positive potentials is facilitated through this electronic structure, which in turn promotes its exceptional selectivity (FE_{CO} > 90%) through suppression of HER pathways. Furthermore, variable potential CPE experiments with direct product detection show that $[Fe1]^{2+}$ operates at fast rates in both organic (TOF > 100 000 s^{-1}) and aqueous electrolytes (TOF > 50 000 s^{-1}) with robust long-term stability and recyclability.

The ability to create molecular compounds with strong exchange coupling between synergistic, redox non-innocent ligands and metal centers has broad implications for catalyst design, including enabling control over the density and arrangement of functional active sites. Indeed, redox balancing through electronic delocalization is pivotal for biological and materials catalysts to achieve complex chemical transformations at or near thermodynamic potentials. However, discrete molecular compounds offer a level of tunability via coordination chemistry that remains unparalleled in protein design and nanostructure engineering. Thus, inorganic molecules are uniquely positioned to open access to a range of new properties and offer a desirable alternative strategy for lowering energy barriers for redox catalysis. The observed 640 mV electrochemical potential shift and associated turn-on of CO_2RR catalysis upon substituting Zn(II) for Fe(II) for

the same redox non-innocent ligand emphasizes metal–ligand cooperativity for redox balancing that goes beyond redox activity dominated at either ligand or metal sites alone.

5.5 Materials and Methods

5.5.1 General Methods

All manipulations were conducted under air and moisture free conditions using a MBraun LABstar pro glove-box and standard Schlenk line techniques unless otherwise noted. 2,2'-(ethane-1,1-diyl)dipyridine, 2,6-bis(1,1-di(pyridine-2-yl)ethyl)pyridine ($PY5Me_2$) and $[Fe(PY5Me_2)][CF_3SO_3)]_2$ were synthesized as previously described.[50,81] All other reagents were purchased from commercial vendors and used without further purification. Carbon dioxide (99.99%), carbon monoxide (99.5%), hydrogen (99.999%), ethane (99.0%), argon (99.999%) and nitrogen (99.998%) were purchased from Praxair. 6-bromo-2,2'-bipyridine was purchased from Santa Cruz Biotechnology. Tetrakis(triphenylphosphine)palladium $[Pd(Ph_3)_4]$, hexamethylditin $[(CH_3)_6Sn_2]$, iron(II) trifluoromethanesulfonate $[Fe(OTf)_2]$, iron(II) chloride ($FeCl_2$) (anhydrous), and iron(III) nitrate nonahydrate $[Fe(NO_3)_3•9H_2O]$ were purchased from Strem Chemicals. 2-ethylpyridine, 2-fluoropyridine, 2,6-dibromopyridine, n-butyllithium (2.5 M, hexanes), lithium chloride, sodium bicarbonate, and 1,2-dimethoxyethane (DME) (anhydrous) were purchased from Sigma Aldrich. Acetonitrile (CH_3CN) and tetrahydrofuran (THF) were dried using a JC Meyer solvent purification system and stored over 3 Å molecular sieves under a nitrogen atmosphere. Deionized water was obtained from a Millipore Autopure system. UV-visible (UV-vis) spectra were collected using an Agilent Cary 60 spectrophotometer at room temperature (RT). NMR spectra were recorded on a Bruker spectrometer operating at either 300, 400, or 500 MHz. Chemical shifts for ^1H spectra were reported in ppm relative to residual protonated solvent. Coupling constants were reported in Hz. X-ray crystallography was performed in the Chexray facility at the University of California, Berkeley. Elemental analyses were conducted at the Microanalytical Laboratory of the University of California, Berkeley and Midwest Microlab (Indianapolis, IN).

5.5.2 Cyclic Voltammetry

Cyclic voltammetry experiments were performed using either a CH Instruments, Inc. 600E potentiostat or a Bioanalytical Systems, Inc. (BASi) Epsilon potentiostat.

Non-aqueous voltammetry studies were conducted in a three-electrode cell equipped with a glassy carbon disk (3.0 mm diameter) working electrode (BASi), a platinum wire counter electrode, and a silver wire in a porous Vycor tipped glass tube filled with electrolyte as a pseudo-reference electrode. The working electrode was polished prior to each experiment with 0.05-micron alumina powder on a felt pad. The electrolyte was 0.1 M tetrabutylammonium hexafluorophosphate ($TBAPF_6$) in CH_3CN freshly prepared with anhydrous solvent and saturated with either CO_2 or Ar at 1 atm. At the conclusion of each experiment, the pseudo-reference potentials were referenced against ferrocene/ferrocenium (Fc/Fc^+) used as an external standard. The scan rates for all cyclic voltammograms were 100 mV/s unless otherwise noted. All voltammograms were obtained with iR compensation.

Aqueous voltammetry studies were performed with a three electrode-cell equipped with a carbon paste working electrode (commercially available from BASi; the electrode body (part # MF-2010); the carbon paste slurry (part # CF-1010)) working electrode, a platinum wire counter

electrode and an Ag/AgCl reference electrode. The working electrode was polished between every scan with a 0.05 micron alumina powder on a felt pad. The electrolyte used was 0.1 M aqueous sodium bicarbonate ($NaHCO_3$) saturated with either CO_2 or Ar at 1 atm. No iR compensation was applied. The Ag/AgCl (saturated KCl) reference electrode was externally calibrated to potassium ferricyanide in 0.5 M aqueous potassium bicarbonate ($KHCO_3$) saturated with CO_2 at pH 7.3. Potentials were converted to the reversible hydrogen electrode (RHE) scale by E (V vs RHE) = E (V vs Ag/AgCl) + 0.210 V + 0.0591×pH.

5.5.3 Controlled Potential Electrolysis

Controlled potential electrolyses were conducted using either a CH Instruments, Inc. 600E potentiostat or a Bioanalytical Systems, Inc. (BASi) Epsilon potentiostat.

Non-aqueous preparative scale controlled potential electrolysis experiments were performed in a miniaturized version of our previously described homemade gastight PEEK electrolysis cell with a working compartment (7 mL liquid volume) and counter compartment (3 mL liquid volume) separated by an ultrafine glass frit (**Figure 5.46**).[47] A 1 cm^2 glassy carbon plate (Toki Carbon; Kanagawa, Japan) was used as the working electrode, a 2.5 cm diameter graphite planchet (Ted Pella; Redding, CA) was used as the auxiliary electrode, and an Ag wire in a Vycor tipped glass tube filled with electrolyte ($TBAPF_6/CH_3CN$) was used as a pseudo-reference electrode. The working compartment was filled with 7 mL of a 1 mM solution of catalyst dissolved in 0.1 M $TBAPF_6/CH_3CN$ containing up to 3.5 M phenol as a proton source. The counter electrode chamber was filled with 3 mL of a 20 mM solution of tetrabutylammonium acetate dissolved in 0.1 M $TBAPF_6/CH_3CN$. This soluble source of acetate was sacrificially oxidized to generate CO_2 and ethane, thereby preventing GC detection of solvent oxidation byproducts. Both compartments were sealed to be gastight. The working compartment was sparged with CO_2 for 10 min, then sealed and injected with 0.50 mL of ethane as a gaseous internal standard. A CV scan was collected prior to the CPE measurement to calibrate the potential. The electrolyte solution was constantly stirred during the CPE experiment with a 1 cm stirbar. At the conclusion of the experiment, the headspace was injected directly into an SRI-GC (model #8610C) equipped with 6' Hayesep D and 13X molecular sieve chromatographic columns. Two in-line detectors were used: a TCD for H_2 detection and an FID with a methanizer for $CO/CO_2/C_2H_6$ detection. Analytes of interest were quantified by comparing a ratios of analyte/internal stand peak integrals to a calibration curve with known amounts of analyte (**Figures 5.47** and **5.48**).

Aqueous preparative scale electrolysis studies were conducted in a miniaturized version of a previously reported custom-made three-piece glass electrochemical cell composed of a working compartment body (20 mL liquid volume), working compartment lid, and a counter compartment body (10 mL liquid volume) (**Figure 5.46**).[47] The working and counter electrode compartments were separated by a cation exchange membrane (Nafion 117). A 1 cm^2 glassy carbon plate (Toki Carbon; Kanagawa, Japan) was used as the working electrode, a 3.0 mm diameter vitreous carbon rod (Goodfellow; Cambridge, UK) was used as the auxiliary electrode with an Ag/AgCl (sat. KCl) reference electrode. 0.1 M aq. $NaHCO_3$ was prepared and utilized as the electrolyte and sparged with CO_2 for 10 min at 1 atm before electrolysis. 0.50 mL ethane was injected as an internal standard prior to the start of the electrolysis. A CV scan was collected prior to the CPE measurement to calibrate the potential. No iR compensation was applied. The electrolysis

experiments were then conducted at constant potential for the specified amount of time. After this period, the headspace of the cell was immediately analyzed by GC, and the amount of gas generated was determined from the standard calibration curves obtained by injecting known amounts of CO, H_2, and ethane into the GC (Figures 5.26 and 5.27). Gas production was measured on an SRI gas chromatography instrument (model #8610C) equipped with a Haysep D column (1/8" x 6') and a 13X Mol Sieve column (1/8" x 6'). Ethane was used as an internal standard. No liquid products were detected by ^{1}H NMR.

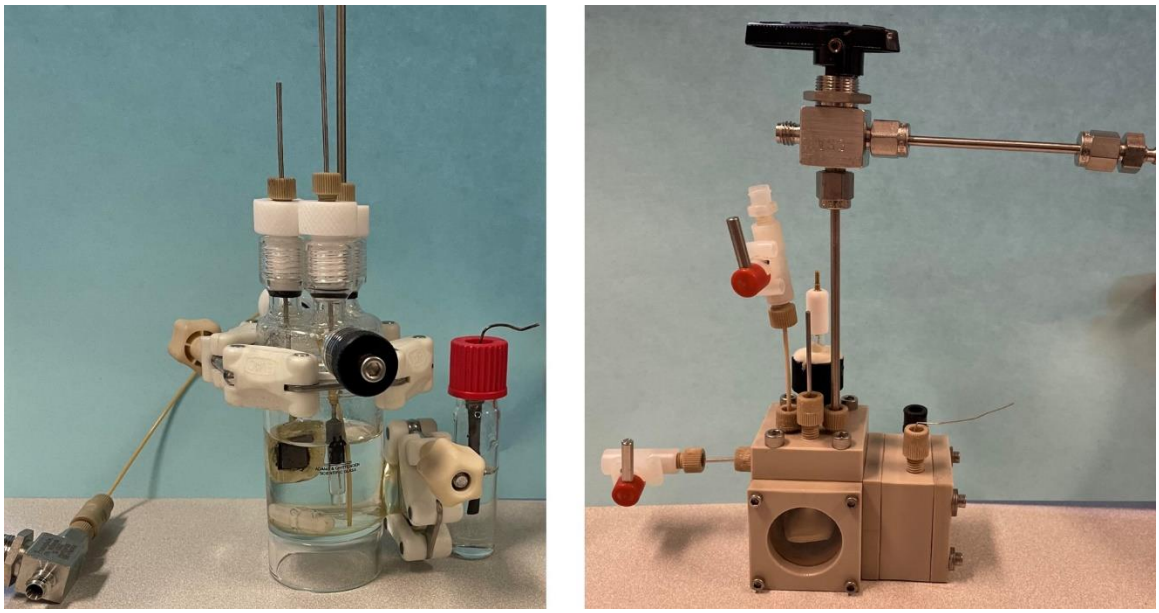


Figure 5.46. Miniaturized version of our previously described homemade gastight electrolysis cells for aqueous (left) and organic (right) electrolysis experiments.[47]

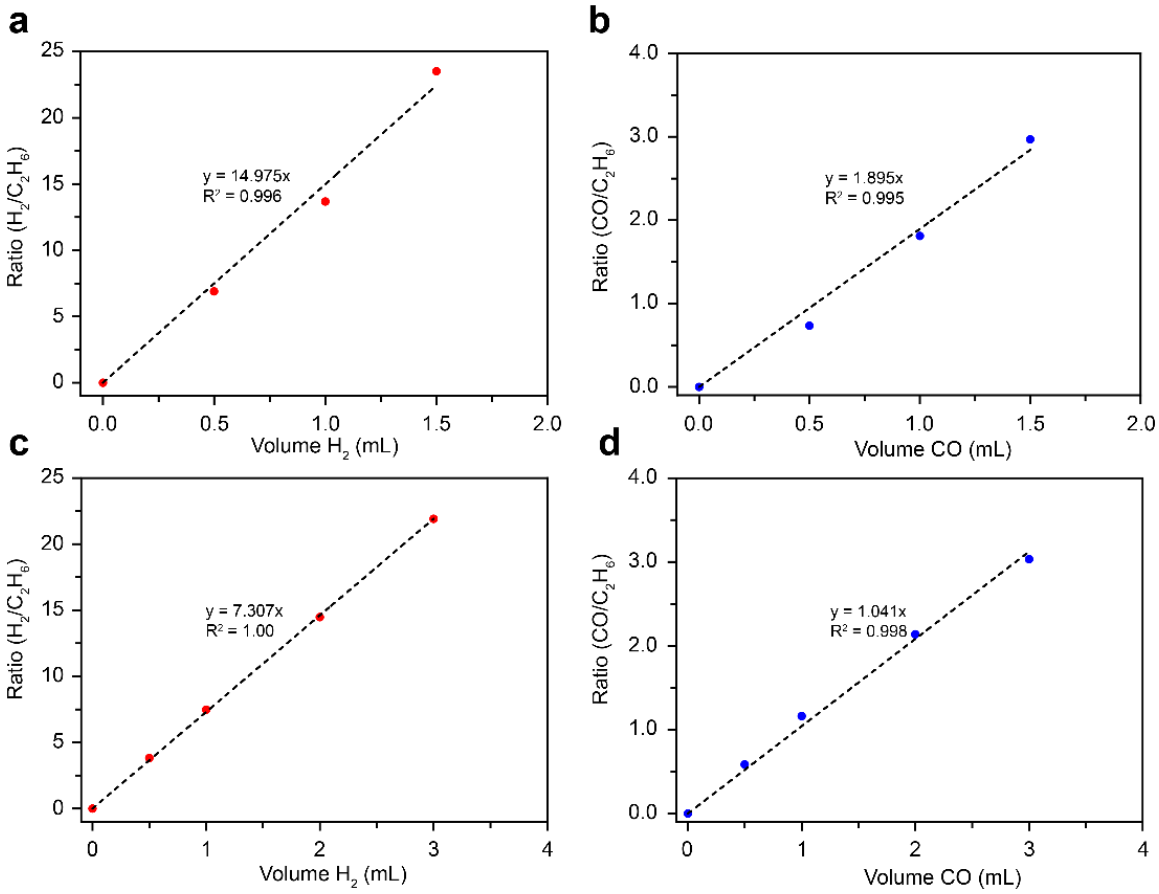


Figure 5.47. GC calibration curves. (a) H_2 and (b) CO calibration curve for CPE experiments conducted in $TBAPF_6/CH_3CN$. (c) H_2 and (d) CO calibration curves for CPE experiments conducted in 0.10 M $NaHCO_3$ aq.

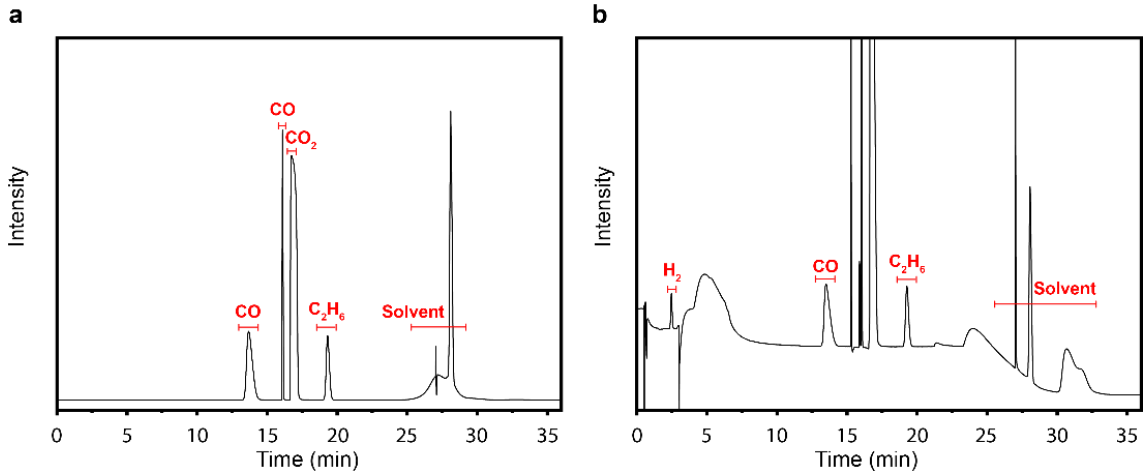


Figure 5.48. Representative gas chromatograms for detection and quantification of (a) CO from the flame ionization detection (FID) channel and (b) H_2 from the thermal conductivity detection (TCD) channel.

5.5.4 Determination of Overpotential (η)

Conversion of applied potentials into overpotentials (η) were performed following the methods reported by Mayer et al.[55] and Matsubara and coworkers.[56,57] Briefly, the standard redox potential for the conversion of CO_2 into CO in CH_3CN in the presence of acid, AH, ($E^0_{CO_2/CO,CH_3CN,AH}$), is described by **Equation 5.1**:

$$E^0_{CO_2/CO,CH_3CN,AH}(vs\ SHE) = -\frac{1}{2F}(\Delta_f G^0(CO_{(g)}) + \Delta_f G^0(H_2O_{(l)}) + \Delta_{tr}^{1\rightarrow sol} G^0(H_2O) - \Delta_f G^0(CO_{2(g)}) + 2RT(\ln 10) pK^{H_2O}_{a,abs}(CO_{2(g)} + H_2O_{(sol,x)})) \quad \textbf{Equation 5.1}$$

Where F is Faradays constant and $\Delta_f G^0(CO_{(g)})$, $\Delta_f G^0(CO_{2(g)})$, and $\Delta_f G^0(H_2O_{(l)})$ are the standard formation Gibbs energy changes of CO and CO_2 in the gas phase, and pure liquid H_2O, respectively. At standard pressure (1 bar) and temperature (298.15 K) these values are reported as –137.163, –394.389, and –237.178 kJ/mol.[57] The term $\Delta_{tr}^{1\rightarrow sol} G^0(H_2O)$ is the standard Gibbs energy change upon transfer of water from pure liquid to an acetonitrile-water mixture, for which both standard states are taken as unit mole fractions of water. R is the gas constant, and T the temperature. $pK^{H_2O}_{a,abs}(CO_{2(g)} + H_2O_{(sol,x)})$ is the absolute acidity constant for acetonitrile-water mixtures which can be measured and have been tabulated by Matsubara.[57]

In order to accurately obtain the standard redox potential for CO_2, the strongest acid in solution has to be considered. While dry acetonitrile was used to prepare the electrolyte solution, the phenol and $TBAPF_6$ were not thoroughly dried prior to each use and were stored on the benchtop, thus preventing complete removal of water in our system. Therefore, CO_2 in the presence of water, forming carbonic acid, represents the strongest acid present under our experimental conditions. Because $pK^{H_2O}_{a,abs}(CO_{2(g)} + H_2O_{(sol,x)})$ varies significantly as a function of water concentration in acetonitrile mixtures, standard redox potentials can fluctuate by ~500

mV across the water-acetonitrile mixtures examined by Matsubara (i.e., –1.57 V vs Fc/Fc^+ for 0.5 M water; –0.95 V vs Fc/Fc^+ for 55 M water). As a conservative estimate, we selected the midpoint value of –1.27 V vs Fc/Fc^+. Conditions of high water concentration do not apply for our experimental conditions, and low water concentrations assuming less than 0.5 M water leads to an estimated CO_2 standard redox potential that is more negative than where our catalyst operates for CO_2 reduction, which would then result in negative overpotential values. We note that this –1.27 V vs Fc/Fc^+ value is 70 mV more positive than the previously estimated standard redox potentials by Savéant and coworkers.[12,13]

5.5.5 Determination of Faradaic Efficiency (FE)

Controlled potential electrolysis experiments were conducted in gas-tight electrochemical cells at varying applied potentials for 1 – 5 h. At the conclusion of the CPE experiment, samples from the headspace of the electrochemical cell were injected into a gas chromatograph for analysis. Calibration curves (**Figure 5.47**) were constructed using known amounts of H_2 and CO and C_2H_6 (0.50 mL) as internal standards to quantify the volume of gaseous products from the respective chromatograms (**Figure 5.48**). The amounts (mols) of gas produced were calculated from the volume of gas using the Ideal Gas Law and Faradaic efficiencies were then determined using **Equation 5.2**:

$$FE(\%) = \frac{Q_{expt}}{Q_{Theory}} x100 = \frac{znF}{Q} x100 \qquad \textbf{Equation 5.2}$$

where *z* is the number of electrons, *n* is the mols of analyte produced, *F* is Faradays constant and *Q* is the specific charge passed during the CPE experiment.

5.5.6 Determination of k_{obs} and Turn Over Frequency (TOF)

In order to estimate k_{obs} (= TOF_{max}) under the experimental conditions reported, Foot-of-the-Wave analysis (FOWA) was applied to cyclic voltammetry as reported by Savéant and coworkers.[66] At the beginning of each experiment, a cyclic voltammogram was measured with catalyst alone under inert atmosphere in the absence of phenol as a proton source from which E_{redox} could be obtained. The peak height of the catalytically relevant wave, the formal L/L^{2-} redox couple, was determined by subtracting the current right before the reduction wave from the peak current. Given that a simultaneous 2 e^- reduction of $[Fe1]^{2+}$ is required in order for catalysis to occur, CO_2 reduction with $[Fe1]^{2+}$ may be best described as an EECC process and thus the following relationship may be derived (**Equation 5.3**):[65]

$$\frac{i}{i_p} = \frac{2.24\sqrt{\frac{RT}{nF\nu}}\sqrt{n' k_{obs}}}{1+e^{\left[\frac{nF}{RT}(E-E_{redox})\right]}} \qquad \textbf{Equation 5.3}$$

where *i* is the current, i_p is the peak current in the absence of substrate, *E* is the potential, ν is the scan rate (V/s), k_{obs} is the observed rate constant, *F* is Faradays constant, *R* is the ideal gas constant, *T* is the temperature (K), *n* is the number of electrons transferred to the catalyst from the electrode (n = 2), and *n'* is the number of catalyst equivalents used per turnover (n' = 1). k_{obs} (TOF_{max}) can

thus be determined by plotting $\frac{i}{i_p}$ vs $\frac{1}{1+e^{\left[\frac{nF}{RT}(E-E_{redox})\right]}}$ yielding a line with a slope of $2.24\sqrt{\frac{RT}{nfv}}\sqrt{n'k_{obs}}$.

Due to the small linear FOW region, multi-segmented catalytic wave, and the inherent assumptions associated with FOWA (**Figure 5.27**), kinetic information was also extracted directly from the controlled potential electrolysis data at varying applied onset potentials utilizing methods developed by Savéant and coworkers.[66] k_{obs} was determined from the CPE experiment using **Equation 5.4**:

$$\frac{I}{F} = \sqrt{2kC_A^0 D_p}\,\frac{C_p}{1+exp\left[\frac{F}{RT}(E-E^0_{redox})\right]} \qquad \textbf{Equation 5.4}$$

Where I is the average CO specific current density (A/cm^2) calculated based on the geometric surface area of the working electrode (1 cm^2); The average was taken across the three 1 h CPE experiments, F is Faradays constant, E is the applied potential, E^0_{redox}, is the redox potential in the absence of substrate, R is the ideal gas constant, T is the temperature (K), C_A^0 is the concentration of CO_2 (2.80 x 10^{-4} mol/cm^3), D_p is the diffusion coefficient of [Fe1]$^{2+}$ (4.57 x 10^{-6} cm^2/s), and C_p is the concentration of catalyst (1.10 x 10^{-6} mol/cm^3). The diffusion coefficient of the reduced iron complex was extracted from the scan rate dependent CV experiments under Ar atmosphere (**Figure 5.22**) and calculated using the Randles-Sevcik equation (**Equation 5.5**).

$$i_p = 0.4463nFAC\left(\frac{nFvD}{RT}\right)^{1/2} \qquad \textbf{Equation 5.5}$$

Where i_p is the peak current maximum, n is the number of electrons transferred in the redox event, A is the electrode area (cm^2), F is Faradays constant (C/mol), D is the diffusion coefficient (mol/cm^3), C is the concentration (mol/cm^3) and n is the scan rate (V/s).

Catalytic Tafel plots were generated from the kinetic data obtained from the variable potential CPE experiments using **Equation 5.6**:

$$TOF = \frac{2k_{obs}}{1+e^{\left[\frac{F}{RT}(E-E^0_{redox})\right]}} \qquad \textbf{Equation 5.6}$$

5.5.7 Mössbauer Spectroscopy

Zero-field, ^{57}Fe Mössbauer spectra were recorded in a constant acceleration spectrometer (SEE Co., Minneapolis, MN) between 295 K and 5 K in a Janis Research Co. cryostat (Willmington, MA) utilizing a ^{57}Co radioactive source embedded in a Rh matrix. Isomer shifts were reported relative to α-iron (30 μm foil) at 295 K. Samples were prepared by loading a finely ground crystalline sample of iron complexes in a nylon washer wrapped in Kapton tape under an inert atmosphere prior to introducing into the spectrometer in air. Once the samples were loaded into the spectrometer, vacuum was immediately pulled in order to limit air exposure.

5.5.8 X-Ray Absorption Spectroscopy (XAS)

Fe K-edge X-ray absorption data were collected using beamline 9-3 at the Stanford Sychrotron Radiation Laboratory (SSRL) operating with standard ring conditions of 3.0 GeV energy and 500 mA current. A Si (220) double crystal monochromator detuned to 10% of flux maximum at Fe K-edge was used to minimize the higher harmonics. A harmonic rejection mirror was used to further reduce the contamination of higher harmonics. The intensities of incident and transmitted X-rays were monitored with N_2-filled ion chambers before the sample (I0) and after the sample (I1 and I2), respectively. The slit in front of the I0 detector was closed to a vertical size of 1 mm and a horizontal size of 6.5 mm. A 10 mM solution of $[Fe1]^{2+}$ and 1 mM solution of $[Fe1]^{0}$ in CH_3CN was loaded in 40 µL plexiglass sample holders having Mylar tape window on one side, and frozen immediately in liquid nitrogen. XAS data of samples were collected as fluorescence excitation spectra using a 100-element Ge solid-state detector (Canberra). The monochromator energy was calibrated with the pre-edge peak of Fe foil (7112 eV). Fe foil calibration standard was placed between the N_2-filled ion chambers (I1 and I2) after the sample and its Fe spectra were simultaneously recorded along with samples for internal energy calibration. To minimize the X-ray damage, data was collected at 10 K using a liquid He flow cryostat (Oxford Instruments). The XAS scans of samples were closely monitored for any X-ray induced damage during the course of measurements.

Data reduction of XAS spectra was performed using SamView (SixPack software, available at (http://www.sams-xrays.com/sixpack). Athena program of Demeter software package (Demeter version 0.9.26, B.Ravel) was used to align/merge XAS data and subtract the pre-edge and post-edge backgrounds. The spectra were then normalized to the edge jump.

5.5.9 X-Ray Crystallography

Crystals were coated with Paratone-N oil, attached to a Kapton loop, and mounted onto a Rigaku XtaLAB P200 equipped with a MicroMax 007HF rotating anode and Pilatus3 R 200K-A hybrid pixel array detector. Data were collected using Mo Kα radiation (λ = 0.71073 Å). Crystals were kept at 100(2) K throughout the collection. Data collection was performed with CrysAlisPro.[82] Data processing was done with CrysAlisPro and included a multi-scan absorption correction applied using the SCALE3 ABSPACK scaling algorithm within CrysAlisPro.

5.5.10 Quantum Chemical Calculations

The magnetic coupling was estimated with the Heisenberg-Dirac-van Vleck Hamiltonian (**Equation 5.7**):[83]

$$\widehat{H}(HDvV) = -J_{ab}S_a \cdot S_b \qquad \textbf{Equation 5.7}$$

And the magnetic coupling constant, J_{ab}, is obtained with broken symmetry (BS) DFT using wB97X-D/def2-TZVPP (**Equation 5.8**):[84]

$$J_{ab} = \frac{^{LS}E - ^{HS}E}{^{HS}\langle S^2\rangle - ^{LS}\langle S^2\rangle} \qquad \textbf{Equation 5.8}$$

For $[Fe1]^0$: J_{ab} = −1023 cm^{-1} (using $^{LS}E - {}^{HS}E$ = −4400 cm^{-1}, $^{HS}\langle S^2\rangle$ = 6.06 and $^{LS}\langle S^2\rangle$ = 1.76).

Reduction potentials are reported against the Ferrocene/Ferrocenium (Fc/Fc^+) couple used as an internal standard.[85,86] This method allows accurate predictions due to systematic error cancelation in both theory and experiment with an accuracy of ~100 mV with a hybrid DFT functional and modest basis set.[86] The predicted reduction potentials are summarized in **Tables 5.5** and **5.6**.

Adiabatic spin gaps for the low-spin (LS) and intermediate-spin (IS) states are referenced against the high-spin (HS) state and correspond to the difference in free energy ($\Delta G_{IS/LS} = G_{IS/LS} - G_{HS}$). The spin gaps for $[Fe1]^{n+}$ (n = 2,1, 0) are shown in **Tables 5.7** and **5.8**. The $[Fe1]^+$ sextet (S = 5/2) is best described as a high-spin Fe(II) (S_{Fe} = 2) and a one-electron reduced tpyPY2Me ligand (S_{tpy} = 1/2). The quartet (S = 3/2) has the same configuration but an antiferromagnetic ordering of the two spin centers (*i.e.*, S_{Fe} = 2; S_{tpy} = 1/2 total S = 3/2) while the doublet (S = 1/2) is best described as a low-spin Fe(II) (S_{Fe} = 0) and a reduced tpyPY2Me (S_{tpy} = 1/2). The $[Fe1]^0$ quintet (S = 2) is best described as an intermediate-spin Fe(II) (S_{Fe}=1) and a doubly reduced tpyPY2Me ligand (S_{tpy} = 1). The triplet and singlet configuration couple one or both spins antiferromagnetically (BS solution), respectively. Alternatively, the $[Fe1]^0$ singlet (S = 0) can have an Fe(II) low-spin center (S_{Fe} = 0) and a doubly-reduced ligand singlet (S_{tpy} = 0) (RKS solution). The adiabatic spin gap between the broken symmetry singlet configuration of $[Fe1]^0$ and the RKS solution is −9.1 kcal/mol with the BS solution lower in energy.

The localized orbital bonding analysis[87] was applied to both **[**$[Fe1]^+$ and $[Fe1]^0$ and in both cases the oxidation state was determined to be iron(II) and the localized metal orbitals had a very high metal d-orbital character (>90%). The three localized metal orbitals from the analysis as well as the canonical α HOMO (tpyPY2Me π*) of $[Fe1]^+$ are depicted in **Figure 5.33c** and **Figure 5.49** (isovalue: 0.03 a.u.).

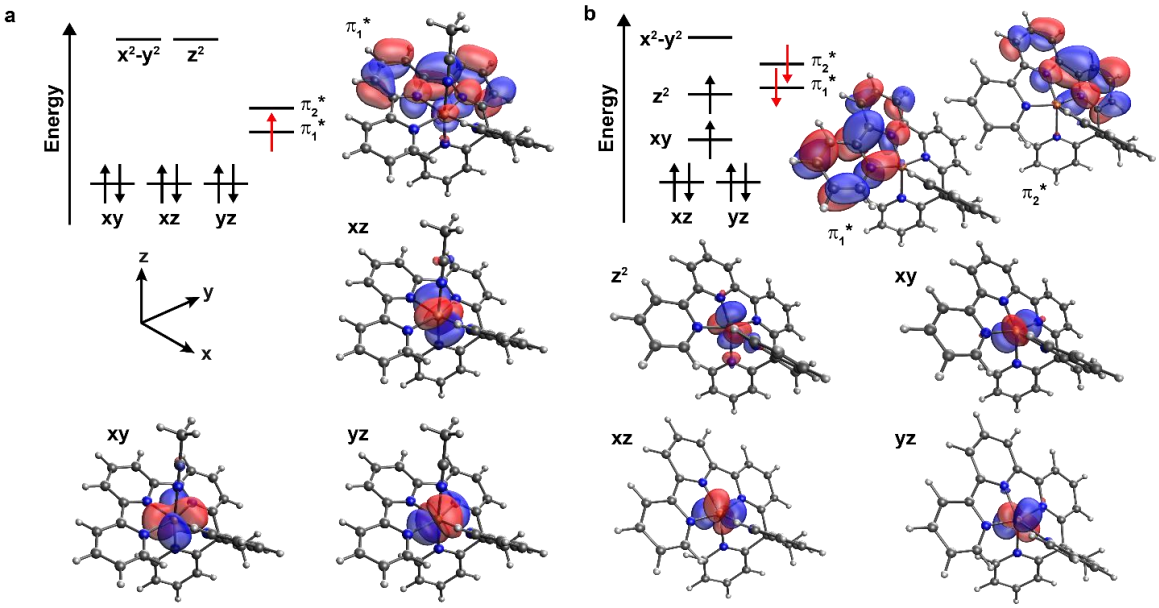


Figure S49. Simplified MO diagrams including localized metal d orbitals for the (a) one electron reduction intermediate, $[Fe1]^{+}$ and (b) the two electron reduced active catalyst, $[Fe1]^{0}$.

The multiconfigurational wave-function method CAS(4,4) was applied to the $[Fe1]^{0}$ singlet state, in order to probe the orbital entanglement of the two metal d-orbitals and the two π* ligand orbitals of the doubly-reduced tpyPY2Me ligand. The natural orbitals including their occupation number (NOON) are depicted in **Figure 5.34**. The deviation from integers (0, 1, or 2) confirms a significant amount of static correlation and an antiferromagnetic ordering. Each d-orbital (distorted d_{z^2} and d_{xy}) interacts with one of the ligand orbitals in π-type interaction whereas both bonding (1.35) and anti-bonding (0.65) orbitals have significant population. The localized active space orbitals are depicted in **Figure 5.33e** (as well as the localized inactive doubly occupied metal orbitals with an isovalue of 0.03 a.u.).

5.5.11 Computational Details

Density functional theory calculations for magnetic coupling, spin gaps, redox potential and the localized orbital bonding analysis were performed with the Q-Chem package[88] (version 5.0.2) using the ωB97X-D[89] functional. Geometries were optimized in the gas phase with no constraints. The structures were verified as minimum with the vibrational frequencies. The geometry optimization and frequency calculations were performed with ωB97X-D and a mixed basis (def2-SVP basis for all main group elements, def2-TZVP basis set for Fe).[90] The electronic structure was refined with the def2-TZVPP basis[90] single point calculations. The solvation energies were calculated using the C-PCM model (acetonitrile, ε = 37.5) as implemented in Q-Chem.[91] The numerical integration of the XC functional was on a (75, 302) grid (75 radial shells with 302 Lebedev points). Orbitals were plotted with an isovalue of 0.03 a.u. and spin densities with an isovalue of 0.005 a.u.

Additional calculation was performed with ωB97M-V, ωB97X-V,[92] B3LYP,[93–95] PBE0,[96] PW6B95,[97] MN15,[98] PWB6K[97] (ordered by increasing amount of (short range) exact exchange

ranking from 15–48%) to gauge functional dependence. The functionals were selected because they performed well on an extensive benchmark[99] or a benchmark specifically for Fe systems.[100,101]

To probe the static correlation of $[Fe1]^0$ we employed CASSCF. These calculations were performed with Orca (version 4.0.0.2)[102] and the def2-TZVPP basis. For larger active spaces (>12) we employed the ICE-CI algorithm (*tgen* = $1e^{-3}$; *tvar* = $1e^{-6}$). For the initial CASSCF calculation an active space of 16 electrons in 16 orbitals (CAS(16,16)) was selected for the singlet state. The active space consisted of 5 metal 3d orbitals and 5 occupied and 6 unoccupied π orbitals of the tpyPY2Me ligand using the ICE-CI algorithm. The quasi restricted orbitals of a B97-D high-spin (quintet) were used as guess orbitals. However, the same solution was obtained using the RKS singlet as starting orbitals. A subsequent CAS(12,12) calculation without ICE-CI and by removing weakly correlated orbitals pairs confirmed that only 4 electrons in 4 orbitals exhibit strong static correlation.

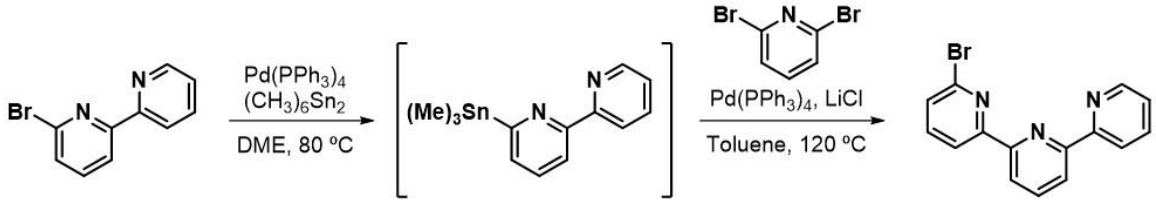
Gibbs free energies (*G*) were used to compute reduction potentials and adiabatic spin gaps and are based on standard thermodynamic cycles.[86,103,104] The Gibbs free energies include enthalpic contributions from the zero-point energy correction and the entropic contribution is calculated from the vibrational frequencies at T = 298 K. Solvation energies were approximated by performing single point calculations applying the implicit C-PCM solvent model.

The correct prediction of adiabatic spin gaps ($\Delta_{LS/HS}G = G(LS) - G(HS)$) in first row transition metal complexes is very sensitive to the choice of DFT functional. The amount of Hartree-Fock (HF) exchange plays a crucial role because it is found that spin gaps depend linearly on the amount of HF exchange incorporated in the functional. An increasing amount of HF exchange stabilizes the high-spin state.[100,105]

In order to predict isomer-shifts for ^{57}Fe Mössbauer spectroscopy, we employed the theoretical framework established through extensive analysis by previous studies using similar Fe complexes.[54,106] The calculation was performed using Orca (version 4.0.0.2).[102] Geometries were optimized with B3LYP functional[93–95] including D3 correction[107] the de2-TZVP basis for all elements, the CPCM model for solvation as implemented in Orca[108] (ε = 7.25) and the resolution of the identity (RI) approximation (RIJCOSX) and corresponding RI basis set.[109] The numerical integration of the XC functional during the SCF iteration had 302 Lebedev points for the angular grid and a radial grid of 4.67 (IntAcc) (Grid4); a larger grid was used for the final energy evaluation (Lebedev points 434 and a radial grid of 5.01 (Grid5)). Single point calculation at the optimized geometries were performed with a slightly different set-up to predict the Mössbauer spectral parameters. We employed the B3LYP functional[93–95], a mixed basis using def2-TZVP for all main group elements and the larger CP(PPP) basis[110] for Fe and the CPCM model[108] (ε = 7.25). The XC integration grid had 770 Lebedev points and IntAcc of 5.67 for all main group elements (Grid7) and 7.0 for Fe.

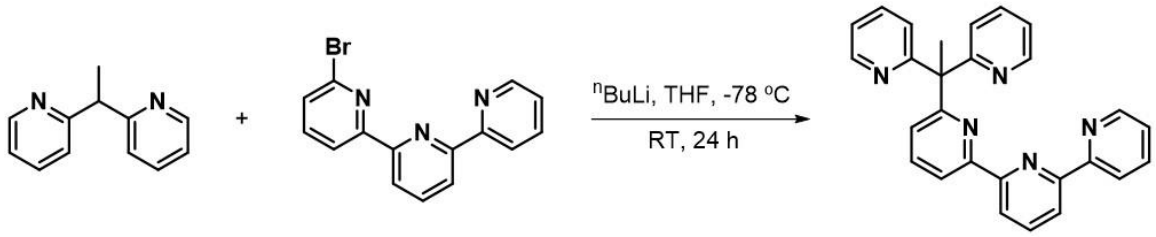
The key findings of the DFT studies are robust in terms of functional choice. All hybrids functionals predict the broken-symmetry solution of $[Fe1]^0$ to be the ground state and predict a small gap between both reduction events (see **Table 5.7**). Furthermore, a small singlet-quintet gap for $[Fe1]^{2+}$ and a significant singlet (BS)-quintet gap for $[Fe1]^0$ is predicted by most functionals (see **Table 5.8**).

5.5.12 Synthesis of 6-Bromo-2,2':6',2"-terpyridine



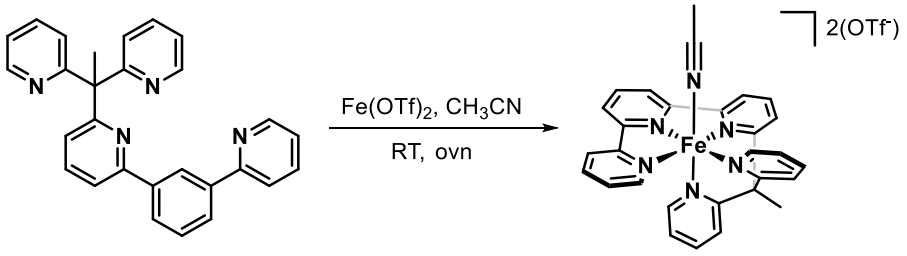
6-Bromo-2,2':6'2"-terpyridine was synthesized by making slight modifications to previous literature reports.[110,111] 6-Bromo-2,2'-bipyridine (3.58 g, 15.26 mmol) and $Pd(PPh_3)_4$ (0.88 g, 0.76 mmol) were loaded into an oven dried 500 mL Schlenk flask equipped with a stir bar. The reaction flask was evacuated and refilled with Ar (3x). Next, anhydrous 1,2-dimethoxyethane (DME) (300 mL) and hexamethylditin (3.16 mL) were added to the reaction mixture. The reaction was then heated at 80 °C overnight. The reaction mixture was then allowed to cool to RT and concentrated under vacuum. The crude 6-(trimethylstannyl)-2,2'-bipyridine solution was vacuum dried overnight and used without further purification the following day. The next day, 2,6-dibromopyridine (3.61 g, 15.26 mmol), LiCl (1.29 g, 30.52 mmol), and $Pd(PPh_3)_4$ (0.88 g, 0.76 mmol) were added under Ar atmosphere to the Schlenk flask (500 mL) containing the dry 6-(trimethylstannyl)-2,2'-bipyridine. The reaction mixture was degassed with Ar (3x) then dry toluene (300 mL) was cannula transferred into the reaction flask. The crude reaction mixture was stirred at reflux for 24 h. After 24 h, the reaction was cooled to RT and concentrated under reduced pressure. The crude product was purified by column chromatography starting with pure DCM and slowly ramping to 5% MeOH on SiO_2. The resulting product was further recrystallized in hot DMC and washed repeatedly with hexanes until the filtrate was clear. The final pure product was isolated as a white solid (1.40 g, 30% yield). ^{1}H NMR (500 MHz, CD_2Cl_2) δ (ppm): 8.69 (1H, ddd, *J* = 4.8, 2.6, 0.8 Hz), 8.60 (2H, dd, *J* = 7.8, 0.8 Hz), 8.49 (1H, dd, *J* = 7.8, 1.0 Hz), 8.40 (1H, dd, *J* = 7.8, 1.0 Hz), 7.97 (1H, t, *J* = 7.8 Hz), 7.88 (1H, td, *J* = 7.7, 1.8 Hz), 7.74 (1H, t, *J* = 7.8 Hz), 7.53 (1H, dd, *J* = 7.8, 0.80 Hz), 7.36 (1H, ddd, *J* = 12.2, 2.7, 1.8 Hz). ^{13}C NMR (126 MHz, CD_2Cl_2)/ δ (ppm): 157.91, 156.40, 156.15, 154.26, 149.77, 142.04, 139.93, 138.59, 137.39, 128.62, 124.48, 122.01, 122.64, 121.43, 120.33. ESI-MS Calcd. for $C_{15}H_{11}N_5$ $[M+H]^+$, 312.0 *m/z* found 311.9 *m/z*.

5.5.13 Synthesis of 6-(1,1-Di(pyridin-2-yl)ethyl)-2,2':6',2"-terpyridine (tpyPY2Me)



To an oven dried 50 mL Schlenk flask was added 5 mL dry THF and 2,2'-(ethane-1,1-diyl)dipyridine (0.18 g, 0.96 mmol, 0.18 mL). The reaction mixture was then cooled to –78 ºC. ^{n}BuLi (2.5 M, hexanes) (0.05 g, 0.96 mmol, 0.38 mL) was slowly added to the reaction solution resulting in an immediate color change to bright red. The reaction was allowed to stir for 30 min at –78 ºC. To a separate oven dried Schlenk flask (50 mL) equipped with a stir bar was added 6-bromo-2,2':6',2"-terpyridine (0.20 g, 0.64 mmol). Dry THF (3 mL) was added to the Schlenk flask and the solution was stirred until 6-bromo-2,2':6',2"-terpyridine was fully dissolved. After 30 min, the 6-bromo-2,2':6',2"-terpyridine solution was slowly added by syringe to the reaction mixture at –78 ºC. The reaction was allowed to stir for 1 h at –78 ºC then slowly warmed up to RT. Upon warming to ambient temperature, the reaction color turns dark red. The reaction was allowed to stir at RT for 24 h. After 24 h, the reaction was quenched with 60 mL water. The organic and aqueous layers were separated. The aqueous layer was washed with DCM (3x, 20 mL), dried over $MgSO_4$, and concentrated to give a yellow-orange oil as a crude product. The crude oil was purified by column chromatography SiO_2: EtOAc (the crude product was loaded onto the column in a minimal amount of DCM). The pure ligand was obtained as a crystalline white solid (0.43 g, 81% yield). ^{1}H NMR (500 MHz, CD_2Cl_2) δ (ppm): 8.67 (1H, ddd, *J* = 4.7, 2.5, 0.9 Hz), 8.63 (1H, d, *J* = 8.0 Hz), 8.55 (2H, dt, *J* = 4.0, 1.6 Hz), 8.48 (1H, dd, *J* = 7.8, 0.7 Hz), 8.41 (1H, dd, *J* = 7.8, 0.9 Hz), 8.21 (1H, dd, *J* = 7.8, 0.9 Hz), 7.87 (2H, m), 7.78 (1H, t, *J* = 7.8 Hz), 7.61 (2H, td, *J* = 7.8, 1.9 Hz), 7.34 (1H, ddd, *J* = 12.2, 4.8, 1.1 Hz), 7.20 (1H, dd, *J* = 7.9, 0.7 Hz), 7.16 (4H, m), 2.39 (3H, s). ^{13}C NMR (126 MHz, CD_2Cl_2) / δ (ppm): 166.83, 165.53, 156.72, 156.20, 155.79, 155.16, 149.69, 149.11, 138.23, 137.34, 137.31, 136.29, 124.46, 124.31, 124.20, 121.74, 121.49, 121.43,121.20, 118.81 60.95, 27.55. ESI-MS Calcd. for $C_{27}H_{22}N_5$ $[M+H]^+$, 416.5 *m/z* found 416.0 *m/z*.

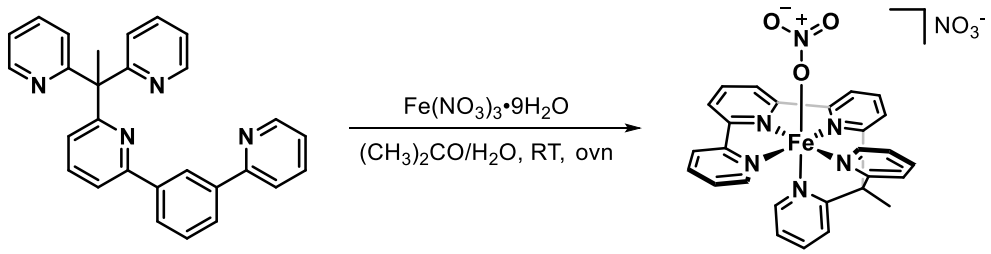
5.5.14 Synthesis of [Fe(tpyPY2Me)(CH$_3$CN)][OTf]$_2$ ([Fe1]$^{2+}$)



In an N_2 filled glovebox, tpyPY2Me (86.0 mg, 0.21 mmol) was weighed into a 20 ml, oven dried scintillation vial equipped with a stir bar. Dry, degassed CH_3CN (9 mL) was added to the scintillation vial and the ligand solution was stirred at RT until fully solubilized. In a second 20

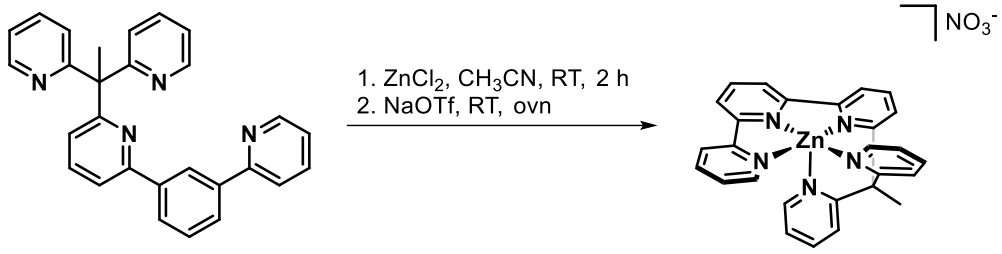
mL, oven dried scintillation vial was loaded $Fe(OTf)_2$ (73 mg, 0.21 mmol) and 9 mL dry, degassed CH_3CN. The iron triflate solution was stirred at RT until fully solubilized. Once fully homogenous, the iron triflate solution was added to the stirring ligand solution resulting in the formation of a dark red solution. The reaction was stirred at RT overnight. The following day, the crude reaction solution was concentrated under vacuum and washed with pentanes (2 mL, 3x). The crude iron complex was purified by crystallization by slow vapor diffusion of diethyl ether (Et_2O) into a saturated CH_3CN solution which resulted in dark red block shaped X-ray diffraction quality crystals over the course of 3 – 5 days (158 mg, 98% yield). ^{1}H NMR (300 MHz, CD_3CN) δ (ppm): 9.49 (s, br), 8.72 (1H, d, *J* = 8.0 Hz), 8.63 (2H, m), 8.45 (1H, d, *J* = 8.0 Hz), 8.38 (1H, t, *J* = 7.2 Hz), 8.31 (1H, d, *J* = 7.8 Hz), 8.25 (1H, d, *J* = 7.4 Hz), 8.16 (2H, t, *J* = 7.8 Hz), 8.04 (2H, d, *J* = 7.8 Hz), 7.79 (2H, t, *J* = 6.5 Hz), 7.06 (s, br), 2.81 (3H, s). Anal. Calcd. for $C_{31}H_{24}F_6FeN_6O_6S_2$: C, 45.94; H, 2.98; N, 10.37; S, 7.91. Found: C, 43.45; H, 2.87; N, 9.03; S, 8.04. ESI-MS Calcd. for $C_{27}H_{21}FeN_5$ $[M]^{2+}$, 235.6 *m/z* found 235.5 *m/z*; $C_{28}H_{21}F_3FeN_5O_3S$ $[M+OTf]^+$, 620.1 *m/z* found 620.0 *m/z*.

5.5.15 Synthesis of [Fe(tpyPY2Me)(NO3)][NO3]



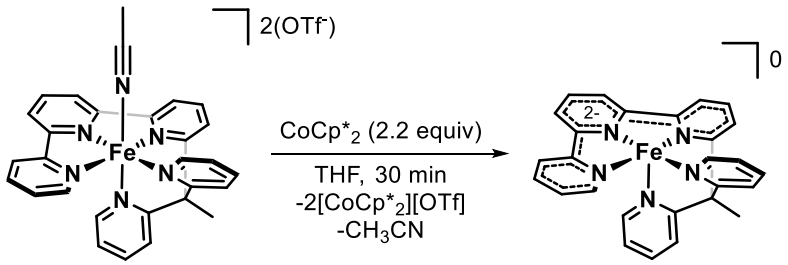
tpyPY2Me (100 mg, 0.21 mmol) was weighed into a 20 ml, scintillation vial equipped with a stir bar and dissolved in acetone (2 mL). $Fe(NO_3)_3$•$9H_2O$ (97.2 mg, 0.24 mmol) was weighed into a second scintillation vial and dissolved in water (1 mL). The iron nitrate solution was then added dropwise into the ligand solution resulting in the formation of an orange solution that turned to dark red over the course of a few minutes. The reaction was stirred at RT overnight. The following day the crude reaction solution was concentrated under vacuum. The crude iron complex was purified by crystallization by slow vapor diffusion of Et_2O into a saturated methanolic solution which resulted in black plate-shaped X-ray diffraction quality crystals over the course of 1 – 2 days (116 mg, 81% yield). ^{1}H NMR (500 MHz, CD_3CN) δ (ppm): 9.45 (Br, s), 8.74 (1H, d, *J* = 8.5 Hz), 8.65 (2H, s), 8.47 (1H, 2), 8.38 (2H, s), 8.29 (3H, m), 8.16 (2H, s), 8.07 (2H, s), 7.81 (3H, s), 7.13 (br, s), 6.81 (br, s), 2.82 (3H, s). Anal. Calcd. for $C_{27}H_{21}FeN_7O_6$: C, 54.47; H, 3.56; N, 16.47. Found: C, 49.58; H, 3.65; N, 15.2. ESI-MS Calcd. for $C_{27}H_{21}FeN_5$ $[M]^{2+}$, 235.6 *m/z* found 235.6 *m/z*; $C_{27}H_{21}FeN_6O_3$ $[M+NO_3]^+$, 533.1 *m/z* found 532.9 *m/z*.

5.5.16 Synthesis of [Zn(tpyPY2Me)][OTf]$_2$ ([Zn1]$^{2+}$)



In an N_2 filled glovebox, tpyPY2Me (100.0 mg, 0.24 mmol) was weighed into a 20 ml, oven dried scintillation vial equipped with a stir bar. Dry, degassed CH_3CN (9 mL) was added to the scintillation vial and the ligand solution was stirred at RT until fully solubilized. In a second 20 mL, oven dried scintillation vial was loaded $ZnCl_2$ (32.9 mg, 0.24 mmol) and 9 mL dry, degassed CH_3CN. The zinc chloride solution was stirred at RT until fully solubilized. Once fully homogenous, the zinc chloride solution was added to the stirring ligand solution resulting in the formation or a white precipitate after *ca.* 10 min. The reaction was stirred at RT for 2 h then sodium triflate (NaOTf) (87.1 mg, 0.51 mmol) was added to the reaction mixture as a solid. The reaction was then stirred at RT overnight. The following day, the crude reaction solution was filtered and concentrated under reduced pressure. The crude zinc complex was purified by crystallization by slow vapor diffusion of Et_2O into a saturated CH_3CN solution which resulted in the formation of colorless needle-shaped crystals (176 mg, 95% yield). ^{1}H NMR (500 MHz, CD_3CN) δ (ppm): 8.85 (1H, ddd, *J* = 5.1, 1.8, 0.8 Hz), 8.82 (1H, d, *J* = 8.1 Hz), 8.71 (1H, m), 8.59 (1H, m), 8.55 (1H, td, *J* = 7.9, 1.6 Hz), 8.49 (2H, ddd, *J* = 5.2, 2.3, 0.6 Hz), 8.44 (1H, d, *J* = 7.7 Hz), 8.32 (1H, t, *J* = 8.0 Hz), 8.22 (3H, m), 8.17 (2H, ddd, *J* = 15.9, 8.0, 1.8 Hz), 8.00 (1H, ddd, *J* = 12.8, 5.1, 1.1 Hz), 7.56 (2H, ddd, *J* = 12.8, 5.3, 1.1 Hz), 2.88 (3H, s). ^{13}C NMR (126 MHz, CD_3CN) / δ (ppm): 157.56, 157.53, 151.58, 150.89, 150.27, 149.39, 148.77, 147.25, 145.61, 144.21, 144.05, 143.20, 129.60, 125.81, 125.71, 125.42, 125.20, 124.59, 124.17, 122.32, 51.19, 22.30. Anal. Calcd. for $C_{29}H_{21}F_6N_5O_6S_2Zn$: C, 44.71; H, 2.72; N, 8.99; S, 8.23. Found: C, 40.49; H, 2.68; N, 8.74; S, 8.74. ESI-MS Calcd. for $C_{27}H_{21}N_5Zn$ [M]$^{2+}$, 239.6 *m/z* found 239.6 *m/z*.

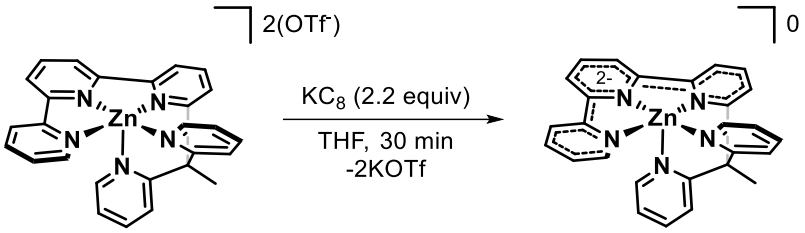
5.5.17 Synthesis of [Fe(tpyPY2Me)]^0 ([Fe1]^0)



In an N_2 filled glovebox, [Fe1]$^{2+}$ (10.0 mg, 0.013 mmol) was weighed into a 20 mL, oven dried scintillation vial equipped with a stir bar. Dry, degassed THF (3 mL) was added to the scintillation vial and the resulting slurry was stirred at RT. In a second 20 mL, oven dried scintillation vial was added 2.6 mL (0.286 mmol, 2.2 equiv) of a 10 mM stock solution of decamethylcobaltocene ($CoCp^*_2$) in dry THF (33.10 mg in 10 mL THF). The scintillation vial

containing the reductant was then frozen in a cold well. The iron solution was then added dropwise to the frozen $CoCp^*_2$ solution at RT resulting in an immediate color change to dark purple. The reaction was ran at RT for 60 min, filtered, and concentrated under reduced pressure to give the final reduced iron complex, $[Fe1]^0$, as a dark purple solid. X-ray diffraction quality crystals (dark purple plates) were obtained by slow evaporation of a saturated acetonitrile solution over 2 – 3 weeks. ^{1}H NMR (500 MHz, CD_3CN) δ (ppm): 8.68 (1 H, dd, *J* = 4.7, 0.7 Hz), 8.64 (1H, d, *J* = 8.0 Hz), 8.51 (2H, ddd, *J* = 4.8, 2.6, 0.9 Hz), 8.48 (1H, d, *J* = 7.7 Hz), 8.41 (1H, d, *J* = 8.5 Hz), 8.19 (1H, dd, *J* = 7.8, 0.8 Hz), 7.93 (2H, m), 7.84 (1H, t, *J* = 7.8 Hz), 7.66 (2H, td, *J* = 7.8, 1.8 Hz), 7.41 (1H, ddd, *J* = 12.2, 4.8, 1.0 Hz), 7.21 (3H, m), 7.17 (2H, d, *J* = 8.1 Hz), 2.36 (3H, s).

5.5.18 Synthesis of $[Zn(tpyPY2Me)]^0$ ($[Zn1]^0$)



In an N_2 filled glovebox, $[Zn1]^{2+}$ (50 mg, 0.064 mmol) was weighed into a 20 mL, oven dried scintillation vial equipped with a stir bar. Dry, degassed THF (8 mL) was added to the scintillation vial and the resulting slurry was stirred at RT. In a second 20 mL, oven dried scintillation vial equipped with a stir bar was weighed potassium graphite (KC_8) (19.1 mg, 0.14 mmol). Dry THF (5 mL) was added to the KC_8 and the resulting slurry was frozen at –195 °C in a cold well. The zinc slurry was then added dropwise to the frozen KC_8 solution at RT resulting in an immediate color change to dark green. The reaction was allowed to slowly warm back to RT and ran for an additional hour. After 1 h, the crude reaction mixture was filtered and concentrated under reduced pressure to give the reduced zinc complex, $[Zn1]^0$, as a dark green solid. ^{1}H NMR (400 MHz, CD_3CN) δ (ppm): 8.68 (1H, ddd, *J* = 4.7, 1.6, 0.8 Hz), 8.64 (1H, d, *J* = 8.0 Hz), 8.51 (2H, ddd, *J* = 4.8, 2.7, 0.9 Hz), 8.48 (1H, dd, *J* = 7.8, 0.7 Hz), 8.42 (1H, dd, *J* = 7.8, 0.9 Hz), 8.19 (1H, dd, *J* = 7.8, 0.9 Hz), 7.93 (2H, m), 7.84 (1H, t, *J* = 7.9 Hz), 7.66 (2H, td, *J* = 7.8, 1.9 Hz), 7.41 (1H, ddd, *J* = 12.2, 4.8, 1.1 Hz), 7.21 (5H, m), 2.36 (3H, s).

5.5.19 X-Ray Crystallographic Data

Table 5.9. Crystallographic data[a] for $[Fe1]^{2+}$.

	[Fe(tpyPY2Me)(CH$_3$CN)][OTf]$_2$
Chemical formula	$C_{29}H_{24}FeN_6 \cdot 2(CF_3O_3S) \cdot C_2H_3N$
FW	851.58
Crystal system, space group	Monoclinic, $P2_1/c$
Temperature (K)	100(2)
a (Å)	12.2643(3)
b (Å)	22.0109(5)
c (Å)	13.0397(3)
α	90.0
β	104.208(2)
γ	90.0
V (Å^3)	3412.37(14)
Z	4
μ (mm^{-1})	0.66
F(000)	1736
Crystal size (mm)	0.6 × 0.34 × 0.26
θ range (°) for cell measurement	3.2–28.9
Radiation type	Mo $K\alpha$
No. of reflections for cell measurement	28033
Index ranges	$-15 \leq h \leq 15$
	$-27 \leq k \leq 26$
	$-16 \leq l \leq 16$
Reflections collected / unique	36911 / 6970
R_{int}	0.056
Data / restraints / parameters	6970 / 0 / 499
Goodness-of-fit on F^2	1.037
Final R indices[b]	$R_1 = 0.032$, $wR_2 = 0.083$
Largest diff. peak and hole, eÅ^{-3}	0.42 and –0.40

[a]Obtained with a rotating-anode X-ray tube, Rigaku Mo K_α (λ = 0.71073 Å) X-ray source.
[b]$R_1 = \sum||F_0| - F_C||/\sum|F_0|$, $R_2 = \{\sum[w(F_0^2 - F_0^2)^2]/\sum[w(F_0^2)^2]\}^{1/2}$.

Table 5.10. Selected bond lengths (Å) and angles (°) for **[Fe1]$^{2+}$**.

Atoms	Distance	Atoms	Distance
Fe1—N1	1.9598(14)	C4—C5	1.391(2)
Fe1—N2	1.9986(14)	C8—C9	1.390(2)
Fe1—N3	1.8853(14)	C9—C10	1.390(2)
Fe1—N4	1.9094(14)	C10—C11	1.386(2)
Fe1—N5	1.9641(14)	C11—C12	1.380(2)
Fe1—N6	1.9555(15)	C13—C14	1.394(2)
N1—C1	1.349(2)	C14—C15	1.392(3)
N1—C5	1.363(2)	C15—C16	1.385(3)
N2—C23	1.368(2)	C16—C17	1.386(2)
N2—C27	1.346(2)	C17—C18	1.468(2)
N3—C18	1.355(2)	C18—C19	1.386(2)
N3—C22	1.347(2)	C19—C20	1.392(3)
N4—C13	1.339(2)	C20—C21	1.391(3)
N4—C17	1.363(2)	C21—C22	1.386(2)
N5—C8	1.353(2)	C22—C23	1.479(2)
N5—C12	1.350(2)	C23—C24	1.384(2)
N6—C28	1.146(2)	C24—C25	1.388(3)
C1—C2	1.378(3)	C25—C26	1.385(3)
C2—C3	1.390(3)	C26—C27	1.385(2)
C3—C4	1.390(3)	C28—C29	1.455(3)

Atoms	Angle (º)	Atoms	Distance
N1—Fe1—N2	93.01(6)	N2—Fe1—N6	90.44(6)
N1—Fe1—N3	102.42(6)	N3—Fe1—N4	81.22(6)
N1—Fe1—N4	84.30(6)	N3—Fe1—N5	169.71(6)
N1—Fe1—N5	86.47(6)	N3—Fe1—N6	83.39(6)
N1—Fe1—N6	173.64(6)	N4—Fe1—N5	94.70(6)
N2—Fe1—N3	81.07(6)	N4—Fe1—N6	94.13(6)
N2—Fe1—N4	161.06(6)	N5—Fe1—N6	87.51(6)
N2—Fe1—N5	103.86(6)		

Table 5.11. Crystallographic data[a] for $[Zn1]^{2+}$.

	[Zn(tpyPY2Me)][OTf]$_2$
Chemical formula	$C_{27}H_{21}N_5Zn \cdot 2(CF_3O_3S) \cdot C_2H_3N$
FW	820.07
Crystal system, space group	Monoclinic, $P2_1/c$
Temperature (K)	100(2)
a (Å)	14.0710(6)
b (Å)	15.7185(7)
c (Å)	16.1418(9)
α	90.0
β	113.062(6)
γ	90.0
V (Å^3)	3412.37(14)
Z	4
μ (mm^{-1})	0.96
F(000)	1664
Crystal size (mm)	0.20 × 0.07 × 0.06
θ range (°) for cell measurement	2.9–28.6
Radiation type	Mo $K\alpha$
No. of reflections for cell measurement	9682
Index ranges	$-14 \leq h \leq 19$
	$-20 \leq k \leq 17$
	$-20 \leq l \leq 21$
Reflections collected / unique	36949 / 7720
R_{int}	0.079
Data / restraints / parameters	7720 / 0 / 462
Goodness-of-fit on F^2	1.089
Final R indices[b]	$R_1 = 0.099$, $wR_2 = 0.257$
Largest diff. peak and hole, eÅ^{-3}	1.72 and –1.25

[a]Obtained with a rotating-anode X-ray tube, Rigaku Mo K_α (λ = 0.71073 Å) X-ray source.
[b] $R_1 = \sum||F_0| - F_C||/\sum|F_0|$, $R_2 = \{\sum[w(F_0^2 - F_0^2)^2]/\sum[\, w(F_0^2)^2]\}^{1/2}$.

Table 5.12. Selected bond lengths (Å) and angles (°) for $[Zn1]^{2+}$.

Atoms	Distance	Atoms	Distance
Zn1—N1	2.088(5)	C5—C6	1.481(9)
Zn1—N2	2.064(5)	C6—C7	1.405(9)
Zn1—N3	2.112(5)	C7—C8	1.380(10)
Zn1—N4	2.017(5)	C8—C9	1.396(10)
Zn1—N5	2.067(6)	C9—C10	1.391(9)
N1—C1	1.342(8)	C10—C11	1.495(10)
N1—C5	1.347(8)	C11—C12	1.378(9)
N2—C6	1.321(8)	C12—C13	1.375(10)
N2—C10	1.331(8)	C13—C14	1.380(9)
N3—C11	1.354(8)	C14—C15	1.401(8)
N3—C15	1.318(8)	C15—C16	1.551(9)
N4—C18	1.352(8)	C18—C19	1.391(9)
N4—C22	1.355(8)	C19—C20	1.383(9)
N5—C23	1.349(9)	C20—C21	1.389(10)
N5—C27	1.333(9)	C21—C22	1.394(9)
C1—C2	1.382(9)	C23—C24	1.380(10)
C2—C3	1.376(10)	C24—C25	1.392(11)
C3—C4	1.369(9)	C25—C26	1.361(12)
C4—C5	1.382(9)	C26—C27	1.375(12)

Atoms	Angle (º)	Atoms	Distance
N1—Zn1—N2	77.5(2)	N2—Zn1—N4	138.7(2)
N1—Zn1—N3	153.3(2)	N2—Zn1—N5	127.8(2)
N1—Zn1—N4	112.0(2)	N3—Zn1—N4	88.29(19)
N1—Zn1—N5	112.6(2)	N3—Zn1—N5	84.5(2)
N2—Zn1—N3	75.8(2)	N4—Zn1—N5	87.1(2)

Table 5.13. Crystallographic data[a] for $[Fe1]^0$.

	[Fe(tpyPY2Me)]^0
Chemical formula	$1(C_{20}H_{29}Co)\cdot 2(C_{27}H_{21}FeN_5)$
FW	1272.05
Crystal system, space group	Monoclinic, $P2_1/c$
Temperature (K)	100(2)
a (Å)	19.7462(11)
b (Å)	15.5398(7)
c (Å)	9.7373(6)
α	90.0
β	93.360(5)
γ	90.0
V (Å^3)	2982.8(3)
Z	2
μ (mm^{-1})	0.81
F(000)	1330
Crystal size (mm)	0.3 × 0.22 × 0.11
θ range (°) for cell measurement	3.3–29.5
Radiation type	Mo $K\alpha$
No. of reflections for cell measurement	12920
Index ranges	$-24 \le h \le 24$
	$-18 \le k \le 19$
	$-11 \le l \le 12$
Reflections collected / unique	36402 / 6074
R_{int}	0.095
Data / restraints / parameters	6074 / 0 / 400
Goodness-of-fit on F^2	1.048
Final R indices[b]	$R_1 = 0.042$, $wR_2 = 0.113$
Largest diff. peak and hole, eÅ^{-3}	0.64 and –0.73

[a]Obtained with a rotating-anode X-ray tube, Rigaku Mo K_α (λ = 0.71073 Å) X-ray source.
[b]$R_1 = \sum||F_0| - F_C||/\sum|F_0|$, $R_2 = \{\sum[w(F_0^2 - F_0^2)^2]/\sum[w(F_0^2)^2]\}^{1/2}$.

Table 5.14. Selected bond lengths (Å) and angles (°) for $[Fe1]^0$.

Atoms	Distance	Atoms	Distance
Fe1—N1	1.8997(18)	C4—C5	1.402(3)
Fe1—N2	1.8377(18)	C5—C6	1.434(3)
Fe1—N3	1.8783(17)	C6—C7	1.396(3)
Fe1—N4	1.9463(18)	C7—C8	1.388(3)
Fe1—N5	1.9600(19)	C8—C9	1.398(3)
N1—C1	1.377(3)	C9—C10	1.397(3)
N1—C5	1.407(3)	C11—C12	1.394(3)
N2—C6	1.382(3)	C12—C13	1.381(3)
N2—C10	1.386(3)	C13—C14	1.411(3)
N3—C11	1.389(3)	C14—C15	1.383(3)
N3—C15	1.360(3)	C15—C16	1.537(3)
N4—C18	1.364(3)	C18—C19	1.397(3)
N4—C22	1.364(3)	C19—C20	1.388(3)
N5—C23	1.365(3)	C22—C22	1.376(3)
N5—C27	1.361(3)	C23—C24	1.399(3)
C1—C2	1.363(3)	C24—C25	1.392(3)
C2—C3	1.418(4)	C25—C26	1.399(4)
C3—C4	1.367(4)	C26—C27	1.372(3)

Atoms	Angle (º)	Atoms	Distance
N1—Fe1—N4	100.80(8)	N2—Fe1—N5	140.49(8)
N1—Fe1—N5	101.72(8)	N3—Fe1—N1	162.82(8)
N2—Fe1—N1	81.71(8)	N3—Fe1—N4	91.09(7)
N2—Fe1—N3	81.11(8)	N3—Fe1—N5	91.42(8)
N2—Fe1—N4	132.81(8)	N4—Fe1—N5	85.73(7)

Table 5.15. Crystallographic data[a] for [Fe(tpyPY2Me)(NO_3)][NO_3].

	[Fe(tpyPY2Me)(NO_3)][NO_3]
Chemical formula	$C_{27}H_{21}FeN_6O_3 \cdot N_{0.5}O_{1.5}$
FW	626.37
Crystal system, space group	Monoclinic, *C*2/*c*
Temperature (K)	100(2)
a (Å)	31.268(3)
b (Å)	13.9785(12)
c (Å)	12.8118(7)
α	90.0
β	92.908(7)
γ	90.0
V (Å^3)	5592.6(7)
Z	8
μ (mm^{-1})	0.60
F(000)	2576
Crystal size (mm)	0.21 × 0.13 × 0.05
θ range (°) for cell measurement	3.2–29.2
Radiation type	Mo *K*α
No. of reflections for cell measurement	11890
Index ranges	$-40 \le h \le 42$
	$-18 \le k \le 19$
	$-15 \le l \le 17$
Reflections collected / unique	50351 / 6973
R_{int}	0.105
Data / restraints / parameters	6973 / 0 / 354
Goodness-of-fit on F^2	1.559
Final R indices[b]	R_1 = 0.074, wR_2 = 0.233
Largest diff. peak and hole, eÅ^{-3}	1.35 and –0.81

[a]Obtained with a rotating-anode X-ray tube, Rigaku Mo K_α (λ = 0.71073 Å) X-ray source.
[b]$R_1 = \sum||F_0| - F_C||/\sum|F_0|$, $R_2 = \{\sum[w(F_0^2 - F_0^2)^2]/\sum[w(F_0^2)^2]\}^{1/2}$.

Table 5.16. Selected bond lengths (Å) and angles (°) for [Fe(tpyPY2Me)(NO_3)][NO_3].

Atoms	Distance	Atoms	Distance
Fe1—N1	1.955(3)	C4—C5	1.402(6)
Fe1—N2	1.958(3)	C8—C9	1.387(5)
Fe1—N3	1.911(3)	C9—C10	1.381(5)
Fe1—N4	1.877(3)	C10—C11	1.384(5)
Fe1—N5	2.000(3)	C11—C12	1.380(5)
Fe1—O1	1.997(2)	C13—C14	1.385(5)
N1—C1	1.344(5)	C14—C15	1.385(6)
N1—C5	1.354(5)	C15—C16	1.383(6)
N2—C8	1.358(4)	C16—C17	1.389(6)
N2—C12	1.358(4)	C17—C18	1.455(6)
N3—C13	1.333(5)	C18—C19	1.388(6)
N3—C17	1.361(5)	C19—C20	1.386(7)
N4—C18	1.356(5)	C20—C21	1.410(7)
N4—C22	1.358(5)	C21—C22	1.388(6)
N5—C23	1.372(5)	C22—C23	1.475(6)
N5—C27	1.343(5)	C23—C24	1.382(6)
C1—C2	1.375(6)	C24—C25	1.386(6)
C2—C3	1.388(7)	C25—C26	1.401(6)
C3—C4	1.371(7)	C26—C27	1.379(6)

Atoms	Angle (º)	Atoms	Distance
N1—Fe1—O1	172.88(11)	N2—Fe1—N5	104.69(13)
N1—Fe1—N2	87.10(12)	N3—Fe1—O1	98.15(12)
N1—Fe1—N3	85.57(13)	N3—Fe1—N4	80.76(13)
N1—Fe1—N4	102.2 (13)	N3—Fe1—N5	161.27(13)
N1—Fe1—N5	92.98(13)	N4—Fe1—O1	84.36(11)
N2—Fe1—O1	86.59(11)	N4—Fe1—N5	81.32(14)
N2—Fe1—N3	93.90(12)	N5—Fe1—O1	85.43(11)
N2—Fe1—N4	168.72(13)		

5.5.20 DFT Calculation Coordinates (x,y,z)

Table 5.17. DFT [unrestricted Kohn-Sham (UKS) or broken symmetry (BS)] geometry optimized atomic x, y, z coordinates for Mössbauer calculations on $[Fe(tpy)_2]^n$ (n = 3+, 2+, 1+, 0). Optimized using B3LYP.

$[Fe(tpy)_2]^{3+}$, S = 1/2, UKS				**$[Fe(tpy)_2]^{2+}$, S = 0, UKS)**			
Fe	-0.010407	0.024899	-0.007264	Fe	-0.001425	0.014001	0.000157122
C	-1.225702	0.946444	-4.505228	C	-1.225275	0.955824	-4.516913946
C	0.114981	0.726389	-4.219894	C	0.113644	0.724440	-4.237967948
C	-2.156299	0.874526	-3.474182	C	-2.148374	0.880719	-3.482657466
C	0.487813	0.451414	-2.912894	C	0.485258	0.430903	-2.934591627
C	-1.724466	0.587145	-2.188598	C	-1.710097	0.579514	-2.200167203
C	0.359224	-4.664179	-0.766461	C	0.412588	-4.688200	-0.752989594
C	-3.982242	0.560774	-0.955305	C	-3.972309	0.566931	-0.987116045
C	-2.594702	0.473165	-1.011121	C	-2.585063	0.469563	-1.023373047
C	1.464879	-3.828198	-0.638832	C	1.503907	-3.833474	-0.675924695
C	-0.914650	-4.116348	-0.695700	C	-0.863252	-4.165002	-0.597360685
C	1.273352	-2.472349	-0.433565	C	1.293099	-2.481144	-0.444463441
C	-1.043586	-2.751239	-0.497940	C	-1.003014	-2.804136	-0.371483402
C	3.724240	-1.704048	-0.344033	C	3.733766	-1.691027	-0.436377161
C	2.353458	-1.482281	-0.283152	C	2.362970	-1.477917	-0.336212381
C	4.584303	-0.617972	-0.197093	C	4.589512	-0.602430	-0.307268937
C	4.076433	0.659503	0.011484	C	4.075989	0.669149	-0.075969436
C	2.695079	0.822765	0.071591	C	2.696801	0.822739	0.021765091
C	-4.606037	0.398397	0.278471	C	-4.618935	0.416628	0.235031647
C	1.943781	2.067755	0.259291	C	1.950972	2.068936	0.253430632
C	-0.200644	2.986127	0.305581	C	-0.171550	2.990073	0.433602382
C	2.511606	3.314566	0.469027	C	2.539007	3.311328	0.448756022
C	0.310195	4.259503	0.507033	C	0.350803	4.261474	0.621733407
C	1.686297	4.425359	0.595616	C	1.729262	4.422820	0.635447569
C	-2.473128	0.074159	1.317009	C	-2.500144	0.081872	1.295603589
C	-3.855424	0.156013	1.429150	C	-3.884901	0.174984	1.391399424
C	-1.491752	-0.193567	2.385247	C	-1.541801	-0.185217	2.378886446
C	0.774670	-0.452494	2.867250	C	0.705158	-0.447465	2.886860109
C	-1.820590	-0.383798	3.716216	C	-1.891847	-0.364657	3.710218542
C	0.507951	-0.642580	4.213930	C	0.425211	-0.621281	4.233504758
C	-0.810150	-0.608888	4.646555	C	-0.896889	-0.584228	4.652590791
H	-1.546393	1.173100	-5.513679	H	-1.549028	1.194171	-5.520942777
H	0.868335	0.771154	-4.994250	H	0.865169	0.772297	-5.013311373
H	-3.205330	1.043373	-3.673453	H	-3.196844	1.060151	-3.672820758
H	1.522459	0.278313	-2.653308	H	1.519280	0.244933	-2.68012091
H	-4.567793	0.746897	-1.844300	H	-4.541214	0.751232	-1.886593733
H	0.494654	-5.725686	-0.928486	H	0.558222	-5.744117	-0.936517236

H	2.464374	-4.235386	-0.698552	H	2.506703	-4.217435	-0.79590301
H	-1.798809	-4.729829	-0.799067	H	-1.740220	-4.794039	-0.65378168
H	4.122807	-2.694280	-0.512319	H	4.132505	-2.678833	-0.615068513
H	5.654586	-0.768554	-0.251509	H	5.658531	-0.744883	-0.389025744
H	-2.017927	-2.288877	-0.443194	H	-1.980561	-2.360046	-0.248789181
H	4.744365	1.502074	0.118044	H	4.739366	1.515552	0.024151806
H	-5.684363	0.461074	0.346213	H	-5.696834	0.487891	0.286258569
H	-1.265625	2.817469	0.234700	H	-1.239635	2.822114	0.423098761
H	3.585353	3.421616	0.533672	H	3.614933	3.411181	0.455567222
H	-0.363577	5.100213	0.596436	H	-0.313844	5.102308	0.759880013
H	2.115065	5.405099	0.760952	H	2.170498	5.398256	0.78916943
H	-4.349078	0.029514	2.381805	H	-4.386925	0.054840	2.340145302
H	1.788273	-0.475899	2.494695	H	1.722674	-0.478138	2.523406691
H	-2.853340	-0.353119	4.033625	H	-2.929028	-0.328244	4.011131163
H	1.322778	-0.813005	4.903630	H	1.232462	-0.787276	4.932717542
H	-1.054015	-0.756033	5.690581	H	-1.152223	-0.723851	5.69421623
N	-0.403325	0.384822	-1.918142	N	-0.394959	0.363150	-1.932318437
N	0.017052	-1.945798	-0.364504	N	0.040486	-1.974591	-0.29700449
N	1.890462	-0.239844	-0.075635	N	1.887650	-0.240877	-0.112951331
N	-1.898986	0.235336	0.112915	N	-1.895696	0.232334	0.10508105
N	0.590265	1.913401	0.191341	N	0.599998	1.914886	0.257961451
N	-0.191624	-0.237009	1.968036	N	-0.245404	-0.237585	1.972645427

$[Fe(tpy)_2]^{1+}$, *S* = 1/2, UKS				**$[Fe(tpy)_2]^0$, *S* = 1, BS(4,2)**			
Fe	-0.001346	0.023948	-0.001046	Fe	-0.006109	-0.007539	-0.01532988
C	-1.210853	1.029390	-4.500003	C	-2.272182	0.266740	-4.40269389
C	0.136534	0.808205	-4.211274	C	-1.065619	-0.448183	-4.292225893
C	-2.140023	0.920844	-3.482598	C	-2.793719	0.874774	-3.272458917
C	0.495734	0.491278	-2.915257	C	-0.446986	-0.515095	-3.056717243
C	-1.717953	0.588903	-2.195319	C	-2.118097	0.769642	-2.046936835
C	0.398048	-4.688678	-0.658378	C	3.607604	3.153845	-1.207619617
C	-3.972647	0.544137	-0.991397	C	2.307621	3.643291	-0.985414595
C	-2.586879	0.461593	-1.034070	C	3.837799	1.792793	-1.089796152
C	1.490424	-3.842282	-0.618061	C	-2.567784	1.363581	-0.796282281
C	-0.881144	-4.151902	-0.504292	C	1.309193	2.743832	-0.656863071
C	1.296091	-2.474244	-0.431580	C	-3.730617	2.116109	-0.632314699
C	-1.009463	-2.788508	-0.319273	C	2.781945	0.931594	-0.753899712
C	3.726796	-1.689034	-0.444085	C	4.075405	-1.246035	-0.773792333
C	2.358126	-1.480716	-0.345625	C	4.051060	-2.632485	-0.59870719
C	4.589317	-0.602851	-0.301764	C	2.902221	-0.511389	-0.602749698
C	4.075228	0.670382	-0.057789	C	2.848545	-3.256445	-0.255072684
C	2.699927	0.833504	0.035129	C	1.697081	-2.486351	-0.092908979
C	-4.621248	0.399612	0.233572	C	0.088439	-4.352156	0.500761496
C	1.960605	2.072280	0.241788	C	-1.202421	-4.729721	0.833031723

C	-0.172324	3.000131	0.373017	C	-2.196446	-3.738407	0.923609518
C	2.538531	3.330810	0.400469	C	0.382344	-3.000919	0.262032839
C	0.341945	4.274379	0.525473	C	-1.844114	-2.423573	0.677193463
C	1.727745	4.440538	0.546182	C	-4.045861	2.629960	0.628582907
C	-2.498792	0.091327	1.305558	C	-2.034257	1.621303	1.497513548
C	-3.881058	0.173123	1.394782	C	-3.187374	2.378529	1.702538474
C	-1.547924	-0.194892	2.373953	C	-1.055671	1.282926	2.520979729
C	0.706046	-0.498465	2.865866	C	0.950612	0.162151	2.946188847
C	-1.887361	-0.425603	3.705714	C	-1.135584	1.674337	3.86619989
C	0.433110	-0.720708	4.202027	C	0.928521	0.516108	4.28340254
C	-0.893900	-0.687300	4.630714	C	-0.144230	1.293649	4.755971283
H	-1.525910	1.288717	-5.501518	H	-2.787155	0.342179	-5.355500455
H	0.894857	0.879004	-4.977882	H	-0.620159	-0.940616	-5.150585052
H	-3.188457	1.098529	-3.676415	H	-3.722902	1.432740	-3.330555139
H	1.528087	0.312084	-2.648063	H	0.486667	-1.054042	-2.916755881
H	-4.542982	0.714620	-1.893289	H	-4.385989	2.301135	-1.477087012
H	0.535660	-5.750676	-0.809986	H	4.417706	3.828588	-1.466843548
H	2.491425	-4.234190	-0.730001	H	2.080782	4.701407	-1.066994286
H	-1.762139	-4.776617	-0.536592	H	4.831654	1.389400	-1.255929218
H	4.123122	-2.677041	-0.629503	H	5.000172	-0.745422	-1.041348782
H	5.657569	-0.747254	-0.382804	H	0.288080	3.069206	-0.47474737
H	-1.981150	-2.330392	-0.199433	H	4.955507	-3.217995	-0.728835624
H	4.740234	1.514933	0.051458	H	2.811302	-4.331978	-0.116318331
H	-5.699302	0.460012	0.284048	H	0.874190	-5.097077	0.424956565
H	-1.239327	2.823434	0.358060	H	-1.440008	-5.772464	1.020016246
H	3.614615	3.432194	0.406594	H	-3.221001	-3.987570	1.180380344
H	-0.326443	5.116092	0.635996	H	-2.573277	-1.619322	0.73408009
H	2.164121	5.421986	0.672373	H	-4.947090	3.217274	0.772234106
H	-4.381828	0.050427	2.344311	H	-3.416799	2.769588	2.688332666
H	1.720035	-0.521711	2.491335	H	1.756094	-0.437512	2.529976524
H	-2.924193	-0.396853	4.009606	H	-1.974204	2.274277	4.205121926
H	1.242821	-0.916122	4.890461	H	1.727404	0.194902	4.943960341
H	-1.144923	-0.865821	5.667353	H	-0.196741	1.591302	5.798748033
N	-0.394546	0.380926	-1.922105	N	-0.943193	0.071798	-1.948199227
N	0.038973	-1.958044	-0.287574	N	1.518955	1.416723	-0.538414717
N	1.878921	-0.233594	-0.113718	N	1.722259	-1.125075	-0.264780786
N	-1.887346	0.241724	0.106552	N	-0.591629	-2.041588	0.353061789
N	0.602291	1.916663	0.245041	N	-1.725563	1.117376	0.258967069
N	-0.246346	-0.241131	1.961691	N	-0.007291	0.525710	2.068948142

Table 5.18. DFT [unrestricted Kohn-Sham (UKS) or broken symmetry (BS)] geometry optimized atomic xyz coordinates for Mössbauer calculations on $[Fe(bpy)_3]^n$ (n = 3+, 2+, 1+, 0). Optimized using B3LYP.

$[Fe(bpy)_3]^{3+}$, *S* = 1/2, UKS				**$[Fe(bpy)_3]^{2+}$, *S* = 0, UKS**			
Fe	0.013685	0.004683	-0.002538	Fe	0.007288	0.001600	-0.001993733
N	0.000491	0.050437	1.984526	N	-0.032832	0.026344	1.995379051
C	-0.929228	0.876274	2.526374	C	-0.929662	0.883397	2.53673414
C	-1.084696	0.964528	3.904666	C	-1.080000	0.994251	3.916000979
C	-0.272282	0.204152	4.734942	C	-0.294564	0.217322	4.753468998
C	0.689544	-0.622489	4.167133	C	0.630855	-0.651419	4.190307611
C	0.796032	-0.671807	2.787613	C	0.729069	-0.714688	2.810119047
N	-1.418083	1.368999	0.253740	N	-1.408137	1.395345	0.264876212
C	-1.718651	1.634407	1.550299	C	-1.709670	1.656073	1.559309009
C	-2.694888	2.567843	1.881012	C	-2.677427	2.596685	1.903147986
C	-3.372251	3.235944	0.869648	C	-3.351116	3.280113	0.902396966
C	-3.058358	2.952305	-0.453251	C	-3.040093	3.004276	-0.421877574
C	-2.079865	2.010062	-0.721246	C	-2.067587	2.056484	-0.695140964
N	-1.434740	-1.356950	-0.159189	N	-1.424274	-1.389029	-0.172846421
C	-1.806455	-1.643618	-1.432397	C	-1.799515	-1.665076	-1.444389493
C	-2.789573	-2.591500	-1.692594	C	-2.774927	-2.619478	-1.720491805
C	-3.405943	-3.246536	-0.634416	C	-3.386218	-3.294171	-0.674401067
C	-3.024018	-2.936693	0.664405	C	-3.004981	-2.997395	0.626699277
C	-2.037747	-1.985215	0.861256	C	-2.024065	-2.041144	0.831405441
C	-1.088774	-0.886450	-2.462536	C	-1.092749	-0.889413	-2.473335762
N	-0.137697	-0.043639	-1.987306	N	-0.166840	-0.024968	-1.995138664
N	1.519727	-1.294519	-0.162322	N	1.527391	-1.299271	-0.132584144
C	2.753034	-0.730364	-0.170611	C	2.756641	-0.733620	-0.159584481
C	3.895793	-1.514590	-0.270815	C	3.908236	-1.508584	-0.258607034
C	3.774073	-2.894342	-0.358489	C	3.800312	-2.888632	-0.327781175
C	2.505797	-3.460027	-0.353359	C	2.536696	-3.462001	-0.302827285
C	1.402906	-2.627108	-0.260620	C	1.430389	-2.632774	-0.209723843
C	2.759492	0.730916	-0.052890	C	2.761898	0.732412	-0.058816319
N	1.531244	1.296350	0.056112	N	1.535820	1.298897	0.030827098
C	1.427696	2.626414	0.196228	C	1.449267	2.630274	0.147498237
C	2.537477	3.455015	0.214063	C	2.561976	3.456086	0.164499541
C	3.799963	2.888950	0.089926	C	3.821741	2.882727	0.059301772
C	3.909032	1.511507	-0.040041	C	3.919603	1.504524	-0.049557364
C	0.588684	0.688531	-2.844783	C	0.528123	0.723769	-2.860685434
C	0.388809	0.630769	-4.213844	C	0.330066	0.662170	-4.230503555
C	-0.592572	-0.217308	-4.712538	C	-0.626037	-0.213817	-4.727791701
C	-1.334582	-0.986604	-3.826915	C	-1.342118	-0.999458	-3.838298661
H	-1.832588	1.616255	4.331772	H	-1.802577	1.677300	4.336818241
H	-0.390014	0.259950	5.809295	H	-0.405438	0.291679	5.826856967

H	1.346536	-1.226124	4.777748	H	1.266552	-1.273977	4.803918006
H	1.523448	-1.309683	2.310056	H	1.430885	-1.383431	2.335222922
H	-2.927299	2.779452	2.914426	H	-2.907227	2.799161	2.938636755
H	-4.132456	3.966619	1.112433	H	-4.104674	4.013988	1.153458203
H	-3.560353	3.449580	-1.271337	H	-3.538915	3.511019	-1.235679314
H	-1.809698	1.768816	-1.737388	H	-1.798535	1.821160	-1.71351448
H	-3.076063	-2.822003	-2.708212	H	-3.060125	-2.837377	-2.738906523
H	-4.172177	-3.986944	-0.822892	H	-4.146321	-4.037332	-0.873147244
H	-3.478155	-3.421690	1.517119	H	-3.454766	-3.495424	1.473800962
H	-1.712598	-1.725673	1.856477	H	-1.697892	-1.791445	1.829382902
H	4.874384	-1.058564	-0.276445	H	4.882003	-1.043635	-0.279753954
H	4.656447	-3.516233	-0.432363	H	4.686944	-3.503353	-0.402492113
H	2.365536	-4.529776	-0.423970	H	2.402967	-4.533151	-0.358492931
H	0.402718	-3.031660	-0.255053	H	0.432259	-3.043299	-0.188581306
H	4.882589	1.053914	-0.131619	H	4.889963	1.038385	-0.126439578
H	4.686920	3.508626	0.099097	H	4.712516	3.495932	0.066723365
H	2.407507	4.522535	0.326354	H	2.436393	4.525386	0.260795787
H	0.432274	3.032133	0.288841	H	0.454331	3.041941	0.223894168
H	-2.098628	-1.652688	-4.199788	H	-2.088761	-1.686618	-4.207170827
H	-0.780954	-0.281035	-5.776433	H	-0.815112	-0.285445	-5.790499238
H	0.990387	1.244115	-4.870189	H	0.912782	1.292421	-4.887358557
H	1.334809	1.342810	-2.420930	H	1.255835	1.399367	-2.436823102

$[Fe(bpy)_3]^{1+}$, *S* = 1/2, UKS				**$[Fe(bpy)_3]^{0}$, *S* = 1, BS(4,2)**			
Fe	0.041292	0.005916	-0.004932	Fe	0.101904	0.063232	0.000463558
N	-0.011783	0.028841	1.977004	N	-0.120590	0.092566	2.103314254
C	-0.977291	0.836511	2.501880	C	-1.132656	0.874128	2.599730859
C	-1.219233	0.851181	3.883036	C	-1.471148	0.798052	3.965160824
C	-0.449081	0.073136	4.721260	C	-0.768058	-0.031052	4.806367861
C	0.572618	-0.709367	4.174860	C	0.304150	-0.785380	4.28901895
C	0.745044	-0.702927	2.803309	C	0.575497	-0.689308	2.943651046
N	-1.368266	1.397665	0.230856	N	-1.413538	1.583207	0.34170873
C	-1.703472	1.631756	1.532767	C	-1.792950	1.732763	1.648130767
C	-2.665637	2.598420	1.861434	C	-2.760681	2.699114	1.993791439
C	-3.296731	3.304850	0.859428	C	-3.342395	3.472591	1.017621369
C	-2.961381	3.040404	-0.470835	C	-2.960316	3.287923	-0.32289115
C	-1.996421	2.084680	-0.730826	C	-1.997701	2.338202	-0.595739756
N	-1.381751	-1.383747	-0.138787	N	-1.446901	-1.477009	-0.198162985
C	-1.786981	-1.643921	-1.415178	C	-1.859679	-1.731643	-1.474447458
C	-2.759801	-2.621766	-1.670601	C	-2.824484	-2.729973	-1.717751494
C	-3.336695	-3.305674	-0.621277	C	-3.380560	-3.422717	-0.667037549
C	-2.932957	-3.011325	0.683376	C	-2.970392	-3.125689	0.641237077
C	-1.955713	-2.051063	0.869630	C	-2.002753	-2.154784	0.811334756
C	-1.129698	-0.855237	-2.436990	C	-1.253122	-0.930838	-2.515546786

N	-0.150542	-0.021301	-1.981735	N	-0.286846	-0.050536	-2.119014135
N	1.547565	-1.296063	-0.113609	N	1.779491	-1.288656	-0.115549994
C	2.783042	-0.724129	-0.138522	C	3.014495	-0.696171	-0.144875802
C	3.937875	-1.514246	-0.186329	C	4.177995	-1.491973	-0.176378495
C	3.826908	-2.888748	-0.224048	C	4.079345	-2.861566	-0.19382356
C	2.555255	-3.463837	-0.219402	C	2.802879	-3.455580	-0.187476619
C	1.452299	-2.630074	-0.164486	C	1.702420	-2.627591	-0.150526331
C	2.786700	0.726944	-0.089256	C	3.022935	0.743192	-0.135488704
N	1.555172	1.301120	0.002778	N	1.793358	1.352448	-0.087064949
C	1.469775	2.633577	0.095875	C	1.739076	2.695264	-0.031114873
C	2.576642	3.463546	0.077659	C	2.850789	3.504981	-0.046590756
C	3.841958	2.887321	-0.048321	C	4.119465	2.894106	-0.118644261
C	3.943900	1.513982	-0.128710	C	4.195989	1.523741	-0.156904651
C	0.530612	0.722810	-2.860792	C	0.337540	0.693739	-3.037729298
C	0.268817	0.712166	-4.218555	C	0.042629	0.643902	-4.386166617
C	-0.759472	-0.107854	-4.692720	C	-0.968070	-0.235768	-4.807185003
C	-1.454582	-0.895814	-3.800608	C	-1.608958	-1.018499	-3.875424217
H	-2.011979	1.462775	4.287614	H	-2.297746	1.378917	4.348568581
H	-0.637551	0.070830	5.786456	H	-1.040232	-0.106486	5.851170378
H	1.211609	-1.320231	4.795769	H	0.896341	-1.433421	4.919341226
H	1.502707	-1.315173	2.337284	H	1.372440	-1.265715	2.490220562
H	-2.907744	2.795377	2.895475	H	-3.038398	2.842601	3.028357036
H	-4.038245	4.053518	1.102768	H	-4.082253	4.217097	1.281137228
H	-3.435223	3.562347	-1.289252	H	-3.401294	3.864185	-1.123735784
H	-1.703235	1.860514	-1.745411	H	-1.665772	2.159570	-1.611386065
H	-3.055689	-2.841157	-2.685922	H	-3.130161	-2.956549	-2.728965775
H	-4.089291	-4.059454	-0.808555	H	-4.124181	-4.187084	-0.851182206
H	-3.363176	-3.514213	1.537075	H	-3.390411	-3.633022	1.49791498
H	-1.606843	-1.806828	1.861521	H	-1.645360	-1.898316	1.799919825
H	4.912373	-1.049949	-0.188633	H	5.151268	-1.023613	-0.184487016
H	4.712961	-3.507868	-0.259119	H	4.971542	-3.473530	-0.2169948
H	2.419023	-4.534867	-0.260327	H	2.677690	-4.528766	-0.218489384
H	0.451283	-3.034884	-0.152040	H	0.698628	-3.035132	-0.146442685
H	4.912910	1.047883	-0.224280	H	5.161173	1.041153	-0.205338986
H	4.729691	3.504282	-0.078387	H	5.019882	3.493863	-0.13633619
H	2.448988	4.533154	0.161491	H	2.742797	4.579379	0.003460385
H	0.473128	3.040168	0.181783	H	0.743390	3.116788	0.03284304
H	-2.253645	-1.533470	-4.148434	H	-2.391577	-1.693992	-4.188239807
H	-1.011720	-0.125236	-5.744584	H	-1.245503	-0.299784	-5.851625195
H	0.847304	1.335847	-4.884423	H	0.580471	1.267122	-5.086305438
H	1.300024	1.359964	-2.450259	H	1.104754	1.357379	-2.657155953

Table 5.19. DFT geometry optimized atomic xyz coordinates for Mössbauer calculations on $[Fe(PY5Me_2)(CH_3CN)]^{2+}$. Optimized using B3LYP.

$[Fe(PY5Me_2)(CH_3CN)]^{2+}$, S = 0, UKS			
Fe	8.372002	1.522664	3.175160
C	6.010417	-0.135075	2.380308
C	5.277764	-1.085186	1.696237
C	5.951606	-1.933584	0.834832
C	7.331342	-1.828773	0.752052
C	8.009106	-0.863685	1.491522
C	9.548330	-0.812272	1.530384
C	10.130912	-1.966950	0.704853
C	9.973397	-0.949543	3.004422
C	10.774326	-2.003607	3.434070
C	11.053433	-2.167086	4.781465
C	10.493869	-1.278515	5.682335
C	9.725303	-0.243330	5.185138
C	10.032983	0.530772	0.984852
C	10.910003	0.590516	-0.089999
C	11.328460	1.818562	-0.561906
C	10.849048	2.961411	0.049626
C	9.970380	2.852994	1.119148
C	9.747972	3.045638	5.343383
C	10.451411	4.057020	5.966887
C	10.873703	5.129101	5.200801
C	10.557125	5.139475	3.851196
C	9.839024	4.087667	3.289211
C	9.415440	4.101903	1.810646
C	9.933202	5.372238	1.121906
C	7.878205	4.070517	1.766128
C	7.147307	5.077035	1.141263
C	5.762446	5.074144	1.197182
C	5.135319	4.067876	1.911602
C	5.921119	3.090449	2.489574
C	6.540168	1.428481	5.662915
C	5.692234	1.406461	6.838149
N	7.337549	0.018041	2.257508
N	9.489361	-0.045092	3.879117
N	9.578340	1.649209	1.583829
N	9.452216	3.034237	4.034319
N	7.259991	3.056163	2.400959
N	7.214844	1.442424	4.733820
H	6.118587	2.039195	7.617646
H	4.698929	1.781617	6.586691

H	5.603122	0.387021	7.215661
H	9.255131	0.441823	5.866698
H	10.644824	-1.379182	6.747917
H	11.675752	-2.985589	5.116530
H	11.176226	-2.709733	2.728519
H	11.217014	-1.971071	0.748283
H	9.775440	-2.924386	1.077251
H	9.838865	-1.8839533	0.339017
H	11.271549	-0.306530	-0.560230
H	12.015008	1.884241	-1.394981
H	11.163954	3.923954	-0.312792
H	11.017584	5.432785	1.172712
H	9.646724	5.391089	0.073229
H	9.524097	6.260911	1.595813
H	10.870398	5.973693	3.247649
H	11.429830	5.946455	5.639384
H	10.657374	3.997148	7.026244
H	9.395743	2.213345	5.922468
H	5.457904	2.309855	3.062936
H	4.060935	4.031356	2.023461
H	5.193262	5.853432	0.708644
H	7.647333	5.870650	0.613642
H	5.514741	0.518954	3.073904
H	4.209680	-1.154558	1.846232
H	5.423923	-2.680828	0.257826
H	7.870412	-2.510994	0.117786

Table 5.20. DFT [unrestricted Kohn-Sham, restricted Kohn-Sham (RKS), or broken symmetry (BS)] geometry optimized atomic xyz coordinates for Mössbauer calculations on $[Fe(tpyPY2Me)L]^n$ (n = 2+ or 0; L = CH_3CN or no axial ligand (CN = 5)). Optimized using B3LYP.

$[Fe(tpyPY2Me)(CH_3CN)]^{2+}$, S = 2, UKS				**$[Fe(tpyPY2Me)(CH_3CN)]^{2+}$, S = 1, UKS**			
H	0.224425	9.759395	-5.894650	H	0.120624	9.310142	-6.150542
C	0.136210	9.819536	-4.818151	C	0.050700	9.476136	-5.083705
H	-0.325899	11.927901	-4.756450	H	-0.568612	11.539377	-5.229022
C	-0.170034	11.017852	-4.194855	C	-0.332352	10.708417	-4.579492
C	-0.279254	11.028178	-2.816408	C	-0.404630	10.852450	-3.203915
H	-0.524239	11.936316	-2.286886	H	-0.701904	11.793098	-2.757869
N	-0.092315	9.936764	-2.062535	N	-0.115258	9.864082	-2.354880
C	0.247872	8.768249	-2.653525	C	0.272372	8.671849	-2.829805
C	0.350102	8.691339	-4.036884	C	0.355300	8.447695	-4.199980
H	0.607978	7.762270	-4.517474	H	0.658796	7.492297	-4.594799
C	0.563237	7.552225	-1.737277	C	0.623821	7.570517	-1.785564
C	1.006974	6.338887	-2.557664	C	1.089812	6.291529	-2.489666
H	0.210828	5.993226	-3.213851	H	0.303723	5.883579	-3.120594
H	1.283493	5.516409	-1.901241	H	1.371690	5.529971	-1.765386
Fe	-0.285773	9.960841	-0.079197	Fe	-0.278823	10.071897	-0.114567
C	-0.689134	7.216972	-0.913278	C	-0.639080	7.284419	-0.945729
C	-1.195419	5.924917	-0.816292	C	-1.180782	6.006236	-0.846840
H	-0.704965	5.103061	-1.310476	H	-0.699891	5.166782	-1.319205
C	-2.343057	5.684834	-0.074790	C	-2.355528	5.798471	-0.138545
C	-2.976635	6.751377	0.545264	C	-2.985746	6.882097	0.454122
H	-3.883205	6.617628	1.118057	H	-3.910977	6.772469	1.001453
C	-2.410048	8.004471	0.425477	C	-2.384809	8.119152	0.342942
H	-2.844182	8.858037	0.923849	H	-2.808909	8.987160	0.826495
N	-1.726991	11.393865	-0.070719	N	-1.710197	11.553844	-0.118724
C	-3.011463	11.284613	-0.419773	C	-2.979504	11.477611	-0.527635
H	-3.340104	10.306298	-0.740495	H	-3.289584	10.533312	-0.953727
C	-3.892137	12.356499	-0.391722	C	-3.861192	12.542185	-0.426942
H	-4.923293	12.211887	-0.681688	H	-4.880281	12.433967	-0.769843
C	-3.420235	13.599227	0.004103	C	-3.402651	13.734239	0.116194
C	-2.082449	13.728510	0.351788	C	-2.080829	13.826011	0.531762
H	-1.685999	14.688156	0.650368	H	-1.702124	14.748855	0.946371
C	-1.255660	12.614750	0.305566	C	-1.250815	12.721983	0.403189
C	0.180561	12.641378	0.635039	C	0.173462	12.705775	0.778287
C	0.903910	13.695534	1.185538	C	0.897876	13.732368	1.371714
H	0.436681	14.648186	1.387165	H	0.432642	14.677735	1.608897
C	2.243601	13.492847	1.496303	C	2.240089	13.519171	1.667579
N	-0.467334	9.673869	1.853641	N	-0.514449	9.609567	2.267170
C	-0.550160	9.388068	2.961493	C	-0.588160	9.216197	3.344017

H	-0.998423	9.840829	4.956954	H	-1.017470	9.510455	5.370852
C	-0.666305	8.995896	4.352640	C	-0.698732	8.711531	4.700545
H	-1.392379	8.187364	4.447772	H	-1.432246	7.905439	4.738192
H	0.298711	8.646048	4.722468	H	0.265193	8.325968	5.035409
C	2.836766	12.252658	1.277659	C	2.837707	12.298844	1.372250
H	3.870380	12.083952	1.543732	H	3.879085	12.128157	1.604002
C	2.067706	11.240558	0.718421	C	2.068534	11.310950	0.769723
C	2.484617	9.872368	0.371396	C	2.508011	9.980535	0.326218
C	3.773631	9.366163	0.420464	C	3.797349	9.478904	0.402239
H	4.581355	9.943644	0.846331	H	4.586574	10.039878	0.881066
C	4.007693	8.108818	-0.121214	C	4.050415	8.239869	-0.168279
H	4.997374	7.674505	-0.078296	H	5.041261	7.809289	-0.112128
C	2.987164	7.444919	-0.791798	C	3.045330	7.571525	-0.857556
H	3.196219	6.515277	-1.295939	H	3.270895	6.639493	-1.348610
C	1.717113	8.013009	-0.825043	C	1.769785	8.125620	-0.915192
N	1.474880	9.135746	-0.150896	N	1.522180	9.266007	-0.267754
N	0.785435	11.473326	0.387435	N	0.773517	11.541736	0.487076
N	-1.287431	8.235555	-0.272620	N	-1.238364	8.318040	-0.325330
H	2.823572	14.298463	1.925227	H	2.820484	14.305303	2.130495
H	1.872564	6.579171	-3.170958	H	1.952640	6.490265	-3.120975
H	-2.736207	4.680636	0.011011	H	-2.771748	4.803144	-0.057935
H	-4.078093	14.457123	0.034196	H	-4.061991	14.586801	0.208787

[Fe(tpyPY2Me)(CH$_3$CN)]$^{2+}$, S = 0, UKS				**[Fe(tpyPY2Me)]^0, S = 0, RKS**			
H	0.224461	9.759397	-5.894651	Fe	-0.146365	10.231059	-0.613696
C	0.136232	9.819538	-4.818153	H	0.096712	9.124605	-6.372325
H	-0.325880	11.927902	-4.756457	C	0.006198	9.329693	-5.313642
C	-0.170020	11.017853	-4.194860	H	-0.752639	11.343927	-5.536628
C	-0.279254	11.028180	-2.816414	C	-0.460974	10.556149	-4.855830
H	-0.524245	11.936316	-2.286894	C	-0.534319	10.764109	-3.494883
N	-0.092320	9.936765	-2.062539	H	-0.874599	11.702662	-3.080288
C	0.247873	8.768251	-2.653525	N	-0.176625	9.833305	-2.588604
C	0.350118	8.691341	-4.036884	C	0.262088	8.627854	-3.019584
H	0.608003	7.762273	-4.517470	C	0.360680	8.364196	-4.384132
C	0.563231	7.552228	-1.737275	H	0.722484	7.410855	-4.732728
C	1.006971	6.338888	-2.557658	C	0.651318	7.589485	-1.940831
H	0.210829	5.993229	-3.213851	C	1.055527	6.266758	-2.596921
H	1.283483	5.516409	-1.901232	H	0.239224	5.856934	-3.189824
Fe	-0.285781	9.960846	-0.079200	H	1.332255	5.533801	-1.842808
C	-0.689144	7.216978	-0.913281	C	-0.567153	7.375478	-1.013046
C	-1.195435	5.924925	-0.816298	C	-1.109190	6.114791	-0.773832
H	-0.704985	5.103067	-1.310484	H	-0.681593	5.240555	-1.236433
C	-2.343075	5.684845	-0.074798	C	-2.203573	5.970601	0.064342
C	-2.976648	6.751390	0.545259	C	-2.757244	7.107287	0.642392

H	-3.883220	6.617643	1.118052	H	-3.619160	7.051527	1.292324
C	-2.410056	8.004482	0.425474	C	-2.172653	8.328290	0.379913
H	-2.844187	8.858048	0.923847	H	-2.549600	9.243208	0.814607
N	-1.727000	11.393866	-0.070719	N	-1.614177	11.566334	-0.312561
C	-3.011473	11.284614	-0.419774	C	-2.883573	11.537802	-0.784100
H	-3.340112	10.306300	-0.740500	H	-3.107943	10.724776	-1.464115
C	-3.892147	12.356499	-0.391724	C	-3.847987	12.451125	-0.436902
H	-4.923303	12.211886	-0.681694	H	-4.844113	12.359049	-0.847903
C	-3.420247	13.599229	0.004098	C	-3.512381	13.491717	0.452329
C	-2.082461	13.728513	0.351782	C	-2.225783	13.558153	0.933574
H	-1.686010	14.688160	0.650358	H	-1.935475	14.342427	1.619554
C	-1.255671	12.614753	0.305561	C	-1.274383	12.601296	0.556022
C	0.180551	12.641383	0.635031	C	0.078824	12.535297	1.013768
C	0.903899	13.695541	1.185530	C	0.750109	13.414155	1.844718
H	0.436669	14.648192	1.387156	H	0.239643	14.288696	2.226362
C	2.243590	13.492855	1.496296	C	2.082255	13.177826	2.192218
N	-0.467324	9.673858	1.853635	C	2.727980	12.036883	1.706349
C	-0.550129	9.388050	2.961486	H	3.756724	11.839516	1.979374
H	-0.998343	9.840789	4.956965	C	2.052393	11.157683	0.881770
C	-0.666230	8.995865	4.352633	C	2.521175	9.935906	0.300373
H	-1.392290	8.187321	4.447780	C	3.768775	9.331210	0.465237
H	0.298801	8.646029	4.722430	H	4.516111	9.809062	1.083726
C	2.836755	12.252666	1.277654	C	4.027720	8.125322	-0.148875
H	3.870369	12.083959	1.543729	H	4.985259	7.639309	-0.016509
C	2.067696	11.240565	0.718417	C	3.039553	7.520684	-0.947612
C	2.484606	9.872373	0.371399	H	3.248118	6.578042	-1.427506
C	3.773616	9.366159	0.420483	C	1.820414	8.148119	-1.099281
H	4.581340	9.943639	0.846354	N	1.560490	9.322265	-0.486941
C	4.007675	8.108808	-0.121180	N	0.726639	11.406440	0.514055
H	4.997352	7.674487	-0.078247	N	-1.092393	8.469926	-0.412757
C	2.987149	7.444911	-0.791770	H	2.608712	13.869288	2.834584
H	3.196202	6.515262	-1.295901	H	1.914326	6.408763	-3.249400
C	1.717102	8.013009	-0.825034	H	-2.617568	4.990019	0.259553
N	1.474869	9.135752	-0.150897	H	-4.251843	14.222083	0.752312
N	0.785425	11.473332	0.387428				
N	-1.287438	8.235563	-0.272623				
H	2.823561	14.298472	1.925219				
H	1.872567	6.579171	-3.170946				
H	-2.736229	4.680648	0.011000				
H	-4.078105	14.457125	0.034187				

[Fe(tpyPY2Me)]^{0}, S = 0, BS(2,2)			
Fe	-0.126838	10.260259	-0.580362
H	0.085658	9.127582	-6.379005
C	-0.002416	9.335399	-5.320540
H	-0.728754	11.361080	-5.549761
C	-0.451313	10.570239	-4.866453
C	-0.527761	10.776248	-3.504602
H	-0.860591	11.718774	-3.091047
N	-0.189330	9.839212	-2.602865
C	0.237666	8.633177	-3.026001
C	0.337921	8.364426	-4.390172
H	0.686660	7.406452	-4.739313
C	0.621723	7.600128	-1.942022
C	1.032828	6.278111	-2.596640
H	0.215557	5.863384	-3.184867
H	1.316670	5.547917	-1.842769
C	-0.592953	7.374850	-1.013632
C	-1.114567	6.107328	-0.761111
H	-0.680562	5.233436	-1.218325
C	-2.202642	5.958474	0.085959
C	-2.766349	7.091770	0.661302
H	-3.623015	7.028941	1.317621
C	-2.196522	8.317239	0.382703
H	-2.581411	9.231820	0.812770
N	-1.566072	11.539643	-0.315787
C	-2.831706	11.496131	-0.807128
H	-3.035684	10.677274	-1.486034
C	-3.805572	12.399809	-0.478806
H	-4.794485	12.296400	-0.904174
C	-3.495614	13.453008	0.416520
C	-2.216540	13.534808	0.916579
H	-1.945693	14.325896	1.603417
C	-1.248071	12.590060	0.559439
C	0.099097	12.547921	1.037540
C	0.768457	13.438569	1.881933
H	0.261422	14.313296	2.264356
C	2.092529	13.186004	2.222228
C	2.753439	12.052345	1.740503
H	3.780320	11.857156	2.015889
C	2.063628	11.177063	0.906231
C	2.509619	9.947191	0.306508
C	3.753380	9.344074	0.454285
H	4.506263	9.821633	1.066805
C	4.010777	8.139279	-0.170069

H	4.968690	7.651381	-0.053849
C	3.006145	7.544335	-0.962558
H	3.210882	6.605916	-1.452327
C	1.786402	8.164661	-1.100868
N	1.527362	9.341029	-0.475029
N	0.765575	11.446701	0.565129
N	-1.128975	8.460228	-0.420183
H	2.618846	13.874883	2.869669
H	1.887193	6.423647	-3.253883
H	-2.604515	4.974523	0.290248
H	-4.248358	14.175192	0.701506

Table 5.21. DFT geometry optimized atomic xyz coordinates for $[Fe(tpyPY2Me)L]^n$ (n = 2+, 1+, 0; L = CH_3CN or no axial ligand (CN = 5)). Optimized using ωB97X-D.

$[Fe(tpyPY2Me)(CH_3CN)]^{2+}$, S = 2, UKS				**$[Fe(tpyPY2Me)(CH_3CN)]^{2+}$, S = 1, UKS**			
Fe	-0.499430	9.960170	-0.174540	H	0.158870	9.479710	-6.108970
H	0.139760	9.434500	-6.144330	C	0.067620	9.589380	-5.026780
C	-0.009770	9.520040	-5.066280	H	-0.632850	11.642780	-5.086960
H	-0.944460	11.478510	-5.139410	C	-0.370550	10.783880	-4.468520
C	-0.607970	10.647420	-4.518920	C	-0.464870	10.856140	-3.084110
C	-0.768660	10.687820	-3.141130	H	-0.802340	11.772860	-2.593180
H	-1.231740	11.552540	-2.659070	N	-0.156560	9.834840	-2.283380
N	-0.373540	9.698900	-2.332070	C	0.274710	8.678770	-2.806900
C	0.212180	8.600880	-2.844060	C	0.395850	8.524940	-4.189020
C	0.402600	8.490420	-4.222990	H	0.741530	7.593140	-4.630280
H	0.870690	7.612790	-4.661300	C	0.627680	7.534890	-1.809640
C	0.665530	7.480370	-1.862610	C	1.104070	6.292590	-2.569140
C	1.233460	6.294020	-2.651710	H	0.329820	5.917520	-3.249210
H	0.495140	5.891930	-3.356490	H	1.367410	5.481800	-1.877270
H	1.531960	5.478650	-1.981020	Fe	-0.292990	9.961270	-0.030350
C	-0.563600	7.021010	-1.039830	C	-0.650990	7.214870	-1.001800
C	-1.044240	5.710190	-1.097140	C	-1.245360	5.950670	-1.041260
H	-0.545980	4.952080	-1.695570	H	-0.793690	5.137870	-1.603510
C	-2.186260	5.356520	-0.383650	C	-2.434480	5.715170	-0.359110
C	-2.835900	6.317890	0.381680	C	-3.017050	6.751060	0.362270
H	-3.737920	6.087320	0.949300	H	-3.950300	6.617220	0.909710
C	-2.294620	7.593470	0.407630	C	-2.365530	7.973100	0.377160
H	-2.752890	8.382940	1.008790	H	-2.762730	8.810820	0.954660
N	-1.777060	11.743670	-0.040040	N	-1.739740	11.463480	-0.055250
C	-3.066920	11.764470	-0.386360	C	-3.004710	11.383640	-0.475970
H	-3.480630	10.835390	-0.789720	H	-3.326330	10.415160	-0.866490
C	-3.860260	12.899790	-0.257170	C	-3.875600	12.467930	-0.437720
H	-4.909470	12.873200	-0.553350	H	-4.900580	12.358740	-0.793330

C	-3.277130	14.055870	0.252340	C	-3.404060	13.680600	0.056080
C	-1.931080	14.035930	0.614130	C	-2.080540	13.772180	0.484080
H	-1.459820	14.936580	1.007240	H	-1.688520	14.718080	0.858030
C	-1.203840	12.858410	0.456810	C	-1.268360	12.644530	0.412100
C	0.240700	12.731480	0.814790	C	0.166250	12.628640	0.796510
C	1.004630	13.715180	1.443170	C	0.887220	13.666230	1.386550
H	0.583790	14.684860	1.707510	H	0.418090	14.623110	1.614450
C	2.336620	13.427390	1.737930	C	2.231560	13.452440	1.688740
N	-0.739950	9.685840	2.085100	N	-0.496430	9.624640	2.258750
C	-0.786710	9.573830	3.232260	C	-0.545170	9.448970	3.398100
H	-0.982300	10.411390	5.146490	H	-0.765060	10.178190	5.354090
C	-0.845400	9.427190	4.677700	C	-0.607840	9.223700	4.833530
H	-1.688810	8.778440	4.951630	H	-1.438480	8.544040	5.067800
H	0.088020	8.978250	5.044200	H	0.332820	8.774170	5.179960
C	2.875690	12.185750	1.407980	C	2.833460	12.227430	1.399830
H	3.917150	11.961530	1.637920	H	3.884920	12.058850	1.632850
C	2.051430	11.254660	0.774570	C	2.059500	11.235790	0.802480
C	2.474800	9.899740	0.314920	C	2.510840	9.894090	0.354640
C	3.758350	9.384520	0.464570	C	3.809580	9.405470	0.415340
H	4.538070	9.935250	0.990340	H	4.607470	9.968090	0.900020
C	4.027550	8.136510	-0.089570	C	4.067420	8.174560	-0.184900
H	5.017430	7.689880	0.020730	H	5.071630	7.748760	-0.145450
C	3.045970	7.474840	-0.821160	C	3.061700	7.508800	-0.882200
H	3.287190	6.523420	-1.289100	H	3.298170	6.581820	-1.399470
C	1.780290	8.058670	-0.948920	C	1.776100	8.058030	-0.915530
N	1.521770	9.209590	-0.328860	N	1.532490	9.178350	-0.235420
N	0.781410	11.555470	0.496770	N	0.767300	11.465940	0.520750
N	-1.195000	7.931480	-0.278910	N	-1.221390	8.202050	-0.285180
H	2.958660	14.177480	2.229680	H	2.816090	14.248300	2.153140
H	2.119020	6.590160	-3.227620	H	1.990790	6.517930	-3.174460
H	-2.564200	4.333470	-0.432710	H	-2.898830	4.727950	-0.394920
H	-3.862030	14.970460	0.365710	H	-4.056780	14.554420	0.100360

[Fe(tpyPY2Me)(CH$_3$CN)]$^{2+}$, S = 0, UKS				[Fe(tpyPY2Me)(CH$_3$CN)]$^{1+}$, S = 5/2, UKS			
H	0.147770	9.768170	-5.899190	H	0.466100	9.555950	-6.148580
C	0.078020	9.818710	-4.810970	C	0.215420	9.604470	-5.087140
H	-0.478510	11.915610	-4.729710	H	-0.700610	11.572090	-5.178720
C	-0.270040	11.001770	-4.172710	C	-0.427820	10.716880	-4.560000
C	-0.349530	10.997430	-2.788050	C	-0.717070	10.708570	-3.202590
H	-0.619880	11.904920	-2.246950	H	-1.218170	11.556500	-2.727870
N	-0.105570	9.910030	-2.045440	N	-0.400320	9.689700	-2.399670
C	0.260090	8.759020	-2.650070	C	0.229780	8.606910	-2.886740
C	0.349480	8.691340	-4.040070	C	0.544470	8.543660	-4.247440
H	0.632690	7.767050	-4.537790	H	1.050820	7.679090	-4.668320
C	0.588230	7.534780	-1.749330	C	0.607350	7.463530	-1.905070
C	1.044460	6.340450	-2.590690	C	1.187490	6.280750	-2.689110
H	0.257840	6.010900	-3.280840	H	0.476110	5.901030	-3.434480
H	1.306150	5.488010	-1.950190	H	1.447640	5.455630	-2.015290
Fe	-0.270590	9.914350	-0.048080	Fe	-0.586800	9.933330	-0.246030
C	-0.685160	7.188660	-0.956510	C	-0.660230	7.009200	-1.141230
C	-1.262780	5.917670	-0.986600	C	-1.126050	5.691100	-1.198960
H	-0.806860	5.107650	-1.550610	H	-0.600230	4.934450	-1.774630
C	-2.441510	5.675920	-0.288730	C	-2.281470	5.329620	-0.513370
C	-3.021920	6.713010	0.433130	C	-2.962210	6.287280	0.228460
H	-3.947420	6.574760	0.992960	H	-3.870800	6.049330	0.781940
C	-2.384710	7.943540	0.430340	C	-2.439420	7.571100	0.254080
H	-2.786880	8.780630	1.004160	H	-2.911250	8.360000	0.844520
N	-1.729390	11.343720	-0.040340	N	-1.934900	11.676300	-0.088770
C	-3.000840	11.228450	-0.431530	C	-3.199620	11.726880	-0.518600
H	-3.322020	10.236300	-0.755590	H	-3.583480	10.824450	-1.004120
C	-3.884730	12.303910	-0.449610	C	-3.999870	12.851850	-0.373850
H	-4.914070	12.156370	-0.778320	H	-5.027080	12.847830	-0.739310
C	-3.423800	13.553080	-0.048670	C	-3.447170	13.974340	0.242220
C	-2.092430	13.686240	0.341390	C	-2.132390	13.924940	0.688970
H	-1.699960	14.659400	0.637550	H	-1.677510	14.795400	1.160780
C	-1.267550	12.565790	0.329370	C	-1.391740	12.752520	0.516050
C	0.175020	12.599920	0.681530	C	0.018260	12.593760	0.973390
C	0.881350	13.654110	1.262010	C	0.675890	13.484760	1.796580
H	0.400560	14.608310	1.478070	H	0.204450	14.400750	2.149690
C	2.222830	13.452240	1.585480	C	2.007050	13.161270	2.193130
N	-0.427950	9.665070	1.914270	N	-0.956180	9.550070	2.094380
C	-0.484180	9.507830	3.054150	C	-0.387600	9.793720	3.069200
H	-0.709130	10.267880	4.997640	H	1.022810	11.005100	4.004990
C	-0.551820	9.305090	4.492280	C	0.374700	10.151030	4.253570
H	-1.385090	8.631140	4.734560	H	-0.301170	10.430040	5.072690
H	0.386450	8.858210	4.848990	H	0.997410	9.302580	4.566910
C	2.830730	12.217890	1.348950	C	2.585030	11.984150	1.781010

H	3.871680	12.050410	1.626800	H	3.599710	11.734350	2.094960
C	2.069760	11.212610	0.758010	C	1.855300	11.092950	0.948670
C	2.499490	9.839990	0.391260	C	2.292060	9.813420	0.480240
C	3.795780	9.342990	0.440070	C	3.567800	9.231820	0.701470
H	4.607680	9.923610	0.878750	H	4.307930	9.738450	1.321700
C	4.036560	8.090580	-0.122760	C	3.862580	8.030800	0.105980
H	5.037960	7.657950	-0.086090	H	4.838180	7.567160	0.264240
C	3.017830	7.425940	-0.801620	C	2.924300	7.400730	-0.746970
H	3.236860	6.493510	-1.318180	H	3.199200	6.477470	-1.249430
C	1.739300	7.990020	-0.826490	C	1.686790	8.004660	-0.918920
N	1.499330	9.105320	-0.138950	N	1.376160	9.132880	-0.276900
N	0.793360	11.446200	0.418470	N	0.593130	11.459570	0.542510
N	-1.251560	8.179520	-0.247380	N	-1.331270	7.915620	-0.410740
H	2.796570	14.259640	2.043930	H	2.563730	13.850970	2.829730
H	1.930530	6.591510	-3.187370	H	2.106970	6.572490	-3.209850
H	-2.899280	4.685320	-0.312450	H	-2.643560	4.300800	-0.562350
H	-4.086970	14.419950	-0.049930	H	-4.036390	14.884370	0.369280

[Fe(tpyPY2Me)(CH$_3$CN)]$^{1+}$, S = 3/2, UKS				[Fe(tpyPY2Me)(CH$_3$CN)]$^{1+}$, S = 1/2, UKS			
Fe	-0.384100	10.202730	-0.399700	H	0.283910	9.836670	-5.897010
H	0.572380	9.259390	-6.232850	C	0.171950	9.867610	-4.811620
C	0.363090	9.438230	-5.176410	H	-0.350960	11.973260	-4.709280
H	-0.319170	11.482820	-5.445250	C	-0.181330	11.044470	-4.164290
C	-0.129620	10.665550	-4.748960	C	-0.313880	11.014000	-2.784070
C	-0.377240	10.823890	-3.392280	H	-0.582940	11.913460	-2.229050
H	-0.767650	11.765020	-2.994650	N	-0.116860	9.908970	-2.056880
N	-0.154380	9.855950	-2.500290	C	0.258970	8.764970	-2.664860
C	0.326610	8.666040	-2.891110	C	0.397230	8.722940	-4.053700
C	0.590840	8.430390	-4.242930	H	0.689630	7.803890	-4.555350
H	0.976410	7.472400	-4.582920	C	0.562240	7.531970	-1.774380
C	0.573530	7.595370	-1.796460	C	1.015310	6.343770	-2.624300
C	1.085560	6.301850	-2.436420	H	0.235230	6.024200	-3.327990
H	0.365420	5.898280	-3.160120	H	1.270040	5.488200	-1.985860
H	1.267820	5.534340	-1.673970	Fe	-0.319870	9.899910	-0.068970
C	-0.754760	7.328230	-1.049390	C	-0.717490	7.181990	-0.996940
C	-1.350970	6.064790	-1.020400	C	-1.287780	5.905640	-1.027020
H	-0.897050	5.217270	-1.527300	H	-0.825210	5.104280	-1.597660
C	-2.545700	5.878050	-0.330870	C	-2.456940	5.649680	-0.320500
C	-3.129110	6.955290	0.324350	C	-3.040530	6.678150	0.411430
H	-4.059140	6.854280	0.884030	H	-3.957500	6.529290	0.982220
C	-2.483820	8.181350	0.254900	C	-2.415830	7.915070	0.404230
H	-2.875480	9.058160	0.773270	H	-2.818510	8.749630	0.981900
N	-1.872120	11.560970	-0.294770	N	-1.777460	11.333430	-0.063690
C	-3.084560	11.487200	-0.854750	C	-3.049000	11.220590	-0.461250
H	-3.287640	10.588470	-1.442600	H	-3.363590	10.229210	-0.795390
C	-4.039910	12.484220	-0.707480	C	-3.935650	12.289860	-0.471590
H	-5.016460	12.379510	-1.180760	H	-4.962790	12.143960	-0.807110
C	-3.714080	13.606460	0.051700	C	-3.476020	13.536850	-0.052770
C	-2.451400	13.692480	0.628760	C	-2.150020	13.667520	0.343010
H	-2.168430	14.563150	1.220120	H	-1.753830	14.635010	0.651390
C	-1.542490	12.653490	0.441570	C	-1.314810	12.549930	0.323330
C	-0.168350	12.628210	1.004920	C	0.125760	12.584230	0.677060
C	0.385860	13.536660	1.878430	C	0.801700	13.627110	1.283720
H	-0.160430	14.412780	2.224760	H	0.308910	14.566550	1.531260
C	1.711540	13.279730	2.338740	C	2.171160	13.418100	1.605870
N	-0.986380	9.694110	2.500670	N	-0.453450	9.672820	1.889470
C	-0.038130	9.449230	3.113850	C	-0.383210	9.572360	3.034040
H	1.667410	10.096440	4.144710	H	-0.387550	10.441300	4.943260
C	1.172150	9.155430	3.868340	C	-0.260160	9.454390	4.478320
H	0.926190	8.594250	4.779920	H	-1.023570	8.768760	4.869530
H	1.856710	8.561120	3.246490	H	0.736040	9.065240	4.729070

C	2.392720	12.150150	1.949750	C	2.777970	12.208880	1.356990
H	3.399400	11.957350	2.324160	H	3.820500	12.047350	1.635550
C	1.768860	11.232130	1.061990	C	2.034570	11.164220	0.743420
C	2.228950	9.967670	0.598730	C	2.432390	9.830710	0.445680
C	3.480880	9.361620	0.872360	C	3.726640	9.257160	0.560040
H	4.201270	9.865420	1.518270	H	4.524250	9.800270	1.069360
C	3.774390	8.148740	0.301540	C	3.967000	8.035770	-0.017670
H	4.733710	7.667250	0.499520	H	4.956500	7.581070	0.058040
C	2.850230	7.525860	-0.573350	C	2.958960	7.390190	-0.784500
H	3.116390	6.585210	-1.047170	H	3.199430	6.487040	-1.339930
C	1.632620	8.147040	-0.808200	C	1.701570	7.967280	-0.821070
N	1.320080	9.301800	-0.206090	N	1.425830	9.066260	-0.112740
N	0.521510	11.551870	0.589550	N	0.739000	11.433100	0.372090
N	-1.339350	8.358270	-0.414730	N	-1.291240	8.163850	-0.281310
H	2.184740	13.987980	3.020990	H	2.739620	14.222850	2.075380
H	2.032230	6.475670	-2.962210	H	1.913430	6.598130	-3.200030
H	-3.011700	4.891090	-0.306400	H	-2.904690	4.654500	-0.343290
H	-4.437650	14.411720	0.190700	H	-4.140810	14.402550	-0.047280

[Fe(tpyPY2Me)]^0, *S* = 2, UKS				**[Fe(tpyPY2Me)]^0, *S* = 1, UKS**			
H	0.227750	9.340660	-6.250010	H	0.126410	9.274020	-6.278320
C	0.088700	9.474980	-5.175210	C	0.029690	9.433130	-5.202270
H	-0.707370	11.491620	-5.321640	H	-0.722960	11.466060	-5.361910
C	-0.427010	10.663570	-4.669640	C	-0.439420	10.644480	-4.703150
C	-0.572770	10.771850	-3.292230	C	-0.533120	10.784250	-3.325000
H	-0.966200	11.678690	-2.823360	H	-0.887690	11.708770	-2.860350
N	-0.241240	9.787530	-2.457690	N	-0.197170	9.807720	-2.481140
C	0.254800	8.635560	-2.921710	C	0.254060	8.633630	-2.938500
C	0.432140	8.450710	-4.297590	C	0.379160	8.418870	-4.316320
H	0.837200	7.523220	-4.695790	H	0.746830	7.473930	-4.709760
C	0.621580	7.551250	-1.876500	C	0.625210	7.561020	-1.883350
C	1.065920	6.269260	-2.585080	C	1.064360	6.270770	-2.579840
H	0.274850	5.873220	-3.236400	H	0.263110	5.861780	-3.210160
H	1.335340	5.495450	-1.855330	H	1.347340	5.507750	-1.843840
Fe	-0.219040	10.110090	-0.271930	Fe	-0.188280	10.129620	-0.337730
C	-0.630880	7.274790	-1.015760	C	-0.620700	7.293050	-1.010990
C	-1.205940	6.001520	-0.923120	C	-1.182590	6.017940	-0.875070
H	-0.771390	5.154150	-1.446970	H	-0.746050	5.160410	-1.381160
C	-2.345930	5.805380	-0.152270	C	-2.311340	5.835690	-0.084800
C	-2.903380	6.887360	0.520440	C	-2.869020	6.934480	0.561490
H	-3.795860	6.785590	1.138430	H	-3.754300	6.844350	1.191710
C	-2.279270	8.118600	0.393700	C	-2.258890	8.166920	0.390070
H	-2.658230	9.004990	0.908830	H	-2.642160	9.065490	0.880460
N	-1.665740	11.458600	-0.125740	N	-1.642710	11.474930	-0.180060

C	-2.934520	11.404180	-0.576010	C	-2.901680	11.429370	-0.657890
H	-3.196410	10.491770	-1.123480	H	-3.147240	10.534080	-1.239990
C	-3.862880	12.400030	-0.389720	C	-3.839570	12.414910	-0.459430
H	-4.872750	12.295050	-0.786250	H	-4.840490	12.316720	-0.879920
C	-3.457440	13.565910	0.334680	C	-3.457250	13.559040	0.308680
C	-2.170090	13.658900	0.794430	C	-2.181240	13.639530	0.802560
H	-1.840920	14.543330	1.342990	H	-1.868790	14.507030	1.387150
C	-1.240850	12.609820	0.557680	C	-1.245070	12.600250	0.556710
C	0.131340	12.606070	0.948420	C	0.116120	12.578700	0.985420
C	0.853040	13.589150	1.676170	C	0.820000	13.527980	1.746830
H	0.371750	14.511670	1.999890	H	0.330170	14.442510	2.083010
C	2.190010	13.336730	1.975240	C	2.152530	13.279560	2.074450
C	2.832490	12.158780	1.588460	C	2.800030	12.107220	1.667250
H	3.878020	11.979930	1.838690	H	3.839000	11.916570	1.936530
C	2.085290	11.202700	0.856850	C	2.073320	11.183810	0.903400
C	2.501810	9.929810	0.360950	C	2.507290	9.918900	0.367120
C	3.782650	9.335310	0.483960	C	3.786830	9.357740	0.451530
H	4.557580	9.840390	1.063320	H	4.565530	9.879440	1.011020
C	4.036400	8.140500	-0.135480	C	4.053670	8.162390	-0.184390
H	5.018830	7.672540	-0.046860	H	5.043450	7.707500	-0.127600
C	3.023770	7.506180	-0.928210	C	3.029390	7.543490	-0.954920
H	3.260870	6.589220	-1.460960	H	3.262040	6.632890	-1.502750
C	1.779540	8.099160	-0.996380	C	1.777710	8.113700	-1.008270
N	1.508190	9.234830	-0.336310	N	1.492990	9.248450	-0.315640
N	0.786710	11.480310	0.557550	N	0.781590	11.447190	0.577200
N	-1.181360	8.305190	-0.349990	N	-1.168820	8.339450	-0.369680
H	2.755210	14.085850	2.536160	H	2.701420	14.015140	2.666990
H	1.952750	6.457260	-3.201670	H	1.938600	6.451020	-3.216960
H	-2.791510	4.811290	-0.078630	H	-2.749300	4.841360	0.023240
H	-4.167130	14.375810	0.516070	H	-4.173560	14.361320	0.497330

[Fe(tpyPY2Me)]^0, S = 0 (S_{Fe} = 1; S_{tpy} = 1), UKS				**[Fe(tpyPY2Me)]^0, S = 0 (S_{Fe} = 0; S_{tpy} = 0), UKS**			
H	-0.036790	9.155880	-6.348510	H	-0.039480	9.295390	-6.292810
C	-0.100840	9.349610	-5.275810	C	-0.086190	9.461740	-5.214920
H	-0.909730	11.357990	-5.472710	H	-0.825660	11.502990	-5.342960
C	-0.582260	10.565250	-4.799230	C	-0.519860	10.679900	-4.696110
C	-0.629040	10.752120	-3.425860	C	-0.547850	10.837430	-3.321160
H	-0.986120	11.687350	-2.986970	H	-0.862900	11.773950	-2.857970
N	-0.238870	9.814880	-2.555050	N	-0.180830	9.864410	-2.468810
C	0.219780	8.633000	-2.993350	C	0.234070	8.676780	-2.954090
C	0.302150	8.377280	-4.367440	C	0.292420	8.456510	-4.334300
H	0.678850	7.427310	-4.739110	H	0.635070	7.503150	-4.730410
C	0.640020	7.594750	-1.926840	C	0.638360	7.604400	-1.921150

C	1.067510	6.289740	-2.602180	C	1.019010	6.297790	-2.617310
H	0.254180	5.863990	-3.205350	H	0.185350	5.901080	-3.212410
H	1.365030	5.544540	-1.854160	H	1.307340	5.535550	-1.882300
Fe	-0.116610	10.243740	-0.511330	Fe	-0.107260	10.176720	-0.550850
C	-0.577820	7.344430	-1.007530	C	-0.564100	7.392030	-0.978580
C	-1.127840	6.071280	-0.816120	C	-1.149730	6.138520	-0.772030
H	-0.704450	5.198830	-1.308120	H	-0.764130	5.256000	-1.277740
C	-2.230100	5.913720	0.016270	C	-2.232280	6.011110	0.088880
C	-2.769820	7.031250	0.645870	C	-2.713720	7.148420	0.733710
H	-3.633690	6.957590	1.307360	H	-3.559140	7.103580	1.421220
C	-2.169300	8.260060	0.416290	C	-2.086260	8.358300	0.492160
H	-2.536980	9.174670	0.888510	H	-2.409780	9.278950	0.980630
N	-1.560930	11.512110	-0.274110	N	-1.561150	11.444920	-0.316850
C	-2.812400	11.475950	-0.801340	C	-2.803380	11.381210	-0.857580
H	-3.023250	10.611190	-1.439090	H	-2.992760	10.509810	-1.491760
C	-3.766130	12.433130	-0.575160	C	-3.778910	12.326920	-0.645740
H	-4.752090	12.339750	-1.032110	H	-4.758330	12.213620	-1.112590
C	-3.438500	13.541490	0.263810	C	-3.481040	13.434820	0.182420
C	-2.180950	13.606060	0.813020	C	-2.228830	13.524640	0.744900
H	-1.901060	14.441240	1.458150	H	-1.966830	14.366610	1.388030
C	-1.228050	12.594940	0.552670	C	-1.261990	12.525730	0.496120
C	0.107510	12.546870	1.059830	C	0.072350	12.481830	1.005020
C	0.777410	13.451910	1.911310	C	0.724910	13.377570	1.841270
H	0.272260	14.343850	2.282520	H	0.201410	14.266260	2.201030
C	2.096440	13.181110	2.266610	C	2.052240	13.145260	2.224010
C	2.763030	12.043860	1.802300	C	2.715460	12.000290	1.754360
H	3.795980	11.844010	2.087770	H	3.750910	11.807890	2.044630
C	2.067250	11.161810	0.955570	C	2.055590	11.113210	0.920670
C	2.515040	9.941430	0.348670	C	2.532360	9.898630	0.329510
C	3.781230	9.346430	0.475320	C	3.799410	9.302870	0.457200
H	4.540440	9.828710	1.093830	H	4.561520	9.781100	1.074400
C	4.051220	8.166010	-0.179430	C	4.060210	8.119950	-0.201190
H	5.029220	7.690570	-0.091350	H	5.038440	7.643720	-0.112250
C	3.037530	7.561440	-0.981000	C	3.058590	7.519600	-0.995130
H	3.259420	6.629370	-1.495800	H	3.271470	6.586280	-1.512760
C	1.807020	8.167180	-1.085310	C	1.825850	8.138740	-1.093720
N	1.537810	9.329920	-0.439670	N	1.572710	9.293570	-0.448070
N	0.776150	11.441450	0.617990	N	0.735270	11.348230	0.543960
N	-1.107980	8.407660	-0.384390	N	-1.038430	8.481790	-0.341520
H	2.623800	13.875460	2.925130	H	2.566360	13.848130	2.880420
H	1.929760	6.457050	-3.259440	H	1.875190	6.448840	-3.287030
H	-2.661860	4.922610	0.170130	H	-2.691130	5.034640	0.255360
H	-4.174180	14.322470	0.463900	H	-4.231480	14.204940	0.371150

Table 5.22. DFT geometry optimized atomic xyz coordinates for $[Zn(tpyPY2Me)]^n$ (n = 2+, 1+, 0). Optimized using ωB97X-D implemented in Q-Chem.

$[Zn(tpyPY2Me)]^{2+}$, S = 0, UKS				**$[Zn(tpyPY2Me)]^{1+}$, S = 1/2, UKS**			
H	0.079310	9.010120	-6.416540	H	0.149920	9.053920	-6.412420
C	-0.005160	9.247100	-5.354250	C	0.033020	9.271900	-5.349060
H	-0.758010	11.262960	-5.652210	H	-0.759590	11.275090	-5.634750
C	-0.468120	10.489960	-4.940340	C	-0.469340	10.497210	-4.928380
C	-0.552480	10.723010	-3.576370	C	-0.589530	10.705610	-3.562660
H	-0.910410	11.681490	-3.191260	H	-0.974510	11.649080	-3.165410
N	-0.205630	9.805390	-2.663930	N	-0.244050	9.783220	-2.659270
C	0.251170	8.593290	-3.041460	C	0.248490	8.588910	-3.039470
C	0.355270	8.296000	-4.401150	C	0.391550	8.315230	-4.403060
H	0.715880	7.329310	-4.742000	H	0.783880	7.362190	-4.747180
C	0.654160	7.562560	-1.943590	C	0.653590	7.555700	-1.949220
C	1.116650	6.257390	-2.602770	C	1.103580	6.251670	-2.616980
H	0.322510	5.808060	-3.211480	H	0.305260	5.806560	-3.225370
H	1.417960	5.521870	-1.846950	H	1.410930	5.517050	-1.863260
Zn	-0.345690	10.181820	-0.649400	Zn	-0.290840	10.191690	-0.612400
C	-0.561360	7.278660	-1.010140	C	-0.558120	7.274250	-1.015110
C	-1.072180	5.991010	-0.840160	C	-1.046310	5.979990	-0.811880
H	-0.642710	5.139700	-1.361060	H	-0.597690	5.125330	-1.310690
C	-2.153330	5.774810	0.012400	C	-2.122600	5.765520	0.044810
C	-2.717690	6.849100	0.689100	C	-2.709270	6.845820	0.692540
H	-3.561540	6.723450	1.367680	H	-3.551260	6.722430	1.373820
C	-2.168240	8.103740	0.474950	C	-2.181050	8.104160	0.446070
H	-2.570040	8.986630	0.978860	H	-2.594100	8.995770	0.926000
N	-1.767300	11.703100	-0.233010	N	-1.784040	11.716220	-0.234640
C	-3.018520	11.742430	-0.702740	C	-3.037800	11.766330	-0.704010
H	-3.322610	10.919420	-1.355430	H	-3.342490	10.943180	-1.357590
C	-3.901000	12.769790	-0.387250	C	-3.914650	12.792120	-0.391660
H	-4.914140	12.765580	-0.790230	H	-4.927390	12.794700	-0.795260
C	-3.454730	13.789210	0.448580	C	-3.458940	13.810880	0.450490
C	-2.149860	13.747800	0.937960	C	-2.161580	13.761610	0.938300
H	-1.788460	14.539650	1.593340	H	-1.792480	14.547490	1.596280
C	-1.324290	12.686480	0.578180	C	-1.328760	12.694300	0.580400
C	0.088300	12.551630	1.050570	C	0.073630	12.552120	1.049530
C	0.755830	13.446230	1.887220	C	0.731060	13.436310	1.876520
H	0.271710	14.343750	2.270330	H	0.247980	14.334920	2.258500
C	2.078560	13.165040	2.229310	C	2.078650	13.149660	2.228140
C	2.706280	12.018400	1.742880	C	2.695720	12.014110	1.744540
H	3.739830	11.800240	2.010900	H	3.730310	11.797530	2.014960
C	1.975530	11.171190	0.911880	C	1.983720	11.136850	0.899480
C	2.475910	9.902870	0.297280	C	2.471210	9.919460	0.307690

C	3.749860	9.371380	0.467740	C	3.761190	9.353330	0.460130
H	4.499860	9.863700	1.086440	H	4.513720	9.842810	1.079040
C	4.043570	8.175020	-0.184380	C	4.048160	8.174630	-0.186420
H	5.032090	7.725180	-0.075250	H	5.036640	7.723740	-0.080160
C	3.083550	7.546720	-0.975860	C	3.076730	7.529880	-0.993720
H	3.334630	6.613720	-1.475200	H	3.330630	6.598710	-1.493810
C	1.823000	8.139960	-1.101520	C	1.832640	8.127800	-1.107180
N	1.574540	9.279570	-0.466690	N	1.564740	9.270300	-0.475930
N	0.711350	11.464410	0.600450	N	0.683900	11.443570	0.583040
N	-1.129370	8.306910	-0.346440	N	-1.147620	8.303880	-0.377790
H	2.625770	13.847500	2.881890	H	2.623210	13.832390	2.881370
H	1.982070	6.432270	-3.253660	H	1.971320	6.428020	-3.263590
H	-2.548270	4.765380	0.143120	H	-2.497350	4.752260	0.202030
H	-4.115620	14.614330	0.720630	H	-4.115660	14.638910	0.723610

[Zn(tpyPY2Me)]^0, *S* = 0, UKS			
H	0.185400	9.077140	-6.416410
C	0.048610	9.283190	-5.352830
H	-0.779760	11.273460	-5.632240
C	-0.482960	10.495250	-4.928850
C	-0.624860	10.689420	-3.561800
H	-1.034190	11.618010	-3.152160
N	-0.273350	9.765690	-2.665940
C	0.239910	8.584260	-3.045790
C	0.409180	8.323680	-4.411000
H	0.822570	7.379850	-4.756030
C	0.641860	7.554730	-1.955540
C	1.090990	6.250400	-2.622230
H	0.290430	5.804420	-3.228700
H	1.402420	5.519510	-1.866920
Zn	-0.306800	10.248350	-0.587180
C	-0.565750	7.271880	-1.022020
C	-1.034770	5.973730	-0.787860
H	-0.570140	5.114510	-1.263940
C	-2.111250	5.766730	0.069920
C	-2.717980	6.855170	0.685320
H	-3.563760	6.737990	1.363120
C	-2.204870	8.115110	0.409330
H	-2.628410	9.019630	0.856490
N	-1.748670	11.669340	-0.247530
C	-3.017800	11.734360	-0.710210
H	-3.322360	10.907770	-1.363740
C	-3.898810	12.741770	-0.410780

H	-4.909390	12.730000	-0.820210
C	-3.449140	13.795960	0.448270
C	-2.164910	13.753440	0.931770
H	-1.802380	14.546390	1.588380
C	-1.291220	12.691350	0.593600
C	0.069040	12.572800	1.059600
C	0.760650	13.459660	1.907190
H	0.282710	14.358430	2.296780
C	2.083790	13.161600	2.241240
C	2.723730	12.017610	1.757920
H	3.757560	11.802680	2.029630
C	2.000070	11.155750	0.914670
C	2.464780	9.931570	0.310750
C	3.748100	9.354040	0.452560
H	4.498760	9.846880	1.073220
C	4.043420	8.177180	-0.190470
H	5.030940	7.724000	-0.085700
C	3.053320	7.534250	-1.004380
H	3.298800	6.603350	-1.509630
C	1.815940	8.138330	-1.108960
N	1.530750	9.282050	-0.482200
N	0.714340	11.469770	0.605410
N	-1.170330	8.304010	-0.411440
H	2.632540	13.841530	2.897500
H	1.959130	6.427600	-3.267780
H	-2.471930	4.752260	0.252260
H	-4.115570	14.618460	0.714530

5.5.21 NMR Spectra

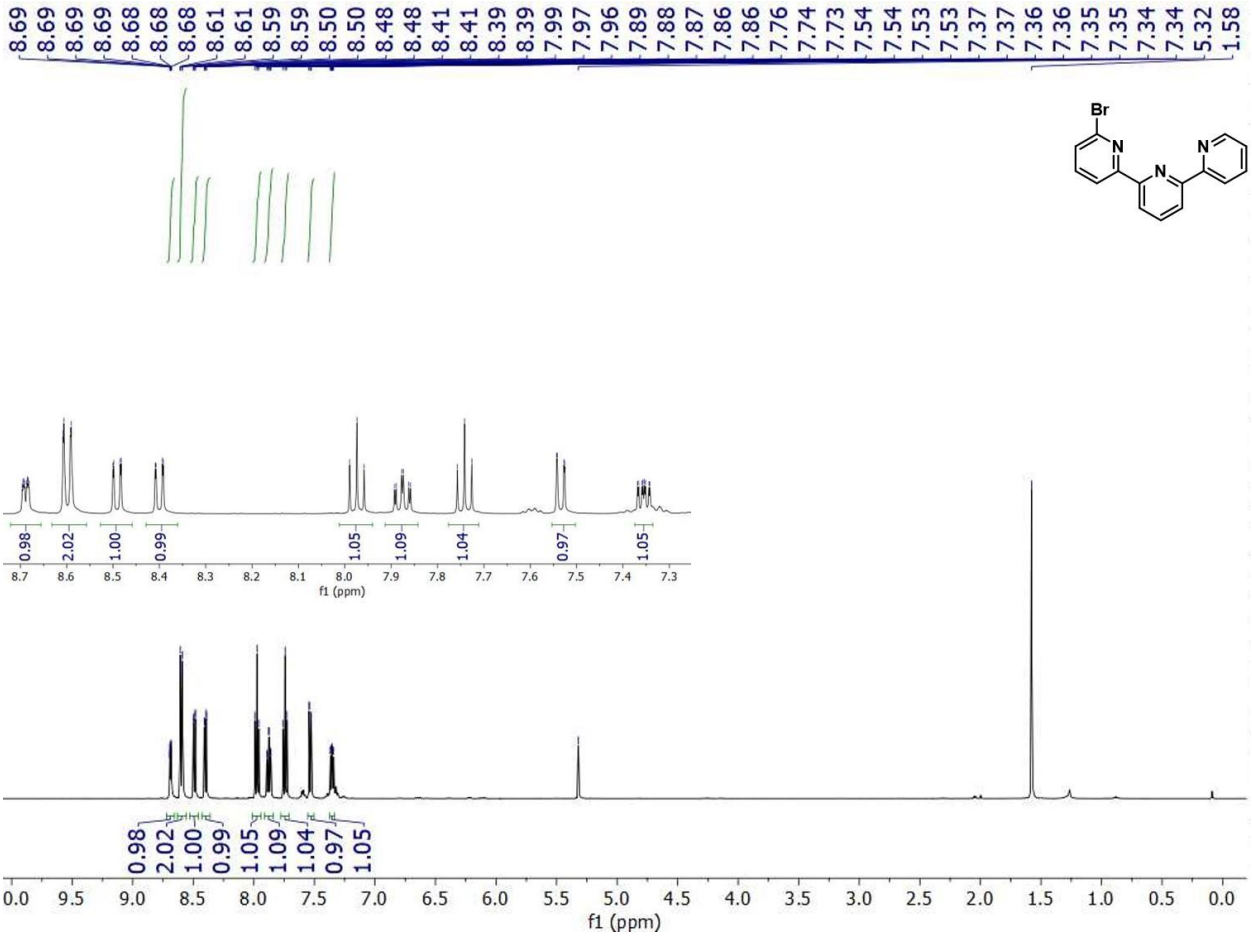


Figure 5.50. ^{1}H NMR of 6-bromo-2,2':6'2"-terpyridine in CD_2Cl_2.

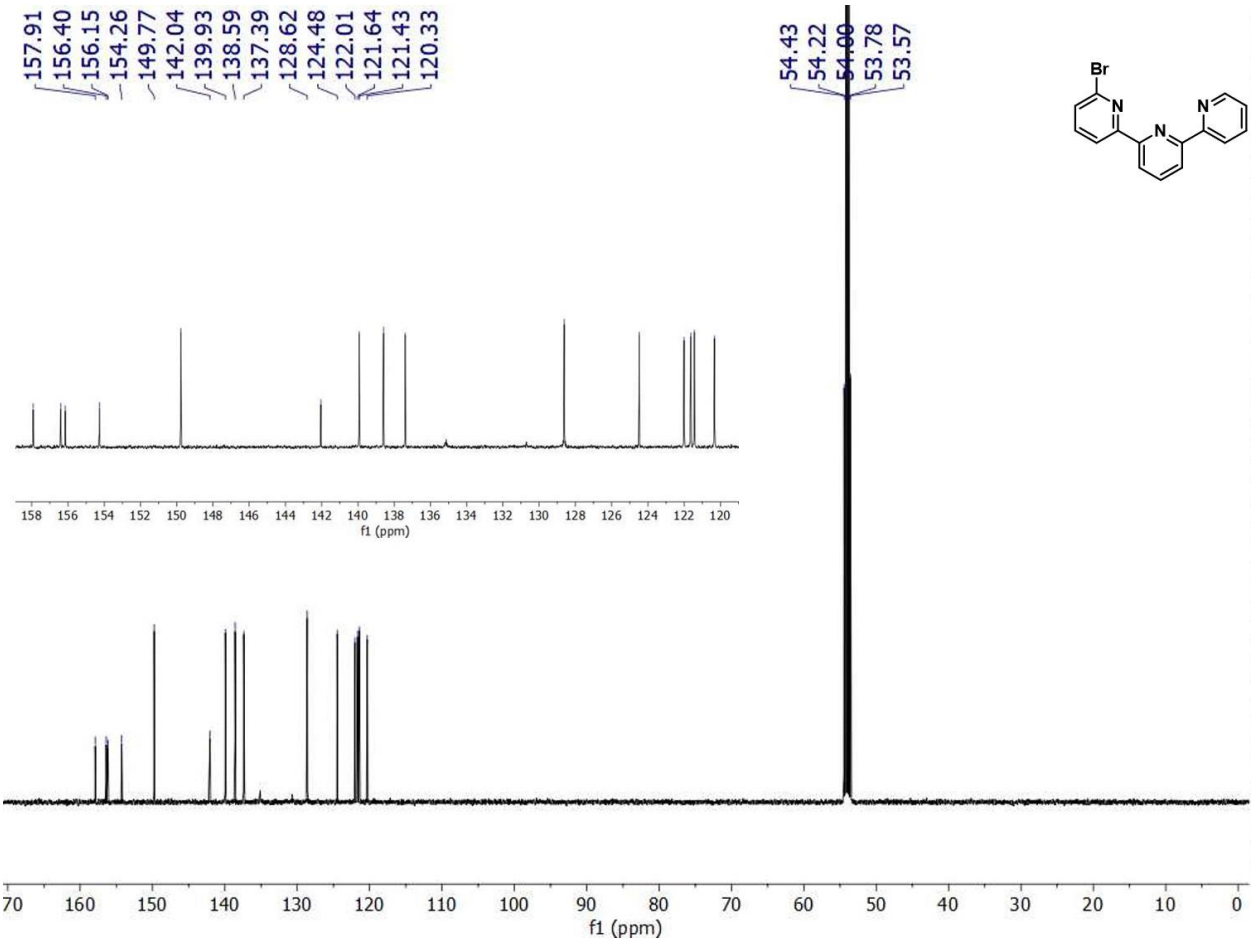


Figure 5.51. ^{13}C NMR of 6-bromo-2,2':6'2"-terpyridine in CD_2Cl_2.

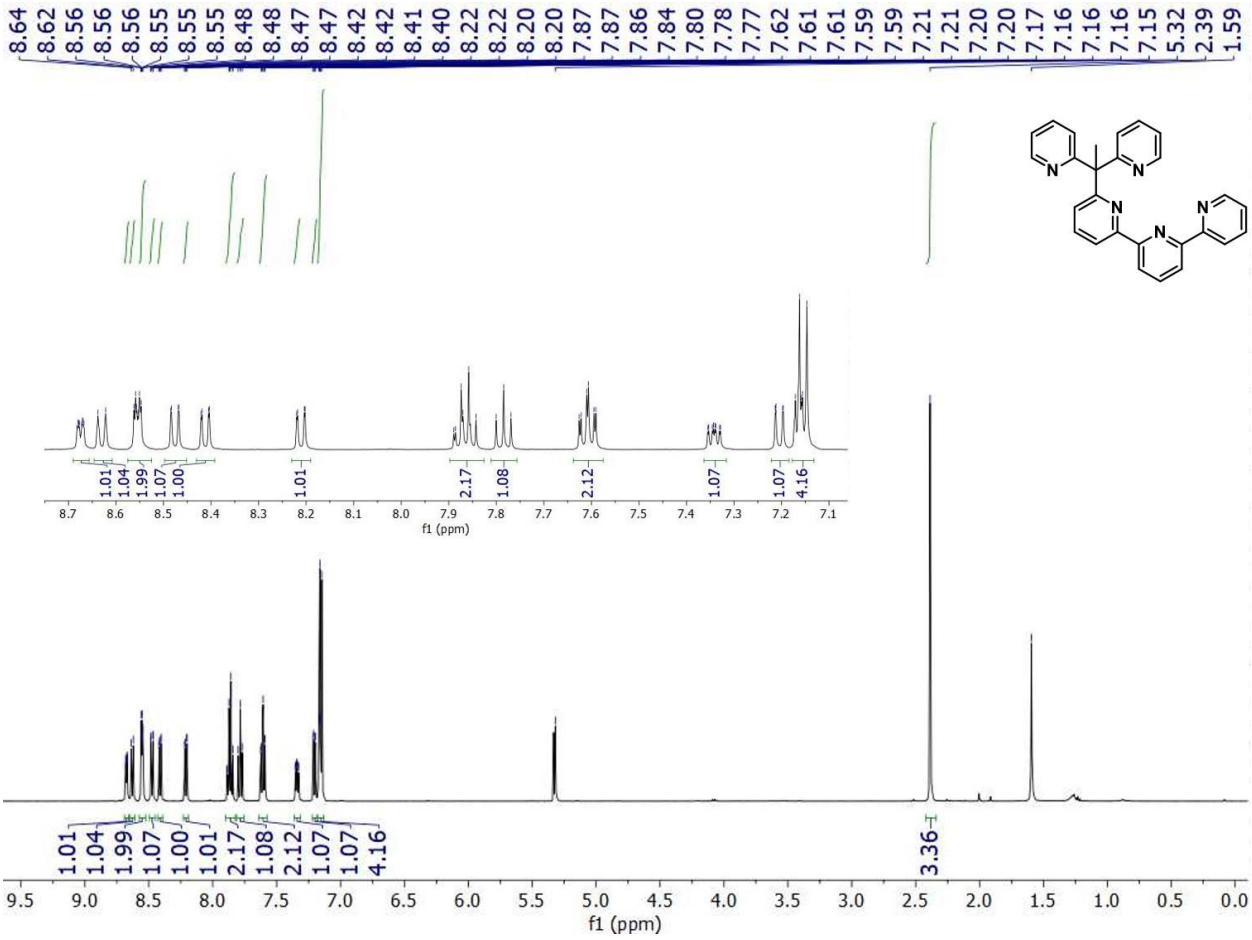


Figure 5.52. ^{1}H NMR of tpyPY2Me in CD_2Cl_2.

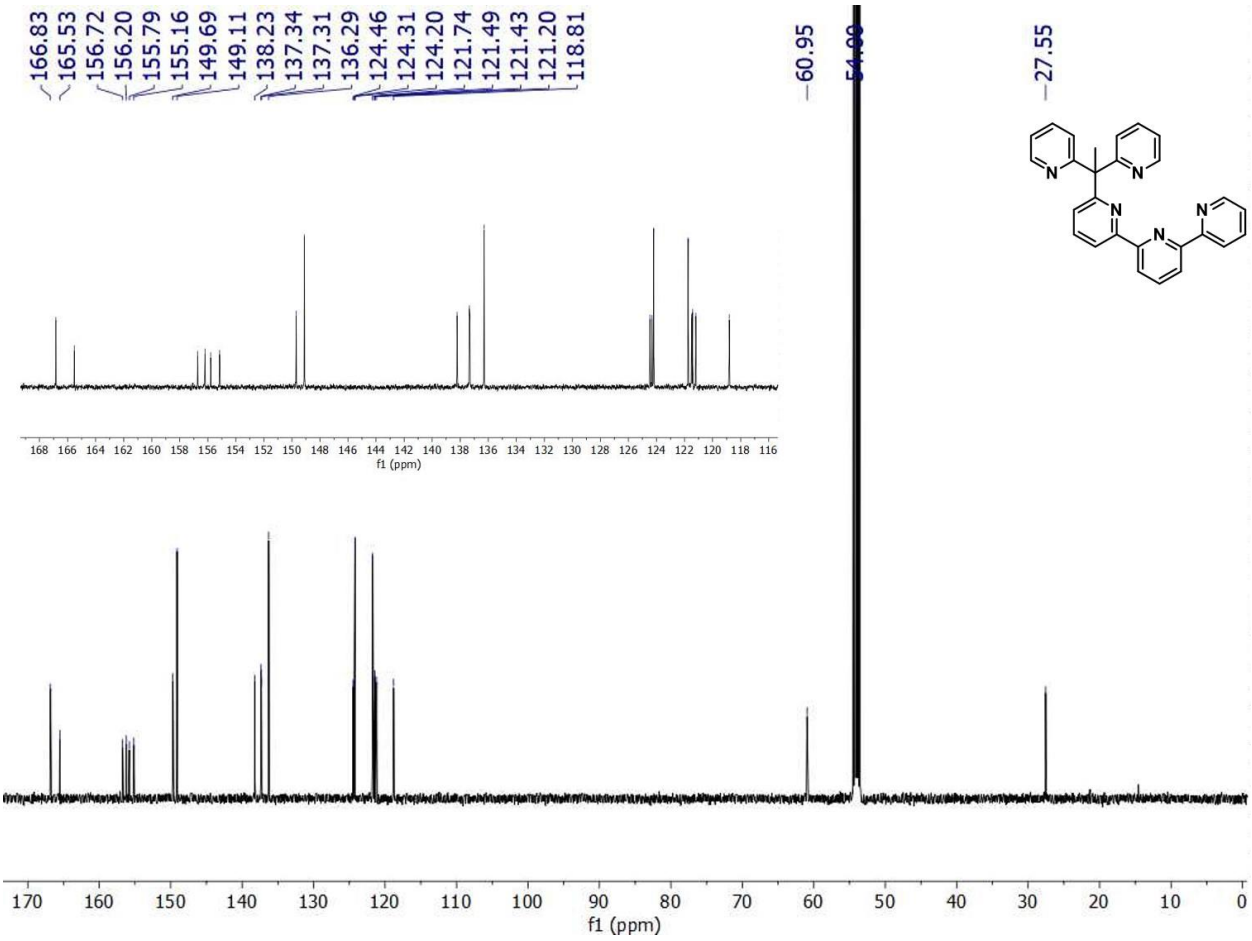


Figure 5.53. ^{13}C NMR of tpyPY2Me in CD_2Cl_2.

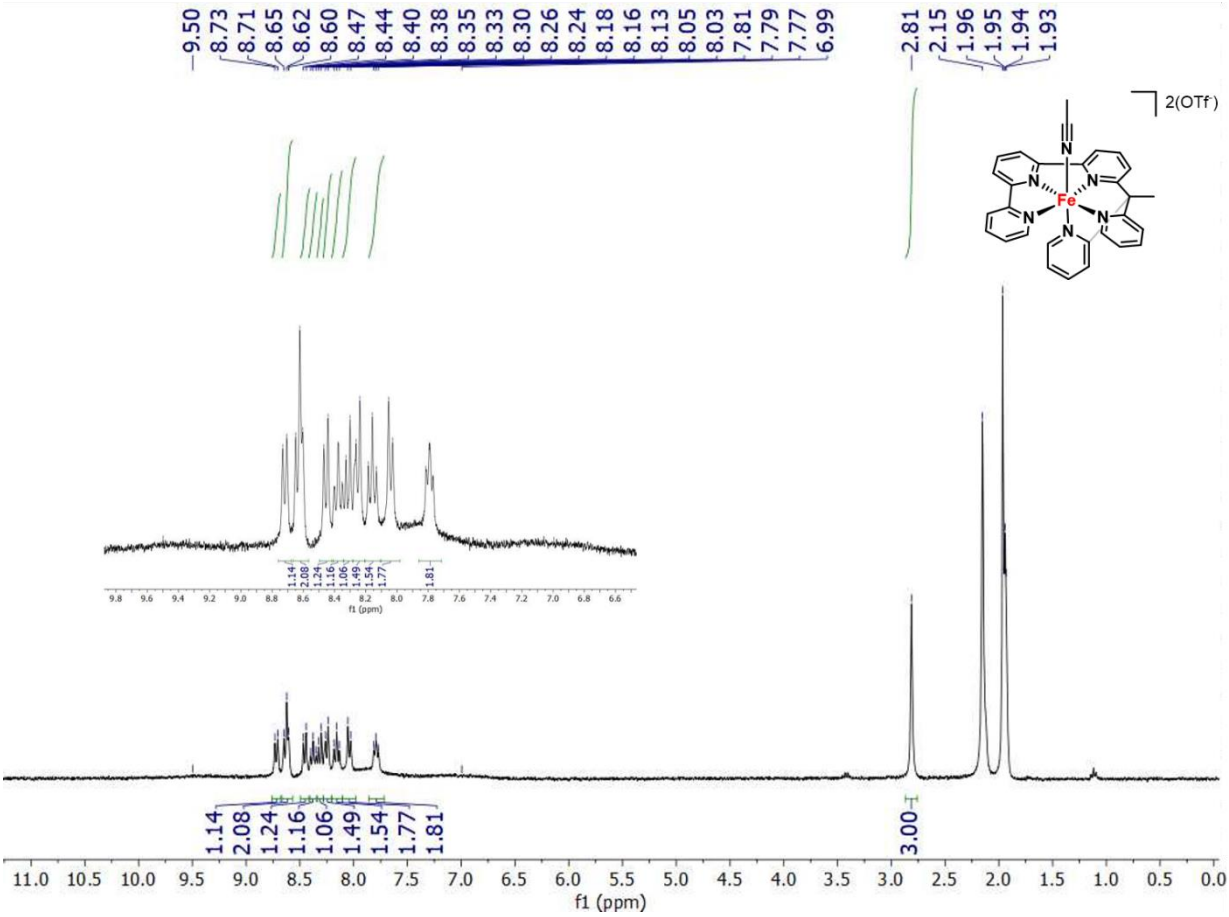


Figure 5.54. ^{1}H NMR of [Fe(tpyPY2Me)(CH_3CN)][OTf]$_2$ in CD_3CN.

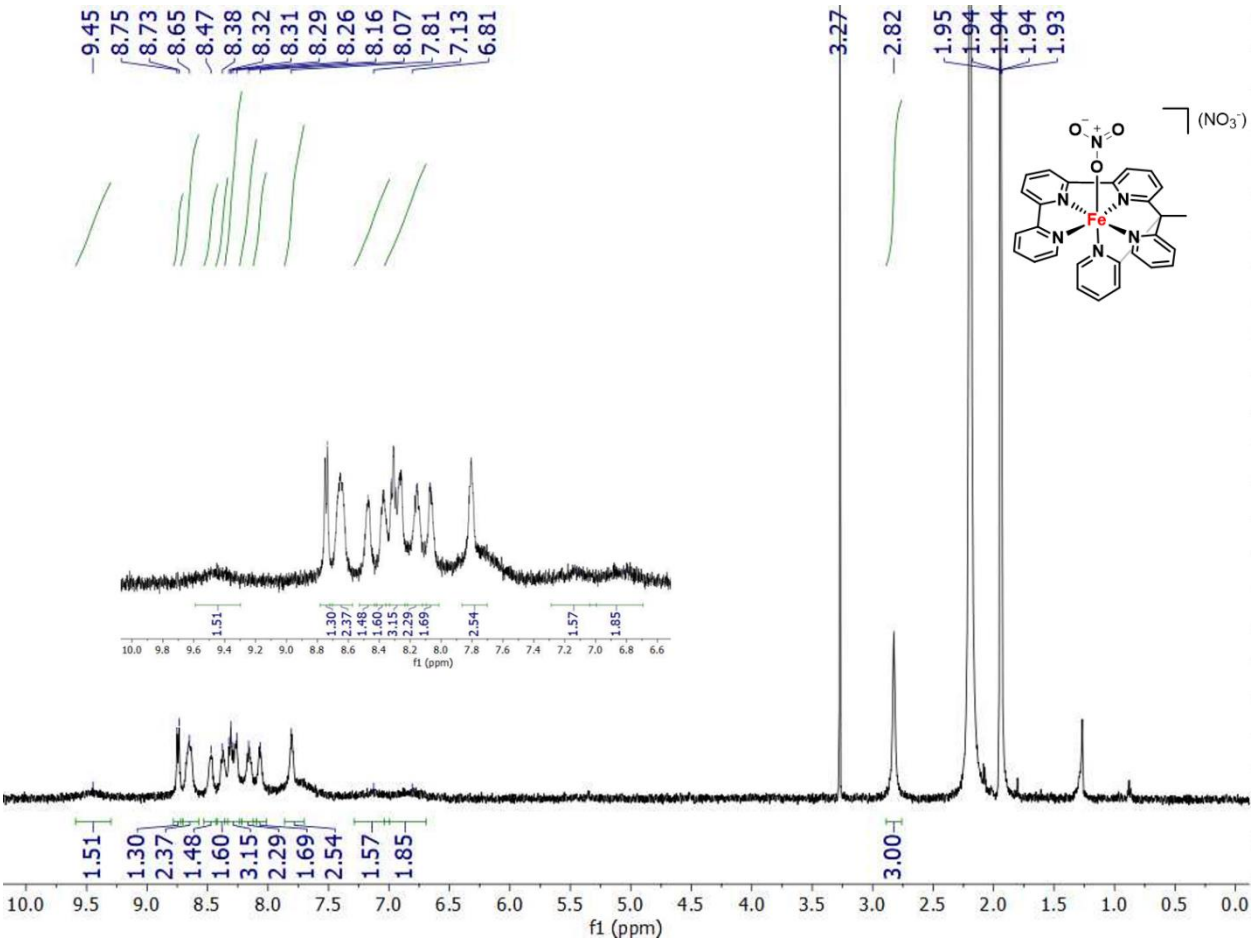


Figure 5.55. ^{1}H NMR of [Fe(tpyPY2Me)(NO_3)][NO_3] in CD_3CN.

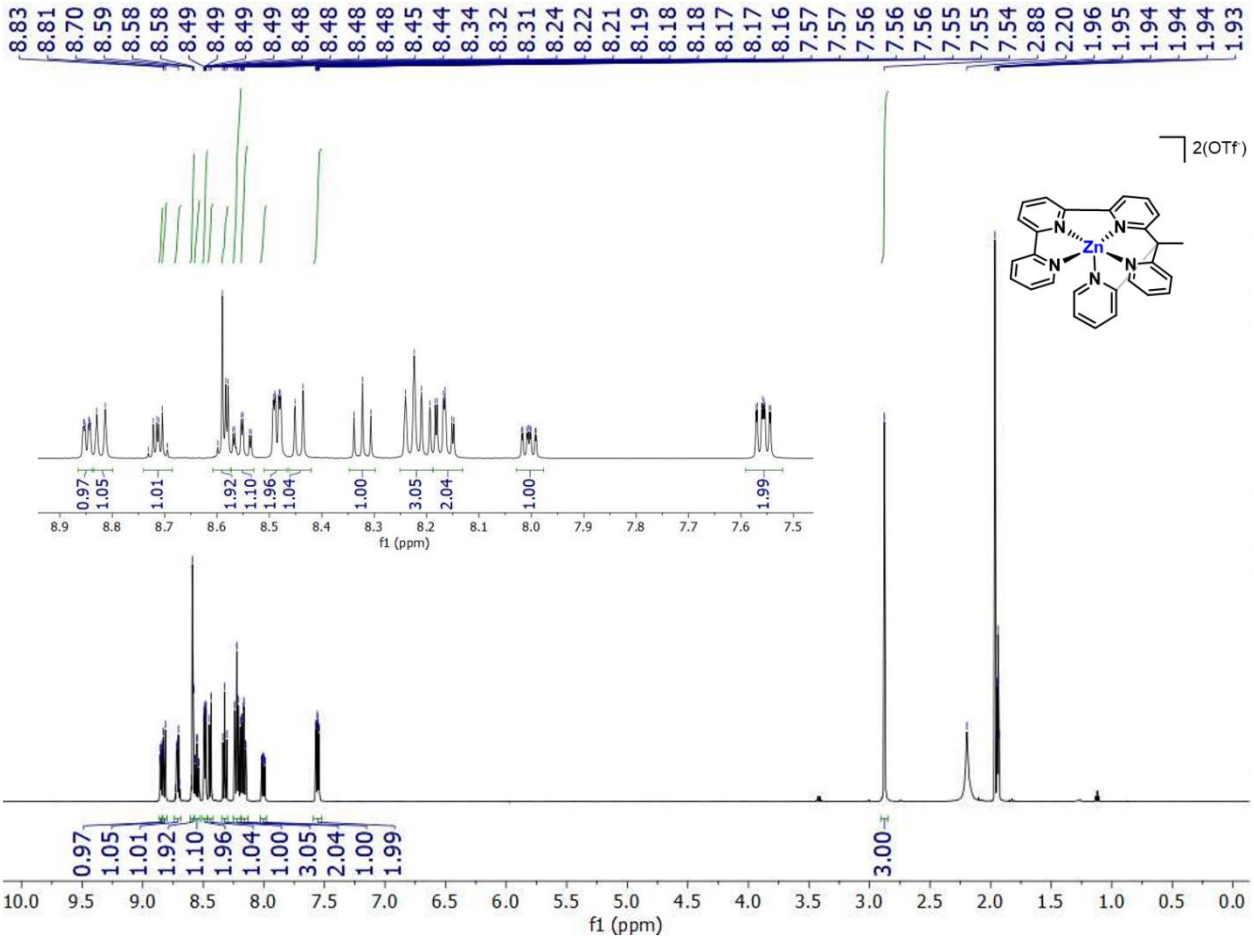


Figure 5.56. ^{1}H NMR of [Zn(tpyPY2Me)][OTf]$_2$ in CD_3CN.

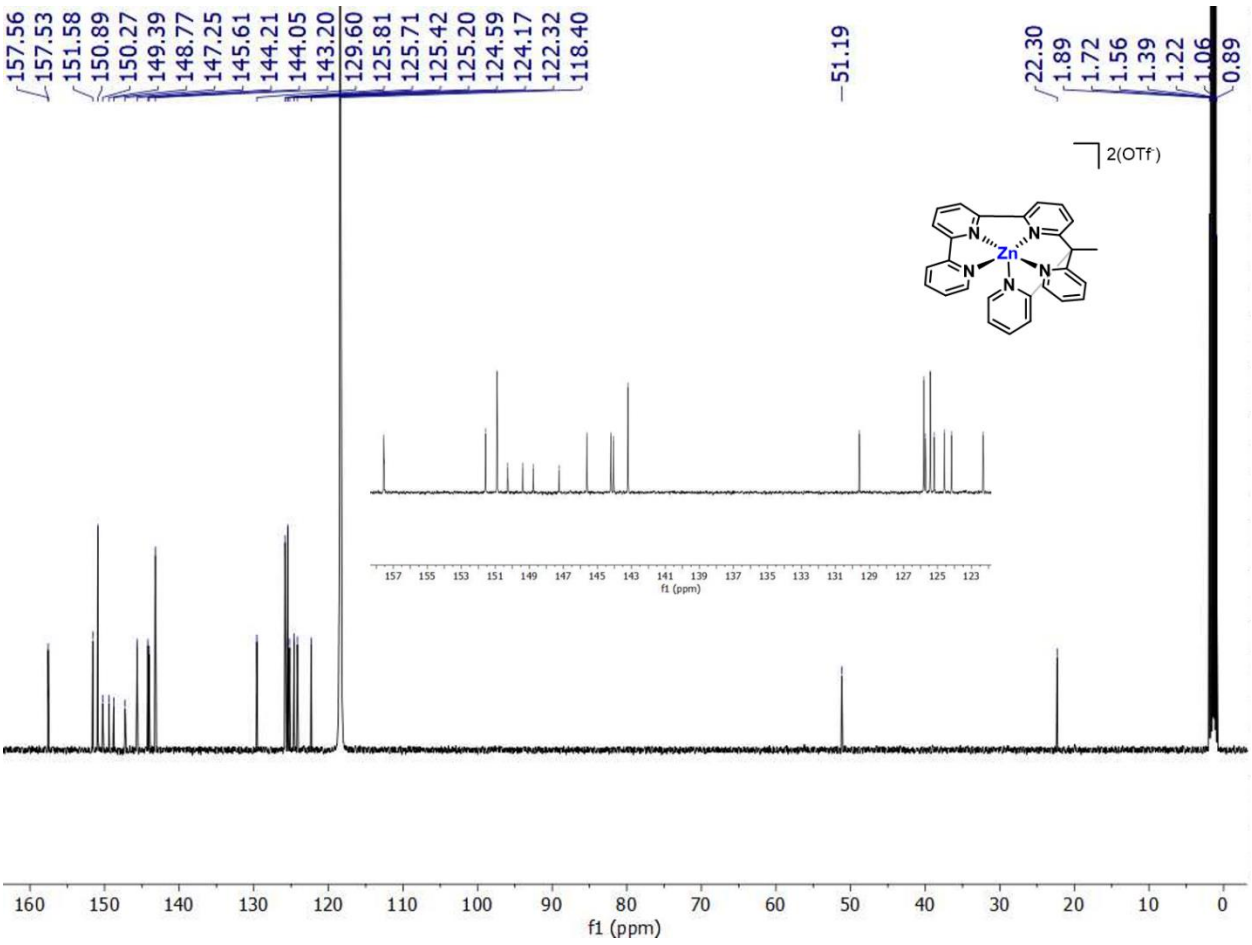


Figure 5.57. ^{13}C NMR of [Zn(tpyPY2Me)][OTf]$_2$ in CD_3CN.

5.6 References

(1) Lewis, N. S.; Nocera, D. G. Powering the Planet: Chemical Challenges in Solar Energy Utilization. *Proc. Natl. Acad. Sci.* **2006**, *103*, 15729–15735.

(2) De Luna, P.; Hahn, C.; Higgins, D.; Jaffer, S. A.; Jaramillo, T. F.; Sargent, E. H. What Would It Take for Renewably Powered Electrosynthesis to Displace Petrochemical Processes? *Science* **2019**, *364*, eaav3506.

(3) Francke, R.; Schille, B.; Roemelt, M. Homogeneously Catalyzed Electroreduction of Carbon Dioxide—Methods, Mechanisms, and Catalysts. *Chem. Rev.* **2018**, *118*, 4631–4701.

(4) Can, M.; Armstrong, F. A.; Ragsdale, S. W. Structure, Function, and Mechanism of the Nickel Metalloenzymes, CO Dehydrogenase, and Acetyl-CoA Synthase. *Chem. Rev.* **2014**, *114*, 4149–4174.

(5) Corbin, N.; Zeng, J.; Williams, K.; Manthiram, K. Heterogeneous Molecular Catalysts for Electrocatalytic CO_2 Reduction. *Nano Res.* **2019**, *12*, 2093–2125.

(6) Smith, P. T.; Nichols, E. M.; Cao, Z.; Chang, C. J. Hybrid Catalysts for Artificial Photosynthesis: Merging Approaches from Molecular, Materials, and Biological Catalysis. *Acc. Chem. Res.* **2020**, *53*, 575–587.

(7) Fisher, B. J.; Eisenberg, R. Electrocatalytic Reduction of Carbon Dioxide by Using Macrocycles of Nickel and Cobalt. *J. Am. Chem. Soc.* **1980**, *102*, 7361–7363.

(8) Beley, M.; Collin, J.-P.; Ruppert, R.; Sauvage, J.-P. Nickel(II)-Cyclam: An Extremely Selective Electrocatalyst for Reduction of CO_2 in Water. *J. Chem. Soc. Chem. Commun.* **1984**, 1315–1316.

(9) Schneider, J.; Jia, H.; Kobiro, K.; Cabelli, D. E.; Muckerman, J. T.; Fujita, E. Nickel(II) Macrocycles: Highly Efficient Electrocatalysts for the Selective Reduction of CO_2 to CO. *Energy Environ. Sci.* **2012**, *5*, 9502–9510.

(10) Froehlich, J. D.; Kubiak, C. P. Homogeneous CO_2 Reduction by Ni(Cyclam) at a Glassy Carbon Electrode. *Inorg. Chem.* **2012**, *51*, 3932–3934.

(11) Hammouche, M.; Lexa, D.; Savéant, J. M.; Momenteau, M. Catalysis of the Electrochemical Reduction of Carbon Dioxide by Iron("0") Porphyrins. *J. Electroanal. Chem. Interfacial Electrochem.* **1988**, *249*, 347–351.

(12) Costentin, C.; Drouet, S.; Robert, M.; Savéant, J.-M. A Local Proton Source Enhances CO_2 Electroreduction to CO by a Molecular Fe Catalyst. *Science* **2012**, *338*, 90–94.

(13) Azcarate, I.; Costentin, C.; Robert, M.; Savéant, J.-M. Through-Space Charge Interaction Substituent Effects in Molecular Catalysis Leading to the Design of the Most Efficient Catalyst of CO_2-to-CO Electrochemical Conversion. *J. Am. Chem. Soc.* **2016**, *138*, 16639–16644.

(14) Meshitsuka, S.; Ichikawa, M.; Tamaru, K. Electrocatalysis by Metal Phthalocyanines in the Reduction of Carbon Dioxide. *J. Chem. Soc. Chem. Commun.* **1974**, 158–159.

(15) Ren, S.; Joulié, D.; Salvatore, D.; Torbensen, K.; Wang, M.; Robert, M.; Berlinguette, C. P. Molecular Electrocatalysts Can Mediate Fast, Selective CO_2 Reduction in a Flow Cell. *Science* **2019**, 365, 367–369.

(16) Hawecker, J.; Lehn, J.-M.; Ziessel, R. Electrocatalytic Reduction of Carbon Dioxide Mediated by $Re(Bipy)(CO)_3Cl$ (Bipy = 2,2′-Bipyridine). *J. Chem. Soc. Chem. Commun.* **1984**, 328–330.

(17) Smieja, J. M.; Kubiak, C. P. Re(Bipy-TBu)$(CO)_3Cl^-$improved Catalytic Activity for Reduction of Carbon Dioxide: IR-Spectroelectrochemical and Mechanistic Studies. *Inorg. Chem.* **2010**, *49*, 9283–9289.
(18) Reda, T.; Plugge, C. M.; Abram, N. J.; Hirst, J. Reversible Interconversion of Carbon Dioxide and Formate by an Electroactive Enzyme. *Proc. Natl. Acad. Sci.* **2008**, *105*, 10654–10658.
(19) Evans, R. M.; Siritanaratkul, B.; Megarity, C. F.; Pandey, K.; Esterle, T. F.; Badiani, S.; Armstrong, F. A. The Value of Enzymes in Solar Fuels Research – Efficient Electrocatalysts through Evolution. *Chem. Soc. Rev.* **2019**, *48*, 2039–2052.
(20) Nitopi, S.; Bertheussen, E.; Scott, S. B.; Liu, X.; Engstfeld, A. K.; Horch, S.; Seger, B.; Stephens, I. E. L.; Chan, K.; Hahn, C.; Nørskov, J. K.; Jaramillo, T. F.; Chorkendorff, I. Progress and Perspectives of Electrochemical CO_2 Reduction on Copper in Aqueous Electrolyte. *Chem. Rev.* **2019**, *119*, 7610–7672.
(21) Todorova, T. K.; Schreiber, M. W.; Fontecave, M. Mechanistic Understanding of CO_2 Reduction Reaction (CO_2RR) Toward Multicarbon Products by Heterogeneous Copper-Based Catalysts. *ACS Catal.* **2020**, *10*, 1754–1768.
(22) Rodriguez, P.; Koper, M. T. M. Electrocatalysis on Gold. *Phys. Chem. Chem. Phys.* **2014**, *16*, 13583–13594.
(23) Karunadasa, H. I.; Chang, C. J.; Long, J. R. A Molecular Molybdenum-Oxo Catalyst for Generating Hydrogen from Water. *Nature* **2010**, *464*, 1329–1333.
(24) Karunadasa, H. I.; Montalvo, E.; Sun, Y.; Majda, M.; Long, J. R.; Chang, C. J. A Molecular MoS_2 Edge Site Mimic for Catalytic Hydrogen Generation. *Science* **2012**, *335*, 698–702.
(25) Zee, D. Z.; Chantarojsiri, T.; Long, J. R.; Chang, C. J. Metal–Polypyridyl Catalysts for Electro- and Photochemical Reduction of Water to Hydrogen. *Acc. Chem. Res.* **2015**, *48*, 2027–2036.
(26) Sun, Y.; Bigi, J. P.; Piro, N. A.; Tang, M. L.; Long, J. R.; Chang, C. J. Molecular Cobalt Pentapyridine Catalysts for Generating Hydrogen from Water. *J. Am. Chem. Soc.* **2011**, *133*, 9212–9215.
(27) Chen, Z.; Chen, C.; Weinberg, D. R.; Kang, P.; Concepcion, J. J.; Harrison, D. P.; Brookhart, M. S.; Meyer, T. J. Electrocatalytic Reduction of CO_2 to CO by Polypyridyl Ruthenium Complexes. *Chem. Commun.* **2011**, *47*, 12607–12609.
(28) Gonell, S.; Massey, M. D.; Moseley, I. P.; Schauer, C. K.; Muckerman, J. T.; Miller, A. J. M. The Trans Effect in Electrocatalytic CO_2 Reduction: Mechanistic Studies of Asymmetric Ruthenium Pyridyl-Carbene Catalysts. *J. Am. Chem. Soc.* **2019**, *141*, 6658–6671.
(29) Gonell, S.; Assaf, E. A.; Duffee, K. D.; Schauer, C. K.; Miller, A. J. M. Kinetics of the Trans Effect in Ruthenium Complexes Provide Insight into the Factors That Control Activity and Stability in CO_2 Electroreduction. *J. Am. Chem. Soc.* **2020**, *142*, 8980–8999.
(30) Li, T.-T.; Shan, B.; Xu, W.; Meyer, T. J. Electrocatalytic CO_2 Reduction with a Ruthenium Catalyst in Solution and on Nanocrystalline TiO_2. *ChemSusChem* **2019**, *12*, 2402–2408.
(31) Liu, Y.; Fan, X.; Nayak, A.; Wang, Y.; Shan, B.; Quan, X.; Meyer, T. J. Steering CO_2 Electroreduction toward Ethanol Production by a Surface-Bound Ru Polypyridyl Carbene Catalyst on N-Doped Porous Carbon. *Proc. Natl. Acad. Sci.* **2019**, *116*, 26353–26358.
(32) Benson, E. E.; Sampson, M. D.; Grice, K. A.; Smieja, J. M.; Froehlich, J. D.; Friebel, D.; Keith, J. A.; Carter, E. A.; Nilsson, A.; Kubiak, C. P. The Electronic States of Rhenium Bipyridyl Electrocatalysts for CO_2 Reduction as Revealed by X-Ray Absorption

Spectroscopy and Computational Quantum Chemistry. *Angew. Chem. Int. Ed.* **2013**, *52*, 4841–4844.
(33) Clark, M. L.; Cheung, P. L.; Lessio, M.; Carter, E. A.; Kubiak, C. P. Kinetic and Mechanistic Effects of Bipyridine (Bpy) Substituent, Labile Ligand, and Brønsted Acid on Electrocatalytic CO_2 Reduction by Re(Bpy) Complexes. *ACS Catal.* **2018**, *8*, 2021–2029.
(34) Keith, J. A.; Grice, K. A.; Kubiak, C. P.; Carter, E. A. Elucidation of the Selectivity of Proton-Dependent Electrocatalytic CO_2 Reduction by Fac-Re(Bpy)$(CO)_3$Cl. *J. Am. Chem. Soc.* **2013**, *135*, 15823–15829.
(35) Su, X.; McCardle, K. M.; Panetier, J. A.; Jurss, J. W. Electrocatalytic CO_2 Reduction with Nickel Complexes Supported by Tunable Bipyridyl-N-Heterocyclic Carbene Donors: Understanding Redox-Active Macrocycles. *Chem. Commun.* **2018**, *54*, 3351–3354.
(36) Su, X.; McCardle, K. M.; Chen, L.; Panetier, J. A.; Jurss, J. W. Robust and Selective Cobalt Catalysts Bearing Redox-Active Bipyridyl-N-Heterocyclic Carbene Frameworks for Electrochemical CO_2 Reduction in Aqueous Solutions. *ACS Catal.* **2019**, *9*, 7398–7408.
(37) Lin, S.; Diercks, C. S.; Zhang, Y.-B.; Kornienko, N.; Nichols, E. M.; Zhao, Y.; Paris, A. R.; Kim, D.; Yang, P.; Yaghi, O. M.; Chang, C. J. Covalent Organic Frameworks Comprising Cobalt Porphyrins for Catalytic CO_2 Reduction in Water. *Science* **2015**, *349*, 1208–1213.
(38) Diercks, C. S.; Lin, S.; Kornienko, N.; Kapustin, E. A.; Nichols, E. M.; Zhu, C.; Zhao, Y.; Chang, C. J.; Yaghi, O. M. Reticular Electronic Tuning of Porphyrin Active Sites in Covalent Organic Frameworks for Electrocatalytic Carbon Dioxide Reduction. *J. Am. Chem. Soc.* **2018**, *140*, 1116–1122.
(39) Gonell, S.; Lloret-Fillol, J.; Miller, A. J. M. An Iron Pyridyl-Carbene Electrocatalyst for Low Overpotential CO_2 Reduction to CO. *ACS Catal.* **2021**, *11*, 615–626.
(40) Eisenberg, R.; Gray, H. B. Noninnocence in Metal Complexes: A Dithiolene Dawn. *Inorg. Chem.* **2011**, *50*, 9741–9751.
(41) McNamara, W. R.; Han, Z.; Alperin, P. J.; Brennessel, W. W.; Holland, P. L.; Eisenberg, R. A Cobalt–Dithiolene Complex for the Photocatalytic and Electrocatalytic Reduction of Protons. *J. Am. Chem. Soc.* **2011**, *133*, 15368–15371.
(42) McNamara, W. R.; Han, Z.; Yin, C.-J. (Madeline); Brennessel, W. W.; Holland, P. L.; Eisenberg, R. Cobalt-Dithiolene Complexes for the Photocatalytic and Electrocatalytic Reduction of Protons in Aqueous Solutions. *Proc. Natl. Acad. Sci.* **2012**, *109*, 15594–15599.
(43) Letko, C. S.; Panetier, J. A.; Head-Gordon, M.; Tilley, T. D. Mechanism of the Electrocatalytic Reduction of Protons with Diaryldithiolene Cobalt Complexes. *J. Am. Chem. Soc.* **2014**, *136*, 9364–9376.
(44) Wu, Y.; Jiang, J.; Weng, Z.; Wang, M.; Broere, D. L. J.; Zhong, Y.; Brudvig, G. W.; Feng, Z.; Wang, H. Electroreduction of CO_2 Catalyzed by a Heterogenized Zn–Porphyrin Complex with a Redox-Innocent Metal Center. *ACS Cent. Sci.* **2017**, *3*, 847–852.
(45) Proppe, A. H.; Li, Y. C.; Aspuru-Guzik, A.; Berlinguette, C. P.; Chang, C. J.; Cogdell, R.; Doyle, A. G.; Flick, J.; Gabor, N. M.; van Grondelle, R.; Hammes-Schiffer, S.; Jaffer, S. A.; Kelley, S. O.; Leclerc, M.; Leo, K.; Mallouk, T. E.; Narang, P.; Schlau-Cohen, G. S.; Scholes, G. D.; Vojvodic, A.; Yam, V. W.-W.; Yang, J. Y.; Sargent, E. H. Bioinspiration in Light Harvesting and Catalysis. *Nat. Rev. Mater.* **2020**, *5*, 828–846.
(46) Jurss, J. W.; Khnayzer, R. S.; Panetier, J. A.; Roz, K. A. E.; Nichols, E. M.; Head-Gordon, M.; Long, J. R.; Castellano, F. N.; Chang, C. J. Bioinspired Design of Redox-Active Ligands for Multielectron Catalysis: Effects of Positioning Pyrazine Reservoirs on Cobalt for

Electro- and Photocatalytic Generation of Hydrogen from Water. *Chem. Sci.* **2015**, *6*, 4954–4972.
(47) Nichols, E. M.; Derrick, J. S.; Nistanaki, S. K.; Smith, P. T.; Chang, C. J. Positional Effects of Second-Sphere Amide Pendants on Electrochemical CO_2 Reduction Catalyzed by Iron Porphyrins. *Chem. Sci.* **2018**, *9*, 2952–2960.
(48) Smith, P. T.; Weng, S.; Chang, C. J. An NADH-Inspired Redox Mediator Strategy to Promote Second-Sphere Electron and Proton Transfer for Cooperative Electrochemical CO_2 Reduction Catalyzed by Iron Porphyrin. *Inorg. Chem.* **2020**, *59*, 9270–9278.
(49) Dey, S.; Das, P. K.; Dey, A. Mononuclear Iron Hydrogenase. *Coord. Chem. Rev.* **2013**, *257*, 42–63.
(50) Chantarojsiri, T.; Sun, Y.; Long, J. R.; Chang, C. J. Water-Soluble Iron(IV)-Oxo Complexes Supported by Pentapyridine Ligands: Axial Ligand Effects on Hydrogen Atom and Oxygen Atom Transfer Reactivity. *Inorg. Chem.* **2015**, *54*, 5879–5887.
(51) Römelt, M.; Ye, S.; Neese, F. Calibration of Modern Density Functional Theory Methods for the Prediction of ^{57}Fe Mössbauer Isomer Shifts: Meta-GGA and Double-Hybrid Functionals. *Inorg. Chem.* **2009**, *48*, 784–785.
(52) McWilliams, S. F.; Brennan-Wydra, E.; MacLeod, K. C.; Holland, P. L. Density Functional Calculations for Prediction of ^{57}Fe Mössbauer Isomer Shifts and Quadrupole Splittings in β-Diketiminate Complexes. *ACS Omega* **2017**, *2*, 2594–2606.
(53) Scarborough, C. C.; Lancaster, K. M.; DeBeer, S.; Weyhermüller, T.; Sproules, S.; Wieghardt, K. Experimental Fingerprints for Redox-Active Terpyridine in $[Cr(tpy)_2](PF_6)_n$ (n = 3–0), and the Remarkable Electronic Structure of $[Cr(tpy)_2]^{1-}$. *Inorg. Chem.* **2012**, *51*, 3718–3732.
(54) England, J.; Scarborough, C. C.; Weyhermüller, T.; Sproules, S.; Wieghardt, K. Electronic Structures of the Electron Transfer Series $[M(bpy)_3]_n$, $[M(tpy)_2]_n$, and $[Fe(^tbpy)_3]_n$ (M = Fe, Ru; n = 3^+, 2^+, 1^+, 0, 1^-): A Mössbauer Spectroscopic and DFT Study. *Eur. J. Inorg. Chem.* **2012**, *2012*, 4605–4621.
(55) Pegis, M. L.; Roberts, J. A. S.; Wasylenko, D. J.; Mader, E. A.; Appel, A. M.; Mayer, J. M. Standard Reduction Potentials for Oxygen and Carbon Dioxide Couples in Acetonitrile and N,N-Dimethylformamide. *Inorg. Chem.* **2015**, *54*, 11883–11888.
(56) Matsubara, Y.; Grills, D. C.; Kuwahara, Y. Thermodynamic Aspects of Electrocatalytic CO_2 Reduction in Acetonitrile and with an Ionic Liquid as Solvent or Electrolyte. *ACS Catal.* **2015**, *5*, 6440–6452.
(57) Matsubara, Y. Standard Electrode Potentials for the Reduction of CO_2 to CO in Acetonitrile–Water Mixtures Determined Using a Generalized Method for Proton-Coupled Electron-Transfer Reactions. *ACS Energy Lett.* **2017**, *2*, 1886–1891.
(58) Bard, A. J.; Parsons, R.; Jordan J. *Standard Potentials in Aqueous Solution*; M. Dekker, New York, 1985.
(59) Pavlishchuk, V. V.; Addison, A. W. Conversion Constants for Redox Potentials Measured versus Different Reference Electrodes in Acetonitrile Solutions at 25°C. *Inorganica Chim. Acta* **2000**, *298*, 97–102.
(60) Hooe, S. L.; Dressel, J. M.; Dickie, D. A.; Machan, C. W. Highly Efficient Electrocatalytic Reduction of CO_2 to CO by a Molecular Chromium Complex. *ACS Catal.* **2020**, *10*, 1146–1151.

(61) Ngo, K. T.; McKinnon, M.; Mahanti, B.; Narayanan, R.; Grills, D. C.; Ertem, M. Z.; Rochford, J. Turning on the Protonation-First Pathway for Electrocatalytic CO_2 Reduction by Manganese Bipyridyl Tricarbonyl Complexes. *J. Am. Chem. Soc.* **2017**, *139*, 2604–2618.
(62) Dey, S.; Ahmed, M. E.; Dey, A. Activation of Co(I) State in a Cobalt-Dithiolato Catalyst for Selective and Efficient CO_2 Reduction to CO. *Inorg. Chem.* **2018**, *57*, 5939–5947.
(63) Ahmed, M. E.; Rana, A.; Saha, R.; Dey, S.; Dey, A. Homogeneous Electrochemical Reduction of CO_2 to CO by a Cobalt Pyridine Thiolate Complex. *Inorg. Chem.* **2020**, *59*, 5292–5302.
(64) Lee, K. J.; McCarthy, B. D.; Dempsey, J. L. On Decomposition, Degradation, and Voltammetric Deviation: The Electrochemist's Field Guide to Identifying Precatalyst Transformation. *Chem. Soc. Rev.* **2019**, *48*, 2927–2945.
(65) Rountree, E. S.; McCarthy, B. D.; Eisenhart, T. T.; Dempsey, J. L. Evaluation of Homogeneous Electrocatalysts by Cyclic Voltammetry. *Inorg. Chem.* **2014**, *53*, 9983–10002.
(66) Costentin, C.; Drouet, S.; Robert, M.; Savéant, J.-M. Turnover Numbers, Turnover Frequencies, and Overpotential in Molecular Catalysis of Electrochemical Reactions. Cyclic Voltammetry and Preparative-Scale Electrolysis. *J. Am. Chem. Soc.* **2012**, *134*, 11235–11242.
(67) Costentin, C.; Drouet, S.; Robert, M.; Savéant, J.-M. Correction to Turnover Numbers, Turnover Frequencies, and Overpotential in Molecular Catalysis of Electrochemical Reactions. Cyclic Voltammetry and Preparative-Scale Electrolysis. *J. Am. Chem. Soc.* **2012**, *134*, 19949–19950.
(68) Galan, B. R.; Schöffel, J.; Linehan, J. C.; Seu, C.; Appel, A. M.; Roberts, J. A. S.; Helm, M. L.; Kilgore, U. J.; Yang, J. Y.; DuBois, D. L.; Kubiak, C. P. Electrocatalytic Oxidation of Formate by $[Ni(PR_2NR'_2)_2(CH_3CN)]^{2+}$ Complexes. *J. Am. Chem. Soc.* **2011**, *133*, 12767–12779.
(69) Sung, S.; Kumar, D.; Gil-Sepulcre, M.; Nippe, M. Electrocatalytic CO_2 Reduction by Imidazolium-Functionalized Molecular Catalysts. *J. Am. Chem. Soc.* **2017**, *139*, 13993–13996.
(70) Haviv, E.; Azaiza-Dabbah, D.; Carmieli, R.; Avram, L.; Martin, J. M. L.; Neumann, R. A Thiourea Tether in the Second Coordination Sphere as a Binding Site for CO_2 and a Proton Donor Promotes the Electrochemical Reduction of CO_2 to CO Catalyzed by a Rhenium Bipyridine-Type Complex. *J. Am. Chem. Soc.* **2018**, *140*, 12451–12456.
(71) Chapovetsky, A.; Welborn, M.; Luna, J. M.; Haiges, R.; Miller, T. F.; Marinescu, S. C. Pendant Hydrogen-Bond Donors in Cobalt Catalysts Independently Enhance CO_2 Reduction. *ACS Cent. Sci.* **2018**, *4*, 397–404.
(72) Rudd, D. J.; Goldsmith, C. R.; Cole, A. P.; Stack, T. D. P.; Hodgson, K. O.; Hedman, B. X-Ray Absorption Spectroscopic Investigation of the Spin-Transition Character in a Series of Single-Site Perturbed Iron(II) Complexes. *Inorg. Chem.* **2005**, *44*, 1221–1229.
(73) Gütlich, P.; Eckhard, B.; Trautwein, X. A. Mössbauer Spectroscopy and Transition Metal Chemistry Fundamentals and Applications; Springer: Berlin, 2011.
(74) Garino, C.; Gobetto, R.; Nervi, C.; Salassa, L.; Rosenberg, E.; Ross, J. B. A.; Chu, X.; Hardcastle, K. I.; Sabatini, C. Spectroscopic and Computational Studies of a Ru(II) Terpyridine Complex: The Importance of Weak Intermolecular Forces to Photophysical Properties. *Inorg. Chem.* **2007**, *46*, 8752–8762.

(75) Römelt, C.; Song, J.; Tarrago, M.; Rees, J. A.; van Gastel, M.; Weyhermüller, T.; DeBeer, S.; Bill, E.; Neese, F.; Ye, S. Electronic Structure of a Formal Iron(0) Porphyrin Complex Relevant to CO_2 Reduction. *Inorg. Chem.* **2017**, *56*, 4745–4750.
(76) Kang, P.; Meyer, T. J.; Brookhart, M. Selective Electrocatalytic Reduction of Carbon Dioxide to Formate by a Water-Soluble Iridium Pincer Catalyst. *Chem. Sci.* **2013**, *4*, 3497–3502.
(77) Costentin, C.; Robert, M.; Savéant, J.-M.; Tatin, A. Efficient and Selective Molecular Catalyst for the CO_2-to-CO Electrochemical Conversion in Water. *Proc. Natl. Acad. Sci.* **2015**, *112*, 6882–6886.
(78) Taheri, A.; Thompson, E. J.; Fettinger, J. C.; Berben, L. A. An Iron Electrocatalyst for Selective Reduction of CO_2 to Formate in Water: Including Thermochemical Insights. *ACS Catal.* **2015**, *5*, 7140–7151.
(79) Nakada, A.; Ishitani, O. Selective Electrocatalysis of a Water-Soluble Rhenium(I) Complex for CO_2 Reduction Using Water as an Electron Donor. *ACS Catal.* **2018**, *8*, 354–363.
(80) Gu, J.; Hsu, C.-S.; Bai, L.; Chen, H. M.; Hu, X. Atomically Dispersed Fe^{3+} Sites Catalyze Efficient CO_2 Electroreduction to CO. *Science* **2019**, *364*, 1091–1094.
(81) Bechlars, B.; D'Alessandro, D. M.; Jenkins, D. M.; Iavarone, A. T.; Glover, S. D.; Kubiak, C. P.; Long, J. R. High-Spin Ground States via Electron Delocalization in Mixed-Valence Imidazolate-Bridged Divanadium Complexes. *Nat. Chem.* **2010**, *2*, 362–368.
(82) Rigaku Oxford Diffraction. CrysAlisPro Software System; Rigaku Corporation: Oxford, UK, 2015.
(83) Heisenberg, W. Zur Theorie des Ferromagnetismus. *Z. Für Phys.* **1928**, *49*, 619–636.
(84) Soda, T.; Kitagawa, Y.; Onishi, T.; Takano, Y.; Shigeta, Y.; Nagao, H.; Yoshioka, Y.; Yamaguchi, K. Ab Initio Computations of Effective Exchange Integrals for H–H, H–He–H and Mn_2O_2 Complex: Comparison of Broken-Symmetry Approaches. *Chem. Phys. Lett.* **2000**, *319*, 223–230.
(85) Fu, Y.; Liu, L.; Yu, H.-Z.; Wang, Y.-M.; Guo, Q.-X. Quantum-Chemical Predictions of Absolute Standard Redox Potentials of Diverse Organic Molecules and Free Radicals in Acetonitrile. *J. Am. Chem. Soc.* **2005**, *127*, 7227–7234.
(86) Konezny, S. J.; Doherty, M. D.; Luca, O. R.; Crabtree, R. H.; Soloveichik, G. L.; Batista, V. S. Reduction of Systematic Uncertainty in DFT Redox Potentials of Transition-Metal Complexes. *J. Phys. Chem. C* **2012**, *116*, 6349–6356.
(87) Thom, A. J. W.; Sundstrom, E. J.; Head-Gordon, M. LOBA: A Localized Orbital Bonding Analysis to Calculate Oxidation States, with Application to a Model Water Oxidation Catalyst. *Phys. Chem. Chem. Phys.* **2009**, *11*, 11297–11304.
(88) Shao, Y.; Gan, Z.; Epifanovsky, E.; Gilbert, A. T. B.; Wormit, M.; Kussmann, J.; Lange, A. W.; Behn, A.; Deng, J.; Feng, X.; Ghosh, D.; Goldey, M.; Horn, P. R.; Jacobson, L. D.; Kaliman, I.; Khaliullin, R. Z.; Kuś, T.; Landau, A.; Liu, J.; Proynov, E. I.; Rhee, Y. M.; Richard, R. M.; Rohrdanz, M. A.; Steele, R. P.; Sundstrom, E. J.; Woodcock, H. L.; Zimmerman, P. M.; Zuev, D.; Albrecht, B.; Alguire, E.; Austin, B.; Beran, G. J. O.; Bernard, Y. A.; Berquist, E.; Brandhorst, K.; Bravaya, K. B.; Brown, S. T.; Casanova, D.; Chang, C.-M.; Chen, Y.; Chien, S. H.; Closser, K. D.; Crittenden, D. L.; Diedenhofen, M.; DiStasio, R. A.; Do, H.; Dutoi, A. D.; Edgar, R. G.; Fatehi, S.; Fusti-Molnar, L.; Ghysels, A.; Golubeva-Zadorozhnaya, A.; Gomes, J.; Hanson-Heine, M. W. D.; Harbach, P. H. P.; Hauser, A. W.; Hohenstein, E. G.; Holden, Z. C.; Jagau, T.-C.; Ji, H.; Kaduk, B.; Khistyaev, K.; Kim, J.; Kim, J.; King, R. A.; Klunzinger, P.; Kosenkov, D.; Kowalczyk, T.; Krauter,

C. M.; Lao, K. U.; Laurent, A. D.; Lawler, K. V.; Levchenko, S. V.; Lin, C. Y.; Liu, F.; Livshits, E.; Lochan, R. C.; Luenser, A.; Manohar, P.; Manzer, S. F.; Mao, S.-P.; Mardirossian, N.; Marenich, A. V.; Maurer, S. A.; Mayhall, N. J.; Neuscamman, E.; Oana, C. M.; Olivares-Amaya, R.; O'Neill, D. P.; Parkhill, J. A.; Perrine, T. M.; Peverati, R.; Prociuk, A.; Rehn, D. R.; Rosta, E.; Russ, N. J.; Sharada, S. M.; Sharma, S.; Small, D. W.; Sodt, A.; Stein, T.; Stück, D.; Su, Y.-C.; Thom, A. J. W.; Tsuchimochi, T.; Vanovschi, V.; Vogt, L.; Vydrov, O.; Wang, T.; Watson, M. A.; Wenzel, J.; White, A.; Williams, C. F.; Yang, J.; Yeganeh, S.; Yost, S. R.; You, Z.-Q.; Zhang, I. Y.; Zhang, X.; Zhao, Y.; Brooks, B. R.; Chan, G. K. L.; Chipman, D. M.; Cramer, C. J.; Goddard, W. A.; Gordon, M. S.; Hehre, W. J.; Klamt, A.; Schaefer, H. F.; Schmidt, M. W.; Sherrill, C. D.; Truhlar, D. G.; Warshel, A.; Xu, X.; Aspuru-Guzik, A.; Baer, R.; Bell, A. T.; Besley, N. A.; Chai, J.-D.; Dreuw, A.; Dunietz, B. D.; Furlani, T. R.; Gwaltney, S. R.; Hsu, C.-P.; Jung, Y.; Kong, J.; Lambrecht, D. S.; Liang, W.; Ochsenfeld, C.; Rassolov, V. A.; Slipchenko, L. V.; Subotnik, J. E.; Van Voorhis, T.; Herbert, J. M.; Krylov, A. I.; Gill, P. M. W.; Head-Gordon, M. Advances in Molecular Quantum Chemistry Contained in the Q-Chem 4 Program Package. *Mol. Phys.* **2015**, *113*, 184–215.

(89) Chai, J.-D.; Head-Gordon, M. Long-Range Corrected Hybrid Density Functionals with Damped Atom–Atom Dispersion Corrections. *Phys. Chem. Chem. Phys.* **2008**, *10*, 6615–6620.

(90) Weigend, F.; Ahlrichs, R. Balanced Basis Sets of Split Valence, Triple Zeta Valence and Quadruple Zeta Valence Quality for H to Rn: Design and Assessment of Accuracy. *Phys. Chem. Chem. Phys.* **2005**, *7*, 3297–3305.

(91) Truong, T. N.; Stefanovich, E. V. A New Method for Incorporating Solvent Effect into the Classical, Ab Initio Molecular Orbital and Density Functional Theory Frameworks for Arbitrary Shape Cavity. *Chem. Phys. Lett.* **1995**, *240*, 253–260.

(92) Mardirossian, N.; Head-Gordon, M. ΩB97X-V: A 10-Parameter, Range-Separated Hybrid, Generalized Gradient Approximation Density Functional with Nonlocal Correlation, Designed by a Survival-of-the-Fittest Strategy. *Phys. Chem. Chem. Phys.* **2014**, *16*, 9904–9924.

(93) Becke, A. D. Density-Functional Exchange-Energy Approximation with Correct Asymptotic Behavior. *Phys. Rev. A* **1988**, *38*, 3098–3100.

(94) Lee, C.; Yang, W.; Parr, R. G. Development of the Colle-Salvetti Correlation-Energy Formula into a Functional of the Electron Density. *Phys. Rev. B* **1988**, *37*, 785–789.

(95) Becke, A. D. Density-functional Thermochemistry. III. The Role of Exact Exchange. *J. Chem. Phys.* **1993**, *98*, 5648–5652.

(96) Adamo, C.; Barone, V. Toward Reliable Density Functional Methods without Adjustable Parameters: The PBE0 Model. *J. Chem. Phys.* **1999**, *110*, 6158–6170.

(97) Zhao, Y.; Truhlar, D. G. Design of Density Functionals That Are Broadly Accurate for Thermochemistry, Thermochemical Kinetics, and Nonbonded Interactions. *J. Phys. Chem. A* **2005**, *109*, 5656–5667

(98) Yu, H. S.; He, X.; Li, S. L.; Truhlar, D. G. MN15: A Kohn–Sham Global-Hybrid Exchange–Correlation Density Functional with Broad Accuracy for Multi-Reference and Single-Reference Systems and Noncovalent Interactions. *Chem. Sci.* **2016**, *7*, 5032–5051.

(99) Mardirossian, N.; Head-Gordon, M. Thirty Years of Density Functional Theory in Computational Chemistry: An Overview and Extensive Assessment of 200 Density Functionals. *Mol. Phys.* **2017**, *115*, 2315–2372.

(100) Kepp, K. P. Theoretical Study of Spin Crossover in 30 Iron Complexes. *Inorg. Chem.* **2016**, *55*, 2717–2727.
(101) Verma, P.; Varga, Z.; Klein, J. E. M. N.; Cramer, C. J.; Que, L.; Truhlar, D. G. Assessment of Electronic Structure Methods for the Determination of the Ground Spin States of Fe(II), Fe(III) and Fe(IV) Complexes. *Phys. Chem. Chem. Phys.* **2017**, *19*, 13049–13069.
(102) Neese, F. The ORCA Program System. *WIREs Comput. Mol. Sci.* **2012**, *2*, 73–78.
(103) Kelly, C. P.; Cramer, C. J.; Truhlar, D. G. Single-Ion Solvation Free Energies and the Normal Hydrogen Electrode Potential in Methanol, Acetonitrile, and Dimethyl Sulfoxide. *J. Phys. Chem. B* **2007**, *111*, 408–422.
(104) Song, J.; Klein, E. L.; Neese, F.; Ye, S. The Mechanism of Homogeneous CO_2 Reduction by Ni(Cyclam): Product Selectivity, Concerted Proton–Electron Transfer and C–O Bond Cleavage. *Inorg. Chem.* **2014**, *53*, 7500–7507.
(105) Ioannidis, E. I.; Kulik, H. J. Towards Quantifying the Role of Exact Exchange in Predictions of Transition Metal Complex Properties. J. Chem. Phys. **2015**, *143*, 034104–034111.
(106) Proppe, J.; Reiher, M. Reliable Estimation of Prediction Uncertainty for Physicochemical Property Models. *J. Chem. Theory Comput.* **2017**, *13*, 3297–3317.
(107) Grimme, S.; Ehrlich, S.; Goerigk, L. Effect of the Damping Function in Dispersion Corrected Density Functional Theory. *J. Comput. Chem.* **2011**, *32*, 1456–1465.
(108) Barone, V.; Cossi, M. Quantum Calculation of Molecular Energies and Energy Gradients in Solution by a Conductor Solvent Model. *J. Phys. Chem. A* **1998**, *102*, 1995–2001.
(109) Weigend, F. Accurate Coulomb-Fitting Basis Sets for H to Rn. *Phys. Chem. Chem. Phys.* **2006**, *8*, 1057–1065.
(110) Zamalyutin, V. V.; Bezdenezhnykh, V. A.; Nichugovskiy, A. I.; Flid, V. R. New Approaches to the Synthesis of 2,2′: 6′,2″-Terpyridine and Some of Its Derivatives. *Russ. J. Org. Chem.* **2018**, *54*, 419–425.
(111) Stefankiewicz, A. R.; Wałęsa-Chorab, M.; Harrowfield, J.; Kubicki, M.; Hnatejko, Z.; Korabik, M.; Patroniak, V. Self-Assembly of Transition Metal Ion Complexes of a Hybrid Pyrazine–Terpyridine Ligand. *Dalton Trans.* **2013**, *42*, 1743–1751.

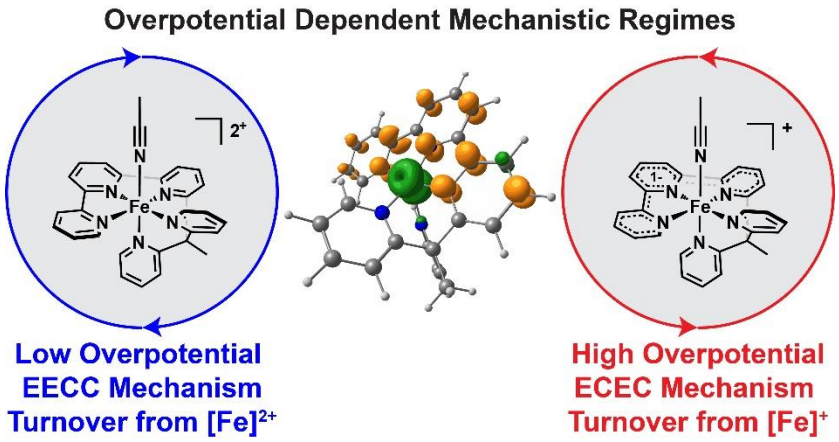
Chapter 6: Deciphering Distinct Overpotential Dependent Pathways for Electrochemical Carbon Dioxide Reduction Catalyzed by an Iron-Terpyridine Complex

Portions of this work were published in the following scientific journal:
Loipersberger, M.‡; Derrick, J. S.‡; Chang, C. J.; Head-Gordon, M. Deciphering Distinct Overpotential Dependent Pathways for Electrochemical CO_2 Reduction Catalyzed by an Iron-Terpyridine Complex. *Inorganic Chemistry* **2022**, https://doi.org/10.1021/acs.inorgchem.2c00279
(‡Denotes equal contribution)

Specific Contributions: Dr. Matthias Loipersberger did the computational work.

6.1 Abstract

[Fe(tpyPY2Me)]$^{2+}$ ([Fe]$^{2+}$) is a homogeneous electrocatalyst for converting CO_2 into CO featuring low overpotentials of <100 mV, near-unity selectivity, and high activity with turnover frequencies faster than 100,000 s^{-1}. To identify the origins of its exceptional performance and inform future catalyst design, we report a combined computational and experimental study that establishes two distinct mechanistic pathways for electrochemical CO_2 reduction catalyzed by [Fe]$^{2+}$ as a function of applied overpotential. Electrochemical data shows the formation of two catalytic regimes at low ($\eta_{TOF/2}$ of 160 mV) and high ($\eta_{TOF/2}$ of 590 mV) overpotential plateaus. We propose that at low overpotentials [Fe]$^{2+}$ undergoes a two-electron reduction, two-proton transfer mechanism (electrochemical-electrochemical-chemical-chemical, EECC), where turnover occurs through the dicationic iron complex, [Fe]$^{2+}$. Computational analysis supports the importance of the singlet ground state electronic structure for CO_2 binding and that the rate-limiting step is the second protonation in this low-overpotential regime. When more negative potentials are applied, an additional electron transfer event occurs through either a stepwise or proton-coupled electron transfer (PCET) pathway, enabling catalytic turnover from the monocationic iron complex ([Fe]$^{+}$) via an electrochemical-chemical-electrochemical-chemical (ECEC) mechanism. Comparison of experimental kinetic data obtained from variable controlled potential electrolysis (CPE) experiments with direct product detection with calculated rates obtained from the energetic span model support the PCET pathway as the most likely mechanism. Moreover, we build upon this mechanistic understanding to propose the design of an improved ligand framework that is predicted to stabilize the key transition states identified from our study and explore their electronic structures using an energy decomposition analysis. Taken together, this work highlights the value of synergistic computational/experimental approaches to decipher mechanisms of new electrocatalysts and direct the rational design of improved platforms



6.2 Introduction

Increasing energy demands and global climate change motivate the need for technologies that capture and utilize atmospheric carbon dioxide (CO_2) and convert it into value-added carbon products.[1–3] In this context, the electrochemical reduction of CO_2[4,5] offers a promising way to restore balance to the carbon cycle and develop a net negative carbon footprint if these technologies can be coupled to renewable sources of electricity. A diverse array of upgraded carbon products for the electrochemical CO_2 reduction reaction (CO_2RR) include CO, CH_3OH, and CH_4.[6] Of these products, the two-electron two-proton reduction of CO_2 to CO is economically most viable due to its usage in the Fischer-Tropsch process.[7]

In order to realize the goal of sustainable electrochemical carbon capture and conversion, efficient catalysts are required to selectively drive CO_2 reduction versus the thermodynamic and kinetically competitive hydrogen evolution reaction (HER).[5,8] The electrochemical CO_2 reduction reaction has been extensively explored across materials,[9] biological,[10] and molecular systems.[11] Molecular electrocatalysts are of particular interest as they are ideal platforms that can be rationally and systematically tuned through synthetic chemistry[12–14] with a level of precision and in the absence of defects that is unavailable to heterogeneous congeners.[9,15] Moreover, owing to their small size relative to enzymes and their homogeneous nature, they can be investigated at a mechanistic level which aids in the understanding and directed development of improved catalytic platforms.[14,16,17]

In this regard, iron-based molecular systems are especially desirable owing to the abundance of this element; the iron porphyrin platform Fe-TPP (TPP = tetraphenylporphyrin) is a robust and active catalyst making it a popular framework for ligand development with a considerable number of derivatives having been prepared in recent years.[18–28] The turnover frequency of the original Fe-TPP platform has been improved by several orders of magnitude from 10^2 s^{-1} to 10^6 s^{-1} for Fe-*o*-TMA, a tetra-substituted trimethylanilinium, derivative. The (current) top performance of 10^9 s^{-1} for Fe-TPP-based catalysts is achieved by introducing four bulky, methylimidazolium-containing groups.[29] The success story of the Fe-TPP system illustrates the effectiveness of systematic synthetic modification of the ligand scaffold and optimization of reaction conditions. Alternatively, simpler polypyridyl ligand platforms, including iron-bipyridine (bpy)[30,31] (**Figure 6.1a**) and iron-quaterpyridine (qpy)[32–35] (**Figure 6.1c**), have received increased attention for electrochemical CO_2 reduction chemistry. These systems are robust under electrochemical conditions and are synthetically accessible through facile and modular routes which facilitates precise tuning of their sterics and electronics in a rational fashion.

Against this backdrop, the development of novel metal-polypyridyl electrocatalysts for proton and CO_2 reduction has been a part of a larger research program between our laboratories in energy conversion chemistry.[30,31,36–38] We recently reported[39] a novel terpyridine (tpy)-based iron polypyridine complex (**Figure 6.1b**), $[Fe(tpyPY2Me)]^{2+}$ ($[Fe]^{2+}$), that leverages ligand non-innocence of the tpy moiety and metal-ligand cooperativity through exchange coupling. These two factors yield mild reduction potentials for the complex in comparison to other pyridine-based catalysts as illustrated in **Figure 6.1** and enables it to electrochemically convert CO_2 into CO at extremely low overpotentials (η), resulting in high product selectivity and rates under both organic solvents and aqueous conditions. The Faradaic efficiency for CO production (FE_{CO}), rates (k_{max})

and overpotentials of the three platforms are compared to the Fe-TPP platforms and summarized in **Table 6.1**. Comparison of these parameters clearly identifies these polypyridyl complexes as some of the best homogeneous catalysts to date, but we note that benchmarking should be done with care and caution. Indeed, determination of accurate overpotentials requires the use of the thermodynamic potential required to convert CO_2 into CO, which is often unknown for the exact experimental conditions and can thus vary by over 500 mV depending on solution conditions. To normalize for this uncertainly, we give the values reported by Matsubara[40] that take into account the effect of solvent mixtures, acid additives, and homoconjugation of phenol in acetonitrile.[40–43] Similarly, estimation of kinetic performance based on the maximum turnover frequency (TOF_{max}) is highly dependent on the method utilized (*e.g.*, foot-of-the-wave analysis, peak catalytic current analysis, etc).[44–48] As such, the methods used to determine the rates are indicated in Table 1. Specifically, in order to minimize uncertainty in rate determination for our $[Fe]^{2+}$ catalyst, we extracted the kinetic parameters directly from the averaged specific current densities for CO production obtained from variable potential CPE experiments that were conducted in triplicate as described by Savéant and coworkers.[49,50]

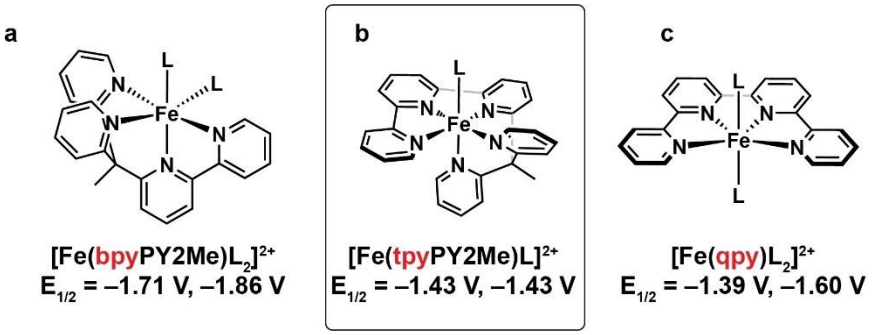


Figure 6.1. Overview of select iron polypyridyl molecular catalyst platforms for CO_2 reduction. Chemical structures of (a) $[Fe(bpyPY2Me)L_2]^{2+}$, (b) $[Fe(tpyPY2Me)L]^{2+}$, and (c) $[Fe(qpy)L_2]^{2+}$. Redox potentials for the iron catalyst are provided versus Fc/Fc^+. $[Fe(tpyPY2Me)L]^{2+}$ exhibits two single electron reduction events that are on top of each other and centered at –1.43 V vs Fc/Fc^+. L = H_2O or CH_3CN.

In our initial study of the $[Fe(tpyPY2Me)]^{2+}$ system, we reported the synthesis, characterization, and electrocatalytic behavior of $[Fe]^{2+}$ for CO_2RR to CO. Synthesis of the two-electron reduced product, $[Fe(tpyPY2Me)]^0$ ($[Fe]^0$), and spectroscopic characterization enabled us to attribute its exceptional catalytic activity to its unique open-shell singlet electronic structure that results from the antiferromagnetic coupling of the intermediate-spin Fe(II) center (S_{Fe} = 1) to a doubly reduced, triplet ligand system (S_{tpy} = 1). We were able to establish that this electronic structure was responsible for the reduction of CO_2 to CO at low overpotentials, through the preparation and comparison to a series of redox-(in)active metal and ligand controls. However, despite a detailed understanding of the electronic structure of the $[Fe]^{2+}$ system and its two-electron reduced product, the mechanism(s) through which it functions in CO_2RR are insufficiently explored. In the present study, we use a combined experimental and computational approach to identify two distinct mechanistic pathways for CO_2RR catalyzed by $[Fe(tpyPY2Me)]^{2+}$ depending on applied overpotential, η. We propose that at low overpotentials [$E_{cat/2}$ of –1.43 V vs Fc/Fc^+ ($\eta_{TOF/2}$ = 0.16 V)], $[Fe]^{2+}$ undergoes a two-electron reduction, two-proton transfer mechanism

(electrochemical-electrochemical-chemical-chemical, EECC) where turnover occurs though the dicationic iron complex, $[Fe]^{2+}$. At higher overpotentials [$E_{cat/2}$ of –1.86 V vs Fc/Fc^+ ($\eta_{TOF/2}$ = 0.59 V)], an additional electron transfer event becomes possible through either a stepwise or a proton-coupled electron transfer (PCET) pathway, enabling catalytic turnover from the monocationic iron complex ($[Fe]^+$) via an electrochemical-chemical-electrochemical-chemical (ECEC) mechanism (see Materials and Methods section for details surrounding the determination of $E_{cat/2}$ and $\eta_{TOF/2}$). The PCET steps considered in this manuscript corresponds to concerted electron-proton transfer. Based on this detailed mechanistic analysis, we propose the design of improved ligand frameworks and explore their electronic structures with an energy decomposition analysis (EDA). This mechanistic analysis lays the foundation for further rational optimization of theoretically driven modifications of the ligand scaffold for improved catalytic activity.

Table 6.1. Key benchmark metrics for the three pyridine based catalytic platforms and direct comparison to the TPP frameworks. Rates for $[Fe(bpy^{NHEt}PY2Me)L_2]^{2+}$ and FeTPP were determined by FOWA. Rates for $[Fe(qpy)(H_2O)_2]^{2+}$ and Fe-*o*-TMA were measured with catalytic plateau analysis and from bulk electrolysis current. $[Fe(tpyPY2Me)]^{2+}$ rates were extracted directly from the averaged specific current densities for CO production obtained from variable potential CPE experiments that were conducted in triplicate.

Platform	FE_{CO} (%)	TOF_{max} (s^{-1})	η_{eff} (V)	Ref.
$[Fe(bpy^{NHEt}PY2Me)L_2]^{2+}$	81	102	0.66	[30]
$[Fe(tpyPY2Me)]^{2+}$	97	105	0.71	[39]
$[Fe(qpy)(H_2O)_2]^{2+}$	70	102	0.24	[33]
FeTPP	93	102	0.67	[40]
Fe-*o*-TMA	93	106	0.60	[22,40]

6.3 Results and Discussion

6.3.1 Observation of Two Distinct Overpotential-Dependent Regimes for Electrochemical CO_2 Reduction Catalyzed by $[Fe(tpyPY2Me)]^{2+}$

Electrochemical analysis of this molecular iron CO_2RR system exhibits two distinct catalytic regimes that are dependent on applied potential (**Figure 6.2**). Cyclic voltammograms collected under CO_2 atmosphere with the addition of 1 M phenol (PhOH), as a proton source, shows the formation of two catalytic waves. The first regime reaches a half-maximum catalytic current at a potential of −1.43 V vs Fc/Fc^+ ($E^1_{cat/2}$; $\eta = 160$ mV) and displays canonical S-shaped wave instructive of pure kinetic conditions without substrate consumption.[43,44] At more negative applied potentials beyond −1.75 V vs Fc/Fc^+ ($\eta = 480$ mV), a second catalytic response is observed reaching a half-maximum catalytic current at a potential of −1.86 V vs Fc/Fc^+ ($E^2_{cat/2}$; $\eta = 590$ mV). This second catalytic regime shows peak-shaped behavior indicative of substrate consumption by the rate-determining step (**Figure 6.2**).[44]

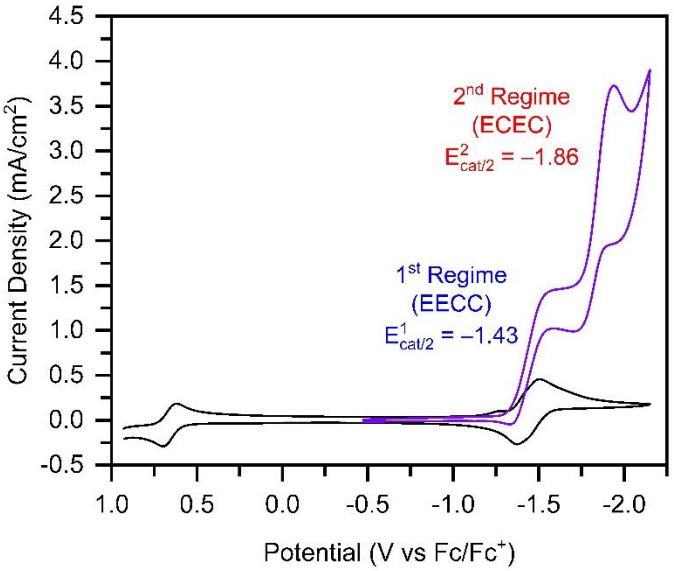


Figure 6.2. Electrochemical Characterization of $^1[Fe]^{2+}$. Cyclic voltammograms of $^1[Fe]^{2+}$ collected under Ar (black) and CO_2 (purple) with the addition of 1 M PhOH as a proton source. Cyclic voltammograms were collected with a scan rate of 100 mV/s with an electrolyte of 0.10 M $TBAPF_6$ dissolved in CH_3CN. The proposed two distinct mechanistic pathways for $^1[Fe]^{2+}$ are designated by the potentials at which they reach half of the maximum catalytic current ($E_{cat/2}$) at –1.43 and –1.86 V vs Fc/Fc^+ and are labeled in blue and red, respectively. The first regime turns over from the 2^+ complex and undergoes a proposed EECC mechanism while the second regime at more negative potentials undergoes turnover from the 1^+ complex *via* an ECEC mechanism.

The catalytic voltammogram clearly illustrates the formation of two catalytic waves with maximum current densities achieved at approximately −1.66 V vs Fc/Fc^+ ($\eta = 390$ mV) and −1.98 V vs Fc/Fc^+ ($\eta = 710$ mV). We attribute this behavior to the occurrence of two distinct catalytic regimes with disparate mechanisms. Building on this observation, we explore various reaction pathways for these two catalytic regimes in the presence of 1 M PhOH and 4-chlorophenol (Cl-

PhOH) to probe the effect of the pK_a on the observed rates and to investigate the origin of selectivity of $[Fe]^{2+}$ for the CO_2RR relative to the HER (*vide infra*). The proposed mechanisms are in line with experimental kinetic data obtained from controlled potential electrolysis (CPE) data collected with direct product detection *via* gas chromatography. In order to compactly provide relevant information regarding the electronic structure of the proposed catalytic intermediates along the way, we introduce a naming scheme that incorporates the multiplicity (M, M= 2S+ 1), charge (C), and the identity of the sixth, axial ligand (X) on the iron center: $^{M}[Fe{-}X]^{C}$; for example, $^{1}[Fe{-}CH_3CN]^{2+}$ corresponds to the unreduced, hexacoordinated initial iron complex in the singlet state.

6.3.2 Low Overpotential Pathway

Figure 6.2 shows that the current density of the first catalytic regime reaches a plateau at approximately −1.66 V vs Fc/Fc^+ (η = 390 mV) with rates that are slower relative to the second catalytic regime. A mechanism for this first regime is illustrated in **Figure 6.3** and presented in this section.

First, we propose two, sequential single electron reduction steps followed by the dissociation of CH_3CN to generate the catalytically active open-shell singlet, $^{1}[Fe]^{0}$. CO_2 binding and subsequent protonation steps can then occur resulting in the loss of a water molecule and the formation of $^{1}[Fe{-}CO]^{2+}$. Ligand exchange with exogenous CH_3CN and CO release closes the catalytic cycle. Interestingly, the formal oxidation state of the central metal does not change during catalysis. The following sections will expand upon these proposed individual elementary steps before we expand our discussion to include a proposed catalytic pathway for the second catalytic region that occurs at more negative potentials.

6.3.3 Reduction

The reduction pathway of $^{1}[Fe]^{2+}$ was established in our initial report.[39] Variable temperature NMR and Mössbauer studies established that the starting $^{1}[Fe]^{2+}$ complex is predominantly low-spin Fe(II) with a small population of thermally accessible spin excited states near room temperature that we attributed to the axial distortions engendered by the rigid tpyPY2Me ligand (**Figure 6.4a**). The first reduction of $^{1}[Fe]^{2+}$ is ligand centered, with occupation of the tpy-π^* orbital with almost no excess spin density on the metal center, yielding $^{2}[Fe{-}CH_3CN]^{+}$, a ground state doublet composed of an low-spin Fe(II) center and a radical anion $tpyPY2Me^{-}$ ligand (**Figure 6.4b**). The addition of a second electron occupies another tpy-π^* orbital and induces a spin-state transition of the iron center from low-spin (S_{Fe} = 0) to intermediate-spin (S_{Fe} = 1) and ligand dissociation of the axially coordinated CH_3CN solvent molecule. This tetraradicaloid electronic configuration allows for strong exchange coupling of the two unpaired d electrons on the intermediate-spin iron center with the two electrons in the tpy-π^* manifold, forming an overall open-shell singlet ground state, $^{1}[Fe]^{0}$ (**Figure 6.4c**). The open-shell singlet electronic structure was validated by synthesizing and isolating $^{1}[Fe]^{0}$ from the chemical reduction of $^{1}[Fe]^{2+}$ with decamethylcobaltocene and fully characterizing the resulting coordination compound by single-crystal X-ray crystallography, Mössbauer spectroscopy, X-ray absorption spectroscopy, and DFT and CASSCF calculations. Through these spectroscopic studies and with comparison to control complexes, we were able to attribute the catalysis of $^{1}[Fe]^{2+}$ for the CO_2RR

at mild overpotentials to this antiferromagnetic complex. The predicted reduction potentials for the two reductions are −1.46 V and −1.51 V vs Fc/Fc^+, which are in good agreement with the experimental cyclic voltammetry data collected under argon atmosphere that show two closely spaced one-electron reduction waves centered at −1.43 V vs Fc/Fc^+. The exchange-coupling shifts the second reduction wave positive by a remarkable 640 mV relative to $[Zn(tpyPY2Me)]^{2+}$ which employs the same redox-active tpyPY2Me ligand, but contains a Zn(II) metal center that is unable to participate in stabilization through antiferromagnetic coupling.

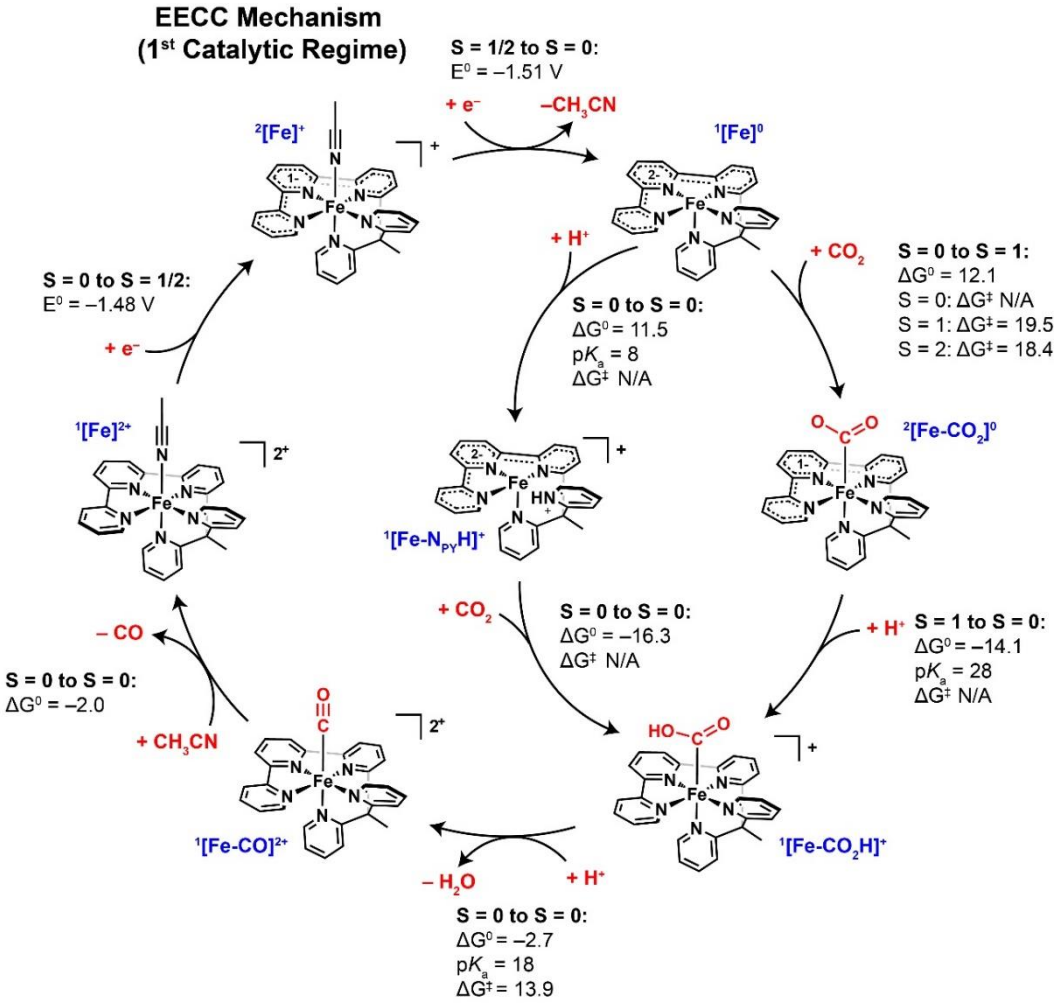


Figure 6.3. Proposed mechanistic pathways for the low overpotential regime. Starting from $^1[Fe]^{2+}$ (left side), we first propose two one-electron reduction steps followed by the dissociation of CH_3CN to generate the catalytically active open-shell singlet, $^1[Fe]^0$. CO_2 binding and subsequent protonation steps can then occur resulting in the loss of a water molecule and the formation of $^1[Fe{-}CO]^{2+}$. Ligand exchange with exogenous CH_3CN and CO release closes the catalytic cycle (outer pathway). Alternatively, direct protonation of the pyridyl arm in $^1[Fe]^0$ to give $^1[Fe{-}N_{PY}H]^+$ followed by CO_2 coordination and proton transfer was found to be a competitive pathway (inner pathway). All reaction and activation energies are given in units of kcal/mol and all reduction potentials are referenced to the computed Fc/Fc^+ couple.

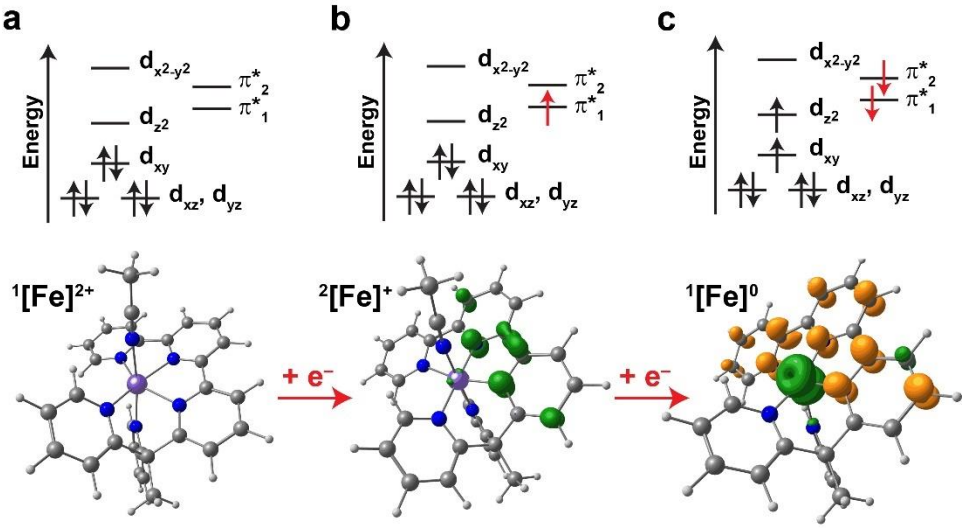


Figure 6.4. Spin densities and schematic MO diagrams: (a) unreduced complex ^{1}[Fe–L]$^{2+}$ exhibiting no spin density; (b) singly reduced complex, ^{1}[Fe–L]$^{2+}$, exhibiting spin density solely in the tpy ligand; (c) doubly reduced complex, ^{1}[Fe–L]$^{2+}$, exhibiting spin density on both the metal center and the tpy moiety of the tpyPY2Me ligand in an exchange coupled state.

6.3.4 CO_2 Binding

CO_2 coordination occurs after ^{1}[Fe]$^{2+}$ has been reduced by two electrons and the iron center has undergone a spin-state transition and subsequent ligand dissociation of the axially bound solvent molecule. The binding of CO_2 under standard conditions is endergonic and remains on the singlet surface yielding ^{1}[Fe–CO_2]^0. We attempted to stabilize the CO_2 adduct with the addition of either explicit water molecules or electrolyte ($TBAPF_6$) but the binding remains endergonic with a free energy of +12.1 kcal/mol (ΔH = ~4 kcal/mol). The addition of an explicit phenol led to direct protonation of the CO_2 moiety. The CO_2 ligand is bound *via* the carbon atom with an angle of 124° (**Figure 6.5a**). This structure is indicative of a closed shell highly reduced CO_2 moiety and a low-spin singlet Fe(II) center with a neutral tpyPY2Me ligand. The LOBA analysis indicate that the two excess electrons are stabilized in a delocalized MO, which mainly consists of the CO_2 π^* orbitals but also has significant contribution of the Fe-3d_{z^2} (40%) and some contribution of the tpy π^* (see **Figure 6.6**).

The endergonic binding can be rationalized by the high stability of ^{1}[Fe]^0, attributed to its antiferromagnetically coupled electronic structure, which yields a positive reduction potential but consequently at the cost of sluggish CO_2 binding. This prediction is in line with experimental findings as high concentrations of PhOH are required to observe CO_2 binding and subsequent catalysis. In order to probe the binding of CO_2, we attempted to measure the equilibrium constants for CO_2 binding (K_{CO_2}), based on the potential shift of the ligand reduction wave under Ar and CO_2 atmosphere (**Figure 6.7**). Under an Ar atmosphere, without the addition of PhOH as a proton source, there is no shift in the ligand reduction waves centered at −1.43 V vs Fc/Fc^+ (**Figure 6.7a**). When PhOH (1 M) is added, a catalytic wave is formed; however, a reversible couple could not be observed even when the experiment was performed with fast scan rates up to 50 V/s (**Figure 6.7b,c**). Taken together, these results suggest that CO_2 binding and thus catalysis is hampered

when the system is proton limited. Interestingly, the higher spin-state surfaces [triplet (^{3}[Fe]^0) and quintet (^{5}[Fe]^0)] both exhibited much higher barriers for CO_2 binding that would effectively prevent catalysis. Thus, the open-shell singlet electronic structure of ^{1}[Fe]^0 is key not only to decrease the overpotentials required for catalysis but also to facilitate CO_2 binding even though it is thermodynamically difficult. We further investigated an alternative pathway of CO_2 binding to a singly reduced intermediate (^{2}[Fe]$^+$). This pathway results in an even more endergonic CO_2 binding (14.1 kcal/mol) making it an unlikely intermediate.

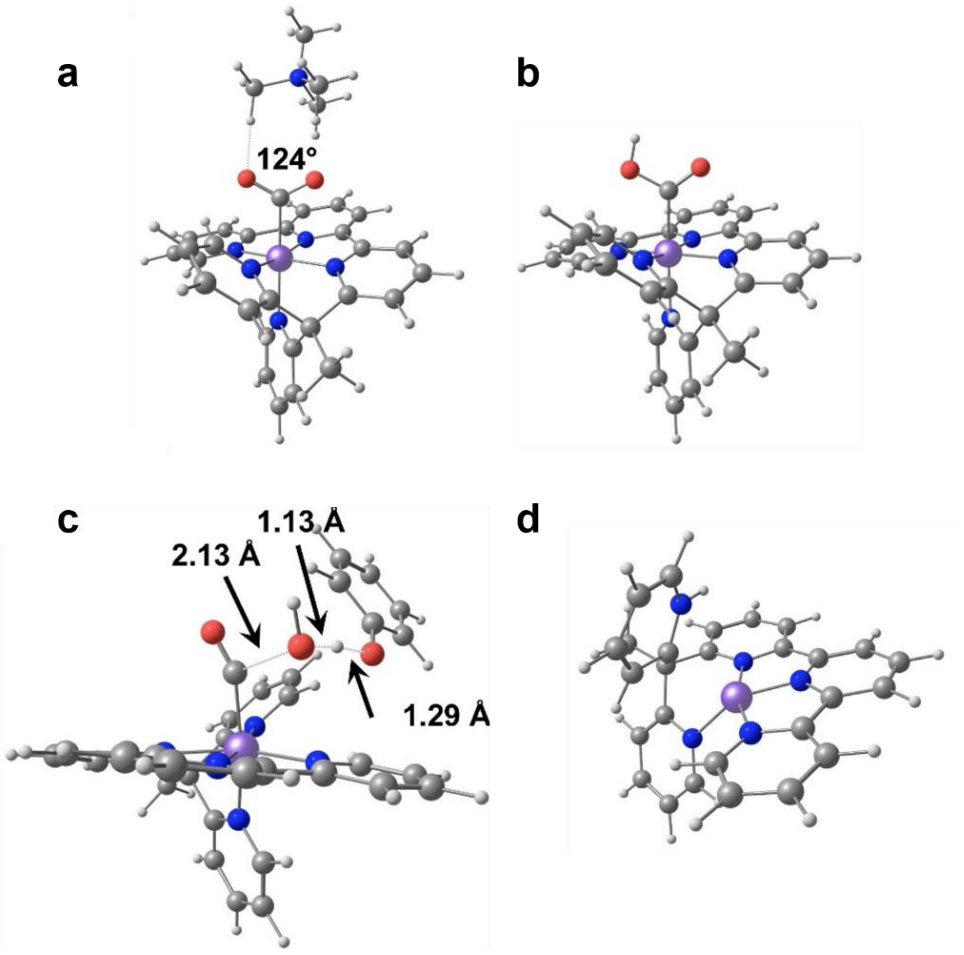


Figure 6.5. Geometry of key intermediates of the low overpotential mechanism: (a) CO_2 adduct, ^{1}[Fe–CO_2]^0 included a counter ion; (b) carboxy intermediate, ^{1}[Fe–CO_2H]$^+$; (c) transition state for the rate-determining, second protonation step; (d) pyridinium intermediate, ^{1}[Fe–N_{PY}H]$^+$.

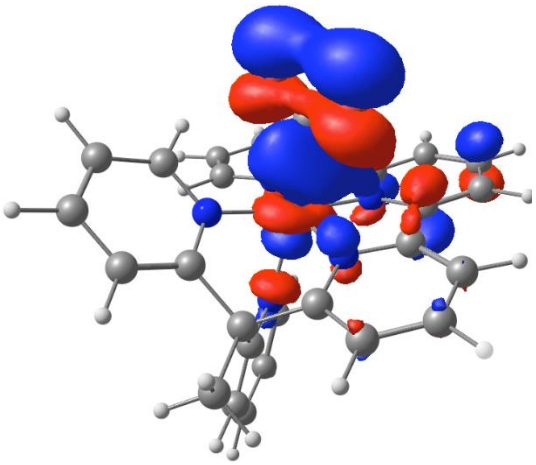


Figure 6.6. LOBA orbital illustrating the stabilization of the two excess electrons in $^{1}[Fe\text{-}CO_2]^{0}$.

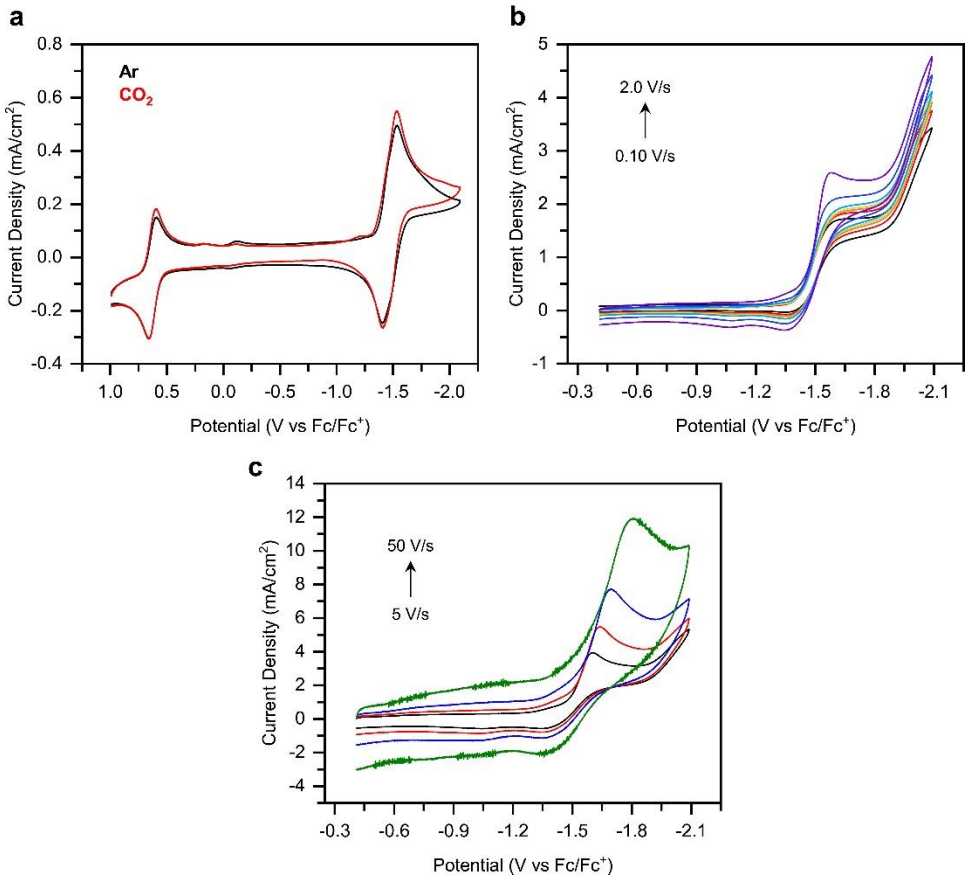


Figure 6.7. Electrochemical analysis of $^{1}[Fe]^{2+}$ to determine CO_2 binding equilibrium. (a) Cyclic voltammograms collected under Ar (black) and CO_2 (red) without the addition of phenol. (b) Catalytic voltammograms of $^{1}[Fe]^{2+}$ collected under CO_2 atmosphere with 1 M phenol with scan rates increasing to 2.0 V/s. (c) Scan rates were increased to 50 V/s to try to isolate a reversible couple from which CO_2 binding equilibrium could be obtained.

6.3.5 Protonation

In a first scenario, the first protonation of $^1[Fe{-}CO_2]^0$ is barrierless and strongly exergonic (−16.9 kcal/mol) yielding the carboxyl intermediate, $^1[Fe{-}CO_2H]^+$ (**Figure 6.5b**). This intermediate can be best described as a CO_2H^- moiety coordinated to the Fe(II) center with the neutral tpy ligand framework. The second proton transfer step is exergonic (−2.1 kcal/mol) but with a barrier of 13.9 kcal/mol as it is coupled to the cleavage of the C−O bond and results in the loss of water and the formation of the carbonyl intermediate ($^1[Fe{-}CO]^{2+}$) (**Figure 6.5c**). The transition state geometry is depicted in **Figure 6.8**. The influence of explicit solvent molecules added to the transition state geometry was probed, but we were unable to find lower barriers with the addition of exogenous water molecules. In a second scenario, $^1[Fe]^0$ is protonated at one of the pyridine arms yielding a pyridinium intermediate, $^1[Fe{-}N_{PY}H]^+$ (**Figure 6.5d**). The calculated pK_a of 8 is quite acidic (versus a calculated pK_a of 16 for H_2CO_3); thus, the free energy of protonation coupled to carbonic acid is 11.5 kcal/mol. Previous experimental work by Matsubara shows that the pK_a of the reaction mixture is significantly lower with the addition of water. The experimental pK_a for CO_2 saturated water-acetonitrile mixtures can range from 7.8 to 16.8 where we would expect the addition of molar quantities of PhOH to further acidify the solution thus making this intermediate competitive.[40] The binding of CO_2 to $^1[Fe{-}N_{PY}H]^+$ is very exergonic (−16.3 kcal/mol) and directly yields a carboxy intermediate, $^1[Fe{-}CO_2H]^+$ (**Figure 6.5b**), by skipping the high energy CO_2 adduct. This adduct is achieved by a simultaneous intramolecular proton transfer from the pyridinium and electron transfer from the tpy upon binding of CO_2 to form CO_2H^-. The second protonation proceeds as described above, see **Figure 6.3** (outer pathway).

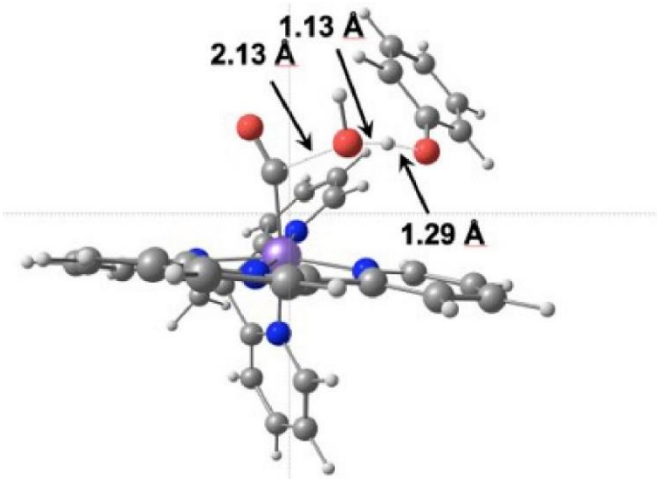


Figure 6.8. Transition state Geometry for the formation of $^1[Fe{-}CO]^{2+}$.

6.3.6 CO Release

CO release from $^1[Fe{-}CO]^{2+}$ is exergonic and barrierless which can be attributed to the relatively high oxidation state of the iron center, which limits backbonding interactions. In addition, the low solubility of CO in CH_3CN promotes removal of CO from solution and into the gas phase. In order to further probe CO coordination and release, CVs of $^1[Fe]^{2+}$ were collected under CO atmosphere and compared to data collected under Ar atmosphere. The addition of CO results in the formation of very small reductive features at −0.59 and a quantitative reductive wave

at −1.23 V vs Fc/Fc^+. Additionally, the reversibility in the ligand reduction waves centered at −1.43 (**Figure 6.9a**) are lost at slower scan rates of 100 mV/s. We tentatively assign the new reduction wave at −1.23 V vs Fc/Fc^+ to the reduction of an Fe(II)-carbonyl species ($^1[Fe{-}CO]^{2+}$). This value agrees well with the predicted reduction potential of −1.18 V vs Fc/Fc+, supporting this assignment. We do note that attempts to spectroscopically characterize the waves at −0.59 and −1.23 V vs Fc/Fc^+ have been unsuccessful to date. Multi-segmented CV data collected under CO_2 atmosphere with the addition of 1 M PhOH, do not show any significant changes or the formation of new reductive features that could be attributed to the buildup of iron carbonyl species in the voltammograms across one-hundred cycles (**Figure 6.9**). Taken together, these data support the computational findings that CO binding is weakly endergonic by 2 kcal/mol and barrierless and thus we do not observe the accumulation of iron carbonyl species under electrocatalytic conditions. Further reduction of an iron carbonyl intermediate $^2[Fe{-}CO]^+$ to $^1[Fe{-}CO]^0$ can be eliminated based on the predicted redox potential which is more negative than −2.0 V vs Fc/Fc^+. A similar Fe(II)-carbonyl species equipped with a comparable terpyridine and pyridyl-N-heterocyclic carbene based ligand system was synthesized and structurally characterized by ^1H NMR and single crystal X-ray diffraction by Miller and coworkers.[51] Chemical reduction with two equivalents of decamethylcobaltocene resulted in the dissociation of the pyridine ligand and the formation of a pentacoordinate, low-valent iron carbonyl complex that was unfortunately shown to undergo rate limiting endergonic release of CO. The hemilability of the pyridyl arm to generate a stable 18-electron complex may be a defining feature to explain the difference in catalytic activity and speaks to the potential advantages engendered by utilizing a homoleptic tpyPY2Me ligand system.

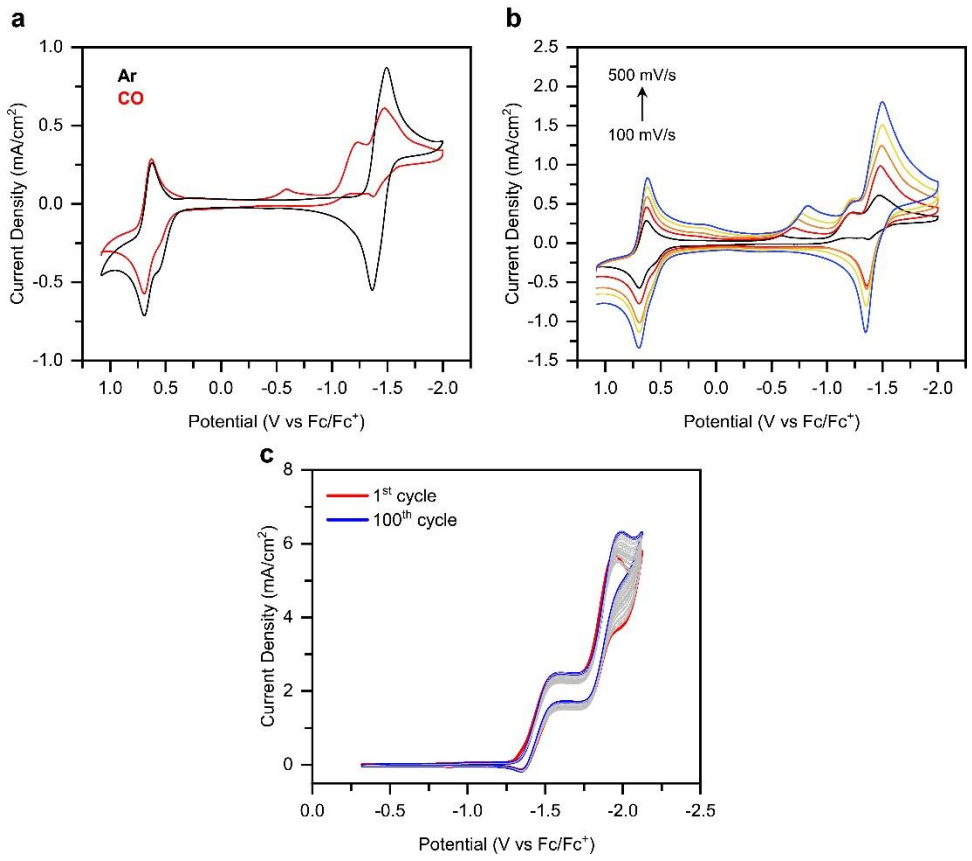


Figure 6.9. Investigation of CO binding to $^{1}[Fe]^{2+}$ under electrochemical conditions. (a) Cyclic voltammograms of $^{1}[Fe]^{2+}$ collected under Ar (black) or CO (red) atmosphere. Data was collected with a scan rate of 100 mV/s (b) Cyclic voltammograms of $^{1}[Fe]^{2+}$ collected at variable scan rates (100 mV−500 mV/s) under CO atmosphere. (c) Multi-segmented cyclic voltammograms of $^{1}[Fe]^{2+}$ collected under CO_2 atmosphere with 1 M PhOH. 100 cycles were collected with a scan rate of 100 mV/s where no significant changes in the reductive features were observed that would be consistent with the formation of significant amounts of $^{1}[Fe\text{-}CO]^{2+}$.

6.3.7 High Overpotential Pathway

The application of more reducing potentials beyond −1.7 V vs Fc/Fc^{+} results in the formation of a second catalytic wave. A mechanism for this high overpotential regime is illustrated in **Figure 6.10** and presented in detail in this section. Here we investigate three potential pathways and found two to be aligned with experimental findings.

In all three cases, the initial reduction steps are identical in redox potential and electronic structure to what we presented for the low overpotential pathway discussed above. However, the first electron transfer is off-pathway; where at more reducing potentials, we find that there is enough driving force to reduce the carboxy intermediate ($^{1}[Fe{-}CO_2H]^{+}$) with a predicted redox potential of −1.83 V vs Fc/Fc^{+} (*vide infra*). This observation results in catalytic turnover occurring from the singly reduced, iron complex ($^{1}[Fe]^{+}$) rather than turnover from the unreduced $^{1}[Fe]^{2+}$.

The three mechanistic pathways explored below diverge following the formation of the $^{1}[Fe]^{0}$ catalytic resting state.

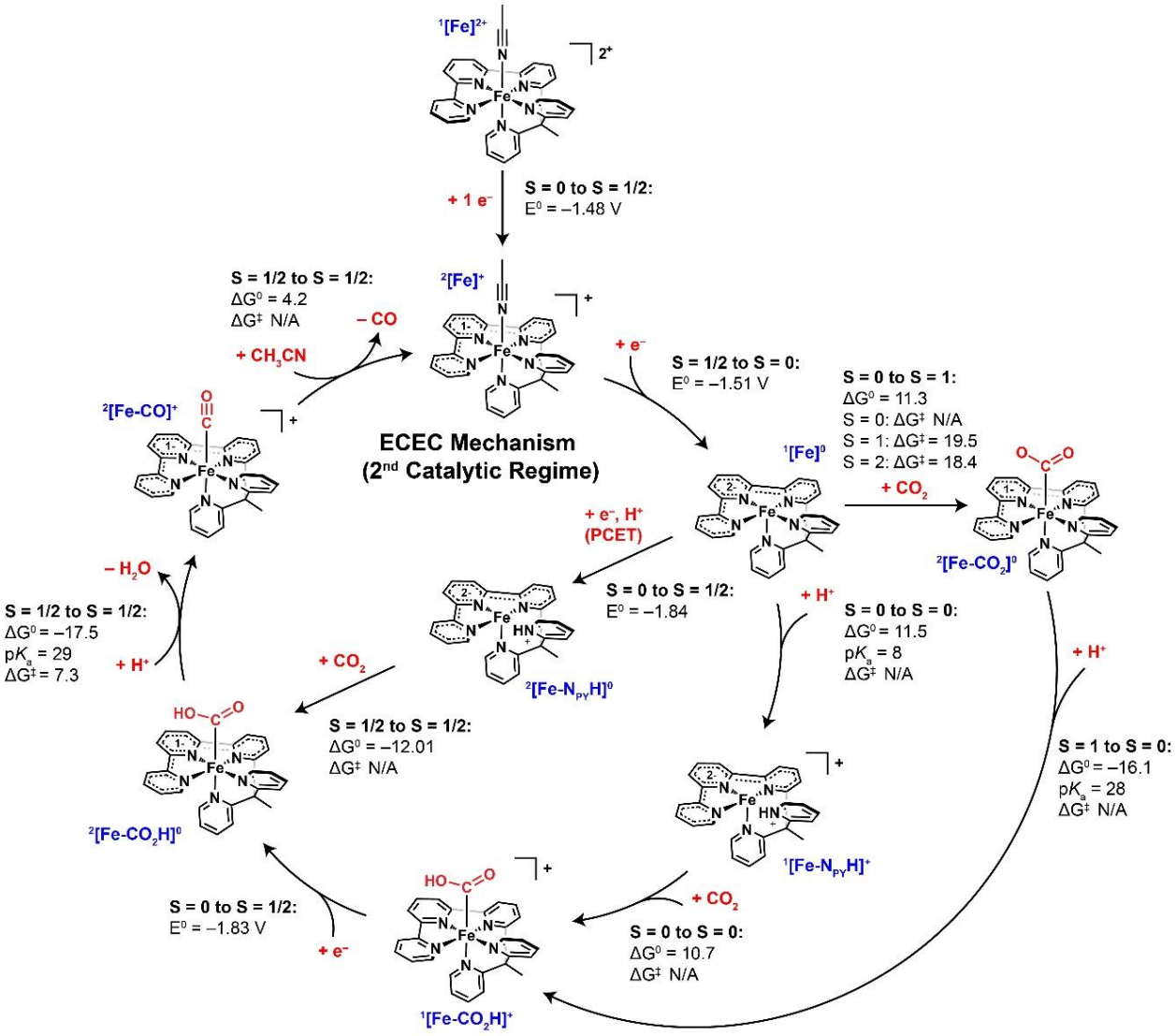


Figure 6.10. Proposed mechanistic cycles for the high overpotential regime. The high overpotential catalytic regime turns over from $^{2}[Fe]^{+}$ following an initial induction period. Single-electron reduction of $^{2}[Fe]^{+}$ gives the catalytic resting state, $^{1}[Fe]^{0}$. Following formation of $^{1}[Fe]^{0}$, the pathway diverges in three directions. CO_2 binding can occur first followed by protonation to give $^{1}[Fe{-}CO_2H]^{+}$ (outer pathway) or protonation-first can occur followed by CO_2 coordination (inner pathway). The $^{1}[Fe{-}CO_2H]^{+}$ intermediate can then be further reduced to $^{2}[Fe{-}CO_2H]^{0}$ and following the final protonation step and loss of water generates the carbonyl complex, $^{2}[Fe{-}CO]^{+}$ which regenerates $^{2}[Fe]^{+}$ following ligand exchange. We additionally explore the possibility of overcoming the high energy barriers associated with either CO_2 binding or protonation of $^{1}[Fe]^{0}$ by undergoing a PCET pathway to generate $^{2}[Fe{-}N_{PY}H]^{0}$ (center pathway). All reaction and activation energies are given in units of kcal/mol and all reduction potentials are referenced to the computed Fc/Fc^{+} couple.

The proposed mechanism is depicted in **Figure 6.10**. In the first two scenarios, from the $^1[Fe]^0$ intermediate, CO_2 coordination (**Figure 6.10**; outer cycle) or protonation (**Figure 6.10**; inner cycle) can occur first as discussed above for the low overpotential regime. Both pathways are uphill by approximately 11 kcal/mol and barrierless. The two pathways converge at the formation of the CO_2H adduct, $^1[Fe{-}CO_2H]^+$, that can be further reduced at a calculated applied potential of −1.83 V vs Fc/Fc^+ yielding $^2[Fe{-}CO_2H]^0$ where the electron populates one of the low-lying tpy-π^* orbitals. The second proton transfer step to lose water and yield the carbonyl intermediate, $^2[Fe{-}CO]^+$, is strongly exergonic by −17.5 kcal/mol (**Figure 6.11**). Moreover, the activation barrier for the second protonation is 7.3 kcal/mol, which is 4 kcal/mol lower than the barrier for the C−O bond cleavage step in the low overpotential regime. The CO release becomes endergonic by 4.2 kcal/mol due to the excess electron density that is transferred from the tpy-π^* orbital to the Fe−CO moiety thus strengthening the backbonding to the CO ligand. Hence, the additional reductive event significantly lowers the barrier of the second protonation at the cost of more difficult CO release. Therefore, the second protonation is not as critical as in the low overpotential regime. Depending on the pathway, either the addition of CO_2 (12.1 kcal/mol) or the protonation of the $^1[Fe{-}py{-}H]^+$ (11.5 kcal/mol) become critical steps as well. Unfortunately, it is not possible to distinguish those two pathways computationally due to the small relative energy difference of 0.6 kcal/mol and the error associated with the predictions of protonation and CO_2 addition. It is possible that both channels are populated.

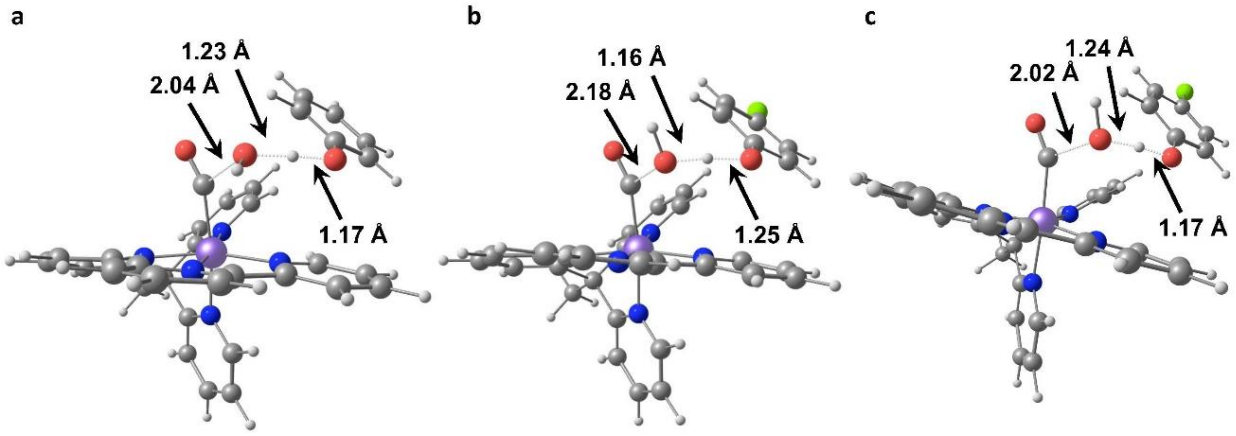


Figure 6.11. Transition states for the second protonation step: (a) after a third reduction step; (b) after two reduction steps with Cl-PhOH as the proton source; (c) after a third reduction step with Cl-PhOH as the proton source.

In a third scenario, following the formation of $^1[Fe]^0$, a proton coupled electron transfer (PCET) pathway is possible where one of the pyridyl arms is protonated yielding $^2[Fe{-}N_{PY}H]^0$. The additional electron is localized in the pyridinium moiety; thus, the electronic structure can be described as a doubly reduced tpy-π^* moiety coupled to the intermediate spin iron center and a singly reduced pyridinium; this structure is summarized in the spin density plot in **Figure 6.12**. The reduction potential is acid dependent; using H_2CO_3 the calculated reduction potential is –2.14 V vs. Fc/Fc^+. However, taking non-standard concentrations into account using a similar approach to Song and coworkers,[52] we compute a shift by 0.3 V resulting in a potential of –1.84 V. For reference using H^+ the computed reduction potential is –1.17 V vs Fc/Fc^+. Next, CO_2 can bind to

^{2}[Fe−N$_{PY}$H]^0 to directly yield ^{2}[Fe−CO$_2$H]^0 in an intramolecular proton and electron transfer step with a free energy of −12.0 kcal/mol and thus also “skipping" the high energy CO_2 adduct intermediate. The role of proton transfer during catalysis was examined by measuring the H/D kinetic isotope effects in both catalytic regimes using C_6H_5OH (PhOH-H$_6$) or C_6D_5OD (PhOH-D$_6$) as the proton source (**Figure 6.13**). Experimentally, normal primary H/D kinetic isotope effects were observed under both catalytic regimes (k_H/k_D of 1.59 and 1.22, respectively), suggesting that proton transfer is involved in the rate determining step, thus supporting the protonation-first pathways, and excluding the CO_2-first mechanism.

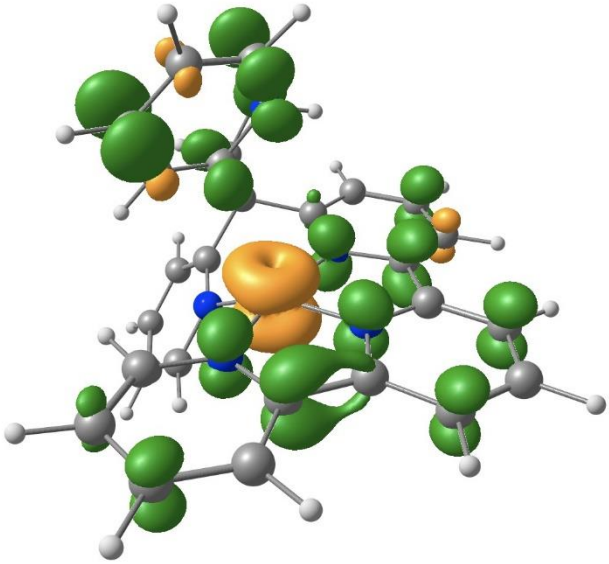


Figure 6.12. Spin-density plot for the reduced pyridinium intermediate, ^{2}[Fe-N$_{PY}$H]^0.

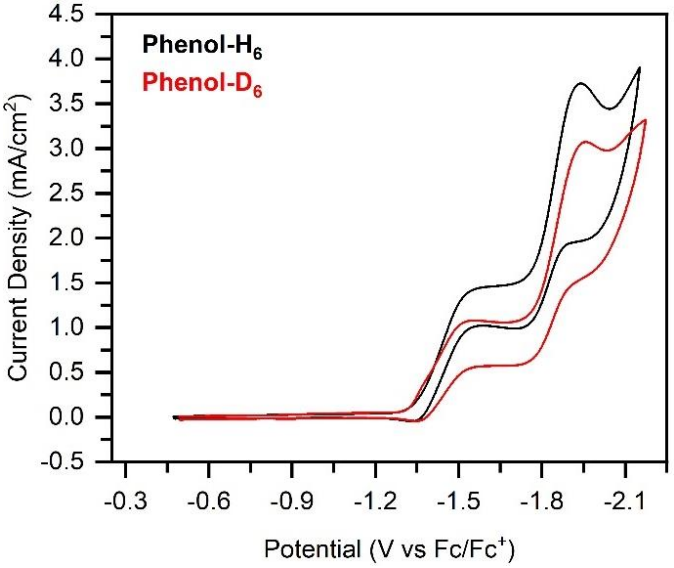


Figure 6.13. H/D Kinetic isotope experiments for the ^{1}[Fe]$^{2+}$ catalyst.

6.3.8 Kinetic Analysis of Proposed Mechanistic Pathways

The free energy landscape summarizing the total catalytic cycle is depicted in **Figure 6.14**. Following elucidation of the possible reaction pathways for CO_2 reduction across both potential-dependent regimes, we next sought to compare experimentally determined kinetic data against computationally derived turnover frequencies (TOFs) obtained from the energetic span computational model developed by Kozuch and coworkers.[53] The energetic span model was employed to identify key intermediates and transition states, which control the rate of catalysis. This model connects the free energy landscape of the DFT based catalytic cycles with the experimentally measured TOFs using Eyring transition state theory. The model identifies TOF-determining transition states (TDTS) and the TOF-determining intermediates (TDI) and computes rates based on the energetic span of these two states.[53] Often there are various intermediates with a significant influence on the catalytic rates. This progression can be quantified in this model by the degree of TOF control (denoted as X_{TOF}),[54] which describes how the TOF varies by a small change in energy of that intermediate or transition state. The range of X_{TOF} is between 0 and 1, where 0 denotes that the species has no influence on the TOF and 1 denotes that the species solely controls the TOF.[55,56]

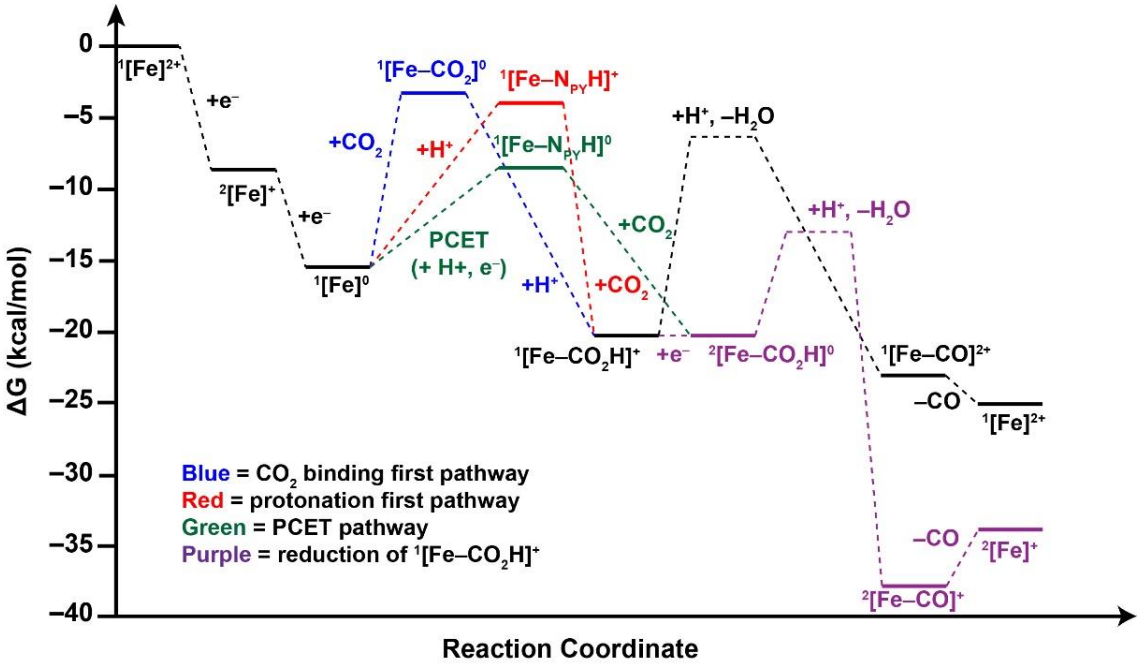


Figure 614. Free energy landscape for the low overpotential (**Figure 6.3**) and high overpotential (**Figure 6.10**) CO_2RR regimes. Colors signify different possible pathways that were proposed in the catalytic cycles shown in **Figures 6.3** and **6.10**. From the doubly reduced $^1[Fe]^0$ intermediate, the blue line signifies the CO_2 binding first pathway, the red line denotes the protonation first pathway, and the green plots the PCET pathway. The purple line indicates the pathway where the $^1[Fe\text{-}CO_2H]^+$ intermediate is further reduced in the high overpotential regime (refer to **Figure 6.10**). For the reduction steps, a potential of −1.8 V vs Fc/Fc^+ is applied; for the protonation steps, PhOH is used to estimate barriers and carbonic acid for free energies; solid lines correspond to intermediate states and dashed lines to transition states.

Experimental kinetic parameters were obtained from variable controlled potential (CPE) experiments as described by Savéant and co-workers.[49,50] Short-term (5 min; **Figure 6.15**) and long-term (1 h; **Figures 6.16** and **6.17**) CPE experiments were performed where the products (CO and H_2) were detected and quantified by gas chromatography for the long-term CPE experiments conducted in an air-tight electrochemical cell. The observed rate constants (k_{obs}) at each applied potential were extracted from the average specific current densities taken across the entire electrolysis experiment and were then compared to the computed rates obtained from the energetic span model (**Figures 6.16** and **6.17** and **Tables 6.2–6.7**). To further probe the influence of the proton transfer step on the observed rates, PhOH (see **Figure 6.15**), and Cl-PhOH (see **Figures 6.16 – 6.18**), which is approximately one pK_a unit more acidic (in water), were utilized.

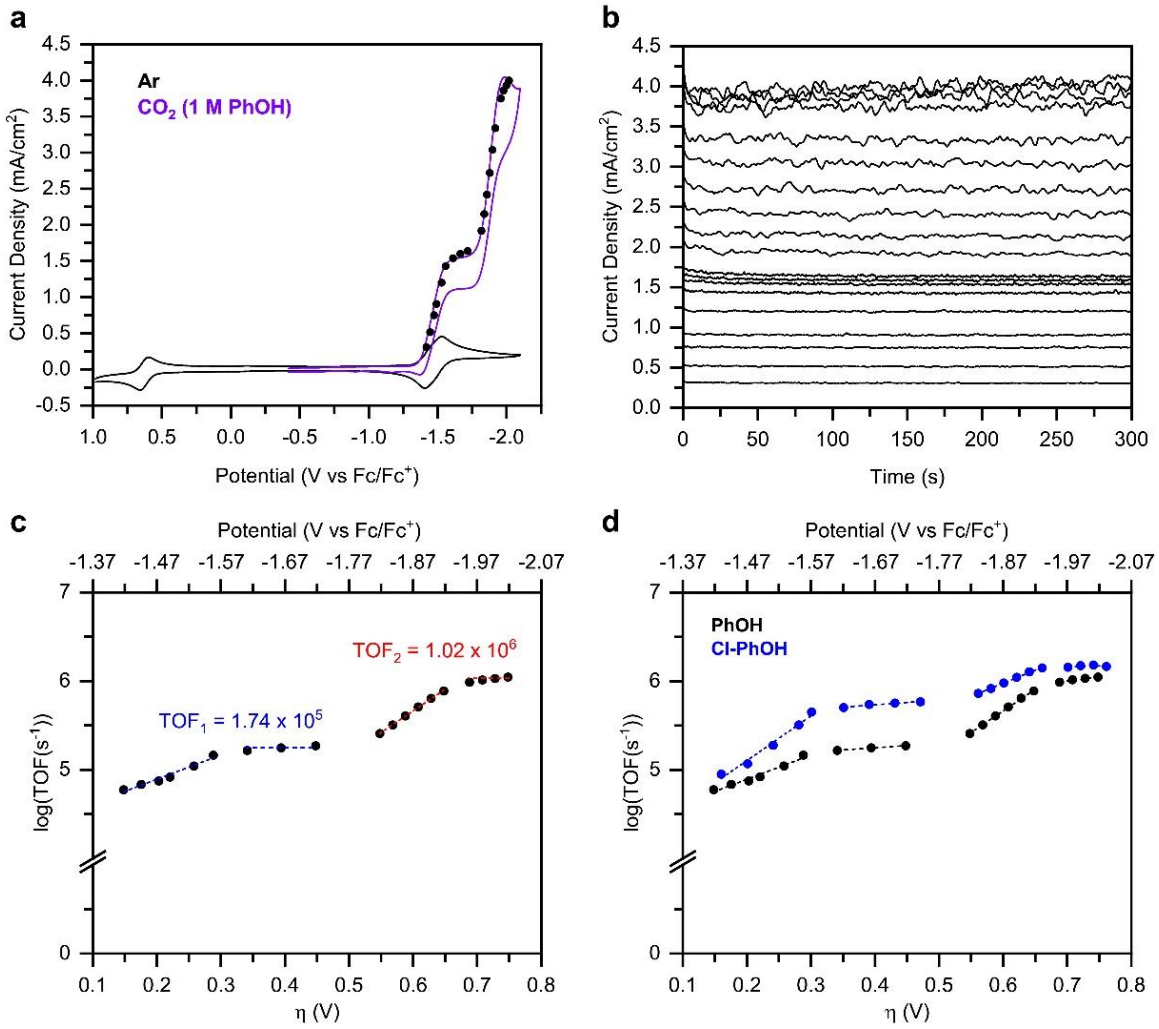


Figure 6.15. Kinetic analysis of $^1[Fe]^{2+}$ (a) Cyclic voltammograms of $^1[Fe]^{2+}$ in the absence (black) and presence (purple) of CO_2 with 1 M PhOH. Average current densities extracted from the short-term controlled potential electrolysis experiments (b) are overlayed on the catalytic CV (black dots) (c) Catalytic Tafel plot for $^1[Fe]^{2+}$ obtained from the short-term CPE experiments with 1 M PhOH. (d) Comparison of catalytic Tafel plots obtained with 1 M PhOH or Cl-PhOH. CPE and CV experiments were collected in an electrolyte of 0.10 M $TBAPF_6$ dissolved in acetonitrile.

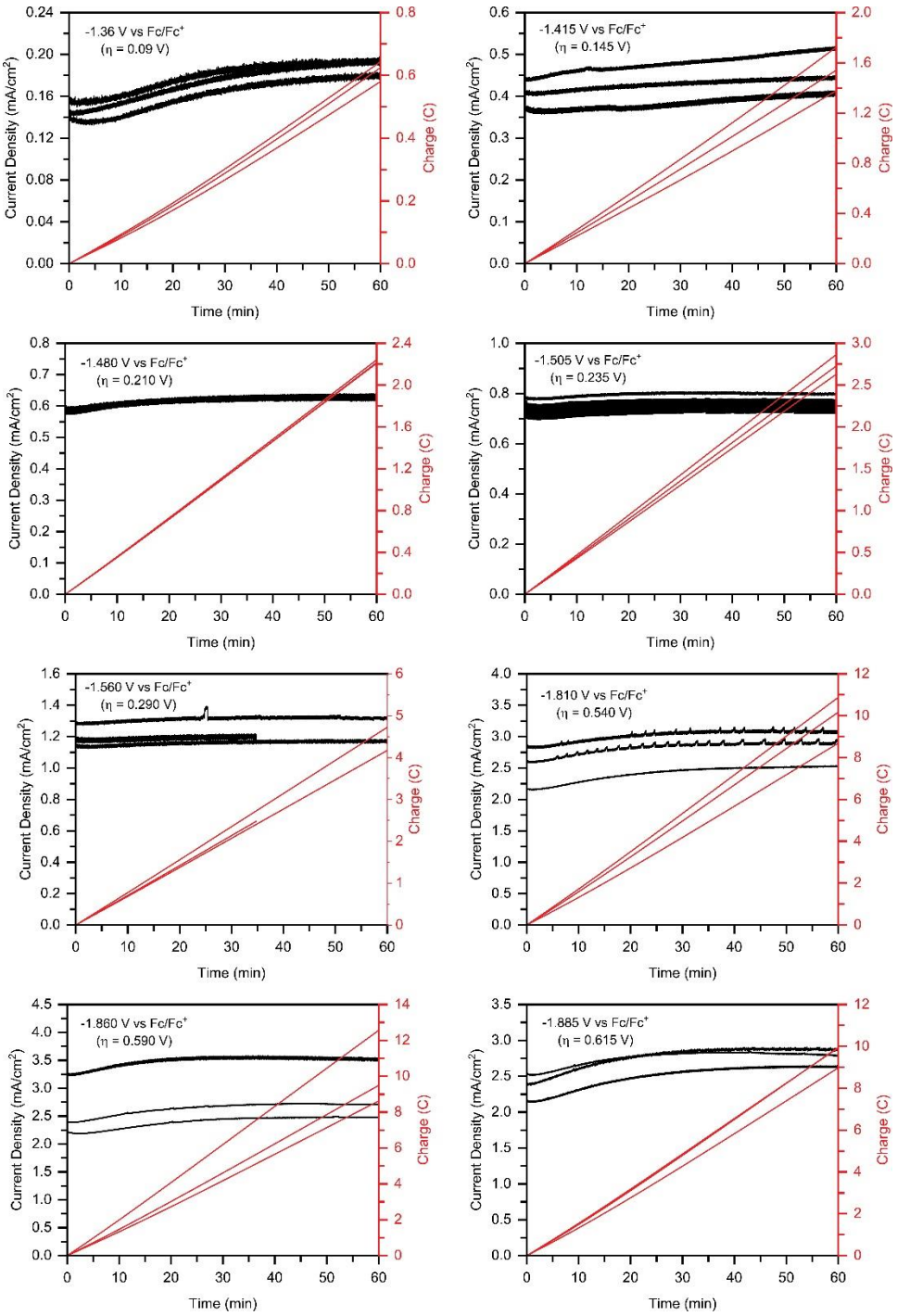


Figure 6.16. Long-term controlled potential electrolysis data of the low overpotential regime of $^{1}[Fe]^{2+}$ under CO_2 atmosphere with 1 M Cl-PhOH as the proton source. CPE experiments were conduced in triplicate at varying onset potentials ranging from −1.36 V vs Fc/Fc^{+} to−1.89 V vs Fc/Fc^{+}. The kinetic Tafel plot generated from this long-term CPE data is depicted in Figure S14. Conditions: 1 mM $^{1}[Fe]^{2+}$; 0.10 M $TBAPF_6/CH_3CN$; 1.0 M Cl-PhOH; 0.020 M tetrabutylammonium acetate in the counter compartment.

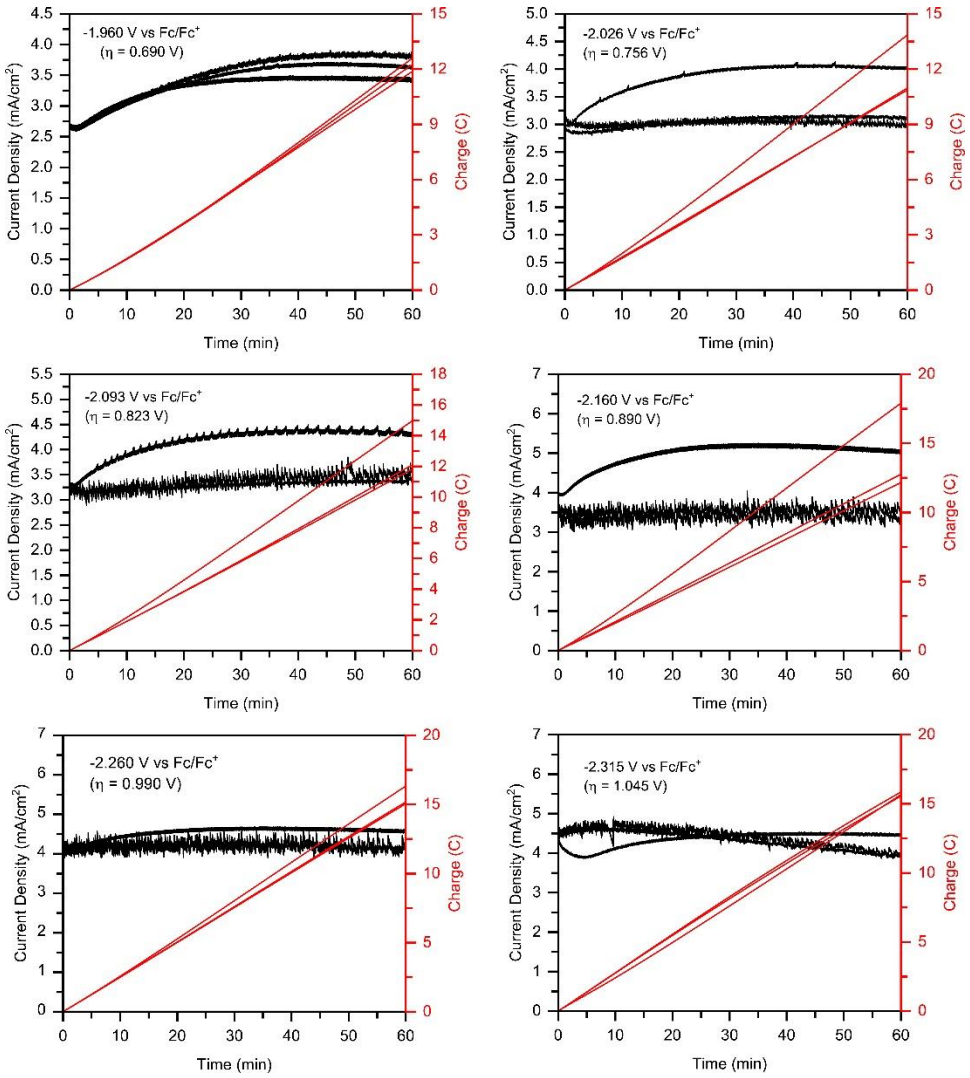


Figure 6.17. Long-term controlled potential electrolysis data of the high overpotential regime of $^{1}[Fe]^{2+}$ under CO_2 atmosphere with 1 M Cl-PhOH as the proton source. CPE experiments were conducted in triplicate at varying onset potentials ranging from −1.96 V vs Fc/Fc^{+} to −2.32 V vs Fc/Fc^{+}. The kinetic Tafel plot generated from this long-term CPE data is depicted in Figure S14. Conditions: 1 mM $^{1}[Fe]^{2+}$; 0.10 M $TBAPF_6/CH_3CN$; 1.0 M Cl-PhOH; 0.020 M tetrabutylammonium acetate in the counter compartment.

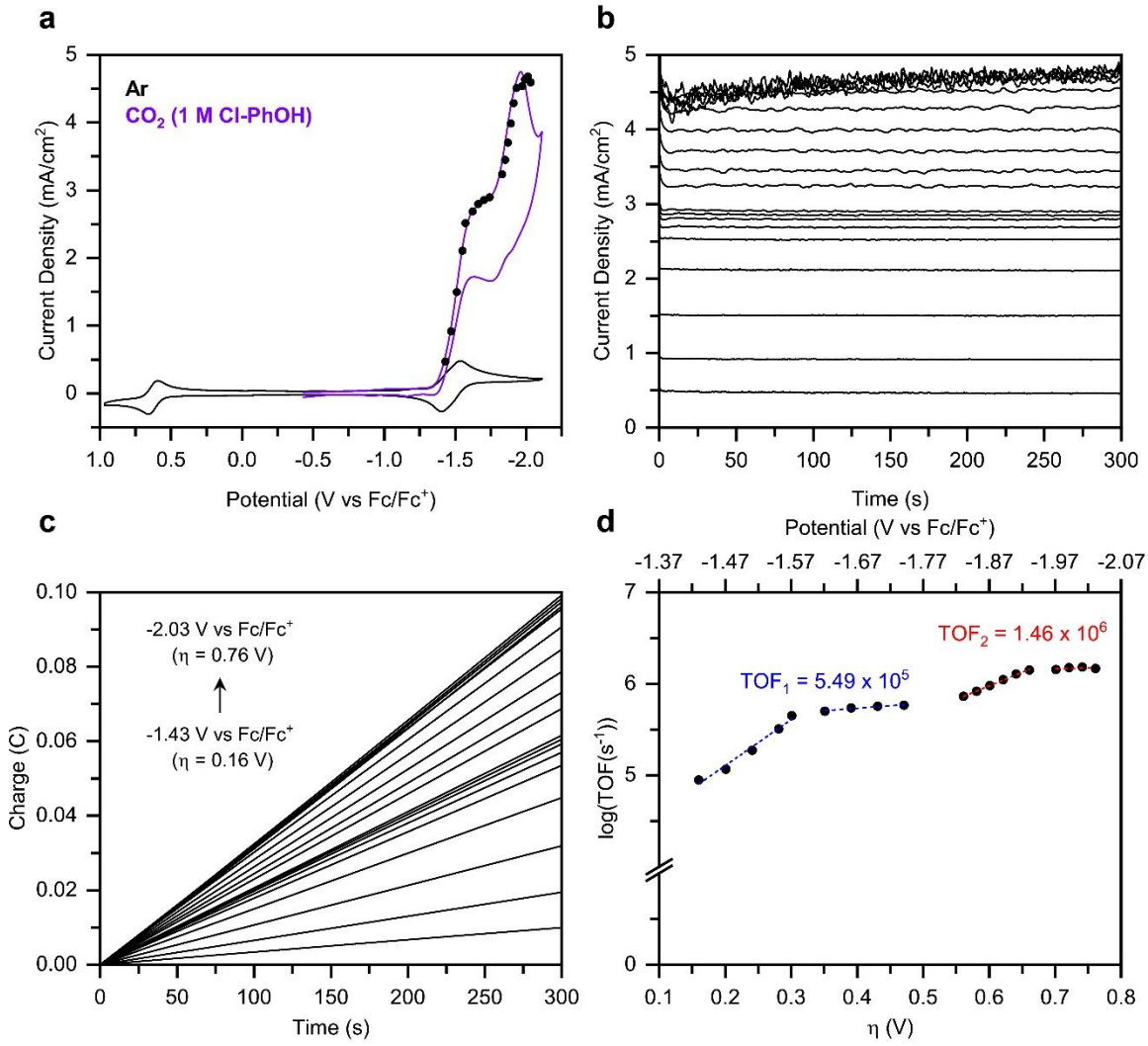


Figure 6.18. Kinetic data extracted from short-term controlled potential electrolysis experiments. (a) Cyclic voltammograms of $^{1}[Fe]^{2+}$ in the absence (black) and presence (purple) of CO_2 with 1 M Cl-PhOH. Average current densities extracted from the controlled potential electrolysis experiments (b and C) overlayed on the catalytic CV (black dots). (d) Catalytic Tafel plot for $^{1}[Fe]^{2+}$ obtained from short-term CPE experiments with 1 M Cl-PhOH. CPE experiments were collected in an electrolyte of 0.10 M $TBAPF_6$ dissolved in acetonitrile.

Table 6.2. Energetic span calculations of the low overpotential catalytic regime ($E^1_{cat/2}$= –1.43 V vs Fc/Fc^+; $\eta_{TOF/2}$ = 0.10 V) with PhOH as the acid (see **Figure 6.3**, outer pathway).

Intermediate	Reaction Step	X_{TOF}(I)	X_{TOF}(TS)
$^1[Fe]^{2+}$	1st reduction	0.00	0.00
$^2[Fe]^{+}$	2nd reduction	0.00	0.00
$^1[Fe]^{0}$	CO_2 coordination	0.03	0.03
$^2[Fe\text{-}CO_2]^{0}$	1st protonation	0.00	0.00
$^1[Fe\text{-}CO_2H]^{+}$	2nd protonation (C–O cleavage)	0.97	0.97
$^1[Fe\text{-}CO]^{2+}$	CO release	0.00	0.00
Overall		**ΔG = –25.4 kcal/mol**	**TOF = 3.82x10^2 s^{-1}**

Table 6.3. Energetic span calculations of the low overpotential catalytic regime ($E^1_{cat/2}$= –1.43 V vs Fc/Fc^+; $\eta_{TOF/2}$ = 0.10 V) with Cl-PhOH as the acid (see **Figure 6.3**, outer pathway).

Intermediate	Reaction Step	X_{TOF}(I)	X_{TOF}(TS)
$^1[Fe]^{2+}$	1st reduction	0.00	0.00
$^2[Fe]^{+}$	2nd reduction	0.00	0.00
$^1[Fe]^{0}$	CO_2 coordination	0.16	0.16
$^2[Fe\text{-}CO_2]^{0}$	1st protonation	0.00	0.00
$^1[Fe\text{-}CO_2H]^{+}$	2nd protonation (C–O cleavage)	0.82	0.82
$^1[Fe\text{-}CO]^{2+}$	CO release	0.00	0.00
Overall		**ΔG = –25.4 kcal/mol**	**TOF = 2.08x10^3 s^{-1}**

Table 6.4. Energetic span calculations of the high overpotential catalytic regime ($E^2_{cat/2}$ = –1.86 V vs Fc/Fc^+; $\eta_{TOF/2}$ = 0.53 V) with PhOH as the acid via the protonation first pathway (see **Figure 6.10**, middle pathway).

Intermediate	Reaction Step	X_{TOF}(I)	X_{TOF}(TS)
$^2[Fe]^+$	1st reduction	0.00	0.00
$^1[Fe]^0$	1st protonation	0.00	0.00
$^1[Fe\text{-}N_{PY}H]^+$	CO_2 coordination	1.00	1.00
$^1[Fe\text{-}CO_2H]^+$	2nd reduction	0.00	0.00
$^2[Fe\text{-}CO_2H]^0$	2nd protonation (C–O cleavage)	0.00	0.00
$^2[Fe\text{-}CO]^{2+}$	CO release	0.00	0.00
Overall		**ΔG = –33.8 kcal/mol**	**TOF = 4.4x10^3 s^{-1}**

Table 6.5. Energetic span calculations of the high overpotential catalytic regime ($E^2_{cat/2}$ = –1.86 V vs Fc/Fc^+; $\eta_{TOF/2}$ = 0.53 V) with Cl-PhOH as the acid via the protonation first pathway (see **Figure 6.10**, middle pathway).

Intermediate	Reaction Step	X_{TOF}(I)	X_{TOF}(TS)
$^2[Fe]^+$	1st reduction	0.00	0.00
$^1[Fe]^0$	1st protonation	0.00	0.00
$^1[Fe\text{-}N_{PY}H]^+$	CO_2 coordination	1.00	1.00
$^1[Fe\text{-}CO_2H]^+$	2nd reduction	0.00	0.00
$^2[Fe\text{-}CO_2H]^0$	2nd protonation (C–O cleavage)	0.00	0.00
$^2[Fe\text{-}CO]^{2+}$	CO release	0.00	0.00
Overall		**ΔG = –33.8 kcal/mol**	**TOF = 4.4x10^4 s^{-1}**

Table 6.6. Energetic span calculations of the high overpotential catalytic regime ($E^2_{cat/2}$ = –1.86 V vs Fc/Fc^+; $\eta_{TOF/2}$ = 0.53 V) with PhOH as the acid via the PCET pathway (see **Figure 6.10**, diagonal pathway).

Intermediate	Transition State	X_{TOF}(I)	X_{TOF}(TS)
$^2[Fe]^+$	1st reduction	0.00	0.00
$^1[Fe]^0$	PCET	0.50	0.50
$^2[Fe\text{-}N_{PY}H]^0$	CO_2 coordination	0.00	0.00
$^2[Fe\text{-}CO_2H]^0$	2nd protonation (C–O cleavage)	0.50	0.50
$^2[Fe\text{-}CO]^+$	CO release	0.00	0.00
Overall		**ΔG = –33.8 kcal/mol**	**TOF = 1.40x10^7 s^{-1}**

Table 6.7. Energetic span calculations of the high overpotential catalytic regime ($E^2_{cat/2}$ = –1.86 V vs Fc/Fc^+; $\eta_{TOF/2}$ = 0.53 V) with Cl-PhOH as the acid via the PCET pathway (see **Figure 6.10**, diagonal pathway).

Intermediate	Transition State	X_{TOF}(I)	X_{TOF}(TS)
$^2[Fe]^+$	1st reduction	0.00	0.00
$^1[Fe]^0$	PCET	0.98	0.98
$^2[Fe\text{-}N_{PY}H]^0$	CO_2 coordination	0.00	0.00
$^2[Fe\text{-}CO_2H]^0$	2nd protonation (C–O cleavage)	0.01	0.01
$^2[Fe\text{-}CO]^+$	CO release	0.01	0.01
Overall		**ΔG = –33.8 kcal/mol**	**TOF = 2.64x10^7 s^{-1}**

First, we explored the kinetics of the low overpotential regime (potential window of −1.40 − −1.75 V vs Fc/Fc^+). Short-term CPE data collected at applied potentials between −1.42 and −1.72 V vs Fc/Fc^+ overlay closely with the voltammogram collected under CO_2 atmosphere with 1 M PhOH (**Figure 6.15a**). Current densities were stable across the entire short-term electrolysis (**Figure 6.15b**) and long-term electrolysis (**Figures 6.16 and 6.17**) and reached a plateau at ca. −1.66 V vs Fc/Fc^+ with an average current density of 1.53 mA/cm^2 which corresponds to a TOF of 1.74 x 10^5 s^{-1} (**Figure 6.15c**). When the more acidic, Cl-PhOH was added as the proton donor, the maximum TOF of the first catalytic regime increased to 5.50 x 10^5 s^{-1}, a three-fold increase in observed rate relative to the data obtained with PhOH as the proton source (**Figure 6.15d**) without loss of product selectivity (**Figures 6.19 and 6.20**). Analysis of this catalytic regime with the energetic span model shows that the catalytic rate is solely controlled by the second protonation step (C−O bond cleavage to release water) as the key rate-limiting intermediate and transition state are both associated with the second protonation. The carboxy intermediate, $^1[Fe{-}CO_2H]^+$, is the TDI and the second protonation barrier is the TDTS both with X_{TOF} values close to 1. Based on this analysis, a TOF of 400 s^{-1} is predicted. This value is slower than the experimentally determined

TOF of 1.74 x 10^5; however, this translates to an energy difference of ~3.5 kcal/mol which is still within acceptable agreement. Furthermore, when Cl-PhOH is utilized as the acid source, the barrier is lowered by 1.1 kcal/mol which translates to a rate increase by one order of magnitude. The stronger acid lowers the TDTS, leading to an increase in the importance of the CO_2 binding step. This shift is illustrated by the change in the degree of TOF control: Indeed, the X_{TOF} of both the TDI ($^1[Fe{-}CO_2H]^+$) and TDTS decreases from 0.97 to 0.82 and the CO_2 binding step is increasingly important for the rate as the X_{TOF} increases to 0.16 from 0.03. Distinction between the protonation first or CO_2 binding first pathways by this kinetic analysis was not possible because both options occur before the rate determining protonation step.

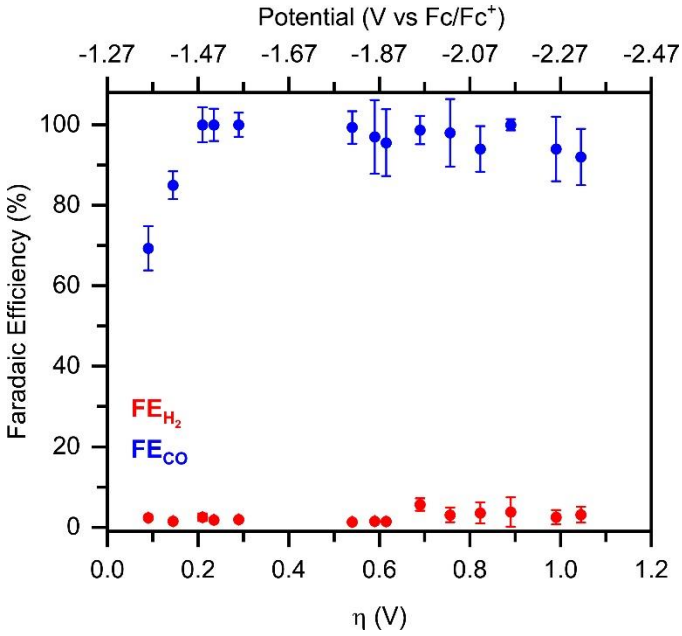


Figure 6.19. Selectivity of $^1[Fe]^{2+}$ for CO_2 reduction into CO (blue) over proton reduction into H_2 (red). Data was obtained from long-term CPE experiments conducted in the gastight cell. Conditions: 1 mM $^1[Fe]^{2+}$; 0.10 M $TBAPF_6/CH_3CN$; 1.0 M Cl-PhOH; 0.020 M tetrabutylammonium acetate in the counter compartment.

Application of more negative onset potentials between −1.81 and −2.01 V vs Fc/Fc^+ allowed us to probe the kinetics of the second, high overpotential regime. Tight correlations between averaged current densities from the CPE experiments with the cyclic voltammograms collected under CO_2 atmosphere with PhOH (**Figure 6.15a**) or Cl-PhOH (**Figure 6.18a**) were observed. Peak current density of 4.0 mV/cm^2 was reached at −2.01 V vs Fc/Fc^+ which corresponds to a maximum TOF of 1.05 x 10^6 s^{-1}. Addition of 1 M Cl-PhOH as the proton source results in a smaller rate enhancement with a maximum TOF of 1.5 x 10^6 s^{-1}, representing only a 1.4-fold enhancement relative to PhOH, about half of what was observed in the low overpotential regime (**Figures 6.15d, 6.19, and 6.20**). Catalytic Tafel plots comparing the two acids are presented in **Figure 6.15d**. In addition, there is still a proton dependence on the rate limiting step as illustrated by the normal, primary H/D kinetic isotope effect.

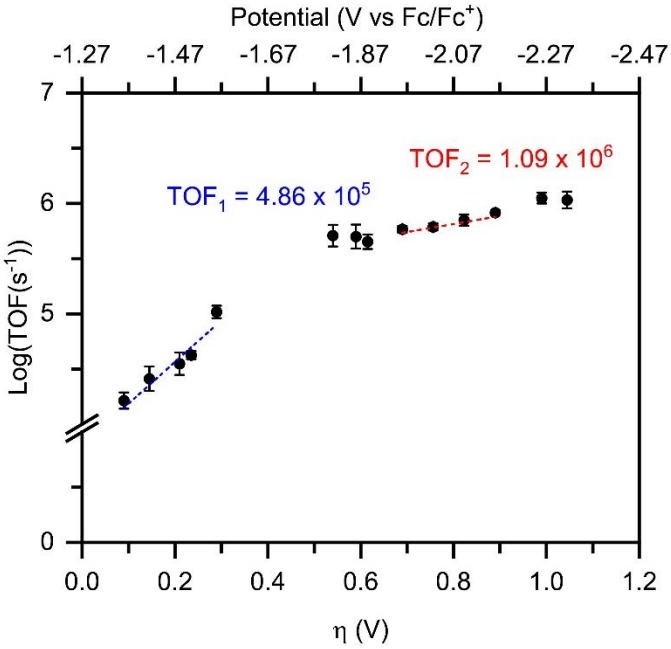


Figure 6.20. Catalytic Tafel plot for $^{1}[Fe]^{2+}$ obtained from long-term CPE experiments in the gastight PEEK cell with acetonitrile and added Cl-PhOH (1 M).

Next, the energetic span model was applied to predict the rates for the three possible mechanistic pathways proposed for the high overpotential regime. These rates are then compared to the experimentally determined TOFs. The three pathways are given in **Figure 6.10** and are illustrated in a free energy diagram (**Figure 6.14**) to allow for more direct comparison. From the $^{1}[Fe]^{0}$ catalytic resting state, the iron complex can either go through: (1) a CO_2 coordination first pathway to give the CO_2 complex ($^{2}[Fe{-}CO_2]^{0}$); (2) a protonation first pathway to generate the cationic pyridinium intermediate, $^{1}[Fe{-}N_{PY}H]^{+}$; or a PCET pathway to generate a similar neutral pyridinium species, $^{2}[Fe{-}N_{PY}H]^{0}$.

A TOF of 4000 s^{-1} is predicted for the CO_2 binding first pathway. The TOF is completely controlled by the CO_2 coordination step as the reduction of $^{1}[Fe{-}CO_2H]^{+}$ to $^{2}[Fe{-}CO_2H]^{0}$ lowers the (previously rate limiting) barrier for the second protonation by 6.6 kcal/mol from 13.9 to 7.3 kcal/mol. This shrinks the X_{TOF} for both $^{1}[Fe{-}CO_2H]^{+}$ and the transition state for the second protonation to 0. The CO_2 first pathway can be eliminated because CO_2 coordination is shown by the energetic span model to be entirely rate limiting and thus fails to explain the experimentally observed normal, primary H/D kinetic isotope effect and a large catalytic enhancement with the addition of more acidic proton donors.

Next, for the protonation first pathway, we predict a TOF that is almost 3 orders of magnitude slower than what we observed experimentally (11000 s^{-1}). Additionally, we find that the cycle is solely controlled by the first protonation of $^{1}[Fe]^{0}$ to give the pyridinium intermediate, $^{1}[Fe{-}N_{PY}H]^{+}$. The protonation first pathway would account for the primary kinetic isotope effect but not the rate enhancement upon addition of stronger acids as the energetic span model predicts the same rate regardless of if PhOH or Cl-PhOH are utilized as the proton source.

The TOF predicted for the PCET pathway of 1.4 x 10^7 s^{-1} resulted in the closest match to the experimentally measured value of 1.05 x 10^6 s^{-1} with the pathway being controlled by both the PCET step as well as the second protonation of $^2[Fe{-}CO_2H]^0$ as both have X_{TOF} coefficients close to 0.5. The *para*-chloro substituted PhOH, Cl-PhOH, lowers the barrier for the second protonation by 2.6 kcal/mol. However, only the PCET pathway is kinetically controlled by this transition state increasing the TOF from 1.4 x 10^7 s^{-1} to 2.6 x 10^7 s^{-1}. This increase is smaller than the increase in the low overpotential regime despite a stronger effect on barrier lowering, which can be understood by the lower X_{TOF} of that step in the low versus high overpotential regime. Based on the experimental and computational findings, these data suggest that the PCET pathway is the more likely mechanism for the high overpotential regime.

6.3.9 Selectivity Versus HER

Achieving selectivity for CO_2 reduction over the reduction of protons to H_2 is critical. The HER is a competitive side reaction across a similar potential window to the CO_2RR and is highly dependent on the presence and strength of the proton source.[14] The generation of an iron hydride under reducing conditions in the presence of a proton donor can thus shift the catalyst selectivity away from CO production and toward the formation of H_2. It is therefore important to understand the kinetic and thermodynamic barriers associated with the protonation of the reduced iron center.

In our proposed pathway there are two critical intermediates through which the formation of a hydride is feasible (**Figure 6.21 and 6.22**). The first possibility is the direct protonation of the iron center of the doubly reduced intermediate, $^1[Fe]^0$ (**Figure 6.21 and 6.23a**). The other possibility is the rearrangement of the pyridinium intermediate, $^1[Fe{-}N_{PY}H]^+$, to a metal hydride (**Figure 6.21 and 6.23b**). In both cases, high activation barriers prevent these side reactions and explain the high product selectivity for CO_2 reduction to CO that is observed experimentally. The direct formation of a hydride $^1[Fe{-}H]^+$ from $^1[Fe]^0$ albeit thermodynamically favorable with a free energy of −6.1 kcal/mol, is kinetically inhibited with a high activation barrier of 24.5 kcal/mol. The rearrangement of $^1[Fe{-}N_{PY}H]^+$ to $^1[Fe{-}H]^+$, is more exergonic (−17.5 kcal/mol); however, this pathway is also inhibited by a larger activation barrier of 21.4 kcal/mol. In both cases, the high barriers can be rationalized by the electronic structure of $^1[Fe]^0$: the metal center stabilizes the two ligand reductions through antiferromagnetic coupling and thus the metal center remains Lewis acidic. This feature is illustrated by the coordination of acid (*e.g.*, PhOH or H_2CO_3) to $^1[Fe]^0$ in which the acid prefers to bind *via* the oxygen atom to the iron center which then facilitates the protonation of the pyridyl arm, but blocks the metal center from protonation (see **Figure 6.24**). Therefore, the formation of a metal-hydride is prohibited by steep kinetic barriers ultimately shutting down pathways to hydrogen production. The difference between the rate limiting transition state in CO_2RR and the barrier for hydride formation is ∼10 kcal/mol which implies that $^1[Fe]^{2+}$ should remain selective for the CO_2RR even when stronger acids are used as proton donors. Indeed, selectivity is achieved by using 4-nitrophenol (NO_2-PhOH), an even stronger acid (two pK_a units stronger than Cl-PhOH), with a barrier of 19.3 kcal/mol for the formation of a hydride. We explored this possibility, and, in all cases, we do not detect any hydrogen formation experimentally. However, NO_2-PhOH was also redox-active at the potentials applied, which also prevented the formation of CO.

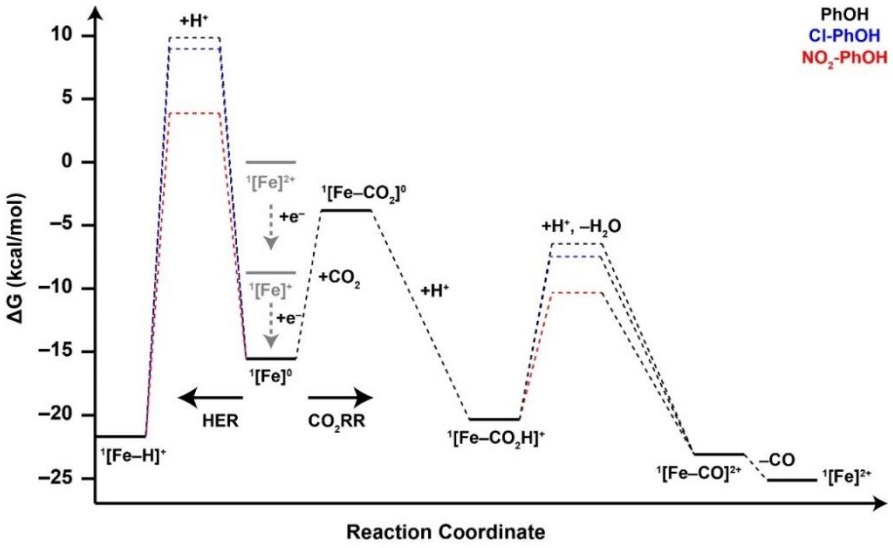


Figure 6.21. Free energy landscape of the low overpotential regime for CO_2RR and HER pathways. For the reduction steps, a potential of –1.8 V vs Fc/Fc^+ is applied. For the protonation steps, PhOH is used to estimate barriers and carbonic acid for free energies. Solid lines correspond to intermediate states and dashed lines to transition structures. Black, blue, and red lines denote the uses of PhOH, Cl-PhOH, and NO_2-PhOH, respectively.

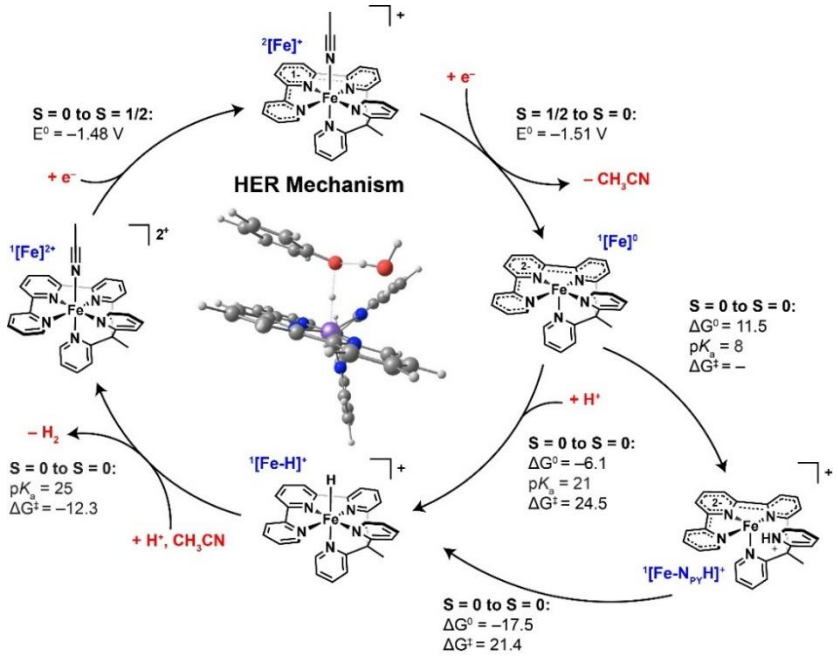


Figure 6.22. Proposed mechanistic cycles for the hydrogen evolution reaction. Two single-electron transfer steps results in the formation of $^1[Fe]^0$ which can then be directly protonated to give the iron hydride, $^1[Fe{-}H]^+$ (inner cycle). Additionally, protonation on the ligand could also occur resulting in a pyridinium intermediate, $^1[Fe{-}N_{PY}H]^+$, which can then rearrange to give the metal hydride (outer cycle).

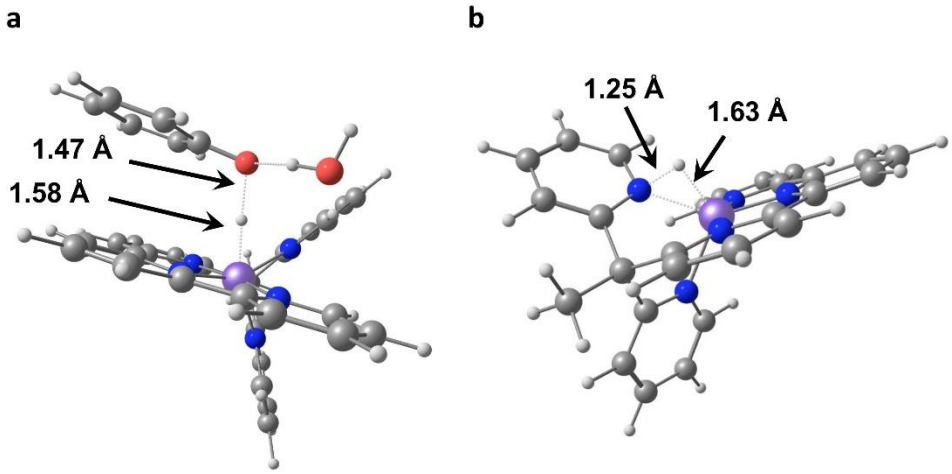


Figure 6.23. Transition states for the formation of an iron hydride intermediate (a) directly from PhOH as the acid source or (b) an intramolecular proton transfer through a pyridinium intermediate.

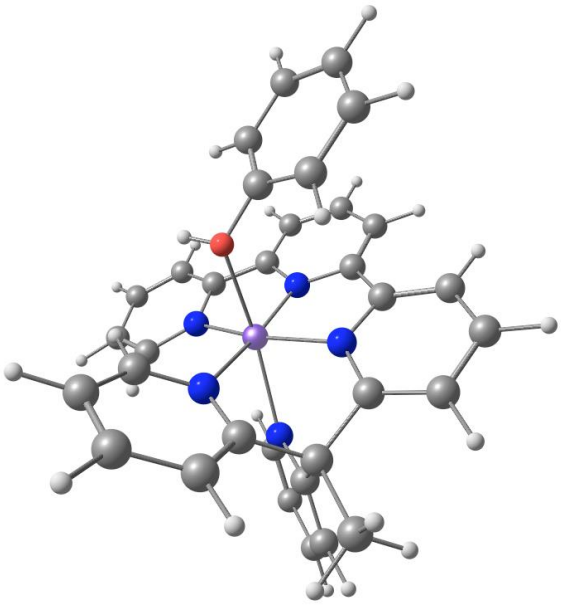


Figure 6.24. Geometry optimized structure for the coordination of phenol to the iron center showing blocking of the open coordination site by oxygen atom coordination.

6.3.10 Rational Catalyst Design Driven by Mechanistic Insights

Based on the mechanistic studies we identified several critical intermediates and transition states that directed us to propose improved ligand designs that ideally stabilize several critical intermediates. The key takeaways from the kinetic analysis are: first, the low overpotential regime is solely controlled by the second protonation step, even when strong acids are used. Thus, modifications must either lower the energy of the transition state or decrease the stability of the carboxy intermediate. Second, the high overpotential regime is mainly controlled by either the CO_2

adduct or the formation of the pyridinium intermediate, especially when stronger acids are used as the proton source. Thus, an optimal modification should have a positive effect on both the CO_2 binding and second protonation. On the basis of our detailed mechanistic investigation, we propose rationally designed synthetic modifications to the tpyPY2Me ligand to further increase the catalytic performance of the iron complex. Synthetic modification to the pyridine moiety is the most promising for two reasons: first, it does not affect the initial reduction potentials and the crucial antiferromagnetic coupling of $^1[Fe]^0$; second, substituents can affect all critical intermediates by stabilizing the bound CO_2 adduct, increasing the pK_a of the pyridine itself for protonation and PCET, and then stabilizing the transition state for the second protonation (**Figure 6.25** shows the investigated candidates). In order to gain quantitative insights, we use the absolutely localized MO energy decomposition analysis with continuum solvation (ALMO-EDA(solv))[56] (see Materials and Methods section for a short introduction and a more detailed review is also available[57]) to understand how a specific modification stabilizes the reduced CO_2 adduct. We employ a difference-of-differences-approach where we compare the change in interaction energy and EDA terms using the unsubstituted tpyPY2Me ligand as the reference. We investigate hydrogen bonding (−OH and−NH_2) and ionic stabilization (−$N(CH_3)_3^+$) as both moieties are known to facilitate CO_2 binding in other CO_2RR catalysts (see **Figure 6.25**).[12,19,22,30,31,58] The EDA decomposition of that change in interaction energy is crucial for understanding the exact stabilization pathway as substituents affect the reduced CO_2 not only directly *via* a non-covalent interaction but also indirectly through substituent effects. Both pathways often have distinct EDA fingerprints and thus can be distinguished by an EDA scheme. We recently showed the viability of this approach for an iron tetraphenylporphyrin catalyst.[56] The chosen reference fragmentation of the complex is a doubly reduced CO_2^{2-} and an unreduced catalyst. This fragmentation is more suitable for this type of complex as the O−C−O bond angle of 124º indicates a transfer of both electrons into the CO_2 moiety. The alternative choice, a neutral but bent CO_2 fragment and a doubly reduced metal complex will be solely dominated by the geometry distortion term as discussed elsewhere.[56,57] Thus, this interaction energy decomposed by the EDA scheme corresponds to the stabilization of the doubly reduced CO_2^{2-} dianion by the unreduced catalyst. It is important to point out that this is just a part of the total free energy of CO_2 addition. The EDA results for the unsubstituted complex are given in **Figure 6.26a** and shows that the attractive interactions are dominated by electrostatic interactions with significant charge transfer contributions. The short Fe−C bond distance of 2.05 Å rationalizes the high Pauli repulsion, and indicates that net binding energy results mainly from CT. The change in interactions energies as well as each EDA component for each substituent relative to the unsubstituted complex is depicted in **Figure 6.26b**. The *ortho*-hydroxy substituent (*o*-OH) strengthens the interaction by 77.1 kJ/mol (18.5 kcal/mol). The main driving force is additional favorable electrostatic interaction, which is also supplemented by favorable contributions from polarization and charge transfer, which are typical of a hydrogen bonding fingerprint.[59] The large increase in Pauli repulsion can be attributed to the repulsion of the diffuse lone pairs of the CO_2 moiety and the hydroxy group. Interestingly, this intermediate was not stable without freezing the hydroxy OH bond as it otherwise directly protonates the CO_2 moiety. The *ortho*-amino substituent has a much smaller stabilizing effect of −22.5 kJ/mol (5.4 kcal/mol). The favorable electrostatic interaction cannot overcome the additional Pauli repulsion of the amino substituent and the CO_2^{-2} moiety. Lastly, the charged trimethylanilinum (TMA) moiety had to be placed at the *meta* position due to the bulkiness of the group. The EDA results demonstrate how this group provides a purely electrostatic stabilization; however, the solvation screens most of the interaction to yield an overall

stabilization of −44.6 kJ/mol (−10.7 kcal/mol). Moreover, the *ortho* hydrogen donating substituents have another advantage: They can stabilize the transition state for the second protonation step by forming hydrogen bonds. These interactions lower the transition state (see **Figure 6.27**) for the *o*-OH by 1.3 kcal/mol which translates to an order of magnitude faster TOF in the low overpotential regime (similar effect to the use of stronger acids).

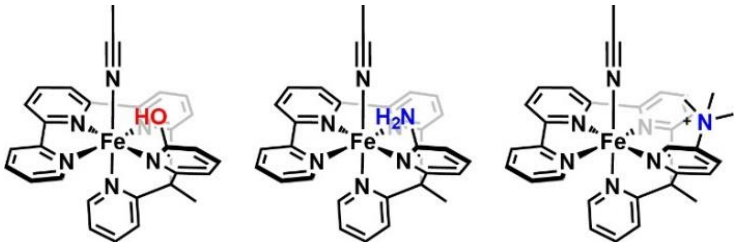


Figure 6.25. Chemical structures of second-sphere functionalized polypyridyl catalysts for improved performance based on our mechanistic understanding.

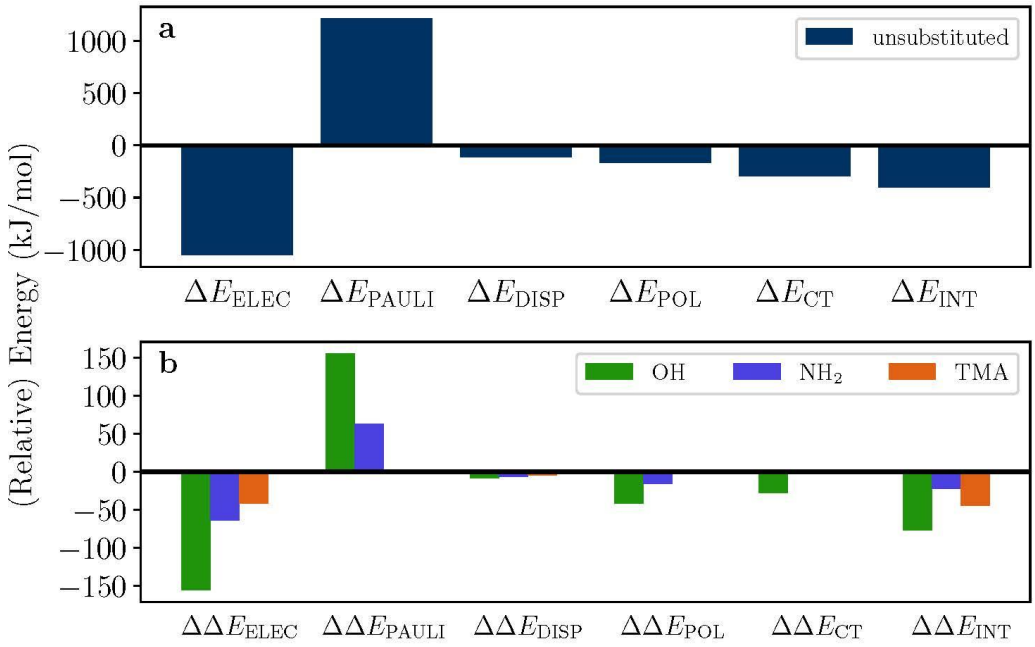


Figure 6.26. ALMO-EDA (solv) results for CO_2 adduct $^1[Fe{-}CO_2]^0$: (a) the unsubstituted adduct; (b) differential ALMO-EDA (solv) results for three different substituents: −OH (green), $-NH_2$ (blue), and $-N(CH_3)_3^+$ (TMA; orange). Energies are reported in kJ/mol.

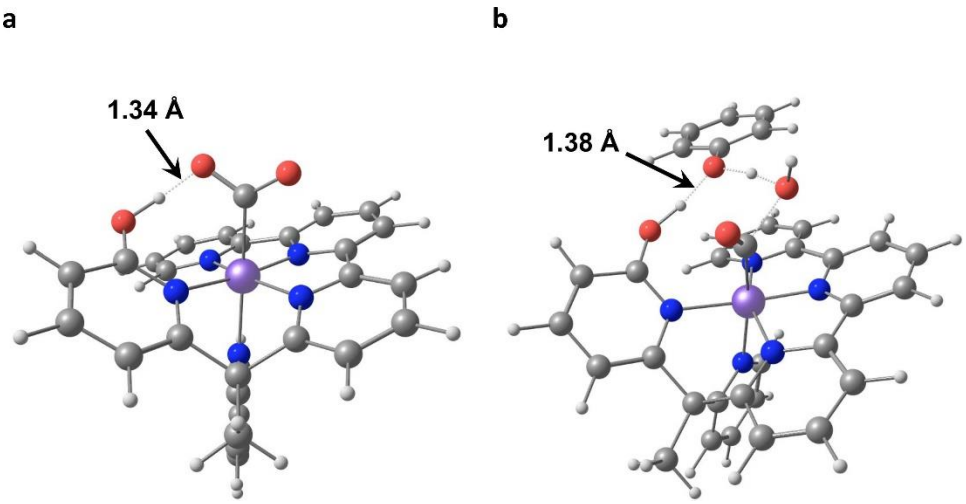


Figure 6.27. Key intermediate for the hydroxyl substituted pyridine complex: (a) CO_2 adduct (b) transition state for the second protonation.

6.4 Conclusion

In summary, inspired by the excellent observed catalytic performance of the molecular $[Fe(tpyPY2Me)]^{2+}$ system, we investigated the mechanistic pathways through which it electrochemically converts CO_2 into CO. Cyclic voltammograms collected under CO_2 atmosphere displayed the formation of two distinct catalytic regimes with $E^1_{cat/2}$ of −1.43 V vs Fc/Fc^+ (η = 160 mV) and $E^2_{cat/2}$ −1.86 V vs Fc/Fc^+ (η = 590 mV). For the low overpotential regime, the computed pathway shows that $^1[Fe]^{2+}$ first undergoes two, single-electron reduction steps to generate the five-coordinate open-shell singlet, $^1[Fe]^0$. From $^1[Fe]^0$, we show that the order of CO_2 addition or protonation is flexible and experimentally indistinguishable with both steps having comparable calculated barriers. We find that both CO_2 binding and protonation of the pyridine arm are feasible steps with similar endergonic free energies. In any case, the rate limiting step was found to be the second protonation step resulting in cleavage of the C−O bond with subsequent CO release being barrierless and exergonic. Analysis of the complete low overpotential regime revealed that catalysis is solely controlled by the carboxyl intermediate ($^1[Fe{-}CO_2H]^+$) and the transition state for the second protonation step. Consequently, the use of a stronger proton source, such as Cl-PhOH, resulted in a three-fold increase in the rate of catalysis without any loss in product selectivity. Computational analysis of the high overpotential regime shows a similar two initial electron transfer steps; however, at more reducing potentials, the first reduction is off-pathway, allowing for turnover from $^2[Fe]^+$ rather than $^1[Fe]^{2+}$ as is observed in the low overpotential regime. Following formation of the catalytic resting state, $^1[Fe]^0$, we computationally probed three mechanistic pathways and compared them to experimental kinetic data and results obtained from the energetic span model. From this analysis, we identified the PCET pathway of one of the pyridine arms as the most consistent mechanism. This intermediate readily binds CO_2 and rearranged into a singly reduced carbonyl intermediate. The additional electron greatly facilitates the second protonation step explaining the increased rates observed for the higher overpotential regime. Analysis of the cycle showed that both the PCET and the second protonation steps control the rate of catalysis. As such, similar to the low overpotential regime, the use of a more acidic proton source increases the rate of catalysis, but to a lesser degree. The stronger acid only lowers the barrier for the second protonation; however, this step has less influence on the turnover frequency and thus the effect of acid pK_a is lower.

Finally, the mechanistic insights gained from this study identified the pyridyl arms as promising targets for further optimization of the catalytic performance of this system. The pyridyl arms are not involved in stabilizing the excess electron density in the reduction events and thus any modifications should not alter the reduction potential of $^1[Fe]^{2+}$, which is already optimally matched to the standard redox potential for the conversation of CO_2. The introduction of hydrogen bond donors into the second coordination sphere can further greatly stabilize the CO_2 adduct and lower the transition state for the second protonation step, both of which are critical intermediates for fast catalysis. Moreover, we also expect that the substituent effects can help to stabilize the pyridinium intermediate; therefore, this synthetic modification has the potential to improve catalysis in all proposed cycles for both the low and high overpotential regimes.

6.5 Materials and Methods

6.5.1 Computational Model

In this section we briefly explain the model, its assumptions and expected errors (see SI for more technical details and justifications). Density functional theory calculations for free energies, activation energies, reduction potential and the LOBA[60] oxidation state analysis were performed with the Q-Chem package[61] (version 5.3.0) using the ωB97X-D54 functional with a mixed basis for the optimization and frequency calculations (def2-SVP basis for all main group elements, def2-TZVP basis set for Fe).[62] This functional was chosen based on our previous study and extensive functional screening (see SI reference [[63]]). In addition, we probed several other popular density functionals but no other functional better agreement in both the predicted redox potentials and rates (see **Table 6.8**). Gibbs free energies (G) were used to compute reduction potentials and adiabatic spin gaps and are based on standard thermodynamic cycles.[52,64,65] Solvation energies were approximated by performing single point calculations applying the implicit C-PCM solvent model with the larger def2-TZVP basis for all elements[62] (see reference [[66]] more technical details). Reduction potentials are reported with an isodesmic scheme against the ferrocene/ferrocenium couple (Fc/Fc^+) used as an internal standard.[52,65,67] This method allows accurate predictions even at a modest level of theory with reported errors within approximately ∼100 mV (∼4 kcal/mol) of experimental values.[52] Of particular relevance to this work, this approach has yielded accurate calculated reduction potentials in several pyridine based electrocatalysts.[31,35,39] The RMSD of ωB97X-D for barrier heights is ∼2 kcal/mol using gas phase high level wave function methods as the reference;[68,69] When comparing to experimental values, additional errors may arise from describing solvation by the implicit solvation model and other simplifications in the computational model versus experiment.

The calculation of free energies for protonation reactions with implicit solvent models results in expected deviations versus experimental values of ±3 pK_a units.[70] We tested our computational protocol for phenol (PhOH) with ωB97X-D yielding a pK_a of 24.6 which is 4-5 pK_a units too low.[71] While this is a large error, it also has a significant systematic component: calculated relative pK_a values are more reliable because of favorable error cancellation by removing the experimental free energy of the proton. Thus, calculated pK_a values should mainly be compared against each other.

We use PhOH as the main proton source for calculating reaction barriers involving protonation reactions as it was added to the reaction mixture in molar quantities for the CPE experiments. The concentration of other proton sources (H^+ and H_2CO_3) is negligible.[65] However, we report free energies of protonation reaction steps versus carbonic acid (H_2CO_3) because it is the strongest acid in solution and reprotonates phenolate (PhO^-) *via* complexation of CO_2 and OH^-. This approach was also used in a previous study of quaterpyridine based catalysts.[35] The calculated standard potential for the reduction reaction using carbonic acid is –1.28 V vs Fc/Fc^+; this is in good agreement with the experimental estimate of –1.27 V used in our previous study.[39] Matsubara[40] estimates the standard potential in wet CH_3CN depending on the mole fraction of water to be between 0.95 V and 1.63 V vs Fc/Fc^+. The highest predicted reduction potential is −1.83 V vs Fc/Fc^+ ($\eta = 0.56$ V) in our catalytic cycles (*vide infra*); this translates to a total reaction energy of −25.4 ($CO_2 + 2H_2CO_3 + 2e^- \rightarrow CO + H_2O + 2HCO_3^-$).

Table 6.8. We probed the functional dependency using a wide array of popular functions. Based on the key transition states and redox potentials listed in the table below, ωB97X-D remains the best overall functional. In case of ωB97M-V, the predicted barrier for the low overpotential pathway matches the experimental kinetics better; however, it also predicts a lower barrier for the high over potential pathway and leads to worse agreement in that pathway. In addition, the prediction of the potential difference between the reduction event deviates significantly from experimental results. Rates assume that the transition state remains the TDTS.

DFT Functional	TDTS (2nd Red) (kcal/mol)	TDTS (3rd Red) (kcal/mol)	E1 (V vs $Fc^{0/+}$)	E2 (V vs $Fc^{0/+}$)
ωB97X-D	13.91	7.26	-1.46	-1.51
ωB97M-V	11.88 ($k = 6.7x10^3$)	5.84 ($k = 3.5x10^8$)	-1.52	-1.77
ωB97X-V	14.12	7.89	-1.49	-1.63
B3LYP-D	23.63	19.01	-1.29	-0.97
MN15	18.08	10.67	-1.67	-1.79
B97-D	14.64	7.41	-1.44	-0.97

In contrast, the calculated standard potential using PhOH of –1.94 V vs Fc/Fc^+ is too negative. However, the calculated standard potential can get further reduced to –1.33 V by incorporating the effect of homoconjugation of phenol ins acetonitrile ($CO_2 + 6PhOH + 2e^- \rightarrow CO + H_2O + 2(PhO^- * 2PhOH)$).[42,43] The formation constant (K_f) for homoconjugation of PhOH in acetonitrile is very large ($\sim 10^{5.8}$)[41] and therefore we would expect significant formation even at very small concentrations of acid. This further complicates accurate determination of an unambiguous value of overpotential that would characterize the catalyst under these conditions (*i.e.*, $\eta_{TOF/2}$) as the value strongly depends on the concentration of the acid. Furthermore, here we report kinetics based on effective overpotentials (η_{eff}) and the corresponding applied potentials reference to the Fc/Fc^+ couple across a wide potential range. We employ the energetic span model to predict the turnover frequency (TOF) based on our calculated catalytic cycles. This model identifies the key intermediates and transition states, which control the rate of catalysis (see the corresponding section for more detail).[71]

6.5.2 Quantum Chemistry

Density functional theory calculations for spin gaps, redox potential and the LOBA[60] analysis utilized the Q-Chem package[72] (version 5.3.0) using the ωB97X-D[73] functional. Geometries were optimized with no constraints and structures were verified as minimum with the vibrational frequencies. The geometry optimization and frequency calculations were performed with ωB97X-D and a mixed basis (def2-SVP basis for all main group elements, def2-TZVP basis set for Fe).[66] The electronic structure was refined with the def2-TZVPP basis[66] single point calculations. The solvation energies were calculated using the C-PCM model (acetonitrile, ε =

37.5) as implemented in Q-Chem.[72] The numerical integration of the XC functional was performed on a (75, 302) grid (75 radial shells with 302 Lebedev points).

The calculation of accurate free energies for protonation reaction must employ the experimental value for the free energy of the proton based on the Sackur-Tetrode equation and an estimated solvation energy of $G_{solv}(H^+) = -264.6$ kcal/mol in acetonitrile was used.[62] This approach yields deviations versus experimental values of ±3 pK_a units.[6] For phenol this approach led to a pK_a of 27.6 which falls in that range (experimental pK_a is 29.1 in acetonitrile.[70] Furthermore, calculated *relative* pK_a values are more accurate because of favorable error cancellation. Thus, calculated pK_a values should mainly be compared against each other. Another limitation of the implicit solvation model is that it corresponds to a pure solution of acetonitrile. However, electrolysis experiments were conducted in 0.10 M $TBAPF_6$ dissolved in acetonitrile and saturated with CO_2 (0.28 M). Therefore, the pK_a of possible intermediates under the experimental conditions should be lower because experimental pK_a values of acids in mixtures of acetonitrile and water are lower than in pure acetonitrile.[40] For reference, the experimental pK_a of water-acetonitrile mixtures saturated with carbon dioxide range from 8 to 16, depending on the relative concentration of water.[40] Therefore, we report not only the pK_a value of the protonation steps but also the free energy of the protonation reaction coupled to carbonic acid. This is in line with experimental approaches for determining the overpotential which also use carbonic acid as the proton source. Even if it is assumed that phenol is involved in the rate limiting barriers (*vide supra*), the conjugate base, phenolate (PhO^-), is reprotonated by the strongest acid in the solution which is carbonic acid or aqueous CO_2.[22] The complete catalytic pathways explored computationally are displayed in **Figure 6.28.**

The energy decomposition analysis based on absolutely localized molecular-orbitals ALMO-EDA decomposes the intermolecular interaction energy, ΔE_{int} of two fragments (or more) at a given geometry into five terms (**Equation 6.1**):

$$\Delta E_{\mathrm{INT}} = \Delta E_{ELEC} + \Delta E_{\mathrm{PAULI}} + \Delta E_{\mathrm{DISP}} + \Delta E_{\mathrm{POL}} + \Delta E_{CT} \qquad \textbf{Equation 6.1}$$

where ΔE_{ELEC} denotes the classical electrostatic interaction, $\Delta E_{\mathrm{PAULI}}$ the Pauli repulsion component, ΔE_{DISP} the dispersion energy, ΔE_{POL} the polarization energy and ΔE_{CT} the charge transfer energy, see reference [57] for a detailed review of this method. The electrostatic component describes the classical Coulombic, Pauli repulsion arises from the Pauli exclusion principle of electrons forcing the overlapping electron densities of fragments to distort. Dispersion arises due to attractive induced dipole-dipole interactions. Polarization describes the relaxation of the electron density in the field of the other fragments. The charge transfer is the energy arises due to orbital interaction of different fragments such as dative bonds.

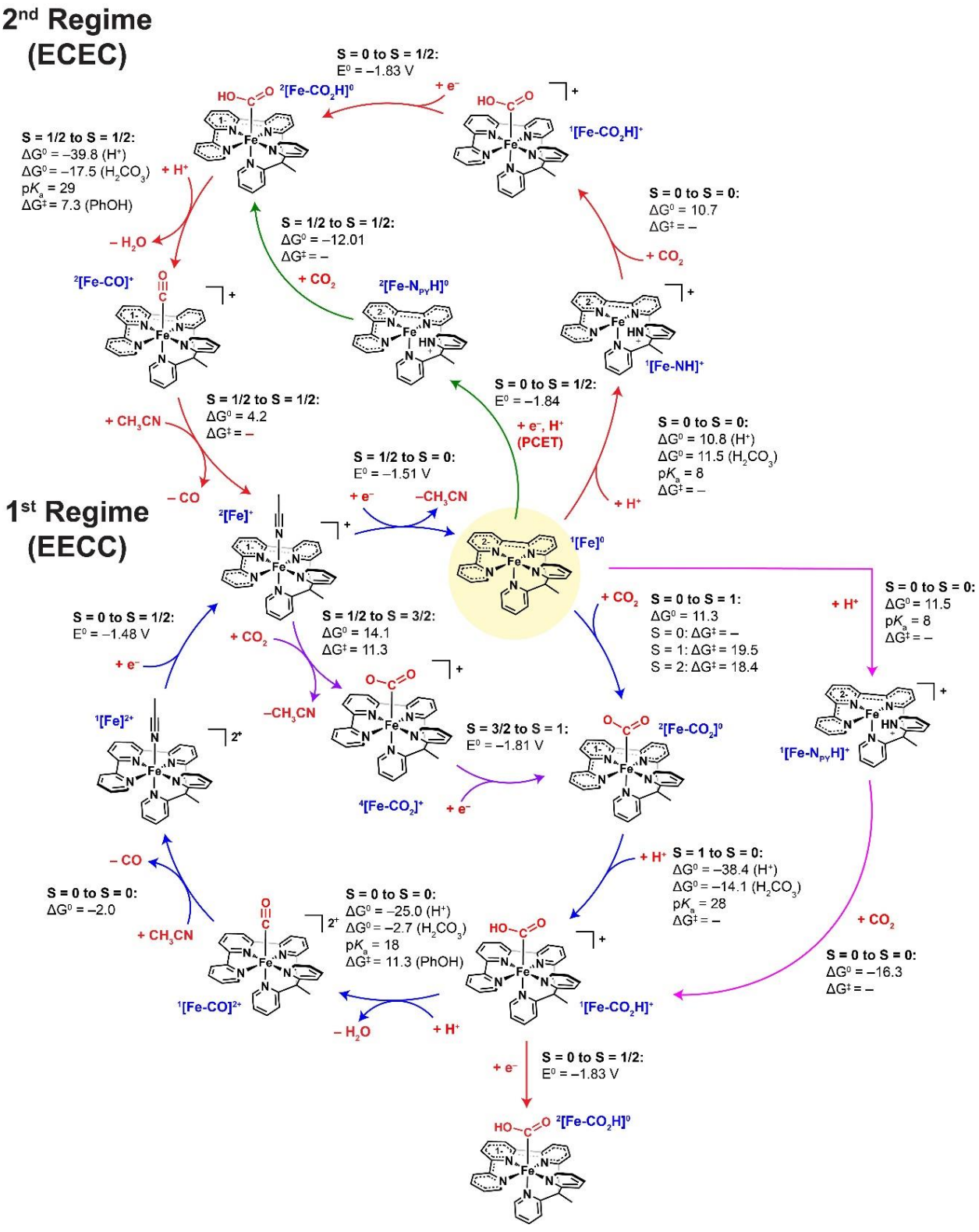


Figure 6.28. Complete mechanistic pathways investigated for the first catalytic regime (low overpotential; bottom half) and the second catalytic regime (high overpotential; top half). For the low overpotential regime we probed: (1) a CO_2 binding first pathway (blue arrows), (2) protonation

first pathway (magenta arrows), and (3) CO_2 binding to the singly reduced complex, $^2[Fe]^+$ (purple arrows). For the high overpotential regime, catalysis turns over from $^2[Fe]^+$. Single-electron reduction of $^2[Fe]^+$ gives the catalytic resting state, $^1[Fe]^0$ highlighted in yellow. Following formation of $^1[Fe]^0$, the pathway diverges in three directions. CO_2 binding can occur first followed by protonation to give $^1[Fe–CO_2H]^+$ (blue arrows) or protonation-first can occur followed by CO_2 coordination (red arrows). The $^1[Fe–CO_2H]^+$ intermediate can then be further reduced to $^2[Fe–CO_2H]^0$ and following the final protonation step and loss of water generates the carbonyl complex, $^2[Fe–CO]^+$ which regenerates $^2[Fe]^+$ following ligand exchange. We additionally explore the possibility of overcoming the high energy barriers associated with either CO_2 binding or protonation of $^1[Fe]^0$ by undergoing a PCET pathway to generate $^2[Fe–N_{PY}H]^0$ (green arrows). All reaction and activation energies are given in units of kcal/mol and all reduction potentials are referenced to the computed Fc/Fc^+ couple.

6.5.3 Redox Potential Calculations

Calculation PCET redox potential shift under non-standard conditions: Follows a similar approach as ref. [52] (see SI). The pK_a of wet acetonitrile is 16.8[40] resulting in (**Equation 6.2**):

$$[H^+] = 10^{-8.4} = 4\text{x}10^{-9} \qquad \textbf{Equation 6.2}$$

Assuming the strongest acid in solution is carbonic acid (**Equation 6.3**):

$$[H^+] \approx [HCO3^-] \qquad \textbf{Equation 6.3}$$

The concentration of carbonic acid can be estimated *via* the solubility of CO_2 in acetonitrile (0.28M) and hydration equilibrium constant K_h (in water [52]) (**Equation 6.4**):

$$[H_2CO_3] = K_h[CO_2] = 1.7x10^{-3}[0.28] = 5x10^{-5} \qquad \textbf{Equation 6.4}$$

This translate into a shift of the standard redox potential computed to be –2.14 V vs Fc/Fc^+ (**Equations 6.5** and **6.6**):

$$E = E^0 - \frac{RT}{nF}2.2log\left(\frac{[Red]}{[Ox]}\right) \qquad \textbf{Equation 6.5}$$

$$E = -2.14\text{ V} + 0.30\text{ V} = -1.84\ V \text{ vs } Fc/Fc^+ \qquad \textbf{Equation 6.6}$$

6.5.4 General Experimental Methods

All manipulations were conducted under air and moisture free conditions using a MBraun LABstar pro glovebox and standard Schlenk line techniques unless otherwise noted. $[Fe(tpyPY2Me)]^{2+}$ was synthesized as previously described.[12] All other reagents were purchased from commercial vendors and used without further purification. Carbon dioxide (99.99%), carbon monoxide (99.5%), ethane (99.0%), argon (99.999%) was purchased from Praxair. Acetonitrile (CH_3CN) was dried using a JC Meyer solvent purification system. Deionized water was obtained from a Millipore Autopure system.

Binding equilibria for CO_2 coordination and CO dissociation were investigated by cyclic voltammetry (CV) with varying scan rates (0.1 to 50 V/s). Catalytic stability was probed with multi-segmented CV experiments over one-hundred cycles as well as with long-term (1 h) preparative scale controlled potential electrolysis (CPE) experiments taken across a range of applied potentials. Averaged Faradaic efficiencies for H_2 (FE_{H2}) and CO (FE_{CO}) production were determined from the one-hour CPE experiments, conducted in triplicate, with direct product detection by gas chromatography. The observed rate constants (k_{obs}) and turnover frequencies (TOF) were extracted from the averaged specific current densities for CO production (j_{CO}) over both short-term CPE experiments (5 min) conducted in a small CV cell and from long-term CPE experiments (1 hr) conducted in a large gastight PEEK electrolysis cell. We observed good agreement between rates obtained from both measurements. Kinetic isotope effects (KIE) were measured using 1 M solutions of phenol-H_6 and phenol-D_6 as the proton source. Observed rate constants for the KIE experiments were obtained using catalytic plateau current analysis despite the noncanonical catalytic behavior of $[Fe]^{2+}$ which makes this analysis inaccurate. This analysis was appropriate here because errors in rate determination are eliminated by taking the ratio of k_H/k_D.

6.5.5 Cyclic Voltammetry (CV)

CV experiments were performed using a CH Instruments, Inc. 600E potentiostat. Voltammetry studies were conducted in a three-electrode cell equipped with a glassy carbon disk (3.0 mm diameter) working electrode (BASi), a platinum wire counter electrode, and a silver wire in a porous Vycor tipped glass tube filled with electrolyte as a pseudo-reference electrode. The working electrode was polished prior to each experiment with 0.05-micron alumina powder on a felt pad. The electrolyte was 0.1 M tetrabutylammonium hexafluorophosphate ($TBAPF_6$) in CH_3CN and was saturated with either CO_2 or Ar at 1 atm. At the conclusion of each experiment, the pseudo-reference potentials were referenced against ferrocene/ferrocenium (Fc/Fc^+) used as an external standard. The scan rates for all cyclic voltammograms were 100 mV/s unless otherwise noted. All voltammograms were obtained with iR compensation.

6.5.6 Controlled Potential Electrolysis (CPE)

CPE experiments were conducted using a CH Instruments, Inc. 600E potentiostat. Preparative scale CPE experiments were performed in either the CV cell (for short-term experiments) or in a miniaturized version of our previously described homemade gastight PEEK electrolysis cell[74] (for long-term experiments) with a working compartment (7 mL liquid volume) and counter compartment (3 mL liquid volume) separated by an ultrafine glass frit. Gaseous products were detected and quantified from data obtained in the long-term, gastight PEEK cell. A 1 cm^2 glassy carbon plate (Toki Carbon; Kanagawa, Japan) was used as the working electrode for the long-term experiments while a 7.07 x 10^{-2} cm^2 glassy carbon disk (BASi) was used for the short-term CPE experiments. The Auxiliary electrode was either a 2.5 cm diameter graphite planchet (Ted Pella; Redding, CA) in the long-term experiment or a platinum wire counter electrode in the short-term experiment. An Ag wire in a Vycor tipped glass tube filled with electrolyte ($TBAPF_6/CH_3CN$) was used as a *pseudo*-reference electrode. The working compartment was filled with 7 mL of a 1 mM solution of $[Fe(tpyPY2Me)]^{2+}$ dissolved in 0.1 M$TBAPF_6/CH_3CN$ containing up to 1.0 M phenol or 4-chlorophenol as a proton source. The

counter electrode chamber was filled with 3 mL of a 20 mM solution of tetrabutylammonium acetate dissolved in 0.1 M $TBAPF_6/CH_3CN$. This soluble source of acetate was sacrificially oxidized to generate CO_2 and ethane, thereby preventing GC detection of solvent oxidation byproducts. Both compartments were sealed to be gastight. The working compartment was sparged with CO_2 for 10 min, then sealed and injected with 0.50 mL of ethane as a gaseous internal standard. A CV scan was collected prior to the CPE measurement to calibrate the potential. The electrolyte solution was constantly stirred during the CPE experiment with a 1 cm stir bar. At the conclusion of the experiment, the headspace was injected directly into an SRI-GC (model #8610C) equipped with 6' Hayesep D and 13X molecular sieve chromatographic columns. Two in-line detectors were used: a TCD for H_2 detection and an FID with a methanizer for $CO/CO_2/C_2H_6$detection. Analytes of interest were quantified by comparing a ratios of analyte/internal stand peak integrals to a calibration curve with known amounts of analyte (**Figure 6.29**).

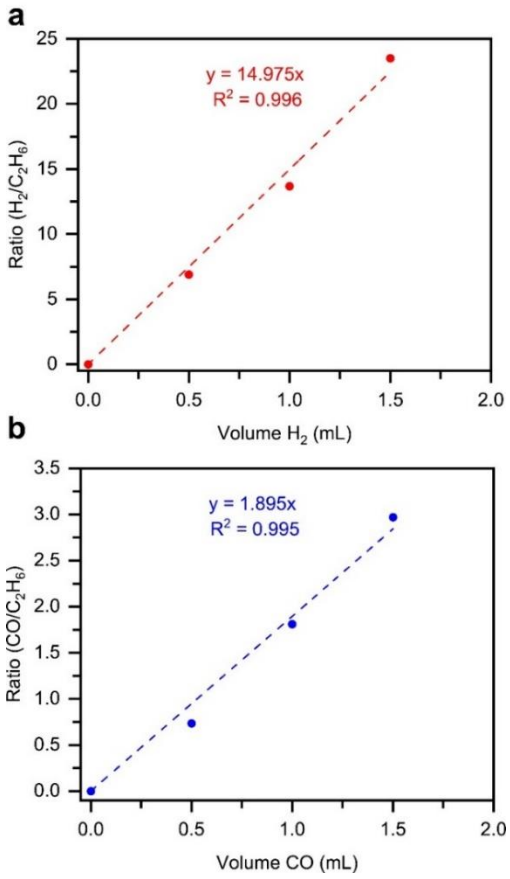


Figure 6.29. Calibration curves for the GC for the detection and quantification of (a) H_2 and(b) CO in $TBAPF_6/CH_3CN$.

6.5.7 Determination of Half-Maximum Catalytic Potentials ($E_{cat/2}$)

The two catalytic regimes for $^1[Fe]^{2+}$ are defined based on the potentials at which half of the maximum catalytic currents ($i_{cat/2}$) are reached ($E_{cat/2}$) in order to avoid potential ambiguity or uncertainty associated with the broadness of the plateau and peak in the low and high potential

regimes, respectively.[43] Values for $E_{cat/2}$ were determined following one of the methods outline by Fourmond and coworkers.[42] Briefly, values for $E^1_{cat/2}$ and $E^2_{cat/2}$ were obtained by subtracting 15 mV from the maximum of the first derivative plot of the forward CV scan collected under catalytic conditions (CO_2 atmosphere with 1 M PhOH). This data is plotted in **Figure 6.30**.

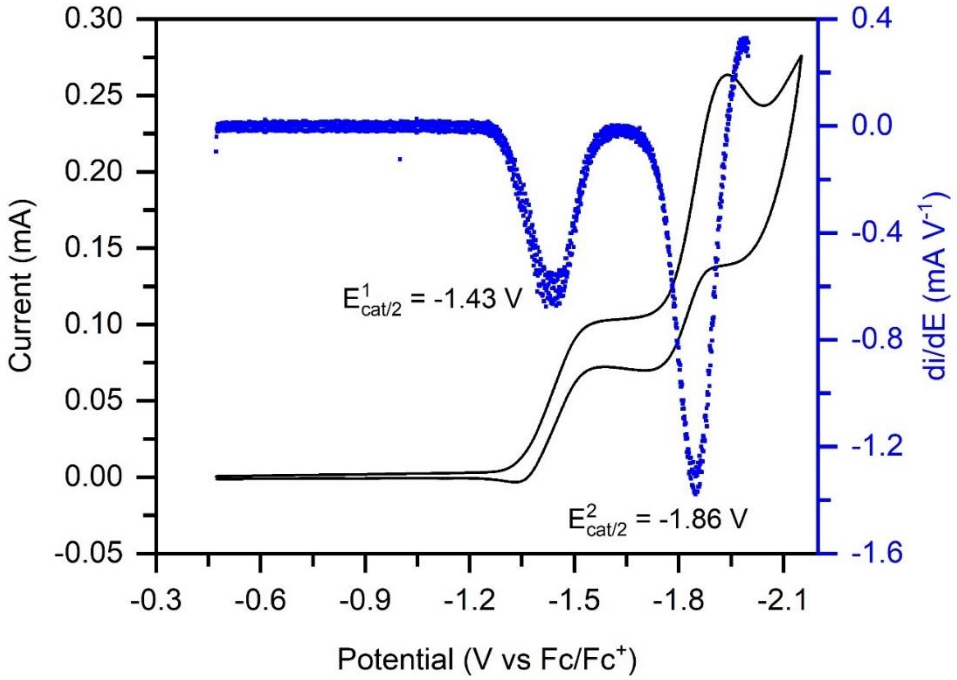


Figure 6.30. First-derivative plot of the cyclic voltammogram of $^1[Fe]^{2+}$ for the determination of $E_{cat/2}$. The black line is the cyclic voltammogram of $^1[Fe]^{2+}$ in the presence of CO_2 and 1 M PhOH and the dotted blue line is the first derivative of the forward scan. To obtain $E_{cat/2}$ from the stationary cyclic voltammogram, 15 mL was subtracted from the maximums extracted from the first derivative plot.

6.5.8 Determination of Overpotential (η)

Conversion of applied potential into overpotential (η) were performed following the methods reported by Mayer et al.[75,76] and Matsubara and coworkers.[40,76] Briefly, the standard redox potential for the conversion of CO_2 into CO in CH_3CN in the presence of acid, AH, $E^0_{CO_2/CO,CH_3CN,AH}$, is described by **Equation 6.7**:

$$E^0_{CO_2/CO,CH_3CN,AH}(vs\ SHE) = \frac{-1}{2F}[\Delta_f G^0(CO_{(g)}) + \Delta_f G^0(H_2O_{(l)}) + \Delta^{1\rightarrow sol}_{tr} G^0(H_2O) - \Delta_f G^0(CO_{2(g)}) + 2RT(ln10)pK^{H_2O}_{a,abs}(CO_{2(g)} + H_2O_{(sol,x)})] \quad \textbf{Equation 6.7}$$

Where F is Faraday's constant and $\Delta_f G^0(CO_{(g)})$, $\Delta_f G^0(CO_{2(g)})$, and $\Delta_f G^0(H_2O_{(l)})$ are the standard formation Gibbs energy changes of CO and CO_2 in the gas phase, and pure liquid H_2O, respectively. At standard pressure (1 bar) and temperature (298.15 K) these values are reported as –137.163, –394.389, and –237.178 kJ/mol. The term $\Delta^{1\rightarrow sol}_{tr} G^0(H_2O)$ is the standard Gibbs energy change upon transfer of water from pure liquid to an acetonitrile-water mixture, for which both

standard states are taken as unit mole fractions of water. R is the gas constant, and T the temperature. $pK_{a,abs}^{H_2O}\left(CO_{2(g)} + H_2O_{(sol,x)}\right)$ is the absolute acidity constant for acetonitrile-water mixtures which can be measured and have been tabulated by Matsubara.[40] In order to accurately obtain the standard redox potential for CO_2, the strongest acid in solution has to be considered. Acetonitrile was used to prepare the electrolyte solution and the phenol, 4-chlorophenol, and $TBAPF_6$ were not thoroughly dried prior to each use and were stored on the benchtop, thus preventing complete removal of water in our system. Therefore, CO_2 in the presence of water, forming carbonic acid, represents the strongest acid present under our experimental conditions. Because $pK_{a,abs}^{H_2O}\left(CO_{2(g)} + H_2O_{(sol,x)}\right)$ varies significantly as a function of water concentration in acetonitrile mixtures, standard redox potentials can fluctuate by 500 mV across the water-acetonitrile mixtures examined by Matsubara (*i.e.*, –1.57 V vs Fc/Fc^+ for 0.5 M water; –0.95 V vs Fc/Fc^+ for 55 M water). As a conservative estimate, we selected the midpoint value of –1.27 V vs Fc/Fc^+. Conditions of high-water concentration do not apply for our experimental conditions, and low-water concentrations assuming less than 0.5 M water leads to an estimated CO_2 standard redox potential that is more negative than where our catalyst operates for CO_2 reduction, which would then result in negative overpotential values. We note that this –1.27 V vs Fc/Fc^+ value is 70 mV more positive than the previously estimated standard redox potentials by Savéant and coworkers.[19,22]

6.5.9 Determination of Faradaic Efficiency (FE)

Controlled potential electrolysis experiments were conducted in gas-tight electrochemical cells at varying applied potentials for 1h. At the conclusion of the CPE experiment, samples from the headspace of the electro-chemical cell were injected into a gas chromatograph for analysis. Calibration curves (**Figure 6.29**) were constructed using known amounts of H_2 and CO and C_2H_6 (0.50 mL) as internal standards to quantify the volume of gaseous products from the respective chromatograms. The amounts (mols) of gas produced were calculated from the volume of gas using the Ideal Gas Law and Faradaic efficiencies were then determined using **Equation 6.8**:

$$FE = \frac{Q_{expt}}{Q_{theory}} x\ 100 = \frac{znf}{Q} x\ 100 \qquad \textbf{Equation 6.8}$$

where z is the number of electrons, n is the mols of analyte produced, F is Faraday's constant and Q is the specific charge passed during the CPE experiment.

6.5.10 Determination of k_{obs} and Turnover Frequency (TOF)

Kinetic information was extracted directly from the short-term and long-term controlled potential electrolysis data at varying applied onset potentials utilizing methods developed by Savéant and coworkers[49] due to the non-canonical catalytic behavior of $[Fe(tpyPY2Me)]^{2+}$ (*e.g.*, a small linear foot-of-the-wave (FOW) region, multi-segmented catalytic waves, and the inherent assumptions associated with FOW analysis). k_{obs} was determined from the CPE experiment using **Equation 6.9**:

$$\frac{Jco}{F} = \sqrt{2kC_A^0 D_p} * \frac{C_p}{1+\exp\left[\frac{F}{RT}(E-E_{redox}^0)\right]} \qquad \textbf{Equation 6.9}$$

Where J_{CO} is the specific current density (A/cm^2) for CO production calculated based on the geometric surface area of the working electrode (1 cm^2 for long-term CPE and 7.07 x10^{-2} cm^2 for the short-term CPE); The average was taken across the three 1 h CPE experiments, F is Faraday's constant, E is the applied potential, E^0_{redox}, is the redox potential in the absence of substrate, R is the ideal gas constant, T is the temperature (K), C^0_A is the concentration of CO_2 (2.80 x 10^{-4} mol/cm^3), D_p is the diffusion coefficient of [Fe1]$^{2+}$ (4.57 x 10^{-6} cm^2/s), and C_p is the concentration of catalyst (1.10 x 10^{-6} mol/cm^3). Catalytic Tafel plots were generated from the kinetic data obtained from the variable potential CPE experiments using **Equation 6.10**:

$$TOF = \frac{2k_{obs}}{1+\exp\left[\frac{F}{RT}(E-E^0_{redox})\right]} \qquad \textbf{Equation 6.10}$$

6.5.11 Determination of Kinetic Isotope Effects (KIE)

KIE were measured for ^{1}[Fe]$^{2+}$ using 1 M phenol (C_6H_6O or C_6D_6O) as the proton source. Observed rate constants, k_{obs}, were determined using catalytic plateau current analysis using **Equation 6.11**:

$$\frac{i_{pl}}{i_p} = \frac{1}{0.446}\sqrt{\frac{RT}{nF\nu}k_{obs}} \qquad \textbf{Equation 6.11}$$

where i_{pl} is the plateau current; i_p is the peak current obtained in the absence of substrate; R is the universal gas constant; n is the number of electrons transferred to the catalyst from the electrode (n = 2); F is Faraday's Constant; ν is the scan rate.

6.6 References

(1) Lewis, N. S.; Nocera, D. G. Powering the Planet: Chemical Challenges in Solar Energy Utilization. *Proc. Natl. Acad. Sci.* **2006**, *103*, 15729–15735.

(2) De Luna, P.; Hahn, C.; Higgins, D.; Jaffer, S. A.; Jaramillo, T. F.; Sargent, E. H. What Would It Take for Renewably Powered Electrosynthesis to Displace Petrochemical Processes? *Science* **2019**, *364*, eaav3506.

(3) Nguyen, V.-H.; Nguyen, B.-S.; Jin, Z.; Shokouhimehr, M.; Jang, H. W. Towards artificial photosynthesis- Sustainable hydrogen utilization for photocatalytic reduction of CO_2 to high-value renewable fuels. *Chem. Eng. J.* **2020**, *402*, 126184.

(4) Gust, D.; Moore, T. A.; Moore, A. L. Solar Fuels via Artificial Photosynthesis. *Acc. Chem. Res.* **2009**, *42*, 1890–1898.

(5) Appel, A. M.; Bercaw, J. E.; Bocarsly, A. B.; Dobbek, H.; DuBois, D. L.; Dupuis, M.; Ferry, J. G.; Fujita, E.; Hille, R.; Kenis, P. J. A.; Kerfeld, C. A.; Morris, R. H.; Peden, C. H. F.; Portis, A. R.; Ragsdale, S. W.; Rauchfuss, T. B.; Reek, J. N. H.; Seefeldt, L. C.; Thauer, R. K.; Waldrop, G. L. Frontiers, Opportunities, and Challenges in Biochemical and Chemical Catalysis of CO_2 Fixation. *Chem. Rev.* **2013**, *113*, 6621–6658.

(6) Sun, Z.; Ma, T.; Tao, H.; Fan, Q.; Han, B. Fundamentals and Challenges of Electrochemical CO_2 Reduction Using Two-Dimensional Materials. *Chem*, **2017**, *3*, 560–587.

(7) Verma, S.; Kim, B.; Jhong, H.-R. "Molly"; Ma, S.; Kenis, P. J. A. A Gross-Margin Model for Defining Technoeconomic Benchmarks in the Electroreduction of CO_2. *ChemSusChem* **2016**, *9*, 1972–1979.

(8) Kumar, B.; Llorente, M.; Froehlich, J.; Dang, T.; Sathrum, A.; Kubiak, C. P. Photochemical and Photoelectrochemical Reduction of CO_2. *Annu. Rev. Phys. Chem.* **2012**, *63*, 541–569.

(9) Long, C.; Li, X.; Guo, J.; Shi, Y.; Liu, S.; Tang, Z. Electrochemical Reduction of CO_2 over Heterogeneous Catalysts in Aqueous Solution: Recent Progress and Perspectives. *Small Methods* **2019**, *3*, 1800369.

(10) Razzak, S. A.; Ali, S. A. M.; Hossain, M. M.; deLasa, H. Biological CO_2 Fixation with Production of Microalgae in Wastewater – A Review. *Renew. Sustain. Energy Rev.* **2017**, *76*, 379–390.

(11) Elouarzaki, K.; Kannan, V.; Jose, V.; Sabharwal, H. S.; Lee, J.-M. Recent Trends, Benchmarking, and Challenges of Electrochemical Reduction of CO_2 by Molecular Catalysts. *Adv. Energy Mater.* **2019**, *9*, 1900090.

(12) Nichols, A. W.; Machan, C. W. Secondary-Sphere Effects in Molecular Electrocatalytic CO_2 Reduction. *Front. Chem.* **2019**, *7*, 397.

(13) Luo, Y.-H.; Dong, L.-Z.; Liu, J.; Li, S.-L.; Lan, Y.-Q. From Molecular Metal Complex to Metal-Organic Framework: The CO_2 Reduction Photocatalysts with Clear and Tunable Structure. *Coord. Chem. Rev.* **2019**, *390*, 86–126.

(14) Kinzel, N. W.; Werlé, C.; Leitner, W. Transition Metal Complexes as Catalysts for the Electroconversion of CO_2: An Organometallic Perspective. *Angew. Chem. Int. Ed.* **2021**, *60*, 11628–11686.

(15) Sun, L.; Reddu, V.; Fisher, A. C.; Wang, X. Electrocatalytic Reduction of Carbon Dioxide: Opportunities with Heterogeneous Molecular Catalysts. *Energy Environ. Sci.* **2020**, *13*, 374–403.

(16) Francke, R.; Schille, B.; Roemelt, M. Homogeneously Catalyzed Electroreduction of Carbon Dioxide—Methods, Mechanisms, and Catalysts. *Chem. Rev.* **2018**, *118*, 4631–4701.

(17) Fukuzumi, S.; Lee, Y.-M.; Ahn, H. S.; Nam, W. Mechanisms of Catalytic Reduction of CO_2 with Heme and Nonheme Metal Complexes. *Chem. Sci.* **2018**, *9*, 6017–6034.
(18) Hammouche, M.; Lexa, D.; Savéant, J. M.; Momenteau, M. Catalysis of the Electrochemical Reduction of Carbon Dioxide by Iron("0") Porphyrins. *J. Electroanal. Chem. Interfacial Electrochem.* **1988**, *249*, 347–351.
(19) Costentin, C.; Drouet, S.; Robert, M.; Savéant, J.-M. A Local Proton Source Enhances CO_2 Electroreduction to CO by a Molecular Fe Catalyst. *Science* **2012**, *338*, 90–94.
(20) Costentin, C.; Robert, M.; Savéant, J.-M.; Tatin, A. Efficient and Selective Molecular Catalyst for the CO_2-to-CO Electrochemical Conversion in Water. *Proc. Natl. Acad. Sci.* **2015**, *112*, 6882–6886.
(21) Costentin, C.; Passard, G.; Robert, M.; Savéant, J.-M. Ultraefficient Homogeneous Catalyst for the CO_2-to-CO Electrochemical Conversion. *Proc. Natl. Acad. Sci.* **2014**, *111*, 14990–14994.
(22) Azcarate, I.; Costentin, C.; Robert, M.; Savéant, J.-M. Through-Space Charge Interaction Substituent Effects in Molecular Catalysis Leading to the Design of the Most Efficient Catalyst of CO_2-to-CO Electrochemical Conversion. *J. Am. Chem. Soc.* **2016**, *138*, 16639–16644.
(23) Rao, H.; Schmidt, L. C.; Bonin, J.; Robert, M. Visible-Light-Driven Methane Formation from CO_2 with a Molecular Iron Catalyst. *Nature* **2017**, *548*, 74–77.
(24) Rao, H.; Lim, C.-H.; Bonin, J.; Miyake, G. M.; Robert, M. Visible-Light-Driven Conversion of CO_2 to CH_4 with an Organic Sensitizer and an Iron Porphyrin Catalyst. *J. Am. Chem. Soc.* **2018**, *140*, 17830–17834.
(25) Martin, D. J.; Mayer, J. M. Oriented Electrostatic Effects on O_2 and CO_2 Reduction by a Polycationic Iron Porphyrin. *J. Am. Chem. Soc.* **2021**, *143*, 11423–11434.
(26) Masaoka, S.; Kosugi, K.; Kondo, M. Quick and Easy Method for Dramatic Improvement of the Electrochemical CO_2 Reduction Activity of an Iron Porphyrin Complex. *Angew. Chem. Int. Ed.*, **2021**, *60*, 22070 – 22074.
(27) Costentin, C.; Savéant, J.-M. Towards an Intelligent Design of Molecular Electrocatalysts. *Nat. Rev. Chem.* **2017**, *1*, 0087.
(28) Costentin, C.; Robert, M.; Savéant, J.-M. Current Issues in Molecular Catalysis Illustrated by Iron Porphyrins as Catalysts of the CO_2-to-CO Electrochemical Conversion. *Acc. Chem. Res.* **2015**, *48*, 2996–3006.
(29) Khadhraoui, A.; Gotico, P.; Boitrel, B.; Leibl, W.; Halime, Z.; Aukauloo, A. Local Ionic Liquid Environment at a Modified Iron Porphyrin Catalyst Enhances the Electrocatalytic Performance of CO_2 to CO Reduction in Water. *Chem. Commun.* **2018**, *54*, 11630–11633.
(30) Zee, D. Z.; Nippe, M.; King, A. E.; Chang, C. J.; Long, J. R. Tuning Second Coordination Sphere Interactions in Polypyridyl–Iron Complexes to Achieve Selective Electrocatalytic Reduction of Carbon Dioxide to Carbon Monoxide. *Inorg. Chem.* **2020**, *59*, 5206–5217.
(31) Loipersberger, M.; Zee, D. Z.; Panetier, J. A.; Chang, C. J.; Long, J. R.; Head-Gordon, M. Computational Study of an Iron(II) Polypyridine Electrocatalyst for CO_2 Reduction: Key Roles for Intramolecular Interactions in CO_2 Binding and Proton Transfer. *Inorg. Chem.* **2020**, *59*, 8146–8160.
(32) Che, C.-M.; Chan, C.-W.; Yang, S.-M.; Guo, C.-X.; Lee, C.-Y.; Peng, S.-M. Synthesis, Properties and Crystal Structures of Iron-(II) and -(III) Complexes of 2,2′:6′,2″:6″,2‴-Quaterpyridine. *J. Chem. Soc. Dalton Trans.* **1995**, 2961–2966.

(33) Cometto, C.; Chen, L.; Lo, P.-K.; Guo, Z.; Lau, K.-C.; Anxolabéhère-Mallart, E.; Fave, C.; Lau, T.-C.; Robert, M. Highly Selective Molecular Catalysts for the CO_2-to-CO Electrochemical Conversion at Very Low Overpotential. Contrasting Fe vs Co Quaterpyridine Complexes upon Mechanistic Studies. *ACS Catal.* **2018**, *8*, 3411–3417.
(34) Cometto, C.; Chen, L.; Anxolabéhère-Mallart, E.; Fave, C.; Lau, T.-C.; Robert, M. Molecular Electrochemical Catalysis of the CO_2-to-CO Conversion with a Co Complex: A Cyclic Voltammetry Mechanistic Investigation. *Organometallics* **2019**, *38*, 1280–1285.
(35) Loipersberger, M.; Cabral, D. G. A.; Chu, D. B. K.; Head-Gordon, M. Mechanistic Insights into Co and Fe Quaterpyridine-Based CO_2 Reduction Catalysts: Metal–Ligand Orbital Interaction as the Key Driving Force for Distinct Pathways. *J. Am. Chem. Soc.* **2021**, *143*, 744–763.
(36) Smith, P. T.; Nichols, E. M.; Cao, Z.; Chang, C. J. Hybrid Catalysts for Artificial Photosynthesis: Merging Approaches from Molecular, Materials, and Biological Catalysis. *Acc. Chem. Res.* **2020**, *53*, 575–587.
(37) Zee, D. Z.; Chantarojsiri, T.; Long, J. R.; Chang, C. J. Metal–Polypyridyl Catalysts for Electro- and Photochemical Reduction of Water to Hydrogen. *Acc. Chem. Res.* **2015**, *48*, 2027–2036.
(38) Smith, P. T.; Weng, S.; Chang, C. J. An NADH-Inspired Redox Mediator Strategy to Promote Second-Sphere Electron and Proton Transfer for Cooperative Electrochemical CO_2 Reduction Catalyzed by Iron Porphyrin. *Inorg. Chem.* **2020**, *59*, 9270–9278.
(39) Derrick, J. S.; Loipersberger, M.; Chatterjee, R.; Iovan, D. A.; Smith, P. T.; Chakarawet, K.; Yano, J.; Long, J. R.; Head-Gordon, M.; Chang, C. J. Metal–Ligand Cooperativity via Exchange Coupling Promotes Iron- Catalyzed Electrochemical CO_2 Reduction at Low Overpotentials. *J. Am. Chem. Soc.* **2020**, *142*, 20489–20501.
(40) Matsubara, Y. Unified Benchmarking of Electrocatalysts in Noninnocent Second Coordination Spheres for CO_2 Reduction. *ACS Energy Lett.* **2019**, *4*, 1999–2004.
(41) Coetzee, J. F.; Padmanabhan, G. R. Dissociation and Homoconjugation of Certain Phenols in Acetonitrile. *J. Phys. Chem.* **1965**, *69*, 3193–3196.
(42) Fourmond, V.; Jacques, P.-A.; Fontecave, M.; Artero, V. H_2 Evolution and Molecular Electrocatalysts: Determination of Overpotentials and Effect of Homoconjugation. *Inorg. Chem.* **2010**, *49*, 10338–10347.
(43) Stratakes, B. M.; Dempsey, J. L.; Miller, A. J. M. Determining the Overpotential of Electrochemical Fuel Synthesis Mediated by Molecular Catalysts: Recommended Practices, Standard Reduction Potentials, and Challenges. *ChemElectroChem* **2021**, *8*, 4161–4180.
(44) Rountree, E. S.; McCarthy, B. D.; Eisenhart, T. T.; Dempsey, J. L. Evaluation of Homogeneous Electrocatalysts by Cyclic Voltammetry. *Inorg. Chem.* **2014**, *53*, 9983–10002.
(45) Lee, K. J.; Elgrishi, N.; Kandemir, B.; Dempsey, J. L. Electrochemical and Spectroscopic Methods for Evaluating Molecular Electrocatalysts. *Nat. Rev. Chem.* **2017**, *1*, 0039.
(46) Costentin, C.; Savéant, J.-M. Multielectron, Multistep Molecular Catalysis of Electrochemical Reactions: Benchmarking of Homogeneous Catalysts. *ChemElectroChem* **2014**, *1*, 1226–1236.
(47) Wang, V. C.-C.; Johnson, B. A. Interpreting the Electrocatalytic Voltammetry of Homogeneous Catalysts by the Foot of the Wave Analysis and Its Wider Implications. *ACS Catal.* **2019**, *9*, 7109–7123.

(48) Costentin, C.; Passard, G.; Savéant, J.-M. Benchmarking of Homogeneous Electrocatalysts: Overpotential, Turnover Frequency, Limiting Turnover Number. *J. Am. Chem. Soc.* **2015**, *137*, 5461–5467.
(49) Costentin, C.; Drouet, S.; Robert, M.; Savéant, J.-M. Turnover Numbers, Turnover Frequencies, and Overpotential in Molecular Catalysis of Electrochemical Reactions. Cyclic Voltammetry and Preparative-Scale Electrolysis. *J. Am. Chem. Soc.* **2012**, *134*, 11235–
(50) Costentin, C.; Drouet, S.; Robert, M.; Savéant, J.-M. Correction to Turnover Numbers, Turnover Frequencies, and Overpotential in Molecular Catalysis of Electrochemical Reactions. Cyclic Voltammetry and Preparative-Scale Electrolysis. *J. Am. Chem. Soc.* **2012**, *134*, 19949–19950.
(51) Gonell, S.; Lloret-Fillol, J.; Miller, A. J. M. An Iron Pyridyl-Carbene Electrocatalyst for Low Overpotential CO_2 Reduction to CO. *ACS Catal.* **2021**, *11*, 615–626.
(52) Song, J.; Klein, E. L.; Neese, F.; Ye, S. The Mechanism of Homogeneous CO_2 Reduction by Ni(Cyclam): Product Selectivity, Concerted Proton–Electron Transfer and C–O Bond Cleavage. *Inorg. Chem.* **2014**, *53*, 7500–7507.
(53) Kozuch, S.; Shaik, S. A Combined Kinetic−Quantum Mechanical Model for Assessment of Catalytic Cycles: Application to Cross-Coupling and Heck Reactions. *J. Am. Chem. Soc.* **2006**, *128*, 3355–3365.
(54) Uhe, A.; Kozuch, S.; Shaik, S. Automatic Analysis of Computed Catalytic Cycles. *J. Comput. Chem.* **2011**, *32*, 978–985.
(55) Kozuch, S. A Refinement of Everyday Thinking: The Energetic Span Model for Kinetic Assessment of Catalytic Cycles. *WIREs Comput. Mol. Sci.* **2012**, *2*, 795–815.
(56) Mao, Y.; Loipersberger, M.; Kron, K. J.; Derrick, J. S.; Chang, C. J.; Sharada, S. M.; Head-Gordon, M. Consistent Inclusion of Continuum Solvation in Energy Decomposition Analysis: Theory and Application to Molecular CO_2 Reduction Catalysts. *Chem. Sci.* **2021**, *12*, 1398–1414.
(57) Mao, Y.; Loipersberger, M.; Horn, P. R.; Das, A.; Demerdash, O.; Levine, D. S.; Prasad Veccham, S.; Head-Gordon, T.; Head-Gordon, M. From Intermolecular Interaction Energies and Observable Shifts to Component Contributions and Back Again: A Tale of Variational Energy Decomposition Analysis. *Annu. Rev. Phys. Chem.* **2021**, *72*, 641–666.
(58) Ambre, R. B.; Daniel, Q.; Fan, T.; Chen, H.; Zhang, B.; Wang, L.; Ahlquist, M. S. G.; Duan, L.; Sun, L. Molecular Engineering for Efficient and Selective Iron Porphyrin Catalysts for Electrochemical Reduction of CO_2 to CO. *Chem. Commun.* **2016**, *52*, 14478–14481.
(59) Khaliullin, R. Z.; Cobar, E. A.; Lochan, R. C.; Bell, A. T.; Head-Gordon, M. Unravelling the Origin of Intermolecular Interactions Using Absolutely Localized Molecular Orbitals. *J. Phys. Chem. A* **2007**, *111*, 8753–8765.
(60) Thom, A. J. W.; Sundstrom, E. J.; Head-Gordon, M. LOBA: A Localized Orbital Bonding Analysis to Calculate Oxidation States, with Application to a Model Water Oxidation Catalyst. *Phys. Chem. Chem. Phys.* **2009**, *11*, 11297–11304.
(61) Epifanovsky, E.; Gilbert, A. T. B.; Feng, X.; Lee, J.; Mao, Y.; Mardirossian, N.; Pokhilko, P.; White, A. F.; Coons, M. P.; Dempwolff, A. L.; Gan, Z.; Hait, D.; Horn, P. R.; Jacobson, L. D.; Kaliman, I.; Kussmann, J.; Lange, A. W.; Lao, K. U.; Levine, D. S.; Liu, J.; McKenzie, S. C.; Morrison, A. F.; Nanda, K. D.; Plasser, F.; Rehn, D. R.; Vidal, M. L.; You, Z.-Q.; Zhu, Y.; Alam, B.; Albrecht, B. J.; Aldossary, A.; Alguire, E.; Andersen, J. H.; Athavale, V.; Barton, D.; Begam, K.; Behn, A.; Bellonzi, N.; Bernard, Y. A.; Berquist, E. J.; Burton, H. G. A.; Carreras, A.; Carter-Fenk, K.; Chakraborty, R.; Chien, A. D.; Closser,

K. D.; Cofer-Shabica, V.; Dasgupta, S.; de Wergifosse, M.; Deng, J.; Diedenhofen, M.; Do, H.; Ehlert, S.; Fang, P.-T.; Fatehi, S.; Feng, Q.; Friedhoff, T.; Gayvert, J.; Ge, Q.; Gidofalvi, G.; Goldey, M.; Gomes, J.; González-Espinoza, C. E.; Gulania, S.; Gunina, A. O.; Hanson-Heine, M. W. D.; Harbach, P. H. P.; Hauser, A.; Herbst, M. F.; Hernández Vera, M.; Hodecker, M.; Holden, Z. C.; Houck, S.; Huang, X.; Hui, K.; Huynh, B. C.; Ivanov, M.; Jász, Á.; Ji, H.; Jiang, H.; Kaduk, B.; Kähler, S.; Khistyaev, K.; Kim, J.; Kis, G.; Klunzinger, P.; Koczor-Benda, Z.; Koh, J. H.; Kosenkov, D.; Koulias, L.; Kowalczyk, T.; Krauter, C. M.; Kue, K.; Kunitsa, A.; Kus, T.; Ladjánszki, I.; Landau, A.; Lawler, K. V.; Lefrancois, D.; Lehtola, S.; Li, R. R.; Li, Y.-P.; Liang, J.; Liebenthal, M.; Lin, H.-H.; Lin, Y.-S.; Liu, F.; Liu, K.-Y.; Loipersberger, M.; Luenser, A.; Manjanath, A.; Manohar, P.; Mansoor, E.; Manzer, S. F.; Mao, S.-P.; Marenich, A. V.; Markovich, T.; Mason, S.; Maurer, S. A.; McLaughlin, P. F.; Menger, M. F. S. J.; Mewes, J.-M.; Mewes, S. A.; Morgante, P.; Mullinax, J. W.; Oosterbaan, K. J.; Paran, G.; Paul, A. C.; Paul, S. K.; Pavošević, F.; Pei, Z.; Prager, S.; Proynov, E. I.; Rák, Á.; Ramos-Cordoba, E.; Rana, B.; Rask, A. E.; Rettig, A.; Richard, R. M.; Rob, F.; Rossomme, E.; Scheele, T.; Scheurer, M.; Schneider, M.; Sergueev, N.; Sharada, S. M.; Skomorowski, W.; Small, D. W.; Stein, C. J.; Su, Y.-C.; Sundstrom, E. J.; Tao, Z.; Thirman, J.; Tornai, G. J.; Tsuchimochi, T.; Tubman, N. M.; Veccham, S. P.; Vydrov, O.; Wenzel, J.; Witte, J.; Yamada, A.; Yao, K.; Yeganeh, S.; Yost, S. R.; Zech, A.; Zhang, I. Y.; Zhang, X.; Zhang, Y.; Zuev, D.; Aspuru-Guzik, A.; Bell, A. T.; Besley, N. A.; Bravaya, K. B.; Brooks, B. R.; Casanova, D.; Chai, J.-D.; Coriani, S.; Cramer, C. J.; Cserey, G.; DePrince, A. E.; DiStasio, R. A.; Dreuw, A.; Dunietz, B. D.; Furlani, T. R.; Goddard, W. A.; Hammes-Schiffer, S.; Head-Gordon, T.; Hehre, W. J.; Hsu, C.-P.; Jagau, T.-C.; Jung, Y.; Klamt, A.; Kong, J.; Lambrecht, D. S.; Liang, W.; Mayhall, N. J.; McCurdy, C. W.; Neaton, J. B.; Ochsenfeld, C.; Parkhill, J. A.; Peverati, R.; Rassolov, V. A.; Shao, Y.; Slipchenko, L. V.; Stauch, T.; Steele, R. P.; Subotnik, J. E.; Thom, A. J. W.; Tkatchenko, A.; Truhlar, D. G.; Van Voorhis, T.; Wesolowski, T. A.; Whaley, K. B.; Woodcock, H. L.; Zimmerman, P. M.; Faraji, S.; Gill, P. M. W.; Head-Gordon, M.; Herbert, J. M.; Krylov, A. I. Software for the Frontiers of Quantum Chemistry: An Overview of Developments in the Q-Chem 5 Package. *J. Chem. Phys.* **2021**, *155*, 084801.

(62) Kelly, C. P.; Cramer, C. J.; Truhlar, D. G. Single-Ion Solvation Free Energies and the Normal Hydrogen Electrode Potential in Methanol, Acetonitrile, and Dimethyl Sulfoxide. *J. Phys. Chem. B* **2007**, *111*, 408–422.

(63) McWilliams, S. F.; Brennan-Wydra, E.; MacLeod, K. C.; Holland, P. L. Density Functional Calculations for Prediction of ^{57}Fe Mössbauer Isomer Shifts and Quadrupole Splittings in β-Diketiminate Complexes. *ACS Omega* **2017**, *2*, 2594–2606.

(64) Konezny, S. J.; Doherty, M. D.; Luca, O. R.; Crabtree, R. H.; Soloveichik, G. L.; Batista, V. S. Reduction of Systematic Uncertainty in DFT Redox Potentials of Transition-Metal Complexes. *J. Phys. Chem. C* **2012**, *116*, 6349–6356.

(65) Fu, Y.; Liu, L.; Yu, H.-Z.; Wang, Y.-M.; Guo, Q.-X. Quantum-Chemical Predictions of Absolute Standard Redox Potentials of Diverse Organic Molecules and Free Radicals in Acetonitrile. *J. Am. Chem. Soc.* **2005**, *127*, 7227–7234.

(66) Weigend, F.; Ahlrichs, R. Balanced Basis Sets of Split Valence, Triple Zeta Valence and Quadruple Zeta Valence Quality for H to Rn: Design and Assessment of Accuracy. *Phys. Chem. Chem. Phys.* **2005**, *7*, 3297–3305.

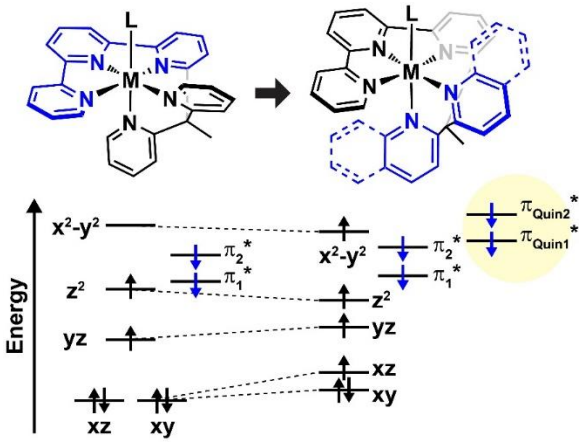
(67) Karton, A.; O'Reilly, R. J.; Radom, L. Assessment of Theoretical Procedures for Calculating Barrier Heights for a Diverse Set of Water-Catalyzed Proton-Transfer Reactions. *J. Phys. Chem. A* **2012**, *116*, 4211–4221.
(68) Mardirossian, N.; Head-Gordon, M. Thirty Years of Density Functional Theory in Computational Chemistry: An Overview and Extensive Assessment of 200 Density Functionals. *Mol. Phys.* **2017**, *115*, 2315–2372.
(69) Bhattacharjee, A.; Andreiadis, E. S.; Chavarot-Kerlidou, M.; Fontecave, M.; Field, M. J.; Artero, V. A Computational Study of the Mechanism of Hydrogen Evolution by Cobalt(Diimine-Dioxime) Catalysts. *Chem. Eur. J.* **2013**, *19*, 15166–15174.
(70) Raamat, E.; Kaupmees, K.; Ovsjannikov, G.; Trummal, A.; Kütt, A.; Saame, J.; Koppel, I.; Kaljurand, I.; Lipping, L.; Rodima, T.; Pihl, V.; Koppel, I. A.; Leito, I. Acidities of Strong Neutral Brønsted Acids in Different Media. *J. Phys. Org. Chem.* **2013**, *26*, 162–170.
(71) Kozuch, S.; Shaik, S. How to Conceptualize Catalytic Cycles? The Energetic Span Model. *Acc. Chem. Res.* **2011**, *44*, 101–110.
(72) Shao, Y.; Gan, Z.; Epifanovsky, E.; Gilbert, A. T. B.; Wormit, M.; Kussmann, J.; Lange, A. W.; Behn, A.; Deng, J.; Feng, X.; Ghosh, D.; Goldey, M.; Horn, P. R.; Jacobson, L. D.; Kaliman, I.; Khaliullin, R. Z.; Kuś, T.; Landau, A.; Liu, J.; Proynov, E. I.; Rhee, Y. M.; Richard, R. M.; Rohrdanz, M. A.; Steele, R. P.; Sundstrom, E. J.; Woodcock, H. L.; Zimmerman, P. M.; Zuev, D.; Albrecht, B.; Alguire, E.; Austin, B.; Beran, G. J. O.; Bernard, Y. A.; Berquist, E.; Brandhorst, K.; Bravaya, K. B.; Brown, S. T.; Casanova, D.; Chang, C.-M.; Chen, Y.; Chien, S. H.; Closser, K. D.; Crittenden, D. L.; Diedenhofen, M.; DiStasio, R. A.; Do, H.; Dutoi, A. D.; Edgar, R. G.; Fatehi, S.; Fusti-Molnar, L.; Ghysels, A.; Golubeva-Zadorozhnaya, A.; Gomes, J.; Hanson-Heine, M. W. D.; Harbach, P. H. P.; Hauser, A. W.; Hohenstein, E. G.; Holden, Z. C.; Jagau, T.-C.; Ji, H.; Kaduk, B.; Khistyaev, K.; Kim, J.; Kim, J.; King, R. A.; Klunzinger, P.; Kosenkov, D.; Kowalczyk, T.; Krauter, C. M.; Lao, K. U.; Laurent, A. D.; Lawler, K. V.; Levchenko, S. V.; Lin, C. Y.; Liu, F.; Livshits, E.; Lochan, R. C.; Luenser, A.; Manohar, P.; Manzer, S. F.; Mao, S.-P.; Mardirossian, N.; Marenich, A. V.; Maurer, S. A.; Mayhall, N. J.; Neuscamman, E.; Oana, C. M.; Olivares-Amaya, R.; O'Neill, D. P.; Parkhill, J. A.; Perrine, T. M.; Peverati, R.; Prociuk, A.; Rehn, D. R.; Rosta, E.; Russ, N. J.; Sharada, S. M.; Sharma, S.; Small, D. W.; Sodt, A.; Stein, T.; Stück, D.; Su, Y.-C.; Thom, A. J. W.; Tsuchimochi, T.; Vanovschi, V.; Vogt, L.; Vydrov, O.; Wang, T.; Watson, M. A.; Wenzel, J.; White, A.; Williams, C. F.; Yang, J.; Yeganeh, S.; Yost, S. R.; You, Z.-Q.; Zhang, I. Y.; Zhang, X.; Zhao, Y.; Brooks, B. R.; Chan, G. K. L.; Chipman, D. M.; Cramer, C. J.; Goddard, W. A.; Gordon, M. S.; Hehre, W. J.; Klamt, A.; Schaefer, H. F.; Schmidt, M. W.; Sherrill, C. D.; Truhlar, D. G.; Warshel, A.; Xu, X.; Aspuru-Guzik, A.; Baer, R.; Bell, A. T.; Besley, N. A.; Chai, J.-D.; Dreuw, A.; Dunietz, B. D.; Furlani, T. R.; Gwaltney, S. R.; Hsu, C.-P.; Jung, Y.; Kong, J.; Lambrecht, D. S.; Liang, W.; Ochsenfeld, C.; Rassolov, V. A.; Slipchenko, L. V.; Subotnik, J. E.; Van Voorhis, T.; Herbert, J. M.; Krylov, A. I.; Gill, P. M. W.; Head-Gordon, M. Advances in Molecular Quantum Chemistry Contained in the Q-Chem 4 Program Package. *Mol. Phys.* **2015**, *113*, 184–215.
(73) Chai, J.-D.; Head-Gordon, M. Long-Range Corrected Hybrid Density Functionals with Damped Atom–Atom Dispersion Corrections. *Phys. Chem. Chem. Phys.* **2008**, *10*, 6615–6620.

(74) Nichols, E. M.; Derrick, J. S.; Nistanaki, S. K.; Smith, P. T.; Chang, C. J. Positional Effects of Second-Sphere Amide Pendants on Electrochemical CO_2 Reduction Catalyzed by Iron Porphyrins. *Chem. Sci.* **2018**, *9*, 2952–2960.
(75) Pegis, M. L.; Roberts, J. A. S.; Wasylenko, D. J.; Mader, E. A.; Appel, A. M.; Mayer, J. M. Standard Reduction Potentials for Oxygen and Carbon Dioxide Couples in Acetonitrile and N,N-Dimethylformamide. *Inorg. Chem.* **2015**, *54*, 11883–11888.
(76) Matsubara, Y.; Grills, D. C.; Kuwahara, Y. Thermodynamic Aspects of Electrocatalytic CO_2 Reduction in Acetonitrile and with an Ionic Liquid as Solvent or Electrolyte. *ACS Catal.* **2015**, *5*, 6440–6452.

Chapter 7: Expanded π* Systems Integrated into Molecular Polypyridyl Coordination Complexes for Electrochemical Carbon Dioxide Reduction Beyond Two-Electron Reduction Products: Synthesis, Characterization, and Catalytic Analysis

7.1 Abstract

Integration of a redox-active terpyridine (tpy) moiety into the primary coordination sphere of a polypyridyl ligand environment yields a series of first-row coordination complexes (M-tpyPY2Me) that display interesting electronic structures and catalytic activities. The Fe-tpyPY2Me complex was shown in Chapter 5 to be an exceptional homogenous electrocatalyst capable of converting CO_2 into CO at low overpotentials with high selectivity at rates faster than 100,000 s^{-1}. This exceptional catalytic performance is attributed to the open-shell singlet electronic structure of the catalytically relevant, two-electron reduced complex that arises from the strong antiferromagnetic coupling of an intermediate-spin Fe(II) center with a doubly, reduced triplet tpyPY2Me ligand. The Co-tpyPY2Me complex similarly catalyzes the electrochemical and photochemical CO_2 reduction reaction, but with limited solution stability due to its more reactive doublet ground state. Conversely, the Ni analog, Ni-tpyPY2Me, doesn't operate as an effective CO_2 reduction catalyst, but has found application as an effective electron mediator capable of controlling the single-electron transfer pathways of alkyl halides through outer-sphere electron transfer enabled by metal–ligand cooperativity (see Appendix B). The success of the tpyPY2Me ligand scaffold has encouraged us to explore if the concept of metal–ligand exchange coupling can be expanded to give access to discrete, well-defined molecular catalysts that are able to reduce CO_2 beyond two-electron products. We hypothesize that the installation of more redox-active components will result in additional low-lying π* orbitals that can accommodate and stabilize highly reduced molecular catalysts. The mechanistic study discussed in Chapter 6 identified synthetic modification to the pyridyl arms as a promising strategy to access additional ligand-based orbitals without disrupting the crucial antiferromagnetic coupling that is key for efficient redox matching with CO_2. To this end, the work presented in this chapter seeks to substitute the redox-silent pyridyl arms for more conjugated, redox-active quinoline or isoquinoline moieties. We report the synthesis and characterization of tpy-based polypyridyl complexes equipped with bis-(iso)quinoline arms which provide a starting point for the analysis of their feasibility to electrochemically reduce CO_2 beyond two-electron products.



7.2 Introduction

The reliance of contemporary society on fossil fuel combustion to meet increasing energy demands has contributed to a steady increase in atmospheric carbon dioxide (CO_2) levels, the main greenhouse gas driving human accelerated climate change.[1] Current infrastructure that relies on fossil fuels are unsustainable due to vastly depleting oil, natural gas, and coal reserves, and further fail to address the current, critical imbalance in carbon emissions which, if left uncorrected, will inevitability exacerbate the economic and environmental issues we face today.[2,3] Solutions directed at meeting these challenges must focus on both the capture and conversion of CO_2 into more useful carbon-based products if we are to transition towards a carbon-neutral global economy.[4,5] Ideally, we envision driving these transformations with electricity because of its ability to be generated renewably and its compatibility with aqueous media.[5] Water presents a cheap, abundant, and inert carbon-neutral matrix to facilitate the transfer of protons and electrons, the primary chemical reactants required to achieve value-added CO_2 reduction products such as carbon monoxide (CO), formate (HCO_2H), formaldehyde (CH_2O), methanol (CH_3OH), and methane (CH_4).

The thermodynamic and kinetic challenges associated with the electrochemical CO_2 reduction reaction (CO_2RR) necessitates the use of efficient catalysts to achieve high selectivity over the competing, background hydrogen evolution reaction (HER).[6–8] Despite the broad interest in CO_2RR in recent years, molecular catalyst development has primarily focused on a limited number of privileged scaffolds.[9–18] Biology, on the other hand, utilizes a rich repertoire of second coordination sphere functional groups to facilitate rapid and efficient capture, activation, and reduction of small molecules.[19,20] For example, carbon monoxide dehydrogenase (CODH) enzymes utilize a series of hydrogen bonding and proton-shuttles to efficiently catalyze the reversible transformation of CO_2 to CO.[20–23] Furthermore, for long-term carbon recycling goals to be realized, CO_2 must be converted to more useful forms beyond the two-electron reduced products, CO or formate.[5,24] This requires new strategies to deliver more than two electrons and two protons to CO_2 in a highly precise and controlled manner. Biology has also elegantly addressed the problem of how to deliver multiple electrons and protons to other small molecule substrates such as dinitrogen (N_2) with nitrogenases through the use of redox reservoirs such as iron sulfur clusters.[25–27]

Catalytic systems capable of supplying more than two electrons to CO_2 are almost entirely limited to copper-based cathodes.[24,28] Excluding surface adsorbed systems, where the interaction between the catalyst and support is far from innocent, molecular catalysts reporting highly reduced products remain scarce.[24] A ruthenium polypyridyl complex, $[Ru(bpy)(tpy)(CO)]^{2+}$ (bpy = 2,2'-bipyridine; tpy = 2,2':6',2"-terpyridine), reported by Nagao and coworkers was the first molecular catalyst capable of converting CO_2 into CH_2O and CH_3OH, albeit at low temperature (–20 ºC) with poor Faradic efficiencies (<5%).[29,30] This surprising activity is not observed at ambient temperature or for the bis-bpy analog, $[Ru(bpy)_2(CO)_2]^{2+}$, and was attributed to the ability of the tpy ligand to stabilize the two-electron reduced carbonyl intermediate at low temperatures.[29,30] This example complements the work we presented in Chapters 5 and 6 where we also exploited the integration of a tpy moiety into a polypyridyl framework to suppress the hydrogen evolution reaction (HER) and subsequently turn-on CO_2 reduction catalysis *via* metal–ligand exchange coupling. Moreover, Nagao's work further illustrates the utility of redox-active ligands to stabilize

key reaction intermediates so that they can persist long enough to be further reduced while simultaneously avoiding over-stabilization that can occur by strong back-bonding interactions which ultimately cause catalyst poisoning (*e.g.*, the Sabatier principle).[29–31] Interestingly this isn't the only report that leverages terpyridine-based catalysts to generate highly reduced carbon products. Abruna *et al.* demonstrated a few years after the seminal report from Nagato that bis-(vinyl-terpyridine) complexes (M = Cr, Fe, Co) can be polymerized electrochemically onto glassy carbon electrodes where the resultant molecular-material hybrids are extremely active for CH_2O production from CO_2 with Faradaic efficiencies reaching 87%.[32] While this system isn't purely molecular it does serve to highlight the potential benefits engendered by tpy-based ligand scaffolds to facilitate production of value-added carbon products.

Recent literature reports further bolster the general applicability of redox-active ligands to reduce CO_2 beyond two-electron products. In 2021, Nganga *et al.*[33] expanded upon a series of rhenium complexes based on the tricarbonyl bipyridine complexes (*i.e.* [*fac*-Re(bpy)$(CO)_3$X]^n where X is an axial halide and n = 0 or +1) which had been first reported by Lehn *et al.*[13] and further developed by Kubiak and coworkers.[16,34] These complexes catalyze the reduction of CO_2 into CO and CH_4 at low efficiencies. The substitution of the bpy ligand for more redox-active (iso)quinoline-oxazoline ligands yielded a series of coordination complexes that express modest CH_4 formation (~33%) at negative applied potentials (–2.5 V vs Fc/Fc^+) in acetonitrile with the use of 2,2,2-trifluorethanol (TFE) as the proton source. Aided by theoretical mechanistic studies, they independently attributed CH_4 formation to a ligand-assisted pathway where electron density was delocalized onto the (iso)quinoline moiety resulting in stabilization of a key carbonyl intermediate for further electron and proton transfer steps.[33] Their computational work agrees well with the mechanistic pathway originally put forward by Nagato *et al.* decades earlier.[29,30]

In addition to polypyridyl complexes, redox-active imine-based coordination complexes in the form of copper bis(thiosemicarbazone), Cu-ATSM (H_2ATSM = diacetyl-2-(4-N-methyl-3-thiosemicarbazone)-3-(4-N-amino-3- thiosemicarbazone)), have recently been reported to catalyze the six-electron reduction of CO_2 into CH_3OH with Faradaic efficiencies (FE) up to 74% at turnover frequencies as high as 2844 h^{-1}.[35] The validity of this system however should be questioned as copper bis(thiosemicarbazones) are well-known to release Cu(I) upon reduction through an ionophore mechanism that has been exploited as a strategy to deliver copper ions into cellular environments.[36] The authors did not perform rigorous controls to evaluate the intactness of the catalyst and therefore some (or all) of the observed reactivity could be due to metallic copper surfaces generated electrochemically. Finally, while not electrochemical, Robert and coworkers have shown that molecular iron tetraphenylporphyrin (Fe-TPP) complexes are capable of visible light driven methane formation from CO_2 when paired with an appropriate Ir-based photosensitizer (Ir-$(ppy)_3$).[37] However, unlike the polypyridyl systems discussed above that directly covert CO_2 into CH_2O and CH_3OH, the Fe-TPP complexes operate through a two-pot stepwise procedure where CO_2 is first reduced to CO and CO is further reduced to give CH_4 with selectivity up to 82% at quantum yields close to 0.18%.[37]

This literature precedence alongside joint work from the Chang and Long groups to develop polypyridyl complexes for electrochemical proton and CO_2 reduction has directed the design concept for the novel ligand scaffolds reported in this final chapter (**Figure 7.1**).[38–48] Early work between our groups that started over a decade ago identified the applicability of the $PY5Me_2$

ligand as a robust scaffold for reductive electrocatalysis in organic and aqueous electrolytes. High-valent molybdenum(IV)-oxo,[38] molybdenum(IV)-disulfide,[39] and cobalt(II)-$PY5Me_2$ complexes[40–42] have shown exceptional reactivity for generating hydrogen gas from organic acids or water at neutral pH. Unfortunately, $PY5Me_2$ coordination complexes find limited application as electrochemical CO_2 reduction catalysts. This is because the redox-chemistry of these $PY5Me_2$ complexes is almost entirely localized to metal-centered d_{z^2} orbitals.[43–46] Such a buildup in Lewis basicity results in rapid formation of metal hydride intermediates, a major step on the path to proton reduction. Zee *et al.* showed that substitution of the molybdenum or cobalt metal centers for Fe and exchange of two pyridine ligands for a more redox-active bipyridine moiety turns on modest CO_2 reduction catalysis (FE_{CO} = ~20%).[47,48] Vast improvements in selectivity and rates were further achieved by modifying the second coordination sphere with protic functional groups of varying acidities. Alternatively, extremely efficient, and robust CO_2 reduction catalysis can also be obtained without modifications to the second coordination sphere. Tuning the primary coordination sphere via exchange of three of the equatorial pyridyl arms in the $PY5Me_2$ ligand for an even more conjugated, redox active terpyridine functional group gave the tpyPY2Me ligand.[43] The Fe-tpyPY2Me complex was shown in Chapters 5 and 6 to be an exceptional homogenous electrocatalyst capable of converting CO_2 into CO at low overpotentials with high selectivity and fast rates. Extension of this work to other metal centers proved fruitful with the Co-tpyPY2Me showing modest catalysis for the CO_2RR under electrochemical and photochemical conditions. While the Ni-tpyPY2Me complex isn't a CO_2RR electrocatalyst, it was demonstrated to be a highly robust redox-mediator for controlling product selectivity of electrochemical radical reactions.[49] The work presented in this chapter further expands this research program to explore the extent to which metal–ligand exchange coupling can be utilized to catalyze the reduction of CO_2 beyond two-electron reductive products. Towards this goal, we report here the synthesis and characterization of a series of tpy-based polypyridyl complexes that incorporate bis-(iso)quinoline arms to yield highly redox-active molecular catalysts that can supply more than two electrons to CO_2. Catalytic conditions are systematically screened, and initial data supports the complexes being able to generate small quantities of carbon monoxide and formaldehyde. Catalytic performance appears to be ultimately limited by catalyst stability a highly reducing potentials.

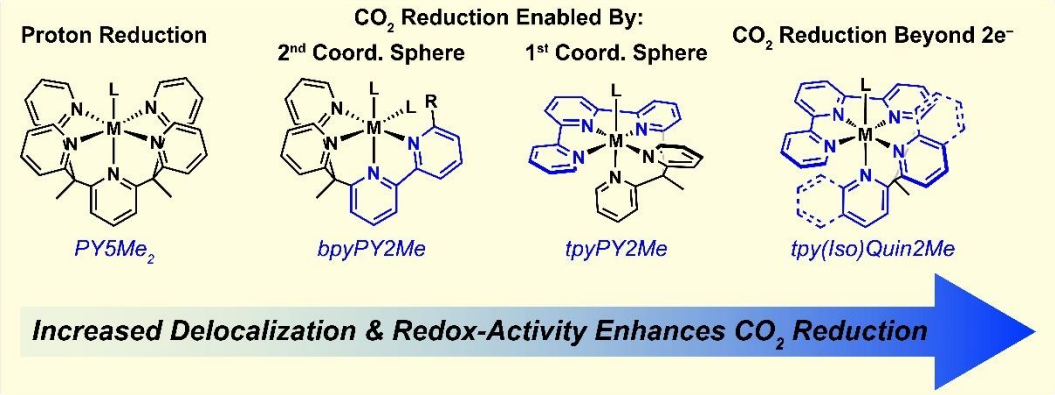


Figure 7.1. Evolution of polypyridyl catalysts for the electrochemical reduction of protons and CO_2. Molybdenum[38,39] and Cobalt[40,42] complexes equipped with the redox innocent $PY5Me_2$ ligand are exceptional catalysts for the HER in organic and aqueous electrolytes but are unable to catalyze the reduction of CO_2. Preparation of iron complexes that incorporate a more redox-active bipyridine moiety turns on catalysis for the CO_2RR; large enhancement in CO_2 selectivity is achieved through modifications to the second coordination sphere with acidic functional groups (R = H, OH, OMe, NHEt, NEt_2).[44,47] Even further enhancements to CO_2 reduction catalysis are achieved through the substitution of three pyridyl arms in the $PY5Me_2$ ligand for a conjugated, redox-active terpyridine moiety.[43] This work explores the exchange of the last two pyridyl arms in the tpyPY2Me ligand for more redox-active quinolines or isoquinoline to give access to more reduced CO_2 products, beyond two electrons.

7.3 Results and Discussion

7.3.1 Rational Design of the tpy(Iso)Quin2Me Ligands

We previously demonstrated the utility of the tpyPY2Me ligand scaffold to facilitate the electrochemical reduction of CO_2 to CO at low overpotentials with high selectivity by antiferromagnetically pairing the two electrons that are injected electrochemically into the ligand orbitals with the two unpaired electrons of an intermediate-spin Fe(II) center.[43] This metal–ligand cooperativity enables efficient two-electron reductive electrocatalysis, but in order to generate more reduced products additional reducing equivalents are required. Further reduction of the Fe-tpyPY2Me complex is unfavorable as the addition of another electron into either metal- or ligand-based orbitals disrupts the strong antiferromagnetic coupling that is responsible for the large anodic shift in redox potential that permits CO_2RR catalysis to occur with low energy input. Indeed, this point is observed experimentally by comparing the electrochemical CO_2RR behavior of the first-row transition metal tpyPY2Me complexes. As shown in **Figure 7.2** and summarized in **Table 7.1**, no additional redox events beyond the second ligand-centered reduction are observed for the Fe, Co, and Ni tpyPY2Me complexes by cyclic voltammetry (CV) even when scanning to reductive potentials of –2.5 V vs Fc/Fc^+. This, however, is not true for the redox-innocent control, Zn-tpyPY2Me, which does have an additional, irreversible, ligand-based reduction with a peak cathodic potential (i_{pc}) of –2.41 V vs Fc/Fc^+. We speculate that this difference can be attributed to the inability of Zn-tpyPY2Me to participate in metal–ligand exchange coupling because it possesses a full d orbital manifold. As such, the application of more reducing potentials produces an additional ligand-based reduction that does not come at the cost of weakened antiferromagnetic coupling. This subtle point illuminates the limitations of the tpyPY2Me ligand to facilitate more than two-electron redox chemistry through this metal–ligand exchange coupled mechanism.

Table 7.1. Summary of the redox properties of metal tpyPY2Me complexes in Ar saturated acetonitrile solution with 0.1 M $TBAPF_6$ as the supporting electrolyte.

M-tpyPY2Me	**$E_{1/2}$ (ΔE_p) (V vs Fc/Fc^+)**			
Fe	+0.66 (0.07)	–1.43 (0.13)		
Co	+0.14 (0.33)	–0.74 (0.13)	–2.14 (0.07)	–2.27 (0.07)
Ni	+1.26 (0.09)	–0.96 (0.07)	–1.90 (0.07)	–2.47 (0.07)
Zn	–1.56 (0.07)	–2.07 (0.07)	–2.41 (0.23)[a]	

[a]Peak cathodic potential reported due to the irreversible electron transfer.

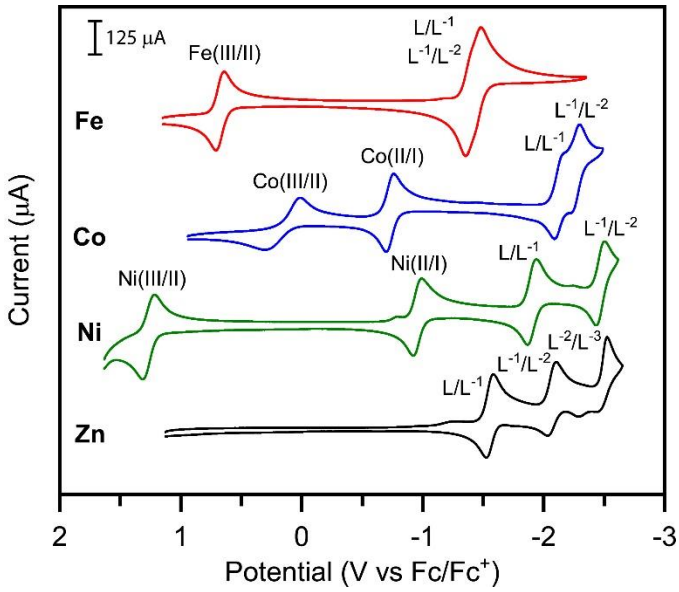


Figure 7.2. Cyclic voltammograms of metal tpyPY2Me complexes in argon saturated acetonitrile solution with 0.1 M $TBAPF_6$ as the supporting electrolyte. All data was obtained with a scan rate of 100 mV/s.

To circumvent this problem, we envision an alternative approach to grant access to additional electron density by increasing the number of accessible, ligand-based orbitals that are available for coupling to unpaired electron density on the metal center. The terpyridine (tpy) moiety in the tpyPY2Me ligand gives access to two low-lying, essentially degenerate, π* orbitals.[43,49–51] Further expansion of the conjugation of the tpy moiety (*e.g.*, quaterpyridine; quaterpyridine = 2,2':6',2":6",2"'-quaterpyridine) would indeed give rise to additional orbitals but it would also significantly alter the primary coordination sphere (overall coordination number and molecular geometry) and therefore will impact the extent of coupling with unpaired electrons in the metal d orbitals.[52,53] The consequences of disrupting the antiferromagnetic coupling in this ligand system can be gleaned by comparing the catalytic activity of Fe-tpyPY2Me for electrochemical CO_2 reduction (described in Chapter 5) to that of the analogous Co- and Ni-tpyPY2Me complexes. **Figure 7.3** displays the electrochemical behavior Co- and Ni-tpyPY2Me under CO_2 atmosphere. Large catalytic responses are observed for both upon saturation with CO_2. Incorporation of molar quantities of phenol (PhOH) as an acid source produces a large enhancement in the catalytic wave at –2.28 V and –2.56 V for Co-tpyPY2Me and only an increase in the first catalytic wave of the Ni-tpyPY2Me complex at –2.19 V vs Fc/Fc^+. The Co and Ni complexes were then subjected to preparative scale controlled potential electrolysis experiments under a wide range of catalytic conditions where factors such as the electrolyte identity, cathode material, proton source, and applied potential were systematically varied. The data from these extensive screening efforts display two consistent trends: 1) fast decay of the current density within the first few minutes of the electrolysis and 2) modest to low selectivity for the CO_2RR over the undesired HER. We have been able to overcome some of the selectivity and stability issues with Co-tpyPY2Me by switching from an electrochemical system to a photocatalytic one where we could take advantage of much lower catalyst loadings relative to the concentrations of reduced catalyst that are electrochemically generated in the electrochemical double layer. Still, the improvements are quite limited in the photocatalytic system as the selectivity and rates

significantly decrease after an hour of photolysis and its photocatalytic performance is far inferior to that of the original Fe-tpyPY2Me catalyst.

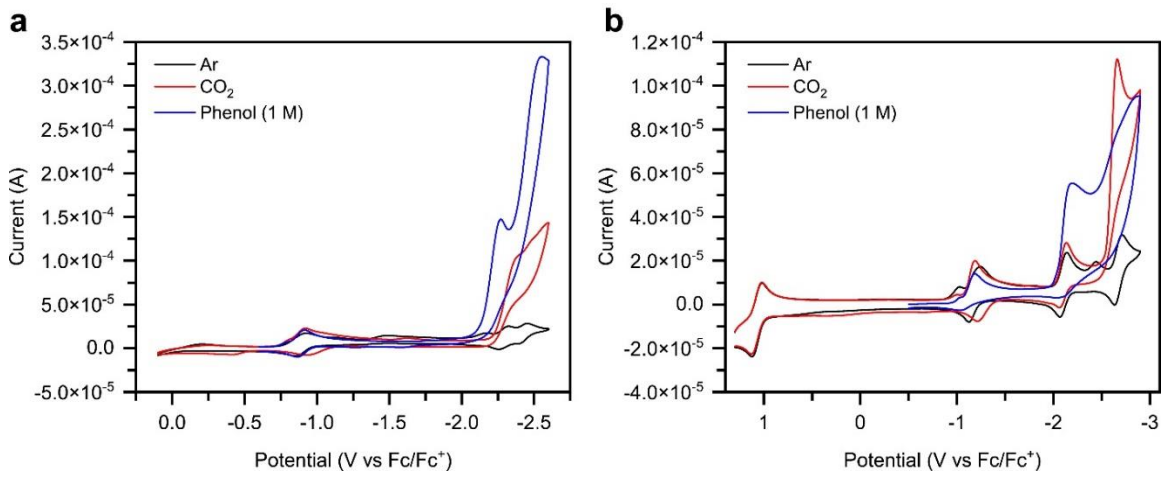


Figure 7.3. Electrochemical analysis of other earth-abundant transition-metal tpyPY2Me complexes for CO_2 reduction. CVs for (a) Co-tpyPY2Me and (b) Ni-tpyPY2Me collected under Ar (black line), CO_2 (red line), with the addition of PhOH (1M; blue line). Voltammograms were collected at a scan rate of 100 mV/s in an electrolyte of 0.10 M $TBAPF_6$ dissolved in CH_3CN.

Density functional theory (DFT) calculations of the Co- and Ni-typPY2Me complexes (the Ni data is presented in Appendix B) offers a potential explanation for the diminished catalytic reactivity and stability relative to Fe-tpyPY2Me. DFT calculations using the ωB97X-D functional were carried out to establish molecular orbital pictures of the 2^+, 1^+, and neutral Co-tpyPY2Me complexes (**Figure 7.4**). The DFT optimized structures and predicted redox potentials for $[Co\text{-}tpyPY2Me]^{2+}$ agree well with the experimental data and are consistent with a doublet ground state (S = ½). Interestingly, DFT analysis shows that the first reduction of $[Co\text{-}tpyPY2Me]^{2+}$ to $[Co\text{-}tpyPY2Me]^{+}$ is purely a metal-centered reduction resulting in the formation of a singlet ground state (S = 0). This assignment agrees well with the experimental CV data that shows that the first-redox event beyond the open circuit potential (0.02 V vs Fc/Fc^+) is 820 mV more positive than where the first ligand-based reduction occurs for the redox innocent Zn-tpyPY2Me complex. Localized orbital bonding analysis (LOBA) further confirms that the $[Co\text{-}tpyPY2Me]^{+}$ complex is in the 1^+ oxidation state and is bound to a neutral tpyPY2Me ligand. This contrasts with the computational studies of the analogous $[Fe\text{-}tpyPY2Me]^{+}$ and $[Ni\text{-}tpyPY2Me]^{+}$ complexes, which first involve ligand-centered reductions to yield Fe(II) and Ni(II) centers bound to a radical anion tpyPY2Me ligand ($tpyPY2Me^{\bullet-}$). The addition of a second electron to yield the neutral, doubly reduced $[Co\text{-}tpyPY2Me]^{0}$ complex is found to be consistent with the population of a ligand-based π* orbital belonging to the tpy moiety. The calculated redox potential ($E_{1/2}$ = –2.22 V) matches the experimentally determined value closely (**Table 7.1**). Spin density plots for $[Co\text{-}tpyPY2Me]^{0}$ suggest that the reduction is accompanied by significant rearrangement of the electrons occupying the metal d orbitals, leading to the population of a low-lying metal-ligand ($\pi^* + d_{z^2}$) orbital and reordering the remaining Co-based electrons into a high-spin configuration (**Figure 7.4**). The computational results suggest that the $[Co\text{-}tpyPY2Me]^{0}$ species exists as an unreduced Co(II) center bound to a diradical $(tpyPY2Me^{\bullet\bullet})^{2-}$ ligand which is in agreement with studies of the [Ni-

tpyPY2Me]^0 analog (see Appendix B). Taken together, these computational studies highlight the intriguing outcome of oxidation of the central Co metal center through reduction of the overall complex, made possible by delocalized reduction events across the Co center and the tpyPY2Me ligand. Moreover, comparison of the one- and two-electron reduced Co and Ni electronic structures to the Fe complexes offers insights into their limited CO_2 selectivity and poor solution stability. The metal centered reduction of [Co-tpyPY2Me]$^+$ may give access to rapid formation of Co(III) hydrides through which product selectivity would be expected to shift away from CO; while a decomposition pathway may also be linked to the presumed limited stability of the open-shell doublet ground state of the proposed active catalyst, [Co-tpyPY2Me]^0.

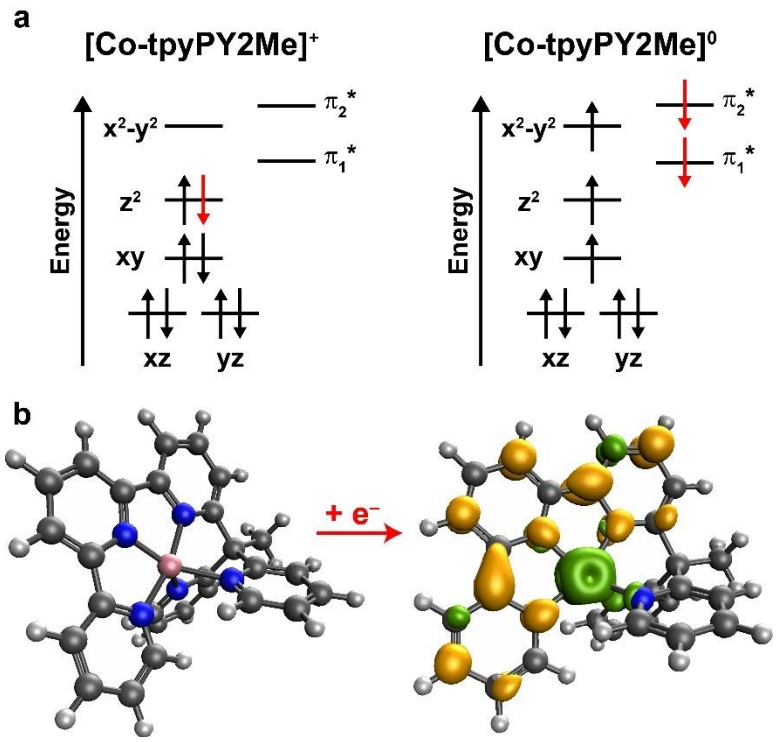


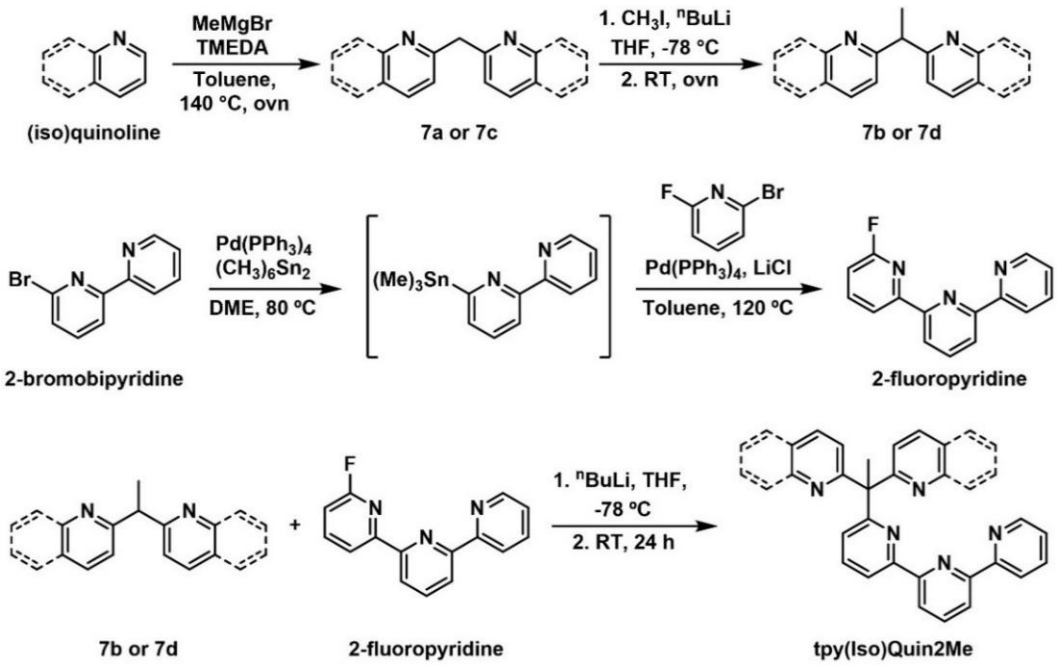
Figure 7.4. DFT predicted pathway for the two-electron reduction of [Co-tpyPY2Me]$^{2+}$. (a) Schematic qualitative molecular orbital diagrams and (b) the accompanying spin density plots for [Co-tpyPY2Me]$^+$ and [Co-tpyPY2Me]^0.

Therefore, for the reasons discussed above, we believe that the tpyPY2Me ligand is unable to facilitate reductive catalysis beyond two-electron products. If more reduced carbon products are to be produced with this ligand system, it would presumably have to be through a stepwise mechanistic pathway where CO_2 is first reduced to CO, which can then act as the substrate for further reduction steps to yield more complex products like CH_2O or CH_3OH. A stepwise reduction mechanism seems unlikely given that CO dissociation from Fe-tpyPY2Me was established to be exergonic and barrierless in the previous chapter, but the identity of the metal center could greatly alter this outcome. As such, we need to develop an alternative strategy to access additional ligand-based orbitals that do not include extending the conjugation network of the tpy moiety. The insights gained from the mechanistic studies conducted in Chapter 6 identified the pyridine arms as promising targets for optimization and improvement of the overall catalytic performance of the

system. They are not involved in stabilizing the excess electron density generated by electrochemical reduction and thus synthetic modifications should not significantly alter the ligand-based reduction potentials of Fe-tpyPY2Me that are already optimally tuned to match the standard redox potential for the conversion of CO_2. This led us to hypothesize that we can achieve the additional ligand-centered orbitals by expanding conjugation of the pyridyl arms into either quinoline or isoquioline moieties that have lower energy LUMOs that may be accessible electrochemically within our desired potential window.

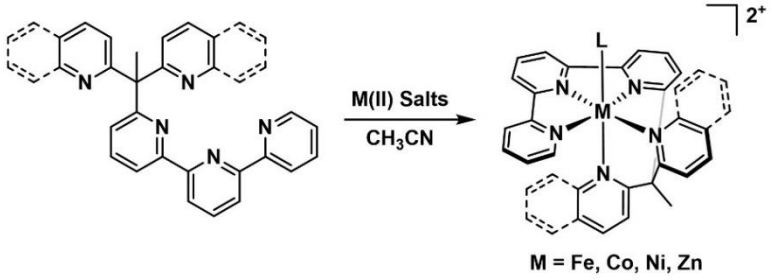
7.3.2 Synthesis and Characterization of Metal tpy(Iso)Quin2Me Complexes

With this design concept in mind, we sought to prepare the tpyQuin2Me and tpyIsoQuin2Me ligands. To this end, we envisioned a synthetic strategy similar to the one used to prepare the tpyPY2Me ligand.[43] The general synthetic pathway is given in **Scheme 7.1**. This strategy involves the lithium-mediated nucleophilic aromatic substation (S_NAr) of 2,2'-(ethane-1,1-diyl)diquinoline (**7b**) or 1,1'-(ethane-1,1-diyl)diisoquinoline (**7d**) with a halide-appended terpyridine to forge the desired C–C bond between the redox-active tpy moiety and the methylene linker of the redox-active (iso)quinoline arms. First, starting from cheap and commercially available quinoline or isoquinoline, di(quinolin-2-yl)methane (**7a**) and di(isoquinolin-1-yl)methane (**7c**) were obtained in modest yields (20% and 30%, respectively) through Grignard-mediated dimerization reactions with methylmagnesium bromide and tetramethylethylenediamine (TMEDA) following slight modifications to a procedure outlined by Stevens and coworkers.[54] Deprotonation of **7a** and **7c** with *n*-butyllithium at –78 °C in dry THF and methylation of the methylene linker with methyl iodide afforded the desired bis-(iso)quinoline intermediates, **7b** (65%) and **7d** (60%) in reasonable yields. With **7b** and **7d** in hand, we first attempted the coupling via an S_NAr reaction with the 2-bromoterpyridine synthon we utilized in Chapter 5. Unfortunately, no product function was observed under these reaction conditions. This is certainly, in part, due to the fact that **7b** and **7d** are much poorer nucleophiles (relative to bispyridyl ethane) because of their steric bulk and ability to stabilize the electron density generated from carbanion formation *via* resonance enabled by the added conjugation granted from the additional aryl rings. To get around this issue without having to pursue an entirely new synthetic strategy, we sought to prepare 6-fluoro-2,2':6',2''-terpyridine (2-fluoroterpyridine) owing to the much faster rates observed for S_NAr reactions with aryl-fluorides. 2-Fluoroterpyridine was accessed in good yield (70%) through a one-step Stille coupling of 2-bromobipyridine with commercially available 2-bromo-6-fluoropyridine. Satisfyingly, subjecting the 2-fluoroterpyridine electrophile to the S_NAr reaction conditions with either **7b** or **7d** gave the desired tpyQuin2Me and tpyIsoQuin2Me ligands in a yield of 67% and 31%, respectively. All compounds were characterized by electrospray ionization (ESI) mass spectrometry and ^{1}H- and ^{13}C-NMR spectroscopy (see Materials and Methods section for details).



Scheme 7.1. Synthetic route for the preparation of tpyQuin2Me and tpyIsoQuin2 ligands.

The late first-row transition metal complexes (M = Fe, Co, Ni, and Zn) were easily prepared by metalating tpyQuin2Me and tpyIsoQuin2Me with divalent metal salts in acetonitrile under N_2 atmosphere at 50 ºC overnight (**Scheme 7.2**). The reactions were heated due to the limited solubility of the ligands and some of the metal salts in acetonitrile; however, the resultant coordination complexes were highly soluble which helped drive the reactions to completion with near quantitative yields achieved for most of the desired coordination complexes (see materials and methods for details). The triflate salts were desired as our work in Chapter 5 identified that the triflate anion imparts excellent solubility in acetonitrile and is non-coordinating enough to facilitate fast, reversible electrochemical behavior.[43] The Fe- and Zn-tpyQuin2Me and tpyIsoQuin2Me complexes were first prepared with divalent metal halide salts (*i.e.*, $FeBr_2$ and $ZnCl_2$, respectively) followed by a salt metathesis step with silver triflate (AgOTf) to afford the desired triflate complexes. Unfortunately, initial cyclic voltammetry (CV) data suggested that residual AgOTf may be interfering with the electrochemical analysis (*vide infra*) so we instead switched to direct metalation of the ligands with divalent triflate salts (see materials and methods).



Scheme 7.2. General synthetic scheme for the preparation of tpyQuin2Me and tpyIsoQuin2Me coordination complexes. See the materials and methods section for further experimental details.

Slow diffusion of diethyl ether into acetonitrile or methanol solutions of the M-tpyQuin2Me (M = Fe, Co, Zn) and M-tpyIsoQuin2Me (M = Fe, Co, Ni, Zn) complexes afforded single crystals suitable for analysis by X-ray diffraction with the exception of Ni-tpyQuin2Me, which we have currently been unable to crystalize. The resulting solid-state structures for the M-tpyQuin2Me complexes are displayed in **Figure 7.5** while the typIsoQuin2Me complexes are given in **Figure 7.6**. The structure of Fe-tpyQuin2Me differs from all the other M-tpyQuin2Me complex as it is the only one that has an axial triflate ligand bound resulting in a distorted pseudo-octahedral coordination geometry. The Co- and Zn-tpyQuin2Me complexes don't have an exogenous anion or solvent occupying a sixth coordination site and therefore their coordination geometries are best described as square-pyramidal with severe distortions away from idealized geometry toward trigonal bipyramidal based on their distortion parameters (τ_5)[55] of 0.35 and 0.36, respectively. The difference in coordination number can be understood by a simple electron counting argument. Coordination of triflate or acetonitrile in solution results in the formation of a stable, 18-electron configuration where if bound to the Co and Zn complexes would lead to the formation of 19 and 22 electron complexes (respectively) that would be expected to be quite unstable given the extent of population of anti-bonding orbitals. Of course, this argument surely oversimplifies the actual electronic structures of these tpyQuin2Me complexes as the bulky quinoline and isoquinoline arms, the π-accepting capabilities of the redox-active ligand, and the crystal packing interactions most certainly also contribute to the observed solid-state geometries.

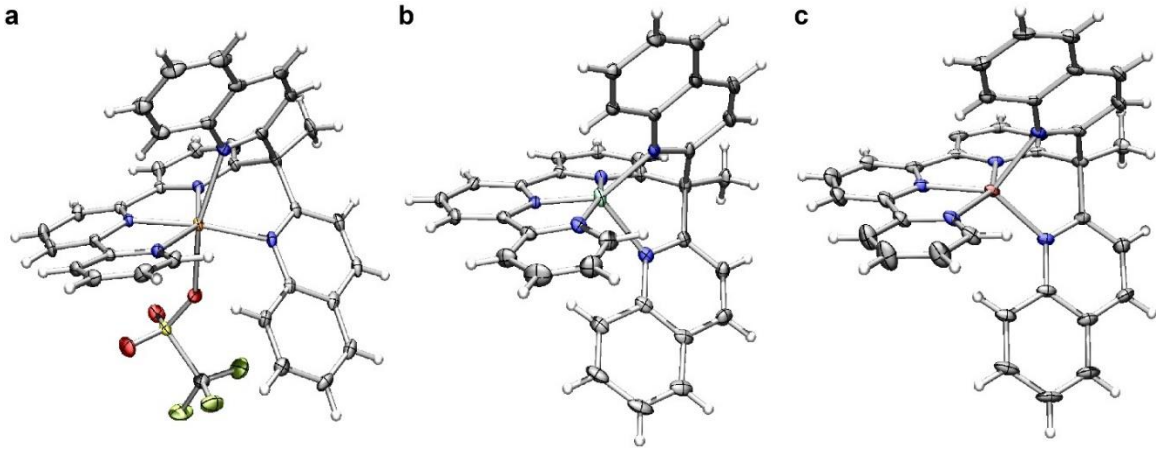


Figure 7.5. Solid state structures of (a) Fe-tpyQuin2Me, (b) Co-tpyQuin2Me, and (c) Zn-tpyQuin2Me. Thermal ellipsoids are potted at the 50%, 20%, and 30% probability levels for Fe-tpyQuin2Me, Co-tpyQuin2Me, and Zn-tpyQuin2Me, respectively. Orange, aquamarine, brown, grey, blue, red, yellow, green, and white signify Fe, Co, Zn, C, N, O, S, F, and H atoms, respectively. Non coordinating solvent and anions are omitted for clarity. Selected bond metrics for these complexes are provided in the crystallography data section.

Important differences are observed when comparing the tpyQuin2Me solid-state structures to those collected for the M-tpyIsoQuin2Me complexes (M = Fe, Co, Ni, Zn; **Figure 7.6**). All four complexes have pseudo-octahedral geometries due to the tpyIsoQuin2Me ligand binding in a tetradentate fashion where the N-donor atoms occupy the equatorial positions while two triflate anions are bound to the open, axial sites. Indeed, the tetradentate binding is unsurprising given the significant steric clashing that would be required for both isoquinoline arms to bind to the metal

center. Therefore, to minimize the ground-state energies of these complexes, one of the quinoline arms pivots away from the metal center. Interestingly, this creates a situation where the achiral tpyIsoQuin2Me ligand becomes chiral at the methylene carbon atom due to coordination of only one of the isoquinoline arms to the metal center, which restricts free rotation about the C_{15}–C_{16} bond effectively locking the methyl group in either an up or down position (**Figure 7.6**). The bond metrics of the terpyridine moiety in the M-tpyQuin2Me and M-tpyIsoQuin2Me complexes are all consistent with what is expected for a neutral, unreduced ligand[43] and thus the formal metal oxidation states of all unreduced complexes can be assigned as 2^+ (see crystallography data section for further details).

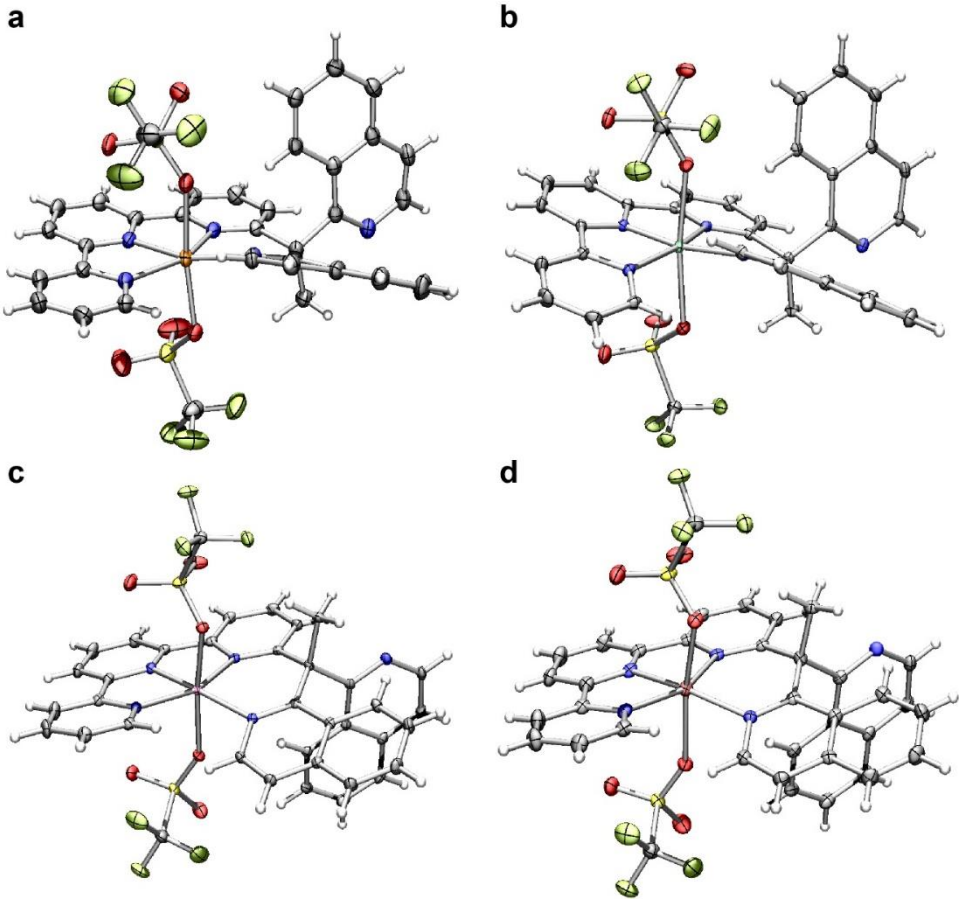


Figure 7.6. Solid state structures of (a) Fe-tpyIsoQuin2Me, (b) Co-tpyIsoQuin2Me, (c) Ni-tpyIsoQuin2Me, and (d) Zn-tpyQuin2Me. Thermal ellipsoids are potted at the 50% probability level. Orange, aquamarine, pink, brown, grey, blue, red, yellow, green, and white signify Fe, Co, Ni, Zn, C, N, O, S, F, and H atoms, respectively. Non-coordinating solvent are omitted for clarity. Selected bond metrics for these complexes are provided in the crystallography data section.

To probe the electronic structures of these complexes in solution, we measured the room-temperature magnetic susceptibilities in acetonitrile with the Evans method (**Table 7.2**).[56] All of these complexes, with the exception of Zn-tpyQuin2Me and Zn-tpyIsoQuin2Me, are paramagnetic as determined by their extremely broad ^{1}H NMR spectra that show resonances shifted as far

downfield as 89 ppm and as far upfield as –15 ppm (see NMR data section). Distinct from what was observed for the tpyPY2Me complexes, the solution magnetic moments that are reported in **Table 7.2** are consistent with high-spin complexes. The average M–N bond lengths extracted from the solid-state structures of these complexes are also consistent with other high-spin polypyridyl complexes.[40,42,45,47] This difference is interesting as we expected that the better π-accepting tpy(Iso)Quin2Me ligands to enforce a stronger ligand field than tpyPY2Me, thus favoring the formation of low-spin complexes. In order to rationalize this behavior, we expanded the qualitative Walsh diagram analysis that we utilized in Chapter 5 to explain the formation of distinct populations of Fe(II) spin states in Fe-tpyPY2Me at room temperature (**Figure 7.7**). Comparison of the axial distortions enforced by the tpyPY2Me and tpyQuin2Me ligands on their respective Fe centers causes a decrease in symmetry from idealized O_h toward C_{2v} where such distortions significantly stabilize the d_{z^2} orbitals and destabilize the d_{xz} and d_{zy} through z-component mixing of the t_{1u} and t_{2g} orbitals. The average axial bond angles given in **Figure 7.7** for Fe-PY5Me2 (~180º), Fe-tpyPY2Me2 (173º), and Fe-tpyQuin2Me (159º) clearly illustrate this point and demonstrate how the increased rigidity enforced by the tpyQuin2Me ligand (relative to PY5Me2 and tpyPY2Me) conformationally restricts the resultant iron complex into a more distorted coordination geometry that favors a high-spin state. Additionally, we also note that the tpyQuin2Me and tpyIsoQuin2Me complexes also exhibit a significant degree of distortion in the xy-plane that along with the lower coordination numbers in the Co- and Zn-tpyQuin2Me complexes and the weaker ligand fields produced by the axial triflate ligands in the M-tpyIsoQuin2Me complexes should further favor high-spin configurations.

Table 7.2. Magnetic susceptibility measurements of the M-tpyQuin2Me and M-tpyIsoQuin2Me complexes recorded at room-temperature in acetonitrile using the Evans method. Note: the large error in μ_{eff} for the M-tpyIsoQuin2Me complexes are due to their limited solubility in acetonitrile.

M-tpyQuin2Me	**μ_{eff} (μ_B)**	**Spin-state**
Fe	5.3	HS-Fe(II), S = 2
Co	4.0	HS-Co(II), S = 3/2
Ni	3.3	HS-Ni(II), S = 1
Zn	0	S = 0
M-tpyIsoQuin2Me	**μ_{eff} (μ_B)**	**Spin-state**
Fe	8.6	HS-Fe(II), S = 2
Co	6.1	HS-Co(II), S = 3/2
Ni	5.3	HS-Ni(II), S = 1
Zn	0	S = 0

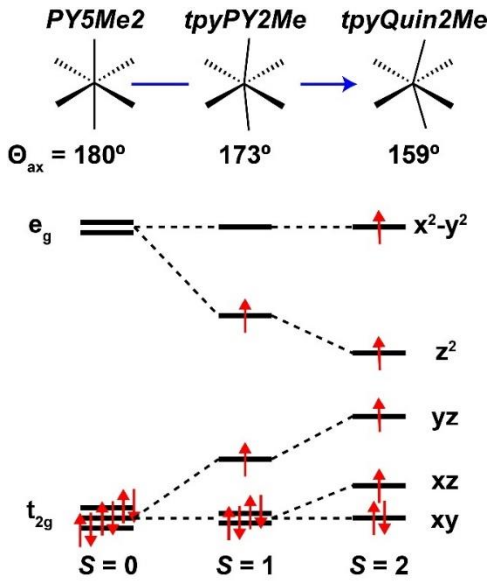


Figure 7.7. Qualitative Walsh diagram to for the bending of one trans L–M–L angle in an octahedral FeL_6 complex. The simplified diagram illustrates how geometric distortions away from idealized O_h geometry as a result of ligand rigidity can explain the high-spin configuration observed for Fe-tpyQuin2Me by solution Evans method measurements.

7.3.3 Electrochemical Properties of the Metal tpy(Iso)Quin2Me Complexes

With this small library of coordination complexes in hand, we first sought to compare their electrochemical properties to those of the tpyPY2Me complexes to determine if the (iso)quinoline arms grant access to additional redox chemistry. The direct comparison between Fe-tpyPY2Me and Fe-tpyQuin2Me is given in **Figure 7.8**. The redox waves were tentatively assigned by comparison to the previous tpyPY2Me complexes and the Zn-tpyQuin2Me redox-control. A few interesting differences were noted between the two voltammograms. First, the Fe(III/II) wave in Fe-tpyQuin2Me is anodically shifted by 60 mV and is irreversible even at fast scan rates. This behavior may be due to the coupling of a chemical reaction to the oxidation of Fe(II) to Fe(III) as the electrode potential is swept from the open circuit potential to the initial potential for the CV experiment of 1.0 V vs Fc/Fc^+. The irreversibility upon oxidation points to the Fe(III) complex being more reactive than Fe-tpyPY2Me and suggests that these quinoline-based complexes may find applications as catalysts for oxidative electrochemical reactions. The second major difference is that the tpy-based reductions are now clearly resolved with the first ligand redox event being shifted anodically by 410 mV relative to Fe-tpyPY2Me. While this indicates that the quinoline arms significantly lower the energy level of one of the terpyridine-based π^* orbitals, it is important to note that the redox potential of the second ligand reduction is conserved at –1.43 V vs Fc/Fc^+ and therefore should still be ideally matched to the standard redox potential of CO_2 to CO. Finally, when scanning to more negative potentials, and additional irreversible, presumably quinoline-based redox event is observed at –2.42 V vs Fc/Fc^+ with a peak cathodic current (i_{cp} = 98 μA) that is approximately twice that of the other ligand-based redox waves (i_{cp} = 43 μA). This wave was not observed for Fe-tpyPY2Me in this potential window. These findings seem to support our hypothesis that the substitution of the pyridyl arms for quinolines gives access to additional redox

chemistry. We do note however, that the electrochemical irreversibility of this wave indicates that electrolysis at these potentials may be coupled to catalyst decomposition.

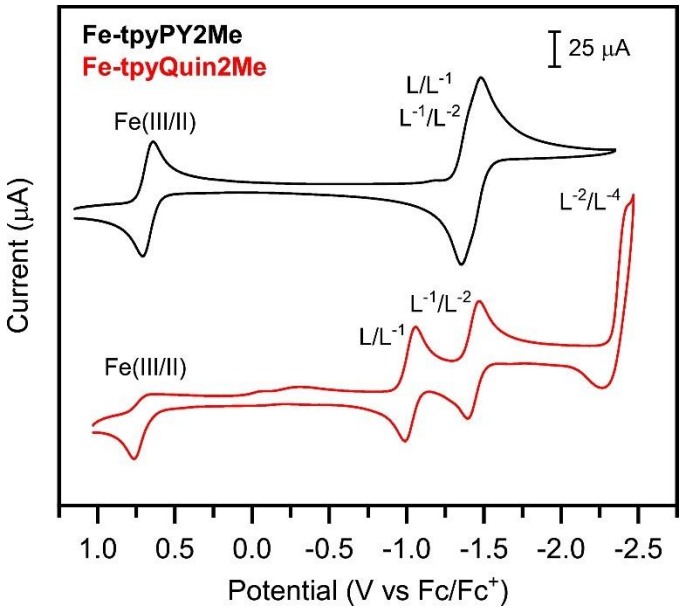


Figure 7.8. Electrochemical analysis of Fe-tpyQuin2Me in Ar saturated acetonitrile solution with 0.1 M $TBAPF_6$ as the supporting electrolyte. The CV of Fe-tpyQuin2Me is plotted in red and compared to Fe-tpyPY2Me in black to evaluate the influence of quinoline installation onto the tpy-based scaffold.

Encouraged by the additional ligand-centered redox waves in the Fe-tpyQuin2Me complex, we turned to the electrochemical analysis of the remaining quinoline and isoquinoline complexes. The voltammograms of the M-tpyQuin2Me complexes are presented together in **Figure 7.9** and their redox properties are summarized in **Table 7.3** to facilitate easy comparison. Like Fe-tpyQuin2Me, the Co-tpyQuin2Me complex also has an additional two-electron wave; however, it occurs at a significantly more positive potential (–2.03 V vs Fc/Fc^+) and has an addition reversible redox wave following it at –2.15 V vs Fc/Fc^+ to give a total of four ligand-centered reduction events. The metal-centered Co(III/II) and Co(II/I) reductions are also shifted to more positive potentials by 480 mV and 70 mv, respectively relative to Co-tpyPY2Me similar to what is observed for the iron complexes. The redox potentials of Ni-tpyQuin2Me are also shifted anodically by 130 to 260 mV but it differs from the Fe and Co complexes in that only two ligand-centered reductions are present. The quinoline-based reductions are most likely beyond the electrochemical window and are thus not observable under our experimental conditions. Strangely, the Zn control also only shows two redox waves at –1.56 and –1.84 V vs Fc/Fc^+ that have tentatively been assigned to the tpy-based reductions due to the similarity in potential to Zn-tpyPY2Me. The absence of an additional two-electron quinoline wave may indicate that metal-ligand cooperativity is instrumental for ensuring that these reduction events are accessible within the potential window. Moreover, an unexpected, symmetric peak appears on the anodic scan at –1.64 V vs Fc/Fc^+. Such waves are highly suggestive of redox events resulting from surface-adsorbed species.[57,58] Initially, we hypothesized that this feature may be due to a stripping wave from residual AgOTf that was being electroplated onto the working electrode at reductive

potentials. This hypothesis was excluded as the CV of the Zn complex prepared directly from the $Zn(OTf)_2$ salt without a AgOTf metathesis step also has this oxidative feature thus attributing the redox wave to the Zn complex itself. Analysis of the background-subtracted current as a function of the scan-rate (ν) showed that it is approximately linear with respect to $\nu^{1/2}$; however, we note that a larger range of scan rates should be explored as the range of applicable scan rates that can be utilized for this analysis are limited by the relative rate of electrode deposition. A further rinse-test showed that no current beyond the background is observed. Taken together, these data suggest that Zn-tpyPY2Me is weakly adsorbed onto the electrode surface following reduction by two electrons. This may occur via hemi-lability of one of the quinoline arms upon reduction. Similar ligand dynamics have been reported for other first-row polypyridyl coordination complexes.[59–61]

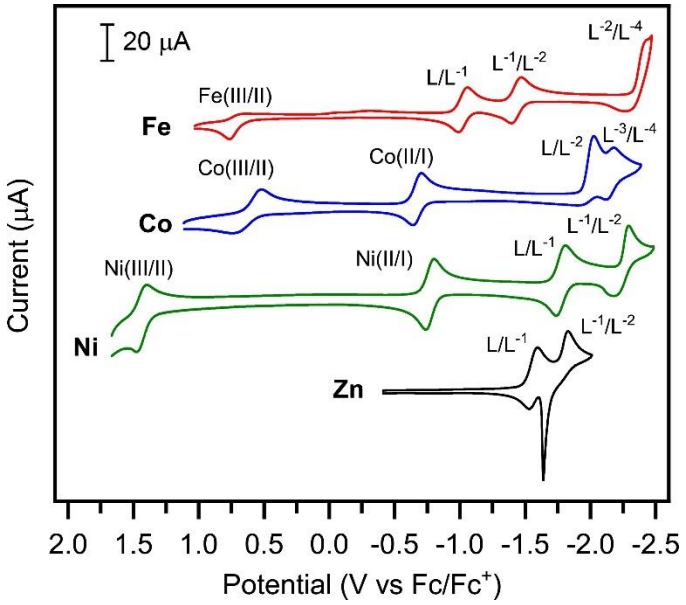


Figure 7.9. Cyclic voltammograms of M-tpyQuin2Me complexes in Ar saturated acetonitrile solutions with 0.1 M $TBAPF_6$ as the supporting electrolyte.

Table 7.3. Summary of the redox properties of M-tpyQuin2Me complexes in Ar saturated acetonitrile solution with 0.1 M $TBAPF_6$ as the supporting electrolyte.

M-tpyQuin2Me	$E_{1/2}$ (ΔE_p) (V)			
Fe	+0.72 (0.08)	–1.02 (0.07)	–1.43 (0.07)	–2.42[a]
Co	+0.62 (0.22)	–0.67 (0.07)	–2.03[a]	–2.15 (0.06)
Ni	+1.44 (0.08)	–0.77 (0.06)	–1.77 (0.07)	–2.47 (0.07)
Zn	–1.56 (0.09)	–1.84[a]	–	–

[a]Peak cathodic potential reported due to the irreversible electron transfer.

The isoquinoline variants are plotted in **Figure 7.10** with their redox potentials tabulated in **Table 7.4**. Unsurprising given the drastic difference in the coordination chemistry, the M-tpyIsoQuin2Me complexes have a few distinct electrochemical properties relative to the quinoline

isomers. Perhaps the most noticeable difference is present in the Fe-tpyIsoQuin2Me complex, which shows complex and ill-defined redox waves, all of which are irreversible. We initially thought this may be due to limited solution or air-stability but measuring the CV inside an N_2-filled glovebox yielded an identical voltammogram. Preparation of Fe-tpyIsoQuin2Me via direct metalation with $FeOTf_2$ rather than $FeBr_2$ followed by AgOTf addition also didn't improve the voltammogram. Currently our understanding of this behavior is limited, but we speculate that it may be related to relatively strong coordination of the triflate anion to the oxophilic iron center. Fe–O bond lengths of Fe-tpyIsoQuin2Me are significantly shorter than those observed in the Fe-tpyQuin2Me solid-state structure. Preparation of hexafluorophosphate analogs would be informative to test this hypothesis. The Zn-tpyIsoQuin2Me redox control is also interesting in that it has two quasi-reversible ligand-centered reductions with no indication of any stripping behavior. This indeed is perplexing as we would expect a greater interaction between the glassy carbon cathode and Zn-tpyIsoQuin2Me if the nature of this interaction was due to hemi-lability of the quinoline arms upon reduction because one of the isoquinolines remains unbound and therefore should be more susceptible to adsorption processes. Finally, the last noteworthy difference between the tpyIsoQuin2Me and tpyQuin2Me complexes is the number of accessible ligand-centered reductions. The Co and Ni tpyIsoQuin2Me complexes have one fewer reduction compared to their tpyQuin2Me counterparts. The irreversible ligand-centered reduction at –1.96 V Vs Fc/Fc^+ in Co-tpyIsoQuin2Me has a peak cathodic current that is consistent with a single-electron reduction while the metal-centered Ni(III/II) wave is not observed even when scanning to potentials beyond 1.5 V vs Fc/Fc^+. We also speculate that this may be attributed to the difference in the primary coordination spheres, but additional solution studies are required to further elucidate these points.

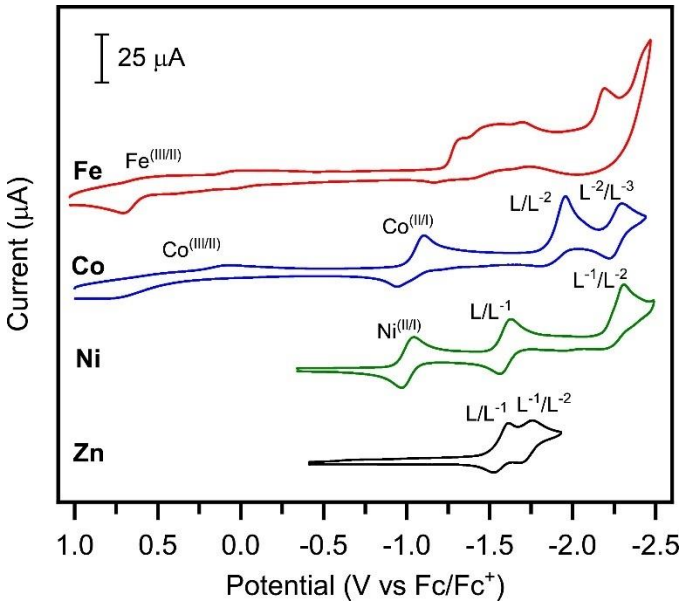


Figure 7.10. Cyclic voltammograms of M-tpyIsoQuin2Me complexes in Ar saturated acetonitrile solutions with 0.1 M $TBAPF_6$ as the supporting electrolyte.

Table 7.4. Summary of the redox properties of M-tpyIsoQuin2Me complexes in Ar saturated acetonitrile solution with 0.1 M $TBAPF_6$ as the supporting electrolyte.

M-tpyIsoQuin2Me	$E_{1/2}$ (ΔE_p) (V)			
Fe[a]	–	–	–	–
Co	+0.40 (0.66)	–1.03 (0.16)	–1.96[b]	–2.26(0.07)
Ni	–1.16 (0.07)	–1.74 (0.07)	–2.46[b]	–
Zn	–1.66 (0.09)	–1.81 (0.07)	–	–

[a]Redox potentials not reported because all redox potentials are irreversible and/or poorly resolved. [b]Peak cathodic potential (E_{pc}) reported due to the irreversible electron transfer.

7.3.4 Screening Metal tpy(Iso)Quin2Me Complexes as Catalysts for Electrochemical CO_2 Reduction

To probe the reactivity of the metal tpy(Iso)Quin2Me complexes towards CO_2, CVs were collected under CO_2 atmosphere. Different from what is observed for Fe-tpyPY2Me, reductive current enhancements are produced for all the (iso)quinoline-based complexes in the absence of an exogenous proton source (red lines; **Figures 7.11** and **7.12**). This however appears to come at the cost of more negative onset potentials ranging between roughly –1.8 to –2.5 V vs Fc/Fc^+. The addition of PhOH or TFE as acids in either low (0.1 M; blue lines) or high concentrations (1.0 M; pink lines) generates a large enhancement in the catalytic response and produces additional catalytic waves at more positive reduction potentials (see **Figures 7.11** and **7.12**). In order to determine and quantify product selectivity, as well as to evaluate the robustness of these catalysts, a series of controlled potential electrolysis (CPE) experiments were conducted where the conditions were systematically screened by altering the identity and quantity of the acid and the applied potential to match the responses observed in the catalytic voltammograms. The experimental data from these experiments can be found in the materials and methods section and the catalytic metrics are summarized in **Tables 7.5** and **7.6**. Disappointingly, the iron complexes appear to perform quite poorly compared to the exceptional performance of Fe-tpyPY2Me. Fe-tpyQuin2Me has extremely limited stability with current densities decaying within the first five minutes (**Figure 7.18**) across all conditions screened and has total Faradic efficiencies for CO production that are much less than 100% (5 – 29%). The limited stability appears to be related to fast electrode deposition and fouling that is visible after the electrolysis experiment and is most likely correlated to the extremely negative operating potentials. This degree of electrode fouling severely limits mass transport to the electrode surface thus explaining the small amount of charge passed during the hour-long electrolysis experiments (0.1 – 1.3 C). Moreover, even if the limitations in catalyst stability could be easily addressed, the Fe-tpyQuin2Me complex doesn't appear to be particularly selective for CO_2RR over the HER as the average percent yield for CO production is less than 50%. For this reason, we have yet to screen the Fe isoquinoline analog because its CV data establishes that it has even worse electrochemical stability.

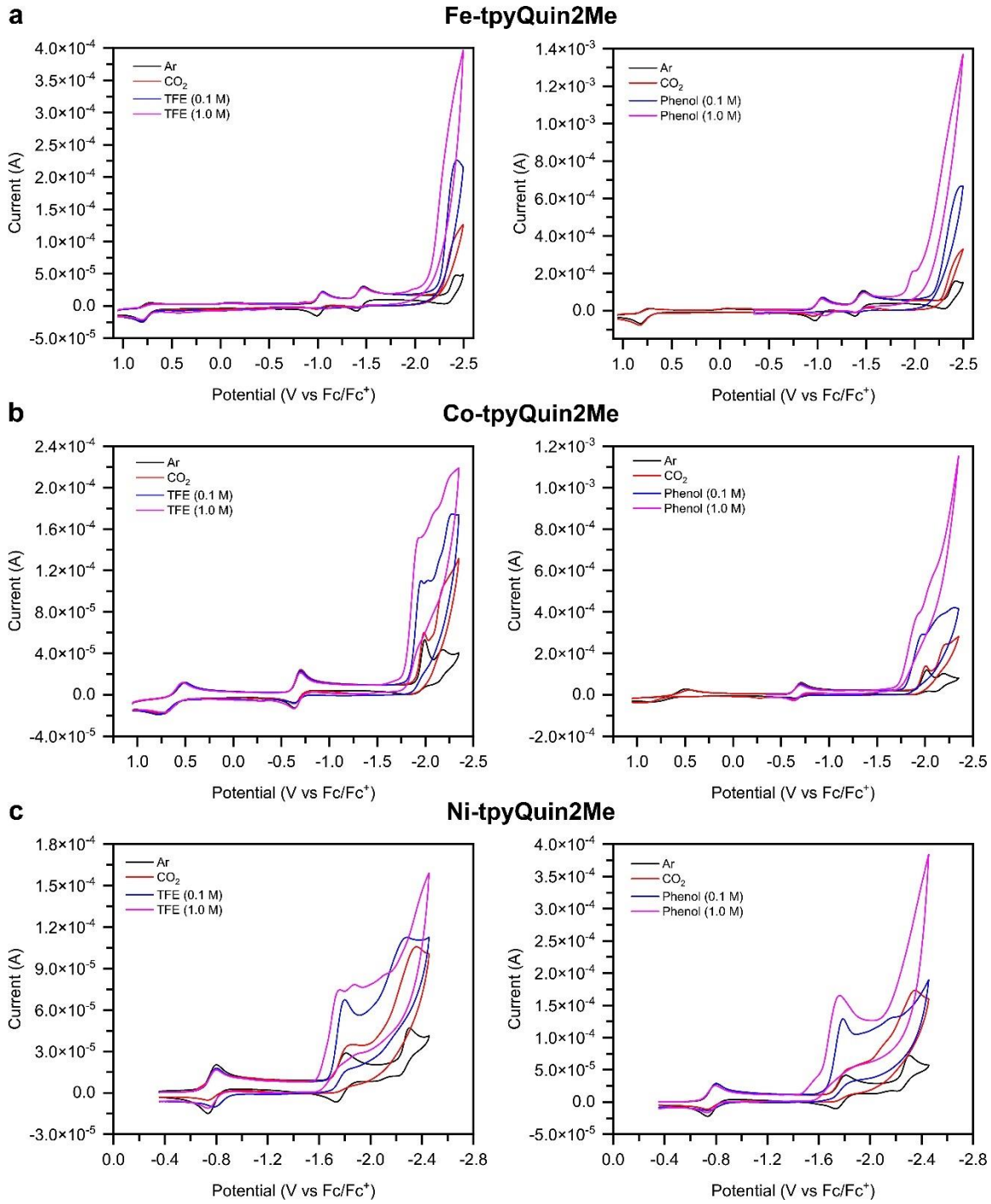


Table 7.11. Electrochemical analysis of M-tpyQuin2Me complexes under CO_2 atmosphere. Cyclic voltammograms of (a) Fe-tpyQuin2Me, (b) Co-tpyQuin2Me, and (c) Ni-tpyQuin2Me collected under Ar (black line), CO_2 (red line), and with added TFE or PhOH at either low concentration (0.1 M; blue line) or high concentration (1.0 M; pink line). Voltammograms were collected with a scan rate of 100 mV/s with an electrolyte of 0.10 M $TBAPF_6$ dissolved in CH_3CN.

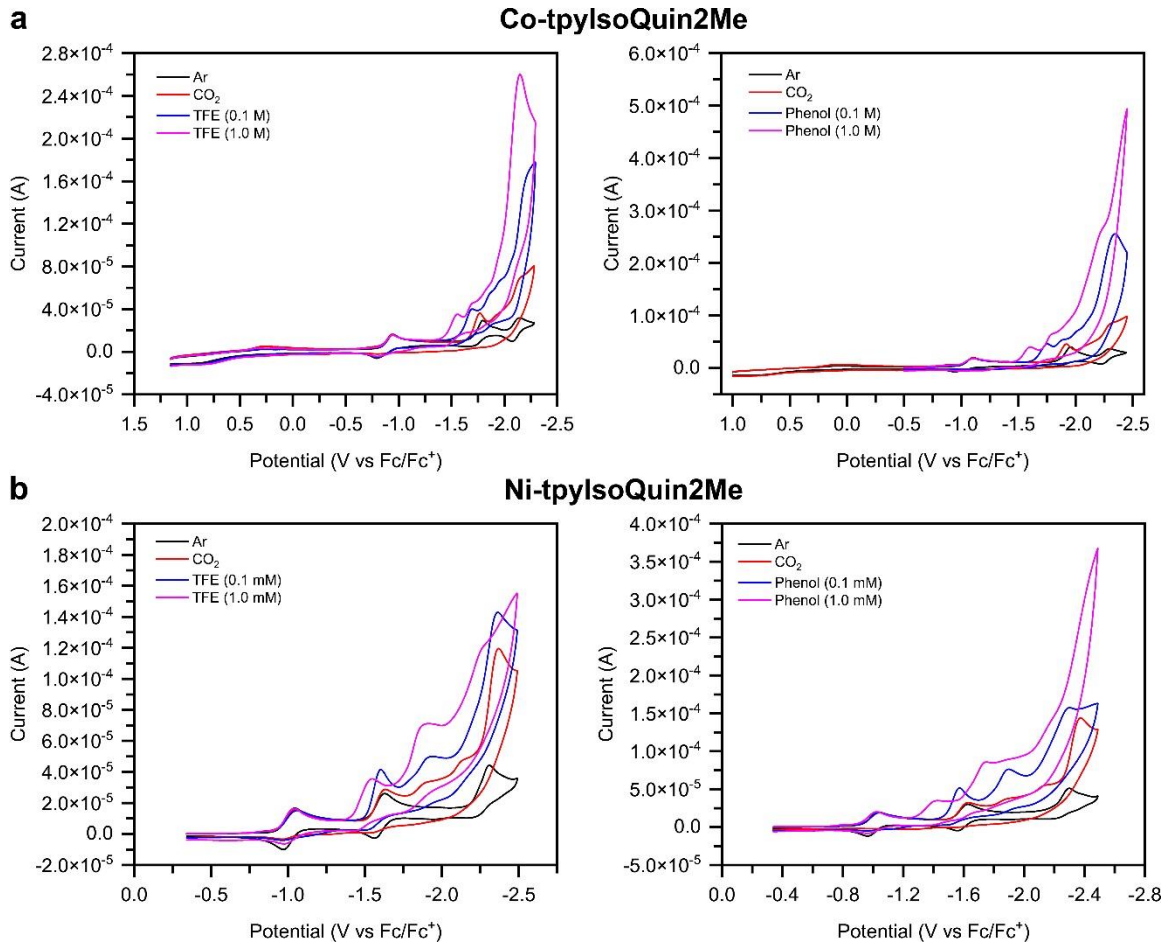


Table 7.12. Electrochemical analysis of M-tpyIsoQuin2Me complexes under CO_2 atmosphere. Cyclic voltammograms of (a) Co-tpyQuin2Me and (b) Ni-tpyQuin2Me collected under Ar (black line), CO_2 (red line), and with added TFE or PhOH at either low concentration (0.1 M; blue line) or high concentration (1.0 M; pink line). Voltammograms were collected with a scan rate of 100 mV/s with an electrolyte of 0.10 M $TBAPF_6$ dissolved in CH_3CN.

Table 7.5. Summary of controlled potential electrolysis conditions screened for M-tpyQuin2Me complexes to catalyze the electrochemical reduction of CO_2. Yellow highlighting denotes conditions where current density was stable over the 1 h electrolysis experiment and CO_2RR yields were promising enough to warrant the search for liquid products.

Metal	Conditions	E_{app} (V vs $Fc^{0/+}$)	Q(C)	I (mA/cm^2)	FE_{H_2} (%)	FE_{CO} (%)	FE_{total} (%)	CO_2RR yield (%)
Fe	0.1 M PhOH	–2.57	0.7	0.20	4	3	7	40
	1.0 M PhOH	–2.15	1.3	0.36	2	3	5	65
	1.0 M PhOH	–2.57	1.0	0.26	10	2	12	15
	0.1 TFE	–2.57	0.1	0.03	0	5	5	100
	1.0 TFE	–2.57	0.2	0.07	25	4	29	14
Co	0.1 M PhOH	–2.11	3.2	0.18	1	2	3	62
	0.1 M PhOH	–2.33	5.4	0.30	4	2	6	30
	1.0 M PhOH	–2.07	2.8	1.55	23	14	37	38
	1.0 M PhOH	–2.24	4.9	2.73	33	10	43	23
	0.1 TFE	–2.11	0.5	0.30	0	17	17	100
	0.1 TFE	–2.42	0.5	0.29	3	22	25	88
	1.0 TFE	–2.22	0.90	0.51	1	22	23	96
	1.0 TFE	–2.48	1.7	0.93	4	18	22	82
Ni	0.1 M PhOH	–2.00	0.6	0.34	0	5	5	100
	0.1 M PhOH	–2.43	0.5	0.26	20	5	25	20
	1.0 M PhOH	–2.00	1.6	0.89	1	9	10	89
	0.1 TFE	–2.00	0.6	0.34	0	12	12	100
	1.0 TFE	–2.00	1.1	0.62	0	12	12	100

Table 7.6. Summary of controlled potential electrolysis conditions screened for M-tpyIsoQuin2Me complexes to catalyze the electrochemical reduction of CO_2. Yellow highlighting denotes conditions where current density was stable over the 1 h electrolysis experiment and CO_2RR yields were promising enough to warrant the search for liquid products.

Metal	Conditions	E_{app} (V vs $Fc^{0/+}$)	Q(C)	I (mA/cm^2)	FE_{H_2} (%)	FE_{CO} (%)	FE_{total} (%)	CO_2RR yield (%)
Fe	0.1 M PhOH	–2.57	0.7	0.20	4	3	7	40
	1.0 M PhOH	–2.15	1.3	0.36	2	3	5	65
	1.0 M PhOH	–2.57	1.0	0.26	10	2	12	15
	0.1 TFE	–2.57	0.1	0.03	0	5	5	100
	1.0 TFE	–2.57	0.2	0.07	25	4	29	14
Co	0.1 M PhOH	–2.11	3.2	0.18	1	2	3	62
	0.1 M PhOH	–2.33	5.4	0.30	4	2	6	30
	1.0 M PhOH	–2.07	2.8	1.55	23	14	37	38
	1.0 M PhOH	–2.24	4.9	2.73	33	10	43	23
	0.1 TFE	–2.11	0.5	0.30	0	17	17	100
	0.1 TFE	–2.42	0.5	0.29	3	22	25	88
	1.0 TFE	–2.22	0.90	0.51	1	22	23	96
	1.0 TFE	–2.48	1.7	0.93	4	18	22	82
Ni	0.1 M PhOH	–2.00	0.6	0.34	0	5	5	100
	0.1 M PhOH	–2.43	0.5	0.26	20	5	25	20
	1.0 M PhOH	–2.00	1.6	0.89	1	9	10	89
	0.1 TFE	–2.00	0.6	0.34	0	12	12	100
	1.0 TFE	–2.00	1.1	0.62	0	12	12	100

Catalyst stability under reductive preparative scale experiments unfortunately also doesn't appear to be a problem isolated solely to the iron complexes and was found to be highly dependent not only on the metal center but also the identity and concentration of the proton source. For example, current densities are generally more stable across the hour-long electrolysis experiments for the Co- and Ni-tpyQuin2Me and tpyIsoQuin2Me complexes (see **Figures 7.19 – 7.22**). Further improvements are achieved when 1 M concentrations of acid are used and when TFE is exchanged for the more acidic PhOH.[62] These preliminary screening experiments allowed us to identify catalytic conditions where the metal complexes maintain steady current density over time and are selective for CO_2RR over undesired HER. These conditions are denoted with yellow highlighting in **Tables 7.5** and **7.6**. A consistent trend noted from these screening experiments is that while we could identify conditions where CO_2RR yields are good (*i.e.*, 82 – 100%), the total Faradaic efficiencies (FE) for CO_2 reduction were relatively low with FE's for CO production ranging from only 10% to 43%. The additional unaccounted-for charge was not made up in hydrogen production. Therefore, to determine if the missing charge is going towards the production of liquid products, we conducted long-term electrolysis experiments over 2 to 5 hours in deuterated electrolyte with the goal being to pass enough charge to generate liquid products at concentrations that can be easily detected and quantified by ^{1}H NMR. Furthermore, because CV analysis of the tpyQuin2Me complexes suggests they can facilitate four-electron chemistry, we also hypothesize that formaldehyde may be a potential product. Due to its reactive nature, we speculate that it may be difficult to detect by NMR at low concentrations; this directed us to utilize a reactivity-based florescent probe, FAP-573, previously developed in the lab for the direct colorimetric detection of potential formaldehyde products from the post-electrolysis solution.[63,64] ^{1}H NMR analyses with long delay times of 20 seconds following methods from a previous literature report[65] didn't indicate the production of any discernable liquid products; however, colorimetric analysis with FAP-573 for formaldehyde production yielded more promising results. **Figure 7.13** displays representative data for the formaldehyde detection in the post-electrolysis solution. The emission intensity at 588 nm is much larger for the post-electrolysis solution relative to the pre-electrolysis control. Quantification of Faradaic efficiencies for formaldehyde production based on these data average around 1 – 2%. While the efficiencies for formaldehyde production are small, the control CPE experiment conducted under Ar atmosphere shows no difference in the emission spectrum of the pre- and post-electrolysis solutions confirming that the formaldehyde is indeed generated from CO_2. While these data are preliminary and current work is ongoing to search and quantify liquid products, they serve to validate our hypothesis that installation of additional low-lying π^* orbitals can facilitate generation of more reduced carbon-products beyond the two-electron chemistry, but major improvements in catalyst stability and efficiency are still required. The final section of this thesis discusses potential solutions to improve catalyst performance for these quinoline and isoquinoline based ligand frameworks.

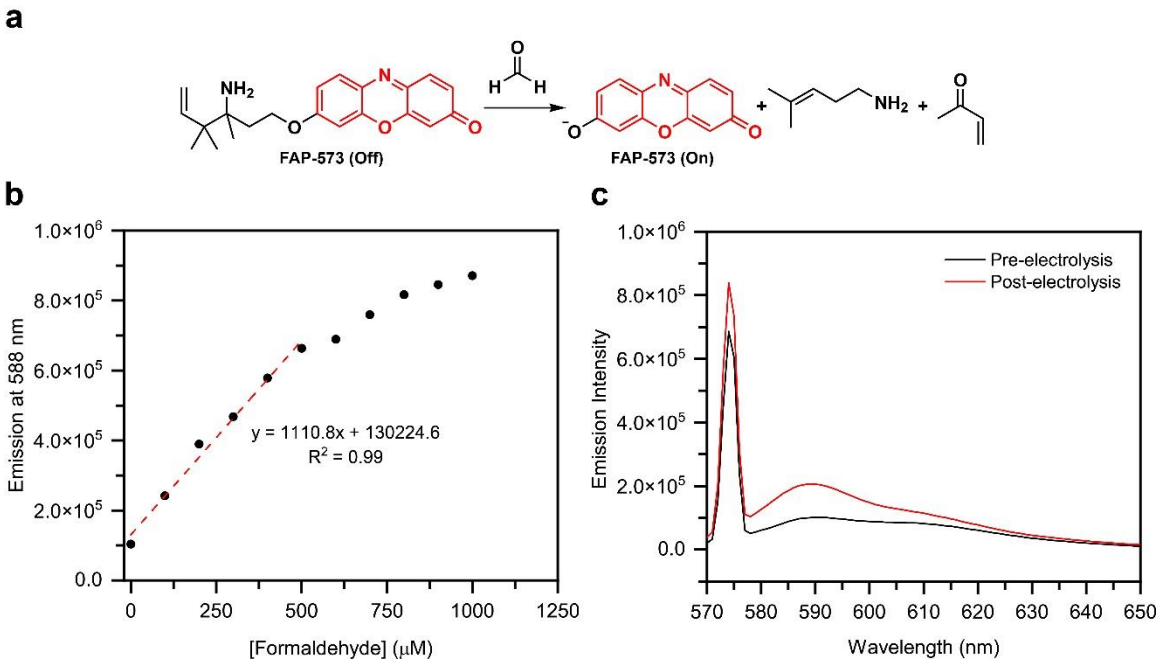


Table 7.13. Fluorescent detection of formaldehyde generated during controlled potential electrolysis experiments. (a) Chemical scheme for the fluorescent detection of formaldehyde with FAP-573.[63,64] The probe leverages the use of a formaldehyde-induced aza-Cope rearrangement to uncage the fluorophore for a turn-on fluorescence reading. (b) The calibration curve obtained in a mixture of 1:4 PBS Buffer: 0.10 M $TBAPF_6$ electrolyte in CH_3CN. Deviations from linearity at higher concentrations are a result of slower reaction kinetics. Concentrations of formaldehyde generated during electrolysis were within the linear region. (c) Representative emission spectra obtained before (black line) and after (red line) the controlled potential electrolysis experiment.

7.3.5 Future Directions Towards the Production of More Reduced Products

The work presented in this final thesis chapter lays the foundation for the exploration of a molecular approach to generate further reduction of CO_2 beyond CO or formate with this terpyridine-based polypyridyl framework. The initial results seem promising from a product distribution perspective as the HER is reasonably suppressed and small amounts of CO and formaldehyde are generated; still, the catalyst stability under reductive electrochemical conditions must be improved for these goals to be realized in a practical manner. To this end, we propose three approaches to improve catalyst stability. These approaches are based on the hypothesis that the catalyst instability and decomposition is directly correlated to the extremely negative reduction potentials that are required to inject more than two electrons into the ligand scaffold for catalysis.

The first approach involves the synthesis and analysis of the early metal variants of the tpyQuin2Me and tpyIsoQuin2Me complexes and is currently ongoing in the laboratory. We hypothesize that the more electron-deficient early metal complexes will be able to antiferromagnetically couple more efficiently with the highly reduced tpyQuin2Me and typyIsoQuin2Me ligands resulting in effective stabilization of these reactive, low valent states thus shifting the redox chemistry to more anodic potentials. This led us to synthesize the Cr complexes through metalation of the tpyQuin2Me and tpyIsoQuin2Me ligands with commercially available

$CrCl_3$•3THF (THF = tetrahydrofuran) following metathesis with AgOTf. The solid-state structures for Cr-tpyQuin2Me are presented in **Figure 7.14** and the Cr-tpyIsoQuin2Me complex is given in **Figure 7.15**. Interestingly, both ligands bind in an identical tetradentate fashion due to the strong coordination of the chloride anions to the axial positions which we were unable to abstract with the use of excess silver salts (**Figure 7.14b**). Anion dependencies on catalytic performance are well established across multiple ligand platforms where generally more coordinating anions limit reactivity through impaired CO_2 binding.[66–68] As such, we sought to prepare the divalent triflate complexes but to do so we first had to synthesize the $Cr(OTf)_2$ salt which is not commercially available. We obtained the Cr triflate salt following previous literature reports[69,70] and isolated the acetonitrile complex via crystallization by slow vapor diffusion of diethyl ether into a concentrated acetonitrile solution to yield $Cr(OTf)_2(CH_3CN)_2$ as light blue crystals (see materials and methods for further details) in quantitative yields. Metalation of the ligands with this salt produced the desired coordination complexes as confirmed by elemental analysis although all attempts to grow diffraction quality crystals have been unsuccessful. Current synthetic efforts are being focused on the synthesis, characterization, and catalytic screening of the remaining early metal triflate salt-containing ($V(OTf)_2$ and $Mn(OTf)_2$) tpy(Iso)Quin2Me complexes.

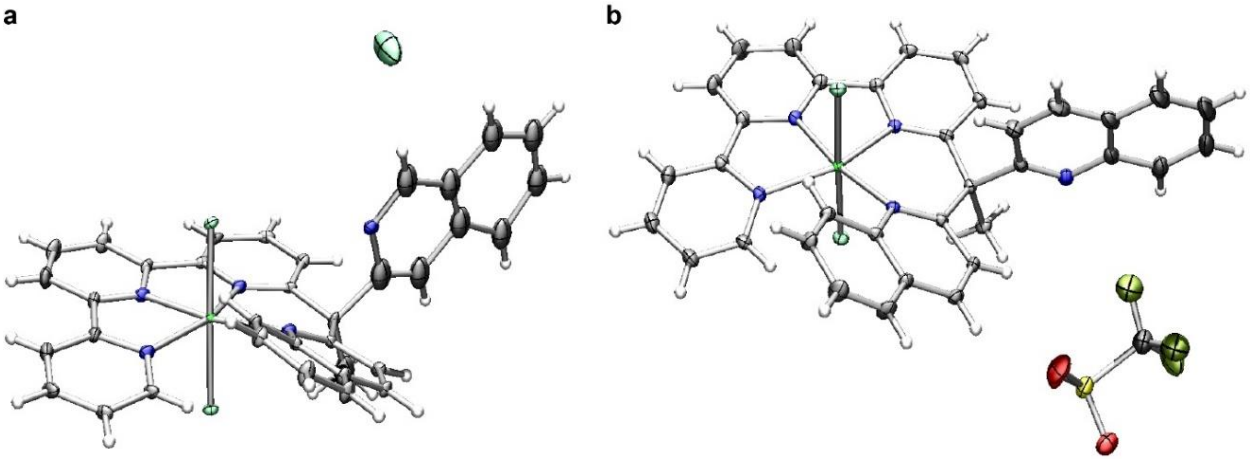


Figure 7.14. Solid state structures of (a) $[Cr(tpyQuin2Me)(Cl)_2][Cl]$ and (b) $[Cr(tpyQuin2Me)(Cl)_2][OTf]$. Thermal ellipsoids are potted at the 30%, 50% probability levels for $[Cr(tpyQuin2Me)(Cl)_2][Cl]$ and $[Cr(tpyQuin2Me)(Cl)_2][OTf]$, respectively. Green, aquamarine, grey, blue, red, yellow, yellow-green, and white signify Cr, Cl, C, N, O, S, F, and H, respectively.

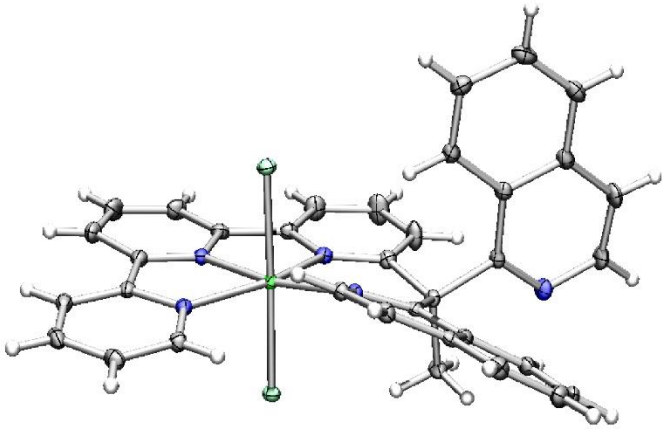


Figure 7.15. Solid state structures of [Cr(tpyIsoQuin2Me)(Cl)$_2$][Cl]. Thermal ellipsoids are potted at the 50% probability level. Green, aquamarine, grey, blue, and white signify Cr, Cl, C, N, and H, respectively.

The second approach involves the use of both light and electricity together to drive the reduction of CO_2 at lower overpotentials (**Figure 7.16a**). Photoelectrocatalysis has recently been applied to the HER by Miller and coworkers[71–73] who have shown that irradiation of an Ir-bpy complex ([Cp*Ir(bpy)(Cl)][Cl], Cp* = pentamethylcyclopentadiene) with visible light generates hydrogen gas in aqueous solution at close to the thermodynamic potential.[71] This mechanism is made possible because the Ir-based transition metal complex acts as both the light absorber and the active electrocatalyst. As such, no photosensitizer or sacrificial reductants are required which greatly reduces the number of components required in solution and removes complications associated with incompatibility between them. Impressively, they've recently expanded this concept to operate with the use of a noble-metal-free catalyst and have shown that these systems can drive the formation of hydrogen at an electrochemical underpotential (*i.e.*, negative overpotential) using 460 nm light in the presence of an organic acid. To the best of our knowledge, this approach has not yet been applied to CO_2 reduction, but we can envision the application of a similar strategy to drive the CO_2RR at significantly lower overpotentials and with much weaker acids given that our tpyPY2, tpyQuin2Me, and tpyIsoQuin2Me complexes presumably possess the photophysical properties required for photoelectrocatalysis given their structural similarity to canonical photosensitizers.[74] This may require the preparation and screening of additional second and third row transition metal complexes to ensure that excited state lifetimes are matched to the timescales for homogenous electrocatalysis.

Finally, the last approach takes inspiration from the organic electrocatalysis community which often utilize robust electron mediators to facilitate and control fast electron transfer processes (**Figure 7.16b**).[75–79] In this dual cooperative electrocatalysis approach, we envision overcoming the overpotential-driven decomposition of our tpyQuin2Me and tpyIsoQuin2Me complexes using an appropriately redox-matched robust electron mediator. The ideal mediator must exhibit chemically and electrochemically reversible behavior at redox potentials slightly more negative than the tpy(Iso)Quin2Me complexes so that it can reduce the catalyst via outer sphere electron transfer. Through this mechanism we hope to avoid the buildup of high concentrations of reduced catalysts within the diffusion layer and avoid decomposition pathways directed by hemi-lability and electrode adsorption of the (iso)quinoline arms. The success of this

strategy is entirely dependent on the identification of an appropriate redox mediator that is chemically stable at extremely reducing conditions. This approach has been applied to dioxygen reduction[80] and alcohol oxidations[81,82] but has yet to find application for CO_2 reduction.

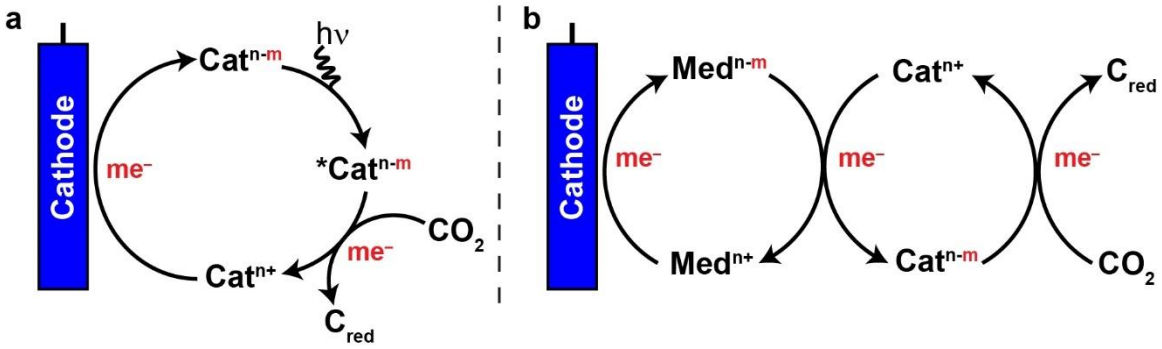


Figure 7.16. Schematic representations for (a) Photoelectrocatalytic and (b) dual cooperative catalytic strategies to improve the stability and electrochemical performance of our tpy-based polypyridyl complexes for electrochemical CO_2 reduction beyond two-electron products.

7.4 Conclusion

In this final thesis chapter, we have explored strategies to enable more than two-electron redox chemistry with our terpyridine-based molecular scaffold with the goal being to generate CO_2 reduction products beyond the typical two-electron products, CO and formate, that are mainly produced with homogenous catalysts. Our design approach is focused on expanding the amount of possible metal-ligand exchange coupling such that more than two electrons localized to metal d orbitals can be antiferromagnetically coupled to unpaired electron density that is electrochemically supplied into the ligand-centered orbitals. Based on the work in Chapter 5, we hypothesized that this type of metal–ligand cooperativity will effectively stabilize highly reduced catalytic intermediates thus shifting the redox chemistry to more mild potentials and ultimately allowing for the delivery of more than two electrons to CO_2. The mechanistic studies in Chapter 6 identified the redox-inactive pyridine arms as the ideal site for synthetic modification because they are not involved in electronically stabilizing the active catalytic species. Therefore, to gain access to the additional low-lying π^* orbitals required to support added ligand-centered electron density, we substituted the redox-inactive pyridyl arms in tpyPY2Me for more conjugated quinoline or isoquinoline arms yielding the tpyQuin2Me and tpyIsoQuin2Me ligand platforms. Metalation with various first-row transition metal salts produced a small library of coordination complexes that were characterized and evaluated for their catalytic activity toward electrochemical CO_2 reduction. Interesting differences in coordination chemistry, electronic structure, and electrochemical properties were observed between the two ligand platforms because of the sterics and relative positioning of the (iso)quinoline arms around the metal centers. CV analysis validated our initial hypothesis by showing that the coordination complexes possess one to two additional ligand centered reductions relative to their tpyPY2Me counterparts. Exposure of the complexes to CO_2 saturated electrolyte with the addition of molar quantities of acid displayed modest catalytic activity with small amounts of CO and formaldehyde being detected. Ultimately, these catalytic systems appear to be severely limited by their stability under prolonged reductive electrolysis conditions and therefore future efforts are required to stabilize these highly reduced catalytic intermediates.

7.5 Materials and Methods

7.5.1 General Methods

All manipulations were conducted under air and moisture free conditions using a MBraun LABstar pro glove-box and standard Schlenk line techniques unless otherwise noted. Acetonitrile adducts of chromium(II) trifluoromethanesulfonate $[Cr(OTf)_2(CH_3CN)_2]$[69,70] and cobalt(II) trifluoromethanesulfonate $[Co(OTf)_2(CH_3CN)_2]$[40] were prepared following slight modifications to literature methods. All other reagents were purchased from commercial vendors and used without further purification. Carbon dioxide (99.99%), hydrogen (99.999%), ethane (99.0%), argon (99.999%) and nitrogen (99.998%) were purchased from Praxair. 6-bromo-2,2'-bipyridine was purchased from Santa Cruz Biotechnology. Tetrakis(triphenylphosphine)palladium $[Pd(Ph_3)_4]$, hexamethylditin $[(CH_3)_6Sn_2]$, iron(II) trifluoromethanesulfonate $[Fe(OTf)_2]$, nickel(II) trifluoromethanesulfonate $[Ni(OTf)_2]$, and zinc(II) trifluoromethanesulfonate $[Zn(OTf)_2]$ were purchased from Strem Chemicals. Quinoline, isoquinoline, 2-bromo-6-fluoropyridine, n-butyllithium (2.5 M, hexanes), lithium chloride, and 1,2-dimethoxyethane (DME) (anhydrous) were purchased from Sigma Aldrich. Acetonitrile (CH_3CN), tetrahydrofuran (THF), and toluene were dried using a JC Meyer solvent purification system and stored over 3 Å molecular sieves under a nitrogen atmosphere. Deionized water was obtained from a Millipore Autopure system. Fluorescence spectra were recorded using a Photon Technology International Quanta Master 4 L-format scan spectrofluorometer equipped with an LPS220B 75-W xenon lamp and power supply, A-1010B lamp housing with integrated igniter, switchable 814 photocounting/analog photomultiplier detection unit, and MD5020 motor driver. UV-visible (UV-vis) spectra were collected using an Agilent Cary 60 spectrophotometer at room temperature (RT). NMR spectra were recorded on a Bruker spectrometer operating at either 300, 400, or 500 MHz. Chemical shifts for ^1H spectra were reported in ppm relative to residual protonated solvent. Coupling constants were reported in Hz. X-ray crystallography was performed in the Chexray facility at the University of California, Berkeley. Elemental analyses were conducted at the Microanalytical Laboratory of the University of California, Berkeley.

7.5.2 Cyclic Voltammetry

Cyclic voltammetry experiments were performed using a CH Instruments, Inc. 600E potentiostat. Voltammetry studies were conducted in a three-electrode cell equipped with a glassy carbon disk (3.0 mm diameter), working electrode (BASi), a platinum wire counter electrode, and a silver wire in a porous Vycor tipped glass tube filled with electrolyte as a pseudo-reference electrode. The working electrode was polished prior to each experiment with 0.05-micron alumina powder on a felt pad. The electrolyte was 0.1 M tetrabutylammonium hexafluorophosphate ($TBAPF_6$) in CH_3CN freshly prepared with anhydrous solvent and saturated with either CO_2 or Ar at 1 atm. At the conclusion of each experiment, the pseudo-reference potentials were referenced against ferrocene/ferrocenium (Fc/Fc^+) used as an external standard. The scan rates for all cyclic voltammograms were 100 mV/s unless otherwise noted. All voltammograms were obtained with iR compensation.

7.5.3 Controlled Potential Electrolysis

Controlled potential electrolyses were conducted using a CH Instruments, Inc. 600E potentiostat. Preparative scale controlled potential electrolysis experiments were performed in a miniaturized version of our previously described homemade gastight PEEK electrolysis cell with a working compartment (7 mL liquid volume) and counter compartment (3 mL liquid volume) separated by an ultrafine glass frit.[83] A 1 cm^2 glassy carbon plate (Toki Carbon; Kanagawa, Japan) was used as the working electrode, a 2.5 cm diameter graphite planchet (Ted Pella; Redding, CA) was used as the auxiliary electrode, and an Ag wire in a Vycor tipped glass tube filled with electrolyte ($TBAPF_6/CH_3CN$) was used as a pseudo-reference electrode. The working compartment was filled with 7 mL of a 1 mM solution of catalyst dissolved in 0.1 M $TBAPF_6/CH_3CN$ containing up to 3.5 M PhOH as a proton source. The counter electrode chamber was filled with 3 mL of a 20 mM solution of tetrabutylammonium acetate dissolved in 0.1 M $TBAPF_6/CH_3CN$. This soluble source of acetate was sacrificially oxidized to generate CO_2 and ethane, thereby preventing GC detection of solvent oxidation byproducts. Both compartments were sealed to be gastight. The working compartment was sparged with CO_2 for 10 min, then sealed and injected with 0.50 mL of ethane as a gaseous internal standard. A CV scan was collected prior to the CPE measurement to calibrate the potential. The electrolyte solution was constantly stirred during the CPE experiment with a 1 cm stirbar. At the conclusion of the experiment, the headspace was injected directly into an SRI-GC (model #8610C) equipped with 6' Hayesep D and 13X molecular sieve chromatographic columns. Two in-line detectors were used: a TCD for H_2 detection and an FID with a methanizer for $CO/CO_2/C_2H_6$ detection. Analytes of interest were quantified by comparing a ratios of analyte/internal stand peak integrals to a calibration curve with known amounts of analyte.

7.5.4 Determination of Faradaic Efficiency (FE)

Controlled potential electrolysis experiments were conducted in gas-tight electrochemical cells at varying applied potentials for 1 – 5 h. At the conclusion of the CPE experiment, samples from the headspace of the electrochemical cell were injected into a gas chromatograph for analysis. Calibration curves were constructed using known amounts of H_2 and CO with C_2H_6 (0.50 mL) as an internal standard to quantify the volume of gaseous products from the respective chromatograms. The amounts (mols) of gas produced were calculated from the volume of gas using the Ideal Gas Law and Faradaic efficiencies were then determined using **Equation 7.1**:

$$FE(\%) = \frac{Q_{expt}}{Q_{Theory}} x100 = \frac{znF}{Q} x100 \qquad \textbf{(Equation 7.1)}$$

where *z* is the number of electrons, *n* is the mols of analyte produced, *F* is Faradays constant and *Q* is the specific charge passed during the CPE experiment.

7.5.5 X-Ray Crystallography

Crystals were coated with Paratone-N oil, attached to a Kapton loop, and mounted onto a Rigaku XtaLAB P200 equipped with a MicroMax 007HF rotating anode and Pilatus3 R 200K-A hybrid pixel array detector. Data were collected using Mo Kα radiation (λ = 0.71073 Å). Crystals were kept at 100(2) K throughout the collection. Data collection was performed with

CrysAlisPro.[84] Data processing was done with CrysAlisPro and included a multi-scan absorption correction applied using the SCALE3 ABSPACK scaling algorithm within CrysAlisPro.

7.5.6 Detection and Quantification of Liquid Products

The post-electrolysis solution was collected for liquid product analysis. ^{1}H NMR was used to search for formate and methanol and the reactivity-based fluorescence analysis with the FAP-573 probe[64] was applied to search for and quantify formaldehyde. All post-electrolysis samples were compared directly to their respective pre-electrolysis control samples to account for potential contaminations or false positive measurements. The long-term controlled potential electrolysis experiments conducted to search for liquid products were done with electrolyte dissolved in CD_3CN to facilitate easy NMR analysis and were vacuum transferred prior to the NMR measurement to suppress the signals from the tetrabutylammonium salt and acid additives. 2.0 uL of an internal standard mixture containing 250 mM DMF and 40 mM DMSO was added to the NMR tube along with 0.5 mL of the electrolysis solution to give a final concentration of 1.0 mM DMF and 0.16 mM DMSO. The DMF internal standard was utilized for quantification of formate and the DMSO internal standard was used for quantification of products that have chemical shifts that occur more upfield, such as methanol.

Formaldehyde was quantified using the calibration curve in **Figure 7.13b** obtained with standard formaldehyde solutions ranging in concentration from 100 μM to 1.0 mM. The standard and electrolysis solutions were prepared by taking 748.5 μL of electrolyte (or Formaldehyde standard solution) and adding 249.5 μL PBS buffer (20 mM, pH 7.4) and 2.0 uL of a 5 mM FAP-573 stock in DMSO, vigorously mixing with a vortex, and incubating the samples in Eppendorf tubes at 37 ºC for two hours. The addition of PBS buffer is critical for fluorescent turn-on to occur as the probe relies on hydrolysis and β-hydride elimination to uncage the fluorophore. After the 2 h incubation period, the samples were loaded into 1 x 1 cm quartz cuvettes and their emission spectra were recorded with excitation at 573 nm. The emission intensity at 588 nm was corrected for the dilution effect associated with addition of PBS buffer and subsequently used for formaldehyde quantification. A representative data set is depicted in **Figure 7.13c**.

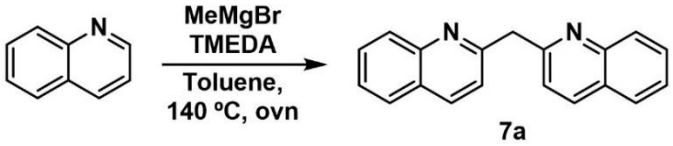
7.5.7 Evans Method Analysis

The Evans method was employed to estimate the magnetic moments of the paramagnetic complexes. All samples were prepared inside a N_2 filled glovebox unless stated otherwise. The Evans standard NMR solution (30 μL of hexafluorobenzene in 3 mL of CD_3CN) was degassed through freeze-pump-thaw cycles (3x) and stored over 3 Å molecular sieves under a nitrogen atmosphere. 5.8 mg of $[Cr(tpyQuin2Me][OTf]_2$, 11.2 mg of $[Fe(tpyQuin2Me][OTf]_2$, 12.0 mg of $[Co(tpyQuin2Me][OTf]_2$, 12.2 mg of $[Ni(tpyQuin2Me][OTf]_2$, 4.4 mg of $[Cr(tpyIsoQuin2Me][OTf]_2$, 5.3 mg of $[Fe(tpyIsoQuin2Me][OTf]_2$, 5.7 mg of $[Co(tpyIsoQuin2Me][OTf]_2$, or 4.5 mg of $[Ni(tpyIsoQuin2Me][OTf]_2$ was dissolved in 600 or 700 μL of standard solution (30 μL of hexafluorobenzene in 3 mL of CD_3CN) and transferred to a J-young NMR tube. A thin capillary containing the standard solution was inserted into the NMR tube. The relative shift of the ^{19}F NMR peak for hexafluorobenzene in CD_3CN[85] was measured at 293 K on either an AVB-400 or AV600 NMR spectrometer. Diamagnetic corrections were approximated using **Equation 7.2**.[86]

$$\chi_D = -\frac{MW}{2} 10^{-6} emu\ mol^{-1}$$ (**Equation 7.2**)

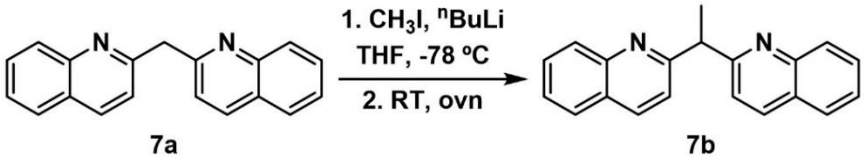
where MW is the unitless molecular weight. For [Cr(tpyQuin2Me][OTf]$_2$ and [Cr(tpyIsoQuin2Me)][OTf]$_2$, a diamagnetic correction value of –433 x 10^{-6} emu mol^{-1} was calculated. For [Fe(tpyQuin2Me][OTf]$_2$ and [Fe(tpyIsoQuin2Me)][OTf]$_2$, a diamagnetic correction value of –434 x 10^{-6} emu mol^{-1} was calculated. For [Co(tpyQuin2Me][OTf]$_2$ and [Co(tpyIsoQuin2Me)][OTf]$_2$, a diamagnetic correction value of –436 x 10^{-6} emu mol^{-1} was calculated. For [Ni(tpyQuin2Me][OTf]$_2$ and [Ni(tpyIsoQuin2Me)][OTf]$_2$, a diamagnetic correction value of –436 x 10^{-6} emu mol^{-1} was calculated. The effective magnetic moments estimated at 293 K in acetonitrile are summarized in **Table 7.2**.

7.5.8 Synthesis of Di(quinolin-2-yl)methane (7a)



To an oven-dried 300 mL pressure flask equipped with a stir bar was added, 30 mL dry toluene, quinoline (5.16 g, 40.0 mmol), MeMgBr (3.0 M, diethyl ether) (14.3 g, 120 mmol, 40.0 mL) and TMEDA (0.464 g, 4.00 mmol, 0.60 mL). The reaction mixture was then heated at 140 ºC overnight. The reaction mixture was then allowed to cool to room temperature and quenched with saturated NH_4Cl solution. The organic and aqueous phases were separated, and the aqueous phase was extracted with EtOAc (3x, 20 mL). The combined organic phases were washed with brine, dried over $MgSO_4$ and concentrated under vacuum to give an orange oil as the crude product. The crude oil was purified by column chromatography (SiO_2; Hexanes:EtOAc 1:1, dry load). The purified product, **7a**, was obtained as an orange solid (2.15 g, 7.95 mmol, 20%). ^{1}H NMR (500 MHz, CD_2Cl_2) / δ (ppm): 8.09 (dd, *J* = 8.5, 0.8 Hz, 2H), 8.03 (dq, *J* = 8.5, 0.9 Hz, 2H), 7.80 (dd, *J* = 8.2, 1.5 Hz, 2H), 7.70 (ddd, *J* = 8.5, 6.9, 1.5 Hz, 2H), 7.51 (ddd, *J* = 8.2, 6.9, 1.2 Hz, 2H), 7.44 (d, *J* = 8.5 Hz, 2H), 4.67 (s, 2H).^{13}C NMR (126 MHz, CD_2Cl_2) / δ (ppm): 160.11, 148.43, 136.76, 129.79, 129.36, 127.96, 127.31, 126.43, 122.36, 49.43. The NMR spectra are consistent with the literature data.[54] ESI-MS Calcd. for $C_{20}H_{16}N_2$ $[M + H]^+$ 285.1 found 285.3 *m/z*.

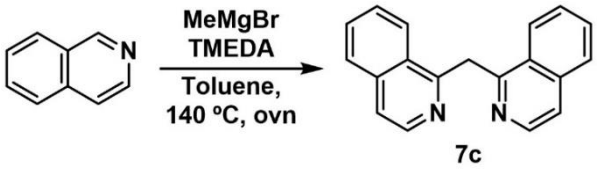
7.5.9 Synthesis of 2,2'-(Ethane-1,1-diyl)diquinoline (7b)



To an oven-dried 100 mL Schlenk flask equipped with a stir bar **7a** (814 mg, 3.02 mmol) was dissolved in 20 mL dry THF. The reaction mixture was then cooled to –78 ºC. ^{n}BuLi (2.5 M, hexanes) (212 mg, 3.31 mmol, 1.3 mL) was slowly added to the reaction solution resulting in an immediate color change to dark red. The reaction was allowed to stir for 30 min at –78 ºC, after which CH_3I (505 mg, 3.55 mmol, 22 µL) was added to the solution. The reaction was left to stir

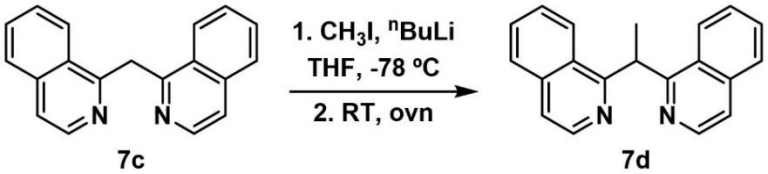
overnight and allowed to warm to room temperature. The following day, the reaction was quenched by addition of water (25 mL). The organic and aqueous phases were separated, and the organics were extracted from the aqueous phase with DCM (3x, 20 mL). The combined organic phases were dried over $MgSO_4$ and concentrated under vacuum to give an orange oily solid as crude product. The crude product was purified by column chromatography (SiO_2; pentane:TBME 1:1, dry load). The purified product, **7b**, was obtained as an orange solid (557 mg, 1.96 mmol, 65%). ^{1}H NMR (500 MHz, CD_2Cl_2)/ δ (ppm): 8.11 – 8.00 (m, 4H), 7.77 (dd, *J* = 8.0, 1.5 Hz, 2H), 7.69 (ddd, *J* = 8.4, 6.9, 1.5 Hz, 2H), 7.49 (ddd, *J* = 8.1, 6.9, 1.2 Hz, 2H), 7.42 (d, *J* = 8.5 Hz, 2H), 4.83 (q, *J* = 7.2 Hz, 1H), 1.94 (d, *J* = 7.1 Hz, 3H). ^{13}C NMR (126 MHz, CD_2Cl_2)/ δ (ppm): 164.37, 148.38, 136.78, 129.84, 129.62, 128.07, 127.57, 126.53, 121.66, 51.84, 19.64. ESI-MS Calcd. for $C_{20}H_{16}N_2$ $[M + H]^+$ 270.1 found 271.2 *m/z*.

7.5.10 Synthesis of Di(isoquinolin-1-yl)methane (7c)



To an oven-dried 300 mL pressure flask equipped with a stir bar was added, 30 mL dry toluene, isoquinoline (5.16 g, 40.0 mmol), MeMgBr (3.0 M, diethyl ether) (14.3 g, 120 mmol, 40.0 mL) and TMEDA (0.464 g, 4.00 mmol, 0.60 mL). The reaction mixture was then heated at 140 ºC overnight. The reaction mixture was then allowed to cool to room temperature and quenched with saturated NH_4Cl solution. The organic and aqueous phases were separated, and the organics were extracted from the aqueous phase with EtOAc (3x, 20 mL). The combined organic phases were washed with brine, dried over $MgSO_4$ and concentrated under vacuum to give an orange oil as crude product. The crude oil was purified by column chromatography (SiO_2; Hexane:EtOAc 1:1, dry load). The purified product, **7c**, was obtained as an orange solid (3.29 mg, 12.16 mmol, 30%). ^{1}H NMR (400 MHz, CD_2Cl_2) / δ(ppm): 8.60 (dt, *J* = 8.3, 1.0 Hz, 2H), 8.48 (d, *J* = 5.8 Hz, 2H), 7.82 (d, *J* = 8.1 Hz, 2H), 7.66 (ddd, *J* = 8.2, 6.8, 1.3 Hz, 2H), 7.62 – 7.52 (m, 4H), 5.44 (s, 2H). ^{13}C NMR (126 MHz, CD_2Cl_2) / δ (ppm): 159.82, 142.36, 136.89, 130.42, 128.36, 127.71, 127.69, 126.79, 120.23, 43.83. The ^{1}H NMR spectrum is consistent with literature reports.[54] ESI-MS Calcd. for $C_{19}H_{14}N_2$ $[M + H]^+$ 271.4 found 271.5 *m/z*.

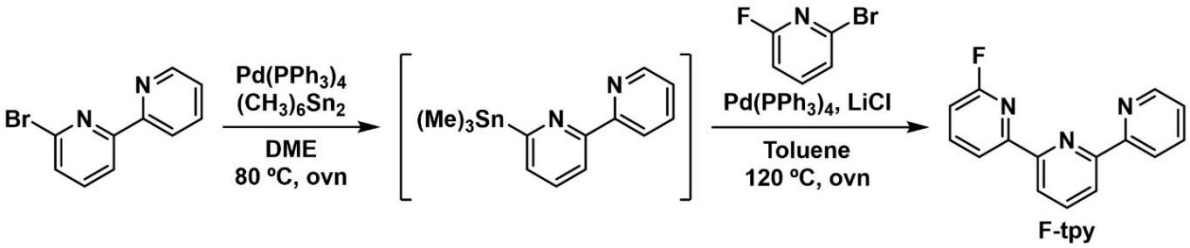
7.5.11 Synthesis of 1,1'-(Ethane-1,1-diyl)diisoquinoline (7d)



To an oven-dried 100 mL Schlenk flask equipped with a stir bar, **7c** (3.29 g, 12.2 mmol) was dissolved in 90 mL dry THF. The reaction mixture was then cooled to –78 ºC. ^{n}BuLi (2.5 M, hexanes) (858 mg, 13.4 mmol, 5.4 mL) was slowly added to the reaction solution resulting in an immediate color change to dark red. The reaction was allowed to stir for 30 min at –78 ºC, after

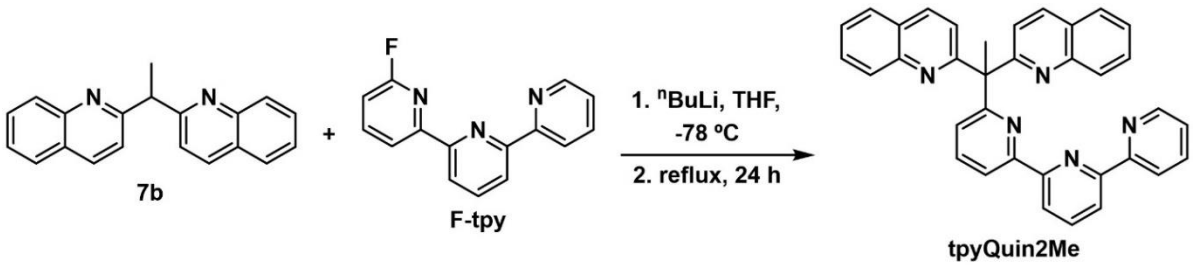
which CH_3I (2.04 g, 14.4 mmol, 894 µL) was added to the solution. The reaction was left to stir overnight and allowed to warm to room temperature. Subsequently, the reaction was quenched by addition of water (50 mL). The organic and aqueous phases were separated, and the organics were extracted from the aqueous phase with DCM (3x, 20 mL). The combined organic phases were dried over $MgSO_4$ and concentrated under vacuum to give a brown oil as crude product. The crude product was purified by column chromatography (SiO_2; pentane:TBME 1:1, dry load). The purified product, **7d**, was obtained as a yellow solid (2.09 mg, 7.35 mmol, 60%). ^{1}H NMR (500 MHz, CD_2Cl_2) / δ (ppm): 8.43 (d, *J* = 5.7 Hz, 2H), 8.27 – 8.16 (m, 2H), 7.83 (dt, *J* = 8.3, 0.9 Hz, 2H), 7.62 (ddd, *J* = 8.2, 6.9, 1.2 Hz, 2H), 7.55 (dd, *J* = 5.7, 0.9 Hz, 2H), 7.47 (ddd, *J* = 8.4, 6.9, 1.4 Hz, 2H), 5.96 (q, *J* = 7.1 Hz, 1H), 2.00 (d, *J* = 7.0 Hz, 3H). ^{13}C NMR (126 MHz, CD_2Cl_2) / δ (ppm): 163.92, 142.39, 137.12, 130.12, 128.10, 127.74, 127.31, 125.60, 120.08, 44.63, 19.69. ESI-MS Calcd. for $C_{20}H_{16}N_2$ $[M + H]^+$ 284.1 found 285.3 m/z.

7.5.12 Synthesis of 6-Fluoro-2,2':6',2''-terpyridine (F-tpy)



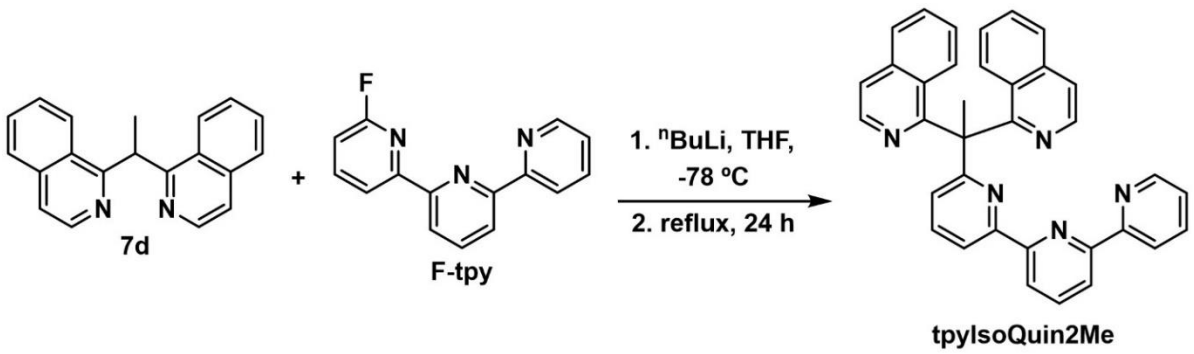
6-fluoro-2,2':6',2"-terpyridine (**F-tpy**) was synthesized by making slight modifications to previous literature reports.[43] 6-Bromo-2,2'-bipyridine (3.59 g, 15.26 mmol) and $Pd(PPh_3)_4$ (0.88 g, 0.76 mmol) were loaded into an oven dried 500 mL Schlenk flask equipped with a stir bar. The reaction flask was evacuated and refilled with Ar (3x). Next, anhydrous 1,2-dimethoxyethane (DME) (300 mL) and hexamethylditin (5.0 g, 15.26 mmol, 3.16 mL) were added to the reaction mixture. The reaction was then heated at 80 °C overnight. The reaction mixture was then allowed to cool to RT and concentrated under vacuum. The crude 6-(trimethylstannyl)-2,2'-bipyridine solution was vacuum dried overnight and used without further purification the following day. The next day, 2-bromo-6-fuloropyridine (2.69 g, 15.26 mmol), LiCl (1.29 g, 30.52 mmol), and $Pd(PPh_3)_4$ (0.88 g, 0.76 mmol) were added under Ar atmosphere to the Schlenk flask (500 mL) containing the dry 6-(trimethylstannyl)-2,2'-bipyridine. The reaction mixture was degassed with Ar (3x) then dry toluene (300 mL) was cannula transferred into the reaction flask. The crude reaction mixture was stirred at reflux for 24 h. After 24 h, the reaction was cooled to RT and concentrated under reduced pressure. The crude product was purified by column chromatography (SiO_2; EtOAc:Hexanes 1:1, dry load). The final product was isolated as a white solid (2.68 g, 10.7 mmol, 70%). ^{1}H NMR (400 MHz, CD_2Cl_2) / δ (ppm): 8.69 (ddd, *J* = 4.7, 1.8, 0.9 Hz, 1H), 8.61 (dt, *J* = 8.0, 1.1 Hz, 1H), 8.54 (ddd, *J* = 7.5, 2.5, 0.8 Hz, 1H), 8.49 (dd, *J* = 7.8, 1.1 Hz, 1H), 8.36 (dd, *J* = 7.8, 1.1 Hz, 1H), 7.98 (dt, *J* = 9.6, 7.9 Hz, 2H), 7.88 (td, *J* = 7.7, 1.8 Hz, 1H), 7.36 (ddd, *J* = 7.5, 4.8, 1.2 Hz, 1H), 7.00 (ddd, *J* = 8.1, 3.0, 0.8 Hz, 1H). ^{13}C NMR (126 MHz, CD_2Cl_2)/ δ (ppm): 156.44, 156.14, 149.77, 142.57, 142.51, 138.60, 137.40, 124.49, 121.92, 121.56, 121.45, 118.73, 118.70, 110.18, 109.88. ^{19}F NMR (376 MHz, CD_2Cl_2) / δ (ppm): –68.45 (d, *J* = 8.5 Hz). ESI-MS Calcd. for $C_{15}H_{10}FN_3$ $[M+H]^+$, 251.3 found 251.6 *m/z*.

7.5.13 Synthesis of 2,2'-(1-([2,2':6',2''-Terpyridin]-6-yl)ethane-1,1-diyl)diquinoline (tpyQuin2Me)



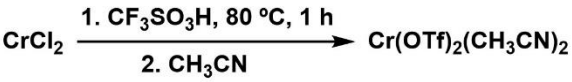
To an oven dried 100 mL Schlenk flask was added 30 mL dry THF and **7b** (0.96 g, 3.4 mmol). The reaction mixture was then cooled to –78 ºC. ^{n}BuLi (2.5 M, hexanes) (0.22 g, 3.4 mmol, 1.3 mL) was slowly added to the reaction solution resulting in an immediate color change to dark purple. The reaction was allowed to stir for 30 min at –78 ºC. To a separate oven dried Schlenk flask (100 mL) equipped with a stir bar was added **F-tpy** (0.76 g, 3.1 mmol). Dry THF (30 mL) was added to the Schlenk flask and the solution was stirred until **F-tpy** was fully dissolved. After 30 min, the **F-tpy** solution was slowly added by syringe to the reaction mixture at –78 ºC. The reaction was allowed to stir for 1 h at –78 ºC then slowly warmed up to RT. Once at RT, the reaction was heated and stirred at reflux for 24 h. After 24 h, the reaction was quenched with 60 mL water. The organic and aqueous layers were separated. The aqueous layer was washed with DCM (3x, 20 mL), dried over $MgSO_4$, and concentrated to give a yellow-orange oil as a crude product. The crude oil was purified by column chromatography (SiO_2; EtOAc:Hexanes 1:3, dry load). The pure ligand was obtained as a crystalline yellow solid (1.05 g, 2.04 mmol, 67%) ^{1}H NMR (400 MHz, CD_3CN) / δ (ppm): 8.66 (ddd, *J* = 4.8, 1.8, 0.9 Hz, 1H), 8.62 (dt, *J* = 8.0, 1.1 Hz, 1H), 8.51 (dd, *J* = 7.8, 0.9 Hz, 1H), 8.37 (dd, *J* = 7.8, 1.1 Hz, 1H), 8.15 (dd, *J* = 8.8, 0.9 Hz, 2H), 8.07 (dd, *J* = 7.8, 1.0 Hz, 1H), 7.97 – 7.77 (m, 7H), 7.68 (ddd, *J* = 8.5, 6.9, 1.6 Hz, 2H), 7.55 (ddd, *J* = 8.1, 6.9, 1.3 Hz, 2H), 7.51 – 7.43 (m, 3H), 7.40 (ddd, *J* = 7.6, 4.8, 1.3 Hz, 1H), 2.53 (s, 3H). ^{13}C NMR (126 MHz, CD_2Cl_2)/ δ (ppm): 166.57, 165.35, 156.69, 156.09, 155.78, 155.28, 149.69, 147.77, 138.25, 137.57, 137.33, 135.51, 129.85, 129.58, 127.93, 127.32, 126.73, 124.31, 123.45, 121.51, 121.41, 121.21, 118.99, 62.23, 27.49. ESI-MS Calcd. for $C_{35}H_{25}N_5$ $[M+H]^+$, 515.6 *m/z* found 516.0 *m/z*.

7.5.14 Synthesis of 1,1'-(1-([2,2':6',2''-Terpyridin]-6-yl)ethane-1,1-diyl)diisoquinoline (tpyIsoQuin2Me)



To an oven dried 100 mL Schlenk flask was added 25 mL dry THF and **7d** (0.88 g, 3.1 mmol). The reaction mixture was then cooled to –78 ºC. ^{n}BuLi (2.5 M, hexanes) (0.20 g, 3.1 mmol, 1.2 mL) was slowly added to the reaction solution resulting in an immediate color change to dark blue. The reaction was allowed to stir for 30 min at –78 ºC. To a separate oven dried Schlenk flask (100 mL) equipped with a stir bar was added **F-tpy** (0.71 g, 2.8 mmol). Dry THF (25 mL) was added to the Schlenk flask and the solution was stirred until **F-tpy** was fully dissolved. After 30 min, the **F-tpy** solution was slowly added by syringe to the reaction mixture at –78 ºC. The reaction was allowed to stir for 1 h at –78 ºC then slowly warmed up to RT. Once at RT, the reaction was heated and stirred at reflux for 24 h. After 24 h, the reaction was quenched with 60 mL water. The organic and aqueous layers were separated. The aqueous layer was washed with DCM (3x, 20 mL), dried over $MgSO_4$, and concentrated to give a orange-brown oil as a crude product. The crude oil was purified by column chromatography (SiO_2; EtOAc:Hexanes 1:1, dry load). The pure ligand was obtained as a crystalline white solid (0.46 g, 0.88 mmol, 31%). ^{1}H NMR (400 MHz, CD_2Cl_2) / δ (ppm): 8.64 (d, *J* = 1.8 Hz, 1H), 8.57 (d, *J* = 7.6 Hz, 1H), 8.51 (d, *J* = 5.5 Hz, 2H), 8.43 (d, *J* = 7.8 Hz, 1H), 8.24 (d, *J* = 7.9 Hz, 1H), 7.89 (t, *J* = 7.9 Hz, 1H), 7.84 (t, *J* = 8.8 Hz, 1H), 7.79 (t, *J* = 8.7 Hz, 3H), 7.64 (t, *J* = 7.7 Hz, 4H), 7.47 – 7.39 (m, 3H), 7.30 (dd, *J* = 7.6, 4.7 Hz, 1H), 7.05 (t, *J* = 7.8 Hz, 2H), 6.87 (d, *J* = 7.8 Hz, 1H), 2.70 (s, 3H). ^{13}C NMR (126 MHz, CD_2Cl_2)/ δ (ppm): 165.86, 164.93, 156.72, 156.04, 155.52, 153.67, 149.61, 141.24, 137.75, 137.62, 137.29, 136.64, 129.38, 128.86, 128.49, 127.85, 126.59, 126.34, 124.22, 121.37, 121.02, 121.00, 120.76, 118.44, 63.83, 30.52. ESI-MS Calcd. for $C_{35}H_{25}N_5$ $[M+H]^+$, 515.6 *m/z* found 515.7 *m/z*.

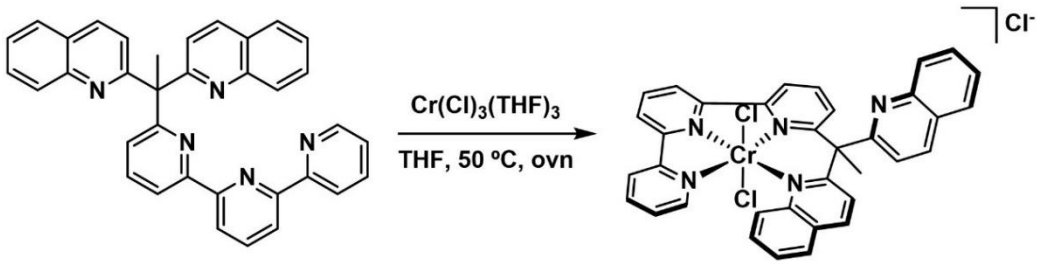
7.5.15 Synthesis of $Cr(OTf)_2(CH_3CN)_2$



$Cr(OTf)_2$ was prepared following slight modifications to previous literature reports.[69,70] Under N_2 atmosphere, $CrCl_2$ (5.0 g, 8.14 mmol) was weighed into a 100 mL, oven dried Schlenk flask equipped with a stir bar and attached to a bubbler containing a saturated sodium hydroxide solution with a plastic cannula. Triflic acid (25 mL) was then slowly cannula transferred into the reaction flask with a steady stream of N_2 flowing through the reaction flask. Once the triflic acid was added, the reaction was heated to 80 °C for 1 hour. After an hour, the reaction mixture was

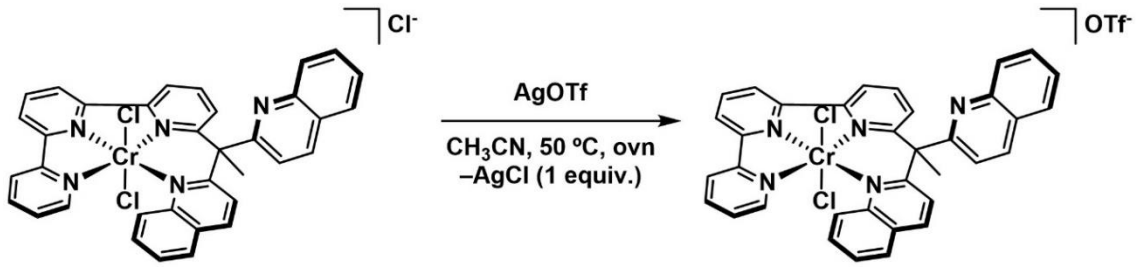
cooled to 0 °C while N_2 flow was maintained. Anhydrous diethyl ether (Et_2O) was then added slowly to the rapidly stirring solution in a dropwise fashion to crash out the desired chromium salt. The isolated $Cr(OTf)_2$ salt was collected by vacuum filtration and further washed with copious amounts of Et_2O until the filtrate was clear to yield a yellow-white solid. The crude $Cr(OTf)_2$ salt was then purified by crystallization via slow vapor diffusion of Et_2O into a saturated CH_3CN solution which resulted in the formation of the desired acetonitrile adduct, $Cr(OTf)_2(CH_3CN)_2$, as light-blue crystals that were suitable for X-ray diffraction in near quantitative yield (3.5 mg, 8.0 mmol, 98%). Anal. Calcd. for $C_2CrF_6O_6S_2$: C, 6.86; H, 0.00;, N, 0.00; S, 18.31. Found: C, 6.93; H, 0.03; N, 0.97; S, 18.49.

7.5.16 Synthesis of [Cr(tpyQuin2Me)(Cl)$_2$][Cl]



In an N_2 filled glovebox, tpyQuin2Me (100.0 mg, 0.19 mmol) was weighed into a 20 ml, oven dried scintillation vial equipped with a stir bar. Dry, degassed CH_3CN (9 mL) was added to the scintillation vial and the ligand solution was stirred at RT until mostly solubilized. In a second 20 mL, oven dried scintillation vial was loaded $Cr(Cl)_3(THF)_3$ (72.6 mg, 0.19 mmol) and 9 mL dry, degassed CH_3CN. The chromium triflate solution was stirred at RT until fully solubilized. Once fully homogenous, the chromium triflate solution was added to the stirring ligand solution resulting in the formation of a mint-green precipitate. The reaction was stirred at 50 ºC overnight. The following day, the product was isolated by vacuum filtration and washed with diethyl ether (Et_2O) (2 mL, 3x) to give a light green solid (101.1 mg, 0.15 mmol, 79%). Diffraction quality crystals were obtained by slow vapor diffusion of Et_2O into a saturated acetonitrile solution.

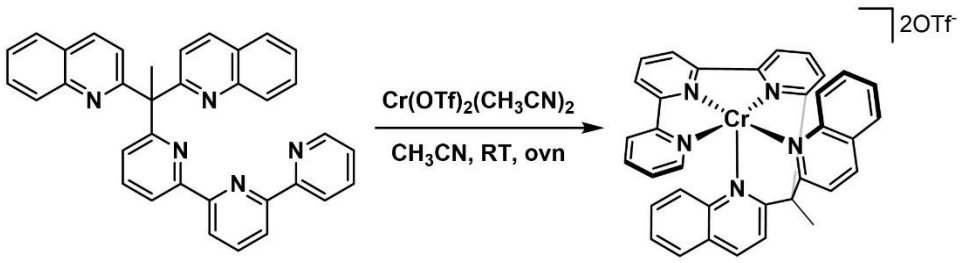
7.5.17 Synthesis of [Cr(tpyQuin2Me)(Cl)$_2$][OTf]



In an N_2 filled glovebox, [Cr(tpyQuin2Me)(Cl)$_2$][Cl] (60.9 mg, 0.09 mmol) was weighed into a 20 ml, oven dried scintillation vial equipped with a stir bar. Dry, degassed CH_3CN (9 mL) was added to the scintillation vail and the solution was stirred at RT. Silver triflate (AgOTf) (71.9 mg, 0.28 mmol) was added as a solid to the [Cr(tpyQuin2Me)(Cl)$_2$][Cl] slurry. Upon addition of AgOTf, the solution turned brown-orange and a white precipitate formed. The reaction mixture

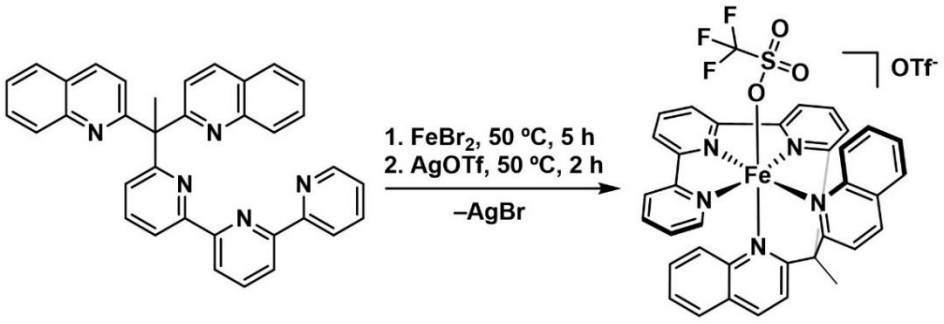
was stirred at 50 ºC overnight. The following day, the reaction solution was filtered to remove AgCl, concentrated under vacuum, and washed with pentanes (2 mL, 3x). Diffraction quality crystals were obtained by slow vapor diffusion of diethyl ether (Et_2O) into a saturated methanolic solution which resulted in dark brown plates. X-ray diffraction analysis confirmed incomplete salt metathesis showing that both axial Cl anion were still bound to the Cr center and only the non-coordinated triflate anion had been exchanged.

7.5.18 Synthesis of [Cr(tpyQuin2Me)][OTf]$_2$ (Cr-tpyQuin2Me)



In an N_2 filled glovebox, tpyQuin2Me (100.0 mg, 0.19 mmol) was weighed into a 20 ml, oven dried scintillation vial equipped with a stir bar. Dry, degassed CH_3CN (9 mL) was added to the scintillation vial and the ligand solution was stirred at RT until mostly solubilized. In a second 20 mL, oven dried scintillation vial was loaded $Cr(OTf)_2(CH_3CN)_2$ (82.1 mg, 0.19 mmol) and 9 mL dry, degassed CH_3CN. The chromium triflate solution was stirred at RT until fully solubilized. Once fully homogenous, the chromium triflate solution was added to the stirring ligand solution resulting in the formation of a dark black solution. The reaction was stirred at RT overnight. The following day, the crude reaction solution was concentrated under vacuum and washed with pentanes (2 mL, 3x) and used without further purification (151.5 mg, 0.17 mmol, 92% yield). All attempts is grow diffraction quality crystals have been unsuccessful. Anal. Calcd. for $C_{37}H_{25}CrF_6N_5O_6S_2$: C, 51.33; H, 2.91; N, 8.09; S, 7.41. Found: C, 48.27; H, 2.98; N, 7.96; S, 7.80.

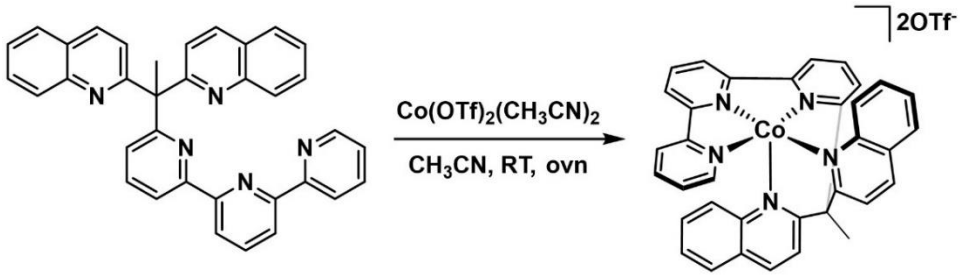
7.5.19 Synthesis of [Fe(tpyQuin2Me)][OTf]$_2$ (Fe-tpyQuin2Me)



In an N_2 filled glovebox, tpyQuin2Me (100.0 mg, 0.19 mmol) was weighed into a 20 mL, oven dried scintillation vial equipped with a stir bar. Dry, degassed CH_3CN (9 mL) was added to the scintillation vial and the ligand solution was stirred at RT until fully solubilized. In a second 20 mL, oven dried scintillation vial was loaded $Fe(Br)_2$ (41 mg, 0.19 mmol) and 9 mL dry, degassed CH_3CN. The iron bromide slurry was stirred vigorously at RT while the ligand solution

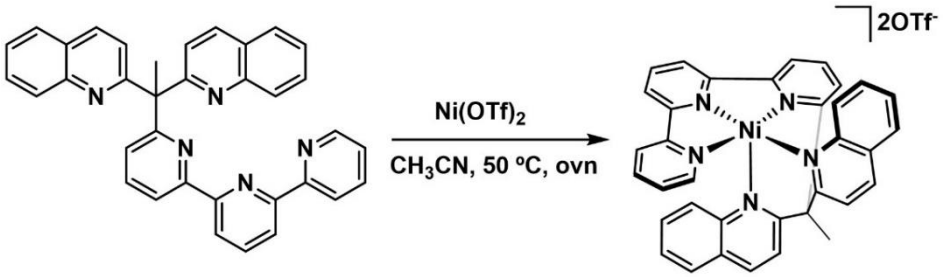
was added to the vial containing the metal salt resulting in the formation of a dark red solution. The reaction was then heated to 50 °C and allowed to react for 5 h. After 5 h, silver triflate (AgOTf) (102.8 mg, 0.40 mmol) was added as a solid to the reaction mixture resulting the immediate formation of a silver-grey solid and bright orange solution. The reaction mixture was stirred at 50 ºC for an additional 2 h. After 2 h, the reaction mixture was filtered to remove the silver bromide and concentrated to give a bright orange-red solid (141 mg, 0.16 mmol, 85%). The iron complex was purified by crystallization by slow vapor diffusion of diethyl ether (Et_2O) into a saturated CH_3CN solution which resulted in orange, block shaped X-ray diffraction quality crystals. ^1H NMR (400 MHz, CD_3CN) / δ (ppm): 86.86, 79.35, 77.35, 72.06, 64.87, 39.53, 37.68, 21.26, 18.08, 7.19, 2.94. Anal. Calcd. for $C_{37}H_{25}F_6FeN_5O_6S_2$: C, 51.11; H, 2.90; N, 8.05; S, 7.37. Found: C, 49.14; H, 2.98; N, 7.79; S, 7.49.

7.5.20 Synthesis of [Co(tpyQuin2Me)][OTf]$_2$ (Co-tpyQuin2Me)



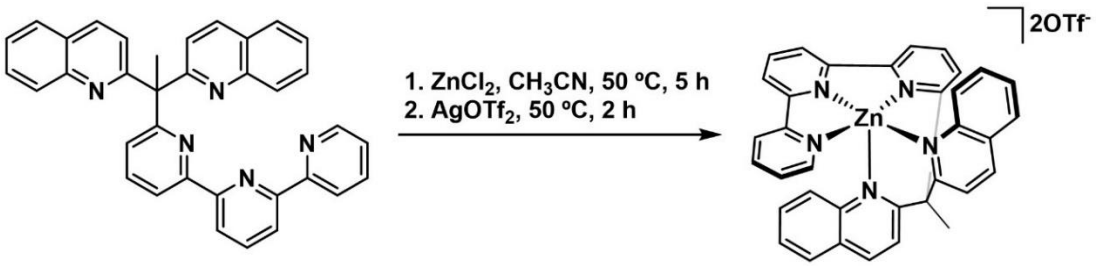
In an N_2 filled glovebox, tpyQuin2Me (100.0 mg, 0.19 mmol) was weighed into a 20 mL, oven dried scintillation vial equipped with a stir bar. Dry, degassed CH_3CN (9 mL) was added to the scintillation vial and the ligand solution was stirred at RT until fully solubilized. In a second 20 mL, oven dried scintillation vial was loaded $Co(OTf)_2(CH_3CN)_2$ (83.4 mg, 0.19 mmol) and 9 mL dry, degassed CH_3CN. The cobalt triflate solution was then added to the ligand solution resulting in the formation of a red-orange solution. The reaction was stirred at RT overnight. The following day, the reaction solution was concentrated under vacuum and washed with diethyl ether (Et_2O) (2 mL, 3x) giving the desired product as an orange-brown solid (165 mg, 0.19 mmol, 100%). X-ray diffraction quality crystals were obtained by slow vapor diffusion of Et_2O into a saturated methanolic solution resulting in the formation of orange block shaped single crystals over the course of a few days. ^1H NMR (400 MHz, CD_3CN) / δ (ppm): 81.67, 63.84, 59.60, 58.99, 55.22, 53.74, 52.47, 51.91, 48.08, 28.93, 26.71, 19.23, 18.54, 18.08, 17.04, 16.52, 12.82, 4.66, 2.68, –15.44. Anal. Calcd. for $C_{37}H_{25}CoF_6N_5O_6S_2$: C, 50.92; H, 2.89; N, 8.03; S, 7.35. Found: C, 49.16; H, 2.61; N, 7.86; S, 7.76.

7.5.21 Synthesis of [Ni(tpyQuin2Me)][OTf]$_2$ (Ni-tpyQuin2Me)



In an N_2 filled glovebox, tpyQuin2Me (100.0 mg, 0.19 mmol) was weighed into a 20 mL, oven dried scintillation vial equipped with a stir bar. Dry, degassed CH_3CN (9 mL) was added to the scintillation vial and the ligand solution was stirred at RT until fully solubilized. In a second 20 mL, oven dried scintillation vial was loaded $Ni(OTf)_2$ (67.8 mg, 0.19 mmol) and 9 mL dry, degassed CH_3CN. The ligand solution was then added to the $Ni(OTf)_2$ slurry. The reaction was heated to 50 ºC and stirred overnight over which time the solution turns light yellow. The following day, the reaction solution was concentrated under vacuum and washed with diethyl ether (Et_2O) (2 mL, 3x) giving the desired product as a tan solid (165.8 mg, 0.19 mmol, 100%). All attempts to grow diffraction quality crystals have been unsuccessful. ^{1}H NMR (400 MHz, CD_3CN) / δ (ppm): 88.68, 76.76, 74.34, 66.05, 60.19, 45.63, 37.65, 29.58, 19.95, 16.23, 14.24, 12.22, 12.14, 6.17, 4.57, 2.81, –7.59. Anal. Calcd. for $C_{37}H_{25}F_6N_5NiO_6S_2$: C, 50.94; H, 2.89; N, 8.03; S, 7.35. Found: C, 49.74; H, 2.62; N, 8.08; S, 7.76.

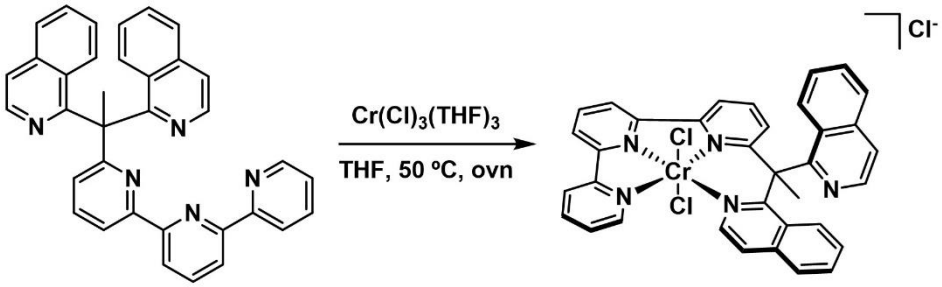
7.5.22 Synthesis of [Zn(tpyQuin2Me)][OTf]$_2$ (Zn-tpyQuin2Me)



tpyQuin2Me (44.0 mg, 0.085 mmol) was weighed into a 20 mL, oven dried scintillation vial equipped with a stir bar. Dry, degassed CH_3CN (3 mL) was added to the scintillation vial and the ligand solution was stirred at RT until fully solubilized. In a second 20 mL, oven dried scintillation vial was loaded $ZnCl_2$ (11.6 mg, 0.085 mmol) and 3 mL dry, degassed CH_3CN. The ligand solution was then added to the $ZnCl_2$ slurry with vigorous stirring. The reaction was heated to 50 ºC and stirred overnight over which the solution turns light yellow and precipitate forms. The following day, silver triflate (AgOTf) (46 mg, 0.18 mmol) was added as a solid to the reaction mixture resulting in the formation of a silver-grey solid. The mixture was then stirred at 50 ºC for an additional 2 h. After 2 h, the reaction mixture was filtered to remove the silver chloride and concentrated to give a white solid (74 mg, 0.084 mmol, 99%). The zinc complex was purified by crystallization by slow vapor diffusion of diethyl ether (Et_2O) into a saturated CH_3CN solution which resulted in clear, block shaped X-ray diffraction quality crystals. ^{1}H NMR (400 MHz,

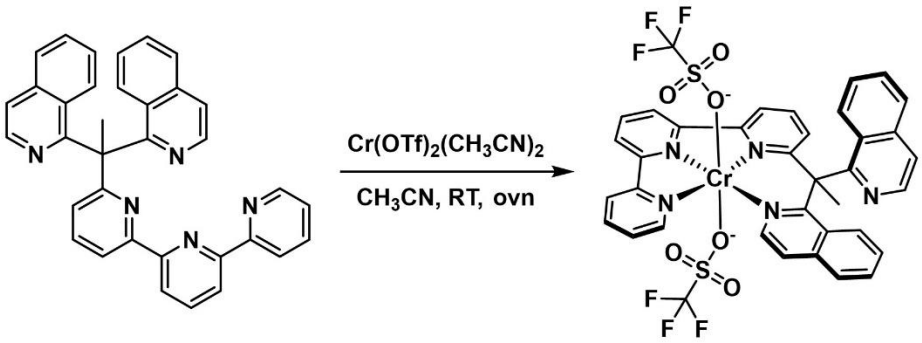
CD_3CN) / δ (ppm): 9.02 (1H, dt, *J* = 8.2, 1.0 Hz), 8.93 (1H, dd, *J* = 6.3, 2.4 Hz), 8.79 (2H, dd, *J* = 9.0, 0.8 Hz), 8.73 – 8.69 (2H, m), 8.58 (1H, td, *J* = 7.9, 1.6 Hz), 8.51 – 8.47 (3H, m), 8.34 – 8.28 (2H, m), 8.28 – 8.23 (1H, m), 8.07 (2H, dd, *J* = 8.1, 1.4 Hz), 7.69 (1H, ddd, *J* = 7.6, 5.2, 1.1 Hz), 7.62 (2H, ddd, *J* = 8.1, 6.7, 1.2 Hz), 7.42 (2H, ddd, *J* = 8.3, 6.8, 1.5 Hz), 7.39 – 7.32 (2H, m), 3.17 (3H, s). Anal. Calcd. for $C_{37}H_{25}F_6N_5O_6S_2Zn$: C, 50.55; H, 2.87; N, 7.97; S, 7.29. Found: C, 47.18; H, 3.05; N, 7.20; S, 7.22.

7.5.23 Synthesis of [Cr(tpyIsoQuin2Me)(Cl)$_2$][Cl]



In an N_2 filled glovebox, tpyIsoQuin2Me (100.0 mg, 0.19 mmol) was weighed into a 20 ml, oven dried scintillation vial equipped with a stir bar. Dry, degassed CH_3CN (9 mL) was added to the scintillation vial and the ligand solution was stirred at RT until mostly solubilized. In a second 20 mL, oven dried scintillation vial was loaded $Cr(Cl)_3(THF)_3$ (72.6 mg, 0.19 mmol) and 9 mL dry, degassed CH_3CN. The chromium triflate solution was stirred at RT until fully solubilized. Once fully homogenous, the chromium triflate solution was added to the stirring ligand solution resulting in the formation of a light-pink precipitate. The reaction was stirred at 50 ºC overnight. The following day, the product was isolated by vacuum filtration and washed with diethyl ether (Et_2O) (2 mL, 3x) to give a peach colored solid (121 mg, 0.18 mmol, 95%). Diffraction quality crystals were obtained by slow vapor diffusion of Et_2O into a saturated methanolic solution.

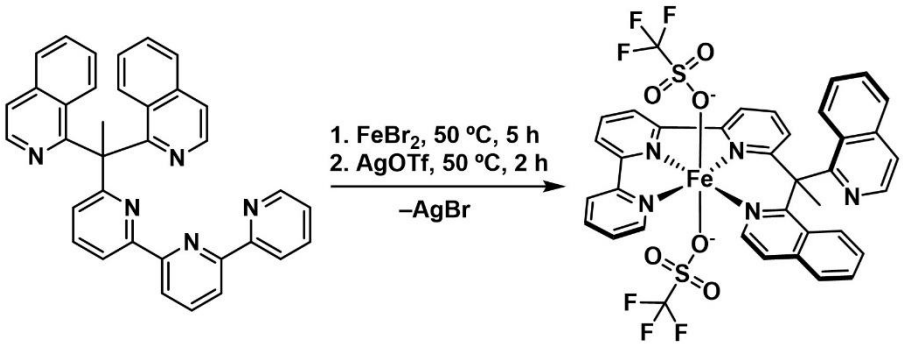
7.5.24 Synthesis of Cr(tpyIsoQuin2Me)(OTf)$_2$ (Cr-tpyIsoQuin2Me)



In an N_2 filled glovebox, tpyIsoQuin2Me (100.0 mg, 0.19 mmol) was weighed into a 20 ml, oven dried scintillation vial equipped with a stir bar. Dry, degassed CH_3CN (9 mL) was added to the scintillation vial and the ligand solution was stirred at RT until mostly solubilized. In a

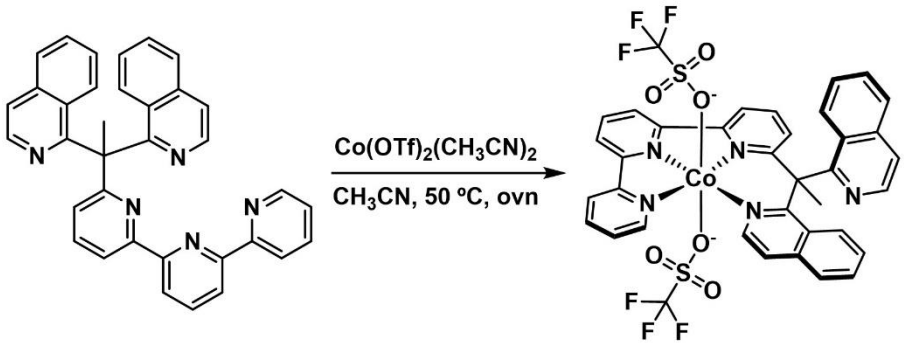
second 20 mL, oven dried scintillation vial was loaded $Cr(OTf)_2(CH_3CN)_2$ (82.1 mg, 0.19 mmol) and 9 mL dry, degassed CH_3CN. The chromium triflate solution was stirred at RT until fully solubilized. Once fully homogenous, the chromium triflate solution was added to the stirring ligand solution resulting in the formation of a brown solution. The reaction was stirred at RT overnight. The following day, the crude reaction solution was concentrated under vacuum and washed with pentanes (2 mL, 3x) and used without further purification (164 mg, 0.19 mmol, 100%). All attempts to obtain diffraction quality crystals have been unsuccessful to date. Anal. Calcd. for $C_{37}H_{25}CrF_6N_5O_6S_2$: C, 51.33; H, 2.91; N, 8.09; S, 7.41. Found: C, 48.50; H, 3.11; N, 8.09; S, 7.66.

7.5.25 Synthesis of Fe(tpyIsoQuin2Me)(OTf)$_2$ (Fe-tpyIsoQuin2Me)



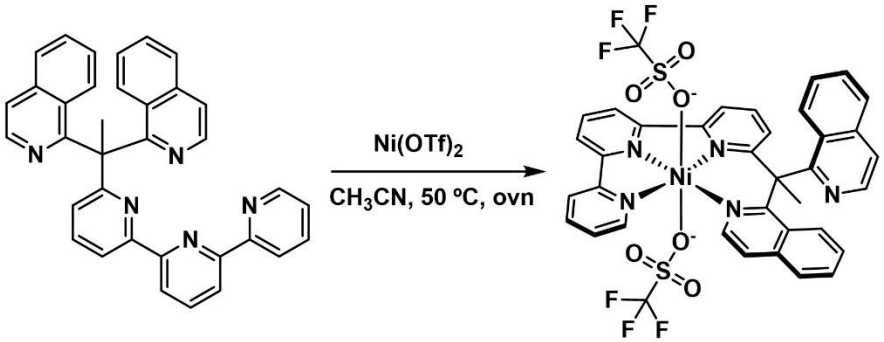
In an N_2 filled glovebox, tpyIsoQuin2Me (100.0 mg, 0.19 mmol) was weighed into a 20 mL, oven dried scintillation vial equipped with a stir bar. Dry, degassed CH_3CN (9 mL) was added to the scintillation vial and the ligand solution was stirred at RT until fully solubilized. In a second 20 mL, oven dried scintillation vial was loaded $Fe(Br)_2$ (41 mg, 0.19 mmol) and 9 mL dry, degassed CH_3CN. The iron bromide slurry was stirred vigorously at RT while the ligand solution was added to the vial containing the metal salt resulting in the formation of a green-blue solution with a dark precipitate. The reaction was then heated to 50 ºC and allowed to react for 5 h. After 5 h, silver triflate (AgOTf) (102.8 mg, 0.40 mmol) was added as a solid to the reaction mixture resulting the immediate formation of a silver-grey solid and red-orange solution. The reaction mixture was stirred at 50 ºC for an additional 2 h. After 2 h, the reaction mixture was filtered to remove the silver bromide and concentrated to give a bright orange-red solid (165 mg, 0.19 mmol, 100%). The iron complex was purified by crystallization by slow vapor diffusion of diethyl ether (Et_2O) into a saturated CH_3CN solution which resulted in orange, block shaped X-ray diffraction quality crystals. Anal. Calcd. for $C_{37}H_{25}F_6FeN_5O_6S_2$: C, 51.11; H, 2.90; N, 8.05; S, 7.37. Found: C, 49.25; H, 3.12; N, 7.92; S, 6.95.

7.5.26 Synthesis of Co(tpyIsoQuin2Me)(OTf)$_2$ (Co-tpyIsoQuin2Me)



In an N_2 filled glovebox, tpyIsoQuin2Me (100.0 mg, 0.19 mmol) was weighed into a 20 mL, oven dried scintillation vial equipped with a stir bar. Dry, degassed CH_3CN (9 mL) was added to the scintillation vial and the ligand solution was stirred at RT until fully solubilized. In a second 20 mL, oven dried scintillation vial was loaded $Co(OTf)_2(CH_3CN)_2$ (83.4 mg, 0.19 mmol) and 9 mL dry, degassed CH_3CN. The cobalt triflate solution was then added to the ligand solution resulting in the formation of a orange solution. The reaction was stirred at RT overnight. The following day, the reaction solution was concentrated under vacuum and washed with diethyl ether (Et_2O) (2 mL, 3x) giving the desired product as an orange solid (148.4 mg, 17 mmol, 92%). X-ray diffraction quality crystals were obtained by slow vapor diffusion of Et_2O into a saturated acetonitrile solution resulting in the formation of orange block shaped single crystals over the course of a few days. ^{1}H NMR (400 MHz, CD_3CN) / δ (ppm): 82.42, 76.80, 71.91, 59.79, 50.47, 38.62, 37.57, 31.87, 31.09, 26.54, 24.49, 20.08, 18.89, 17.06, 12.89, 12.64, 12.59, 12.39, 9.83, 5.30, –6.17. Anal. Calcd. for $C_{37}H_{25}CoF_6N_5O_6S_2$: C, 50.92; H, 2.89; N, 8.03; S, 7.35. Found: C, 49.8; H, 2.93; N, 7.92; S, 7.38.

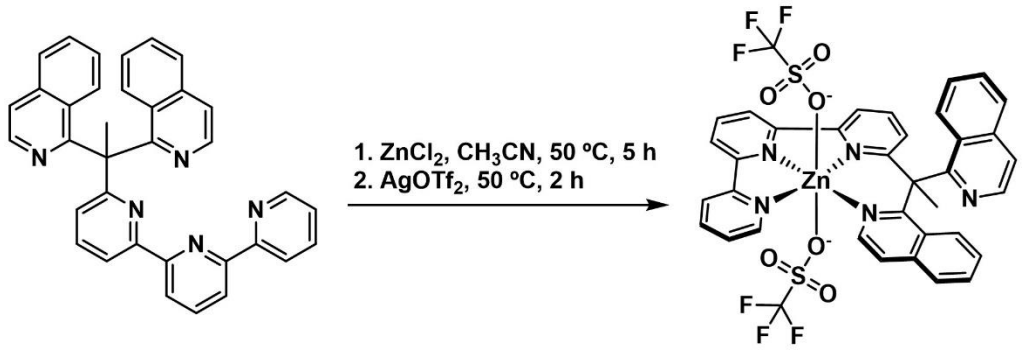
7.5.27 Synthesis of Ni(tpyIsoQuin2Me)(OTf)2 (Ni-tpyIsoQuin2Me)



In an N_2 filled glovebox, tpyIsoQuin2Me (100.0 mg, 0.19 mmol) was weighed into a 20 mL, oven dried scintillation vial equipped with a stir bar. Dry, degassed CH_3CN (9 mL) was added to the scintillation vial and the ligand solution was stirred at RT until fully solubilized. In a second 20 mL, oven dried scintillation vial was loaded $Ni(OTf)_2$ (69.2 mg, 0.19 mmol) and 9 mL dry, degassed CH_3CN. The ligand solution was then added to the $Ni(OTf)_2$ slurry. The reaction was heated to 50 ºC and stirred overnight over which the solution turns light yellow. The following

day, the reaction solution was concentrated under vacuum and washed with diethyl ether (Et_2O) (2 mL, 3x) giving the desired product as an tan solid (166 mg, 0.19 mmol, 100%). X-ray diffraction quality crystals were obtained by the slow diffusion of diethyl ether (Et_2O) into a saturated CH_3CN solution. ^{1}H NMR (400 MHz, CD_3CN) / δ (ppm): 81.60. 76.26, 72.79, 62.48, 60.66, 38.06, 29.41, 16.98, 14.14, 13.17, 12.61, 11.12, 9.21, 8.70, 8.62, 8.55, 8.47, 8.32, 7.92, 7.90, 7.81, 7.63, 7.54, 7.28, 7.12, 5.77, 2.73. Anal. Calcd. for $C_{37}H_{25}F_6N_5NiO_6S_2$: C, 50.94; H, 2.89; N, 8.03; S, 7.35. Found: C, 52.85; H, 3.03; N, 8.23; S, 6.91.

7.5.28 Synthesis of Zn(tpyIsoQuin2Me)(OTf)$_2$ (Zn-tpyIsoQuin2Me)



tpyIsoQuin2Me (104.0 mg, 0.20 mmol) was weighed into a 20 mL, oven dried scintillation vial equipped with a stir bar. Dry, degassed CH_3CN (9 mL) was added to the scintillation vial and the ligand solution was stirred at RT until fully solubilized. In a second 20 mL, oven dried scintillation vial was loaded $ZnCl_2$ (27.3 mg, 0.20 mmol) and 9 mL dry, degassed CH_3CN. The ligand solution was then added to the $ZnCl_2$ slurry with vigorous stirring. The reaction was heated to 50 C and stirred overnight over which the solution turns light yellow and precipitate forms. The following day, silver triflate (AgOTf) (107.9 mg, 0.41 mmol) was added as a solid to the reaction mixture resulting in the formation of a silver-grey solid. The mixture was then stirred at 50 ºC for an additional 2 h. After 2 h, the reaction mixture was filtered to remove the silver chloride and concentrated to give a white solid (166 mg, 0.19 mmol, 95%). The zinc complex was purified by crystallization by slow vapor diffusion of diethyl ether (Et_2O) into a saturated CH_3CN solution which resulted in clear, block shaped X-ray diffraction quality crystals. ^{1}H NMR (400 MHz, CD_3CN) / δ (ppm): 8.94 (dt, *J* = 5.0, 1.3 Hz, 1H), 8.88 (d, *J* = 5.7 Hz, 1H), 8.75 (d, *J* = 6.1 Hz, 1H), 8.73 – 8.68 (m, 2H), 8.64 – 8.57 (m, 2H), 8.43 (ddd, *J* = 15.9, 8.0, 1.2 Hz, 2H), 8.22 (d, *J* = 9.1 Hz, 1H), 8.12 (d, *J* = 6.0 Hz, 1H), 7.99 – 7.83 (m, 4H), 7.75 (d, *J* = 8.3 Hz, 1H), 7.62 (t, *J* = 7.7 Hz, 1H), 7.32 (q, *J* = 7.7 Hz, 2H), 6.97 (d, *J* = 8.4 Hz, 1H), 6.93 – 6.78 (m, 2H), 3.05 (s, 3H). Anal. Calcd. for $C_{37}H_{25}F_6N_5O_6S_2Zn$: C, 50.55; H, 2.87; N, 7.97; S, 7.29. Found: C, 48.3; H, 3.09; N, 7.65; S, 7.70.

7.5.29 X-Ray Crystallography Data

Table 7.7. Crystallographic data[a] for Fe-tpyQuin2Me.

	[Fe(tpyQuin2Me)(OTf)][OTf]
Chemical formula	$(C_{35}H_{25}FeN_5)•2(CF_3O_3S)•(C_4H_{10}O)$
FW	943.71
Crystal system, space group	Triclinic, *P-1*
Temperature (K)	100(2)
a (Å)	12.2354(3)
b (Å)	12.9627(3)
c (Å)	15.2146(3)
α	78.540(2)
β	72.494(2)
γ	61.869(3)
V (Å^3)	2024.85(10)
Z	2
μ (mm^{-1})	0.56
F(000)	968
Crystal size (mm)	0.19 × 0.12 × 0.08
θ range (°) for cell measurement	2.9–26.4
Radiation type	Mo *K*α
No. of reflections for cell measurement	17555
Index ranges	$-15 \le h \le 15$
	$-16 \le k \le 16$
	$-19 \le l \le 19$
Reflections collected / unique	42839 / 8269
R_{int}	0.035
Data / restraints / parameters	8269 / 0 / 562
Goodness-of-fit on F^2	1.018
Final R indices[b]	R_1 = 0.035, wR_2 = 0.081
Largest diff. peak and hole, eÅ^{-3}	0.50 and –0.40

[a]Obtained with a rotating-anode X-ray tube, Rigaku Mo K_α (λ = 0.71073 Å) X-ray source. [b]$R_1 = \sum||F_0| - F_C||/\sum|F_0|$, $R_2 = \{\sum[w(F_0^2 - F_0^2)^2]/\sum[w(F_0^2)^2]\}^{1/2}$.

Table 7.8. Crystallographic data[a] for Co-tpyQuin2Me.

	[Co(tpyQuin2Me)][OTf]$_2$
Chemical formula	$2(C_{35}H_{25}CoN_5)\bullet 4(CF_3O_3S)$
FW	1745.34
Crystal system, space group	Triclinic, *P-1*
Temperature (K)	100(2)
a (Å)	15.6171(6)
b (Å)	15.7928(6)
c (Å)	18.4546(7)
α	74.846(3)
β	89.276(3)
γ	64.342(4)
V (Å^3)	3933.6(3)
Z	2
μ (mm^{-1})	0.62
F(000)	1772
Crystal size (mm)	0.30 × 0.10 × 0.04
θ range (°) for cell measurement	3.0–28.5
Radiation type	Mo *K*α
No. of reflections for cell measurement	25790
Index ranges	$-21 \le h \le 20$
	$-21 \le k \le 20$
	$-24 \le l \le 24$
Reflections collected / unique	86980 / 18766
R_{int}	0.058
Data / restraints / parameters	18766 / 0 / 1046
Goodness-of-fit on F^2	1.055
Final R indices[b]	$R_1 = 0.108$, $wR_2 = 0.313$
Largest diff. peak and hole, eÅ^{-3}	2.0 and –1.8

[a]Obtained with a rotating-anode X-ray tube, Rigaku Mo K_α (λ = 0.71073 Å) X-ray source. [b]$R_1 = \sum||F_0| - F_C||/\sum|F_0|$, $R_2 = \{\sum[w(F_0^2 - F_0^2)^2]/\sum[w(F_0^2)^2]\}^{1/2}$.

Table 7.9. Crystallographic data[a] for Zn-tpyQuin2Me.

	[Zn(tpyQuin2Me)][OTf]$_2$
Chemical formula	$2(C_{35}H_{25}N_5Zn)•4(CF_3O_3S)•3(C_2H_3N)$
FW	1881.01
Crystal system, space group	Triclinic, *P-1*
Temperature (K)	100(2)
a (Å)	12.7721(3)
b (Å)	17.4899(3)
c (Å)	19.7906(4)
α	69.8152(17)
β	75.3718(17)
γ	76.8170(16)
V (Å^3)	3966.24(14)
Z	2
μ (mm^{-1})	0.81
F(000)	1915
Crystal size (mm)	0.08 × 0.17 × 0.19
θ range (°) for cell measurement	2.8–29.5
Radiation type	Mo *K*α
No. of reflections for cell measurement	14627
Index ranges	$-17 \leq h \leq 17$
	$-23 \leq k \leq 23$
	$-26 \leq l \leq 27$
Reflections collected / unique	89187 / 19030
R_{int}	0.049
Data / restraints / parameters	19030 / 0 / 1131
Goodness-of-fit on F^2	1.012
Final R indices[b]	$R_1 = 0.091$, $wR_2 = 0.260$
Largest diff. peak and hole, eÅ^{-3}	3.5 and –2.0

[a]Obtained with a rotating-anode X-ray tube, Rigaku Mo K_α (λ = 0.71073 Å) X-ray source. [b]$R_1 = \sum||F_0| - F_C||/\sum|F_0|$, $R_2 = \{\sum[w(F_0^2 - F_0^2)^2]/\sum[\, w(F_0^2)^2]\}^{1/2}$.

Table 7.10. Crystallographic data[a] for [Cr(tpyQuin2Me)(Cl)$_2$][Cl].

	[Cr(tpyQuin2Me)(Cl)$_2$][Cl]
Chemical formula	$C_{35}H_{25}Cl_3CrN_5$
FW	673.97
Crystal system, space group	Triclinic, *P-1*
Temperature (K)	100(2)
a (Å)	10.0834(2)
b (Å)	11.7525(2)
c (Å)	15.2209(4)
α	88.459(2)
β	72.147(2)
γ	83.740(2)
V (Å^3)	1706.62(7)
Z	2
μ (mm^{-1})	0.60
F(000)	968
Crystal size (mm)	0.26 × 0.24 × 0.03
θ range (°) for cell measurement	2.8–29.5
Radiation type	Mo *K*α
No. of reflections for cell measurement	20031
Index ranges	$-13 \le h \le 13$
	$-14 \le k \le 16$
	$-20 \le l \le 20$
Reflections collected / unique	38506 / 8255
R_{int}	0.035
Data / restraints / parameters	8255 / 0 / 330
Goodness-of-fit on F^2	2.353
Final R indices[b]	$R_1 = 0.143$, $wR_2 = 0.493$
Largest diff. peak and hole, eÅ^{-3}	3.5 and –5.2

[a]Obtained with a rotating-anode X-ray tube, Rigaku Mo K_α (λ = 0.71073 Å) X-ray source. [b]$R_1 = \sum||F_0| - F_C||/\sum|F_0|$, $R_2 = \{\sum[w(F_0^2 - F_0^2)^2]/\sum[\, w(F_0^2)^2]\}^{1/2}$.

Table 7.11. Crystallographic data[a] for [Cr(tpyQuin2Me)(Cl)$_2$][OTf].

	[Cr(tpyQuin2Me)(Cl)$_2$][OTf]
Chemical formula	$C_{35}H_{25}Cl_2CrN_5$•(CF_3O_3S)
FW	789.65
Crystal system, space group	Monoclinic, *P2$_1$/2*
Temperature (K)	100(2)
a (Å)	10.1462(3)
b (Å)	28.1423(9)
c (Å)	11.7555(4)
α	90
β	94.859(3)
γ	90
V (Å^3)	1706.62(7)
Z	4
μ (mm^{-1})	0.61
F(000)	1613
Crystal size (mm)	0.41 × 0.26 × 0.07
θ range (°) for cell measurement	2.9–29.5
Radiation type	Mo *K*α
No. of reflections for cell measurement	7097
Index ranges	–13 ≤ h ≤ 13
	–14 ≤ k ≤ 16
	–20 ≤ l ≤ 20
Reflections collected / unique	73589 / 8464
R_{int}	0.059
Data / restraints / parameters	8464 / 0 / 456
Goodness-of-fit on F^2	1.049
Final R indices[b]	R_1 = 0.0469, *w*R_2 = 0.1284
Largest diff. peak and hole, eÅ^{-3}	1.5 and –1.3

[a]Obtained with a rotating-anode X-ray tube, Rigaku Mo K_α (λ = 0.71073 Å) X-ray source. [b]$R_1 = \sum||F_0| - F_C||/\sum|F_0|$, $R_2 = \{\sum[w(F_0^2 - F_0^2)^2]/\sum[w(F_0^2)^2]\}^{1/2}$.

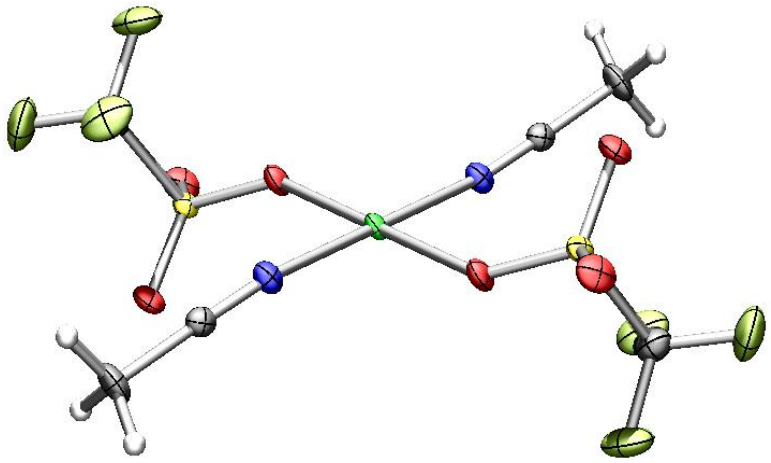


Figure 7.17. Solid state structures of $Cr(OTf)_2(CH_3CN)_2$. Thermal ellipsoids are potted at the 50% probability level. Green, grey, blue, red, yellow, yellow-green, and white signify Cr, C, N, O, S, F, and H, respectively.

Table 7.12. Crystallographic data[a] for $Cr(OTf)_2(CH_3CN)_2$.

	$Cr(OTf)_2(CH_3CN)_2$
Chemical formula	$C_3H_3Cr_{0.5}F_3NO_3S$
FW	216.12
Crystal system, space group	Monoclinic, $P2_1/n$
Temperature (K)	100(2)
a (Å)	10.6495(6)
b (Å)	5.1297(3)
c (Å)	13.4631(9)
α	90
β	99.003(6)
γ	90
V (Å^3)	726.41(8)
Z	4
μ (mm^{-1})	1.17
F(000)	428
Crystal size (mm)	0.14 × 0.12 × 0.60
θ range (°) for cell measurement	3.0–29.6
Radiation type	Mo $K\alpha$
No. of reflections for cell measurement	4627
Index ranges	$-14 \le h \le 14$
	$-6 \le k \le 6$
	$-16 \le l \le 18$
Reflections collected / unique	8454 / 1772
R_{int}	0.045
Data / restraints / parameters	1772 / 0 / 107
Goodness-of-fit on F^2	1.143
Final R indices[b]	$R_1 = 0.0363$, $wR_2 = 0.1106$
Largest diff. peak and hole, eÅ^{-3}	0.5 and –0.8

[a]Obtained with a rotating-anode X-ray tube, Rigaku Mo K_α (λ = 0.71073 Å) X-ray source. [b]$R_1 = \sum||F_0| - F_C||/\sum|F_0|$, $R_2 = \{\sum[w(F_0^2 - F_0^2)^2]/\sum[\, w(F_0^2)^2]\}^{1/2}$.

Table 7.13. Crystallographic data[a] for Fe-tpyIsoQuin2Me.

	Fe-tpyIsoQuin2Me
Chemical formula	$C_{35}H_{25}FeN_5$•2(CF_3O_3S)•(C_2H_3N)
FW	910.64
Crystal system, space group	Triclinic, *P-1*
Temperature (K)	100(2)
a (Å)	11.5263(12)
b (Å)	12.9946(8)
c (Å)	13.8524(9)
α	78.429(5)
β	72.511(7)
γ	77.386(7)
V (Å^3)	1910.7(3)
Z	2
μ (mm^{-1})	0.59
F(000)	928
Crystal size (mm)	0.10 × 0.12 × 0.15
θ range (°) for cell measurement	2.9–29.6
Radiation type	Mo *K*α
No. of reflections for cell measurement	10387
Index ranges	$-14 \leq h \leq 15$
	$-18 \leq k \leq 16$
	$-18 \leq l \leq 18$
Reflections collected / unique	44401 / 9365
R_{int}	0.077
Data / restraints / parameters	9365 / 0 / 543
Goodness-of-fit on F^2	1.036
Final R indices[b]	R_1 = 0.0538, wR_2 = 0.1517
Largest diff. peak and hole, eÅ^{-3}	1.4 and –0.5

[a]Obtained with a rotating-anode X-ray tube, Rigaku Mo K_α (λ = 0.71073 Å) X-ray source. [b]$R_1 = \sum||F_0| - F_C||/\sum|F_0|$, $R_2 = \{\sum[w(F_0^2 - F_0^2)^2]/\sum[\, w(F_0^2)^2]\}^{1/2}$.

Table 7.14. Crystallographic data[a] for Co-tpyIsoQuin2Me.

	Co-tpyIsoQuin2Me
Chemical formula	$C_{35}H_{25}CoN_5$•2(CF_3O_3S)•(C_2H_3N)
FW	913.72
Crystal system, space group	Triclinic, *P-1*
Temperature (K)	100(2)
a (Å)	12.0989(3)
b (Å)	12.4699(3)
c (Å)	13.9064(3)
α	111.360(2)
β	100.203(2)
γ	100.429(2)
V (Å^3)	1852.79(9)
Z	2
μ (mm^{-1})	0.67
F(000)	930
Crystal size (mm)	0.12 × 0.19 × 0.42
θ range (°) for cell measurement	2.9–29.6
Radiation type	Mo *K*α
No. of reflections for cell measurement	24625
Index ranges	$-16 \leq h \leq 16$
	$-17 \leq k \leq 17$
	$-19 \leq l \leq 19$
Reflections collected / unique	41599 / 9023
R_{int}	0.046
Data / restraints / parameters	9023 / 0 / 543
Goodness-of-fit on F^2	1.070
Final R indices[b]	R_1 = 0.0329, *w*R_2 = 0.0864
Largest diff. peak and hole, eÅ^{-3}	0.8 and –0.6

[a]Obtained with a rotating-anode X-ray tube, Rigaku Mo K_α (λ = 0.71073 Å) X-ray source. [b]$R_1 = \sum||F_0| - F_C||/\sum|F_0|$, $R_2 = \{\sum[w(F_0^2 - F_0^2)^2]/\sum[\, w(F_0^2)^2]\}^{1/2}$.

Table 7.15. Crystallographic data[a] for Ni-tpyIsoQuin2Me.

	Ni-tpyIsoQuin2Me
Chemical formula	$C_{35}H_{25}N_5Ni•2(CF_3O_3S)•(C_2H_3N)$
FW	914.56
Crystal system, space group	Triclinic, *P-1*
Temperature (K)	100(2)
a (Å)	12.0723(3)
b (Å)	12.5586(3)
c (Å)	13.8626(3)
α	110.702(2)
β	100.098(2)
γ	101.424(2)
V (Å^3)	1856.80(9)
Z	2
μ (mm^{-1})	0.72
F(000)	932
Crystal size (mm)	0.10 × 0.13 × 0.29
θ range (°) for cell measurement	2.9–29.6
Radiation type	Mo *K*α
No. of reflections for cell measurement	21043
Index ranges	$-16 \le h \le 15$
	$-15 \le k \le 16$
	$-18 \le l \le 19$
Reflections collected / unique	41293 / 9016
R_{int}	0.057
Data / restraints / parameters	9016 / 0 / 543
Goodness-of-fit on F^2	1.063
Final R indices[b]	R_1 = 0.0319, wR_2 = 0.0802
Largest diff. peak and hole, eÅ^{-3}	0.4 and –0.4

[a]Obtained with a rotating-anode X-ray tube, Rigaku Mo K_α (λ = 0.71073 Å) X-ray source. [b]$R_1 = \sum||F_0| - F_C||/\sum|F_0|$, $R_2 = \{\sum[w(F_0^2 - F_0^2)^2]/\sum[\, w(F_0^2)^2]\}^{1/2}$.

Table 7.16. Crystallographic data[a] for Zn-tpyIsoQuin2Me.

	Zn-tpyIsoQuin2Me
Chemical formula	$C_{35}H_{25}N_5Zn•2(CF_3O_3S)•(C_2H_3N)$
FW	920.17
Crystal system, space group	Triclinic, *P-1*
Temperature (K)	100(2)
a (Å)	12.1748(5)
b (Å)	12.5317(5)
c (Å)	13.8818(6)
α	110.685(4)
β	100.700(3)
γ	101.154(3)
V (Å^3)	1868.08(15)
Z	2
μ (mm^{-1})	0.86
F(000)	936
Crystal size (mm)	0.31 × 0.17 × 0.14
θ range (°) for cell measurement	2.9–29.5
Radiation type	Mo *K*α
No. of reflections for cell measurement	12387
Index ranges	$-16 \le h \le 15$
	$-16 \le k \le 17$
	$-18 \le l \le 17$
Reflections collected / unique	42244 / 9006
R_{int}	0.082
Data / restraints / parameters	9006 / 0 / 543
Goodness-of-fit on F^2	0.871
Final R indices[b]	R_1 = 0.0432, wR_2 = 0.1304
Largest diff. peak and hole, eÅ^{-3}	0.8 and –0.7

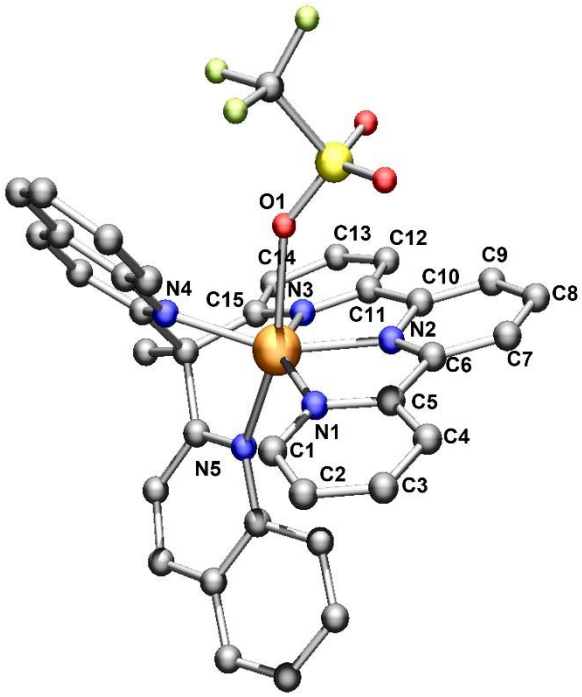
[a]Obtained with a rotating-anode X-ray tube, Rigaku Mo K_α (λ = 0.71073 Å) X-ray source. [b]$R_1 = \sum||F_0| - F_C||/\sum|F_0|$, $R_2 = \{\sum[w(F_0^2 - F_0^2)^2]/\sum[w(F_0^2)^2]\}^{1/2}$.

Table 7.17. Crystallographic data[a] for [Cr(tpyIsoQuin2Me)(Cl)$_2$][Cl].

	[Cr(tpyIsoQuin2Me)(Cl)$_2$][Cl].
Chemical formula	$C_{35}H_{25}Cl_3CrN_5$•(CH_4O)
FW	706.01
Crystal system, space group	Triclinic, *P-1*
Temperature (K)	100(2)
a (Å)	8.7692(3)
b (Å)	12.7878(4)
c (Å)	15.0660(4)
α	69.672(3)
β	79.998(2)
γ	89.268(2)
V (Å^3)	1558.11(9)
Z	2
μ (mm^{-1})	0.66
F(000)	726
Crystal size (mm)	0.32 × 0.16 × 0.13
θ range (°) for cell measurement	3.0–29.6
Radiation type	Mo *K*α
No. of reflections for cell measurement	18407
Index ranges	$-12 \leq h \leq 11$
	$-17 \leq k \leq 17$
	$-18 \leq l \leq 20$
Reflections collected / unique	35113 / 7466
R_{int}	0.040
Data / restraints / parameters	7466 / 0 / 418
Goodness-of-fit on F^2	1.080
Final R indices[b]	R_1 = 0.0311, wR_2 = 0.0864
Largest diff. peak and hole, eÅ^{-3}	0.7 and –0.7

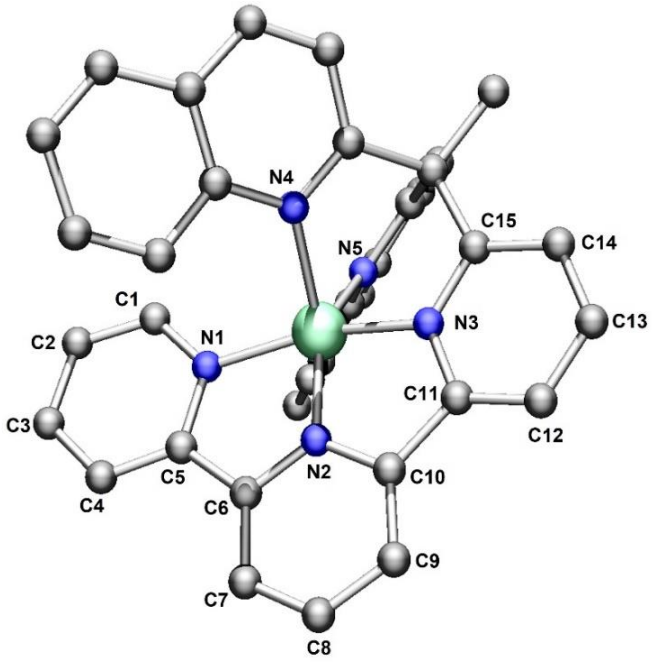
[a]Obtained with a rotating-anode X-ray tube, Rigaku Mo K_α (λ = 0.71073 Å) X-ray source. [b]$R_1 = \sum||F_0| - F_C||/\sum|F_0|$, $R_2 = \{\sum[w(F_0^2 - F_0^2)^2]/\sum[w(F_0^2)^2]\}^{1/2}$.

Table 7.18. Selected bond lengths (Å) and angles (°) for Fe-tpyQuin2Me.



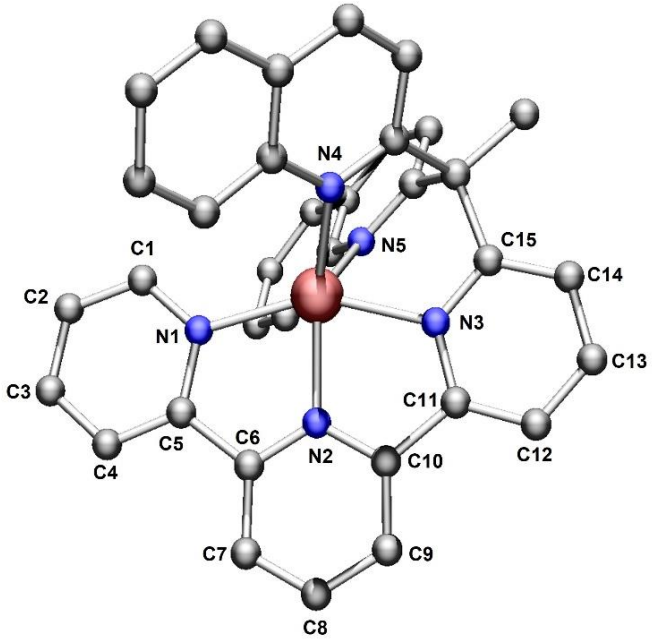
Atoms	Distance	Atoms	Distance
Fe1–N1	2.1909(15)	C2–C3	1.377(3)
Fe1–N2	2.1018(14)	C3–C4	1.388(3)
Fe1–N3	2.1218(15)	C4–C5	1.382(3)
Fe1–N4	2.1688(14)	C5–C6	1.481(3)
Fe1–N5	2.2119(16)	C6–C7	1.385(3)
Fe1–O1	2.2422(14)	C7–C8	1.388(3)
N1–C1	1.344(2)	C8–C9	1.384(3)
N1–C5	1.359(2)	C9–C10	1.386(3)
N2–C6	1.341(2)	C10–C11	1.482(2)
N2–C10	1.345(2)	C11–C12	1.383(3)
N3–C11	1.348(2)	C12–C13	1.382(3)
N3–C15	1.339(2)	C13–C14	1.383(3)
C1–C2	1.379(3)	C14–C15	1.392(3)
Atoms	**Angle (º)**	**Atoms**	**Angle (º)**
N1–Fe1–N2	74.82(6)	N2–Fe1–N5	109.61(6)
N2–Fe1–N3	74.74(6)	N3–Fe1–N5	77.81(6)
N3–Fe1–N4	90.03(6)	N1–Fe1–O1	95.36(6)
N4–Fe1–N5	83.32(6)	N2–Fe1–O1	82.58(5)
N1–Fe1–N4	121.88(6)	N3–Fe1–O1	89.99(6)
O1–Fe1–N5	159.32(5)	N4–Fe1–O1	80.02(6)
N1–Fe1–N5	103.84(6)		

Table 7.19. Selected bond lengths (Å) and angles (°) for Co-tpyQuin2Me.



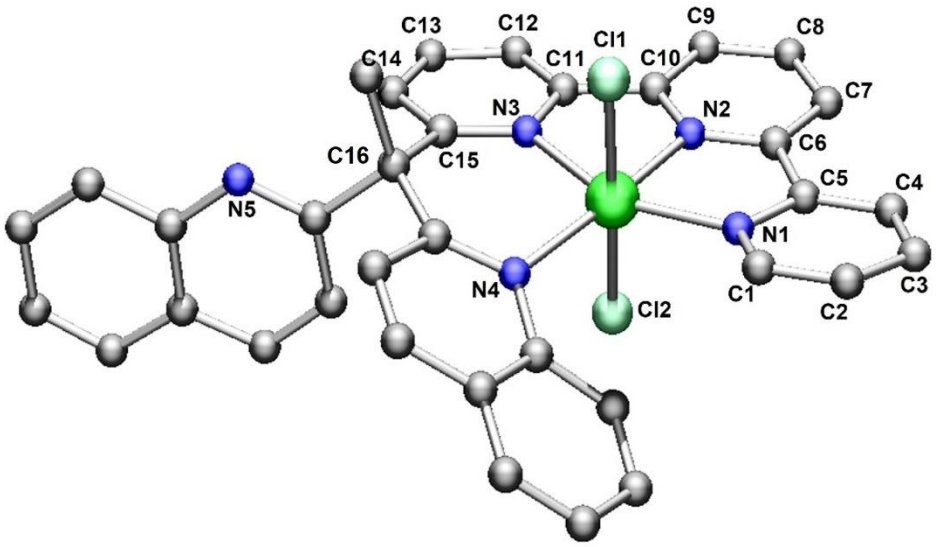
Atoms	Distance	Atoms	Distance
Co1–N1	1.960(4)	C3–C4	1.411(11)
Co1–N2	1.857(4)	C4–C5	1.372(8)
Co1–N3	1.898(4)	C5–C6	1.464(8)
Co1–N4	2.079(5)	C6–C7	1.383(7)
Co1–N5	1.985(4)	C7–C8	1.386(9)
N1–C1	1.329(7)	C8–C9	1.384(8)
N1–C5	1.360(7)	C9–C10	1.387(7)
N2–C6	1.349(6)	C10–C11	1.467(7)
N2–C10	1.357(6)	C11–C12	1.386(6)
N3–C11	1.348(6)	C12–C13	1.380(7)
N3–C15	1.344(6)	C13–C14	1.376(8)
C1–C2	1.342(10)	C14–C15	1.402(7)
C2–C3	1.406(12)		
Atoms	**Angle (º)**	**Atoms**	**Angle (º)**
N1–Co1–N2	81.51(18)	N1–Co1–N5	106.76(17)
N2–Co1–N3	81.91(17)	N2–Co1–N5	145.59(16)
N3–Co1–N4	86.05(17)	N3–Co1–N5	89.17(16)
N4–Co1–N5	91.68(17)	N2–Co1–N4	120.52(16)
N1–Co1–N4	99.07(18)		

Table 7.20. Selected bond lengths (Å) and angles (°) for Zn-tpyQuin2Me.



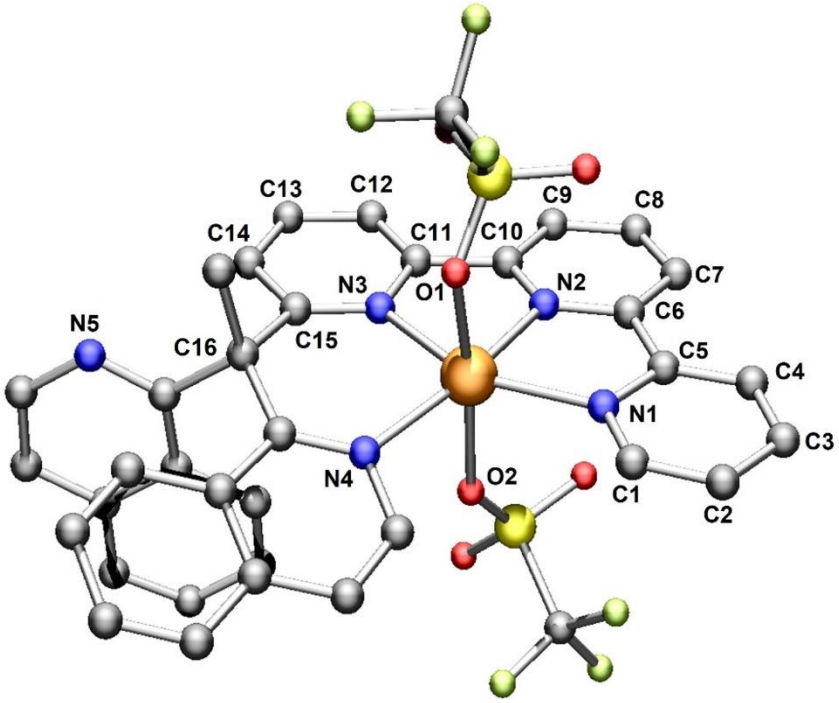
Atoms	Distance	Atoms	Distance
Zn1–N1	2.099(6)	C3–C4	1.393(13)
Zn1–N2	2.045(6)	C4–C5	1.384(11)
Zn1–N3	2.090(6)	C5–C6	1.487(11)
Zn1–N4	2.037(6)	C6–C7	1.377(13)
Zn1–N5	2.061(6)	C7–C8	1.360(15)
N1–C1	1.340(10)	C8–C9	1.391(14)
N1–C5	1.356(10)	C9–C10	1.393(12)
N2–C6	1.339(10)	C10–C11	1.487(11)
N2–C10	1.340(10)	C11–C12	1.401(11)
N3–C11	1.335(10)	C12–C13	1.376(13)
N3–C15	1.337(10)	C13–C14	1.384(12)
C1–C2	1.392(10)	C14–C15	1.386(10)
C2–C3	1.361(13)		
Atoms	**Angle (º)**	**Atoms**	**Angle (º)**
N1–Zn1–N2	77.6(2)	N1–Zn1–N5	113.5(2)
N2–Zn1–N3	75.6(2)	N2–Zn1–N5	131.6(2)
N3–Zn1–N4	85.1(2)	N3–Zn1–N5	85.4(2)
N4–Zn1–N5	95.2(2)	N2–Zn1–N4	126.1(2)
N1–Zn1–N4	110.5(2)		

Table 7.21. Selected bond lengths (Å) and angles (°) for [Cr(tpyQuin2Me)(Cl)$_2$][OTf].



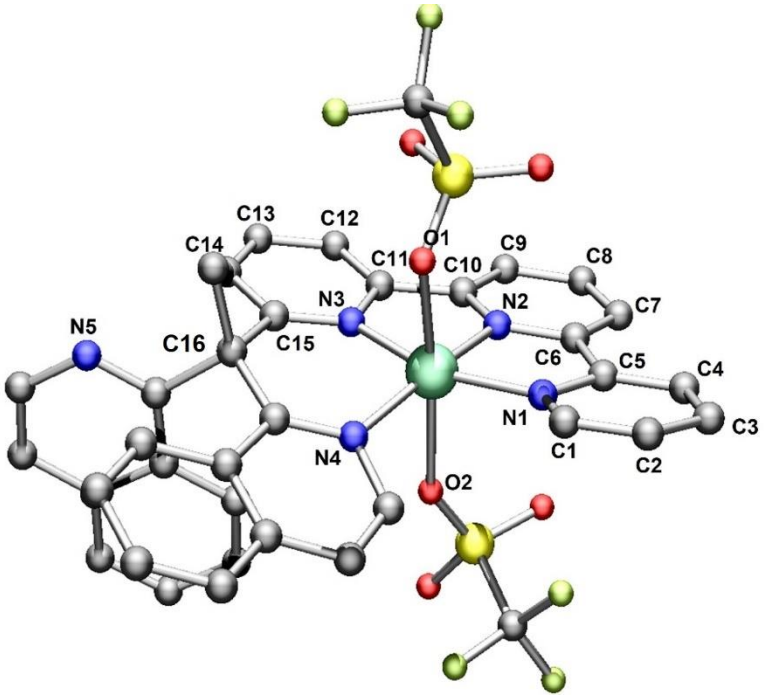
Atoms	Distance	Atoms	Distance
Cr1–N1	2.1231(18)	C2–C3	1.383(4)
Cr1–N2	1.9952(19)	C3–C4	1.382(3)
Cr1–N3	2.0443(19)	C4–C5	1.388(3)
Cr1–N4	2.0981(18)	C5–C6	1.475(3)
Cr1–Cl1	2.3000(6)	C6–C7	1.385(3)
Cr1–Cl2	2.3192(6)	C7–C8	1.389(4)
N1–C1	1.347(3)	C8–C9	1.384(4)
N1–C5	1.355(3)	C9–C10	1.396(3)
N2–C6	1.345(3)	C10–C11	1.469(3)
N2–C10	1.340(3)	C11–C12	1.383(3)
N3–C11	1.373(3)	C12–C13	1.381(3)
N3–C15	1.340(3)	C13–C14	1.378(3)
C1–C2	1.383(3)	C14–C15	1.408(3)
Atoms	**Angle (º)**	**Atoms**	**Angle (º)**
N1–Cr1–N2	77.00(7)	N4–Cr1–Cl1	91.42(5)
N2–Cr1–N3	79.38(7)	N1–Cr1–Cl2	96.99(5)
N3–Cr1–N4	93.32(7)	N2–Cr1–Cl2	85.94(6)
N4–Cr1–N1	110.82(7)	N3–Cr1–Cl2	88.07(5)
N1–Cr1–Cl1	84.93(5)	N4–Cr1–Cl2	88.51(5)
N2–Cr1–Cl1	93.88(6)	Cl1–Cr1–Cl2	177.97(2)
N3–Cr1–Cl1	89.92(5)		

Table 7.22. Selected bond lengths (Å) and angles (°) for Fe-tpyIsoQuin2Me.



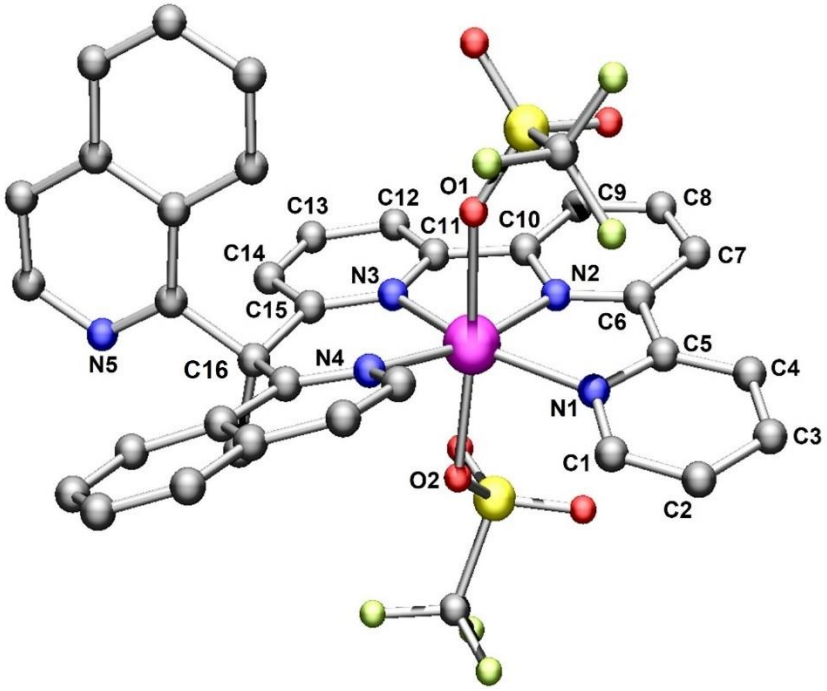
Atoms	Distance	Atoms	Distance
Fe1–N1	2.204(2)	C2–C3	1.390(4)
Fe1–N2	2.071(2)	C3–C4	1.378(5)
Fe1–N3	2.145(2)	C4–C5	1.386(4)
Fe1–N4	2.088(2)	C5–C6	1.477(4)
Fe1–O1	2.1587(19)	C6–C7	1.379(4)
Fe1–O2	2.197(2)	C7–C8	1.381(5)
N1–C1	1.346(4)	C8–C9	1.379(4)
N1–C5	1.358(4)	C9–C10	1.391(4)
N2–C6	1.348(4)	C10–C11	1.483(4)
N2–C10	1.330(4)	C11–C12	1.374(4)
N3–C11	1.372(3)	C12–C13	1.379(4)
N3–C15	1.339(3)	C13–C14	1.378(4)
C1–C2	1.385(4)	C14–C15	1.396(4)
Atoms	**Angle (º)**	**Atoms**	**Angle (º)**
N1–Fe1–N2	75.55(9)	N4–Fe1–O1	90.85(8)
N2–Fe1–N3	76.82(9)	N1–Fe1–O2	90.75(8)
N3–Fe1–N4	87.64(9)	N2–Fe1–O2	90.28(8)
N4–Fe1–N1	119.85(9)	N3–Fe1–O2	91.15(8)
N1–Fe1–O1	90.17(8)	N4–Fe1–O2	79.66(8)
N2–Fe1–O1	100.05(8)	O1–Fe1–O2	169.53(7)
N3–Fe1–O1	92.87(8)		

Table 7.23. Selected bond lengths (Å) and angles (°) for Co-tpyIsoQuin2Me.



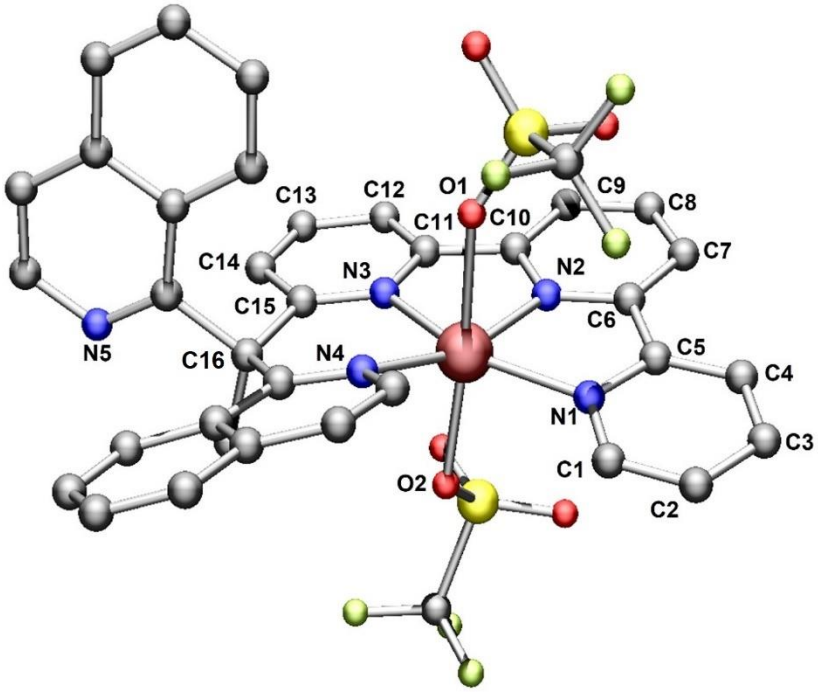
Atoms	Distance	Atoms	Distance
Co1–N1	2.0379(13)	C2–C3	1.378(2)
Co1–N2	1.8817(13)	C3–C4	1.386(2)
Co1–N3	1.9340(13)	C4–C5	1.384(2)
Co1–N4	1.9723(13)	C5–C6	1.469(2)
Co1–O1	2.2869(11)	C6–C7	1.389(2)
Co1–O2	2.2519(11)	C7–C8	1.383(2)
N1–C1	1.343(2)	C8–C9	1.390(2)
N1–C5	1.363(2)	C9–C10	1.389(2)
N2–C6	1.344(2)	C10–C11	1.468(2)
N2–C10	1.344(2)	C11–C12	1.379(2)
N3–C11	1.376(2)	C12–C13	1.389(2)
N3–C15	1.340(2)	C13–C14	1.375(2)
C1–C2	1.383(2)	C14–C15	1.407(2)
Atoms	**Angle (º)**	**Atoms**	**Angle (º)**
N1–Co1–N2	79.91(5)	N4–Co1–O1	82.04(5)
N2–Co1–N3	82.62(6)	N1–Co1–O2	85.56(5)
N3–Co1–N4	93.49(5)	N2–Co1–O2	102.08(5)
N4–Co1–N1	104.94(5)	N3–Co1–O2	91.19(5)
N1–Co1–O1	94.32(5)	N4–Co1–O2	97.80(5)
N2–Co1–O1	88.25(5)	O1–Co1–O2	169.47(4)
N3–Co1–O1	92.22(5)		

Table 7.24. Selected bond lengths (Å) and angles (°) for Ni-tpyIsoQuin2Me.



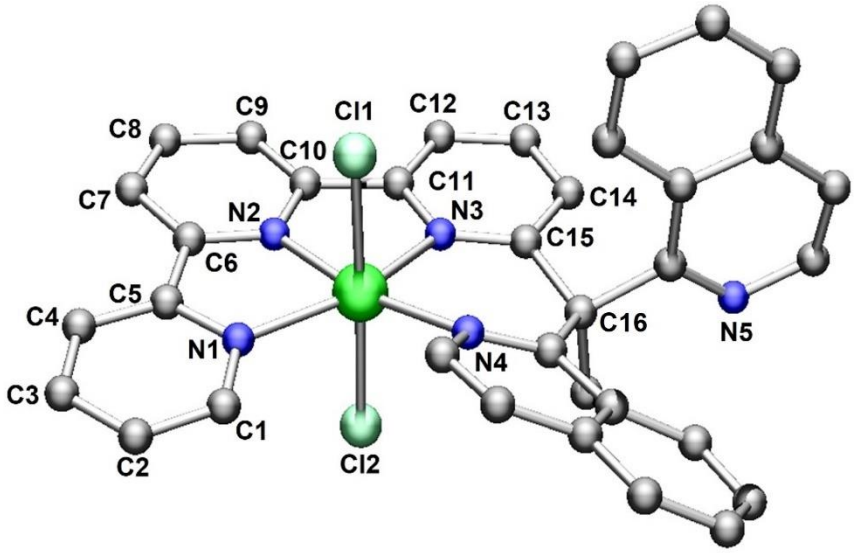
Atoms	Distance	Atoms	Distance
Ni1–N1	2.1426(13)	C2–C3	1.384(2)
Ni1–N2	1.9794(12)	C3–C4	1.385(2)
Ni1–N3	2.0296(13)	C4–C5	1.383(2)
Ni1–N4	2.0306(12)	C5–C6	1.483(2)
Ni1–O1	2.1593(11)	C6–C7	1.394(2)
Ni1–O2	2.1277(10)	C7–C8	1.386(2)
N1–C1	1.3396(19)	C8–C9	1.387(2)
N1–C5	1.3584(19)	C9–C10	1.391(2)
N2–C6	1.332(2)	C10–C11	1.482(2)
N2–C10	1.3376(19)	C11–C12	1.380(2)
N3–C11	1.3656(18)	C12–C13	1.387(2)
N3–C15	1.3338(19)	C13–C14	1.378(2)
C1–C2	1.381(2)	C14–C15	1.403(2)
Atoms	**Angle (º)**	**Atoms**	**Angle (º)**
N1–Ni1–N2	77.59(5)	N4–Ni1–O1	82.01(4)
N2–Ni1–N3	80.62(5)	N1–Ni1–O2	87.00(4)
N3–Ni1–N4	91.99(5)	N2–Ni1–O2	100.22(5)
N4–Ni1–N1	110.48(5)	N3–Ni1–O2	91.04(5)
N1–Ni1–O1	93.67(4)	N4–Ni1–O2	89.10(4)
N2–Ni1–O1	88.92(5)	O1–Ni1–O2	170.75(4)
N3–Ni1–O1	91.83(5)		

Table 7.25. Selected bond lengths (Å) and angles (°) for Zn-tpyIsoQuin2Me.



Atoms	Distance	Atoms	Distance
Zn1–N1	2.157(2)	C2–C3	1.382(4)
Zn1–N2	2.0400(19)	C3–C4	1.388(4)
Zn1–N3	2.107(2)	C4–C5	1.382(4)
Zn1–N4	2.0343(19)	C5–C6	1.482(3)
Zn1–O1	2.3157(17)	C6–C7	1.389(3)
Zn1–O2	2.1639(17)	C7–C8	1.385(4)
N1–C1	1.340(3)	C8–C9	1.383(4)
N1–C5	1.355(3)	C9–C10	1.388(3)
N2–C6	1.337(3)	C10–C11	1.484(3)
N2–C10	1.331(3)	C11–C12	1.384(4)
N3–C11	1.359(3)	C12–C13	1.384(4)
N3–C15	1.334(3)	C13–C14	1.380(3)
C1–C2	1.385(4)	C14–C15	1.401(3)
Atoms	**Angle (º)**	**Atoms**	**Angle (º)**
N1–Zn1–N2	77.05(8)	N4–Zn1–O1	79.98(7)
N2–Zn1–N3	77.86(8)	N1–Zn1–O2	89.04(7)
N3–Zn1–N4	90.76(8)	N2–Zn1–O2	103.12(7)
N4–Zn1–N1	114.59(8)	N3–Zn1–O2	92.67(7)
N1–Zn1–O1	91.88(7)	N4–Zn1–O2	91.12(7)
N2–Zn1–O1	86.21(7)	O1–Zn1–O2	170.58(6)
N3–Zn1–O1	90.52(7)		

Table 7.26. Selected bond lengths (Å) and angles (°) for [Cr(tpyIsoQuin2Me)(Cl)$_2$][OTf].



Atoms	Distance	Atoms	Distance
Cr1–N1	2.1126(13)	C2–C3	1.381(2)
Cr1–N2	1.9831(12)	C3–C4	1.381(2)
Cr1–N3	2.0347(13)	C4–C5	1.388(2)
Cr1–N4	2.0605(12)	C5–C6	1.467(2)
Cr1–Cl1	2.3171(4)	C6–C7	1.393(2)
Cr1–Cl2	2.2793(4)	C7–C8	1.387(2)
N1–C1	1.335(2)	C8–C9	1.389(2)
N1–C5	1.3640(19)	C9–C10	1.389(2)
N2–C6	1.3395(19)	C10–C11	1.474(2)
N2–C10	1.339(2)	C11–C12	1.378(2)
N3–C11	1.3709(19)	C12–C13	1.380(2)
N3–C15	1.3409(19)	C13–C14	1.380(2)
C1–C2	1.394(2)	C14–C15	1.401(2)
Atoms	**Angle (º)**	**Atoms**	**Angle (º)**
N1–Cr1–N2	77.61(5)	N4–Cr1–Cl1	86.26(4)
N2–Cr1–N3	80.45(5)	N1–Cr1–Cl2	86.40(4)
N3–Cr1–N4	90.58(5)	N2–Cr1–Cl2	93.30(4)
N4–Cr1–N1	111.72(5)	N3–Cr1–Cl2	90.44(4)
N1–Cr1–Cl1	90.55(4)	N4–Cr1–Cl2	93.24(4)
N2–Cr1–Cl1	87.74(4)	Cl1–Cr1–Cl2	176.485(17)
N3–Cr1–Cl1	93.04(4)		

7.5.30 Supplemental Controlled Potential Electrolysis Data

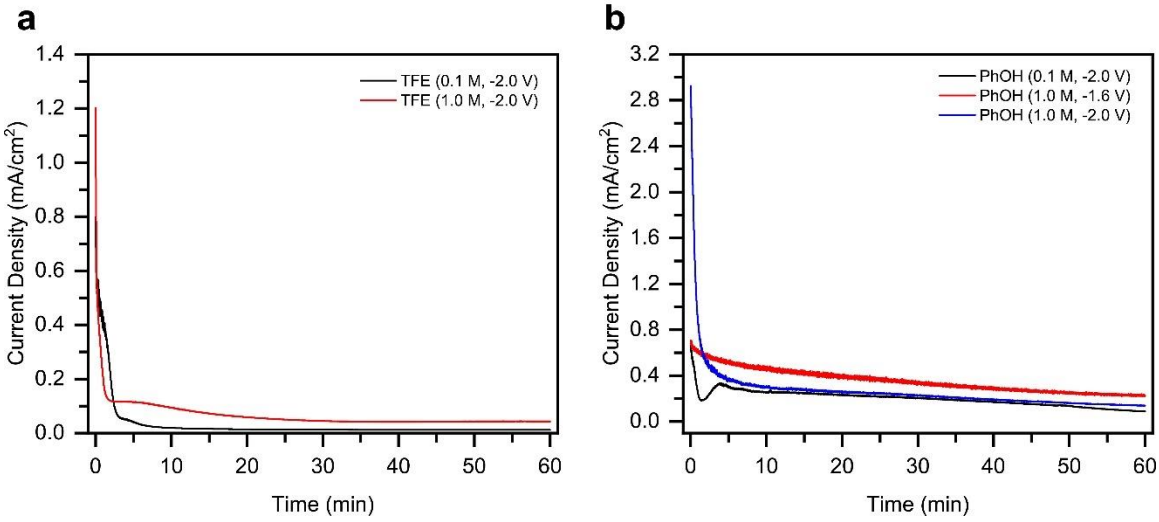


Figure 7.18. Controlled potential electrolysis of Fe-tpyQuin2Me under CO_2 atmosphere. CPE experiments were conducted at varying potentials in the presence of either (a) TFE or (b) PhOH as a proton source. Conditions: 1 mM Fe-tpyQuin2Me; 0.10 M $TBAPF_6/CH_3CN$; 0.1 M or 1.0 M of TFE or PhOH.

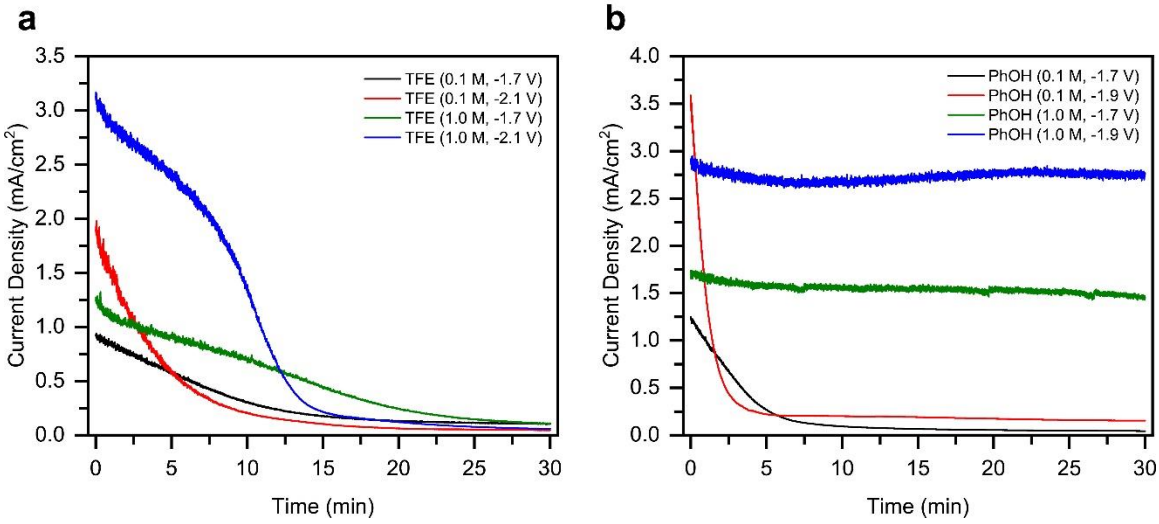


Figure 7.19. Controlled potential electrolysis of Co-tpyQuin2Me under CO_2 atmosphere. CPE experiments were conducted at varying potentials in the presence of either (a) TFE or (b) PhOH as a proton source. Conditions: 1 mM Co-tpyQuin2Me; 0.10 M $TBAPF_6/CH_3CN$; 0.1 M or 1.0 M of TFE or PhOH.

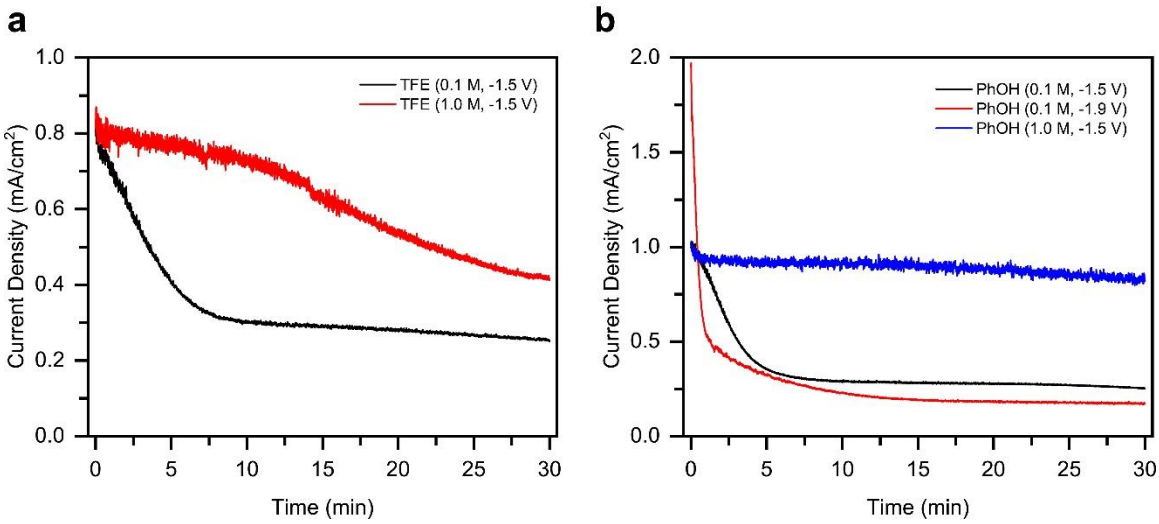


Figure 7.20. Controlled potential electrolysis of Ni-tpyQuin2Me under CO_2 atmosphere. CPE experiments were conducted at varying potentials in the presence of either (a) TFE or (b) PhOH as a proton source. Conditions: 1 mM Ni-tpyQuin2Me; 0.10 M $TBAPF_6/CH_3CN$; 0.1 M or 1.0 M of TFE or PhOH.

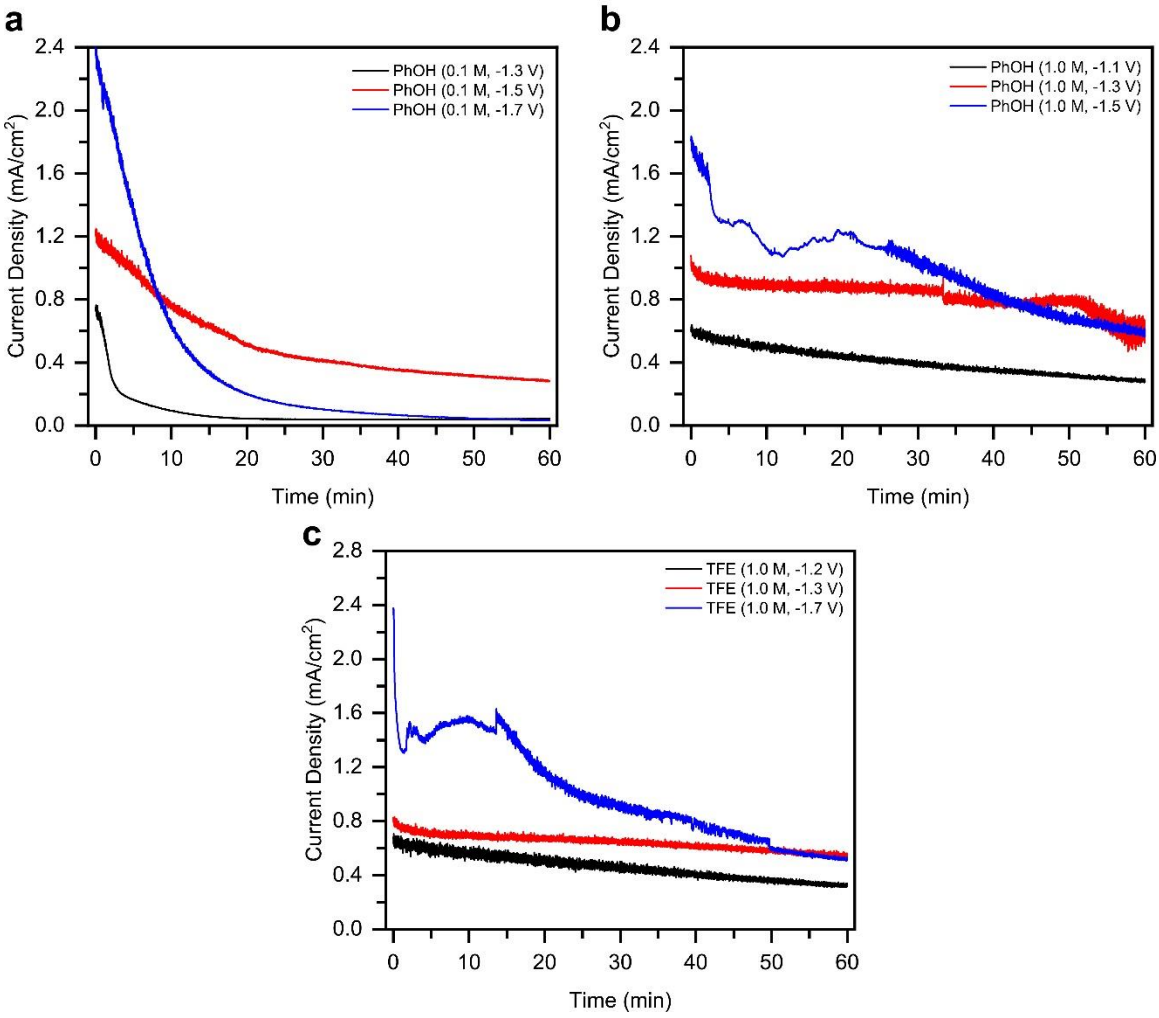


Figure 7.21. Controlled potential electrolysis of Co-tpyIsoQuin2Me under CO_2 atmosphere. CPE experiments were conducted at varying potentials in the presence of either (a) TFE or (b) PhOH as a proton source. Conditions: 1 mM Co-tpyIsoQuin2Me; 0.10 M $TBAPF_6/CH_3CN$; 0.1 M or 1.0 M of TFE or PhOH.

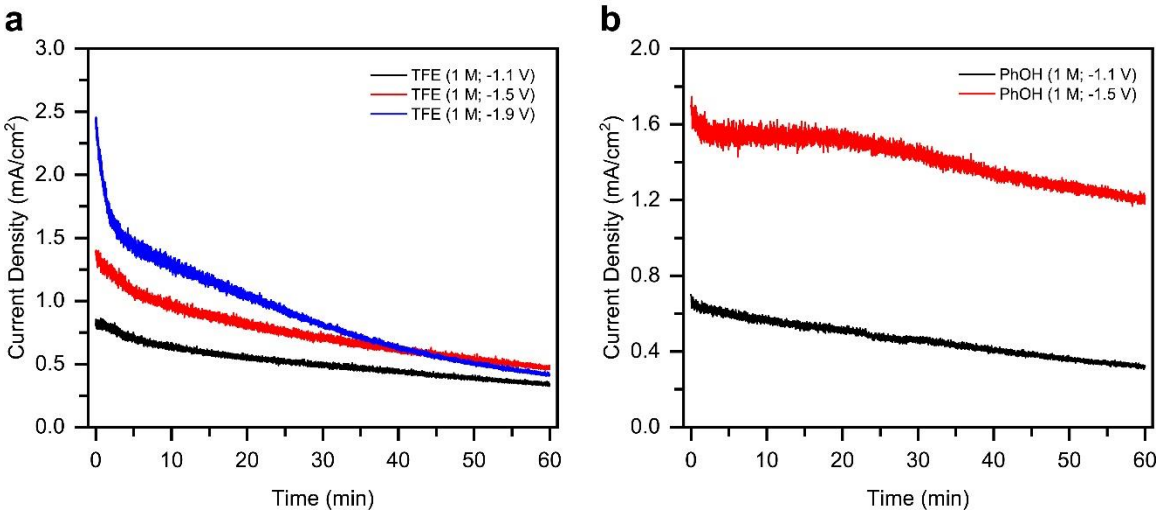


Figure 7.22. Controlled potential electrolysis of Ni-tpyIsoQuin2Me under CO_2 atmosphere. CPE experiments were conducted at varying potentials in the presence of either (a) TFE or (b) PhOH as a proton source. Conditions: 1 mM Ni-tpyIsoQuin2Me; 0.10 M $TBAPF_6/CH_3CN$; 0.1 M or 1.0 M of TFE or PhOH.

7.5.31 NMR Spectra

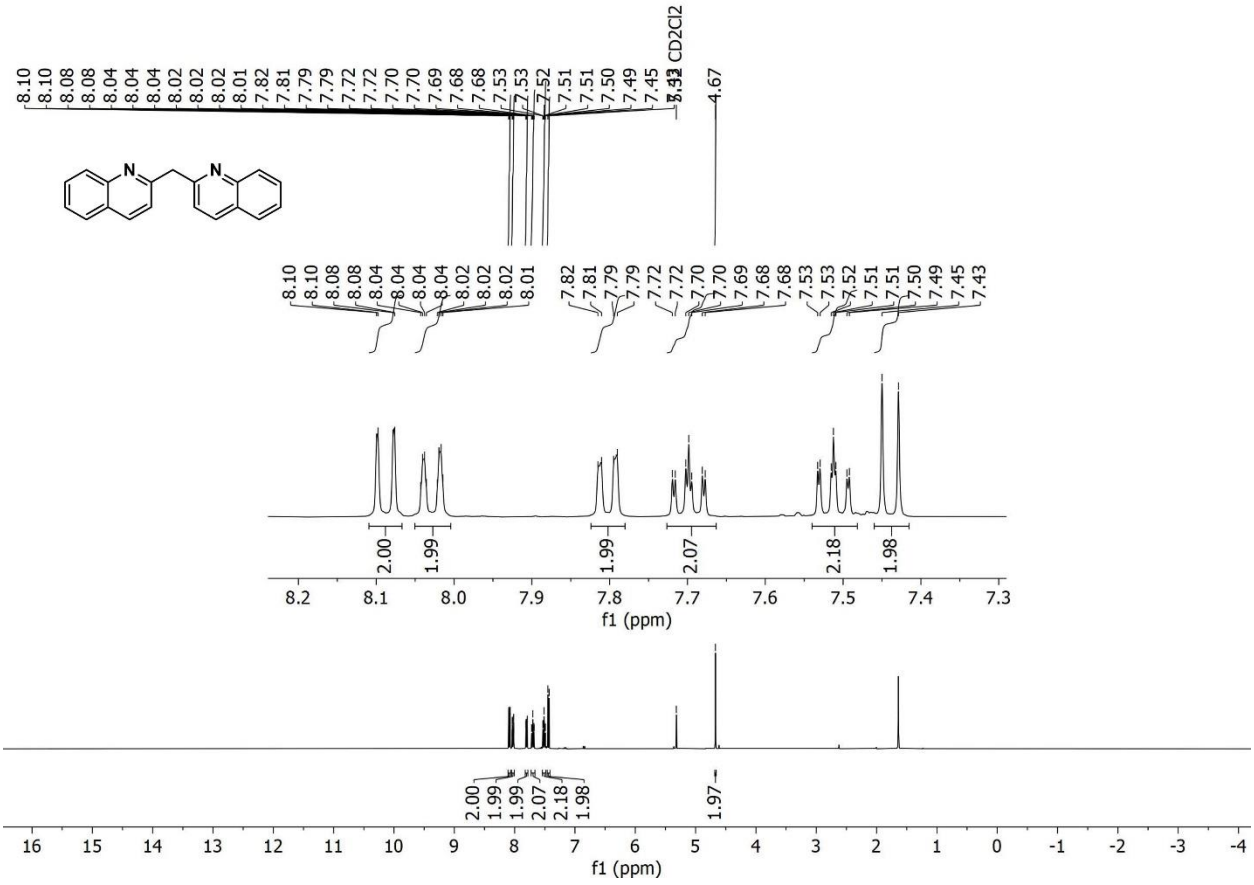


Figure 7.23. ^{1}H NMR of di(quinolin-2-yl)methane (**7a**) in CD_2Cl_2.

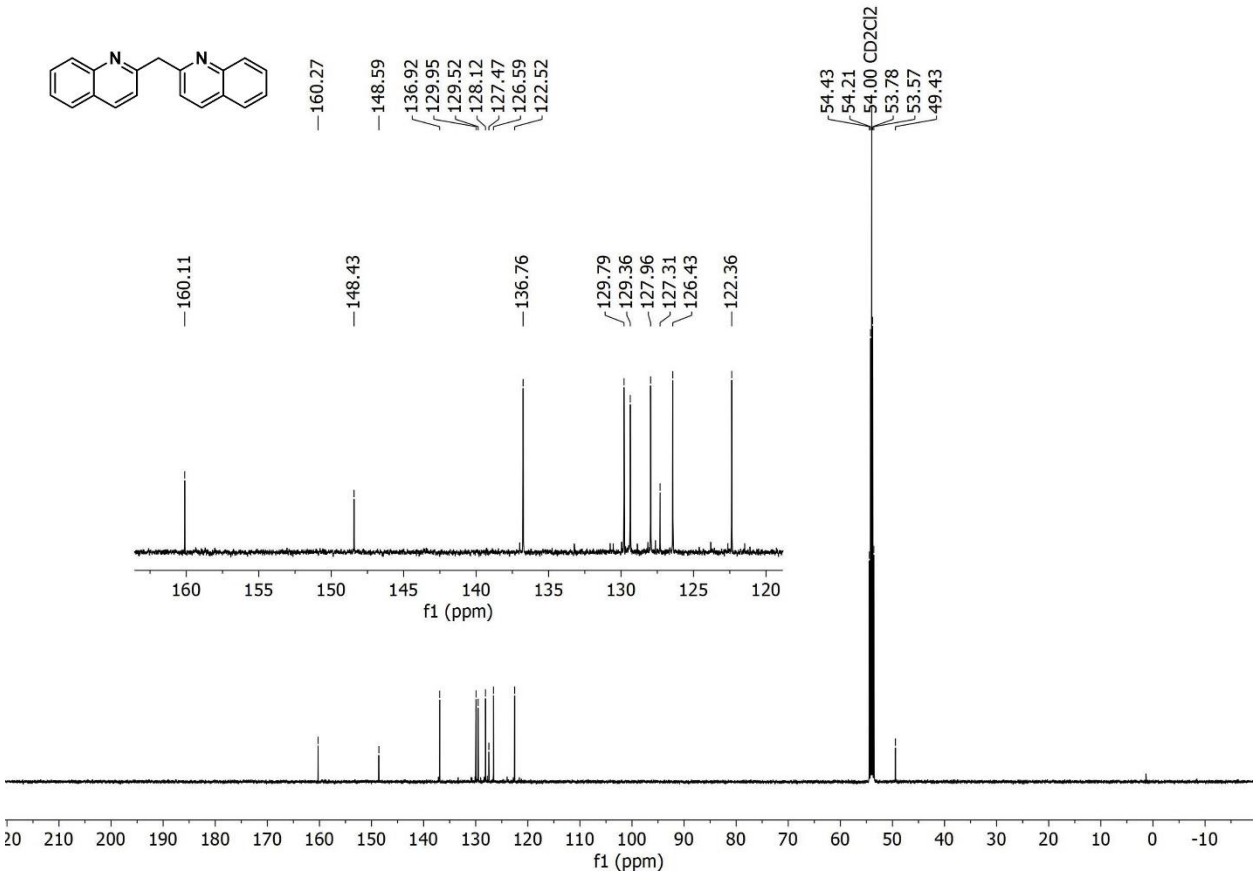


Figure 7.24. ^{13}C NMR of di(quinolin-2-yl)methane (**7a**) in CD_2Cl_2.

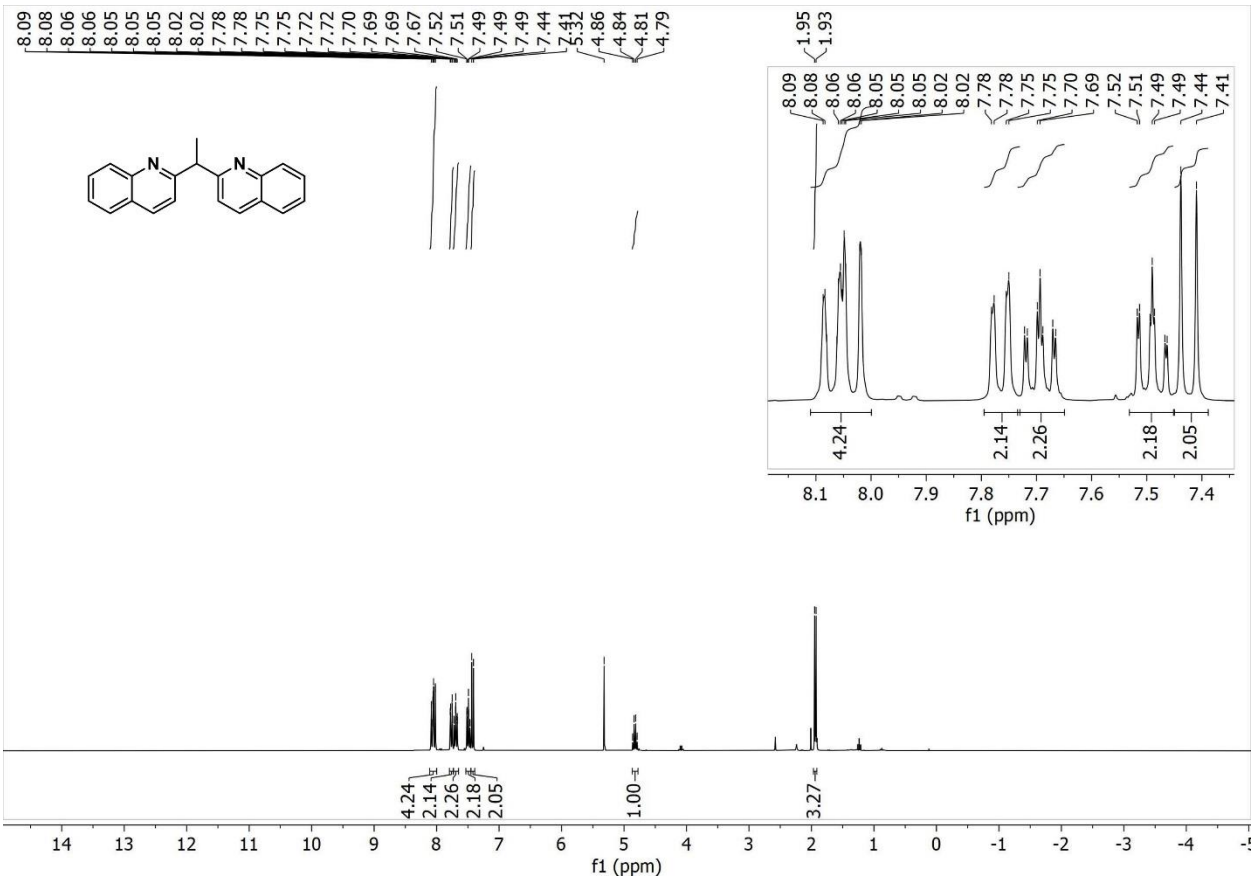


Figure 7.25. ^{1}H NMR of 2,2'-(ethane-1,1-diyl)diquinoline (**7b**) in CD_2Cl_2.

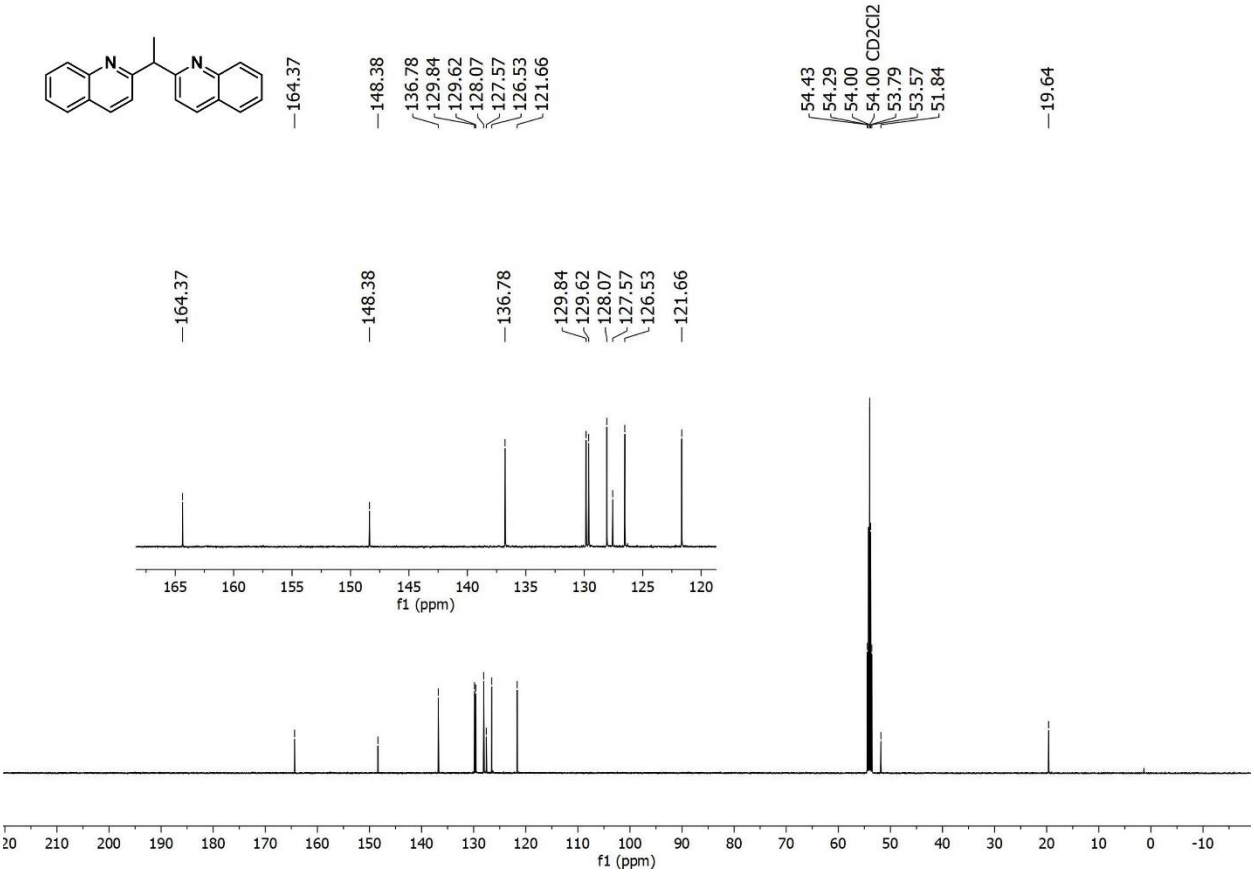


Figure 7.26. ^{13}C NMR of 2,2'-(ethane-1,1-diyl)diquinoline (**7b**) in CD_2Cl_2.

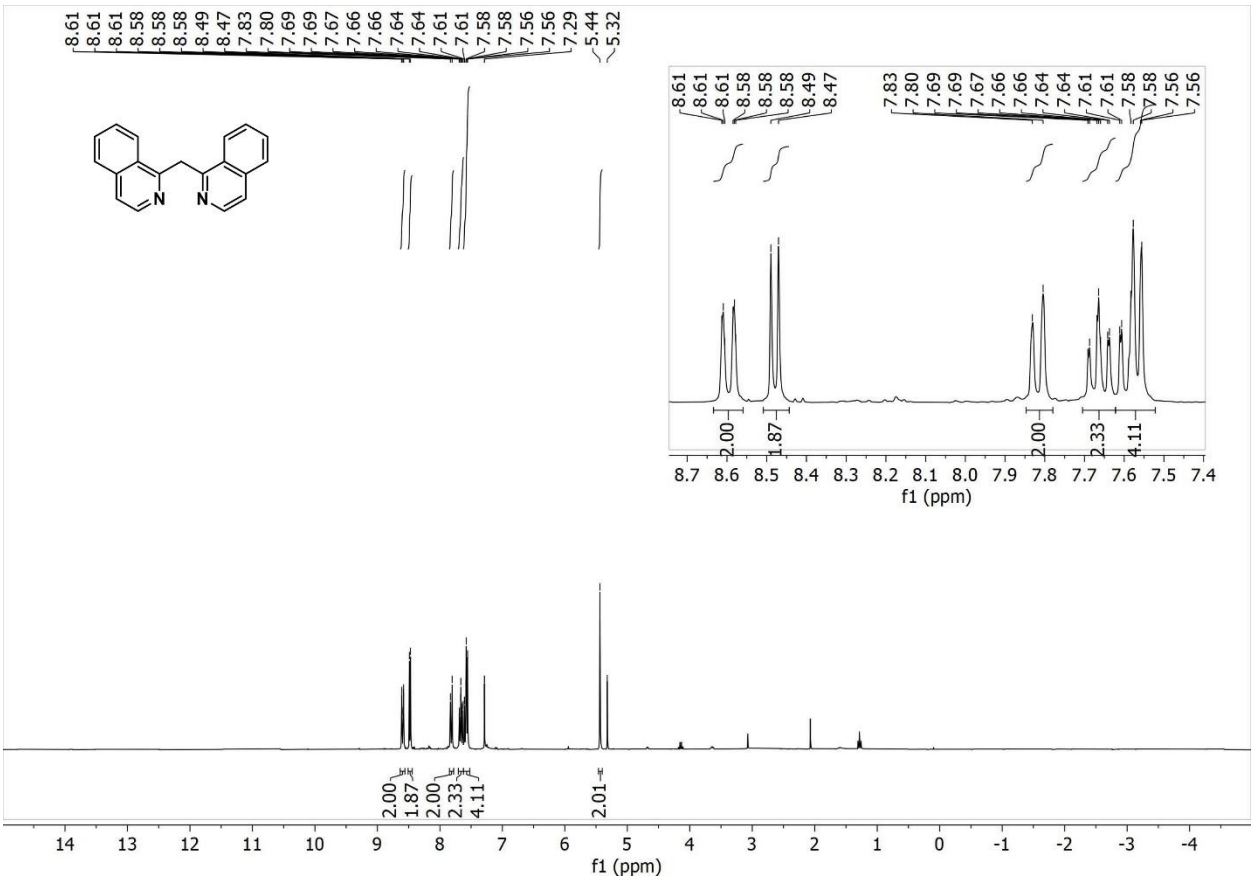


Figure 7.27. ^{1}H NMR of di(isoquinolin-1-yl)methane (**7c**) in CD_2Cl_2.

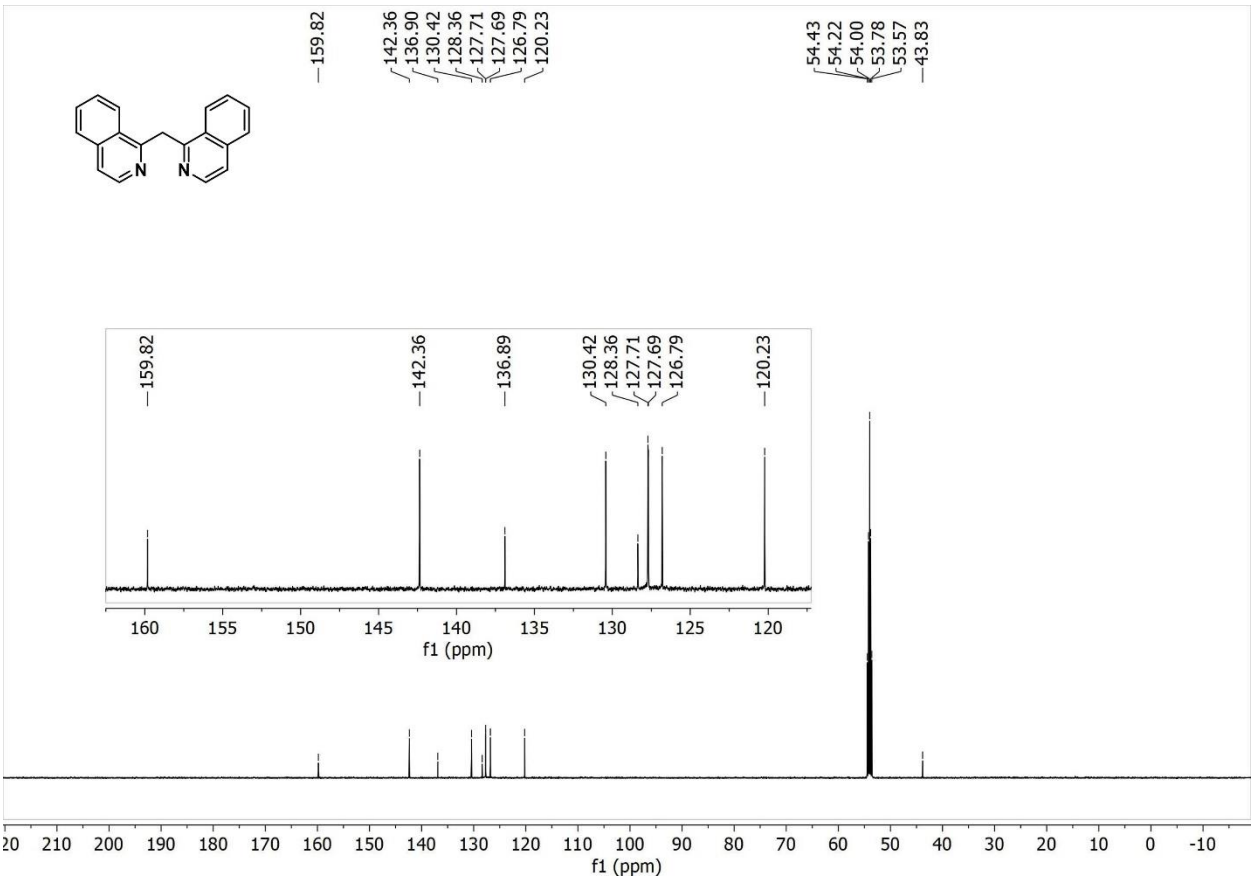


Figure 7.28. ^{13}C NMR of di(isoquinolin-1-yl)methane (**7c**) in CD_2Cl_2.

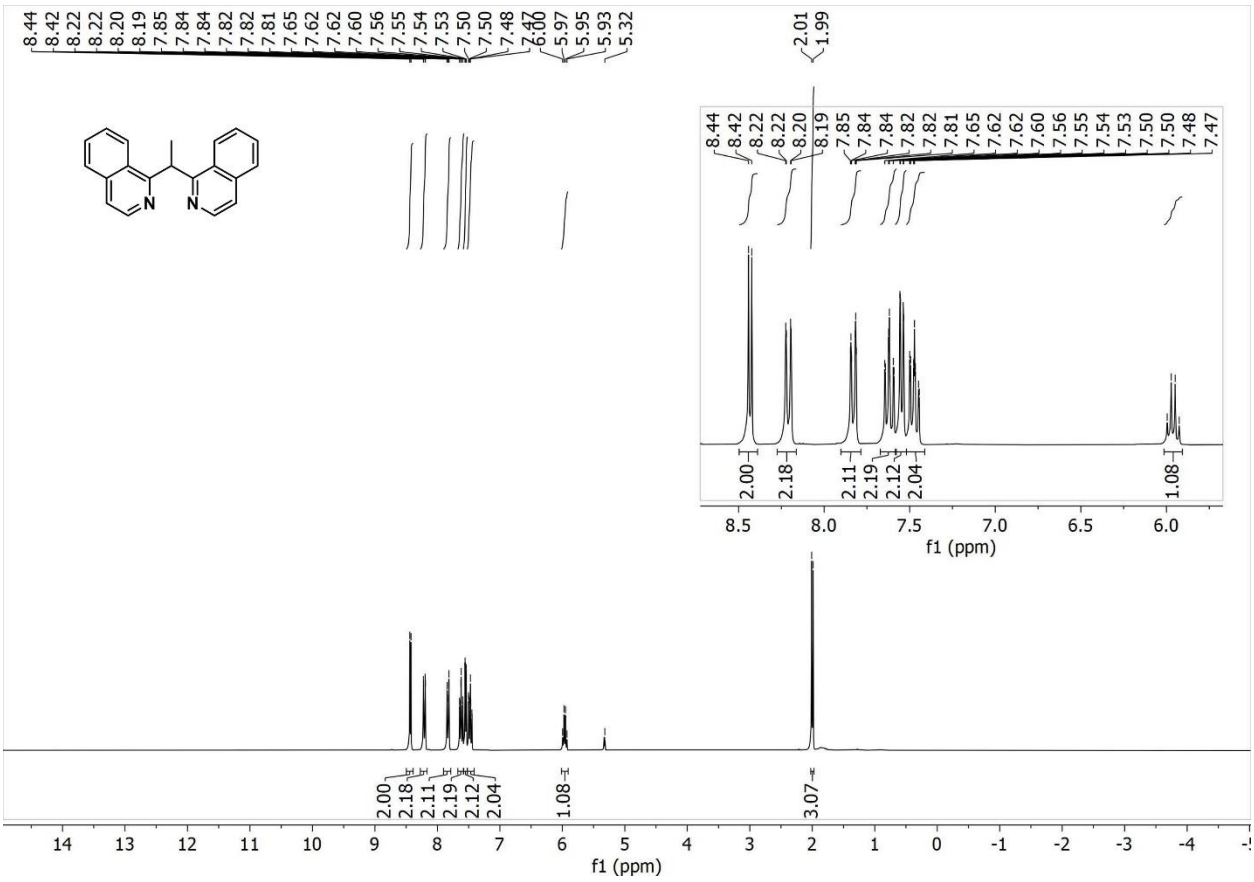


Figure 7.29. ^{1}H NMR of 1,1'-(ethane-1,1-diyl)diisoquinoline (**7d**) in CD_2Cl_2.

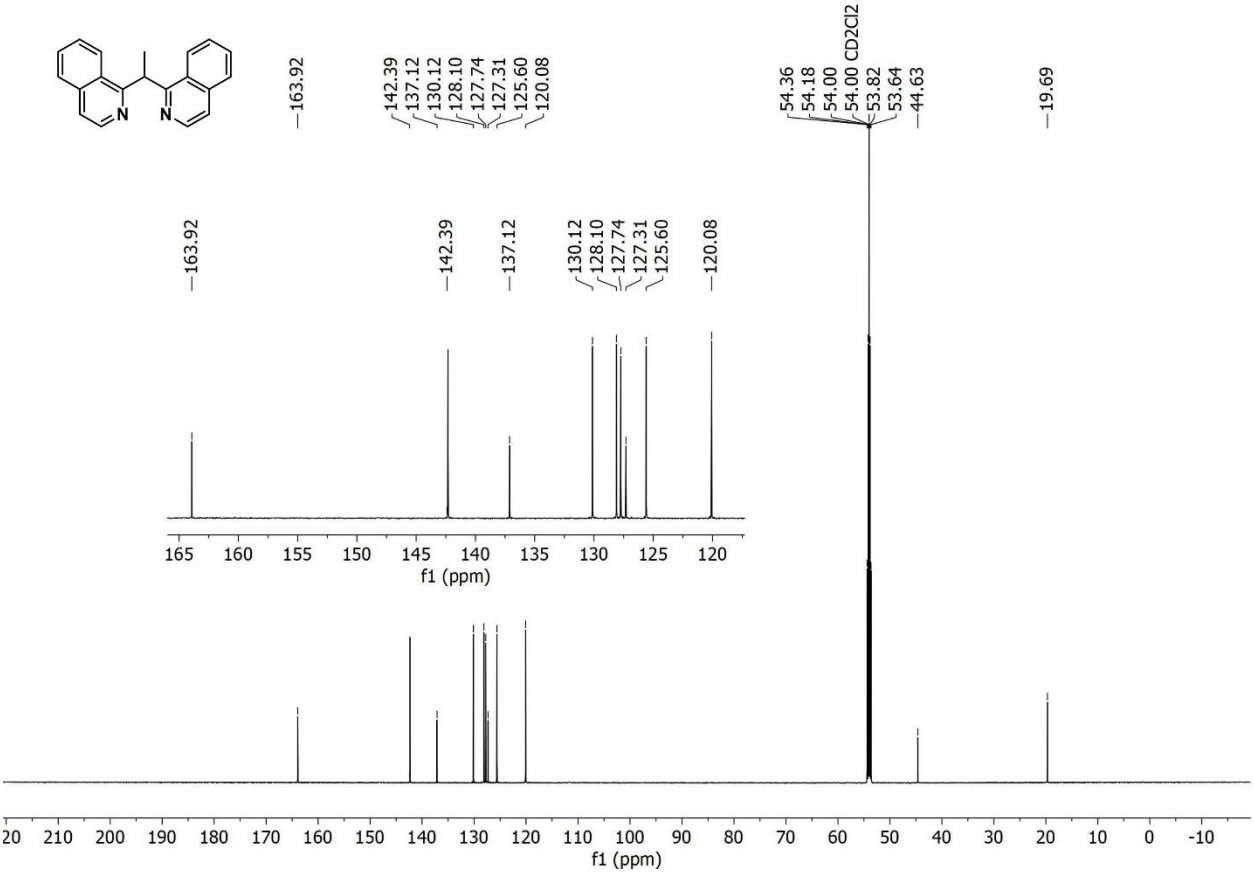


Figure 7.30. ^{13}C NMR of 1,1'-(ethane-1,1-diyl)diisoquinoline (**7d**) in CD_2Cl_2.

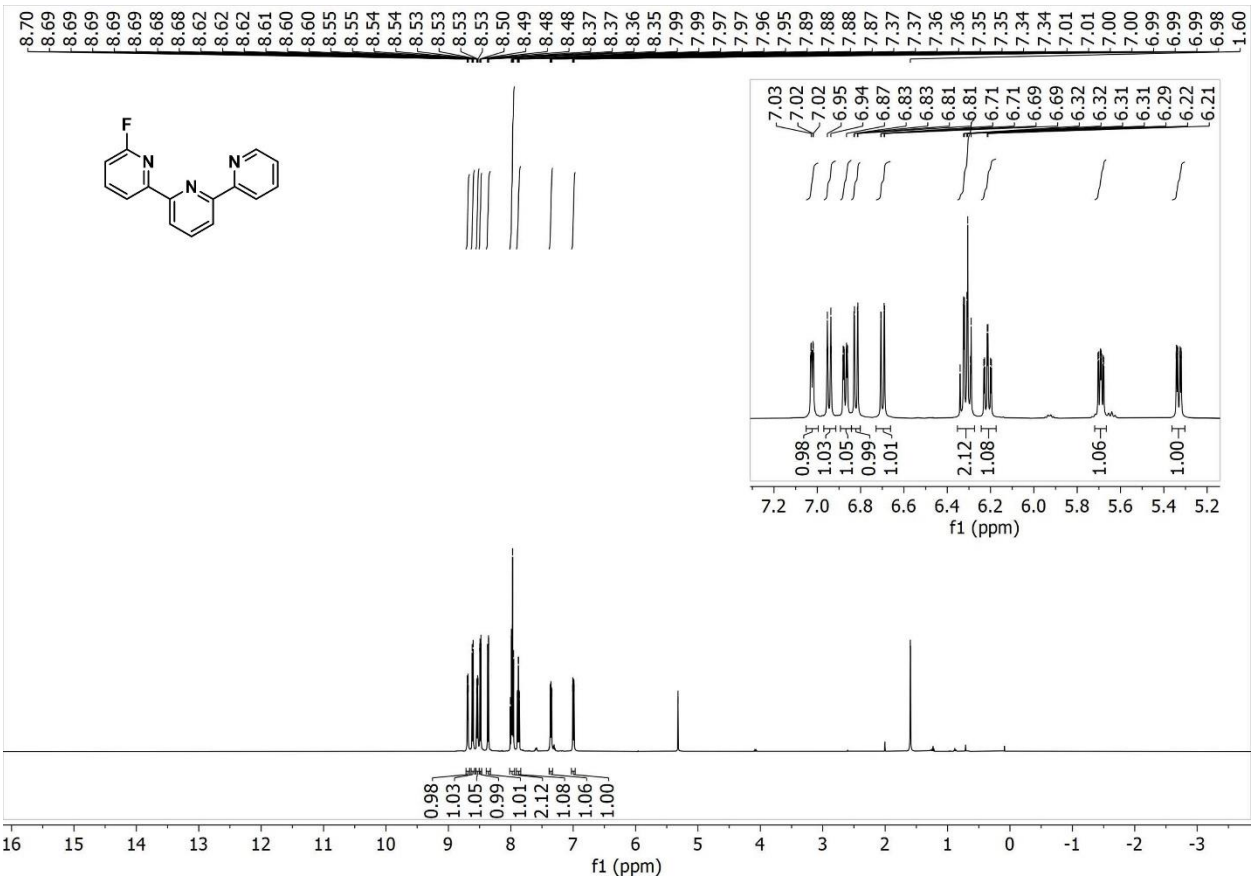


Figure 7.31. ^{1}H NMR of 6-fluoro-2,2':6',2"-terpyridine (F-tpy) in CD_2Cl_2.

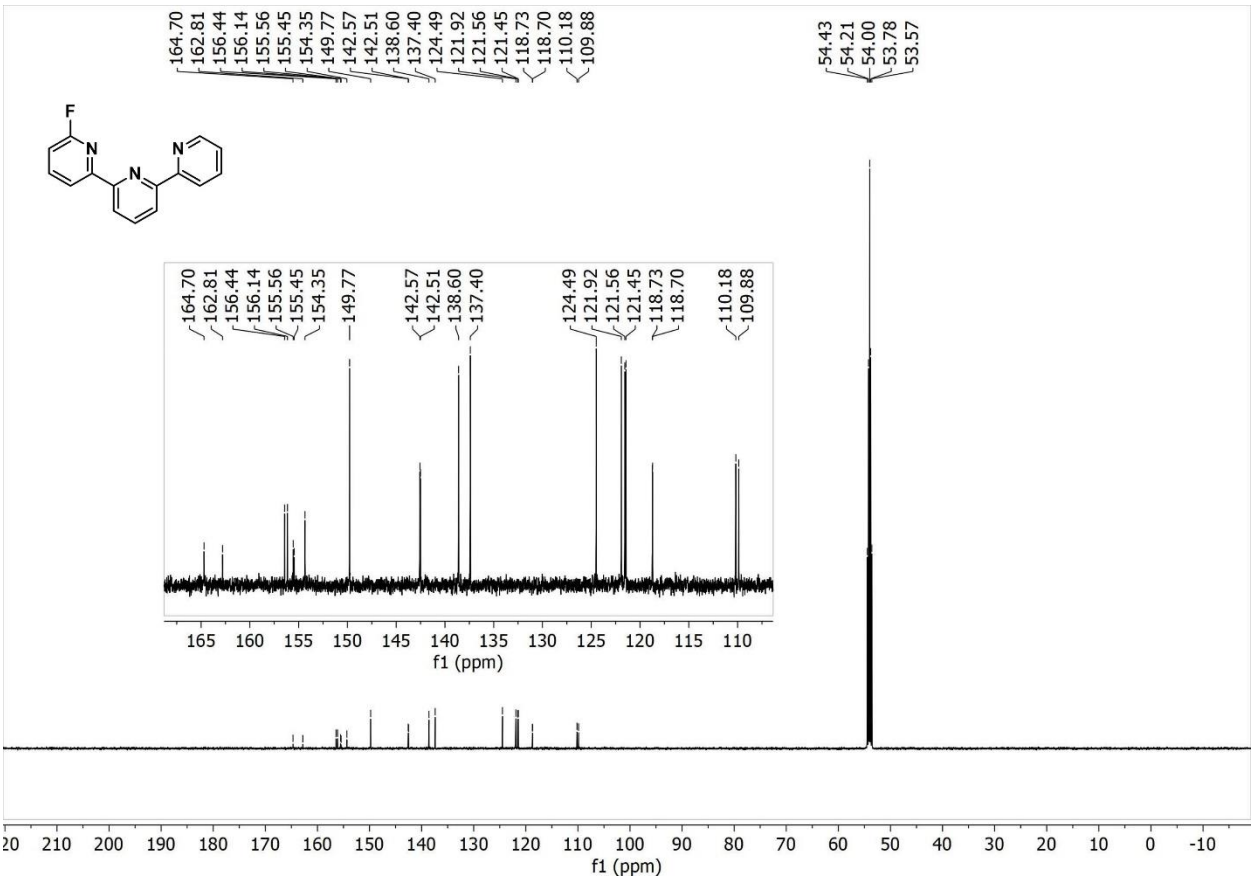


Figure 7.32. ^{13}C NMR of 6-fluoro-2,2':6',2"-terpyridine (F-tpy) in CD_2Cl_2.

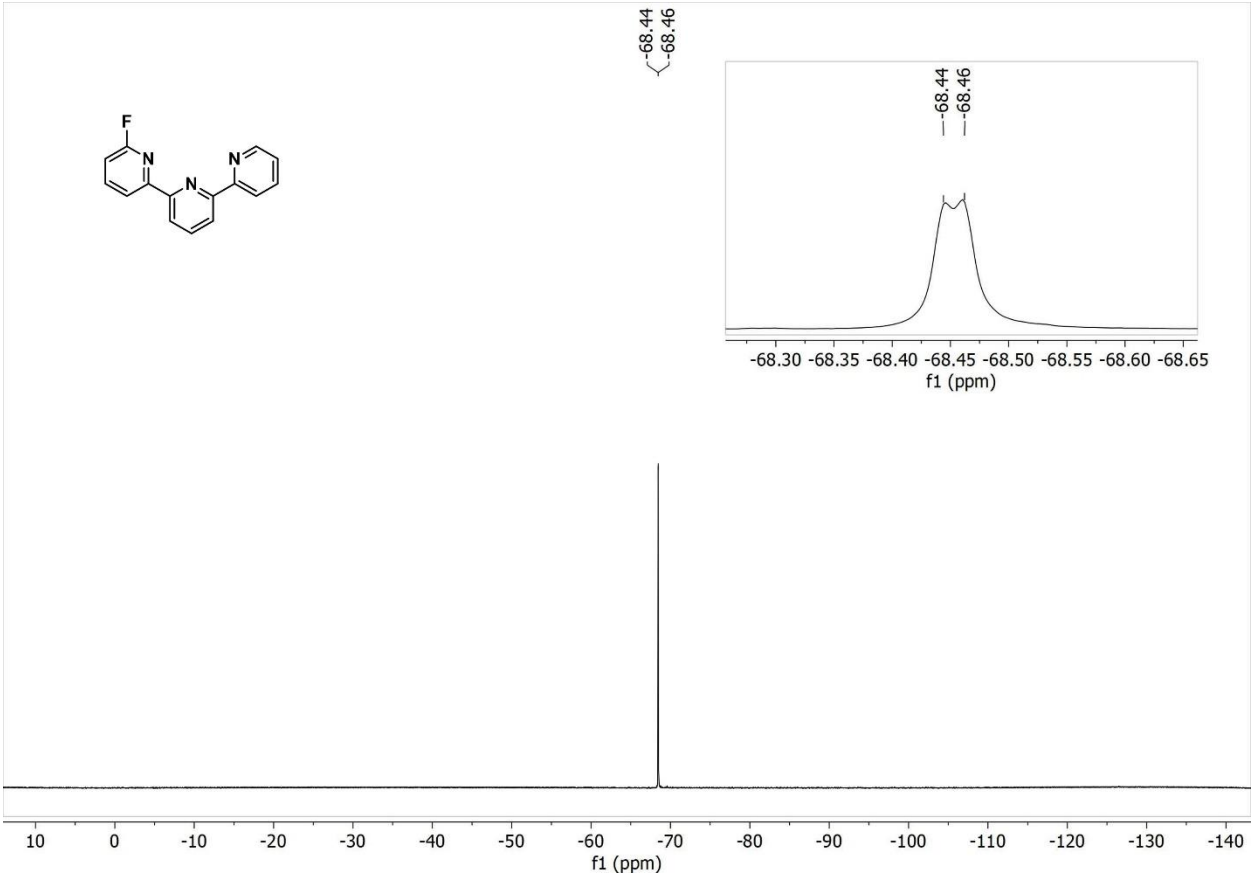


Figure 7.33. ^{19}F NMR of 6-fluoro-2,2':6',2''-terpyridine (F-tpy) in CD_2Cl_2.

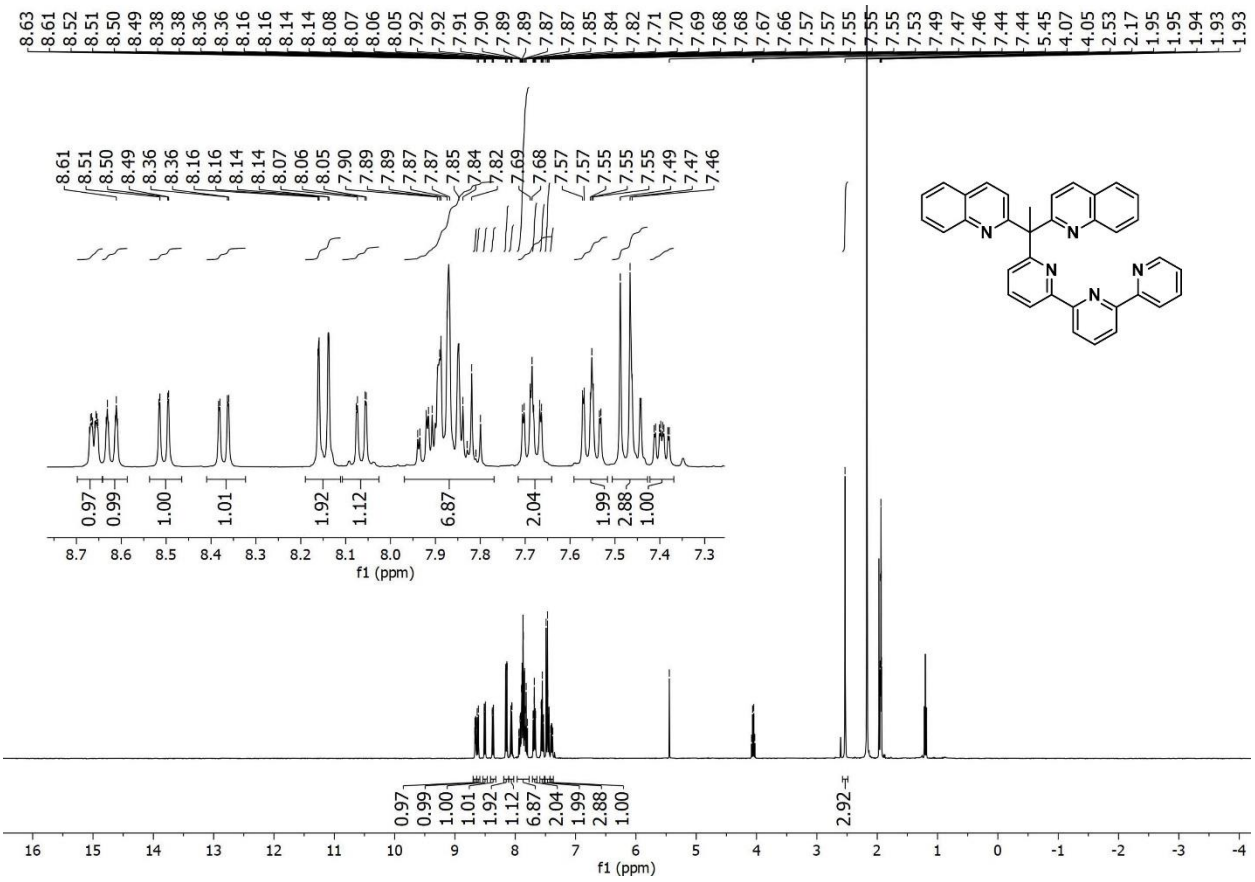


Figure 7.34. ^{1}H NMR of 2,2'-(1-([2,2':6',2''-terpyridin]-6-yl)ethane-1,1-diyl)diquinoline (tpyQuin2Me) in CD_2Cl_2.

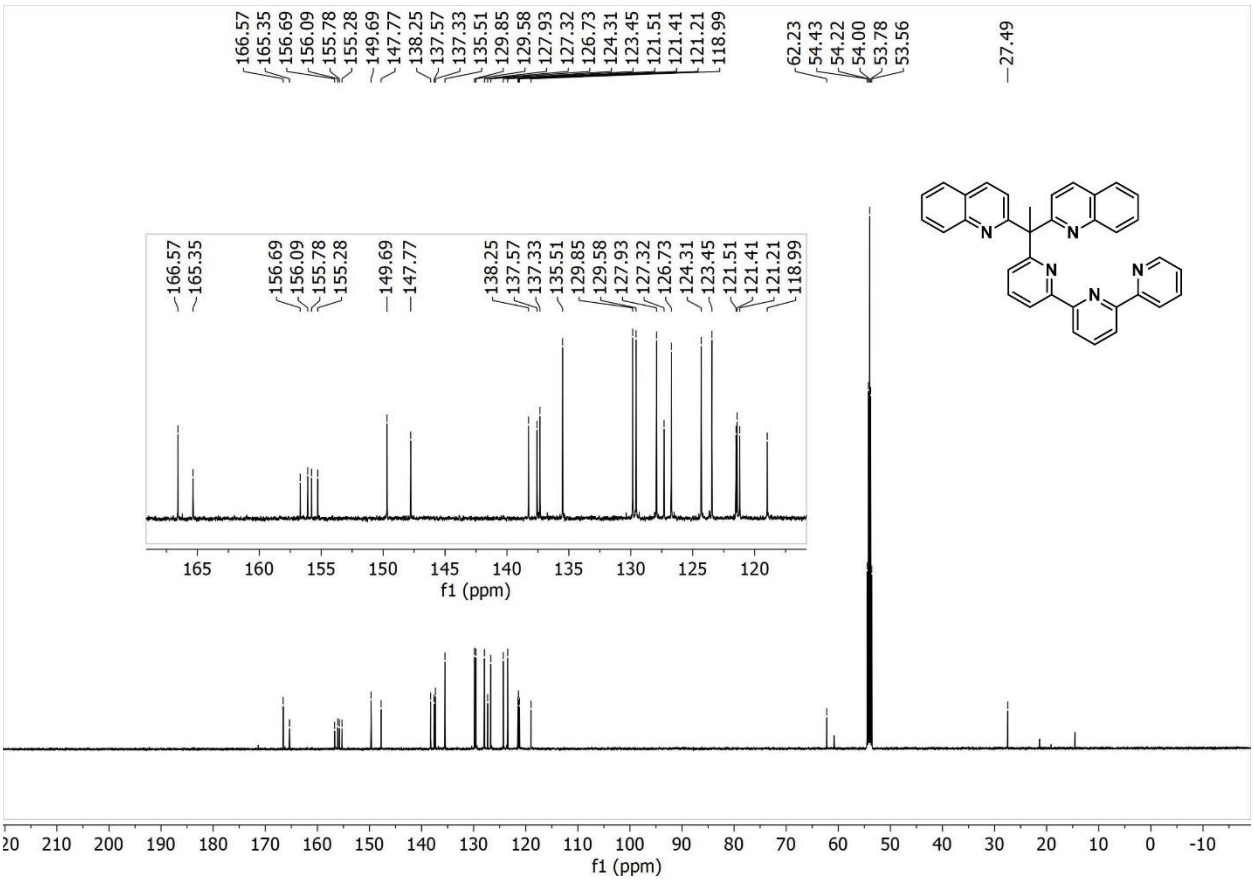


Figure 7.35. ^{13}C NMR of 2,2'-(1-([2,2':6',2''-terpyridin]-6-yl)ethane-1,1-diyl)diquinoline (tpyQuin2Me) in CD_2Cl_2.

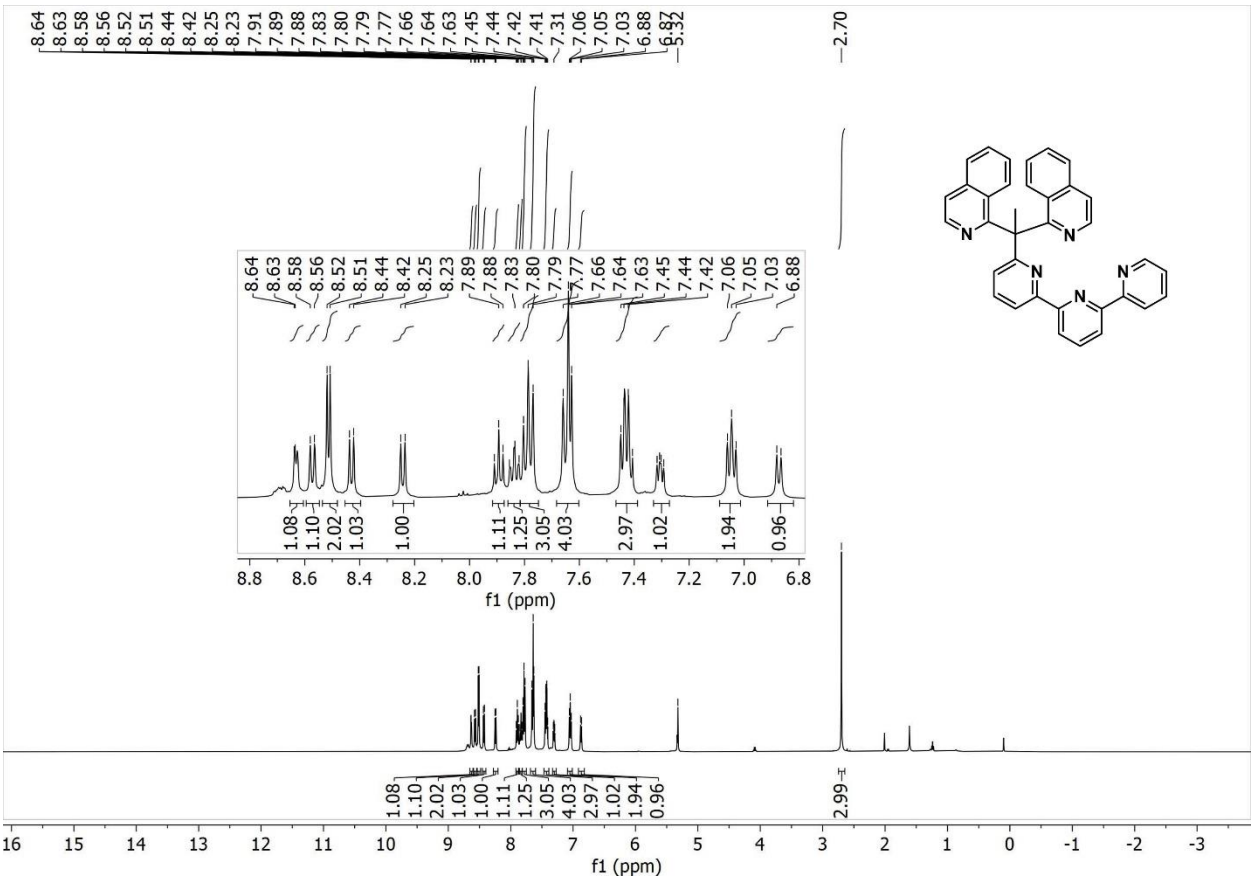


Figure 7.36. ^{1}H NMR of 1,1'-(1-([2,2':6',2''-terpyridin]-6-yl)ethane-1,1-diyl)diisoquinoline (tpyIsoQuin2Me).

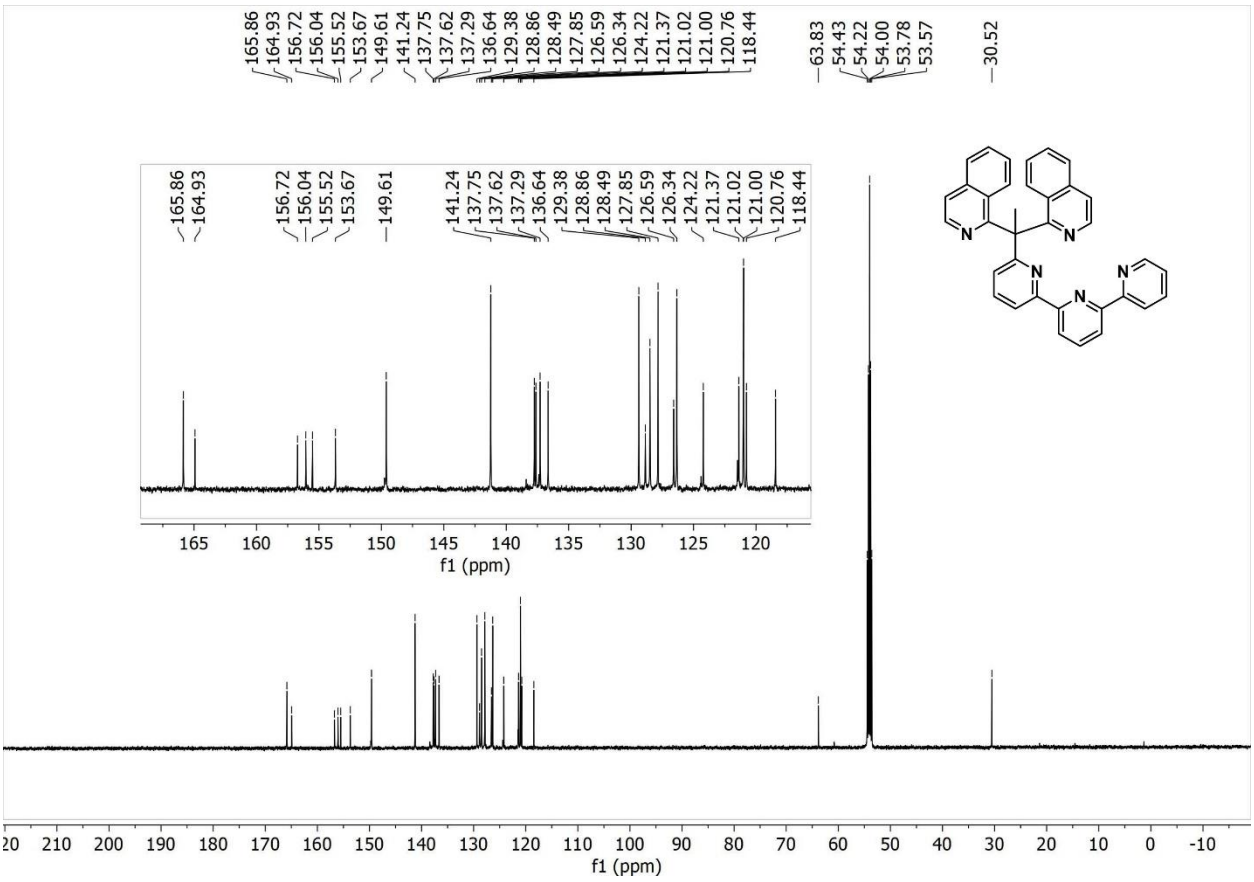


Figure 7.37. ^{13}C NMR of 1,1'-(1-([2,2':6',2''-terpyridin]-6-yl)ethane-1,1-diyl)diisoquinoline (tpyIsoQuin2Me).

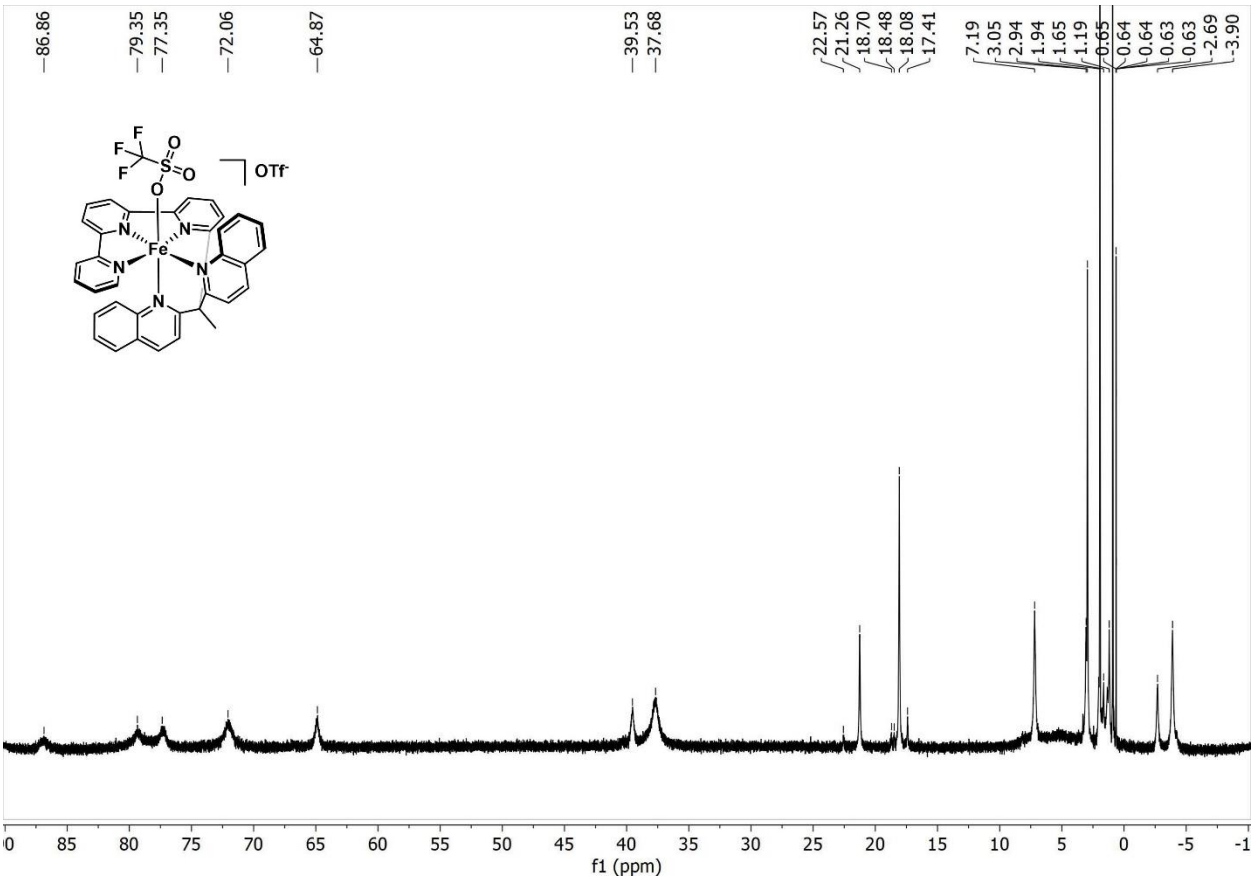


Figure 7.38. ^{1}H NMR of [Fe(tpyQuin2Me)][OTf]$_2$ (Fe-tpyQuin2Me) in CD_3CN.

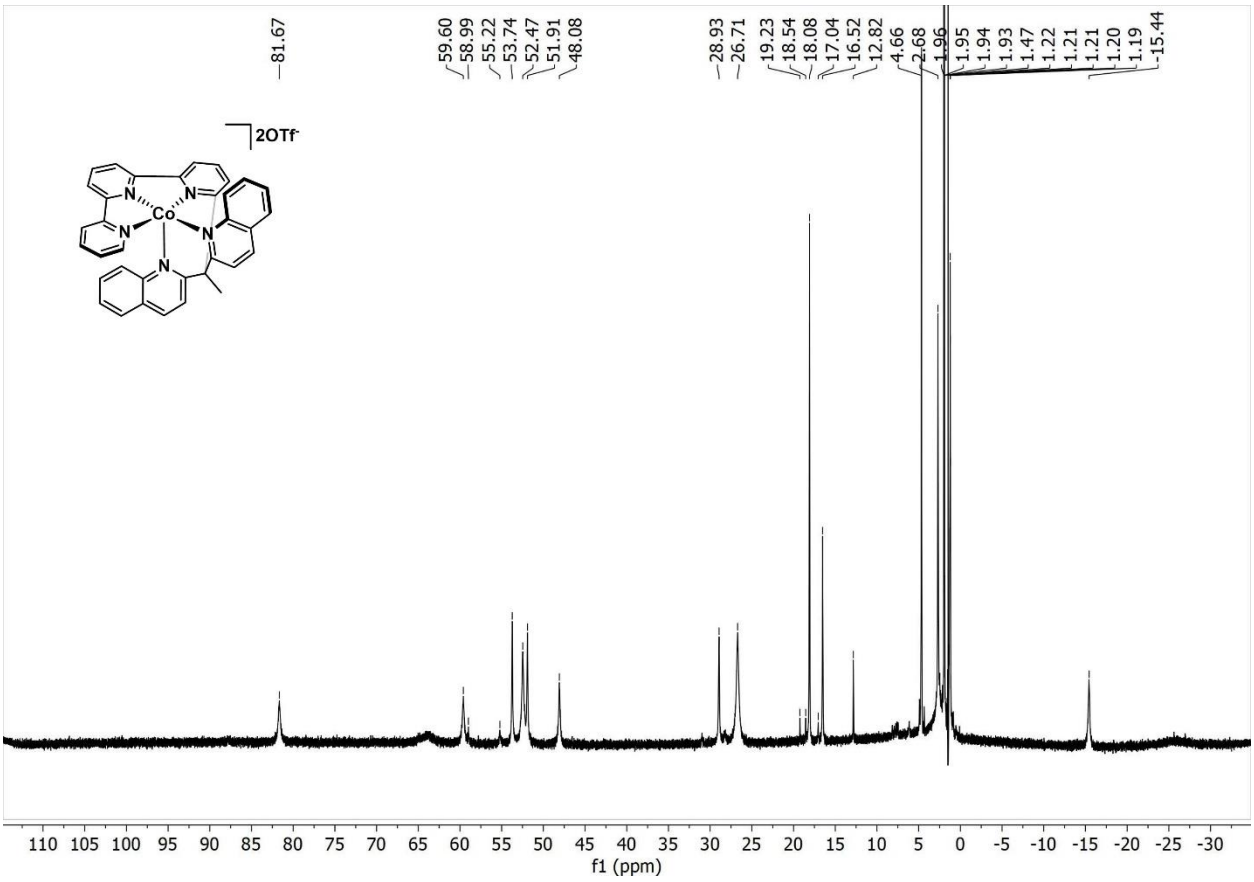


Figure 7.39. ^{1}H NMR of [Co(tpyQuin2Me)][OTf]$_2$ (Co-tpyQuin2Me) in CD_3CN.

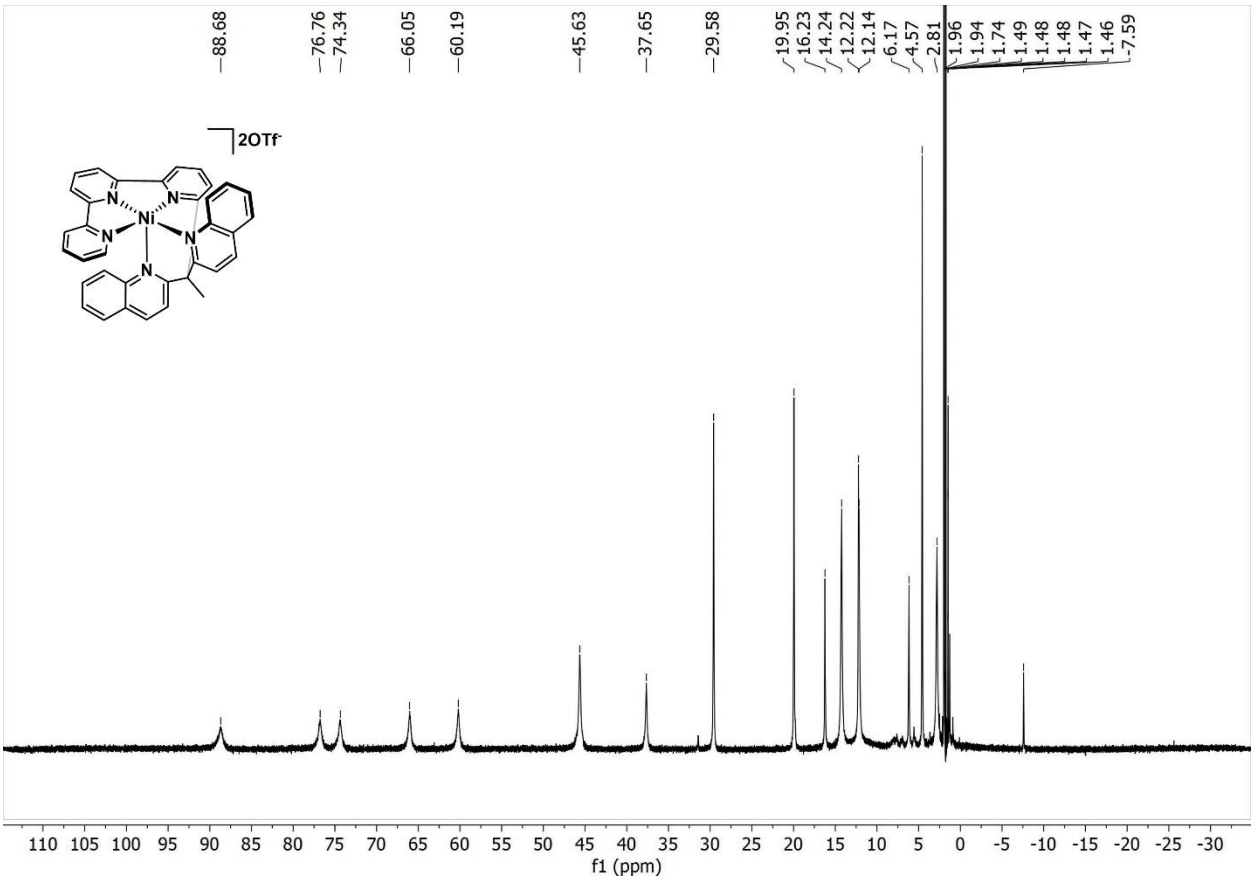


Figure 7.40. ^{1}H NMR of [Ni(tpyQuin2Me)][OTf]$_2$ (Ni-tpyQuin2Me) in CD_3CN.

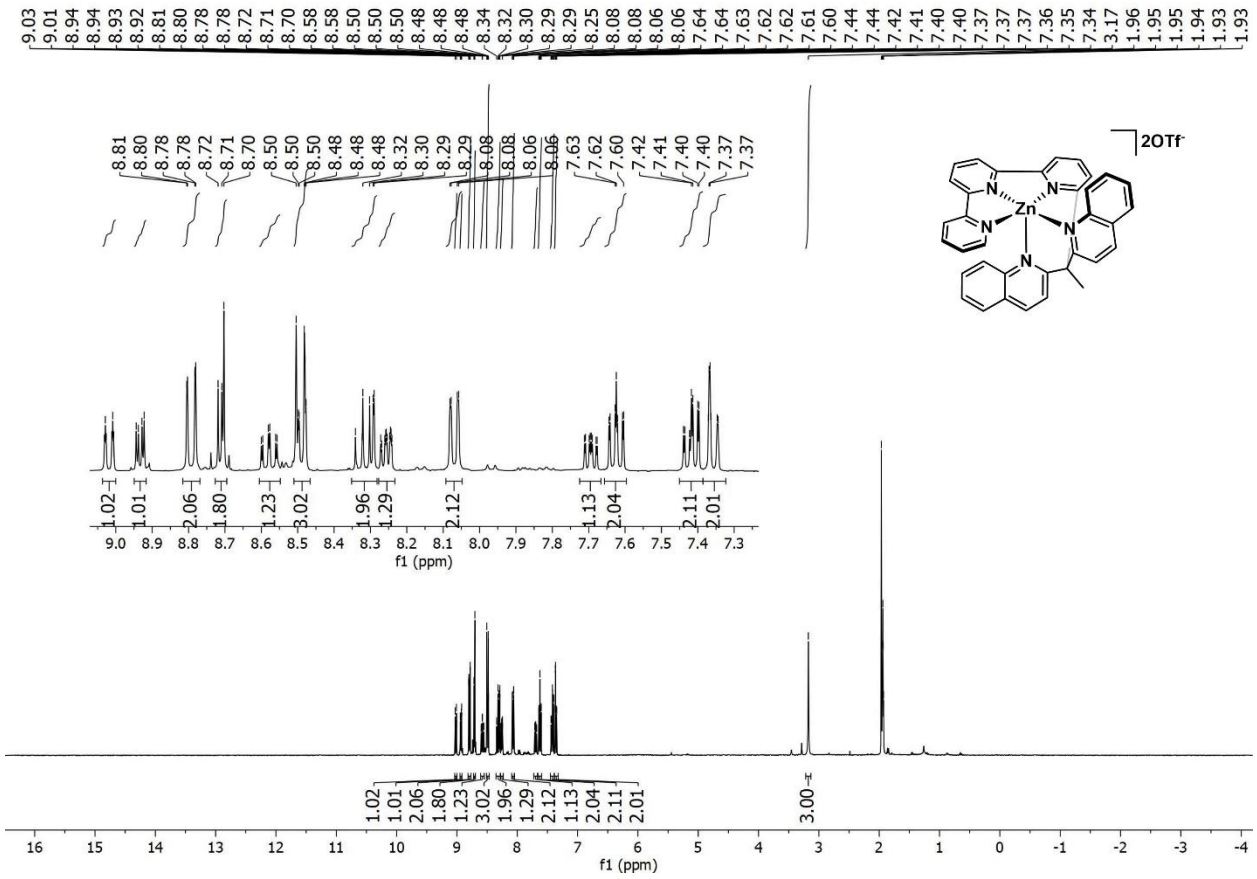


Figure 7.41. ^{1}H NMR of [Zn(tpyQuin2Me)][OTf]$_2$ (Zn-tpyQuin2Me) in CD_3CN.

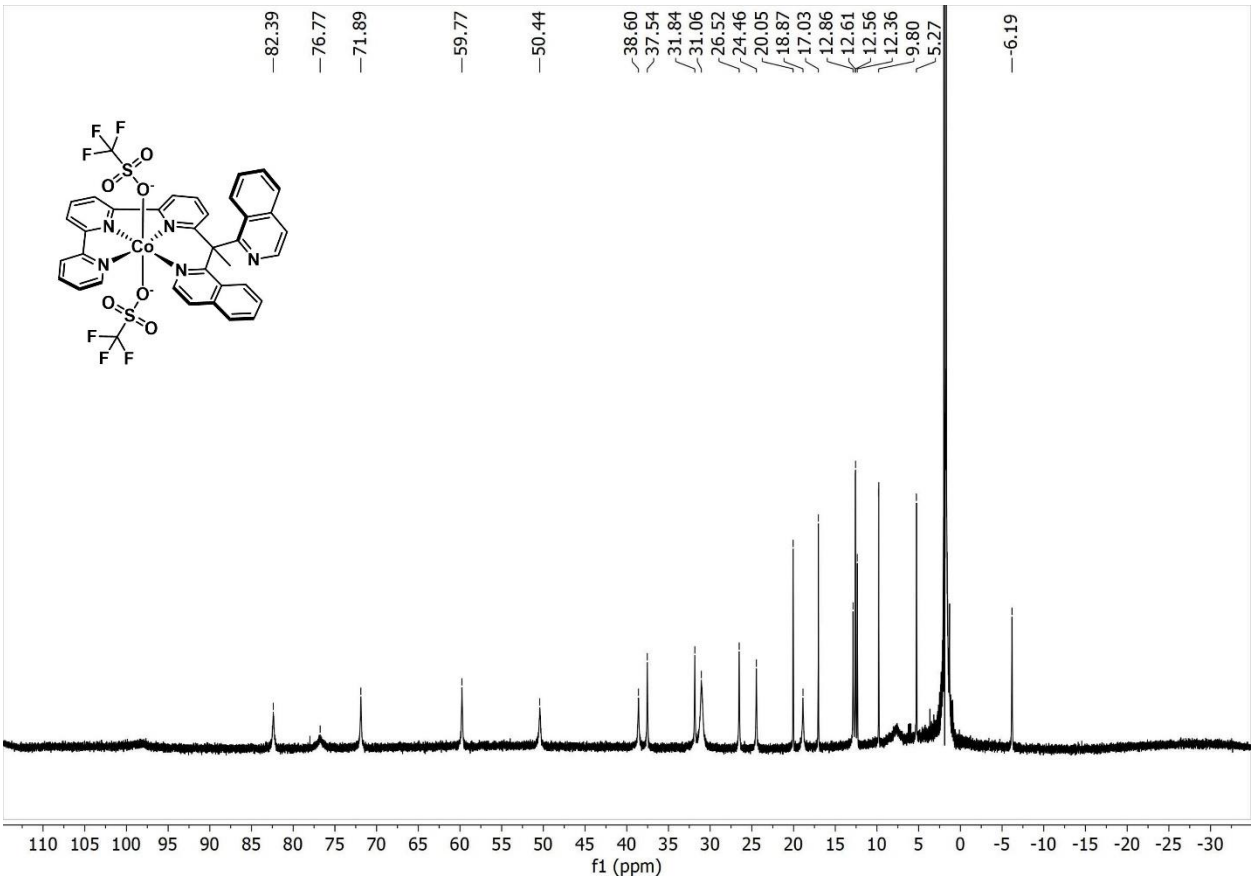


Figure 7.42. ^{1}H NMR of Co(tpyIsoQuin2Me)(OTf)$_2$ (Co-tpyIsoQuin2Me) in CD_3CN.

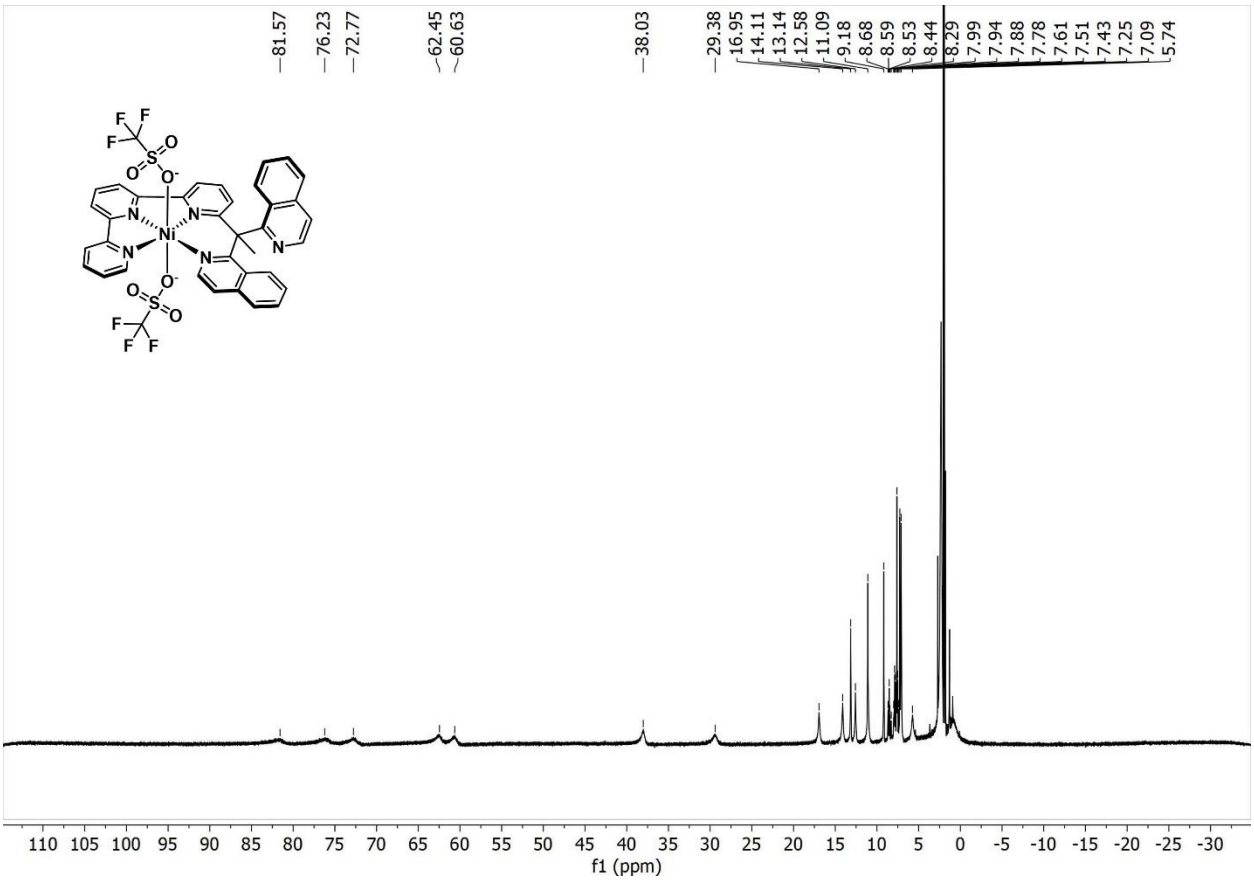


Figure 7.43. ^{1}H NMR of Ni(tpyIsoQuin2Me)(OTf)$_2$ (Ni-tpyIsoQuin2Me) in CD_3CN.

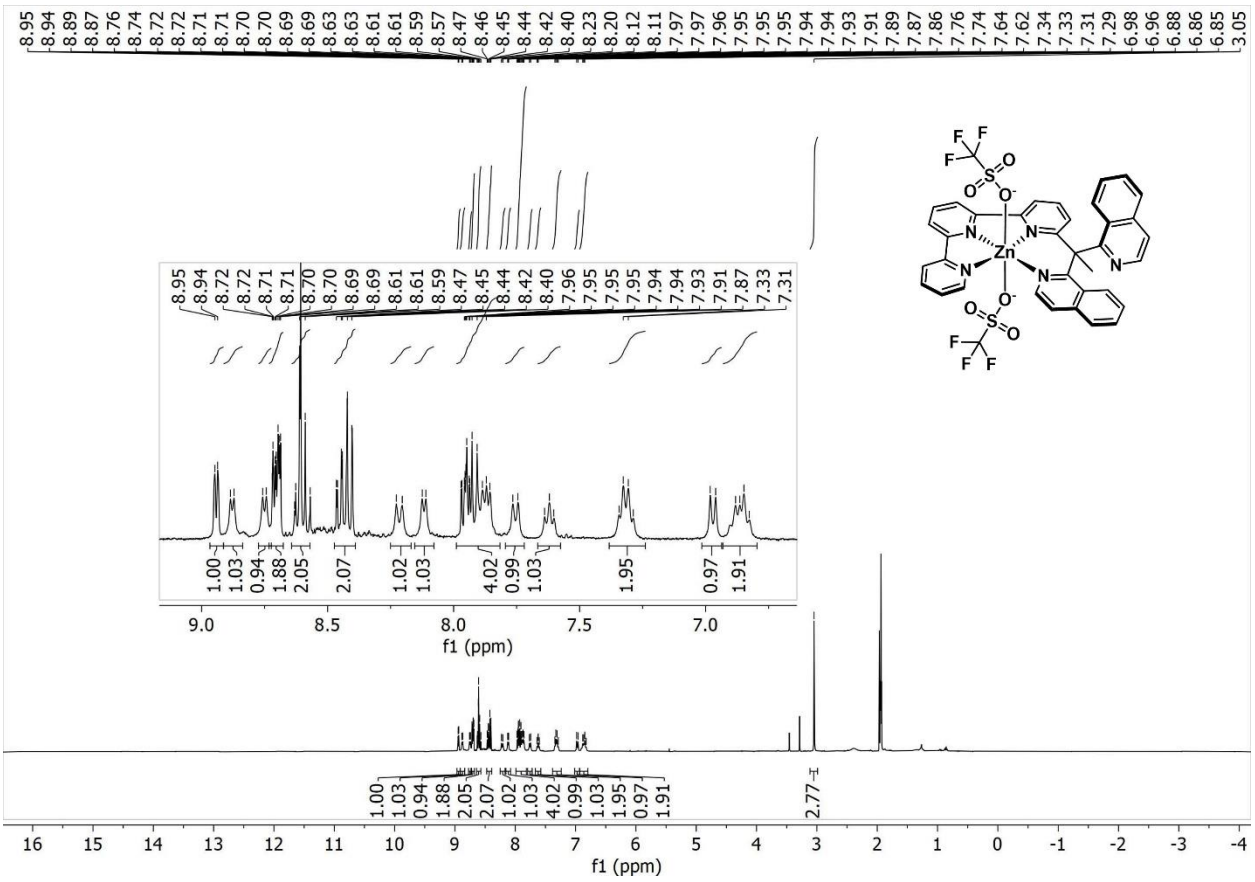


Figure 7.44. ^{1}H NMR of Ni(tpyIsoQuin2Me)$(OTf)_2$ (Zn-tpyIsoQuin2Me) in CD_3CN.

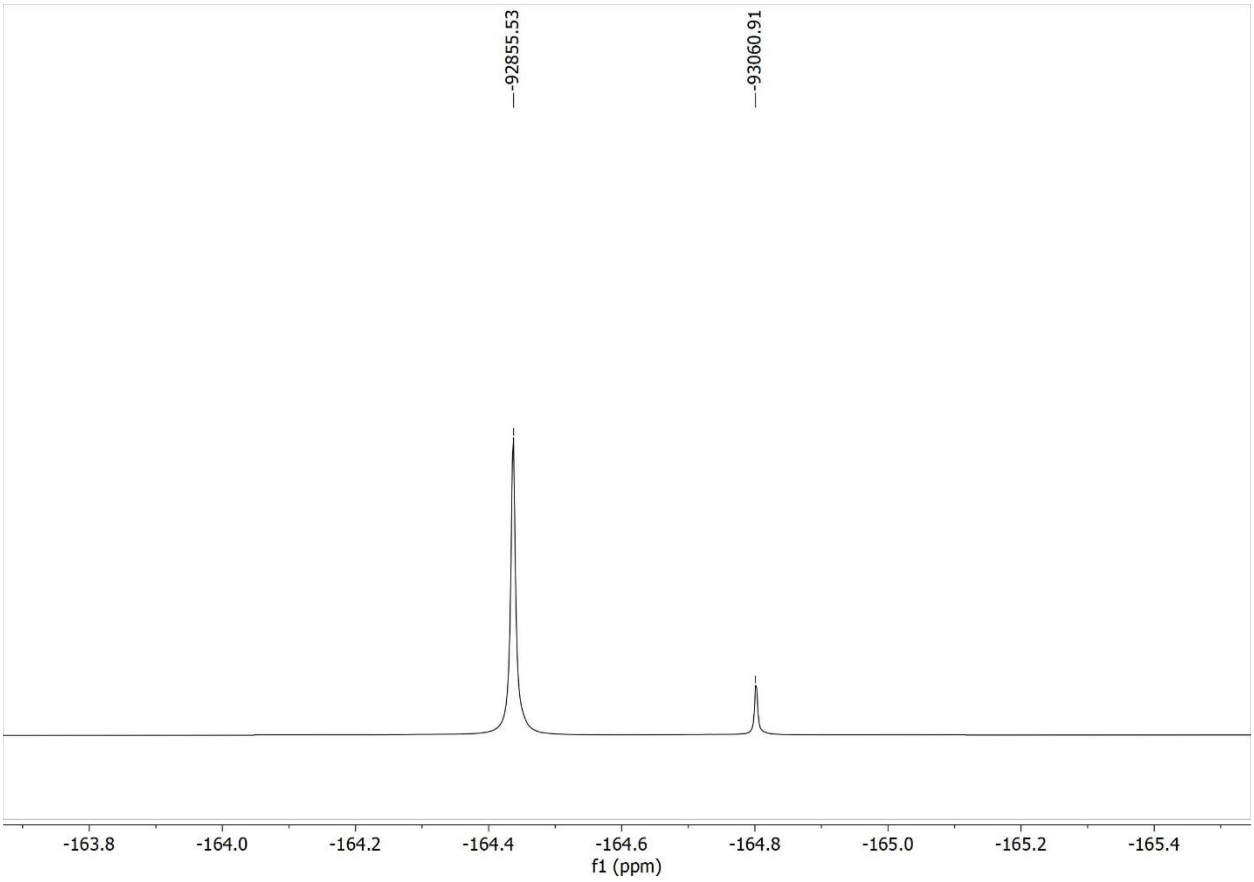


Figure 7.45. Solution Evans Method of Cr-tpyQuin2Me in CD_3CN measured by ^{19}F NMR at 293 K with hexafluorobenzne as the internal standard.

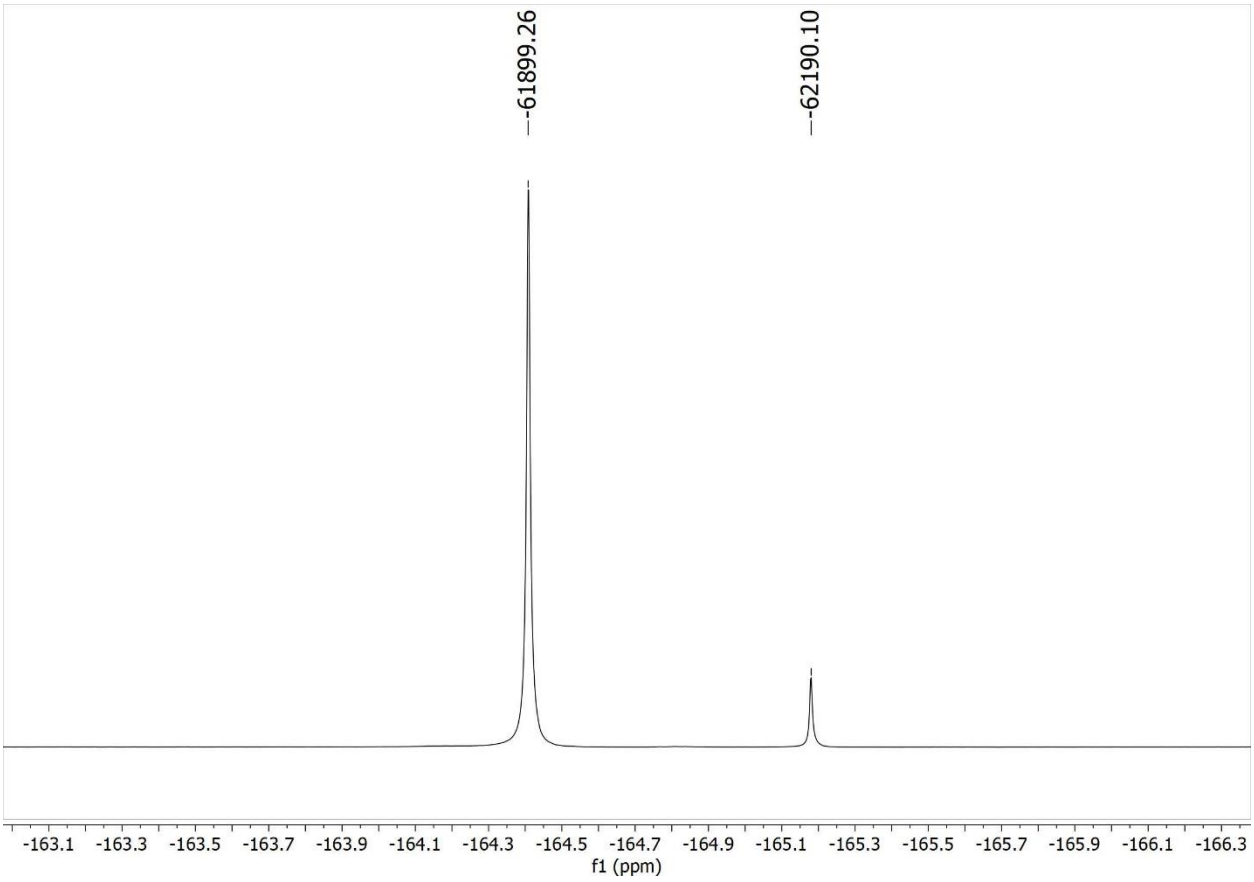


Figure 7.46. Solution Evans Method of Fe-tpyQuin2Me in CD_3CN measured by ^{19}F NMR at 293 K with hexafluorobenzne as the internal standard.

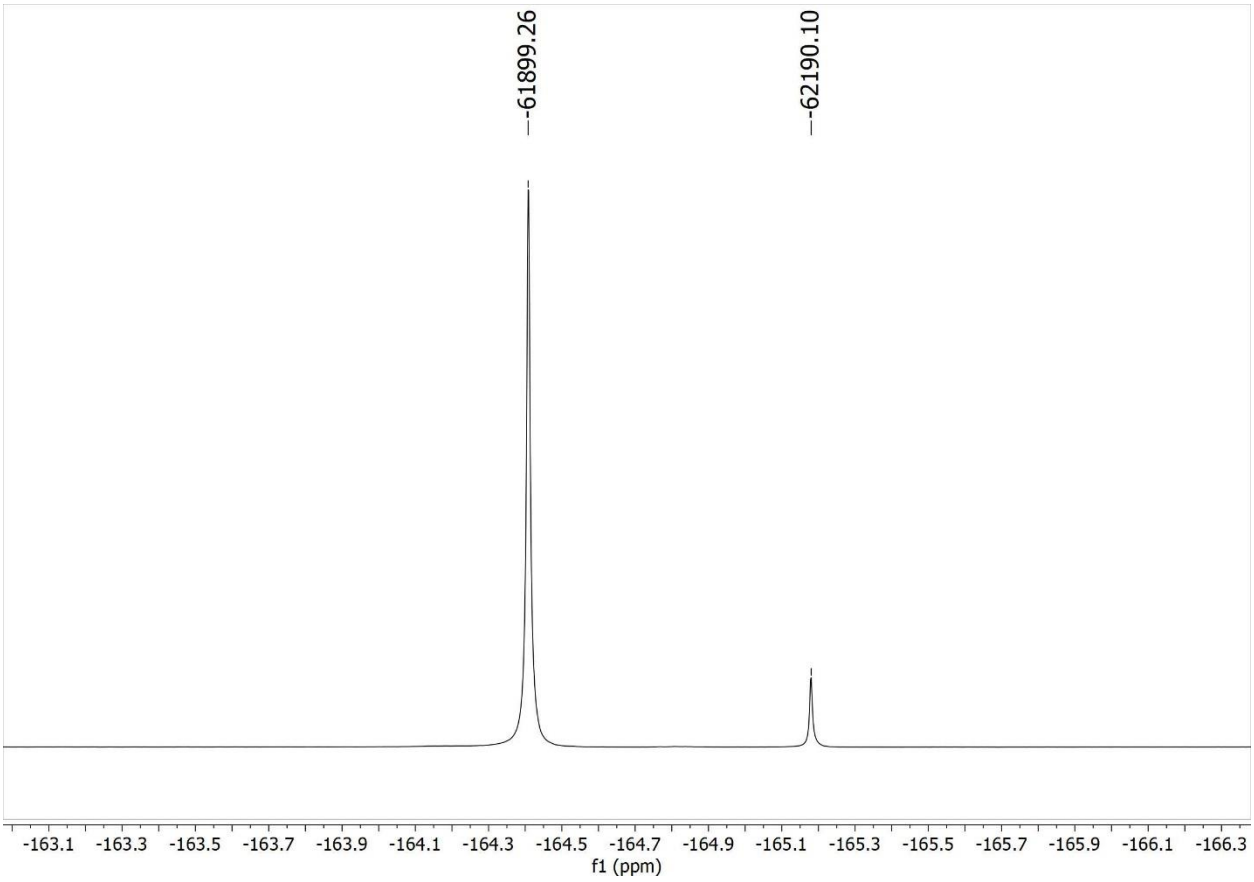


Figure 7.47. Solution Evans Method of Co-tpyQuin2Me in CD_3CN measured by ^{19}F NMR at 293 K with hexafluorobenzne as the internal standard.

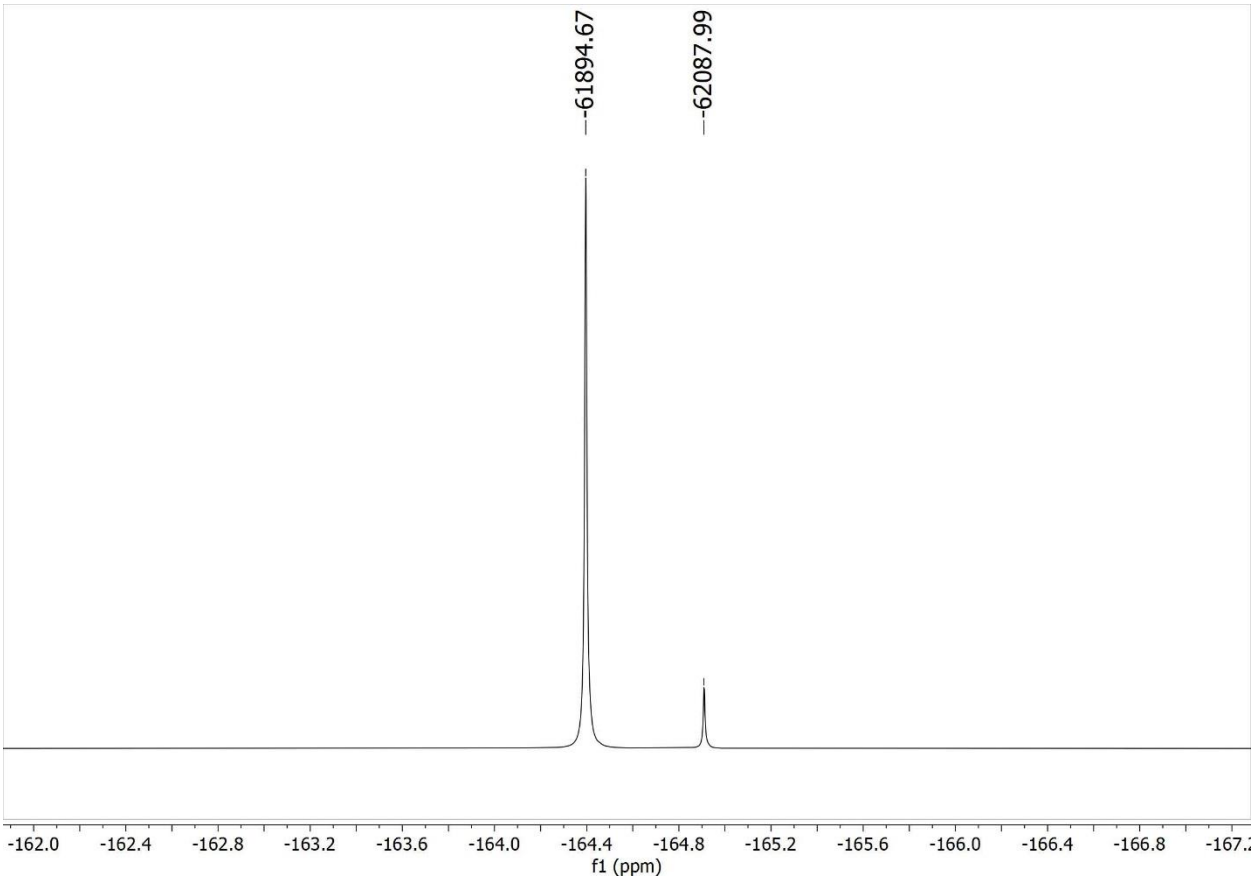


Figure 7.48. Solution Evans Method of Ni-tpyQuin2Me in CD_3CN measured by ^{19}F NMR at 293 K with hexafluorobenzne as the internal standard.

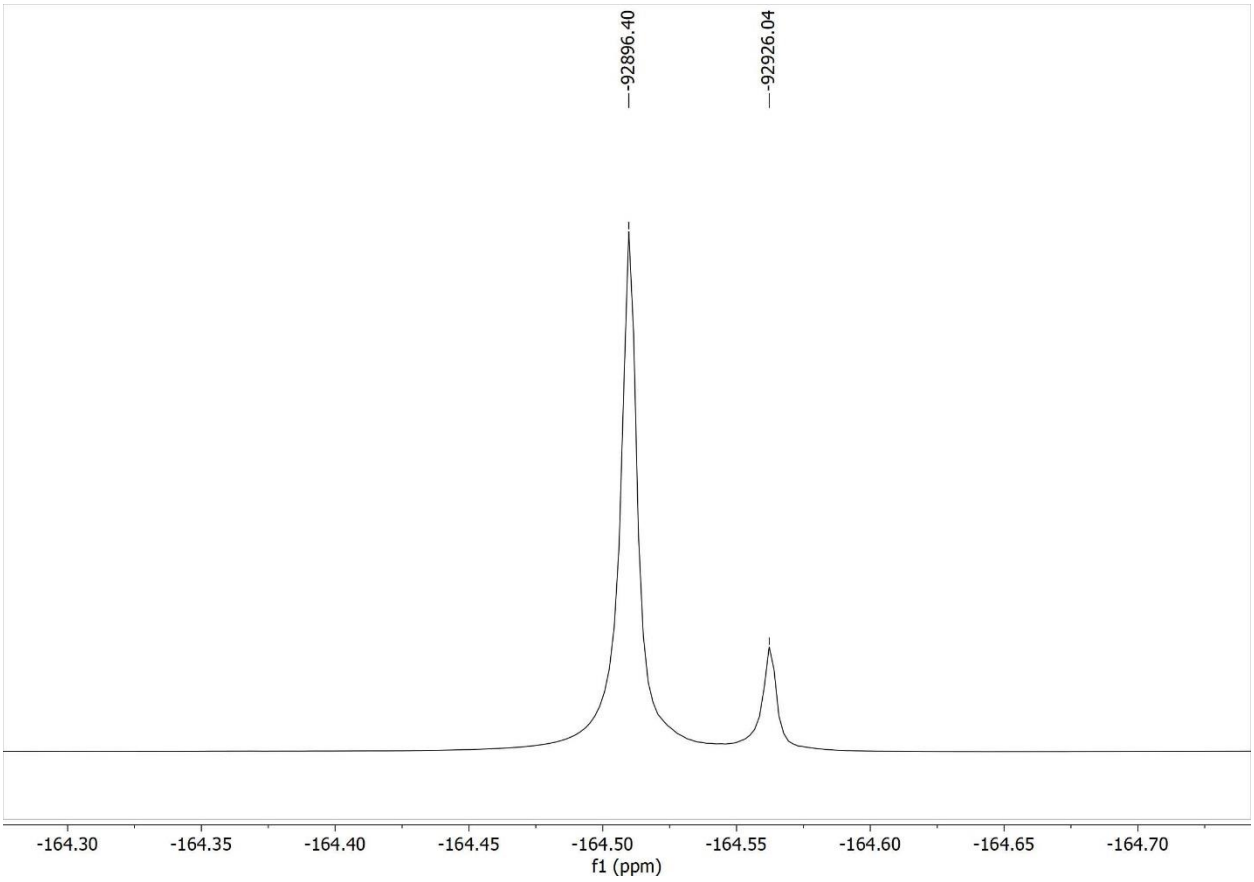


Figure 7.49. Solution Evans Method of Cr-tpyIsoQuin2Me in CD_3CN measured by ^{19}F NMR at 293 K with hexafluorobenzne as the internal standard.

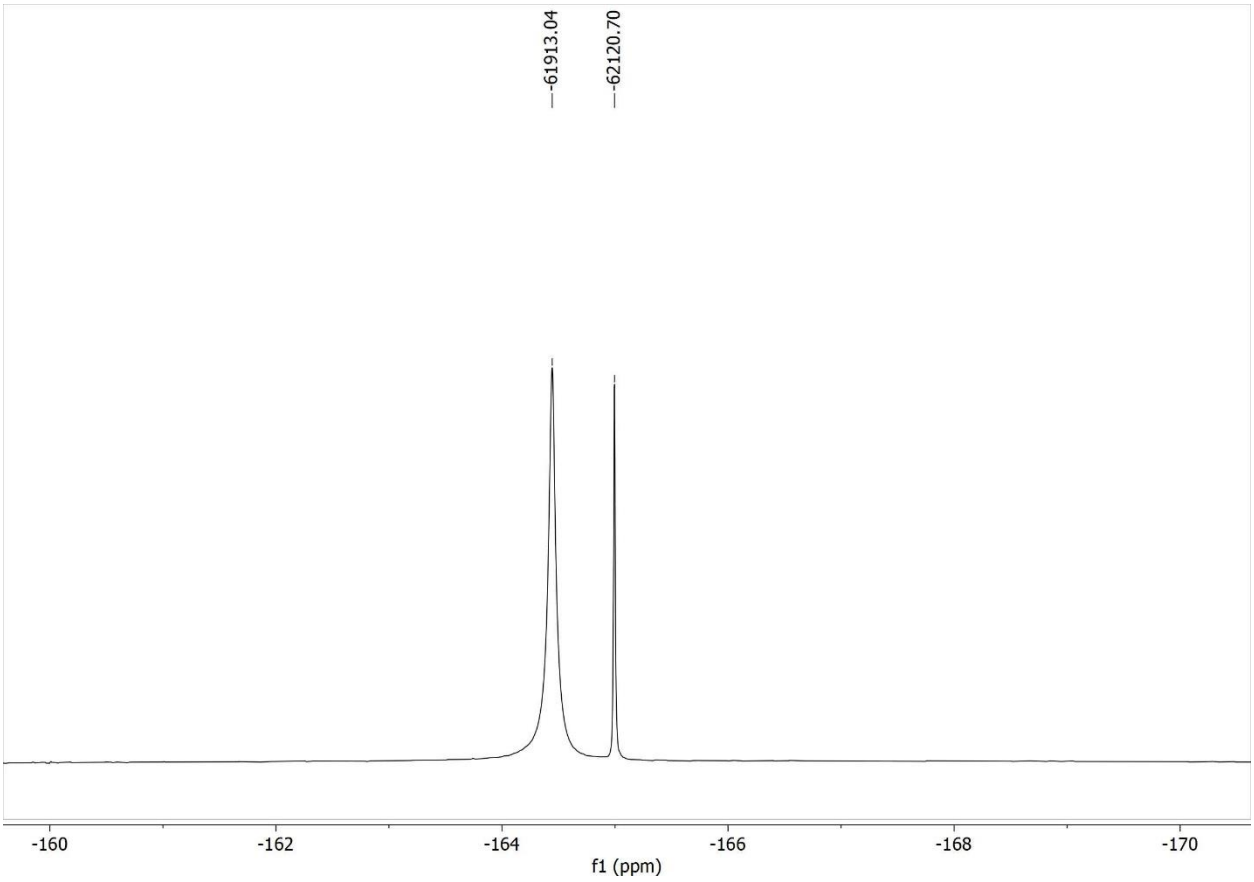


Figure 7.50. Solution Evans Method of Fe-tpyIsoQuin2Me in CD_3CN measured by ^{19}F NMR at 293 K with hexafluorobenzne as the internal standard.

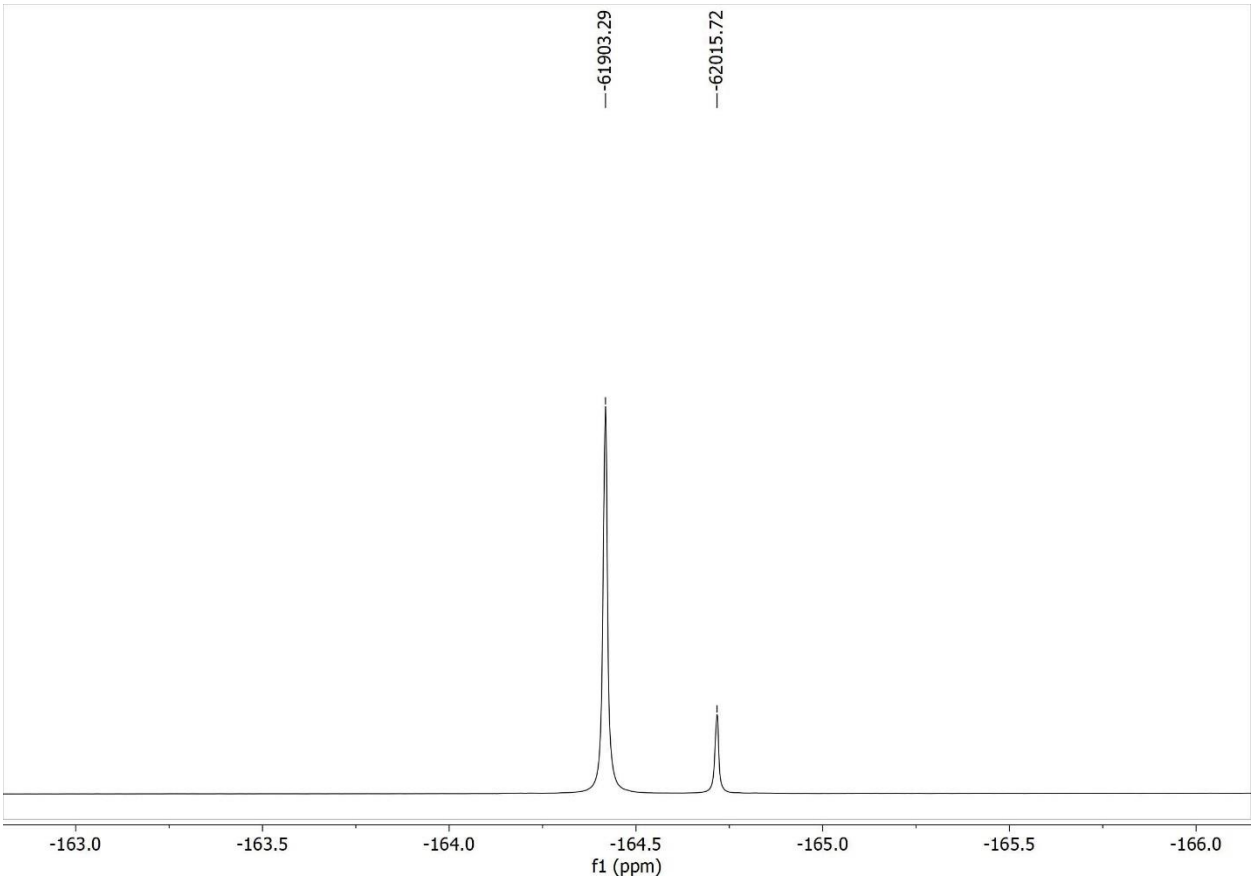


Figure 7.51. Solution Evans Method of Co-tpyIsoQuin2Me in CD_3CN measured by ^{19}F NMR at 293 K with hexafluorobenzne as the internal standard.

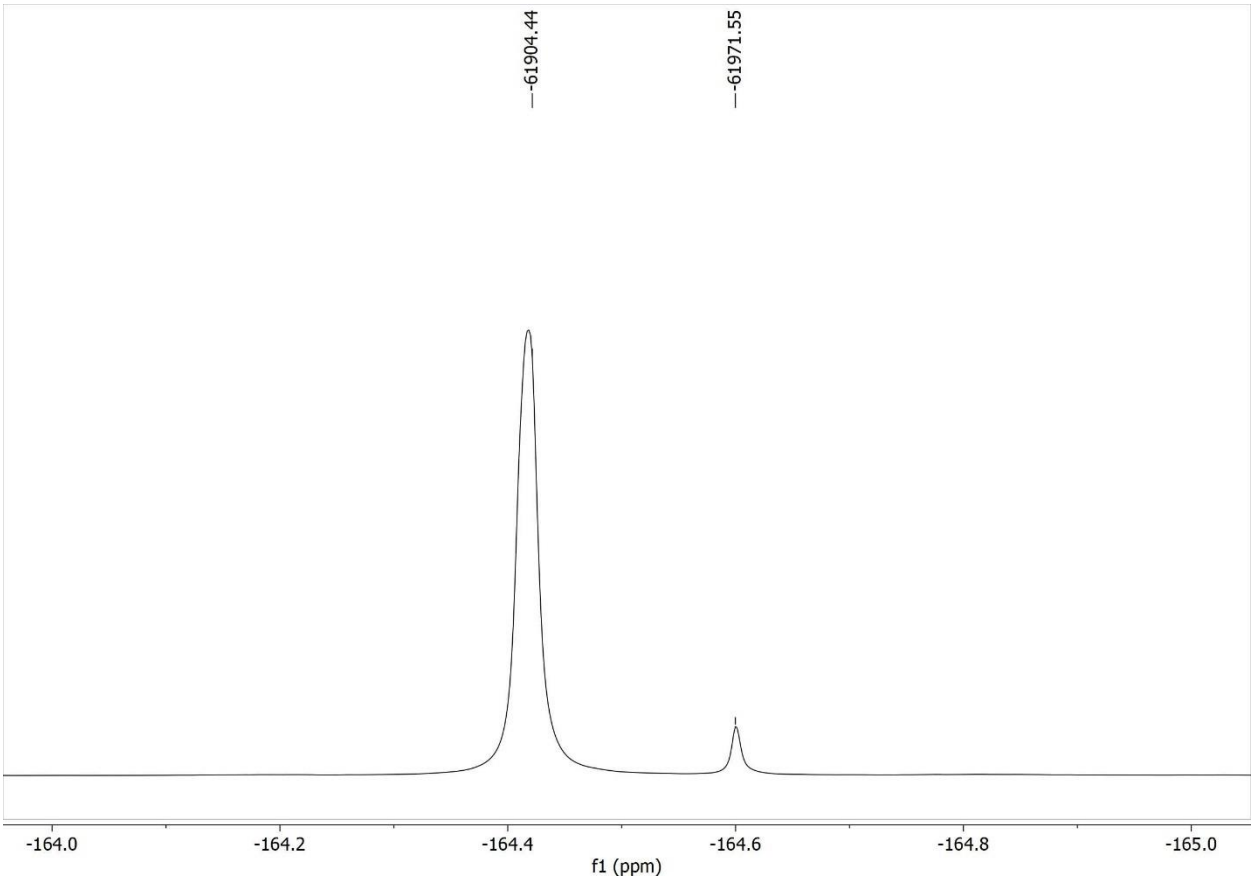


Figure 7.52. Solution Evans Method of Ni-tpyIsoQuin2Me in CD_3CN measured by ^{19}F NMR at 293 K with hexafluorobenzne as the internal standard.

7.6 References

(1) Davis, S. J.; Caldeira, K.; Matthews, H. D. Future CO_2 Emissions and Climate Change from Existing Energy Infrastructure. *Science* **2010**, *329*, 1330–1333.

(2) Höök, M.; Tang, X. Depletion of Fossil Fuels and Anthropogenic Climate Change—A Review. *Energy Policy* **2013**, *52*, 797–809.

(3) Whiting, K.; Carmona, L. G.; Sousa, T. A Review of the Use of Exergy to Evaluate the Sustainability of Fossil Fuels and Non-Fuel Mineral Depletion. *Renew. Sustain. Energy Rev.* **2017**, *76*, 202–211.

(4) Lewis, N. S.; Nocera, D. G. Powering the Planet: Chemical Challenges in Solar Energy Utilization. *Proc. Natl. Acad. Sci.* **2006**, *103*, 15729–15735.

(5) De Luna, P.; Hahn, C.; Higgins, D.; Jaffer, S. A.; Jaramillo, T. F.; Sargent, E. H. What Would It Take for Renewably Powered Electrosynthesis to Displace Petrochemical Processes? *Science* **2019**, *364*, eaav3506.

(6) Francke, R.; Schille, B.; Roemelt, M. Homogeneously Catalyzed Electroreduction of Carbon Dioxide—Methods, Mechanisms, and Catalysts. *Chem. Rev.* **2018**, *118*, 4631–4701.

(7) Can, M.; Armstrong, F. A.; Ragsdale, S. W. Structure, Function, and Mechanism of the Nickel Metalloenzymes, CO Dehydrogenase, and Acetyl-CoA Synthase. *Chem. Rev.* **2014**, *114*, 4149–4174.

(8) Corbin, N.; Zeng, J.; Williams, K.; Manthiram, K. Heterogeneous Molecular Catalysts for Electrocatalytic CO_2 Reduction. *Nano Res.* **2019**, *12*, 2093–2125.

(9) Meshitsuka, S.; Ichikawa, M.; Tamaru, K. Electrocatalysis by Metal Phthalocyanines in the Reduction of Carbon Dioxide. *J. Chem. Soc. Chem. Commun.* **1974**, 158–159.

(10) Fisher, B. J.; Eisenberg, R. Electrocatalytic Reduction of Carbon Dioxide by Using Macrocycles of Nickel and Cobalt. *J. Am. Chem. Soc.* **1980**, *102*, 7361–7363.

(11) Beley, M.; Collin, J.-P.; Ruppert, R.; Sauvage, J.-P. Nickel(II)-Cyclam: An Extremely Selective Electrocatalyst for Reduction of CO_2 in Water. *J. Chem. Soc. Chem. Commun.* **1984**, 1315–1316.

(12) Hammouche, M.; Lexa, D.; Savéant, J. M.; Momenteau, M. Catalysis of the Electrochemical Reduction of Carbon Dioxide by Iron("0") Porphyrins. *J. Electroanal. Chem. Interfacial Electrochem.* **1988**, *249*, 347–351.

(13) Hawecker, J.; Lehn, J.-M.; Ziessel, R. Electrocatalytic Reduction of Carbon Dioxide Mediated by $Re(Bipy)(CO)_3Cl$ (Bipy = 2,2′-Bipyridine). *J. Chem. Soc. Chem. Commun.* **1984**, 328–330.

(14) Ishida, Hitoshi.; Tanaka, Koji.; Tanaka, Toshio. Electrochemical CO_2 Reduction Catalyzed by Ruthenium Complexes $[Ru(bpy)_2(CO)_2]^{2+}$ and $[Ru(bpy)_2(CO)Cl]^+$. Effect of PH on the Formation of CO and $HCOO^-$. *Organometallics* **1987**, *6*, 181–186.

(15) Bolinger, C. M.; Story, N.; Sullivan, B. P.; Meyer, T. J. Electrocatalytic Reduction of Carbon Dioxide by 2,2'-Bipyridine Complexes of Rhodium and Iridium. *Inorg. Chem.* **1988**, *27*, 4582–4587.

(16) Sampson, M. D.; Nguyen, A. D.; Grice, K. A.; Moore, C. E.; Rheingold, A. L.; Kubiak, C. P. Manganese Catalysts with Bulky Bipyridine Ligands for the Electrocatalytic Reduction of Carbon Dioxide: Eliminating Dimerization and Altering Catalysis. *J. Am. Chem. Soc.* **2014**, *136*, 5460–5471.

(17) Slater, S.; Wagenknecht, J. H. Electrochemical Reduction of Carbon Dioxide Catalyzed by $Rh(Diphos)_2Cl$. *J. Am. Chem. Soc.* **1984**, *106*, 5367–5368.

(18) DuBois, D. L.; Miedaner, A.; Haltiwanger, R. C. Electrochemical Reduction of Carbon Dioxide Catalyzed by [Pd(Triphosphine)(Solvent)]$(BF_4)_2$ Complexes: Synthetic and Mechanistic Studies. *J. Am. Chem. Soc.* **1991**, *113*, 8753–8764.
(19) Drover, M. W. A Guide to Secondary Coordination Sphere Editing. *Chem. Soc. Rev.* **2022**, *51*, 1861–1880.
(20) Mondal, B.; Song, J.; Neese, F.; Ye, S. Bio-Inspired Mechanistic Insights into CO_2 Reduction. *Curr. Opin. Chem. Biol.* **2015**, *25*, 103–109.
(21) Gong, W.; Hao, B.; Wei, Z.; Ferguson, D. J.; Tallant, T.; Krzycki, J. A.; Chan, M. K. Structure of the $\alpha_2\varepsilon_2$ Ni-Dependent CO Dehydrogenase Component of the Methanosarcina Barkeri Acetyl-CoA Decarbonylase/Synthase Complex. *Proc. Natl. Acad. Sci.* **2008**, *105*, 9558–9563.
(22) Drennan, C. L.; Heo, J.; Sintchak, M. D.; Schreiter, E.; Ludden, P. W. Life on Carbon Monoxide: X-Ray Structure of Rhodospirillum Rubrum Ni-Fe-S Carbon Monoxide Dehydrogenase. *Proc. Natl. Acad. Sci.* **2001**, *98*, 11973–11978.
(23) Jeoung, J.-H.; Dobbek, H. Carbon Dioxide Activation at the Ni,Fe-Cluster of Anaerobic Carbon Monoxide Dehydrogenase. *Science* **2007**, *318*, 1461–1464.
(24) Boutin, E.; Robert, M. Molecular Electrochemical Reduction of CO_2 beyond Two Electrons. *Trends Chem.* **2021**, *3*, 359–372.
(25) Ribbe, M. W.; Hu, Y.; Hodgson, K. O.; Hedman, B. Biosynthesis of Nitrogenase Metalloclusters. *Chem. Rev.* **2014**, *114*, 4063–4080.
(26) Zanello, P. Structure and Electrochemistry of Proteins Harboring Iron-Sulfur Clusters of Different Nuclearities. Part V. Nitrogenases. *Coord. Chem. Rev.* **2019**, *398*, 113004.
(27) Tanifuji, K.; Ohki, Y. Metal–Sulfur Compounds in N_2 Reduction and Nitrogenase-Related Chemistry. *Chem. Rev.* **2020**, *120*, 5194–5251.
(28) Nitopi, S.; Bertheussen, E.; Scott, S. B.; Liu, X.; Engstfeld, A. K.; Horch, S.; Seger, B.; Stephens, I. E. L.; Chan, K.; Hahn, C.; Nørskov, J. K.; Jaramillo, T. F.; Chorkendorff, I. Progress and Perspectives of Electrochemical CO_2 Reduction on Copper in Aqueous Electrolyte. *Chem. Rev.* **2019**, *119*, 7610–7672.
(29) Carbon-Carbon Bond Formation in Multi-electron Reduction of Carbon Dioxide Catalyzed by $[Ru(bpy)(trpy)(CO)]^{2+}$ (bpy = 2,2′-bipyridine; trpy = 2,2′:6′,2″-terpyridine). *Chemistry Letters*, **1993**, 955 – 958.
(30) Nagao, H.; Mizukawa, T.; Tanaka, K. Carbon-Carbon Bond Formation in the Electrochemical Reduction of Carbon Dioxide Catalyzed by a Ruthenium Complex. *Inorg. Chem.* **1994**, *33*, 3415–3420.
(31) Costentin, C.; Savéant, J.-M. Towards an Intelligent Design of Molecular Electrocatalysts. *Nat. Rev. Chem.* **2017**, *1*, 0087.
(32) Ramos Sende, J. A.; Arana, C. R.; Hernandez, L.; Potts, K. T.; Keshevarz-K, M.; Abruna, H. D. Electrocatalysis of CO_2 Reduction in Aqueous Media at Electrodes Modified with Electropolymerized Films of Vinylterpyridine Complexes of Transition Metals. *Inorg. Chem.* **1995**, *34*, 3339–3348.
(33) Nagana, J. K.; Lucienna, Wolf, L. M.; Mullick, K.; Reinheimer, E.; Saucedo, C.; Wilson, M. E.; Grice, K. A.; Ertem, M. Z.; Angeles-Boza, A. M. Methane Generation from CO_2 with a Molecular Rhenium Catalyst. Inorg. Chem. **2021**, *60*, 3572–3584.
(34) Smieja, J. M.; Kubiak, C. P. $Re(bipy\text{-}tBu)(CO)_3Cl$−improved Catalytic Activity for Reduction of Carbon Dioxide: IR-Spectroelectrochemical and Mechanistic Studies. *Inorg. Chem.* **2010**, *49*, 9283–9289.

(35) Jiang, W.-X.; Liu, W.-X.; Wang, C.-L.; Zhan, S.-Z.; Wu, S.-P. A Bis(Thiosemicarbazonato)-Copper Complex, a New Catalyst for Electro- and Photo-Reduction of CO_2 to Methanol. *New J. Chem.* **2020**, *44*, 2721–2726.
(36) Crouch, P. J.; Barnham, K. J. Therapeutic Redistribution of Metal Ions to Treat Alzheimer's Disease. *Acc. Chem. Res.* **2012**, *45*, 1604–1611.
(37) Rao, H.; Schmidt, L. C.; Bonin, J.; Robert, M. Visible-Light-Driven Methane Formation from CO_2 with a Molecular Iron Catalyst. *Nature* **2017**, *548*, 74–77.
(38) Karunadasa, H. I.; Chang, C. J.; Long, J. R. A Molecular Molybdenum-Oxo Catalyst for Generating Hydrogen from Water. *Nature* **2010**, *464*, 1329–1333.
(39) Karunadasa, H. I.; Montalvo, E.; Sun, Y.; Majda, M.; Long, J. R.; Chang, C. J. A Molecular MoS_2 Edge Site Mimic for Catalytic Hydrogen Generation. *Science* **2012**, *335*, 698–702.
(40) Sun, Y.; Bigi, J. P.; Piro, N. A.; Tang, M. L.; Long, J. R.; Chang, C. J. Molecular Cobalt Pentapyridine Catalysts for Generating Hydrogen from Water. *J. Am. Chem. Soc.* **2011**, *133*, 9212–9215.
(41) Sun, Y.; Sun, J.; Long, J. R.; Yang, P.; Chang, C. J. Photocatalytic Generation of Hydrogen from Water Using a Cobalt Pentapyridine Complex in Combination with Molecular and Semiconductor Nanowire Photosensitizers. *Chem. Sci.* **2012**, *4*, 118–124.
(42) King, A. E.; Surendranath, Y.; Piro, N. A.; Bigi, J. P.; Long, J. R.; Chang, C. J. A Mechanistic Study of Proton Reduction Catalyzed by a Pentapyridine Cobalt Complex: Evidence for Involvement of an Anation-Based Pathway. *Chem. Sci.* **2013**, *4*, 1578–1587.
(43) Derrick, J. S.; Loipersberger, M.; Chatterjee, R.; Iovan, D. A.; Smith, P. T.; Chakarawet, K.; Yano, J.; Long, J. R.; Head-Gordon, M.; Chang, C. J. Metal–Ligand Cooperativity via Exchange Coupling Promotes Iron- Catalyzed Electrochemical CO_2 Reduction at Low Overpotentials. *J. Am. Chem. Soc.* **2020**, *142*, 20489–20501.
(44) Loipersberger, M.; Zee, D. Z.; Panetier, J. A.; Chang, C. J.; Long, J. R.; Head-Gordon, M. Computational Study of an Iron(II) Polypyridine Electrocatalyst for CO_2 Reduction: Key Roles for Intramolecular Interactions in CO_2 Binding and Proton Transfer. *Inorg. Chem.* **2020**, *59*, 8146–8160.
(45) Jurss, J. W.; Khnayzer, R. S.; Panetier, J. A.; Roz, K. A. E.; Nichols, E. M.; Head-Gordon, M.; Long, J. R.; Castellano, F. N.; Chang, C. J. Bioinspired Design of Redox-Active Ligands for Multielectron Catalysis: Effects of Positioning Pyrazine Reservoirs on Cobalt for Electro- and Photocatalytic Generation of Hydrogen from Water. *Chem. Sci.* **2015**, *6*, 4954–4972.
(46) Sundstrom, E. J.; Yang, X.; Thoi, V. S.; Karunadasa, H. I.; Chang, C. J.; Long, J. R.; Head-Gordon, M. Computational and Experimental Study of the Mechanism of Hydrogen Generation from Water by a Molecular Molybdenum-Oxo Electrocatalyst. *J. Am. Chem. Soc.* **2012**, *134*, 5233–5242.
(47) Zee, D. Z.; Nippe, M.; King, A. E.; Chang, C. J.; Long, J. R. Tuning Second Coordination Sphere Interactions in Polypyridyl–Iron Complexes to Achieve Selective Electrocatalytic Reduction of Carbon Dioxide to Carbon Monoxide. *Inorg. Chem.* **2020**, *59*, 5206–5217.
(48) Zee, D. Z.; Chantarojsiri, T.; Long, J. R.; Chang, C. J. Metal–Polypyridyl Catalysts for Electro- and Photochemical Reduction of Water to Hydrogen. *Acc. Chem. Res.* **2015**, *48*, 2027–2036.
(49) Wuttig, A.; Derrick, J. S.; Loipersberger, M.; Snider, A.; Head-Gordon, M.; Chang, C. J.; Toste, F. D. Controlled Single-Electron Transfer via Metal–Ligand Cooperativity Drives

Divergent Nickel-Electrocatalyzed Radical Pathways. *J. Am. Chem. Soc.* **2021**, *143*, 6990–7001.
(50) Scarborough, C. C.; Lancaster, K. M.; DeBeer, S.; Weyhermüller, T.; Sproules, S.; Wieghardt, K. Experimental Fingerprints for Redox-Active Terpyridine in $[Cr(tpy)_2](PF_6)_n$ (n = 3–0), and the Remarkable Electronic Structure of $[Cr(tpy)_2]^{1-}$. *Inorg. Chem.* **2012**, *51*, 3718–3732.
(51) England, J.; Scarborough, C. C.; Weyhermüller, T.; Sproules, S.; Wieghardt, K. Electronic Structures of the Electron Transfer Series $[M(bpy)_3]^n$, $[M(tpy)_2]^n$, and $[Fe(^tbpy)_3]^n$ (M = Fe, Ru; n = 3^+, 2^+, 1^+, 0, 1^-): A Mössbauer Spectroscopic and DFT Study. *Eur. J. Inorg. Chem.* **2012**, *2012*, 4605–4621.
(52) Chen, L.; Chen, G.; Leung, C.-F.; Cometto, C.; Robert, M.; Lau, T.-C. Molecular Quaterpyridine-Based Metal Complexes for Small Molecule Activation: Water Splitting and CO_2 Reduction. *Chem. Soc. Rev.* **2020**, *49*, 7271–7283.
(53) Loipersberger, M.; Cabral, D. G. A.; Chu, D. B. K.; Head-Gordon, M. Mechanistic Insights into Co and Fe Quaterpyridine-Based CO_2 Reduction Catalysts: Metal–Ligand Orbital Interaction as the Key Driving Force for Distinct Pathways. *J. Am. Chem. Soc.* **2021**, *143*, 744–763.
(54) Stephens, D. E.; Nguyen, V. T.; Chhetri, B.; Clark, E. R.; Arman, H. D.; Larionov, O. V. Organocatalytic Synthesis of Methylene-Bridged N-Heterobiaryls. *Org. Lett.* **2016**, *18*, 5808–5811.
(55) Addison, A. W.; Rao, T. N.; Reedijk, J.; Rijn, J. van; Verschoor, G. C. Synthesis, Structure, and Spectroscopic Properties of Copper(II) Compounds Containing Nitrogen–Sulphur Donor Ligands; the Crystal and Molecular Structure of Aqua[1,7-Bis(N-Methylbenzimidazol-2′-Yl)-2,6-Dithiaheptane]Copper(II) Perchlorate. *J. Chem. Soc. Dalton Trans.* **1984**, 1349–1356.
(56) Evans, D. F. The Determination of the Paramagnetic Susceptibility of Substances in Solution by Nuclear Magnetic Resonance. *J. Chem. Soc.* **1959**, 2003–2005.
(57) Lee, K. J.; McCarthy, B. D.; Dempsey, J. L. On Decomposition, Degradation, and Voltammetric Deviation: The Electrochemist's Field Guide to Identifying Precatalyst Transformation. *Chem. Soc. Rev.* **2019**, *48*, 2927–2945.
(58) Martin, D. J.; McCarthy, B. D.; Piro, N. A.; Dempsey, J. L. Synthesis and Electrochemical Characterization of a Tridentate Schiff-Base Ligated Fe(II) Complex. *Polyhedron* **2016**, *114*, 200–204.
(59) Klein Gebbink, R. J. M.; Jonas, R. T.; Goldsmith, C. R.; Stack, T. D. P. A Periodic Walk: A Series of First-Row Transition Metal Complexes with the Pentadentate Ligand PY5. *Inorg. Chem.* **2002**, *41*, 4633–4641.
(60) Gonell, S.; Lloret-Fillol, J.; Miller, A. J. M. An Iron Pyridyl-Carbene Electrocatalyst for Low Overpotential CO_2 Reduction to CO. *ACS Catal.* **2021**, *11*, 615–626.
(61) Gonell, S.; Assaf, E. A.; Lloret-Fillol, J.; Miller, A. J. M. An Iron Bis(Carbene) Catalyst for Low Overpotential CO_2 Electroreduction to CO: Mechanistic Insights from Kinetic Zone Diagrams, Spectroscopy, and Theory. *ACS Catal.* **2021**, *11*, 15212–15222.
(62) Bordwell, F. G. Equilibrium Acidities in Dimethyl Sulfoxide Solution. *Acc. Chem. Res.* **1988**, *21*, 456–463.
(63) Brewer, T. F.; Chang, C. J. An Aza-Cope Reactivity-Based Fluorescent Probe for Imaging Formaldehyde in Living Cells. *J. Am. Chem. Soc.* **2015**, *137*, 10886–10889.

(64) Bruemmer, K. J.; Walvoord, R. R.; Brewer, T. F.; Burgos-Barragan, G.; Wit, N.; Pontel, L. B.; Patel, K. J.; Chang, C. J. Development of a General Aza-Cope Reaction Trigger Applied to Fluorescence Imaging of Formaldehyde in Living Cells. *J. Am. Chem. Soc.* **2017**, *139*, 5338–5350.
(65) Ceballos, B. M.; Yang, J. Y. Directing the Reactivity of Metal Hydrides for Selective CO_2 Reduction. *Proc. Natl. Acad. Sci.* **2018**, *115*, 12686–12691.
(66) Machan, C. W.; Stanton, C. J.; Vandezande, J. E.; Majetich, G. F.; Schaefer, H. F.; Kubiak, C. P.; Agarwal, J. Electrocatalytic Reduction of Carbon Dioxide by Mn(CN)(2,2′-Bipyridine)$(CO)_3$: CN Coordination Alters Mechanism. *Inorg. Chem.* **2015**, *54*, 8849–8856.
(67) Clark, M. L.; Cheung, P. L.; Lessio, M.; Carter, E. A.; Kubiak, C. P. Kinetic and Mechanistic Effects of Bipyridine (Bpy) Substituent, Labile Ligand, and Brønsted Acid on Electrocatalytic CO_2 Reduction by Re(Bpy) Complexes. *ACS Catal.* **2018**, *8*, 2021–2029.
(68) Kosugi, K.; Kondo, M.; Masaoka, S. Quick and Easy Method to Dramatically Improve the Electrochemical CO_2 Reduction Activity of an Iron Porphyrin Complex. *Angew. Chem. Int. Ed.* **2021**, *60*, 22070–22074.
(69) Dixon, N. E.; Lawrance, G. A.; Lay, P. A.; Sargeson, A. M.; Taube, H. Trifluoromethanesulfonates and Trifluoromethanesulfonato-O Complexes. In *Inorganic Syntheses*; John Wiley & Sons, Ltd, 1990; 70–76.
(70) Park, J. G.; Collins, B. A.; Darago, L. E.; Runčevski, T.; Ziebel, M. E.; Aubrey, M. L.; Jiang, H. Z. H.; Velasquez, E.; Green, M. A.; Goodpaster, J. D.; Long, J. R. Magnetic Ordering through Itinerant Ferromagnetism in a Metal–Organic Framework. *Nat. Chem.* **2021**, *13*, 594–598.
(71) Pitman, C. L.; Miller, A. J. M. Molecular Photoelectrocatalysts for Visible Light-Driven Hydrogen Evolution from Neutral Water. *ACS Catal.* **2014**, *4*, 2727–2733.
(72) Stratakes, B. M.; Miller, A. J. M. H_2 Evolution at an Electrochemical "Underpotential" with an Iridium-Based Molecular Photoelectrocatalyst. *ACS Catal.* **2020**, *10*, 9006–9018.
(73) Stratakes, B. M.; Dempsey, J. L.; Miller, A. J. M. Determining the Overpotential of Electrochemical Fuel Synthesis Mediated by Molecular Catalysts: Recommended Practices, Standard Reduction Potentials, and Challenges. *ChemElectroChem* **2021**, *8*, 4161–4180.
(74) Shon, J.-H.; Teets, T. S. Photocatalysis with Transition Metal Based Photosensitizers. *Comments Inorg. Chem.* **2020**, *40*, 53–85.
(75) Kawamata, Y.; Yan, M.; Liu, Z.; Bao, D.-H.; Chen, J.; Starr, J. T.; Baran, P. S. Scalable, Electrochemical Oxidation of Unactivated C–H Bonds. *J. Am. Chem. Soc.* **2017**, *139*, 7448–7451.
(76) Saito, M.; Kawamata, Y.; Meanwell, M.; Navratil, R.; Chiodi, D.; Carlson, E.; Hu, P.; Chen, L.; Udyavara, S.; Kingston, C.; Tanwar, M.; Tyagi, S.; McKillican, B. P.; Gichinga, M. G.; Schmidt, M. A.; Eastgate, M. D.; Lamberto, M.; He, C.; Tang, T.; Malapit, C. A.; Sigman, M. S.; Minteer, S. D.; Neurock, M.; Baran, P. S. N-Ammonium Ylide Mediators for Electrochemical C–H Oxidation. *J. Am. Chem. Soc.* **2021**, *143*, 7859–7867.
(77) Robinson, S. G.; Wu, X.; Jiang, B.; Sigman, M. S.; Lin, S. Mechanistic Studies Inform Design of Improved Ti(Salen) Catalysts for Enantioselective [3 + 2] Cycloaddition. *J. Am. Chem. Soc.* **2020**, *142*, 18471–18482.
(78) Liu, J.; Lu, L.; Wood, D.; Lin, S. New Redox Strategies in Organic Synthesis by Means of Electrochemistry and Photochemistry. *ACS Cent. Sci.* **2020**, *6*, 1317–1340.

(79) Kim, H.; Kim, H.; Lambert, T. H.; Lin, S. Reductive Electrophotocatalysis: Merging Electricity and Light to Achieve Extreme Reduction Potentials. *J. Am. Chem. Soc.* **2020**, *142*, 2087–2092.
(80) Preger, Y.; Gerken, J. B.; Biswas, S.; Anson, C. W.; Johnson, M. R.; Root, T. W.; Stahl, S. S. Quinone-Mediated Electrochemical O_2 Reduction Accessing High Power Density with an Off-Electrode Co-N/C Catalyst. *Joule* **2018**, *2*, 2722–2731.
(81) Badalyan, A.; Stahl, S. S. Cooperative Electrocatalytic Alcohol Oxidation with Electron-Proton-Transfer Mediators. *Nature* **2016**, *535*, 406–410.
(82) Galvin, C. M.; Waymouth, R. M. Electron-Rich Phenoxyl Mediators Improve Thermodynamic Performance of Electrocatalytic Alcohol Oxidation with an Iridium Pincer Complex. *J. Am. Chem. Soc.* **2020**, *142*, 19368–19378.
(83) Nichols, E. M.; Derrick, J. S.; Nistanaki, S. K.; Smith, P. T.; Chang, C. J. Positional Effects of Second-Sphere Amide Pendants on Electrochemical CO_2 Reduction Catalyzed by Iron Porphyrins. *Chem. Sci.* **2018**, *9*, 2952–2960.
(84) Rigaku Oxford Diffraction. CrysAlisPro Software System; Rigaku Corporation: Oxford, UK, 2015.
(85) Nakai, H.; Jeong, K.; Matsumoto, T.; Ogo, S. Catalytic C–F Bond Hydrogenolysis of Fluoroaromatics by [(H_5-C_5Me_5)RhI(2,2′-Bipyridine)]. *Organometallics* **2014**, *33*, 4349–4352.
(86) Bain, G. A.; Berry, J. F. Diamagnetic Corrections and Pascal's Constants. *J. Chem. Educ.* **2008**, *85*, 532.

Appendix A: Development of Nickel Bis(iminopyridine) Complexes Directed Toward Electrochemical Carbon Dioxide and Carbon Monoxide Reduction

A.1 Introduction

The continued reliance of contemporary society on novel industrial and technological pursuits has forged a perpetually increasing demand for energy resources. Unfortunately, current infrastructures that rely on the utilization of fossil fuels are unsustainable due the vastly depleting oil, natural gas, and coal reserves.[1-3] Moreover, the continued combustion of fossil fuels has further led to increased atmospheric levels of carbon dioxide (CO_2), which has been shown to have significant and detrimental impacts on the environment and public health.[1-3] An attractive solution to meet such energy demands is to balance the carbon cycle by capturing and utilizing CO_2 as a source for carbon-based fuels.[4-6] The use of CO_2 as a fuel source is an attractive goal due to its abundance, renewability, and ability to be incorporated into existing energy infrastructure.[7]

Electrochemical reduction of CO_2 provides the means through which value-added chemicals and fuels such as ethanol, ethane, ethylene, acetate, methanol, formaldehyde, formate, and carbon monoxide (CO) can be generated from an abundant carbon feedstock.[8-11] While the last fifty years has seen significant advances in the development of both homogenous and heterogeneous electrochemical catalysts to facilitate these reductive transformations, there are still many formidable challenges to be surmounted before such processes can be employed as efficient replacements for current technology. Thermodynamically, proton-coupled electron transfer steps are generally more favorable because they produce more stable molecules and avoid the formation of a high energy bent, radical anion.[4,6,7,12] Achieving such coupling of multi-electron and proton steps at low overpotentials also presents a major kinetic challenge, such that the use of extremely effective and efficient catalysts is warranted.[6] Such catalysts should ideally possess high selectivity for CO_2 reduction products particularly over the competing processes of proton reduction to form hydrogen (H_2). Additional important considerations include the use of earth abundant metals, aqueous compatibility over organic solvents, and high catalyst efficiency and stability at low operating potentials.[6]

Current molecular systems capable of catalyzing the electrochemical reduction of CO_2 have advanced significantly in the last few decades through the use of creative catalyst designs, such as secondary coordination sphere modifications, proton relays, and the use of Lewis acids.[13-18] Even with so much effort focused on the development of CO_2 reduction catalysts there appears to be only a very limited number of privileged catalytic systems available to promote such transformations. For example, most CO_2 reduction catalysts can be classified into three categories based on their ligands.[6] These are (i) macrocycles, such as nickel cyclam or iron porphyrins,[19-23] (ii) bipyridine complexes largely pioneered by Kubiak and co-workers,[24-28] and (iii) polydentate phosphine complexes, such as the palladium complexes first reported by Dubois.[29-33] The goal of our work is to expand ligand design beyond these limiting regimes such that we investigate novel systems for CO_2 reduction. The ideal molecular catalysts that we envision would possess a few key properties.

First, they should be targeted to get beyond CO_2 to CO conversion. Next, they should be modular and synthetically facile to generate so that they can be easily and quickly tuned, both electronically and sterically. Finally, the employment of redox non-innocent ligands should be incorporated in order to facilitate multi-electron redox changes on earth abundant metal complexes.[34] Herein, we report our efforts towards these goals with the design, synthesis, and

analysis of a series of nickel bis(iminopyridine) complexes as electrochemical catalysts for CO_2 and CO reduction.

A.2 Results and Discussion

A.2.1 Design Rationale and Preparation of Nickel Bis(iminopyridine) Complexes

A series of nickel bis(iminopyridine) complexes (Ni(1) – Ni(9); **Figure A.1**) were synthesized and investigated for their reactivity towards CO_2 and CO reduction. The bis(iminopyridine) ligand scaffold was selected as a starting framework because it possesses many of the idealized properties we envisioned for our catalytic system (vide supra). For example, a small library of nickel complexes equipped with redox-active imine ligands, was quickly synthesized through a facile, high-yielding, one-step imine condensation reaction following slight modifications to previous literature reports (**Scheme A.1**).[35,36]

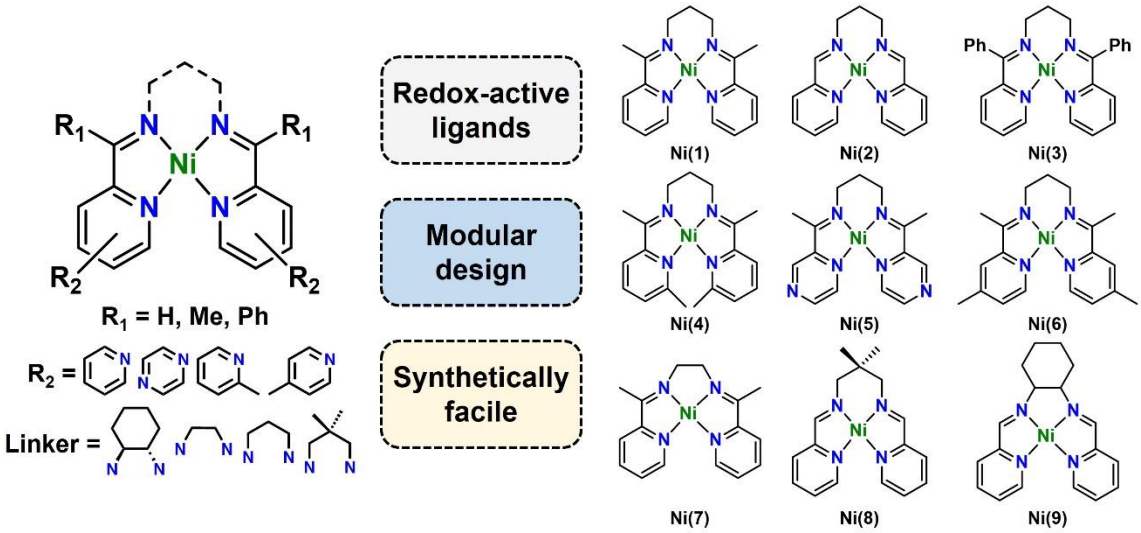
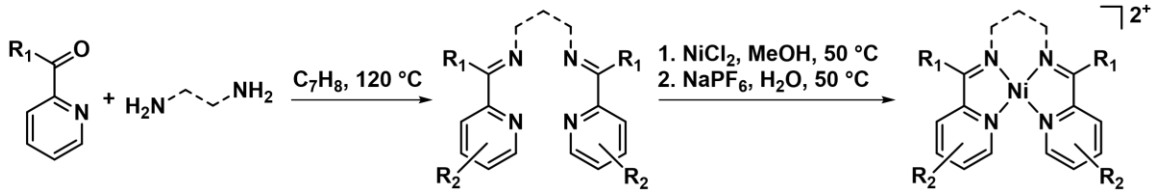


Figure A.1. Structural variations on a nickel bis(iminopyridine) framework for electrochemical catalysis of CO_2 and CO. The ligand scaffold was modified at three positions: (i) the R_1 position on the imine (blue), (ii) the R_2 position on the pyridine (purple), and (iii) the diamine linker (green).



Scheme A.1. General synthetic route to ligands **1**–**9** and complexes Ni(1)–Ni(9).

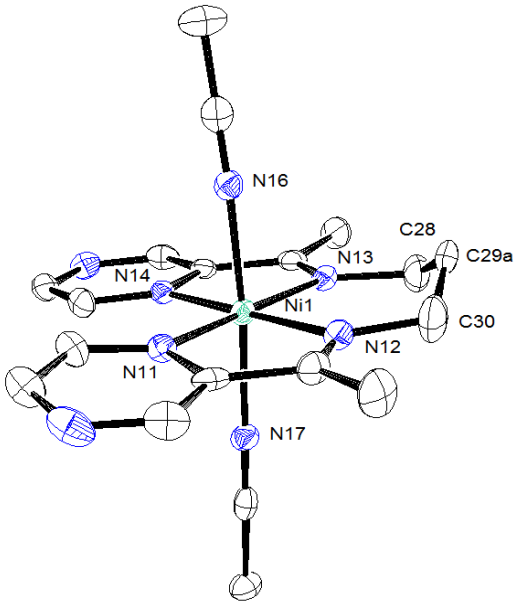
Briefly, two equivalents of a substituted acetyl pyridine derivative were allowed to react with a diamine linker (1 equiv.) and heated at reflux for 24 to 48 h with a condenser fitted with a Dean-Stark apparatus (**Scheme A.1**). The sterically hindered imine ligand, **3**, was generated by continuous heating and distillation in a drying agent of tetraethyl orthosilicate.[36] The ligand solutions were then concentrated and used for the subsequent metalation reactions without further purification. The nickel complexes [Ni(1) – Ni(9)] were then generated by slowly adding a solution of nickel(II) chloride hexahydrate ($NiCl_2$•$6H_2O$) to a methanol solution of ligand (**1** – **9**) and

filtered. A salt metathesis reaction with three equivalents of sodium hexafluorophosphate ($NaPF_6$) yielded the final complexes as PF_6 salts (**Scheme A.1**). The nickel complexes were then crystallized by slow diffusion of either diethyl ether or diisopropyl ether into a saturated acetonitrile solution.

Through this synthetic approach we were able to modify the nickel complexes at three locations in order to tune both the sterics and electronics of the complexes. First, at the R_1 position the imines were modified with either a hydrogen atom, methyl, or phenyl moiety (Ni(1), Ni(2), and Ni(3), respectively; **Figure A.1**). We envisioned that increased steric bulk, as well as incorporation of an aromatic functional group at this position might help to stabilize and prevent the possible dimerization of the reduced complexes.[37] The pyridine unit was also altered through the installation of a pyrazine [Ni(5)] or a methyl group *ortho* or *para* to the *N*-donor atom (Ni(4) and Ni(6), respectively). We predicted that *ortho* methyl groups may distort the tetradentate ligand from a coplanar orientation[38] while the *para* substitution may increase the σ-donor properties of the pyridine ligand; however, diffraction quality crystals have not yet been obtained to confirm this hypothesis (**Figure A.1**). Substitution of the pyridine for pyrazine was also investigated due to its ability to fine-tune the electronics of a series of cobalt water reduction catalyst, possibly due to its lower lying π* orbitals that enhanced the degree of π-backbonding causing anodic shifts in the reduction potentials of the catalyst.[39] Final structural modifications were engendered through selection of the diamine moiety.[39-41] Rigidity was controlled through the choice of either ethylenediamine [Ni(7)] or 1,2-diaminocyclohexane and a more flexible 1,3-diaminopropane moieties (**Figure A.1**).

A.2.2 X-Ray Crystallographic Characterization of Ni(5)

In order to investigate the coordination chemistry of our nickel bis(iminopyridine) complexes, crystals of Ni(5) suitable for X-ray analysis were obtained by slow diffusion of diisopropyl ether into a saturated acetonitrile solution to give large yellow plates. Ni(5) crystallized in the monoclinic space group, C2/c, showing a pseudo-octahedral coordination environment with the tetradentate ligand occupying the equatorial plane and two acetonitrile molecules coordinating at the open axial sites. Selected bond metrics shown in **Figure A.2** are consistent with previous literature reports.[37,42,43] Nickel-pyrazine bond lengths (i.e., 2.128(5) Å and 2.096(5) Å) are slightly longer than the imine-nickel bonds and the axial acetonitrile molecules are slightly bent towards the pyrazine rings. The second carbon atom on the propyl linker was disordered, as were the non-coordinated acetonitrile molecules, which are located along the 2-fold axis (**Figure A.3**). Both disorders are appropriately modeled by altering the site occupancy factors. Additional efforts are still underway to grow and isolate diffraction quality crystals for the remaining complexes in order to evaluate the effect of our structural modifications on the coordination sphere of our nickel complexes.



Ni(1)–N(11)⍰	2.128(5)⍰Å⍰
Ni(1)–N(12)⍰	2.067(5)⍰Å⍰
Ni(1)–N(13)⍰	2.060(5)⍰Å⍰
Ni(1)–N(14)⍰	2.096(5)⍰Å⍰
Ni(1)–N(16)⍰	2.058(6)⍰Å⍰
Ni(1)–N(17)⍰	2.069(6)⍰Å⍰
N(11)–Ni(1)–N(14)⍰	107.20(19)°⍰
N(14)–Ni(1)–N(13)⍰	78.3(2)°⍰
N(13)–Ni(1)–N(12)⍰	96.6(2)°⍰
N(12)–Ni(1)–N(11)⍰	77.9(2)°⍰
N(14)–Ni(1)–N(16)⍰	90.3(2)°⍰
N(14)–Ni(1)–N(17)⍰	87.0(2)°⍰

Figure A.2. ORTEP diagram for Ni(5) with ellipsoids drawn at the 50% probability level. Non-coordinated PF_6 anions and hydrogen atoms are omitted for clarity. Selected distances (Å) and angles (°) are summarized in the **Table A.3**.

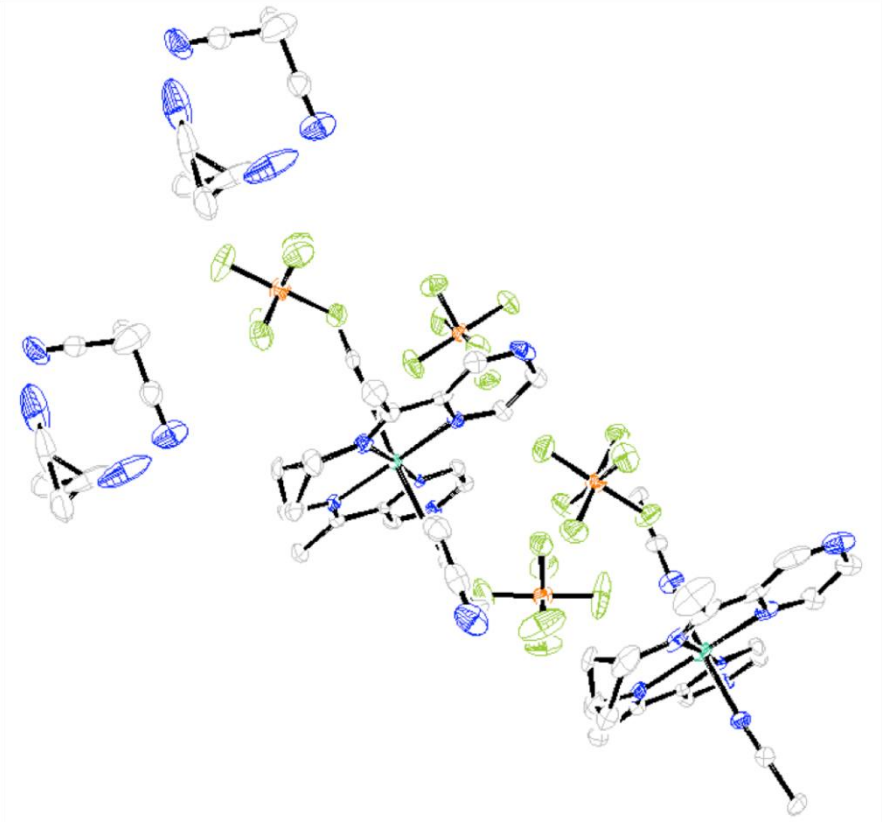


Figure A.3. Unit cell packing diagram for Ni(5).

A.2.3 Electrochemical CO_2 Reduction

To evaluate the competency of our nickel complexes as CO_2 reduction catalysts, non-aqueous cyclic voltammetry experiments in acetonitrile with 0.1 M tetrabutylammonium hexafluorophosphate (NBu_4PF_6) as a supporting electrolyte were conducted (**Figure A.4**). Under Ar atmosphere, all the complexes, except Ni(2) and Ni(9), showed two cathodic waves between ca. –1.0 – –1.5 V *vs.* Fc/Fc^+. These waves have been tentatively assigned as single-electron ligand-based reductions, most likely centered at the imines.[35,37] The separation between the reductive waves varied significantly between each complex. For example, for Ni(1), Ni(3), Ni(7), and Ni(8) the two waves are barely resolved, with a separation in peak cathodic potentials (E_{pc}) of ca. 0.25 V; while the first and second ligand-based reductions in Ni(4), Ni(5), and Ni(6) are separated by ca. 0.5 – 1.0 V. This suggests that modification to the pyridine (R_2 position; **Figure A.1**) may have a more significant effect on the electronics of the complexes than does modification at the imine or diamine linker.

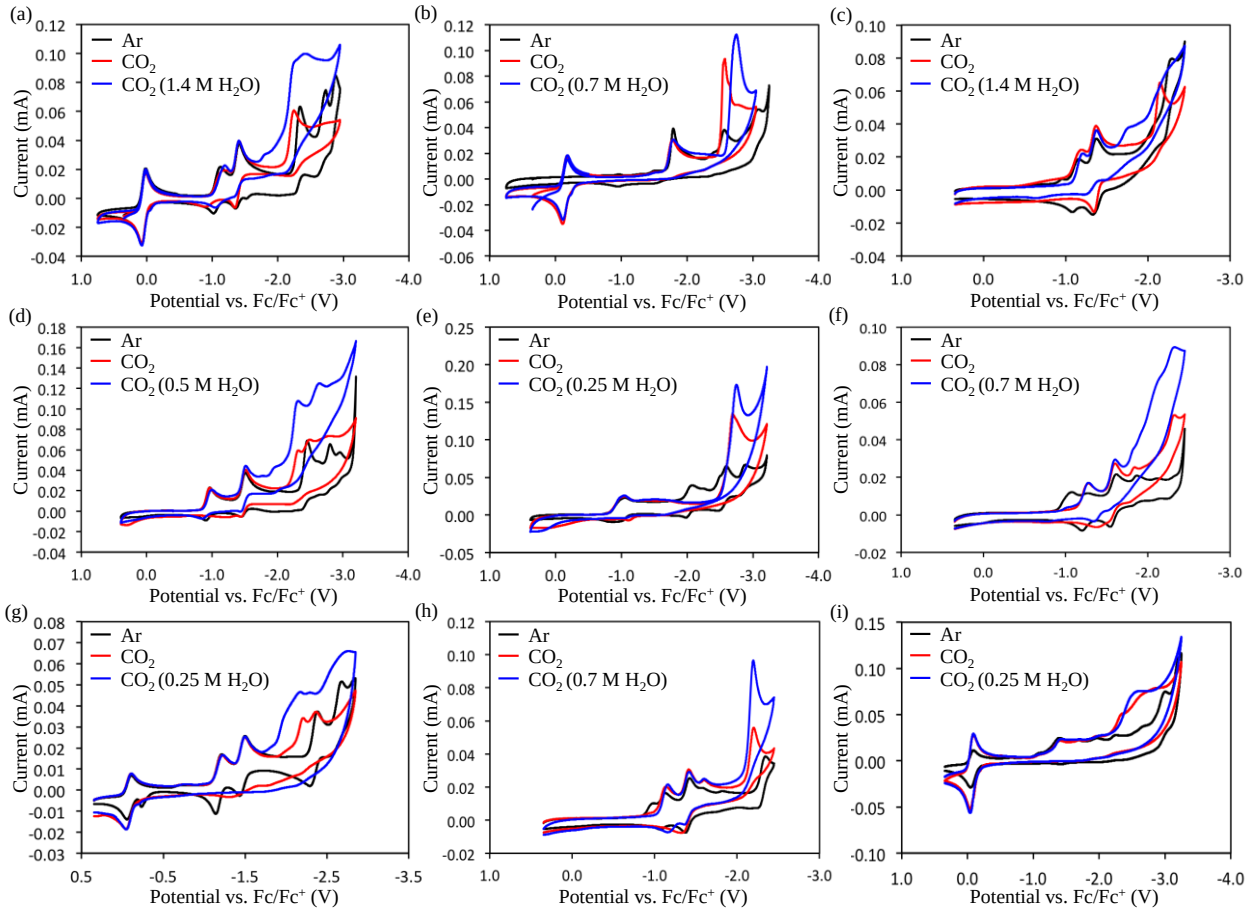


Figure A.4. Cyclic voltammograms of (a) Ni(1), (b) Ni(2), (c) Ni(3), (d) Ni(4), (e) Ni(5), (f) Ni(6), (g) Ni(7), (h) Ni(8), (i) Ni(9) in a 0.1 M NBu_4PF_6 acetonitrile solution under N_2 (black), CO_2 (red), and CO_2 and water (1.4–0.25 M; blue) atmosphere using a glassy carbon disk electrode at a scan rate of 100 mV/s.

Under a CO_2 atmosphere, the cyclic voltammograms of Ni(1) – Ni(9) show current enhancement at the third reductive wave (ca. 2.0 V *vs.* Fc/Fc^+) with an onset potential that is shifted anodically relative to the voltammograms collected under Ar, which is indicative of catalytic consumption of CO_2. Furthermore, there is a loss in reversibility of the return oxidation waves due to the coupled chemical reaction of CO_2 with the molecular catalysts. Further increases in the cathodic current of Ni(1) – Ni(9) were also observed upon the addition of water (0.25 – 1.4 M) as a proton source. Encouraged by these results, we employed controlled potential electrolysis (CPE) experiments under CO_2 atmosphere in order to identify and quantify the products as well as evaluate the long-term stability of our catalysts. The results from these experiments are summarized in **Table A.1** and **Figure A.5**. All complexes, except Ni(3)–Ni(5), exhibited relatively constant current over the examined CPE time scale, suggesting their relative stability under our experimental conditions. Small Faradaic efficiencies for CO and H_2 (FE_{CO} and FE_{H_2}) were observed for all nickel complexes with FE_{CO} between ca. 0 – 13% and FE_{H_2} of ca. 1 – 52%. Moreover, the total FE for gas phase products was found to be much less than 100%. This result led us to hypothesize that the remaining charge was being utilized to generate liquid products, possibly formate. To test this hypothesis, NMR was employed to analyze the CPE solutions, but unfortunately no signals corresponding to potential liquid phase products were observed. A potential explanation for this phenomenon could be that the CO generated during electrolysis may be binding to the reduced complexes and poisoning them, thus preventing further turnover and explaining the small FE for CO.

Table A.1. Summary of controlled potential electrolysis (CPE) experiments under CO_2 atmosphere for Ni(1) – Ni(9). Q is the charge passed during the experiment in coulombs (C).

Complex	Potential (V vs Fc/Fc^+)	Q (C)	FE_{CO} (%)	FE_{H_2} (%)	FE_{Total} (%)
Ni(1)	-2.125	14.0	13	10	23
Ni(2)	-2.050	11.1	11	19	30
Ni(3)	-2.250	15.0	2	48	50
Ni(4)	-2.210	1.6	4	1	5
Ni(5)	-2.236	0.12	0	0	0
Ni(6)	-2.278	2.7	9	52	61
Ni(7)	-1.700	3.1	6	20	26
Ni(8)	-2.175	6.6	11	1	12
Ni(9)	-2.324	5.7	3	44	47

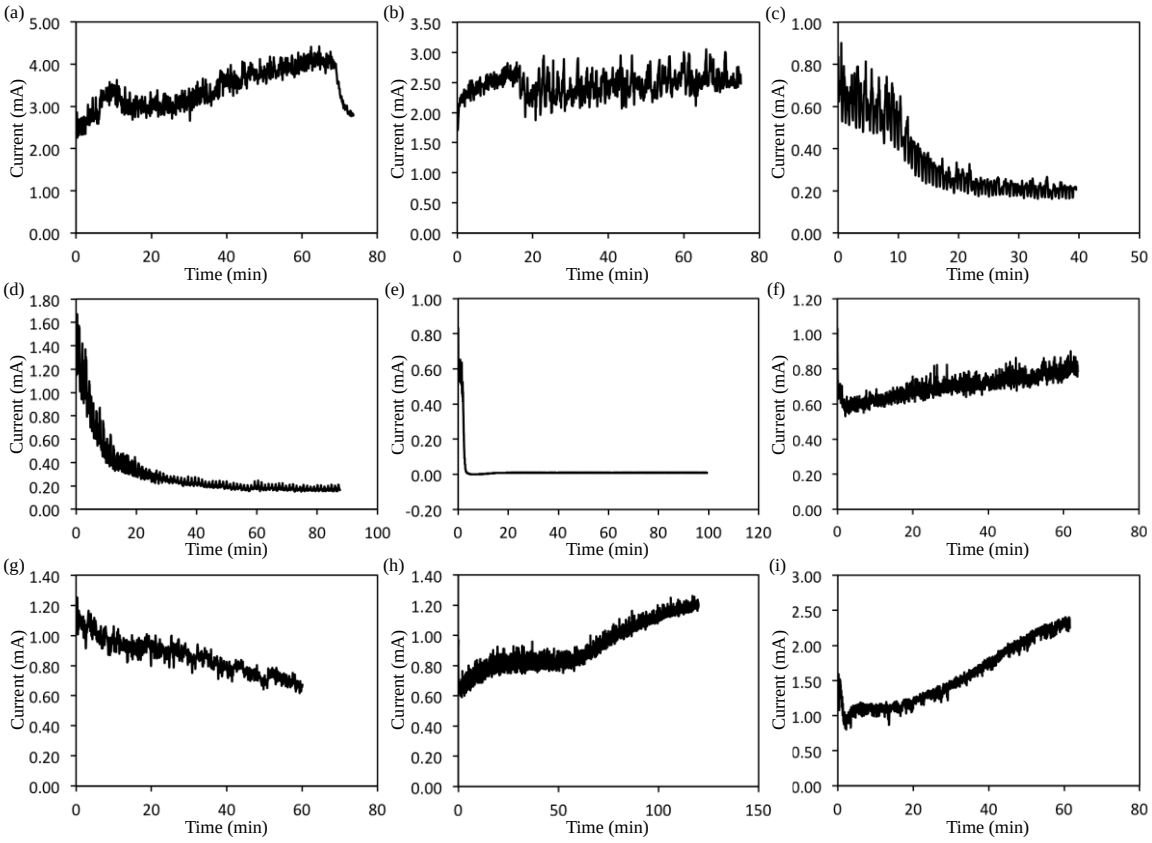


Figure A.5. Controlled potential electrolysis of (a) Ni(1), (b) Ni(2), (c) Ni(3), (d) Ni(4), (e) Ni(5), (f) Ni(6), (g) Ni(7), (h) Ni(8), (i) Ni(9) in a 0.1 M NBu_4PF_6 acetonitrile solution under CO_2 atmosphere using a glassy carbon plate.

To gauge the feasibility of CO poisoning of the reduced Ni(I) complexes, cyclic voltammograms were measured under CO atmosphere and association constants (K_{CO}) were obtained from the shift in the E_{pc} following previously reported methods.[44,45] The cyclic voltammograms of Ni(1) – Ni(9) under CO atmosphere are given in **Figure A.6** and the apparent K_{CO} determined from the voltammograms are summarized in **Table A.2**. The determined binding constants were found to vary over two orders of magnitude between our nickel complexes without any apparent structure-reactivity trends presenting themselves; however, there did appear to be a slight inverse correlation between FE_{total} and K_{CO}. For example, the strongest interaction with CO was observed for Ni(4), which had a FE_{total} of 5% while the weakest CO binder, Ni(9), with the diaminocyclohexane linker had the second largest FE_{total} (47%). While these trends may suggest that some degree of CO poisoning may be occurring, it alone does not appear to be the sole explanation for the small FE_{total} when one considers the overall magnitude of measured association constants with respect to other CO_2 reduction catalysts. Namely, compared to nickel cyclam, a well-established selective CO_2 reduction catalyst, our Ni complexes showed similar, if not lower, affinities for CO coordination (**Table A.2**). Current efforts are still underway to identify what is happening to the unaccounted charge.

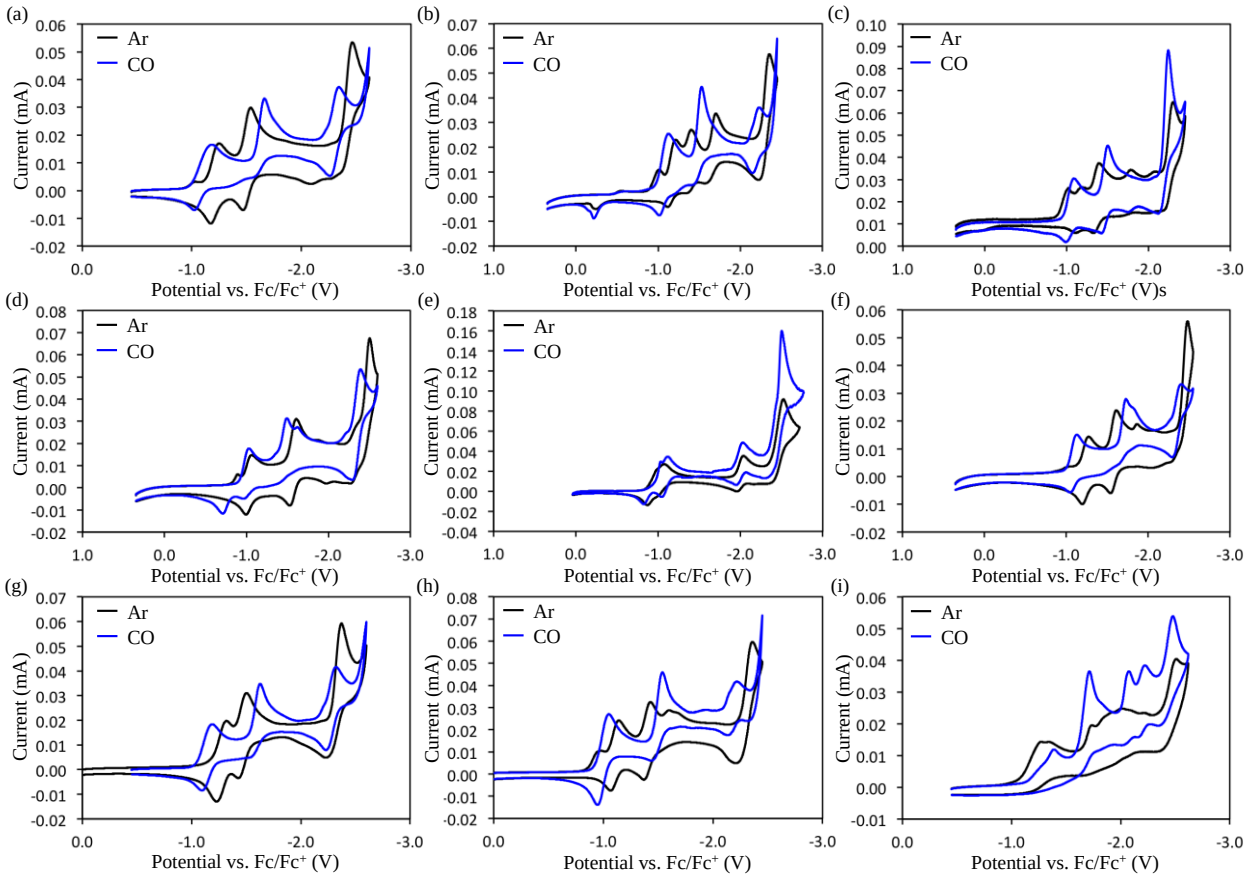


Figure A.6. Cyclic voltammograms of (a) Ni(1), (b) Ni(2), (c) Ni(3), (d) Ni(4), (e) Ni(5), (f) Ni(6), (g) Ni(7), (h) Ni(8), (i) Ni(9) in a 0.1 M NBu_4PF_6 acetonitrile solution under Ar (black) and CO (blue) atmospheres using a glassy carbon disk electrode at a scan rate of 100 mV/s.

Table 2. Approximate binding affinities of Ni(I) complexes for CO, K_{CO} (M^{-1}). Association constants were obtained from the shift in the peak cathodic potentials (E_{pc}) obtained from the voltammograms of Ni(1) – Ni(9) under Ar and CO atmospheres (**Figure A.6**).[44,45] K_{CO} for Ni(3) and Ni(5) are not reported due to the appearance of a potential catalytic wave.

Complex	K_{CO} (M^{-1})
Ni(1)	1.3×10^4
Ni(2)	1.9×10^4
Ni(3)	–
Ni(4)	5.5×10^4
Ni(5)	–
Ni(6)	2.6×10^3
Ni(7)	8.7×10^2
Ni(8)	2.9×10^4
Ni(9)	2.3×10^2
Ni(cyclam)	**7.5×10^4**

A.2.4 Electrochemical CO Reduction and Efforts Toward Product Detection

While the CO voltammetry experiments shown in **Figure A.6** did not give a clear explanation for the low Faradaic efficiencies observed for our nickel complexes as CO_2 reduction catalysts, it did display interesting results for Ni(3) and Ni(5). Upon saturation of acetonitrile solutions of Ni(3) or Ni(5) with CO, there was a noticeable increase in the cathodic wave at ca. 2.5 V *vs.* Fc/Fc^+ with a slight anodic shift in the onset potential as well as a loss in the reversibility of the return oxidation waves. These characteristics were suggestive of a catalytic reduction of CO. In order to further investigate this reactivity as well as identify any potential CO reduction products, CPE experiments were performed for Ni(5) under CO and Ar atmosphere (**Figure A.7**).

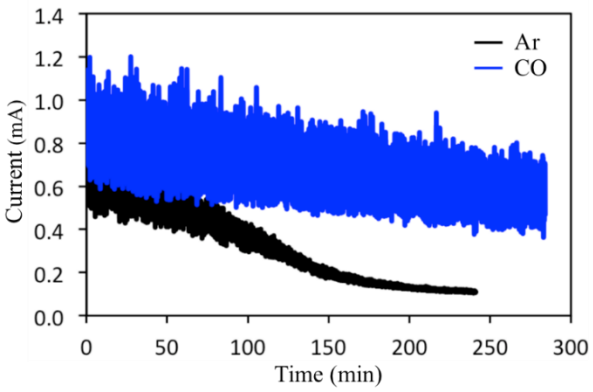


Figure A.7. Controlled potential electrolysis of Ni(5) in a 0.1 M NBu_4PF_6 acetonitrile solution under CO (blue) and Ar (black) atmosphere using a glassy carbon plate working electrode.

Under CO conditions, steady current was passed (Q = 15 C) over a 4 h time period along with drastic changes in color from a starting yellow solution to dark green during the first ca. 30 – 60 min of electrolysis, to a final deep red color at later time points (> 4 h). Analysis of the headspace for gaseous products by gas chromatography (GC) showed the absence of CO reduction products or H_2. Therefore, CPE experiments were repeated in deuterated acetonitrile and following electrolysis, the solutions were vacuum transferred to remove the NBu_4PF_6 and catalyst without losing any potential volatile products and analyzed by NMR (**Figure A.8**). The NMR spectrum showed two small singlets at 9.68 ppm and 3.25 ppm that were consistent with the presence of acetaldehyde (AA) and methanol, both of which are possible CO reduction products. The AA peak (9.86 ppm) was not observed in the Ar electrolyte controls, but a small peak at 3.26 ppm was discernable in the Ar control sample (**Figures A.9 and A.10**). Current efforts to repeat these experiments with the use of an internal integration standard for quantitative purposes have failed to generate reproducible results.

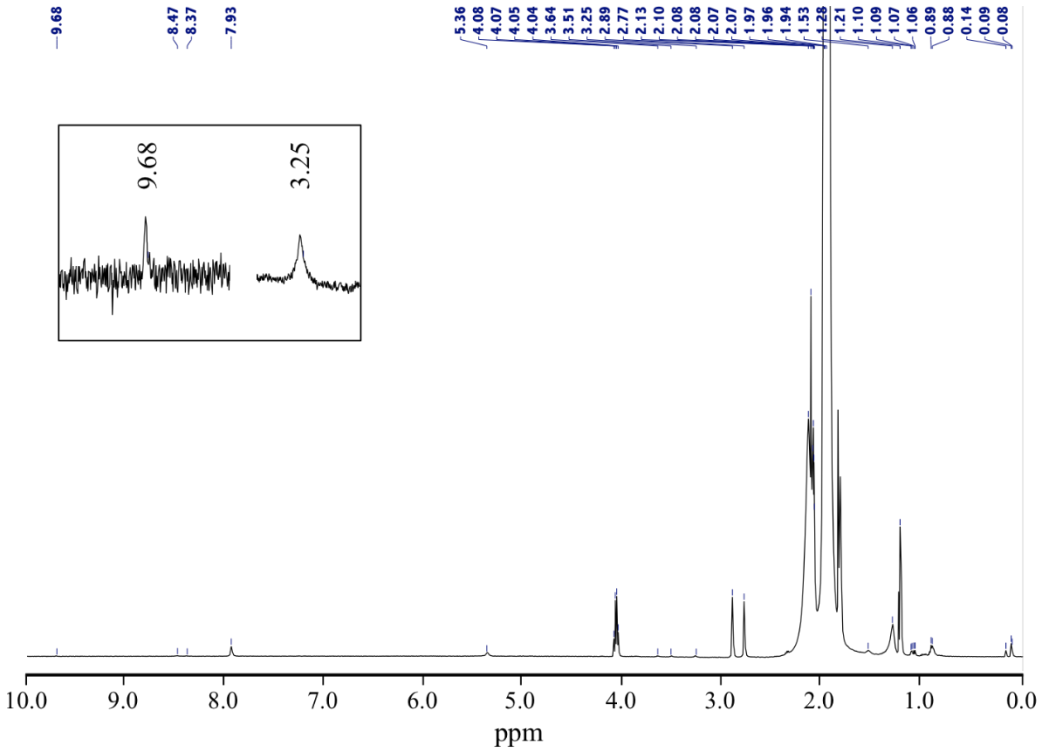


Figure A.8. NMR analysis of the CPE solution of Ni(5) under CO atmosphere.

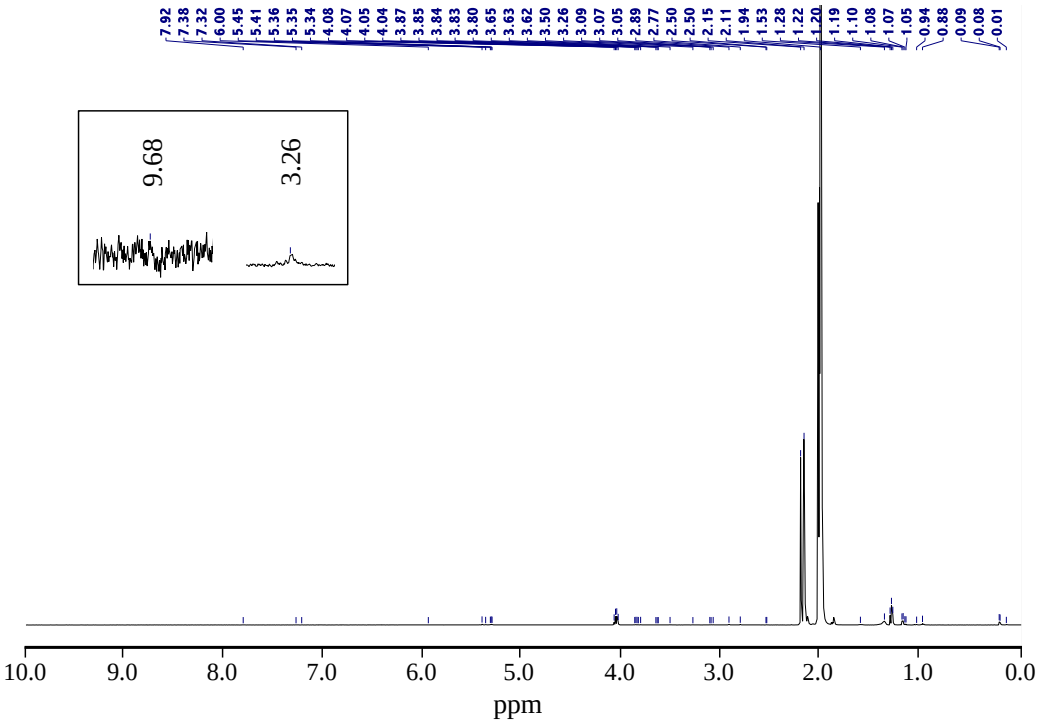


Figure A.9. NMR analysis of the CPE solution of Ni(5) under Ar atmosphere.

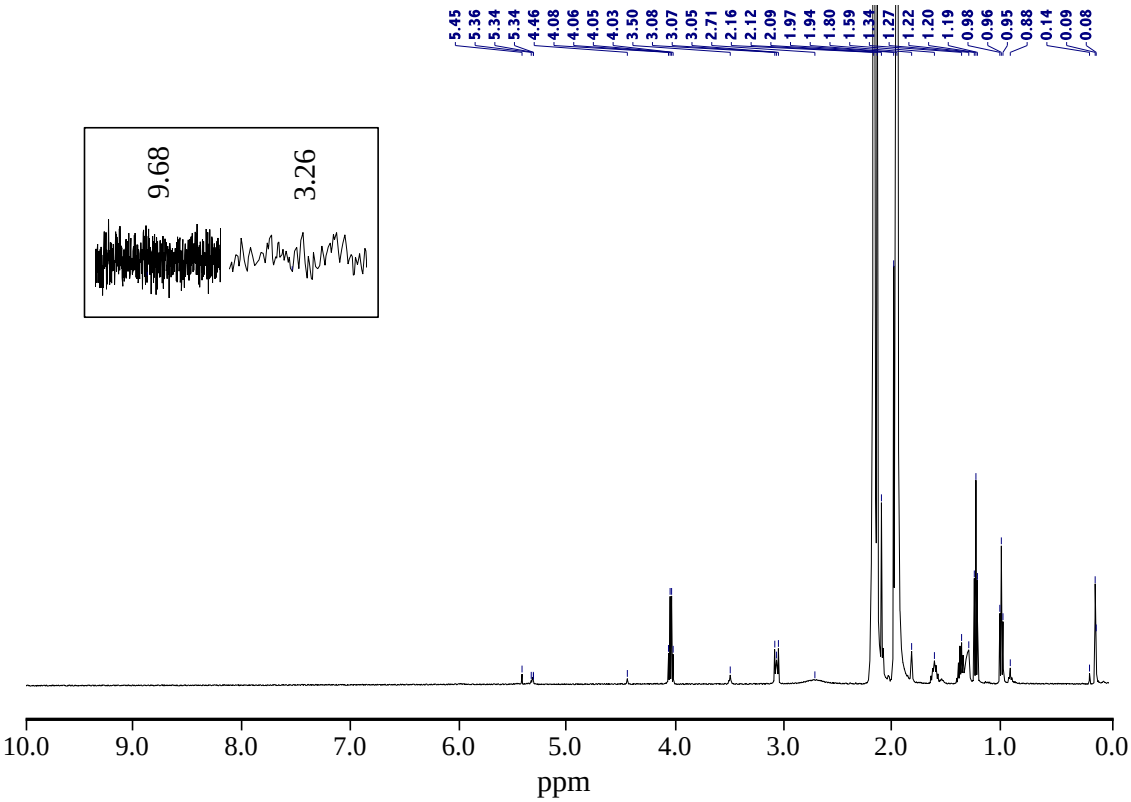
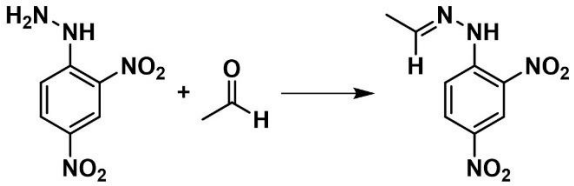


Figure A.10. NMR analysis of the 0.1 M Bu_4NPF_6 electrolyte solution in CD_3CN.

To further evaluate the production of AA as a potential product, UV-Visible (UV-Vis) spectroscopy experiments in the absence and presence of 2,4-dinitrophenylhydrazine (DNPH) were performed in order to stabilize AA as a hydrazone adduct for more facile detection (**Scheme A.2**).[46-48] The UV-visible spectrum of the CO saturated CPE solution incubated with DNPH produced a large absorption band at *ca.* 360 nm (**Figure A.11a**). This peak was not present in the untreated CPE solution or the DNPH solution, which showed a broad band with what appeared to be two poorly resolved peaks with λ_{max} at *ca.* 324 and 355 nm. The red-shift in the optical spectra upon incubation of the CO saturated CPE solution with DNPH is similar to that observed for the AA control treated with DNPH (λ_{max} (AA) = 290 nm; λ_{max} (DNPH) = 326 nm; λ_{max} (AA+DNPH) = 364 nm; **Figure A.12**). Analysis of the CPE solution under Ar atmosphere did not show a similar red-shift in the UV-Vis spectrum upon incubation with DNPH and instead appeared almost identical to that of the optical spectrum of DNPH alone (**Figure A.11b**). Taken together, these UV-Vis experiments support the production of AA (or other ketone/aldehydes) as a potential product for electrochemical CO reduction. These data are also in agreement with our preliminary NMR studies. Further efforts to detect potential products by high resolution mass spectrometry (HRMS), liquid chromatography-mass spectrometry (LC-MS), and gas chromatography-mass spectrometry (GC-MS) have been unsuccessful to date, mostly likely due to the small mass and low boiling points of potential products.



Scheme A.2. Detection of acetaldehyde (AA) by UV-vis through the formation of a DNPH adduct.

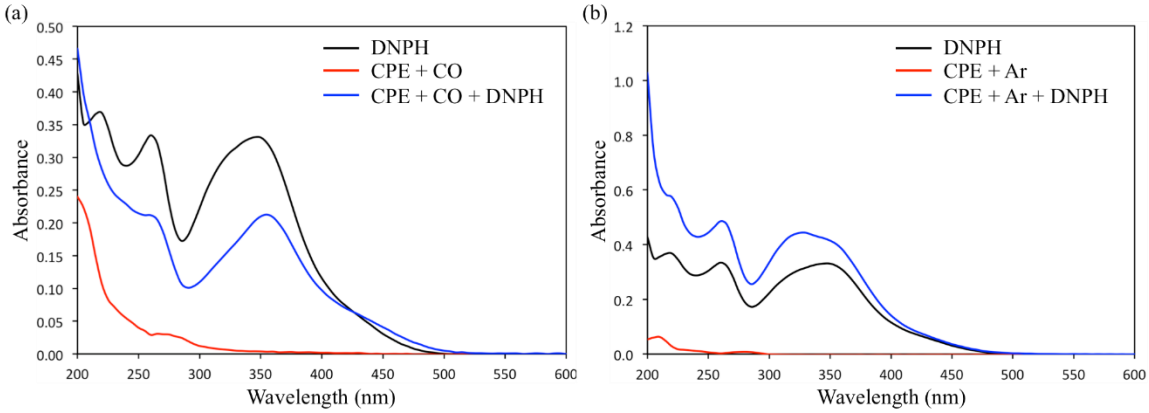


Figure A.11. UV-Vis analysis of CPE solutions of Ni(5) under (a) CO and (b) Ar atmospheres.

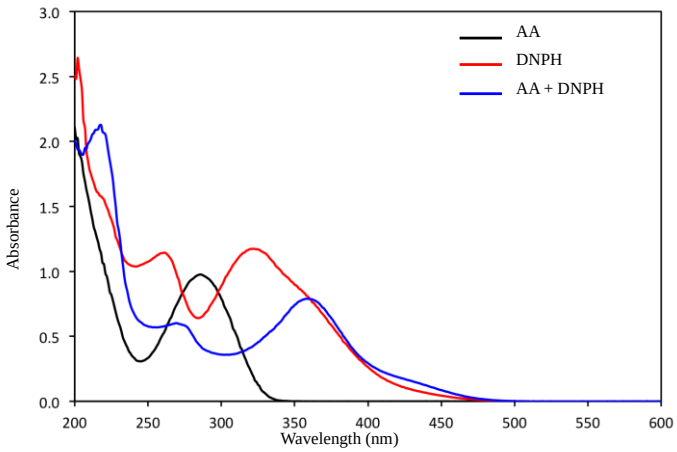


Figure A.12. UV-visible control experiments of acetaldehyde and DNPH.

A.2.5. Controlled Potential Electrolysis in ^{13}CO Atmosphere

In order to definitively determine if AA is being generated under our electrolysis experiments in addition to other potential CO derived products, CPE experiments were performed in ^{13}CO atmosphere. The resulting solution was vacuum transferred and then analyzed by ^{13}C NMR (**Figure A.13**). These experiments ruled out AA as a possible product as no signals at 201 and 31 ppm were observed consistent with AA formation in CD_3CN.[49] Note that the peaks at 163, 36, and 31 ppm were a result of a trace DMF contamination. The NMR spectrum instead showed two peaks at 192 and 185 ppm. The peak at 192 ppm was identified as nickel tetracarbonyl ($Ni(CO)_4$) and is consistent with previous reports, while the peak at 185 ppm is consistent with CO and may be from trace residual amounts of ^{13}CO or additional nickel carbonyl complexes.[50-52]

In light of these results, we propose a potential mode of action for our nickel bis(iminopyridine) complexes where, under electrolysis conditions, the nickel complex is reduced to generate Ni(I)bis(iminopyridine) complexes that facilitate the reduction of CO_2 to CO thus explaining the current increase under CO atmosphere in our CV experiments. The electrochemically generated CO then strongly binds to the reduced nickel metal centers leading to the chelation of the Ni atoms from the tetradentate ligands to give $Ni(CO)_4$ in addition to other nickel carbonyls as observed by ^{13}C NMR. Stoichiometric electrochemical ligand degradation may account for the additional unaccounted charge passed in our CPE experiments. Evidence for this can be seen in the ^{1}H NMR spectra of the CPE solutions measured before the vacuum transfer that exhibit numerous signals in the aromatic region. Overall, due to the high overpotential required for catalysis coupled with poor FE's for CO_2 reduction, limited catalyst stability (irrespective of synthetic tuning), and high affinity for CO poisoning, we have decided to pursue other avenues for electrochemical CO_2 and CO reduction.

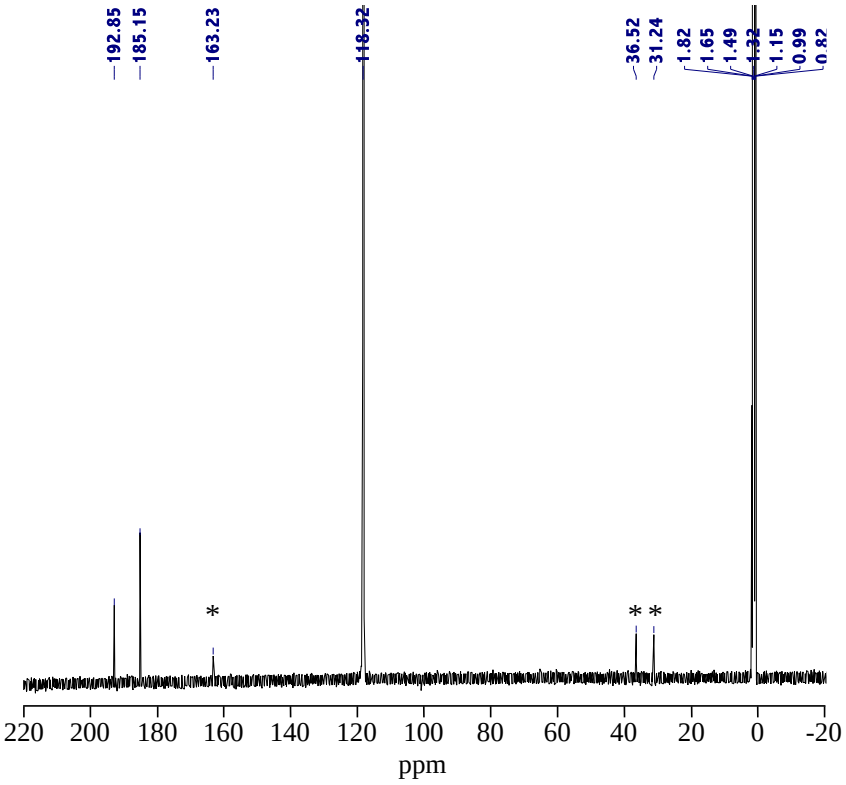


Figure A.13. NMR analysis of the CPE solution of Ni(5) under ^{13}CO atmosphere. Peaks at 192.85 and 185.15 ppm have been identified as $Ni(CO)_4$ and CO respectively. *Indicates peaks due to trace DMF contamination of the electrolyte.

A.3 Conclusion

In summary, this work demonstrates progress toward the design, synthesis, and characterization of a series of nickel-based CO_2 and CO reduction catalysts. Recent efforts were focused on identifying and quantifying the products of the electrochemical reaction between CO and Ni(5). To our knowledge, this would be the first homogenous electrochemical CO reduction catalyst, and therefore we have focused significant resources towards deciphering the reactivity that is occurring in this system. Unfortunately, our newly added CPE experiments with isotopically enriched CO support the poisoning and demetalation of our nickel complexes under electrochemical conditions. Subsequent ligand reduction and degradation then seems to account of the additional charge that is passed during our electrolysis experiments.

A.4 Materials and Methods

A.4.1 General Methods

All reagents and solvents were purchased from commercial sources and used without further purification. All NMR spectra were recorded at RT on a Bruker AV-500, DRX-500, AVB-400, AVQ-400, or AV-300 spectrometers. Chemical shifts were reported in ppm relative to residual protonated solvent; coupling constants are reported in Hz. UV-visible (UV-vis) spectra were collected on an Agilent Cary 60 spectrophotometer in CH_3CN at RT, unless otherwise noted. Electrospray ionization mass spectra (ESI-MS) were taken on an Advion Expression mass spectrometer. Fourier transform infrared (FT-IR) spectra were obtained with a Bruker Alpha-P spectrometer. Single crystals suitable for X-ray diffraction analysis were coated with paratone-N hydrocarbon oil and mounted on Kaptan loops. X-ray diffraction data was collected on a Bruker APEX II QUAZAR diffractometer equipped with an Oxford Cryostream 700 cryostat. Diffraction data was collected with a Mo-Kα radiation source (λ = 0.71073 Å) at 100 K. Bruker APEX2 v. 2009.1 software package was used to integrate raw data which was corrected for Lorentz and polarization effects.[54] Semi-empirical absorption correction (SADABS) was applied.[55] Space groups were identified by systematic absences, E-statistics, and successive refinement of the structure. SHELXL[56-58] was utilized to solve the structure with direct methods and refine the data with least-squares refinement based on F^2 and standard difference Fourier techniques. Thermal parameters for all non-hydrogen atoms were refined anisotropically and hydrogen atoms were included at ideal positions and refined isotropically.

A.4.2 Electrochemical Measurements

Electrochemistry was performed with either a Bioanalytical Systems, Inc. (BASi) Epsilon potentiostat or a CH Instruments, Inc. 600E potentiostat. Voltammetry studies were performed with a three-electrode cell equipped with a glassy carbon disk (3.0 mm diameter) working electrode, platinum wire counter electrode, and a silver wire in a porous Vycor tip glass tube filled with 0.1 M tetrabutylammonium hexafluorophosphate (NBu_4PF_6) in CH_3CN as a pseudoreference electrode. The scan rate for all cyclic voltammograms is 100 mV/s unless otherwise mentioned. All potentials were referenced against ferrocene/ferrocenium (Fc/Fc^+) as an internal standard. Controlled-potential electrolysis experiments were carried out using a custom-made Teflon two-compartment cell separated by a fine glass frit membrane. The cell is connected to a SIR gas chromatograph for headspace analysis. A glassy carbon plate (1 x 1 cm^2), carbon plate, and silver wire in a porous Vycor tip glass tube filled with 0.1 M tetrabutylammonium hexafluorophosphate (NBu_4PF_6) in CH_3CH was used as the working, counter-, and reference electrodes, respectfully.

Electrochemical determination of equilibrium constants for the binding of CO to the reduced Ni complexes was determined following previous literature methods.[59,60] Briefly, the equilibrium constants were determined from **Equation A.1**

$$K_{CO} = \frac{e^{\Delta E(\frac{nF}{RT})} - 1}{[CO]} \qquad \textbf{Equation A.1}$$

where ΔE is the difference in the peak cathodic potentials (E_{pc}) of the nickel bound CO complex and the free reduced Ni complex (i.e., $\Delta E = E_{pc,Ni-CO} - E_{pc,Ni}$). This value is obtained from the difference in E_{pc} of the formal Ni^{II}/Ni^{I} couple under CO and Ar atmospheres. F, is Faradays constant (96485 C mol^{-1}); n, is the number of electrons (n = 1); R, is the gas constant (8.314 J K^{-1} mol^{-1}); T, is the temperature (298 K); and [CO], the concentration of CO in solution (0.0083 M). It should be noted that this equation assumes that the Ni^{2+} complexes do not interact with CO.

A.4.3 Detection of CPE Products by NMR

Liquid phase products generated during controlled potential electrolysis (CPE) experiments were detected by NMR. CPE solutions were quickly transferred to a clean round-bottom flask with a syringe and frozen in liquid nitrogen to avoid any potential loss of volatile products. The electrolyte (0.1 M Bu_4NPF_6) and catalyst were removed from the electrolysis solution by vacuum transferring the volatile products into a new clean round bottom flask. The solutions were then frozen in liquid nitrogen and stored at –40 ºC and analyzed by NMR at RT.

A.4.4 UV-Visible DNPH Experiments for Acetaldehyde (AA) Detection

2,4-dinitrophenylhydrazine (DNPH) solutions for AA detection were obtained by following previous literature reports.[61-63] Commercially available DNPH was recrystallized three times from hot CH_3CN and dried overnight, protected from the light. The DNPH solution was then prepared by dissolving 20 mg of the recrystallized DNPH in 15 mL of a solution containing concentrated HCl (ca. 12 M), water, and CH_3CN in a ratio 2:5:1 (v/v/v). Potential carbonyl contamination was removed by extracting with hexanes (3x, 5 mL). The DNPH solution (100 μL) was then added to the CPE solutions (4 mL) in a scintillation vial charged with a stir bar and allowed to react for 24 h, protected from the light before analysis by UV-visible (UV-vis) spectroscopy.

A.4.5 General Synthetic Procedure for the Preparation of Bis(iminopyridine) Ligands

The synthesis of the bis(iminopyridine) ligands (**1–2** and **4–9**) were prepared through slight modifications to a previous literature report.[35] A 50 mL round-bottom flask was charged with a stir bar and a solution of an acetyl pyridine derivative (2 equiv) in toluene (20 mL). This colorless solution was sparged with N_2 for *ca.* 10 min before a diamine linker (1 equiv) was added to the reaction mixture. The reaction was then heated at reflux for 24 to 48 h with a condenser fitted with a Dean-Stark apparatus. The reaction mixture was then concentrated by rotary evaporation and used without further purification.

(1*E*,1'*E*)-*N*,*N*'-(Propane-1,3-diyl)bis(1-(pyridin-2-yl)ethan-1-imine) (1). A solution of 2-acetylpyridine (0.40 g, 3.3 mmol) and 1,3-diaminopropane (139 μL, 1.7 mmol) in toluene (20 mL) was heated at reflux for 24 h with a condenser fitted with a Dean-Stark apparatus. Toluene was then removed by rotary evaporation, and the resultant yellow oil was used without further purification (0.37 g, 80% yield). ^{1}H NMR (400 MHz, CD_3CN)/ δ (ppm): 8.84 (2H, d, J = 5.0 Hz), 8.27 (2H, td, J = 1.60, 7.8 Hz), 8.20 (2H, d, J = 7.9 Hz), 7.85 (2H, t, J = 6.3 Hz), 3.93 (4H, s), 2.51 (6H, s), 2.17 (4H, s). ESI-MS (MeOH): $[M + H]^+$ Calcd for $C_{17}H_{20}N_4$ 281.16 *m/z*; Found 281.24 *m/z*.

(1*E*,1'*E*)-*N*,*N*'-(Propane-1,3-diyl)bis(1-(pyridin-2-yl)methanimine) (2). A solution of picolinaldehyde (0.40 g, 3.7 mmol) and 1,3-diaminopropane (157 μL, 1.9 mmol) in toluene (20 mL) was heated at reflux for 24 h with a condenser fitted with a Dean-Stark apparatus. Toluene was removed by rotary evaporation and the resultant brown oil was used without further purification (0.28 g, 59% yield). ^{1}H NMR (400 MHz, CD_3OD)/ δ (ppm): 8.60 (2H, d, *J* = 5.8 Hz), 8.41 (2H, s), 8.02 (2H, d, *J* = 7.9 Hz), 7.89 (2H, t, *J* = 7.7 Hz), 7.46 (2H, t, *J* = 6.2 Hz), 3.81 (4H, t, *J* = 6.9 Hz), 2.16 (2H, quin, *J* = 6.8 Hz). ESI-MS (MeOH): $[M + H]^+$ Calcd for $C_{15}H_{16}N_4$ 252.14 *m/z*; Found 252.40 *m/z*.

(1*E*,1'*E*)-*N*,*N*'-(Propane-1,3-diyl)bis(1-phenyl-1-(pyridin-2-yl)methanimine) (3). To a 20 mL round-bottom flask charged with a stir bar was added tetraethoxyorthoscilicate (2.0 mL, 8.7 mmol). 2-benzoylpyridine (1.6 g, 8.7 mmol) was added to the reaction flask and dissolved with heating. One drop of concentrated H_2SO_4 was added and then the reaction flask was briefly degassed with N_2 before 1,3-diaminopropane (368 μL, 4.4 mmol) was added. An oven-dried distillation head was attached and the reaction flask was heated to 120 ºC with a Variac. After 30 min, the solution turned a bright yellow color. The reaction was allowed to proceed for 1.5 h, and then cooled to RT. The resultant solution was extracted with diethyl either (3x, 5 mL), washed with saturated $NaHCO_3$ and then with water 2x. The organic phase was dried over $MgSO_4$ and the concentrated to give a yellow-orange oil that was used without further purification (1.4 g, 78% yield). ^{1}H NMR (400 MHz, CD_3CN)/ δ (ppm): 8.61 (2H, d, *J* = 5.0 Hz), 8.38 (2H, d, *J* = 5.0 Hz), 7.99 (2H, d, *J* = 5.6 Hz), 7.78 (4H, m), 7.43 (4H, m), 7.24 (2H, m), 7.12 (2H, m), 3.34 (4H, m), 1.97 (2H, m). ESI-MS (MeOH): $[M + H]^+$ Calcd for $C_{27}H_{24}N_4$ 404.20 *m/z*; Found 404.12 *m/z*.

(1*E*,1'*E*)-*N*,*N*'-(Propane-1,3-diyl)bis(1-(6-methylpyridin-2-yl)ethan-1-imine) (4). A solution of 2-acetyl-6-methylpyridine (0.40 g, 3.0 mmol) and 1,3-diaminopropane (124 μL, 1.5 mmol) in toluene (20 mL) was heated at reflux for 48 h with a condenser fitted with a Dean-Stark apparatus. Toluene was removed by rotary evaporation and the resultant yellow-orange oil was used without further purification (0.38 g, 84% yield) ^{1}H NMR (400 MHz, CD_3CN)/ δ (ppm): 7.86 (2H, d, *J* = 7.9 Hz), 7.62 (2H, t, *J* = 7.7 Hz), 7.19 (2H, d, *J* = 7.55 Hz), 3.62 (4H, t, *J* = 6.7 Hz), 2.50 (6H, s), 2.29 (6H, s), 2.10 (2H, t, *J* = 6.8 Hz). ESI-MS (MeOH): $[M + H]^+$ Calcd for $C_{19}H_{24}N_4$ 309.20 *m/z*; Found 309.15 *m/z*.

(1*E*,1'*E*)-*N*,*N*'-(Propane-1,3-diyl)bis(1-(pyrazin-2-yl)ethan-1-imine) (5). A Solution of 2-acetylpyrazine (2.0 g, 16.4 mmol) and 1,3-diaminopropane (683 μl, 8.2 mmol) in toluene (20 mL) was heated at reflux for 24 h with a condenser fitted with a Dean Stark apparatus. Toluene was removed by rotatory evaporation and the resultant orange oil was used without further purification (1.7 g, 72% yield). ^{1}H NMR (400 MHz, $(CD_3)_2SO$)/ δ (ppm): 9.22 (2H, s), 8.67 (2H, d, *J* = 2.6 Hz), 8.65 (2H, d, *J* = 1.4 Hz), 3.69 (4H, t, *J* = 6.7 Hz), 2.30 (6H, s), 2.40 (2H, t, *J* = 6.7 Hz). FT-IR (solid): 1632, 1406, 1370, 1317, 1175, 1053, 1040 cm^{-1} ESI-MS (MeOH): $[M + H]^+$ Calcd for $C_{15}H_{18}N_6$ 283.16 *m/z*; Found 283.20 *m/z*.

(1*E*,1'*E*)-*N*,*N*'-(Propane-1,3-diyl)bis(1-(4-methylpyridin-2-yl)ethan-1-imine) (6). A solution of 2-acetyl-4-methylpyridine (0.40 g, 3.0 mmol) and 1,3-diaminopropane (124 μL, 1.5 mmol) in toluene (20 mL) was heated at reflux for 24 h with a condenser fitted with a Dean Stark apparatus. Toluene was removed by rotatory evaporation and the resultant brown oil was used

without further purification (0.41 g, 89% yield). ^{1}H NMR (400 MHz, CD_3OD)/ δ (ppm): 8.43 (2H, d, *J* = 5.0 Hz), 8.41 (2H, d, *J* = 5.1 Hz), 7.57 (2H, s), 2.66 (4H, t, *J* = 13.8 Hz), 2.40 (6H, s), 2.32 (6H, s), 2.21 (2H, t, *J* = 6.8 Hz). ESI-MS (MeOH): $[M + H]^+$ Calcd for $C_{19}H_{24}N_4$ 309.20 *m/z*; Found 309.18 *m/z*.

(1*E*,1'*E*)-*N*,*N*'-(Ethane-1,2-diyl)bis(1-(pyridin-2-yl)ethan-1-imine) (7). A solution of 2-acetylpyridine (0.40 g, 3.3 mmol) and ethylenediamine (110 μL, 1.7 mmol) in toluene (20 mL) was heated at reflux for 24 h with a condenser fitted with a Dean Stark apparatus. Toluene was removed by rotatory evaporation and the resultant yellow oil was used without further purification (0.31 g, 72% yield). ^{1}H NMR (400 MHz, $CDCl_3$)/ δ (ppm): 8.58 (2H, d, *J* = 4.8 Hz), 8.06 (2H, d, *J* = 8.0 Hz), 7.69 (2H, t, *J* = 7.7 Hz), 7.28 (2H, d, *J* = 3.7 Hz), 3.97 (4H, s), 2.72 (2H, s), 2.43 (6H, s). ESI-MS (MeOH): $[M + H]^+$ Calcd for $C_{16}H_{18}N_4$ 267.15 *m/z*; Found 267.87 *m/z*.

(1*E*,1'*E*)-*N*,*N*'-(2,2-Dimethylpropane-1,3-diyl)bis(1-(pyridin-2-yl)methanimine) (8). A solution of picolinaldehyde (0.40 g, 3.7 mmol) and 2,2-dimethylpropane-1,3-diamine (0.19 μl, 1.9 mmol) in toluene (20 mL) was heated at reflux for 24 h with a condenser fitted with a Dean Stark apparatus. Toluene was removed by rotatory evaporation and the resultant yellow oil was used without further purification (0.35 g, 66% yield). ^{1}H NMR (400 MHz, CD_3OD)/ δ (ppm): 8.61 (2H, d, *J* = 4.8 Hz), 8.37 (2H, d), 8.05 (2H, d, *J* = 7.9 Hz), 7.71 (2H, t, *J* = 7.6 Hz), 7.28 (2H, t, *J* = 6.2 Hz), 3.59 (4H, d, *J* = 1.3 Hz), 1.04 (6H, s). ESI-MS (CH_3OH): $[M + H]^+$ Calcd for $C_{17}H_{20}N_4$ 281.17 *m/z*; Found 281.28 *m/z*.

(1*E*,1'*E*)-*N*,*N*'-((1*R*,2*S*)-Cyclohexane-1,2-diyl)bis(1-(pyridin-2-yl)methanimine) (9). A solution of picolinaldehyde (0.40 g, 3.7 mmol) and (1*S*,2*S*)-cyclohexane-1,2-diamine (0.21 g, 1.9 mmol) in toluene (20 mL) was heated at reflux for 24 h with a condenser fitted with a Dean Stark apparatus. Toluene was removed by rotatory evaporation and the resultant brown oil was used without further purification (0.37 g, 67% yield). ^{1}H NMR (400 MHz, $(CD_3)_2SO$))/ δ (ppm): 8.54 (2H, d, *J* = 4.0 Hz), 8.22 (2H, s), 7.84 (2H, d, *J* = 7.8 Hz), 7.79 (2H, t, *J* = 7.6 Hz), 7.38 (2H, t, *J* = 6.1 Hz), 2.21 (2H, m), 1.75 (6H, m), 1.48 (2H, t, *J* = 9.6 Hz). ESI-MS (CH_3OH): $[M + H]^+$ Calcd for $C_{18}H_{20}N_4$ 293.17 *m/z*; Found 293.35 *m/z*.

A.4.6 General Procedure for the Preparation of Nickel Complexes

Ligand solutions (**1-9**; 1 equiv.) in methanol (2 mL) were loaded into 20 mL scintillation vials charged with stir bars. To a separate 20 mL scintillation vial was added $NiCl_2$•$6H_2O$ (1 equiv.) in methanol (2 mL). The ligand and nickel solutions were both stirred at 50 °C until fully dissolved. The $NiCl_2$•$6H_2O$ solution was then added dropwise to the ligand solution and the reaction was allowed to stir at 50 °C for 5 h. The reaction mixtures were then filtered and washed with cold water. The resulting solids were then transferred into a new 20 mL scintillation vial and dissolved in water (2 mL). Sodium hexafluorophosphate ($NaPF_6$; 3.0 equiv.) was added to another 20 mL scintillation vial equipped with a stir bar and suspended in 2.0 mL of water. The $NaPF_6$ solution was then added dropwise to the reaction mixture and allowed to react for 5 h at 50 °C. The resulting solid was filtered, washed with cold water, and dried under vacuum. The crude products were then recrystallized by slow vapor diffusion of diethyl ether or diisopropyl ether into saturated acetonitrile solutions.

Ni(1). Methanol solutions (2 mL) of **1** (0.40 g, 1.4 mmol) and $NiCl_2$•$6H_2O$ (0.34 g, 1.4 mmol) were mixed and allowed to stir at 50 °C for 5 h. After 5 h, the reaction mixture was filtered; the solid was collected, dissolved in water (2 mL) and added to an aqueous solution of $NaPF_6$ (0.72 g, 4.3 mmol) and allowed to react for an additional 5 h. The resulting light-green solid was then filtered, washed with cold water and recrystallized by slow vapor diffusion of diethyl ether into a saturated acetonitrile solution (0.79 g, 87% yield). UV-vis (CH_3CN): λ_{abs} = 229, 279, 295, 374 nm. FT-IR (solid): 3609, 1600, 1320, 1257, 1020, 834, 782, 737, 653, 555 cm^{-1} ESI-MS (CH_3OH): $[M - H]^+$ Calcd for $C_{17}H_{19}N_4Ni$ 338.07 *m/z*; Found 338.09 *m/z*; $[M]^{2+}$ Calcd for $C_{17}H_{20}N_4Ni$ 169.54; Found 169.44 *m/z*.

Ni(2). Methanol solutions (2 mL) of **2** (0.40 g, 1.6 mmol) and $NiCl_2$•$6H_2O$ (0.37 g, 1.6 mmol) were mixed and allowed to stir at 50 °C for 5 h. After 5 h, the reaction mixture was filtered; the solid was collected, dissolved in water (2 mL) and added to an aqueous solution of $NaPF_6$ (0.80 g, 4.8 mmol) and allowed to react for an additional 5 h. The resulting brown solid was then filtered, washed with cold water and recrystallized by slow vapor diffusion of diethyl ether into a saturated acetonitrile solution (0.69 g, 70% yield). UV-vis (CH_3CN): λ_{abs} = 224, 235, 290, 300, 385 nm. FT-IR (solid): 1659, 1603, 1310, 1300, 830, 774, 642, 555, 507, 426 cm^{-1}. ESI-MS (CH_3OH): $[M - H]^+$ Calcd for $C_{15}H_{15}N_4Ni$ 310.01 *m/z*; Found 310.11 *m/z*; $[M]^{2+}$ Calcd for $C_{15}H_{16}N_4Ni$ 155.51; Found 155.23 *m/z*.

Ni(3). Methanol solutions (2 mL) of **3** (0.40 g, 0.99 mmol) and $NiCl_2$•$6H_2O$ (0.23 g, 0.99 mmol) were mixed and allowed to stir at 50 °C for 5 h. After 5 h, the reaction mixture was filtered; the solid was collected, dissolved in water (2 mL) and added to an aqueous solution of $NaPF_6$ (0.50 g, 3.0 mmol) and allowed to react for an additional 5 h. The resulting light-brown solid was then filtered, washed with cold water and recrystallized by slow vapor diffusion of diethyl ether into a saturated acetonitrile solution (0.56 g, 74% yield). UV-vis (CH_3CN): λ_{abs} = 229, 300, 387 nm. FT-IR (solid): 3590, 3529, 1632, 1602, 1444, 1330, 1017, 830, 801, 772, 753, 702, 687, 555 cm^{-1}. ESI-MS (CH_3OH): $[M - H]^+$ Calcd for $C_{27}H_{23}N_4Ni$ 462.21 *m/z*; Found 462.13 *m/z*; $[M]^{2+}$ Calcd for $C_{27}H_{24}N_4Ni$ 231.61; Found 231.53 *m/z*.

Ni(4). Methanol solutions (2 mL) of **4** (0.42 g, 1.4 mmol) and $NiCl_2$•$6H_2O$ (0.33 g, 1.4 mmol) were mixed and allowed to stir at 50 °C for 5 h. After 5 h, the reaction mixture was filtered; the solid was collected, dissolved in water (2 mL) and added to an aqueous solution of $NaPF_6$ (0.69 g, 4.1 mmol) and allowed to react for an additional 5 h. The resulting light brown solid was then filtered, washed with cold water and recrystallized by slow vapor diffusion of diethyl ether into a saturated acetonitrile solution (0.72 g, 80% yield). UV-vis (CH_3CN): λ_{abs} = 224, 259, 389 nm. FT-IR (solid): 2923, 1637, 1584, 1573, 1451, 1352, 1307, 794, 739, 679, and 631 ESI-MS (CH_3OH): $[M - H]^+$ Calcd for $C_{19}H_{23}N_4Ni$ 365.14 *m/z*; Found 365.18 *m/z*; $[M]^{2+}$ Calcd for $C_{19}H_{24}N_4Ni$ 183.07; Found 183.00 *m/z*.

Ni(5). Methanol solutions (2 mL) of **5** (1.1 g, 4.0 mmol) and $NiCl_2$•$6H_2O$ (0.94 g, 4.0 mmol) were mixed and allowed to stir at 50 °C for 5 h. After 5 h, the reaction mixture was filtered; the solid was collected, dissolved in water (2 mL) and added to an aqueous solution of $NaPF_6$ (2.0 g, 11.9 mmol) and allowed to react for an additional 5 h. The resulting yellow solid was then filtered, washed with cold water and recrystallized by slow vapor diffusion of diisopropyl ether into a saturated acetonitrile solution to yield orange diffraction quality crystals (2.0 g, 81% yield).

UV-vis (CH_3CN): λ_{abs} = 229, 305, 400 nm. FT-IR (solid): 1637, 1410, 1324, 1176, 1038, 824, 738, 555, and 466 cm^{-1}. ESI-MS (CH_3OH): $[M - H]^+$ Calcd for $C_{15}H_{17}N_6Ni$ 339.09 *m/z*; Found 339.10 *m/z*; $[M]^{2+}$ Calcd for $C_{15}H_{18}N_6Ni$ 170.05 *m/z*; Found 170.18 *m/z*.

Ni(6). Methanol solutions (2 mL) of **6** (0.49 g, 1.6 mmol) and $NiCl_2 \cdot 6H_2O$ (0.38 g, 1.6 mmol) were mixed and allowed to stir at 50 °C for 5 h. After 5 h, the reaction mixture was filtered; the solid was collected and dissolved in water (2 mL) and added to an aqueous solution of $NaPF_6$ (0.80 g, 4.7 mmol) and allowed to react for an additional 5 h. The resulting dark brown solid was then filtered, washed with cold water and recrystallized by slow vapor diffusion of diethyl ether into a saturated acetonitrile solution to yield brown crystals (0.89 g, 85% yield). UV-vis (CH_3CN): λ_{abs} = 229, 300, 395 nm. FT-IR (solid): 3586, 1614, 1370, 1320, 1023, 828, 739, 663, 555 cm^{-1} ESI-MS (CH_3OH): $[M - H]^+$ Calcd for $C_{19}H_{23}N_4Ni$ 365.14 *m/z*; Found 365.20 *m/z*; $[M]^{2+}$ Calcd for $C_{19}H_{24}N_4Ni$ 183.07; Found 188 *m/z*.

Ni(7). Methanol solutions (2 mL) of **7** (0.40 g, 1.5 mmol) and $NiCl_2 \cdot 6H_2O$ (0.35 g, 1.5 mmol) were mixed and allowed to stir at 50 °C for 5 h. After 5 h, the reaction mixture was filtered; the solid was collected and dissolved in water (2 mL) and added to an aqueous solution of $NaPF_6$ (0.76 g, 4.5 mmol) and allowed to react for an additional 5h. The resulting solid was then filtered and washed with cold water and recrystallized by slow vapor diffusion of diethyl ether into a saturated acetonitrile solution to yield a light-green solid (0.74 g, 80% yield). UV-vis (CH_3CN): λ_{abs} = 229, 295, 400 nm. FT-IR (solid): 3208, 1667, 1600, 1446, 1372, 1315, 1253, 1173, 1108, 1013, 785, 638, 532, 449 cm^{-1} ESI-MS (CH_3OH): $[M - H]^+$ Calcd for $C_{16}H_{17}N_4Ni$ 323.09 *m/z*; Found 323.23 *m/z*; $[M]^{2+}$ Calcd for $C_{16}H_{18}N_4Ni$ 162.05; Found 162.12 *m/z*.

Ni(8). Methanol solutions of **8** (0.40 g, 1.4 mmol) and $NiCl_2 \cdot 6H_2O$ (0.40 g, 1.4 mmol) were mixed and allowed to stir at 50 °C for 5 h. After 5 h, the reaction mixture was filtered; the solid was collected and dissolved in water (2 mL) and added to an aqueous solution of $NaPF_6$ (0.34 g, 1.4 mmol) and allowed to react for an additional 5h. The resulting solid was then filtered and washed with cold water and recrystallized by slow vapor diffusion of diethyl ether into a saturated acetonitrile solution to yield a light-brown solid (0.43 g, 48% yield). UV-vis (CH_3CN): λ_{abs} = 229, 300, 380 nm. FT-IR (solid): 1646, 1601, 1312, 1018, 829, 791, 683, 642, 555, 505, 428 cm^{-1}. ESI-MS (CH_3OH): $[M - H]^+$ Calcd for $C_{17}H_{19}N_4Ni$ 337.10 *m/z*; Found 337.17 *m/z*; $[M]^{2+}$ Calcd for $C_{17}H_{20}N_4Ni$ 169.05 *m/z* ; Found 169.20 *m/z*.

Ni(9). Methanol solutions of **9** (0.40 g, 1.4 mmol) and $NiCl_2 \cdot 6H_2O$ (0.32 g, 1.4 mmol) were mixed and allowed to stir at 50 °C for 5 h. After 5 h, the reaction mixture was filtered; the solid was collected and dissolved in water (2 mL) and added to an aqueous solution of $NaPF_6$ (0.69 g, 4.1 mmol) and allowed to react for an additional 5h. The resulting solid was then filtered and washed with cold water and recrystallized by slow vapor diffusion of diethyl ether into a saturated acetonitrile solution to yield a light-brown solid (0.64 g, 73% yield). UV-vis (CH_3CN): λ_{abs} = 229, 290, 400 nm. FT-IR (solid): 3268, 1598, 1446, 1386, 1305, 1228, 1107, 1052, 1021, 770, 643, 555, 481, 420 cm^{-1}. ESI-MS (CH_3OH): $[M - H]^+$ Calcd for $C_{18}H_{19}N_4Ni$ 349.10 *m/z*; Found 349.13 *m/z*; $[M]^{2+}$ Calcd for $C_{18}H_{20}N_4Ni$ 175.05; Found 175.24 *m/z*.

A.4.7 X-Ray Crystallography Data

Table A.3. Crystal data and structure refinement for Ni(5).

Identification Code	Ni(5)
Empirical Formula	$C_{15}H_{18}F_{12}N_6NiP_2$
Formula Weight	630.97
Temperature	100(2) K
Wavelength	0.71073 Å
Crystal System	Monoclinic
Space Group	C2/c
Unit Cell Dimensions	a = 42.847(12) Å α = 90° b = 8.763(2) Å β = 123.220(6)° c = 38.089(11) Å γ = 90°
Volume	11964(6) $Å^3$
Z	2
Density (calc)	1.673 mg/m^3
Absorption Coefficient	0.862 mm^{-1}
F(000)	6100
Crystal Size	0.320 x 0.220 x 0.200 mm
Theta Range	1.901° to 24.108°
Reflections Collected (unique)	87574 (9469(
Completeness to Theta	99.8%
Refinement Method	Full-matrix least-squares on F^2
Data / Restraints / Parameters	9469 / 86 / 892
Goodness-of-fit on F^2	1.317
Final R indices [I>2σ(I)]	R_1 = 0.0757 wR_2 = 0.1590
R indices (all data)	R_1 = 0.0852 wR_2 = 0.1622

A.5 References

(1) Veziroglu, N. T. *Journal of Advanced Science* **2001**, *13*, 101.
(2) Shafiee, S.; Topal, E. *Energy Policy* **2009**, *37*, 181.
(3) Hofmann, D. J.; Butler, J. H.; Tans, P. P. *Atmospheric Environment* **2009**, *43*, 2084.
(4) Jhong, H.-R. M.; Ma, S.; Kenis, P. J. A. *Current Opinion in Chemical Engineering* **2013**, *2*, 191.
(5) Costentin, C.; Robert, M.; Saveant, J. M. *Chem. Soc. Rev.* **2013**, *42*, 2423.
(6) Benson, E. E.; Kubiak, C. P.; Sathrum, A. J.; Smieja, J. M. *Chem. Soc. Rev.* **2009**, *38*, 89.
(7) Appel, A. M.; Bercaw, J. E.; Bocarsly, A. B.; Dobbek, H.; DuBois, D. L.; Dupuis, M.; Ferry, J. G.; Fujita, E.; Hille, R.; Kenis, P. J.; Kerfeld, C. A.; Morris, R. H.; Peden, C. H.; Portis, A. R.; Ragsdale, S. W.; Rauchfuss, T. B.; Reek, J. N.; Seefeldt, L. C.; Thauer, R. K.; Waldrop, G. L. *Chem. Rev.* **2013**, *113*, 6621.
(8) Li, C. W.; Ciston, J.; Kanan, M. W. *Nature* **2014**, *508*, 504.
(9) Ren, D.; Ang, B. S.-H.; Yeo, B. S. *ACS Catal.* **2016**, *6*, 8239.
(10) Verdaguer-Casadevall, A.; Li, C. W.; Johansson, T. P.; Scott, S. B.; McKeown, J. T.; Kumar, M.; Stephens, I. E.; Kanan, M. W.; Chorkendorff, I. *J. Am. Chem. Soc.* **2015**, *137*, 9808.
(11) Hori, Y.; Takahashi, I.; Koga, O.; Hoshi, N. *J. Mol. Catal. A: Chem.* **2003**, *199*, 39.
(12) Kumar, B.; Llorente, M.; Froehlich, J.; Dang, T.; Sathrum, A.; Kubiak, C. P. *Annu. Rev. Phys. Chem.* **2012**, *63*, 541.
(13) Sampson, M. D.; Kubiak, C. P. *J. Am. Chem. Soc.* **2016**, *138*, 1386.
(14) Lim, C. H.; Holder, A. M.; Musgrave, C. B. *J. Am. Chem. Soc.* **2013**, *135*, 142.
(15) Roy, S.; Sharma, B.; Pecaut, J.; Simon, P.; Fontecave, M.; Tran, P. D.; Derat, E.; Artero, V. *J. Am. Chem. Soc.* **2017**, *139*, 3685.
(16) Costentin, C.; Passard, G.; Robert, M.; Saveant, J. M. *Proc. Natl. Acad. Sci. U.S.A.* **2014**, *111*, 14990.
(17) Costentin, C.; Passard, G.; Robert, M.; Saveant, J. M. *J. Am. Chem. Soc.* **2014**, *136*, 11821.
(18) Hammouche, M.; Lexa, D.; Momenteau, M.; Saveant, J. M. *J. Am. Chem. Soc.* **1991**, *113*, 8455.
(19) Froehlich, J. D.; Kubiak, C. P. *J. Am. Chem. Soc.* **2015**, *137*, 3565.
(20) Schneider, J.; Jia, H.; Kobiro, K.; Cabelli, D. E.; Muckerman, J. T.; Fujita, E. *Energy Environ. Sci.* **2012**, *5*, 9502.
(21) Froehlich, J. D.; Kubiak, C. P. *Inorg. Chem.* **2012**, *51*, 3932.
(22) Fisher, B.; Eisenberg, R. *J. Am. Chem. Soc.* **1980**, *102*, 7363.
(23) Bhugun, I.; Lexa, D.; Saveant, J. M. *J. Am. Chem. Soc.* **1996**, *118*, 1769.
(24) Hawecker, J.; Lehn, J.-M.; Ziessel, R. *J. Chem. Soc., Chem. Commun.* **1984**, 328.
(25) Ishida, H.; Tanaka, K.; Tanaka, T. *Organometallics* **1987**, *6*, 181.
(26) Bolinger, M. C.; Story, N.; P., S. B.; Meyer, T. J. *Inorg. Chem.* **1988**, *27*, 4582.
(27) Riplinger, C.; Sampson, M. D.; Ritzmann, A. M.; Kubiak, C. P.; Carter, E. A. *J. Am. Chem. Soc.* **2014**, *136*, 16285.
(28) Smieja, J. M.; Benson, E. E.; Kumar, B.; Grice, K. A.; Seu, C. S.; Miller, A. J. M.; Mayer, J. M.; Kubiak, C. P. *Proc. Natl. Acad. Sci. U.S.A.* **2012**, *109*, 15646.
(29) Slater, S.; Wagenknecht, J. H. *J. Am. Chem. Soc.* **1984**, *106*, 5367.
(30) DuBois, D. L.; Miedander, A.; Haltiwanger, R. C. *J. Am. Chem. Soc.* **1991**, *113*, 8753.

(31) Raebiger, J. W.; Turner, J. W.; Noll, B. C.; Curtis, C. J.; Miedander, A.; Cox, B.; DuBois, D. L. *Organometallics* **2006**, *25*, 3345.
(32) Dubois, D. L. *Comments on Inorganic Chemistry* **1997**, *19*, 307.
(33) Haines, R. J.; Wittrig, R. E.; Kubiak, C. P. *Inorg. Chem.* **1994**, *33*, 4723.
(34) Luca, O. R.; Crabtree, R. H. *Chem. Soc. Rev.* **2013**, *42*, 1440.
(35) Stubbert, B. D.; Peters, J. C.; Gray, H. B. *J. Am. Chem. Soc.* **2011**, *133*, 18070.
(36) Love, B. E.; Ren, J. *J. Org. Chem.* **1993**, *58*, 5556.
(37) Williams, V. A.; Hulley, E. B.; Wolczanski, P. T.; Lancaster, K. M.; Lobkovsky, E. B. *Chem. Sci.* **2013**, *4*, 3636.
(38) Thoi, V. S.; Kornienko, N.; Margarit, C. G.; Yang, P.; Chang, C. J. *J. Am. Chem. Soc.* **2013**, *135*, 14413.
(39) Jurss, J. W.; Khnayzer, R. S.; Panetier, J. A.; El Roz, K. A.; Nichols, E. M.; Head-Gordon, M.; Long, J. R.; Castellano, F. N.; Chang, C. J. *Chem. Sci.* **2015**, *6*, 4954.
(40) Toma, H. E.; Malin, J. M. *Inorg. Chem.* **1973**, *12*, 1039.
(41) Ford, P.; Rudd, D. F. P.; Gaunder, R.; Taube, H. *J. Am. Chem. Soc.* **1968**, *90*, 1187.
(42) Rahaman, S. H.; Chowdhury, H.; Bose, D.; Ghosh, R.; Hung, C.-H.; Ghosh, K. *Polyhedron* **2005**, *24*, 1755.
(43) Zhang, R.-L.; Zhao, J.-S.; Yang, P.; Shi, Q.-Z. *J. Chem. Crystallogr.* **2009**, *40*, 357.
(44) Gagne, R. R.; Allison, J. L.; Ingle, D. M. *Inorg. Chem.* **1979**, *18*, 2767.
(45) Addison, A. W.; Carpenter, M.; Lau, L. K.-M.; Wicholas, M. *Inorg. Chem.* **1978**, *17*, 1545.
(46) Zwiener, C.; Glauner, T.; Frimmel, F. H. *Anal. Bioanal. Chem.* **2002**, *372*, 615.
(47) Sakuragawa, A.; Yoneno, T.; Inoue, K.; Okutani, T. *J. Chromatogr. A* **1999**, *844*, 403.
(48) Kleber, R. J.; Mopper, K. *Environ. Sci. Technol.* **1990**, *24*, 1477.
(49) Aitken, R. A.; Armstrong, J. M.; Drysdale, M. J.; Ross, F. C.; Ryan, B. M. *J. Chem. Soc., Perkin Trans.* **1999**, *1*, 593.
(50) La Duca, M. J. J.; Simunic, J. L.; Hershberger, J. W.; Pinhas, A. R. *Inorg. Chim. Acta* **1994**, *222*, 165.
(51) Hill, A. M.; Levason, W.; Webster, M.; Albers, I. *Organometallics* **1997**, *16*, 5641.
(52) Shaw, W. J.; Chen, Y.; Fulton, J.; Linehan, J.; Gutowska, A.; Bitterwolf, T. *J. Organomet. Chem* **2008**, *693*, 2111.
(53) Sieh, D.; Lacy, D. C.; Peters, J. C.; Kubiak, C. P. *Chem. Eur. J.* **2015**, *21*, 8497.
(54) *APEX2, v. 2009*, Bruker Analytical X-Ray Systems, Inc, Madison, Wi, 2009.
(55) Sheldrick, G. M., *SADABS, Version 2.03*, Bruker Analytical X-Ray Systems, Inc, Madison, Wi, 2010 .
(56) Sheldrick, G. M., *Acta Crystallogr. Sect. A* **1990**, *46*, 467.
(57) Sheldrick, G. M., *Acta Crystallogr. Sect. A* **2008**, *64*, 112.
(58) Sheldrick, G. M. *SHELXL-97: Program for crystal structure determination*, University of Göttingen, Göttingen, Germany, 1997.
(59) Gagne, R. R.; Allison, J. L.; Ingle, D. M. *Inorg. Chem.* **1979**, *18*, 2767.
(60) Addison, A. W.; Carpenter, M.; Lau, L. K.-M.; Wicholas, M. *Inorg. Chem.* **1978**, *17*, 1545.
(61) Zwiener, C.; Glauner, T.; Frimmel, F. H. *Anal. Bioanal. Chem.* **2002**, *372*, 615.
(62) Sakuragawa, A.; Yoneno, T.; Inoue, K.; Okutani, T. *J. Chromatogr. A* **1999**, *844*, 403.
(63) Kleber, R. J.; Mopper, K. *Environ. Sci. Technol.* **1990**, *24*, 1477.

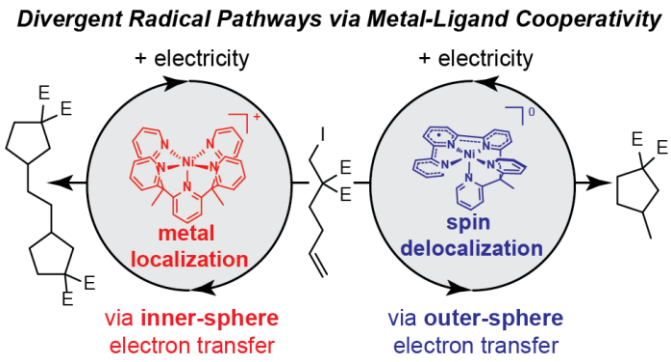
Appendix B: Controlled Single-Electron Transfer via Metal–Ligand Cooperativity Drives Divergent Nickel-Electrocatalyzed Radical Pathways

Portions of this work were published in the following scientific journal:
Wuttig, A. Derrick, J. S., Loipersberger, M.; Snider, A.; Head-Gordon, M.; Chang, C. J.; Toste, D. F. Controlled Single-Electron Transfer via Metal–Ligand Cooperativity Drives Divergent Nickel-Electrocatalyzed Radical Pathways. *J. Am. Chem. Soc.* **2021**, *143*, 6990–7001.

Specific Contributions: Dr. Anna Wuttig did the electrochemistry. Dr. Matthias Loipersberger and Andrew Snider did the computational and theory work.

B.1 Abstract

Electrocatalysis enables the construction of C–C bonds under mild conditions via controlled formation of carbon-centered radicals. For sequences initiated by alkyl halide reduction, coordinatively unsaturated Ni complexes commonly serve as single-electron transfer agents, giving rise to the foundational question of whether outer- or inner-sphere electron transfer oxidative addition prevails in redox mediation. Indeed, rational design of electrochemical process requires the discrimination of these two electron transfer pathways, as they can have outsized effects on the rate of substrate bound activation and thus impact radical generation rates and downstream product selectivities. We present results from combined synthetic, electroanalytical, and computational studies that examine the mechanistic differences of single electron transfer to alkyl halides imparted by Ni metal–ligand cooperativity. Electrogenerated reduced Ni species, stabilized by delocalized spin density onto a redox-active tpyPY2Me polypyridyl ligand, activates alkyl iodides via outer-sphere electron transfer, allowing for the selective activation of alkyl iodide substrates over halogen atom donors and the controlled generation and sequestration of electrogenerated radicals. In contrast, the Ni complex possessing a redox-innocent pentapyridine congener activates the substrate in an inner-sphere fashion owing to a purely metal-localized spin, thereby activating both substrates and halogen atom donors in an indiscriminate fashion, generating a high concentration of radicals and leading to unproductive dimerization. Our data established that controlled electron transfer via Ni-ligand cooperativity can be used to limit undesired radical recombination products and promote selective radical processes in electrochemical environments, providing a generalizable framework for designing redox mediators with distinct rate and potential requirements.



B.2 Introduction

The controlled formation of carbon-centered radicals facilitates the construction of value-added products. While it is well-established that these open-shell intermediates are readily accessed via halogen atom transfer from alkyl halide (RX) feedstocks,[1–4] the toxicity of tin, silicon, or trialkylborane reagents traditionally employed to initiate this reactivity motivates the development of complementary synthetic methods with improved sustainability. Among the numerous alternatives pursued,[5–16] strategies that enable RX activation via single electron transfer (SET) present an opportunity for radical generation to be interfaced with SET catalysts, where energy input from visible light[17] or electricity[18,19] enables turnover under mild conditions. RX reduction under photoredox conditions typically employs coordinatively saturated Rh or Ir polypyridyl catalysts.[10–12,14,20,21] In these systems, it is hypothesized that the initial light sensitization steps form reductants that activate substrates via outer-sphere electron transfer (OSET).[22,23] Thus, the interaction of the starting material with the metal center, promoting an inner-sphere electron transfer (ISET) event or coordination of the ensuing carbon-centered radical, is not invoked. Hence, the photocatalyst ligand is tuned to optimize the redox potential necessary to facilitate the OSET step.[10,11,14] In contrast, for electrosynthetic sequences initiated by RX reduction, coordinatively unsaturated Ni complexes possessing diverse ligand scaffolds commonly serve as SET agents,[24–26] giving rise to the question of whether OSET or ISET oxidative addition prevails in catalytic redox mediation. Moreover, the design of more complex electrochemical radical processes requires an understanding of the ligand design criteria necessary to direct outer-sphere vs inner-sphere redox reactivity, as these distinct electron transfer reaction pathways are expected to lead to dramatic differences in the rate of RX bond activation near the electroactive interface[27] and thereby impact radical production rates and downstream product selectivity.

Studies suggest that Ni ligand tuning directs both outer-sphere and inner-sphere electron transfer reactivity manifolds toward RX activation. Reported electrosynthetic reaction sequences imply that electrogenerated Ni(I) complexes reduce RX via OSET, thereby regenerating Ni(II) for subsequent turnover.[28,29] Indeed, ligand tuning by both redox-active and redox-inactive tetradentate ligands has been shown to alter the redox potential for Ni(II)/Ni(I) by over 1 V,[24,25,28,29] and this sole property has been utilized to choose a suitable redox mediator for RX activation prior to direct substrate reduction at more negative potentials.[26] However, it has been shown that Ni complexes spanning ∼0.8 V can still mediate the reduction of the same RX substrate,[30,31] suggesting that select Ni-based redox mediators may operate, instead, via ISET mechanisms. Indeed, evidence suggests that metal-centered reduction may facilitate ISET pathways toward RX activation. It has been shown that RX oxidative addition processes at Ni(I) complexes bearing a strongly sigma-donating and redox-inactive ligand, i.e., bisphosphine, proceed via an inner-sphere pathway of metal-centered halogen atom abstraction.[32] Similarly, Ni(I) cyclam or tetramethylcyclam, a widely utilized redox mediator for RX reduction[30,33–36] bearing no redox-active ligand, has been shown to catalyze the electroreduction of RX at potential values ∼1 V more positive than the direct reduction of the substrate, rendering an OSET mechanism unlikely.[37] Yet, the nature of the oxidative addition adduct, i.e., halogen atom transfer[38] vs two-electron oxidative insertion into the RX bond,[39,40] remains unresolved. In addition, Ni(II) salen complexes with aliphatic imine bridges exhibit metal-based SET reduction by EPR and UV–vis studies,[41] and inner-sphere reactivity of the corresponding Ni(I) species has been implicated toward RX reduction.[37,42–44] Thus, despite the central role of SET processes in facilitating carbon-centered

radical formation in electrochemical environments, the diversity of explored Ni ligand platforms precludes systematic studies of metal-centered reduction on SET, limiting the ability to design more complex electrocatalytic radical processes.

In order to isolate and study the effect of metal-centered reduction on SET to RX and thereby electrocatalytic carbon-centered radical generation and downstream reactivity, we reasoned that an ideal ligand set requires: (1) a chelating ligand that favors one open metal coordination site to isolate single-electron reactivity over traditional three-centered concerted two-electron oxidative addition pathways and (2) fine-tuned control over the localization of spin density between the metal center and/or low-ligand ligand orbitals. In this context, recent studies on Fe complexes demonstrate that the incorporation of a pentadentate, redox-active pentapyridine ligand (tpyPY2Me = 6-(1,1-di(pyridin-2-yl)ethyl)-2,2′:6′,2″-terpyridine) shifts electron density away from metal orbitals relative to complexes possessing a redox-innocent pentapyridine congener ($PY5Me_2$ = 2,6-bis(1,1-bis(2-pyridyl)ethyl)pyridine) and can be exploited for electrocatalysis.[45] Thus, the tpyPY2Me and $PY5Me_2$ ligand platforms present an ideal pair to interrogate (1) and (2). Translation of these design elements toward the study of electrocatalyzed RX activation, however, requires the preparation of Ni complexes as the Fe variants are not sufficiently reducing[45] to act as SET redox mediators toward RX reduction.

Here, we report the synthesis and characterization of Ni complexes of tpyPY2Me and $PY5Me_2$ and compare their electrocatalytic performance for RX activation. We combine electrokinetic and bulk electrolysis studies with structural insight from DFT calculations to formulate a mechanistic model that describes the structure of the electroactive reduced complexes and the rate-limiting alkyl iodide (RI) activation processes for both. We find that electrogenerated reduced Ni species, stabilized by delocalized spin density onto the redox-active tpyPY2Me ligand, activate RI via OSET, followed by rapid sequestration of an ensuing radical to furnish an overall bimolecular oxidative addition step. In contrast, the redox-innocent ligand congener, with a purely metal-localized reduction, activates RI at 3–5 orders of magnitude higher rate by ISET, thus leading to uncontrolled free radical formation. We exploit these divergent SET pathways for RI activation in the context of radical cyclization following carboiodination,[46] showing that Ni-ligand cooperativity limits undesired radical recombination products and promotes a selective radical process. More broadly, these findings establish metal–ligand cooperativity as a design element that can be employed to control the rate of electrochemical radical generation and downstream radical reactivity.

B.3 Results and Discussion

B.3.1 Synthesis and characterization of Ni complexes

The $[Ni(tpyPY2Me)(MeCN)]^{2+}$, $[Ni\text{-}1]^{2+}$, complex was synthesized by adopting slight modifications to the literature-reported methods for the analogous iron complex (see the materials and methods).[45] In order to elucidate the role of the redox-active tpyPY2Me ligand on redox mediation, the redox-inactive congener, $[Ni(PY5Me_2)(MeCN)]^{2+}$, $[Ni\text{-}2]^{2+}$, was prepared by modifying literature-reported methods for the syntheses of metal complexes bearing the $PY5Me_2$ ligand.[47–52] The solid-state structures of both complexes were characterized by single-crystal X-ray diffraction. In the primary coordination sphere, both $[Ni\text{-}1]^{2+}$ (**Figure B.1a**) and $[Ni\text{-}2]^{2+}$ (**Figure B.1b**) adopt a *pseudo*-octahedral structure. The enhanced rigidity of the tpyPY2Me framework gives rise to increased distortion away from an idealized octahedral symmetry relative to the $PY5Me_2$, consistent with observations using Fe.[45] Definitive determination of the structure in solution is precluded by the observation of broad ^1H NMR signals, suggesting that both Ni(II) complexes are paramagnetic. Measurements of the effective magnetic moment by the Evans method confirm this hypothesis: values of 3.2 and 3.0 μ_B (S = 1) are estimated for $[Ni\text{-}1]^{2+}$ and $[Ni\text{-}2]^{2+}$, respectively (**Figures B.2** and **B.3**). Together, these data evince the formation of the desired Ni(II) complexes in which the two high-lying d orbitals, $d_{x^2-y^2}$ and d_{z^2}, are singularly occupied in the ground state.

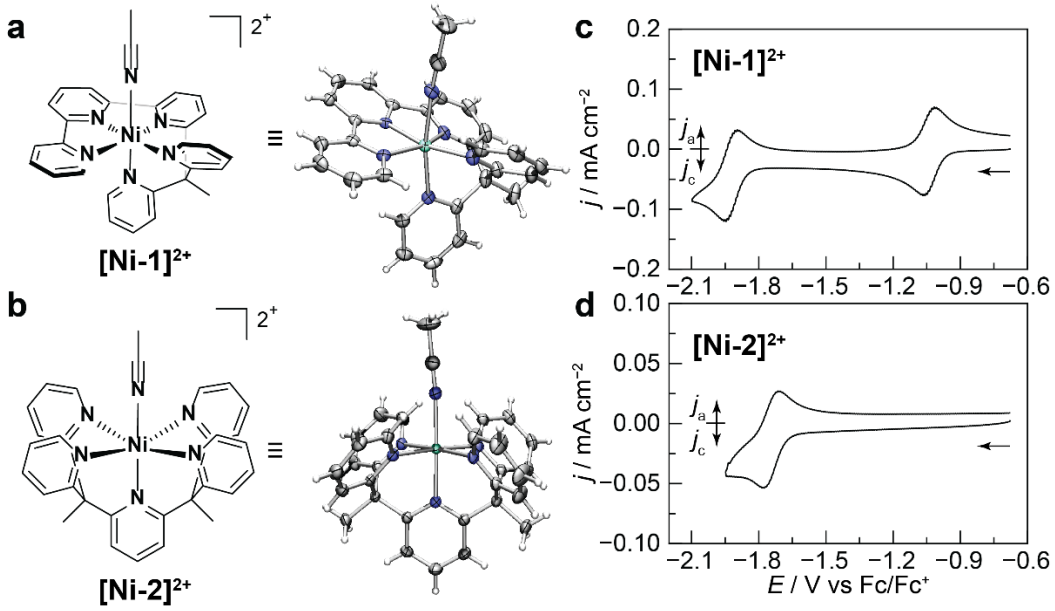


Figure B.1. Structures and crystal structures of $[Ni\text{-}1]^{2+}$ (a) and $[Ni\text{-}2]^{2+}$ determined by single crystal x-ray diffraction (b). Thermal ellipsoids are plotted at 50% and 75% probability level for $[Ni\text{-}1]^{2+}$ and $[Ni\text{-}2]^{2+}$, respectively. Turquoise, dark blue, and gray ellipsoids signify Ni, N, and C atoms, respectively. Noncoordinating solvent and anions omitted for clarity. Cyclic voltammogram (CV) of 1.8 mM $[Ni\text{-}1]^{2+}$ (c) and 1.4 mM $[Ni\text{-}2]^{2+}$ (d) at 100 mV s^{-1} taken in 0.1 M $TBAPF_6$ in DMF, where CV scans were initiated cathodically from the open circuit potential (–0.68 V vs Fc/Fc^+).

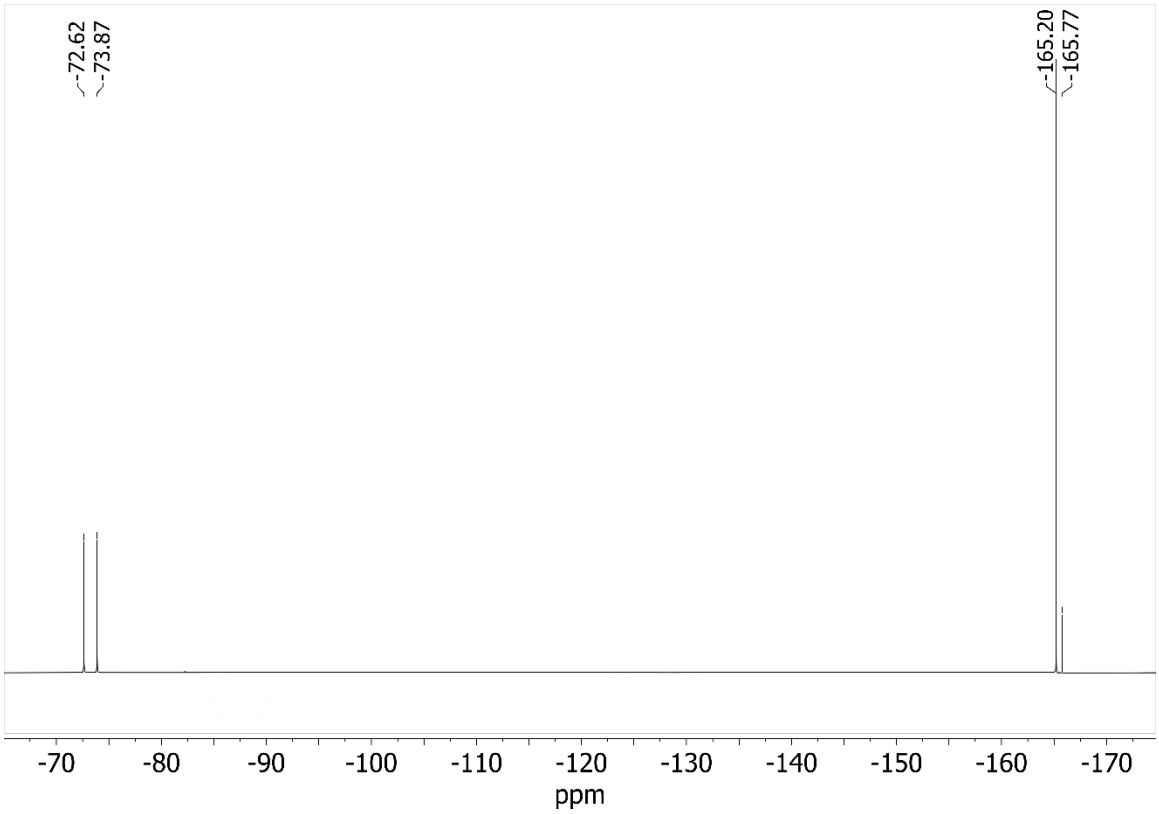


Figure B.2. Evans method analysis for $[Ni\text{-}1]^{2+}$. ^{19}F NMR of 36 mM $[Ni\text{-}1]^{2+}$ in hexafluorobenzene/CD_3CN containing capillary of hexafluorobenzene/CD_3CN. Measured frequency shift of hexafluorobenzene is 342 Hz.

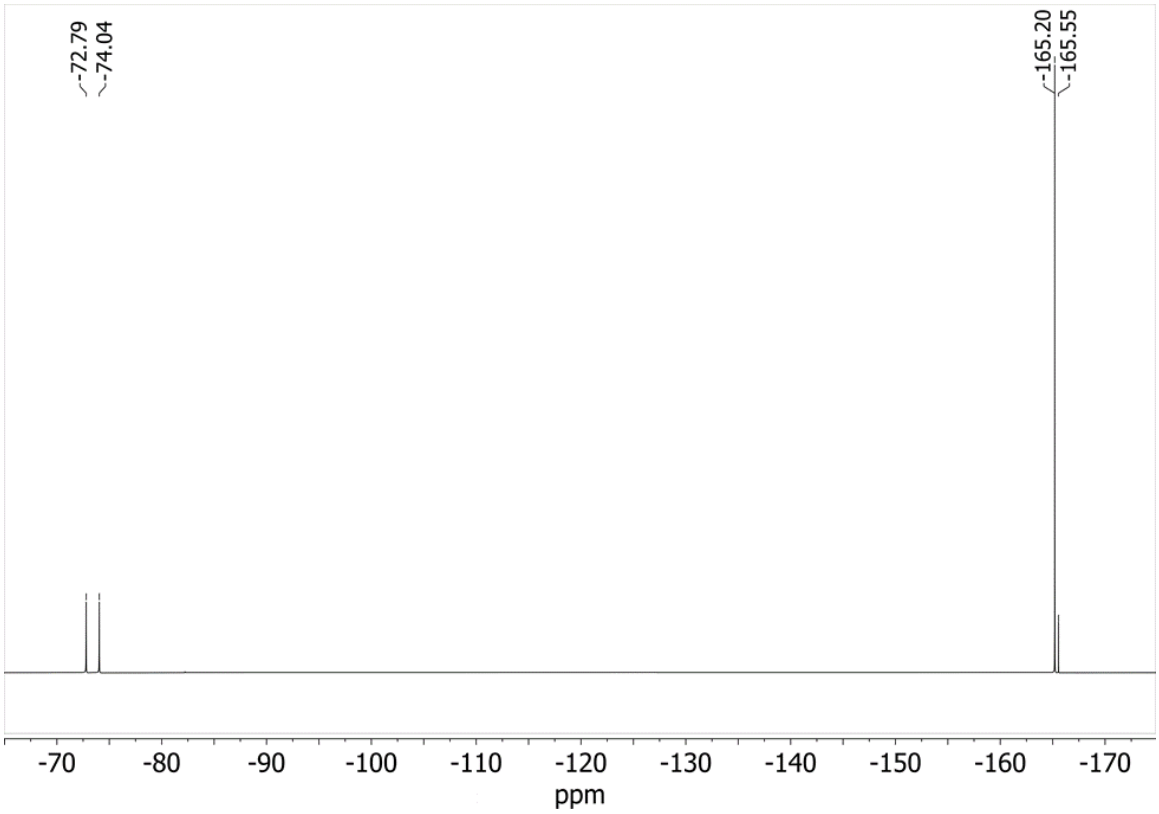


Figure B.3. Evans method analysis for $[Ni\text{-}2]^{2+}$. ^{19}F NMR of 24 mM $[Ni\text{-}2]^{2+}$ in hexafluorobenzene/CD_3CN containing capillary of hexafluorobenzene/CD_3CN. Measured frequency shift of hexafluorobenzene is 210 Hz.

The $[Ni\text{-}1]^{2+}$ complex exhibits two redox features, while $[Ni\text{-}2]^{2+}$ exhibits a single feature over the same potential range**. Figure B.1c** shows the cyclic voltammogram (CV) of $[Ni\text{-}1]^{2+}$ taken in 0.1 M $TBAPF_6$ in DMF at 100 mV s^{-1} initiated at the open-circuit potential (−0.68 V). Two redox features are observed at $E_{1/2}$ values of −1.92 V (all potentials quoted vs Fc/Fc^+) and −1.04 V. Scan-rate-dependent CV measurements (**Figure B.4**) reveal that the observed 60 mV separation (ΔE_p) between the peak potential of the anodic and cathodic features persists for both redox events. This observation is characteristic of Nernstian SETs to solution-dissolved reactants,[53,54] supporting the reversibility, and thus fast ET kinetics, of the redox events associated with $[Ni\text{-}1]^{2+}$ reduction. Bulk electrolysis measurements of $[Ni\text{-}1]^{2+}$ conducted at −2.04 V consume 2 F mol^{-1} (**Figure B.5**) and are in line with the assignment of two redox events, i.e., sequential formation of $[Ni\text{-}1]^+$ and [Ni-1], accessible at this potential. In contrast, the $[Ni\text{-}2]^{2+}$ complex exhibits a single redox feature with slower ET kinetics. **Figure B.1d** displays the CV of $[Ni\text{-}2]^{2+}$ taken over a similar potential range as $[Ni\text{-}1]^{2+}$. A redox feature is observed at an $E_{1/2}$ value equaling −1.75 V (**Figure B.1d**). As the scan rate is increased, the peak-to-peak separation between the anodic and cathodic features increases (**Figure B.6**), revealing that the redox event is influenced by the kinetics of the electron transfer process.[1,3] Determination of the diffusion coefficient of $[Ni\text{-}2]^{2+}$ (5×10^{-6} cm^2 s^{-1}) by electroanalytical methods (**Figure B.6**) allows for the estimation of the electron transfer rate constant, $k_{s[Ni\text{-}2]^{2+}} = 1.1 \times 10^{-2}$ cm s^{-1}, for forming the reduced $[Ni\text{-}2]^+$ species, in contrast to the Nernstian behavior observed for $[Ni\text{-}1]^{2+}$. The voltammetry results demonstrate that reduced [Ni-1] and $[Ni\text{-}2]^+$ complexes are accessible within 170 mV of one another.

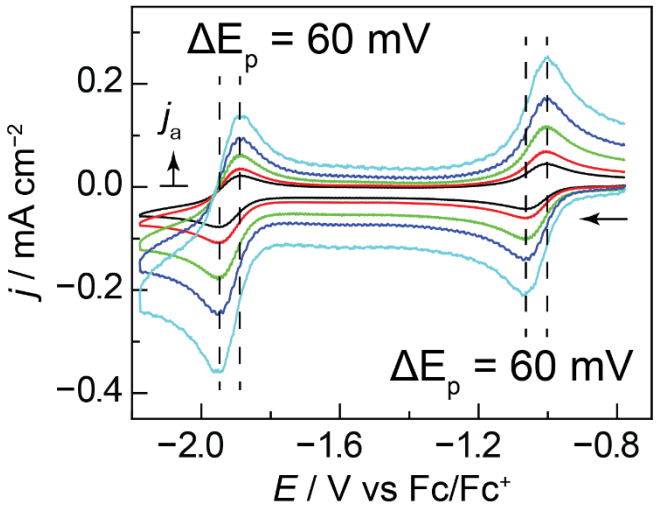


Figure B.4. Cyclic voltammograms of 1.1 mM $[Ni\text{-}1]^{2+}$ at 0.1 (black), 0.2 (red), 0.5 (green), 1 (dark blue), and 2 (light blue) V s^{-1} taken in 0.1 M $TBAPF_6$ in DMF, where CV scans were initiated at –0.78 V vs Fc/Fc^+.

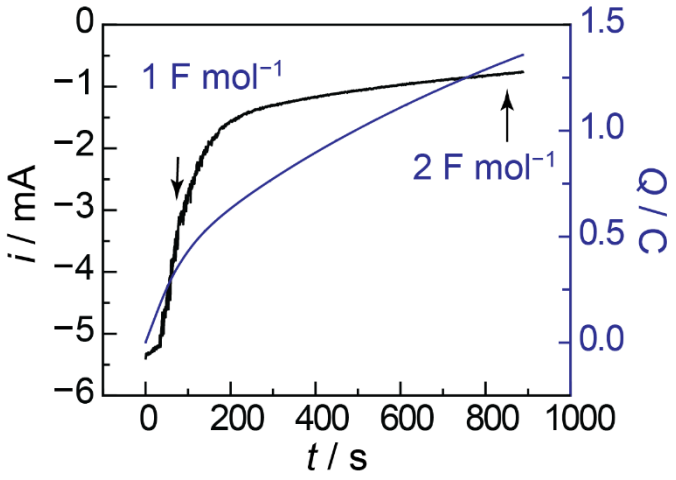


Figure B.5. Chronoamperometry trace of 1.36 mM $[Ni\text{-}1]^{2+}$ in 0.1 M $TBAPF_6$ in DMF collected at –2.04 V vs Fc/Fc^+ using a RVC cathode. Corresponding coulometry trace (blue) shown.

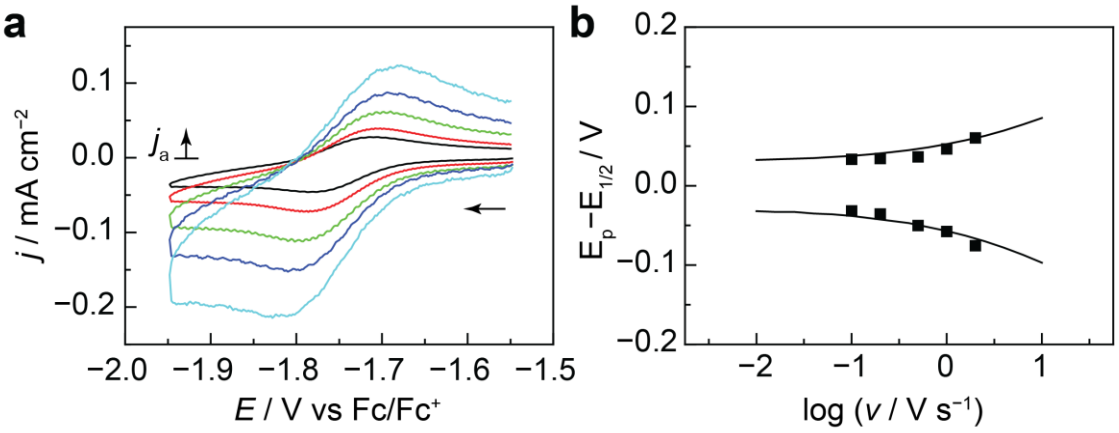


Figure B.6. (a) Cyclic voltammograms of 1.4 mM $[Ni\text{-}2]^{2+}$ at 0.1 (black), 0.2 (red), 0.5 (green), 1 (dark blue), and 2 (light blue) V s^{-1} taken in 0.1 M $TBAPF_6$ in DMF, where CV scans were initiated at –1.55 V vs Fc/Fc^+. (b) Dependence of peak potential (E_p) as a function of the scan rate for data collected in Figure S5a (black squares) compared with simulated curves plotted for k_s = 0.011 cm s^{-1} (black line). The diffusion coefficient for $[Ni\text{-}2]^{2+}$ was calculated at a value of 5×10^{-6} cm^2 s^{-1} from the peak current in the reversible limit of cyclic voltammograms collected.

B.3.2 Single-Electron Activation of Alkyl Iodide Substrates by [Ni-1]

To investigate the electrocatalytic reactivity of synthesized $[Ni\text{-}1]^{2+}$ and $[Ni\text{-}2]^{2+}$, we screened various alkyl halide substrates to identify variants that were electrochemically activated by both complexes and gave rise to mechanistically distinguishable reactivity. We found that both an activated RI substrate, dimethyl 2-butyl-2-(iodomethyl)malonate (**3**), and a less activated RI substrate, cycloiodohexane (CyI), fit this criteria. With these substrates in hand, we studied the catalysts' mechanism of action by employing electroanalytical studies to track the in situ formation and consumption of the reduced forms of $[Ni\text{-}1]^{2+}$ and $[Ni\text{-}2]^{2+}$ and combining these insights with bulk electrolysis reactivity studies.

The electrogenerated [Ni-1] complex activates **3** in a bimolecular fashion. **Figure B.7a** depicts the CV of 1.1 mM $[Ni\text{-}1]^{2+}$ taken in 0.1 M $TBAPF_6$ in DMF in the absence (black solid trace) and presence of 12 mM of **3** (red solid trace). Upon the addition of **3**, the wave corresponding to $[Ni\text{-}1]^+/[Ni\text{-}1]$ becomes irreversible, and an increase in the cathodic peak current (j_p) relative to the current in the absence of substrate (j_0) is observed. The j_p increases together with the concentration of added **3** up to two electrons (j_p/j_0 = 2) (**Figure B.8a**). This observation suggests that two equivalents of [Ni-1] are involved in activating **3**. Bulk electrolysis measurements of equimolar $[Ni\text{-}1]^{2+}$ and **3** conducted at −2.08 V are consistent with this hypothesis; this process consumes 3 F mol^{-1} (**Figure B.9**) in agreement with the assignment of the combined one-electron stoichiometry at the $[Ni\text{-}1]^{2+}/[Ni\text{-}1]^+$ wave and the two-electron stoichiometry at the $[Ni\text{-}1]^+/[Ni\text{-}1]$ wave in the presence of **3**. Furthermore, electrochemical studies in the absence of added $[Ni\text{-}1]^{2+}$ failed to activate **3** at the same potential, consistent with the assignment of [Ni-1] as the active redox mediator. The peak potential (E_p) for the direct reduction of **3** is −2.52 V (**Figure B.10a**), a value that is 0.58 V more negative than the E_p of **3** activation in the presence of [Ni-1] (−1.94 V; **Figure B.7.a**). This observation rules out competing direct reduction pathways of **3** since they are

not electrochemically accessible at the potential values examined. A mechanistic sequence compatible with these observations is the following

$$[\text{Ni-1}]^{2+} + e^- \rightleftharpoons [\text{Ni-1}]^{+} \qquad \textbf{Equation B.1}$$

$$[\text{Ni-1}]^{+} + e^- \rightleftharpoons [\text{Ni-1}] \qquad \textbf{Equation B.2}$$

$$[\text{Ni-1}] + \text{RI} \xrightarrow{k_1} \text{R}^{\bullet} + \text{I}^- + [\text{Ni-1}]^{+} \qquad \textbf{Equation B.3}$$

$$[\text{Ni-1}] + \text{R}^{\bullet} \xrightarrow{k_r} [(\text{Ni-1})(\text{R})] \qquad \textbf{Equation B.4}$$

Where k_1 is the rate constant of the homogeneous single-electron transfer between [Ni-1] and **3** (denoted above as a general alkyl iodide, RI) and k_r is the rate constant associated with rapid rebound of the resultant radical ($R^{\bullet}$) to [Ni-1]. This proposed sequence captures the two redox features observed for $[\text{Ni-1}]^{2+}$ (steps 1 and 2) and the two-electron stoichiometry at the $[\text{Ni-1}]^{+}$/[Ni-1] wave observed in the presence of **3** (steps 3 and 4). Electrochemical simulations provide further support of this hypothesis. By assuming that step 1 does not play a role in substrate activation other than accessing the redox potential necessary to form $[\text{Ni-1}]^{+}$, steps 2 to 4 can be described using the well-established theoretical framework of homogeneous redox catalysis in which a reactive intermediate (here, $R^{\bullet}$) rapidly adds to the catalyst active form (here, [Ni-1]), following a rate-determining substrate activation event.[55,56] This mechanistic framework permits the construction of working curves, which relate theoretical j_p/j_0 values to the ratio of the substrate and catalyst concentration (here, $C_{RI}/C_{[\text{Ni-1}]^{2+}}$).[55,56] However, the electrochemical response of [Ni-1] in the presence of **3** is convoluted by the observation of a broad capacitive feature ($E < -1.54$ V) and possible tail of an overlapping reductive feature ($E < -2.08$ V) as the concentration of **3** increases (**Figures B.7a** and **B.8a**). For these reasons, incremental changes in j_p/j_0 are not suitable observables to compare against theory. Therefore, theoretical working curves depicting predicted shifts in E_p were constructed (see **Figure B.8c** and the materials and methods for the procedure), predicting an anodic shift in E_p as the kinetic parameter increases. Comparison of the experimental E_p values with the working curves established for varying $C_{RI}/C_{[\text{Ni-1}]2+}$ values (**Figure B.8c**) leads to an estimation of k_1 ($\log k_1 = 2.841 \pm 0.007$ [M^{-1} s^{-1}]) (**Table B.1** and **Figure B.7c** (labeled red circle)). We observe agreement of k_1 values estimated at varying scan rates (**Figure B.8b** and **Table B.1**), providing further support of the proposed mechanistic sequence. This mechanism is in line with reports that expose the role of other one-electron reductants, e.g., $KCo(CN)_5^{3-}$, $KM(CO)_5$ (M = Mn, Re), and [Ni(1*R*,4*R*,8*S*,11*S*-tetramethylcyclam)]$^+$,[38,57–59] in similarly facilitating bimolecular oxidative addition pathways of polar reagents. Together, these data support a bimolecular oxidative addition pathway of **3** by electrogenerated [Ni-1].

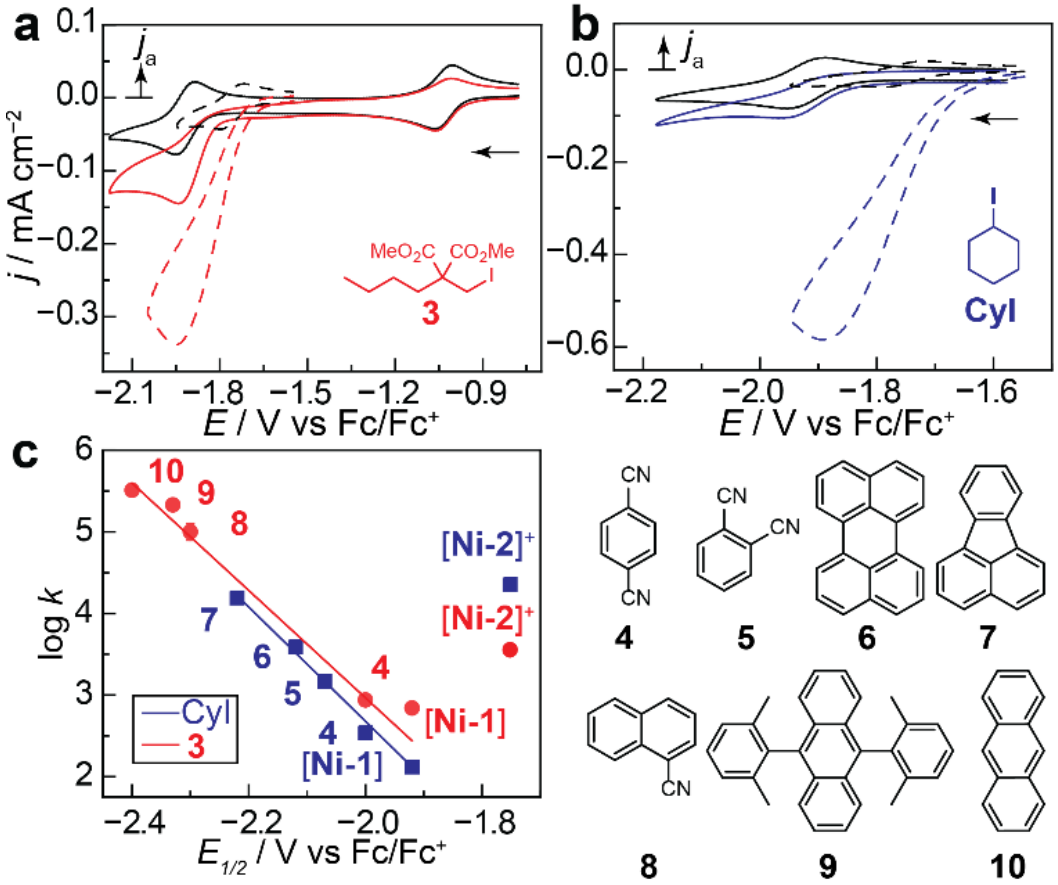


Figure B.7. (a) CV of 1.1 mM $[Ni\text{-}1]^{2+}$ in the absence (solid black) and presence (solid red) of 12 mM **3**. CV of 0.9 mM $[Ni\text{-}2]^{2+}$ in the absence (dashed black) and presence (dashed red) of 10 mM **3**. (b) CV of 1.1 mM $[Ni\text{-}1]^{2+}$ in the absence (solid black) and presence (solid blue) of 11 mM CyI. CV of 1.0 mM $[Ni\text{-}2]^{2+}$ in the absence (dashed black) and presence (dashed blue) of 11 mM CyI. CVs collected at 100 mV s^{-1} in 0.1 M $TBAPF_6$/DMF, where CV scans were initiated in the cathodic direction. (c) Variation in the estimated rate constant of the rate-determining step of **3** (red) and CyI (blue) activation with the redox potential of investigated Ni complexes or aromatic anions **4**-**10**. Straight line by regression for **3** activation by **10** to [Ni-1], $R^2 = 0.995$ and for CyI activation by **7** to [Ni-1], $R^2 = 0.998$. The data points are larger than the error bars in estimated *k*.

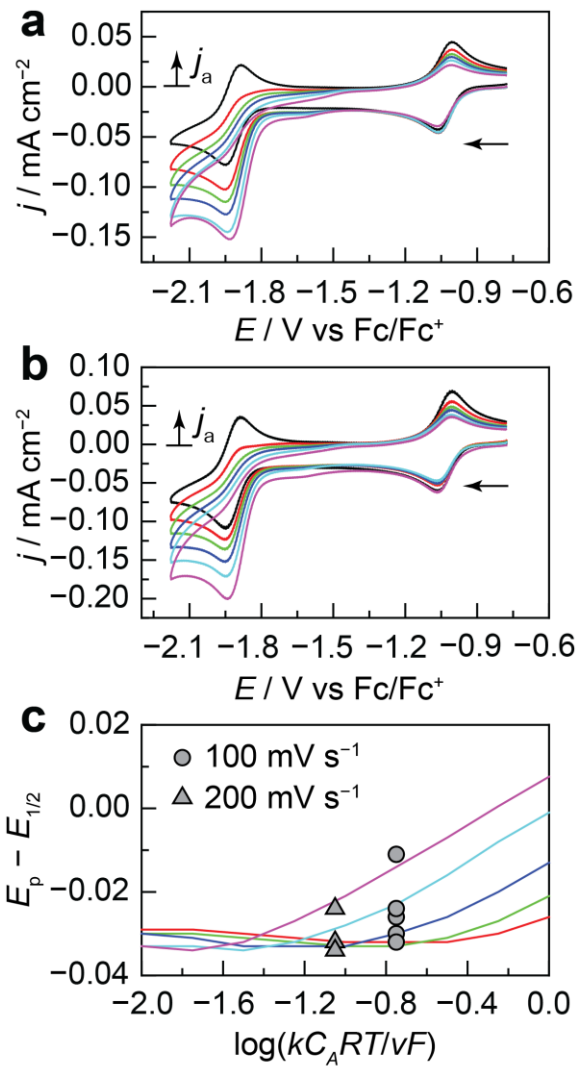


Figure B.8. Cyclic voltammogram (CV) of 1.1 mM $[Ni\text{-}1]^{2+}$ at 100 mV s^{-1} (a) and 200 mV s^{-1} (b) in the absence (black) and the presence of **3**, 1.1 mM (red), 2.1 mM (green), 4.4 mM (dark blue), 12 mM (light blue), 23 mM (pink) taken in 0.1 M $TBAPF_6$ in DMF, where CV scans were initiated at –0.78 V vs Fc/Fc^+. (c) Corresponding experimental (grey circles and triangles) and theoretical variation of difference of peak current potential (E_p) and reversible potential of catalyst ($E_{1/2}$) as a function dimensionless kinetic parameter for an electrocatalytic sequence with homogeneous electron transfer as the rate-limiting step followed by quenching of the reduced catalyst by the ensuing alkyl radical.

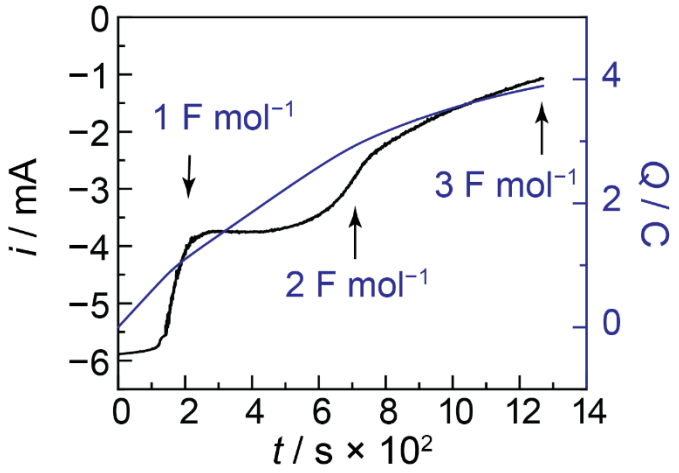


Figure B.9. Chronoamperometry trace of 2.50 mM $[Ni\text{-}1]^{2+}$ and 2.50 mM **3** in 0.1 M $TBAPF_6$ in DMF collected at –2.08 V vs Fc/Fc^+ using an RVC cathode. Corresponding colometry (blue) trace also shown.

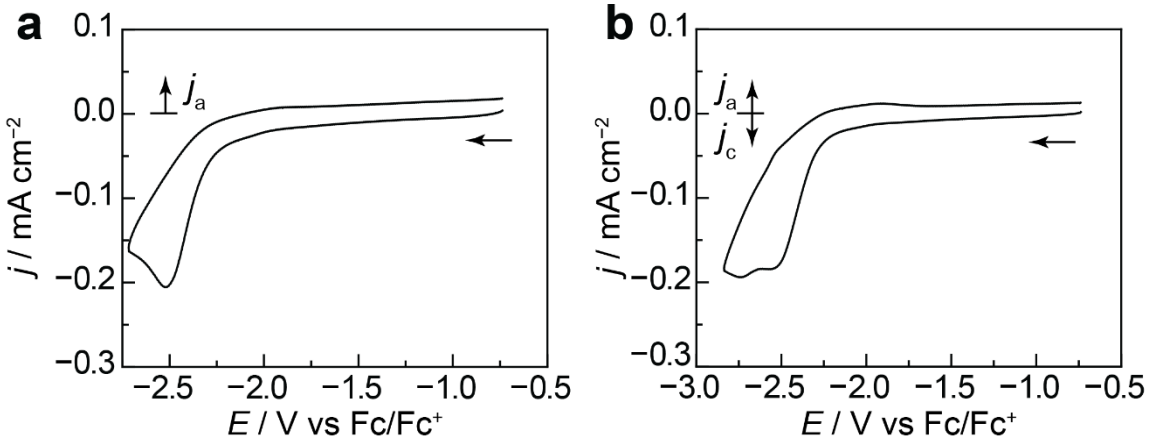


Figure B.10. Cyclic voltammogram (CV) of 2.1 mM of **3** (a) or 3.3 mM of CyI (b) taken at 100 mV s^{-1} in 0.1 M $TBAPF_6$ in DMF, where CV scans were initiated at –0.74 V vs Fc/Fc^+.

Table B.1. Summary of k_1 obtained as a function of various experimental parameters. CyI is cycloiodohexane. **3** is dimethyl 2-butyl-2-(iodomethyl)malonate. CC is chemical catalysis. TC is total catalysis. EC is electrochemical step followed by a chemical step. [#]Total catalysis conditions only observed for one set of parameters examined. [a]Estimated in M^{-1} s^{-1}. [b]Reported values in **Figure B.7c**. [c]Estimated lower limit.

Catalyst	$E_{1/2}$ / V vs Fc/Fc^+	Substrate	Analysis Method	Fig. #	Parameter Varied	log k_1[a]	Average Value[b]
					v		
[**Ni-2**]$^{2+}$	–1.75	CyI	CC	C.23	100 mV s^{-1}	4.140	4.141±0.001[c]
					200 mV s^{-1}	4.141	
					v		
[**Ni-2**]$^{2+}$	–1.75	**3**	CC	C.22	100 mV s^{-1}	5.32	5.28±0.06[c]
					200 mV s^{-1}	5.24	
					v		
[**Ni-1**]$^{2+}$	–1.92	CyI	EC	C.11	100 mV s^{-1}	2.14	2.12±0.04
					200 mV s^{-1}	2.09	
					v		
[**Ni-1**]$^{2+}$	–1.92	**3**	EC	C.8	100 mV s^{-1}	2.840	2.841±0.007
					200 mV s^{-1}	2.841	
					v		
4	–2.00	CyI	EC	C.12	100 mV s^{-1}	2.540	2.541±0.001
					200 mV s^{-1}	2.541	
					v		
4	–2.00	**3**	EC	C.13	100 mV s^{-1}	2.99	2.94±0.07
					200 mV s^{-1}	2.89	
					v		
5	–2.07	CyI	EC	C.15	100 mV s^{-1}	3.14	3.17±0.04
					200 mV s^{-1}	3.19	
					v		
6	–2.12	CyI	EC	C.18	100 mV s^{-1}	3.590	3.591±0.001
					200 mV s^{-1}	3.591	
					v		
7	–2.22	CyI	EC	C.19	100 mV s^{-1}	4.190	4.191±0.001
					200 mV s^{-1}	4.191	

					v		
8	–2.30	**3**	TC	C.14	100 mV s^{-1}	4.95	5.0±0.1
					200 mV s^{-1}	5.14	
9	–2.33	**3**	TC	C.16	# [RI]	5.33	5.33
10	–2.40	**3**	TC	C.17	1.2 mM	5.54	5.51±0.05
					2.5 mM	5.47	

The [Ni-1] complex activates CyI at a lower rate than **3**. **Figure B.7b** shows the CV of 1.1 mM $[Ni\text{-}1]^{2+}$ in the absence (black solid trace) and presence of 11 mM of CyI (blue solid trace). We observe: (1) increased current density at the redox couple associated with [Ni-1] formation; (2) j_p/j_0 approaching a value of 2 as the CyI concentration is increased (**Figure B.11a**); and (3) direct CyI reduction at E values 580 mV more negative than in the presence of [Ni-1] (**Figure B.10b**). Comparison of the experimental E_p values with the identical working curve utilized to analyze the activation of **3** (vide supra) (**Figure B.11c**) leads to an estimation of k_1 (log k_1 = 2.12 ± 0.04 [M^{-1} s^{-1}]) (**Table B.1** and **Figure B.7c** (labeled blue square)). We observe agreement of k_1 values estimated at varying scan rates (**Figure B.11b** and **Table B.1**), providing further support of the mechanistic sequence, steps 2 through 4. Together, these data suggest that electrogenerated [**Ni-1**] activates CyI in a similar manner as **3**, however, at a 5-fold slower rate.

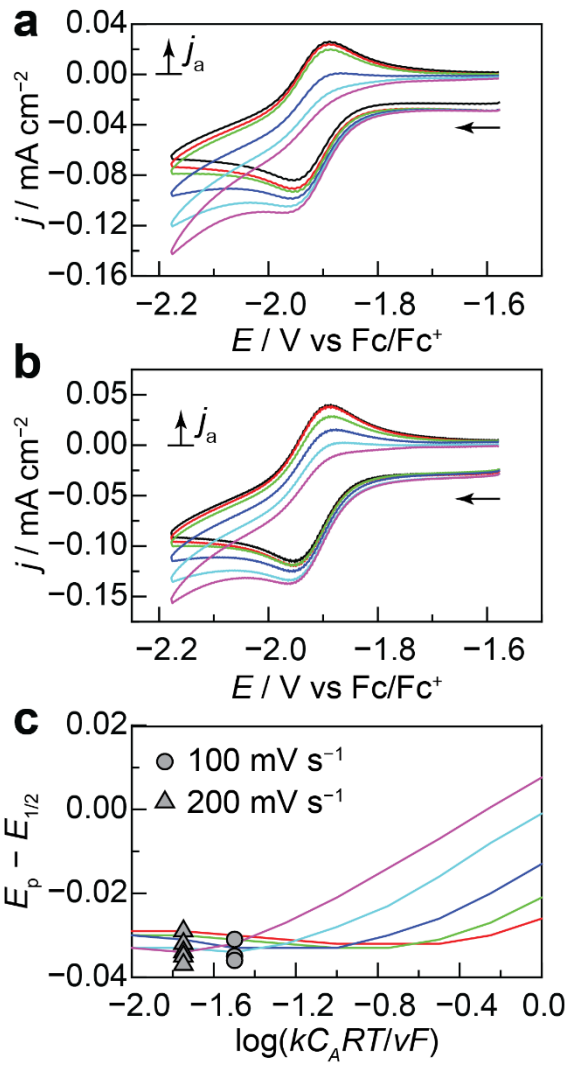


Figure B.11. Cyclic voltammogram (CV) of 1.1 mM $[Ni\text{-}1]^{2+}$ at 100 mV s^{-1} (a) and 200 mV s^{-1} (b) in the absence (black) and the presence of cycloiodohexane 1.1 mM (red), 2.1 mM (green), 4.3 mM (dark blue), 11 mM (light blue), 20 mM (pink) taken in 0.1 M $TBAPF_6$ in DMF, where CV scans were initiated at –1.58 V vs Fc/Fc^+. (c) Corresponding experimental (grey circles and

triangles) and theoretical variation of difference of peak current potential (E_p) and reversible potential of catalyst ($E_{1/2}$) as a function dimensionless kinetic parameter for an electrocatalytic sequence with homogeneous electron transfer as the rate-limiting step followed by quenching of the reduced catalyst by the ensuing alkyl radical.

To distinguish the mechanism of the homogeneous ET step involved in substrate activation by [Ni-1], i.e., step 3 in the proposed sequence, we compared estimated k_1 values with those obtained for **3** and CyI activation by a series of organic redox mediators (Ar). As there is no metal center on the electrogenerated organic radical anion ($Ar^{\bullet-}$) to facilitate an inner-sphere interaction with the substrate, the experimentally determined rate of ET between $Ar^{\bullet-}$ and RI (k_1 in step 3 of the proposed sequence, where $Ar^{\bullet-}$ replaces the Ni complex) represents values expected for a purely outer-sphere homogeneous electron transfer event (OSET). Thus, estimated k_1 values are expected to be proportional to the activation free energy, which is lowered by increases in the driving force, i.e., the difference of $E_{1/2}$ of varying Ar from the fixed standard potential of the $RI/R^{\bullet} + I^-$ couple (approximately −1.7 V for 1-iodobutane)[56] by the Hush–Marcus relationship.[60–62] Establishing this relationship for the substrates examined in this study serves as a diagnostic method[27,63,64] to identify if [Ni-1] similarly activates RI in an OSET fashion. The organic compounds, **4**–**10** in **Figure B.7c**, were judiciously chosen as precursors for electrogenerated $Ar^{\bullet-}$. First, their $E_{1/2}$ values span a 400 mV potential range that closely overlaps with that of $[Ni\text{-}1]^+/[Ni\text{-}1]$. Second, after screening several literature-reported organic redox mediators,[27,56] we narrowed the selection to **4**–**10** due to their well-defined CV responses in the presence of **3** and/or CyI. These organic redox mediators exhibited responses consistent with known limiting cases of two kinetic regimes (total catalysis or catalyst deactivation),[55,65] allowing for the estimation of k_1 in the absence of convoluting side reactions (see **Figures B.12** – **B.19** and the materials and methods for experimental and theoretical details). In short, these methods provided consistent values of k_1 across varying experimental conditions, supporting the proposed mechanism involving rate-limiting activation of RI by the examined Ar redox mediators. The k_1 values found using this procedure are listed in **Table B.1** and graphically represented in **Figure B.7c**. The values found for CyI agree with reported k_1 values for the secondary alkyl iodide, 2-iodobutane,[56] providing further support for the methods utilized herein. As anticipated for OSET processes in which the transfer coefficients do not significantly change with the driving force,[53,60–62] an approximate log–linear relationship between the $E_{1/2}$ and k_1 is observed for RI activation by **4**–**10** (**Figure B.7c**). Importantly, we find that the measured k_1 values for both **3** and CyI activation by [Ni-1] follow this approximate linear trend, providing strong evidence for OSET activation of **3** and CyI by [Ni-1]. While we note the log k_1–$E_{1/2}$ relationships, in theory, are nonlinear,[27,56,63] the slopes for the obtained linear fits (**Figure B.7**) (for **3**, -6.6 ± 0.3, red and for CyI, -7.0 ± 0.1, blue) allow us to estimate a transfer coefficient value of 0.4, consistent with previous reports detailing homogeneous concerted dissociative electron transfers to similar alkyl halide substrates[27,56,63] by Ar redox mediators. The consistently observed ∼3-fold difference in rate between **3** and CyI suggests that the RI bond of **3** is indeed more activated than that of CyI and thus more readily cleaved. The observed approximate log–linear relationship of k_1 with $E_{1/2}$ for RI activation by [Ni-1] with various electrogenerated $Ar^{\bullet-}$ further supports the hypothesized mechanistic sequence invoked in steps 1–4 (vide supra) over an SN_2-type activation by [Ni-1] to directly form [(Ni-1)(R)]; the latter inner-sphere reaction sequence would lead to higher rates that would significantly deviate from the values obtained for $Ar^{\bullet-}$, e.g., as has been observed for alkyl bromide activation by iron

porphyrin systems.[63] Together, these studies are consistent with a mechanism implicating dissociative OSET activation of RI by [Ni-1].

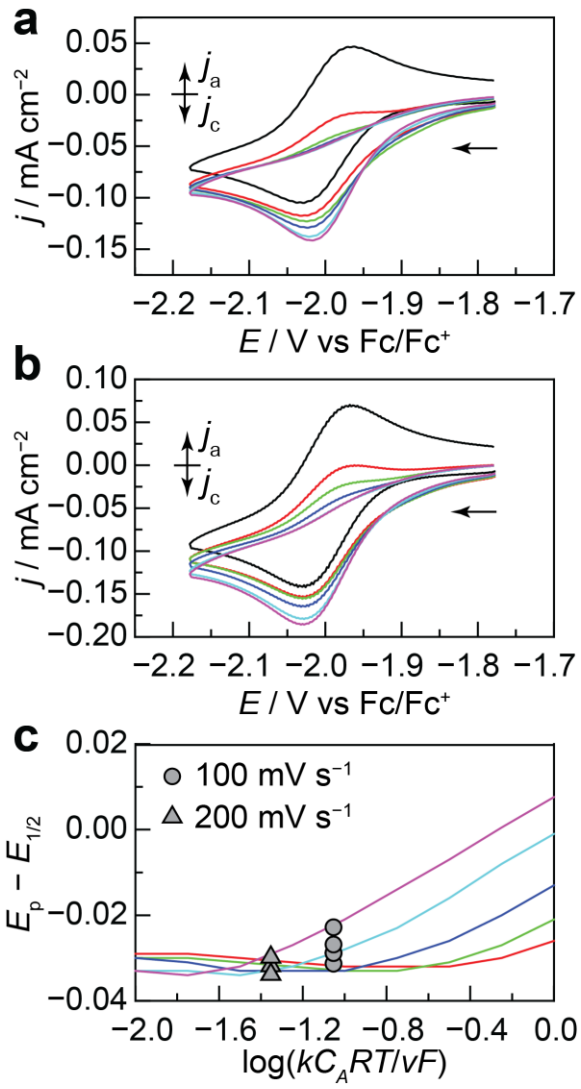


Figure B.12. Cyclic voltammogram (CV) of 1.0 mM 1,4 CN benzene at 100 mV s^{-1} (a) and 200 mV s^{-1} (b) in the absence (black) and the presence of cycloiodohexane 1.0 mM (red), 2.0 mM (green), 3.9 mM (dark blue), 9.6 mM (light blue), 19 mM (pink) taken in 0.1 M $TBAPF_6$ in DMF, where CV scans were initiated at –1.78 V vs Fc/Fc^+. (c) Corresponding experimental (grey circles and triangles) and theoretical variation of difference of peak current potential (E_p) and reversible potential of catalyst ($E_{1/2}$) as a function dimensionless kinetic parameter for an electrocatalytic sequence with homogeneous electron transfer as the rate-limiting step followed by quenching of the reduced catalyst by the ensuing alkyl radical.

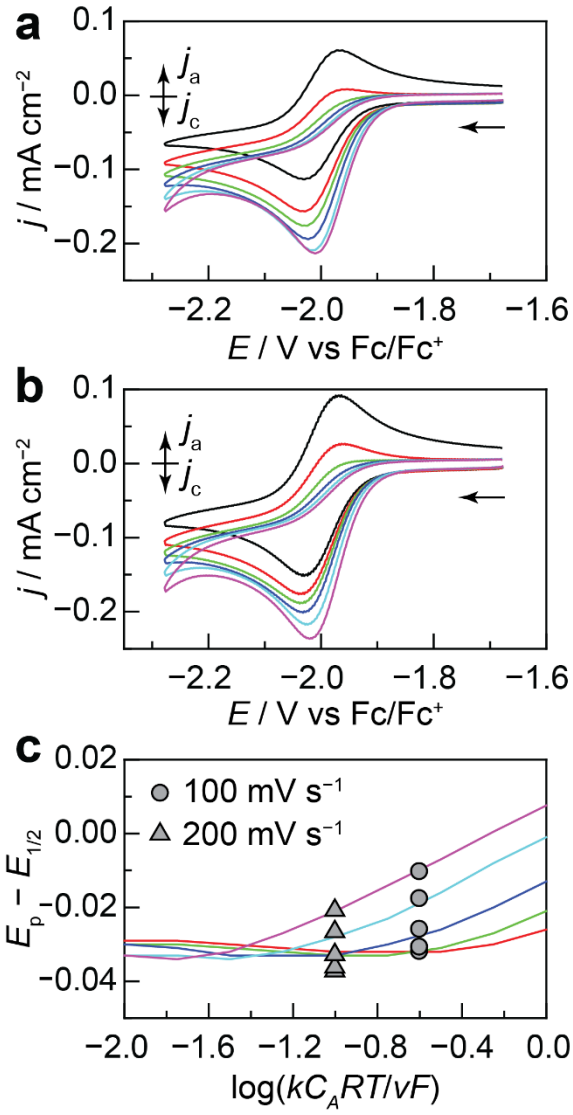


Figure B.13. Cyclic voltammogram (CV) of 0.9 mM 1,4 CN benzene at 100 mV s^{-1} (a) and 200 mV s^{-1} (b) in the absence (black) and the presence of **3** 0.9 mM (red), 1.8 mM (green), 3.7 mM (dark blue), 9.0 mM (light blue), 17 mM (pink) taken in 0.1 M $TBAPF_6$ in DMF, where CV scans were initiated at –1.68 V vs Fc/Fc^+. (c) Corresponding experimental (grey circles and triangles) and theoretical variation of difference of peak current potential (E_p) and reversible potential of catalyst ($E_{1/2}$) as a function dimensionless kinetic parameter for an electrocatalytic sequence with homogeneous electron transfer as the rate-limiting step followed by quenching of the reduced catalyst by the ensuing alkyl radical.

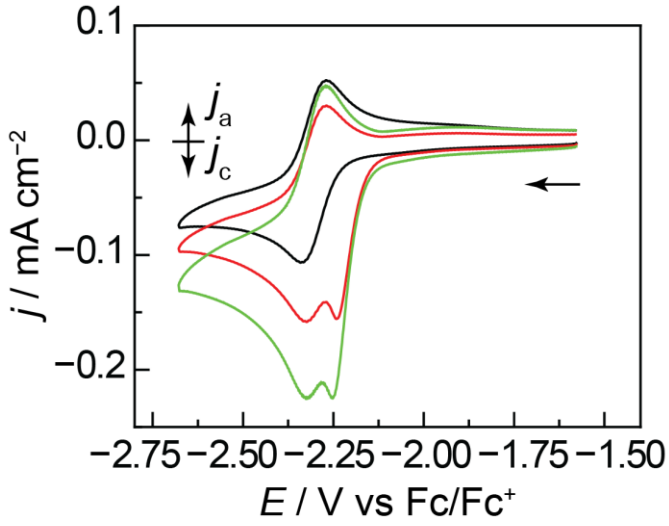


Figure B.14. Cyclic voltammogram (CV) of 1.0 mM CN-napthalene at 100 mV s^{-1} without (black) and with (red) 1.0 mM **3** taken in 0.1 M $TBAPF_6$ in DMF, where CV scans were initiated at –1.58 V vs Fc/Fc^+. CV with 1.0 mM **3** at 200 mV s^{-1} (green).

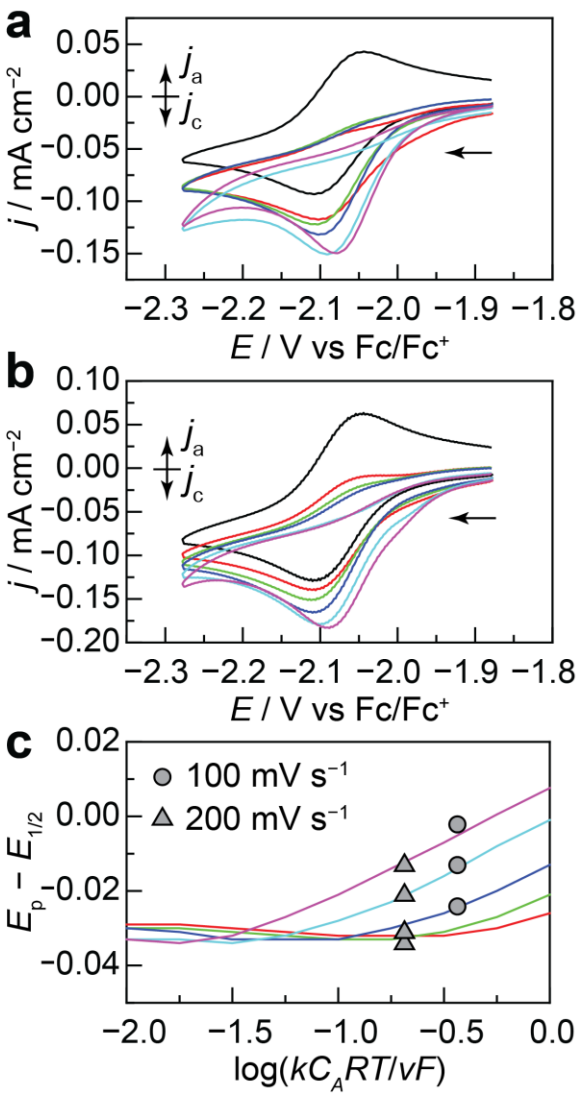


Figure B.15. Cyclic voltammogram (CV) of 1.0 mM 1,2 CN benzene at 100 mV s^{-1} (a) and 200 mV s^{-1} (b) in the absence (black) and the presence of cycloiodohexane 1.0 mM (red), 2.0 mM (green), 3.9 mM (dark blue), 9.6 mM (light blue), 19 mM (pink) taken in 0.1 M $TBAPF_6$ in DMF, where CV scans were initiated at –1.88 V vs Fc/Fc^+. (c) Corresponding experimental (grey circles and triangles) and theoretical variation of difference of peak current potential (E_p) and reversible potential of catalyst ($E_{1/2}$) as a function dimensionless kinetic parameter for an electrocatalytic sequence with homogeneous electron transfer as the rate-limiting step followed by quenching of the reduced catalyst by the ensuing alkyl radical.

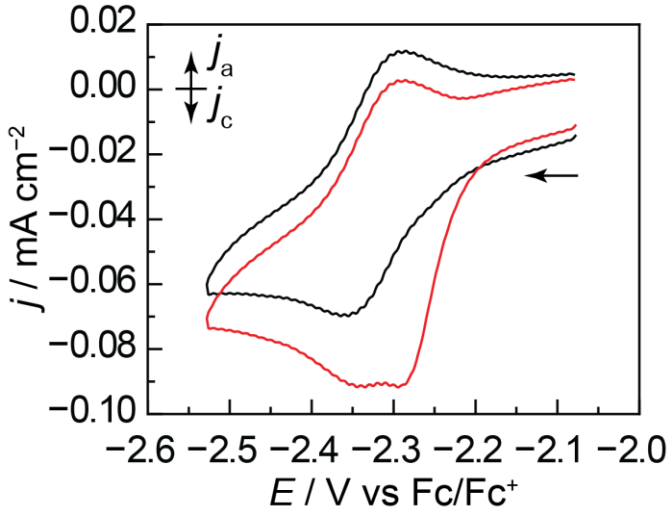


Figure B.16. Cyclic voltammogram (CV) of 0.9 mM 9,10-bis(2,6-dimethylphenyl)anthracene at 100 mV s^{-1} without (black) and with (red) 0.9 mM **3** taken in 0.1 M $TBAPF_6$ in DMF, where CV scans were initiated at –2.08V vs Fc/Fc^+.

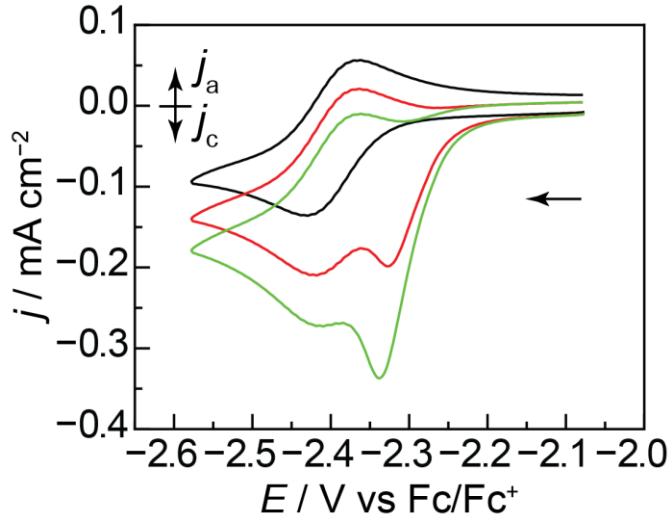


Figure B.17. Cyclic voltammogram (CV) of 1.0 mM anthracene at 100 mV s^{-1} without (black) and with (red) 1.2 mM or 2.5 mM (green) **3** taken in 0.1 M $TBAPF_6$ in DMF, where CV scans were initiated at – 2.08 V vs Fc/Fc^+.

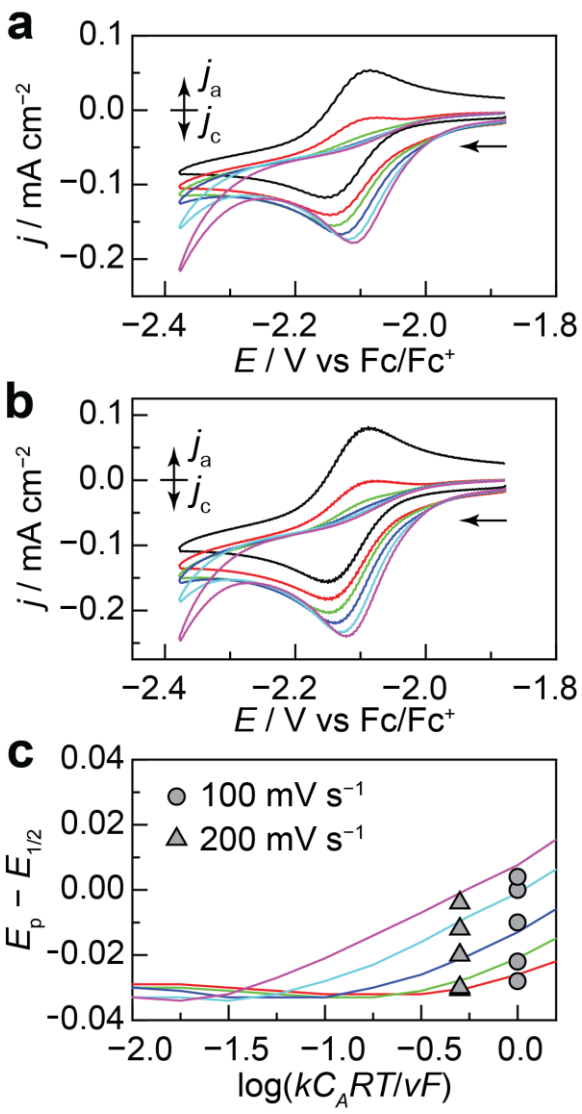


Figure B.18. Cyclic voltammogram (CV) of 1.1 mM perylene at 100 mV s^{-1} (a) and 200 mV s^{-1} (b) in the absence (black) and the presence of cycloiodohexane 1.0 mM (red), 2.1 mM (green), 4.2 mM (dark blue), 9.9 mM (light blue), 19 mM (pink) taken in 0.1 M $TBAPF_6$ in DMF, where CV scans were initiated at –1.88 V vs Fc/Fc^+. (c) Corresponding experimental (grey circles and triangles) and theoretical variation of difference of peak current potential (E_p) and reversible potential of catalyst ($E_{1/2}$) as a function dimensionless kinetic parameter for an electrocatalytic sequence with homogeneous electron transfer as the rate-limiting step followed by quenching of the reduced catalyst by the ensuing alkyl radical.

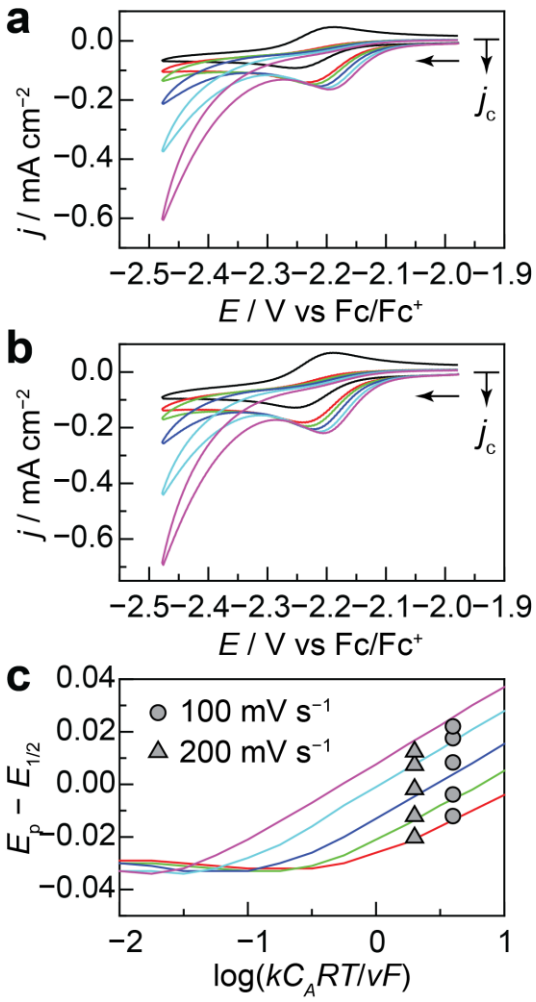
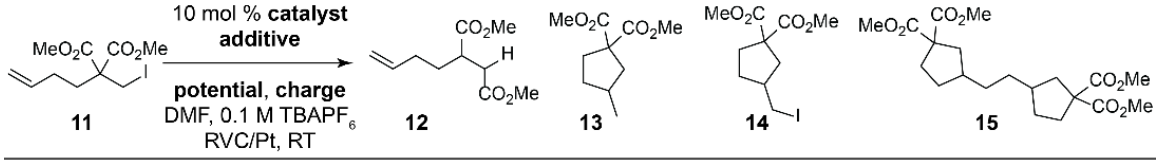


Figure B.19. Cyclic voltammogram (CV) of 1.1 mM fluoranthrene at 100 mV s^{-1} (a) and 200 mV s^{-1} (b) in the absence (black) and the presence of cycloiodohexane 1.0 mM (red), 2.0 mM (green), 4.2 mM (dark blue), 9.9 mM (light blue), 19 mM (pink) taken in 0.1 M $TBAPF_6$ in DMF, where CV scans were initiated at –1.88 V vs Fc/Fc^+. (c) Corresponding experimental (grey circles and triangles) and theoretical variation of difference of peak current potential (E_p) and reversible potential of catalyst ($E_{1/2}$) as a function dimensionless kinetic parameter for an electrocatalytic sequence with homogeneous electron transfer as the rate-limiting step followed by quenching of the reduced catalyst by the ensuing alkyl radical.

To decipher the downstream reactivity of the hypothesized [(Ni-1)(R)] species, i.e., step 4 in the proposed sequence, and the presence of free radical intermediates upon dissociative cleavage of RI, we examined the bulk electrolysis product distribution of [Ni-1]-catalyzed cyclization of **11**. As the cyclization of the 5-hexenyl radical is expected to be fast and irreversible,[66] we reasoned that interrogation of the bulk electrolysis reactivity of **3** modified with an alkene would facilitate detection of cyclized products, indicative of free radical intermediates. First, to obtain the baseline reactivity of **11** in the absence of $[Ni\text{-}1]^{2+}$, controlled potential electrolysis (CPE) of **11** was conducted at −2.73 V, corresponding to the potential associated with direct reduction (**Figure B.10a**). This process gives rise to **12** following the passage of 2 C mol^{-1} of charge (**Figure B.20**,

entry a). These data are consistent with the reported[67] and observed (**Figure B.10a**) two-electron CV waves associated with reduction of primary alkyl iodides, implicating that the reduction of **11** proceeds via the intermediacy of an electrogenerated carbanion. The observed 1,2-ester shift[68,69] of **12** further supports the presence of the carbanion intermediate. This reactivity lies in contrast to the high chemical yields observed for radical capture by alkenes for carbon-centered radicals electrogenerated from secondary halides,[19] highlighting the utility of redox mediation for primary alkyl halide substrates to synthesize cyclized products, vide infra, when direct reduction selectively forms the protodehalogenated product.[70] We note the low chemical yields observed (< 100% carbon balance) for the CPE experiments, shown in **Figure B.20**, which can be explained by the known functionalization of carbon surfaces under similar electrochemical conditions[64] and may be further exacerbated by the activated RI substrate utilized in this work.



entry	catalyst	additive	F mol^{-1}	V vs Fc/Fc^{+}	**12**	**13**	**14**	**15**
a	none	none	2	−2.73 V	50(30)*	nd	nd	nd
b	[**Ni-1**]$^{2+}$	none	1	−2.03 V	nd	31	17	nd
c	e-[**Ni-1**]	none	none	none	nd	<4%	nd	nd
d	[**Ni-1**]$^{2+}$	NaOTf	1	−2.03 V	nd	nd	nd	46(30)*
e	[**Ni-1**]$^{2+}$	CyI	1	−2.03 V	nd	19	75(40)*	nd
f	[**Ni-2**]$^{2+}$	none	1	−1.91 V	nd	12	nd	38
g	[**Ni-2**]$^{2+}$	CyI	3	−1.91 V	nd	24	nd	nd

Figure B.20. Controlled-potential electrolysis (CPE) reactivity data for **11** conducted in a divided electrochemical cell (0.044 mmol **11**, 0.004 mmol catalyst, 0.097 mmol additive in 5 mL catholyte). Charged passed until background current values observed and reported with respect to the amount of **11** added. In all cases, > 99% conversion of **11** observed. ^{1}H NMR yields against 1-methyloxindole standard reported due to low concentration of substrates utilized to match electroanalytical conditions. *Isolated yields also reported. For entry c, CPE was first conducted on [Ni-1]$^{2+}$ alone at 2 C mol^{-1} to form electrogenerated [Ni-1] (e-[Ni-1]), after which the applied potential bias was removed and **11** was added; product distribution investigated after stirring at RT for approximately 5 hours.

CPE performed in the presence of catalytic amounts of [Ni-1]$^{2+}$ shows product distributions consistent with the formation of radical intermediates produced via SET. In the presence of 10 mol % of [Ni-1]$^{2+}$, CPE of **11** at −2.03 V, corresponding to the potential associated with mediated reduction (**Figure B.7a**), gives rise to 31% and 17% yield of cyclized products **13** and **14**, respectively, following the passage of 1 C mol^{-1} of charge with respect to **11** (**Figure B.20**, entry b). The observed electron stoichiometry is in line with the 1 C mol^{-1} value expected for the proposed bimolecular activation of **3**, vide supra. For **13**, we propose that the cyclized radical is quenched by an H atom donor present in solution, which we hypothesize is DMF.[28,71] For **14**, the cyclized radical is quenched by a halogen atom donor; we postulate that an equivalent of unreacted

11 could serve as the donor via an atom transfer radical (ATR) cyclization pathway.[14,72,73] To rule out the predominance of a non-Faradaic ATR chain pathway on the observed reactivity for **14**, we investigated the reactivity of **11** in the presence of electrogenerated [Ni-1] in the absence of potential bias. [Ni-1] was electrogenerated in the absence of **11** until 2 C mol^{-1} of charge with respect to $[Ni\text{-}1]^{2+}$ was consumed, after which **4** was added, and the potential was turned off. Products were not detected in quantifiable amounts (**Figure B.20**, entry c), indicating that non-Faradaic chain processes do not predominate the observed reactivity. We repeated these experiments in the presence of triflate anions (OTf^-), which we observed redirects the product selectivity through a hypothesized coordination blocking mode. The presence of OTf^- dramatically changes the product distribution, with the dimer, **15**, being observed as the primary detectable product (**Figure B.20**, entry d). These data suggest that OTf^- interacts with electrogenerated [Ni-1],[74] suppressing formation of the hypothesized [(Ni-1)(R)] species, thereby favoring dimerization of free radicals formed via steps 1–3. Thus, we postulate that the observed reactivity in **Figure B.20**, entry b, is due to the propensity of [(Ni-1)(R)] to act as a reductant toward another equivalent of **11**, thereby controlling the free radical behavior via the bimolecular oxidative addition pathway in steps 1–4. Together, these reactivity studies evince the formation of [Ni-1]-mediated free radical species and suggest the presence of a [(Ni-1)(R)] intermediate in directing the product selectivity.

Increased selectivity of radical processes is observed for [Ni-1]-catalyzed **11** activation performed in the presence of a viable halogen donor, CyI. Results show that 75% of **14** and 19% of **13** are formed (**Figure B.20**, entry e). Importantly, only 1 C mol^{-1} of charge is transferred (**Figure B.21**), indicative of selective activation of **11** over CyI and consistent with the discrimination in k_1 observed between the two substrates given in **Figure B.7c**. The observation of high selectivity for **14** after the passage of 1 C mol^{-1} rules out the predominance of an ATR cyclization chain pathway,[14,72,73] which would lead to a significantly diminished and fractional electron equivalency as previously observed.[28] Thus, CyI serves as a halogen atom donor to quench the radical cascade sequence. Together, these data demonstrate that [Ni-1] catalyzes a selective radical process in an electrochemical environment: [Ni-1] selectively activates **11** over CyI in an OSET-initiated bimolecular event, and the subsequent hypothesized [(Ni-1)(R)] further activates another equivalent of **11**, regenerating $[Ni\text{-}1]^+$ and generating cyclized radicals that are quenched by CyI.

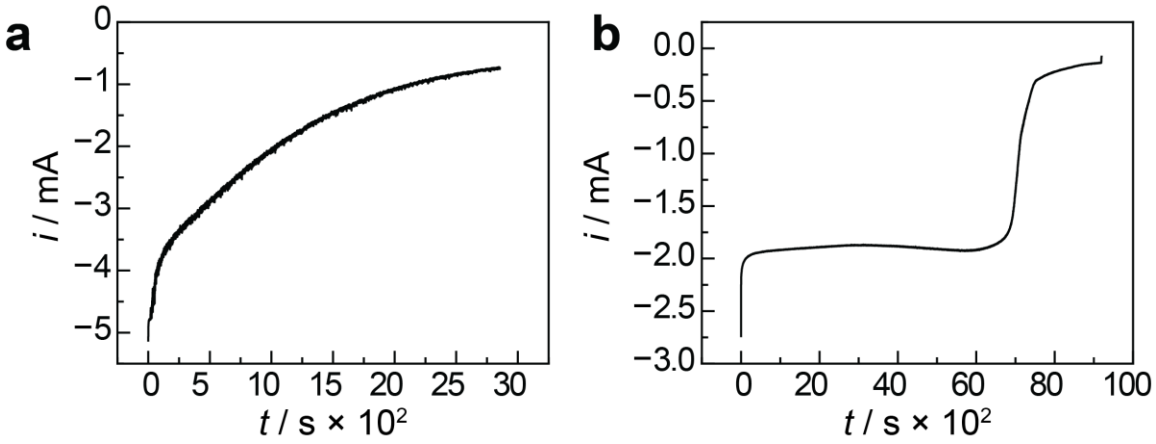


Figure B.21. (a) Chronoamperometry trace of 1 mM $[Ni\text{-}1]^{2+}$, 10 mM **11**, and 22 mM cycloiodohexane in 0.1 M $TBAPF_6$ in DMF collected at –2.05 V vs Fc/Fc^+ using a RVC cathode. (b) Chronoamperometry trace of 1 mM $[Ni\text{-}2]^{2+}$, 10 mM **11**, and 22 mM cycloiodohexane in 0.1 M $TBAPF_6$ in DMF collected at –1.92 V vs Fc/Fc^+ using a RVC cathode.

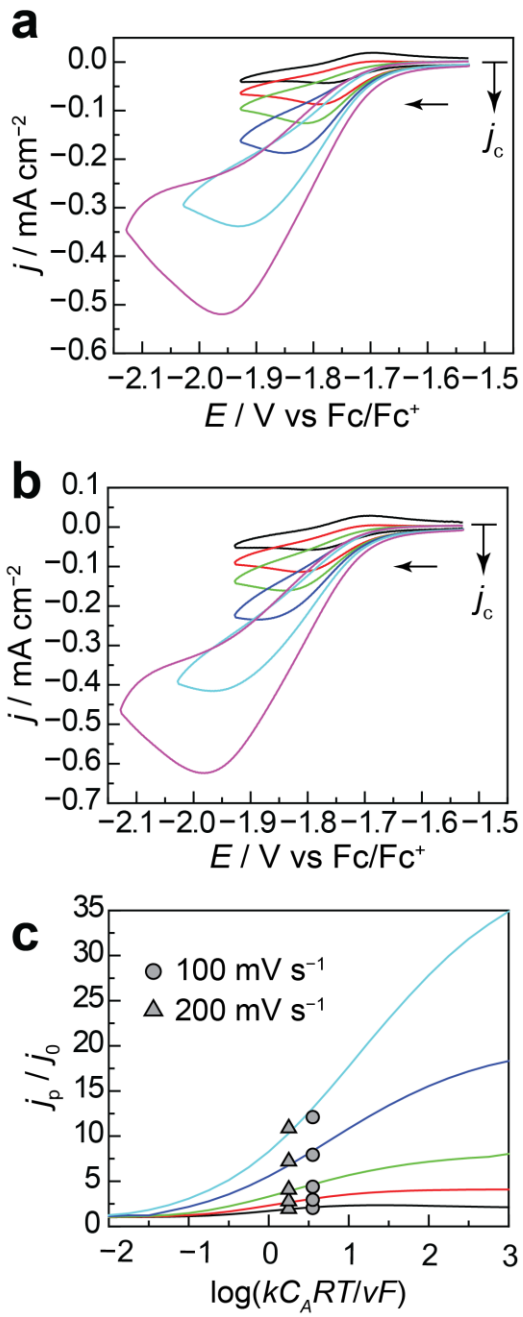


Figure B.22. Cyclic voltammogram (CV) of 0.93 mM $[Ni\text{-}2]^{2+}$ at 100 mV s^{-1} (a) and 200 mV s^{-1} (b) in the absence (black) and the presence of **3** 1.0 mM (red), 2.0 mM (green), 3.9 mM (dark blue), 10.0 mM (light blue), 20.4 mM (pink) taken in 0.1 M $TBAPF_6$ in DMF, where CV scans were initiated at –1.53 V vs Fc/Fc^+. (c) Corresponding experimental (grey circles and triangles) and theoretical variation of difference of peak current (j_p) relative to peak current in the absence of substrate (j_0) as a function dimensionless kinetic parameter for a redox-mediated sequence with homogeneous electron transfer as the rate-limiting step.

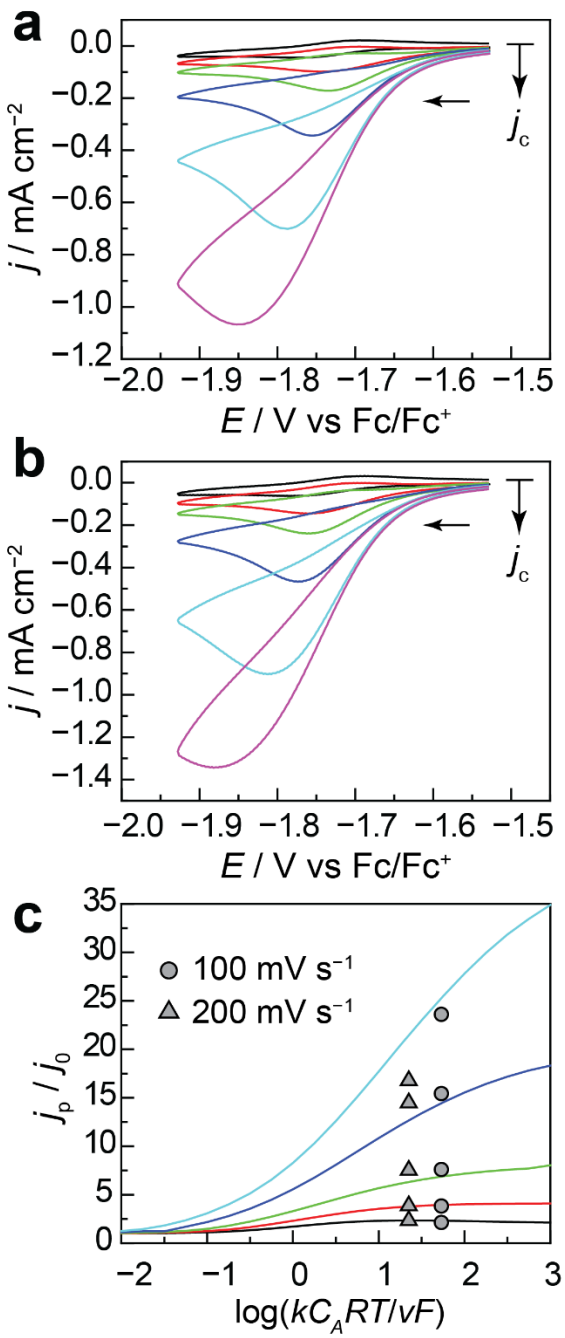


Figure B.23. Cyclic voltammogram (CV) of 0.96 mM $[Ni\text{-}2]^{2+}$ at 100 mV s^{-1} (a) and 200 mV s^{-1} (b) in the absence (black) and the presence of cycloiodohexane 1.1 mM (red), 2.2 mM (green), 4.4 mM (dark blue), 10.7 mM (light blue), 21 mM (pink) taken in 0.1 M $TBAPF_6$ in DMF, where CV scans were initiated at –1.53 V vs Fc/Fc^+. (c) Corresponding experimental (grey circles and triangles) and theoretical variation of difference of peak current (j_p) relative to peak current in the absence of substrate (j_0) as a function dimensionless kinetic parameter for a redox-mediated sequence with homogeneous electron transfer as the rate-limiting step.

B.3.3 Single-Electron Activation of Alkyl Iodide Substrates by [Ni-2]$^+$

In contrast to results obtained with [Ni-1]$^{2+}$, corresponding electroanalytical data collected for [Ni-2]$^{2+}$ implicate inner-sphere electron transfer (ISET) activation of the substrates examined, **3** and CyI. **Figure B.7b** shows the CV of 0.9 mM [Ni-2]$^{2+}$ in the absence (black dotted trace) and presence of 10 mM of **3** (red dotted trace). Upon the addition of **3**, the wave corresponding to [Ni-2]$^{2+}$/[Ni-2]$^+$ becomes irreversible, and a j_p/j_0 value equaling 8 is observed. This value increases monotonically with added concentration of **3** (**Figure B.22**), suggesting that, unlike [Ni-1], activation of **3** by [Ni-2]$^+$ involves the continuous catalytic regeneration of [Ni-2]$^{2+}$ at an appreciable rate. Similar results are obtained for data collected using CyI as the substrate. **Figure B.7b** shows the CV of 1 mM [Ni-1]$^{2+}$ in the absence (black dotted trace) and presence of 11 mM CyI (blue dotted trace). When CyI is added, a j_p/j_0 value equaling 16 is observed at the peak corresponding to [Ni-2]$^+$ formation. This value also increases monotonically with added concentration of CyI (**Figure B.23**). A mechanistic sequence consistent with these observations is

$$[\text{Ni-2}]^{2+} + e^- \rightleftharpoons [\text{Ni-2}]^+ \qquad \textbf{Equation B.5}$$

$$[\text{Ni-2}]^+ + \text{RI} \xrightarrow{k_1} \text{R}^\bullet + \text{I}^- + [\text{Ni-2}]^{2+} \qquad \textbf{Equation B.6}$$

where k_s is the heterogeneous electron transfer rate obtained in the absence of substrate, vide supra. This mechanism is in line with a redox catalysis scheme,[65,75] where the homogeneous electron transfer step between electrogenerated catalyst (here, [Ni-2]$^+$) and RI is rate determining.[27] Within this mechanistic framework, a lower limit on k_1 can be estimated by constructing working curves, which depict theoretical j_p/j_0 values at varying $C_{RI}/C_{[\text{Ni-2}]^{2+}}$ (see materials and methods and **Figures B.22** and **B.23** for details). Agreement of the values across various substrate concentrations and scan rates were observed; average values of log k_1 = 5.7 ± 0.2 [M^{-1} s^{-1}] and log k_1 = 7.1 ± 0.2 [M^{-1} s^{-1}] (**Table B.1** and **Figure B.7c**, labeled red circle and blue square) were obtained for **3** and CyI, respectively. Comparison of these rates with those obtained for [Ni-1] (**Figure B.7c**) reveals that (1) the k_1 values do not scale with those observed for Ar and [Ni-1]-mediated RI activation, and (2) [Ni-2]$^+$ exhibits roughly 10-fold and 100-fold higher rates of activation for **3** and CyI, respectively, as $Ar^{\bullet-}$ and [Ni-1] with similar $E_{1/2}$. These data delineate that, unlike [Ni-1], RI activation by [Ni-2]$^+$ is inconsistent with an OSET mechanism to regenerate an oxidized Ni species, [Ni-2]$^{2+}$. These data suggest that, instead, ISET-based activation prevails for [Ni-2]$^+$-catalyzed RI activation, resulting in a [(Ni-2)(I)]$^+$ intermediate in which the halogen atom is abstracted, i.e.

$$[\text{Ni-2}]^+ + \text{RI} \xrightarrow{k_1} \text{R}^\bullet + [(\text{Ni-2})(\text{I})]^+ \qquad \textbf{Equation C.7}$$

The existence of the proposed [(Ni-2)(I)]$^+$ intermediate is supported by the observation that independently synthesized and characterized [Ni(PY5Me2)(I)]$^+$ (see materials and method, **Figure B.24**) exhibits electrochemical features similar to [Ni-2]$^{2+}$. A single redox feature ($E_{1/2}$ = −1.75 V) is observed, which falls within the potential range in which catalysis is detected for [Ni-2]$^{2+}$. Second, [Ni(PY5Me2)(I)]$^+$ exhibits a significant catalytic current response in the presence of **3**, consistent with the notion that catalysis can be initiated by entering the cycle from this intermediate. While the detailed structure of the substrate–[Ni-2]$^+$ association complex that may

enable an inner-sphere interaction cannot be determined from these data, it is clear that $[Ni\text{-}2]^+$ does not activate RI via OSET.

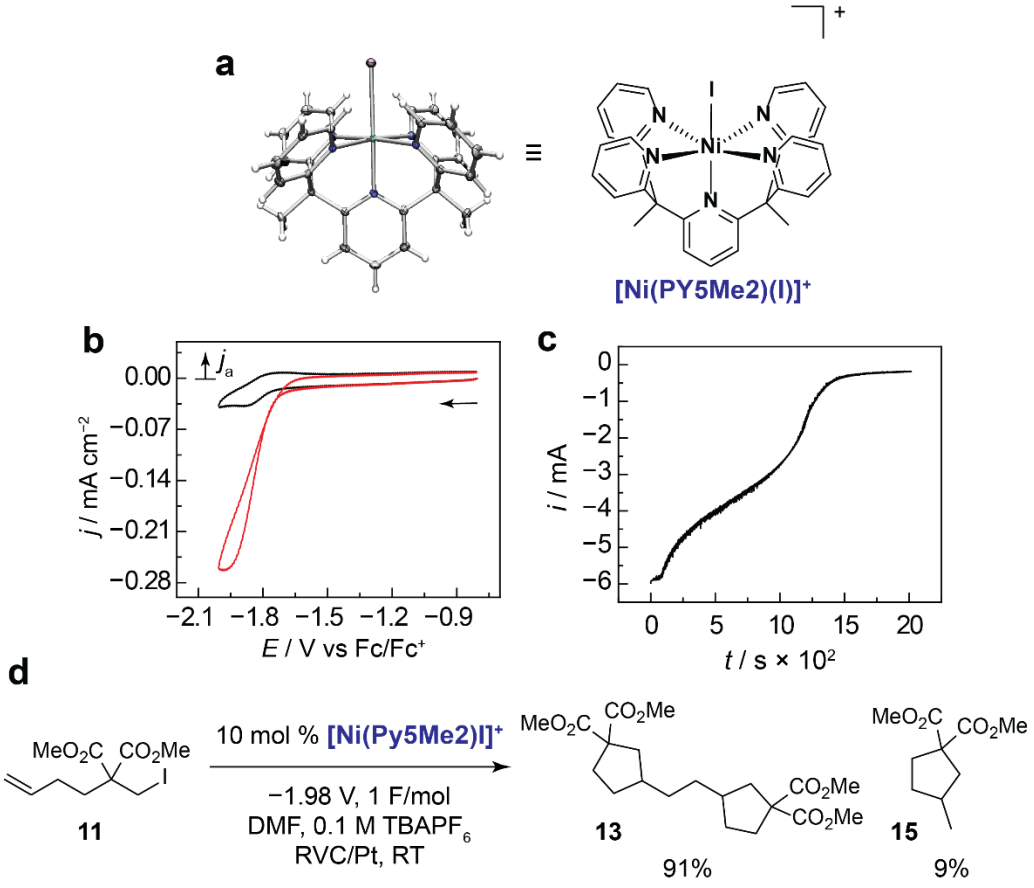


Figure B.24. (a) Crystal structure of $[Ni(PY5Me2)(I)]^+$ determined by single crystal x-ray diffraction. Thermal ellipsoids are plotted at 50% probability level. Green, turquoise, dark blue, and gray ellipsoids signify I, Ni, N, and C atoms, respectively. Noncoordinating solvent and anions omitted for clarity. (b) Cyclic voltammograms of 0.6 mM [Ni(PY5Me2)(I)](I) in the absence (black) and presence (red) of 8.2 mM **11** in 0.1 M $TBAPF_6$ in DMF using a glassy carbon working electrode. (c) Chronoamperomery trace of 0.6 mM [Ni(PY5Me2)(I)](I) and 8.2 mM **11** in 0.1 M $TBAPF_6$ in DMF collected at –1.98 V vs Fc/Fc^+ using a RVC cathode. (d) Controlled-potential electrolysis (CPE) results for **11** conducted in a divided electrochemical cell (0.041 mmol **11**, 0.003 mmol catalyst, in 5 mL catholyte). Charged passed until background current values observed and reported with respect to the amount of **11** added. ^1H NMR yields against 1-methyloxindole standard reported.

To probe the downstream reactivity of hypothesized free radical intermediates generated in step 6, CPE experiments of **11** were performed in the presence of catalytic amounts of $[Ni\text{-}2]^{2+}$. In the presence of 10 mol % of $[Ni\text{-}2]^{2+}$, the CPE of **11** at −1.91 V, corresponding to the potential associated with mediated reduction (**Figure B.7a**), gives rise to 12% and 38% yield of cyclized products **13** and **15**, respectively, following the passage of 1 C mol^{-1} of charge with respect to **11**

(**Figure B.20**, entry f). These data suggest that the observed higher rates of radical formation for $[Ni\text{-}2]^+$- vs [Ni-1]-catalyzed RI activation (**Figure B.7c**) lead to a higher concentration that favors dimerization. To verify that dimerized products are not a result of metal-mediated reductive elimination, we performed CPE of **11** in the presence of 10 mol % of Ar, **8**, and obtained exclusive formation of **15**, suggesting that dimerization is favored due to the high rates of substrate activation. The existence of the proposed $[(Ni\text{-}2)(I)]^+$ intermediate, **Equation B.6**, is further supported by the observation that CPE of **11** in the presence of 10 mol % of independently synthesized $[Ni(PY5Me2)(I)]^+$ exhibits a similar product distribution, favoring formation of **15**, under electrocatalytic conditions after the passage of 1 C mol^{-1} (**Figure B.24**). In addition, $[Ni(PY5Me2)(I)]^+$ exhibits a redox feature ($E_{1/2} = -1.75$ V) more positive than the potential utilized for CPE experiments in **Figure B.20** (−1.91 V), demonstrating that reduced Ni species from the proposed $[Ni(PY5Me2)(I)]^+$ can be accessed within the potential value utilized for CPE. This result demonstrates that the proposed $[(Ni\text{-}2)(I)]^+$ intermediate is catalytically viable and further supports the proposed ISET mechanism. Finally, in contrast to the reactivity observed for [Ni-1], increased selectivity for radical products is not observed when the reaction is conducted in the presence of CyI (**Figure B.20**, entry g). Instead, indiscriminate activation of CyI and **11** is observed as evidenced by the 3 C mol^{-1} charge consumption (**Figure B.21b**) and ensuing complex distribution of products, where only a small amount of **13** could be identified. These data are consistent with the high k_1 observed for both substrates in **Figure B.7c**, and thus simultaneous activation of both **11** and CyI is observed, resulting in unselective radical processes. Together, these data evince the formation of free radical intermediate species and demonstrate that $[Ni\text{-}2]^+$ catalyzes SET reductive activation of RI at higher rates than [Ni-1], owing to an inner-sphere interaction, manifesting in higher selectivity for the formation of unproductive dimerized products and indiscriminate activation of **11** and CyI.

B.3.4 Computational Characterization of Reduced Electroactive Species [Ni-1] and $[Ni\text{-}2]^+$

Computational analysis provides insight into the molecular orbital composition and occupancies of the electroactive Ni species responsible for SET activation of RI. **Tables B.5 – B.7** show the coordinates for optimized structures for $[Ni\text{-}1]^{2+}$, $[Ni\text{-}1]^+$, and [Ni-1] obtained using DFT calculations employing ωB97X-D functionals and DMF as the solvent. The computed redox potentials ($E^0 = -1.27$ V and −2.06 V) and the spin state ($S = 1$) for $[Ni\text{-}1]^{2+}$ are consistent with experimentally determined values (**Figure B.25a**,**b**). DFT calculations predict that the first reduction of $[Ni\text{-}1]^{2+}$ to $[Ni\text{-}1]^+$ is accompanied by the loss of the axial solvent molecule and the population of a low-lying mixed metal–ligand ($\pi^* + d_z^2$, 35% Ni-d) orbital, resulting in a doublet ground state ($S = 1/2$) (**Figure B.26a,b**, left). The spin density plot for $[Ni\text{-}1]^+$ (**Figure B.26c**, left) suggests that the excess spin is delocalized between the ligand and the metal. This molecular description of the reduced tpy ligand over a purely metal-based reduction is in agreement with (1) EPR and computational studies of $[Ni(tpy)(CH_3)]^+$, which describe the complex as $(Ni(II)–CH_3)^+$ bound to a one-electron-reduced π radical monoanion $(tpy^{\bullet})^-$;[76] (2) computational studies on the structurally analogous $[Fe(tpyPY2Me)(MeCN)]^+$,[45] which describe the complex as Fe(II) bound to $(tpyPY2Me^{\bullet})^-$; and (3) spectroscopic and computational studies,[77] describing reduced $[Cr(tpy)_2]^{2+}$ as Cr(III) bound to $(tpy^{\bullet})^-$ in addition to the neutral parent ligand, (tpy^0). DFT calculations predict that the second reduction of $[Ni\text{-}1]^+$ to [Ni-1] is associated with the population of a primarily ligand-based orbital (π*) to form a triplet ground state ($S = 1$) (**Figure B.26b**, middle). This second reduction is also accompanied by a rearrangement of the $\pi^* + d_z^2$ orbital,

occupied by the first excess electron, to form a more metal-based orbital ($\pi^* + d_z^2$, 48% Ni-d) (**Figure B.27**). The spin density plots for [Ni-1] reveal that the excess spin is delocalized between the ligand and the metal (**Figure B.26c**, middle). Thus, the computational data suggest that electroactive [Ni-1] species can be described by a resonance form of the following: (1) a reduced Ni(I) center bound to $(tpyPY2Me^{\bullet})^{-}$ and (2) an unreduced Ni(II) center bound to $(tpyPY2Me^{\bullet\bullet})^{2-}$. Together, these data suggest that the two observed redox events for $[Ni\text{-}1]^{2+}$ occur in a delocalized fashion onto both the Ni center and the tpyPY2Me ligand and that this spin-delocalized [Ni-1] complex is responsible for the observed RI activation reactivity.

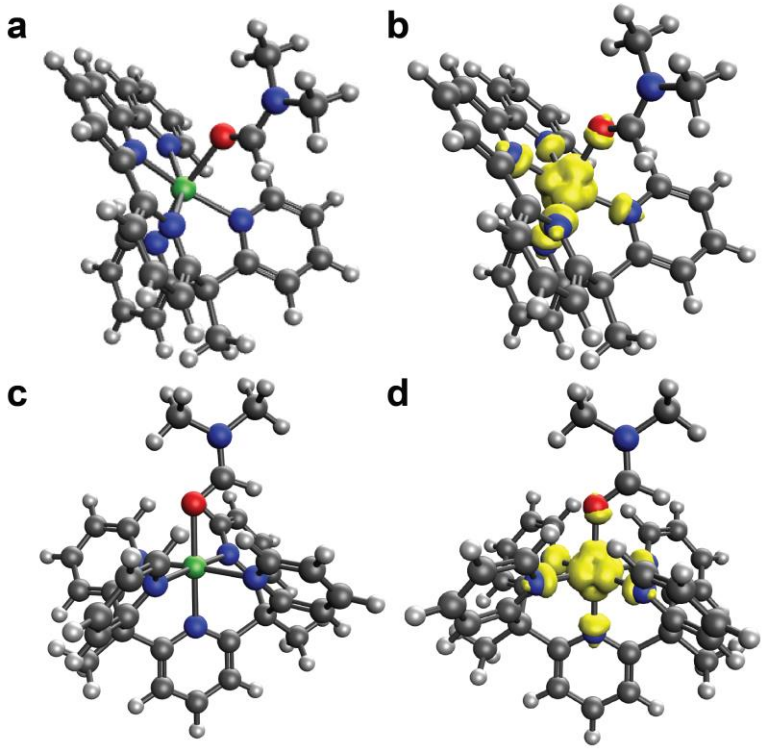


Figure B.25. Calculated optimized structure (a) and spin density plots (b) for $[Ni\text{-}1]^{2+}$. Calculated optimized structure (c) and spin density plots (d) for $[Ni\text{-}2]^{2+}$.

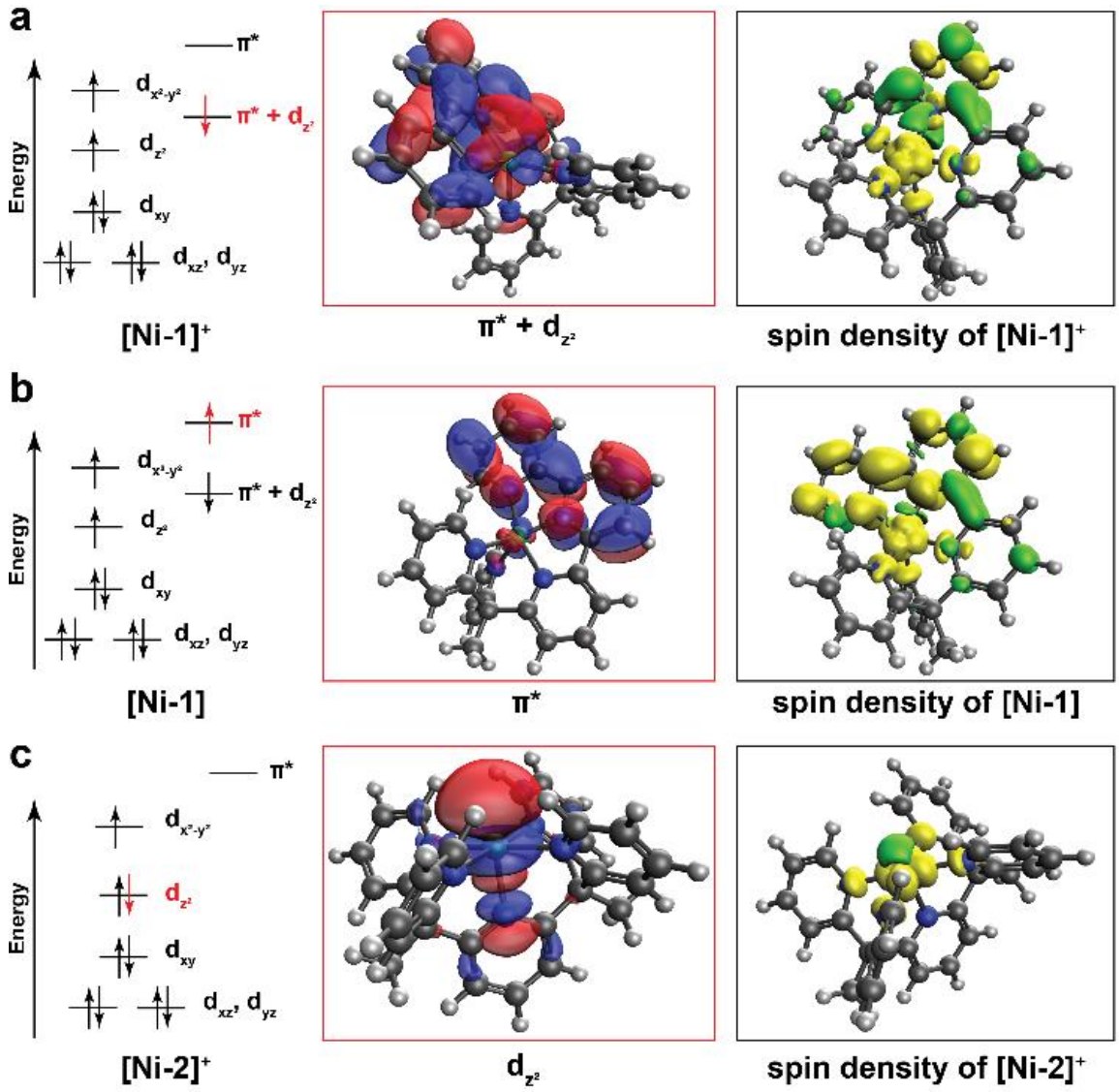


Figure B.26. DFT analysis of electrochemically accessible reduced species, $[Ni\text{-}1]^+$ (a), [Ni-1] (b), and $[Ni\text{-}2]^+$ (c). For each species the following are shown: (1) simplified, qualitative molecular orbital diagram (left) consistent with DFT calculations, where newly added electron (relative to unreduced state) is highlighted in red; (2) relevant calculated MO (middle red box); and (3) the calculated spin density plot (right black box). Molecular orbitals not to scale.

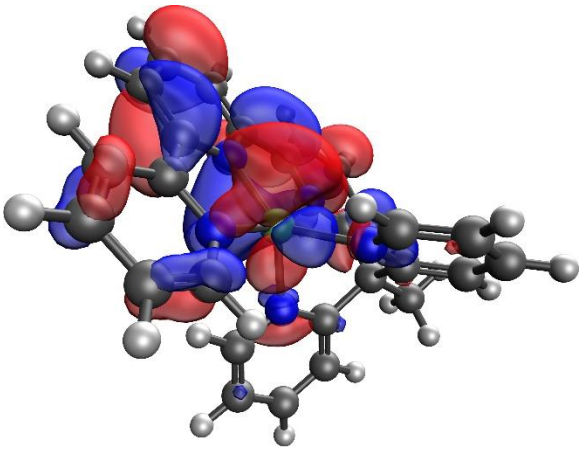


Figure B.27. Calculated molecular orbital for HOMO-1 for [Ni-1], 48% Ni-d.

In contrast, DFT analyses for $[Ni\text{-}2]^{2+}$ are consistent with a purely metal-based reduction event. **Tables B.8 and B.9** show the coordinates obtained for optimized structures of $[Ni\text{-}2]^{2+}$ and $[Ni\text{-}2]^{+}$, respectively. The computed redox potential ($E^0 = -1.77$ V) and the spin state ($S = 1$) for $[Ni\text{-}2]^{2+}$ are in line with experimentally determined values (**Figure B.24c,d**). DFT calculations predict that the reduction of $[Ni\text{-}2]^{2+}$ to $[Ni\text{-}2]^{+}$ is accompanied by the loss of the axial solvent molecule and the population of a purely metal-based (d_z^2) orbital, resulting in a doublet ground state ($S = 1/2$) (**Figure B.26a,b**, right) and the formation of a Ni(I) species. The spin density plot for $[Ni\text{-}1]^{+}$ given in **Figure B.26c** (right) similarly suggests that the excess spin is localized on the metal. Metal-localized reduction and concomitant nuclear reconfiguration offer a possible explanation for the sluggishness of the electron transfer rate (k_s) observed by CV studies, vide supra.[78] Together, these data establish that, unlike $[Ni\text{-}1]^{2+}$, $[Ni\text{-}2]^{2+}$ reduction proceeds solely at the Ni center, strongly implicating that a metal-localized $[Ni\text{-}1]^{+}$ system is responsible for the observed RI activation reactivity.

B.3.5 Mechanistic Model for Controlled Single-Electron Transfer Manipulated via Metal–Ligand Cooperativity

The combined insights from electroanalytical, electrosynthetic, and computational studies point to a model where the extent of the Ni metal-centered reduction alters the mechanism for SET activation of RI substrates. For electrogenerated [Ni-1] (**Figure B.28**, right), computational results describe the electroactive reduced complex as one where the excess spin is delocalized throughout the π system (**Figure B.26b**). Electroanalytical data are consistent with a purely OSET activation manifold of investigated model substrates **3** and CyI by the spin-delocalized [Ni-1], where rate-limiting RI bond cleavage rates scale with those obtained for metal-free redox mediators (**Figure B.7c**). Electroanalytical data are also in line with an electron stoichiometry whereby the ensuing alkyl radical rapidly recombines with another equivalent of [**Ni-1**] to enable an overall bimolecular oxidative addition pathway (**Figures B.7a,b, B.8, B.9, and B.11**). While obtaining definitive structural evidence for the postulated in situ formed [LNi(R)] has remained challenging due to its reactive nature, the present data rule out the alternative mechanism of an OSET pathway that does not involve an alkyl rebound. This alternative mechanism would result in an electrocatalytic wave that monotonically increases as a function of the substrate concentration. Instead, we demonstrate

that the presence of RI substrates leads to a 2-fold current enhancement that does not increase with further addition of RI. In addition, if such a pathway were operative, product distributions following CPE conducted under catalytic conditions would remain unaffected by changes in the counteranion. However, we observe that the presence of OTf^- induces the formation of unproductive dimerization of cyclized products from substrate **11**, whereas its absence disfavors dimerization. Thus, these studies are consistent with the hypothesis that free radical species ($R^\bullet$) are formed that interact with [Ni-1] under electrocatalytic conditions.

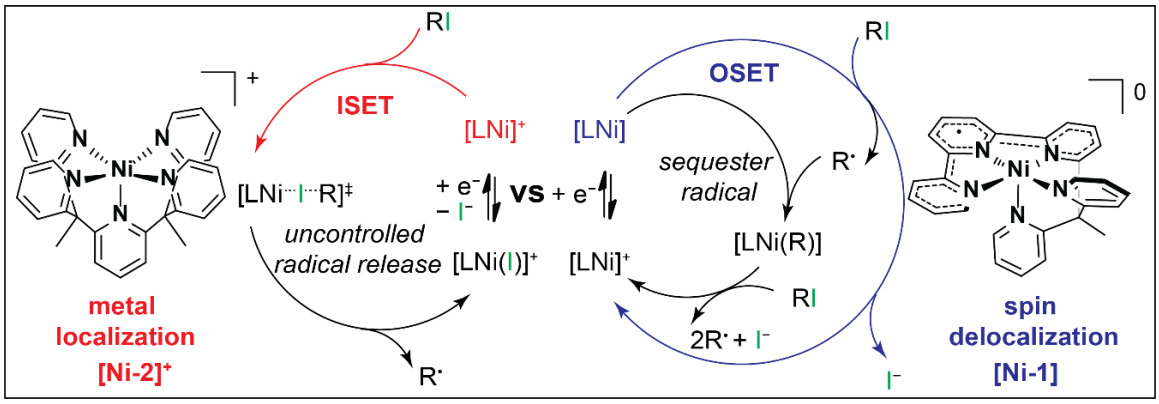


Figure B.28. Mechanistic model for alkyl radical generation by $[Ni(PY5Me2)]^+$ (left) and [Ni(tpyPY2Me)] (right).

These insights enable us to build the mechanistic model shown in **Figure B.28** (right). The OSET mechanism contrasts with related RI activation processes catalyzed by $[Ni(tpy)(CH_3)]^+$; it has been hypothesized[79] and computed[80] to proceed via rate-limiting halogen atom transfer followed by radical formation and rebound. We propose that the OSET pathway found here is favored due to the spin delocalization in both [Ni-1] and $[Ni-1]^+$ imparted by the redox-active, rigid, pentadentate tpyPY2Me scaffold because: (1) spin delocalization imparts reduced interaction with σ* of the RI substrates, and (2) the tpyPY2Me serves to stabilize these redox states as evidenced by their Nernstian CV behavior. We postulate that the OSET mechanism allows for the discrimination in k_1 observed for CyI vs **3**, giving rise to selective activation of **11** in the presence of the halogen atom donor, CyI. We hypothesize that the [LNi(R)] species can either: (1) reduce another equivalent of RI and/or (2) release products by protodemetalation. The former mechanism is consistent with the observation of 1 C mol^{-1} of RI charge consumption, and therefore, we depict this model in **Figure B.28**. Thus, this mechanistic model proposes that RI activation via [Ni-1] enables the controlled electrogeneration and sequestration of $R^\bullet$, facilitating selective free radical reactivity in an electrochemical environment.

Our combined data are consistent with a contrasting mechanistic pathway for RI activation by $[Ni-2]^+$ bearing the redox-inactive PY5Me2 ligand. For electrogenerated $[Ni-2]^+$ (**Figure B.28**, left), computational studies are in line with the expected purely metal-localized reduction (**Figure B.26c**). Electroanalytical data are inconsistent with an OSET manifold for activating **3** and CyI (**Figure B.7c**). Thus, we postulate that an electrocatalytic ISET activation pathway is favored due to an enhanced interaction of the σ* of the RI substrates with the localized reduced metal center, leading to a formal halogen atom abstraction past the rate-limiting RI bond cleavage step to form $[(Ni-2)(I)]^+$. As such, $[Ni-2]^+$ activates both CyI and 3 at much higher rates than [Ni-1] at

comparable applied potentials, precluding the selective activation of one substrate over another (**Figure B.7c** and **Figure B.20**). In addition, this mechanistic postulate explains the discrimination in k_1 observed for **3** vs CyI activation by $[Ni\text{-}2]^+$ (**Figure B.7c**), and the more sterically encumbered substrate **3** exhibits lower rates than CyI within experimental error. Electrosynthetic studies are consistent with the high rate of formation for free radical species following electrocatalytic RI activation; higher selectivity for unproductive dimerization of cyclized products is obtained from **11** (**Figure B.20**), in comparison to that obtained using [Ni-1]. Finally, we provide additional support for the proposed $[(Ni\text{-}2)(I)]^+$ intermediate by demonstrating that catalysis can be initiated by entering the cycle from this species. We independently synthesized the compound and revealed that it exhibited electrocatalytic features in the presence of the substrate and high selectivity toward unproductive dimerization, similar to what we observed for catalysis by $[Ni\text{-}2]^+$. **Figure B.28** (left) summarizes the proposed mechanism of RI activation by $[Ni\text{-}2]^+$.

Comparison of this proposal with the mechanistic model for [Ni-1]-mediated RI activation (**Figure C.28**) demonstrates that the rate of electrocatalytic radical generation, and thus selectivity of downstream radical products, can be controlled via ligand-directed manipulation of the single-electron transfer mechanism. As increased rates of SET, RI activation would result in increased concentration of $R^{\bullet}$. The model shows that ISET activation by $[Ni\text{-}2]^+$ generates a high $R^{\bullet}$ concentration for both **3** and CyI, while [Ni-1] allows for controlled radical generation dictated by the potential difference of $E_{1/2}$ of $[Ni\text{-}1]^+$ and the standard potential for RI reduction. Taken together, these mechanistic studies highlight how tuning the extent of metal-centered reduction via metal–ligand cooperativity directs OSET vs ISET pathways for electrocatalyzed alkyl halide activation, thereby establishing a generalizable molecular design principle for the development of selective free-radical-based catalytic sequences in an electrochemical environment.

B.4 Conclusion

In this work, we report the synthesis, electrochemical characterization, reactivity for single electron transfer activation of alkyl iodides, and electronic structure calculations of Ni complexes that differ in the ligand manifold by the presence and absence of a redox-active terpyridine moiety. We combine electroanalytical studies and bulk electrolysis reactivity data to formulate the mechanistic basis for the divergent selectivity toward redox-mediated radical reactivity we observe for the two complexes. We identify that Ni-ligand cooperativity enables control over the single-electron transfer substrate activation pathway, limiting undesired radical recombination products and promoting a selective model radical process. These studies reveal that tuning the extent of metal-centered reduction can be used to control the electron transfer mechanism and, thereby, radical-based electroorganic reaction selectivity.

At a fundamental level, our studies establish distinct rate and potential requirements for redox mediator design compared to those typically pursued in formulating molecular electrocatalyst design principles. For applications in energy conversion catalysis, for example, molecular electrocatalysts with the highest turnover frequencies at the lowest applied potentials are targeted; as they enable the most efficient fuel formation.[81] In contrast, we find that in order to achieve selective free radical reactivity in an electrochemical environment, molecular electrocatalysts operative at the highest rates at low potentials, in this case $[Ni\text{-}2]^+$, are not the ideal catalysts, as unproductive dimerization outcompetes the desired reactivity and indiscriminate activation of various substrates is observed. Instead, we demonstrate that catalysts with fine-tuned and lower rates of activation at low potentials, [Ni-1], exhibit higher selectivities for cyclized products. These results highlight how fine-tuned rates may be more applicable criteria to target when developing new catalysts for electroorganic applications involving free-radical intermediates. Furthermore, while we note that these findings cannot be extrapolated to electrocatalytic systems beyond Ni-catalyzed alkyl iodide activation at this time, our findings lie in contrast to the contemporary view that the electron distribution plays a minor role for reactions proceeding via outer-sphere electron transfer and a major role for those proceeding via inner-sphere pathways.[82] For reactions where all-organic redox mediators are readily deactivated, as is the case for mediated primary alkyl radical generation, we show that metal–ligand cooperativity enables sustained outers-sphere electron transfer to proceed in cases where inner-sphere pathways yield substrate activation rates that are intractable for selective radical reactions. Together, this work serves to demonstrate how electrocatalyst ligand design coupled with electroanalysis serve as powerful tools toward establishing molecular level insights that underpin electroorganic reaction selectivity in complex electrochemical environments.

B.5 Materials and Methods

B.5.1 General Methods

Reagents were purchased from commercial sources and used without further purification unless otherwise noted. Standard Schleck line techniques were utilized for synthetic manipulations unless otherwise noted. 2,6-bis(1,1-bis(2-pyridyl)ethyl)pyridine (PY5Me2),[47,48,50,51,83,84] 6-(1,1-di(pyridin-2-yl)ethyl)-2,2':6',2"-terpyridine (tpyPY2Me)[45], 9,10-bis(2,6-dimethylphenyl)anthracene (**9**)[85], and dimethyl 2-(but-3-en-1-yl)malonate,[86] dimethyl 2-butylmalonate[87] were synthesized according to previously reported protocols. Dimethylformamide (DMF), acetonitrile (CH_3CN), and tetrahydrofuran (THF) were dried and purified using a solvent purification system (JC Meyer) under argon. Thin-layer chromatography (TLC) analysis of reaction mixtures were performed using Merck silica gel 60 F254 TLC plates and visualized using $KMnO_4$ stain or UV. Column chromatography and preparative TLC was carried out using Merck Silica Gel 60 Å, 230 X 400 mesh or Merck silica gel 60 F254 TLC plates, respectively. ^1H, ^{13}C, and ^{19}F NMR experiments were conducted using Bruker AV-600 or NEO-500 instruments. Peaks were referenced using residual solvent peaks or added internal standards. Elemental (carbon, hydrogen, and nitrogen) analyses were provided by the Microanalytical Laboratory of the University of California, Berkeley. High resolution mass spectrometry (electrospray ionization) was conducted using a Perkin Elmer UHPLC-TOF AxION 2 instrument or a LTQ FT-ICR mass spectrometer equipped with an electrospray ionization source (Finnigan LTQ FT, Thermo Fisher Scientific, Waltham, MA) operated in positive ion mode. X-ray crystallography was conducted at the Chexray facility at the University of California, Berkeley.

B.5.2 Electrochemical Methods for Cyclic Voltammetry

Electrochemical experiments were conducted using a CHI 760E potentiostat, a Ag/Ag^+ reference electrode (BASi, 10 mM $AgBF_4$ in 0.1 M $TBAPF_6$ in MeCN, Fc/Fc^+ at 0.098 V vs Ag/Ag^+), a high surface area Pt-mesh counter electrode (Alfa Aesar, 99.997 %), and a glassy carbon working electrode (BASi, 3 mm diameter). Glassy carbon electrodes were polished (alumina slurry with Millipore Type 1, 18.2 MΩ, water) and dried prior to experiments. The Ag/Ag^+ electrode was stored in 0.1 M $TBAPF_6$ in DMF between measurements and was periodically checked relative to Fc/Fc^+ to ensure against potential drift. All experiments were performed at 24±1℃. Electrode potentials were converted to the Fc/Fc^+ standard using the conversion, $E_{Fc/Fc+} = E_{Ag/Ag+} - 0.098$ V. For each experiment, an initial starting point for the uncompensated Ohmic loss was measured using the R_u test function in the CHI Electrochemical Workstation Version 18.05 (~150 Ω). This initial value was further corrected by collecting sequential cyclic voltammograms with increasing R_u values until oscillations corresponding to total compensation were observed.[53] This corrected R_u value (R_{corr}) was approximately 150 Ω higher than the initial value measured using the R_u test function, i.e. 300 Ω. This R_{corr} was inputted manually into the iR compensation menu in the CHI Electrochemical Workstation Version 18.05. For each experiment conducted sequentially using similar experimental conditions, at least 5 min was elapsed at the open circuit potential in order to obtain reproducible cyclic voltammetry scans. Current density values are reported relative to the geometric surface area of the glassy carbon working electrode. A three-compartment electrochemical cell was utilized and held 5 mL of electrolyte in the working compartment and counter compartments (James Glass Inc.) The

compartments were separated by an ultra-fine glass frit (P5, Adams and Chittenden). Prior to data collection, the working compartment was purged with N_2 for > 10 min to ensure the complete removal of residual O_2. During data collection, the headspace of the working compartment was subject to a constant stream of N_2.

B.5.3 Bulk Electrolysis Procedures

Bulk electrolysis experiments were conducted using a CHI 760E potentiostat, a leakless Ag/AgCl reference electrode (Innovative Instruments, Fc/Fc^+ at 0.529 V vs Ag/Ag^+), a high surface area Pt-mesh counter electrode (Alfa Aesar, 99.997 %), and a reticular vitreous carbon (RVC) working electrode (100 ppi, ~70 cm^2 surface area, Duocell). For every experiment, a freshly cut piece of RVC (approx. 0.635×0.635×1.11 cm^3 slice) was attached to a graphite rod (June Gold, 2.0 mm diameter) using carbon glue (Anders Products) and annealed for 15 min in an oven prior to use (105 °C). The Ag/AgCl electrode was stored in saturated NaCl between measurements and was periodically checked relative to a pristine Ag/AgCl electrode to ensure against potential drift. Electrode potentials were converted to the Fc/Fc^+ standard using the conversion, $E_{Fc/Fc+} = E_{Ag/AgCl} – 0.529$ V. All experiments were performed at 24 ± 1℃. A three-compartment electrochemical cell was utilized and held 5 mL of electrolyte in the working compartment and counter compartments (James Glass Inc.) The compartments were separated by an ultra-fine glass frit (P5, Adams and Chittenden). Prior to data collection, the working compartment was purged with N_2 for > 10 min to ensure the complete removal of residual O_2. During data collection, the headspace of the working compartment was subject to a constant stream of N_2. Prior to each experiment, a cyclic voltammogram of the catalyst was taken in the presence and absence of substrate using a glassy carbon electrode (BASi, 3 mm diameter) to verify the potential of the catalyzed reduction of substrate. The working electrode was switched to the RVC, and a chronoamperometry trace was initiated 100 mV more negative than the peak potential of the catalyzed reduction determined by cyclic voltammetry. Bulk electrolysis was performed in the dark by wrapping the working compartment in aluminum foil. The working compartment was continuously stirred (~350 rpm). After the current value reached the background value (~1 mA), the chronoamperometry experiment was terminated. The catholyte was quenched with brine and the compartment, RVC, and reference electrodes were rinsed with diethyl ether and brine. The organic products were extracted with diethyl ether (3x). The combined organic extracts were washed with brine (3x) and water (1x), dried over Na_2SO_4, filtered through 0.22 μm frit, and concentrated *in vacuo*. Products listed below were isolated on silica gel (10% EtOAc in hexanes) by preparative thin layer chromatography. When determining the yield by ^1H NMR, a solution of 1-methyloxindole in DMF was added to the catholyte before the workup procedure and used as an NMR standard. Sufficient and reproducible extraction (>85%) of 1-methyloxindole was confirmed by addition of a second internal standard, 1,3,5-tris(trifluoromethyl)benzene, after workup.

B.5.4 Electrochemical Simulation Methods

Electrochemical simulations were conducted using the DigiElch Professional Simulation Version 8FD software by Elchsoft. The cyclic voltammetry simulation was conducted assuming planar electrode geometry, semi-infinite 1D diffusion, and total compensation of internal resistance. The pre-equilibrium was set to Smart. Model parameters were set to 0% noise level, 2

Gauss-Newton iterations, 0.5 exponential factor (x-grid), 1E–5 % truncation error, and 6 Xmax/SQRT.

B.5.6 Determination of Electron Transfer Rate Constant for $[Ni\text{-}2]^{2+}$

Estimation of the electron transfer rate constant, k_s, requires an estimation of the diffusion coefficient, *D*. This value can be determined by employing the following relationship within the reversible limit operating under purely diffusion control, i.e. the peak-to-peak separation for the anodic and cathodic features equal 60 mV separation at 25°C)[53]:

$$i_p = 0.446FSC^0\sqrt{D}\sqrt{\frac{Fv}{RT}} \qquad \textbf{Equation B.8}$$

where F is Faraday's constant, S is the electrode surface area, C^0 is the concentration of $[Ni\text{-}2]^{2+}$, and RT take on their usual meaning. Using this relationship, a value of 5×10^{-6} cm^2 s^{-1} was obtained. As the scan rate is increased, the peak-to-peak separation increases as the system transitions from a purely reversible electron transfer process to irreversible one, whereby the reaction is influenced by the kinetics of electron transfer.[53,88] We observe such a transition experimentally in **Figure B.6a** and **B.6b** (black squares). We performed simulations to plot the expected peak potential shifts as a function of the scan rate, and obtained a good fit with the experimental data when using a k_s value equaling 0.011 cm^2 s^{-1}, **Figure B.6b**.

B.5.7 Determination of Electron Transfer Rates for EC Mechanism Involving Catalyst Deactivation

Simulation methods were used to construct working curves used to estimate the rate of homogeneous electron transfer for a reaction scheme involving the deactivation of catalyst. The inputs to the simulation were determined assuming the following mechanistic scheme. For a reaction scheme involving rate-limiting irreversible reduction of an alkyl halide mediated by a catalyst at a potential less negative than its direct reduction, the possible elementary steps have been described by the following:[53,54,89]

$$P + e^- \rightleftharpoons Q \qquad \textbf{Equation B.9}$$

$$Q + A \xrightarrow{k_1} B + P \qquad \textbf{Equation B.10}$$

$$Q + B \xrightarrow{k_2} C + P \qquad \textbf{Equation B.11}$$

$$Q + B \xrightarrow{k_3} QB \qquad \textbf{Equation B.12}$$

where P is the catalyst, Q is the reduced catalyst, A is the alkyl halide, B is the neutral radical, C is the carbanion, and QB is the product of radical addition to the reduced catalyst. The cyclic voltammogram responses of reaction sequences involving **Equations B.9** to **B.12** are governed by three dimensionless parameters:[53,54,89] (1) the ratio of the concentration of starting material to catalyst (C_A/C_P); (2) the competition between second electron transfer step (**Equation B.11**) and

the addition reaction (**Equation B.12**), i.e. $k_2/(k_2+k_3)$; and (3) the kinetic parameter (**Equation B.13**), see below, capturing the rate of **Equation B.10** relative to that of diffusion. In our studies, we find that $k_2/(k_2+k_3)$ equals zero because catalytic peak currents do not exceed 2 for select catalyst and substrate pairs, detailed below, (**Figures B.8a,b**; **B.11–C.13a.b**; **B.15a,b**; **B.18a,b**; **B.19a,b**), consistent with previous studies for alkyl iodide reduction by a series of aromatic hydrocarbon and heterocycle anion radicals.[89] Therefore, **Equation B.11** is negligible in our analysis relevant to the present study. In the simulation, **Equation B.9** was designated as a reversible charge-transfer reaction with Butler Volmer kinetics assuming transfer coefficient (α = 0.5) and k_s (1 cm s^{-1}) values in line with the Nernstian single electron transfer observed for $[Ni\text{-}1]^{2+}$ and aromatic redox mediators employed. **Equation B.10** was designated as the rate-limiting chemical reaction involving homogeneous electron transfer with varying k_1 values, see below. **Equation B.12** was designated as an irreversible and fast addition reaction, $k_3 = 1\times10^{10}$ $M^{-1}s^{-1}$, consistent with the absence of competition between **Equation B.11** and **B.12** observed in our systems and previous studies of related alkyl iodide substrates[89]. A family of cyclic voltammograms was simulated for each value of experimentally relevant C_A/C_P (1, 2, 4, 10, and 20), in which k_1 was systematically altered from 38.92 to 389,256 M^{-1} s^{-1} to adjust the dimensionless kinetic parameter,

$$\log \lambda = \log\left(\frac{k_1 C_P^0 RT}{vF}\right) \qquad \textbf{Equation B.13}$$

in 0.25 increments from –2 to 2, where C_P^0 is the concentration of P (1 mM), ν is the scan rate (100 mV s^{-1}), T is the temperature (298.2 K), F is Faraday's constant, and R is the universal gas constant. To construct the working curves, these simulated voltammograms were analyzed, and the difference between the simulated peak potential for reduction (E_p) and reversible potential for the catalyst in the absence of substrate ($E_{1/2}$) were plotted against log λ (Figure **B.8c**, **B.11–B.13c**, **B.15c**, **B.18c**, **B.19c**). These working curves were then compared to experimentally determined E_p-$E_{1/2}$ values as a function of varying experimental conditions (C_A/C_P, ν) to estimate k_1 values. This procedure was utilized to estimate rates of single electron transfer activation, k_1, of **3** by [**Ni-1**] (**Figure B.8**), and 1,4 CN-benzene, **4** (**Figure B.13**), and activation of CyI by fluoranthrene, **7** (**Figure B.19**), perylene, **6**, (**Figure B.18**), 1,2 CN-benzene, **5**, (**Figure B.15**), **4** (**Figure B.12**), and [Ni-1] (**Figure B.11**); these estimated k_1 values are listed in **Table B.1** and **Figure B.7c**.

B.5.8 Determination of Electron Transfer Rates for Total Catalysis (TC)

Total catalysis describes a kinetic regime of a homogeneous catalytic electrochemical process in which the system is governed by substrate diffusion due to extremely rapid substrate consumption kinetics.[53,90] For the reaction sequences involving elementary steps **Equation B.9** and **B.10** above, the total catalysis cyclic voltammetric response is characterized by the observation of two waves. The first wave is associated with substrate, A, diffusion-controlled catalytic reduction of A. The second wave is associated with residual catalyst, P, reduction. In these cases, k_1 can be estimated by calculating the shift in the peak potential for the first wave (E_p) relative to the Nernstian reduction potential for P (E^0) described by,[53,90]

$$E_p = E^0 - 0.409\frac{RT}{F} + \frac{RT}{2F}\ln\left(\frac{RT}{Fv}\frac{C_P^0 k_1}{v}\frac{C_P^0}{C_A^0}\frac{D_P}{D_A}\right) \qquad \textbf{Equation B.14}$$

where C_P^0 is the initial concentration of P (0.9 to 1.0 mM), ν is the scan rate (100 to 200 mV s^{-1}), C_A^0 is the initial concentration of A (0.9 to 2.5 mM), T is the temperature (298 K), F is Faraday's constant, D_p is the diffusion coefficient of P, D_A is the diffusion coefficient of A, and R is the universal gas constant. The ratio of D_p to D_A is assumed to be unity. These total catalysis conditions were observed for CN-napthalene (**8**), anthracene (**10**), and 9,10-bis(2,6-dimethylphenyl)anthracene (**9**)-catalyzed reduction of substrate **3** (**Figures B.14**, **B.16**, and **B.17**), and therefore, **Equation B.14** is used to estimate values of k_1 listed in **Table B.1** and **Figure B.7c**.

B.5.9 Determination of Electron Transfer Rates for Chemical Catalysis (CC)

We note that in our experiments, catalysis by $[Ni\text{-}2]^{2+}$ shows non-ideal cyclic voltammogram responses, where with increased scan rate or substrate concentration, classic S-shaped behavior was not achieved.[53,91–93] In addition, the CV responses did not fit into the previous two cases (EC or total catalysis). Foot-of-the-wave analysis (FOWA), where the charge passed is small and thus side-phenomena are reduced, is a well-established method to estimate the rate constant in these cases.[91–93] However, application of the ideal case assuming fast catalyst kinetics (Nernstian) is not applicable for $[Ni\text{-}2]^{2+}$, i.e. k_s equals 1.1×10^{-2} cm s^{-1}, see above, and attempts to conduct foot-of-the-wave analysis incorporating k_s values[94] did not yield linear FOWA behavior. Therefore, the working curves assuming a redox catalysis mechanism, **Equations B.9** and **B.10**, were constructed where k_s equals 1.1×10^{-2} cm s^{-1} to establish a *lower limit* on k_1 for $[Ni\text{-}2]^{2+}$-catalyzed RI activation. A family of cyclic voltammograms was simulated for each value of experimentally relevant C_A/C_P (1, 2, 4, 10, and 20), in which k_1 was systematically altered from 38.92 to 389,256 M^{-1} s^{-1} to adjust the dimensionless kinetic parameter, **Equation B.13**. To construct the working curves, these simulated voltammograms were analyzed, and the difference between the simulated peak current (i_p) and peak current of the catalyst in the absence of substrate (i_{p0}) were plotted against log λ (**Figures B.22c** and **B.23c**). These working curves were then compared to experimentally determined i_p/i_{p0} values as a function of varying experimental conditions (C_A/C_P, ν) to estimate k_1 values (**Figures B.22** and **B.23**). We note that even at the lower limit of k_1 estimation of $[\mathbf{Ni\text{-}2}]^{2+}$, much higher rates for RI activation are observed than that obtained for $[Ni\text{-}1]^{2+}$, **Figure B.7c**.

B.5.10 X-Ray Crystallography

Crystals were coated with Paratone-N oil, attached to a Kapton loop, and mounted onto a Rigaku XtaLAB P200 equipped with a MicroMax 007HF rotating anode and Pilatus3 R 200K-A hybrid pixel array detector. Data were collected using Mo Kα radiation (λ = 0.71073 Å). Crystals were kept at 100(2) K throughout the data collection. Data collection was performed with CrysAlisPro.[95] Data processing was done with CrysAlisPro and included a multi-scan absorption correction applied using the SCALE3 ABSPACK scaling algorithm within CrysAlisPro. Data obtained are summarized in **Tables B.2** and **B.3**.

B.5.11 Evans Method Analysis

The Evans method was employed to estimate the magnetic moments of the complexes. 19.1 mg of $[Ni(tpyPY2Me)](PF_6)_2$ or 13.4 mg of $[Ni(PY5Me_2)](PF_6)_2$ was dissolved in 700 μL of a standard solution (30μL of hexafluorobenzene in 3 mL of CD_3CN) and transferred to an NMR

tube. A thin capillary containing the standard solution was inserted into the NMR tube. The relative shift of the ^{19}F NMR peak for hexafluorobenzene in CD_3CN[96] was measured, **Figures B.2** and **B.3**, at 293 K on an AV600 NMR instrument. Diamagnetic corrections were approximated using the equation:[97]

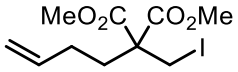
$$\chi_D = -\frac{MW}{2} 10^{-6}\ emu\ mol^{-1} \qquad \textbf{Equation B.15}$$

where MW is the unitless molecular weight. For $[Ni(tpyPY2Me)(MeCN)](PF_6)_2$, a diamagnetic correction value of -403×10^{-6} emu mol^{-1} was calculated. For $[Ni(PY5Me_2)(MeCN)](PF_6)_2$, a diamagnetic correction value of -417×10^{-6} emu mol^{-1} was calculated. With these values in hand, the effective magnetic moments for $[Ni(tpyPY2Me)(MeCN)](PF_6)_2$ and $[Ni(PY5Me_2)(MeCN)](PF_6)_2$, 3.2 and 3.0 μ_B, respectively, were estimated at 293 K.

B.5.12 Quantum Chemical Computations

The Q-Chem package (version 5.2.2)[98] was employed for all density functional calculations. The range-separated hybrid functional ωB97X-D[99] was employed similarly to a previous study using an identical ligand framework with an iron complex.[45] The numerical integration of the exchange correlation functional was performed on a (75, 302) grid (75 radial shells with 302 Lebedev points). Geometries were optimized in the gas phase with no constraints and verified as minimum structures by vibrational frequency calculations. A mixed basis was used (def2-SVP basis for all main group elements, def2-TZVP basis set for Ni)[99] for geometry optimization and frequency calculations. The electronic structure was subsequently refined with def2-TZVPP basis[99] single point calculations. The solvation energies were calculated with the C-PCM model (DMF, ε = 37.2) as implemented in QChem.[100] Reduction potentials are reported against the calculated Fc/Fc^+ couple used as an internal standard.[101,102] The Gibbs free energies (G) used to compute these reduction potentials are based on standard thermodynamic cycles, see references.[102–104] Those free S-1 energies entail contributions from the zero-point energy correction and contribution from the vibrational frequencies at T = 298 K. Solvation energies were approximated by performing single point calculations in the gas phase and with C-PCM solvent model in the def2-TZVPP basis.

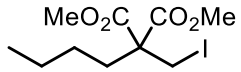
B.5.13 Synthesis of Dimethyl 2-(but-3-en-1-yl)-2-(iodomethyl)malonate (11)



Dimethyl 2-(but-3-en-1-yl)malonate[86] (1 equiv, 5.35 mmol, 1 g) was added dropwise to a stirred suspension of NaH (60% dispersion in mineral oil, 1.12 equiv, 6 mmol, 316 mg) in DMF at 0°C under N_2. The mixture was stirred at 0°C for 1 hr. Diiodomethane (1.2 equiv, 6.42 mmol, 0.53 mL) was added dropwise at 0°C. The resulting mixture was warmed to room temperature and stirred for an additional 5 hrs. The mixture was quenched with saturated $NaHCO_3$ and extracted with EtOAc. The organic extract dried over Na_2SO_4 and then concentrated *in vacuo*. The crude product was purified by silica gel chromatography twice: (1) using gradient of 0.5:10 to 1:10 hexanes:EtOAc; and (2) using 6:4:0.1 hexanes: DCM: ethyl ether. The purified product was stored in the absence of light at –10°C. Yield: 900 mg, 52%. ^1H NMR (600 MHz, $CDCl_3$) δ 5.78 (ddt, J = 16.8, 10.2, 6.4 Hz, 1H), 5.12 – 4.95 (m, 2H), 3.76 (s, 6H), 3.63 (s, 2H), 2.18 – 2.12 (m, 2H), 1.96 – 1.89 (m, 2H). ^{13}C NMR (151 MHz,

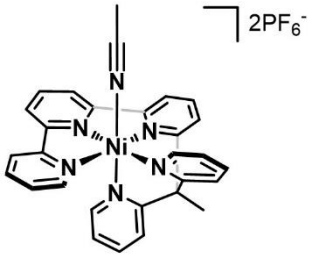
$CDCl_3$) δ 169.25, 136.87, 115.76, 58.13, 53.17, 32.98, 28.08, 6.70. ESI-MS Calcd. for $C_{10}H_{15}O_4INa$ $[M + Na]^+$, 348.99 found 348.99 m/z.

B.5.14 Synthesis of Dimethyl 2-butyl-2-(iodomethyl)malonate (3)



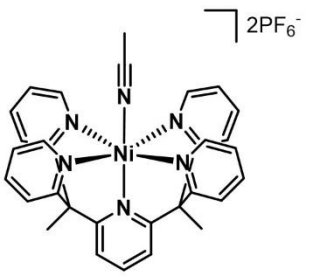
Dimethyl 2-butylmalonate[87] (1.48 equiv, 5.31 mmol, 1 g) was added dropwise to a stirred suspension of NaH (60% dispersion in mineral oil, 1.04 equiv, 3.73 mmol, 150 mg) in THF at 0°C under N_2. The mixture was warmed to room temperature and stirred for 30 min. Diiodomethane (1 equiv, 3.6 mmol, 0.3 mL) was added at room temperature. The resulting mixture was heated to reflux (60°C) and stirred at this elevated temperature overnight. After approximately 12 hours, the mixture was quenched with water and extracted with diethyl ether. The organic extract was washed sequentially with water and brine, dried over Na_2SO_4, and concentrated *in vacuo*. The crude product was purified by silica gel chromatography (7: 3: 0.1 hexanes: DCM: diethyl ether). The purified product was stored in the absence of light at –10°C. Yield: 804 mg, 68%. ^{1}H NMR (600 MHz, CD_2Cl_2) δ 3.72 (s, 6H), 3.61 (s, 2H), 2.03 – 1.97 (m, 2H), 1.35 (h, J = 7.4 Hz, 2H), 1.13 – 1.05 (m, 2H), 0.91 (t, J = 7.4 Hz, 3H). ^{13}C NMR (151 MHz, CD_2Cl_2) δ 169.60, 58.57, 53.21, 33.67, 26.07, 23.07, 14.02, 7.32. ESI-MS Calcd. for $C_{10}H_{17}O_4INa$ $[M + Na]^+$, 351.01 found 351.00 m/z.

B.5.15 Synthesis of [Ni(tpyPY2Me)(MeCN)](PF$_6$)$_2$ ([Ni-1]$^{2+}$)



A suspension of $NiCl_2$ (1 equiv, 0.2406 mmol, 31 mg) in MeCN (8 mL) was added to tpyPY2Me[45] (1 equiv, 0.2406 mmol, 100 mg) dissolved in MeCN (8 mL). The mixture was heated to 50 °C and stirred at this elevated temperature overnight. After approximately 12 hrs, the mixture was cooled to room temperature, and $NaPF_6$ was added (4 equivs, 0.9624 mmol, 162 mg). The resulting mixture was heated to 50 °C and stirred at this elevated temperature overnight. After approximately 12 hrs, the mixture was cooled to room temperature and filtered through glass fiber. The brown filtrate was concentrated *in vacuo*. Pure brown crystals were obtained by slow vapor diffusion of diethyl ether into the concentrated acetonitrile solution. X-ray diffraction quality crystals were obtained by slow vapor diffusion of diisopropyl ether into the concentrated acetonitrile solution. Yield: 147 mg, 80%. ^{1}H NMR (600 MHz, CD_3CN): δ 85.58, 78.29, 71.21, 67.05, 59.57, 54.38, 43.55, 36.62, 18.81, 14.86, 13.88, 12.86, 12.27. Anal. Calcd for $C_{27}H_{21}F_{12}N_5NiP_2$: C, 42.44; H, 2.77; N, 9.17. Found: C, 42.36; H, 2.71; N, 9.09. ESI-MS Calcd. for $C_{27}H_{21}N_5F_6PNi$ $[M + PF_6]^+$, 618.08 found 618.08 m/z.

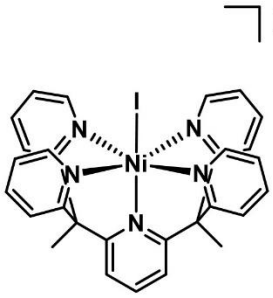
B.5.16 Synthesis of [Ni(PY5Me2)(MeCN)](PF$_6$)$_2$ ([Ni-2]$^{2+}$)



A suspension of $NiBr_2$ (1 equiv, 0.0696 mmol, 15 mg) in MeCN (8 mL) was added to PY5Me2[83] (1 equiv, 0.0696 mmol, 31 mg) dissolved in MeCN (8 mL). The mixture was heated to 50 °C and stirred at this elevated temperature overnight. After approximately 12 hrs, the mixture was cooled to room temperature, and $AgPF_6$ was added (2.2 equivs, 0.153 mmol, 39 mg). The resulting mixture was stirred at room temperature. After approximately 2 hrs, the mixture was filtered through

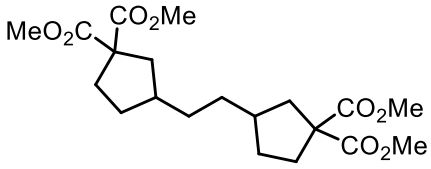
glass fiber. The pink filtrate was concentrated in vacuo. Pure pink crystals were obtained by slow vapor diffusion of diethyl ether into the concentrated acetonitrile solution. X-ray diffraction quality crystals were obtained by slow vapor diffusion of diisopropyl ether into the concentrated acetonitrile solution. Yield: 41 mg, 74%. ^{1}H NMR (600 MHz, CD_3CN): δ 51.29, 49.35, 43.06, 39.14, 19.76, 18.61, 10.01. Anal. Calcd for $C_{29}H_{25}F_{12}N_5NiP_2$: C, 43.97; H, 3.18; N, 8.84. Found: C, 42.31; H, 3.37; N, 8.64. ESI-MS Calcd. for $C_{29}H_{25}N_5F_6PNi$ $[M + PF_6]^+$, 646.11 found 646.11 m/z.

B.5.17 Synthesis of [Ni(PY5Me2)(I)](I)



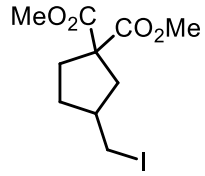
A suspension of NiI_2 (1 equiv, 0.0674 mmol, 21 mg) in MeCN (8 mL) was added to PY5Me2 (1 equiv, 0.0674 mmol, 30 mg) dissolved in MeCN (8 mL). The mixture was heated to 50 °C and stirred at this elevated temperature overnight. Then, the mixture was cooled to room temperature and a beige precipitate formed. The orange solution was decanted, and the beige precipitate was washed three times with diethyl ether. X-ray diffraction quality crystals were obtained by slow vapor diffusion of diethyl ether into a concentrated methanol solution. Yield: 28 mg, 55%. ^{1}H NMR (600 MHz, CD_3OD): δ 51.74, 48.43, 40.25, 18.87, 10.08, 4.84. Anal. Calcd for $C_{29}H_{25}I_2N_5Ni$: C, 46.07; H, 3.33; N, 9.26. Found: C, 45.88; H, 3.53; N, 9.02. ESI-MS Calcd. for $C_{29}H_{25}IN_5Ni$ $[M]^+$, 628.05 found 628.05 m/z.

B.5.18 Synthesis of Tetramethyl 3,3'-(ethane-1,2-diyl)bis(cyclopentane-1,1-dicarboxylate)



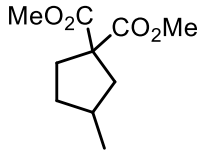
^{1}H NMR (600 MHz, CD_2Cl_2) δ 3.68 (d, J = 1.5 Hz, 12H), 2.45 – 2.38 (m, 2H), 2.26 (ddd, J = 13.3, 8.4, 3.5 Hz, 2H), 2.10 (ddd, J = 13.6, 9.4, 7.3 Hz, 2H), 1.86 (dtq, J = 14.6, 7.3, 3.9 Hz, 4H), 1.66 (dd, J = 13.3, 9.8 Hz, 2H), 1.36 – 1.29 (m, 3H), 1.25 – 1.19 (m, 2H). ^{13}C NMR (151 MHz, CD_2Cl_2) δ 173.43, 60.31, 52.85, 52.83, 41.13, 40.34, 34.52, 34.20, 32.44, 30.10. ESI-MS Calcd. for $C_{20}H_{30}O_8Na$ $[M + Na]^+$, 421.18 found 421.18 m/z.

B.5.19 Synthesis of Dimethyl 3-(iodomethyl)cyclopentane-1,1-dicarboxylate



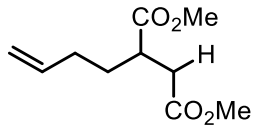
^{1}H NMR (600 MHz, CD_2Cl_2) δ 3.70 (d, J = 0.8 Hz, 6H), 3.26 – 3.18 (m, 2H), 2.50 (dd, J = 13.6, 7.6 Hz, 1H), 2.38 – 2.26 (m, 2H), 2.20 (ddd, J = 13.6, 8.9, 7.7 Hz, 1H), 2.00 – 1.92 (m, 1H), 1.84 (dd, J = 13.6, 9.5 Hz, 1H), 1.40 (dq, J = 12.7, 8.8 Hz, 1H). ^{13}C NMR (151 MHz, CD_2Cl_2) δ 172.90, 172.88, 60.60, 53.02, 42.45, 41.30, 34.17, 32.97, 11.83. ESI-MS Calcd. for $C_{10}H_{15}O_4INa$ $[M + H]^+$, 348.99 found 348.99 m/z.

B.5.20 Synthesis of Dimethyl 3-methylcyclopentane-1,1-dicarboxylate



^{1}H NMR (600 MHz, CD_2Cl_2) δ 3.68 (s, 6H), 2.42 (dd, J = 13.3, 7.2 Hz, 1H), 2.29 (ddd, J = 13.2, 8.5, 3.7 Hz, 1H), 2.12 (ddd, J = 13.5, 9.3, 7.6 Hz, 1H), 2.06 – 1.99 (m, 1H), 1.87 – 1.80 (m, 1H), 1.65 (dd, J = 13.3, 10.1 Hz, 1H), 1.26 – 1.18 (m, 1H), 1.00 (d, J = 6.6 Hz, 3H). ^{13}C NMR (151 MHz, CD_2Cl_2) δ 173.56, 60.65, 52.84, 52.82, 42.93, 34.86, 34.48, 34.46, 30.11, 19.72. In line with previously reported spectra.[105]

B.5.21 Synthesis of dimethyl 2-(but-3-en-1-yl)succinate



^{1}H NMR (600 MHz, $CDCl_3$) δ 5.77 (ddt, J = 16.9, 10.2, 6.6 Hz, 1H), 5.07 – 4.93 (m, 2H), 3.69 (d, J = 17.1 Hz, 6H), 2.91 – 2.84 (m, 1H), 2.73 (dd, J = 16.6, 9.2 Hz, 1H), 2.46 (dd, J = 16.6, 5.2 Hz, 1H), 2.11 – 2.04 (m, 2H), 1.81 – 1.72 (m, 1H), 1.65 – 1.56 (m, 1H). ^{13}C NMR (151 MHz, $CDCl_3$) δ 175.43, 172.47, 137.42, 115.67, 52.01, 51.94, 40.74, 35.92, 31.20, 29.86. In line with previously reported spectra.[106]

B.5.22 X-Ray Crystallography Data

Table B.2. Crystallographic data for $[Ni\text{-}1]^{2+}$.

	$[Ni(tpyPY2Me)(CH_3CN)][PF_6]_2$
Chemical formula	$C_{29}H_{24}N_6Ni\cdot 2(PF_6)\cdot 2(C_2H_3N)$
FW	887.28
Crystal system, space group	Triclinic, *P*-1
Temperature (K)	100(2)
a (Å)	10.3734(8)
b (Å)	12.9537(5)
c (Å)	15.3495(10)
α (°)	65.205(5)
β (°)	78.135(6)
γ (°)	85.488(5)
V (Å^3)	1832.4(2)
Z	2
μ (mm^{-1})	0.72
F(000)	920.0
Crystal size (mm)	0.10 × 0.18 × 0.36
θ range (°) for cell measurement	3.2–29.1
Radiation type	Mo *K*α
No. of reflections for cell measurement	12919
Index ranges	$-14 \le h \le 14$
	$-17 \le k \le 15$
	$-21 \le l \le 20$
Reflections collected / unique	12919 / 8884
R_{int}	0.069
Data / restraints / parameters	8884 / 0 / 614
Goodness-of-fit on F^2	1.029
Final R indices[a]	$R_1 = 0.066$, $wR_2 = 0.178$
Largest diff. peak and hole, eÅ^{-3}	1.60 and –0.90

Obtained with a rotating-anode X-ray tube, Rigaku Mo K_α (λ = 0.71073 Å) X-ray source.
[a] $R_1 = \sum||F_0| - F_C||/\sum|F_0|$, $R_2 = \{\sum[w(F_0^2 - F_0^2)^2]/\sum[w(F_0^2)^2]\}^{1/2}$.

Table B.3. Crystallographic data for $[Ni\text{-}2]^{2+}$.

	$[Ni(PY5Me_2)(CH_3CN)][PF_6]_2$
Chemical formula	$C_{31}H_{28}N_6Ni\cdot 2(PF_6)\cdot 2(C_2H_3N)$
FW	915.33
Crystal system, space group	Triclinic, *P*-1
Temperature (K)	100(2)
a (Å)	12.6877(4)
b (Å)	12.8153(3)
c (Å)	15.3949(4)
α (°)	113.843(3)
β (°)	90.997(2)
γ (°)	118.712(3)
V (Å^3)	1936.9(11)
Z	2
μ (mm^{-1})	0.68
F(000)	934.0
Crystal size (mm)	0.60 × 0.57 × 0.24
θ range (°) for cell measurement	3.1–29.9
Radiation type	Mo *K*α
No. of reflections for cell measurement	28444
Index ranges	$-17 \le h \le 16$
	$-16 \le k \le 17$
	$-20 \le l \le 20$
Reflections collected / unique	28444 / 9390
R_{int}	0.060
Data / restraints / parameters	9390 / 0 / 522
Goodness-of-fit on F^2	1.078
Final R indices[a]	$R_1 = 0.046$, $wR_2 = 0.137$
Largest diff. peak and hole, eÅ^{-3}	1.40 and –1.50

Obtained with a rotating-anode X-ray tube, Rigaku Mo K_α (λ = 0.71073 Å) X-ray source.
[a] $R_1 = \sum||F_0| - F_C||/\sum|F_0|$, $R_2 = \{\sum[w(F_0^2 - F_0^2)^2]/\sum[w(F_0^2)^2]\}^{1/2}$.

Table B.4. Crystallographic data for $[Ni(PY5Me_2)(I)]^+$.

	[Ni(PY5Me$_2$)(I)][I]
Chemical formula	$C_{29}H_{25}IN_5Ni\cdot(I)\cdot(CH_4O)$
FW	788.10
Crystal system, space group	Triclinic, *P*-1
Temperature (K)	100(2)
a (Å)	10.3601(3)
b (Å)	12.3461(3)
c (Å)	12.6708(3)
α (°)	105.211(2)
β (°)	99.118(2)
γ (°)	108.123(2)
V (Å^3)	1434.48(7)
Z	2
μ (mm^{-1})	2.862
F(000)	776.0
Crystal size (mm)	0.10 × 0.18 × 0.36
θ range (°) for cell measurement	3.2–29.7
Radiation type	Mo *K*α
No. of reflections for cell measurement	12919
Index ranges	$-14 \le h \le 14$
	$-17 \le k \le 15$
	$-21 \le l \le 20$
Reflections collected / unique	12919 / 6983
R_{int}	0.03
Data / restraints / parameters	6983 / 0 / 357
Goodness-of-fit on F^2	1.139
Final R indices[a]	$R_1 = 0.029$, $wR_2 = 0.086$
Largest diff. peak and hole, eÅ^{-3}	1.60 and –0.90

Obtained with a rotating-anode X-ray tube, Rigaku Mo K_α (λ = 0.71073 Å) X-ray source.
[a] $R_1 = \sum||F_0| - F_C||/\sum|F_0|$, $R_2 = \{\sum[w(F_0^2 - F_0^2)^2]/\sum[w(F_0^2)^2]\}^{1/2}$.

B.5.23 DFT Calculation Coordinates (x,y,z)

Table B.5. Coordinates for optimized structure of $[Ni\text{-}1]^{2+}$ obtained using DFT calculations employing ωB97X-D functionals and DMF as the solvent.

Atom	x	y	z
H	-0.36199	8.04713	-6.10411
C	-0.4484	8.43147	-5.08589
H	-1.23672	10.37151	-5.6634
C	-0.92892	9.71469	-4.84937
C	-1.00173	10.14478	-3.53286
H	-1.34118	11.15304	-3.28441
N	-0.64837	9.37112	-2.49935
C	-0.20003	8.12204	-2.70498
C	-0.08045	7.63083	-4.00775
H	0.29038	6.62753	-4.20144
C	0.13015	7.25612	-1.46426
C	0.50396	5.83482	-1.89812
H	-0.30248	5.36623	-2.47555
H	0.7078	5.19753	-1.02864
Ni	-0.57799	10.16063	-0.59572
C	-1.1284	7.22825	-0.54576
C	-1.78145	6.03647	-0.23026
H	-1.43889	5.08337	-0.62537
C	-2.89458	6.05723	0.60837
C	-3.33487	7.26971	1.12272
H	-4.19617	7.3324	1.78823
C	-2.64007	8.41651	0.76202
H	-2.94347	9.39746	1.13439
N	-2.16764	11.52789	-0.22821
C	-3.31118	11.6322	-0.90484

H	-3.44509	10.94337	-1.74317
C	-4.29886	12.55562	-0.57286
H	-5.21956	12.6067	-1.15495
C	-4.07846	13.39548	0.51373
C	-2.88583	13.28381	1.22717
H	-2.70311	13.92388	2.09025
C	-1.9455	12.33663	0.82997
C	-0.63927	12.13826	1.52574
C	-0.08793	12.97751	2.49681
H	-0.61769	13.85826	2.85895
C	1.18274	12.67556	2.98362
C	1.88482	11.57226	2.49497
H	2.88926	11.35283	2.85722
C	1.2661	10.77805	1.53199
C	1.84068	9.56159	0.8823
C	3.01754	8.92323	1.25926
H	3.65796	9.32611	2.044
C	3.34224	7.72745	0.62097
H	4.26433	7.20399	0.88045
C	2.46578	7.16501	-0.30478
H	2.70193	6.19819	-0.74397
C	1.28966	7.85162	-0.62512
N	1.06845	9.04775	-0.08786
N	0.03341	11.06913	1.11258
N	-1.57877	8.39498	-0.04841
H	1.63897	13.31647	3.74014
H	1.40517	5.83847	-2.52468
H	-3.40745	5.12613	0.85676
H	-4.82935	14.12955	0.8114

H	3.72162	11.6653	-3.39956
O	0.4966	11.81419	-1.45417
C	1.56065	11.78022	-2.08878
H	2.03813	10.81438	-2.34473
N	2.22159	12.84698	-2.51968
C	1.73128	14.1931	-2.27141
H	0.81159	14.14294	-1.67963
H	1.52542	14.70017	-3.22567
H	2.49017	14.77124	-1.7242
C	3.45984	12.72332	-3.27178
H	4.28005	13.22993	-2.74212
H	3.34919	13.18233	-4.26523

Table B.6. Coordinates for optimized structure of $[Ni\text{-}1]^+$ obtained using DFT calculations employing ωB97X-D functionals and DMF as the solvent.

Atom	x	y	z
H	0.39068	8.84806	-6.18669
C	0.23673	9.13211	-5.14397
H	-0.48447	11.13438	-5.57865
C	-0.24659	10.39299	-4.81547
C	-0.41625	10.68977	-3.47043
H	-0.78749	11.66594	-3.14789
N	-0.13683	9.81771	-2.49779
C	0.33133	8.59455	-2.79246
C	0.52713	8.22673	-4.12732
H	0.90505	7.24258	-4.3924
C	0.63863	7.62496	-1.61743
C	1.11219	6.273	-2.15997
H	0.35124	5.80598	-2.79821
H	1.33829	5.57911	-1.34068
Ni	-0.3045	10.35642	-0.50959
C	-0.6537	7.4386	-0.77409
C	-1.21941	6.17855	-0.55535
H	-0.77129	5.27849	-0.96832
C	-2.37912	6.06382	0.20598
C	-2.95996	7.20835	0.73873
H	-3.86661	7.16541	1.34286
C	-2.34443	8.42527	0.48145
H	-2.74976	9.36047	0.8763
N	-1.79303	11.81246	-0.40297
C	-2.99553	11.80081	-0.99379
H	-3.22064	10.92142	-1.60464
C	-3.91384	12.82866	-0.85307

H	-4.88121	12.77417	-1.35317
C	-3.56338	13.92498	-0.05818
C	-2.32098	13.94527	0.55677
H	-2.02969	14.79085	1.18001
C	-1.44304	12.8693	0.37037
C	-0.1016	12.77647	0.97074
C	0.50447	13.7145	1.80105
H	-0.00995	14.63551	2.07697
C	1.7919	13.46275	2.2829
C	2.4467	12.28023	1.9252
H	3.45187	12.07556	2.2959
C	1.79636	11.3762	1.09312
C	2.32122	10.08708	0.60934
C	3.57498	9.53924	0.89894
H	4.28352	10.06375	1.54014
C	3.89568	8.30795	0.34704
H	4.86662	7.85419	0.55344
C	2.98163	7.63952	-0.47648
H	3.25262	6.67483	-0.89958
C	1.74884	8.23755	-0.72695
N	1.46401	9.42099	-0.1855
N	0.54512	11.63607	0.63462
N	-1.23217	8.53114	-0.25072
H	2.28342	14.18552	2.93481
H	2.02685	6.38816	-2.75489
H	-2.82202	5.08111	0.37905
H	-4.25807	14.75558	0.07861

Table B.7. Coordinates for optimized structure of [Ni-1] obtained using DFT calculations employing ωB97X-D functionals and DMF as the solvent.

Atom	x	y	z
H	0.24096	9.22103	-6.34775
C	0.1196	9.40466	-5.27813
H	-0.67464	11.41529	-5.50089
C	-0.38514	10.616	-4.81777
C	-0.50964	10.78615	-3.44503
H	-0.89798	11.71185	-3.01063
N	-0.1668	9.83878	-2.57076
C	0.31412	8.66105	-2.99001
C	0.47011	8.41894	-4.36046
H	0.86095	7.47231	-4.72621
C	0.6764	7.59734	-1.91657
C	1.15155	6.30998	-2.59684
H	0.37554	5.88876	-3.24969
H	1.4173	5.54954	-1.85179
Ni	-0.27201	10.22102	-0.51683
C	-0.5864	7.30666	-1.0592
C	-1.11523	6.01696	-0.92559
H	-0.65327	5.163	-1.41532
C	-2.25411	5.81612	-0.15171
C	-2.8534	6.90373	0.47429
H	-3.74842	6.79321	1.08746
C	-2.27157	8.15272	0.29975
H	-2.68544	9.05301	0.76299
N	-1.76077	11.60934	-0.24474
C	-2.98847	11.66143	-0.78092
H	-3.23548	10.83847	-1.46359
C	-3.91304	12.65465	-0.52688

H	-4.89568	12.63386	-0.99887
C	-3.53087	13.69533	0.36804
C	-2.28394	13.67279	0.9342
H	-1.97863	14.46428	1.62128
C	-1.36964	12.6182	0.6339
C	-0.05616	12.49779	1.16425
C	0.60784	13.36095	2.07098
H	0.10295	14.25032	2.45226
C	1.90047	13.07662	2.47473
C	2.57102	11.92975	1.99196
H	3.59	11.70338	2.3073
C	1.88153	11.10856	1.10367
C	2.39368	9.87554	0.48401
C	3.66066	9.31428	0.67802
H	4.37856	9.79109	1.34608
C	3.98277	8.14581	0.00544
H	4.96514	7.68852	0.1394
C	3.04825	7.54556	-0.85215
H	3.31605	6.6297	-1.37502
C	1.80329	8.14756	-1.00454
N	1.51178	9.27189	-0.34645
N	0.62468	11.38731	0.71343
N	-1.17607	8.33701	-0.43886
H	2.40841	13.74477	3.17349
H	2.04424	6.49681	-3.20688
H	-2.6687	4.81167	-0.04303
H	-4.22586	14.50538	0.60156

Table B.8. Coordinates for optimized structures of $[Ni\text{-}2]^{2+}$ obtained using DFT calculations employing ωB97X-D functionals and DMF as the solvent.

Atom	x	y	z
Ni	8.77992	1.4681	2.99591
C	6.49237	-0.35615	2.15743
C	5.80013	-1.32186	1.44208
C	6.51379	-2.07876	0.52243
C	7.88481	-1.87395	0.39813
C	8.51642	-0.89322	1.16711
C	10.05661	-0.71286	1.15626
C	10.68717	-1.77719	0.24767
C	10.56216	-0.91279	2.60778
C	11.48583	-1.90822	2.9366
C	11.81446	-2.13768	4.26941
C	11.18798	-1.38783	5.25609
C	10.30041	-0.4017	4.85131
C	10.43053	0.69395	0.64528
C	11.23944	0.85767	-0.48027
C	11.55143	2.13802	-0.90775
C	11.05314	3.22798	-0.21005
C	10.24875	3.01092	0.90855
C	10.27587	2.98339	5.17845
C	11.03163	3.96675	5.79818
C	11.38132	5.08137	5.04767
C	10.95232	5.16556	3.72717
C	10.18874	4.13432	3.17138
C	9.67226	4.19975	1.71391
C	10.11671	5.52186	1.07363
C	8.12708	4.125	1.71806
C	7.33935	5.13092	1.14947

C	5.95213	5.04552	1.20571
C	5.37079	3.95985	1.84732
C	6.21595	2.99874	2.37928
N	7.79738	-0.11921	1.996
N	10.02834	-0.14214	3.56905
N	9.95928	1.76146	1.30914
N	9.87365	3.0544	3.90483
N	7.54981	3.06443	2.30486
H	9.75631	0.19086	5.58658
H	11.37803	-1.5612	6.31546
H	12.53592	-2.91471	4.52893
H	11.95033	-2.52321	2.17096
H	11.78074	-1.69531	0.2368
H	10.43259	-2.78708	0.59142
H	10.33682	-1.67804	-0.78685
H	11.62989	0.00722	-1.03122
H	12.18402	2.28563	-1.78484
H	11.30047	4.2286	-0.55116
H	11.20913	5.61432	1.0668
H	9.77074	5.5979	0.03605
H	9.71234	6.38032	1.62315
H	11.22334	6.0434	3.14737
H	11.97859	5.88517	5.48173
H	11.33898	3.85412	6.83796
H	9.97454	2.09638	5.73331
H	5.80142	2.13532	2.89704
H	4.28952	3.8497	1.92991
H	5.33686	5.82798	0.75808
H	7.78705	5.99047	0.65887

H	5.98685	0.23805	2.91797
H	4.73338	-1.47411	1.60725
H	6.01803	-2.84253	-0.07951
H	8.44525	-2.49624	-0.29383
H	4.61159	2.73511	7.27204
O	7.59017	1.17533	4.69502
C	7.06629	2.03046	5.43043
H	7.22458	3.10924	5.24305
N	6.29407	1.75555	6.47083
C	5.99131	0.38403	6.85245
H	6.50495	-0.30585	6.17519
H	4.90615	0.21154	6.80059
H	6.32593	0.20258	7.88413
C	5.70805	2.81309	7.28109
H	5.99571	3.79622	6.88778
H	6.05536	2.73383	8.32117

Table B.9. Coordinates for optimized structure of $[Ni\text{-}2]^+$ obtained using DFT calculations employing ωB97X-D functionals and DMF as the solvent.

Atom	x	y	z
Ni	8.11738	1.53118	3.0225
C	5.93938	-0.30615	2.05688
C	5.33544	-1.4574	1.56984
C	6.15678	-2.44369	1.04064
C	7.53237	-2.23725	1.02672
C	8.06719	-1.04795	1.53225
C	9.59796	-0.80272	1.57226
C	10.33672	-1.94684	0.86011
C	10.03355	-0.74903	3.05696
C	11.16592	-1.43528	3.50796
C	11.4696	-1.45485	4.86561
C	10.61578	-0.81392	5.75418
C	9.5285	-0.13143	5.22531
C	9.91414	0.52762	0.85196
C	10.33193	0.57622	-0.4798
C	10.53654	1.82028	-1.06563
C	10.31312	2.97672	-0.32753
C	9.88918	2.84984	0.99705
C	9.27883	3.04298	5.42179
C	10.32245	3.68986	6.06983
C	11.21453	4.41637	5.29087
C	10.98533	4.51958	3.92224
C	9.88993	3.86601	3.34885
C	9.5127	4.07243	1.86215
C	10.23009	5.31826	1.31938
C	7.97612	4.25625	1.78092
C	7.40348	5.47767	1.41451

C	6.01911	5.6061	1.35758
C	5.23046	4.50623	1.66658
C	5.87354	3.33001	2.02943
N	7.2588	-0.09659	2.03329
N	9.26624	-0.06247	3.91828
N	9.71815	1.64817	1.54328
N	9.09512	3.08715	4.09991
N	7.20111	3.20188	2.09023
H	8.82633	0.38081	5.88378
H	10.78291	-0.83673	6.83151
H	12.35287	-1.98853	5.2216
H	11.81565	-1.96458	2.81534
H	11.40561	-1.71839	0.76017
H	10.23798	-2.89222	1.40922
H	9.94511	-2.10887	-0.15107
H	10.49541	-0.32571	-1.06537
H	10.86424	1.88853	-2.10465
H	10.46188	3.9485	-0.7933
H	11.30886	5.13779	1.22612
H	9.86003	5.5926	0.32443
H	10.08329	6.18451	1.9774
H	11.6608	5.11992	3.31712
H	12.06831	4.92461	5.74314
H	10.42816	3.62095	7.15297
H	8.54603	2.46548	5.98803
H	5.28881	2.44769	2.29089
H	4.14149	4.55146	1.63639
H	5.56781	6.55872	1.074
H	8.02223	6.33875	1.17449

H	5.33218	0.48191	2.50452
H	4.2522	-1.57269	1.61589
H	5.73789	-3.37171	0.64692
H	8.17524	-3.01596	0.62478

B.5.24 NMR Spectra

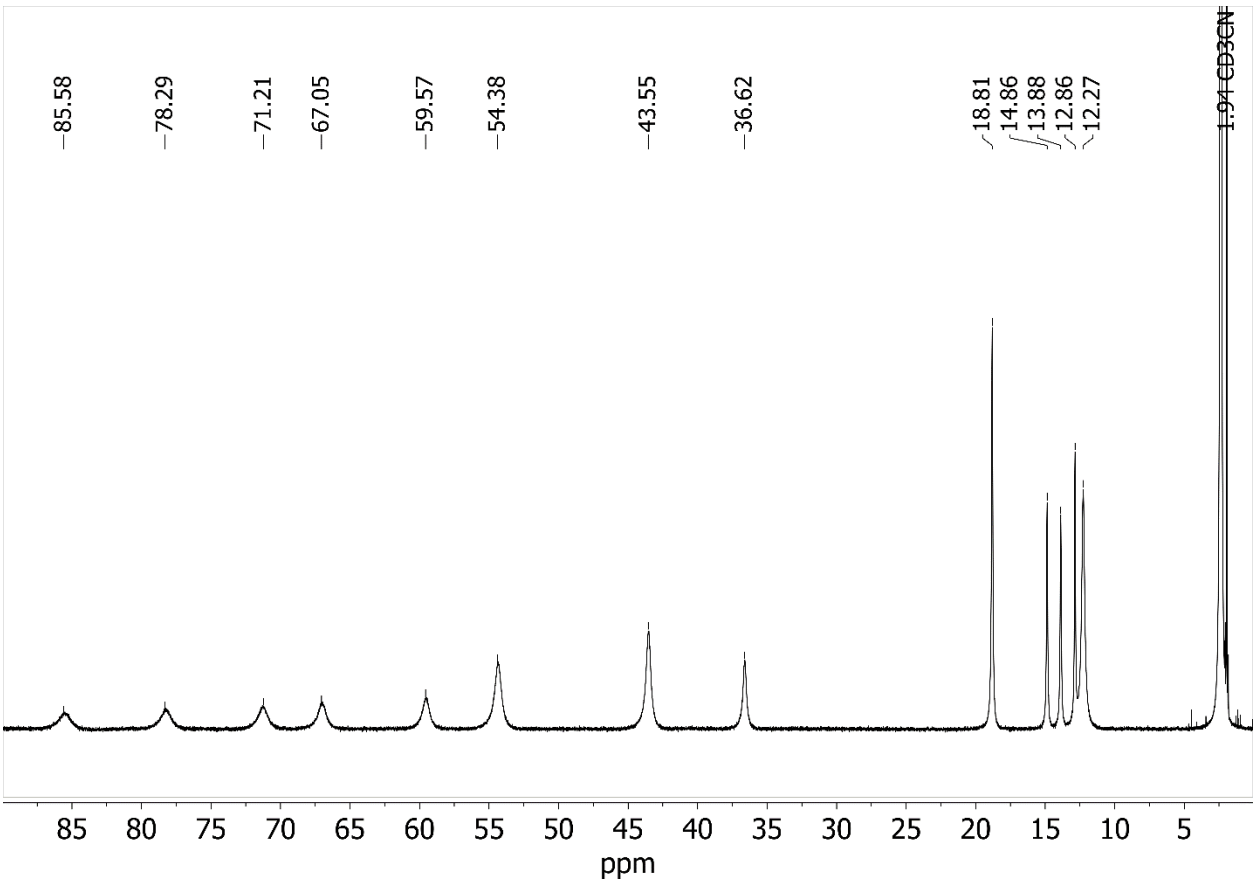


Figure B.29. ^{1}H NMR of [Ni(tpyPY2Me)]$(PF_6)_2$ in CD_3CN.

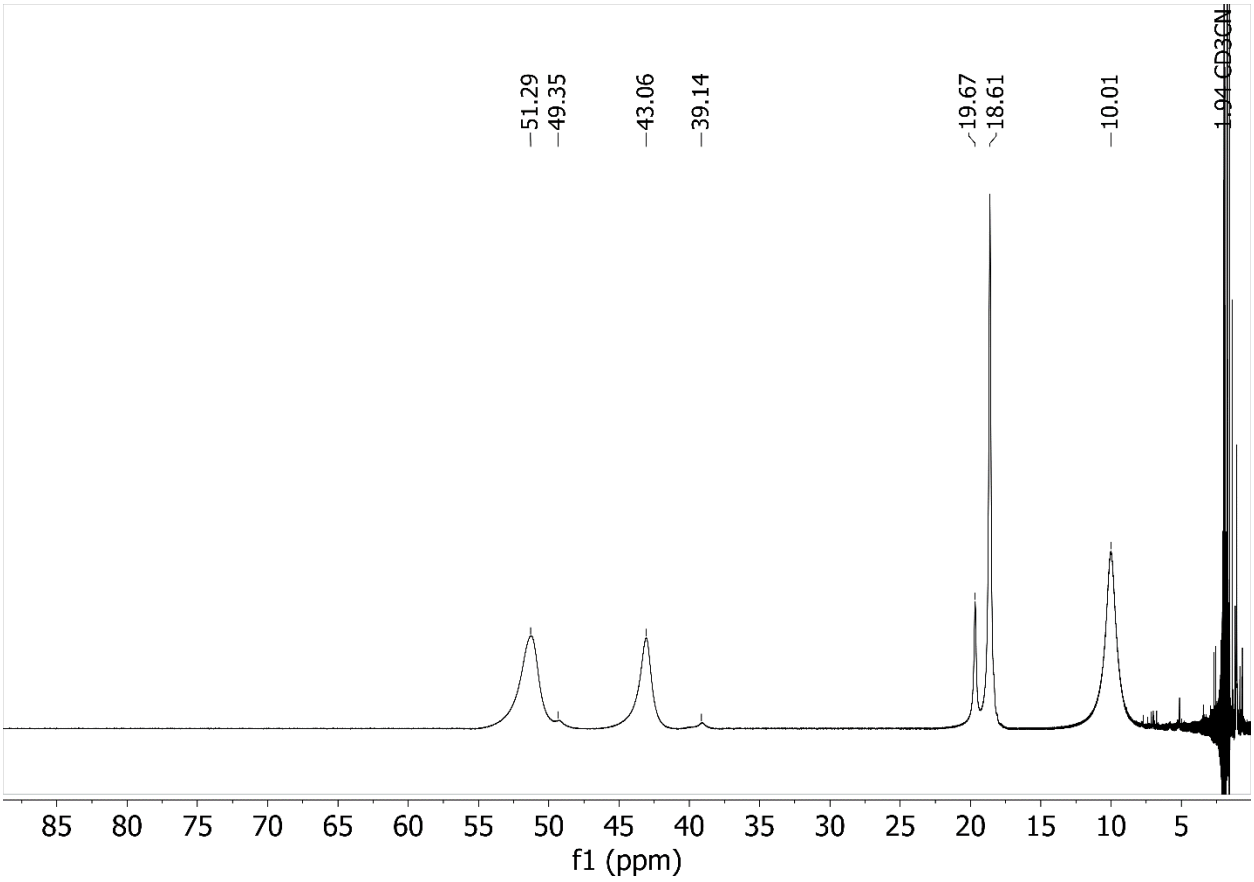


Figure B.30. ^{1}H NMR of [Ni(PY5Me$_2$)](PF$_6$)$_2$ in CD$_3$CN.

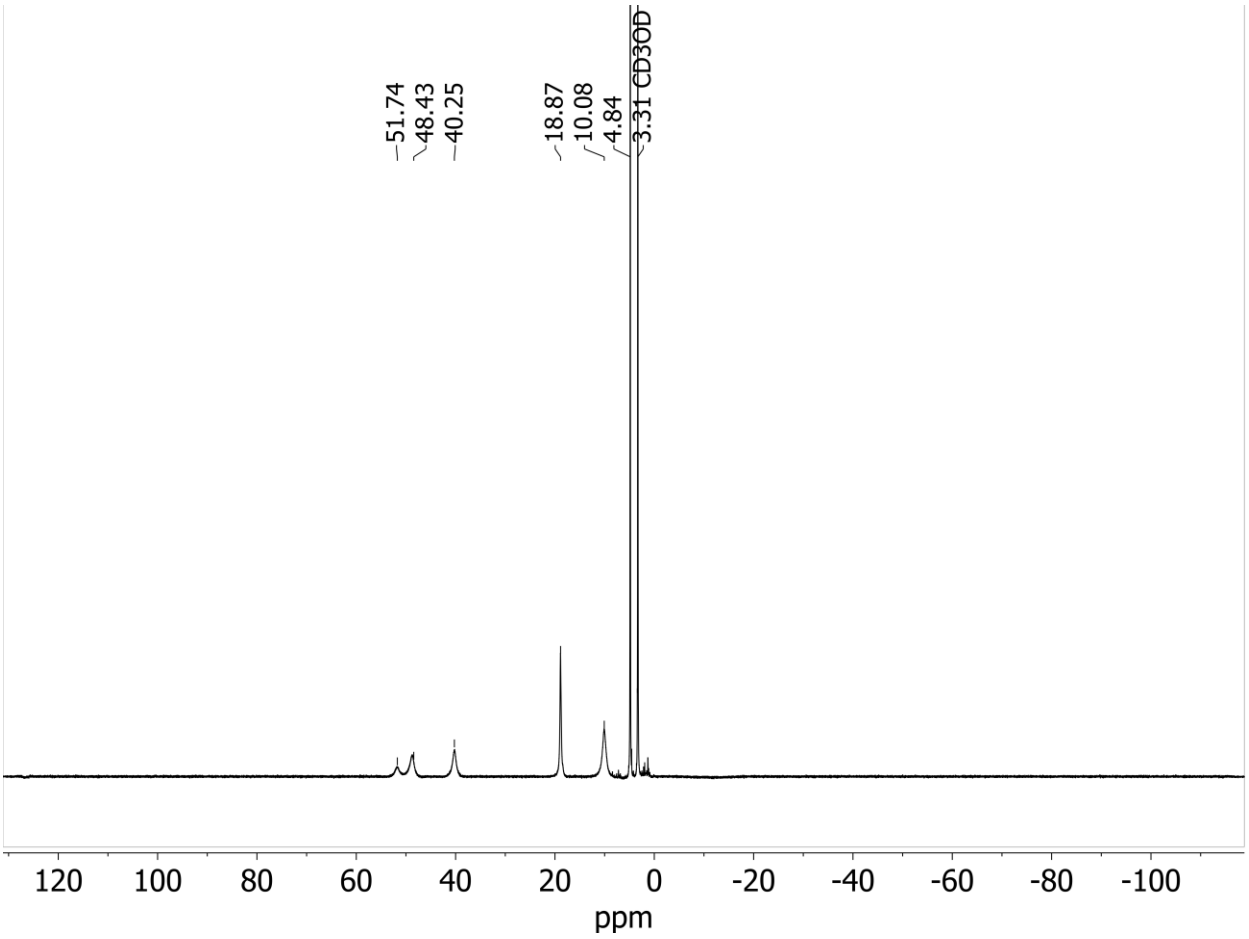


Figure B.31. ^{1}H NMR of [Ni(PY5Me$_2$)(I)](I) in CD_3OD.

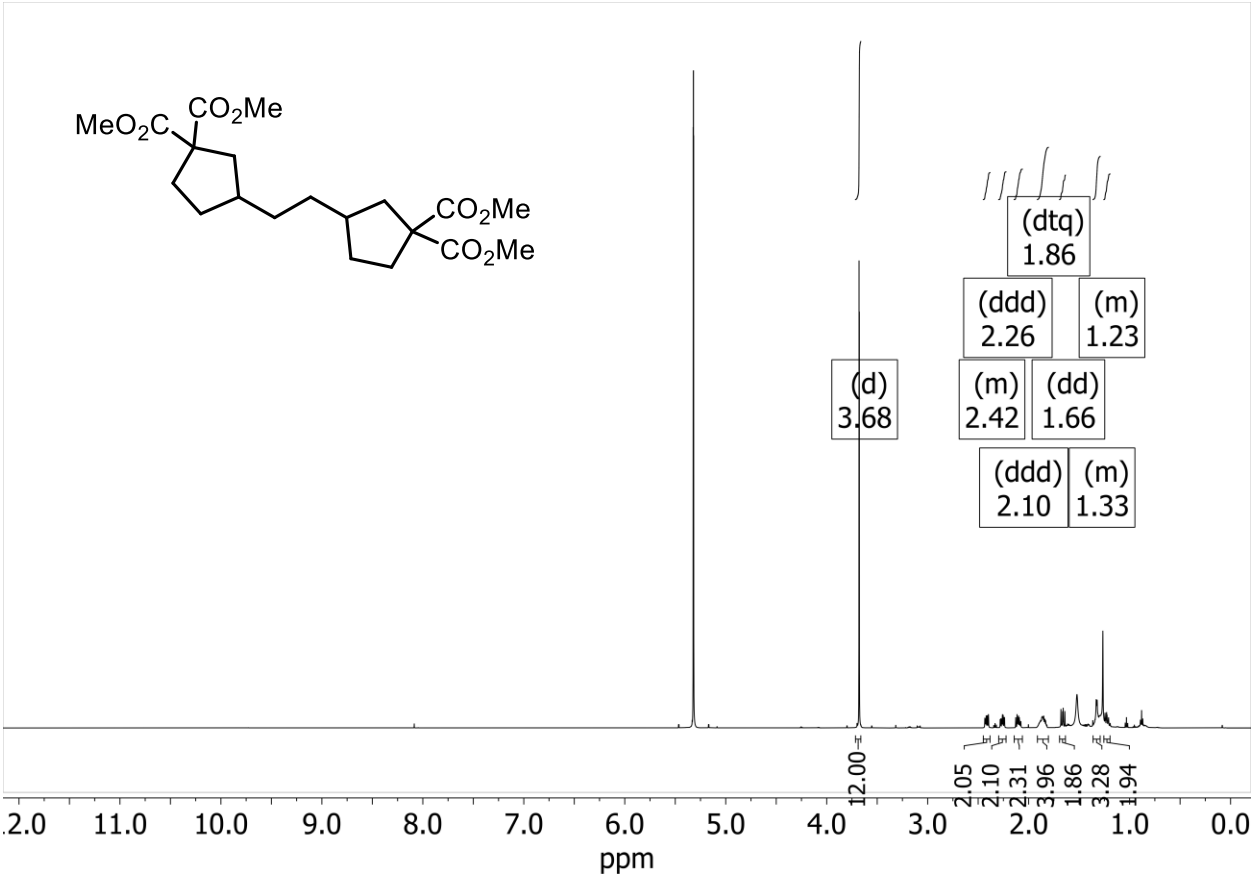


Figure B.32. ^{1}H NMR of tetramethyl 3,3'-(ethane-1,2-diyl)bis(cyclopentane-1,1-dicarboxylate) in CD_2Cl_2.

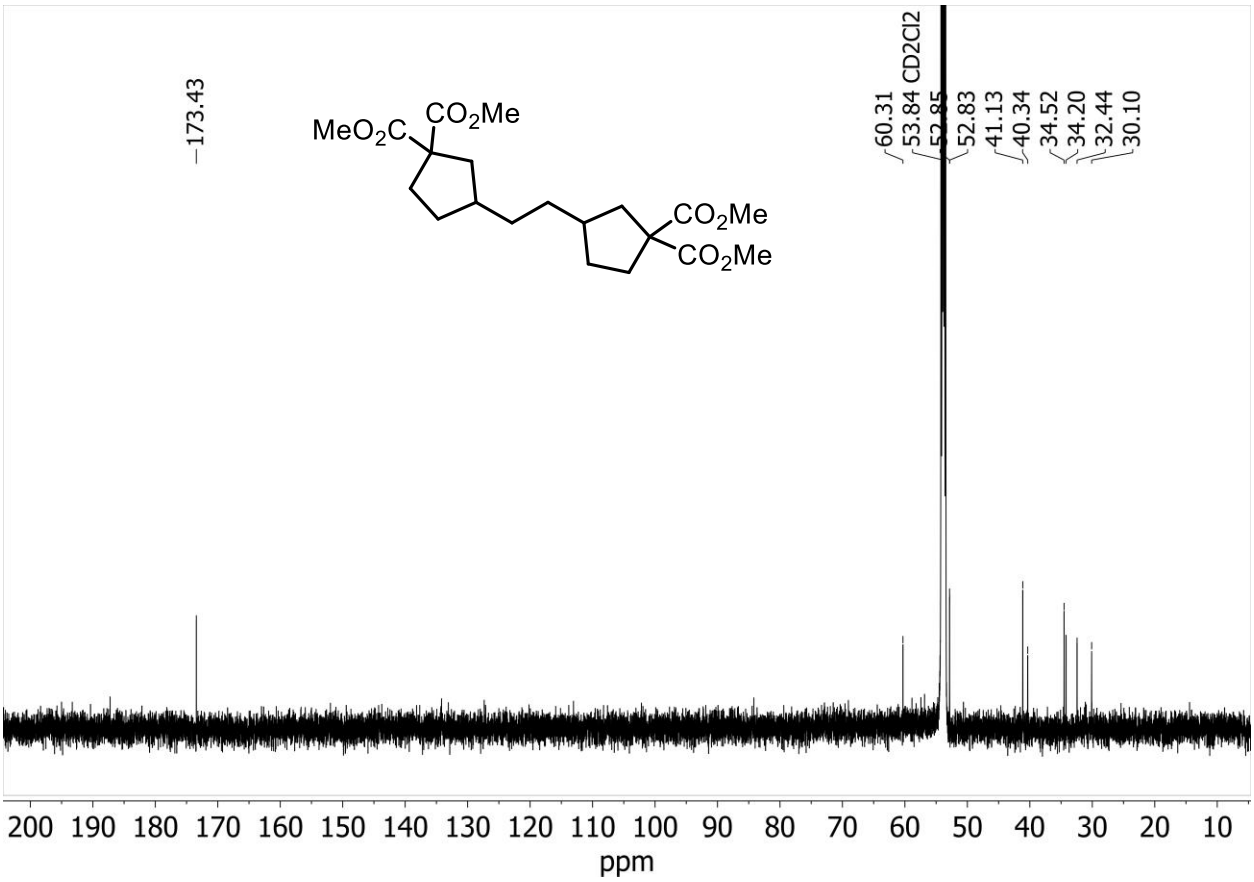


Figure B.33. ^{13}C NMR of tetramethyl 3,3'-(ethane-1,2-diyl)bis(cyclopentane-1,1-dicarboxylate) in CD_2Cl_2.

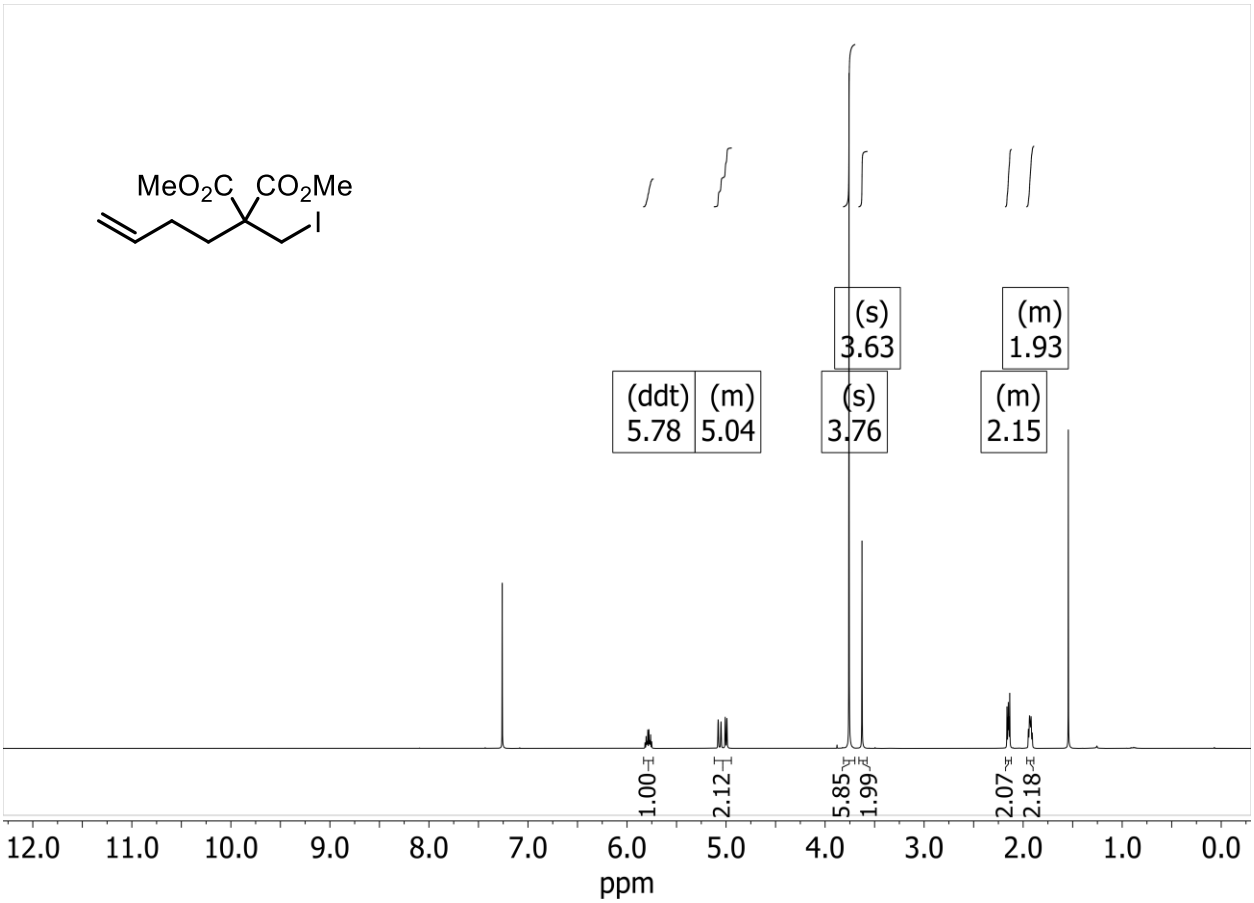


Figure B.34. ^{1}H NMR of dimethyl 2-(but-3-en-1-yl)-2-(iodomethyl)malonate in $CDCl_3$.

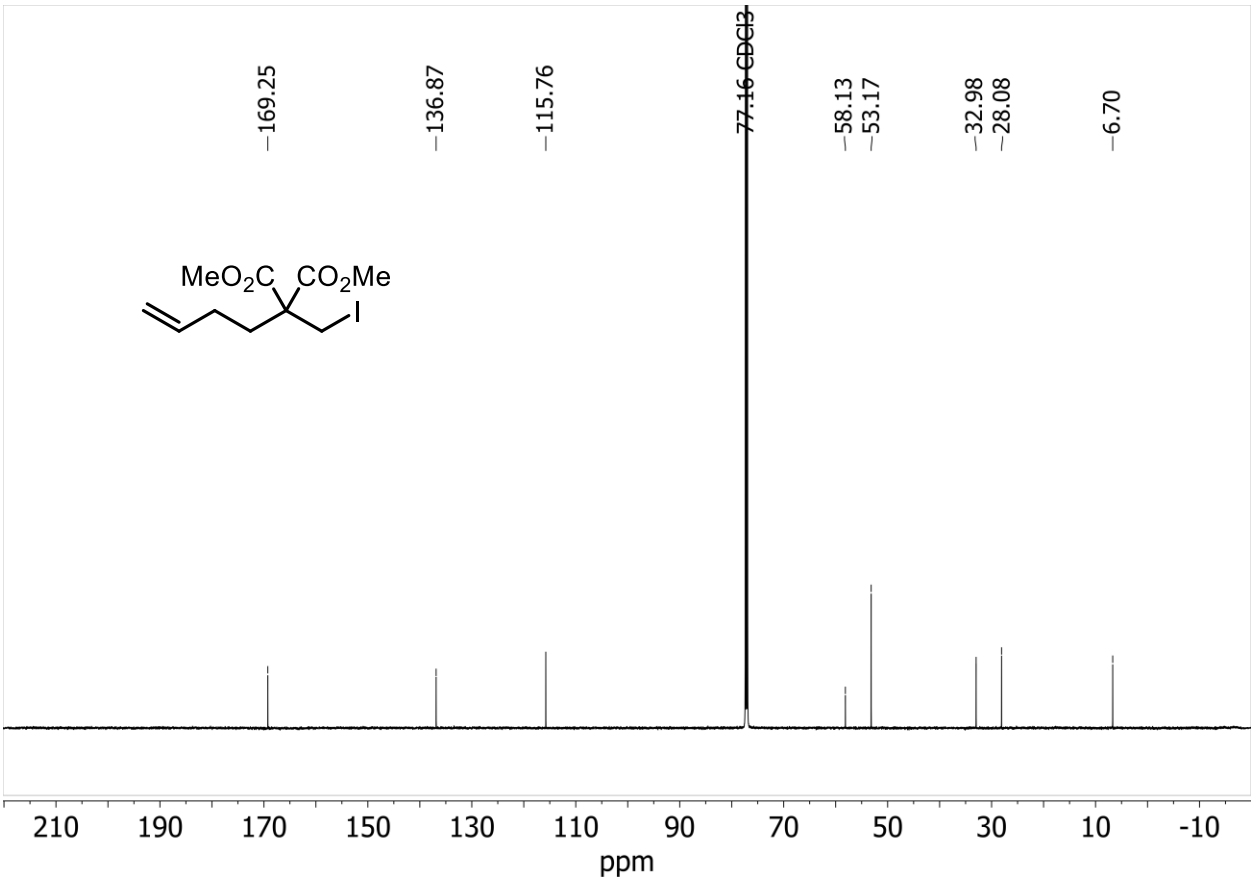


Figure B.35. ^{13}C NMR of dimethyl 2-(but-3-en-1-yl)-2-(iodomethyl)malonate in $CDCl_3$.

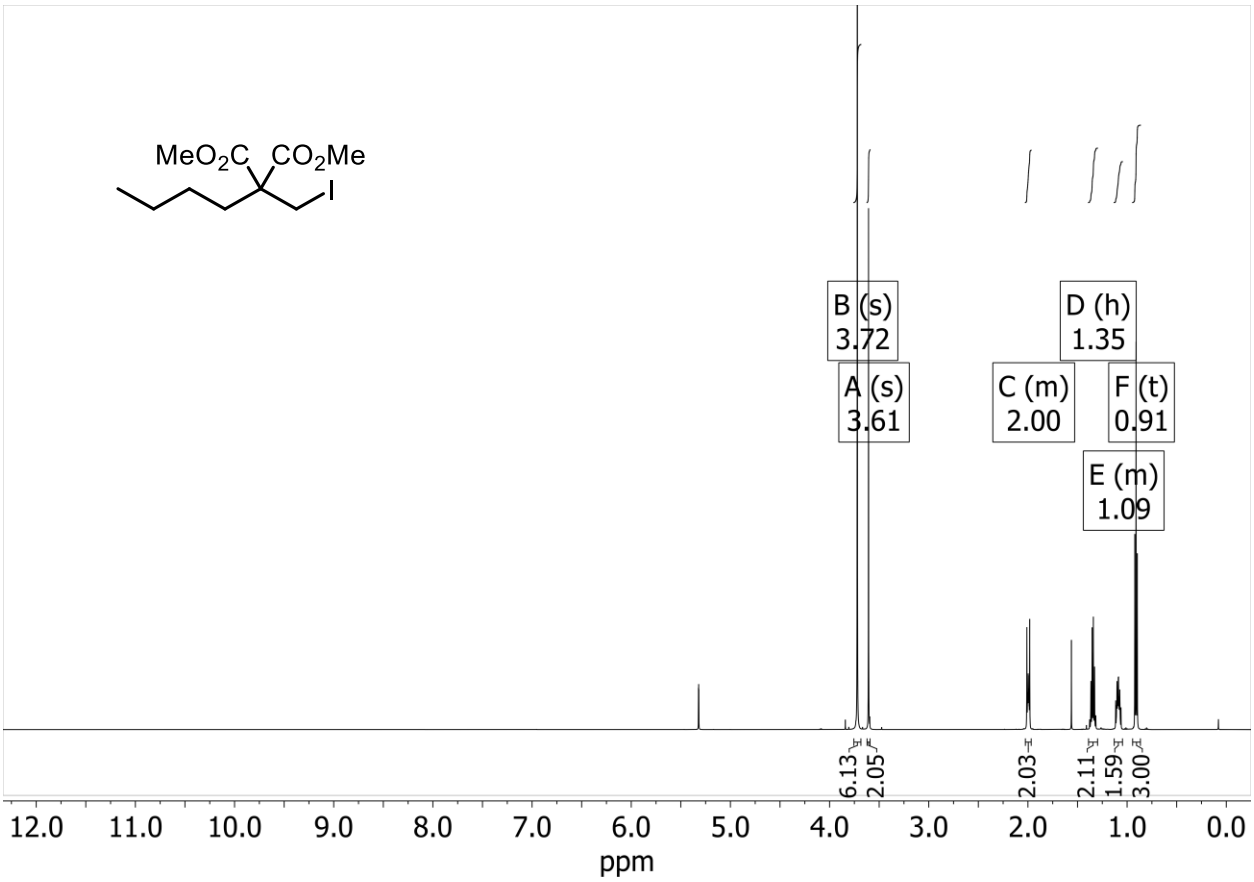


Figure B.36. H NMR of dimethyl 2-butyl-2-(iodomethyl)malonate in CD_2Cl_2.

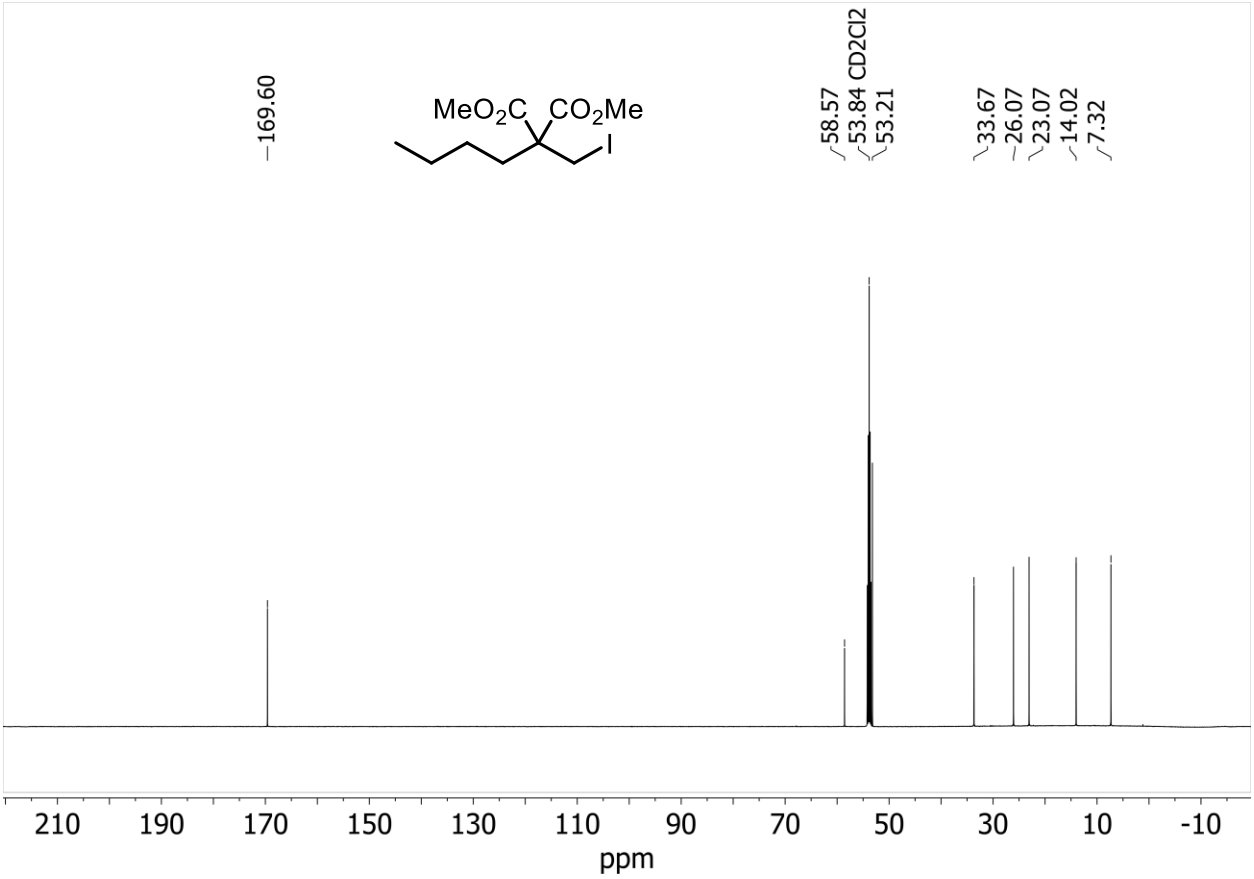


Figure B.37. ^{13}C NMR of dimethyl 2-butyl-2-(iodomethyl)malonate in CD_2Cl_2.

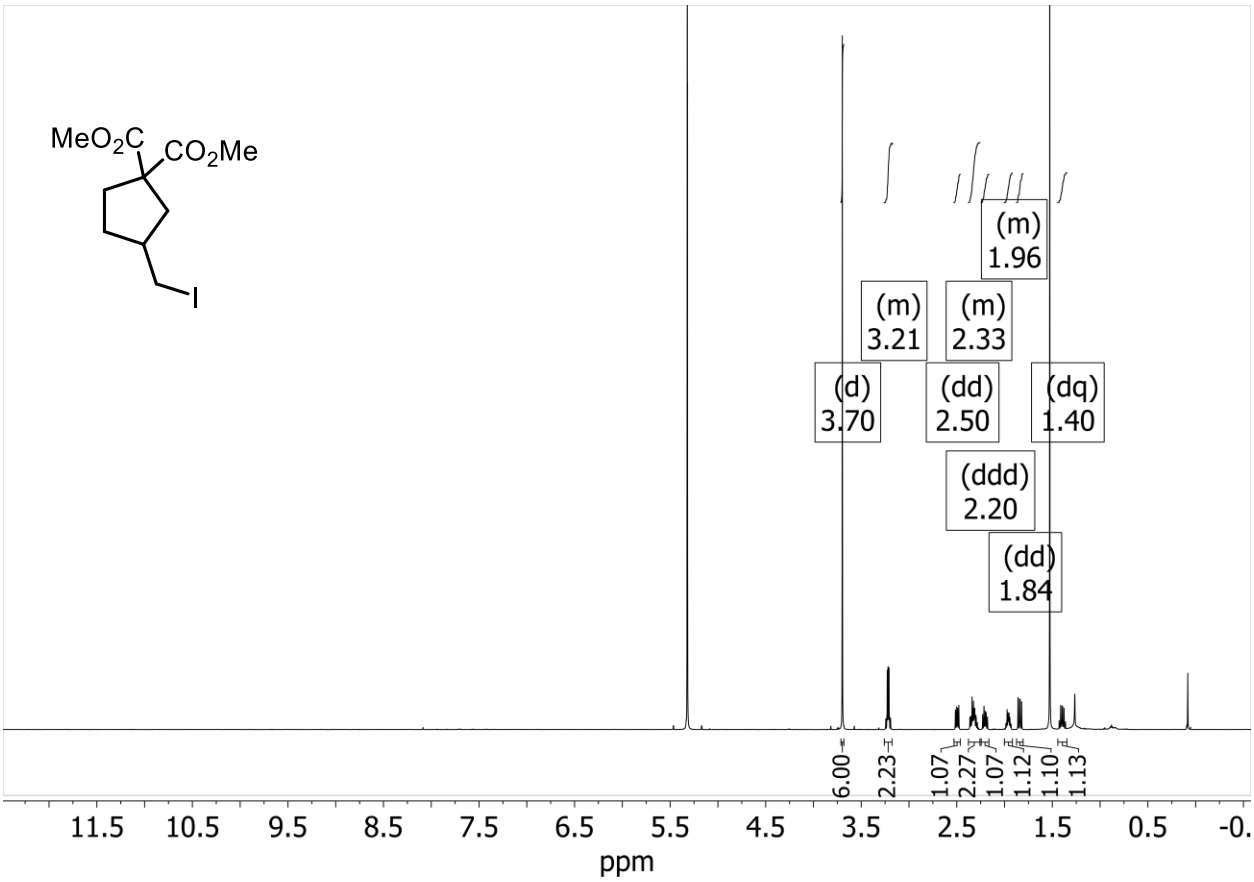


Figure B.38. ^{1}H NMR of dimethyl 3-(iodomethyl)cyclopentane-1,1-dicarboxylate in CD_2Cl_2.

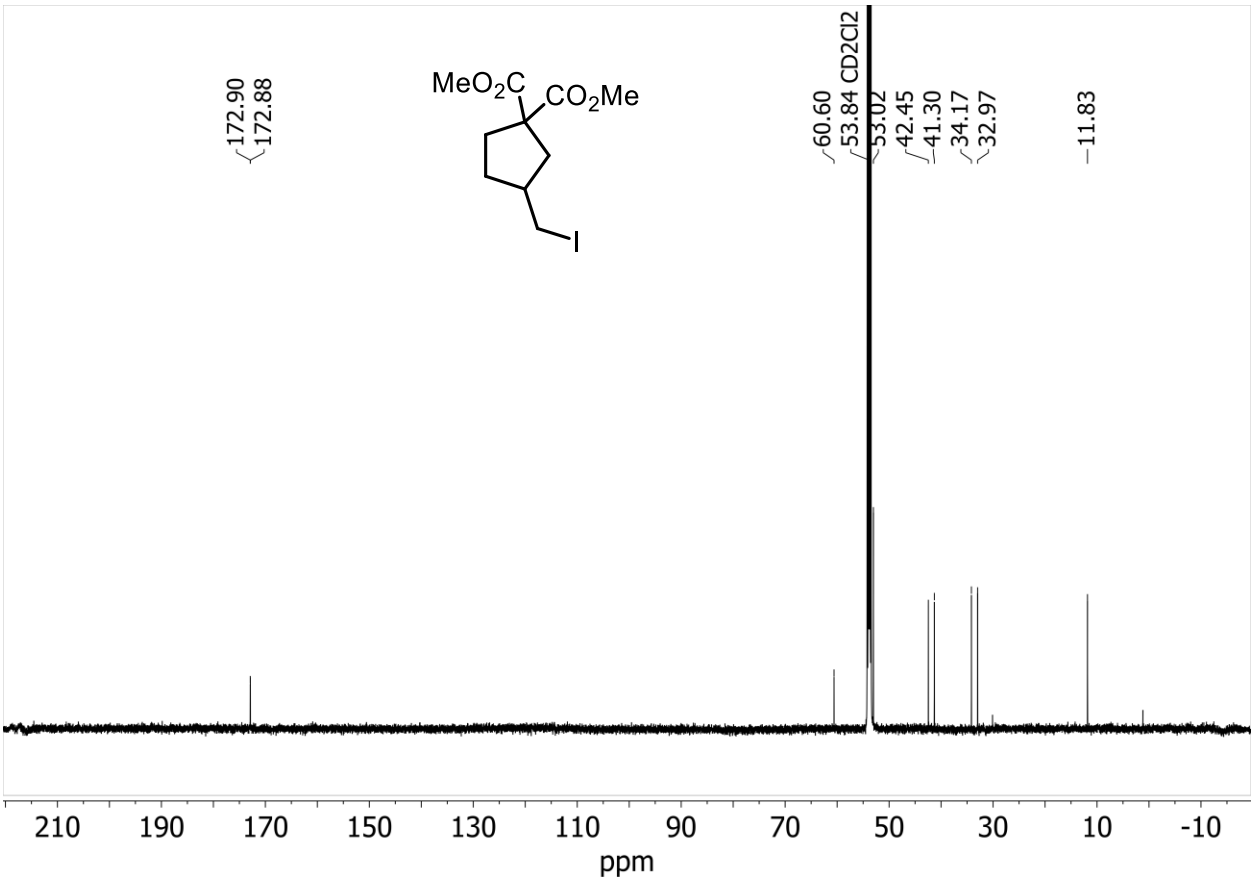


Figure B.39. ^{13}C NMR of dimethyl 3-(iodomethyl)cyclopentane-1,1-dicarboxylate in CD_2Cl_2.

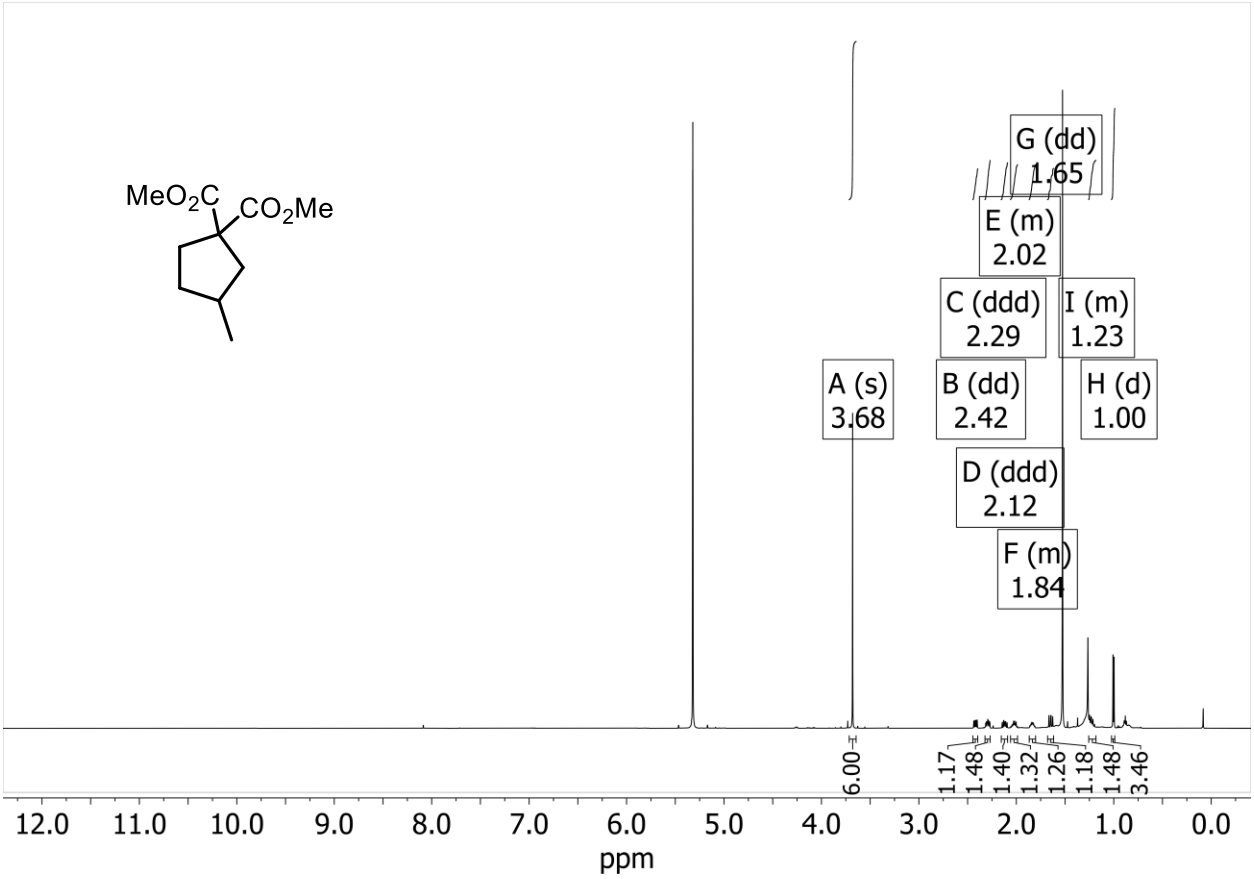


Figure B.40. ^{1}H NMR of dimethyl 3-methylcyclopentane-1,1-dicarboxylate in CD_2Cl_2.

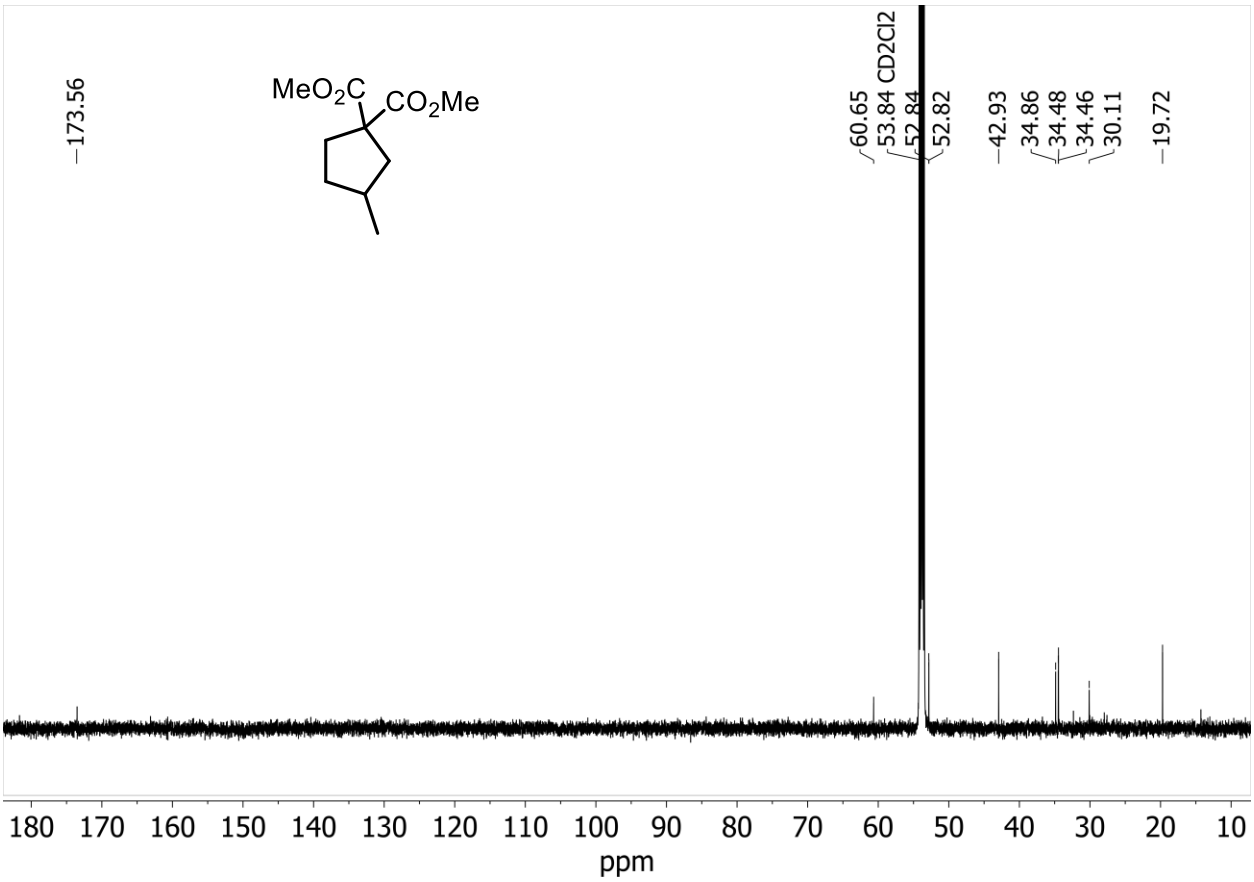


Figure B.41. ^{13}C NMR of dimethyl 3-methylcyclopentane-1,1-dicarboxylate in CD_2Cl_2.

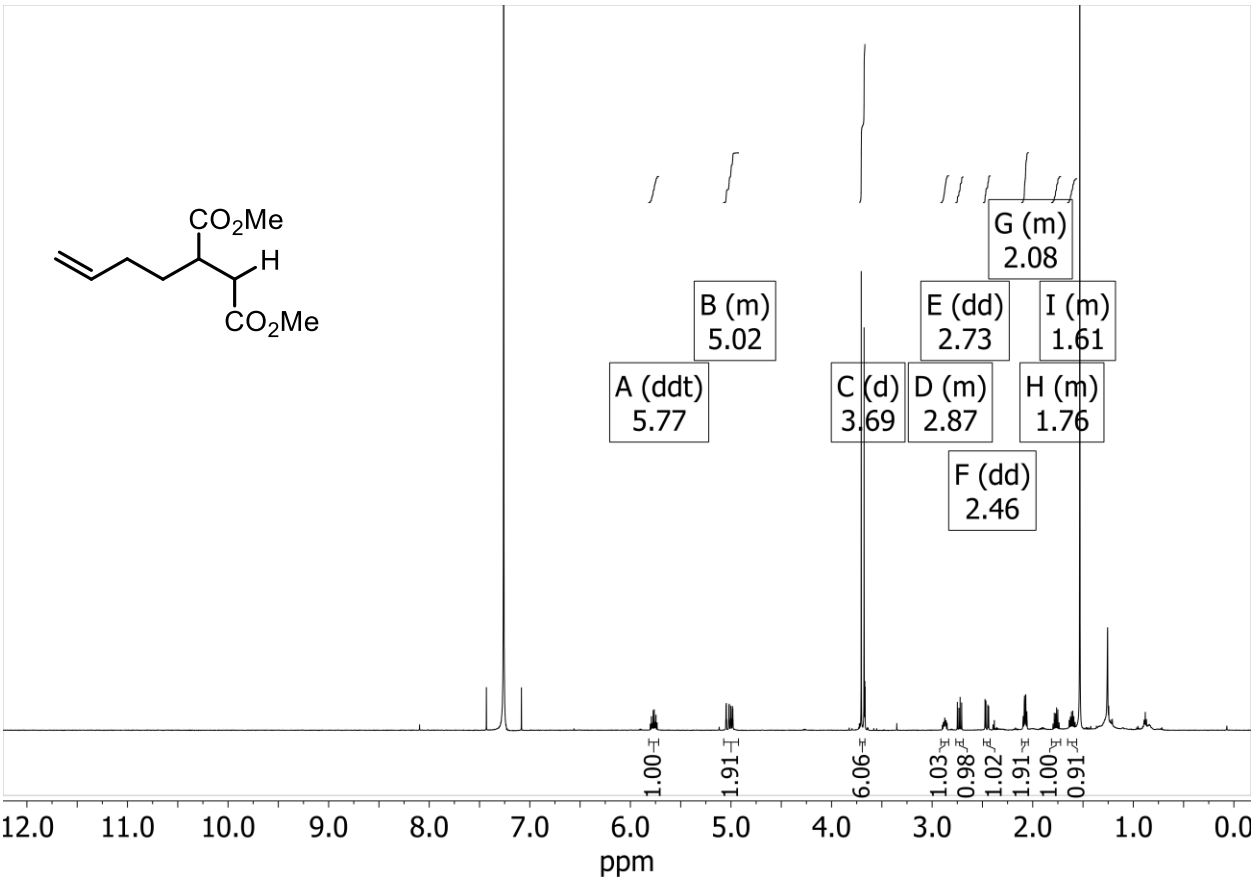


Figure B.42. ^{1}H NMR of dimethyl 2-(but-3-en-1-yl)succinate in $CDCl_3$.

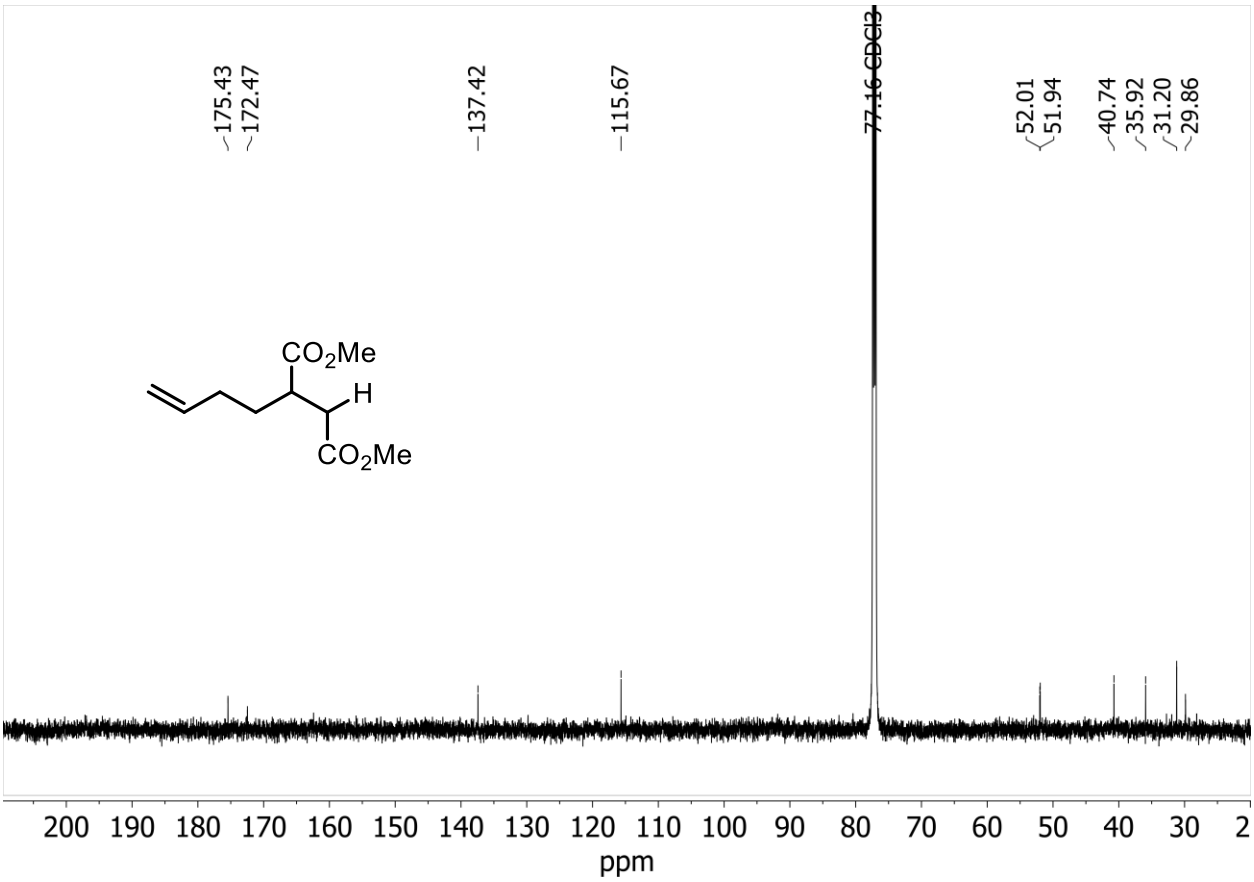


Figure B.43. ^{13}C NMR of dimethyl 2-(but-3-en-1-yl)succinate in $CDCl_3$.

B.6 References

(1) Chatgilialoglu, C.; Ferreri, C.; Landais, Y.; Timokhin, V. I. Thirty Years of $(TMS)_3SiH$: A Milestone in Radical-Based Synthetic Chemistry. *Chem. Rev.* **2018**, *118*, 6516–6572.

(2) Neumann, W. P. Tri-n-Butyltin Hydride as Reagent in Organic Synthesis. *Synthesis* **1987**, *1987*, 665–683.

(3) Renaud, P.; Sibi, M. P. *Radicals in Organic Synthesis*; Wiley VCH, 2001.

(4) Renaud, P.; Sibi, M. P. *Radicals in Organic Synthesis*; Wiley VCH, 2001.

(5) Constantin, T.; Zanini, M.; Regni, A.; Sheikh, N. S.; Juliá, F.; Leonori, D. Aminoalkyl Radicals as Halogen-Atom Transfer Agents for Activation of Alkyl and Aryl Halides. Science **2020**, *367*, 1021−1026.

(6) Kuo, J. L.; Lorenc, C.; Abuyuan, J. M.; Norton, J. R. Catalysis of Radical Cyclizations from Alkyl Iodides under H_2: Evidence for Electron Transfer from $[CpV(CO)_3H]^-$. *J. Am. Chem. Soc.* **2018**, *140*, 4512–4516.

(7) Li, D.; Ma, T.-K.; Scott, R. J.; Wilden, J. D. Electrochemical Radical Reactions of Alkyl Iodides: A Highly Efficient, Clean, Green Alternative to Tin Reagents. *Chem. Sci.* **2020**, *11*, 5333–5338.

(8) Crespi, S.; Fagnoni, M. Generation of Alkyl Radicals: From the Tyranny of Tin to the Photon Democracy. *Chem. Rev.* **2020**, *120*, 9790–9833.

(9) Kim, H.; Lee, C. Nickel-Catalyzed Reductive Cyclization of Organohalides. *Org. Lett.* **2011**, *13*, 2050–2053.

(10) Kim, H.; Lee, C. Visible-Light-Induced Photocatalytic Reductive Transformations of Organohalides. *Angew. Chem. Int. Ed.* **2012**, *51*, 12303–12306.

(11) Nguyen, J. D.; D'Amato, E. M.; Narayanam, J. M. R.; Stephenson, C. R. J. Engaging Unactivated Alkyl, Alkenyl and Aryl Iodides in Visible-Light-Mediated Free Radical Reactions. *Nat. Chem.* **2012**, *4*, 854–859.

(12) Shen, Y.; Cornella, J.; Juliá-Hernández, F.; Martin, R. Visible-Light-Promoted Atom Transfer Radical Cyclization of Unactivated Alkyl Iodides. *ACS Catal.* **2017**, *7*, 409–412.

(13) Alpers, D.; Gallhof, M.; Witt, J.; Hoffmann, F.; Brasholz, M. A Photoredox-Induced Stereoselective Dearomative Radical (4+2)-Cyclization/1,4-Addition Cascade for the Synthesis of Highly Functionalized Hexahydro-1H-Carbazoles. *Angew. Chem. Int. Ed.* **2017**, *56*, 1402–1406.

(14) Gu, X.; Li, X.; Qu, Y.; Yang, Q.; Li, P.; Yao, Y. Intermolecular Visible-Light Photoredox Atom-Transfer Radical [3+2]-Cyclization of 2-(Iodomethyl)Cyclopropane-1,1-Dicarboxylate with Alkenes and Alkynes. *Chem. Eur. J.* **2013**, *19*, 11878–11882.

(15) Murphy, J. A.; Khan, T. A.; Zhou, S.; Thomson, D. W.; Mahesh, M. Highly Efficient Reduction of Unactivated Aryl and Alkyl Iodides by a Ground-State Neutral Organic Electron Donor. *Angew. Chem. Int. Ed.* **2005**, *44*, 1356–1360.

(16) Hwang, J. Y.; Baek, J. H.; Shin, T. I.; Shin, J. H.; Oh, J. W.; Kim, K. P.; You, Y.; Kang, E. J. Single-Electron-Transfer Strategy for Reductive Radical Cyclization: $Fe(CO)_5$ and Phenanthroline System. *Org. Lett.* **2016**, *18*, 4900–4903.

(17) Sebren, L. J.; Devery, J. J.; Stephenson, C. R. J. Catalytic Radical Domino Reactions in Organic Synthesis. *ACS Catal.* **2014**, *4*, 703–716.

(18) Bohn, M. A.; Paul, A.; Hilt, G. Electrochemically Initiated Radical Reactions. In *Encyclopedia of Radicals in Chemistry, Biology and Materials*; John Wiley & Sons, Ltd, 2012.

(19) Zhang, W.; Lin, S. Electroreductive Carbofunctionalization of Alkenes with Alkyl Bromides via a Radical-Polar Crossover Mechanism. *J. Am. Chem. Soc.* **2020**, *142*, 20661–20670.
(20) Narayanam, J. M. R.; Tucker, J. W.; Stephenson, C. R. J. Electron-Transfer Photoredox Catalysis: Development of a Tin-Free Reductive Dehalogenation Reaction. *J. Am. Chem. Soc.* **2009**, *131*, 8756–8757.
(21) Tucker, J. W.; Narayanam, J. M. R.; Krabbe, S. W.; Stephenson, C. R. J. Electron Transfer Photoredox Catalysis: Intramolecular Radical Addition to Indoles and Pyrroles. *Org. Lett.* **2010**, *12*, 368–371.
(22) Juris, A.; Balzani, V.; Barigelletti, F.; Campagna, S.; Belser, P.; von Zelewsky, A. Ru(II) Polypyridine Complexes: Photophysics, Photochemistry, Eletrochemistry, and Chemiluminescence. *Coord. Chem. Rev.* **1988**, *84*, 85–277.
(23) Connell, T. U.; Fraser, C. L.; Czyz, M. L.; Smith, Z. M.; Hayne, D. J.; Doeven, E. H.; Agugiaro, J.; Wilson, D. J. D.; Adcock, J. L.; Scully, A. D.; Gómez, D. E.; Barnett, N. W.; Polyzos, A.; Francis, P. S. The Tandem Photoredox Catalysis Mechanism of $[Ir(Ppy)_2(Dtb\text{-}Bpy)]^+$ Enabling Access to Energy Demanding Organic Substrates. *J. Am. Chem. Soc.* **2019**, *141*, 17646–17658.
(24) Duñach, E.; Medeiros, M. J.; Olivero, S. Intramolecular Reductive Cyclisations Using Electrochemistry: Development of Environmentally Friendly Synthetic Methodologies. *New J. Chem.* **2006**, *30*, 1534–1548.
(25) Duñach, E.; Medeiros, M. J.; Olivero, S. Electrochemical Cyclizations of Organic Halides Catalyzed by Electrogenerated Nickel(I) Complexes: Towards Environmentally Friendly Methodologies. *Electrochimica Acta* **2017**, *242*, 373–381.
(26) Francke, R.; Little, R. D. Redox Catalysis in Organic Electrosynthesis: Basic Principles and Recent Developments. *Chem. Soc. Rev.* **2014**, *43*, 2492–2521.
(27) Lexa, D.; Saveant, J. M.; Su, K. B.; Wang, D. L. Chemical vs. Redox Catalysis of Electrochemical Reactions. Reduction of Trans-1,2-Dibromocyclohexane by Electrogenerated Aromatic Anion Radicals and Low Oxidation State Metalloporphyrins. *J. Am. Chem. Soc.* **1987**, *109*, 6464–6470.
(28) Ozaki, S.; Matsushita, H.; Ohmori, H. Indirect Electroreductive Cyclisation of N-Allylic and N-Propargylbromo Amides and o-Bromoacryloylanilides Using Nickel(II) Complexes as Electron-Transfer Catalysts. *J. Chem. Soc. Perkin* **1993**, *1*, 2339–2344.
(29) Foley, M. P.; Du, P.; Griffith, K. J.; Karty, J. A.; Mubarak, M. S.; Raghavachari, K.; Peters, D. G. Electrochemistry of Substituted Salen Complexes of Nickel(II): Nickel(I)-Catalyzed Reduction of Alkyl and Acetylenic Halides. *J. Electroanal. Chem.* **2010**, *647*, 194–203.
(30) Duñach, E.; Esteves, A. P.; Medeiros, M. J.; Olivero, S. Electrochemical Intramolecular Cyclisation of Propargyl Bromoethers Catalysed by Nickel Complexes. *New J. Chem.* **2005**, *29*, 633–636.
(31) Duñach, E.; Esteves, A. P.; Freitas, A. M.; Medeiros, M. J.; Olivero, S. Electroreductive Cyclisation of Unsaturated Halides Catalysed by Nickel Macrocyclic Complexes. *Tetrahedron Lett.* **1999**, *40*, 8693–8696.
(32) Diccianni, J. B.; Katigbak, J.; Hu, C.; Diao, T. Mechanistic Characterization of (Xantphos)Ni(I)-Mediated Alkyl Bromide Activation: Oxidative Addition, Electron Transfer, or Halogen-Atom Abstraction. *J. Am. Chem. Soc.* **2019**, *141*, 1788–1796.

(33) Ihara, M.; Katsumata, A.; Setsu, F.; Tokunaga, Y.; Fukumoto, K. Synthesis of Six-Membered Compounds by Environmentally Friendly Cyclization Using Indirect Electrolysis. *J. Org. Chem.* **1996**, *61*, 677–684.
(34) Esteves, A. P.; Neves, C. S.; Medeiros, M. J.; Pletcher, D. Organic Cyclisations of Propargyl and Allyl Bromoesters in Microemulsions Catalysed by Electrogenerated Nickel(I) Tetramethylcyclam. *J. Electroanal. Chem.* **2008**, *614*, 131–138.
(35) Duñach, E.; Esteves, A. P.; Freitas, A. M.; Lemos, M. A.; Medeiros, M. J.; Olivero, S. Intramolecular cyclization of propargyl derivatives using environmentally friendly methodologies. *Pure Appl. Chem.* **2001**, *73*, 1941–1945.
(36) Duñach, E.; Esteves, A. P.; Medeiros, M. J.; Olivero, S. Electrogenerated Nickel(I) Complexes as Catalysts for the Intramolecular Radical Cyclisation of Unsaturated α-Bromoesters. *Tetrahedron Lett.* **2004**, *45*, 7935–7937.
(37) Gosden, C.; Healy, K. P.; Pletcher, D. Reaction of Electrogenerated Square-Planar Nickel(I) Complexes with Alkyl Halides. *J. Chem. Soc. Dalton Trans.* **1978**, 972–976.
(38) Bakac, Andreja.; Espenson, J. H. Kinetics and Mechanism of the Alkylnickel Formation in One-Electron Reductions of Alkyl Halides and Hydroperoxides by a Macrocyclic Nickel(I) Complex. *J. Am. Chem. Soc.* **1986**, *108*, 713–719.
(39) Becker, J. Y.; Kerr, J. B.; Pletcher, D.; Rosas, R. The Electrochemistry of Square Planar Macrocyclic Nickel Complexes and the Reaction of Ni(I) with Alkyl Bromides: Nickel Tetraamine Complexes. *J. Electroanal. Chem. Interfacial Electrochem.* **1981**, *117*, 87–99.
(40) Esteves, A. P.; Freitas, A. M.; Medeiros, M. J.; Pletcher, D. Reductive Intramolecular Cyclisation of Unsaturated Halides by Ni(II) Complexes. *J. Electroanal. Chem.* **2001**, *499*, 95–102.
(41) Azevedo, F.; Freire, C.; de Castro, B. Reductive Electrochemical Study of Ni(II) Complexes with N_2O_2 Schiff Base Complexes and Spectroscopic Characterisation of the Reduced Species. Reactivity towards CO. *Polyhedron* **2002**, *21*, 1695–1705.
(42) Gosden, C.; Kerr, J. B.; Pletcher, D.; Rosas, R. The Electrochemistry of Square Planar Macrocyclic Nickel Complexes and the Reaction of Ni(I) with Alkyl Bromides: Tetradentate Schiff Base Complexes. *J. Electroanal. Chem. Interfacial Electrochem.* **1981**, *117*, 101–107.
(43) Gosden, C.; Pletcher, D. The Catalysis of the Electrochemical Reduction of Alkyl Bromides by Nickel Complexes: The Formation of Carbon-carbon Bonds. *J. Organomet. Chem.* **1980**, *186*, 401–409.
(44) Martin, E. T.; McGuire, C. M.; Peters, D. G. Catalytic Reduction of Organic Halides by Electrogenerated Nickel(I) Salen. *Electrochem. Soc. Interface* **2016**, *25*, 41.
(45) Derrick, J.; Loipersberger, M.; Iovan, D.; Smith, P. T.; Chakarawet, K.; Yano, J.; Long, J. R.; Head-Gordon, M.; Chang, C. Metal–Ligand Exchange Coupling Promotes Iron-Catalyzed Electrochemical CO_2 Reduction at Low Overpotentials. *J. Am. Chem. Soc.* **2020**, *142*, 20489–20501.
(46) Hartmann, M.; Studer, A. Cyclizing Radical Carboiodination, Carbotelluration, and Carboaminoxylation of Aryl Amines. *Angew. Chem. Int. Ed.* **2014**, *53*, 8180–8183.
(47) Karunadasa, H. I.; Chang, C. J.; Long, J. R. A Molecular Molybdenum-Oxo Catalyst for Generating Hydrogen from Water. *Nature* **2010**, *464*, 1329–1333.
(48) Bechlars, B.; D'Alessandro, D. M.; Jenkins, D. M.; Iavarone, A. T.; Glover, S. D.; Kubiak, C. P.; Long, J. R. High-Spin Ground States via Electron Delocalization in Mixed-Valence Imidazolate-Bridged Divanadium Complexes. *Nat. Chem.* **2010**, *2*, 362–368.

(49) Sun, Y.; Bigi, J. P.; Piro, N. A.; Tang, M. L.; Long, J. R.; Chang, C. J. Molecular Cobalt Pentapyridine Catalysts for Generating Hydrogen from Water. *J. Am. Chem. Soc.* **2011**, *133*, 9212–9215.
(50) Karunadasa, H. I.; Montalvo, E.; Sun, Y.; Majda, M.; Long, J. R.; Chang, C. J. A Molecular MoS_2 Edge Site Mimic for Catalytic Hydrogen Generation. *Science* **2012**, *335*, 698–702.
(51) Chantarojsiri, T.; Sun, Y.; Long, J. R.; Chang, C. J. Water-Soluble Iron(IV)-Oxo Complexes Supported by Pentapyridine Ligands: Axial Ligand Effects on Hydrogen Atom and Oxygen Atom Transfer Reactivity. *Inorg. Chem.* **2015**, *54*, 5879–5887.
(52) Zee, D. Z.; Chantarojsiri, T.; Long, J. R.; Chang, C. J. Metal–Polypyridyl Catalysts for Electro- and Photochemical Reduction of Water to Hydrogen. *Acc. Chem. Res.* **2015**, *48*, 2027–2036.
(53) Savéant, J.-M.; Costentin, C. *Elements of Molecular and Biomolecular Electrochemistry: An Electrochemical Approach to Electron Transfer Chemistry*, 2nd ed.; John Wiley & Sons: Hoboken, 2019.
(54) Nadjo, L.; Savéant, J. M.; Su, K. B. Homogeneous Redox Catalysis of Multielectron Electrochemical Reactions. Part II. Competition between Homogeneous Electron Transfer and Addition on the Catalyst. *J. Electroanal. Chem.* **1985**, *196*, 23–34.
(55) Nadjo, L.; Savéant, J. M.; Su, K. B. Homogeneous Redox Catalysis of Multielectron Electrochemical Reactions: Part II. Competition between Homogeneous Electron Transfer and Addition on the Catalyst. *J. Electroanal. Chem. Interfacial Electrochem.* **1985**, *196*, 23–34.
(56) Andrieux, C. P.; Gallardo, Iluminada.; Savaent, J. Michel.; Su, K. Binh. Dissociative Electron Transfer. Homogeneous and Heterogeneous Reductive Cleavage of the Carbon-Halogen Bond in Simple Aliphatic Halides. *J. Am. Chem. Soc.* **1986**, *108*, 638–647.
(57) Biddulph, M. A.; Davis, R.; Wells, C. H. J.; Wilson, F. I. C. Reactions between Dinuclear Metal Carbonyl Complexes and Alkyl Halides: Formal Oxidative Addition across a Metal–Metal Single Bond. *J. Chem. Soc. Chem. Commun.* **1985**, 1287–1288.
(58) Herrick, R. S.; Herrinton, T. R.; Walker, H. W.; Brown, T. L. Rates of Halogen Atom Transfer to Manganese Carbonyl Radicals. *Organometallics* **1985**, *4*, 42–45.
(59) Halpern, J.; Maher, J. P. Kinetics of the Reactions of Pentacyanocobaltate(II) with Organic Halides. *J. Am. Chem. Soc.* **1965**, *87*, 5361–5366.
(60) Marcus, R. A. The Second R. A. Robinson Memorial Lecture. Electron, Proton and Related Transfers. *Faraday Discuss. Chem. Soc.* **1982**, *74*, 7–15.
(61) Hush, N. S. Adiabatic Rate Processes at Electrodes. I. Energy-Charge Relationships. *J. Chem. Phys.* **1958**, *28*, 962–972.
(62) Marcus, R. A. On the Theory of Oxidation-Reduction Reactions Involving Electron Transfer. I. *J. Chem. Phys.* **1956**, *24*, 966–978.
(63) Lexa, D.; Mispelter, J.; Saveant, J. M. Electroreductive Alkylation of Iron in Porphyrin Complexes. Electrochemical and Spectral Characteristics of σ-Alkylironporphyrins. *J. Am. Chem. Soc.* **1981**, *103*, 6806–6812.
(64) Barnes, J. T.; Griffith, K. J.; Beeler, J. A.; Gerroll, B. H. R.; Couto Petro, A. G.; Williams, C. G.; Siedle, A. R.; Tait, S. L.; Peters, D. G. Alkyl-Group Grafting onto Glassy Carbon Cathodes by Reduction of Primary Monohaloalkanes: Electrochemistry and X-Ray Photoelectron Spectroscopy Studies. *J. Electroanal. Chem.* **2020**, *856*, 113531.

(65) Savéant, J. M.; Su, K. B. Homogeneous Redox Catalysis of Electrochemical Reaction: Part VI. Zone Diagram Representation of the Kinetic Regimes. *J. Electroanal. Chem. Interfacial Electrochem.* **1984**, *171*, 341–349.
(66) Lal, D.; Griller, D.; Husband, S.; Ingold, K. U. Kinetic Applications of Electron Paramagnetic Resonance Spectroscopy. XVI. Cyclization of the 5-Hexenyl Radical. *J. Am. Chem. Soc.* **1974**, *96*, 6355–6357.
(67) Andrieux, C. P.; Gallardo, I.; Saveant, J. M. Outer-Sphere Electron-Transfer Reduction of Alkyl Halides. A Source of Alkyl Radicals or of Carbanions? Reduction of Alkyl Radicals. *J. Am. Chem. Soc.* **1989**, *111*, 1620–1626.
(68) Alender, J.; Morgan, P.; Timberlake, J. Decomposition of N,N-Dialkylthiadiaziridine 1,1-Dioxides: A Mechanistic Revision. *J. Org. Chem.* **1983**, *48*, 755–756.
(69) Murakami, Y.; Hisaeda, Y.; Fan, S.-D. Characterization of a Simple Vitamin B12 Model Complex and Its Catalysis in Electrochemical Carbon-Skeleton Rearrangement. *Chem. Lett.* **1987**, *16*, 655–658.
(70) James, H. P. U.; Little, R. D.; Nielsen, M. F. Reductive Coupling. In Organic Electrochemistry; Hammerich, O., Speiser, B., Eds.; CRC Press: Boca Raton, 2015; 621−704.
(71) Salamone, M.; Milan, M.; DiLabio, G. A.; Bietti, M. Reactions of the Cumyloxyl and Benzyloxyl Radicals with Tertiary Amides. Hydrogen Abstraction Selectivity and the Role of Specific Substrate-Radical Hydrogen Bonding. *J. Org. Chem.* **2013**, *78*, 5909–5917.
(72) Studer, A.; Curran, D. P. Catalysis of Radical Reactions: A Radical Chemistry Perspective. *Angew. Chem. Int. Ed.* **2016**, *55*, 58–102.
(73) Curran, D. P.; Kim, D. Atom Transfer Cyclization of Simple Hexenyl Iodides. A Caution on the Use of Alkenyl Iodides as Probes for the Detection of Single Electron Transfer Processes. *Tetrahedron Lett.* **1986**, *27*, 5821–5824.
(74) Ramprasad, D.; Gilicinski, A. G.; Markley, T. J.; Pez, G. P. Cobalt(II) Polypyridine Complexes and Their Reversible Reactivity with Dioxygen. *Inorg. Chem.* **1994**, *33*, 2841–2847..
(75) Andrieux, C. P.; Blocman, C.; Dumas-Bouchiat, J. M.; M'Halla, F.; Savéant, J. M. Homogeneous Redox Catalysis of Electrochemical Reactions: Part V. Cyclic Voltammetry. *J. Electroanal. Chem. Interfacial Electrochem.* **1980**, *113*, 19–40.
(76) Jones, G. D.; Martin, J. L.; McFarland, C.; Allen, O. R.; Hall, R. E.; Haley, A. D.; Brandon, R. J.; Konovalova, T.; Desrochers, P. J.; Pulay, P.; Vicic, D. A. Ligand Redox Effects in the Synthesis, Electronic Structure, and Reactivity of an Alkyl−Alkyl Cross-Coupling Catalyst. *J. Am. Chem. Soc.* **2006**, *128*, 13175–13183.
(77) Scarborough, C. C.; Lancaster, K. M.; DeBeer, S.; Weyhermüller, T.; Sproules, S.; Wieghardt, K. Experimental Fingerprints for Redox-Active Terpyridine in $[Cr(tpy)_2](PF_6)^n$ (n = 3–0), and the Remarkable Electronic Structure of $[Cr(tpy)_2]^{1-}$. *Inorg. Chem.* **2012**, *51*, 3718–3732.
(78) Hupp, J. T.; Weaver, M. J. Prediction of Electron-Transfer Reactivities from Contemporary Theory: Unified Comparisons for Electrochemical and Homogeneous Reactions. *J. Phys. Chem.* **1985**, *89*, 2795–2804.
(79) Anderson, T. J.; Jones, G. D.; Vicic, D. A. Evidence for a Ni^I Active Species in the Catalytic Cross-Coupling of Alkyl Electrophiles. *J. Am. Chem. Soc.* **2004**, *126*, 8100–8101.

(80) Lin, X.; Phillips, D. L. Density Functional Theory Studies of Negishi Alkyl–Alkyl Cross-Coupling Reactions Catalyzed by a Methylterpyridyl-Ni(I) Complex. *J. Org. Chem.* **2008**, *73*, 3680–3688.
(81) Costentin, C.; Drouet, S.; Robert, M.; Savéant, J.-M. A Local Proton Source Enhances CO_2 Electroreduction to CO by a Molecular Fe Catalyst. *Science* **2012**, *338*, 90–94.
(82) Costentin, C.; Savéant, J.-M.; Tard, C. Ligand "Noninnocence" in Coordination Complexes vs. Kinetic, Mechanistic, and Selectivity Issues in Electrochemical Catalysis. *Proc. Natl. Acad. Sci.* **2018**, *115*, 9104–9109.
(83) Canty, A. J.; Minchin, N. J.; Skelton, B. W.; White, A. H. Interaction of Palladium(II) Acetate with Substituted Pyridines, Including a Cyclometallation Reaction and the Structure of $[Pd\{meso\text{-}[(Py)PhMeC]_2C_5H_3N\}(O_2CMe)][O_2CMe]\cdot 3H_2O$. *J. Chem. Soc. Dalton Trans.* **1986**, 2205–2210.
(84) Sun, Y.; Bigi, J. P.; Piro, N. A.; Tang, M. L.; Long, J. R.; Chang, C. J. Molecular Cobalt Pentapyridine Catalysts for Generating Hydrogen from Water. *J. Am. Chem. Soc.* **2011**, *133*, 9212–9215.
(85) Grein, K.; Kirste, B.; Kurreck, H. Synthesen, ESR- Und ENDOR-Untersuchungen Hochverdrillter Phenylsubstituierter Radikalanionen. *Chem. Ber.* **1981**.
(86) Nagasawa, S.; Sasano, Y.; Iwabuchi, Y. Synthesis of 1,3-Cycloalkadienes from Cycloalkenes: Unprecedented Reactivity of Oxoammonium Salts. *Angew. Chem. Int. Ed.* **2016**, *55*, 13189–13194.
(87) Brenna, E.; Cannavale, F.; Crotti, M.; De Vitis, V.; Gatti, F. G.; Migliazza, G.; Molinari, F.; Parmeggiani, F.; Romano, D.; Santangelo, S. Synthesis of Enantiomerically Enriched 2-Hydroxymethylalkanoic Acids by Oxidative Desymmetrisation of Achiral 1,3-Diols Mediated by Acetobacter Aceti. *ChemCatChem* **2016**, *8*, 3796–3803.
(88) Costentin, C.; Robert, M.; Savéant, J. M. Electrochemical Concerted Proton and Electron Transfers. Potential-Dependent Rate Constant, Reorganization Factors, Proton Tunneling and Isotope Effects. *J. Electroanal. Chem.* **2006**, *588*, 197–206.
(89) Andrieux, C. P.; Gallardo, I.; Savéant, J. M.; Su, K. B. Dissociative Electron Transfer. Homogeneous and Heterogeneous Reductive Cleavage of the Carbon-Halogen Bond in Simple Aliphatic Halides. *J. Am. Chem. Soc.* **1986**, *108*, 638–647.
(90) Savéant, J. M.; Su, K. B. Homogeneous Redox Catalysis of Electrochemical Reaction. Part VI. Zone Diagram Representation of the Kinetic Regimes. *J. Electroanal. Chem.* **1984**, *171*, 341–349.
(91) Costentin, C.; Drouet, S.; Robert, M.; Savéant, J. M. Turnover Numbers, Turnover Frequencies, and Overpotential in Molecular Catalysis of Electrochemical Reactions. Cyclic Voltammetry and Preparative-Scale Electrolysis. *J. Am. Chem. Soc.* **2012**, *134*, 11235–11242.
(92) Saveant, J. M.; Vianello, E. Potential-Sweep Chronoamperometry: Kinetic Currents for First-Order Chemical Reaction Parallel to Electron-Transfer Process (Catalytic Currents). *Electrochimica Acta* **1965**, *10*, 905–920.
(93) Nicholson, R. S.; Shain, I. Theory of Stationary Electrode Polarography: Single Scan and Cyclic Methods Applied to Reversible, Irreversible, and Kinetic Systems. *Anal. Chem.* **1964**, *36*, 706–723.
(94) Costentin, C.; Drouet, S.; Robert, M.; Savéant, J.-M. A Local Proton Source Enhances CO_2 Electroreduction to CO by a Molecular Fe Catalyst. *Science* **2012**, *338*, 90–94.

(95) Rigaku Oxford Diffraction. *CrysAlisPro Software System*; Rigaku Corporation: Oxford, UK, 2015.
(96) Nakai, H.; Jeong, K.; Matsumoto, T.; Ogo, S. Catalytic C-F Bond Hydrogenolysis of Fluoroaromatics by [(H_5-C_5Me_5)RhI(2,2′-Bipyridine)]. *Organometallics* **2014**, *33*, 4349–4352.
(97) Bain, G. A.; Berry, J. F. Diamagnetic Corrections and Pascal's Constants. *J. Chem. Educ.* **2008**, *85*, 532–536.
(98) Shao, Y.; Gan, Z.; Epifanovsky, E.; Gilbert, A. T. B.; Wormit, M.; Kussmann, J.; Lange, A. W.; Behn, A.; Deng, J.; Feng, X.; Ghosh, D.; Goldey, M.; Horn, P. R.; Jacobson, L. D.; Kaliman, I.; Khaliullin, R. Z.; Kuś, T.; Landau, A.; Liu, J.; Proynov, E. I.; Rhee, Y. M.; Richard, R. M.; Rohrdanz, M. A.; Steele, R. P.; Sundstrom, E. J.; Woodcock, H. L.; Zimmerman, P. M.; Zuev, D.; Albrecht, B.; Alguire, E.; Austin, B.; Beran, G. J. O.; Bernard, Y. A.; Berquist, E.; Brandhorst, K.; Bravaya, K. B.; Brown, S. T.; Casanova, D.; Chang, C.-M.; Chen, Y.; Chien, S. H.; Closser, K. D.; Crittenden, D. L.; Diedenhofen, M.; DiStasio, R. A.; Do, H.; Dutoi, A. D.; Edgar, R. G.; Fatehi, S.; Fusti-Molnar, L.; Ghysels, A.; Golubeva-Zadorozhnaya, A.; Gomes, J.; Hanson-Heine, M. W. D.; Harbach, P. H. P.; Hauser, A. W.; Hohenstein, E. G.; Holden, Z. C.; Jagau, T.-C.; Ji, H.; Kaduk, B.; Khistyaev, K.; Kim, J.; Kim, J.; King, R. A.; Klunzinger, P.; Kosenkov, D.; Kowalczyk, T.; Krauter, C. M.; Lao, K. U.; Laurent, A. D.; Lawler, K. V.; Levchenko, S. V.; Lin, C. Y.; Liu, F.; Livshits, E.; Lochan, R. C.; Luenser, A.; Manohar, P.; Manzer, S. F.; Mao, S.-P.; Mardirossian, N.; Marenich, A. V.; Maurer, S. A.; Mayhall, N. J.; Neuscamman, E.; Oana, C. M.; Olivares-Amaya, R.; O'Neill, D. P.; Parkhill, J. A.; Perrine, T. M.; Peverati, R.; Prociuk, A.; Rehn, D. R.; Rosta, E.; Russ, N. J.; Sharada, S. M.; Sharma, S.; Small, D. W.; Sodt, A.; Stein, T.; Stück, D.; Su, Y.-C.; Thom, A. J. W.; Tsuchimochi, T.; Vanovschi, V.; Vogt, L.; Vydrov, O.; Wang, T.; Watson, M. A.; Wenzel, J.; White, A.; Williams, C. F.; Yang, J.; Yeganeh, S.; Yost, S. R.; You, Z.-Q.; Zhang, I. Y.; Zhang, X.; Zhao, Y.; Brooks, B. R.; Chan, G. K. L.; Chipman, D. M.; Cramer, C. J.; Goddard, W. A.; Gordon, M. S.; Hehre, W. J.; Klamt, A.; Schaefer, H. F.; Schmidt, M. W.; Sherrill, C. D.; Truhlar, D. G.; Warshel, A.; Xu, X.; Aspuru-Guzik, A.; Baer, R.; Bell, A. T.; Besley, N. A.; Chai, J.-D.; Dreuw, A.; Dunietz, B. D.; Furlani, T. R.; Gwaltney, S. R.; Hsu, C.-P.; Jung, Y.; Kong, J.; Lambrecht, D. S.; Liang, W.; Ochsenfeld, C.; Rassolov, V. A.; Slipchenko, L. V.; Subotnik, J. E.; Van Voorhis, T.; Herbert, J. M.; Krylov, A. I.; Gill, P. M. W.; Head-Gordon, M. Advances in Molecular Quantum Chemistry Contained in the Q-Chem 4 Program Package. *Mol. Phys.* **2015**, *113*, 184–215.
(99) Weigend, F.; Ahlrichs, R. Balanced Basis Sets of Split Valence, Triple Zeta Valence and Quadruple Zeta Valence Quality for H to Rn: Design and Assessment of Accuracy. *Phys. Chem. Chem. Phys.* **2005**, *7*, 3297–3305.
(100) Truong, T. N.; Stefanovich, E. V. A New Method for Incorporating Solvent Effect into the Classical, Ab Initio Molecular Orbital and Density Functional Theory Frameworks for Arbitrary Shape Cavity. *Chem. Phys. Lett.* **1995**, *240*, 253–260.
(101) Fu, Y.; Liu, L.; Yu, H. Z.; Wang, Y. M.; Guo, Q. X. Quantum-Chemical Predictions of Absolute Standard Redox Potentials of Diverse Organic Molecules and Free Radicals in Acetonitrile. *J. Am. Chem. Soc.* **2005**, *127*, 7227–7234.
(102) Konezny, S. J.; Doherty, M. D.; Luca, O. R.; Crabtree, R. H.; Soloveichik, G. L.; Batista, V. S. Reduction of Systematic Uncertainty in DFT Redox Potentials of Transition-Metal Complexes. *J. Phys. Chem. C* **2012**, *116*, 6349–6356.

(103) Kelly, C. P.; Cramer, C. J.; Truhlar, D. G. Single-Ion Solvation Free Energies and the Normal Hydrogen Electrode Potential in Methanol, Acetonitrile, and Dimethyl Sulfoxide. *J. Phys. Chem. B* **2007**, *111*, 408–422.
(104) Song, J.; Klein, E. L.; Neese, F.; Ye, S. The Mechanism of Homogeneous CO_2 Reduction by Ni(Cyclam): Product Selectivity, Concerted Proton-Electron Transfer and C–O Bond Cleavage. *Inorg. Chem.* **2014**, *53*, 7500–7507.
(105) Tran, H.; McCallum, T.; Morin, M.; Barriault, L. Homocoupling of Iodoarenes and Bromoalkanes Using Photoredox Gold Catalysis: A Light Enabled Au(III) Reductive Elimination. *Org. Lett.* **2016**, *18*, 4308–4311.
(106) Stille, J. K.; Divakaruni, R. Palladium(II)-Catalyzed Carboxylation Reactions of Olefins: Scope and Utility. *J. Org. Chem.* **1979**, *44*, 3474–3482.